Dark Matter in Astro- and Particle Physics

DARK 2004

Edited by H. V. Klapdor-Kleingrothaus
and R. Arnowitt

Springer

Dark Matter in Astro- and Particle Physics

H.V. Klapdor-Kleingrothaus R. Arnowitt (Eds.)

Dark Matter in Astro- and Particle Physics

Proceedings of the International Conference
DARK 2004
College Station, USA, October 3–9, 2004

Springer

Professor Dr. Hans Volker Klapdor-Kleingrothaus
Max-Planck-Institut für Kernphysik
Saupfercheckweg 1
69117 Heidelberg, Germany
E-mail: H.Klapdor@mpi-hd.mpg.de

Professor Dr. Richard Arnowitt
Department of Physics
Texas A & M University
College Station
TX 77807, USA
E-mail: arnowitt@physics.tamu.edu

Library of Congress Control Number: 2005930478

ISBN-10 3-540-26372-1 Springer Berlin Heidelberg New York
ISBN-13 978-3-540-26372-2 Springer Berlin Heidelberg New York

This work is subject to copyright. All rights are reserved, whether the whole or part of the material is concerned, specifically the rights of translation, reprinting, reuse of illustrations, recitation, broadcasting, reproduction on microfilm or in any other way, and storage in data banks. Duplication of this publication or parts thereof is permitted only under the provisions of the German Copyright Law of September 9, 1965, in its current version, and permission for use must always be obtained from Springer. Violations are liable for prosecution under the German Copyright Law.

Springer is a part of Springer Science+Business Media
springeronline.com
© Springer-Verlag Berlin Heidelberg 2006
Printed in The Netherlands

The use of general descriptive names, registered names, trademarks, etc. in this publication does not imply, even in the absence of a specific statement, that such names are exempt from the relevant protective laws and regulations and therefore free for general use.

Typesetting: by the authors and TechBooks using a Springer LaTeX macro package

Cover design: *design & production* GmbH, Heidelberg

Printed on acid-free paper SPIN: 11314035 55/TechBooks 5 4 3 2 1 0

Preface

The Fifth HEIDELBERG International Conference on Dark Matter in Astro- and Particle Physics, DARK 2004, took place at Texas A&M University, College Station Texas, USA, October 3–9, 2004. It was, after Cape Town 2002, the second conference of this series held outside Germany. The earlier meetings, starting in 1996, were held in Heidelberg.

Dark Matter is still one of the most exciting and central fields of astrophysics, particle physics and cosmology. The conference covered, as usual for this series, a large range of topics, theoretical and experimental.

Theoretical talks covered SUSY/SUGRA phenomenology, which provides at present a preferred theoretical framework for the existence of cold dark matter. Also included were other possible explanations of dark matter such as SUSY Q balls, exciting New Symmetries, etc.

The most important experiments in the underground search for cold and hot dark matter were presented. Talks describing the current experimental dark matter bounds, what might be obtained in the near future, and the reach of future large (i.e. one ton) detectors were given. The potential of future colliders to correlate accelerator physics with dark matter searches was also outlined. Thus the reader will be able to see the present status and future prospects in the search for dark matter.

The exciting astronomical evidence for dark matter and corresponding observations concerning the Milky Way's black hole, high-redshift clusters, wakes in dark matter halos were other important topics at the conference.

A considerable fraction of the conference was taken by presentations on cosmology and baryogenesis. The status and perspectives of the search for dark energy from supernovae, leptonic CP violation and baryon asymmetry and a new type of baryogenesis, Q-genesis, were discussed. Finally a possible special property of neutrinos (which are known now to contribute to hot dark matter) in dense matter – neutrino spin light – was presented.

We are confident that the present Proceedings give a useful overview of this exciting field of research, and its fundamental connections to various frontier disciplines of particle physics and cosmology. We hope that this book may also be a kind of handbook for students.

The organizers express their thanks to all colleagues from many countries, who contributed so actively to the success of the meeting. We also thank

those speakers who helped carry our field into public attention by the evening lectures open to the public given during the conference.

Thanks go to the George P. and Cynthia W. Mitchell Institute For Fundamental Physics of Texas A&M University and the Max Planck Institut für Kernphysik in Heidelberg for their generous financial support. We thank all people who contributed in one way or another to the organization of the conference, and in creating a pleasant and inspiring atmosphere during the conference. We are indebted in particular to Beverly Guster, Ron Bryan, Ching-Ming Chen, James Dent and Gang Zhao for their help in the scientific organisation. Particular thanks go to the Scientific Secretary, Dr. Irina Krivosheina, who unfortunately could not participate because of visa problems. To the latter we are also indebted for preparing this Proceedings volume.

Last but not least, one of the Cochairmen would like to give his personal thanks to Professor Richard Arnowitt for making this successful event possible, while the other Cochairman would like to thank Professor Hans V. Klapdor-Kleingrothaus for choosing Texas A&M as the conference site for this second DARK conference outside Germany.

Heidelberg, Germany *H.V. Klapdor-Kleingrothaus*
College Station, USA *R. Arnowitt*
April 2005

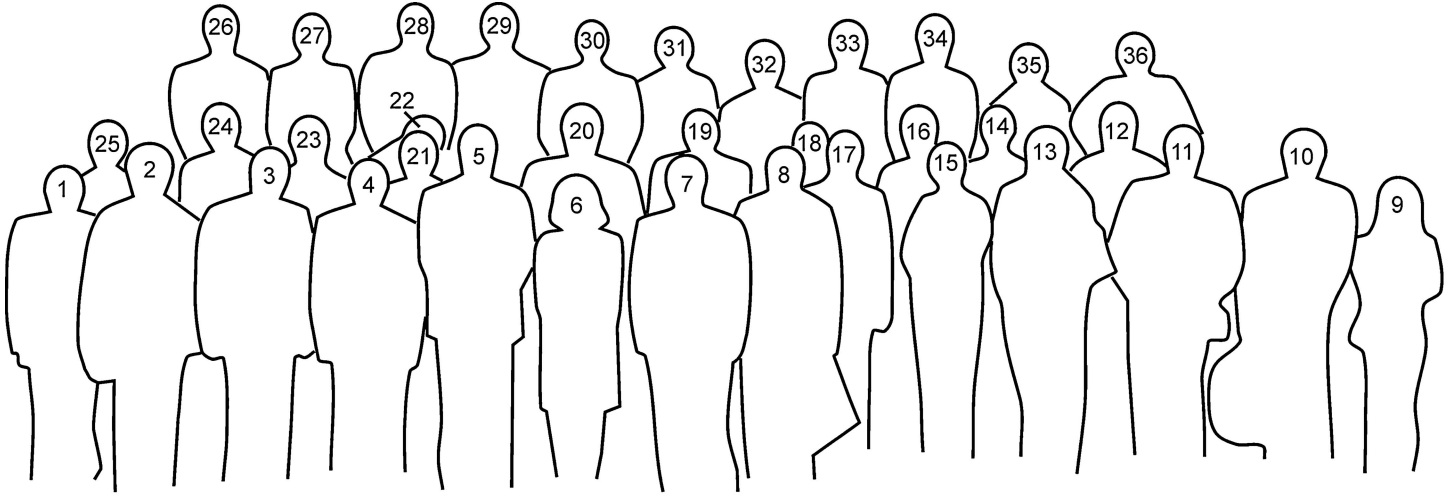

1. Antonio Masiero
2. George V. Kraniotis
3. John D. Vergados
4. Richard Arnowitt
5. Hans Volker Klapdor-Kleingrothaus
6. Wendy Freedman
7. Jihn E. Kim
8. Jerome Drexler
9. Yvonne Wong
10. Hanguo Wang
11. Nigel Smith
12. Patrick Green
13. James T. White
14. Eric Linder
15. Prisca Cushman
16. Richard W. Schnee
17. Riccardo Cerulli
18. Elena Accomando
19. Piero Belli
20. David Cline
21. Kris Sigurdson
22. Leszek Rozkowski
23. Joel Walker
24. Kim Griest
25. Chikaori Mitsuda
28. Rocky Kolb
29. Wim de Boer
30. Nicolao Fornengo
31. Bhaskar Dutta
32. Paolo Gondolo
33. Roland Lüscher
34. Paul Luis Brink
35. Neil Spooner
36. Rafael Lopez-Mobilia

Contents


The Nature of
Energy
Dark energy
Many
High
Relative Light Yield or Charge Collection


Big Bang
Big Bang plus 300,000 years
Big Bang plus 13.5 billion years


Part I

Astronomical Evidence for Dark Matter

The Milky Way's Black Hole and the Central Stellar Cluster: Variable Emission from SgrA*

A. Eckart[1], R. Schödel[1], C. Straubmeier[1], T. Viehmann[1], J.-U. Pott[1,2], and N. Mouawad[1]

[1] I. Physikalisches Institut, University of Cologne, Zülpicher Str. 77, D-50937 Köln, Germany
eckart@ph1.uni-koeln.de
[2] European Southern Observatory, ESO Headquarter Garching, Karl-Schwarzschild-Str. 2, D-85748 Garching, Germany

Abstract. The dark mass located at the center of the Milky Way is currently the very best candidate for a super massive black hole in our immediate vicinity. The strongest evidence for this is provided by measurements of stellar orbits and strongly variable NIR and X-ray emission from Sagittarius A* at the center of the cental stellar cluster. As proven by the Keplerian orbits of several of the high velocity stars within the central arcsecond the Galactic Center harbors a $\sim 3.5 \times 10^6 M_\odot$ massive black hole at the position of the compact radio source SgrA*. Simultaneous NIR/X-ray observations of SgrA* in 2003/2004 have revealed first insights into the emission mechanisms of both the powerful near-infrared flares and the "quiescent" emission from within a few ten to one hundred Schwarzschild radii of the super-massive black hole at the center of the Milky Way. The central source shows synchronous NIR/X-ray flare variation and indications of quasi-periodicity within the NIR flares.

1 Introduction

The compact radio source Sagittarius A* is located within a dense central stellar cluster – surrounded by a $\sim 1''$ diameter cusp. In this contribution we summarize some of the most intriguing characteristics of the central dark mass associated with SgrA* and the stars in its vicinity. Our knowledge on the Galactic Center (GC) profits greatly from the very recent results obtained with large 8–10 m class ground based telescopes that operate in the infrared. At these wavelengths the dust and gas along the $\sim$8 kpc line of sight towards the center can be penetrated, resulting in detailed data on the stars and the infrared counterpart of SgrA*.

The central stellar cluster is extremely dense, with an unusual observed stellar population consisting mainly (80% of all K$\leq$14 stars; Ott et al. 1999) of late-type red giants, many of which are suspected to lie on the asymptotic giant branch (AGB), as well as young massive stars with energetic winds (see Fig. 1; e.g. Krabbe et al. 1995, Najarro et al. 1997). Spectra of AGB stars show strong 2.3 μm CO bandhead absorption and the massive, hot and windy stars ("He-stars") exhibit He/H emission and interact strongly with the local ISM. The emission line stars appear to dominate the central few

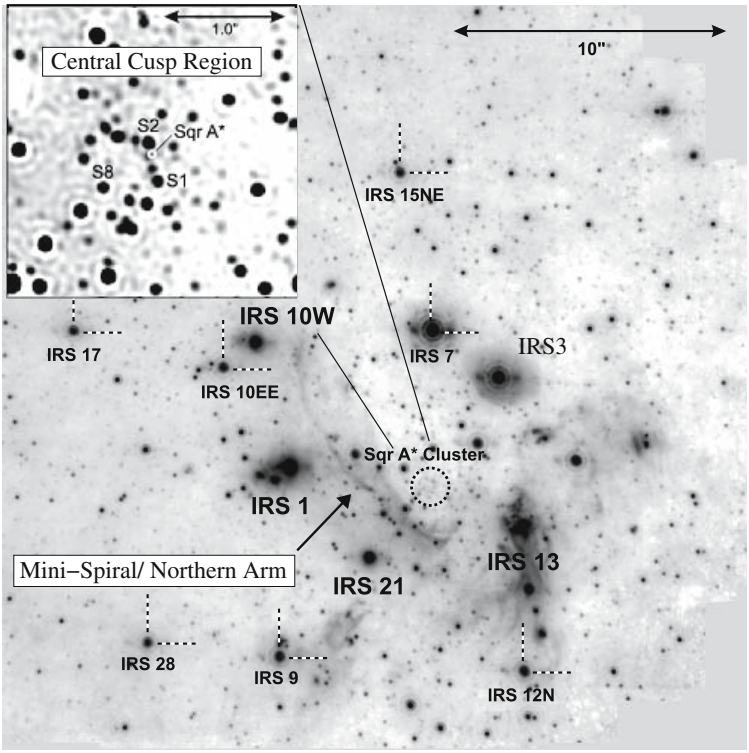

Fig. 1. NACO L band image of the Galactic Center region with a K-band zoom into the central arcsecond.

arcseconds, where the bright IRS 16 cluster is located. These stars are generally classified as Ofpe/WN9, although some of them might be luminous blue variables (LBV) and a few show characteristics of Wolf-Rayet stars. A third, less numerous component of the Galactic Center stellar cluster consists of luminous, extended objects with steep, red and featureless (K-band-) spectra and a strong infrared excess. They are likely bow-shock sources with the implication that they are linked to luminous, windy WR or He-stars (Tanner et al. 2002, 2003, Rigaut et al. 2003, Eckart et al. 2004, Viehmann et al. 2005). In addition the detection of a stellar cusp (Genzel et al. 2003b) supplies evidence for the presence of a spherical potential which is neither Keplerian nor harmonic. In such a potential orbits will precess resulting in rosetta shaped trajectories on the sky and the assumption of non-Keplerian orbits is a more physical approach. It is also the only approach through which cusp mass information can be obtained via stellar dynamics of the cusp members. First results of modeling such a system are now available (Mouawad et al. 2003a, 2003b, 2004).

The investigation of the dynamics of stars within the central cluster is a key for the investigation of the mass distribution in that area. Over the last decade, these investigations have provided compelling evidence for the existence of a massive black hole (MBH) at the center of the Milky Way (Eckart & Genzel 1996, Genzel et al. 1997, 2000, Ghez et al. 1998, 2000, 2003a, 2003b, Eckart et al. 2002, Schödel et al. 2002, 2003). However, Sgr A* is remarkably faint in all wavebands other than the radio region, challenging current theories of matter accretion and radiation surrounding black holes. It is unclear whether the feeble emission (10^{-8} of the Eddington rate) is due to a low accretion rate, inefficient angular momentum transport, low radiation efficiency, or a combination of these. Intense discussion among the theoretical community at present focuses on radiatively inefficient accretion flow models (RIAFs: Yuan et al. 2004, including ADAFs: Narayan et al. 1995, CDAFs: Ball et al. 2000, ADIOSs: Blandford & Begelman 1999), jet models (Markoff et al. 2001), and Bondi-Hoyle models (Melia & Falke 2001).

The observation of variable emission from SgrA* is also a key element for the understanding of this compact object. These observations result in additional strong evidence for a massive black hole at that position. A major result is here the discovery of interim-quiescent (or IQ) and flare activity from that position both in the X-ray and recently in the near-infrared wavelength domain (Baganoff et al. 2001, 2003, Eckart et al. 2003, 2004, Porquet et al. 2003, Goldwurm et al. 2003, Genzel et al. 2003a, Ghez et al. 2004). Especially the discovery (Genzel et al. 2003a) of powerful NIR flares from SgrA* has now opened the possibility for an improved study of the emission mechanisms. The IR flares occurred at the remarkable rate of $4(\pm 2)$ times a day, at least twice the rate of X-ray flares detected by Chandra and XMM-Newton between 2000 and 2002.

Eckart et al. (2004) have recently reported on the first successful simultaneous NIR/X-ray campaign using NACO and Chandra as well as quasi-simultaneous mm-data from BIMA (see below). Coincident with the peak of the about $6{\times}10^{33}$ erg/s X-ray flare a fading NIR flare of Sgr A* with >2 times the interim-quiescent flux was detected (Fig. 2). The event implies that the NIR/X-ray flare emission was coupled with a time lag not larger than 15 min and probably originated from the same ensemble of electrons. Compared to 8 h before the flare a 10% increased mm-flux density was measured about 8 h after the event. However, a remarkable property discovered in two of the brightest K-band flares is a quasi-periodic substructure with a period of 17 minutes. If this periodicity is a fundamental property of all flares, it most likely arises from the relativistic modulation of gas emission orbiting just outside the event horizon. In that case, the inevitable conclusion is that the Galactic center black hole has at least half of the maximum (Kerr) spin. The X-ray flares have similar durations as the IR-flares and some also do show minute-scale substructure. The reanalysis of the two most powerful ones in the framework of disk modes indicates high spin parameters as

well (Aschenbach et al. 2003, 3004). NACO time studies will be a powerful tool for exploring the physics and space time structure in the strong gravity regime around a super-massive black hole. The observational data obtained with NACO and Chandra in July 2005 is very much consistent with the previously obtained results.

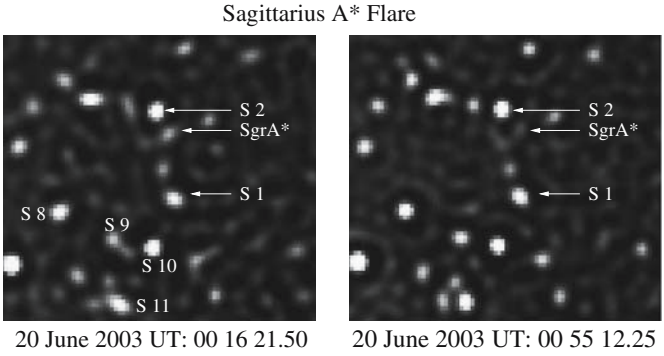

Fig. 2. Two characteristic images that demonstrate the infrared variability event described in Eckart et al. (2004). This event was the first one to be detected simultaneously in the X-ray domain using Chandra. Shown is the average of eight Lucy-Richardson deconvolved and beam restored images taken at two different intervals. The universal times of the first image in each series are indicated in the panels. Sgr A* can be seen as a flaring source in the left panel. The field of view is 1.43″ (72 light days) times 0.85″ (43 light days).

2 Alternatives to the Black Hole Scenario?

The so called "fermion ball" and the "boson star" scenarios are two "dark particle matter" models that have been under discussion as an alternative to a super-massive black hole at the center of the Milky Way. Here we will briefly summarize their properties and discuss whether they are suitable descriptions of the extreme mass concentration found at the position of SgrA* (see also Fig. 3).

The fermion ball as an attempt to explain large compact nuclear masses observed at the centers of galaxies was introduced by Viollier et al. (1992). A motivation for the development of the neutrino ball scenario was that a resolved mass – and therefore a gravitational potential that decreases near the very center – would allow to account for a decreasing radiative efficiency towards its center. This would have helped to explain the low luminosity of Sgr A*. These objects are stabilized by the degeneracy pressure of the corresponding fermion candidates, e.g. neutrinos. The self-gravity of a ball

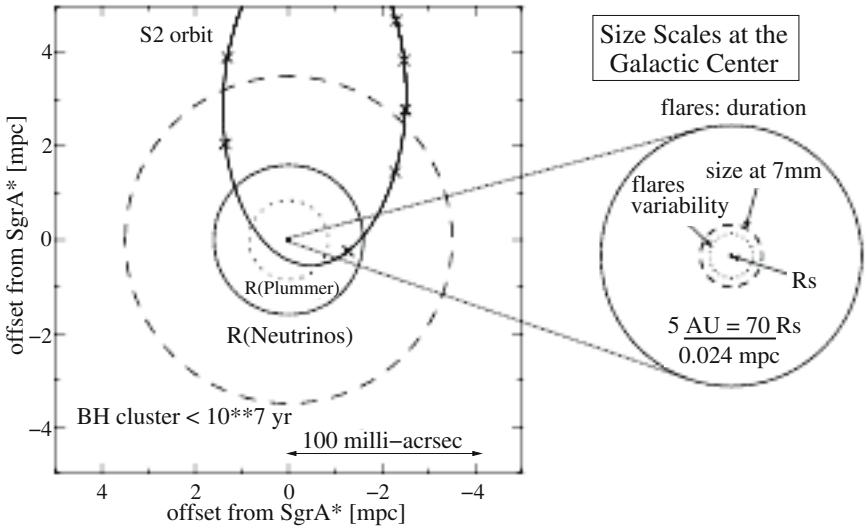

Fig. 3. A comparison of size scales at the Galactic Center near Sgr A*. Left: Indicated are the core radii of hypothetical dense clusters (Plummer models): A cluster of 3 $M_\odot$ black holes with a life time of 10^7 yr, marked by a dashed line, and a dark cluster that could marginally fit the gravitational potential as constrained by the orbit of S2. The latter cluster, marked by a dotted line, would have a life time of less than 10^5 yr. The radius of a neutrino ball composed of degenerate 17 keV neutrinos is indicated by a circle with a solid line. These models are excluded by the observed orbit of S2 and life time arguments. Right: Indicated are the size constraints due to the duration of the observed X-ray and NIR flares with a duration of the order 60 min (outer circle, marked by "flares:duration"), the size inferred from 7 mm interferometry (Bower et al. 2004; Science), the size limit imposed by the variability (rise-and-fall time) time of the flares (dotted line), and the Schwarzschild radius R_S, of a 3.6×10^6 $M_\odot$ black hole.

of degenerate fermions can be balanced by the degeneracy pressure of the fermions due to the Pauli principle. In this case, the relation between the mass M and the radius R of a fermion ball, composed of fermions with mass m and degeneracy g, can be described by the non-relativistic Lane-Emden equation. The maximum mass of a degenerate fermion ball is given by the Oppenheimer-Volkoff limit For a given fermion mass m all objects heavier than M_{OV} must be black holes.

In case of the GC, the Oppenheimer-Volkoff limit gives us maximum fermion masses of 351 keV for $g = 4$ and 417 keV for $g = 2$. The orbit of S2 tells us $M = 3.6 \times 10^6$ $M_\odot$ and $R = 0.00055$ pc $= 0.655$ ld. Therefore, we obtain as a minimum fermion mass 48 keV for $g = 4$ and 57 keV for $g = 2$. The most massive central dark object currently known is located at the center of M87, with a mass of $> 3 \times 10^9$ $M_\odot$. The Oppenheimer-Volkoff limit would

allow a maximum neutrino mass of 14 keV in that case. Comparing this value with the above derived constraints on the properties of a putative neutrino ball at the Galactic Center, one can exclude the possibility that all compact dark objects at the centers of galaxies can be explained by a neutrino ball model.

A further significant drawback of that scenario is that it does not explain what happens to the permanently in-falling (baryonic) matter. It appears plausible that it will be trapped and condense at the bottom of the potential well, where it might eventually form a seed black hole. This scenario defeats the purpose of having a ball of degenerated matter (especially neutrinos; Melia & Falcke 2001). A neutrino ball could not account for the compactness of Sgr A* observed at radio/mm wavelengths. Observations of X-ray and NIR flares from Sgr A* (Baganoff et al. 2001, Baganoff et al. 2003, Eckart et al. 2003, Porquet et al. 2003, Goldwurm et al. 2003, Ghez et al. 2004, Genzel et al. 2003a) suggest that the emission comes from structures smaller than about ten Schwarzschild radii of a 3.6×10^6 $M_\odot$ million solar mass black hole. This is more than two orders of magnitude more compact than the radius of a neutrino ball with a neutrino mass of 48 keV.

Another model that could explain a very compact mass is the boson star scenario. It is the only dark particle matter explanation that cannot be ruled out by the present data, since such a ball of bosons could form a very compact configuration that is difficult to distinguish from a black hole. However, it would be hard to understand how the bosons managed to cool sufficiently in order to settle down into such a small volume, and did not form a black hole during that process (Maoz 1998). Boson stars (Kaup et al. 1968) are supposed to be supported by the Heisenberg uncertainty principle. Ruffini & Bonazzola (1969) showed that – e.g. for a boson mass of 1GeV – a stable object of total mass of $10^{-19}M_\odot$ and 1 fm diameter could be formed. If a hypothetical weak repulsive force between bosons is introduced (*ad hoc*) (Colpi et al. 1986), it would be possible to form objects with total masses as large as they are found in galactic nuclei (Colpi et al. 1986). For a large range of hypothetical boson masses they can have sizes of only several times their Schwarzschild radii. This makes it difficult to clearly distinguish observationally between boson stars and black holes as candidates for super-massive objects at the nuclei of galaxies (see also Torres et al. 2000, Mielke & Schunck 2000).

However, during its lifetime, even if a boson star had formed at the center, it should eventually have collapsed to a black hole through accretion of the abundant gas and dust in the Galactic Center. Therefore we conclude that similar to the fermion ball solution, a super-massive boson star is not an astrophysically attractive explanation for the high mass concentration at the center of the Milky Way. As for possibilities of definitely ruling out the boson star scenario, simultaneous multi-wavelength measurements of the emission from Sgr A* (see Eckart et al. 2004) will allow to constrain the emission mechanism and therefore the compactness of the emitting region around Sgr A*

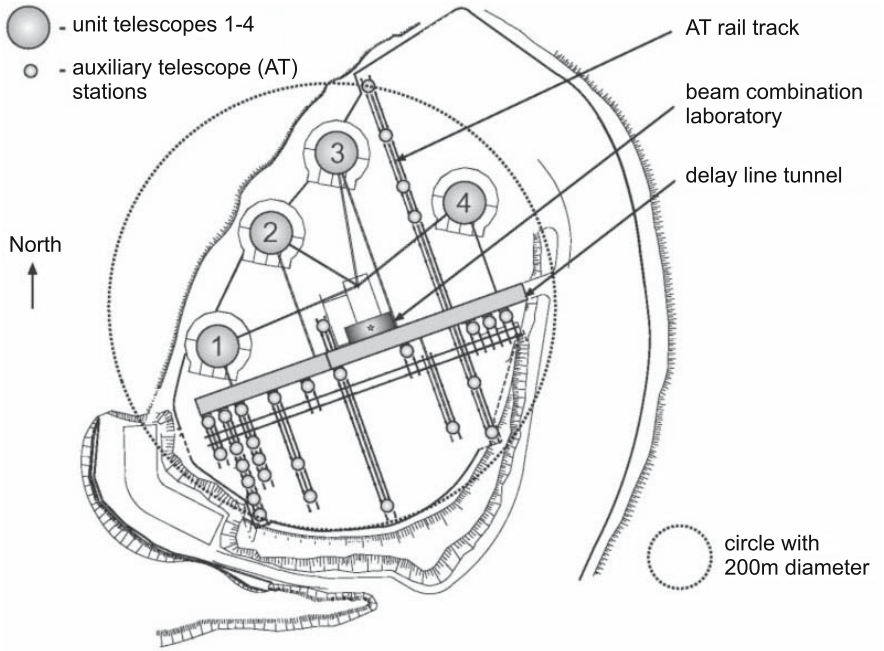

Fig. 4. Schematic representation of the ESO Paranal site showing the locations of the 8.4m diameter UTs and the possible locations of the ATs with the delay line tunnel. The stellar object IRS 3 at the Galactic Center was observed with MIDI on the 47m baseline between UT2 and UT3.

even further. Probably within the next decade it will be possible to image the 'shadow' cast by the putative black hole through deflection of light rays using global radio interferometry at sub-millimeter wavelengths. Such an experiment will involve very long baseline interferometry in the sub-mm regime (Falcke et al. 2000, Melia & Falcke 2001).

The future for Galactic Center research lies in high angular resolution observations at all accessible wavelengths. For radio wavelengths, progress will be made with VLBI at mm-wavelengths. In the infrared wavelength domain interferometry is now possible with large aperture interferometers that will - in the near future - allow to observe SgrA* with a resolution of a few milliarcseconds. These are the Very Large Telescope Interferometer (VLTI; Fig. 4), the Keck Interferometer, and the Large Binocular Telescope. Recently - on 8 July 2004 - Eckart, Pott et al. have carried out first mid-infrared interferometric observations of a number of bright 10 μm sources within the central stellar cluster using MIDI (Leinert et al. 1998) and the 47 m UT2/UT3 baseline. In these observations fringes on the first Galactic Center source were obtained on the stellar source IRS3 (see Fig. 1). In the very near future further infrared interferometer measurements in the Galactic Center area will be possible.

Acknowledgments

This work was supported in part by the Deutsche Forschungsgemeinschaft (DFG) via grant SFB 494. We are also grateful to all members of the NAOS/CONICA as well as the ESO Paranal teams.

References

Aschenbach, B., Grosso, N., Porquet, D., Predehl, P., 2004 A&A 417, 71.
Aschenbach, B., 2004, A&A 425, 1075.
Baganoff, F. K. et al., 2001, Nature, 413, 45.
Baganoff, F. K. et al., 2003, HEAD, 35.
Ball, G. H., Narayan, R. & Quataert, E. 2001, ApJ 552, 221.
Blandford, R., & Begelman, M., 1999, MNRAS, 303, L1.
Clénet et al., 2001, A&A 376, 124.
Colpi, M., Shapiro, S.L., Wassermann, I., 1986, Phys. Rev. Let. 57, 2485
Eckart, A., et al., Proc. Galactic Center Workshop 2002b, Nov. 3–8, 2002, Kailua-Kona, Hawaii, Astron. Nachr., Vol. 324, 557.
Eckart, A., Moultaka, N., Viehmann, T., et al., 2003, Astron. Nachrichten Suppl. 324, 557
Eckart, A., Baganoff, F.K., Morris, M., et al., 2004, A&A 427, 1 (astro-ph/0403577).
Eckart et al., 2004, ApJ 602, 760.
Eyres et al., 2004, MNRAS 350, L9.
Genzel, R., Eckart, A., Ott, Th., Eisenhauer, F., 1997, MNRAS, 291, 219.
Genzel, R., Schödel, R., Ott, T., et al., 2003a, Nature 425, 934
Genzel, R., Schödel, R., Ott, T., et al., 2003b, ApJ 594, 812
Geballe et al., 1989, A&A 208, 255.
Ghez, A. M., Duchene, G., Matthews, K. et al., 2003a, Astrophys.J., 586, L127.
Ghez, A. M. et al., 2003b, 2003b, ANS 324, 527
Ghez, A. M. et al., 2004, ApJ 601, L159
Goldwurm, A. et al., 2003, ApJ 584,751.
Horrobin et al., 2004, AN 325, 88.
Kaup, D. J., 1968, Phys. Rev. 172, 1331.
Krabbe et al., 1995, ApJ 447, L95.
Leinert, C., & Graser, U., 1998, in Proc. SPIE Vol. 3350, p. 389-393, Astronomical Interferometry, Robert D. Reasenberg; Ed.
Maoz, E., 1998, ApJ 447, L91.
Markoff, S., Falcke, H., Yuan, F. & Biermann, P.L., 2001, Astr.Ap.379, L13.
Melia, F. & Falcke, H. 2001, ARAA 39, 309.
Mielke, E., & Schunck, F., 2000, Nucl. Phys. B, 594, 1985
Moneti et al., 2001, ApJ 549, L203.

Mouawad, N, Eckart, A., Pfalzner, S., et al., 2003a, LNP Vol. 626: Galaxies and Chaos, 302.
Mouawad, N, Eckart, A., Pfalzner, S., et al., 2003b, Astron. Nachrichten Supplement, 324, 315.
Mouawad, N, Eckart, A., Pfalzner, S., et al., 2004, Astron. Nachrichten submitted.
Moultaka, J., Eckart, A., Viehmann, T., Mouawad, N., Straubmeier, C., Ott, T., Schödel, R., 2004 A&A 425, 529
Najarro et al., 1997, A&A 325, 700.
Narayan, R., Yi, I., & Mahadevan, R., 1995, Nature, 374, 623.
Ott et al., 1999, ApJ 523, 248.
Porquet, D., Predehl, P., Aschenbach, B., et al., 2003, A&A 407, L17
Rigaut et al., 2003, ANS 324, 551.
Ruffini, R., &, Bonazzola, S., 1969, Phys. Rev. 187, 1767
Sandford et al., 1988, ApJ, 329, 498.
Scally & Clarke 2001, MNRAS 325, 449.
Tanner et al., 2003, ANS 324, 597.
Tanner et al., 2002, ApJ 575, 860.
Tielens et al., 1991, ApJ 381,181.
Torres, D. F., Capoziello, S., Lambiase, G., 2000, Phys. Rev. D 62, 104012
Viemann, T., Eckart, A., Schödel, R., Moultaka, J., Straubmeier, C., *L*- and *M*-band Imaging Observations of the Galactic Center Region, 2005, A&A in press
Viollier, R. D., Leimbruber, F. R., and Trautmann, D., 1992, Physics Letters B, 297, 132
Yuan, F., Markoff, S. & Falcke, H. 2002, Astron.Astrophys. 854, 854.
Yuan, F., Quataert, E. & Narayan, R., 2004, Ap.J. 606, 894.
Yuan, F., Quataert, E. & Narayan, R. 2003, Ap.J. 598, 301.
Zhao, J.-H., et al., 2003, Ap.J. 586 L29.

Indirect Evidence for WIMP Annihilation from Diffuse Galactic Gamma Rays

Wim de Boer

IEKP, Univ. of Karlsruhe
Postfach 6980, D-76131 Karlsruhe
Germany
Wim.de.Boer@cern.ch

1 Introduction

Cold Dark Matter (CDM) makes up 23% of the energy of the universe, as deduced from the WMAP measurements of the temperature anisotropies in the Cosmic microwave Background, in combination with data on the Hubble expansion and the density fluctuations in the universe [1]. The Dark Matter (DM) has to be much more widely distributed than the visible matter, since the rotation speeds do not fall off like $1/\sqrt{r}$, as expected from the visible matter in the centre, but stay more or less constant as function of distance. For a "flat" rotation curve the DM has to fall off slowly, like $1/r^2$, instead of the exponential drop-off for the visible matter. The fact that the DM is distributed over large distances implies that its properties must be quite different from the visible matter, since the latter clumps in the centre owing to its rapid loss of kinetic energy by the electromagnetic and strong interactions after infall into the centre. Since the DM apparently undergoes little energy loss, it can have at most weak interactions. In addition its mass is probably large, as deduced from the formation of stars as soon as a few hundred million years after the Big Bang. This time scale of star formation could be deduced from the polarization of the Cosmic Microwave Background, which is thought to originate from Compton scattering of the CMB on the electrons from the ionized plasma in stars [1]. Such an early formation of stars can only be explained, if the DM became non-relativistic in the early universe and started to cluster by gravity after decoupling from other particles roughly 10^{-9} s after the Big Bang. The baryonic matter fell then into these potential wells of DM after decoupling from the photons 380.000 years after the Big Bang. Given its weak interactions and heavy mass the DM particles are generically called WIMP's, Weakly Interacting Massive Particles.

According to the rules of particle physics weakly interacting particles can annihilate, yielding predominantly quark-antiquark pairs in the final state, which hadronize into mesons and baryons. The stable decay and fragmentation products are neutrinos, photons, protons, antiprotons, electrons and positrons. From these, the protons and electrons disappear in the sea of many matter particles in the universe, but the photons and antimatter particles may be detectable above the background, generated by particle interactions. Such

searches for indirect Dark Matter detection have been actively pursued, see e.g the review by Bergström [2] or more recently by Bertone, Hooper and Silk [3].

The present analysis on diffuse galactic gamma rays differs from previous ones by considering simultaneously the complete sky map *and* the energy spectrum, which allows us to constrain both the halo distribution *and* the WIMP mass. The WIMP annihilation cross section from cosmology is discussed in Sect. 2, while the constraints on the mass and the DM halo profile from the EGRET excess are discussed in Sect. 3, followed by the expectation from Supersymmetry in Sect. 4. The summary is given in Sect. 5.

2 DM Annihilation Cross Section from WMAP and Photon Flux

In the early universe all particles were produced abundantly and were in thermal equilibrium through annihilation and production processes. At temperatures below the mass of the WIMP's the number density drops exponentially. The annihilation rate $\Gamma =< \sigma v > n_\chi$ drops exponentially as well, and if it drops below the expansion rate, the WIMP's cease to annihilate. They fall out of equilibrium (freeze-out) at a temperature of about $m_\chi/22$ [4] and a relic cosmic abundance remains.

For the case that $< \sigma v >$ is energy independent, which is a good approximation in case there is no coannihilation, the present mass density in units of the critical density is given by [5]:

$$\Omega_\chi h^2 = \frac{m_\chi n_\chi}{\rho_c} \approx \left(\frac{2 \cdot 10^{-27} cm^3 s^{-1}}{< \sigma v >} \right) . \tag{1}$$

One observes that the present relic density is inversely proportional to the annihilation cross section at the time of freeze out, a result independent of the WIMP mass (except for logarithmic corrections). For the present value of $\Omega_\chi h^2 = 0.113 \pm 0.009$ the thermally averaged total cross section at the freeze-out temperature of $m_\chi/22$ must have been around $2 \cdot 10^{-26} \mathrm{cm}^3 \mathrm{s}^{-1}$.

From this cross section the differential gamma flux in a direction forming an angle ψ with the direction of the galactic center can be calculated:

$$\phi_\chi(E, \psi) = \frac{\langle \sigma v \rangle}{4\pi} \sum_f \frac{dN_f}{dE} b_f \int_{line\ of\ sight} B_l \frac{1}{2} \frac{\langle \rho_\chi^2 \rangle}{M_\chi^2} dl_\psi \tag{2}$$

where b_f is the branching ratio into the tree-level annihilation final state, while dN_f/dE is the differential photon yield for the final state f. The WIMP mass density enters critically in the prediction for the flux, since the number of WIMP pairs is equal to $1/2\, \rho_\chi^2/M_\chi^2$. The factor B_l is the boost factor, which represents the local enhancement of the number density with respect

to the average by the expected clustering of DM. For the present analysis B_l is assumed to be the same in all directions ψ, although near the centre of the galaxy the DM clusters may have been tidally disrupted by the flyby of nearby stars, thus reducing the boost factor towards the centre. However, this will only modify the density profile near the centre and not affect the overall analysis. Since the average of ρ_χ^2 can be significantly larger than $\langle\rho_\chi\rangle^2$ the boost factor can enhance the flux by one or two orders of magnitude [6].

As mentioned above and discussed further in the section on Supersymmetry, the dominant final state is always into quark pairs. These quarks will be mono-energetic, since the non-relativistic WIMP's annihilate practically at rest. Therefore one has to consider only one final state and the corresponding gamma spectrum from mono-energetic quarks is well known from electron-positron colliders[1], so in principle the only free parameters left are the WIMP mass, the halo profile, i.e. the distribution of the DM density ρ_χ in space and the boost factor. The EGRET data are precise enough to determine these.

3 Indirect Dark Matter Detection

The neutral particles play a very special role for indirect DM searches, since they point back to the source. The charged particles change their direction by the interstellar magnetic fields, energy losses and scattering. Therefore the gamma rays provide a perfect means to reconstruct the intensity (halo) profile of the DM by observing the intensity of the gamma ray emissions in the various sky directions. Of course, this assumes that one can distinguish between the gamma rays from DMA the ones from the background, which is possible because of the different energy spectra: the gamma rays from the mono-energetic quarks from DMA produce a significantly harder spectrum than the gammas from nuclear interaction, which are produced by the interactions between quarks with a steeply falling power law spectrum ($\propto E^{-2.7}$).

The spectral shape of the gamma rays from either the backgrounds or the mono-energetic quarks are well known from accelerator experiments and can be obtained from the well-known PYTHIA code for quark fragmentation [7].

A very detailed gamma ray distribution over the whole sky was obtained by the Energetic Gamma Ray Emission Telescope EGRET, one of the four instruments on the Compton Gamma Ray Observatory CGRO, which collected data during nine years, from 1991 to 2000. The EGRET telescope was carefully calibrated in the energy range of 0.1 to 30 GeV, but using Monte Carlo simulations the energy range was recently extended up to 120 GeV [8] with a correspondingly larger uncertainty, mainly from the self-vetoing of the

[1]The annihilation is preferentially into heavy b-quarks, which yield a slightly harder gamma spectrum than the light quarks. This is the spectrum, which will be used. In case of light quarks the fit to the data would require a somewhat heavier WIMP mass to obtain the same spectrum.

detector by the back-scattering from the electromagnetic calorimeter into the veto counters for high energetic showers.

It was already noticed in 1997 that the EGRET data showed an excess in the galactic disk [9] of gamma ray fluxes for energies above 1 GeV if compared with conventional galactic models and repeated later for all sky directions [8]. This analysis was repeated recently [10, 11] using a different analysis technique on the publicly available EGRET data, namely by comparing the data not with the absolute fluxes from galactic models, but only with the shape of the gamma energy spectra from the galactic background, which is much better known and allows to take the strongly correlated systematic normalization errors between the different energy points of the spectrum into account. Simultaneously to the galactic background the shapes of Dark Matter Annihilation and the extragalactic background are fitted. Fitting these three contributions yielded astonishingly good fits with the free normalization of the background agreeing reasonably well with the absolute predictions of the galactic models [12, 13] for the energies between 0.1 and 0.5 GeV. Above these energies a clear contribution from Dark Matter annihilation is needed, but the excess in different sky directions can be explained by a single WIMP mass and a single boost factor, as shown in Fig. 1 for 6 different sky directions.

Alternative explanations for the excess have been plentiful. Among them: locally soft electron and proton spectra, implying that in other regions of the galaxy the spectra are harder, thus producing harder photon spectra.

A summary of these discussions have been given by Strong et al.[8], who find that hard proton spectra are incompatible with the antiproton yield and hard electron spectra are incompatible with the EGRET data up to 120 GeV, which they analyzed. However, they find that by modifying the electron and proton injection spectra simultaneously, they can improve the description of the data, as noted also recently by Kamae et al.[14].

The problem with these "solutions" is that they give a too large (small) contribution at low (high) gamma ray energies, i.e. the shape of the energy spectra is not well reproduced. But it is exactly the shape, which was well measured by EGRET, because the quoted normalization errors of 15% are common to all energy points. If one calculates the probability of the "optimized" model, taking the correlations between the energy points into account, the probability is below 10^{-14}! Two other arguments, independent of the EGRET errors, against "optimized" models are: 1) the energy loss time of protons above 10 GeV is above 10^{11} yrs, i.e. longer than the lifetime of the universe. Therefore it is hard to image that protons, accelerated in the centre of the galaxy by the many supernovae there, would have a significant different spectrum after diffusion to the solar neighbourhood in about 10^8 yrs, a time much shorter than the energy loss time 2) if the proton spectrum is nevertheless inhomogeneous over our galaxy, it is very surprising that the excess has the *same* energy shape towards the outer galaxy, where there are practically no supernovae and towards the centre of the galaxy. An alternative way of

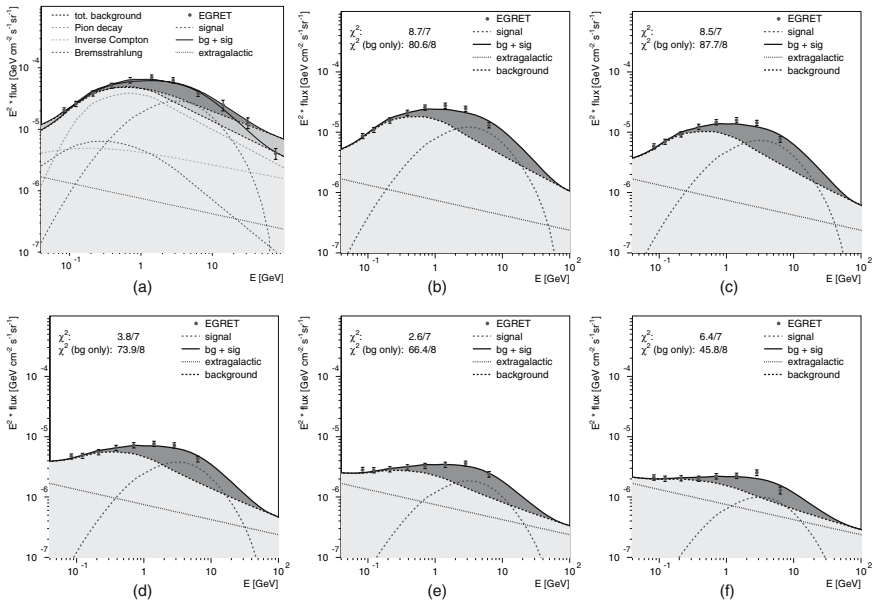

Fig. 1. The diffuse gamma-ray energy spectrum of the disc regions (top row, from left to right): (a): towards the galactic centre (latitudes $0^\circ < |b| < 5^\circ$; longitudes $0^\circ < |l| < 30^\circ$), (b): the outer disc (latitudes $0^\circ < |b| < 5^\circ$; longitudes $30^\circ < |l| < 330^\circ$), (c): the galactic anticentre ($0^\circ < |b| < 10^\circ$; $90^\circ < |l| < 270^\circ$) and outside the disc (bottom, from left to right): (d): intermediate latitudes I ($10^\circ < |b| < 20^\circ$; $0^\circ < |l| < 360^\circ$), (e): intermediate latitudes II ($20^\circ < |b| < 60^\circ$; $0^\circ < |l| < 360^\circ$), and (f): the Galactic pole regions ($60^\circ < |b| < 90^\circ$; $0^\circ < |l| < 360^\circ$), as measured by the EGRET space telescope. The solid straight line represents the fitted contribution from the extragalactic background, while the dotted line indicates the contribution from the annihilation from 65 GeV WIMP's with a boost factor around 70. The total background is indicated by the light (yellow) and the DMA by the dark (red) shaded area, respectively. In the top left panel the various contributions to the background are indicated as well, while the uncertainties from the background are indicated by the medium shaded (blue) area. One observes that the $\chi^2/d.o.f.$ for the fit including DMA is significantly better than the fit for the background only.

formulating this problem: if the EGRET excess can be explained prefectly in all sky directions by a gamma contribution originating from mono-energetic quarks, it is very difficult to replace such a contribution by an excess of quarks (or electrons) with a power law spectrum.

To exemplify these problems we consider the *shape* of the background from a recent analysis by Kamae et al.[14]. They use a harder proton spectrum than locally observed (a power law with index 2.5 instead of 2.7 observed locally) and an updated pp cross section including diffractive scattering and scaling violation. They claim this can describe the EGRET data towards the galactic centre. However, there is a clear overshoot at low energies. Fitting

only their shape to the EGRET data, i.e. with a free normalization, still leaves a significant excess, as shown in the left panel of Fig. 1. Here the upper edge of the medium shaded (blue) area corresponds the hardest possible spectrum from Kamae et al.[14] with the power index of 2.5, while the lower edge corresponds to the conventional GALPROP model [8]. Note that the hard spectrum overshoots the highest EGRET point, which was not yet available during the analysis by Kamae et al. In summary, also for the "conventional" explanations [8, 14] the fit to *all* sky directions can be much improved, if DM is added, since then both the low and high energy range can be perfectly described. Thus different backgrounds just change the normalization of the DM contribution.

The quality of the EGRET data is better appreciated if one plots only the statistical errors. Figure 2 shows the excess for five different sky regions: only at high latitudes the errors start to be visible. The curves are just spline fits through the data and were used to determine the systematic point-to-point errors by leaving a given energy point out of the fit and determine its variance. The point-to-point error is about 7% for most energy points. In the previous plot the WIMP mass was kept constant at 65 GeV. The right hand side of Fig. 2 shows the plot for a WIMP mass of 100 GeV, which clearly overshoots the high energy data. Therefore a rough estimate of the WIMP mass from the EGRET excess is between 50 and 100 GeV.

From the excess in the various sky directions one can obtain the halo profile under the assumption that the clustering of the DM is similar in all sky directions. The result is surprising: in addition to the $1/r^2$ profile

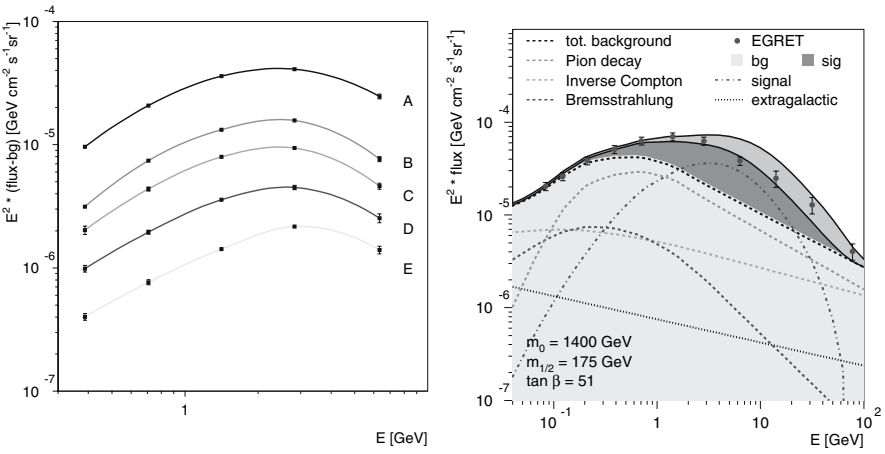

Fig. 2. Left: the energy spectrum of the EGRET excess, defined as the difference between the data and the fitted background contribution for 5 of the panels of Fig. 1. Only the small statistical errors have been plotted. Right: the medium shaded (blue) band shows the effect of varying the WIMP mass between 65 and 100 GeV.

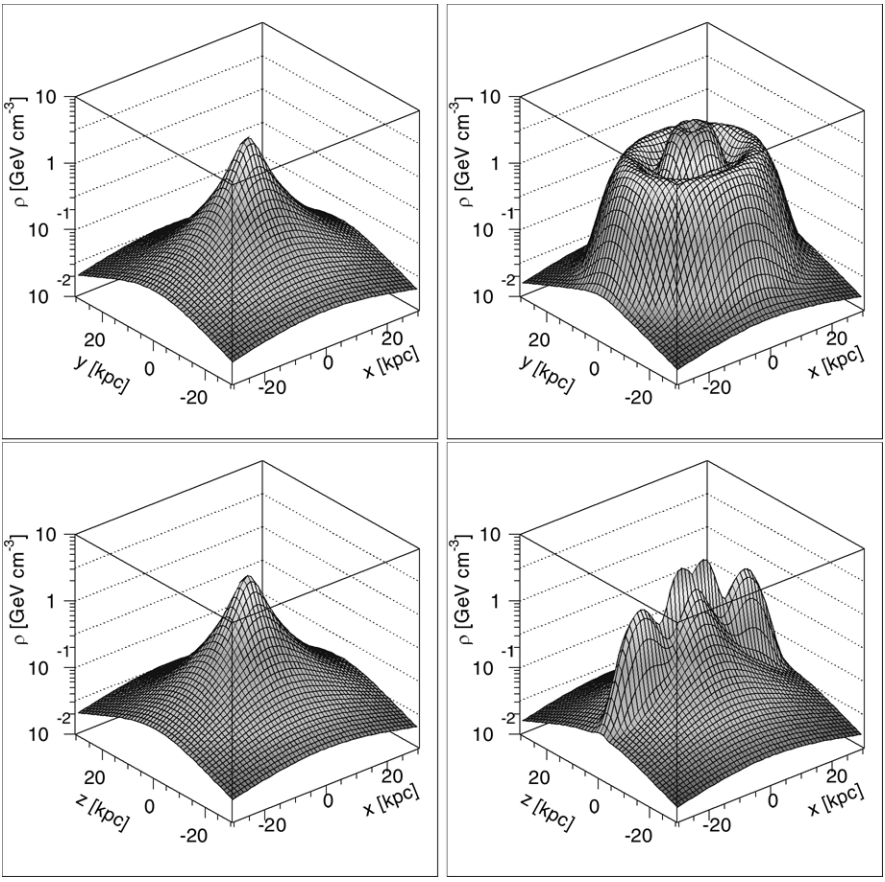

Fig. 3. 3D-distributions of the $1/r^2$ haloprofile in the galactic xy-plane (top row) and xz-plane (bottom row) without (left) and with (right) rings.

expected for a flat rotation curve the EGRET excess show a substructure in the form of toroidal rings at 4 and 14 kpc, as shown in Fig. 3: on the left hand side the contribution from the $1/r^2$ profile is shown, while for the right hand side the ring structure is added. The need for these additional rings is most easily seen by comparing the longitudinal profiles in the galactic plane and towards the galactic poles. As shown in Fig. 4 the pole regions are described reasonably well without rings, but for the galactic plane the $1/r^2$ profile only describes the data towards the centre. For the larger latitudes one needs the rings, as indicated by the right top panel. Note that for each bin only the flux integrated for data above 0.5 GeV has been plotted. The normalization of the background has been obtained from a fit to the flux integrated between 0.1 and 0.5 GeV.

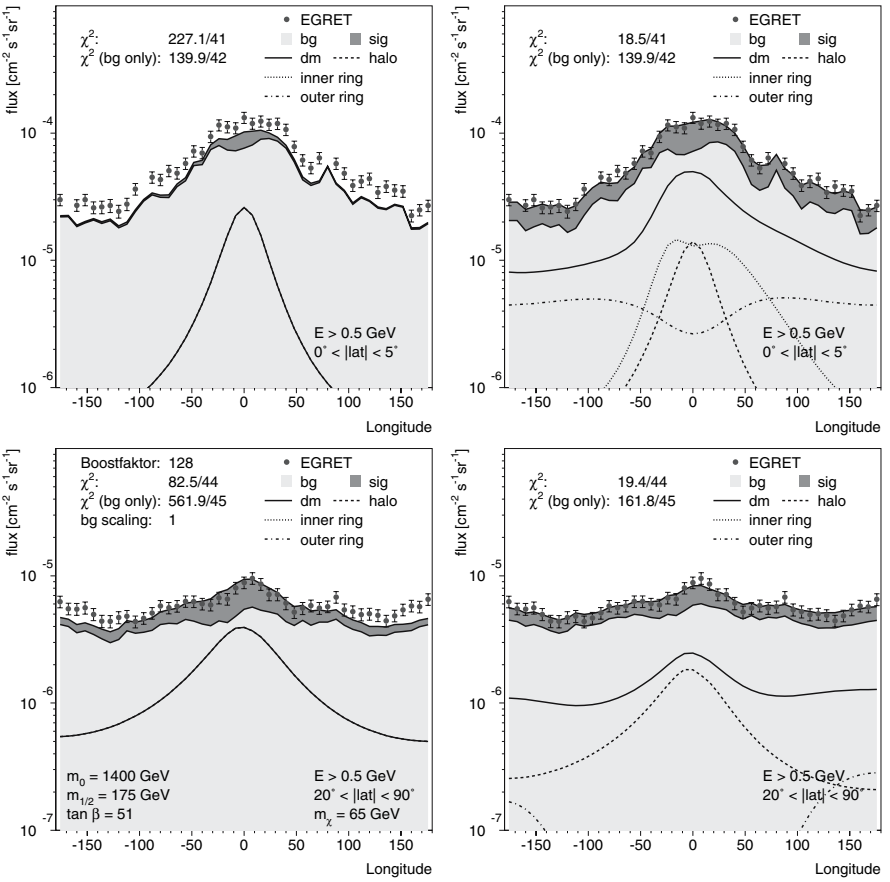

Fig. 4. Top row: the longitude distribution of diffuse gamma-rays in the disc of the galaxy (latitudes $0^\circ < |b| < 5^\circ$) for the $1/r^2$ profile without (left) and with rings (right). The points represent the EGRET data. Bottow row: as above for the polar regions of our galaxy (latitudes $20^\circ < |b| < 90^\circ$).

The position and shape of the inner ring coincides with the ring of molecular hydrogen. Molecules form from atomic hydrogen in the presence of dust or heavy nuclei. So a ring of neutral hydrogen suggests an attractive gravitational potential. The position and shape of the outer ring coincides with the ring of stars, discovered in 2003 by two independent groups [15, 16]. This ring is thought to originate from the infall of a dwarf galaxy, so additional DMA is expected there.

To prove that the enhanced gamma ray density is indeed connected to non-baryonic mass the rotation curve was reconstructed from the excess of the diffuse gamma rays in the following way: since the flux determines the number density of DM for a given boost factor and since the mass of each

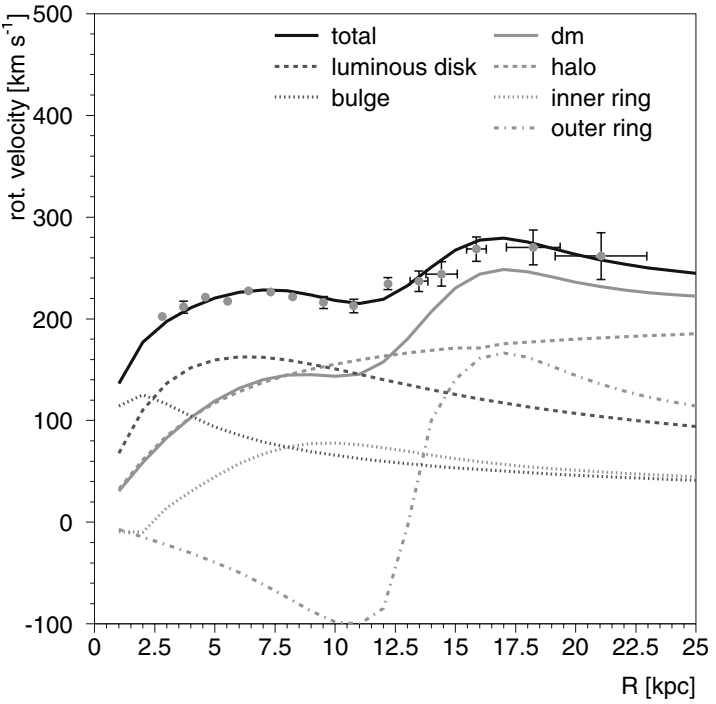

Fig. 5. The rotation curve from our galaxy with the DM contribution determined from the EGRET excess of diffuse gamma rays. The data are averaged from [10].

WIMP is between 50 and 100 GeV, one can determine the mass in the ring and consequently predict the rotation curve[2]. The two ring model describes the peculiar change of slope at 11 kpc well, as shown in Fig. 5. The contributions from each of the mass terms have been shown separately. The basic explanation for the negative contribution from the outer ring is that a tracer star at the inside of the ring at 14 kpc feels an outward force from the ring, thus a negative contribution to the rotation velocity. It has often been argued that the outer rotation curve cannot be taken seriously, because the errors are large due to the fact that the absolute values of the rotation velocities strongly depend on the value of R_0, the distance between the solar system and the galactic centre. This is true, as shown by Honma and Sofue [17], but they show that the *change in slope* at about $1.3R_0$ is independent of R_0. In addition, it has been argued that the inner and outer rotation curve are difficult to compare, since the methods are completely different. The methods are indeed different, but the first 3 data points from the outer rotation curve (between 8 and 11 kpc) show the same slope as the ones from the inner rota-

[2]For the outer ring a total DM mass of a few times 10^{10} solar masses was found in comparison with about 10^9 solar masses in the form of stars.

tion curve, so there seems to be no systematic effect related to the different methods.

4 Comparison with Supersymmetry

Supersymmetry [18] presupposes a symmetry between fermions and bosons, which can be realized in nature only if one assumes each particle with spin j has a supersymmetric partner with spin $|j - 1/2|$ ($|j - 1/2|$ for the Higgs bosons). This leads to a doubling of the particle spectrum. Obviously SUSY cannot be an exact symmetry of nature; or else the supersymmetric partners would have the same mass as the normal particles. The mSUGRA model, i.e. the Minimal Supersymmetric Standard Model (MSSM) with supergravity inspired breaking terms, is characterized by only 5 parameters: $m_0,\ m_{1/2},\ \tan\beta,\ \mathrm{sign}(\mu),\ A_0$. Here m_0 and $m_{1/2}$ are the common masses for the gauginos and scalars at the GUT scale, which is determined by the unification of the gauge couplings. Gauge unification is still possible with the precisely measured couplings at LEP [19]. The ratio of the vacuum expectation values of the two Higgs doublets is called $\tan\beta$ and A_0 is the trilinear coupling at the GUT scale. We only consider the dominant trilinear couplings of the third generation of quarks and leptons and assume also A_0 to be unified at the GUT scale. The absolute value of the Higgs mixing parameter μ is determined by electroweak symmetry breaking, while its sign is taken to be positive, as preferred by the anomalous magnetic moment of the muon [19].

The lightest supersymmetric particle (LSP) is stable, if the multiplicative quantum number R-parity, which is +1 for SM particles and -1 for SUSY particles, is conserved. Non-conservation of R-parity would lead to rapid proton decay [18]. The LSP is a perfect candidate for Dark Matter and it can self annihilate into fermion-antifermion pairs by Higgs or Z-exchange in the s-channel or sfermion, chargino and neutralino exchange in the t-channel. The dominant first three possibilities have amplitudes proportional to the fermion mass, so heavy final states are preferred. For values of $\tan\beta \approx 50$ the annihilation cross sections into $b\overline{b}$ quarks are indeed of the order of magnitude required by WMAP, as shown in Fig. 6. For $m_{1/2} \approx 175$ GeV, corresponding to a neutralino mass of about 70 GeV, as required by the EGRET data, the scalar masses have to be in the TeV range for a thermally averaged annihilation cross section $\sigma v \approx 2.10^{-26}$ cm^3/s, as required by (1).

This point of parameter space respects in addition all constraints from the direct searches on Higgs and charginos and electroweak precision observables, as shown in Fig. 7. The relic density has been calculated with the program MicroMegas [20]. If m_0 is small compared with $m_{1/2}$ the lightest lepton (usually the stau) can be lighter than the neutralino, which happens in the left top corner on the left hand side of Fig. 7. In the region adjacent to it the stau cannot decay fast into a neutralino and tau, in which case a stau and neutralino can annihilate into a tau plus photon. This coannihilation reduces

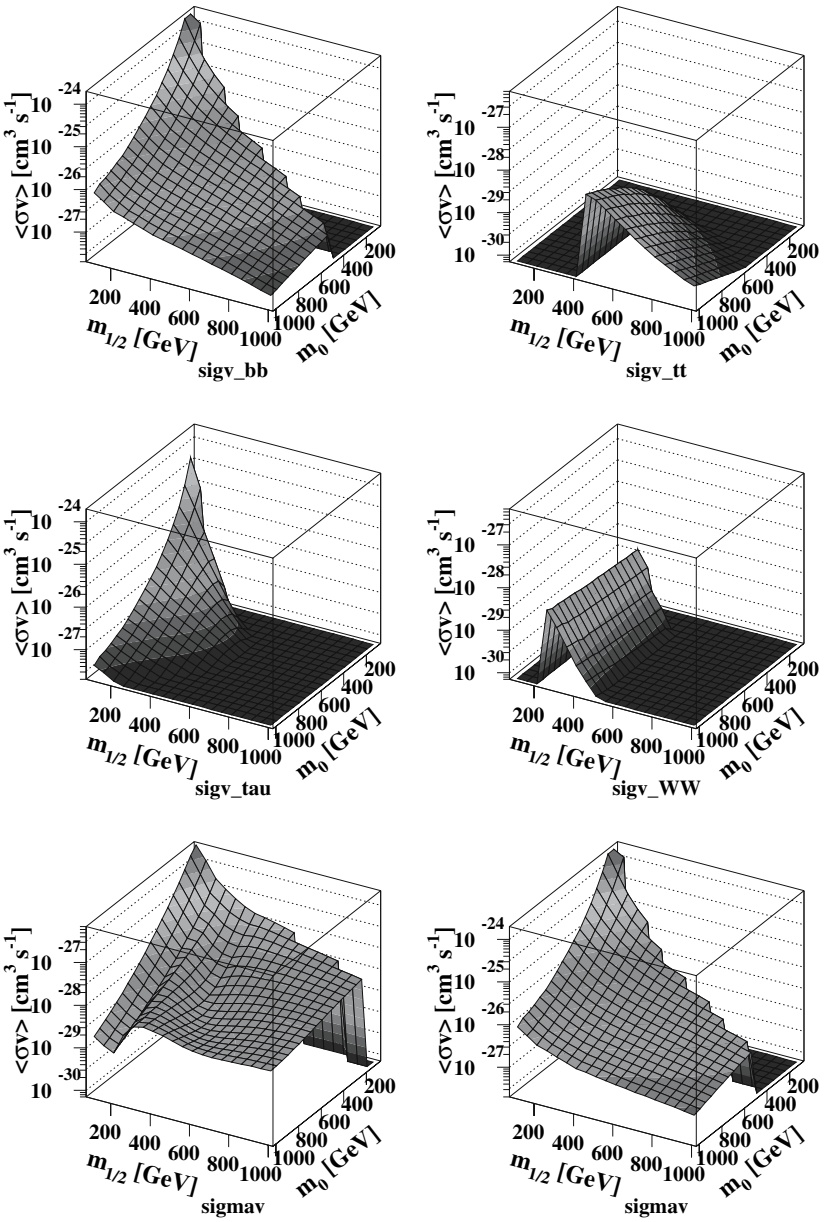

Fig. 6. The first two rows show the thermally averaged annihilation cross section times velocity for neutralino annihilation as function of m_0 and $m_{1/2}$ for $\tan\beta$= 50 and $b\bar{b}$, $t\bar{t}$, W^+W^-, and $\tau\bar{\tau}$ final states (clockwise from top left). The last row shows the total cross section or $\tan\beta$= 5 (left) and 50 (right). The neutralino mass equals $\approx 0.4 m_{1/2}$ in the CMSSM, so the neutralino varies from 40 to 400 GeV along the front axis. Note the strong decrease of the cross section for heavier SUSY mass scales and the different vertical scales.

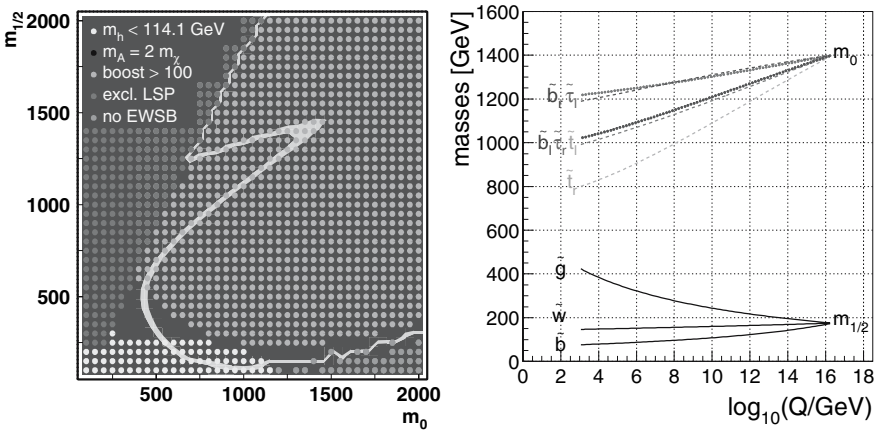

Fig. 7. The light shaded (blue) line in the region allowed by WMAP in the $m_0, m_{1/2}$ plane for $\tan\beta = 51$, $\mu > 0$ and $A_0 = 0$. The excluded regions, where the stau would be the LSP or EWSB fails or are indicated by the dots. The large central region, where the boost factor would be above 100, has been indicated as well. The region for $m_{1/2} \approx 180$ and $m_0 \approx 1400$ all constraints from EGRET, WMAP and electroweak data are fulfilled. The evolution of the particle spectrum from the GUT scale is shown on the right hand side, showing that the squarks and sleptons have masses in the TeV range, while the gluinos and charginos are relatively light.

the relic density to values required by the WMAP data, but these regions require large boost factors, since in the present galaxy the NLSP's have decayed and only the self annihilation contributes. The regions, where the boost factors are above 100 are shown in Fig. 7 together with the regions where the annihilation cross section is consistent with the WMAP data. For boost factors below 100 only two regions are allowed: one around $m_{1/2} = 400\,\mathrm{GeV}$ and one around $m_{1/2} = 180\,\mathrm{GeV}$. Only the latter is compatible with the EGRET excess. It requires m_0 to be above 1 TeV, which yields squark and slepton masses above 1 TeV. The gluinos and charginos are relatively light, as shown on the right hand side of Fig. 7. It should be noted that the EGRET data combined with the WMAP cross section select basically a single point in parameter space. Compared with scans over the multidimensional SUSY parameter space, even with millions of points, it is very easy to miss such a single point, as demonstrated by recent scans [21, 22], which missed the EGRET point.

5 Summary and Outlook

In summary, the EGRET data shows an intriguing hint of DM annihilation, since it explains many unrelated facts simultaneously:

(a) An excess of diffuse galactic gamma rays which shows a *spectrum* consistent with the expectation from WIMP annihilation into mono-energetic quarks.

(b) The excess is present in *all* sky directions with the same spectrum, thus excluding that it originates from anomalous contributions in the centre of the galaxy.

(c) The excess shows a strongly increased intensity at positions where extra DM is expected, namely at two doughnut shaped structures at radii of 14 and 4 kpc from the centre of the galaxy. At 14 kpc one has observed a ring of stars thought to originate from the infall of a dwarf galaxy, while at 4 kpc one finds an enhanced concentration of molecular hydrogen thought to form from atomic hydrogen in the presence of dust or heavy nuclei, which can be collected in the gravitational potential of a ring of DM.

(d) The enhanced excess of gamma rays cannot be due to additional gas in these rings as proven by the rotation curve calculated from the gamma ray excess: the mass in the rings perfectly describe the hitherto unexplained change of slope in the rotation curve at a distance of about 11 kpc. The amount of visible matter is far too low to have such an impact on the rotation curve.

In this analysis only the known spectral shapes of the various processes with arbitrary normalizations are fitted, so the analysis becomes largely model independent. Interestingly, the normalization factors come out to be in excellent agreement with expectations, both for the WIMP signal and the background.

Alternative models trying to explain the EGRET excess have to assume that the locally measured fluxes of protons and electrons are not representative for our galaxy, in which case these spectra outside our local bubble can be tuned to obtain the more energetic gamma rays needed for the EGRET excess, although these models provide significantly worse fits to the data, if one takes the strong correlations in the errors between the different energy bins into account. In addition such models cannot explain simultaneously the stability of the ring of stars at 14 kpc and the change of slope in the rotation curve at $r \approx 11$ kpc.

The results mentioned above make no assumption on the nature of the Dark Matter, except that its annihilation produces hard gamma rays consistent with the fragmentation of mono-energetic quarks between 50 and 100 GeV. WIMP masses in this range and the observed WIMP self annihilation cross section are consistent with WIMP's being the Lightest Supersymmetric Particle predicted in the Minimal Supersymmetric Model with supergravity inspired symmetry breaking, called the mSUGRA model.

Within this supersymmetric model one finds a spin-independent cross section for elastic scattering of a WIMP on a proton of about 10^{-43} cm^2, which is within reach [23] of future experiments as shown in Fig. 8. This elastic scattering cross section was calculated with Darksusy [24].

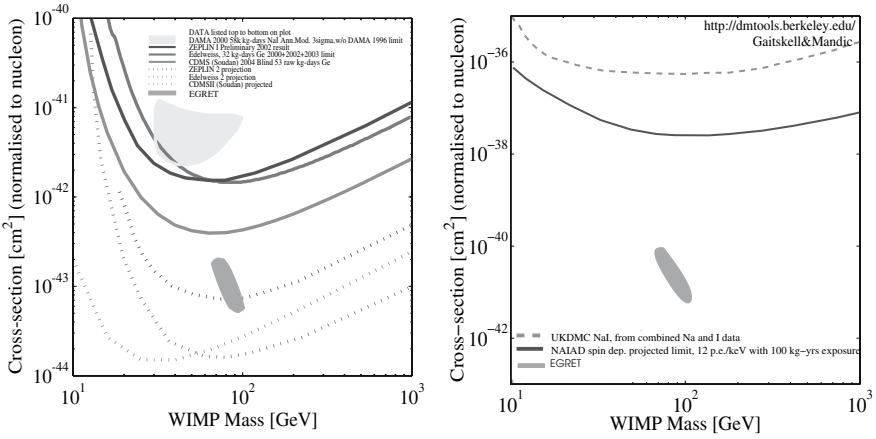

Fig. 8. The spin-independent (left) and spin-dependent (right) neutralino-nucleon cross section as function of the neutralino mass for the SUSY parameters from this analysis [10] (oval shaded (brown) area in comparison with results from present and future direct DM detection experiments.

Direct and indirect detection experiments do not prove the supersymmetric nature of the WIMP's. If the WIMP's are indeed the lightest supersymmetric particle, then this will become clear at the future LHC collider under construction at CERN in Geneva, where supersymmetric particles of the mass range deduced from the EGRET data should be observable from 2008 onwards, if they exist.

The statistical significance of the EGRET excess of at least 10 σ combined with all features mentioned above provides an intriguing hint that DM is not so dark, but visible by its annihilation.

I thank my close collaborators A. Gladyshev, D. Kazakov, C. Sander and V. Zhukov for their contributions to this interesting project. Furthermore I thank V. Moskalenko, A. Strong and O. Reimer for numerous discussions on galactic gamma rays.

This work was supported by the DLR (Deutsches Zentrum für Luft- und Raumfahrt) and a grant from the DFG (Deutsche Forschungsgemeinschaft, Grant 436 RUS 113/626/0-1).

References

1. D.N. Spergel et al., 2003, ApJS, 148, 175;
   C.L. Bennett et al., 2003, ApJS, 148, 1; See also: http://map.gsfc.nasa.gov/m_mm/pub_papers/firstyear.html
2. L. Bergström, Rept. Prog. Phys. **63** (2000) 793, hep-ph/0002126
3. G. Bertone, D. Hooper and J. Silk, hep-ph/0404175

4. E. Kolb, M.S. Turner, The Early Universe, Frontiers in Physics, Addison Wesley, 1990
5. G. Jungman, M. Kamionkowski and K. Griest, Phys. Rep. **267** (1996) 195
6. V. Dokuchaev, these proceedings. V. Berezinsky, V. Dokuchaev and Y. Eroshenko, Phys. Rev. D **68**, 103003 (2003); astro-ph/0301551
7. T. Sjöstrand, P. Eden, C. Friberg, L. Lönnblad, G. Miu, S. Mrenna and E. Norrbin, Computer Phys. Commun. **135** (2001) 238
8. A.W. Strong, I.V. Moskalenko and O. Reimer, Astrophys. J. **613**, 962 (2004); astro-ph/0406254
9. Hunter, S.D et al., Astrophysical Journal **481**, 205 (1997)
10. W. de Boer, M. Herold, C. Sander, V. Zhukov, A. V. Gladyshev and D. I. Kazakov, astro-ph/0408272
11. W. de Boer, hep-ph/0408166
12. A.W. Strong and I.V. Moskalenko, Astrophys. J. **509**, 212 (1998); astro-ph/9807150
13. I.V. Moskalenko and A.W. Strong, Astrophys. Space Sci. **272** (2000) 247; astro-ph/9908032
14. T. Kamae, T. Abe and T. Koi, astro-ph/0410617
15. B. Yanny et al., Astrophys. J. **588** (2003) 824 [Erratum-ibid. **605** (2004) 575]; astro-ph/0301029
16. R.A. Ibata, M.J. Irwin, G.F. Lewis, A.M.N. Ferguson and N. Tanvir, Mon. Not. Roy. Astron. Soc. **340** (2003) L21; astro-ph/0301067
17. M. Honma and Y. Sofue, Publ. of the Astronomical Society of Japan, v.48, p.L103-L106; astro-ph/9611156
18. Reviews and original references can be found in: W. de Boer, Prog. Part. Nucl. Phys. **33** (1994) 201, hep-ph/9402266;
    H.E. Haber, Lectures given at Theoretical Advanced Study Institute, University of Colorado, June 1992, Preprint Univ. of Sante Cruz, SCIPP 92/33; see also SCIPP 93/22;
    Perspectives on Higgs Physics, G. Kane (Ed.), World Scientific, Singapore (1993);
    A.B. Lahanus and D.V. Nanopoulos, Phys. Rep. **145** (1987) 1;
    H.E. Haber and G.L. Kane, Phys. Rep. **117** (1985) 75;
    M.F. Sohnius, Phys. Rep. **128** (1985) 39;
    H.P. Nilles, Phys. Rep. **110** (1984) 1;
    P. Fayet and S. Ferrara, Phys. Rep. **32** (1977) 249
19. W. de Boer and C. Sander, hep-ph/0307049 and references therein
20. G. Bélanger, F. Boudjema, A. Pukhov and A. Semenov, Comp. Phys. Commun. **149** (2002) 103 [arXiv:hep-ph/0112278] and arXiv:hep-ph/0210327 and http://wwwlap.in2p3.fr/lapth/micromegas
21. J.R. Ellis, S. Heinemeyer, K.A. Olive and G. Weiglein, hep-ph/0411216
22. L. Roszkowski, Pramana **62** (2004) 389, hep-ph/0404052
23. The curves were calculated with the interactive web-based program on http://dmtools.berkely.edu
24. P. Gondolo, J. Edsjo, P. Ullio, L. Bergstrom, M. Schelke, E.A. Baltz, JCAP**0407** (2004) 008, astro-ph/0406204 and http://www.physto.se/~edsjo/darksusy/

Probing Dark Objects with Gravitational Lensing

Kim Griest

Physics Department, University of California, San Diego, La Jolla, CA 92093 USA
kgriest@ucsd.edu

1 Introduction

In recent years gravitational lensing has moved from being an obscure curiosity to being a fundamental tool in astronomy. If you look at the sophisticated uses and complicated formalisms that have developed around gravitational lensing it may be surprising that everything in lensing comes from the very simple Einstein light bending formula,

$$\Delta\theta = \frac{4GM}{bc^2}\,, \tag{1}$$

where b is the impact parameter, M is the mass of the lens and G is Newton's constant. This simple light bending causes distant light sources to split into several images, magnify, move around, and shear in predictable ways. Since it is the total mass-energy that does the light bending, gravitational lensing is just as sensitive to non-shining dark substances as it is visible stars and galaxies. Therein lies the power of gravitational lensing. In astrophysical theories, mass is usually more fundamental than the more commonly measured luminosity.

In this short talk I cannot possibly cover all the recent progress in the uses of gravitational lensing. For example, I won't talk about strong lensing in clusters of galaxies, where arcs give the mass and density profiles of the clusters. This allows dark matter to be directly measured in clusters of galaxies, which are the largest known gravitationally bound structures. Also, I won't talk about weak lensing, where small distortions in the shapes of many background galaxies are statistically analyzed to measure the gravitational shear. This is potentially a very powerful technique and can measure the dark matter power spectrum, the growth of structure, and cosmological parameters such as the vacuum energy equation of state, etc. I also will only touch briefly on the uses of quasar lensing, where multiple quasar images allow one to measure the Hubble parameter and dark halo substructure. For the bulk of the talk I will concentrate on what I know best, that is the microlensing of stellar mass objects. This allows one to take an inventory of all compact objects in the Milky way, including faint stars, stellar remnants, planets, etc.

2 Microlensing of Dark Matter?

So far four collaborations have returned dark matter results from microlensing surveys, but the results are still ambiguous as I will describe. These experiments work by monitoring millions of stars in nearby galaxies. They try to prove or disprove the hypothesis that the dark matter of the Milky Way consists of some Massive Astrophysical Compact Halo Objects (Machos). If this was the case, then occasionally such a compact object would cross in front of one the stars being monitored and act as a gravitational lens. As the Macho passed near to the line-of-sight to the background source star, the source star would brighten, reach a peak brightness, and then return to its ordinary brightness. This transient brightening is called a microlensing event and these are what the microlensing collaborations search for. Unfortunately such events are rare, and so many millions of stars must be monitored for many years to discover a significant number of events. This is especially true in the search for Macho dark matter, since one needs target stars that are sufficiently far away that the line-of-sight passes through a significant portion of the dark halo. Thus for dark matter work, the collaborations monitor either the Large or Small Magellanic Clouds (LMC/SMC), or the nearby galaxy M31.

The four collaborations that have returned results are: MACHO [1] who have returned strong evidence in favor of LMC microlensing, but the dark matter interpretation is still unclear, EROS [2], who have returned evidence against substantial LMC microlensing and against Macho dark matter, but still consistent with the MACHO results, MEGA [3] who report evidence in favor of microlensing towards M31, and moderate evidence in favor of Macho dark matter, and POINT/AGAPE [4] who monitor M31 and report weak evidence against Macho halo dark matter.

2.1 MACHO Results on Dark Matter

The MACHO collaboration monitored 12 million stars for 6 years and found 13–17 microlensing events. They did a careful efficiency and likelihood analysis. The lightcurves of several of their events follow the expected functional form of microlensing very well and are beautiful examples of microlensing. So there is no doubt that they have observed microlensing towards the LMC. Their events are spread out over the LMC and occur on random stars in the color-magnitude as expected from microlensing. The distribution of maximum magnifications is also as expected, arguing that the bulk of the events they select are indeed microlensing. Using these 13 (or 17 depending upon selection criteria) events, their likelihood analysis prefers a total mass in Machos of between 8% and 40% (95% confidence level) of the total dark matter in the halo (The central value is $f = 0.2$). This corresponds to a total mass in Machos of 8 to 10 $\times 10^{10} M_{\odot}$. We should note that one of the events (LMC-23) bumped again after 7 years, and so is now known to be a variable star. Thus

the halo fractions (and optical depths) reported by the MACHO collaboration [1] should be reduced by 8%, the contribution of this event to the total microlensing signal. Having contamination of one variable star is consistent with the contamination systematic error which was estimated at 17%, but it is worrying that a lightcurve which looked very much like microlensing was in fact a variable star. In any case, given that the total mass of the Milky Way disk is around $6 \times 10^{10} M_{\odot}$, this Macho component, if it exists, would be a major component of the Milky Way. Also, it is very clear from this measurement that the bulk of the dark matter cannot consist of compact halo objects, but must be something else such as undiscovered exotic elementary particles. The likelihood analysis also prefers that the Macho objects have masses in the 0.1 to 1.0 $M_{\odot}$ range. Now, before accepting this experimental result at face value it is important to consider some problems. What could such a large amount of solar mass objects be? Certainly they can't be main sequence stars or they would be seen. Stellar remnants such as white dwarfs, neutron stars, or black holes have been suggested, but there are severe problems with each of these. In particular, an enormous number of early generation stars would be needed to leave such a large number of remnants. Such an early generation of stars would over-enrich the interstellar medium with heavy elements and would have created lots of background light which is not seen. Primordial black holes are a possibility, but these do not naturally occur in any model. So there are no natural candidates for this Macho population.

However, there is an alternative explanation. In performing its likelihood analysis, The MACHO collaboration calculated the number of microlensing events expected from known stellar populations. They expected to find 0.4 events from Milky Way disk stars, 0.2 events from the thick disk, 0.2 events from the spheroid, and between 1.2 and 2.2 events from LMC self-lensing, for a total of 2–3 events from known stellar sources. This is much larger than the 13 events actually seen; however, if the LMC has an extended halo of faint stars that has not yet been detected, then this could account for the LMC microlensing [5]. Since careful searches for this extended LMC halo have not yet been successful, for now, the source of the LMC microlensing remains a mystery.

2.2 EROS Results on Dark Matter

The EROS collaboration [2] monitored 17.5 million stars in the LMC for 2 years and 5.3 million stars for 6 years, as well as several million stars in the SMC. They found 3 microlensing events in their 50 LMC fields and 4 events in their 10 SMC fields. They interpret their results only as an upper limit on the Macho contribution to the dark matter halo. In the mass range $0.1 M_{\odot}$ to $1.0 M_{\odot}$ they limit Machos to being less than 25% of the dark halo, inconsistent with larger values of the MACHO allowed region, but consistent with the central value and the lower regions. Over the mass range between $10^{-6} M_{\odot}$ and $10^{-1} M_{\odot}$ they limit the total contribution of Machos to the dark matter

to be less than 20%. The MACHO collaboration also ran analysis in this mass range and found similar limits, for example objects in the $3.5 \times 10^{-7}\mathrm{M}_{\odot}$ to $4.5 \times 10^{-5}\mathrm{M}_{\odot}$ make up less than 10% of the dark matter [6].

2.3 Results on Dark Matter Towards M31

The MEGA [3] collaboration found 4 microlensing candidates on sources in the M31, the Andromeda galaxy. M31 microlensing is especially promising, since there is a clever way to distinguish halo lenses from disk lensing. Since M31 is tilted on the sky with respect to our location, the line-of-sight to the northeast side of M31 goes through the bulk of M31's dark matter halo, while the line-of-sight towards the southwest side of M31 does not. Thus if Machos make up the halo of M31, one expects many more events from the back side as compared to the front side. Three of the four events found by the MEGA collaboration are from the back side and one is from the front side. Thus they can then perform a likelihood analysis and find a Macho dark matter halo fraction of $f = 0.29^{+0.30}_{-0.13}$, consistent with the MACHO collaboration result. However, with only four events, this is not yet a very significant result.

On the other hand, the POINT-AGAPE [4] collaboration is also monitoring stars towards M31 and have found 3 events. They interpret these events as an upper limit and find $f < 0.25$ for $0.0001 < m < 0.1\mathrm{M}_{\odot}$, and $f < 0.6$, for $0.1 < m < 1\mathrm{M}_{\odot}$. Thus they find weak evidence against a Macho contribution to the M31 dark halo.

2.4 Summary of Halo Microlensing Results

Putting all the dark matter results together we plot Fig. 1 (by hand, for illustration purposes only!). Experimentally the situation is still not clear. We need more results and more conclusive results. A microlensing experiment from space such as DIME [7], if approved, could solve the problem by finding parallax events and solving for the distance to the lenses, or if we are willing to wait for the Space Interferometry Mission, the distances could be found using astrometric microlensing. If one can measure the distances to only 2 or 3 LMC lenses as being at 10 kpc, that would prove that substantial Macho dark matter exists. Alternatively, if the distances to 3 or 4 random LMC lenses were found to be at 50 kpc, the LMC seslf-lensing hypothesis would be proved. In the near term we are waiting for more results from the MEGA and POINT-AGAPE collaborations on M31 microlensing, and from the SuperMacho collaboration [8] for more LMC microlensing events.

Theoretically there are also problems. A 10% Macho contribution to the Milky Way dark halo is consistent with $\Omega_{baryon} = 0.04$, but such a contribution would cause problems with star and galaxy formation scenarios.

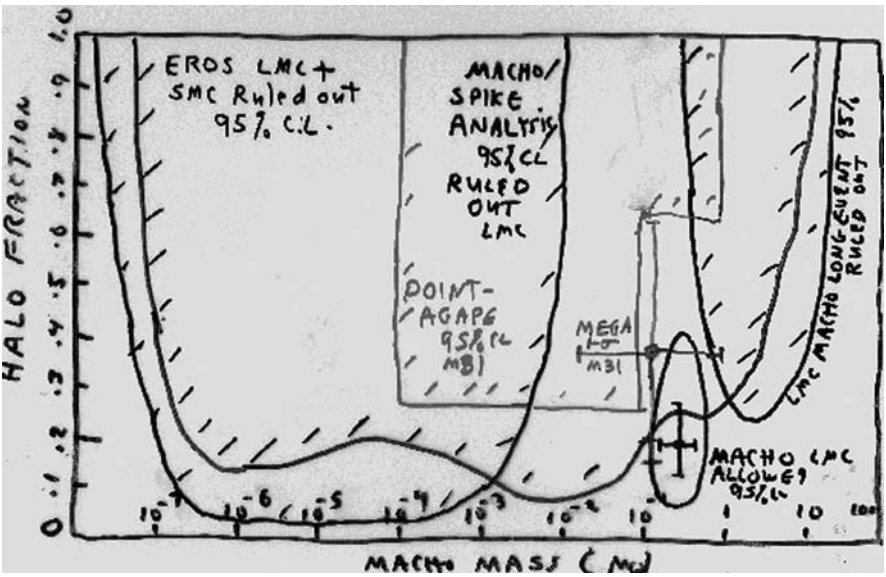

Fig. 1. Rough illustration of current limits on Macho dark matter.

3 Other Microlensing Results

While microlensing was originally conceived as a search for dark matter its sensitivity to all compact objects have made it useful for several other purposes.

3.1 Bulge Microlensing

Three collaborations have returned results on microlensing towards the center of the Milky Way galaxy: OGLE [9], EROS [10], and MACHO [11, 12]. When looking towards the bulge, one looks through the disk of the Galaxy where there are many stars to serve as lenses. So one expects there to be a large number of microlensing events in this direction [13, 14]. This has been born out in practice where there are now more than 1000 bulge microlensing events reported. Due to time, I will discuss only the recent work by the MACHO collaboration, where we reported on the final analysis of 7 years of monitoring over 50 million stars. We found over 450 high quality microlensing events, 60 of which were on clump giant source stars. We found around 40 potential binary lens events, events with parallax and extended source signals, as well as lensing of periodic variables. Using the 60 clump giant source events we calculated a new value for the optical depth towards the bulge. Clump giant stars are very bright and thus are much less affected by blending. Blending greatly complicates the calculation of optical depth because one does not know how many stars one is monitoring, and the microlensing fit parameters

are distorted if the source star is heavily blended. Our new optical depth measurement is currently the world's best and is

$$\tau = 2.18^{+0.45}_{-0.38} \times 10^{-6} \tag{2}$$

This value is smaller than previous MACHO collaboration measurements, larger the current EROS measurements, but very consistent with current model estimates (e.g. Gould and Han [15] $\tau = 1.63 \times 10^{-6}$). We also for the first time measured the optical depth as a function of galactic latitude, and reported on events that are probably from the Sag dwarf galaxy.

3.2 Planet Microlensing

This is a big subject now, and I won't have time to talk much about it. Suffice it to say that after years of effort, the first planet has now been discovered by microlensing. The event is OGLE 2003-BLG-23/ MOA 2003-BLG-53, and has a planet-star mass ratio of 0.0039. Since the star has a likely mass of $0.4M_{\odot}$, this means that the planet has a likely mass of our 1.5 Jupiter masses. It is also seems that the future of planet finding by microlensing is in space. Several missions have been proposed, and studies have been done. It is clear that for Earth mass planets microlensing is the most sensitive of any proposed planet finding method, especially for planets that are a distance of 1AU or more from their stars.

4 Lensing and Substructure

Very briefly, let me mention one other lensing subject that is very relevant to dark matter. This is work done by my student Neal Dalal when he was at UCSD, as well as Chris Kochanek of Harvard. In my opinion, this work, (which was done also by several other groups) solved one of the nagging problems of the cold dark matter (CDM) structure formation scenario.

For some time now, N-body simulations of dark matter halos of large galaxies show that these form by aggregating many smaller dark matter halos. The net result of this hierarchical clustering is that a dark matter halo for a galaxy such as the Milky Way consists of a smooth dark matter component as well as hundreds of smaller sub-halos that have not yet been disrupted. The problem with this scenario, is that the Milky Way galaxy does not have hundreds of dwarf galaxies swarming around it, but only a handful. This order-of-magnitude discrepency between the predictions of the CDM simulations and the observations has led to suggestions that the CDM scenario may be wrong.

What Dalal and Kochanek (along with others such as Metcalf) did was show that these dark matter sub-halos do in fact exist, even though no visible dwarf galaxy can be seen. They did not do this for the Milky Way galaxy,

but for distant galaxies that are acting as gravitational lenses for background quasars. They noted that when workers tried to model the mass distribution of the lenses, they typically had a hard time finding an adequate model. In particular when two of the lens images of the galaxy are very near each other, one can show that any smooth mass distribution predicts the image brightnesses should be the same. In many observations, this was not the case. Dalal, Kochanek, Metcalf, and others realized that one possible cause of this was small scale structure in the mass distribution, that is, sub-halos. They calculated what fraction of the total halo mass would have to be in sub-structure to match the frequency of the quasar image mis-matches and found a number (2%) that was in good agreement with the predictions from the CDM simulations. There were several other potential explanation of the lensing observations, but these have been gradually ruled-out, leaving the halo sub-structure explanation as the most likely.

5 Conclusions

Lensing has a bright future for the observation of dark objects. It actually can't be beat for this purpose, and will probably become more and more important in the future. We see several large projects that will have lensing as a main component: SIM, LSST, SNAP, etc. and expect that more will be conceived of in the future.

References

1. Alcock, et al., ApJ, 542, 281 (2000)
2. Lasserre, T., et al., A&A, 355, L39 (2000)
3. deJong, J.T.A. et al., A&A, 417. 461 (2004)
4. Paulin-Henriksson, S., et al., A&A, 405, 15 (2003)
5. Sahu, K.C., Nature, 370, 275 (1994)
6. Alcock, C., et al., ApJ Lett. 499, L9 (1998)
7. Cook, K., et al., BAAS, 20314302 (2003)
8. Becker, A.C., et al. 2004, Impact of Gravitational Lensing on Cosmology, Proceedings IAU Symposium No. 225 (2004)
9. Udalski, A., et al., Acta Astron., 50, 307 (2000)
10. Afonso, C., et al. 2003, A&A, 404, 145
11. Thomas, C.L. astro-ph/410341 (2004)
12. Popowski, P. astro-ph/410309 (2004)
13. Griest, K. et al. ApJ, 372, L79 (1991)
14. Paczyński, B. ApJ, 371, L63 (1991)
15. Han, C, & Gould, A., ApJ, 592, 172 (2003)

Cosmological Interpretation from High Redshift Clusters Observed within the XMM-Newton Ω-Project

Alain Blanchard

LATT, UPS, CNRS, UMR 5572, 14 Av Ed.Belin, 31 400 Toulouse, France
alain.blanchard@ast.obs-mip.fr

Summary. During the last ten years astrophysical cosmology has brought three remarkable results of deep impact for fundamental physics: the existence of non-baryonic dark matter, the (nearly) flatness of space, the domination of the density of the universe by some gravitationally repulsive fluid. This last result is probably the most revolutionizing one: the scientific review *Sciences* has considered twice results on this question as *Breakthrough of the Year* (for 1998 and 2003). However, direct evidence of dark energy are still rather weak, and the strength of the standard scenario relies more on the "concordance" argument rather than on the robustness of direct evidences. Furthermore, a scenario can be build in an Einstein–de Sitter universe, which reproduces as well as the concordance model the following various data relevant to cosmology: WMAP results, large scale structure of the universe, local abundance of massive clusters, weak lensing measurements, most Hubble constant measurements not based on stellar indicators. Furthermore, recent data on distant x-ray clusters obtained from XMM and Chandra indicates that the observed abundances of clusters at high redshift taken at face value favors an Einstein de Sitter model and are hard to reconcile with the concordance model. It seems wise therefore to consider that the actual existence of the dark energy is still an open question.

1 Introduction

1.1 On the Determination of Cosmological Parameters

The determination of cosmological parameters has always been a central question in cosmology. However, this problem has become more and more important in recent years due to the deep implications it can lead to. One of the most spectacular results established in recent years are for instance the existence of a dominant form of non-baryonic matter in the clustered content of the universe. After a very long debate on whether evidence for non baryonic dark matter universe were sufficiently robust, it is nowadays almost unanimously admitted that there are enough evidences to consider it as an established fact (such a conclusion has strongly contributed to emphasize the deep couplings that exist between astrophysical cosmology and fundamental physics). As long as no direct evidence is found (from laboratory experiments)

doubts are still possible and indeed few researchers still maintain the point of view that modified theories of gravitation could do the job as well.

A second essential result in recent modern cosmology is the evidence for the (nearly) flatness of the Universe which comes from the C_l curve of the CMB. The Saskatoon experiment was probably the first one to provide evidence for the presence of a peak around $l \sim 200$ [34], which was shown to provide a statistically significant indication for the flatness of the universe, a conclusion drawn as early as 1997: [28] see also [22]. This conclusion has been firmly established by second generation experiments, including those of Boomerang [14], Maxima [21], DASI [20], Archeops [2], allowing tight cosmological constraints [3]. Of course all these results have been superseded by WMAP measurements [26, 4]. It should be realized that these CMB measurements provide an observation (basically the position of the Doppler peak) which is predicted by models, involving standard physics, consistent with flat models. It is not a direct measurement of curvature of space (as could be obtained from a triangulation measurement for instance). The two above results are therefore the unavoidable consequences of the existing observations, if they have to be interpreted within standard physics as we know it by now. Rejecting these conclusions is possible, but only at the expense of modifying fundamental laws of physics as we know them by now.

The third result which has emerged in recent years, and which is revolutionizing for fundamental physics : the dominance of the density of the universe by some "dark energy", i.e. a fluid with very exotic equation of state: $p = w\rho c^2$ with $w \sim -1$ [16, 49]. There is a large consensus around this so-called concordance model, which leads to the idea that the determination of cosmological parameters has been achieved with a rather good precision, may be of the order of 10%. Indeed this model does fit an impressive set of independent data, the most impressive been: local estimation of the density of the universe, CMB C_l curve, most current matter density estimations, Hubble constant estimation from HST, apparent acceleration of the Universe, good matching of the power spectrum of matter fluctuations. However, the necessary introduction of a non zero cosmological constant is an extraordinary new mystery for physics, or more exactly the come back of one of the ghost of modern physics since its introduction by Einstein. Here the situation is slightly different from the two previous cases: the introduction of a non-vanishing cosmological constant is a major modification of a fundamental law of physics (gravity). Although the cosmological constant certainly allows one to fit easily the Hubble diagram of distant SNIa, its introduction is not unavoidable, given the data. Rather, trusting fundamental physical laws as we know them lead to the conclusion that distant SNIa are, for some unknown reason, intrinsically fainter than local ones. There is no argument that dismiss this "fact". Therefore, in order for the SNIa Hubble diagram to be regarded as a convincing evidence for a cosmological constant, one should provide a convincing independent evidence that the luminosity of a distant SNIa is

directly comparable to a local one without any correction. It is therefore the opinion of the author, that in order to consider SNIa as an argument in favor a cosmological constant, evidence for the absence of astrophysical corrections to SNIa luminosity has to be demonstrated (and one should remember there that the "absence of evidence " is not "an evidence of absence"...).

The possible detection of a cosmological constant from distant supernovae has brought the first direct piece of evidence largely comforting the so-called concordance model: the apparent luminosity of distant supernovae now appears fainter, i.e. at larger distance, than expected in any decelerating universe [42, 39] and can therefore be explained only within an accelerating universe. There is a set of fundamental assumptions in this reasoning, that is that SNIa are standard candles which are not affected by any bias, any evolution, any obscuration. Although the data are well consistent with this hypothesis, it is almost impossible to demonstrate that it is actually right, i.e. that data are not biased by some astrophysical process. A more problematic point is that astrophysical processes in an Einstein de Sitter universe, if roughly proportional to the look back time may mimic rather well an apparent cosmological constant, producing an Hubble diagram that is almost indistinguishable from the standard diagram of the concordance model (see Fig. 1). This means that SNIa argument is relatively weak by

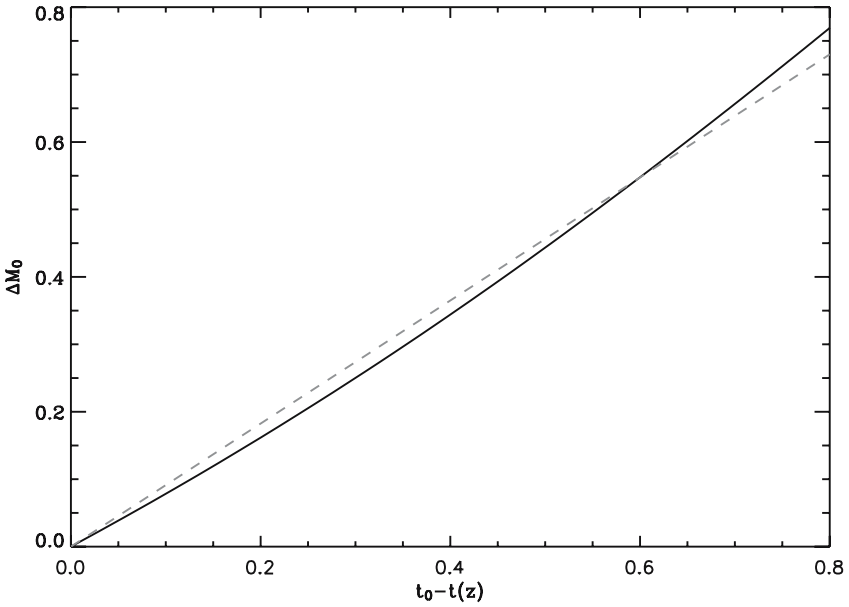

Fig. 1. Difference of magnitude between an Einstein de Sitter Universe and the concordance (full line) versus look back time. Any process which would produce an apparent dimming proportional to this look back time may mimic the presence of a cosmological constant (dashed line).

itself. For instance would the SNIa Hubble diagram points toward a negative matter content, $\Omega_m < 0.$, it would probably be interpreted by everybody as an evidence for some astrophysical process affecting SNIa luminosity...

I have already discussed in some detail the various arguments that may raise doubts on the validity of the concordance model [6, 5] (before WMAP results): for most observations which match the concordance model, there is some other evidences which go in a different direction (for instance different upper limits on the cosmological constant uncomfortably below the present preferred value were published in the past, including one coming from the SNIa in the SCP! [38]. I would like to add one recent example: the Hubble constant. Several measurements based on non stellar distance indicators lead to a lower value for Hubble constant than that has been derived from HST key-Project [19]. A recent analysis of the Cepheid distances suggests that one bias exist which when corrected would lead to a value 20% lower for the Hubble constant [37]. Such a value would imply, in combination with CMB a matter density parameter close to 0.5, ruining the nice concordance of the standard paradigm.

1.2 What the CMB does Actually Tell Us?

Since the discovery of the CMB fluctuations by COBE [48] the idea that early universe physics has left imprints revealed by these fluctuations has gained an enormous attention. In this respect, DMR results have played a fundamental role in modern cosmology comparable to the discovery of the expansion of the universe or the discovery of the microwave background by Penzias and Wilson. The remarkable results of the WMAP experiment, are often quoted as providing a direct evidence for an accelerating universe. This is incorrect: cosmological constraints as established by the WMAP team [49] entirely rely on the powerlaw spectrum asumption. Therefore these conclusions could be erroneous [27, 23]. Indeed, relaxing this hypothesis, i.e; assuming non power law power spectrum allows to produce C_l curve which as good as the concordance model. This is illustrated by Fig. 2 on which 3 models are compared to the WMAP data, two being Einstein de Sitter models. Such models not only reproduce the TT spectrum, but are also extremely close in term of ET and EE spectra. Furthermore the matter power spectrum are similar on scales probed by current galaxies surveys. An un-clustered component of matter like a neutrino contribution or a quintessence field with $w \sim 0$ is necessary to obtain an acceptable amplitude of matter fluctuations on clusters scales [9]. Such models require a low Hubble constant $\sim$ 46 km/s/Mpc. Such a value might be look as terribly at odd with central HST key program value ($\sim$ 72 km/s/Mpc) but is actually only $\sim 3\sigma$ away from this value. Given the above mentioned uncertainties (which raised the preferred value to lie $\sim 1.75\sigma$ away, this can certainly not be considered as a fatal problem for an Einstein-de Sitter universe. The introduction of non-power law power spectrum might appear as unnatural. This is a somewhat subjective question.

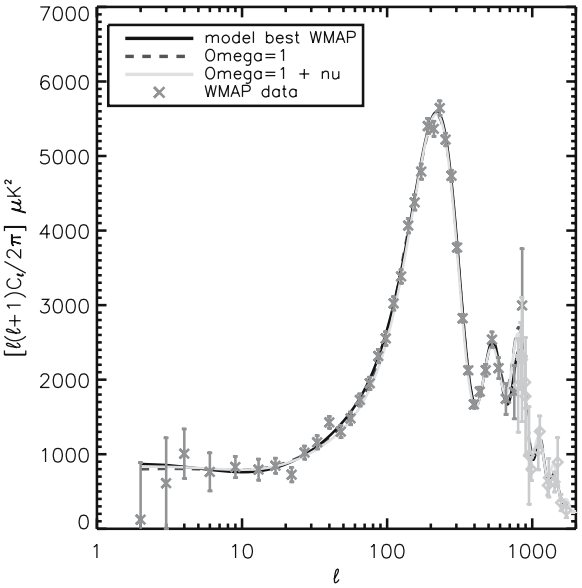

Fig. 2. The TT spectrum of the WMAP data compared to three different models: one is the concordance, the two others are Einstein de Sitter models, one of which comprises neutrino contribution of $\sim 10\%$ corresponding to three degenerate families with $m_\nu \sim 0.7$eV. Courtesy of M.Douspis.

However, present measurement of C_l curve is testing the initial spectrum over 3 order of magnitude in length. The existence of distinct features in the primordial spectrum are suggested by present WMAP data [50], which could be the consequences of early physics on super-Planck scales [32], as scales which are now accessible to the observations are very likely to be sub-planckian before inflation. This argument could be regarded as an argument for which non-power-law models are to be preferred (although this is not giving any support to our –specific– model, given our poor knowledge of the relevant physics). This argument is strengthened by the global value of the χ^2 from the WMAP C_l : a point that is not much emphasized, is that the global value of the χ^2 is not good. In fact, the χ^2 for TT data has only a probability of 3% [49]. The conclusion in such a situation is that the hypotheses in the model are probably to be abandoned! An other option is that the data are still suffering from unsubstracted systematics (which is the proposed explanation given by the WMAP team).

1.3 Motivation for the XMM-Ω Project

If one keeps an open mind, one should consider that the existence of a cosmological constant is not yet a scientific fact established beyond reasonable

doubt or to be more precise, that the case for its actual existence is not as strong as the case for non-baryonic dark matter (furthermore it is always healthy to have an alternative model to the dominant paradigm). It is therefore of high interest to have a reliable measurement of the matter content of the universe, which in conjunction with the CMB data provides a case for or against a non-vanishing cosmological constant, depending on the value obtained for Ω_M. Most of existing measurements are local in nature, i.e. they actually provide mass to light ratio (M/L) from finite and relatively small entities, like clusters, which occupy a tiny fraction of the universe: massive clusters cover only 10^{-5} of the total volume of space! Therefore using the M/L argument relies on an extrapolation over five orders of magnitude... The baryon fraction has been argued as favoring a low density universe. However, this relies on some specific value of the estimation of mass of x-ray clusters which is uncertain. Consequently, given this uncertainty the baryon fraction is actually consistent as well as with a high density universe [44].

The evolution of the number of clusters of a given mass is a sensitive function of the cosmological density of the Universe, very weakly depending on other quantities when properly normalized [7], therefore offering a powerful cosmological test [35]. The XMM-Ω project [1] was designed in order to provide an accurate estimation of the possible evolution of the luminosity–temperature relation at high redshift for clusters of medium luminosity which constitutes the bulk of X-ray selected samples, in order to remove a major source of degeneracy in the determination of Ω_M from cluster number counts in flux limited number counts.

2 Observed Evolution of the $L - T$ Relation of X-ray Clusters

For the first time a measurement of the $L - T$ evolution with XMM has been obtained. D.Lumb et al. (2004) [30] present the results of the X-ray measurements of 8 distant clusters with redshifts between 0.45 and 0.62. By comparing to various local $L-T$ relations, clear evidence for evolution in the $L - T$ relation has been found. The possible evolution has been modeled in the following way:

$$L_{\rm x} = L_6(0) \left(\frac{T}{6{\rm keV}} \right)^{\alpha} (1+z)^{\beta} \qquad (1)$$

where $L_6(0) \left(\frac{T}{6keV}\right)^{\alpha}$ is the local $L-T$ relation. β is found to be of the order of 0.6 ± 0.3 in an Einstein-de Sitter cosmology [30, 52]. This result is entirely consistent with previous analyzes [45, 56] and others XMM data (see Fig. 3).

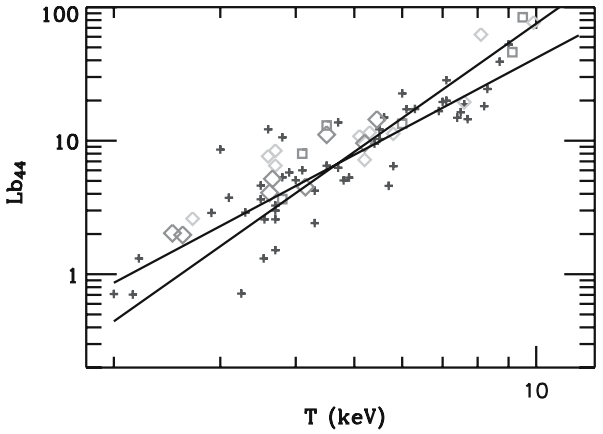

Fig. 3. Temperature–luminosity of X-ray clusters: crosses are local clusters from a flux selected sample [10], grey diamonds are distant clusters from Chandra [56] in the redshift range $0.4 \leq z \leq 0.625$, large dark diamonds are clusters from the XMM Ω project, squares are other XMM clusters within the same redshift range.

3 Cosmological Interpretation

Attempts to apply directly the test of the evolution of the abundance of clusters have been performed but still from a very limited number of clusters (typically 10 at redshift 0.35) [25, 18, 51, 10]. In [10] it was found that $\Omega_M = 0.86 \pm 0.25$ (1σ), so that a concordance model is away at only a 2-σ level, while systematics differences explain the values obtained from the various authors. On the other hand, number counts allow one to use samples comprising much more clusters. Indeed using simultaneously different existing surveys: EMSS, SHARC, RDCS, MACS NEP and 160 deg^2 [24, 43, 41, 17, 33, 55] one can use information provided by more than 300 clusters with $z > 0.3$ (not necessarily independent). In order to model clusters number counts, for which temperatures are not known, it is necessary to have a good knowledge of the $L - T$ relation over the redshift range which is investigated, which information has been provided by XMM and Chandra. Number counts can then be computed:

$$\begin{aligned} N(> f_x, z, 2\Delta z) = & \quad \Omega \int_{z-\Delta z}^{z+\Delta z} \frac{\partial N}{\partial z}(L_x > 4\pi D_l^2 f_x) dz \\ = & \quad \Omega \int_{z-\Delta z}^{z+\Delta z} N(> T(z)) dV(z) \\ = & \; \Omega \int_{z-\Delta z}^{z+\Delta z} \int_{M(z)}^{+\infty} N(M, z) dM dV(z) \end{aligned} \tag{2}$$

where $T(z)$ is the temperature threshold corresponding to the flux f_x as given by the observations, being therefore independent of the cosmological model. For most surveys the above formula has to be adapted to the fact that the area varies with the flux limit, and eventually with redshift. Several

ingredients are needed: the local abundance of clusters as given by the temperature distribution function ($N(T)$), the mass-temperature relation and its evolution, the mass function and the knowledge of the dispersion. Uncertainties in these quantities result in -systematics- uncertainties in the modeling which have been found to be comparable to statistical uncertainties. Figure 4

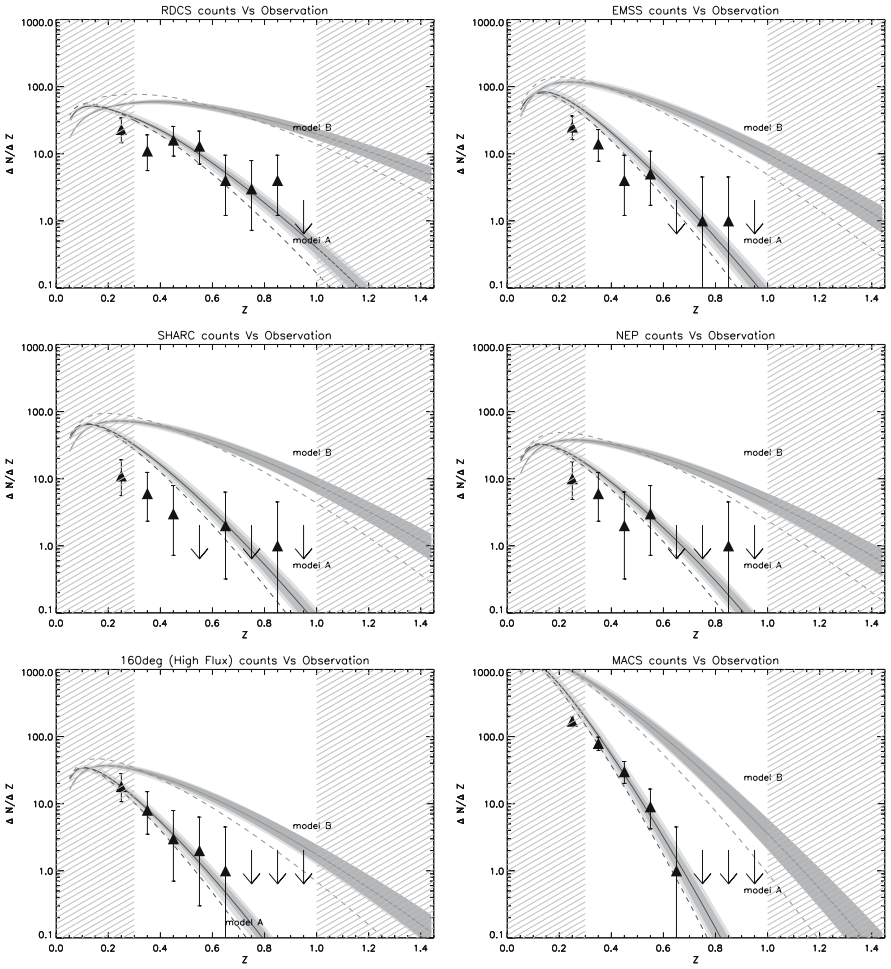

Fig. 4. Theoretical number counts in bins of redshift ($\Delta z = 0.1$) for the different surveys: RDCS, EMSS, MACS and 160deg^2-high flux (corresponding to fluxes $f_x > 2\,10^{-13}$ erg/s/cm^2). Observed numbers are triangles with 95% confidence interval on the density assuming poissonian statistics (arrows are 95% upper limits). The upper curves are the predictions in the concordance model (model B). The lower curves are for critical universe (model A). Uncertainties on σ_8 and on $L{-}T$ evolution lead to the grey area (see [53]).

illustrates [53] the counts obtained with a standard mass temperature relation:

$$T = 4\mathrm{keV} M_{15}^{2/3}(1+z) \tag{3}$$

the SMT mass function [47], and the $L-T$ relation observed by XMM with its uncertainty. These counts were computed for different existing surveys to which they can be compared. Several likelihood analyzes have been performed. Among the various conclusions that were found are: all existing x-ray clusters surveys systematically point toward high Ω_M, statistical uncertainties allow a determination of Ω_M with a 10% precision: $0.9 < \Omega_M < 1.07(1\sigma)$. During this analysis numerous possible source of systematics were investigated with great detail (local samples, normalization of the $M-T$ relation, local $L-T$ relation, dispersion in the various relations). The dominant source of systematic uncertainty is coming from the uncertain calibration of the mass temperature relation. This uncertainty can be greatly removed using the method based on a self consistent adjustment to the baryon fraction [8]. With this method the likelihood obtained is wider and the precision is decreased down to 15% (see Fig. 5). In addition the distribution is non-Gaussian: with the above prescription, although one conclude that $\Omega_M \sim 0.975 \pm 0.15$, the concordance model is still ruled out at 7σ level. Remaining systematics have been added in quadrature and are also representing roughly an additional 15% uncertainty. This means that global uncertainty is roughly 20%. We have also check that the local luminosity in our models is in good agreement with local surveys (without requesting it explicitly).

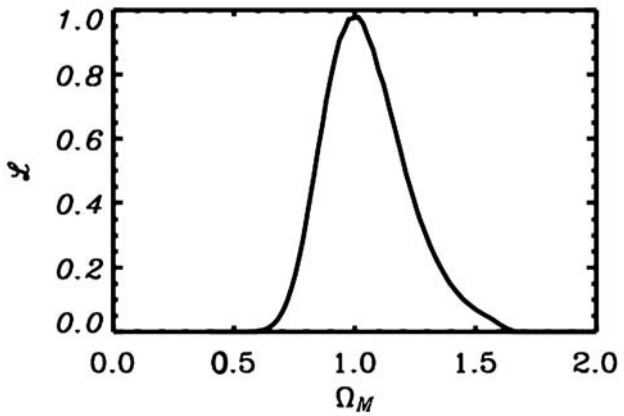

Fig. 5. Final likelihood from x-ray cluster number counts obtained with independent samples: MACS, EMSS, NEP, 160 deg^2. The $M-T$ relation was treated self consistently as in [8].

4 Looking for Loopholes

4.1 Systematics

I have mentioned above that the source of various systematics have been investigated and lead to a $\sim 17\%$ uncertainty. This value is larger than the statistical uncertainty $\sim 10\%$. It is therefore very important to investigate one by one this systematics and what typical amplitude may restore the concordance. Special attention has been paid to selection functions. For instance if flux limit, or identically flux calibration in faint surveys, is erroneous by a factor of 2–3 the concordance would be much closer to existing surveys. However typical uncertainty is considered to be of the order of 20%. This provides a typical number: if the value of one of the systematic effects is ten times larger than estimated amplitude, then the concordance would accommodate the data.

4.2 Comparison with Previous Works

A comment that is heard sometimes in conferences, is that we are the only group who find such a high value for Ω_M. This an incorrect statement: when dealing with the $N(T)$ evolution, [54] did found a high central value, close to our best one. Major differences with previous analyzes to [10] were explained in term of systematics. As those results lie within the 2σ range found in [10], one can conclude that the problem is yet open. However, the redshift distribution of X-ray clusters using normalization from the local temperature distribution has been investigated in the past. With the analysis presented in [36, 45], there has been three different independent analyzes [11, 40], each leading to consistent results with EMSS as well as with ROSAT. All these analyzes indicate that redshift number counts are consistent with a high Ω_M and at odd with value of the order of 0.3 (note that [12] have obtained an acceptable fit to RDCS distribution, but at the price of unacceptable local abundance).

Our new analyzes basically recover identical results to the one mentioned above. However, the statistical significance is now much better: these samples contains ~ 300 clusters. Each sample is individually well fitted, this is a very important point: any large unidentified systematics affecting data, would have to affect the different surveys (from different groups and different methodology, on both ROSAT and EMSS data) in different way to mimic the Einstein de Sitter case, a somewhat tricky coincidence. I conclude that this new analysis is much mores robust than previous one, both in term of statistic and in term of control on systematics.

4.3 Is Cluster Gas Physics Essentially Non-Gravitational?

We have identified only one possible realistic way to reproduce number counts in a concordance model, that is by assuming that the redshift evolution of

the $M-T$ relation is not standard:

$$T \propto M_{15}^{2/3} \tag{4}$$

(i.e. removing the standard $1+z$ factor appearing in equation 3). This is conceivably possible if a large fraction of the thermal energy of the gas in present day clusters originates from other processes than the gravitational collapse and has been continuously injected during recent past (although it remains to be shown that this is actually possible in a realistic way). It is possible to test observationally this latter possibility: heating processes of the gas will obviously heat the gas but not galaxies. The quantity:

$$\beta^{-1} \propto \frac{T_x}{\sigma^2}$$

should therefore evolve with redshift accordingly to $(1+z)^{-1}$ if the $M-T$ relation evolved accordingly to the above non-standard scheme while it should remains constant in the standard case. Note that this conclusion persists even if galaxies velocity dispersion are a biased version of the dark matter one [15]. In order to test whether existing data do provide some indication on such a possible evolution, we have collected some existing measurements of velocity dispersion σ for massive clusters using BAX cluster data base [46] with further recent measurements: we selected clusters with temperature greater than 6 keV for which velocity dispersion was available. The result is shown on Fig. 6. We found no sign of such a non-standard behavior which is in principle ruled out at the 3–σ level at least.

5 Conclusions

The major results obtained with the Ω project are the first XMM measurement of the evolution of the luminosity-temperature with redshift. A positive evolution has been detected, in agreement with previous results including those obtained by Chandra [56]. The second important result is that this evolving $L-T$ produced counts in the concordance model which are inconsistent with the observed counts in all existing published surveys. This is in principle the signature of a high density universe, but might be as well due to a deviation of the expected scaling of the $M-T$ relation with redshift. Our investigation of the ratio $\frac{T_x}{\sigma^2}$ shows no sign of such deviation. Therefore, the distribution of x-ray selected clusters as known at present day favors a high density universe, alleviating the need for a cosmological constant.

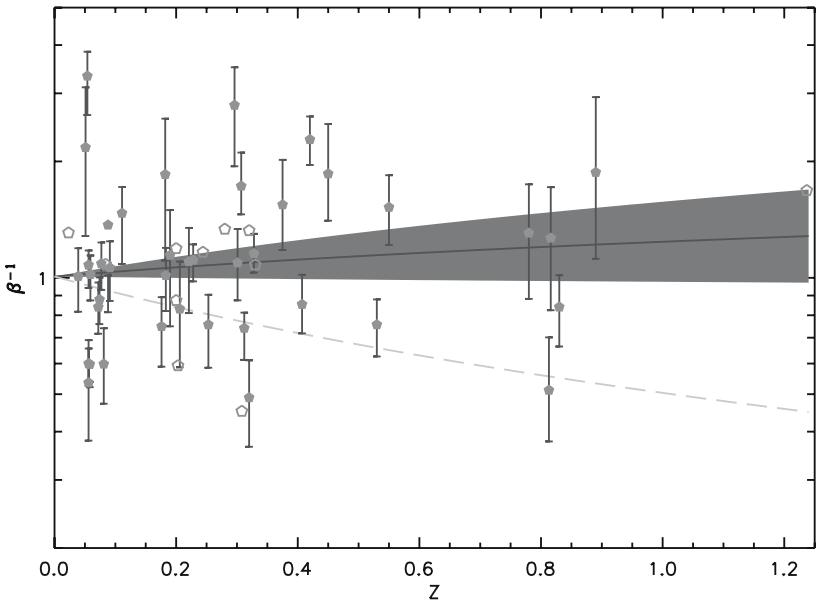

Fig. 6. The ratio between thermal energy of the gas measured by T_x and the kinetic energy of galaxies measured by their velocity dispersion for a sample of clusters with $T_x \geq 6$ keV with redshift spanning from 0 to 1.2. No sign of evolution is found. The best fit is the continuous line, grey area is the formal one σ region, dashed line is the level necessary to make the concordance in agreement with the x-ray clusters counts.

References

1. J. Bartlett et al.: proceedings of the XXIth rencontres de Moriond, astro-ph/0106098 (2001)
2. A. Benoît et al.: astro-ph/0210305, A&A **399**, L19 (2003)
3. A. Benoît et al.: astro-ph/0210306, A&A **399**, L25 (2003)
4. C. L. Bennett et al.: ApJS **148**, 97 (2003)
5. A. Blanchard: Ap&SS **290**, 135 (2004)
6. A. Blanchard: proceedings of the Faro Conference "New Worlds in Astroparticle Physics", 2002, astro-ph/0301137, World Scientific edt, pp 50–69. (2003)
7. A. Blanchard, J. Bartlett: A&A **332**, 49L (1998)
8. A. Blanchard, M. Douspis: astroph/0405489 A&A submitted (2005)
9. A. Blanchard, M. Douspis, M. Rowan-Robinson, S. Sarkar: A&A **412**, 35 (2003)
10. A. Blanchard, R. Sadat, J. Bartlett., M. Le Dour: A&A **362**, 809 (2000)
11. S. Borgani et al.: ApJ **517**, 40 (1999)
12. S. Borgani et al.: ApJ **561**, 13 (2001)
13. S. Boughn, R. Crittenden: Nature **427**, 45 (2004)
14. P. de Bernardis et al.: Nature **404**, 955 (2000)
15. J. Diemand, B. Moore, J. Stadel: MNRAS **352**, 535 (2004)
16. M. Douspis, A. Riazuelo, Y. Zolnierowski, A. Blanchard: A&A **405**, 409 (2003)

17. H. Ebeling, A. C. Edge, J. P. Henry: ApJ **553**, 668 (2001)
18. V. R. Eke, S. Cole, C. Frenk, J. P. Henry: MNRAS **298**, 1145 (1998)
19. W. L. Freedman, et al.: ApJ **553**, 47 (2001)
20. N. W. Halverson et al.: ApJ **568**, 38 (2002)
21. S. Hanany, et al.: ApJ **545**, L5 (2000)
22. S. Hancock, G. Rocha, A. N. Lasenby, C. M. Gutierrez: MNRAS **294**, L1 (1998)
23. S. Hannestad: PRD **63**, 043009 (2001)
24. J. P. Henry, I. M. Gioia, T. Maccacaro et al.: ApJ **386**, 408 (1992)
25. J. P. Henry: ApJ **489**, L1 (1997)
26. G. Hinshaw et al.: ApJS **148**, 135 (2003)
27. W. H. Kinney: PRD **63**, 043001 (2001)
28. C. Lineweaver, D. Barbosa, A. Blanchard, J. Bartlett: A&A **322**, 365 (1997)
29. C. Lineweaver, D. Barbosa, ApJ **496**, 624 (1998)
30. D. H. Lumb et al.: A&A **420**, 853 (2004)
31. A. Markevitch: ApJ **504**, 27 (1998)
32. J. Martin, R. H. Brandenberger: PRD **63**, 123501 (2001)
33. C. R. Mullis et al.: ApJ **594**, 154 (2003)
34. C. B. Netterfield et al.: ApJ **445**, L69 (1995)
35. J. Oukbir, A. Blanchard: A&A **262**, L21 (1992)
36. J. Oukbir, A. Blanchard: A&A **317**, 10 (1997)
37. G. Paturel, P. Teerikorpi: A&A **413**, L31 (2004)
38. S. Perlmutter et al.: ApJ **483**, 565 (1997)
39. S. Perlmutter et al.: ApJ **517**, 565 (1999)
40. Reichart, D. E. et al.: ApJ **518**, 521 (1999)
41. P. Rosati et al.: ApJ **492**, L21 (1998)
42. D. Reiss et al.: AJ **116**, 1009 (1998)
43. A. K. Romer et al.: ApJS **126**, 209 (2000)
44. R. Sadat, A. Blanchard: A&A **371**, 19 (2001)
45. R. Sadat, A. Blanchard, J. Oukbir: A&A **329**, 21 (1998)
46. R. Sadat, A. Blanchard, J.-P. Kneib, G. Mathez, B. Madore, J. M Mazzarella: `http://bax.ast.obs-mip.fr/` A&A **424**, 1097 (2004)
47. R. K. Sheth, H. J. Mo, G. Tormen: MNRAS **323**, 1 (2001)
48. G. F. Smoot et al.: ApJL **396**, L1 (1992)
49. D. N. Spergel et al.: ApJS **148**, 175 (2003)
50. D. Tocchini-Valentini, M. Douspis, J. Silk: astro-ph/0402583, MNRAS to be published (2005)
51. T. P. Viana, A. R. Liddle: MNRAS **303**, 535 (1999)
52. S. C. Vauclair et al.: A&A **412**, L37 (2003)
53. S. C. Vauclair et al.: in preparation (2005)
54. P. T. P. Viana, A. R.Liddle: MNRAS **303**, 535 (1999)
55. A. Vikhlinin et al.: ApJ **502**, 558 (1998)
56. A. Vikhlinin et al.: ApJL **578**, 107 (2002)

Wakes in Dark Matter Halos

Burkhard Fuchs

Astronomisches Rechen-Institut, Mönchhofstr. 12-14, 69120 Heidelberg, Germany
fuchs@ari.uni-heidelberg.de

Summary. I discuss the dynamical interaction of galactic disks with the surrounding dark matter halos. In particular it is demonstrated that if the self–gravitating shearing sheet, a model of a patch of a galactic disk, is embedded in a live dark halo, this has a strong effect on the dynamics of density waves in the sheet. I describe how the density waves and the halo interact via halo particles either on orbits in resonance with the wave or on non-resonant orbits. Contrary to expectation the presence of the halo leads to a very considerable enhancement of the amplitudes of the density waves in the shearing sheet. This effect appears to be the equivalent of the recently reported enhanced growth of bars in numerically simulated stellar disks embedded in live dark halos. Finally I discuss the counterparts of the perturbations of the disk in the dark halo.

1 Introduction

Dark halos are usually thought to stabilize galactic disks against non-axisymmetric instabilities. This was first proposed by Ostriker & Peebles (1973) on the basis of – low–resolution – numerical simulations. Their physical argument was that the presence of a dark halo reduces the destabilizing self–gravity of the disks. Doubts about an entirely passive role of dark halos were raised by Toomre (1977), but he (Toomre 1981) also pointed out that a dense core of a dark halo may cut the feed–back loop of the corotation amplifier of bars or spiral density waves and suppress thus their growth. Recent high-resolution numerical simulations by Athanassoula (2002, 2003), also inherent in the work of Debattista & Sellwood (2000), have shown that quite the reverse, a *destabilization* of disks immersed in dark halos, might be actually true. Athanassoula (2002) demonstrated clearly that much stronger bars grow in the simulations if the disk is embedded in a live dark halo instead of a static halo potential. This is attributed to angular momentum transfer from the bar to the halo via halo particles on resonant orbits. Angular momentum exchange between disk and halo has been addressed since the pioneering work of Weinberg (1985) in many studies theoretically or by numerical simulations and I refer to Athanassoula (2003) for an overview of the literature. Toomre (1981) has shown how the bar instability can be understood as an interference of spiral density waves in a resonance cavity between the corotation amplifier and an inner reflector (cf. also Fuchs 2004b). Thus it is to be expected that

a live dark halo will be also responsive to spiral density waves and develop wakes. That this is indeed the case has been demonstrated by Fuchs (2004a) employing the shearing sheet model. This adds to the confidence in the results of the numerical work on bar growth in galactic disks.

The shearing sheet (Goldreich & Lynden–Bell 1965, Julian & Toomre 1966) model has been developed as a tool to study the dynamics of galactic disks and is particularly well suited to describe theoretically the dynamical mechanisms responsible for the formation of spiral arms. For the sake of simplicity the model describes only the dynamics of a patch of a galactic disk. It is assumed to be infinitesimally thin and its radial size is assumed to be much smaller than the disk. Polar coordinates can be therefore rectified to pseudo-Cartesian coordinates and the velocity field of the differential rotation of the disk can be approximated by a linear shear flow. These simplifications allow an analytical treatment of the problem, which helps also in the present case to clarify the underlying physical processes operating in the disk.

2 Shearing Sheet Model

The basic disk model is the stellardynamical shearing sheet, which describes the local dynamics of a patch of a thin, differentially rotating stellar disk. Stellar orbits are calculated in a frame at a distance r_0 from the galactic center, rotating with an angular velocity Ω_0. Pseudo–Cartesian coordinates x and y point in the radial direction and tangential to the direction of galactic rotation, respectively. The differential rotation of the disk is approximated as a parallel shear flow, $v = -2Ax$, with A denoting Oort's constant. The surface density Σ_0 is assumed to be constant over the entire region. As is well known (cf. Julian & Toomre 1966) the stellar orbits in this model are simply epicyclic orbits and the phase space distribution function of the stars f_0, as derived from the time-independent Boltzmann-equation, is a Schwarzschild-distribution. A cartoon of the shearing sheet model is shown in Fig. 1.

The disk is subjected to potential perturbations

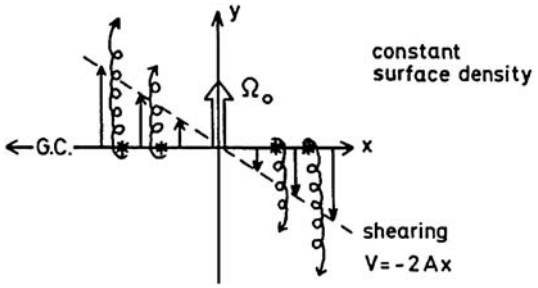

Fig. 1. The shearing sheet model.

$$\delta\Phi = \int d\omega \int dk_{\rm x} \int dk_{\rm y} \Phi_{\mathbf{k},\omega} e^{i(\omega t + k_{\rm x} x + k_{\rm y} y)}, \tag{1}$$

and the response of the disk, f_1, is calculated from the linearized Boltzmann-equation

$$\frac{\partial f_1}{\partial t} + [f_0, \delta\Phi] + [f_1, H_0] = 0\,, \tag{2}$$

written in general form with Poisson brackets. H_0 denotes the Hamiltonian of the stellar orbits in the unperturbed disk. In order to obtain self–consistent perturbations the response density has to be inserted into the Poisson-equation

$$\Delta\delta\Phi = 4\pi G \int d^2 v f_1, \tag{3}$$

where G is the constant of gravitation. Unfortunately, the disk response to a single Fourier component of the potential perturbation (1) is not a Fourier component of the general disk response. I follow therefore Kalnajs (1971) and take scalar products,

$$\frac{1}{4\pi^2} \int dx \int dy\, e^{-i(k'_{\rm xx} + k'_{\rm y} y)} \ldots\,, \tag{4}$$

of both sides of the Poisson-equation with conjugate basis functions of the Fourier transform. Details of the evaluation of the quadratures, which are carried out using action and angle variables are given in (Fuchs 2001). The result is that the Poisson-equation is converted to an integral equation of Volterra-type, which is equivalent to the integral equation given by Julian & Toomre (1966), although it is not formulated in shearing coordinates,

$$\Phi_{\mathbf{k}',\omega} = \int_{-\infty}^{k'_{\rm x}} dk_{\rm x} \mathcal{K}(k_{\rm x}, k'_{\rm x}, k'_{\rm y}, \omega) \Phi_{{\rm k_x},{\rm k'_y},\omega}, \tag{5}$$

with a kernel $\mathcal{K}$ that can be expressed analytically (Fuchs 2001)[1]. By Fredholm discretization (5) can be transformed into a set of algebraic equations. The kernel $\mathcal{K}$ vanishes on the diagonal, so that the triangular coefficient matrix of this set of equations has an unity diagonal, implying a non-vanishing determinant. Thus the homogenous integral equation (5) has no eigensolutions, indicating that there exist in the shearing sheet no – except ringlike ($k'_{\rm y} = 0$) – proper spiral modes in the sense of rigidly rotating spatial patterns with well defined growth rates. External potential perturbations or initial ($t = 0$) density or velocity perturbations of the basic state of the disk are represented by an inhomogeneous term in the integral equation (5), or the corresponding integral equation for the surface density

$$\Sigma_{\mathbf{k}',\omega} = \int_{-\infty}^{k'_{\rm x}} dk_{\rm x} \mathcal{K}(k_{\rm x}, k'_{\rm x}, k'_{\rm y}, \omega) \Sigma_{{\rm k_x},{\rm k'_y},\omega} + r_{\mathbf{k}',\omega}. \tag{6}$$

[1] Positive wave numbers $k'_{\rm y}$ will be assumed in the following.

The resolvent kernel $\mathcal{R}(k_{\rm x}, k'_{\rm x}, k'_{\rm y}, \omega)$ of the inhomogeneous integral equation (6) can be obtained as a Neumann series. Solutions of (6) are then found in a unique way by a convolution of $\mathcal{R}$ with the inhomogeneous terms $r_{\mathbf{k}'}$. Transforming these solutions back from ω- to time-domain one can show that the resulting spatial pattern is a superposition of 'swinging' density waves, shearing with the general flow, but exhibiting transient growth as they swing by until they finally decay. Figure 2, taken from Fuchs (1991), illustrates this for single plane sinusoidal waves, $r_{\mathbf{k}'} \propto \delta(k'_{\rm x} - k^{in}_{\rm x})$, all of the same initial radial wave number k^{in}_x.

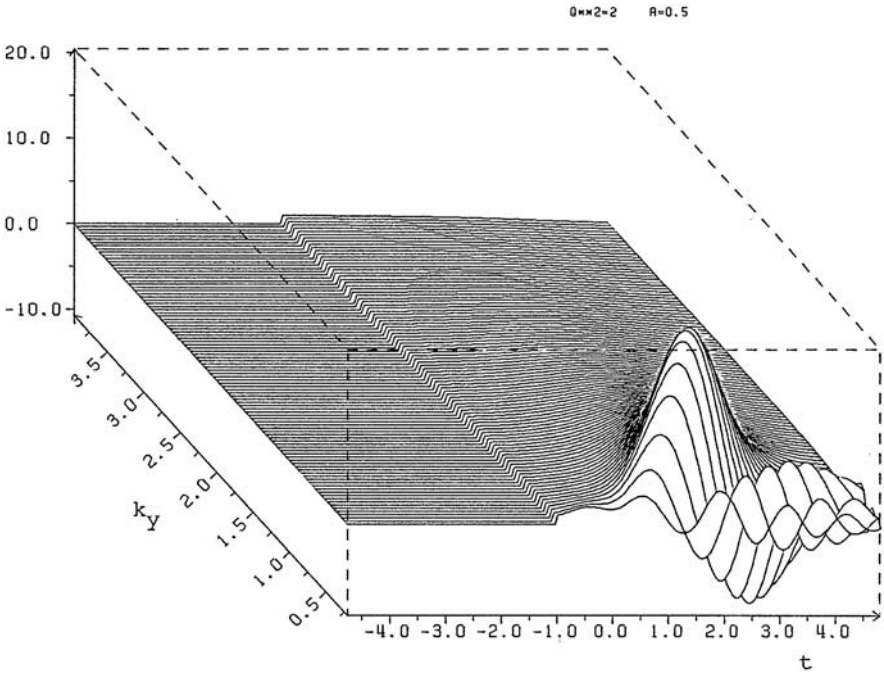

Fig. 2. Amplitudes of swing amplified density waves with initial radial wave numbers $k^{in}_{\rm x} = -1$ (leading waves). Wave numbers are given in units of $k_{\rm crit} = \kappa^2/2\pi G\Sigma_0$, where κ denotes the epicyclic frequency. Time is in units of $(2Ak_{\rm y})^{-1}$. The Toomre stability parameter is $Q = 1.4$, and an Oort constant of $A = \Omega_0/2$ is assumed.

The resulting spatial pattern evolves then as

$$\Sigma(x, y, t) = \delta(t) e^{i(k^{in}_{\rm x} x + k'_{\rm y} y)} + \tilde{\mathcal{R}}(k^{in}_{\rm x}, k^{in}_{\rm x} + 2Ak'_{\rm y} t) e^{i[(k^{in}_{\rm x} + 2Ak'_{\rm y} t)x + k'_{\rm y} y]}\,, \quad (7)$$

where the swinging around of the wave crests of the density waves is described by the growth of the effective radial wave number $k^{in}_{\rm x} + 2Ak'_{\rm y} t$ with time. As is well known, amplification is high for density waves, which are initially leading, but low for initially trailing waves.

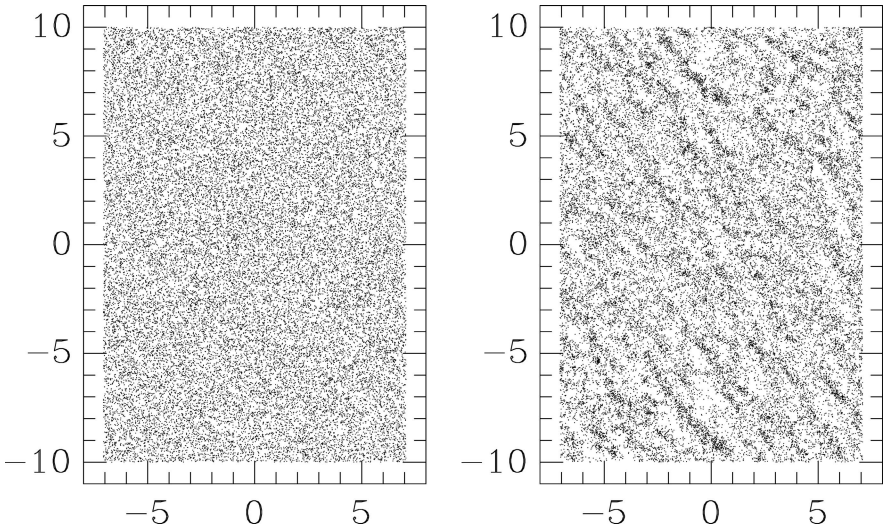

Fig. 3. Snapshots of the growth of density waves in a numerical simulation of the dynamical evolution of the shearing sheet. The sheet was seeded initially with random noise as shown in the left panel. The right panel shows the sheet after an elapsed time of one epicyclic period. Length unit is the critical wave length $\lambda_{\rm crit} = 2\pi/k_{\rm crit}$.

A visual impression of density waves growing from initial random fluctuations of the surface density of the sheet is given in Fig. 3., where snapshots of a numerical simulation of the dynamical evolution of the shearing sheet are shown (Fuchs, Dettbarn & Tsuchiya, in preparation).

3 The Shearing Sheet Immersed in a Live Dark Halo

The evolution of the distribution function of the disk stars in phase space is described by the linearized Boltzmann equation

$$\frac{\partial f_{\rm d1}}{\partial t} + u\frac{\partial f_{\rm d1}}{\partial x} + v\frac{\partial f_{\rm d1}}{\partial y} - \frac{\partial \Phi_{\rm d0} + \Phi_{\rm h0}}{\partial x}\frac{\partial f_{\rm d1}}{\partial u} - \frac{\partial \Phi_{\rm d0} + \Phi_{\rm h0}}{\partial y}\frac{\partial f_{\rm d1}}{\partial v} - \frac{\partial \Phi_{\rm d1} + \Phi_{\rm h1}}{\partial x}\frac{\partial f_{\rm d0}}{\partial u} - \frac{\partial \Phi_{\rm d1} + \Phi_{\rm h1}}{\partial y}\frac{\partial f_{\rm d0}}{\partial v} = 0\,, \tag{8}$$

where $(u,\, v)$ are the velocity components corresponding to the x and y coordinates, respectively. Equation (8) has been derived from the general 6–dimensional Boltzmann equation assuming delta–function like dependencies of the distribution function on the vertical z coordinate and the vertical w velocity component, respectively, and integrating the Boltzmann equation with respect to them. A perturbation Ansatz of the form

$$f_{\rm d} = f_{\rm d0} + f_{\rm d1}\,,\ \Phi_{\rm d} = \Phi_{\rm d0} + \Phi_{\rm d1}\,,\ \Phi_{\rm h} = \Phi_{\rm h0} + \Phi_{\rm h1} \tag{9}$$

is chosen for the distribution function of the disk stars and the gravitational potentials of the disk and the halo, respectively, and the Boltzmann equation (8) has been linearized accordingly.

Similarly the linearized Boltzmann equation for the halo particles can be written as

$$\begin{aligned}&\frac{\partial f_{\rm h1}}{\partial t} + u\frac{\partial f_{\rm h1}}{\partial x} + v\frac{\partial f_{\rm h1}}{\partial y} + w\frac{\partial f_{\rm h1}}{\partial z} - \frac{\partial \Phi_{\rm d0}+\Phi_{\rm h0}}{\partial x}\frac{\partial f_{\rm h1}}{\partial u} - \frac{\partial \Phi_{\rm d0}+\Phi_{\rm h0}}{\partial y}\frac{\partial f_{\rm h1}}{\partial v}\\ &-\frac{\partial \Phi_{\rm d0}+\Phi_{\rm h0}}{\partial z}\frac{\partial f_{\rm h1}}{\partial w} - \frac{\partial \Phi_{\rm h1}+\Phi_{\rm d1}}{\partial x}\frac{\partial f_{\rm h0}}{\partial u} - \frac{\partial \Phi_{\rm h1}+\Phi_{\rm d1}}{\partial y}\frac{\partial f_{\rm h0}}{\partial v}\\ &-\frac{\partial \Phi_{\rm h1}+\Phi_{\rm d1}}{\partial z}\frac{\partial f_{\rm h0}}{\partial w} = 0\,.\end{aligned} \tag{10}$$

The choice of the dark halo model was lead by the following considerations. One of the deeper reasons for the success of the infinite shearing sheet model to describe spiral density waves realistically is the rapid convergence of the Poisson integral in self–gravitating disks (Julian & Toomre 1966). Consider, for example, the potential of a sinusoidal density perturbation

$$\Phi(x,y) = -G\int_{-\infty}^{\infty}dx'\int_{-\infty}^{\infty}dy'\frac{\Sigma_{10}\sin(kx')}{\sqrt{(x-x')^2+(y-y')^2}}\,, \tag{11}$$

$$\Phi(x,y=0) = -4G\Sigma_{10}\sin(kx)\lim_{x_{\rm L}\to\infty}\frac{{\rm Si}(kx_{\rm L})}{k} = -\frac{2\pi G\Sigma_{10}\sin(kx)}{k}\,. \tag{12}$$

The sine integral in (12) converges so rapidly that it reaches at $kx_{\rm L} = \frac{\pi}{2}$ already 87% of its asymptotic value. Thus the "effective range" of gravity is about only a quarter of a wave length. The shearing sheet models effectively patches of galactic disks of such size. The wave lengths of density waves are of the order of the critical wave length

$$\lambda_{\rm crit} = \frac{2\pi}{k_{\rm crit}} = \frac{4\pi^2 G\Sigma_0}{\kappa^2}\,, \tag{13}$$

where κ denotes the epicyclic frequency of the stellar orbits and Σ_0 the surface density of the disk. In the solar neighbourhood in the Milky Way, for instance, the critical wave length is $\lambda_{\rm crit} = 5$ kpc. Thus it is reasonable to neglect over such length scales, like in the shearing sheet model, the curvature of the mean circular orbits of the stars around the galactic center or the gradient of the surface density. The curvature of the stellar orbits due to the epicyclic motions of the stars, on the other hand, cannot be neglected and is indeed not neglected in the shearing sheet model. The radial size of an epicycle is approximately given by $\sigma_{\rm u}/\kappa$, where $\sigma_{\rm u}$ denotes the radial velocity dispersion of the stars, and the ratio of epicycle size and critical wave length is given by

$$\frac{\sigma_{\rm u}}{\kappa\lambda_{\rm crit}} = 0.085Q \tag{14}$$

in terms of the Toomre (1964) stability parameter Q which is typically of the order of 1 to 2. Concurrent to these approximations I have assumed a dark halo which is homogeneous in its unperturbed state. Accordingly the curvature of the unperturbed orbits of the halo particles is neglected on the scales considered here and the particles are assumed to be on straight–line orbits. The equations of motion of the halo particles are the characteristics of the Boltzmann equation. In a homogeneous halo $\ddot{\mathbf{x}} = \nabla(\Phi_{\mathrm{d}0} + \Phi_{\mathrm{h}0}) = 0$, and in accordance with this assumption I neglect the force terms $\nabla\Phi_{\mathrm{d}0}$ and $\nabla\Phi_{\mathrm{h}0}$ in the Boltzmann (10). This simplifies its solution considerably. The disadvantage of such a model is that there are no higher–order resonances of the orbits of the halo particles with the density waves as described by Weinberg (1985) or observed in the high–resolution simulations by Athanassoula (2002, 2003). However their effect was shown to be much less important than the main resonances of the particles with the density waves, which are properly described in the present model.

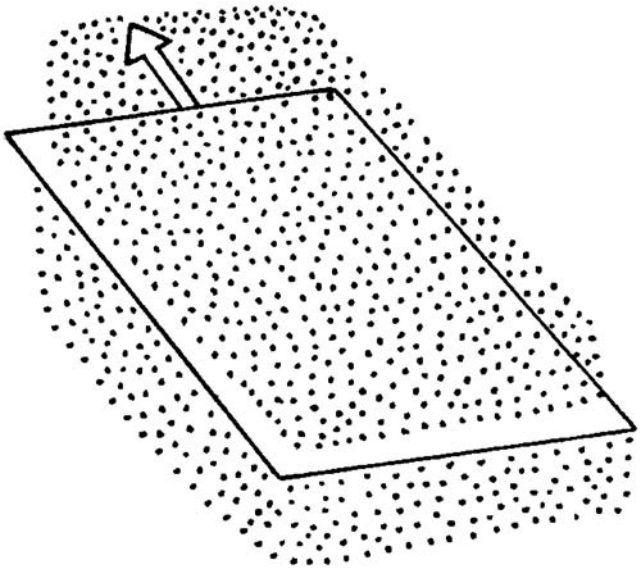

Fig. 4. Sketch of the disk and halo model.

3.1 Halo Dynamics

The Boltzmann equation (10) can be viewed as a linear partial differential equation for the perturbation of the distribution function of the halo particles, $f_{\mathrm{h}1}$, with inhomogeneities depending on the perturbations of the gravitational potentials of the disk and the halo, $\nabla\Phi_{\mathrm{d}1}$ and $\nabla\Phi_{\mathrm{h}1}$, respectively. Thus the

equation can be solved for the disk and halo inhomogeneities separately and the solutions combined afterwards by superposition. It was shown by Fuchs (2004a) that the Boltzmann equation with the inhomogeneity $\nabla\Phi_{\rm h1}$ describes just the Jeans instability of the dark halo. However, dark halos are thought to be dynamically hot systems and their Jeans lengths will be of the order of the size of the halos themselves. Thus this part of the solution of the Boltzmann equation (10) is uninteresting in the present context and will be not considered in the following.

More interesting is the remaining part of the Boltzmann equation (10),

$$\begin{aligned}&\frac{\partial f_{\rm h1}}{\partial t}+u\frac{\partial f_{\rm h1}}{\partial x}+v\frac{\partial f_{\rm h1}}{\partial y}+w\frac{\partial f_{\rm h1}}{\partial z}\\&-\frac{\partial\Phi_{\rm d1}}{\partial x}\frac{\partial f_{\rm h0}}{\partial u}-\frac{\partial\Phi_{\rm d1}}{\partial y}\frac{\partial f_{\rm h0}}{\partial v}-\frac{\partial\Phi_{\rm d1}}{\partial z}\frac{\partial f_{\rm h0}}{\partial w}=0\,,\end{aligned}\tag{15}$$

which describes the halo response to a perturbation in the disk. If the gravitational potential perturbation of the disk is Fourier expanded the Fourier terms have the form (cf. (33) of Fuchs 2001)

$$\Phi_{{\rm d}\mathbf{k}_{||}}e^{i(\omega t+k_{\rm x}x+k_{\rm y}y)-k_{||}|z|}\tag{16}$$

with $k_{||}=|\mathbf{k}_{||}|=\sqrt{k_{\rm x}^2+k_{\rm y}^2}$. This can be converted to Fourier coefficients of the halo potential in 3–dimensional $\mathbf{k}$–space as

$$\Phi_{{\rm d}\mathbf{k}}=\frac{1}{2\pi}\int_{-\infty}^{\infty}dz\Phi_{{\rm d}\mathbf{k}_{||}}e^{-ik_{\rm z}z-k_{||}|z|}=\frac{1}{\pi}\frac{k_{||}}{k_{||}^2+k_{\rm z}^2}\Phi_{{\rm d}\mathbf{k}_{||}}\,.\tag{17}$$

Notice that the coordinate y, which is defined in the reference system of the disk, is related to the y coordinate in the reference system of the halo due to the motion of the center of the shearing sheet as

$$y\rightarrow y-r_0\Omega_0 t\,.\tag{18}$$

The further solution of the Boltzmann equation is straightforward and is described in full detail in Fuchs (2004a). The distribution function is then integrated over velocity space to obtain the Fourier coefficients $\rho_{{\rm h}\mathbf{k}}$ of the density perturbation of the dark halo. Next the gravitational potential associated with this density distribution is calculated from the Poisson equation,

$$-k^2\Phi_{{\rm h}\mathbf{k}}=4\pi G\rho_{{\rm h}\mathbf{k}}\,.\tag{19}$$

Since the gravitational forces in (8) have to be taken at the midplane $z=0$, it is necessary to convert the solution of the Boltzmann equation $\Phi_{{\rm h}\mathbf{k}}$ from the representation in $\mathbf{k}$ space to a mixed representation in $(\mathbf{k}_{||},z)$ space leading to two contributions

$$\Phi^{\rm nr}_{{\rm h}\mathbf{k}_{||}}(z=0) = \int_{-\infty}^{\infty} dk_{\rm z} \frac{k_{||}}{(k_{||}^2+k_{\rm z}^2)^2} \Phi_{{\rm d}\mathbf{k}} \frac{4G\rho_{\rm b}}{\sigma_{\rm h}^2}$$
$$\times \left\{ 1 + i\sqrt{\pi}\, \frac{k_{\rm y} r_0 \Omega_0 - \omega}{\sqrt{2} k \sigma_{\rm h}}\, {\rm erf}\left(i \frac{k_{\rm y} r_0 \Omega_0 - \omega}{\sqrt{2} k \sigma_{\rm h}} \right) \exp - \frac{(k_{\rm y} r_0 \Omega_0 - \omega)^2}{2k^2 \sigma_{\rm h}^2} \right\} \qquad (20)$$

due to halo particles not in resonance with the potential perturbation and

$$\Phi^{\rm res}_{{\rm h}\mathbf{k}_{||}}(z=0) = -\int_{-\infty}^{\infty} dk_{\rm z} \frac{k_{||}}{(k_{||}^2+k_{\rm z}^2)^2} \Phi_{{\rm d}\mathbf{k}} i\sqrt{\pi} \frac{4G\rho_{\rm b}}{\sigma_{\rm h}^2}$$
$$\times \frac{\omega - k_{\rm y} r_0 \Omega_0}{\sqrt{2} k \sigma_{\rm h}}\, \exp - \frac{(k_{\rm y} r_0 \Omega_0 - \omega)^2}{2k^2 \sigma_{\rm h}^2} \qquad (21)$$

due to non–resonant halo particles. $\rho_{\rm b}$ and $\sigma_{\rm h}$ denote the mean spatial density and the velocity dispersion of the halo particles, respectively. The final result can be formally written as

$$\Phi_{{\rm h}\mathbf{k}_{||}}(z=0) = \Upsilon(\omega - k_{\rm y} r_0 \Omega_0, k_{||}) \Phi_{{\rm d}\mathbf{k}_{||}}\,, \qquad (22)$$

where the real and imaginary parts of Υ are defined by (20) and (21), respectively. Thus for any given frequency there is a contribution both from the non–resonant and the resonant halo particles.

3.2 Disk Dynamics

The halo response (22) to the perturbation in the disk has to be inserted into (8). Solving the Boltzmann equation (8) is greatly facilitated by the fact that its form is identical to the case of an isolated shearing sheet with the replacement

$$\Phi_{{\rm d}\mathbf{k}} \rightarrow (1+\Upsilon)\Phi_{{\rm d}\mathbf{k}} \qquad (23)$$

and one can use directly the results of Fuchs (2001) even though the Boltzmann equation is treated there using action and angle variables instead of the Cartesian coordinates as in (8). In particular the factor $1+\Upsilon$ is carried straightforward through to the fundamental Volterra integral equation ((68) of Fuchs 2001)

$$\Phi_{\mathbf{k}',\omega} = \int_{-\infty}^{k'_{\rm x}} dk_{\rm x} \mathcal{K}\left(k_{\rm x}, k'_{\rm x}\right) \left(1 + \Upsilon(k_{\rm x}, k'_{\rm y}, \omega)\right) \Phi_{{\rm k_x}, {\rm k'_y}, \omega} + r_{\mathbf{k}',\omega}\,, \qquad (24)$$

where the kernel $\mathcal{K}$ is given by (67) of Fuchs (2001). $r_{\mathbf{k}'}$ describes an inhomogeneity of (24) related to an initial non–equilibrium state of the shearing sheet. Equation (24) is separating in the circumferential wave number $k'_{\rm y}$. In (24) the wave numbers are expressed in units of the critical wave number $k_{\rm crit}$. This implies that the Volterra equation describing a shearing sheet embedded in a rigid halo potential is formally the same as that of an isolated

shearing sheet, because in this case $\Upsilon = 0$ and the halo mass affects only the numerical values of the critical wave number $k_{\rm crit}$ and the stability parameter Q. It is advantageous to consider (24) transformed back from frequency to time domain. Splitting off the ω–dependent term $\exp i\omega\frac{k_{\rm x}-k'_{\rm x}}{2Ak'_{\rm y}}$ from the kernel and making use of the convolution theorem of the Fourier transform of products of two functions leads to

$$\Phi_{\mathbf{k}',{\rm t}} = \int_{-\infty}^{k'_{\rm x}} dk_{\rm x}\tilde{\mathcal{K}}\left(k_{\rm x},k'_{\rm x}\right)\left\{\int_0^\infty dt'\Phi_{{\rm k_x},{\rm k'_y},{\rm t'}}\delta\left(t-t'+\frac{k_{\rm x}-k'_{\rm x}}{2Ak'_{\rm y}}\right)\right.$$
$$\left. + \int_0^\infty dt'\Phi_{{\rm k_x},{\rm k'_y},{\rm t'}}\mathcal{F}\left(\Upsilon(k_{\rm x},k'_{\rm y},\omega)e^{i\omega\frac{k_{\rm x}-k'_{\rm x}}{2Ak'_{\rm y}}}\right)_{\rm t-t'}\right\} + r_{\mathbf{k}',{\rm t}}\,, \quad (25)$$

where the operator $\mathcal{F}$ denotes the Fourier transform from ω to time domain. In (33) I have assumed an initial perturbation of the disk at time $t = 0$ so that $\Phi_{{\rm k_x},{\rm k'_y},t'<0} = 0$. The Fourier transform $\mathcal{F}$ is given by (34) of Fuchs (2004a). If this is inserted into (25) it takes the form

$$\Phi_{\mathbf{k}',{\rm t}} = \int_{-\infty}^{k'_{\rm x}} dk_{\rm x}\tilde{\mathcal{K}}\left(k_{\rm x},k'_{\rm x}\right)\left\{\Phi_{{\rm k_x},{\rm k'_y},{\rm t}+\frac{{\rm k_x}-{\rm k'_x}}{2{\rm Ak'_y}}}\right.$$
$$\left. + \int_0^{t+\frac{k_{\rm x}-k'_{\rm x}}{2Ak'_{\rm y}}} dt'\Phi_{{\rm k_x},{\rm k'_y},{\rm t'}}\mathcal{F}\left(\Upsilon(k_{\rm x},k'_{\rm y},\omega)e^{i\omega\frac{k_{\rm x}-k'_{\rm x}}{2Ak'_{\rm y}}}\right)_{\rm t-t'}\right\} + r_{\mathbf{k}',{\rm t}}\,. \quad (26)$$

Equation (26) can be integrated numerically with very modest numerical effort. In Fig. 5 I illustrate the response of the shearing sheet now embedded in a live halo to an initial sinusoidal perturbation of unit amplitude. For this purpose I use the inhomogeneity term of the Volterra equation

$$r_{\mathbf{k}',\omega} = \int_{-\infty}^{k'_{\rm x}} dk_{\rm x}\mathcal{L}\left(k_{\rm x},k'_{\rm x}\right)f_{{\rm k_x},{\rm k'}_{\rm y}}(0) \quad (27)$$

derived in Fuchs (2001) with $f_{{\rm k_x},{\rm k'}_{\rm y}}(0) \propto \delta(k_{\rm x}-k_{\rm x}^{\rm in})$. The response of the shearing sheet to this initial impulse is a swing amplification event as described in Sect. (2). The radial wave number $k_{\rm x}$ evolves as

$$k_{\rm x} = k_{\rm x}^{\rm in} + 2Ak'_{\rm y}t\,, \quad (28)$$

while the circumferential wave number $k'_{\rm y}$ is constant, which means that the wave crests swing around from leading to trailing orientation during the amplification phase. Around $t = 6$ the amplitudes become negative which indicates that the swing amplified density wave is also oscillating. As can be seen from Fig. 5 comparing the evolution of shearing sheets embedded either in a rigid halo potential or a live halo this characteristic behaviour of the density wave is not changed by the responsive halo, but the maximum

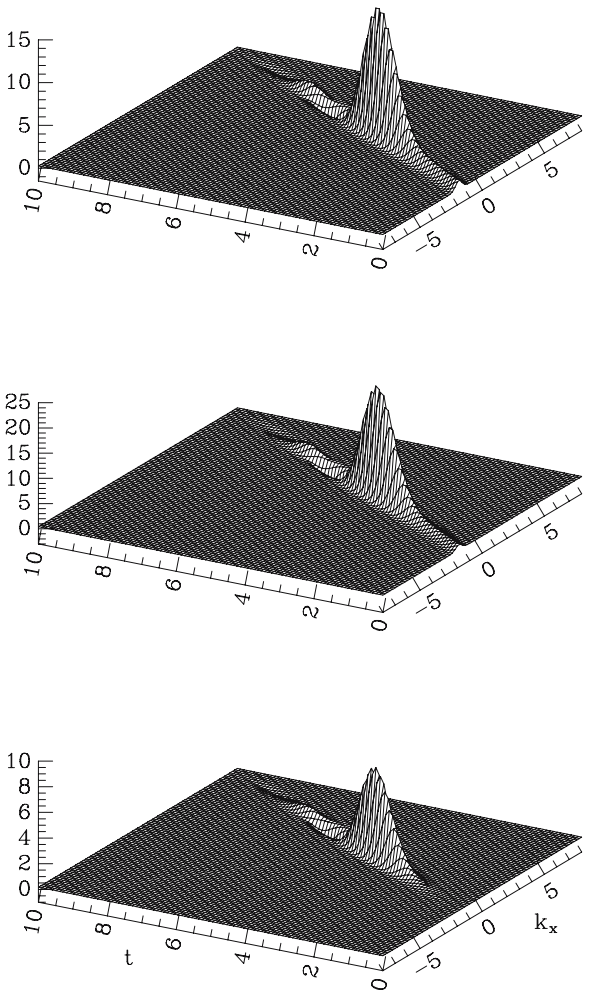

Fig. 5. Swing amplified density wave in the shearing sheet. The upper diagram shows the evolution in a shearing sheet embedded in a static halo potential triggered by an impulse with unit amplitude and wave vector $\mathbf{k}^{\rm in} = (-2, 0.5)k_{\rm crit}$. Time is given in units of $(2Ak_{\rm y}^{\rm in}/k_{\rm crit})^{-1}$. The middle diagram shows the evolution of a shearing sheet embedded in a live dark halo triggered by the same impulse. The lower diagram shows the difference. The model parameters are $A/\Omega_0 = 0.5, Q = 1.4, \sigma_{\rm d} : \sigma_{\rm h} = 1 : 5, G\rho_{\rm b}/\kappa^2 = 0.01$, and $r_0\Omega_0 : \sigma_{\rm d} = 220 : 44$.

growth factor of the amplitude of the wave is enhanced by a surprisingly large amount.

The enhanced maximum growth factor of swing amplified density waves due to a responsive halo seems to be the equivalent of the enhanced growth of bars of stellar disks embedded in live dark halos seen in the numerical simulations. However, the interaction of the shearing sheet and the surrounding halo is not only mediated by the resonant halo particles, but the non–resonant halo particles play an important role as well. The amplification of density waves depends critically on the Toomre stability parameter Q. This is illustrated in Fig. 6 where the response of the shearing sheet to the same initial impulse as in the previous example is shown, but assuming a stability parameter of $Q = 2$. As can be seen in Fig. 6 there is neither effective amplification of density waves in a shearing sheet in a rigid halo potential or in a shearing sheet embedded in a live dark halo.

4 Wakes in Dark Matter Halos

The perturbations of the gravitational potential and the surface density of the shearing sheet have their counterparts in the dark matter halo. From (19) one obtains

$$\rho_{\mathrm{h}\mathbf{k}||}(z,\omega) = -\int_{-\infty}^{\infty} dk_{\mathrm{z}} \frac{k^2}{4\pi G} \Phi_{\mathrm{h}\mathbf{k}} e^{ik_{\mathrm{z}}z}\,, \tag{29}$$

where the Fourier coefficients $\Phi_{\mathrm{h}\mathbf{k}}$ derived in Sect. (3.1) have to be inserted,

$$\rho_{\mathrm{h}\mathbf{k}_{||}}(z,\omega) = -\int_{-\infty}^{\infty} dk_{\mathrm{z}} \frac{k_{||}}{k_{||}^2 + k_{\mathrm{z}}^2} \Phi_{\mathrm{d}\mathbf{k}||} \frac{\rho_{\mathrm{b}}}{\pi\sigma_{\mathrm{h}}^2} e^{ik_{\mathrm{z}}z} \tag{30}$$

$$\times \left\{ 1 + i\sqrt{\pi}\, \frac{k_{\mathrm{y}} r_0 \Omega_0 - \omega}{\sqrt{2} k \sigma_{\mathrm{h}}} \left(1 + \mathrm{erf}\left(i \frac{k_{\mathrm{y}} r_0 \Omega_0 - \omega}{\sqrt{2} k \sigma_{\mathrm{h}}} \right) \right) \exp - \frac{(k_{\mathrm{y}} r_0 \Omega_0 - \omega)^2}{2k^2 \sigma_{\mathrm{h}}^2} \right\}.$$

Equation (30) can be Fourier transformed back from frequency to time domain in the same way as (35) of Fuchs (2004a) was Fourier transformed back to time domain by a convolution of $\Phi_{\mathrm{d}\mathbf{k}||}$(t') with the Fourier transform of the remaining terms under the integral with respect to k_{z}. To these terms the operator

$$\int_{-\infty}^{\infty} d\omega e^{i(\omega - k_{\mathrm{y}} r_0 \Omega_0)t} \ldots \tag{31}$$

is applied and the integral over ω is evaluated with the help of formulae (6.317) and (3.952) of Gradshteyn & Ryzhik (2000) leading effectively to expression (34) of Fuchs (2004a) with $t - t' + \frac{k_{\mathrm{x}} - k'_{\mathrm{x}}}{2Ak'_{\mathrm{y}}}$ replaced by $t - t'$ only. The integral over k_{z} can be then calculated using formulae (3.723) and (3.896) of Gradshteyn & Ryzhik (2000) with the result

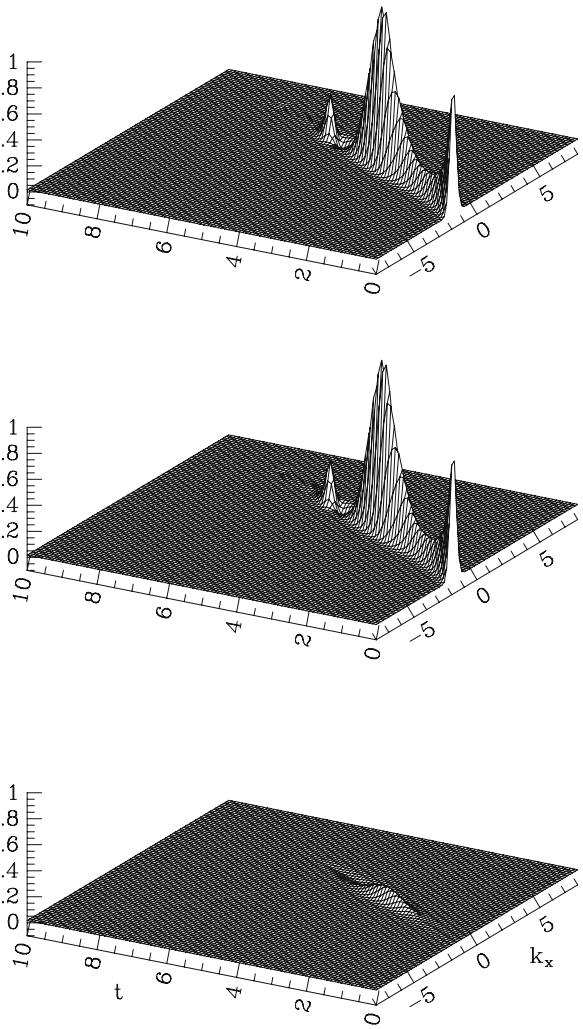

Fig. 6. Same as in Fig. 5, but adopting $Q = 2$.

$$\rho_{\mathrm{h}\mathbf{k}||}(z,t) = -\frac{\rho_{\mathrm{b}}}{\sigma_{\mathrm{h}}^2}\Bigg\{2\pi\Phi_{\mathrm{d}\mathbf{k}||}(t)e^{-k_{||}|z|} \tag{32}$$

$$+\sqrt{8\pi}\sigma_{\mathrm{h}}k_{||}\int_{-\infty}^{t}dt'\Phi_{\mathrm{d}\mathbf{k}||}(t')e^{-\frac{1}{2}\sigma_{\mathrm{h}}^2k_{||}^2(t-t')^2}e^{ik_{\mathrm{y}}r_0\Omega_0)(t-t')}e^{-\frac{z^2}{2\sigma_{\mathrm{h}}^2(t-t')^2}}\Bigg\},$$

and finally I convert the potential perturbation of the disk to the perturbation of its surface density with the relation $k_{||}\Phi_{\mathrm{d}\mathbf{k}||} = -2\pi G\Sigma_{\mathrm{d}\mathbf{k}||}$ (cf. Fuchs 2001) and obtain

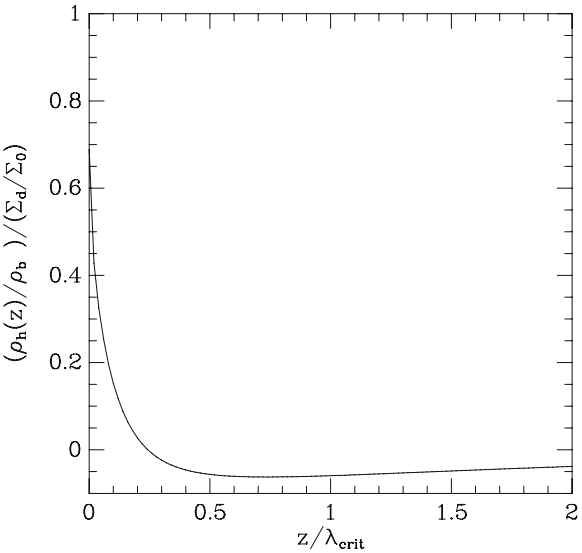

Fig. 7. Vertical profile of the density perturbation in the dark halo induced by a density wave in the sheet, which is at maximal amplification, exactly above the density wave crest. The relative density contrast $\rho_{\mathrm{h}\mathbf{k}}/\rho_{\mathrm{b}}|_{\mathrm{peak}}$ is given in terms of the relative density contrast of the surface density of the sheet $\Sigma_{\mathrm{d}\mathbf{k}}/\Sigma_0|_{\mathrm{peak}}$.

$$\frac{\rho_{\mathrm{h}\mathbf{k}||}}{\rho_{\mathrm{b}}} = \frac{2\pi G\Sigma_{\mathrm{d}}}{\sigma_{\mathrm{h}}^2}\left\{\frac{2\pi}{k_{||}}\frac{\Sigma_{\mathrm{d}\mathbf{k}||}(t)}{\Sigma_{\mathrm{d}}}e^{-k_{||}|z|}\right. \tag{33}$$

$$\left.+\sqrt{8\pi}\sigma_{\mathrm{h}}\int_{-\infty}^{t}dt'\frac{\Sigma_{\mathrm{d}\mathbf{k}||}(t')}{\Sigma_{\mathrm{d}}}e^{-\frac{1}{2}\sigma_{\mathrm{h}}^2k_{||}^2(t-t')^2}e^{ik_y r_0\Omega_0)(t-t')}e^{-\frac{z^2}{2\sigma_{\mathrm{h}}^2(t-t')^2}}\right\}.$$

The time integral in (33) has been calculated numerically. At the time of maximal amplification of the density wave I find, adopting the same parameters used to calculate Fig. 6, $\rho_{\mathrm{h}\mathbf{k}}/\rho_{\mathrm{b}}|_{\mathrm{peak}} = 0.6\,\Sigma_{\mathrm{d}\mathbf{k}}/\Sigma_0|_{peak}$. Figure 7 shows the vertical profile of the density perturbation of the dark halo according to (33). As can be seen from Fig. 7 the profile indicates a density enhancement of dark halo matter close above the density wave crest. At larger distances above the midplane there is a density deficit above the density wave crest, which means that the cloud of dark matter particles is lagging behind like a trail of smoke.

The existence of wakes in dark matter halos might have quite practical implications. For instance the bar in the Milky Way focusses dark matter particles dynamically into some regions in phase space and depopulates others, which may very well affect the flux of dark matter particles through detectors on Earth. Such features have been observed as "star streams" in velocity space among the stars in the solar neighbourhood (Dehnen 2000, Mühlbauer

& Dehnen 2003). These stars are, of course, stars members of the Milky Way disk, but similar effects are to be expected among halo objects.

References

1. E. Athanassoula: Astroph. J., **569**, L83 (2002)
2. E. Athanassoula: Mon. Not. R. Astron. Soc., **341**, 1179 (2003)
3. V.P. Debattista, J. A. Sellwood: Astroph. J., **543**, 704 (2000)
4. W. Dehnen: Astron. J., **119**, 800 (2000)
5. B. Fuchs: Recurrent swing amplification induced by nonlinear amplitude effects. In: *Dynamics of disc galaxies* ed by B. Sundelius (Göteborgs Univ. and Chalmers Univ. of Tech., Göteborg 1991) pp 359–363
6. B. Fuchs: Astron. Astroph., **368**, 107 (2001)
7. B. Fuchs: Astron. Astroph., **419**, 941 (2004a)
8. B. Fuchs: Astron. Astroph., submitted (2004b)
9. P. Goldreich, D. Lynden–Bell: Mon. Not. R. Astron. Soc., **130**, 125 (1965)
10. Gradshteyn, I.S., Ryzhik, I.M.: *Table of Integrals, Series, and Products*, 6th edn (Academic Press, New York 2000)
11. W.H. Julian, A. Toomre: Astroph. J., **146**, 810 (1966)
12. A. Kalnajs: 1971, Astroph. J., **166**, 275 (1971)
13. G. Mühlbauer, W. Dehnen: Astron. Astroph., **401**, 975 (2003)
14. J.P. Ostriker, P.J.E. Peebles: Astroph. J., **186**, 467 (1973)
15. A. Toomre: Astroph. J., **139**, 1217 (1964)
16. A. Toomre: Ann. Rev. Astron. Astroph., **15**, 437 (1977)
17. A. Toomre: What amplifies the spirals? In: *The Structure and Evolution of Normal Galaxies* ed by S.M. Fall, D. Lynden–Bell (Cambridge Univ. Press, Cambridge 1981) pp 111–136
18. M.D. Weinberg: Mon. Not. R. Astron. Soc., **213**, 451 (1985)

Relic Neutrino Clustering and Implications for Their Detection[1]

A. Ringwald and Yvonne Y. Y. Wong

Deutsches Elektronen-Synchrotron DESY, Hamburg, Germany
andreas.ringwald@desy.de,
yvonne.wong@desy.de

We study the gravitational clustering of big bang relic neutrinos onto existing cold dark matter and baryonic structures within the flat ΛCDM model. We then discuss the implications of clustering for scattering-based relic neutrino detection methods, ranging from flux detection via Cavendish-type torsion balances, to target detection using accelerator beams and cosmic rays.

1 Introduction

The standard big bang theory predicts the existence of 10^{87} neutrinos per flavour in the visible universe. This is an enormous abundance unrivalled by any other known form of matter, falling second only to the cosmic microwave background (CMB) photon. Yet, unlike the CMB which boasts its first detection in the 1960s and which has since been observed and its properties measured to high accuracy in a series of experiments, the relic neutrino continues to be elusive in the laboratory. The chief reason for this is of course the feebleness of the weak interaction. The smallness of the neutrino mass also makes momentum-transfer-based detection methods highly impractical. At present, the only evidence for the relic neutrino comes from inferences from other cosmological measurements, such as big bang nucleosynthesis, CMB and large scale structure (LSS) data (e.g., [2]). Nevertheless, it is difficult to accept that these neutrinos will never be detected in a more direct way.

In order to design feasible direct, scattering-based detection methods, a precise knowledge of the relic neutrino phase space distribution is indispensable. In this connection, it is important note that an oscillation interpretation of the atmospheric and solar neutrino data (e.g., [3]) implies that at least two of the neutrino mass eigenstates are nonrelativistic today. These neutrinos are subject to gravitational clustering on existing cold dark matter (CDM) and baryonic structures, possibly causing the local neutrino number density to depart from the standard value of $\bar{n}_\nu = \bar{n}_{\bar{\nu}} \simeq 56\ \mathrm{cm}^{-3}$, and the momentum distribution to deviate from the relativistic Fermi–Dirac function.

[1] Talk given by Yvonne Y.Y. Wong at DARK2004, College Station TX, USA. Based on [1].

In this talk, we describe a method that allows us to study the gravitational clustering of relic neutrinos onto CDM/baryonic structures. We calculate the present day neutrino overdensities in general CDM halos and in the Milky Way, and then discuss their implications for scattering-based relic neutrino detection methods – from flux detection via Cavendish-type torsion balances, to target detection using accelerator beams and cosmic rays.

2 Vlasov Equation

The standard procedure for any clustering investigation involving gravity only is to solve the Vlasov, or collisionless Boltzmann, equation (e.g., [4, 5]),

$$\frac{Df_i}{D\tau} \equiv \frac{\partial f_i}{\partial \tau} + \dot{\boldsymbol{x}} \cdot \frac{\partial f_i}{\partial \boldsymbol{x}} + \dot{\boldsymbol{p}} \cdot \frac{\partial f_i}{\partial \boldsymbol{p}} = 0 \; . \tag{1}$$

The single-particle phase density $f_i(\boldsymbol{x}, \boldsymbol{p}, \tau)$ is defined so that $dN_i = f_i \, d^3x \, d^3p$ is the number of i type particles (e.g., CDM, neutrinos) in an infinitesimal phase space volume element. The variables $\boldsymbol{x} = \boldsymbol{r}/a(t)$, $\boldsymbol{p} = am_i\dot{\boldsymbol{x}}$, and $d\tau = dt/a(t)$ are the comoving distance, its associated conjugate momentum, and the conformal time respectively, with a as the scale factor and m_i the mass of the ith particle species. All temporal and spatial derivatives are taken with respect to comoving coordinates, i.e., $\dot{} \equiv \partial/\partial\tau$, $\nabla \equiv \partial/\partial\boldsymbol{x}$.[2]

In the nonrelativistic, Newtonian limit, (1) is equivalent to

$$\frac{\partial f_i}{\partial \tau} + \frac{\boldsymbol{p}}{am_i} \cdot \frac{\partial f_i}{\partial \boldsymbol{x}} - am_i \nabla\phi \cdot \frac{\partial f_i}{\partial \boldsymbol{p}} = 0 \; , \tag{2}$$

with the Poisson equation

$$\nabla^2\phi = 4\pi G a^2 \sum_i \overline{\rho}_i(\tau)\delta_i(\boldsymbol{x}, \tau) \; , \tag{3}$$

$$\delta_i(\boldsymbol{x}, \tau) \equiv \frac{\rho_i(\boldsymbol{x}, \tau)}{\overline{\rho}_i(\tau)} - 1, \qquad \rho_i(\boldsymbol{x}, \tau) = \frac{m_i}{a^3} \int d^3p \; f_i(\boldsymbol{x}, \boldsymbol{p}, \tau) \; , \tag{4}$$

relating the peculiar gravitational potential $\phi(\boldsymbol{x}, \tau)$ to the density fluctuations $\delta_i(\boldsymbol{x}, \tau)$ with respect to the physical mean $\bar{\rho}_i(\tau)$.

The Vlasov equation expresses conservation of phase space density f_i along each characteristic $\{\boldsymbol{x}(\tau), \boldsymbol{p}(\tau)\}$ given by

$$\frac{d\boldsymbol{x}}{d\tau} = \frac{\boldsymbol{p}}{am_i}, \qquad \frac{d\boldsymbol{p}}{d\tau} = -am_i\nabla\phi \; . \tag{5}$$

The complete set of characteristics coming through every point in phase space is thus exactly equivalent to (1). It is generally not possible to follow the whole

[2] Unless otherwise indicated, comoving spatial and temporal quantities are used throughout the present work. Masses and densities, however, are always physical.

set of characteristics, but the evolution of the system can still be traced, to some extent, if we follow a sufficiently large but still manageable sample selected from the initial phase space distribution. This forms the basis of particle-based solution methods.

3 Solution Method and Halo Density Profiles

A "first principles" approach to neutrino clustering requires the simultaneous solution of the Vlasov equation (1) for both CDM and neutrinos. This is usually done by means of multi-component N-body simulations. In our treatment, however, we make two simplifying approximations:

1. We assume only the CDM component ρ_m contributes to ϕ in the Poisson equation (3), and ρ_m to be completely specified by halo density profiles from high resolution ΛCDM simulations [6]. The neutrino component is treated as a small perturbation whose clustering depends on the CDM halo profile, but is too small to affect it in return. This assumption is well justified, since, on cosmological scales, LSS data require $\rho_\nu/\rho_m = \Omega_\nu/\Omega_m < 0.2$ [2]. On cluster/galactic scales, neutrino free-streaming ensures that ρ_ν/ρ_m always remains smaller than Ω_ν/Ω_m [7].
2. Given that assumption 1. holds, it follows that not only will the CDM halo be gravitationally blind to the neutrinos, the neutrinos themselves will also have negligible gravitational interaction with each other.

These approximations together allow us to track the neutrinos one at a time in N independent simulations, instead of following N particles simultaneously in one single run. We shall call this "N-one-body simulation" [1].

For the halo density profiles, we use the "universal profile" advocated by Navarro, Frenk and White (hereafter, NFW) [8, 9],

$$\rho_{\rm halo}(r) = \frac{\rho_s}{(r/r_s)(1+r/r_s)^2} \ . \tag{6}$$

The parameters r_s and ρ_s are determined by the halo's virial mass $M_{\rm vir}$ and a dimensionless concentration parameter $c \equiv r_{\rm vir}/r_s$, where $r_{\rm vir}$ is the virial radius, within which lies $M_{\rm vir}$ of matter with an average density equal to $\delta_{\rm TH}$ times the mean matter density $\bar{\rho}_m$ at that redshift, i.e.,

$$M_{\rm vir} \equiv \frac{4\pi}{3}\delta_{\rm TH}\bar{\rho}_m a^3 r_{\rm vir}^3 = \frac{4\pi}{3}\delta_{\rm TH}\bar{\rho}_{m,0} r_{\rm vir}^3 \ , \tag{7}$$

where $\bar{\rho}_{m,0}$ is the present day mean matter density. The factor $\delta_{\rm TH}$ is the overdensity predicted by the dissipationless spherical top-hat collapse model,

$$\delta_{\rm TH} \simeq \frac{18\pi^2 + 82y - 39y^2}{\Omega_m(z)}, \quad y = \Omega_m(z) - 1 \,, \tag{8}$$

with $\Omega_m(z) = \Omega_{m,0}/(\Omega_{m,0} + \Omega_{\Lambda,0}a^3)$ [10].

Furthermore, halo concentration correlates with its mass. At $z = 0$, the trend

$$c(z=0) \simeq 9 \left(\frac{M_{\rm vir}}{1.5 \times 10^{13} h^{-1} {\rm M}_\odot} \right)^{-0.13} \tag{9}$$

was found in [11]. In addition, for a fixed virial mass, the median concentration parameter exhibits a redshift dependence of $c(z) \simeq c(z=0)/(1+z)$ between $z = 0$ and $z = 4$.

4 Clustering in NFW Halos

Using the NFW halo profile (6) as an input, we find solutions to the Vlasov equation in the limit $\rho_\nu \ll \rho_m$. The CDM distribution is modelled as follows: We assume a uniform distribution of CDM throughout space, with a spherical NFW halo sitting at the origin. For the neutrinos, we take their initial distribution to be the homogeneous and isotropic Fermi–Dirac distribution with no chemical potential. The initial redshift is taken to be $z = 3$, since, at higher redshifts, a sub-eV neutrino has too much thermal velocity to cluster efficiently. The cosmological parameters used are $\{\Omega_m, \Omega_\Lambda, h\} = \{0.3, 0.7, 0.7\}$.

We solve the Vlasov equation using N-one-body simulations, as well as a semi-analytical linear method.[3] The essential features of the results (Figs. 1 and 2) can be understood in terms of neutrino free-streaming, which causes $n_\nu/\bar{n}_\nu$ to flatten out at small radii, and the mass density ratio ρ_ν/ρ_m to drop substantially below the background mean. Both $n_\nu/\bar{n}_\nu$ and ρ_ν/ρ_m approach their respective cosmic mean of 1 and $\bar{\rho}_\nu/\bar{\rho}_m$ at large radii.

Furthermore, we find that the linear method systematically underestimates the neutrino overdensities over the whole range of halo and neutrino masses considered here. Reconciliation with N-one-body simulations can only be achieved if we impose a smoothing scale of > 1 Mpc, or if $n_\nu/\bar{n}_\nu < 3 \div 4$. This finding is consistent with the standard lore that perturbative methods fail once the perturbations exceed unity and nonlinear effects set in.

5 Clustering in the Milky Way

In order to calculate the neutrino overdensity in the Milky Way and, especially, their phase space distribution at Earth ($r_\oplus \sim 8$ kpc from the Galactic

[3] The linear approximation [12] consists of replacing $\partial f/\partial \boldsymbol{p}$ with $\partial f_0/\partial \boldsymbol{p}$ in (1), where f_0 is the unperturbed Fermi–Dirac function.

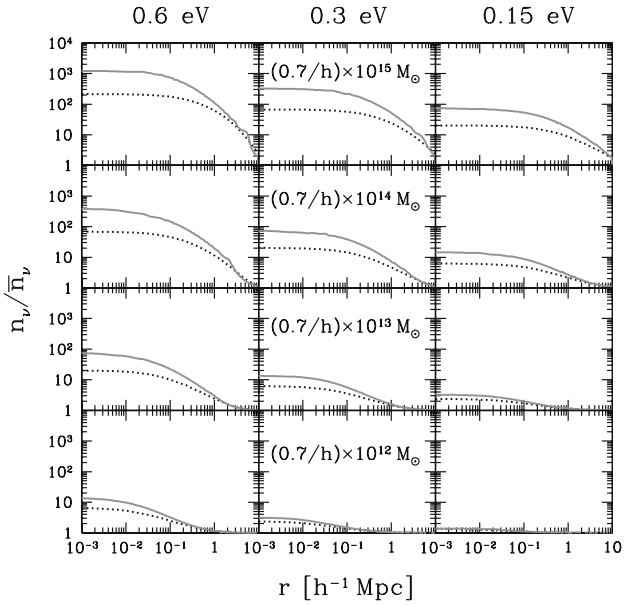

Fig. 1. Relic neutrino number density per flavour, $n_\nu = n_{\bar{\nu}}$, normalised to $\bar{n}_\nu = \bar{n}_{\bar{\nu}} \simeq 56\ \mathrm{cm}^{-3}$, for the indicated neutrino and halo virial masses. Results from N-one-body simulations are denoted by red (solid) lines. Dotted lines correspond to overdensities calculated with the linear approximation.

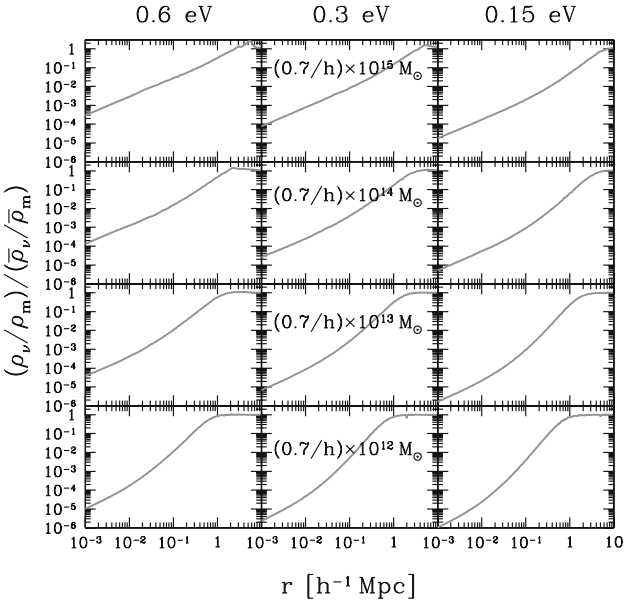

Fig. 2. Mass density ratio ρ_ν/ρ_m normalised to the background mean $\bar{\rho}_\nu/\bar{\rho}_m$ obtained from N-one-body simulations for the indicated neutrino and halo masses.

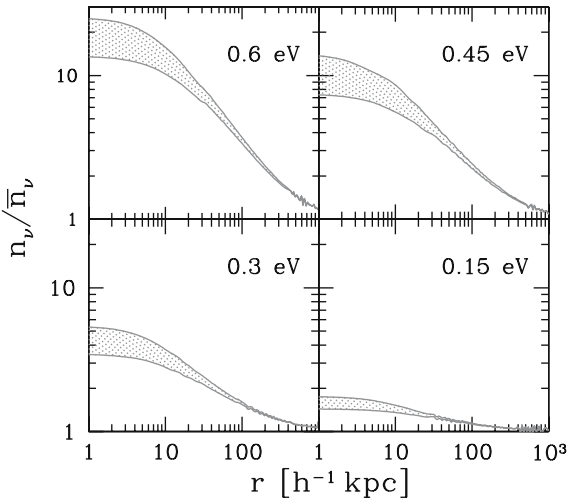

Fig. 3. Relic neutrino number density per flavour, $n_\nu = n_{\bar{\nu}}$, in the Milky Way for various neutrino masses. All curves are normalised to $\bar{n}_\nu = \bar{n}_{\bar{\nu}} \simeq 56\ \mathrm{cm}^{-3}$. The top curve in each plot corresponds to the MWnow run, and the bottom to the NFWhalo run. The enclosed region represents a possible range of overdensities at $z = 0$.

Centre), we need, in principle, to know the complete assembly history of the Milky Way. Theory suggests that the galactic bulge and disk grew out of an NFW halo via baryonic compression [13, 14]. Our strategy, then, is to conduct two series of simulations, one for the present day Milky Way mass distribution (MWnow) [15, 16] which we assume to be static, and one for the NFW halo (NFWhalo) that would have been there, had baryon compression not taken place. The real neutrino overdensity should then lie somewhere between these two extremes. Figure 3 shows the possible ranges of overdensities at $z = 0$.

In all cases, the final momentum distribution at $r_\oplus$ is almost isotropic, with a zero mean radial velocity $\langle v_r \rangle$, and second velocity moments that satisfy approximately the relation $2\langle v_r^2 \rangle = \langle v_T^2 \rangle$. Hence, we plot the coarse-grained phase space densities $\bar{f}(r_\oplus, p)$ only as functions of the absolute velocity.

The coarse-grained spectra in Fig. 4 show varying degrees of deviation from the relativistic Fermi–Dirac function, but share a common feature that $\bar{f} \sim 1/2$ up to the momentum state corresponding to the escape velocity from the Milky Way at $r_\oplus$. This agrees with the requirement that the final coarse-grained density must not exceed the maximal initial fine-grained distribution, $\bar{f} \leq \max(f_0)$ [17, 18, 19, 20, 21]. For neutrinos, $\max(f_0) = 1/2$ at $p = 0$. Thus, our $\bar{f}$ not only satisfies but completely saturates the bound up to p_{esc},

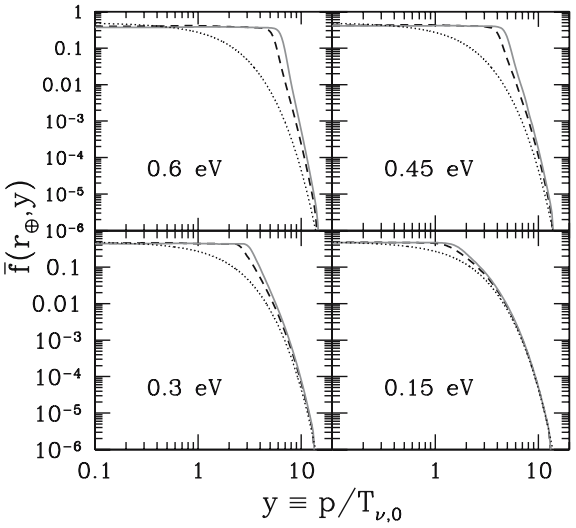

Fig. 4. Momentum distribution of relic neutrinos at $r_\oplus$ for various neutrino masses. The red (solid) line denotes the MWnow run, while the dashed line represents the NFWhalo run. The relativistic Fermi–Dirac function is indicated by the dotted line. The escape velocity $v_{\rm esc} = \sqrt{2|\phi(r_\oplus)|}$ is 490 km s^{-1} and 450 km s^{-1} for MWnow and NFWhalo respectively, corresponding to "escape momenta" $y_{\rm esc} \equiv m_\nu v_{\rm esc}/T_{\nu,0}$ of $(5.9, 4.4, 3.0, 1.5)$ and $(5.4, 4.1, 2.7, 1.4)$ for $m_\nu = (0.6, 0.45, 0.3, 0.15)$ eV.

forming a semi-degenerate state that can only be made denser by filling in states above $p_{\rm esc}$.[4]

6 Relic Neutrino Detection

6.1 Flux Detection

The relic neutrinos' low average momentum $\langle p \rangle = \langle y \rangle T_{\nu,0}$ corresponds to a de Broglie wavelength of macroscopic dimension, $\lambda\!\!\!^{-} = 1/\langle p \rangle = 0.12 \text{ cm}/\langle y \rangle$. Therefore, one may envisage scattering processes in which many target atoms act coherently [22, 23] over a macroscopic volume $\lambda\!\!\!^{-3}$, so that the elastic scattering rate is proportional to the square of the number of target atoms in $\lambda\!\!\!^{-3}$. Compared to the case where the neutrinos are elastically scattered coherently only on the individual target nuclei, the new rate is enhanced by a factor of

$$\frac{N_A}{A}\,\rho_{\rm t}\,\lambda\!\!\!^{-3} \simeq 6 \times 10^{18} \left(\frac{100}{A}\right) \left(\frac{\rho_{\rm t}}{\rm g/cm^3}\right) \left(\frac{\lambda\!\!\!^{-}}{0.1 \text{ cm}}\right)^3 , \qquad (10)$$

[4] This degeneracy should not be confused with that arising from the Pauli exclusion principle.

where N_A is the Avogadro constant, A is the atomic mass, and $\rho_{\rm t}$ is the mass density of the target material.[5]

Exploiting this effect, a practical detection scheme for the local relic neutrino flux is based on the fact that a test body of density $\rho_{\rm t}$ at Earth experiences a neutrino wind force through random scattering events, leading to an acceleration given, for Dirac neutrinos, by [22, 23, 27, 28]

$$a_{\rm t} \simeq \sum_{\nu,\bar{\nu}} \underbrace{n_\nu\, v_{\rm rel}}_{\rm flux}\ \frac{4\pi}{3}\, N_A^2\, \rho_{\rm t}\, r_{\rm t}^3\ \sigma_{\nu N}\ \underbrace{2\, m_\nu\, v_{\rm rel}}_{\rm mom.\ transfer}$$
$$\simeq 2\times 10^{-28}\ \left(\frac{n_\nu}{\bar{n}_\nu}\right)\left(\frac{10^{-3}\, c}{v_{\rm rel}}\right)\left(\frac{\rho_{\rm t}}{{\rm g/cm^3}}\right)\left(\frac{r_{\rm t}}{\hbar/(m_\nu v_{\rm rel})}\right)^3 {\rm cm\ s^{-2}}\ , \quad (11)$$

with $r_t < \lambda$, $\sigma_{\nu N} \simeq G_F^2\, m_\nu^2/\pi$ is the elastic neutrino–nucleon cross section, $v_{\rm rel} = \langle|\boldsymbol{v} - \boldsymbol{v}_\oplus|\rangle$ the mean neutrino velocity in the detector's rest frame, and $v_\oplus \simeq 2.3\times 10^2$ km s^{-1} $\simeq 7.7\times 10^{-4}\, c$ the Earth's velocity through the Milky Way. For $n_\nu/\bar{n}_\nu \sim 20$, (11) gives $a_t \sim 10^{-26}$ cm s^{-2}. For Majorana neutrinos, a_t is further suppressed by a factor of $(v_{\rm rel}/c)^2 \simeq 10^{-6}$ for an unpolarised target, and $v_{\rm rel}/c \simeq 10^{-3}$ for a polarised one.

To digest these estimates, we note that the smallest measurable acceleration at present is $> 10^{-13}$ cm s^{-2}, using conventional Cavendish-type torsion balances. Possible improvements with currently available technology to a sensitivity of $> 10^{-23}$ cm s^{-2} have been proposed [29, 30]. However, this is still off the prediction (11) by three orders of magnitude. Therefore, we conclude that an observation of this effect will not be possible in the next decade, but can still be envisaged in the foreseeable future (thirty to forty years according to [32], exploiting advances in nanotechnology), if our known light neutrinos are Dirac particles. Should they turn out, in the meantime, to be Majorana particles, flux detection via mechanical forces will be a real challenge.

Lastly, the background contribution to the acceleration (11) from the solar pp neutrinos [flux $\sim 10^{11}$ cm^{-2}s^{-1}, $\langle E_\nu\rangle \sim 0.3$ MeV (e.g., [31])], $a_t^{\nu\,{\rm sun}} \simeq 10^{-27}$ cm s^{-2} [27], may be rejected by directionality. The background from weakly interacting massive particles (WIMPs χ, with mass m_χ) [27],

$$a_{\rm t}^{\rm WIMP} \simeq \underbrace{n_\chi\, v_{\rm rel}}_{\rm flux}\ N_A\, A\ \sigma_{\chi N}\ \underbrace{2\, m_\chi\, v_{\rm rel}}_{\rm mom.\ transfer} \quad (12)$$
$$\simeq 6\times 10^{-29}\left(\frac{\rho_\chi}{0.3\ {\rm GeV/cm^3}}\right)\left(\frac{v_{\rm rel}}{10^{-3}\, c}\right)^2\left(\frac{A}{100}\right)\left(\frac{\sigma_{\chi N}}{10^{-45}\ {\rm cm^2}}\right){\rm cm\ s^{-2}}\ ,$$

should they be the main constituent of galactic dark matter with mass density $\rho_\chi \equiv n_\chi m_\chi \simeq 0.3$ GeV cm^{-3} at $r_\oplus$, can be neglected as soon as the WIMP–nucleon cross section $\sigma_{\chi N}$ is smaller than $\sim 3\times 10^{-45}$ cm^2. This should be well established by the time relic neutrino direct detection becomes a reality.

[5] In the case of coherent scattering, it is possible, in principle, to measure also the scattering amplitude itself [24, 25, 26], which is linear in G_F. However, a large lepton asymmetry is required for a non-negligible effect.

6.2 Target Detection

Detection methods based on the scattering of extremely energetic particles (accelerator beams or cosmic rays) off the relic neutrinos as a target take advantage of the fact that, for centre-of-mass (c.m.) energies,

$$\sqrt{s} = \sqrt{2\, m_\nu\, E_{\rm beam}} \simeq 4.5 \, \left(\frac{m_\nu}{\rm eV}\right)^{1/2} \left(\frac{E_{\rm beam}}{10 \text{ TeV}}\right)^{1/2} \text{ MeV} \,, \qquad (13)$$

just below the W- and Z-resonances, the weak interaction cross sections grow rapidly with the beam energy $E_{\rm beam}$.

At accelerators Target detection using accelerator beams does not seem viable. For a hypothetical beam energy of 10^7 TeV and an accelerator ring of ultimate circumference $L \simeq 4 \times 10^4$ km around the Earth, the interaction rate is roughly one event per year. See [1] for details.

With cosmic rays It was pointed out by Weiler [33, 34] (for earlier suggestions, see [35, 36, 37, 38, 39]) that the resonant annihilation of extremely energetic cosmic neutrinos (EECν)—with $E > 10^{20}$ eV—with relic anti-neutrinos (and vice versa) into Z-bosons appears to be a unique process having sensitivity to the relic neutrinos. On resonance,

$$E_\nu^{\rm res} = \frac{m_Z^2}{2m_\nu} \simeq 4 \times 10^{21} \, \left(\frac{\rm eV}{m_\nu}\right) \text{ eV} \,, \qquad (14)$$

the associated cross section is enhanced by several orders of magnitude,

$$\langle \sigma_{\rm ann} \rangle = \int ds \; \sigma^Z_{\nu\bar\nu}(s)/m_Z^2 \simeq 2\pi\sqrt{2}\, G_F \simeq 4 \times 10^{-32} \text{ cm}^2 \,, \qquad (15)$$

leading to a "short" mean free path $\ell_\nu = (\bar n_\nu \, \langle \sigma_{\rm ann} \rangle)^{-1} \simeq 1.4 \times 10^5$ Mpc which is *only* about $48\, h$ times the Hubble distance. Neglecting cosmic evolution effects, this corresponds to an annihilation probability for EECν from cosmological distances on the relic neutrinos of $2\, h^{-1}\%$.

The signatures of annihilation are (i) absorption dips [33, 34, 40] (see also [41, 42, 43]) in the EECν spectrum at the resonant energies, and (ii) emission features [44, 45, 46, 47, 48] (Z-bursts) as protons and photons with energies spanning a decade or more above the Greisen–Zatsepin–Kuzmin (GZK) cutoff at $E_{\rm GZK} \simeq 4 \times 10^{19}$ eV [49, 50]. This is the energy beyond which the CMB is absorbing to nucleons due to resonant photopion production.[6]

The possibility to confirm the existence of relic neutrinos within the next decade from a measurement of the aforementioned dips in the EECν flux was recently investigated in [40]. Presently planned neutrino detectors (Pierre Auger Observatory [55], IceCube [56], ANITA [57], EUSO [58], OWL [59],

[6] The association of Z-bursts with the mysterious cosmic rays observed above $E_{\rm GZK}$ is a controversial possibility [44, 45, 46, 47, 48, 51, 52, 53, 54].

and SalSA [60]) operating in the energy regime above 10^{21} eV appear to be sensitive enough to lead us, within the next decade, into an era of relic neutrino absorption spectroscopy, provided that the EECν flux at the resonant energies is close to current observational bounds and the neutrino mass is > 0.1 eV. In this case, the associated Z-bursts must also be seen as post-GZK events at the planned cosmic ray detectors (Auger, EUSO, and OWL).

What are the implications of relic neutrino clustering for absorption and emission spectroscopy? Firstly, absorption spectroscopy is predominantly sensitive to the relic neutrino background at early times, with the depths of the absorption dips determined largely by the higher number densities at $z \gg 1$. Since neutrinos do not cluster significantly until $z < 2$, clustering at recent times can only show up as secondary dips with such minimal widths in energy [61] that they do not seem likely to be resolved by planned observatories.

On the other hand, emission spectroscopy is directly sensitive to the relic neutrino content of the local universe ($z < 0.01 \Leftrightarrow r_{\rm GZK} < 50$ Mpc). However, since the neutrino density contrasts approximately track those of the underlying CDM above the neutrino free-streaming scale $k_{\rm fs}^{-1}$, it is clear that there cannot be a substantial neutrino overdensity over the whole GZK volume ($\sim r_{\rm GZK}^3$). Indeed, given the local CDM distribution inferred from peculiar velocity measurements (smeared over $\sim$5 Mpc), we estimate the corresponding neutrino overdensity to be < 2 (Fig. 5). Hence the overall emission rate cannot be significantly enhanced by gravitational clustering.

Another possibility is to exploit the fact that there are several galaxy clusters ($> 10^{14} M_\odot$) within the GZK zone with significant neutrino clustering. One could then search for directional dependences in the emission events as a signature of EECν–relic ν annihilation. For example, AGASA has an an-

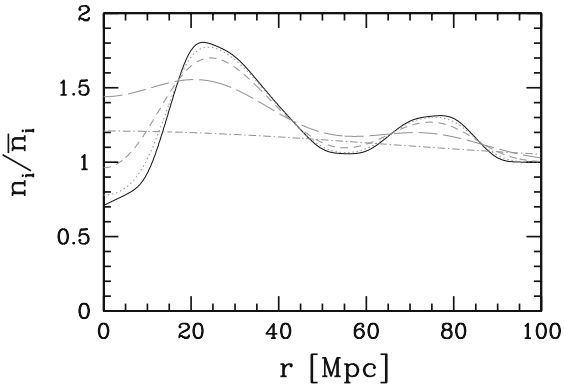

Fig. 5. "Large scale" overdensities ($i = \nu, \mathrm{CDM}$) in the local universe, with the Milky Way at $r = 0$. The black solid line corresponds to the local CDM distribution inferred from peculiar velocity measurements [62] (see also [63]) smeared over the surface of a sphere with radius r [48]. The dotted line is the neutrino overdensity for $m_\nu = 0.6$ eV, short dash 0.3 eV, long dash 0.15 eV, and dot-dash 0.04 eV.

gular resolution of $\sim 2^\circ$ [64]. This is already sufficient to resolve the internal structures of, say, the Virgo cluster (distance $\sim$15 Mpc, $M_{\rm vir} \sim 8 \times 10^{14} {\rm M}_\odot$) which spans some 10° across the sky. From Fig. 1, the average neutrino overdensity along the line of sight towards and up to Virgo is estimated to be $\sim$45 and $\sim$5 for $m_\nu = 0.6\,{\rm eV}$ and $0.15\,{\rm eV}$ respectively, given an angular resolution of $\sim 2^\circ$. The corresponding increases in the number of events coming from the direction of the Virgo cluster relative to the unclustered case, assuming an isotropic distribution of EECν sources, are given roughly by the same numbers, since protons originating from $\sim$15 Mpc away arrive at Earth approximately unattenuated. The numbers improve to $\sim$55 and $\sim$8 respectively with a finer $\sim 1^\circ$ angular resolution.

7 Conclusion

We have conducted a systematic and exhaustive study of the gravitational clustering of big bang relic neutrinos onto existing CDM and baryonic structures within the flat ΛCDM model. Our main computational tools are (i) a restricted, N-one-body method, in which we neglect the gravitational interaction between the neutrinos and treat them as test particles moving in an external potential generated by the CDM/baryonic structures, and (ii) a semi-analytical, linear technique, which requires additional assumptions about the neutrino phase space distribution. In both cases, the CDM/baryonic gravitational potentials are calculated from parametric halo density profiles from high resolution N-body studies and/or from realistic mass distributions reconstructed from observational data.

Using these two techniques, we track the relic neutrinos' accretion onto CDM halos ranging from the galaxy to the galaxy cluster variety ($M_{\rm vir} \sim 10^{12} \to 10^{15} {\rm M}_\odot$), and determine the neutrino number densities on scales $\sim 1 \to 1000$ kpc for a range of neutrino masses. We find that the linear method systematically underestimates the neutrino overdensities over the whole range of halo and neutrino masses considered. Reconciliation with N-one-body simulations can only be achieved if we impose a smoothing scale of > 1 Mpc, or if the overdensity is no more than three or four. We therefore conclude that the linear theory does not generally constitute a faithful approximation to the Vlasov equation in the study of neutrino clustering on galactic and sub-galactic scales (< 50 kpc). However, it may still be useful for finding the minimum effects of neutrino clustering in other contexts not considered in this work (e.g., the nonlinear matter power spectrum [65]).

Next we estimate the neutrino phase space distribution in the Milk Way, especially in our local neighbourhood at Earth $r_\oplus$, taking also into account contributions to the total gravitational potential from the galactic bulge and disk. We find a maximum overdensity of $\sim$20 per neutrino flavour in our immediate vicinity, provided that the neutrino mass is at its current upper

limit of 0.6 eV. For neutrino masses less than 0.15 eV, the expected overdensity from gravitational clustering is less than two. The associated coarse-grained momentum spectra show varying degrees of deviation from the relativistic Fermi–Dirac function, but share a common feature that they are semi-degenerate, with phase space density $\bar{f} \sim 1/2$, up to the momentum state corresponding to the escape velocity from the Milky Way at $r_\oplus$. This means that the neutrino number densities we have calculated here for $r_\oplus$ are already the *highest possible*, given the neutrino mass, without violating phase space constraints. In order to attain even higher densities, one must now appeal to non-standard theories (e.g., [66]).

In terms of scattering-based detection possibilities, this meager enhancement in the neutrino number density in the Milky Way from gravitational clustering means that relic neutrinos are still far from being detected in fully earthbound laboratory experiments. For flux detection methods based on coherent elastic scattering of relic neutrinos off target matter in a terrestrial detector, a positive detection could be thirty to forty years away, provided that light neutrinos are Dirac particles. For light Majorana neutrinos, another $\sim 10^3$ times more sensitivity would be required in the detector for a positive signal. Target detection methods using accelerator beams seem equally hopeless, unless the accelerator is the size of the Earth and operates at an energy of $\sim 10^7$ TeV.

Meanwhile, target detection using extremely energetic cosmic neutrinos (EECν, $> 10^{21}$ eV) remains the only viable means to confirm the existence of big bang relic neutrinos within the next decade or so. Resonant annihilation of EECν on relic neutrinos can be revealed as absorption dips in the EECν flux (e.g., [40]), or as emission features in the Z-decay products. However, since absorption spectroscopy is largely insensitive to late time ($z < 2$) relic neutrino clustering, our findings here have little impact on the conclusions of [40]. On the other hand, emission spectroscopy is sensitive to the relic neutrino content of the local GZK zone, $V_{\rm GZK} \sim 50^3$ Mpc^3. While we find no significant large scale clustering within $V_{\rm GZK}$ and therefore no significant enhancement in the overall emission rates, it is still conceivable to exploit the considerable neutrino overdensities in nearby galaxy clusters, and search for directional dependences in the post-GZK emission events. For the Virgo cluster, for example, we estimate the event rate from the central 1° region to be $\sim$55 and $\sim$8 times the unclustered rate for neutrino mass $m_\nu = 0.6$ eV and 0.15 eV respectively, assuming an isotropic distribution of EECν sources. Planned observatories such as the Pierre Auger Observatory [55], EUSO [58] and OWL [59] will have sufficient angular resolution to, in principle, see this enhancement. However, considering the rapidly improving constraints on both the EECν flux and neutrino masses, it remains to be seen if the enhancement can indeed be observed with enough statistical significance [67].

References

1. A. Ringwald and Y. Y. Y. Wong, JCAP **0412** (2004) 005 [arXiv:hep-ph/0408241].
2. S. Hannestad, New J. Phys. 6 (2004) **108** [arXiv:hep-ph/0404239].
3. G. L. Fogli, E. Lisi, A. Marrone, D. Montanino, A. Palazzo and A. M. Rotunno, eConf **C030626** (2003) THAT05 [arXiv:hep-ph/0310012].
4. E. Bertschinger, in *Les Houches Cosmology 1993*, pp. 273–348, arXiv:astro-ph/9503125.
5. A. Klypin, in *Modern Cosmology*, edited by S. Bonometto, V. Gorini, and U. Moschella (IOP, Bristol, 2002), p. 420.
6. S. Singh and C. P. Ma, Phys. Rev. D **67** (2003) 023506 [arXiv:astro-ph/0208419].
7. L. Kofman, A. Klypin, D. Pogosian and J. P. Henry, Astrophys. J. **470** (1996) 102 [arXiv:astro-ph/9509145].
8. J. F. Navarro, C. S. Frenk and S. D. M. White, Astrophys. J. **462** (1996) 563 [arXiv:astro-ph/9508025].
9. J. F. Navarro, C. S. Frenk and S. D. M. White, Astrophys. J. **490** (1997) 493.
10. G. L. Bryan and M. L. Norman, Astrophys. J. **495** (1998) 80 [arXiv:astro-ph/9710107].
11. J. S. Bullock et al., Mon. Not. Roy. Astron. Soc. **321** (2001) 559 [arXiv:astro-ph/9908159].
12. I. H. Gilbert, Astrophys. J. **144** (1966) 233.
13. S. D. M. White and M. J. Rees, Mon. Not. Roy. Astro. Soc. **183** (1978) 341.
14. H. J. Mo, S. Mao and S. D. M. White, Mon. Not. Roy. Astron. Soc. **295** (1998) 319 [arXiv:astro-ph/9707093].
15. W. Dehnen and J. Binney, Mon. Not. Roy. Astro. Soc. **294** (1998) 429 [arXiv:astro-ph/9612059].
16. A. Klypin, H. Zhao and R. S. Somerville, Astrophys. J. **573** (2002) 597 [arXiv:astro-ph/0110390].
17. D. Lynden-Bell, Mon. Not. Roy. Astron. Soc. **136** (1967) 101.
18. S. Tremaine and J. E. Gunn, Phys. Rev. Lett. **42** (1979) 407.
19. F. H. Shu, Astrophys. J. **225** (1978) 83.
20. F. H. Shu, Astrophys. J. **316** (1987) 502.
21. A. Kull, R. A. Treumann and H. Böhringer, Astrophys. J. **466** (1996) L1 [arXiv:astro-ph/9606057].
22. B. F. Shvartsman, V. B. Braginsky, S. S. Gershtein, Y. B. Zeldovich and M. Y. Khlopov, JETP Lett. **36** (1982) 277 [Pisma Zh. Eksp. Teor. Fiz. **36** (1982) 224].
23. P. F. Smith and J. D. Lewin, Phys. Lett. B **127** (1983) 185.
24. L. Stodolsky, Phys. Rev. Lett. **34** (1975) 110 [Erratum-ibid. **34** (1975) 508].
25. N. Cabibbo and L. Maiani, Phys. Lett. B **114** (1982) 115.
26. P. Langacker, J. P. Leveille and J. Sheiman, Phys. Rev. D **27** (1983) 1228.
27. G. Duda, G. Gelmini and S. Nussinov, Phys. Rev. D **64** (2001) 122001 [arXiv:hep-ph/0107027].
28. I. Ferreras and I. Wasserman, Phys. Rev. D **52** (1995) 5459.
29. C. Hagmann, in *COSMO98: Proceedings of the Conference on Particle Physics and the Early Universe*, edited by D. O. Caldwell (AIP, Woodbury NY, 1999), p.460 [AIP Conf. Proc. **478** (1998) 460; arXiv:astro-ph/9902102].

30. C. Hagmann, presented at *American Physical Society (APS) Meeting of the Division of Particles and Fields (DPF 99)*, Los Angeles, USA, 1999, arXiv:astro-ph/9905258.
31. J. N. Bahcall, M. H. Pinsonneault and S. Basu, Astrophys. J. **555** (2001) 990 [arXiv:astro-ph/0010346].
32. P. F. Smith, Phil. Trans. Roy. Soc. Lond. A **361** (2003) 2591.
33. T. J. Weiler, Phys. Rev. Lett. **49** (1982) 234.
34. T. J. Weiler, Astrophys. J. **285** (1984) 495.
35. J. Bernstein, M. Ruderman and G. Feinberg, Phys. Rev. **132** (1963) 1227.
36. B. P. Konstantinov and G. E. Kocharov, J. Exp. Theor. Phys. **19** (1964) 992.
37. R. Cowsik, Y. Pal and S. N. Tandon, Phys. Lett. **13** (1964) 265.
38. T. Hara and H. Sato, Prog. Theor. Phys. **64** (1980) 1089.
39. T. Hara and H. Sato, Prog. Theor. Phys. **65** (1981) 477.
40. B. Eberle, A. Ringwald, L. Song and T. J. Weiler, Phys. Rev. D **70** (2004) 023007 [arXiv:hep-ph/0401203].
41. P. Gondolo, G. Gelmini and S. Sarkar, Nucl. Phys. B **392** (1993) 111 [arXiv:hep-ph/9209236].
42. E. Roulet, Phys. Rev. D **47** (1993) 5247.
43. S. Yoshida, H. Y. Dai, C. C. Jui and P. Sommers, Astrophys. J. **479** (1997) 547 [arXiv:astro-ph/9608186].
44. D. Fargion, B. Mele and A. Salis, Astrophys. J. **517** (1999) 725 [arXiv:astro-ph/9710029].
45. T. J. Weiler, Astropart. Phys. **11** (1999) 303 [arXiv:hep-ph/9710431].
46. S. Yoshida, G. Sigl and S. J. Lee, Phys. Rev. Lett. **81** (1998) 5505 [arXiv:hep-ph/9808324].
47. Z. Fodor, S. D. Katz and A. Ringwald, Phys. Rev. Lett. **88** (2002) 171101 [arXiv:hep-ph/0105064].
48. Z. Fodor, S. D. Katz and A. Ringwald, JHEP **0206** (2002) 046 [arXiv:hep-ph/0203198].
49. K. Greisen, Phys. Rev. Lett. **16** (1966) 748.
50. G. T. Zatsepin and V. A. Kuzmin, JETP Lett. **4** (1966) 78 [Pisma Zh. Eksp. Teor. Fiz. **4** (1966) 114].
51. O. E. Kalashev, V. A. Kuzmin, D. V. Semikoz and G. Sigl, Phys. Rev. D **65** (2002) 103003 [arXiv:hep-ph/0112351].
52. D. S. Gorbunov, P. G. Tinyakov and S. V. Troitsky, Astropart. Phys. **18** (2003) 463 [arXiv:astro-ph/0206385].
53. D. V. Semikoz and G. Sigl, JCAP **0404** (2004) 003 [arXiv:hep-ph/0309328].
54. G. Gelmini, G. Varieschi and T. Weiler, arXiv:hep-ph/0404272.
55. Pierre Auger Observatory, http://www.auger.org/
56. IceCube, http://icecube.wisc.edu/
57. ANtarctic Impulse Transient Array, http://www.ps.uci.edu/~anita/
58. Extreme Universe Space Observatory, http://www.euso-mission.org/
59. Orbiting Wide-angle Light-collectors, http://owl.gsfc.nasa.gov/
60. Saltdome Shower Array, P. Gorham, D. Saltzberg, A. Odian, D. Williams, D. Besson, G. Frichter and S. Tantawi, Nucl. Instrum. Meth. A **490** (2002) 476 [arXiv:hep-ex/0108027].
61. T. Reiter, unpublished notes.
62. L. N. da Costa, W. Freudling, G. Wegner, R. Giovanelli, M. P. Haynes and J. J. Salzer, Astrophys. J. Lett. **468** (1996) L5 [arXiv:astro-ph/9606144].

63. A. Dekel et al., Astrophys. J. **522** (1999) 1 [arXiv:astro-ph/9812197].
64. Akeno Giant Air Shower Array, http://www-akeno.icrr.u-tokyo.ac.jp/AGASA/
65. K. Abazajian, E. R. Switzer, S. Dodelson, K. Heitmann and S. Habib, arXiv:astro-ph/0411552.
66. G. J. Stephenson, T. Goldman and B. H. J. McKellar, Int. J. Mod. Phys. A **13** (1998) 2765 [arXiv:hep-ph/9603392].
67. A. Ringwald, T. J. Weiler and Y. Y. Y. Wong, in preparation.

Shadow Shapes Around the Black Hole in the Galactic Centre

A.F. Zakharov[1,2,3], A.A. Nucita[4], F. DePaolis[4], and G. Ingrosso[4]

[1] Institute of Theoretical and Experimental Physics, B.Cheremushkinskaya st., 25, Moscow, 117259, Russia,
zakharov@itep.ru
[2] Space Research Centre of Lebedev Physics Institute, Moscow
[3] Joint Institute for Nuclear Research, Dubna
[4] Dipartimento di Fisica Universita di Lecce and INFN, Sezione di Lecce, Italy,
Achille.Nucita,Francesco.DePaolis,Gabriele.Ingrosso@le.infn.it

Abstract. Recently Holz & Wheeler [1] considered a very attracting possibility to detect retro-MACHOs, i.e. retro-images of the Sun by a Schwarzschild black hole. In this paper we discuss glories (mirages) formed near rapidly rotating Kerr black hole horizons and propose a procedure to measure masses and rotation parameters analyzing these forms of mirages. In some sense that is a manifestation of gravitational lens effect in the strong gravitational field near black hole horizon and a generalization of the retro-gravitational lens phenomenon. We analyze the case of a Kerr black hole rotating at arbitrary speed for some selected positions of a distant observer with respect to the equatorial plane of a Kerr black hole. We discuss glories (mirages) formed near rapidly rotating Kerr black hole horizons and propose a procedure to measure masses and rotation parameters analyzing these forms of mirages. Some time ago Falcke, Melia & Agol [2] suggested to search shadows at the Galactic Center. In this paper we present the boundaries for shadows calculated numerically. We also propose to use future radio interferometer RADIOASTRON facilities to measure shapes of mirages (glories) and to evaluate the black hole spin as a function of the position angle of a distant observer.

Recently Holz & Wheeler [1] have suggested that a Schwarzschild black hole may form retro-images (called retro-MACHOs) if it is illuminated by the Sun. We analyze a rapidly rotating Kerr black hole case for some selected positions of a distant observer with respect to the equatorial plane of the Kerr black hole. We discuss glories (mirages) formed near a rapidly rotating Kerr black hole horizon and propose a procedure to measure the mass and the black hole spin analyzing the mirage shapes. Since a source illuminating the black hole surroundings may be located in an arbitrary direction with respect to the observer line of sight, a generalization of the retro-gravitational lens idea suggested by Holz & Wheeler [1] is needed. A strong gravitational field approximation for a gravitational lens model was considered recently in several papers [3, 4, 5, 6, 7, 8, 10, 11, 12, 13, 14, 15]. However, if we consider the standard geometry for a gravitational lens model, namely if a gravitational lens is located between a source and observer, then the probability to have evidences for strong gravitational field effects is quite small, because

the probability is about $P \sim \tau_{GL} \times R_G/D_S$ where, τ_{GL} is the optical depth for gravitational lensing and the factor R_G/D_S corresponds to a probability to have a manifestations for strong gravitational field effects (R_G is the Schwarzschild radius for a gravitational lens, D_S is a distance between an observer and a gravitational lens). Therefore, the factor R_G/D_S is quite small for typical astronomical cases. However, these arguments cannot be used for the cases of a a source located nearby a black hole.

First, it is necessary to explain differences of a considered geometry, standard geometry of gravitational lensing (when a gravitational lens is located roughly speaking between a source and an observer) and a model introduced by Holz & Wheeler [1] when an observer is located between a source (Sun) and a gravitational lens that is a black hole. In this paper we will consider images formed by retro-photons, but in contrast to Holz & Wheeler [1] we will analyze forms of images near black holes but not a light curve of an image formed near black hole as Holz & Wheeler [1] did. In our consideration a location of source could be arbitrary in great part (in accordance with a geometry different parts of images could be formed),[1] for example, accretion flows (disks) could be sources forming such images. Since in such cases images formed by retro-photons are considered, we call it like retro gravitational lensing even if a source is located near a gravitational lens (a black hole) in contrast to a standard gravitational lens model.

As usual, we use geometrical units with $G = c = 1$. It is convenient also to measure all distances in black hole masses, so we may set $M = 1$ (M is a black hole mass). Calculations of mirage forms are based on qualitative analysis of different types of photon geodesics in a Kerr metric (for references see [16, 17, 18, 19]). In fact, we know that impact parameters of photons are very close to the critical ones (which correspond to parabolic orbits). One can find some samples of photon trajectories in [20, 17]. This set (critical curve) of impact parameters separates escape and plunge orbits (see [16, 17, 18, 19] for details) or otherwise the critical curve separates scatter and capture regions for unbounded photon trajectories. Therefore the mirage shapes almost look like to critical curves but are just reflected with respect to z-axis. We assume that mirages of all orders almost coincide and form only one quasi-ring from the point of view of the observer. We know that the impact parameter corresponding to the π deflection is close to that corresponding to a $n\pi$ deflections (n is an odd number). For more details see Holz & Wheeler [1] (astronomical applications of this idea was discussed by De Paolis et al. [21] and its generalizations for Kerr black hole are considered by De Paolis et al. [22]). We use prefix "quasi" since we consider a Kerr black hole case, so that mirage shapes are not circular rings but Kerr ones. Moreover, the side which is formed by co-moving (or co-rotating) photons is much brighter than the opposite side since rotation of a black hole squeeze deviations between geodesics because

[1] However, if a source is located between black hole and an observer, images formed by retro-photons and located near black holes could be non-detectable.

of Lense – Thirring effect. Otherwise, rotation stretches deviations between geodesics for counter-moving photons.

The full classification of geodesic types for Kerr metric is given in [18]. As it was shown in this paper, there are three photon geodesic types: capture, scattering and critical curve which separates the first two sets. This classification fully depends only on two parameters $\xi = L_z/E$ and $\eta = Q/E^2$, which are known as Chandrasekhar's constants [17]. Here the Carter constant Q is given by Carter [23]

$$Q = p_\theta^2 + \cos^2\theta \left[a^2\left(m^2 - E^2\right) + L_z^2/\sin^2\theta\right], \tag{1}$$

where $E = p_t$ is the particle energy at infinity, $L_z = p_\phi$ is z-component of its angular momentum, $m = p_i p^i$ is the particle mass. Therefore, since photons have $m = 0$

$$\eta = p_\theta^2/E^2 + \cos^2\theta \left[-a^2 + \xi^2/\sin^2\theta\right]. \tag{2}$$

The first integral for the equation of photon motion (isotropic geodesics) for a radial coordinate in the Kerr metric is described by the following equation [23, 17, 18, 24]

$$\rho^4 (dr/d\lambda)^2 = R(r)\ ,$$

where

$$R(r) = r^4 + (a^2 - \xi^2 - \eta)r^2 + 2[\eta + (\xi - a)^2]r - a^2\eta\ , \tag{3}$$

and $\rho^2 = r^2 + a^2\cos^2\theta, \Delta = r^2 - 2r + a^2, a = S/M^2$. The constants M and S are the black hole mass and angular momentum, respectively. Equation (3) is written in dimensionless variables (all lengths are expressed in black hole mass units M).

We will consider different types of geodesics on r – coordinate in spite of the fact that these type of geodesics were discussed in a number of papers and books, in particular in a classical monograph by Chandrasekhar [17] (where the most suited analysis for our goals was given). However, our consideration is differed even from Chandrasekhar's analysis in the following items.

(i) Chandrasekhar [17] considered the set of critical geodesics separating capture and scatter regions as parametric functions $\eta(r), \eta(r)$, but not as the function $\eta(\xi)$ (as we do). However, we believe that a direct presentation of function $\eta(\xi)$ is much more clear and give a vivid illustration of different types of motion. Moreover, one could obtain directly form of mirages from the function $\eta(\xi)$ (as it will be explained below).

(ii) Chandrasekhar [17] considered the function $\eta(r)$ also for $\eta < 0$ and that is not quit correct, because for $\eta < 0$ allowed constants of motion correspond only to capture (as it was mentioned in the book [17]). This point will be briefly discussed below.

If we fix a black hole spin parameter a and consider a plane (ξ, η) and different types of photon trajectories corresponding to (ξ, η), namely, a capture

region, a scatter region and the critical curve $\eta_{\rm crit}(\xi)$ separating the scatter and capture regions. The critical curve is a set of (ξ,η) where the polynomial $R(r)$ has a multiple root (a double root for this case). Thus, the critical curve $\eta_{\rm crit}(\xi)$ could be determined from the system [18, 24]

$$\begin{aligned} R(r) &= 0\ , \\ \frac{\partial R}{\partial r}(r) &= 0\ , \end{aligned} \tag{4}$$

for $\eta \geq 0, r \geq r_+ = 1+\sqrt{1-a^2}$, because by analyzing of trajectories along the θ coordinate we know that for $\eta < 0$ we have $M = \{(\xi,\eta)|\eta \geq -a^2 + 2a|\xi| - \xi^2, -a \leq \xi \leq a\}$ and for each point $(\xi,\eta) \in M$ photons will be captured. If instead $\eta < 0$ and $(\xi,\eta) \bar{\in} M$, photons cannot have such constants of motion, corresponding to the forbidden region (see, [17, 18] for details).

One can therefore calculate the critical curve $\eta(\xi)$ which separates the capture and the scattering regions [18, 24]. We remind that the maximal value for $\eta_{\rm crit}(\xi)$ is equal to 27 and is reached at $\xi = -2a$. Obviously, if $a \to 0$, the well-known critical value for Schwarzschild black hole (with $a = 0$) is obtained.

Thus, at first, we calculate the critical curves for chosen spin parameters a which are shown in Fig. 1. The shape of the critical curve for $a = 0$ (Schwarzschild black hole) is well-known because for this case we have $\eta_{\rm crit}(\xi) = 27-\xi^2$ for $|\xi| \leqslant 3\sqrt{3}$, but we show the critical curve to compare with the other cases.

By following this approach we can find the set of critical impact parameters (α,β), for the image (mirage or glory) around a rotating black hole. The sets of critical parameters form caustics around black holes and it is well-known that caustics are the brightest part of each image (numerical simulations of caustic formations were done by Rauch & Blandford [25]). We remind that (α,β) parameters could be evaluated in terms of $(\xi,\eta_{\rm crit})$ by the following way [17]

$$\alpha(\xi) = \xi/\sin\theta_0\ , \tag{5}$$

$$\begin{aligned} \beta(\xi) &= (\eta_{\rm crit}(\xi) + a^2\cos^2\theta_0 - \xi^2\cot^2\theta_0)^{1/2} \\ &= (\eta_{\rm crit}(\xi) + (a^2 - \alpha^2(\xi))\cos^2\theta_0)^{1/2}\ . \end{aligned} \tag{6}$$

Actually, the mirage shapes are boundaries for shadows considered by Falcke, Melia & Agol [2] (see also [26]).

We note that the precision we obtain by considering critical impact parameters instead of their exact values for photon trajectories reaching the observer is good enough. In particular, co-rotating photons form much brighter part of images with respect to retrograde photons. Of course, the larger is the black hole spin parameter the larger is this effect (i.e. the co-rotating part of the images become closest to the black hole horizon and brighter).

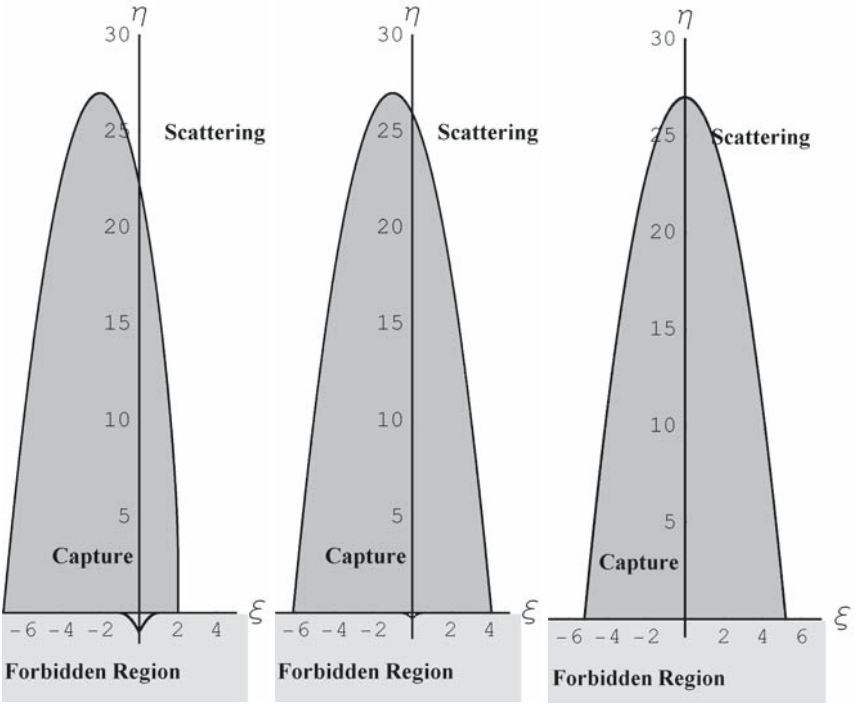

Fig. 1. Different types for photon trajectories and spin parameters ($a = 1., a = 0.5, a = 0.$). Critical curves separate capture and scatter regions. Here we show also the forbidden region corresponding to constants of motion $\eta < 0$ and $(\xi, \eta) \bar{\in} M$ as it was discussed in the text.

This approximation is based not only on numerical simulation results of photon propagation [27, 28, 29, 30, 31, 41, 43, 38, 39, 40] (about 10^9 photon trajectories were analyzed) but also on analytical results (see, for example [17, 18]).

Let us assume that the observer is located in the equatorial plane ($\theta = \pi/2.$). For this case we have from (5) and (6)

$$\alpha(\xi) = \xi, \tag{7}$$

$$\beta(\xi) = \sqrt{\eta_{\rm crit}(\xi)}\,. \tag{8}$$

As mentioned earlier, the maximum impact value $\beta = 3\sqrt{3}$ corresponds to $\alpha = -2a$ and if we consider the extreme spin parameter $a = 1$ a segment of straight line $\alpha = 2, 0 < |\beta| < \sqrt{3}$ belongs to the mirage (see images in Fig. 2 for different spin parameters). It is clear that for this case one could easy evaluate the black hole spin parameter after the mirage shape reconstruction since we have a rather strong dependence of the shapes on spins. As it was explained earlier, the maximum absolute value for $|\beta| =$

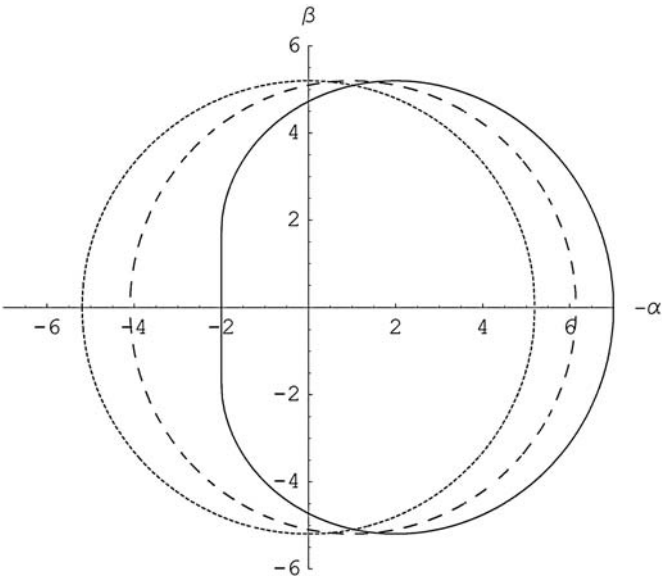

Fig. 2. Mirages around black hole for equatorial position of distant observer and different spin parameters. The solid line, the dashed line and the dotted line correspond to $a = 1, a = 0.5, a = 0$ correspondingly.

$\sqrt{27} \approx 5.196$ corresponds to $\alpha = -2a$ since the maximum value for $\eta(\xi)$ corresponds to $\eta(-2a) = 27$ as it was found by Zakharov [18]. Therefore, in principle it is possible to estimate the black hole spin parameter by measuring the position of the maximum value for β, but probably that part of the mirage could be too faint to be detected.

If the observer is located along the polar axis we have $\theta_0 = 0$ and from (6) we obtain

$$\beta(\alpha) = (\eta_{\rm crit}(0) + a^2 - \alpha^2(\xi))^{1/2}. \tag{9}$$

or

$$\beta^2(\alpha) + \alpha^2 = \eta_{\rm crit}(0) + a^2 \ . \tag{10}$$

Thus, mirages around Kerr black hole look like circles and even for this case in principle we could evaluate the black hole spin (if the black hole mass is known) taking into account that radii of these circles weakly depend on the black hole spin parameter (Fig. 3). However, one should mention that due to the small difference between radii for different spins, even in the future it is unlikely to be able to measure black hole spins in this way (see Table 1).

Let us consider different values for the angular positions of a distant observer $\theta = \pi/2, \pi/3$ and $\pi/8$ for the spin parameter $a = 0.5$ (Fig. 4) and $\theta = \pi/2, \pi/3, \pi/4$ and $\pi/6$ for $a = 1$. (Fig. 5). From these Figures one can

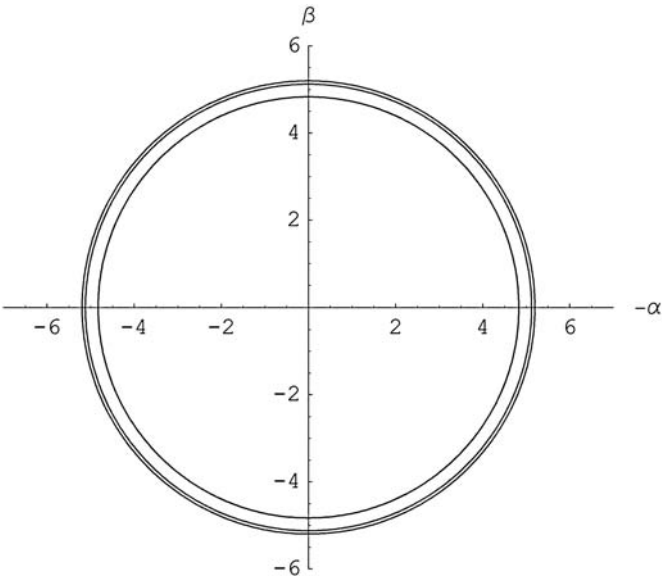

Fig. 3. Mirages around a black hole for the polar axis position of distant observer and different spin parameters ($a = 0, a = 0.5, a = 1$). Smaller radii correspond to greater spin parameters.

Table 1. Dependence of $\eta(0)$ and mirage radii $R_{\rm circ} = (\eta(0) + a^2)^{1/2}$ on spins.

a	0	0.2	0.4	0.5	0.6	0.8	1.
$\eta(0)$	27	26.839	26.348	25.970	25.495	24.210	22.314
$R_{\rm circ}$	5.196	5.185	5.14 9	5.121	5.085	4.985	4.828

see that angular positions of a distant observer could be evaluated from the mirage shapes only for rapidly rotating black holes ($a \sim 1$), but there are no chances to evaluate the angles for slowly rotating black holes, because even for $a = 0.5$ the mirage shape differences are too small to be distinguishable by observations. Indeed, mirage shapes weakly depend on the observer angle position for moderate values of a black hole spin.

According to the schedule the space radio telescope RADIOASTRON will be launched in 2006 or 2007. This project was initiated by Astro Space Center (ASC) of Lebedev Physical Institute of Russian Academy of Sciences (RAS) in collaboration with other institutions of RAS and RosAviaKosmos. Scientists from 20 countries develop the scientific payload for the satellite and will provide a ground base support of the mission. The project was approved by RAS and RosAviaKosmos and is smoothly developing. This space based 10-meter radio telescope will be used for space – ground VLBI measurements.

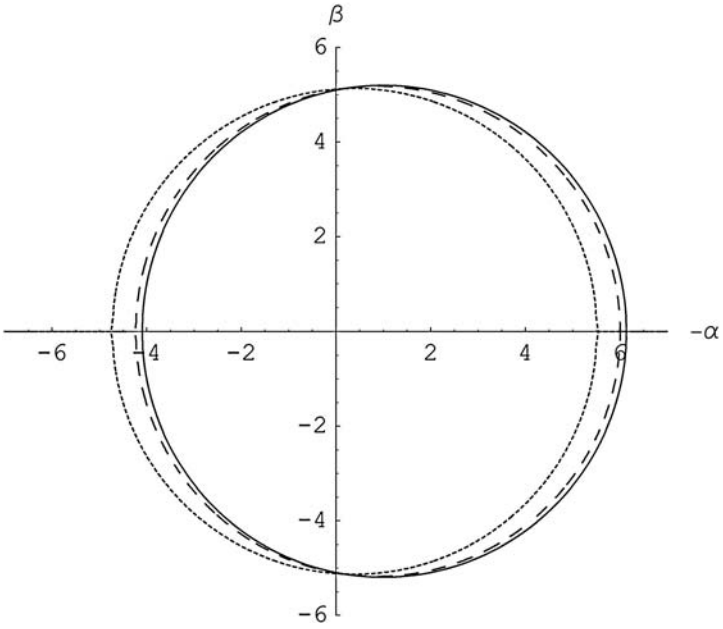

Fig. 4. Mirages around black hole for different angular positions of a distant observer and the spin $a = 0.5$. Solid, dashed and dotted lines correspond to $\theta_0 = \pi/2, \pi/3$ and $\pi/8$, respectively.

The measurements will have extraordinary high angular resolutions, namely about 1–10 microarcseconds (in particular about 8 microarcseconds at the shortest wavelength 1.35 cm and a standard orbit and could be about 0.9 microarcseconds for the high orbit at the same wavelength. For observations four wave bands will be used corresponding to $\lambda = 1.35$ cm, $\lambda = 6.2$ cm, $\lambda = 18$ cm, $\lambda = 92$ cm.

The fringe sizes (in micro arc seconds) for the apogee of the above-mentioned orbit and for all RADIOASTRON bands are given in Table 2.

Thus, there are non-negligible chances to observe such mirages around the black hole at the Galactic Center and in nearby AGNs and microquasars in the radio-band using RADIOASTRON facilities.

Observations of Sgr A* in radio, near-infrared and X-ray spectral bands develop very rapidly [44, 45, 46, 47, 48, 49, 50, 52, 51][2] also because it harbours the closest massive black hole. The mass of this black holes is estimated to be 4×10^6 $M_\odot$ [51, 54, 55, 56] and its intrinsic size from VLBA observations at wavelengths $\lambda = 2$ cm, 1.3 cm, 0.6 cm and 0.3 cm [51].

Similarly to Falcke, Melia & Agol [2] we propose to use VLBI technique to observe the discussed mirages around black holes. They used ray-tracing

[2] An interesting idea to use radio pulsars to test a region near black hole horizon was proposed in [53].

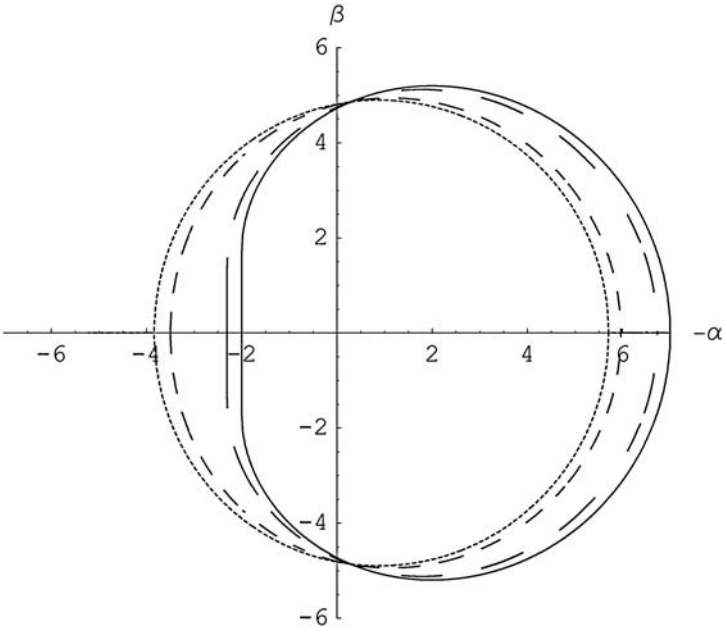

Fig. 5. Mirages around black hole for different angular positions of a distant observer and the spin $a = 1$. Solid, long dashed, short dashed and dotted lines correspond to $\theta_0 = \pi/2, \pi/3, \pi/6$ and $\pi/8$, respectively.

Table 2. The fringe sizes (in micro arc seconds) for the standard and advanced apogees B_{max} (350 000 and 3 200 000 km correspondingly).

B_{max}(km)\λ(cm)	92	18	6.2	1.35
3.5×10^5	540	106	37	8
3.2×10^6	59	12	4	0.9

calculations to evaluate the shapes of shadows. The boundaries of the shadows are black hole mirages (glories or "faces") analyzed earlier. We use the length parameter $r_g = \dfrac{GM}{c^2} = 6 \times 10^{11}$ cm to calculate all values in these units as it was explained in the text. If we take into account the distance towards the Galactic Center $D_{\rm GC} = 8$ kpc then the length r_g corresponds to angular sizes $\sim 5\mu$as. Since the minimum arc size for the considered mirages are about $2r_g$, the standard RADIOASTRON resolution of about 8 μas is comparable with the required precision. The resolution in the case of the higher orbit and shortest wavelength is $\sim 1\mu$as (Table 2) good enough to reconstruct the shapes. Therefore, in principle it will be possible to evaluate a and θ parameters after mirage shape reconstructions from observational

data even if we will observe only the bright part of the image (the bright arc) corresponding to positive parameters α. However, Gammie, Shapiro & McKinney [57] showed that black hole spin is usually not very small and could reach 0.7–0.9 (numerical simulations of relativistic magnetohydrodynamic flows give $a \sim 0.9$). Taking into account detections of 106 day cycle in Sgr A* radio variability seen at 1.3 cm and 2.0 cm by Zhao, Bower & Goss [58] at Very Large Array (VLA), Liu & Melia [59] suggested a procedure to evaluate the black hole spin assuming that the variability could be caused by spin induced disk precession. Moreover, the recent analysis by Aschenbach et al. [60] of periodicity of X-ray flares from the Galactic Center black hole gives an estimate for the spin as high as $a = 0.9939^{+0.0026}_{-0.0074}$. Actually, the authors used generalizations of the idea proposed by Melia et al. [61] that the minimum rotation period for Schwarzschild black hole (for an assumed black hole mass of $2.6 \times 10^6 \mathrm{M}_\odot$) is about $P_0 \approx 20$ minutes and could be in the range $P_0 \in [2.6, 36]$ minutes depending on the black hole spin and prograde and retrograde accretion flows generating the quasi-periodic oscillations. Using this idea and analyzing quasi-periodic variabilities in a infrared band Genzel et al. [46] concluded that the black hole spin should be $a \sim 0.5$. However, this conclusion is based on the assumption that the emitting region is located at the marginally stable orbit, therefore if the periodicity is related to the emitting gas motion around the black hole, we should conclude that the black hole spin is $a \gtrsim 0.5$. One could also mention that such a determination of the black hole spin is indirect and actual typical frequencies for real accretion flows could be rather different from frequencies considered by the authors. We may summarize by saying that there are indications that the spin of the Galactic Center black hole can be very high, although this problem is not completely solved up to date.

As stated earlier, the part of Kerr quasi-rings formed by co-rotating photons is much brighter with respect to the opposite side (i.e. the part of the image formed by counter-rotating photons) and in principle can be detected much more easily. However, even the bright part of the quasi-ring can give information about mass, rotation parameter and inclination angle of the black hole. Of course, if the black hole – observer distance is unknown, the black hole mass can be evaluated in units of the distance. Even if the faint part of image (which is formed by counter-rotating photons) is not detectable, one can try to reconstruct the shape of the total image searching for the best fit of the full image using only the bright part of the image.

Of course, we have such superpower laser (greater than Gigawatt) which Holz & Wheeler [1] wanted to use to investigate a black hole by an active way and, in principle, it is possible to infer the spin parameter and inclination angle by analyzing of mirage shapes formed by retro-photons.

Holz & Wheeler [1] mentioned that the structure of such retro-Macho images will be unresolvable, because of even for very close black holes (say at the age of the solar system), the angular extent of retro-Macho images remain

less than a milliarcsecond. If we we could assume that this black hole could be at the edge of the solar system. We could not restrict ourselves to speculate on future observational facilities. For example, future Space Interferometry Mission (SIM)[3], GAIA satellite[4] and FAME[5] could resolve such images, because they will have a sufficient angular resolution for our example (for example, over a narrow field of view SIM could achieve an accuracy of 1 μas, a similar accuracy will have GAIA), but unfortunately its limiting magnitude will be about 20 mag (the limiting magnitude for GAIA $V \sim 20$), and since the limiting distance to discover such phenomenon is restricted by Holz & Wheeler [1]

$$D_L = 0.02\mathrm{pc} \times \left[10^{(m-30)}/2.5(M/\mathrm{M}_\odot)^2\right]^{1/3} , \qquad (11)$$

thus, for SIM limiting magnitude and even for massive black hole ($M = 10\mathrm{M}_\odot$), we obtain that such a retro-Macho should be inside of solar system since $D_L \sim 10^{-4}$pc. Therefore, to discover such phenomenon we need instrument like SIM concerning angular resolution, but limiting magnitude should on 10 mag better than SIM. In this case there is a possibility not only to observe such retro-Macho at the the edge of the solar system but also to determine its angular momentum.

We could summarize that angular resolution of the space RADIOASTRON interferometer will be high enough to resolve radio images around black holes therefore analyzing the shapes of the images one could evaluate the mass and the spin a for the Kerr black hole inside the Galactic Center and a position angle θ_0 for a distant observer and as it is clear a position angle could be determined by more simple way for rapidly rotating black holes $a \sim 1$ (in principle, measuring the mirage shapes we could evaluate mass, inclination angle and spin parameter if we know the distance toward the observed black hole. Otherwise one can only evaluate the spin parameter in units of the black hole mass since even for not very small spin $a = 0.5$ we have very weak dependence on θ_0 angle for mirage shapes and hardly ever one could determine θ_0 angle from the mirage shape analysis. Moreover, we have a chance to evaluate parameters a and θ (for rapidly rotating black holes) if we reconstruct only bright part of the mirages (bright arcs) corresponding to co-moving photons ($\alpha > 0$). However, for slow rotating black holes $\alpha \lesssim 0.5$ it would be difficult to evaluate parameters a and θ because we have very slow dependence of mirage shapes on these parameters.

However, there are two kind of difficulties to measure mirage shapes around black holes. First, the luminosity of these images or their parts (arcs) may not be sufficient to being detectable by RADIOASTRON. However, numerical simulations by Falcke, Melia & Agol [2], Melia & Falcke [54] give

[3]http://planetquest.jpl.nasa.gov/SIM/

[4]http://astro.estec.esa.nl/gaia

[5]The FAME Concept study. Report by Johnson et al. [62] is available at http://www.usno. navy.mil/FAME/publications, see also [63].

hope that the luminosity could be not too small at least for arcs of images formed by co-rotating photons ($\alpha > 0$). Second, turbulent plasma could give essential broadening of observed images [51], the longest interferometer baseline $b_{max} \sim 350000$ km (or for higher orbit $b_{max} \sim 3.2 \times 10^6$ km) and for this case we have similar to [51] length scale in the scattering medium is $l = (D_{scattering}/D_{GC}) \times b_{max} \sim 4.4 * 10^3$ km (or $l = 4.4 \times 10^4$ km for the higher orbit). Thus, the scale could be less or more than the predicted and measured values of the inner scale, which are in the range 10^2 to $10^{5.5}$ km [64, 65, 51], thus the broadening the images could be essential but it is not very easy to calculate it in details for such parameters.

Recent observations of simultaneous X-ray and radio flares at 3 mm, 7 mm, 1.3 cm and 2 cm with the few-hundred second rise/fall timescales gave indirect evidences that X-ray and radio radiation from the close vicinity of Sgr A* was detected because of that is the most natural interpretation of these flares. However, another interpretations of these flares could not be ruled out and in this case an optical depth for radio waves at 1.3 cm wavelength toward Sgr A* may be not very small.

Few years ago a possibility to get images of nearby black holes in X-ray band was discussed by White [66], Cash et al. [67], moreover Cash et al. [67] presented a laboratory demonstration of the X-ray interferometer. If the project will be realized, one could get X-ray images of black holes with 0.1×10^{-6} arcsec resolution, thus using this tool one could detect X-ray images around the Galactic Centre and around the black hole in M87 Galaxy.

One could mention also that if the emitting region has a degenerate position with respect to the line of sight (for example, the inclination angle of an accretion disk is $\gtrsim 85^0$) strong bending effects found by Matt, Perolla & Stella [68] and analyzed later by Zakharov & Repin [37] do appear.

In spite of the difficulties of measuring the shapes of images near black holes is so attractive challenge to look at the "faces" of black holes because namely the mirages outline the "faces" and correspond to fully general relativistic description of a region near black hole horizon without any assumption about a specific model for astrophysical processes around black holes (of course we assume that there are sources illuminating black hole surroundings). No doubt that the rapid growth of observational facilities will give a chance to measure the mirage shapes using not only RADIOASTRON facilities but using also other instruments and spectral bands (for example, X-ray interferometer [66, 67] or sub-mm VLBI array [69]).

Acknowledgements

AFZ would like to thank organizers of the DARK-2004, especially Profs. R. Arnowitt and H.V. Klapdor-Kleingrothaus for their kind invitation to present the invited talk at the Conference.

References

1. D. Holz and J.A. Wheeler: ApJ, **578**, 330 (2002)
2. H. Falcke, F. Melia, E. Agol: ApJ, **528**, L13 (2000)
3. S. Frittelli, T.P. Kling & E.T. Newman: PRD, **61**, 064021 (2000)
4. K.S. Virbhadra & G.F.R. Ellis: PRD, **62**, 084003 (2000)
5. K.S. Virbhadra & G.F.R. Ellis: PRD, **65**, 103004 (2002)
6. I. Ciufolini & F. Ricci: CQG, **19**, 3863 (2002)
7. I. Ciufolini & F. Ricci: gr-qc/0301030
8. V. Bozza: PRD, **66**, 103001 (2002)
9. V. Bozza: PRD, **67**, 103006 (2003)
10. V. Bozza & L. Mancini: GRG, **36**, 435 (2004)
11. V. Bozza & L. Mancini: astro-ph/0404526
12. E.F. Eiroa, G.E. Romero & D.F. Torres: PRD, **66**, 024010 (2002)
13. E.F. Eiroa & D.F. Torres: PRD, **69**, 063004 (2004)
14. M. Sereno: MNRAS, **344**, 942 (2003)
15. M. Sereno: PRD, **69**, 023002 (2004)
16. P. Young: Phys. Rev. D, **14**, 3281 (1976)
17. S. Chandrasekhar: *The Mathematical Theory of Black Holes.* (Clarendon Press, Oxford, 1983)
18. A.F. Zakharov: Sov. Phys. – J. Exp. & Theor. Phys., **64**, 1 (1986)
19. A.F. Zakharov: Sov. Phys. – J. Exp. & Theor. Phys. **68**, 217 (1989)
20. A.F. Zakharov: SvA, **35**, 147 (1991)
21. F. De Paolis, A. Geralico, G. Ingrosso, A.A. Nucita: A&A, **409**, 804 (2003)
22. F. De Paolis, A. Geralico, G. Ingrosso, A.A. Nucita, A. Qadir: A&A, **415**, 1 (2004)
23. B. Carter: Phys.Rev., **174**, 1559 (1968)
24. A.F. Zakharov: Preprint ITEP 44–91 (1991)
25. K.P. Rauch and R.D. Blandford: ApJ, **421**, 46 (1994)
26. R. Takahashi: astro-ph/0405099
27. A.F. Zakharov: MNRAS, **269**, 283 (1994)
28. A.F. Zakharov: In: *Proc. 17th Texas Symposium on Relativistic Astrophysics,* ed. H. Bohringer, G.E. Morfill, and J.E. Trumper (Annals of the New York Academy of Sciences, 1995) **759**, pp. 550–553
29. A.F. Zakharov & S.V. Repin: Astronomy Reports, **43**, 705 (1999)
30. A.F. Zakharov & S.V. Repin: Astronomy Reports, **46**, 360 (2002)
31. A.F. Zakharov and S.V. Repin: In: *Proc. of the Eleven Workshop on General Relativity and Gravitation in Japan*, ed. by J. Koga, T. Nakamura, K. Maeda, K. Tomita (Waseda University, Tokyo, 2002) pp. 68–72
32. A.F. Zakharov and S.V. Repin: In: *Proc. of the XXXVIIth Rencontres de Moriond "The Gamma-ray Universe"*, ed. by A. Goldwurm, D.N. Neumann and J. Tran Thanh Van, (The GIOI publishers, 2002) pp. 203–208
33. A.F. Zakharov and S.V. Repin: In: *Proc. of the Tenth Lomonosov Conference on Elementary Particle Physics "Frontiers of Particle Physics"*, ed. by A.I. Studenikin, (World Scientific Publishing House, Singapore, 2003) pp. 278–282
34. A.F. Zakharov and S.V. Repin: In *Proc. of the 214th Symposium on "High Energy Processes and Phenomena in Astrophysics"*, ed. by X.D. Li, V. Trimble, Z.R. Wang, (Astronomical Society of the Pacific, 2003) pp. 97–100

35. A.F. Zakharov and S.V. Repin: In: *Proceedings of the Third International Sakharov Conference on Physics*, vol. I, ed. by A. Semikhatov, M. Vasiliev and V. Zaikin, (Scientific World, Moscow, 2003) pp. 503–511
36. A.F. Zakharov and S.V. Repin: In: *Proceedings of the International Conference "I.Ya. Pomeranchuk and physics at the turn of centuries"*, (World Scientific Publishing House, Singapore, 2004) pp. 159–170
37. A.F. Zakharov and S.V. Repin, Astron. & Astrophys., **406**, 7 (2003)
38. A.F. Zakharov and S.V. Repin, Astronomy Reports, **47**, 733 (2003)
39. A.F. Zakharov and S.V. Repin: Nuovo Cimento, **118B**, 1193 (2003)
40. A.F. Zakharov: Lecture at 22nd Summer School and International Symposium on the Physics of Ionyzed Gases, to be published in AIP conference proceedings, astro-ph/0411611
41. A.F. Zakharov and S.V. Repin, Advances in Space Res. **34**, 2544 (2004)
42. A.F. Zakharov, N.S. Kardashev, V.N. Lukash & S.V. Repin: MNRAS, **342**, 1325 (2003)
43. A.F. Zakharov and S.V. Repin: In: "XEUS – studying the evolution of the hot universe", ed. by G.Hasinger, Th. Boller, and A.N. Parmer (MPE Report 281, 2003) pp. 339–345
44. K.Y. Lo, Zh.-Q. Shen, J.-H. Zhao, P.T.P Ho: ApJL, **508**, L61 (1998)
45. K.Y. Lo, Zh.-Q. Shen, J.-H. Zhao, P.T.P Ho: In: "The Central Parsecs of the Galaxy", ed. by H. Falcke, A. Cotera, W.J. Duschl, F. Melia, M.J. Rieke (ASP Conference Series, 1999) pp. 72–79
46. R. Genzel, R. Schödel, T. Ott et al.: Nature, **425**, 934 (2003)
47. A.M. Ghez et al.: ApJL, **601**, L159 (2004)
48. F.K. Baganoff et al.: Nature, **413**, 45 (2001)
49. F.C. Bower, H. Falcke, R.J. Sault & D.C. Backer: ApJ, **571**, 843 (2002)
50. F.C. Bower, M.C.H. Wright, H. Falcke & D.C. Backer: ApJ, **588**, 331 (2003)
51. F.C. Bower, H. Falcke, R.M. Herrstein et al.: Sciencexpress, www.sciencexpress. org/1 April 2004/
52. R. Narayan: Nature, **425**, 908 (2003)
53. E. Phahl & A. Loeb: astro-ph/0309744
54. F. Melia & H. Falcke: Annual Rev. A&A, **39**, 309 (2001)
55. A.M. Ghez et al.: ApJL, **586**, L127 (2003)
56. R. Schödel et al.: ApJ, **596**, 1015 (2003)
57. C.F. Gammie, S. Shapiro & J.C. McKinney: ApJ, **602**, 312 (2004)
58. J.H. Zhao, G.C. Bower & W.M. Goss: ApJL, **547**, L29 (2001)
59. S. Liu & F. Melia: ApJ, **573**, L23 (2002)
60. B. Aschenbach, N. Grosso, D. Porquet & P. Predehl: A&A, **417**, 71 (2004)
61. F. Melia, B. Bromley, S. Liu & C. Walker: ApJ, **554**, L37 (2001)
62. K.J. Johnson et al.: FAME Concept Study Report, (Washington DC: USNO, 1999)
63. S. Salim, A. Gould & R.P. Olling, ApJ, **573**, 631 (2002)
64. P.N. Wilkinson, R. Narayan & R.E. Spencer: MNRAS, **238**, 963 (1994)
65. K.M. Desai & A.L. Fey: ApJS, **133**, 395 (2001)
66. N. White: Nature, **407**, 146 (2000)
67. W. Cash, A. Shipley, S. Osterman, M. Joy: Nature, **407**, 160 (2000)
68. G. Matt, G.C. Perolla & L. Stella: A&A, **267**, 643 (1993)
69. M. Miyoshi: astro-ph/0412289

Part II

Direct Hot and Cold Dark Matter Detection Search

Neutrinoless Double Beta Decay – and Hot Dark Matter

H.V. Klapdor-Kleingrothaus

Max-Planck-Institut für Kernphysik, PO 10 39 80,
D-69029 Heidelberg, Germany,
H.Klapdor@mpi-hd.mpg.de,
mpi-hd.mpg.de.non_acc

Abstract. Nuclear double beta decay provides an extraordinarly broad potential to search for beyond-standard-model physics. *The occurrence of the neutrinoless decay* ($0\nu\beta\beta$) mode has fundamental consequences: first **total lepton number is not conserved**, and second, **the neutrino is a Majorana particle**. Further the effective mass measured allows to put an absolute scale of the neutrino mass spectrum. In addition, *double beta experiments yield sharp restrictions also for other beyond standard model physics.* These include SUSY models (R-parity breaking and conserving), leptoquarks (leptoquark-Higgs coupling), compositeness, left-right symmetric models (right-handeld W boson mass), test of special relativity and of the equivalence principle in the neutrino sector and others. **First evidence for neutrinoless double beta decay was given in 2001, by the HEIDELBERG-MOSCOW experiment**. The HEIDELBERG-MOSCOW experiment is the *by far most sensitive* $0\nu\beta\beta$ experiment since more than 10 years. It is operating 11 kg of enriched ^{76}Ge in the GRAN SASSO Underground Laboratory. The analysis of the data taken from 2 August 1990–20 May 2003, is presented here. The collected statistics is 71.7 kg y. The background achieved in the energy region of the Q value for double beta decay is 0.11 events/ kg y keV. *The two-neutrino accompanied half-life* is determined on the *basis of more than 100 000 events* to be $(1.74._{-0.16}^{+0.18}) \times 10^{21}$ *years*. **The confidence level for the** *neutrinoless* **signal is 4.2 σ level (more than 5σ in the pulse-shape-selected spectrum)**. The half-life is $T_{1/2}^{0\nu} = (1.19_{-0.23}^{+0.37}) \times 10^{25}$ *years*. **The effective neutrino mass deduced is (0.2–0.6) eV (99.73% c.l.)**, with the consequence that neutrinos have degenerate masses, and consequently still considerably, and contribute to hot dark matter in the Universe. The sharp boundaries for other beyond SM physics, mentioned above, are comfortably competitive to corresponding results from high-energy accelerators like TEVATRON, HERA, etc. Some *discussion* is given on future $\beta\beta$ experiments.

1 Introduction

Since 40 years huge experimental efforts have gone into the investigation of nuclear double beta decay which probably is the most sensitive way to look for (total) lepton number violation and probably the only way to decide the Dirac or Majorana nature of the neutrino. It has further perspectives to probe also other types of beyond standard model physics. This thorny way has been documented recently in some detail [29, 39, 31].

With respect to half-lives to explore lying, with the order of 10^{25} years, in a range on "half way" to that of proton decay, the two main experimental problems were to achieve a sufficient amount of double beta emitter material (source strength) and to reduce the background in such experiment to an extremely low level. In both directions large progress has been made over the decades. While the first experiment using source as detector [35], had only grams of material to its disposal (10.6 g of CaF_2), in the last years up to more than 10 kg of enriched emitter material have been used. Simultaneously the background of the experiments has been reduced strongly over the last 40 years. For example, compared to the first Germanium $\beta\beta$ experiment [45], working still with natural Germanium, containing the double beta emitter ^{76}Ge only with 7.8%, 40 years later the background in the HEIDELBERG-MOSCOW experiment is reduced by a factor of 10^4.

The final dream behind all these efforts was less to see a standard-model allowed second-order effect of the weak interaction in the nucleus – the two-neutrino-accompanied decay mode – which has been observed meanwhile for about 10 nuclei – (see e.g. [29]) but to observe neutrinoless double beta decay, and with this a first hint of beyond standard model physics, yielding at the same time a solution of the absolute scale of the neutrino mass spectrum.

2 Performance of the Experiment and Data Taking

2.1 General

The HEIDELBERG-MOSCOW experiment, proposed already in 1987 [9], has been looking for double beta decay of ^{76}Ge since August 1990 until November 30, 2003 in the Gran Sasso Underground Laboratory. It was using the largest source strength of all double beta experiments at present, and has reached a record low level of background, not only for Germanium double beta decay search. It has demonstrated this during more than a decade of measurements and is since more then ten years the most sensitive double beta decay experiment worldwide. The experiment was since 2001 operated only by the Heidelberg group, which also performed the analysis of the experiment from its very beginning.

The experiment has been carried out with five high-purity p-type detectors of Ge enriched to 86% in the isotope ^{76}Ge (in total 10.96 kg of active volume). These were the first enriched high-purity Ge detectors ever produced. So, the experiment starts from the cleanest thinkable source of double beta emitter material, which at the same time is used as detector of $\beta\beta$ events.

A description of the experimental details has been given in [1, 2, 3, 10]. This will not be repeated in this paper, instead we concentrate on the results and their consequences. But let us just mention some of the most important features of the experiment here.

1. Since the sensitivity for the $0\nu\beta\beta$ half-life is $T^{0\nu}_{1/2} \sim a \times \epsilon\sqrt{\frac{Mt}{\Delta E B}}$ (and $\frac{1}{\sqrt{T^{0\nu}}} \sim \langle m_\nu \rangle$), with a denoting the degree of enrichment, ϵ the efficiency of the detector for detection of a double beta event, M the detector (source) mass, ΔE the energy resolution, B the background and t the measuring time, the sensitivity of our 11 kg *of enriched* ^{76}Ge experiment corresponds to that of an at least 1.2 ton *natural* Ge experiment. After enrichment – the other most important parameters of a $\beta\beta$ experiment are: energy resolution, background and source strength.

2. The high energy resolution of the Ge detectors of 0.2% or better, assures that there is no background for a $0\nu\beta\beta$ line from the two-neutrino double beta decay in this experiment, in contrast to most other present experimental approaches, where limited energy resolution is a severe drawback.

3. The efficiency of Ge detectors for detection of $0\nu\beta\beta$ decay events is close to 100% (95%, see [2]).

4. The source strength in this experiment of 11 kg is the largest source strength ever operated in a double beta decay experiment.

5. The background reached in this experiment, is 0.113 ± 0.007 events/ kg y keV (in the period 1995-2003) in the $0\nu\beta\beta$ decay region (around $Q_{\beta\beta}$). This is the lowest limit ever obtained in such type of experiment.

6. The statistics collected in this experiment during 13 years of stable running is the largest ever collected in a double beta decay experiment. The experiment took data during ∼80% of its installation time.

7. The Q value for neutrinoless double beta decay has been determined recently with high precision [33].

3 Data and Analysis

Figures 1, 2 show the total sum spectrum measured over the full energy range of all five detectors for the period November 1995 to May 2003. The identified lines are indicated with their source of origin (for details see[18]).

Figures 3, 4 show the part of the spectrum around $Q_{\beta\beta}$, in the range 2000–2060 keV, measured in the period August 1990 to May 2003 and November 1995 to May 2003. Non-integer numbers in the sum spectra are simply a binning effect.

3.1 Energy Calibration

Precise energy calibration for all detectors before summing the individual 2142 runs taken with the detectors, and finally summing the sum spectra of the different detectors (in total summing 9 570 data sets) is decisive to achieve a good energy resolution of the total spectrum, and an optimum sensitivity of the experiment. For details see [1, 2, 3]. A list of the energies of the identified lines (Figs. 1, 2) is given in a recent paper [18], here we concentrate on the range of interest around $Q_{\beta\beta}$.

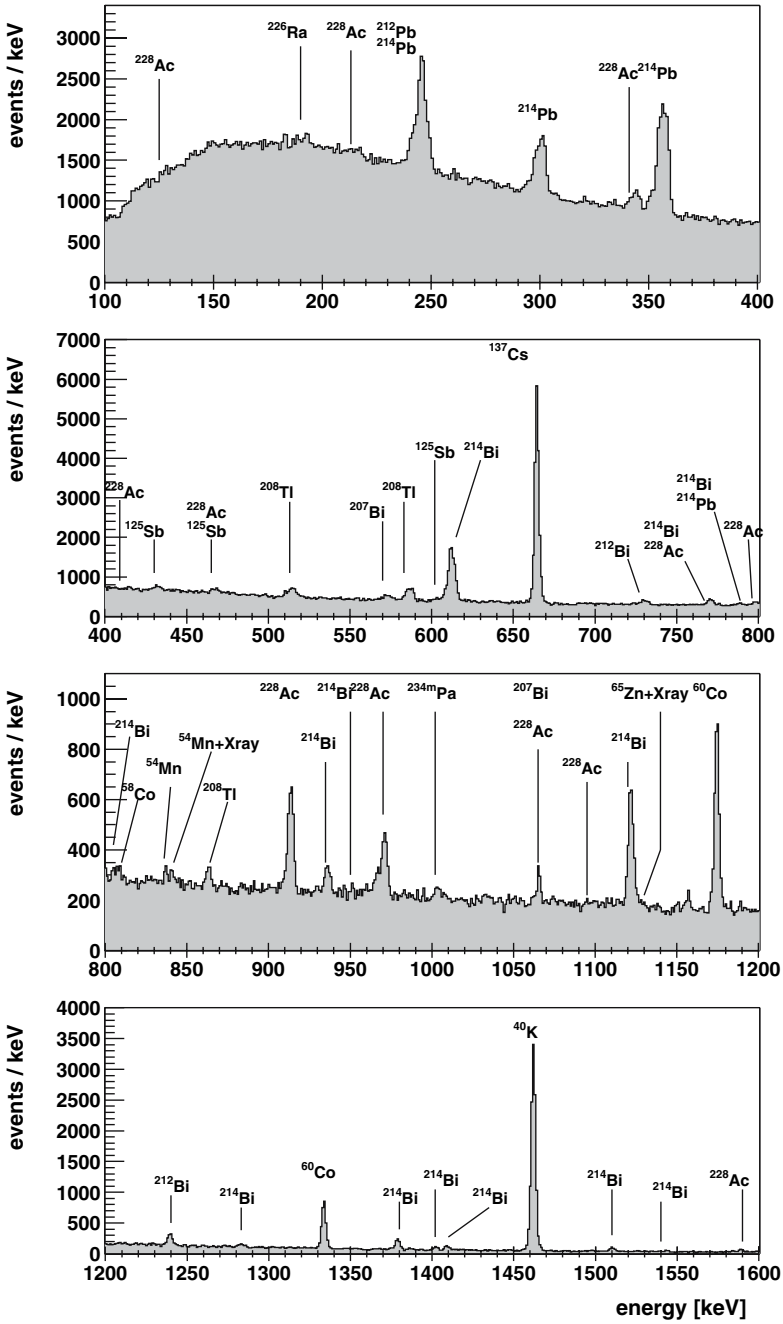

Fig. 1. The total sum spectrum measured over the full energy range (low-energy part) of all five detectors (in total 10.96 kg enriched in ^{76}Ge to 86%) – for the period November 1995 to May 2003.

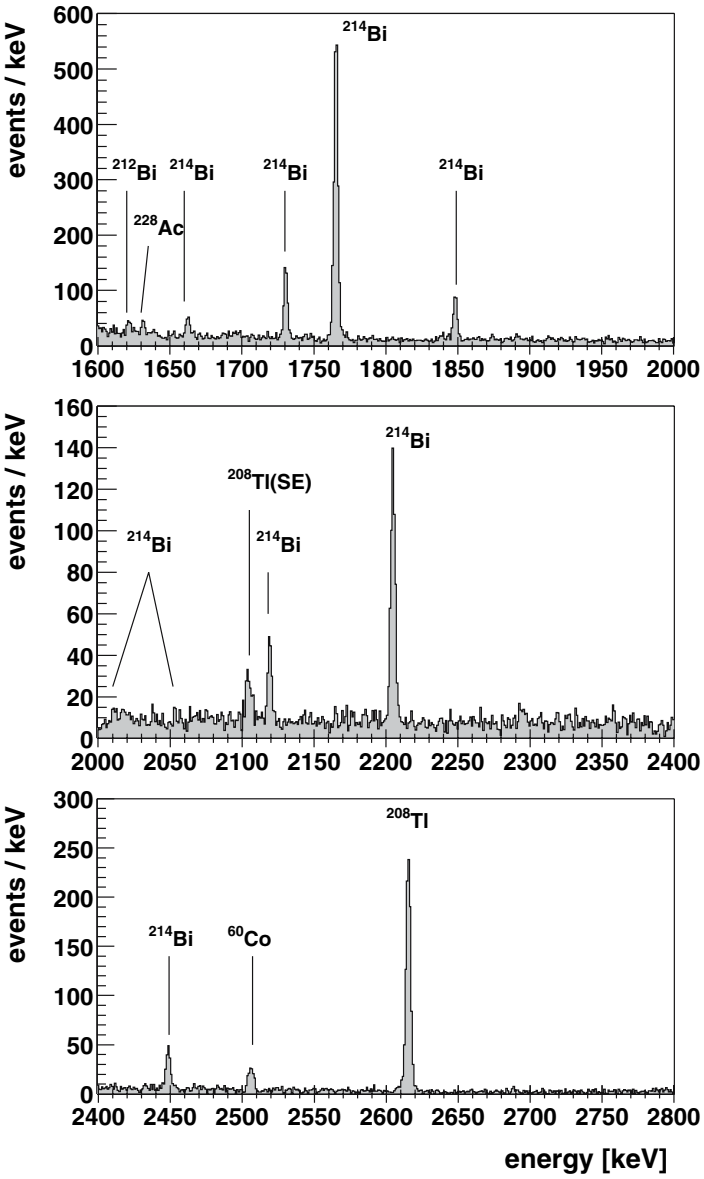

Fig. 2. The total sum spectrum measured over the full energy range (higher energy part) of all five detectors (in total 10.96 kg enriched in ^{76}Ge to 86%) – for the period November 1995 to May 2003.

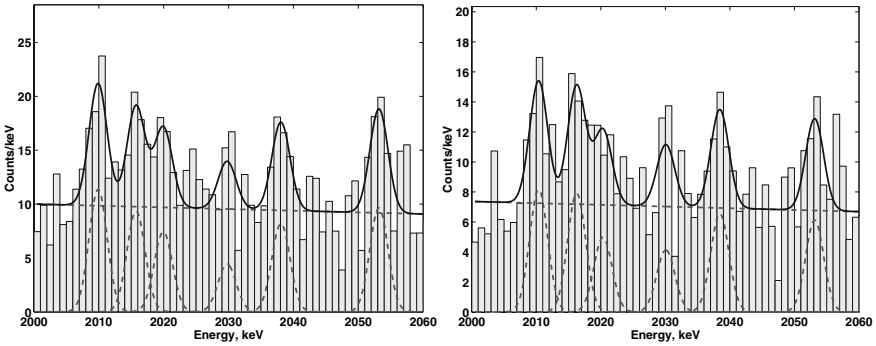

Fig. 3. The total sum spectrum of all five detectors (in total 10.96 kg enriched in ^{76}Ge), for the period: left: November 1990 to May 2003 (71.7 kg y) in the range 2000–2060 keV right: – November 1995 to May 2003 (56.66 kg y) in the range 2000–2060 keV and its fit (see Sect. 3.2).

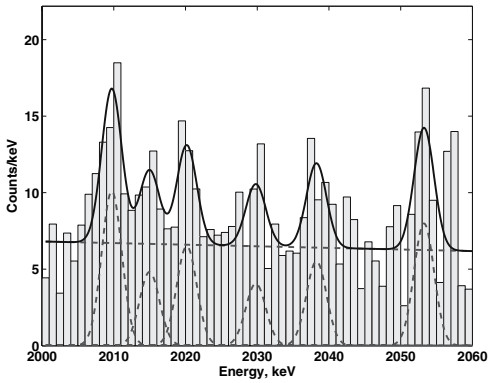

Fig. 4. The total sum spectrum of all five detectors (in total 10.96 kg enriched in ^{76}Ge), in the range (2000–2060) keV and its fit, for the period August 1990 to May 2000 (50.57 kg y).

3.2 Analysis of the Spectra

In the measured spectra (Figs. 3–4) we see in the range around $Q_{\beta\beta}$ the ^{214}Bi lines at 2010.7, 2016.7, 2021.8, 2052.9 keV, the line at $Q_{\beta\beta}$ and a candidate of a line at $\sim$ 2030 keV (see also [13, 19])[1] The spectra have been analyzed by *different methods*: Least Squares Method, Maximum Likelihood Method (MLM) and Feldman-Cousins Method. The analysis is performed

[1]The objections raised after our first paper [4] concerning these lines and other points, by Aalseth et al. (Mod.Phys.Lett.A17:1475-1478,2002 and hep-ex/0202018 v.1), have been shown to be wrong already in [7] and in [6], and later in [13] and [19]. So this "criticism" was already history, before we reached the higher statistics presented in this paper.

without subtraction of any background. We always process background-plus-signal data since the difference between two Poissonian variables does *not* produce a Poissonian distribution [34]. This point has to be stressed, since it is sometimes overlooked. So, e.g., in [44] a formula is developed making use of such subtraction and as a consequence the analysis given in [44] provides overestimated standard errors.

The large improvement of the present analysis (for details see [1, 2, 3]) compared to our paper from 2001 [4, 5, 6], is clearly seen from Fig. 4 showing the *new* analysis of the data 1990–2000, as performed here – to be compared to the corresponding figure in [4, 5, 6]. One reason lies in the stricter conditions for accepting data into the analysis. The spectrum in Fig. 4 now corresponds to 50.57 kg y to be compared to 54.98 kg y in [4], for the same measuring period. The second reason is a better energy calibration of the individual runs. The third reason is the refined summing procedure of the individual data sets mentioned above and the correspondingly better energy resolution of the final spectrum. (For more details see [1, 2, 3]). The signal strength seen in the *individual* detectors in the period 1990-2003 is shown in [3].

We tested the confidence intervals calculated by the fitting programs with numerical simulations (see [1, 2, 3]). As done earlier for other statistical methods [5, 6], we have simulated 100 000 spectra with Poisson-distributed background and a Gaussian-shaped (Poisson-distributed) line of given intensity, and have investigated, in how many cases we find in the analysis the known intensities inside the given confidence range. The result shows that the confidence levels determined are correct within small errors (for details see [2, 3]).

4 Results

4.1 Full Spectra

Figures 3, 4 show together with the measured spectra in the range around $Q_{\beta\beta}$ (2000–2060 keV), the fit by the least-squares method. A linear decreasing shape of the background as function of energy was chosen corresponding to the complete simulation of the background performed in [18] by GEANT4 (see Fig. 5).

In the fits in Figs. 3, 4 the peak positions, widths and intensities are determined simultaneously, and also the *absolute* level of the background.

The signal at $Q_{\beta\beta}$ in the full spectrum at $\sim$ 2039 keV reaches a 4.2 σ confidence level for the period 1990–2003 (28.8 $\pm$ 6.9) events, and of 4.1 σ for the period 1995-2003 (23.0 $\pm$5.7) events. The results of the new analysis are consistent with the results given in [4, 5, 6]. The intensities of all other lines are given in [2, 3].

We have given a detailed comparison of the spectrum measured in this experiment with other Ge experiments in [19]. It is found that the most sensitive experiment with natural Ge detectors [14], and the first experiment

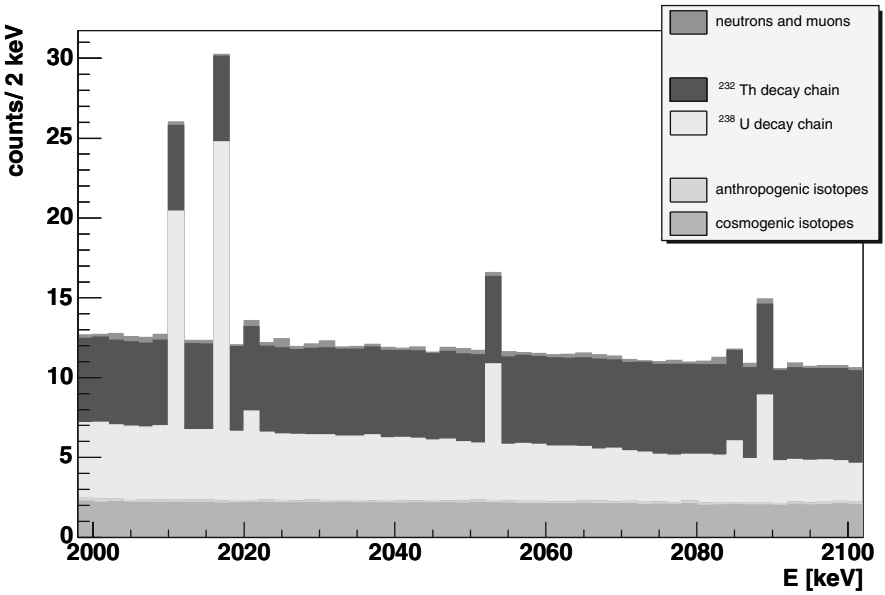

Fig. 5. Monte Carlo simulation of the background in the range of $Q_{\beta\beta}$ by GEANT4, including all known sources of background in the detectors and the setup. This simulation [18] seems to be the by far most extensive and complete one ever made for any double beta experiment. The background around $Q_{\beta\beta}$ is expected to be flat, the only lines visible should be some weak ^{214}Bi lines (from [18]).

using enriched (not yet high-purity) ^{76}Ge detectors [15] find essentially the same background lines (^{214}Bi etc.), but *no* indication for the line near $Q_{\beta\beta}$. This is consistent with the rates expected from the present experiment due to their lower sensitivity: ∼0.7 and ∼1.1 events, respectively. It is also consistent with the result of the IGEX ^{76}Ge experiment [16], which collected only a statistics of 8.8 kg y, before finishing in 1999, and which should expect ∼2.6 events, which they might have missed. Their published half-life limit is overestimated as result of an arithmetic mistake (see [17]).

4.2 Time Structure of Events

There are at present *no other* running experiments (with reasonable energy resolution) which can – not to speak about their lower sensitivity – *in principle* give *any further-going* information in the search for double beta decay than shown up to this point: namely a line at the correct energy $Q_{\beta\beta}$. Also most future projects cannot determine more. The HEIDELBERG-MOSCOW experiment developed some *additional tool* of independent verification. The method is to exploit the time structure of the events and to select $\beta\beta$ events by their pulse shape. The result is shown in Fig. 6.

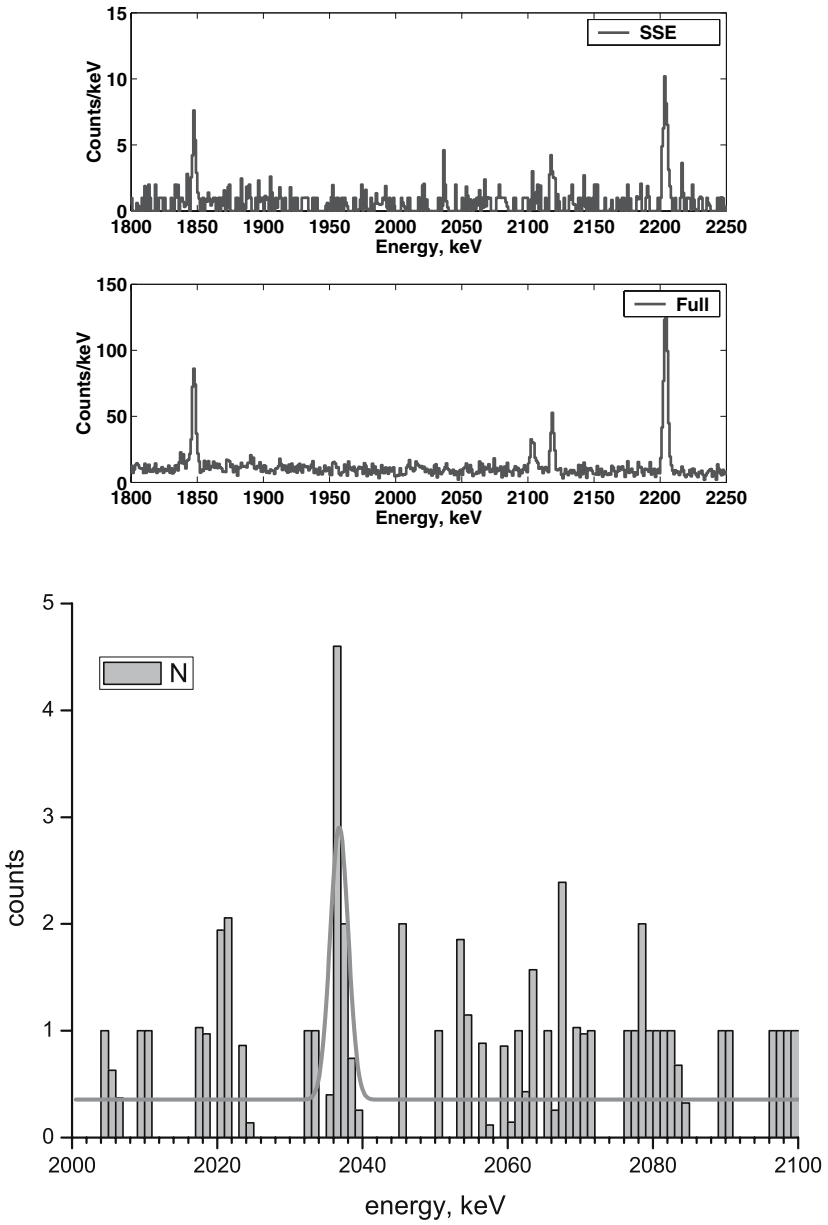

Fig. 6. Top, upper part: The pulse-shape selected spectrum of single site events measured with detectors 2,3,4,5 from 1995–2003, see text. Top, lower part: The full spectrum measured with detectors 2,3,4,5 from 1995–2003. Bottom: As in top figure, upper part, but energy range 2000–2100 keV.

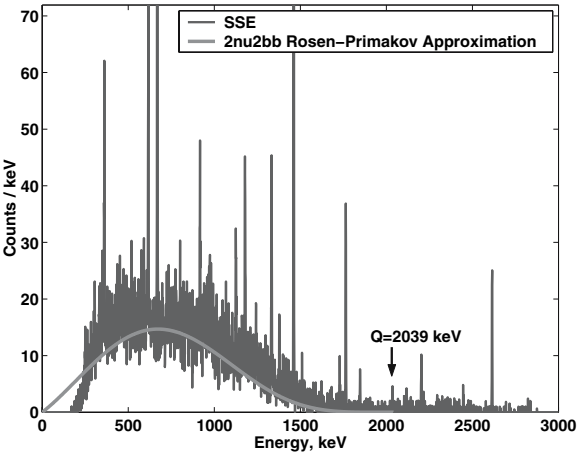

Fig. 7. The pulse-shape selected spectrum measured with detectors 2,3,4,5 from 1995–2003 in the energy range of (100–3000) keV, see text.

Here a *subclass* of shapes selected by the neuronal net method used earlier [6, 8] is shown. Except a line which sticks out sharply near $Q_{\beta\beta}$, *all* other lines are very strongly suppressed.

Fig. 6 also shows the full spectrum in this range. **When taking the range 2000–2100 keV and conservatively assuming all structures except the line at $Q_{\beta\beta}$ to be part of a constant background, a corresponding fit yields a signal at $Q_{\beta\beta}$ of more than 5σ (see Fig. 6)**. The method seems also to fulfill the criterium to select properly the *continuous* $2\nu\beta\beta$ *spectrum* (see Fig. 7).

The energy of this line determined by the spectroscopy ADC is slightly below $Q_{\beta\beta}$, but still within the statistical variation for a weak line (see [19]). This can be understood as result of ballistic effects (for details see[26]). The 2039 keV line as a single site events signal cannot be the double escape line of a γ-line whose full energy peak would be expected at 3061 keV, since no indication of a line is found there in the spectrum measured up to 8 MeV (see [2, 3]).

5 Half-Life of Neutrinoless Double Beta Decay of ^{76}Ge

We have shown in chapter 4 that the signal found at $Q_{\beta\beta}$ is consisting of single site events and is not a γ line. The signal does not occur in the Ge experiments *not* enriched in the double beta emitter ^{76}Ge [14, 12, 19], while neighbouring background lines appear consistently in these experiments.

On this basis we translate the observed numbers of events into half-lives for neutrinoless double beta decay. In Table 1 we give the half-lives deduced

Table 1. Half-life for the neutrinoless decay mode and deduced effective neutrino mass from the HEIDELBERG-MOSCOW experiment (the nuclear matrix element of [24] is used). Shown are in addition to various accumulated total measuring times also the results for four *non-overlapping* data sets: the time periods 11.1995-09.1999 and 09.1999–05.2003 for *all* detectors, and the time period 1995–2003 for two sets of detectors: 1+2+4, and 3+5. *) denotes best value.

Significance $[kg\,y]$	Detectors	$T^{0\nu}_{1/2}$ $[y]$ (3σ range)	$\langle m \rangle$ [eV] (3σ range)	Conf. level (σ)
Period 8.1990 ÷ 5.2003				
71.7	1,2,3,4,5	$\mathbf{(0.69 - 4.18) \times 10^{25}}$ $\mathbf{1.19 \times 10^{25}}$*	**(0.24–0.58)** **0.44***	**4.2**
Period 11.1995 ÷ 5.2003				
56.66	1,2,3,4,5	$(0.67 - 4.45) \times 10^{25}$ 1.17×10^{25}*	(0.23 - 0.59) 0.45*	4.1
51.39	2,3,4,5	$(0.68 - 7.3) \times 10^{25}$ 1.25×10^{25}*	(0.18 - 0.58) 0.43*	3.6
42.69	2,3,5	$(0.88 - 4.84) \times 10^{25}$ (2σ range) 1.5×10^{25}*	(0.22 - 0.51) (2σ range) 0.39*	2.9
28.27	1,2,4	$(0.67 - 6.56) \times 10^{25}$ (2σ range) 1.22×10^{25}*	(0.19 - 0.59) (2σ range) 0.44*	2.5
28.39	3,5	$(0.59 - 4.29) \times 10^{25}$ (2σ range) 1.03×10^{25}*	(0.23 - 0.63) (2σ range) 0.48*	2.6
Period 11.1995 ÷ 09.1999				
26.59	1,2,3,4,5	$(0.43 - 12.28) \times 10^{25}$ 0.84×10^{25}*	(0.14 - 0.73) 0.53*	3.2
Period 09.1999 ÷ 05.2003				
30.0	1,2,3,4,5	$(0.60 - 8.4) \times 10^{25}$ 1.12×10^{25}*	(0.17 - 0.63) 0.46*	3.5

from the full data sets taken in the years 1995–2003 and in 1990–2003 and of some partial data sets. In all cases the signal is seen consistently. Also given are the deduced effective neutrino masses.

The result obtained **is consistent** with the limits given earlier [11], and with the results given in [4, 5, 6].

Concluding **we confirm**, with **4.2σ (99.9973% c.l.) probability (more than 5σ in the pulse-shape selected spectrum)**, our claim from 2001 [4, 5, 6] **of first evidence for the neutrinoless double beta decay mode**.

6 Consequences for Particle Physics, Neutrino Physics and Other Beyond Standard Model Physics

Lepton number violation: *The most important consequence* of the observation of neutrinoless double beta decay is, that **lepton number is not conserved**. This is fundamental for particle physics.

Majorana nature of neutrino: Another fundamental consequence is that **the neutrino is a Majorana particle** (see, e.g. [41, 42], but also [43]). Both of these conclusions are *independent of any* discussion of nuclear matrix elements.

Effective neutrino mass: The matrix element enters when we derive a *value* for the effective neutrino mass - making the *most natural assumption* that the $0\nu\beta\beta$ decay amplitude is dominated by exchange of a massive Majorana neutrino. The half-life for the neutrinoless decay mode is under this assumption given by [24, 25]

$$[T^{0\nu}_{1/2}(0^+_i \to 0^+_f)]^{-1} = C_{mm}\frac{\langle m\rangle^2}{m_e^2} + C_{\eta\eta}\langle\eta\rangle^2 + C_{\lambda\lambda}\langle\lambda\rangle^2 + C_{m\eta}\langle\eta\rangle\frac{\langle m\rangle}{m_e} + C_{m\lambda}\langle\lambda\rangle\frac{\langle m\rangle}{m_e} + C_{\eta\lambda}\langle\eta\rangle\langle\lambda\rangle,$$

$$\langle m\rangle = |m^{(1)}_{ee}| + e^{i\phi_2}|m^{(2)}_{ee}| + e^{i\phi_3}|m^{(3)}_{ee}|, \tag{1}$$

where $m^{(i)}_{ee} \equiv |m^{(i)}_{ee}|\exp(i\phi_i)$ $(i = 1, 2, 3)$ are the contributions to the effective mass $\langle m\rangle$ from individual mass eigenstates, with ϕ_i denoting relative Majorana phases connected with CP violation, and $C_{mm}, C_{\eta\eta}, \ldots$ denote nuclear matrix elements squared, which can be calculated, (see, e.g. [29, 38, 37], for a review). Ignoring contributions from right-handed weak currents, on the right-hand side of Equation (1) only the first term remains.

Using the nuclear matrix element from [24, 25], we conclude from the half-life given above the effective mass $\langle m\rangle$ to be $\langle m\rangle = (0.2 \div 0.6)\,\mathrm{eV}$ (99.73% c.l.), with **best value of $\sim$ 0.4 eV**.

The matrix element given by [24] was the *prediction closest to* the *later* measured $2\nu\beta\beta$ decay half-life of $(1.74^{+0.18}_{-0.16}) \times 10^{25}$ y [18, 10]. It underestimates the 2ν matrix elements by 32% and thus these calculations will also underestimate (to a smaller extent) the matrix element for $0\nu\beta\beta$ decay, and consequently correspondingly overestimate the (effective) neutrino mass. The

value for the effective mass thus in reality will be somewhat lower, than deduced above, down to $\sim$ **0.3 eV**. Allowing conservatively for an uncertainty of the nuclear matrix element of $\pm$ 50% the range for the effective mass may widen to $\langle m \rangle$ = (0.1 - 0.9) eV (99.73% c.l.).

Neutrinos degenerate in mass: With the value deduced for the effective neutrino mass, the HEIDELBERG-MOSCOW experiment excludes several of the neutrino mass scenarios allowed from present neutrino oscillation experiments (see Fig. 8, and Fig. 1 in [52]), – allowing only for degenerate mass scenarios [28, 52, 27]. Degenerate mass scenarios had been discussed already earlier (see e.g. [53, 54]). In connection with the L/E flatness of the electron-like event ratio observed in Superkamiokande, degeneracy has been discussed by [55].

Neutrinos as hot dark matter: The effective neutrino mass determined by $0\nu\beta\beta$ decay allows a considerable fraction of hot dark matter in the Universe carried by neutrinos.

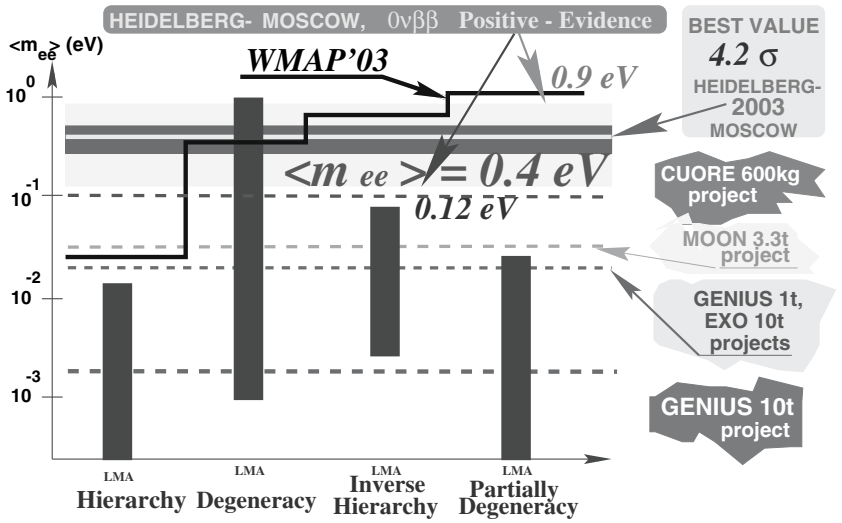

Fig. 8. The impact of the evidence obtained for neutrinoless double beta decay (best value of the effective neutrino mass $\langle m \rangle = 0.4\,\mathrm{eV}$, 3σ confidence range (0.1–0.9) eV – allowing already for an uncertainty of the nuclear matrix element of a factor of $\pm$ 50%) on possible neutrino mass schemes. The bars denote allowed ranges of $\langle m \rangle$ in different neutrino mass scenarios, still allowed by neutrino oscillation experiments (see [28, 52]). All models except the degenerate one are excluded by the new $0\nu\beta\beta$ decay result. Also shown is the exclusion line from WMAP, plotted for $\sum m_\nu < 1.0\,\mathrm{eV}$ [56] (which is according to [74] too strict). WMAP does not rule out any of the neutrino mass schemes. Further shown are the expected sensitivities for the future potential double beta experiments CUORE, MOON, EXO and the 1 ton and 10 ton project of GENIUS [29, 31, 63] (from [52]).

Other beyond Standard Model Physics: Assuming *other* mechanisms to dominate the $0\nu\beta\beta$ decay amplitude, which have been studied extensively in our group, and other groups, in recent years, the result allows to set stringent limits on parameters of SUSY models, leptoquarks, compositeness, masses of heavy neutrinos, the right-handed W boson and possible violation of Lorentz invariance and equivalence principle in the neutrino sector. Figures 9, 10, 11, show as examples some of the relevant graphs which can in principle contribute to the $0\nu\beta\beta$ amplitude and from which bounds on the corresponding parameters can be deduced assuming conservatively the measured half-life as upper limit for the individual processes.

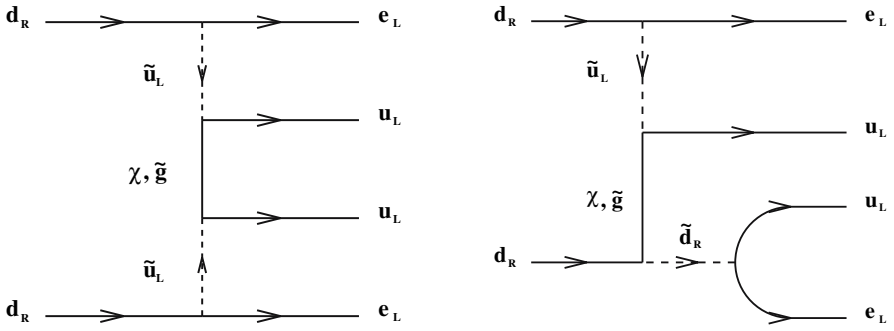

Fig. 9. Examples of Feynman graphs for $0\nu\beta\beta$ decay within R–parity violating supersymmetric models [31].

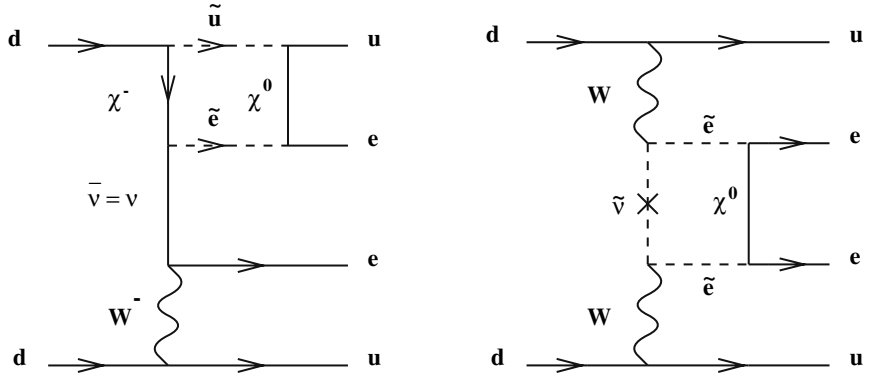

Fig. 10. Examples of R_P conserving SUSY contributions to $0\nu\beta\beta$ decay [31].

Figures 12, 13 and 14 show some results. The most strict limit for the R-parity – breaking Yukawa coupling λ'_{111} in R-violating SUSY models is coming from $0\nu\beta\beta$-decay. It is much stricter then the limits obtained by accelerators, whose limitation in energy is visible in Fig. 12 (from [31]).

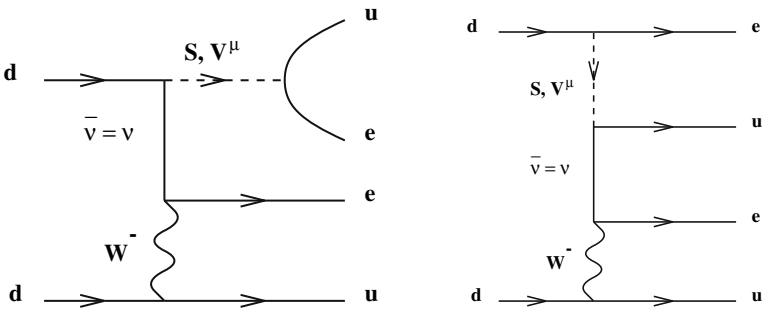

Fig. 11. Examples of Feynman graphs for $0\nu\beta\beta$ decay within LQ models. S and V^{μ} stand for scalar and vector LQs, respectively [31].

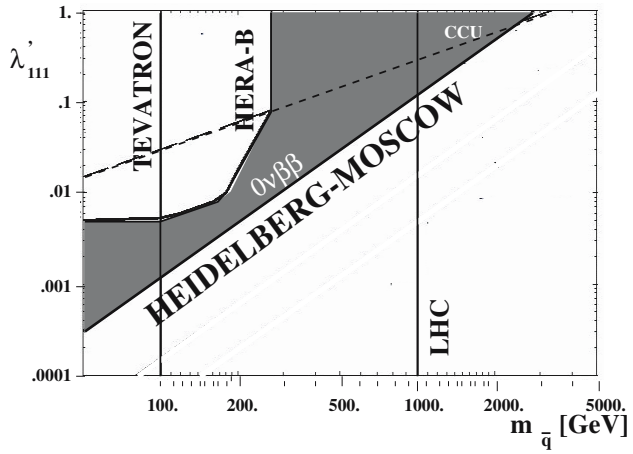

Fig. 12. Comparison of sensitivities of existing and future experiments on R_p-violating SUSY models in the plane λ'_{111}-$m_{\tilde{q}}$. *Note the double logarithmic scale!* Shown are the areas currently excluded by the experiments at the TEVATRON and HERA-B, the limit from charged-current universality, denoted by CCU, and the limit from $0\nu\beta\beta$-decay from the HEIDELBERG-MOSCOW Experiment. *The area beyond (or left of) the lines is excluded.* The estimated sensitivity of LHC is also given (from [31]).

The lower limit for super-heavy left-handed neutrino from the $0\nu\beta\beta$ HEIDELBERG-MOSCOW experiment corresponds to the discovery potential for the inverse process $e^-e^- \longrightarrow W^-W^-$ of a linear collider of 1–2 TeV (see Fig. 13). The constraints concerning *composite* excited neutrinos of mass M$-N$ obtained from $0\nu\beta\beta$ decay (HEIDELBERG-MOSCOW experiment) are more strict than the results of LEPII, as shown in Fig. 14. For a further discussion and for references we refer to [29, 30, 31, 32].

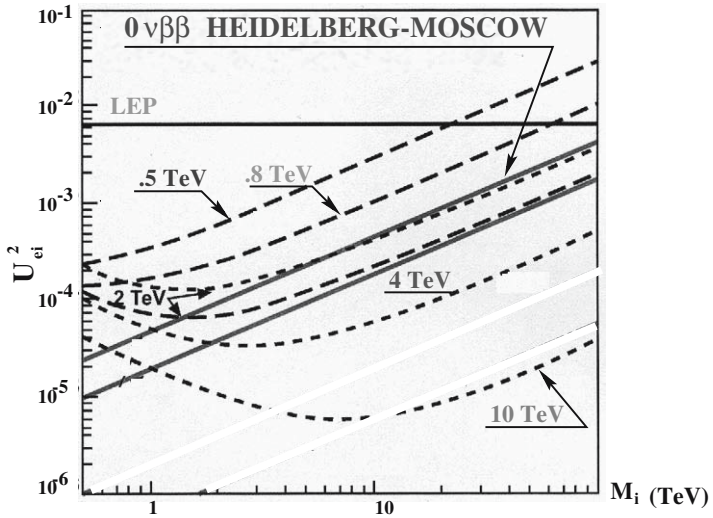

Fig. 13. Discovery limit for $e^-e^- \longrightarrow W^-W^-$ at a linear collider as function of the mass M_i of a heavy left-handed neutrino, and of U^2_{ei} for $\sqrt{s}$ between 500 GeV and 10 TeV. In all cases the parameter space above the line corresponds to observable events. The limits from the HEIDELBERG-MOSCOW $0\nu\beta\beta$ experiment are shown also, the areas above the $0\nu\beta\beta$ contour line are excluded. The horizontal line denotes the limit on neutrino mixing, U^2_{ei}, from LEP (from [64]).

7 Conclusion – Perspectives

Recent information from many *independent* sides seems to condense now to a nonvanishing neutrino mass of the order of the value found by the HEIDELBERG-MOSCOW experiment. This is the case for the results from CMB, LSS, neutrino oscillations, particle theory and cosmology (for a detailed discussion see [1, 2, 3]). To mention a few examples: Neutrino oscillations require in the case of degenerate neutrinos common mass eigenvalues of $m > 0.04\,eV$. An analysis of CMB, large scale structure and X-ray from clusters of galaxies yields a "preferred" value for $\sum m_\nu$ of 0.6 eV [57]. WMAP yields $\sum m_\nu < 1.0\,eV$ [56], SDSS yields $\sum m_\nu < 1.7\,eV$ [74]. Theoretical papers require degenerate neutrinos with $m > 0.1$, or 0.2 eV or 0.3 eV [49, 47, 58, 59, 48], and the recent alternative cosmological concordance model requires relic neutrinos with mass of order of eV [60]. As mentioned already earlier [40, 2] the results of double beta decay and CMB measurements together indicate that the neutrino mass eigenvalues have the same CP parity, as required by the model of [49]. Also the approach of [73] comes to the conclusion of a Majorana neutrino. The Z-burst scenario for ultra-high energy cosmic rays requires $m_\nu \sim 0.4\,eV$ [50, 51], and also a non-standard model (g-2) has been connected with degenerate neutrino masses $>0.2\,eV$ [46]. The neutrino mass determined from $0\nu\beta\beta$ decay is consistent also with present models of leptogenesis in

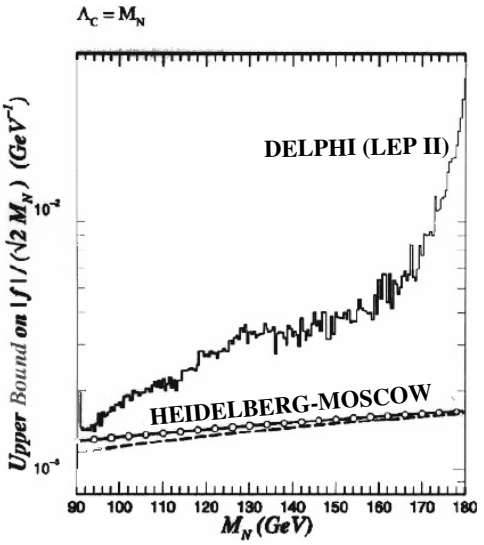

Fig. 14. Comparison between the $\beta\beta_{0\nu}$ HEIDELBERG-MOSCOW experiment and the LEP II upper bound on the quantity $|f|/(\sqrt{2}M_N)$ as a function of the heavy composite neutrino mass M_N, with the choice $\Lambda_C = M_N$. *Regions above the curves are excluded.* The dashed and solid circle curves are the $\beta\beta_{0\nu}$ bounds from the HEIDELBERG-MOSCOW experiment (for details see [65]).

the early Universe [66]. It has been discussed that the Majorana nature of the neutrino tells us that spacetime does realize a construct that is central to construction of supersymmetric theories [36].

Future: With the HEIDELBERG-MOSCOW experiment, *the era of small smart experiments is over.* Fig. 15 shows the present result and a comparison to the potential of the most sensitive other double beta decay experiments and the possible potential of some future projects. It is visible that the presently running experiments have hardly a chance, to reach the sensitivity of the HEIDELBERG-MOSCOW experiment. New approaches and considerably *enlarged* experiments would be required to fix the $0\nu\beta\beta$ half life with higher accuracy. **This will, however, only marginally improve the precision of the deduced neutrino mass**, because of the uncertainties in the nuclear matrix elements, which probably hardly can be reduced to less than 50%.

One has to keep in mind further, that **no more can be learnt** on *other* beyond standard model physics parameters from future more sensitive experiments. The reason is that there is **a half-life** now, and **no more a limit** on the half-life, which could be further reduced.

From future projects one has to require that they should be able to differentiate between a β and a γ signal, or that the tracks of the emitted electrons should be measured. At the same time, as is visible from the present

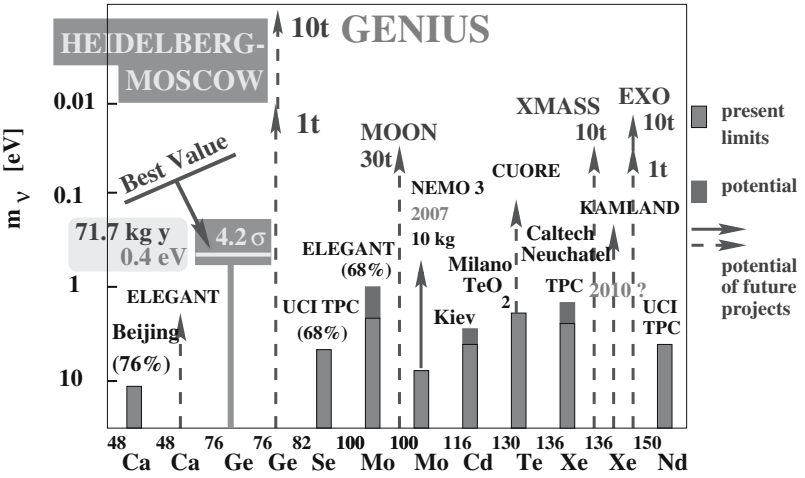

Fig. 15. Present sensitivity, and expectation for the future, of the most promising $\beta\beta$ experiments. Given are limits for $\langle m \rangle$, except for the HEIDELBERG-MOSCOW experiment where the measured *value* is given (3σ c.l. range and best value). Framed parts of the bars: present status; not framed parts: future expectation for running experiments; solid and dashed lines: experiments under construction or proposed, respectively. For references see [29, 5, 6].

information, the energy resolution should be *at least* in the order of that of Ge semiconductor detectors, or better. These requirements exclude at present calorimeter experiments like CUORE, CUORICINO, which *cannot* differentiate between a β and γ signal, etc, but also experiments like EXO [72], *if* the latter will not be able to reconstruct the tracks of the electrons, as it seems at present.

The *most discussed "short-term" "confirmation experiments"* at present are CUORICINO/CUORE and NEMO. Let us therefore, to avoid usual misunderstandings, give a few comments.

CUORICINO, CUORE:

The general background problems of CUORICINO are illustrated by the fact, that this experiment until now is not able to see the $2\nu\beta\beta$ decay of ^{130}Te, whose half life is experimentally known to be $T^{0\nu}_{1/2}=(2.7\pm0.1)\times10^{21}$ years [69], i.e. similar to the $2\nu\beta\beta$ halflife of ^{76}Ge, which is very clearly seen in the HEIDELBERG-MOSCOW experiment (see, e.g. [18, 10]). The background in the range of $Q_{\beta\beta}$ is for CUORICINO at present [70] a factor of two higher than in the HEIDELBERG-MOSCOW experiment.

The present half-life limit for neutrinoless double beta decay is given as 1.8×10^{24} years on a 90% c.l. (statistical method is not described, could however be important, see e.g. [17]), after a measuring time of 10.8 kgy.

The half-life corresponding to the effective neutrino mass deduced from the HEIDELBERG-MOSCOW experiment, for the case of ^{130}Te is according to [24] $T^{0\nu}_{1/2}$=2.5×10^{24} y. At a 90% c.l. a corresponding limit could be reached by CUORINO in additional 5 months of continuous running, i.e. realistically in more than a year. Allowing an uncertainty in the calculated matrix element of a factor of 2, however, could require a 16 times larger measuring time, i.e. ∼30 years, to make a statement on a 90% confidence level. This means that *the CUORICINO experiment can, with good luck, confirm the Heidelberg-Moscow result (on a reasonable, not only 90% c.l.) in several years, but it can never disprove it.*

The full version CUORE with about a factor of 15 larger detector mass than CUORICINO could, with background of CUORICINO, have a sensitivity to probe the HEIDELBERG-MOSCOW result in about one year of continuous measuring on a 90% confidence level. So unfortunately also this experiment would require many years of measurement to make a statement on a reasonable confidence level.

NEMO:

The NEMO project *can* see tracks, but unfortunately has at present only a small efficiency (14%) , and **a low energy resolution of more than 200 keV** not to talk about the background problems from Rn.

Therefore limits given for $0\nu\beta\beta$ decay are lying at present [71] only at $T^{0\nu}_{1/2}$=1.9×10^{23} y (^{82}Se) and $T^{0\nu}_{1/2}$=3.5×10^{23} y (^{100}Mo) on a 90% c.l, i.e. on a 1.5 sigma level, for 0.55 and 5 kg y of measurement, respectively. To improve these limits by a factor of 20, which is required (see [24]) at least, to check the results of the HEIDELBERG-MOSCOW experiment presented in this paper, the measurement times have to be increased by a factor of 400. This means that this experiment is not able to check the HEIDELBERG-MOSCOW result.

GENIUS:

An in principle much more sensitive project is probably the GENIUS project, proposed already in 1997 [61, 67, 68, 62, 63, 30, 29].

A GENIUS Test Facility, (which could already be used to search for cold dark matter by the annual modulation effect) has started operation with 10 kg of natural Germanium detectors in liquid nitrogen in Gran-Sasso on May 5, 2003 [23, 21, 20, 22], increased to 15 kg in October 2005. The results from the GENIUS-Test-Facility show [13], however, that though the search for cold dark matter should be feasible, it may be technically rather difficult, to increase the sensitivity of a *GENIUS-like* experiment for neutrinoless double beta decay beyond that of the HEIDELBERG-MOSCOW experiment.

However, if one wants to get *independent* evidence for the neutrinoless double beta decay mode, one would probably, wish to see the effect in *another* isotope, which would then simultaneously give additional information also on the nuclear matrix elements. In view of these considerations, future efforts to obtain *deeper* information on the process of neutrinoless double beta decay,

would require *a new experimental approach, different from all, what is at present persued.*

Acknowledgement

The author would like to thank all colleagues, who have contributed to the experiment over the last 15 years. He thanks in particular Irina Krivosheina, for her important contribution to the analysis of this experiment.

Our thanks extend also to the technical staff of the Max-Planck Institut für Kernphysik and of the Gran Sasso Underground Laboratory. We acknowledge the invaluable support from BMBF and DFG, and LNGS of this project. We are grateful to the former State Committee of Atomic Energy of the USSR for providing the enriched material used in this experiment.

References

1. H.V. Klapdor-Kleingrothaus, I.V. Krivosheina, A. Dietz et al., *Phys. Lett.* **B 586** (2004) 198–212.
2. H.V. Klapdor-Kleingrothaus, A. Dietz, I.V. Krivosheina et al., *Nucl. Instr. Meth.* **A 522** (2004) 371–406.
3. H.V. Klapdor-Kleingrothaus, in Proc. of BEYOND03, Castle Ringberg, Germany, 9–14 June 2003, *Springer* (2004), ed. H.V. Klapdor-Kleingrothaus, 307–364.
4. H.V. Klapdor-Kleingrothaus et al. hep-ph/0201231 and *Mod. Phys. Lett.* **A 16** (2001) 2409–2420.
5. H.V. Klapdor-Kleingrothaus, A. Dietz, I.V. Krivosheina, *Part. and Nucl.* **110** (2002) 57–79.
6. H.V. Klapdor-Kleingrothaus, A. Dietz, I.V. Krivosheina, *Foundations of Physics* **31** (2002) 1181–1223 and Corrigenda, 2003 home-page: http://www.mpi-hd.mpg.de/non_acc/main_results.html.
7. H.V. Klapdor-Kleingrothaus et al., hep-ph/0205228
8. H.V. Klapdor-Kleingrothaus, A. Dietz, I.V. Krivosheina, hep-ph/0302248 and in Proc. of DARK2002, 4th Int. Heidelberg Conf., International Heidelberg Conference on Dark Matter in Astro and Particle Physics, Cape Town, South Africa, 4–9 Feb 2002, Springer, Heidelberg (2002), eds. by H.V. Klapdor-Kleingrothaus, R.D. Viollier, 404–411.
9. H.V. Klapdor-Kleingrothaus, *Proposal*, **MPI-1987-V17**, September 1987.
10. HEIDELBERG-MOSCOW Coll., *Phys. Rev.* **D 55** (1997) 54.
11. H.V. Klapdor-Kleingrothaus et al., (HEIDELBERG-MOSCOW Coll.), *Eur. Phys. J.* **A 12** (2001) 147 and hep-ph/0103062, in Proc. of 3-rd Int. Conf. Proceedings, Third International Conference on Dark Matter in Astro- and Particle Physics, DARK2000, H.V. Klapdor-Kleingrothaus, ed., (Springer, Heidelberg, 2001) pp. 520–533.
12. H.V. Klapdor-Kleingrothaus, A. Dietz, I.V. Krivosheina, Ch. Dörr, C. Tomei, *Nucl. Instr. Meth.* **510 A** (2003) 281–289 and hep-ph/0308275.

13. H.V. Klapdor-Kleingrothaus et al., *Nucl. Instr. Meth.* **A 511** (2003) 335–340 and hep-ph/0309157.
14. D. Caldwell, *J. Phys.* **G 17** (1991) S137–S144.
15. A.A. Vasenko et al., *Mod. Phys. Lett.* **A 5** (1990) 1299, and I. Kirpichnikov, Preprint ITEP (1991).
16. C.E. Aalseth et al., *Phys. Rev.* **D 65** (2002) 092007.
17. H.V. Klapdor-Kleingrothaus, A. Dietz, I.V. Krivosheina, *Phys. Rev.* **D 70** (2004) 078301.
18. Ch. Dörr, H.V. Klapdor-Kleingrothaus, *Nucl. Instr. Meth.* **A 513** (2003) 596–621.
19. H.V. Klapdor-Kleingrothaus et al., *Phys. Lett.* **578 B** (2004) 54–62 and *Nucl. Instr. Meth.* **A 510** (2003) 281–289.
20. H.V. Klapdor-Kleingrothaus, *CERN Courier* **43** N6 (2003) 9 and hep-ph/0307329, *" 'Naked' Crystals go Underground".*
21. H.V. Klapdor-Kleingrothaus et al., *Nucl. Instr. Meth.* **A 511** (2003) 341–346.
22. C. Tomei, A. Dietz, I. Krivosheina, H.V. Klapdor-Kleingrothaus, *Nucl. Instr. Meth.* **A 508** (2003) 343–352.
23. H.V. Klapdor-Kleingrothaus, C. Tomei, I. Krivosheina et al., *Nucl. Instr. Meth.* **A 530** (2004) 410–418.
24. A. Staudt, K. Muto, H.V. Klapdor-Kleingrothaus, *Eur. Lett.* **13** (1990) 31.
25. K. Muto, E. Bender, H.V. Klapdor, *Z. Phys.* **A 334** (1989) 187.
26. H.V. Klapdor-Kleingrothaus et al., in preparation.
27. H.V. Klapdor-Kleingrothaus, H. Päs, A.Yu. Smirnov, *Phys. Rev.* **D 63** (2001) 073005; and hep-ph/0003219; in Proc. of DARK'2000, Heidelberg, 10–15 July, 2000, Germany, ed. H.V. Klapdor-Kleingrothaus, Springer, Heidelberg (2001) 420–434.
28. H.V. Klapdor-Kleingrothaus, U. Sarkar, *Mod. Phys. Lett.* **A 16** (2001) 2469–2482.
29. H.V. Klapdor-Kleingrothaus, "60 Years of Double Beta Decay – From Nuclear Physics to Beyond the Standard Model", World Scientific, Singapore (2001) 1281 pages.
30. H.V. Klapdor-Kleingrothaus, *Int. J. Mod. Phys.* **A 13** (1998) 3953.
31. H.V. Klapdor-Kleingrothaus, *Springer Tracts in Modern Physics*, **163** (2000) 69–104, Springer-Verlag, Heidelberg, Germany (2000).
32. H.V. Klapdor-Kleingrothaus, U. Sarkar, hep-ph/0302237.
33. G. Douysset et al., *Phys. Rev. Lett.* **86** (2001) 4259–4262; J.G. Hykawy et al., *Phys. Rev. Lett.* **67** (1991) 1708; G. Audi, A.H. Wapstra, *Nucl. Phys.* **A 595** (1995) 409–480; R.J. Ellis et al., *Nucl. Phys.* **A 435** (1985) 34–42.
34. M.D. Hannam, W.J. Thompson, *Nucl. Instr. Meth.* **A 431** (1999) 239–251.
35. E. der Mateosian, M. Goldhaber, *Phys. Rev.* **146** (1966) 810–815.
36. D.V. Ahluwalia, in Proc. of Physics Beyond the Standard Model, Beyond the Desert 02, BEYOND'02, Oulu, Finland, 2–7 Juni, 2002, IOP, Bristol, 2003, ed. H.V. Klapdor-Kleingrothaus, 143–160; D.V. Ahluwalia, M. Kirchbach, Phys. Lett. B529 (2002) 124.
37. K. Muto, H.V. Klapdor, in *"Neutrinos", Graduate Texts in Contemporary Physics"*, ed. H.V. Klapdor, Berlin, Germany: Springer (1988) 183–238.
38. K. Grotz, H.V. Klapdor, *"Die Schwache Wechselwirkung in Kern-, Teilchen- und Astrophysik"*, B.G. Teubner, Stuttgart (1989), *"The Weak Interaction in Nuclear, Particle and Astrophysics"*, IOP Bristol (1990), Moscow, MIR (1992) and China (1998).

39. H.V. Klapdor-Kleingrothaus, A. Staudt, *"Teilchenphysik ohne Beschleuniger"*, B.G. Teubner, Stuttgart (1995), *"Non–Accelerator Particle Physics"*, IOP Publishing, Bristol and Philadelphia (1995) and 2. ed. (1998) and Moscow, Nauka, Fizmalit (1998).
40. H.V. Klapdor-Kleingrothaus, in Proc. of Intern. Conf. on Physics Beyond the Standard Model: Beyond the Desert 02, BEYOND'02, Oulu, Finland, 2–7 Jun. 2002, IOP, Bristol, 2003 ed. H.V. Klapdor-Kleingrothaus, 215–240 pp.
41. J. Schechter, J.W.F. Valle, *Phys. Rev.* **D 25** (1982) 2951–2954.
42. M. Hirsch, H.V. Klapdor-Kleingrothaus, *Phys. Lett.* **B 398** (1997) 311; *Phys. Rev.* **D 57** (1998) 1947; M. Hirsch, H.V. Klapdor-Kleingrothaus, St. Kolb, *Phys. Rev.* **D 57** (1998) 2020.
43. G. Bhattacharyya, H.V. Klapdor-Kleingrothaus, H. Päs, A. Pilaftsis, *Phys. Rev.* **D 67** (2003) 113001 and hep-ph/0402071 in Proc. of Int. Worksh. on Astr. and *HE Phys.* (AHEP-2003), Valencia, Spain, 14–18 Oct 2003.
44. Yu. Zdesenko et al., *Phys. Lett.* **B 546** (2002) 206–215.
45. E. Fiorini et al., *Phys. Lett.* **B 25** (1967) 602.
46. E. Ma, M. Raidal, *Phys. Rev. Lett.* **87** (2001) 011802; *Erratum-ibid.* **87** (2001) 159901 and hep-ph/0102255.
47. K.S. Babu et al., *Phys. Lett.* **B 552** (2003) 207–213.
48. E. Ma in Proc. of Intern. Conf. on Physics Beyond the Standard Model: Beyond the Desert 02, BEYOND'02, Oulu, Finland, 2–7 Jun. 2002, IOP, Bristol, 2003, and BEYOND 2003, Ringberg Castle, Tegernsee, Germany, 9–14 Juni 2003, Springer, Heidelberg, Germany, 2004, ed. H.V. Klapdor-Kleingrothaus.
49. R.N. Mohapatra, M.K. Parida, G. Rajasekaran, (2003) hep-ph/0301234.
50. D. Fargion et al., in Proc. of DARK2000, Heidelberg, Germany, July 10–15, 2000, Ed. H.V. Klapdor-Kleingrothaus, *Springer*, (2001) 455–468 and in Proc. of Beyond the Desert 2002, BEYOND02, Oulu, Finland, June 2002, IOP 2003, and BEYOND03, Ringberg Castle, Tegernsee, Germany, 9–14 Juni 2003, Springer, Heidelberg, Germany, 2003, ed. H.V. Klapdor-Kleingrothaus.
51. Z. Fodor, S.D. Katz, A. Ringwald, *Phys. Rev. Lett.* **88** (2002) 171101 and Z. Fodor et al., *JHEP* (2002) 0206:046, and in Proc. of Intern. Conf. on Physics Beyond the Standard Model: Beyond the Desert 02, BEYOND'02, Oulu, Finland, 2–7 Jun 2002, IOP, Bristol, 2003, ed. H V Klapdor-Kleingrothaus and hep-ph/0210123.
52. H. V. Klapdor-Kleingrothaus, U. Sarkar, hep-ph/0304032, and in *Mod. Phys. Letter.* **A18** (2003) 2243–2254.
53. H. Minakata, O. Yasuda, *Phys. Rev.* **D 56** (1997) 1692.
54. O. Yasuda, in Proc. of Int. Conf. BEYOND'99, Ringberg Castle, Germany, June 6–12, 1999, IOP, Bristol (2000), eds. H.V. Klapdor-Kleingrothaus and I.V. Krivosheina, p.223.
55. I. Stancu, D.V. Ahluwalia, *Phys. Lett.* **B 460** (1999) 431–436.
56. S. Hannestad, CAP 0305 (2003) 920030 004, and astro-ph/0303076, in Proc. of 4th Int. Conf. on Particle Physics Beyond the Standard Model, BEYOND03, Ringberg Castle, Germany, 9–14 Juni 2003, Springer, Heidelberg, Germany, 2003, ed. H.V. Klapdor-Kleingrothaus.
57. S.W. Allen, R.W. Schmidt, S.L. Bridle, astro-ph/0306386.
58. K.S. Babu, E. Ma and J.W.F. Valle, *Phys. Lett.* **B 552** (2003) 207–213.
59. M. Hirsch et al., *Phys. Rev.* **D69** (2004) 093006.
60. A. Blanchard, M. Douspis, M. Rowan-Robinson, S. Sarkar, astro-ph/0304237.

61. H.V. Klapdor-Kleingrothaus in Proc. of BEYOND'97, Castle Ringberg, Germany, 8–14 June 1997, ed. by H.V. Klapdor-Kleingrothaus et al.,IOP Bristol (1998) 485–531, and *Int. J. Mod. Phys.* **A13** (1998) 3953.
62. H.V. Klapdor-Kleingrothaus, J. Hellmig et al.,*J. Phys.* **G24** (1998) 483–516.
63. H.V. Klapdor-Kleingrothaus et al. MPI-Report MPI-H-V26-1999, hep-ph/9910205, in Proc. of the 2nd Int. Conf. on Particle Physics Beyond the Standard Model BEYOND'99, Castle Ringberg, Germany, 6–12 June 1999, eds. H.V. Klapdor-Kleingrothaus and I.V. Krivosheina, IOP Bristol (2000) 915–1014.
64. G. Belanger et al., *Phys. Rev.* **D53** (1996) 6292 and in Proc. of Lepton-Baryon Int. Conf., April 1998, Trento, IOP, Bristol, (1999), eds. H.V. Klapdor-Kleingrothaus and I.V. Krivosheina.
65. O. Panella et al., *Phys. Rev.* **D 62** (2000) 015013.
66. M.N. Rebelo, Proc. of BEYOND'2003, Castle Ringberg, Germany, July 2003, ed. H.V. Klapdor-Kleingrothaus, Springer, Heidelberg (2004) 267.
67. H.V. Klapdor-Kleingrothaus, M. Hirsch, *Z. Phys.* **A 359** (1997) 361–372.
68. J. Hellmig, H.V. Klapdor-Kleingrothaus, Z. *Phys.* **A 359** (1997) 351–359 and nucl-ex/9801004.
69. T. Bernatowicz et al. , *Phys. Rev.* **C 47** (1993) 806 and *Phys. Rev. Lett.* **69** (1992) 2341.
70. C. Brofferio, see Proc. International Conf. "Neutrino Telescopes", Febr. 2005, Venice, Italy.
71. X. Sarazin (NEMO Collaboration), In Proc. of "Neutrino 2004"' Intern. Conference, Paris, July 2005.
72. G. Gratta, ApPEC (Astroparticle Physics European Coordination), Paris, France 22.01.2002, and in Proc. Int. Works. on Low Energy Solar Neutrinos, of LowNu2, Dec. 4–5 (2000) Tokyo, Japan, ed: Y. Suzuki, World Scientific (2001) p.98.
73. R. Hofmann, hep–ph/0401017 v.1.
74. M. Tegmark et al., astro-ph/0310723, subm. *Phys. Rev.* **D**.

DAMA/NaI Results on Dark Matter Particles by Annual Modulation Signature

R. Bernabei[1], P. Belli[1], F. Cappella[1], F. Montecchia[1+], F. Nozzoli[1], A. Incicchitti[2], D. Prosperi[2], R. Cerulli[3], C. J. Dai[4], H. H. Kuang[4], J. M. Ma[4], and Z. P. Ye[4++]

[1] Dipartimento di Fisica, Università di Roma "Tor Vergata" and INFN, Sezione di Roma II, I-00133, Roma, Italy
[2] Dipartimento di Fisica, Università di Roma "La Sapienza" and INFN, Sezione di Roma, I-00185, Roma, Italy
[3] INFN - Laboratori Nazionali del Gran Sasso, I-67010 Assergi (Aq), Italy
[4] IHEP, Chinese Academy, P.O. Box 918/3, Beijing 100039, China
[+] also: Università "Campus Bio-Medico" di Roma, 00155, Rome, Italy,
[++] also: University of Zhao Qing, Guang Dong, China

DAMA is an observatory for rare processes based on the development and use of various kinds of radiopure scintillators; it is operative deep underground at the Gran Sasso National Laboratory of the I.N.F.N.. In particular, the DAMA/NaI set-up ($\simeq$ 100 kg highly radiopure NaI(Tl)) has effectively investigated the model-independent annual modulation signature, obtaining from the data of seven annual cycles (total exposure of 107731 kg $\times$ day) a 6.3 σ C.L. model-independent evidence for the presence of a Dark Matter particle component in the galactic halo. Some of the many possible corollary model-dependent quests for the candidate particle have also been investigated. At present, the second generation DAMA/LIBRA set-up ($\simeq$ 250 kg highly radiopure NaI(Tl)) is in operation deep underground.

1 Introduction

DAMA is an observatory for rare processes. Several low background set-ups have been realised; the main ones are: i) DAMA/NaI ($\simeq$ 100 kg of highly radiopure NaI(Tl)), which took data underground over seven annual cycles and was put out of operation in July 2002 [1, 2, 3, 4, 5, 6, 7, 8, 9, 10, 11, 12, 13]; ii) DAMA/LXe ($\simeq$ 6.5 kg liquid Xenon) [14, 15]; iii) DAMA/R&D, which is devoted to tests on prototypes and small scale experiments [16]; iv) the new second generation DAMA/LIBRA set-up ($\simeq$ 250 kg highly radiopure NaI(Tl)) in operation since March 2003. Moreover, in the framework of devoted R&D for radiopure detectors and PMTs, sample measurements are regularly carried out by means of the low background DAMA/Ge detector, installed deep underground since $\gtrsim$ 10 years and, in some cases, by means of Ispra facilities.

In the following, only the DAMA/NaI results on the annual modulation signature will be addressed. This signature was originally suggested in [17]

and it is very distinctive since it requires the simultaneous satisfaction of all the following requirements: the rate must contain a component modulated according to a cosine function (1) with one year period, T (2) and a phase, t_0, that peaks around $\simeq 2^{nd}$ June (3); this modulation must only be found in a well-defined low energy range, where recoils induced by Dark Matter particle can be present (4); it must apply to those events in which just one detector of many actually "fires" (*single-hit* events), since the Dark Matter particle multi-scattering probability is negligible (5); the modulation amplitude in the region of maximal sensitivity is expected to be $\lesssim 7\%$ for usually adopted halo distributions (6), but it can be larger in case of some possible scenarios such as e.g. those in [18, 19]. Only systematic effects or side reactions able to fulfil these 6 requirements and to account for the whole observed modulation amplitude might mimic this signature. With the present technology, the annual modulation signature remains the main signature for Dark Matter particles in the galactic halo.

A detailed description of the set-up, of its radiopurity, of its performance, of the used hardware procedures, of the determination of the experimental quantities and of the data reduction was given in [1, 9, 10, 2]. Here only few arguments are addressed. The nine 9.7 kg highly radiopure NaI(Tl) are encapsulated in radiopure Cu housings; moreover, 10 cm long Tetrasil-B light guides act as optical windows on the two end faces of each crystals and are coupled to specially developed low background photomultipliers (PMT). The measured light response is 5.5–7.5 photoelectrons/keV depending on the detector. The two PMTs of a detector work in coincidence with hardware thresholds at the single photoelectron level in order to assure high efficiency for the coincidence at few keV level. The energy threshold of the experiment, 2 KeV, is determined by means of X-rays sources and of keV range Compton electrons on the basis also of the features of the noise rejection procedures and of the efficiencies when lowering the number of available photoelectrons [1]. The detectors are enclosed in a sealed copper box, continuously maintained in high purity (HP) Nitrogen atmosphere in slightly overpressure with the respect to the external environment. A suitable low background hard shield against electromagnetic and neutron background was realised using very high radiopure Cu and Pb bricks [1], Cd foils and 10/40 cm polyethylene/paraffin; the hard shield is also sealed in a plexiglas box and maintained in HP Nitrogen atmosphere. Moreover, about 1 m concrete (made from the Gran Sasso rock material) almost fully surrounds the hard shield outside the barrack and at bottom of the hard shield, acting as a further neutron moderator.

A three-level sealing system from environmental Radon is effective. In fact, the inner part of the barrack, where the set-up is allocated, has the floor (above the concrete) and all the walls sealed by Supronyl (permeability: $2 \cdot 10^{-11}\,\mathrm{cm}^2/\mathrm{s}$ [20]) plastic and the entrance door is air-tight. A low level oxygen alarm informs the operator before entering the inner part of the barrack since the HP Nitrogen which fills both the inner Cu box and the external

plexiglas box is released in this closed environment. The Radon level inside the barrack is continuously monitored and recorded with the production data [6, 7, 1, 9, 10, 2].

On the top of the shield a glove-box (also maintained in the HP Nitrogen atmosphere) is directly connected to the inner Cu box, housing the detectors, through Cu pipes. The pipes are filled with low radioactivity Cu bars (covered by 10 cm of low radioactive Cu and 15 cm of low radioactive Pb) which can be removed to allow the insertion of radioactive sources handlers for calibrating the detectors in the same running condition, without any contact with external environment [1].

The whole installation is air-conditioned and the operating temperature as well as many other parameters are continuously monitored and acquired with the production data. Moreover, self-controlled computer processes automatically monitor several parameters and manage alarms [1, 10, 2].

The electronic chain and the data acquisition system operative up to summer 2000 have been described in [1], while the new electronics and DAQ installed in summer 2000 have been described in [2].

In the following the main results on annual modulation investigation will be summarised. It is worth to remind, however, that - thanks to its radiopurity and features - DAMA/NaI has also investigated other approaches for Dark Matter particles [3, 4] and several other rare processes [5].

2 The Model-Independent Result by DAMA/NaI

As reported in [2], a model independent investigation of the annual modulation signature has been realised by exploiting the time behaviour of the experimental residual rates of the *single-hit* events in the lowest energy regions over the seven annual cycles (total exposure: 107731 kg · day) [6, 7, 8, 9, 10, 11, 12, 13, 2]. These experimental residual rates of the *single-hit* events are given by: $< r_{ijk} - flat_{jk} >_{jk}$, where r_{ijk} is the measured rate in the considered i-th time interval for the j-th detector in the k-th considered energy bin and $flat_{jk}$ is the rate of the j-th detector in the k-th energy bin averaged over the cycles. The average is made on all the detectors (j index) and on all the energy bins in the considered energy interval.

This model independent approach offers an immediate evidence of the presence of an annual modulation of the rate of the *single-hit* events in the lowest energy region over the seven annual cycles as shown in Fig. 1, where the energy and time behaviours of the *single-hit* residual rates are depicted.

In particular, the data favour the presence of a modulated cosine-like behaviour at 6.3 σ C.L.; in fact, their fit for the (2–6) KeV larger statistics energy interval offers a modulation amplitude equal to (0.0200 ± 0.0032) cpd/kg/keV, a phase: $t_0 = (140 \pm 22)$ days and a period: $T = (1.00 \pm 0.01)$ year, all parameters kept free in the fit. The period and phase agree with those expected in the case of a Dark Matter particle induced effect ($T = 1$ year and

t_0 roughly at $\simeq$ 152.5-th day of the year). The χ^2 test on the (2–6) KeV residual rate in Fig. 1 disfavours the hypothesis of unmodulated behaviour giving a probability of $7 \cdot 10^{-4}$ ($\chi^2/d.o.f. = 71/37$). Moreover, if the experimental residuals of Fig. 1 are fitted fixing the period at 1 year and the phase at 2^{nd} June, the following modulation amplitudes are obtained: (0.0233 ± 0.0047)

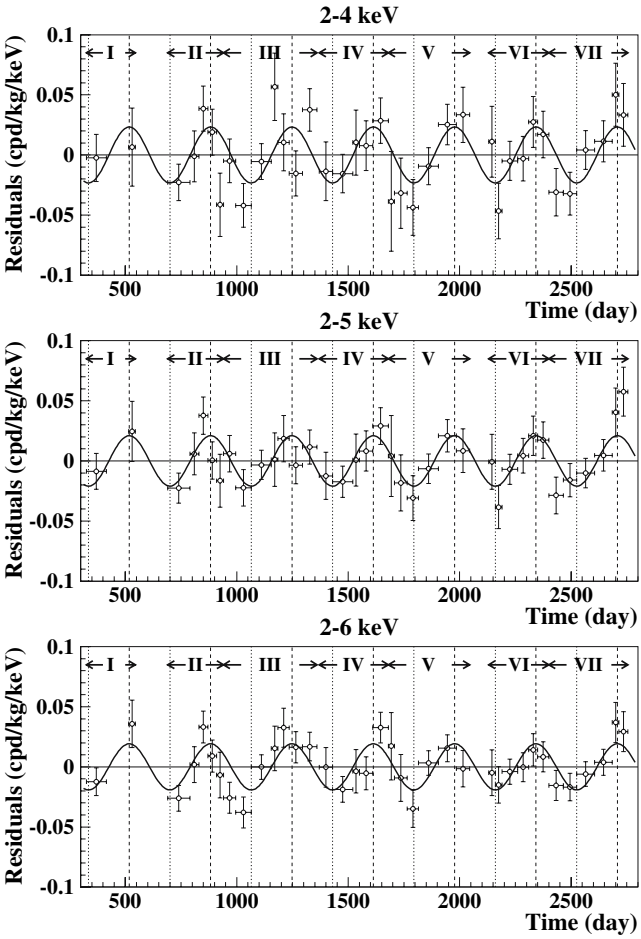

Fig. 1. Experimental residual rate for *single-hit* events, in the (2–4), (2–5) and (2–6) KeV energy intervals as a function of the time elapsed since January 1-st of the first year of data taking. The experimental points present the errors as vertical bars and the associated time bin width as horizontal bars. The superimposed curves represent the cosinusoidal functions behaviours expected for a Dark Matter particle signal with a period equal to 1 year and phase at 2^{nd} June; the modulation amplitudes have been obtained by best fit. See text. The total exposure is 107731 kg $\cdot$ day.

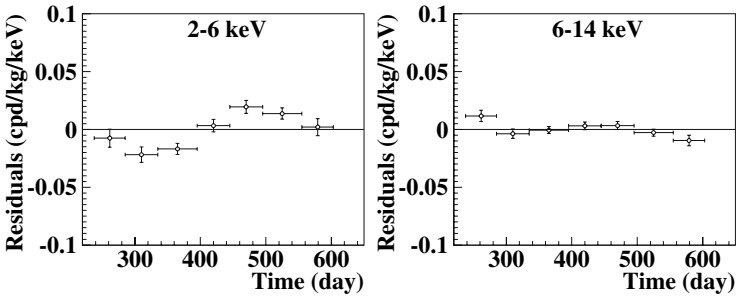

Fig. 2. Experimental *single-hit* residual rate in a single annual cycle from the total exposure of 107731 kg · day for the (2–6) KeV and (6–14) KeV energy intervals. The experimental points present the errors as vertical bars and the associated time bin width as horizontal bars. The initial time is taken at August 7th. Fitting the data with a cosinusoidal function with period of 1 year and phase at 152.5 days, the following amplitudes are obtained: (0.0195 ± 0.0031) cpd/kg/keV and $-(0.0009 \pm 0.0019)$ cpd/kg/keV, respectively. Thus, a clear modulation is present in the lowest energy region, while it is absent just above.

cpd/kg/keV, (0.0210±0.0038) cpd/kg/keV and (0.0192±0.0031) cpd/kg/keV for the (2–4), (2–5) and (2–6) KeV energy intervals, respectively.

In Fig. 2 the experimental *single-hit* residual rate in a single annual cycle from the total exposure of 107731 kg · day is presented for two different energy intervals; as it can be seen the modulation is clearly present in the (2–6) KeV energy region, while it is absent just above. The same conclusion is obtained by investigating the data by means of the Fourier analysis (performed according to [21] including also the treatment of the experimental errors and of the time binning); in fact, the results depicted in Fig. 3 show a clear peak for a period of 1 year in the (2–6) KeV energy interval, while it is absent in the energy interval just above.

A quantitative investigation of the whole energy spectrum up to MeV energy region has not shown modulation in any other energy interval (see e.g. [9, 10, 2] and arguments given later).

Finally, in order to show if the modulation amplitudes are statistically well distributed in all the crystals, in all the annual cycles and in the energy bins, the distributions of the variable $\frac{S_m - <S_m>}{\sigma}$ are reported in Fig. 4. The S_m are the experimental modulation amplitudes for each detector, for each annual cycle and for each considered energy bin (taken as an example equal to 0.25 KeV), σ are their errors and the $< S_m >$ represent the mean values of the modulation amplitudes over the detectors and the annual cycles for each energy bin. The left panel of Fig. 4 shows the distribution referred to the region of interest for the observed modulation, (2–6) keV, while the right panel includes also the energy region just above, (2–14) KeV. Since this variable is distributed as a gaussian with an unitary standard deviation, the

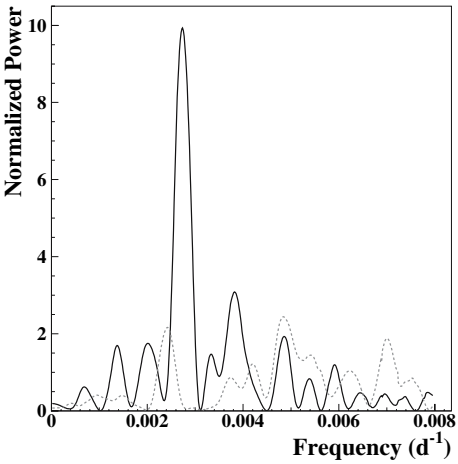

Fig. 3. Power spectrum of the measured *single-hit* residuals for the (2–6) KeV (continuous line) and (6–14) KeV (dotted line) energy intervals calculated according to [21], including also the treatment of the experimental errors and of the time binning. As it can be seen, the principal mode present in the (2–6) KeV energy interval corresponds to a frequency of $2.737 \cdot 10^{-3}$ d^{-1}, that is to a period of $\simeq$1 year. A similar peak is not present in the (6–14) KeV energy interval.

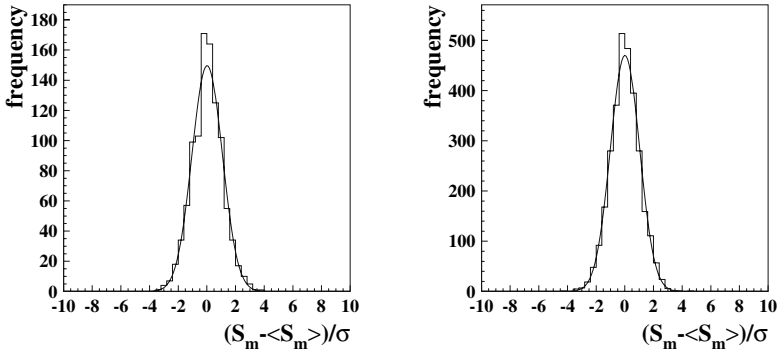

Fig. 4. Distributions of the variable $\frac{S_m - <S_m>}{\sigma}$ (where σ is the error associated to the S_m) evaluated for each detector, for each annual cycle and each considered energy bin: i) in the region of interest for the observed modulation, (2–6) keV (left panel); ii) including also the energy region just above, (2–14) KeV (right panel). See text.

modulation amplitudes are statistically well distributed in all the crystals, in all the data taking periods and in all the considered energy bins.

In conclusion, the data satisfy all the peculiar requirements, given above, for the Dark Matter particle model independent annual modulation signature. A careful investigation of all the known possible sources of systematics and

Table 1. Summary of the results obtained by investigating the possible sources of systematics or of side reactions [2]. No systematics or side reaction has been found able to give a modulation amplitude different from zero; thus cautious upper limits (90% C.L.) have been calculated and are shown here in terms of the measured model independent modulation amplitude, S_m^{obs}. As it can be seen, none of them nor their cumulative effect could account for the measured modulation; moreover, as discussed in details in [10, 2], they cannot mimic the signature.

Source	Cautious upper limit (90%C.L.)
Radon	$< 0.2\% S_m^{obs}$
Temperature	$< 0.5\% S_m^{obs}$
Noise	$< 1\% S_m^{obs}$
Energy scale	$< 1\% S_m^{obs}$
Efficiencies	$< 1\% S_m^{obs}$
Background	$< 0.5\% S_m^{obs}$
Side reactions	$< 0.3\% S_m^{obs}$
In addition: no effect can mimic the signature	

side reactions has been regularly carried out by DAMA/NaI and published at time of each data release [6, 7, 9, 10, 2]. No effect able to mimic the signature has been found, as reported in Table 1 (for detailed quantitative discussions see [10, 2]).

For the sake of completeness, we also remind that possible diurnal effects – correlated both with the sidereal and with the solar time – have already been excluded by the analysis reported in [4].

In particular, as mentioned above, no modulation has been observed in the background; in fact, the whole energy spectrum up to MeV energy region has been analysed and the presence of a background modulation in the whole energy spectrum has been excluded at a level much lower than the effect found in the lowest energy region [10, 2]. This result already accounts also for the background component due to the neutrons and the Radon; nevertheless, further additional independent and cautious analyses to estimate their possible contribution have been given in [10, 2]. In fact, it has been demonstrated in [10, 2] that a modulation of neutron flux – possibly observed by the ICARUS coll. at Gran Sasso, as reported in the ICARUS internal report TM03-01 – cannot quantitatively contribute to the DAMA/NaI observed modulation amplitude, even if the neutron flux would be assumed to be 100 times larger than measured at LNGS by several authors with different techniques over more than 15 years. Moreover, in no case the neu-

trons can mimic the signature since some of the peculiar requirements of the signature would fail. Similarly, any possible effect of the muon flux modulation reported by the MACRO experiment [22] is excluded both by quantitative investigation [10, 2] and by inability to fulfil all the peculiarities of the signature.

As regards the possibility of a contribution from the Radon, we remind that the DAMA/NaI has three levels of insulation from the environmental air (see above). Moreover, the Radonmeter which continuously recorded the Radon level inside the barrack (that is external to the hard shield) typically measured values at level of its sensitivity and no modulation has been observed [6, 7, 9, 10, 2]. To be on the safest side, even the possible presence of Radon trace in the HP Nitrogen atmosphere inside the Cu box, housing the detectors, has been investigated by searching for the double coincidences of the gamma-rays (609 and 1120 KeV) from ^{214}Bi Radon daughter, obtaining an upper limit of: $< 4.5 \cdot 10^{-2}$ Bq/m^3 (90% C.L.). It gives rise to the upper limit reported in Table 1 when assuming an hypothetical 10%, modulation of possible Radon trace in the HP Nitrogen atmosphere of the Cu box. Anyhow, it is worth to remark that in every case even a sizeable quantity of Radon nearby a detector cannot mimic the Dark Matter particle annual modulation signature since some of the peculiarities of the signature would fail [10, 2].

To perform a further relevant investigation, in 1999 we proposed to renew the electronic chain of DAMA/NaI removing the multiplexer system and equipping each detector with its own transient digitizer. This occurred in summer 2000, thus in the last two annual cycles the *multiple-hits* events and the *single-hit* events have been acquired and analysed using the same identical hardware and the same identical software procedures. The *multiple-hits* events class – on the contrary of the *single-hit* one – does not include events induced by Dark Matter particles since the probability that these particles scatter off more than one detector is negligible. The obtained results are depicted in Fig. 5. The fitted modulation amplitudes are: $A = (0.0195 \pm 0.0031)$ cpd/kg/keV and $A = -(3.9 \pm 7.9) \cdot 10^{-4}$ cpd/kg/keV for *single-hit* and *multiple-hits* residual rates, respectively. Thus, evidence of annual modulation is present in the *single-hit* residuals (events class to which recoils induced by the Dark Matter particle belong), while it is absent in the *multiple-hits* residual rate (event class to which only background events belong). Since the same identical hardware and the same identical software procedures have been used to analyse the two classes of events, the obtained result offers an additional strong support for the presence of a Dark Matter particle component in the galactic halo further excluding any side effect either from hardware or from software procedures or from background.

In conclusion, the presence of a Dark Matter particle component in the galactic halo is supported by DAMA/NaI at 6.3 σ C.L. and the modulation amplitude measured over the 7 annual cycles in NaI(Tl) at the location of the Gran Sasso Laboratory for the (2–6) KeV energy region is (0.0200 ± 0.0032)

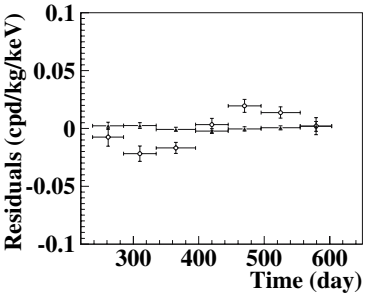

Fig. 5. Experimental residual rates over seven annual cycles for *single-hit* events (open circles) – class of events to which WIMP events belong – and over the last two annual cycles for *multiple-hits* events (filled triangles) – class of events to which WIMP events do not belong – in the (2–6) KeV cumulative energy interval. They have been obtained by considering for each class of events the data as collected in a single annual cycle and using in both cases the same identical hardware and the same identical software procedures. The initial time is taken on August 7th. See text.

cpd/kg/keV. This is the experimental result of DAMA/NaI. It is model independent; no other experiment whose result can be directly compared with this one is available so far in the field of Dark Matter investigation.

3 Corollary Results: Quests for a Candidate Particle in Some of the Possible Model Frameworks

Corollary investigations can also be pursued on the nature and coupling of the Dark Matter candidate but this latter investigation is instead model dependent and – considering the large uncertainties which exist on the astrophysical, nuclear and particle physics assumptions and on the parameters needed in the calculations – has no general meaning (as it is also the case of exclusion plots and of the Dark Matter particle parameters evaluated in the indirect detection experiments). Thus, it should be handled in the most general way [2, 6, 7, 8, 9, 10, 11, 12, 13].

Many possible scenarios can be considered and at present level of knowledge they cannot be disentangled. Some of the open questions are: (i) which is the right nature for the Dark Matter particle; (ii) which is its right couplings with ordinary matter (mixed SI&SD, purely SI, purely SD, *preferred inelastic*, etc.); (iii) which are the right form factors and related parameters for each target nucleus; (iv) which is the right spin factor for each target nucleus; (v) which are the right scaling laws (let us remind that even for the neutralino case in a MSSM framework with purely SI interaction the scenario could be drastically modified as pointed out in [23]); (vi) which is the right

halo model and related parameters; (vii) which are the right values of the experimental parameters within their uncertainties; etc.

As regards, in particular, the Dark Matter particle-nucleus elastic scattering, the differential energy distribution of the recoil nuclei can be calculated [3, 24, 2] by means of the differential cross section of the Dark Matter particle-nucleus elastic processes given by the sum of the SI and the SD contributions. In the SI case, the nuclear parameters can be decoupled from the particle parameters and the nuclear cross sections are usually scaled to a defined point-like SI Dark Matter particle-nucleon cross section, σ_{SI}. In the SD case the notations [11]: $tg\theta = \frac{a_n}{a_p}$, can be used, where $a_{p,n}$ are the effective Dark Matter particle-nucleon coupling strengths for SD interactions. The mixing angle θ is defined in the $[0, \pi)$ interval; in particular, θ values in the second sector account for a_p and a_n with different signs. Also in the SD case all the nuclear cross sections are usually scaled to a defined point-like SD Dark Matter particle-nucleon cross section, σ_{SD} [2]. Thus, the energy distribution of the recoil rate can be written as a function of σ_{SI}, σ_{SD} and θ. Another important parameter is the local density of the Dark Matter particles, $\rho_W = \xi\rho_0$, where ρ_0 is the local halo density and ξ ($\xi \leq 1$) is the fractional amount of local density of Dark Matter particles.

Among the ingredients entering in the model dependent analyses there are the nuclear SI and SD form factors, which generally depend on the nature of the involved particle. In [2] the existing uncertainties in the usually adopted formulation for the SI case have been discussed as well as those for the SD one. It has also shown that the SD case is even more uncertain since the nuclear and particle physics degrees of freedom cannot be decoupled and a dependence on the assumed nuclear potential exists. Moreover, further significant uncertainties in the evaluation of the SD interaction rate also arise from the adopted spin factor for the single target-nucleus. In fact, the available calculated values are well different in different models and, in addition, at fixed model they depend on θ. Thus, not only the target nuclei should have spin different from zero (for example, this is not the case of Ar isotopes) to be sensitive to Dark Matter particles with a SD component in the coupling, but also well different sensitivities can be expected among odd-nuclei having an unpaired proton (as e.g. ^{23}Na and ^{127}I) and odd-nuclei having an unpaired neutron (as e.g. the odd Xe and Te isotopes and ^{73}Ge).

Another scenario also considered in the corollary DAMA/NaI model dependent analyses is that of Dark Matter particle with *preferred inelastic* scattering which has been suggested by [18]. In this case the Dark Matter particles can only inelastically scatter off nuclei going to excited levels with a δ mass splitting. A specific model featuring a real component of the sneutrino (for which the mass splitting naturally arises) has been given in [18]. It has been shown that for this inelastic scattering a kinematical constraint exists which favours target-detectors media with heavy nuclei (such as ^{127}I) with the respect to those with lighter ones (such as e.g. ^{nat}Ge). In fact, this process can

only occur if the particle velocity is larger than a threshold value; this kinematical constraint becomes increasingly severe as the nucleus mass decreases [18]. Moreover, this model scenario implies some interesting peculiar features when exploiting the annual modulation signature; in fact – with the respect to the case of Dark Matter particle elastically scattering – it would give rise to an enhanced modulated component of the signal with the respect to the unmodulated one and to largely different behaviours with energy for both the components (showing both higher mean values) [18]. The differential energy distribution of the recoil nuclei in the case of inelastic processes is function of $\xi\sigma_p$, m_W and δ, analogously as above other ingredients, as e.g. the form factor, play also a role [2].

As mentioned, the expected energy distribution for the scatterings of Dark Matter particles also depends on ρ_W and on the velocity distribution of the Dark Matter particles at Earth's position. The experimental observations regarding the dark halo of our Galaxy do not allow to get information on them without introducing a model for the Galaxy matter density. The dark halo model widely used only in calculations carried out in the field of direct detection approaches is the naive isothermal sphere that corresponds to a spherical infinite system with a flat rotational curve. Despite its simplicity has favoured its wide use in the calculation of expected rate of Dark Matter particle-nucleus interaction, it doesn't match with astrophysical observations and presents an unphysical behaviour. In fact, the density profile has a singularity in the origin and implies a total infinite mass of the halo unless introducing some cut-off at large radii. Thus, the use of more realistic halo models is mandatory since the model dependent results significantly vary. An extensive discussion about some of the more credited realistic halo models has been reported in [13, 2]. In particular, the considered halo model classes correspond to: (i) spherically symmetric matter density with isotropic velocity dispersion (A); (ii) spherically symmetric matter density with non-isotropic velocity dispersion (B); (iii) axisymmetric models (C); (iv) triaxial models (D); (v) moreover, in the case of axisymmetric models it is possible to include either an halo co-rotation or an halo counter-rotation. The parameters of each halo model have been chosen taking into account some available observational data; nevertheless other choices are possible. Thus, considering the allowed range for the local velocity of Dark Matter particles $v_0 = (220 \pm 50)\,\mathrm{km\ s^{-1}}$ (90% C.L.), the allowed range of local density ρ_0 has been evaluated [13] taking into account the following physical constraints: (i) the amount of flatness of the rotational curve of our Galaxy, considering conservatively $0.8 \cdot v_0 \lesssim v_{rot}^{100} \lesssim 1.2 \cdot v_0$, where v_{rot}^{100} is the value of rotational curve at distance of 100 kpc from the galactic center; (ii) the maximal non dark halo components in the Galaxy, considering conservatively $1 \cdot 10^{10}\mathrm{M}_\odot \lesssim M_{vis} \lesssim 6 \cdot 10^{10}\mathrm{M}_\odot$ [25, 26]. Although a large number of self-consistent galactic halo models, in which the variation of the velocity distribution function is originated from the change of the halo density profile or of the potential, have been considered, still many other possibilities exist.

The proper knowledge of other quantities is also necessary such as e.g. the recoil/electron response ratio for the given nucleus in the given detector and energy range, (named *quenching factor*). Of course, significant differences are often present in literature for the measured value of this recoil /electron response ratio even for the same nucleus in the same kind of detector as shown in [2].

In conclusion, just as a corollary of the model independent result over the seven annual cycles, in the following some of the many possible model dependent quests for a Dark Matter candidate are summarised. They have been obtained by considering the halo models previously mentioned and some of the many uncertainties which exist on the astrophysical, nuclear and particle physics assumptions and on the parameters needed in the calculations. Moreover, no restriction on the Dark Matter particle mass has been adopted in these analyses; hence, we have just marked for memory on some figures the lower bound on the neutralino mass as derived from the LEP data in the adopted supersymmetric schemes based on GUT assumptions [27]. In fact, other model assumptions are possible which would imply significant variations of some accelerators bounds, allowing neutralino mass down to 6 GeV (see e.g. the recent [28, 29, 30]); in addition, other low mass candidates can be considered as well. It is worth to note that the LEP model dependent mass limit – when considered – selects the Dark Matter particle-Iodine elastic scatterings as dominant because of the adopted scaling laws and of kinematical arguments, while DAMA/NaI is intrinsically sensitive both to low and high candidate mass having both a light (the ^{23}Na) and a heavy (the ^{127}I) target-nucleus.

The results presented by DAMA/NaI on the corollary quests for the candidate particle over the seven annual cycles are calculated taking into account the time and energy behaviours of the *single-hit* experimental data. In particular, the likelihood function requires the agreement: (i) of the expectations for the modulated part of the signal with the measured modulated behaviour for each detector and for each energy bin; (ii) of the expectations for the unmodulated component of the signal with the respect to the measured differential energy distribution and – since [9] – also with the bound on recoils obtained by pulse shape discrimination from the devoted DAMA/NaI-0 data [3]. The latter one acts in the likelihood procedure as an experimental upper bound on the unmodulated component of the signal and – as a matter of fact – as an experimental lower bound on the estimate of the background levels by the maximum likelihood procedure. Thus, the C.L.'s, we quote for allowed regions, already account for compatibility with the measured differential energy spectrum and with the measured upper bound on recoils. In particular, in the following for simplicity, the results of these corollary quests for the candidate particle are presented in terms of allowed regions obtained as superposition of the configurations corresponding to likelihood function

values *distant* more than 4σ from the null hypothesis (absence of modulation) in each of the several (but still a limited number) of the possible model frameworks considered here. Obviously, these results are not exhaustive of the many scenarios possible at present level of knowledge (e.g. for some other recent ideas see [19, 23, 31]) and larger sensitivities than those reported in the following would be reached when including the effect of other existing uncertainties on assumptions and related parameters [2].

In the most general scenario – to which the DAMA/NaI target nuclei are fully sensitive – both the SI and the SD components of the cross section are present. In this general scenario the data give an allowed volume in the 4-dimensional space (m_W, $\xi\sigma_{SI}$, $\xi\sigma_{SD}$, θ). Fig. 6 just shows slices of this

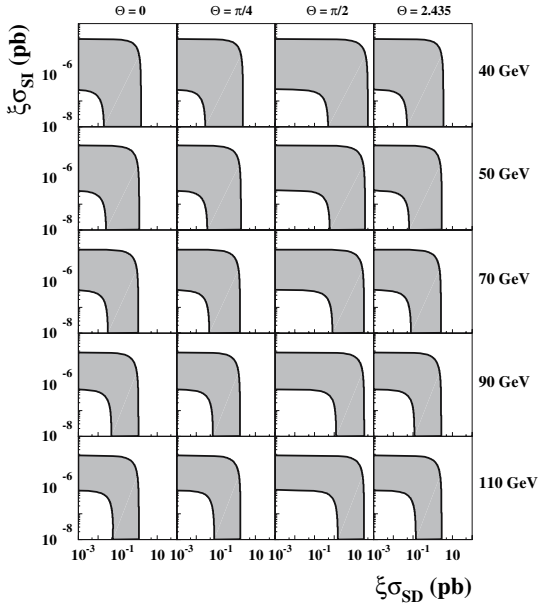

Fig. 6. *Case of a Dark Matter particle with mixed SI&SD interaction in the given model frameworks.* Coloured areas: example of slices (of the 4-dimensional allowed volume) in the plane $\xi\sigma_{SI}$ vs $\xi\sigma_{SD}$ for some of the possible m_W and θ values. Four SD couplings are reported as examples: i) $\theta = 0$ (a_n =0 and $a_p \neq 0$ or $|a_p| >> |a_n|$) corresponding to a particle with null SD coupling to neutron; ii) $\theta = \pi/4$ ($a_p = a_n$) corresponding to a particle with the same SD coupling to neutron and proton; iii) $\theta = \pi/2$ ($a_n \neq 0$ and $a_p = 0$ or $|a_n| >> |a_p|$) corresponding to a particle with null SD couplings to proton; iv) $\theta = 2.435$ rad ($\frac{a_n}{a_p}$ = -0.85) corresponding to a particle with SD coupling through Z_0 exchange. The case $a_p = -a_n$ is nearly similar to the case iv). Inclusion of other existing uncertainties on parameters and models would further extend the regions; for example, the use of more favourable form factors and/or of more favourable spin factors than the considered ones would move them towards lower cross sections.

4-dimensional allowed volume in the plane $\xi\sigma_{SI}$ vs $\xi\sigma_{SD}$ for some of the possible θ and m_W values in the considered model frameworks. We just note that experiments using either even-spin target nuclei (as Ar and most of Ge, Xe, Te isotopes) or odd-spin Ge, Xe or Te isotopes cannot explore most of the allowed volume. From the given figures it is clear that at present either a purely SI or a purely SD or mixed SI&SD configurations are compatible with the experimental data of the seven annual cycles.

Often the purely SI interaction with ordinary matter is assumed to be dominant since e.g. most of the used target-nuclei are practically not sensitive to SD interactions (on the contrary of ^{23}Na and ^{127}I) and the theoretical calculations and comparisons are even much more complex and uncertain. Therefore, following the analogous procedure as for the general case, we have exploited for the same model frameworks the purely SI scenario, obtaining the allowed region in the plane m_W and $\xi\sigma_{SI}$ shown in Fig. 7 – *left*. Of course,

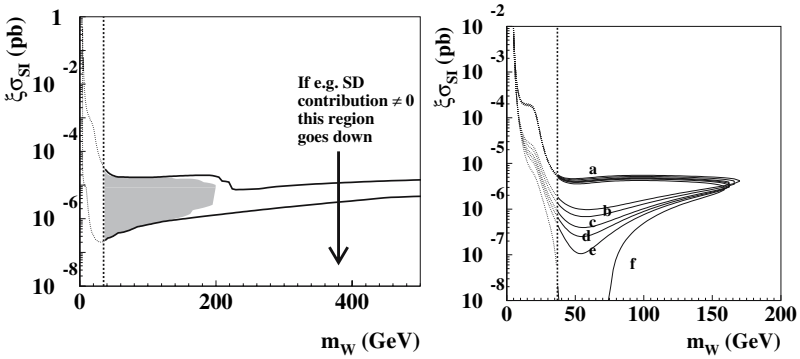

Fig. 7. *On the left : Case of a Dark Matter particle with dominant SI interaction for the given model frameworks.* Region allowed in the plane (m_W, $\xi\sigma_{SI}$). The vertical dotted line represents a bound in case of a neutralino candidate when supersymmetric schemes based on GUT assumptions are adopted to analyse the LEP data; the low mass region is allowed for neutralino when other schemes are considered and for every other Dark Matter candidate; see text. While the area at masses above 200 GeV is allowed only for few configurations, the lower one is allowed by most configurations (the coloured region gathers only those above the vertical line) [2]. The inclusion of other existing uncertainties on parameters and models would further extend the region; for example, the use of more favourable SI form factor for Iodine alone would move it towards lower cross sections. *On the right : Example of the effect induced by the inclusion of a SD component different from zero on allowed regions given in the plane $\xi\sigma_{SI}$ vs m_W.* In this example the Evans' logarithmic axisymmetric $C2$ halo model with $v_0 = 170$ km/s, ρ_0 equal to the maximum value for this model and a given set of the parameters' values (see [2]) have been considered. The different regions refer to different SD contributions for the particular case of $\theta = 0$: $\sigma_{SD} = 0$ pb (a), 0.02 pb (b), 0.04 pb (c), 0.05 pb (d), 0.06 pb (e), 0.08 pb (f). Analogous situation is found for the other model frameworks.

best fit values of cross section and candidate mass span over a large range in the considered model frameworks.

Moreover, configurations with $\xi\sigma_{SI}$ even much lower than those shown in Fig. 7 – *left* are accessible in case an even small SD contribution is present in the interaction as shown as in an example in Fig. 7–*right*. Analogous situation is found for other model frameworks. A comparison of the DAMA/NaI purely SI allowed region (given in Fig. 7–*left*) with the theoretical expectations for a purely SI coupled neutralino candidate in a MSSM with gaugino mass unification at GUT scale released is shown in Fig. 8; it has been taken from [32].

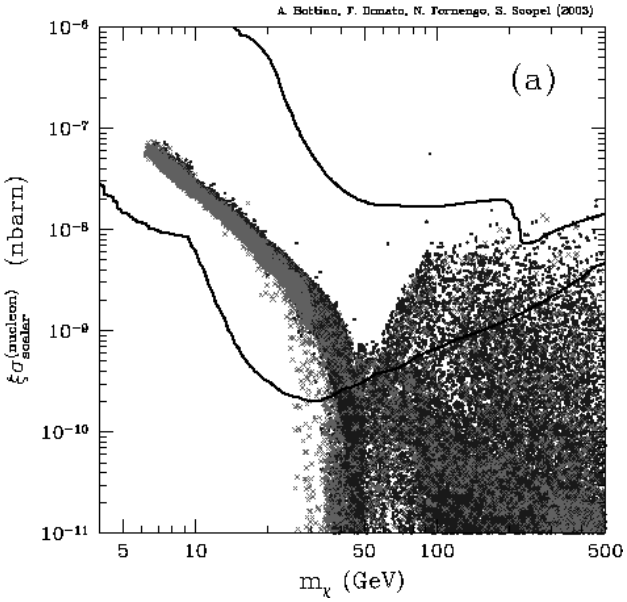

Fig. 8. Figure taken from [32]: theoretical expectations of $\xi\sigma_{SI}$ versus m_W in the purely SI coupling for the particular case of a neutralino candidate in MSSM with gaugino mass unification at GUT scale released; the curve surrounds the DAMA/NaI purely SI allowed region as in Fig. 7-left.

Analogously, one can consider the pure SD coupling. In this scenario one obtain an allowed volume in the 3-dimensional space (m_W, $\xi\sigma_{SD}$, θ). Just examples of some slices of this allowed volume at given θ is shown in Fig. 9. Considerations similar to the first case hold.

Finally, also the inelastic Dark Matter particle scenario has been analysed obtaining an allowed volume in the 3-dimensional space ($\xi\sigma_p$, m_W, δ). For simplicity, Fig. 10 shows just few slices of such an allowed volume at some given masses.

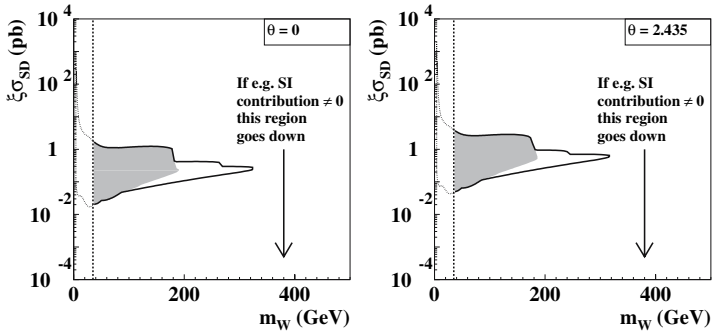

Fig. 9. *Case of a Dark Matter particle with dominant SD interaction in the given model frameworks.* Examples of slices (of the 3-dimensional allowed volume) in the plane (m_W, $\xi\sigma_{SD}$) with $\theta = 0$ and $\theta = 2.435$ (Z_0 coupling). For the definition of the vertical line and of the coloured area see previous figure caption. Inclusion of other existing uncertainties on parameters and models would further extend the SD allowed regions. For example, the use of more favourable SD form factors and/or more favourable spin factors would move them towards lower cross sections. Values of $\xi\sigma_{SD}$ lower than those corresponding to these allowed regions are possible also e.g. in case of an even small SI contribution.

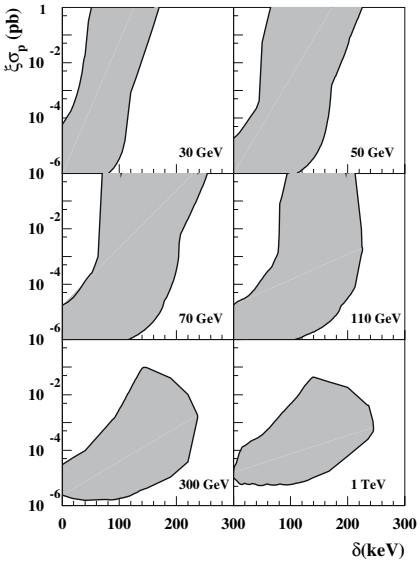

Fig. 10. *Case of a Dark Matter particle with* preferred inelastic *interaction in the given model frameworks.* Examples of slices (coloured areas) of the allowed volumes ($\xi\sigma_p$, δ, m_W) for some m_W values for a Dark Matter particle with *preferred inelastic* interaction. Inclusion of other existing uncertainties on parameters and models would further extend the regions; for example, the use of a more favourable SI form factor for Iodine and different escape velocity would move them towards lower cross sections [2].

We remind that in these calculations v_{esc} has been assumed at fixed value (as in the previous cases), while its present uncertainties can play a significant role in this scenario of Dark Matter particle with *preferred inelastic* scattering.

4 Comparison With Other Direct and Indirect Detection Experiments

As already mentioned, no other experiment, whose result can be directly compared in a model independent way with that of DAMA/NaI, is available so far in the field of Dark Matter detection.

As regards the *direct detection method*, most of the activities, started in the 90's, are still at R&D stage and/or have released marginal exposures with the respect to the many years of existence and to the several used detectors. This is the case of CDMS and EDELWEISS experiments, while the Zeplin experiment is more recent [33, 34, 35]. Since these experiments have claimed to have "excluded" DAMA/NaI, we will briefly point to the attention of the reader only few arguments. In particular, Table 2 summarizes some items for comparison.

Firstly, let us preliminarily assume as fully correct the "selected" number of events, the energy threshold, the energy scale, etc. quoted by those experiments (see Table 2) and let us consider if – at least under this hypothesis – their claims might be justified. The answer is obviously not; in fact: i) they give a single model dependent result using ^{nat}Ge or ^{nat}Xe target, while DAMA/NaI gives a model independent result using ^{23}Na and ^{127}I targets; ii) in the single (of the many possible) model scenario, they consider, they "fix" all the astrophysical, nuclear and particle physics assumptions at a single choice; the same is even for the the experimental and theoretical parameters values needed in the calculations. In addition, DAMA/NaI is generally quoted there in an uncorrect, partial and unupdated way and existing scenarios to which DAMA/NaI is fully sensitive – on the contrary of the others – are ignored.

Let us now briefly comment also some of the experimental aspects. In particular, the counting rate of the Ge bolometers experiments is very high and few/zero events are claimed after applying several strong and hardly safe rejection procedures (involving several orders of magnitude). They usually claim to have an "event by event" discrimination between *noise + electromagnetic background* and *recoil + recoil-like (neutrons, end-range alphas, fission fragments,...)* events by comparing the bolometer and the ionizing signals for each event, but their results are, actually, largely based on "a priori" huge data selections and on the application of other preliminar rejection procedures (such as e.g. the one on the so-called surface electrons), which are generally poorly described and often not completely quantified. Moreover, most efficiencies and physical quantities entering in the interpretation of the claimed

Table 2. Features of the DAMA/NaI results on the Dark Matter particle annual modulation signature over the seven annual cycles [2] with those of [33, 34, 35].

	DAMA/NaI	CDMS-II	Edelweiss-I	Zeplin-I
Signature	Annual modulation	None	None	None
Target-nuclei	^{23}Na, ^{127}I	^{nat}Ge	^{nat}Ge	^{nat}Xe
Technique	well known	poorly experienced	poorly experienced	critical optical liquid/gas interface in this realization
Target mass	$\simeq 100$ kg	0.75 kg	0.32 kg	$\simeq 3$ kg
Exposure	$\simeq (1.1 \cdot 10^5)$ kg $\cdot$ day	19.4 kg $\cdot$ day	30.5 kg $\cdot$ day	280 kg $\cdot$ day
Depth of the experimental site	1400 m	780 m	1700 m	1100 m
Software energy threshold	2 KeV e.e. (5.5–7.5 p.e./keV)	10 KeV e.e.	20 KeV e.e.	2 KeV e.e. (but: $\sigma/E = 100\%$ mostly 1 p.e./keV; [35]) (2.5 p.e./keV for 16 days; [36])
Quenching factor	Measured	Assumed = 1	Assumed = 1 (see also [37])	Measured
Measured event rate in low energy range	$\simeq 1$ cpd/kg/keV	??, claimed γ's larger than CDMS-I ($\simeq 60$ cpd/kg/keV, 10^5 events)	$\simeq 10^4$ events total	$\simeq 100$ cpd/kg/keV
Claimed events after rejection procedures		either 0 or 1	2 (claimed taken in a noisy period)	$\simeq$ 20–50 cpd/kg/keV after rejection and ?? after standard PSD [35, 36]
Events satisfying the signature in DAMA/NaI	modulation amplitude integrated over the given exposure $\simeq 10^3$ events	insensitive	insensitive	insensitive
Expected number of events from DAMA/NaI effect		from few down to zero depending on the models (and on quenching factor)	from few down to zero depending on the models (and on quenching factor)	depends on the models (even zero)

selected events have never been properly accounted; as an example, we mention the case of the bolometer quenching factor of the recoil target nuclei. In fact, for the bolometer signals the quenching factor (on which the energy threshold and the energy scale rely and, hence, also the claimed sensitivity for the given model dependent exclusion plots) is arbitrarily assumed to be exactly equal to one. Up to now, only one measurement has been made available for a given detector [37]; it offers the value: $0.87 \pm 10\%(stat.) \pm 10\%(syst.)$, which is – within the error – compatible with one, but – at the same time – also compatible with much smaller values. Thus, any bolometer result, obtained without considering e.g. the uncertainties about the unknown value of the quenching factor and, hence, about the energy threshold and energy scale, has to be considered partial and arbitrary. For completeness we also mention that the reproducibility of the results over different running periods has not been proved as well as the values of the effective sensitive volumes for the read-outs of the two signals for each event and related quantities; obviously, further uncertainties are present when, as done in some cases, a neutron background modeling and subtraction is pursued in addition.

As regards Zeplin-I [35, 36], a very low energy threshold is claimed (2 KeV), although the light response is very poor: between $\simeq$ 1 ph.e./keV [35] (for most of the time) and $\simeq$ 2.5 ph.e./keV (claimed for 16 days) [36] [1]. Moreover, a strong data filtering is applied to the high level of measured counting rate (see Table 2) by hardware vetoes, by fiducial volume cuts and, largely, by applying down to few keV a standard pulse shape discrimination procedure, although the LXe scintillation pulse profiles (pulse decay time $<$ 30 ns) are quite similar to the PMT noise events in the lower energy bins and in spite of the poor light response. Quantitative information on experimental quantities related to the used procedures has not yet been given [35, 36].

In conclusion, those claims for contradiction have intrinsecally no scientific bases.

As regards the *indirect detection method*, some positive hints have been given: in fact, an excess of positrons and of gamma's in the space has been reported with the respect to a modelled background; they are not in contradiction with the DAMA/NaI result. Moreover, recently, it has been suggested [38] that these positive hints and the effect observed by DAMA/NaI can also be described in a scenario with multi-component Dark Matter in the galactic halo, made of a subdominant component of heavy neutrinos of the 4th family and of a sterile dominant component. In particular (see Fig. 11), it has been shown that an heavy neutrino with mass around 50 GeV can account for all the observations, while the inclusion of possible clumpiness of neutrino density as well as new interactions in the heavy neutrino annihilation, etc. can

[1] For comparison we remind that the data of the DAMA/LXe set-up, which has a similar light response, are analysed by using the much more realistic and safer software energy threshold of 13 KeV [15].

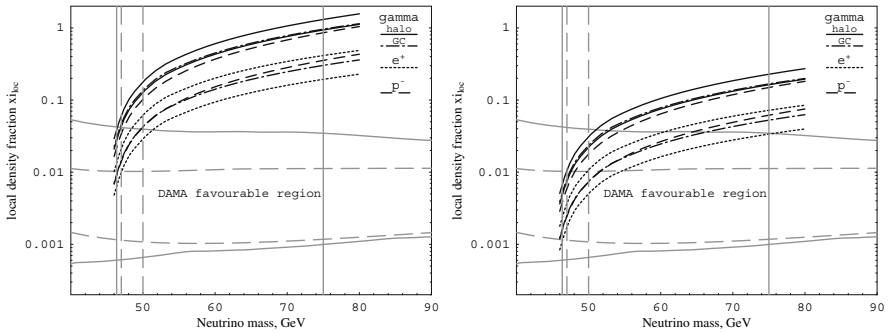

Fig. 11. Figures taken from [38]: case of a subdominant heavy 4th neutrino candidate in the plane local density fraction versus the heavy neutrino mass. The favourable region for this candidate obtained from the DAMA/NaI data (grey dashed line when using the Evan's halo model; solid line when using the other halo models) and the best-fit density parameters deduced from cosmic gamma-radiation (from halo and galactic center), positron and antiproton analysis are shown (left panel). The effect of the inclusion of possible neutrino clumpiness is also reported (right panel). See [38] for details.

lead to wider mass ranges: from about 46 up to about 75 GeV (see [38] for details).

5 Conclusions and Perspectives

DAMA/NaI has been a pioneer experiment investigating as first the Dark Matter particle annual modulation signature with suitable sensitivity and control of the running parameters. During seven independent experiments of one year each one, it has pointed out at 6.3 σ C.L. the presence of a modulation satisfying all the many peculiarities of a WIMP induced effect. Neither systematic effects nor side reactions able to account for the observed modulation amplitude and to contemporaneously satify all the requirements of the signature have been found. DAMA/NaI has also pointed out the complexity of corollary investigations on the nature of the candidate particle, because of the present poor knowledge on the many astrophysical, nuclear and particle physics aspects.

Presently after devoted R&D efforts, the second generation DAMA/LIBRA (a $\simeq$250 kg more radiopure NaI(Tl) set-up) has been realised and put in operation since March 2003. The main features and perspectives of the DAMA/LIBRA set-up are summarized in the Cerulli's paper in these Proceedings. Moreover, a third generation R&D towards the possible 1 ton ultimate radiopure NaI(Tl) set-up, we proposed in 1996, is already in progress.

References

1. R. Bernabei et al., *Nuovo Cimento* A **112** (1999) 545.
2. R. Bernabei et al., La Rivista del Nuovo Cimento **26** n.1, 1-73 (2003) (astro-ph/0307403) and references therein; R. Bernabei et al, to appear on Int. J. Mod. Phys. D (December 2004).
3. R. Bernabei et al., *Phys. Lett.* B **389** (1996) 757.
4. R. Bernabei et al., Nuovo Cimento A **112** (1999) 1541.
5. R. Bernabei et al., Phys. Lett. B **408** (1997) 439; P. Belli et al., Phys. Lett. B **460** (1999) 236. R. Bernabei et al., *Phys. Rev. Lett.* **83** (1999) 4918; P. Belli et al., *Phys. Rev.* C **60** (1999) 065501; R. Bernabei et al., *Phys. Lett.* B **515** (2001) 6; F. Cappella et al., *Eur. Phys. J. direct* C **14** (2002) 1; R. Bernabei et al., Eur. Phys. J. A **23** (2005) 7; R. Bernabei et al., ROM2F/2004/30, submitted for publication.
6. R. Bernabei et al., *Phys. Lett.* B **424** (1998) 195.
7. R. Bernabei et al., *Phys. Lett.* B **450** (1999) 448.
8. P. Belli et al., *Phys. Rev.* D **61** (2000) 023512.
9. R. Bernabei et al., *Phys. Lett.* B **480** (2000) 23.
10. R. Bernabei et al., *Eur. Phys. J.* C **18** (2000) 283.
11. R. Bernabei et al., *Phys. Lett.* B **509** (2001) 197.
12. R. Bernabei el al., *Eur. Phys. J.* C **23** (2002) 61.
13. P. Belli et al., *Phys. Rev.* D **66** (2002) 043503.
14. P. Belli et al., *Nuovo Cimento* A **103** (1990) 767; P. Belli et al., *Nuovo Cimento* C **19** (1996) 537; P. Belli et al., *Astrop. Phys.* **5** (1996) 217; P. Belli et al., *Phys. Lett.* B **387** (1996) 222 and *Phys. Lett.* B **389** (1996) 783 (err.); P. Belli et al., *Phys. Lett.* B **465** (1999) 315; R. Bernabei et al., *Phys. Lett.* B **493** (2000) 12; R. Bernabei et al., *New Journal of Physics* **2** (2000) 15.1; P. Belli et al., *Phys. Rev.* D **61** (2000) 117301; R. Bernabei et al., *Eur. Phys. J. direct* C **11** (2001) 1; R. Bernabei et al., *Nucl. Instr. & Methods* A **482** (2002) 728; R. Bernabei et al., *Phys. Lett.* B **527** (2002) 182; R. Bernabei et al., *Phys. Lett.* B **546** (2002) 23; in "Beyond the Desert 03", Springer (2004) 541.
15. R. Bernabei et al., Phys. Lett. B **436** (1998) 379.
16. R. Bernabei et al., *Astrop. Phys.* **7** (1997) 73; R. Bernabei et al., *Nuovo Cimento* A **110** (1997) 189; P. Belli et al., *Nucl. Phys.* B **563** (1999) 97; P. Belli et al., *Astrop. Phys.* **10** (1999) 115; R. Bernabei et al., *Nucl. Phys.* A **705** (2002) 29; P. Belli et al., *Nucl. Instr. & Methods* A **498** (2003) 352; R. Cerulli et al., *Nucl. Instr. & Methods* A **525** (2004) 535.
17. K.A. Drukier et al., *Phys. Rev.* D **33** (1986) 3495, K. Freese et al.,*Phys. Rev.* D **37** (1988) 3388.
18. D. Smith and N. Weiner, *Phys. Rev.* D **64** (2001) 043502.
19. K. Freese et. al. astro-ph/0309279; Phys. Rev. Lett. 92 (2004) 11301
20. M. Wojcik, Nucl. Instrum. & Methods B61 (1991) 8
21. W.H. Press and G.B. Rybicki, Astrophys. J. 338 (1989) 277; J.D. Scargle, Astrophys. J. 263 (1982) 835
22. M. Ambrosio et al., *Astrop. Phys.* **7** (109) 1997
23. G. Prezeau et al., Phys. Rev. Lett. 91 (2003) 231301
24. A. Bottino et al., Phys. Lett. B402 (1997) 113
25. W. Dehnen and J. Binney, Mon. Not. R. Astron. Soc. 294 (1998) 429
26. E.I. Gates, G. Gyuk, M.S. Turner, Phys. Rev. D53 (1996) 4138

27. D.E. Groom et al., Eur. Phys. J. C 15 (2000) 1
28. A. Bottino et al., *Phys. Rev.* D **67** (063519) 2003, hep-ph/0304080
29. D. Hooper and T. Plehn,MADPH-02-1308,CERN-TH/2002-29, hep-ph/0212226
30. G. Bélanger, F. Boudjema., A. Pukhov and S. Rosier-Lees, hep-ph/0212227
31. F.S. Ling, P. Sikivie, S. Wick, astro-ph/0405231
32. A. Bottino et al., *Phys. Rev.* D **69** (037302) 2004
33. CDMS collaboration, astro-ph/0405033; *Phys. Rev. Lett.* **84** (2000) 5699
34. EDELWEISS coll., in the Proc. of NDM03, Japan (2003); *Phys. Lett.* B **513** (2001) 15
35. N. Smith, talk given at IDM02, York, september 2002
36. R. Luscher , talk given at Moriond, march 2003
37. E. Simon et al., Nucl. Instrum. & Meth. A507 (2003) 643
38. K. Belotsky et al., hep-ph/0411093

DAMA/LIBRA and Beyond

R. Bernabei[1], P. Belli[1], F. Cappella[1], F. Montecchia[1+], F. Nozzoli[1], A. d'Angelo[2 ++], A. Incicchitti[2], D. Prosperi[2], R. Cerulli[3], C.J. Dai[4], H.H. Kuang[4], J.M. Ma[4] and Z.P. Ye[4 +++]

[1]Dipartimento di Fisica, Università di Roma "Tor Vergata" and INFN, Sezione di Roma2, I-00133 Rome, Italy
[2]Dipartimento di Fisica, Università di Roma "La Sapienza" and INFN, Sezione di Roma, I-00185 Rome, Italy
[3]INFN – Laboratori Nazionali del Gran Sasso, I-67010 Assergi (Aq), Italy
[4]IHEP, Chinese Academy, P.O. Box 918/3, Beijing 100039, China
[+]also: Università "Campus Bio-Medico" di Roma, 00155, Rome, Italy
[++]also: Scuola di Specializzazione in Fisica Sanitaria, Università di Roma "Tor Vergata", 00133, Rome, Italy
[+++]also: University of Zhao Qing, Guang Dong, China

As a result of about five years of new devoted R&D projects, the second generation DAMA/LIBRA (Large sodium Iodide Bulk for RAre processes) set-up of the DAMA experiment has been realised in the Gran Sasso National Laboratory of the I.N.F.N.. It is made of $\simeq 250$ kg highly radiopure NaI(Tl) detectors and is operative since March 2003. It works as an observatory for rare processes and is mainly devoted to a further investigation on the Dark Matter particle component in the galactic halo. A third generation R&D towards a possible NaI(Tl) ton set-up, we proposed in 1996, has been funded and started in 2003.

1 The new DAMA/LIBRA set-up

In the framework of the DAMA project [1], the $\simeq$100 kg NaI(Tl) set-up (DAMA/NaI) took data over seven annual cycles (107731 kg $\cdot$ d total exposure) [1] obtaining a model independent result on the presence of a Dark Matter particle component in the galactic halo. In these Proceedings P. Belli summarised the main result as well as also some of the many possible corollary model dependent interpretations. The set-up completed its data taking in July 2002. This highly radiopure NaI(Tl) set-up was the highest radiopure set-up available in the field, effectively pursued a model independent approach to investigate Dark Matter particles in the galactic halo collecting an exposure several orders of magnitude larger than those available in the field and obtained many other complementary or by-products results.

In 1996 DAMA proposed a ton set-up [2] and a second generation R&D project for highly radiopure NaI(Tl) detectors was funded at that time and carried out for several years, in collaboration with Crismatec-St.Gobain com-

pany, in order to realise, as an intermediate step, the second generation experiment successor of DAMA/NaI, with an exposed mass of about 250 kg.

In this framework new powders and other materials were selected, new chemical/physical radiopurification procedures of the NaI and TlI powders were exploited, new growing/handling protocols were developed and new prototypes were built and tested. This allowed – among others – to obtain NaI powders with ^{238}U residual contaminations about 30 times lower than those used in the past to build the radiopure DAMA/NaI detectors [3]. As a consequence of the results of this second generation R&D, the new experimental set-up DAMA/LIBRA (Large sodium Iodide Bulk for RAre processes) with $\simeq$250 kg (matrix of twenty-five $\simeq$ 9.70 kg NaI(Tl) crystals) highly radiopure NaI(Tl) crystal scintillators was realised.

In the realization of DAMA/LIBRA many materials of the set-up and of the installation were further selected and new operative protocols were defined also for all the handling and installing procedures. The production of detectors and of new parts of the installation ended in 2002 and, after the completion of the DAMA/NaI data taking in July 2002, the procedures needed to install the new set-up started. DAMA/LIBRA is taking data since March 2003 and the first data release will, most probably, occur when an exposure larger than that of DAMA/NaI will have been collected and analysed in all the aspects.

All the procedures performed during the dismounting of DAMA/NaI and the installation of DAMA/LIBRA detectors (see Fig. 1 and 2) were carried out in HP Nitrogen atmosphere by using a Scuba system (a self-contained underwater breathing apparatus) modified in order to avoid that the entire breath is expelled into the surrounding air when the operator exhales. The air cylinders were kept five meters away and the output line was two meters long.

As mentioned, the experimental site as well as many components of the installation itself have been implemented (environment, shield of PMTs, wiring, HP Nitrogen system, cooling water of air conditioner, electronics and DAQ, etc...). In particular, before the installation, all the Cu parts have been chemically etched following a new devoted protocol and maintained in HP Nitrogen atmosphere until installation.

Each crystal is enclosed in a suitable radiopure Cu housing; it has two 10 cm long UV low-radioactive quartz light guides directly coupled to the opposite sides of the bare crystal. Two low background photomultipliers work in coincidence at single photoelectron level and are fully surrounded by a new shaped low background Cu shield for PMTs. The detectors are enclosed in a low radioactive copper box inside a low radioactive shield made by 10 cm copper and 15 cm lead. The lead is surrounded by 1.5 mm Cd foils and about 10/40 cm of polyethylene/paraffin; moreover, the installation is almost completely surrounded by about 1 m of concrete – made of the Gran Sasso rock – acting as a further neutron moderator. The passive shield is also enclosed in a

Fig. 1. Left: the installation of the 25 NaI(Tl) crystals (9.70 kg each one) of DAMA/LIBRA in HP Nitrogen atmosphere. Right: One of the final stages of the detectors' installation. Bottom: Picture of the photomultiplier shield made of highly radio-pure Copper. All the used materials have been deeply selected for radiopurity (see for example the cables with teflon envelop). All the procedures as well as these photos have been carried out in HP Nitrogen atmosphere.

Fig. 2. Left: During the chemical etching of the metallic surfaces in clean room. Particular dedicated protocols have been defined and followed; after the etching the materials have been sealed in HP Nitrogen atmosphere Right: Partial view of DAMA/LIBRA set-up.

sealed plexiglas box. As previously in DAMA/NaI, the Cu box, the plexiglas box and the glove-box (which is located on the top of the shield to allow the detectors calibration in the same running conditions without any contact with external environment) are maintained in high purity (HP) Nitrogen atmosphere. The installation is subjected to air conditioning.

Figure 3 summarizes the analogic schema of the DAMA/LIBRA electronic chain and the *single trigger* referred to a single detector, the main trigger of the acquisition system and the trigger system of the Waveform Analysers (WA) in DAMA/LIBRA. The HV power supply for the PMTs is given by a CAEN multichannel voltage supply with voltage stability of 0.1%. The signal from each PMT is amplified by a preamplifier having 0-250 MHz bandwidth, a factor 10 gain and a voltage integral linearity ±0.2%. In particular, the signal from one PMT is divided in two branches: 19/20 of the signal is sent to the

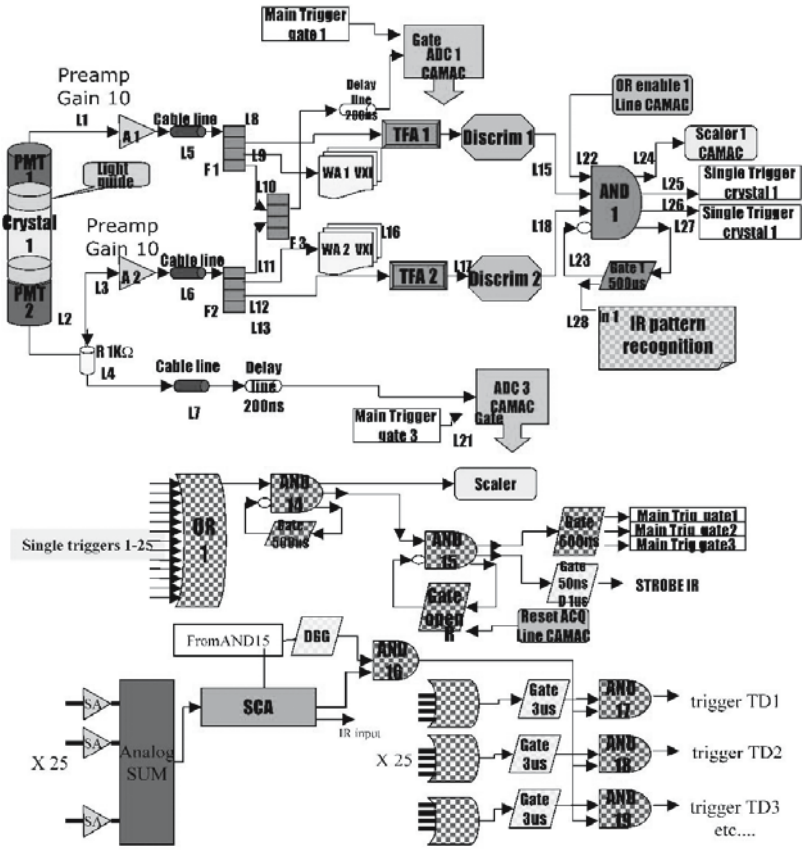

Fig. 3. Top: Schema of the electronic chain referred to a single detector and its trigger. Down: the schema of the main trigger of DAQ and of the trigger of the Waveform Analysers.

input of the preamplifier, while the remaining 1/20 – suitably delayed – feeds a charge ADC channel. This last part processes the pulses with amplitude such to saturate the remaining part of the electronics (they correspond to high energy events). The preamplified signals of each PMT – through linear Fan-in/Fan-out devices – are recorded through a channel of a Waveform Analyser (which processes the signal in a 2 μs time window). In particular, this is accomplished using fast VXI Tektronix four-channel TVS641A digitizers with a sampling frequency of 1 GSample/s and 250 MHz bandwidth. In addition, the sum pulses of the two PMTs are sent to the inputs for the charge ADCs.

The electronic devices, that provide the trigger of a single detector, are also shown in Fig. 3. In particular, the copies of the PMT signals are the inputs of Timing Filter Amplifiers which amplify and integrate the signal (integration time 50 ns); their outputs are discriminated with single photo-electron trigger level. The coincidence between the two logical NIM outputs provides the trigger of each detector. A particular circuit allows: (i) to reject afterglows and Bi-Po events in a 500μs time window after the occurrence of the event (introducing a negligible systematic error on the measured rate); (ii) to enable the detector in the main trigger by a CAMAC I/O Register during the calibrations. The outputs of the coincidence devices provide: (i) the signal for a CAMAC scaler to count the events for each detector; (ii) the lines used in the main trigger (see later); (iii) the line giving the start to a Gate Generator which – in addition to the veto of the coincidence – gives the signal issued to a 16-bit CAMAC I/R Pattern Recognition allowing to identify the detector or the detectors which have generated the trigger.

The *main trigger* of the acquisition – see Fig. 3 – is provided by the logic *OR* of all the crystals. The main trigger pulses are counted by a Scaler, while devoted devices allow to manage the trigger only when the acquisition is ready. Thus, the dead time of the acquisition is properly accounted in the estimate of the running time by using the information from the Scaler. When a general trigger occurs, the following logic signals are issued to: i) a Gate Generator generating the 600 ns gates for the charge ADCs; ii) the Delay Gate Generator which gives the strobe signal to the I/R Pattern Recognition and generates the LAM (and, therefore, the interrupt to the CPU of the acquisition computer) in the CAMAC system; iii) the Delay Gate Generator which gives the signal to the trigger of the Waveform Analyzers. This last condition is verified only if the total energy deposited in the detectors is in an energy window suitably chosen. For this purpose, each line feds a Spectroscopy Amplifier whose gain is equalized in order to have the same response for each detector. Thus, a Single Channel Analyzer made by the two discriminators allows to select only events in the chosen energy window.

A devoted electronic circuit, shown in Fig. 3, allows to trigger only the Waveform Analysers which correspond to fired detectors; it gives a trigger to each Waveform Analysers when: (i) at least one of its corresponding lines has a trigger; (ii) the *main trigger* is present; (iii) the total energy of the

events is in the chosen energy window. Let us remind that for the events with energy outside this energy window the ADC values are acquired. Therefore, although the set-up is optimized for low energy, the high energy events up to MeV region are acquired too.

The data acquisition system is made of a Workstation by Compaq with Linux SuSe operative system, which is interfaced with the hardware system through MXI-2 and GPIB buses. The GPIB bus allows to communicate with the CAMAC crate housing the ADCs, the scalers and the I/O registers, while the MXI-2 bus allows to communicate with the three VXI mainframes, where the Waveform Analysers are installed.

As previously for DAMA/NaI, an hardware/software system to continuosly monitor the running conditions is also operative; in particular, several probes are read out by the data acquisition system and stored with the production data. Moreover, self-controlled computer processes are operational to automatically control several parameters and to manage alarms.

Figure 4 shows the energy distribution of the ^{241}Am source as measured by one of the new DAMA/LIBRA detectors (σ/E = 6.7% at 59.5 KeV).

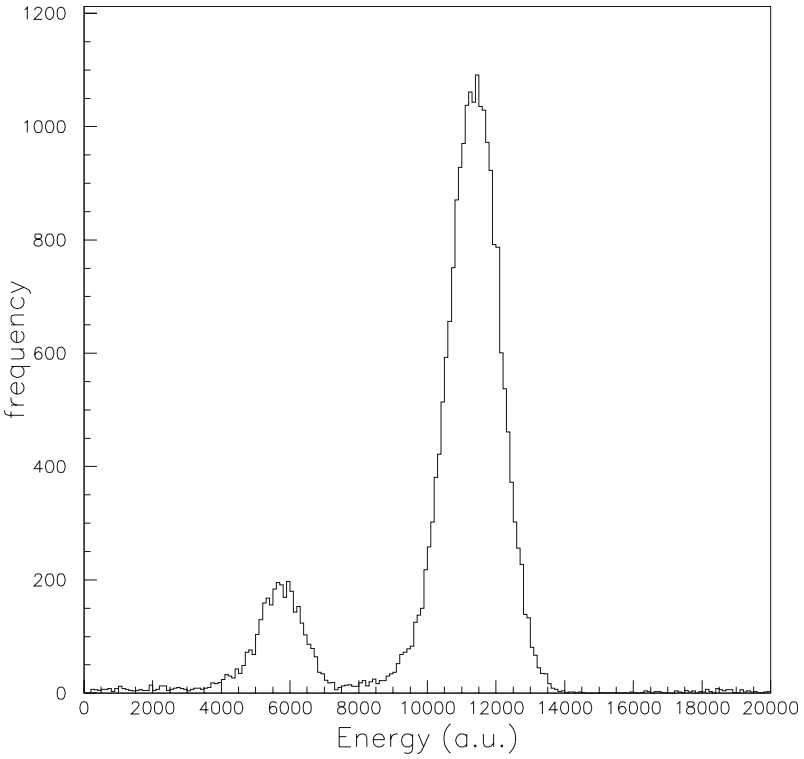

Fig. 4. Energy distribution of the ^{241}Am source as measured by one of the new highly radiopure DAMA/LIBRA NaI(Tl) detectors (σ/E = 6.7% at 59.5 KeV).

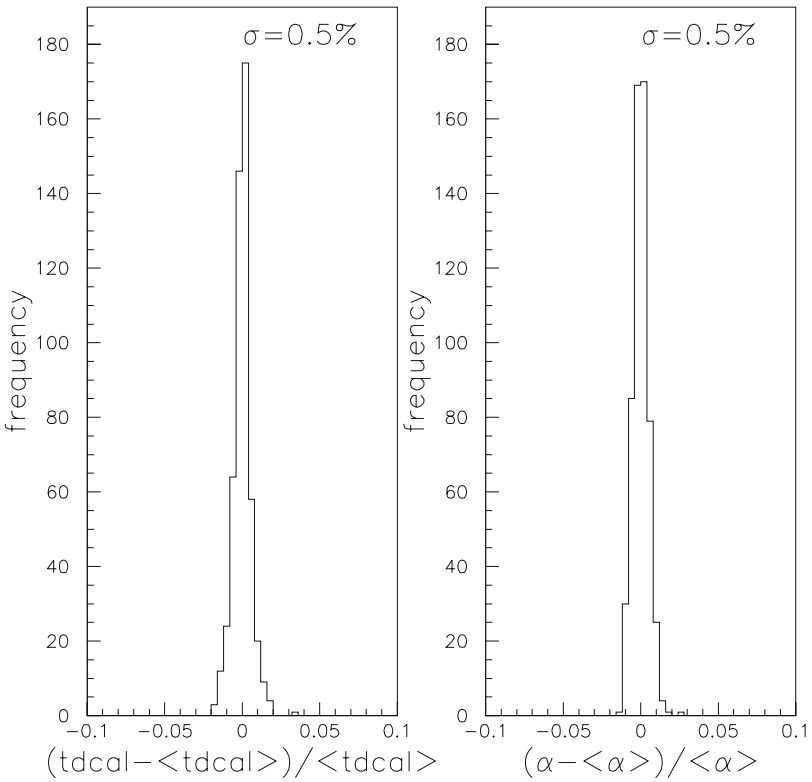

Fig. 5. An example of the stability of the calibration factor (*tdcal*) and of the ratio of the peaks' positions (α) of the measured energy distribution of the ^{241}Am source during about one year of data taking.

Just as an example of the quality of the data taking, Fig. 5 shows the stability of the calibration factor and of the ratio of the peaks' positions of the ^{241}Am source during about one year of data taking.

The highly radiopure DAMA/LIBRA set-up is a powerful tool for further investigation on the Dark Matter particle component in the galactic halo having all the intrinsic merits of the NaI(Tl) scintillator:

- well known technology;
- reachable high radiopurity by material selections and protocols, by chemical/physical purifications, etc.;
- large mass feasible;
- high duty cycle;
- well controlled operational conditions and monitoring feasible;
- routine calibrations feasible down to KeV range in the same conditions as the production runs;
- high light response, that is KeV threshold reachable;

- absence of the necessity of re-purification or cooling down/warming up procedures (implying high reproducibility, high stability, etc.);
- absence of microphonic noise and an effective noise rejection at threshold (time decay of NaI(Tl) pulses is hundreds ns, while that of noise pulses is tens ns);
- sensitivity to spin-independent (SI), spin-dependent (SD) and mixed (SI&SD) couplings as well as to several other existing scenarios;
- sensitivity to both high (by Iodine target) and low (by Na target) mass candidates;
- possibility to effectively investigate the annual modulation signature in all the needed aspects;
- pulse shape discrimination feasible at reasonable level;
- possibility to achieve significant results on several other rare processes;
- no safety problems;
- relatively small underground space necessary;
- the lowest cost with the respect to every other considered technique;
- etc.

Moreover, DAMA/LIBRA has a larger exposed mass, an higher overall radiopurity and improved performances with the respect to DAMA/NaI.

The main aim of DAMA/LIBRA is to further investigate the 6.3 σ C.L. model independent evidence for the presence of a dark matter component in the galactic halo pointed out by DAMA/NaI [1], reaching higher C.L.. Moreover DAMA/LIBRA will also offer an increased sensitivity to improve corollary quests on the nature of the candidate particle, trying to disentangle at least among some of the many different possible astrophysical, nuclear and particle physics models as well as to investigate other new possible scenarios; as an example, we remind here:

- *the effects induced on the Dark Matter particles distribution in the galactic halo by contributions from satellite galaxies tidal streams.* Recently it has been pointed out [4] that contributions to the Dark Matter particles in the galactic halo should be expected from tidal streams from the Sagittarius Dwarf elliptical galaxy. Considering that this galaxy was undiscovered until 1994 and considering galaxy formation theories, one has to expect that also other satellite galaxies do exist and contribute as well. In particular, the Canis Major satellite Galaxy has been pointed out as reported in 2003 in [5]; it can, in principle, play a very significant role being close to our galactic plane. At present, the best way to investigate the presence of a stream contribution is to determine more accurately the phase of the annual modulation, t_0, as a function of the energy; in fact, for a given halo model t_0 would be expected to be (slightly) different from 152.5 d and to vary with energy (see Fig. 6).
- *the effects induced on the Dark Matter particles distribution in the galactic halo by the existence of caustics.* It has been shown that the continuous

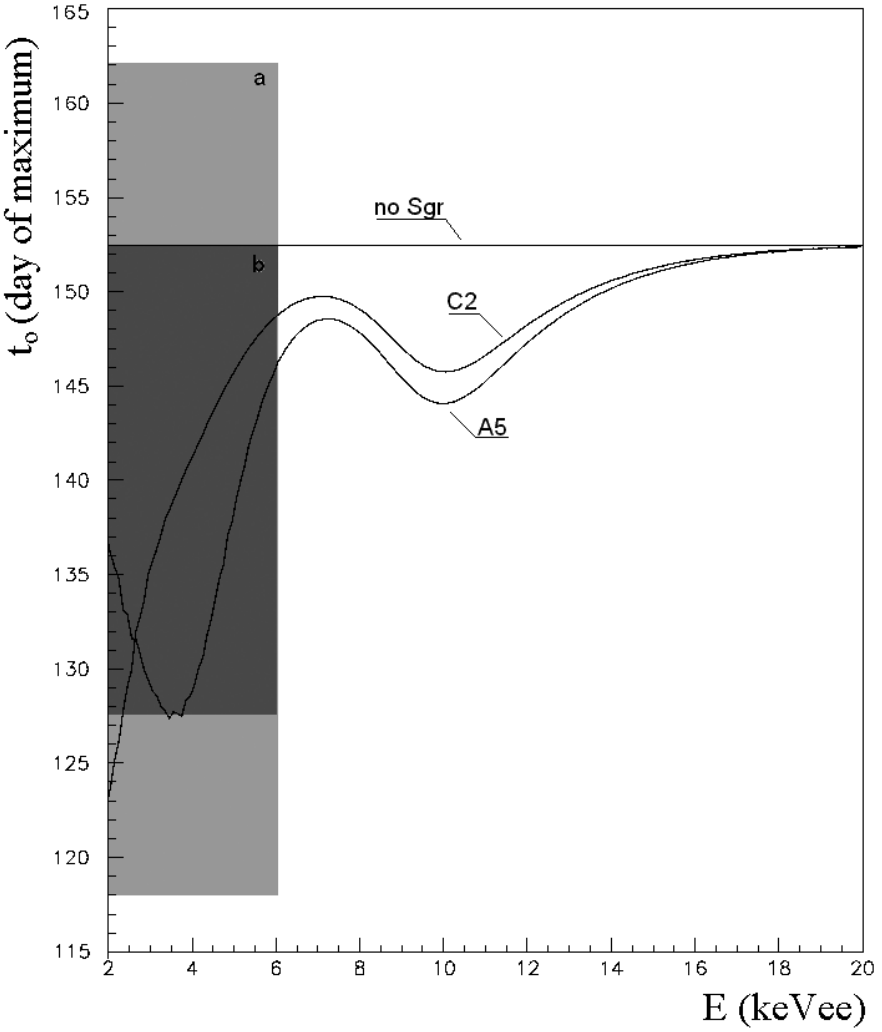

Fig. 6. Expected behaviours of the phase, t_0, of the annual modulation signal as function of the energy when considering: i) only galactic halo ("no Sgr"); ii) galactic halo ($C2$ halo model with $v_0 = 220\,\mathrm{km/s}$, ρ_0 equal to the maximum value for this model) and a contribution from Sagittarius Dwarf galaxy ("C2"); iii) galactic halo ($A5$ halo model with $v_0 = 220\,\mathrm{km/s}$, ρ_0 equal to the maximum value for this model) and a contribution from Sagittarius Dwarf galaxy ("A5"). The contributions from Sagittarius Dwarf galaxy have been taken in both cases with a density equal to 4% of ρ_0. The light shadow region is the final result of DAMA/NaI on the t_0 value for the cumulative energy interval (2–6) KeV, while the dark shadow region is the expectation on t_0 assuming an experiment with the same features as DAMA/NaI, an exposure of $3 \cdot 10^5\,\mathrm{kg} \cdot \mathrm{day}$ and the same central value for t_0.

infall of Dark Matter particles in the galactic gravitational field can form caustic surfaces and discrete streams in the Dark Matter particles halo [6]. The phenomenology to point out a similar scenario is analogous to that in the previous item.

– *the detection of possible "solar wakes"*. As an additional verification of the possible presence of contributions from streams of Dark Matter particles in our galactic halo, DAMA/LIBRA can investigate also the gravitational focusing effect of the Sun on the Dark Matter particle of a stream. In fact, one should expect two kinds of enhancements in the Dark Matter particles flow: one named "spike", which gives an enhancement of Dark Matter particle density along a line collinear with the direction of the incoming stream and of the Sun, and another, named "skirt", which gives a larger Dark Matter particle density on a surface of cone whose opening angle depends on the stream velocity.

Moreover, other interesting topics will be addressed by the highly radiopure DAMA/LIBRA, such as the study (i) on the velocity and spatial distribution of the Dark Matter particles in the galactic halo (for details see the discussions in [1, 7]); (ii) on possible structures as clumpiness with small scale size; (iii) on the coupling(s) of the Dark Matter particle with the ^{23}Na and ^{127}I target-nuclei; (iv) on the nature of the Dark Matter particles (for example, are they susy particles? mirror Dark Matter [8]? particles from multi-dimensional Kaluza-Klein like theories? ...); (v) on scaling laws and cross sections (recently, it has been pointed out [9] that, even for the neutralino candidate, the usually adopted scaling laws could not hold); etc.

A large work will be faced by DAMA/LIBRA, which is intrinsecally, in addition, the most sensitive experiment in the field of Dark Matter because of its radiopurity, exposed mass and high duty cycle. These qualities will also allow DAMA/LIBRA to further investigate with higher sensitivity several other rare processes.

Finally, at present a third generation R&D effort toward the possible NaI(Tl) ton set-up, we proposed in 1996 [2], has been funded and related works have already been started.

References

1. R. Bernabei et al., La Rivista del Nuovo Cimento **26** n.1, 1–73 (2003) (astro-ph/0307403) and references therein; R. Bernabei et al, to appear on Int. J. Mod. Phys. D (December 2004); see also P. Belli et al., in these Proceedings.
2. R. Bernabei et al., Astrop. Phys. **4**, 45 (1995); R. Bernabei, in "The identification of Dark Matter", World Sc. Pub., 574 (1997).
3. R. Bernabei et al., N. Cim. A **112**, 545 (1999).
4. K. Freese et. al. astro-ph/0309279; Phys. Rev. Lett. **92**, 11301 (2004).
5. R.A. Ibata et al., Mon. Not. Roy. Astr. Soc. **348**, 12 (2004).
6. F.S. Ling, P. Sikivie, S. Wick, astro-ph/0405231.

7. P. Belli et al., Phys. Rev. D **66**, 043503 (2002).
8. R. Foot, hep-ph/0308254.
9. G. Prezeau et al., Phys. Rev. Lett. **91**, 231301 (2003).

The GENIUS-Test-Facility and the HDMS Detector in GRAN SASSO

H.V. Klapdor-Kleingrothaus[1,3], I.V. Krivosheina[1,2]

[1] Max-Planck-Institut für Kernphysik, PO 10 39 80,
D-69029 Heidelberg, Germany
H.Klapdor@mpi-hd.mpg.de,
mpi-hd.mpg.de.non_acc
[2] Institute of Radiophysical Research, Nishnij Novgorod, Russia
Irina.Krivosheina@mpi-hd.mpg.de
[3] Spokesman of the GENIUS-TF and HDMS Collaborations

Summary. After the installation of **the first four naked** high purity Germanium detectors in liquid nitrogen in the GRAN SASSO Underground Laboratory in the **GENIUS-Test-Facility** (GENIUS-TF-I) on May 5, 2003, an improved setup **GENIUS-TF-II** with now **six** detectors (15 kg), has been installed on October 14, 2004. This is the only setup existing worldwide until now (April 2005) which applies this novel technique aiming at extreme background reduction in search for rare decays underground. The GENIUS-TF experiment, aims to search for the annual modulation of the Dark Matter signal. The **HDMS (Heidelberg Dark Matter Search experiment)** is the only experiment worldwide, operating *an enriched* ^{73}Ge *detector* and is looking for spin-dependent WIMP-neutron interactions. Results for the measurement Febr. 2001–July 2003 are presented. **They improve the best existing present limits for low WIMP masses.**

1 Introduction

The present status of cold dark matter search, of investigation of neutrinoless double beta decay and of low-energy solar neutrinos all require new techniques of *drastic* reduction of background in the experiments. For this purpose we proposed the GENIUS (GErmanium in liquid NItrogen Underground Setup) project in 1997 [2]. The idea is to operate "naked" Ge detectors in liquid nitrogen (as applied **routinely already for more than 20 years by the CANBERRA Company** for technical functions tests [1]), and thus, by removing all materials from the immediate vicinity of the Ge crystals, to reduce the background considerably with respect to conventionally operated detectors. The liquid nitrogen acts both as a cooling medium and as a shield against external radiactivity.

Monte Carlo simulations for the GENIUS project, and investigation of the *new physics potential* of the project **have been performed in great detail**, and have been published elsewhere [2, 3]. We were **the first** to show (in our HEIDELBERG low-level facility already **in 1997**) that such device can be used for spectroscopy [2].

A small scale version of GENIUS, the GENIUS-Test-Facility has the goal to confirm the claimed evidence for WIMP dark matter from the DAMA experiment[9]. A detailed description of the GENIUS-TF project is given in [5, 6]. In Sect. 2 we give a decription of GENIUS-TF-II. In Sect. 3 we discuss our recent results from the HDMS experiment operating an enriched ^{73}Ge detector and looking for spin-*dependent* WIMP-neutron interactions [11, 13].

2 The GENIUS-TF-II Setup

The first four naked detectors had been installed in liquid nitrogen on 5.05.2003 (see Fig. 1-upper part). This has been reported in Cern Courier and [6]. The data acquisition system we developed in 2002 for GENIUS-TF and GENIUS is decribed in detail in [7]. In October 2004 we have installed a new setup GENIUS-TF-II (see Fig. 1-lower part, and Fig. 2), containing in contrast to the earlier setup now **six naked** Ge detectors, and, as most important improvement **a second copper vessel**, for further shielding of the Radon (see [4]). Each detector has a weight of 2.5 kg. The depth of the

Fig. 1. Upper part – left and right: Taking out the crystals from the transport dewars and fixing the electrical contacts in the clean room of the GENIUS-TF building – from left to right: H. Strecker, I. Krivosheina, H.V. Klapdor-Kleingrothaus. Middle: **The first four contacted naked Ge detectors** before installation into the GENIUS-TF setup. Bottom part – left and right: View from the top of the new GENIUS-TF-II setup in the more Radon-clean beta-beta room, during installation in october 2004. Middle: **The first six contacted naked Ge detectors**.

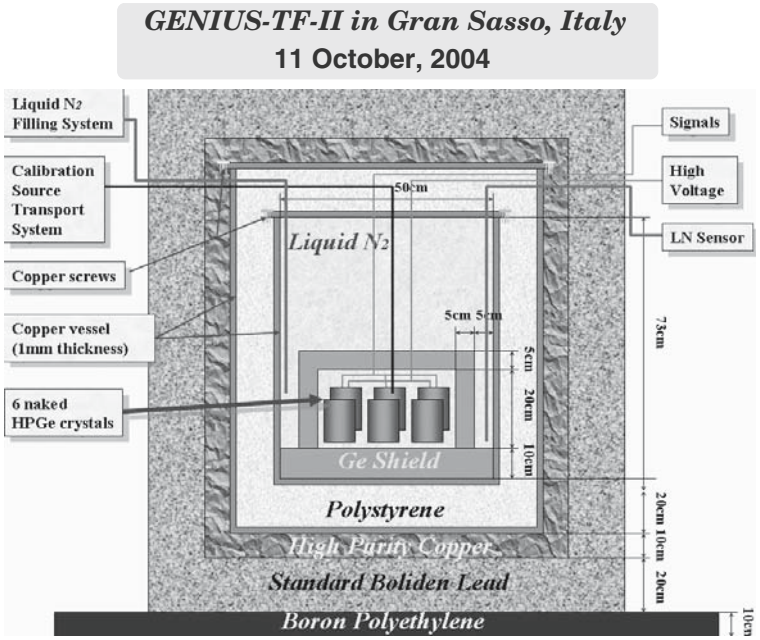

Fig. 2. Cross section of the new setup GENIUS-TF-II.

core of the detectors was reduced to guarantee a very low threshold. The inner shielding by bricks of monocristalline Germanium is used also in this setup. First results seem to show a reduction of the ^{222}Rn background.

The problem of diffusion of ^{222}Ra into the setup GENIUS-TF-I *could not be solved satisfactorily* during the first half of 2004. At present, in the low-energy region, microphonics still causes some problem, which would **be, as the ^{222}Ra background, very serious for any full GENIUS-like experiment.** Also this problem was not solved in 2003 and the first half of 2004. We are presently working on the reduction of the problem for the GENIUS-TF-II application in dark matter search, by pulse shape analysis methods. It might be mentioned that GENIUS-TF (I and II) is the **only** setup of naked detectors operated in liquid nitrogen, running in the world until now.

3 The HEIDELBERG Dark Matter Search Experiment (HDMS)

3.1 General

Investigation of the spin-dependent interaction is important, since it provides additional constraints on SUSY models [19, 16, 13], and further, since it has

been shown [20], that even with a very sensitive detector being sensitive only to the scalar interaction (spinless target nucleus) one can, in principle, miss a dark matter signal. Therefore spin-sensitive detectors (spin-non-zero target nuclei) are required.

In general, both proton and neutron spin contributions enter into the formula for the spin-dependent WIMP-nucleus cross section. Under the assumption that the spin is carried by the 'odd' unpaired group of protons or neutrons, and only one of them, either $\langle S_n^A \rangle$ or $\langle S_p^A \rangle$ is non-zero, possible target nuclei can be classified into n-odd or p-odd group nuclei.

Experimentally, many p-odd group nuclei have been investigated, while the spin-dependent WIMP-neutron interactions were subject only of very few experiments, using natural Germanium [21, 22], and ^{129}Xe [10](DAMA group), the most sensitive of them being the Xe experiment.

The sensitivities reached in investigations of the spin-dependent interaction of WIMPs with p-odd and n-odd nuclei are at present on a similar level (of about 1 pb), and much less than for the spin-independent interaction (about 10^{-6} pb). In spite of this, the "distance" to the SUSY expectation region is similar to that in the spin-independent case since SUSY models predict much higher cross sections for the spin-dependent case (see e.g. [13]).

We present here the results of the investigation of another odd-neutron nucleus, ^{73}Ge (with spin J=9/2). To increase the sensitivity for the spin-dependent interaction, a high-purity Germanium detector enriched in ^{73}Ge to 86% (natural abundance 7.6%) has been produced and applied for this purpose.

3.2 The HDMS Detector and the Measured Spectra

The HDMS (Heidelberg Dark Matter Search) project operates two ionization HPGe detectors at the Gran Sasso National Laboratory (LNGS). The unique configuration of the two crystals is shown in Fig. 3: a small p-type enriched ^{73}Ge crystal with a mass of 202 g (enrichment 86%) is surrounded by a well-type natural Ge crystal of 2.111 kg. Both the detectors are mounted in the same copper cryostat. The coaxial configuration of the two detectors was especially designed to reduce the background of the inner detector by means of two effects, the shielding provided by the outer crystal (germanium is one of the radio-purest known materials), and the anti-coincidence between the two detectors. Since WIMP interactions will take place only in one of the two detectors at a time, events occurring in both inner and outer crystals (like multiple scattered photons) can be rejected.

A further shield against external background sources is provided by 10 cm of electrolytic copper and 20 cm of Boliden lead, both lead and copper having been stored for several years below ground at Gran Sasso. The whole setup is enclosed in an air tight steel box and flushed with gaseous nitrogen in order to suppress environmental radon diffusion. Finally a 15 cm thick

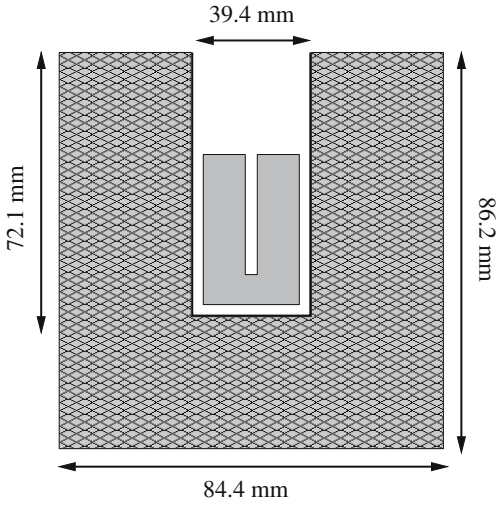

Fig. 3. Schematic view of the HDMS detector configuration. The inner detector is made from ^{73}Ge, the outer from natural germanium.

borated polyethylene shield surrounds the steel box to minimize the influence of neutrons.

The final setup of HDMS was installed at the LNGS during August 2000, after a first prototype phase [18] which took data over a period of about 15 months with an inner detector made of *natural* germanium. The inner detector was then replaced by an *enriched* ^{73}Ge crystal of the same mass and dimensions. For technical properties of the HDMS detectors and previous performances of HDMS we refer to [18, 8]. The electronic data acquisition system is similar to the one used in the HEIDELBERG-MOSCOW double beta decay experiment [23]. It allows data sampling in event-by-event mode and in a calibration mode (for fast data acquisition). 250 MHz flash ADC's of type Analog Devices 9038 JE (in DL515 modules) allowed digital measurements of pulse shapes. The signals of the charge-sensitive preamplifiers were differentiated by Timing Filter Amplifiers. Since the energy resolution of the FADC was 8 bit, the energy signals for high- and low-energy spectra (from 70 KeV to 8 MeV and from threshold of 4 KeV to 400 KeV) were recorded with 13 bit ADC's developed at MPI Heidelberg. As trigger pulse-detect signals from the ADC's were used. For details see [24].

The anti-coincidence between the two detectors is performed off-line. All events having an energy deposition in both detectors are rejected. The total spectrum measured over the period February 2001 to July 2003 (423.18$\dot{\text{d}}$, corresponding to 85.48 kg d) is shown in Fig. 4.

To understand quantitatively the measured spectrum, extensive Monte Carlo simulations have been performed already for the HDMS prototype detector [25], including the effects of the natural decay chains of ^{232}Th and ^{238}U,

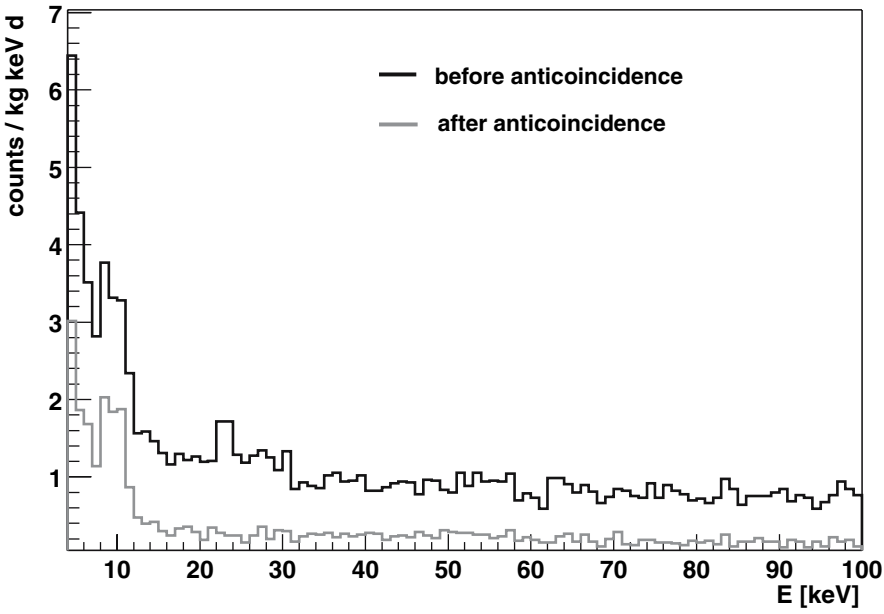

Fig. 4. Background spectrum of the HDMS detector (exposure 85.48 kg d) before and after the anti-coincidence cut is applied.

the primordial nuclide ^{40}K, the cosmogenically produced nuclides ^{54}Mn, ^{57}Co, ^{58}Co, ^{60}Co and ^{65}Zn in the copper of the cryostat and in the Ge crystals, and the anthropogenic radionuclides ^{125}Sb, ^{134}Cs, ^{137}Cs and ^{207}Bi, and also muon showers and neutron-induced interactions. The main background sources and their localization in the HDMS setup were understood, and agreement of the measured spectrum and the simulated sum spectrum was obtained within the uncertainty of the simulations of about 20%.

In Fig. 5 we see the anticoincidence spectrum shown in Fig. 4 divided into 3 subsets, corresponding to 3 partial acquisition periods. The exposures are, respectively, 30.9 kg d, 29.5 kg d and 27.6 kg d. Fig. 5 shows the decrease with measuring time of the activity of the cosmogenic isotope ^{68}Ge (half life = 270.8 d), which is responsible for the structure around 10 KeV (X-rays) (see [26]). Also decreasing with time was the background in the other energy regions, for example from 50 to 100 KeV, where the background index for the third spectrum (runs 721-1000) is less than a half of the first spectrum (runs 260-500). At the same time we notice, that, the background in the lowest energy bin almost remained constant, probably being due to microphonic noise.

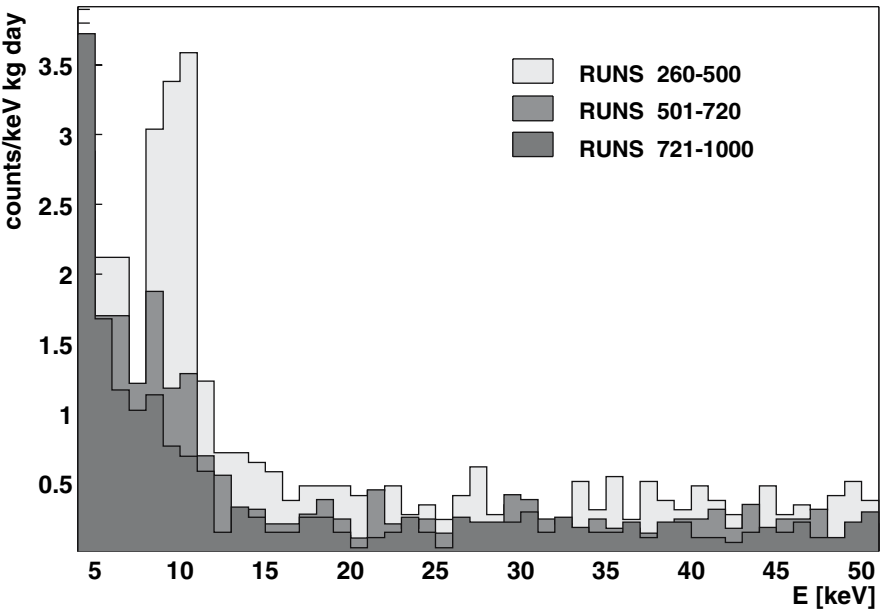

Fig. 5. Anti-coincidence spectra from the HDMS experiment for the indicated partial data sets (see text).

3.3 Dark Matter Limits

The spectra have been used to extract limits on WIMP-nucleon coupling. In the procedure of calculating the limits on the WIMP parameters (mass and cross section) we consider either spin-independent (SI)-coupling only or spin-dependent (SD)-coupling only. This simplification is done in most analyses of dark matter experiments, although *in principle* one has to make a joint analysis of SI and SD coupling (see [27, 13], and below). The evaluation for dark matter limits on the WIMP-nucleon cross section uses the conservative assumption, that the whole experimental spectrum consists of WIMP events. Consequently, excess events above the experimental spectrum in any energy range of a width not smaller than the energy resolution of the detector are forbidden (to a given confidence limit). For the calculation of the expected WIMP spectra we use formulae given in the extensive reviews [17, 28], for a truncated Maxwell velocity distribution in an isothermal WIMP-halo model. However, it should be mentioned that other models exist, and that varying the halo model can affect the results significantly (see [27, 29]). The astrophysical parameters used are given in Table 2. For a given WIMP mass we then fit the only remaining parameter, the scattering cross section σ_{Ge}, to the measured spectrum by using a one-parameter maximum likelihood fit algorithm. We use a sliding variable energy window to check the excess events above the experimental spectrum (for a one-sided 90% c.l.), as used (and described) in

our earlier dark matter investigations [18]. The minimum among the cross section values obtained via the multiple fits is taken as the cross section for the corresponding WIMP mass. As starting value for the cross section $\sigma_{\rm Ge}$ at zero momentum transfer, we assume $\sigma_{\rm Ge} = 10^{-34}{\rm cm}^2$, for both SI and SD coupling.

Regarding the form factor, for the SI coupling we used the Helm approximation of the Bessel form factor. The form factor in this approximation is [30]:

$$F^2(qr_n) = \left(\frac{3j_1(qr_n)}{qr_n}\right)^2 e^{-(qs)^2} \ , \tag{1}$$

where $s \sim 1$ fm is the nuclear skin thickness. For the SD coupling we used the following form factor [17]:

$$\begin{aligned} F^2(qr_n) &= j_0^2(qr_n) && (qr_n < 2.55,\ qr_n > 4.5) \\ F^2(qr_n) &= \text{constant} \simeq 0.047 && (2.55 < \mathrm{qr_n} < 4.5) \end{aligned} \tag{2}$$

calculated in the so-called thin-shell approximation and corrected so that the first zero of the Bessel function is partially filled with the value of the function at the second maximum.

As a result of the procedure described above, we obtain, for each value of the WIMP mass, the upper limit on the WIMP-Ge cross-section $\sigma_{\rm Ge}$ at 90% C.L. . This upper limit can then be converted into a limit on WIMP-nucleon (proton or neutron) cross section. The conversion allows one to compare the results of experiments using different targets. In the spin-independent case the conversion from the WIMP-nucleas cross section $\sigma_{\rm Ge}$ to the WIMP-nucleon cross section σ_p is straightforward ($\sigma_p = \sigma_A \frac{\mu_p^2}{\mu_A^2} \frac{1}{A^2}$)[17].

In Fig. 6 we show the measured spectrum (see Fig. 4 together with some WIMP spectra calculated by use of the minimum cross sections determined by the described fitting procedure. Fig. 6 also shows the deduced contour lines for the data subsets shown in Fig. 5 for the SI interaction. They are not very competitive, and our interest lies with our detector, mainly in the SD interaction.

In the spin-dependent case we have to deal with the problem of the WIMP-type dependence of the cross-section (see [19, 17, 13, 31]). The conversion formula for SD interactions is:

$$\sigma_p = \sigma_A \frac{\mu_p^2}{\mu_A^2} \frac{1}{C_A/C_p} \tag{3}$$

$$\sigma_n = \sigma_A \frac{\mu_n^2}{\mu_A^2} \frac{1}{C_A/C_n} \ , \tag{4}$$

where $\mu_{p,n}^2$ and $C_{p,n}$ are the reduced mass and the enhancement factor for proton and neutron, respectively.
The definition of C_A is given by:

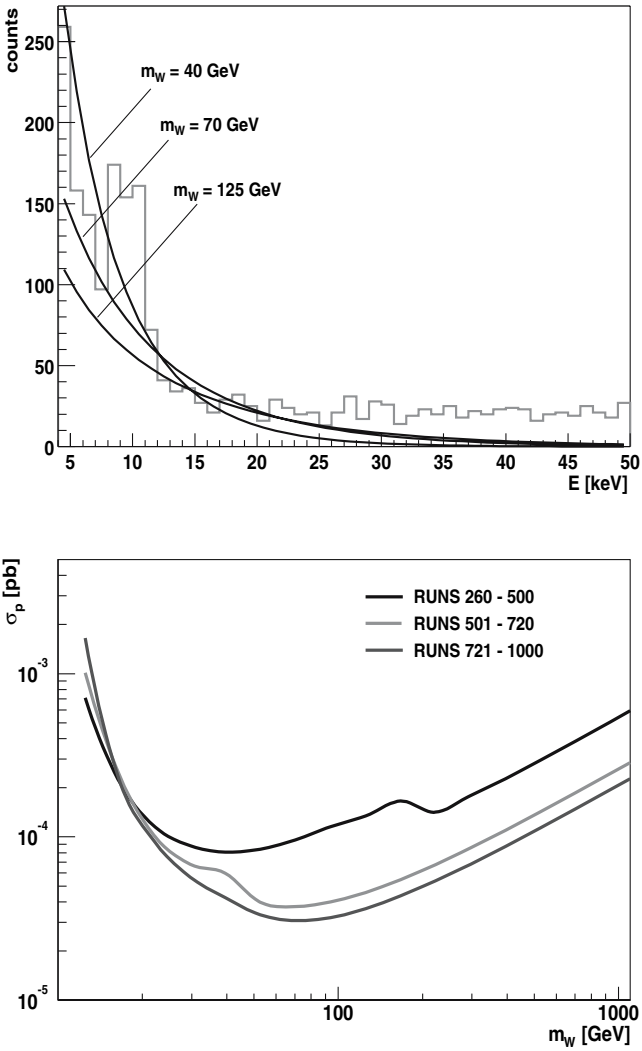

Fig. 6. Left: comparison of the measured spectrum shown in Fig. 4 with theoretical spectra, corresponding to the minimum cross section calculated from the fit and to the WIMP masses indicated. Right: limits on SI WIMP-proton cross sections from the HDMS experiment for the 3 data subsets shown in Fig. 5.

$$C_A = \frac{8}{\pi} \left(a_p \langle S_p \rangle + a_n \langle S_n \rangle \right)^2 \frac{J+1}{J} \,, \tag{5}$$

where a_p and a_n are the (WIMP-type dependent) effective WIMP-nucleon couplings, $\langle S_p \rangle$ and $\langle S_n \rangle$ are the expectation values of the proton and neutron spins within the nucleus and J is the total nuclear spin.

Table 1. Values of the astrophysical quantities used to extract the limits on WIMP-nucleon coupling, used in the fit of the present data.

Parameter	Value	
Earth velocity	v_E	232 km/s
WIMP local density	ρ_w	$0.3\,\mathrm{GeV/cm^3}$
WIMP velocity distribution	v_{rms}	270 km/s
Escape velocity	v_{esc}	600 km/s

Table 2. Several nuclear model calculations of the spin factors $\langle S_p \rangle$ and $\langle S_n \rangle$ for the odd-N nucleus ^{73}Ge.

Model	$\langle S_n \rangle$	$\langle S_p \rangle$
ISPSM [35]	0.5	0
OGM [32]	0.23	0
IBFM [36]	0.469	-0.009
IBFM(quenched) [36]	0.245	-0.005
Hybrid [34]	0.378	0.030
Shell (small) [33]	0.496	0.005
Shell (large) [33]	0.468	0.011
Quenched [33]	0.372	0.009

In the case of free nucleons we have $C_{p,n} = \frac{6}{\pi}\, a_{p,n}^2$ and, as we easily see, the ratio C_A/C_p (as well as C_A/C_n) depends on the WIMP composition.

Under the simplifying assumption that the nuclear spin is carried mostly by protons (neutrons), that is $\langle S_p \rangle >> \langle S_n \rangle$ ($\langle S_n \rangle >> \langle S_p \rangle$) the WIMP-dependence cancels out in the ratio, since the effective WIMP-nucleon couplings a_p and a_n are almost of same magnitude. In the effective MSSM for the ratio of neutralino-neutron spin coupling to the neutralino-proton spin coupling a_p has been calculated to be $0.55 < a_p > 0.8$ [13]. Since ^{73}Ge is a odd-N nucleus (J=9/2), the assumption $\langle S_n \rangle >> \langle S_p \rangle$ is well justified (see Table 2) and we can obtain WIMP-type independent limits for the WIMP-neutron SD cross section in the following way:

$$\sigma_n = \frac{3}{4}\, \sigma_A\, \frac{\mu_n^2}{\mu_A^2}\, \frac{1}{\langle S_n \rangle^2}\, \frac{J}{J+1} \tag{6}$$

The values of $\langle S_n \rangle$ and $\langle S_p \rangle$ are provided by nuclear model calculations. The results of several calculations for ^{73}Ge are listed in Table 2.

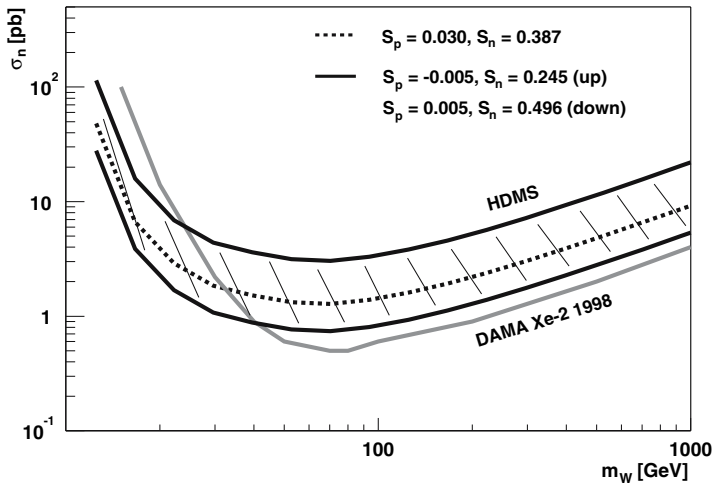

Fig. 7. Experimental limits on WIMP-neutron spin-dependent coupling from the HDMS experiment (data from runs 721-1000). The HDMS exclusion plot (dashed line) is calculated assuming $\langle S_n \rangle = 0.378$ and $\langle S_p \rangle = 0.030$. Also shown is the effect of choosing different values for the spin factors $\langle S_n \rangle$ and $\langle S_p \rangle$ (dashed range). The result of the DAMA Xenon experiment [10] is shown as comparison.

In Fig. 7 we plot the exclusion curve for σ_n obtained from the HDMS last partial data set runs 721-1000. To draw the exclusion plots we assumed the most recent values of $\langle S_n \rangle = 0.378$ and $\langle S_p \rangle = 0.030$, as in [34], but also shown is the effect of choosing different values for the spin factors on the HDMS exclusion plot. We plot as comparison the current best limit on SD WIMP-neutron cross sections coming from an odd-neutron nucleus (^{129}Xe), provided by the DAMA Xenon experiment [10]. Our results are already competitive with the DAMA results, improving the limit in the region of low WIMP masses.

Figure 8, shows the sensitivities of HDMS in the framework of mixed spin-dependent (SD) WIMP-neutron and spin-independent (SI) WIMP-nucleon couplings (see [13]).

4 Conclusions

The GENIUS-TF experiment [6, 5] will be – in addition to DAMA [9] – the *only* experiment which will be able to probe the annual modulation signature in a foreseeable future. The much discussed cryodetector experiments, have at present hardly a chance to look for modulation because the mass used and projected in these experiments is still by far too low (see also [14]).

A new GENIUS-TF-II setup has been installed in October 14, 2004 with additional shielding against radon and additional two Ge detectors in liquid

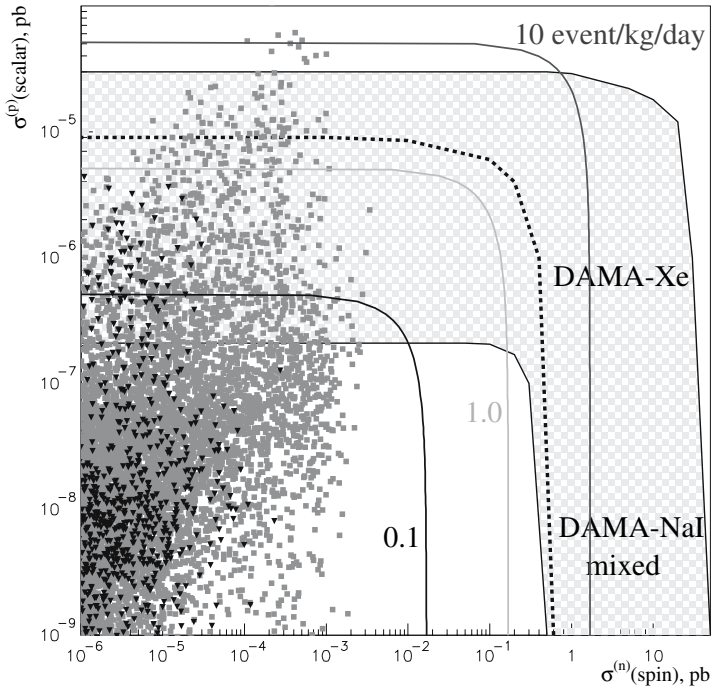

Fig. 8. Right: The solid lines (marked with numbers of $R(15, 50)$ in events/kg day) show the sensitivities of the HDMS setup with ^{73}GeV in the framework of mixed SD WIMP-neutron and SI WIMP-nucleon couplings together with the DAMA-NaI allowed region for sub-dominant SD WIMP-neutron coupling ($\theta = \pi/2$). The *present HDMS* result cuts already part of the DAMA allowed range. The scatter plots give correlations between $\sigma^p_{\rm SI}$ and $\sigma^n_{\rm SD}$ in the effMSSM for $m_\chi < 200$ GeV. The squares (red) correspond to sub-dominant relic neutralino contribution $0.002 < \Omega_\chi h_0^2 < 0.1$ and triangles (black) correspond to WMAP relic neutralino density $0.094 < \Omega_\chi h_0^2 < 0.129$. The dashed line from [10] shows the DAMA-^{129}Xe (1998) exclusion curve for $m_{\rm WIMP} = 50$ GeV (from [13]).

nitrogen in the GRAN SASSO, increasing the total mass to 15 kg. This is the first time that this novel technique is applied under realistic background conditions of an underground laboratory.

The HDMS (HEIDELBERG Dark Matter Search) project runs an enriched ^{73}Ge detector in Gran Sasso, looking for *spin-dependent* WIMP-neutron interaction. The measurement over the period 2001-2003 improved the best up to now existing limits, by the ^{129}Xe DAMA measurement, in the range of low WIMP masses. At present efforts are going on to improve the sensitivity of HDMS, to be able to restrict the SUSY prediction region (see Fig. 2).

Acknowledgement

The authors would like to thank their colleagues from MPI Heidelberg: Herrn H. Strecker, T. Apfel, M. Reissfelder, M. Saueressig for their help during installation of GENIUS-TF-II and also the technical staff of the Max-Planck Institut für Kernphysik and of the Gran Sasso Underground Laboratory. The authors also thank to Dr. C. Tomei for her taking care of the HDMS experimental data during her PhD time. We acknowledge the invaluable support from BMBF and DFG, and LNGS of this project. We are grateful to the former State Committee of Atomic Energy of the USSR for providing the monocristalline Ge shielding material used in this experiment.

References

1. J.Verplancke, **CANBERRA Company,** *priv. commun. 5.03.2004.*
2. H.V. Klapdor-Kleingrothaus, Proc. of BEYOND'97, Castle Ringberg, June 1997, eds. H.V. Klapdor-Kleingrothaus et al. *IOP* (1998)485, *Int. J. Mod. Phys.* **A13** (1998) 3953. H.V. Klapdor-Kleingrothaus, J.Hellmig, M.Hirsch, **GENIUS-Proposal 20 Nov. 1997**; *J. Phys.* **G24** (1998) 483–516; H.V. Klapdor-Kleingrothaus, CERN Courier, Nov. 1997, 16–18.
3. H.V. Klapdor-Kleingrothaus, "60 Years of Double Beta Decay – From Nuclear Physics to Beyond the Standard Model Particle Physics", WS (2001) 1281 p. H.V. Klapdor-Kleingrothaus, *Spring. Tr. Mod. Phys.* **163** (2000) 69.
4. H.V. Klapdor-Kleingrothaus, I.V. Krivosheina and C. Tomei, *Phys. Lett.* **B 609** (2005) 226–231.
5. H.V. Klapdor-Kleingrothaus et al., *Nucl. Instrum. Meth.* **A 481** (2002) 149–159.
6. H.V. Klapdor-Kleingrothaus et al., *Nucl. Instrum. Meth.* **A 511** (2003) 341; Proc. BEYOND02, IOP 2003, ed. H.V. Klapdor-Kleingrothaus, 499. *Nucl. Instrum. Meth.* **A 530** (2004) 410–418 and **A 508** (2003) 343–352, CERN Courier **43** N6 (2003) 9 and hep-ph/0307329.
7. T. Kihm, V. Bobrakov, H.V. Klapdor-Kleingrothaus, *Nucl. Instrum. Meth.* **A 498** (2003) 334.
8. H. V. Klapdor-Kleingrothaus et al., *Astr. Phys.* **18** (2003) 525–530.
9. R. Bernabei et al., *Riv. Nuovo Cim.* **26** (2003) 1–73; *Phys. Lett.* **B 424** (1998) 195; **450** (1999) 448; **480** (2000) 23.
10. R. Bernabei et al., *Phys. Lett.* **B 436** (1998) 379.
11. H.V. Klapdor-Kleingrothaus et al., to be publ. (2005) and Gran Sasso Ann. Rep. 2003, INFN (2004) 99.
12. C. Tomei, Diss. L'Aquila University, 2004.
13. V. Bednyakov, H.V. Klapdor-Kleingrothaus, *Phys. Rev.* **D** 70 (2004) 096006.
14. H.V. Klapdor-Kleingrothaus, *Int. J. Mod. Phys.* **A17** (2002) 3421–3431 (2002).
15. K. Griest, Phys. Rev. **D 38** (1988) 2357.
16. V. Bednyakov, H.V. Klapdor-Kleingrothaus, S. Kovalenko, Phys. Rev. **D 50** (1994) 7128–7143.
17. J.D. Lewin, P. F. Smith, Astropart. Phys. **6** (1997) 87.

18. L. Baudis, A. Dietz, B. Majorovits, F. Schwamm, H. Strecker, and H.V. Klapdor-Kleingrothaus, Phys. Rev. **D 63** (2000) 022001.
19. G. Jungman, M. Kamionkowski, K. Griest, Phys. Rep. **267** (1996) 195.
20. V. Bednyakov, H.V. Klapdor-Kleingrothaus, Phys. Rev. **D 63** (2001) 095005.
21. D.O. Caldwell et al., Phys. Rev. Lett. 61 (1988) 510
22. D. Reusser et al., Phys. Lett. B 255 (1991) 143.
23. H.V. Klapdor-Kleingrothaus, I.V. Krivosheina, A. Dietz et al., Phys. Lett. B 586 (2004) 198–212 and NIM A 522 (2004) 371–406.
24. J. Hellmig, Dissertation, November 1996, MPI-Heidelberg; L. Baudis, Dissertation, December 1999, MPI-Heidelberg; Y. Ramachers, Dissertation, 1997, MPI-Heidelberg.
25. Schwamm, Dipl. Thesis, Univ. Heidelberg, 1999 (unpublished).
26. Table of Isotopes at http://nucleardata.nuclear.lu.se/nucleardata/toi.
27. R. Bernabei et al., Riv. Nuovo Cim. **26** (2003) 1–73.
28. R. Bernabei, Rev. Nuovo Comento 18 (1995) 1.
29. A.M. Green, Phys. Rev. D 66 (2002) 083003.
30. R.H. Helm, Phys. Rev. **104** (1956) 1466–1475.
31. D.R. Tovey et al., Phys. Lett. B**488** (2000) 17–26.
32. J. Engel, S. Pittel, P. Vogel, Int. J. Mod. Phys. **E 1** (1992) 1–37.
33. M.T. Ressell et al., Phys. Rev. **D 48** (1993) 5519.
34. V. Dimitrov, J. Engel and S. Pittel, Phys. Rev. **D 51** (1995) 291–295.
35. M.W. Goodman and E. Witten, Phys. Rev. **D 33** (1986) 2071.
36. F. Iachello, L. M. Krauss and G. Maino, Phys. Lett. **B 254** (1991) 220.

First CDMS II WIMP Search Results from the Soudan Underground Laboratory

D.S. Akerib[2], M.S. Armel-Funkhouser[7], M.J. Attisha[1], L. Baudis[6,10], D.A. Bauer[8,3], P.L. Brink[6], R. Bunker[8], B. Cabrera[6], D.O. Caldwell[8], C.L. Chang[6], M.B. Crisler[3], P. Cushman[11], R. Dixon[3], M.R. Dragowsky[2], D.D. Driscoll[2], L. Duong[11], R. Ferril[8], J. Filippini[7], R.J. Gaitskell[1], D. Holmgren[3], M.E. Huber[9], S. Kamat[2], A. Lu[7], R. Mahapatra[8], V. Mandic[7], P. Meunier[7], N. Mirabolfathi[7], H. Nelson[8], R. Nelson[8], R.W. Ogburn[6], T.A. Perera[2], E. Ramberg[3], W. Rau[7], A. Reisetter[11], R.R. Ross[4,7], T. Saab[6], B. Sadoulet[7,4], J. Sander[8], C. Savage[8], R.W. Schnee[2], D.N. Seitz[7], B. Serfass[7], A.J. Sirois[2], K.M. Sundqvist[7], J-P.F. Thompson[1], G. Wang[2], S. Yellin[8], and B.A. Young[5]

[1] Department of Physics, Brown University, Providence, RI 02912, USA
[2] Department of Physics, Case Western Reserve University, Cleveland, OH, USA
[3] Fermi National Accelerator Laboratory, Batavia, IL 60510, USA
[4] Lawrence Berkeley National Laboratory, Berkeley, CA 94720, USA
[5] Department of Physics, Santa Clara University, Santa Clara, CA 95053, USA
[6] Department of Physics, Stanford University, Stanford, CA 94305, USA
pbrink@stanford.edu
[7] Department of Physics, University of California, Berkeley, CA 94720, USA
[8] Department of Physics, University of California, Santa Barbara, CA, USA
[9] Department of Physics, University of Colorado at Denver, Denver, CO, USA
[10] Department of Physics, University of Florida, Gainesville, FL 32611, USA
[11] School of Physics & Astronomy, University of Minnesota, Minneapolis, USA

1 Introduction

The Cryogenic Dark Matter Search (CDMS) collaboration [1] is performing a direct-search experiment for the Weakly Interacting Massive Particles (WIMPs) that could constitute the majority of the mass of the Universe [2]. The scientific case for WIMPS continues to grow stronger; most compelling are WMAP results in conjunction with studies of large-scale clustering and supernova data [3]. One attractive WIMP candidate is the lightest supersymmetric particle (LSP) which arises naturally in many supersymmetric extensions of the Standard Model of Particle Physics, assuming that R-parity is conserved [4]. WIMPS are expected to interact elastically with nuclei, generating a recoil energy of a few tens of keV, at a rate smaller than 1 event per kg per day [5].

In order to perform such a direct-detection experiment the CDMS experiment utilizes detectors which can discriminate against the majority of background events (electromagnetic in origin). Both the ionization signal, and the athermal phonon flux generated by each recoil-candidate event in the Ge and Si targets are measured. For nuclear recoils (due to neutron backgrounds, and

the possible WIMP candidates of interest) the ionization signal is relatively suppressed compared to that of electron recoils (which arise due to the natural photon and beta backgrounds present). Thus by measuring the relative ionization yield for each recoil event we can identify the nuclear recoils of interest. Another experiment, EDELWEISS, also use this relative-ionization yield technique [6]. But their measurement of the phonon energy is essentially calorimetric utilizing neutron-doped-thermistors. CDMS uses a more advanced phonon sensor that is more sensitive to the initial athermal phonon flux, thus providing an additional event-type discrimination handle [7]. The athermal phonon information can be used to identify surface electron-recoil events, which occur within the first few microns of the detector surface and have low ionization yield. These events otherwise could potentially be erroneously classified as nuclear recoils.

The other class of events that could be misidentified as the WIMP signal of interest comes from the ambient neutron background. Our detector technology cannot discriminate between WIMPS and neutrons; thus it is imperative that the shielding of the experiment is designed to minimize this source of background. Earlier results from CDMS [8] were from operating our detectors at a shallow site (17 m.w.e.) on the Stanford campus (Stanford Underground Facility, SUF). The use of an active muon veto to identify detector events coincident with through-going muons was sufficient to veto most of the neutron background, and along with Monte-Carlo studies of the multiple scattering of events between detectors (neutrons can multiply-scatter, whereas WIMPS will not) CDMS could set competitive limits for the WIMP-nucleon cross-section [8]. However, to make further progress a deeper site is desired where the ambient muon and associated neutron background flux will be further attenuated. Thus the CDMS II collaboration commissioned the deep-site facility at Soudan, Minnesota.

The rest of this paper will describe our operations at Soudan, our first WIMP-search data set from Soudan, and the resulting exclusion limits for both scalar [1] and axial-vector WIMP-nucleon cross-section [9, 10]. These results, under standard assumptions, continue to disagree with the annual modulation signal claimed by the DAMA collaboration [11, 12].

2 CDMS II at Soudan

2.1 Experiment Overview

The Soudan Underground Laboratory provides an overburden of 780 m, corresponding to 2090 m.w.e. to shield against cosmic rays. The surface muon flux is attenuated by a factor of 5×10^4. Within the original Soudan cavern the CDMS II apparatus is housed within an RF-shielded enclosure (see Fig. 1). The apparatus consists of a commercial dilution refrigerator connected via

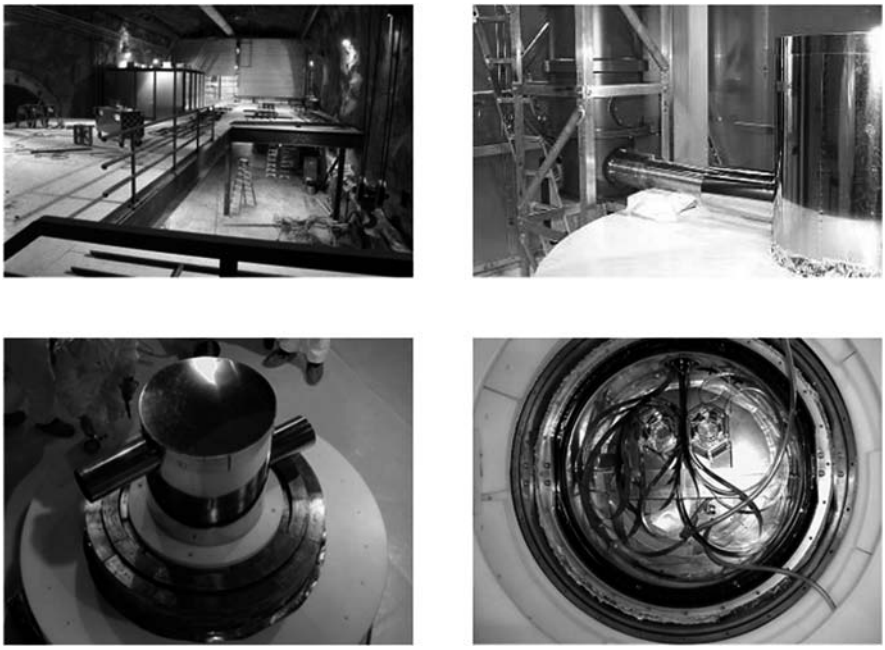

Fig. 1. The CDMS II infrastructure during construction at Soudan. Clockwise from upper left: the upper-half of the class-10,000 cleanroom which houses the apparatus, seen from the mezzanine level in the Soudan cavern; the cryogenic system, with the dilution refrigerator and detector cold volume (icebox) connected via the cold stem; a partial assembly of the shielding below the icebox; Detector Towers 1 & 2 installed with readout striplines in the inner can of the icebox.

a cold-stem to a set of nested copper cans which contain the Ge and Si detectors, cooled to 50 mK. For the first WIMP-search cryogenic run (labelled as Run 118) two "towers" of detectors were installed but only Tower 1 was brought on-line. This is the same tower that was run previously at SUF [8], containing 4 Ge and 2 Si detectors.

The electrical readout of the detectors is accomplished via copper-kapton electrical striplines which bring the signals back to room temperature via an "e-stem", which penetrates the shielding surrounding the copper cans. The signals are amplified in front-end electronic racks and then sent to the adjacent electronics room where digitizers, slow ADCs and scalers record the detector and muon-veto shield activity and monitor various thresholds and settings. The trigger for each detector is formed from the sum of the four phonon channels. The waveforms for each triggered event are recorded for all detectors and transferred by the DAQ to DLT tape. The DAQ deadtime is $\sim$ 20 ms, which allows for a 50 Hz event acquisition rate and thus enables fast execution of calibration-source runs to be interspersed with WIMP-search runs. For Run 118 the WIMP-search runs' trigger-rate was $\sim$ 0.1 Hz (due

to the ambient electron-recoil event rate) at the hardware trigger threshold of $\sim 2\,\mathrm{keV}$. Real-time online analysis of a small fraction of the data ensures quality. Off-line computing farms process all the recorded files and calculate the event parameters of interest (and introduce blinding of potential single-scatter nuclear recoil events in the WIMP-search data sets) for subsequent analysis.

2.2 Shielding

The detector towers reside in a one-cubic-foot copper-walled enclosure, evacuated and cooled to 50 mK. The set of radio-pure copper cans required for the cryogenic operation of these detectors is called the "icebox" and constitute the innermost layer of passive shielding for the detectors. A 2 mm thick mu-metal can (a soft-iron alloy) surrounds the icebox to screen the detectors and their cold-readout electronics from magnetic fields. For the latter part of Run 118 this can also served the purpose of containing old-air that was flushed back through the surrounding shielding material to reduce the ambient radon gas levels within the shield.

Referring to Fig. 2, surrounding the mu-metal shield of the icebox there is an "inner" layer of 10 cm thick polyethylene that serves as the final moderator of incident neutrons on the icebox. Further out are 4.5 cm thick ancient lead

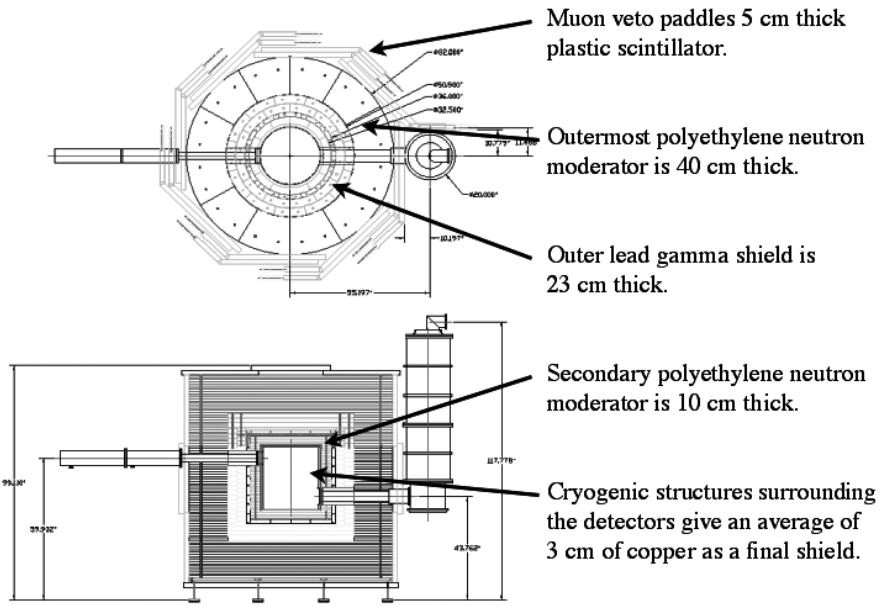

Fig. 2. Schematic plan and side elevations of shielding layers surrounding the Soudan icebox with the dilution refrigerator outside the shielding and connected to the icebox by the cold stem.

bricks, beyond which there is another 9 cm thickness of low-activity lead bricks, to reduce the ambient gamma-ray flux incident on the icebox. The lead bricks are arranged so that there is no direct line of sight through the (three) layers. Beyond the lead bricks is the 40 cm thick outer polyethylene shield required to moderate the neutron flux incident from the neighbouring rock of the cavern.

Surrounding the outer polyethylene shield is the active muon veto system, similar to that employed at SUF [8], but with a number of differences. As indicated in Fig. 2 there are 40 individual paddles arranged to prevent any line of sight from the cavern to the cryogenic detectors. The new readout electronics allows discrimination between through-going muons and high-energy (> 2 MeV) gamma cascades incident on the shield. The threshold was set to give a veto trigger rate of 600 Hz, which is due to the ambient gammas incident on the veto shield. The muon rate at Soudan is too low (one per minute on the entire shield) to allow muons to be used to calibrate and monitor the stability of the active shield. Instead a blue-LED pulser system tuned to match the scintillator light produced by a muon is used to calibrate the paddles twice a day. To date no significant deviations have been observed. A veto trigger for tagging incident muons is constructed by requiring coincident activity in multiple paddles. Through-going muons are tagged with greater than 99.9% efficiency, and rarer stopped muons are tagged with greater than 99.4% efficiency.

2.3 Cryogenics

The dilution refrigerator and icebox design is very similar to that already used by CDMS at SUF [8]. However the associated cryogenic support equipment at Soudan is considerably more sophisticated to allow remote operation. At Soudan, adjacent to the class-10,00 clean-room housing the apparatus is the "cryo-pad" area where the dilution refrigerator's gas-handing equipment, pumps, and cryogenic liquid transfer stations are located.

For the duration of Run 118 the dilution refrigerator had a small leak from the liquid He bath to the outer vacuum can. The detectors and associated cold electronics were not exposed to this helium leak as they are inside a separate, inner vacuum can. However this leak did affect our cryogenic operations. Although this leak was continually pumped on, the vacuum was sufficiently soft to require two liquid helium transfers a day. These transfers reduced our effective livetime as the detectors cannot be operated stably during cryogen refills. In addition, every few weeks the system would go into a thermal runaway mode when sufficient He had accumulated to cause a more substantial degradation in the vacuum. During such "burp" episodes the fridge performance was significantly affected and the detector temperature would rise to 1 K. Typically, it would take a day for the fridge to recover and for the detectors to return to their nominal operating conditions.

2.4 Detectors

The Tower of six detectors operated at Soudan (Tower 1) for Run 118 was first run at SUF [8]. Each Ge (Si) detector is 76 mm in diameter and 10 mm thick, with a mass of 250 g (100 g). As shown in Fig. 3, ionization electrodes and phonon sensors are photolithographically patterned onto the two faces of the crystal for each detector. Division of the electrodes into an annular outer "guard" electrode and a disk-shaped inner electrode help define an inner fiducial region $\simeq 85\%$ that is shielded from low-energy electron sources incident on the detector perimeter.

On the opposite face the phonon sensors serve as the ground electrode grid for the ionization measurement, in addition to their role in measuring the total energy deposited in the crystal by an event. The athermal phonons produced by an event have travel times of $\sim 10\,\mu$s through the crystal before they enter superconducting Al films on the surface of the crystal. There

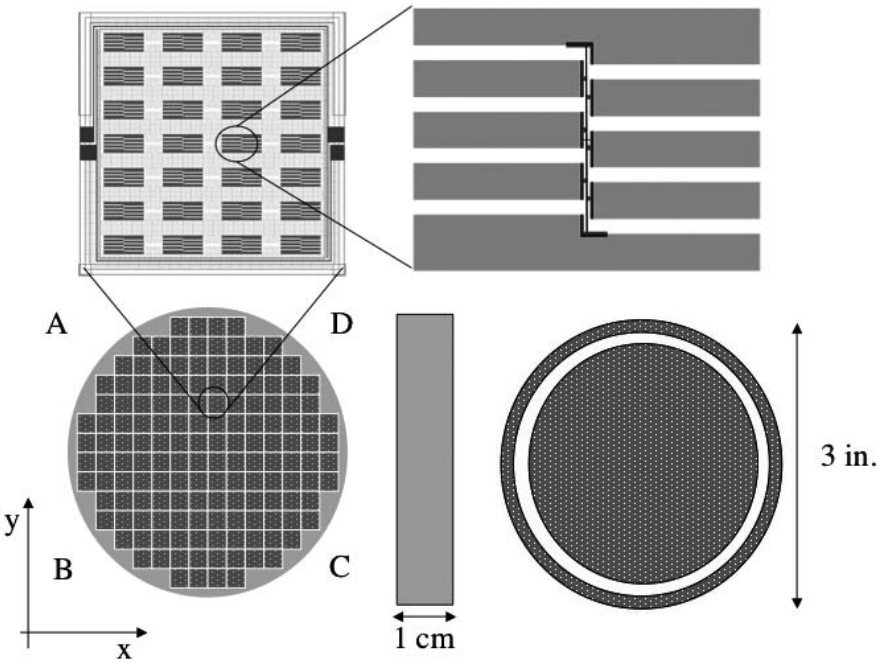

Fig. 3. Schematic layout of a ZIP detector showing the phonon-side (lower left), edge-profile (lower centre), and ionization-side (lower right). The ionization-side has a metallized grid segmented into an inner and an outer (guard ring) electrode. The phonon-side is divided into four quadrants, labelled A, B, C and D, each consisting of 37 dies. The coordinate system (x, y) used in the text is shown. The upper left shows one of phonon sensor dies, each of which contains 28 QET [7] phonon sensors. Each QET (upper right) consists of a 1 µm wide superconducting tungsten transition-edge-sensor connected to 8 aluminium athermal-phonon collection fins.

they can break bound Cooper pairs. The resultant electronic excitations, quasiparticles, then diffuse to the W transition edge sensor (TES) where they heat the W electron system. The W TES is self-biased at $\simeq 80$ mK within its superconducting to normal transition. The rise in temperature of its electron system results in a change in its resistivity, which is sensed by a SQUID readout. These phonon sensors go by the acronym QET, Quasiparticle-trap-assisted Electro-thermal-feedback Transition-edge-sensors [7]. As shown in Fig. 3 the QETs are grouped to give four phonon sensor channels. The relative phonon signal timing delay between them allows a reconstruction of the (x, y) coordinate of the event.

The QET phonon sensors are sensitive to both the athermal phonons produced by the initial recoil event, and the subsequent Luke phonons generated by the drifting of the liberated electrons and holes of the ionization signal under the applied ionization bias voltage [7]. The Luke phonons have lower frequency and thus travel faster (ballistically) than the quasidiffusive propagation of the initial recoil athermal phonons. At an ionization bias of 3 V, half the measured phonon signal of electron-recoil events in Ge is due to these Luke phonons. In comparison, the lower relative ionization yield for nuclear-recoil events results in a smaller fraction of the phonon signal containing prompt phonons. Thus the phonon signals measured will have longer delay times (with respect to the ionization signal) and longer risetimes for nuclear recoils than electron recoils. In addition, electron-recoil events occurring near the surface of the detector will have enhanced down-conversion of the athermal phonons generated by the recoil, due to the presence of metal films on the surface. Thus surface electron-recoil events will generate phonon signals that are both more prompt and with even faster risetimes than electron-recoil events that occur in the bulk of the crystal. This dependence of the phonon signal on the depth, or z-coordinate of the recoil event is the origin of the CDMS detector acronym: Z-dependent Ionization and Phonon (ZIP) detectors.

In Tower 1 the sequence of detectors (running from top to bottom) is Ge, Ge, Ge, Si, Ge, Si, and are labelled Z1-Z6. The detectors are spaced 2 mm apart and have direct line of sight to each other to maximize the detection of multiple scattered events between detectors. The Ge detector at the top of the stack, Z1, has a significantly non-uniform phonon sensor response that is a strong function of the event position within the crystal, thus its analysis threshold was set at 20 keV, twice as high as the other Ge detectors. The Si detector at the bottom, Z6, is known to be slightly contaminated with ^{14}C on its faces. It exhibits a relatively large number of low-ionization-yield beta events and was not used as a WIMP-search detector. Instead it retained utility for tagging multiple-scattered events for other detectors in the Tower.

3 Calibrations

3.1 Gammas

In order to achieve charge collection at the relatively low ionization bias voltage of ∼3 V charged impurity sites in the crystals must be neutralized. This is achieved by "baking" the detectors with photon pulses from LEDs with energies ∼1 eV. The photons liberate some charge carries which neutralize these sites and reduce their scattering cross-sections significantly. However, if the crystals are warmed above 1 K then thermal phonons will reactivate these sites. Thus the LED baking recipe must be optimized for maximum photon yield without excessive heating. Typically we aim to maintain the temperature of the icebox below 200 mK when performing the LED baking.

Once the detectors are neutralized after their initial cooldown we verify that the ionization collection is good by performing gamma calibrations. At Soudan we have performed most of our gamma calibrations using a ^{133}Ba source that is placed on the outer surface of the icebox (the source is pellet-sized and is pulled by a wire through a tube running through the shielding surrounding the icebox). The 3 cm of intervening copper, the finite size of the detectors, and a residual position dependence in the ionization energy resolution can all be simulated by Monte Carlo. Figure 4 shows the measured energy spectra compared to the simulations. The agreement in spectral features is very good and allows an accurate energy calibration of the ionization channels of the detectors.

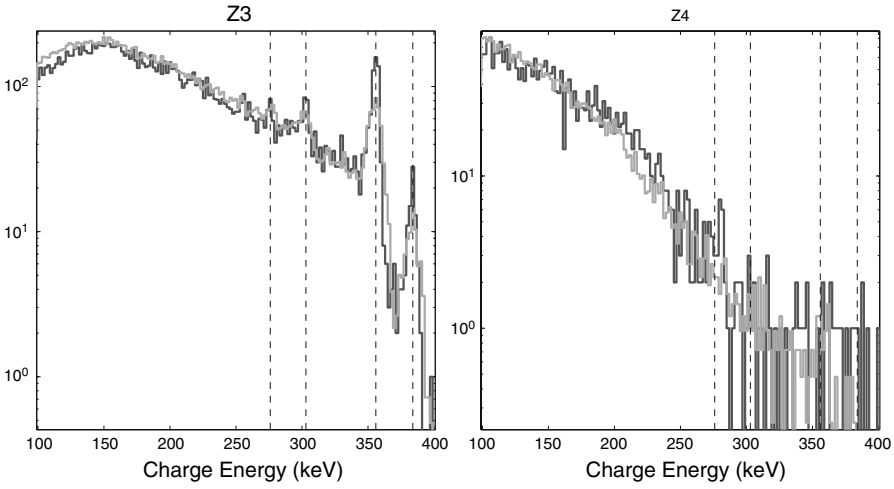

Fig. 4. Comparison of the measured ^{133}Ba charge spectrum (dark) and the Monte Carlo simulation (grey) for (Left) the Ge detector Z3, and (Right) the Si detector Z4. The vertical dashed lines denote the location of the expected peaks at 276 keV, 303 keV, 356 keV and 384 keV.

With the ionization channels now calibrated, the phonon sensors can also be calibrated for electron-recoil events. The position dependence in the phonon signal response is corrected for by establishing lookup tables that use events which are known to be single-scatter bulk electron recoil events [8, 10].

Performing these corrections requires a relatively large number of gamma calibration events. As a by-product these calibration sets also contain a useful fraction (∼1%) of surface electron-recoil events due to high-energy photons ejecting electrons from nearby materials. This class of events are used to study (see [10] and Sect. 4.2 below) the surface electron-recoil response of the detectors and to establish the phonon-timing cuts required to identify such surface events during the WIMP-search running (see Sect. 3.3 for an example).

3.2 Neutrons

In order to determine the nuclear recoil acceptance band in relative ionization yield as a function of recoil energy for each detector, *in situ* neutron calibrations were performed. Like the gamma calibration sources discussed above, the 5μCi ^{252}Cf source was also placed within the shielding but outside of the icebox. Observation of the predicted energy spectrum from the ^{252}Cf source confirmed the energy scale for nuclear recoils [1]. The statistics required from the neutron source to determine the nuclear recoil signal acceptance region are relatively low (∼ 1000 events per detector up to 200 keV recoil energy) and was thus left in place for only an hour in order to minimize the activation of the Ge and surrounding Cu.

The inherent discrimination ability of the detectors between electron recoils and nuclear recoils is demonstrated in Fig. 5, which shows events from three of the Ge detectors of Tower 1 co-added together during one of the Run 118 neutron source calibrations. The neutron source emits both gammas and neutrons. The ionization yield for electron recoils is already normalized to $Y \simeq 1$ by the gamma calibrations. The suppressed ionization yield for the neutron events allows nuclear-recoil acceptance bands to be constructed for each detector.

3.3 Electrons

Figure 5 already indicates the location of the $\pm 2\sigma$ nuclear-recoil acceptance band that will be used as the nuclear recoil cut parameter in the WIMP-search data. However for this band to be accurately calculated, surface event electron-recoils must be removed from the neutron calibration data sets. As described earlier in Sect. 2.4 phonon-timing information can be used to set cuts to reject these surface electron events.

As an example from Run 118, Fig. 6 shows the phonon-timing cuts established for the Ge detector Z3 for the 5–10 keV recoil-energy range. The two

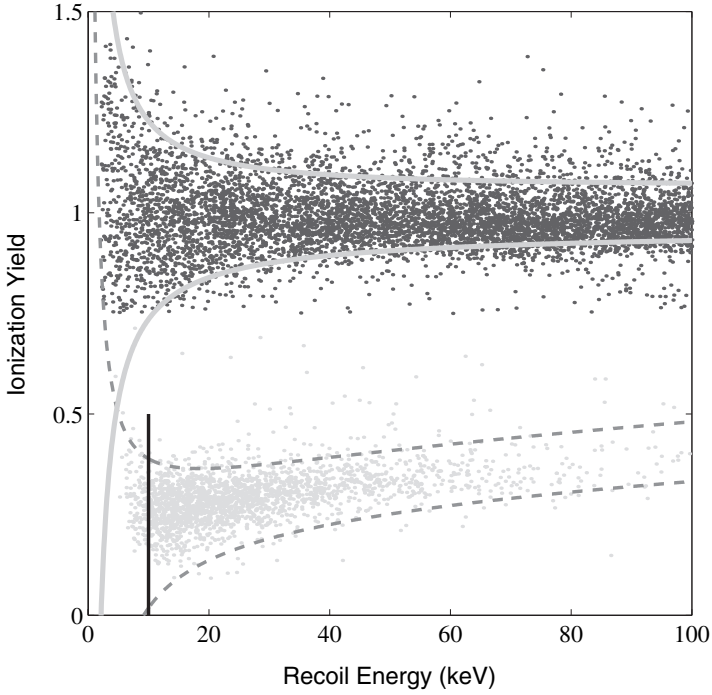

Fig. 5. Ionization yield as a function of recoil energy for calibration data with a ^{252}Cf source with the events for three Ge detectors (Z2, Z3 & Z5) co-added together. The solid curves indicate the electron-recoil acceptance band ($\pm 2\sigma$) and the dashed curves the corresponding nuclear-recoil acceptance band ($\pm 2\sigma$) derived for Z5, the detector with the worst noise of the three. Events with ionization yield $Y < 0.75$ (grey) are shown only if they pass the phonon-timing cuts to ensure that only true nuclear recoils are depicted below $Y = 0.75$. The vertical line indicates the 10 keV analysis threshold used for these three detectors.

timing parameters of interest are `pminrtc` (10%–40% rise-time of the largest of the four phonon pulses) and `pdelc` (relative delay of the 20% point of the largest phonon pulse with respect to the start-time of the ionization pulse). The cuts are positioned such that the estimated leakage of surface-electron events into the nuclear-recoil band for the WIMP-search data itself is optimized by minimizing the ratio P_{90}/α, where P_{90} is the Poisson 90% upper limit on the number of surface events that will leak into the $\pm 4\sigma$ nuclear recoil band, and α is the efficiency of the phonon-timing cuts on accepting neutrons. Note we do not intend to statistically subtract any leakage surface-electron events present in the WIMP-search data set. Hence the conservative optimization outlined above. The scaling of the number of surface-electron events for estimation of P_{90} between the gamma-calibration data sets (see Sect. 3.1) and the WIMP-search data sets can be done by scaling the number

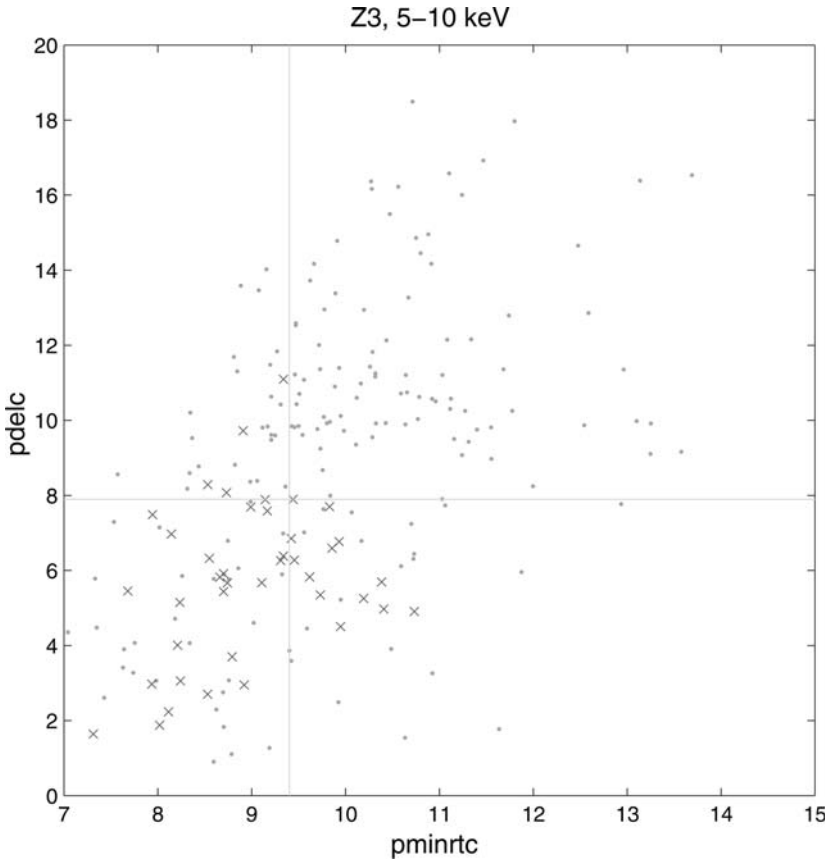

Fig. 6. Phonon timing quantities for the Ge detector Z3 for the 5–10 keV recoil energy bin. The grey points are neutron events from a ^{252}Cf calibration source, and the ×'s are intermediate-yield (beta) calibration events (below 3σ of the electron recoil acceptance band). The lines indicate the optimized cut positions for the timing variables of interest. Above 20 keV the phonon signal to noise is sufficiently large that a cut using only `pdelc` is sufficient for rejecting all calibration betas.

of intermediate-yield events observed between the electron-recoil acceptance band (3σ) and the 4σ nuclear-recoil acceptance band for each of the data sets. As will be shown below in the WIMP-search data sets, this phonon-timing cut approach rejects most of the surface events (as well as a large fraction of the bulk volume electron-recoil events) whilst preserving most of the nuclear-recoil signal-region events of interest.

4 The First WIMP Search at Soudan

4.1 Overview of Run 118

The first WIMP-search data at Soudan was taken between October 11th, 2003 and January 11th, 2004. We performed ^{133}Ba (and ^{60}Co) gamma calibrations on a regular basis to monitor the stability of both the ionization and phonon channels. We also performed three short-duration ($\sim$1 hour each) neutron calibrations *in situ* during the course of the run (November 25th, 2003, December 19th, 2003, and January 5th, 2004) to monitor the nuclear recoil signal acceptance band. These calibrations, and the observation of the 10.4 keV Ga line from neutron activation of Ge, indicate that the energy calibrations were accurate and stable to within a few percent during the course of the run.

We performed a blind analysis of the WIMP-search data, in which the nuclear-recoil region was not inspected until all cuts and analysis thresholds were defined using *in situ* gamma and neutron calibrations. The cut efficiencies were determined after the unblinding of the nuclear-recoil region, but the cuts themselves were not subsequently altered. Upon unblinding, no candidate nuclear-recoil events were observed in the WIMP-search data set, which allowed a new exclusion limit to be set on the WIMP nucleon cross-section [1].

4.2 Backgrounds

Figure 7 summarizes the observed gamma backgrounds and Monte Carlo simulations of likely sources of contamination. The Radon gas levels at Soudan are significant $\sim 500\,\mathrm{Bq/m^3}$. Thus shortly into Run 118, on November 6th, 2003, an old-air purge system was introduced that flushed the innermost part of the shield. The overall gamma rate dropped by a factor of 5 over the next few days. The Monte Carlo simulations now indicate a radon level of $\sim 35\,\mathrm{Bq/m^3}$ within the shield. The upper limit on ^{210}Pb in the inner lead shield is 0.2 ppb. No ^{40}K has been detected, the upper limit being 0.25 ppm. For the inner and outer polyethylene shields the U/Th contamination were measured before-hand to be 30 ppt and 1 ppb respectively. The Cu of the cans had also been measured before-hand to contain less then 0.5 ppb U/Th/K. Figure 7 suggests an additional contribution is required for the detectors towards the bottom of the Tower.

The overall beta event rate (defined as events with relative ionization yield below 3σ of the electron-recoil band and above 2σ of the nuclear-recoil band) also dropped with the introduction of the old air purge into the shield, by a factor of two. By relating the decrements in both gamma and beta rates we have estimated [10] that surface ejected electrons, due to high energy gammas, contribute half of the total beta background, with the rest being due to beta-emitter contamination on the detector surfaces themselves or nearby. Our studies of the ^{133}Ba and ^{60}Co calibration data sets and Monte

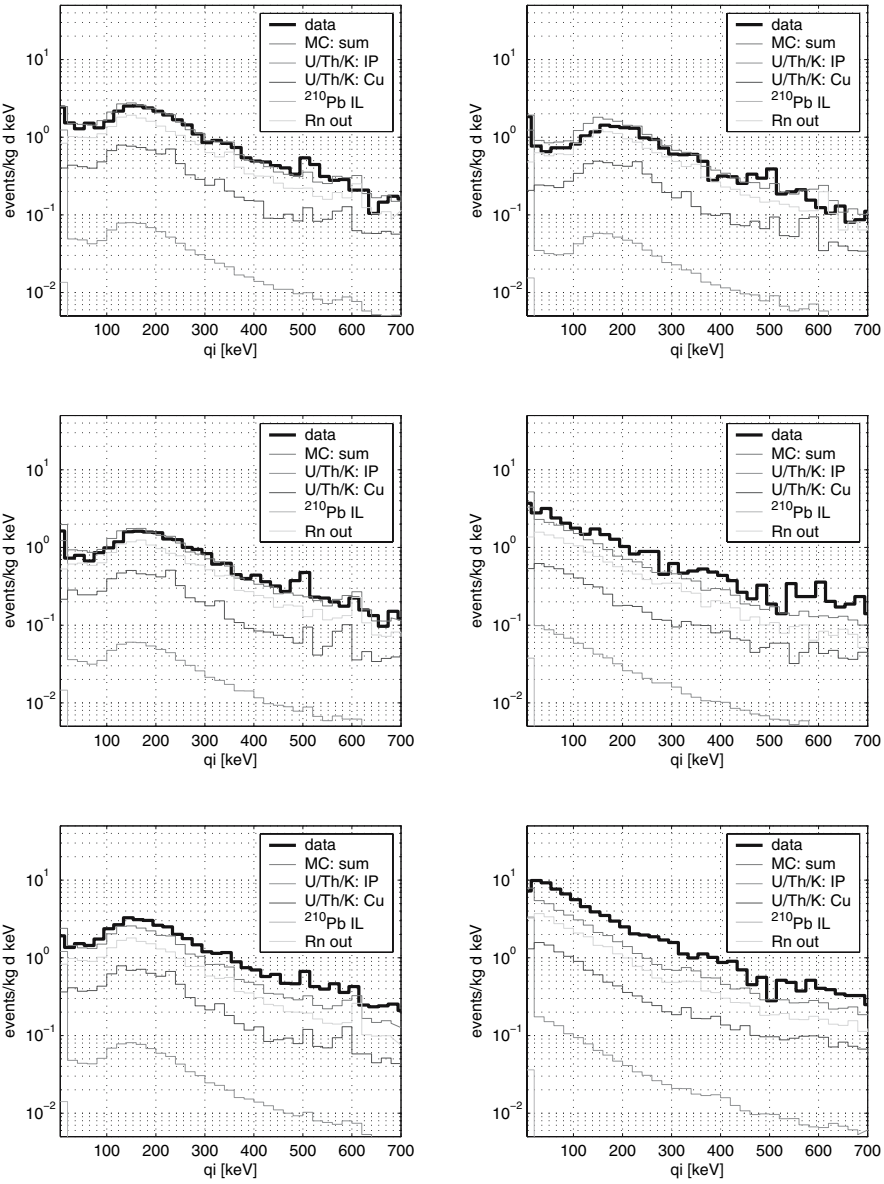

Fig. 7. Measured gamma spectra for Z1-Z6 accumulated during background running whilst searching for WIMPS. The insets indicate the most likely source contributions as determined from Monte Carlo simulations. "IP" refers to contamination within the Inner Polyethylene part of the shield, "IL" refers to contamination of the Inner Lead part of the shield, and "Rn out" refers to Radon gas outside of the old-air purged volume. For this first WIMP-search run at Soudan the purged volume effectively included only the innermost shielding surrounding the icebox.

Carlo studies [10] indicate that only 2% of the *single-scatter* surface-ejected electrons have an ionization yield sufficiently low for them to appear in the nuclear-recoil acceptance band (prior to any phonon timing cuts being introduced). Thus this source of background is negligible compared to surface contamination by the beta emitters present.

Possible sources for surface contamination include: ^{210}Pb plate-out from Radon gas present during the detectors' fabrication and testing; ^{40}K; ^{14}C; and other, more exotic, sources. Monte Carlo studies and surface material analysis studies of test wafers indicate that ^{40}K and ^{14}C contribute $< 20\%$ to the total. In contrast, the rate of alpha particles observed during Run 118 is consistent with the majority of the beta-emitters being due to ^{210}Pb plate-out. Subsequent to Tower 1 fabrication and assembly, additional measures have been put in place to reduce the radon exposure for later towers. Their running at Soudan will further inform us on this issue.

The Monte Carlo simulations [10] further indicate that the depth-profile of such beta surface-contamination events and resultant ionization yield can be closely mimicked by surface-ejected electrons that *double-scatter* between detectors. Thus the identification and study of such events from the gamma calibration data sets will allow further progress in the possible future statistical subtraction of such events.

For the short-exposure WIMP search performed at Soudan reported here, no neutron background events are expected to contaminate the muon-anticoincident nuclear-recoil acceptance band of the detectors [10]. The majority of the neutrons at Soudan, from (α, n) reactions in the cavern rock, are moderated by the 50 cm of polyethylene shielding present (see Sect. 2.2). Neutrons produced by through-going muons interacting in the lead shield and copper cryostat are classified as "internal" neutrons, the vast majority of which will be tagged by the present muon-veto system. Muons interacting in the rock surrounding the cavern produce "external" neutrons. They, and their associated cascades, have a $\sim 50\%$ chance of producing a signal in our present muon veto shield. The external neutrons that do not generate a veto signal form the dominant neutron background expected at Soudan [10]. Such an external event is not expected to occur until several years of WIMP-search running have been performed at Soudan.

4.3 Cuts and Their Efficiencies

The accumulated low-background-running livetime of 52.6 livedays from Run 118 is shown in Fig. 8. Noticeable interruptions to data-taking include cryogenic servicing, LED flashing of detectors (see 3.1), gamma and neutron source calibrations, electronic outrages, and cryogenic runaways (see 2.3). Other, known, detector response failures and noise-trigger bursts have also been taken into account and relevant data sets excluded from further analysis. The overall livetime efficiency was 62% and approached 75% towards the end of the run.

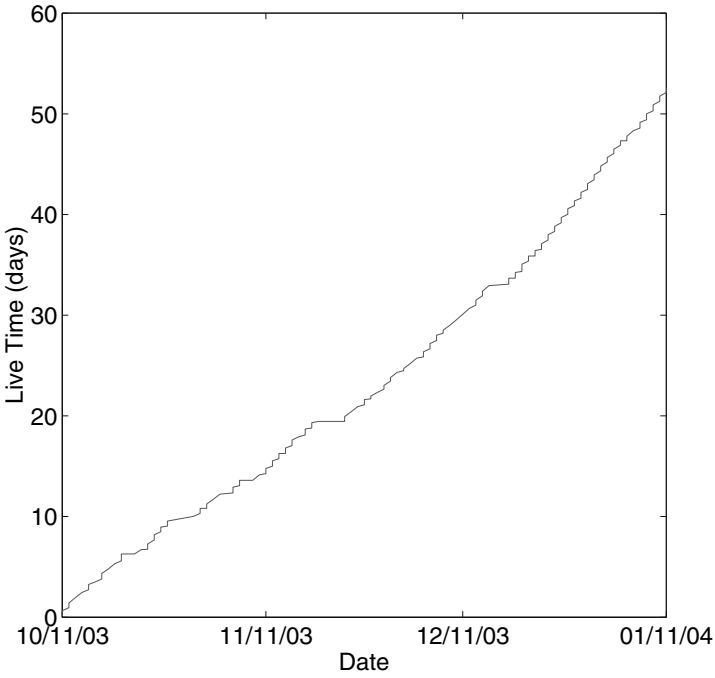

Fig. 8. Accumulated live-time of the first WIMP-search data sets taken at Soudan. The interruptions to data-taking are explained in the text.

A number of minor subsequent data-quality cuts are implemented to remove individual pile-up events, pulses with poor pulse-shape, glitches, and noise-triggered events. A total of 5% of events are removed by these cuts. In addition the muon-veto cut removes another 3% of remaining events, due to accidental veto coincidences within the 50 µs timing window chosen. The ^{133}Ba calibration sets (see Sect. 3.1) are used to define an inner-electrode ionization signal threshold cut, which is set at 5σ of the inner-electrode noise. As described in Sect. 2.4, the outer electrode is used to identify and reject events which deposit some ionization energy in the outer electrode. The ^{133}Ba calibration data sets are used to define an acceptance cut where the fitted amplitude for pulses in the outer-electrode must remain within the outer-electrode ionization noise, with some allowance for electrical cross-talk (5%) for large amplitude inner-electrode pulses. As discussed in Sect. 3, gamma and neutron calibrations are used to define the nuclear recoil signal acceptance region, both in relative ionization yield and phonon-timing.

Figure 9 summarizes the efficiencies of all the relevant cuts for the Ge detectors as a function of recoil energy [1]. Some of the cut efficiencies can be determined from the WIMP-search data electron-recoil events, scaled to the centroid of the estimated nuclear recoil bands; most of the others can

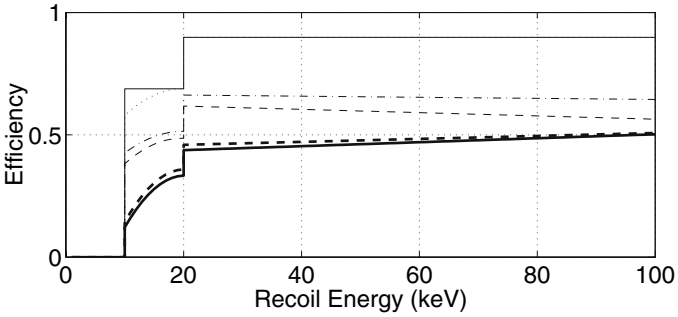

Fig. 9. Overall efficiency averaged over the Ge detectors (Z1, Z2, Z3 & Z5), and over the F5 and OF usages in the first, blind analysis. The solid thin line only includes the charge χ^2, the phonon pre-trigger, and the muon-veto cuts. The step at 20 keV is due to Z1's 20 keV analysis threshold. The dotted line also includes the charge threshold cut. The dot-dashed line also includes the outer charge-electrode cut. The thin dashed line also includes the nuclear-recoil acceptance band cut efficiency. The thick solid line also includes the phonon-timing cut and is the overall WIMP-detection efficiency for this blind analysis. (The thick dashed line shows the corresponding overall efficiency if OF-only quantities had been used, see text.)

be determined from the (low statistics) ^{252}Cf neutron calibrations, as they effectively populate the detectors uniformly with nuclear-recoil events. Monte Carlo simulations of the neutron calibrations also assist in generating mock event sets where the ionization signal and position are known for each event. These can then be convoluted with the experimental noises, and the cut efficiencies determined [10].

Shortly after unblinding the WIMP-search data a computer coding error was discovered. In the off-line analysis there are two estimates available for the charge pulse amplitudes. The intended, lower-noise estimate (labelled as "OF" for optimal filter) was not used for just over half the WIMP-search data. Instead a noisier estimate designed to analyze high-energy pulses that saturate the digitizers was used (labelled as "F5" for fit-5). One of the consequences of this error is a small change in the efficiency for the Run 118 WIMP search, mainly due to the outer charge electrode cut being set with OF amplitude estimates, but then being used with noisier F5 estimates. An averaged, corrected, overall efficiency estimate is shown in Fig. 9 along with the efficiency of the subsequent non-blind analysis performed on the same data set using the intended OF estimates [1].

4.4 Leakage Estimates

The overall average efficiency shown in Fig. 9 results in a spectrum-averaged effective exposure of 19.4 kg-days between 10–100 keV for a 60 GeV/c^2 WIMP incident on the 4 Ge detectors (Z1, Z2, Z3 and Z5) of Run 118.

The leakage of gamma events (that cause bulk electron recoil events) into the nuclear recoil band is very small. From the ^{133}Ba calibration sets of Run 118 we estimate a rejection efficiency of $> 99.997\%$ at 90% C.L. for single-scatter gamma events observed in the Ge detector Z1. The rejection factor for the other Ge detectors is even higher. In the WIMP-search data of Run 118 we observed 2443 single-scatter gamma events for all four Ge detectors and thus expect < 0.07 leakage events (at 90% C.L.) due to gammas in the energy range of interest (10–100 keV).

The usage of the ^{133}Ba calibration sets to further estimate leakage due to surface electrons was described in Sects. 3.3 & 4.2. Using the beta distributions observed in the ^{133}Ba calibration sets and the known number of single-scatter muon-anticoincident beta-events that fall outside of the nuclear-recoil acceptance region in the WIMP-search data of interest, an estimate of 0.69 ± 0.24 for the four Ge detectors can be derived [10].

As indicated in Sect. 4.2, Monte Carlo simulations have been performed for both internal and external sources of neutrons. For the Run 118 WIMP-search data set we estimate 0.05 external neutrons and 1.9 internal neutrons. The internal neutrons would be tagged with high efficiency by the muon veto shield (see Sect. 2.2). No muon-coincident neutron candidate events were observed in the Run 118 WIMP-search data set.

4.5 Run 118 WIMP-Search Results

Figure 10 shows all the single-scatter unvetoed events observed in the Run 118 WIMP-search after unblinding the nuclear-recoil acceptance region. All cuts have been applied, except the phonon-timing cuts. The 10 keV Ga line in Z1 due to neutron activation is discernible. As reported in Sect. 2.4 the Si detector Z6 is contaminated, with a large number of intermediate yield events apparent.

Figure 11 is the same as Fig. 10 but now also includes the phonon-timing cut. For this initial, blind, analysis *no* events are observed in the nuclear recoil acceptance band for this 19.4 kg days exposure of the 4 Ge detectors (Z1, Z2, Z3 & Z5). As indicated in Sect. 3.3, the phonon-timing cut has also removed a significant fraction of the bulk electron recoil events ($Y \simeq 1$).

5 Conclusions

The resulting WIMP-nucleon cross-section exclusion plot is shown in Fig. 12 for a coherent scalar interaction [1]. The first Soudan data sets a new upper limit of $4 \times 10^{-43}\mathrm{cm}^2$ at 90% C.L. for a WIMP mass of 60 GeV/c^2. This is a factor of four better than the previous best limit set by EDELWEISS [6]. Under standard galactic halo and nuclear model assumptions, CDMS is clearly incompatible with the original DAMA signal region [11]. For the DAMA signal region under other halo models see [12].

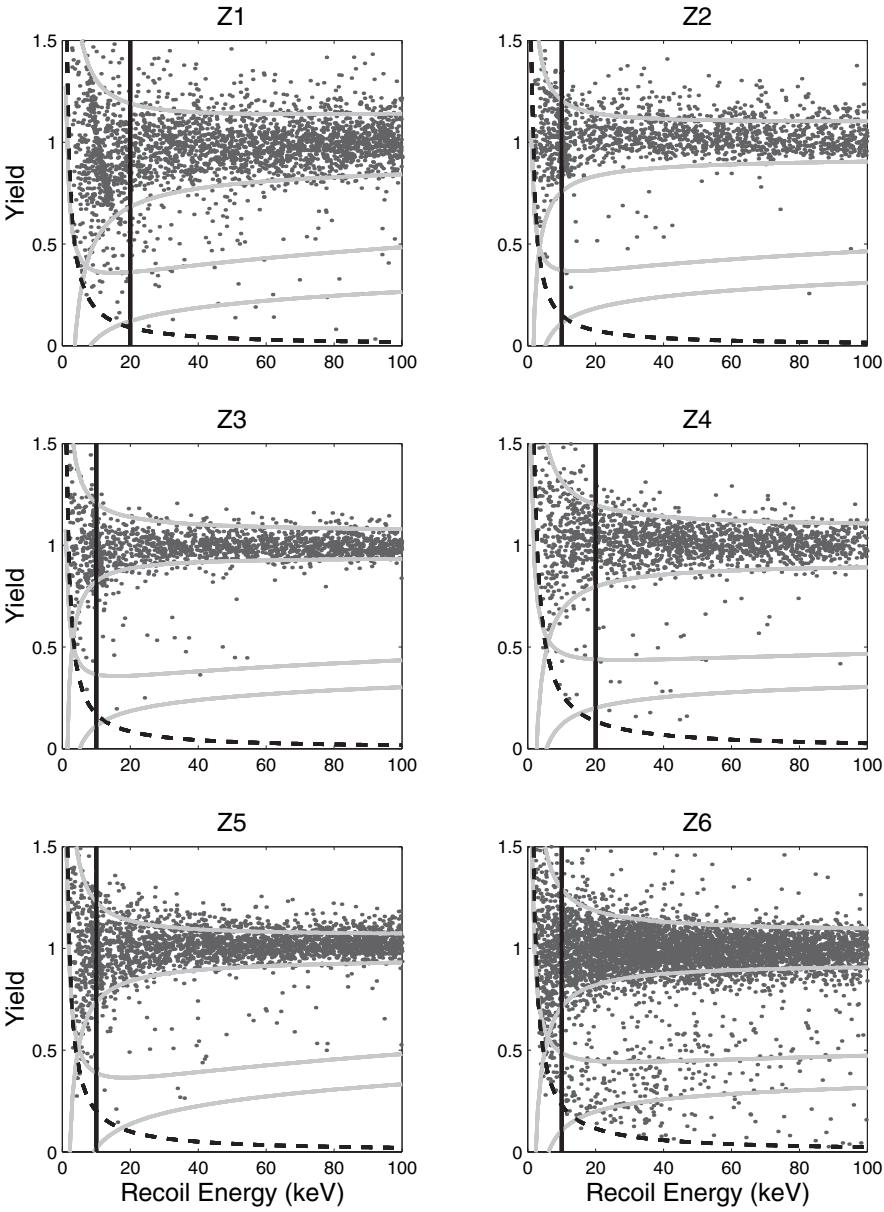

Fig. 10. Single-scatter muon-anticoincident events observed in the WIMP-search data set in all detectors of Tower 1, after all cuts except the phonon-timing cut. The grey lines denote the nuclear and electron recoil acceptance bands, the vertical black lines denote the analysis thresholds, and the dashed black lines denote the charge threshold cuts.

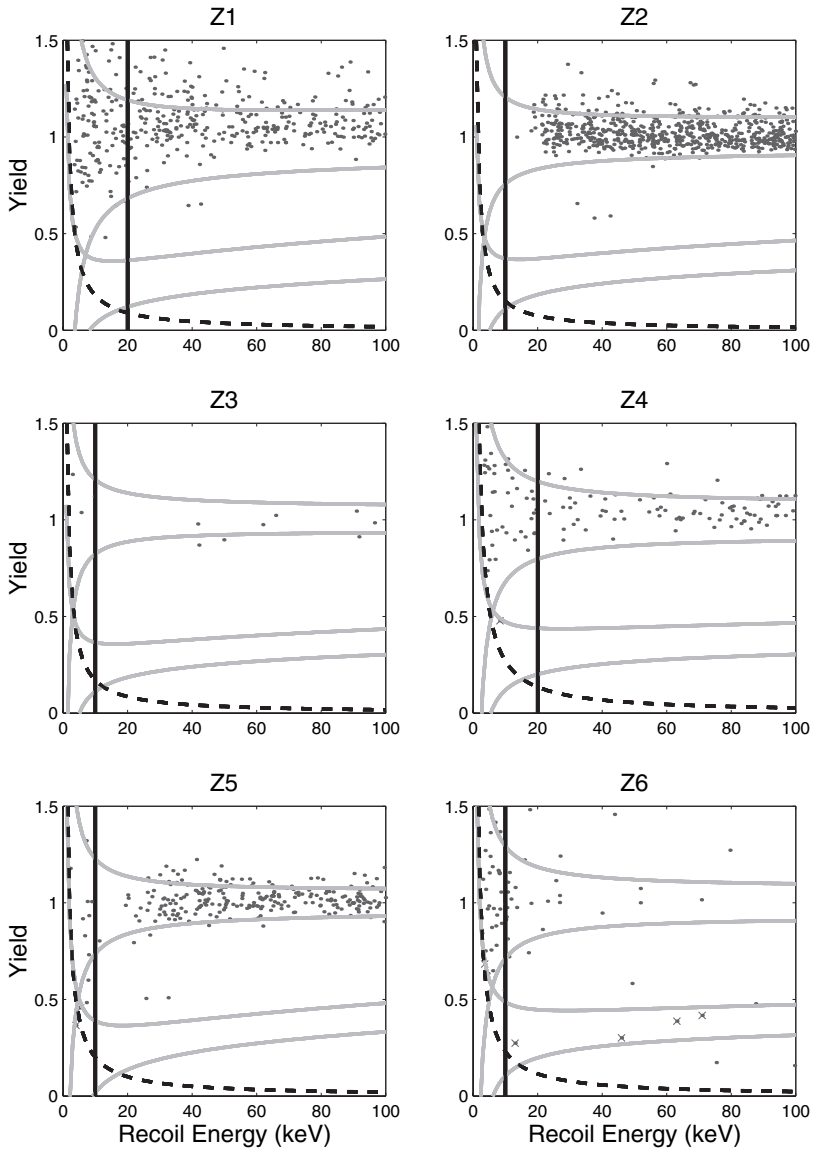

Fig. 11. Single-scatter muon-anticoincident events observed in the WIMP-search data set in all detectors of Tower 1, after all cuts including the phonon-timing cut. The grey lines denote the nuclear and electron recoil acceptance bands, the vertical black lines denote the analysis threshold, and the dashed black lines denote the charge threshold cut. Note that no events survive in the nuclear recoil band for this first, blind, analysis for the Ge detectors (Z1,Z2,Z3 & Z5).

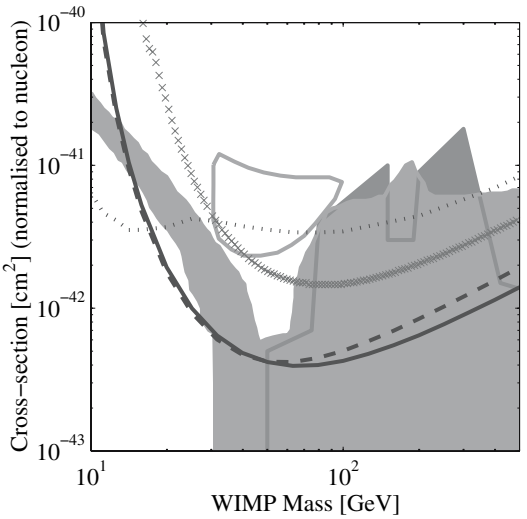

Fig. 12. First WIMP-exclusion limit from CDMS II at Soudan, with no candidate events in 19.4 kg-days effective Ge exposure (solid curve) [1]. Parameter space for the WIMP-nucleon scalar cross section above the curve is excluded at 90% C.L. Some theoretical predictions from Supersymmetry models for the same standard galactic halo model ($v_0 = 220\text{kms}^{-1}$ etc. [1]) are indicated by the dark grey [13] and light grey [14] shaded regions. Also shown are earlier limits from CDMS at SUF (dots) [8], EDELWEISS ($\times$'s) [6] and the second, non-blind analysis of the first CDMS Soudan data (dashed curve). The original DAMA (1–4) 3σ annual modulation signal [11] is shown as a closed contour under the same standard model assumptions.

A spin-dependent WIMP-nucleon cross-section investigation of DAMA and CDMS data has been performed by Savage et al. [9]. They comment that CDMS (using both Ge and Si data from this and past runs at SUF) also sets the most competitive exclusion limits for the WIMP-nucleon cross-section for the case where the coupling is mostly to the neutron spin. A more refined analysis of the CDMS data for this case is in progress [10].

The first CDMS Soudan data also confirms that the earlier WIMP exclusion limits of CDMS at SUF [8], and EDELWEISS [6], are correct and that the events observed in each case were correctly interpreted as not being due to a WIMP signal.

6 Outlook

As reported in Sect. 4.3, a computer coding error was discovered shortly after the unblinding of the Run 118 WIMP-search events. Apart from a slight change in the detection efficiency, a subsequent reanalysis [1] with the in-

tended OF estimates resulted in the appearance of a "leakage" event within Z5's nuclear recoil acceptance region at an energy of 64 keV. The event had been rejected by the initial blind analysis as it was counted as a partial outer electrode event, with F5 quantities being subjected to a cut determined by OF quantities. This event results in only a slightly different WIMP exclusion limit from that reported for the initial blind analysis (see [1] and Fig. 12) as kinematically it would correspond to a very massive WIMP. In reality, this leakage event is most likely to be a surface electron event (see the discussion in Sect. 4.4). Subsequent to Run 118 more sophisticated phonon-timing cuts have been developed. Going forward, we do not anticipate such surface electron events will be a significant factor in the future Soudan WIMP-search data sets.

The subsequent WIMP-search run at Soudan, Run 119, had both Towers 1 & 2 operational. That run ended in August 2004 and its data analysis completion (and unblinding) will occur in early 2005. At the time of writing, the cryogenic system at Soudan is receiving a number of upgrades (to overcome the livetime issues mentioned in Sect. 2.3) and three more towers of detectors have been installed. During 2005 we intend to run all five towers, which together contain 19 Ge ZIPS, each 250 g, and 11 Si ZIPs, each 100 g. The end of 2005 is the programmatic end of CDMS II. Thus, we are in the process of proposing our plans beyond CDMS II [15].

Acknowledgements

This work is supported by the National Science Foundation under Grant No. AST-9978911, by the Department of Energy under contracts DE-AC03-76SF00098, DE-FG03-90ER40569, DE-FG03-91ER40618, and by Fermilab, operated by the Universities Research Association, Inc., under Contract No. DE-AC02-76CH03000 with the Department of Energy. The ZIP detectors were fabricated in the Stanford Nanofabrication Facility operated under NSF. We are grateful to the Minnesota Department of Natural Resources and the staff of the Soudan Underground Laboratory for their assistance.

References

1. D.S. Akerib et al.: Phys. Rev. Lett. **93**, 211301 (2004)
2. J.R. Primack et al.: Ann. Rev. Nucl. Part. Sci. **38** 751 (1988)
3. K. Hagiwara et al.: Phys. Rev. **D66**, 010001 (2002)
4. J. Ellis et al.: Phys. Rev. **D67**, 123502 (2003)
5. J.D. Lewin and P.F. Smith, Astropart. Phys. **6**, 87 (1996)
6. A. Benoit et al.: Phys. Lett. **B545**, 43 (2002)
7. R.M. Clarke et al.: Appl. Phys. Lett. **76**, 2958 (2000)
8. D.S. Akerib et al.: Phys. Rev. **D68**, 82002 (2003)

9. C. Savage, P. Gondolo and K. Freese: *astro-ph/0408346*
10. D.S. Akerib et al.: *in preparation*
11. R. Bernabei et al.: Phys. Lett. **B480**, 23 (2000)
12. R. Bernabei et al.: Riv. Nuovo Cim. **26**, 1 (2003)
13. E.A. Baltz and P. Gondolo: Phys. Rev. **D67**, 063503 (2003)
14. A. Bottino et al.: Phys. Rev. **D69**, 037302 (2004)
15. R.W. Schnee et al.: *these Proceedings*

Dark Matter Search at Boulby Mine

Roland Lüscher[1], on behalf of the UK Dark Matter Collaboration[1,2,3,4]

[1] CCLRC / Rutherford Appleton Laboratory, Chilton, Didcot, OX11 0QX, UK
r.luscher@rl.ac.uk
[2] Imperial College, Blackett Laboratory, London, SW7 3BZ, UK
[3] Dept of Physics and Astronomy, University of Sheffield, Hounsfield Road, S3 7RH, UK
[4] Department of Physics, University of London Queen Mary, London, E1 4NS, UK

The Boulby Dark Matter Collaboration is running a WIMP Dark Matter research programme in the underground laboratory of Boulby Mine for over a decade. Results have been reported previously from the NaIAD detector array – using scintillation properties in NaI crystals [4, 5, 6]. Currently, the programme is based on (1) liquid Xenon (LXe) as the WIMP target and (2) directional detection in low pressure gas detectors (Drift, reported at this conference [3]). This contribution concentrates on Zeplin-1, the LXe first project: a 3.1kg of LXe scintillation detector with a background discrimination based on Pulse Shape Analysis. The current status of the experiment is shown and first limits on nuclear recoil events are reported. Setups with improved background discrimination tools are commissioned: Zeplin-2 and Zeplin-3 will be installed underground early 2004. Progress are reported in another contribution to this conference [1]. These are important steps towards the design of a ton-scale LXe Dark Matter detector array (reported in [2]).

1 Liquid Xenon as Dark Matter Target

The Zeplin project (Zoned Proportional scintillation in LIquid Noble gases), takes advantage of the particularly appropriate properties of Xe: it is an heavy nuclei for a large spin-independent coupling and has an appreciable abundance of isotopes with spin for a large spin-dependent coupling. Low background Xe is available commercially. LXe is known as a good scintillator: emitting in the UV region (175 nm), it enables a low energy threshold. Moreover, the interaction process in LXe owns characteristics which translate into a potentially high background discrimination.

Any recoil in LXe give rise to both ionisation and excitation of Xe atoms. The excitation result in the emission of a 175 nm photon from either a singlet (with decay time ~ 3 ns) or a triplet state (~ 27 ns). The ratio single/triplet is 10 times bigger for nuclear recoil compared to electron recoils. In the absence of an electric field, the ionisation recombines to produce further excited Xe atoms. The recombination time depends on the ionization density: for nuclear recoil, the latter is very high and recombination very fast. For electron recoil,

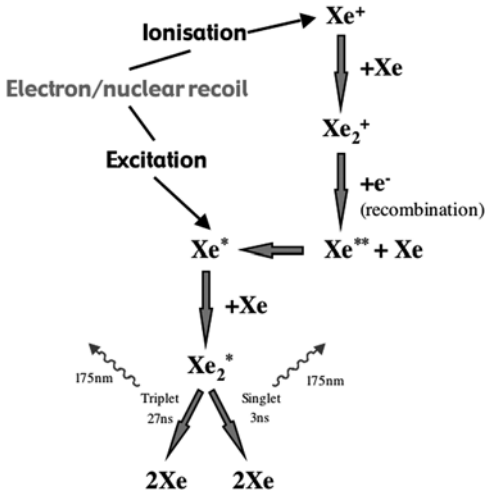

Fig. 1. Scintillation in LXe: the singlet/triplet ratio and the recombination speed differ for nuclear and electron recoils, enabling Pulse Shape Discrimination [7, 8].

the lower density leads to longer times. The scinitillation process in LXe is described schematically in Fig. 1.

2 The Zeplin-1 Detector

Zeplin-1 is based on a pure scintillator design. The LXe is viewed by 3 PMTs through silica windows (Fig. 2). Between the fiducial volume, which contains 3.1 kg, and each window, there is a turret of LXe which acts both as light guide and shielding. None of the turret volume is directly seen by any other PMT than the one it faces to. The signal from any event in these zones (likely background from PMT glass) is thus mostly seen by the corresponding PMT and this asymmetry is used to reject these events. This defines the fiducial volume (Fig. 3).

The detector is enclosed in a 1 tonne active Compton veto shielding, based on PXE liquid scintillator and viewed by 10×8" hemispherical PMTs. Its function is to veto gamma activities from the PMTs and from the surroundings. An important criteria in the choice of the scintillator has been its safe use in an underground laboratory and working mine. From Monte-Carlo simulations, a veto efficiency of 80–90% below 100 keV has been estimated.

The system is surrounded by 25 cxm of lead and installed in the underground laboratory of Boulby mine (Fig. 5), at a depth of 2800 mwe.

Purification of the Xe gas is performed by using an Oxisorb, as well as by pumping on the frozen Xe and subsequent fractionation of the Xe gas. This removes quencher contamination (O_2, CO_2) to acceptable levels. The

Fig. 2. The Zeplin-1 design: a pure LXe scintillator with 4 kg active mass.

Xenon is purified prior to the liquefaction into the target, but not circulated or repurified afterwards. No decrease of light yield has been observed during a 50 day run.

The detector is triggered by a 3-fold coincidence of a single p.e. in each tube. With a light yield of at least 1.5 p.e./keV in the data runs, it gives a 2 keV threshold. The trigger efficiency has been calculated using Poissonian statistics The signals are digitized using an Acqiris cPCI based DAQ system.

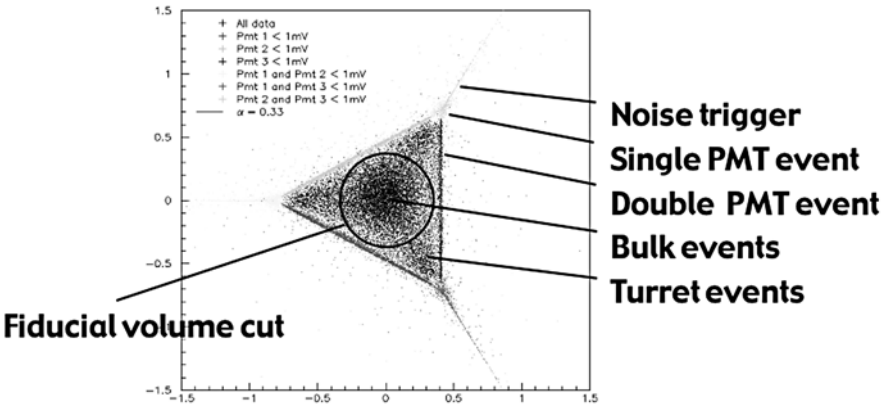

Fig. 3. PMT response plan: turret events are mainly seen by the direct PMT, enabling their discrimination.

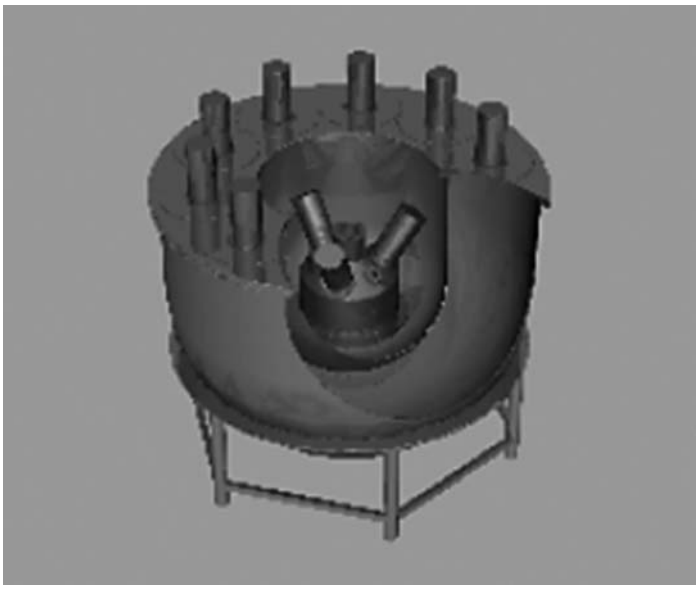

Fig. 4. Zeplin-1 in a 1-ton scintillator active veto.

The dead-time is smaller than 2 μs, its efficiency hence bigger than 99.9% during normal data runs.

2.1 Detector Performance

Daily energy calibration is performed with a ^{57}Co source automatically placed between target and veto. The 122 keV gammas convert within the bottom

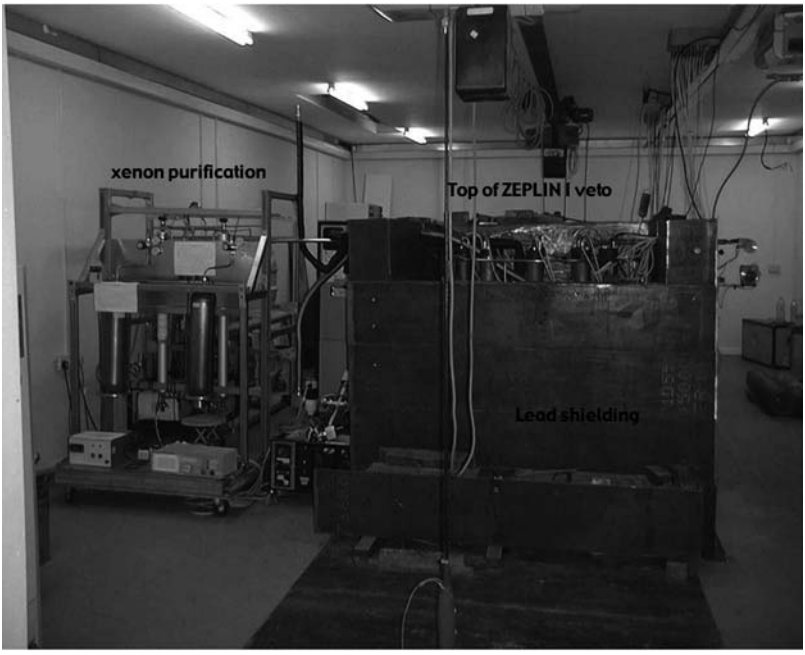

Fig. 5. Zeplin-1 underground, surrounded by its lead shielding.

$\sim$3 mm in the target, making it a calibration point source. A 30 keV K-shell X-ray is also observed in the spectrum, its presence has been confirmed through a Geant4 simulation (Fig. 6).

A full light collection simulation has been performed (Fig. 7), showing variations of efficiencies from a maximum of 18% at the bottom of the target down to 4% just below the Xenon delivery line. This affects the measured energy of an event and has been observed in higher energy gamma calibrations (^{60}Co, ^{137}Cs sources): as different fractions of the target are illuminated, the peak position reflects the reduction in light yield. The observations match well the light collection efficiency simulation.

The light collection study has been extended to each tube separately. This permits to assess the capability of rejecting events occurring in the turrets. A turret parameter (S_3) translates the asymmetry of events into a number. $S_3 = 0.81$ indicates an event with all the signal in a single PMT, while a completely symmetric event would give a null value. In a turret event, in the ideal case of no loss of light within the chamber, one single PMT is expected to get 66% of the light, resulting in S_3 being 0.41.

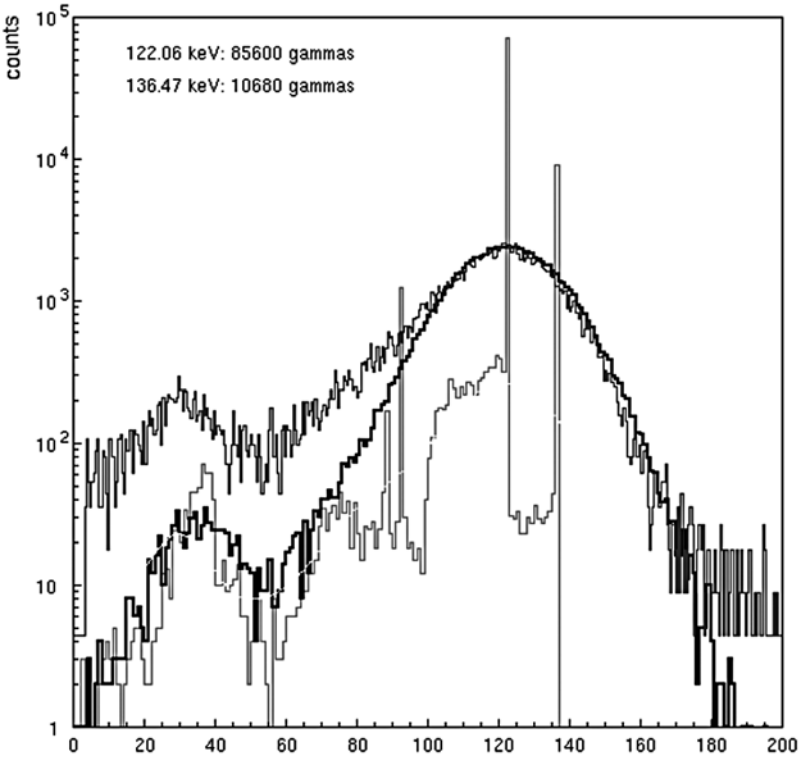

Fig. 6. ^{57}Co source calibration: a Geant4 simulation (narrow peaks) with set resolution (lower broad peak spectrum) is compared to data (higher broad peak spectrum).

3 Background Discrimination and Results

Background discrimination is provided by the difference in time constant of the scintillation pulse induced by nuclear or electron recoils. The parent pulse shape is approximately double-exponential, which could in principle be fitted to each pulse recorded. In practice it is preferable to characterise each pulse by a single parameter defined as the mean charge arrival time of the (integrated) pulse between 5% and 90% of the maximum amplitude. This parameter is then free from any assumptions about the parent pulse shape. This mean charge arrival time is extracted from the sum of the pulses of each event. The individual pulses are also analysed and used to reject noise or turret events. Neutron and gamma source calibrations have been done on the surface. Typical mean charge arrival time distribution are shown in Fig. 8. The time constant ratio is observed to be about 0.5 in the energy range of interest (3–10 keV). The 90% C.L. limit on nuclear recoil is extracted by studying the monotonically rising edge of the time constant distributions and comparing it with pure gamma data. These come from dedicated high

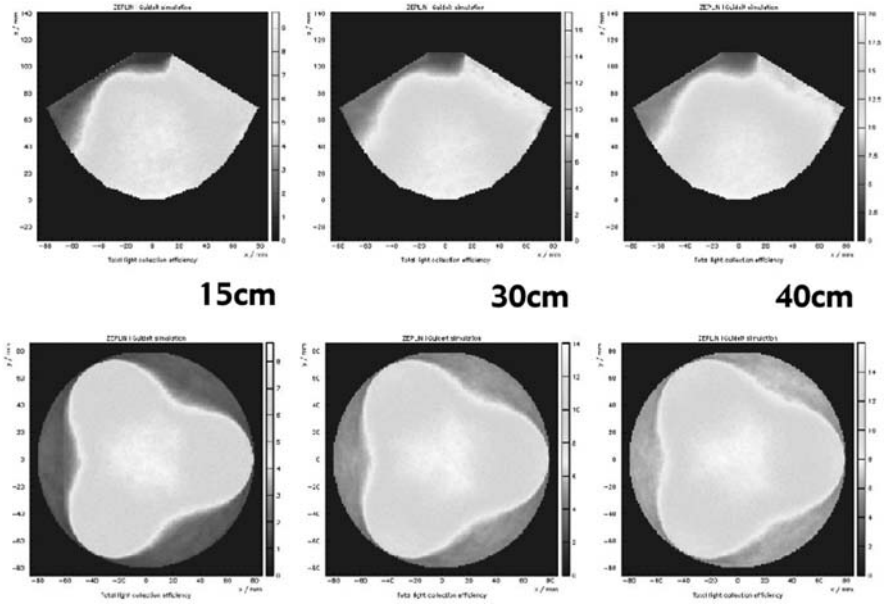

Fig. 7. Light collection simulation: a slice through a PMT-plan (top) and the girth (bottom) is shown for different attenuation length (from left: 15, 30 and 40 cm). A response matrix has been created to correct for the non-uniform light collection. No difference in the matrixes for these attenuation lengths has been observed.

statistic calibration runs (Compton events from ^{60}Co gammas) and from normal data events tagged by the Compton veto (Fig. 9). The upper limit on the number of nuclear recoils in each energy bin is then used to calculate the WIMP-nucleon cross section. The limit extracted from 293 kg×days of data (assuming standard halo parameters) in a preliminary analysis is shown in Fig. 10.

4 Outlook

A two-phase system is designed to measure both the scintillation and the ionization produced by interacting particles. Any particle interacting within the liquid xenon target will produce excitation and ionisation. A vertical electric field partially suppresses recombination; it drifts the ionisation electrons upwards through the liquid to the gaseous phase - where a wire planes define a high field region in which avalanche occurs and electroluminescence is created. Both scintillation and electroluminescence can be recorded by the same PMTs. The proportion of scintillation and electroluminescence released depends on the dE/dx of the particle interaction and differs for electron recoil (more electroluminescence) or nuclear recoils (mostly scintillation). For the

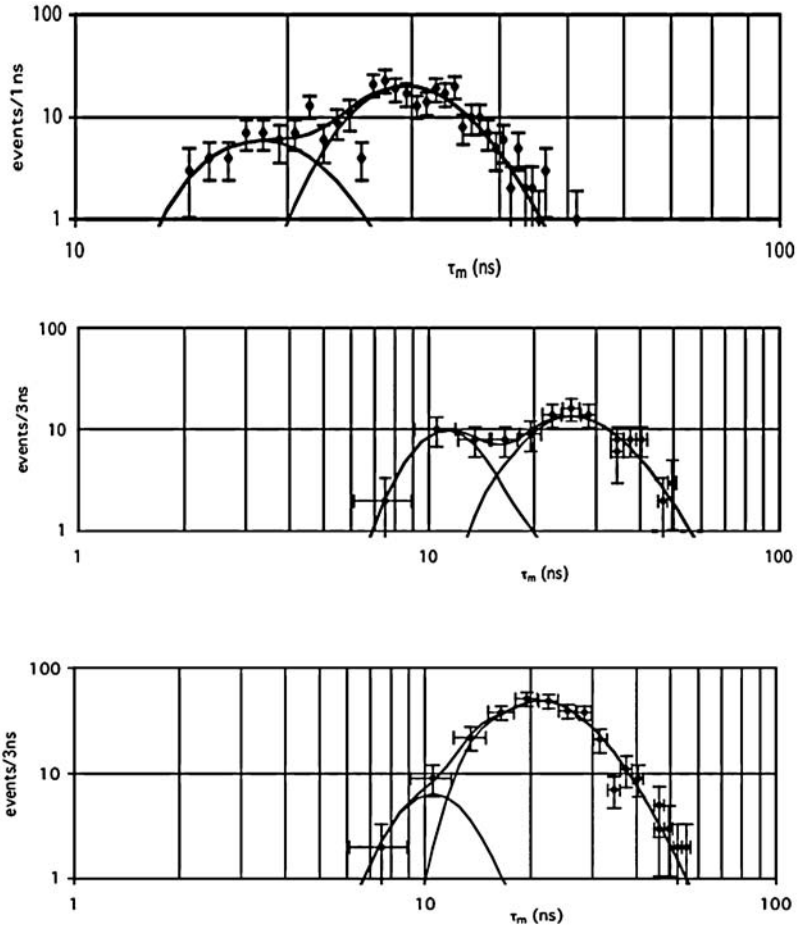

Fig. 8. Examples of neutron calibration of Zeplin-1, showing fits to the neutron and gamma populations. Tagged Am-Be source, 20–30 keV (top). Ambient neutrons and low intensity ^{60}Co gammas, 3–7 keV (middle). Low threshold Am-Be run, 3–8 keV (bottom).

latter, only a very high electric field may prevent part of the recombination and, thus, induce a secondary signal. The Zeplin-2 design is based on this dual-phase technology. The detector contains a target mass of about 30 kg. It will be surrounded by the liquid scintillator Compton veto from Zeplin-1. Sensitivity to rates of about 0.1–0.01 events/kg/day can be reached within 2 years of data. The construction is well underway and commissioning has started. The installation in the Boulby Mine laboratory is scheduled for early 2005. The Zeplin-3 design has been optimised in order to observe both scintillation and ionisation from the nuclear recoil events. As this requires a very high electric field (8 kV/cm in the liquid target), the liquid depth is con-

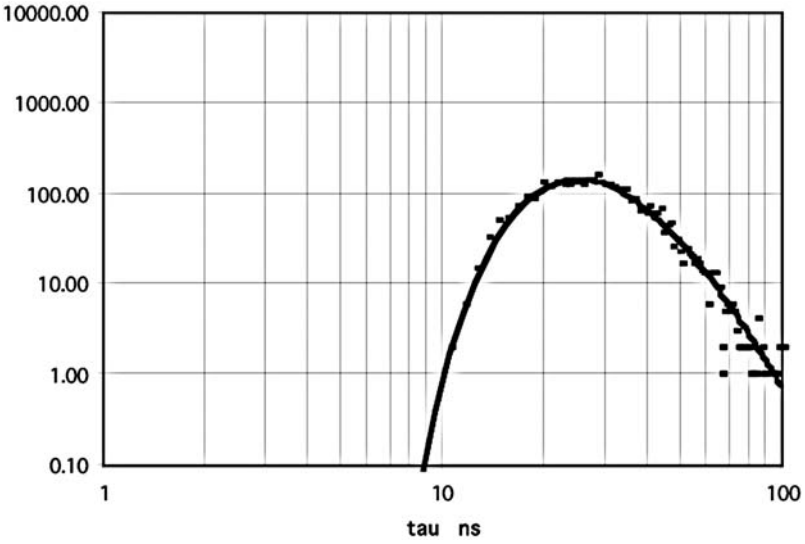

Fig. 9. Comparision of data with events tagged by the Compton veto: no difference in the mean time distribution is observed.

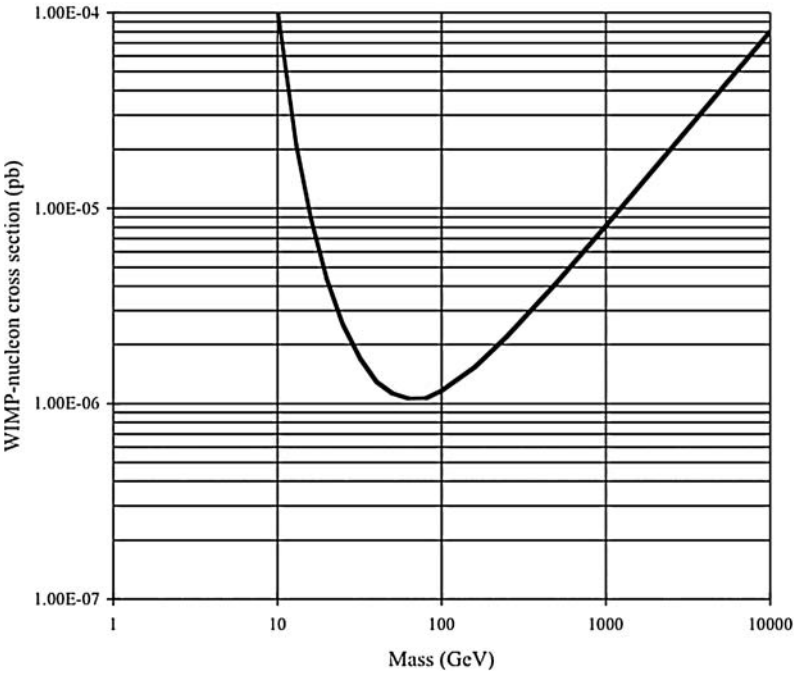

Fig. 10. Exclusion plot for spin-independent WIMP-nucleon cross-section versus particle mass (90% CL) from 293 kg-days (fiducial) running of Zeplin-1, based on standard halo parameters.

strained to 3.5 cm, with a radius of 20 cm. Both VUV signals are observed by an array of 31 photomultiplier tubes submerged in the liquid. The larger electroluminescence signal is used to determine the position of events, allowing definition of a fiducial volume. The design has a smaller fiducial mass (6 kg), but with an improved background discrimination and a lower threshold, similar sensitivities as Zeplin-2 will be reached. More details can be found in [1]. Schedule for installation in Boulby Mine is mid-2005.

4.1 Towards one tonne

The sensitivity of Zeplin-2 and Zeplin-3 in terms of WIMP-nucleon cross section is estimated to be in the regions of 10^{-8} pb. Many SUSY models predict lower cross sections, down to 10^{-10} pb regions. To cover these predictions, a detector mass of 1 tonne might well be needed. We are currently studying different design possibilities for a scale-up towards massive modules, with the constraint of achieving a low energy threshold [2].

Acknowledgements

The BDMC would like to thank Cleveland Potash Ltd for the continued support at Boulby mine.

References

1. H. Wang, this conference.
2. N.J.T. Smith, this conference.
3. N.J.C Spooner, this conference.
4. J.J. Quenby et al., Phys. Lett. B**351**(1995)70.
5. P.F. Smith et al., Phys. Lett. B**379** (1996) 299.
6. B. Ahmed et al, Astropart. Phys.**19** (2003) 691.
7. G.J. Davies, J.D. Davies, J.D. Lewin, P.F. Smith, W.G. Jones, Phys Lett B**320** (1994) 395.
8. T.J. Sumner et al., Proc 26th ICRC 2 (1999) 516.

Prospects for the Detection of SUSY Dark Matter

David B. Cline

Astrophysics Division, Department of Physics & Astronomy University of California, Los Angeles, CA 90095 USA

We present the status of the search for dark matter particles. The different methods include cryogenic detectors and liquid Noble gas detectors such as Xenon (ZEPLIN, etc.). We review the evidence for Dark Matter in the galaxy and the method to detect particle dark matter. The current limits on the search for dark matter are reviewed and some possibility to evade these limits using dark matter flows. The possible future one ton detectors are discussed as is the range of sensitivity of these detectors.

1 Introduction

The direct searches for dark matter particles are some of the most difficult experiments ever made as well as the most important. The detection of dark matter could:

(a) Resolve the issue of the existence of dark matter compared to the concept of modifying gravity in some way (MOND)
(b) Provide the discovery of supersymmetry, a profound advance in elementary particle physics
(c) Lead to the understanding of the dynamics of dark matter in our Halo (streams, flow, Halo model)
(d) Lead to a precision determination of the dark matter needed to study the equation of state and dark energy

Over the past 15 years many techniques have been developed to search for dark matter.

This article will first outline the evidence for dark matter and possible properties in the Milky Way. We will then concentrate on the current detectors and review the current search results and discuss the future prospects.

The report will rely strongly on the proceedings of the 5th Symposium on Source and Detection of Dark Matter and Dark Energy in the Universe, held at Marina del Rey, February 2004 and previous meetings.

2 The Evidence for Dark Matter

In 1993 F. Zwicky studied the galaxies in the COMA cluster and noted that the rotation velocities were too large for the system to be stable and bound. He suggested there must be missing mass in the cluster [2]. Today we know that these clusters are dominated by dark matter. The mass is not missing but is dark [3]. The rotation velocity or stars in undeveloped galaxies also indicate that there is dark matter in galaxies [3]. Perhaps the most convincing evidence comes from the WMAP data that shows [4]

$$\Omega_0 = 1.02 \pm 0.002 \tag{1}$$

and

$$\Omega_m \approx 0.29 \pm 0.05 \tag{2}$$

Baryons cannot account for this value of Ω_m. Therefore there must be appreciable non-baryonic dark matter in the universe. Equations should be centered and numbered consecutively, as in (1). An alternative method is given in (2) for long sets of equations where only one referencing equation number is wanted.

3 Dark Matter in the Milky Way Galaxy: Halo Uncertainty and Streams

In order to detect dark matter particles we must have an understanding of the flux of particles through any given detector on earth. Therefore we must understand the halo of dark matter for our galaxy [1]. In addition some models give clumps of dark matter, others give causes of dark matter [5]. These effects can increase or decrease the rate of interaction in an earth-bound detector. At the recent Marina del Rey meeting we devoted an entire session to the knowledge of our halo [1].

The halo model is very important when attempting to compare different types of experiments, say, direct search and annual variation searches [6]. There is no doubt that the ultimate test for the existence of dark matter will be the observation of an annual variation signal [7]. However there is a strong debate among the experiments as to whether this annual variation signal should be carried out with discriminated events (reduced background) or with raw data (large background). We will show an example of the former from simulation of the ZEPLIN II detector later in this article.

There are also models of dark matter caustics by P. Sikivie and colleagues that can give the opposite sign of the annual variation to that expected in the standard isothermal sphere model [5]. At the Marina del Rey meeting two notable contributions were given by Anne Green and Larry Krauss [1]. In Fig. 1 we show the kinematics of the halo velocity distributions for various

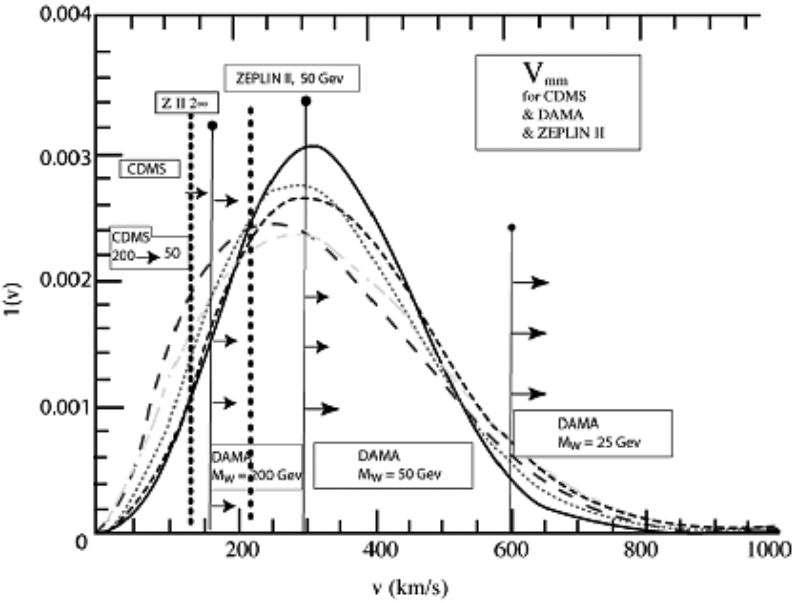

Fig. 1. Schematic of the halo velocity distribution with minimal velocities for CDMS, DAMA and ZEPLIN II; the figure is modified from [2].

detectors [8]. In Fig. 2 we show the work of L. Krauss and colleagues that compares annual variation signals to direct search signals for a large variety of halo models [1]. Note that the variation is not very large. We will discuss this later in the article when the current results of direct searches is described.

4 Methods for the Direct Search for Dark Matter Particles

The direct search for dark matter particles is among the hardest experiments ever undertaken in science [9]. Backgrounds exist for cosmic rays, natural radioactivity even at great depths underground. Early reviews can be found in [10]. Therefore the next generation detector will almost certainly use a method to discriminate against background as well as an active veto shield to reduce the neutron flux from cosmic ray induced events even at great depths underground.

The types of detectors can be generally classed as

1. Cryogenic
2. Liquid Xenon, Neon or Argon
3. Other methods such as bubble chamber or non-discriminating detector.

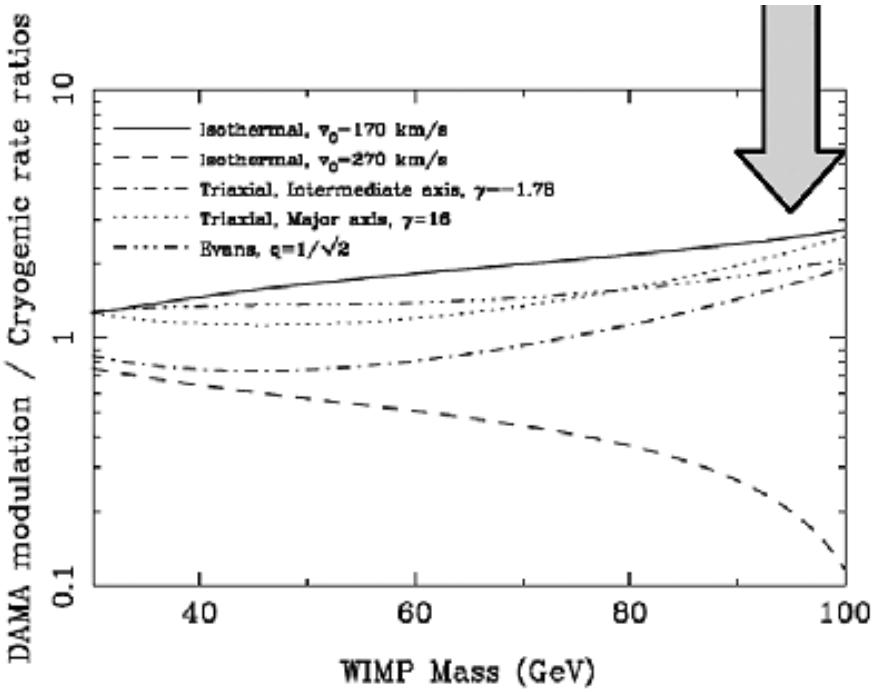

Fig. 2. Work of L. Krauss and colleagues in different halo models [1].

To get some sense of the number of detectors [2] and time scale we give a partial list in Table 1 [11].

4.1 Cryogenic Detectors

For more than 15 years several groups around the world have been studying the possibility of constructing a low temperature detector to measure the recoil energy of the nucleus having been hit by a WIMP [3].

Since this energy is in the range of kiloelectron volts the detector must act as a bolometer to measure the "heat" produced by the recoil [14]. Three groups have now made such detectors using this technique. These groups are:

(a) CDMS
(b) Edelweiss
(c) Cresst

All three groups have now reported limits in the in the search for dark matter particles. So far the nucleus of choice has been Ge or Si. However the Cresst group has worked with $Al0_2$ as well as CaW mixtures.

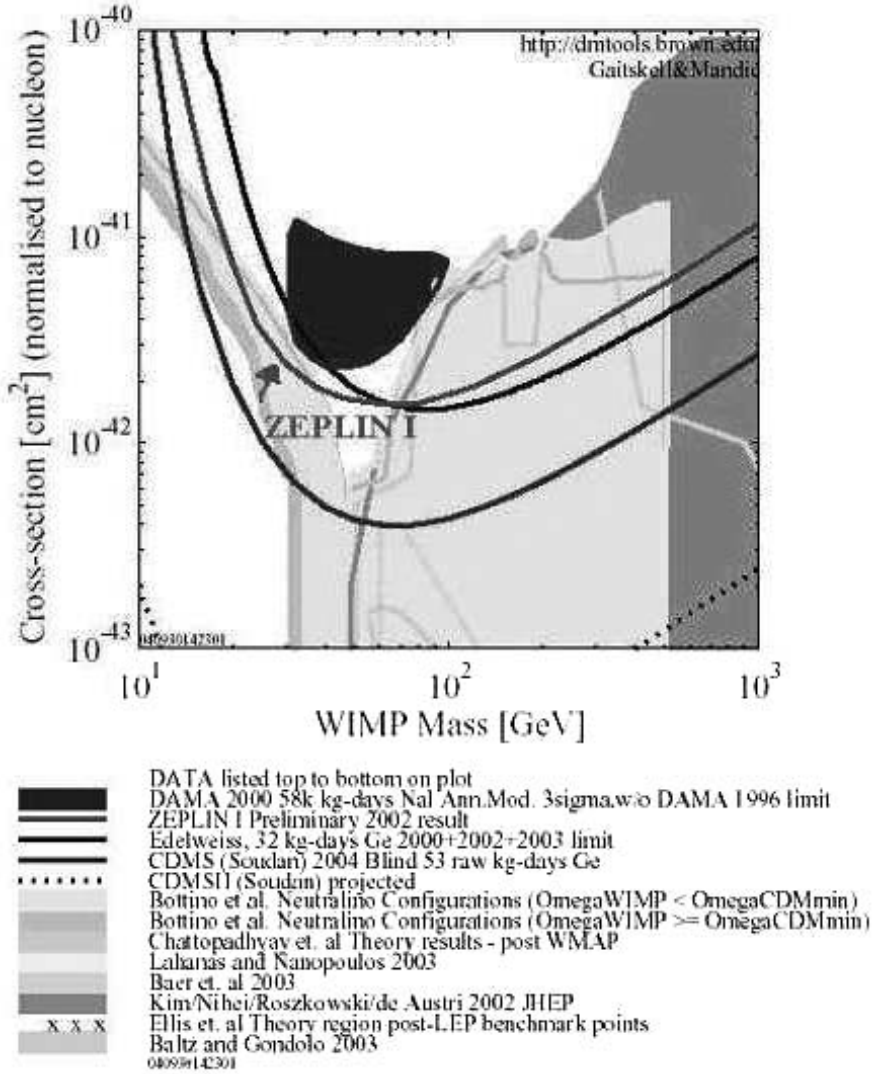

Fig. 3. Work of L. Krauss and colleagues in different halo models [1].

The best limits that have been set by these detectors came from the CDMS II detector operated at the Soudan underground laboratory [18]. These limits are well below the claimed signal by the DAMA group as shown in Fig. 3. All of these detectors are being upgraded to larger mass and 2005 will be a big year for these types of detectors.

4.2 Liquid Noble Gas Detectors: Xenon, Argon and Neon

Another promising method to detect dark matter is to use the scintillation light produced in Noble gas liquids [12]. The process is very well known since excimer lasers use a similar concept. For example the very first excimer laser was made in Russia in 1970 using liquid Xenon. A key part of this method is to apply an electric field to the detector to drift out any electrons that are produced at the recoil vertex as a basis to discriminate against background [12].

This method was just invented by our group within the ICARUS collaboration and is the basis for the ZEPLIN II, III, IV and XENON, as well as XMASS detector [11]. In Fig. 4 we show the schematic of the ZEPLIN II detector and the complete detector being tested at RAL [19]. The XENON detector uses a similar design [1, 20].

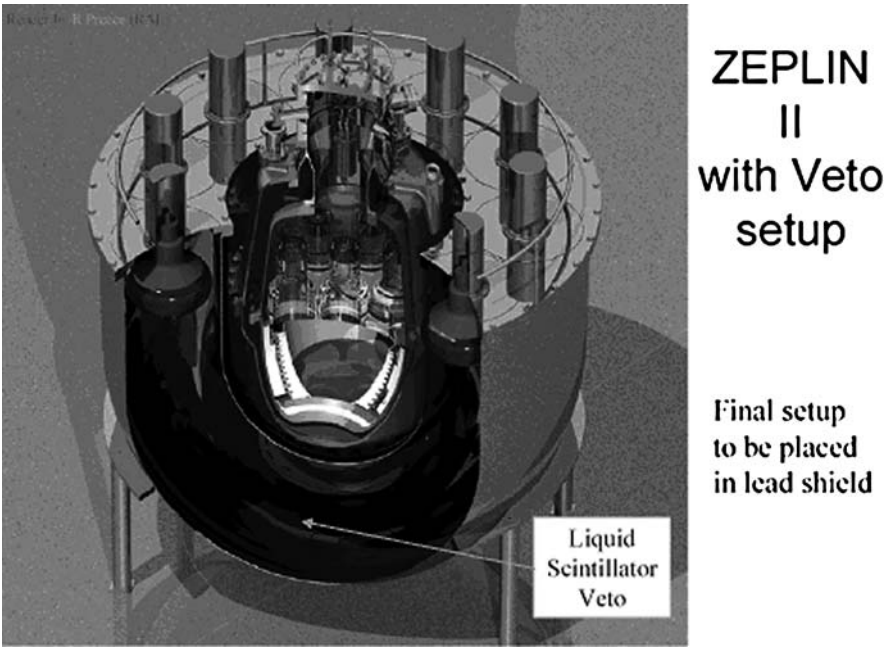

Fig. 4. Schematic of ZEPLIN IV Detector (see [12] for example).

More recently there have been studies of the use of liquid Argon (WARP) and liquid Neon (Clean) as WIMP detectors. One virtue of the use of liquid Xenon is the existence of different isotopes with different spins, thus testing the spin dependence of the WIMP interaction.

The ZEPLIN I team detector has reported a limit in the WIMP search using a partial discrimination method of pulse shape analysis. Of all the current

detector concepts the one most easily expanded to the one ton scale seems to be liquid Xenon. The US/UKDMC team is designing the XEPLIN IV/MAX [12] detector that will have a mass on the range of one ton. Currently it is not clear if there will be a single one ton detector or four 250 kg detectors.

A schematic of the one ton ZEPLIN IV/MAX detector is shown later in this paper.

The goal of the one ton detectors is to reach the cross-section level of absorb 10^{-9} to 10^{-10} pb. Current calculations of the cross-section for SUSY WIMPS (see Fig. 5) indicate that a discovery of dark matter is likely to be made in this cross-section range [14].

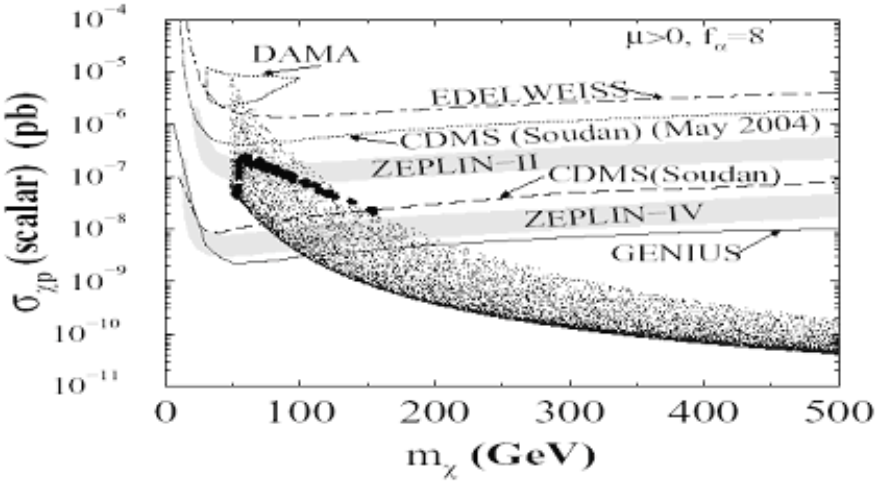

Fig. 5. Expectations for SUSY WIMP cross-sections by Pran Nath and colleagues.

4.3 Other Types of Detectors

There are many other ideas for large WIMP detectors. We only discuss two here. One concept is GENIUS, which will use one ton of ^{76}Ge (also to be used for double β decay search)[see Table 3 for references]. While this detector has no discrimination it is to be produced of ultrapure material so that there is little or no radioactive background. The detector is submerged in a large bath of liquid Nitrogen to shield out neutrons from cosmic rays. Another concept is to construct a "bubble chamber" to detect WIMPS by the formation of bubbles in the detector. More information on this novel scheme can be found in Ref. 1 (see papers in the 2004 Dark Matter meeting).

5 Status of the Search for Dark Matter Particles

A serious search for dark matter particles started around 1995 with the use of NaI detectors at several locations. In Table 1 we provide a list of the leading detectors being used for the search [11]. By the end of 2003 there were considerable data on this search summarized in Table 2 [1]. In addition the CDMS I group carried out a joint fit of their data and the DAMA data, and claimed these data were inconsistent to 98 percent confidence level. Fig. 3 shows the limits on the dark matter search at the time of the DM04 February 2004 meeting [1]. One month later the new results from CDMS II at the Soudan underground laboratory were presented [11].

The experiment collected 52.6 kg days of data with one event being recorded fully consistent with the estimated background. This limit is also shown in Fig. 5 [20]. As can be seen from Fig. 5 the bulk of the DAMA region

Table 1. Leading searches for Dark Matter.

Project	Location	Date	Type	Material	Mass (kg)	Discrimination Detector Types(s)
UKDMC	Boulby, UK	1997	Scintillation	Sodium iodide	5	None
DAMA	Gran Sasso, Italy	1996	Scintillation	Sodium iodide	100	None
ROSEBUD	Canfranc, Spain	1999	Cryogenic	Aluminum oxide	0.05	Thermal
PICASSO	Sudbury, Canada	2000	Liquid droplets	Freon	0.001	None
SIMPLE	Ristrel, France	2001	Liquid droplets	Freon	0.001	None
DRIFT	Boulby, UK	2001	Ionization	Carbon disulfide gas	0.16	Directional
Edelweiss	Frejus, France	2001	Cryogenic	Germanium	1.3	Ionization, thermal
ZEPLIN I	Boulby, UK	2001	Scintillation	Liquid Xenon	4	Timing
CDMS II	Soudan, Minn., US	2003	Cryogenic	Silicon, germanium	7	Ionization, thermal
ZEPLIN II	Boulby, UK	2003	Scintillation	Liquid Xenon	30	Ionization, scintillation
CRESST II	Gran Sasso, Italy	2004	Cryogenic	Calcium tungsten oxide	10	Scintillation, thermal
GENIUS-TF	Gran Sasso	2003	Ionization	Germanium	10kg	Ionization
GENIUS	Gran Sasso	–	Ionization	Germanium	100kg	Ionization

Table 2. Leading searches for Dark Matter.

Detector	Method	Exposure kg/day	Pos. sig. events	Limit events /kg/day	Comment
DAMA	Annual variation of non-discriminating data	–	–	Effective 1 - 0.3 90% CL	Not confirmed
CDMS I (SLAC) 2000	Direct interaction	–	13	0.4	Events consistent with neutrons
CDMS I (SLAC) 2002	Direct interaction	28	20	0.35	Events consistent with neutrons
Edelweiss 2000 2003	Direct interaction	10, 20	0, 2	0.2, 0.2	Events consistent with neutrons
ZEPLIN I	Direct interaction (pulse shape analysis)	300	Null	0.1	Background substration

Table 3. One Ton Dark Matter Detector Proposals.

Detector	Material	Method	Proposal	Current Prototype
GENIUS (LNGS) (a)	Ge	Ultrapure detector in LNGS	1997	10kg GENIUS test detector
ZEPLIN IV (Max) (Boulby/DUSEL) (b)	Xe	2 phase discriminating detector	1999	ZII/III Detectors at Boulby
CryoArray (DUSEL) (c)	Ge/Si	Ionization and Phonons	2001	CDMS II
XMass (Japan) (d)	Xe	2 phase (?)	2000	prototype
Xenon (DUSEL) (e)	Xe	2 phase detector	2001	prototype
WARP (LNGS) (f)	Ar	2 phase (possibly larger than one ton	2003	protoype

Table References

a. H.V. Klapdor-Kleingrothaus et al, Z. Physics A 359, 351 (1997).
b. D. Cline, H. Wang et al, UCLA DM 2000, published in Proceedings.
c. R. Gaitskell et al, 2001 Snowmass Proceedings.
d. Y. Suzuki, hep-ph/008296.
e. ZENONCollaboration, NSF Proposal 0201740, 2001.
f. C. Rubbia talk, UCLA Dark Matter 2004, to be published in the Proceedings.

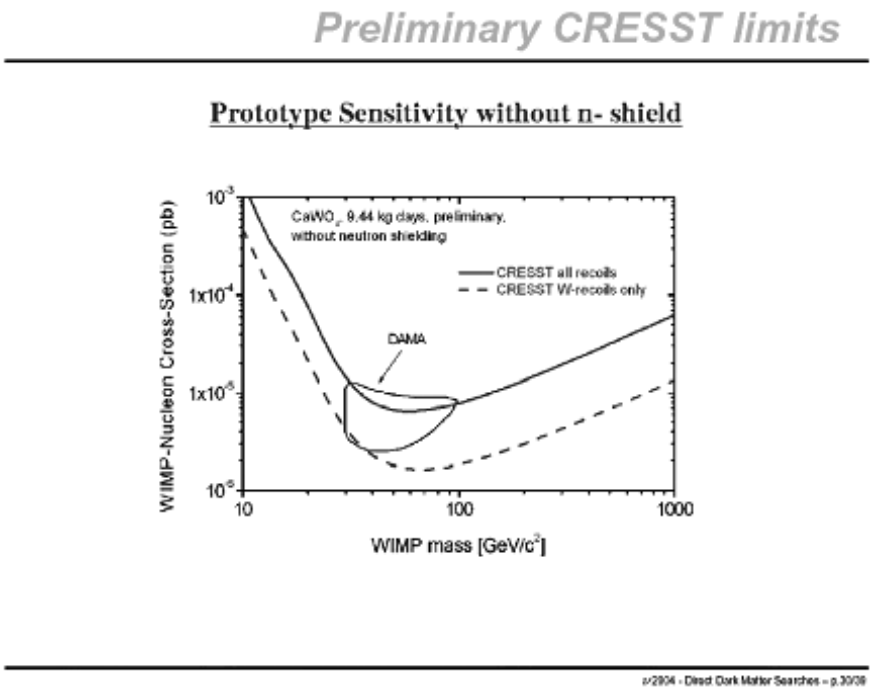

Fig. 6. Results for CRESST II shown at the Paris Neutrino 04 meeting, to be published in the proceedings.

is in conflict with several experiments. At the Paris Neutrino (04) meeting the first results from CRESST were shown (Fig. 6) that also seem inconsistent with the DAMA allowed region.

We show one schematic design of the ZEPLIN IV/MAX detector in Fig. 7 [21]. The expected reach of ZEPLIN IV/MAX is shown in Fig. 8. Table 3 lists most of the worldwide proposed one ton detectors.

6 Summary

The direct search for dark matter particles within the supersymmetry model is reaching a critical stage. The next generation of detectors could discover these particles as we have shown in this review. In any case another generation of one ton class detectors will be required to either confirm and explore the discovery or to confirm the search down to 10^9–10^{10} pb.

One key test for dark matter will be the observation of an annual variation of the signal of discriminated events. See [1] for a discussion of the annual variation signal.

This is undoubtedly an exciting time in the 70 year search for the origin of the missing mass just identified by Zwicky in 1933.

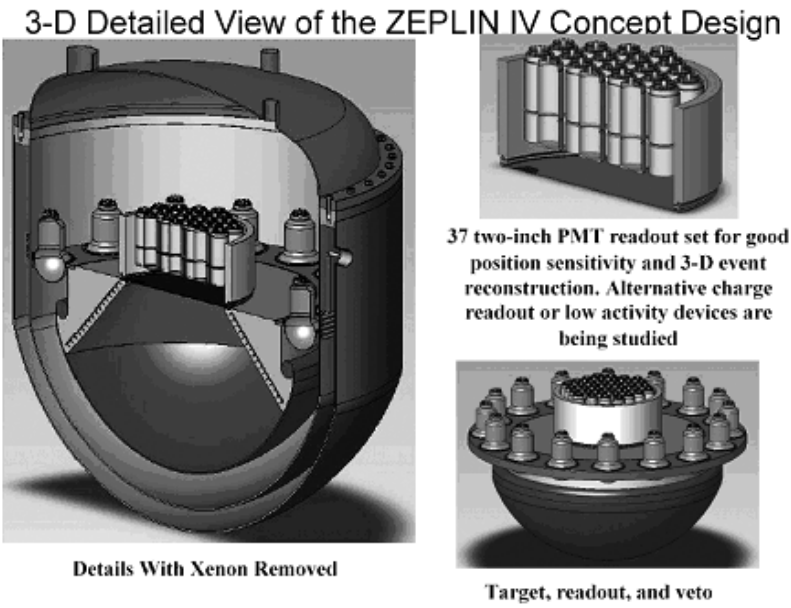

Fig. 7. Schematic of one version of ZEPLIN IV/MAX (H. Wang, private communication).

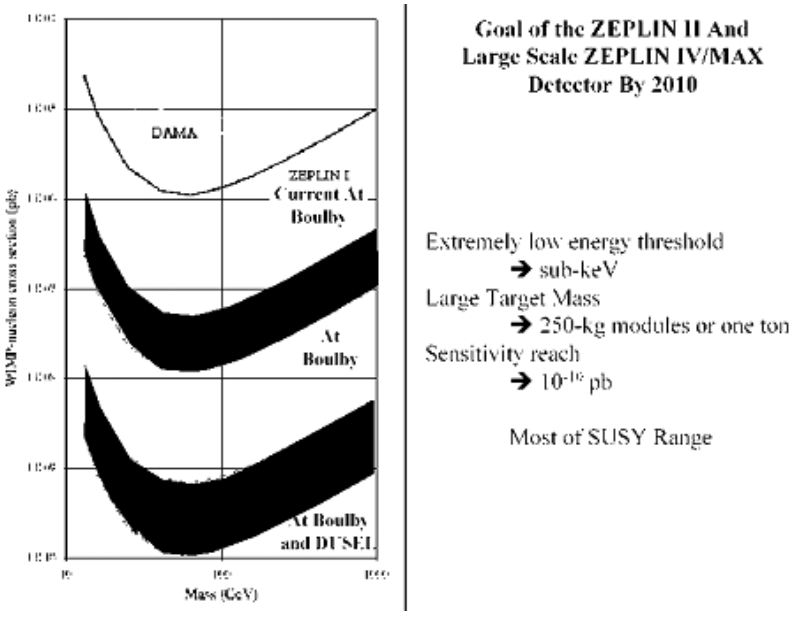

Fig. 8. Schematic of the reach for the secret for SUSY dark matter by ZEPLIN II and ZEPLIN IV/MAX.

Acknowledgments

I wish to thank the Aspen Center for Physics where this article was written and H. Wang, J. White and the UK/DMC for advice.

References

1. See the Proceedings of the 5th Symposium on Sources and Detection of Dark Matter and Dark Energy in the Universe, Elsevier 2004.
2. F. Zwicky, Helv. Phys. Act. **6**, 110 (1933)
3. C. Rubbia and W.K. Ford, Ap. J. **159**, 379 (1970); D.H. Rogstad and G.S. Shostak, Ap. J. **176**, 315 (1972)
4. C.L. Bennett et al, Ap. J. Suppl. **148**, 1 (2003)
5. P. Sikivie, Phys. Lett. B. **432**, 139 (1998)
6. A. Green, Phys Rev D **68**, 023004 (2003); C. Copi, L. Krauss, Phys Rev D **67**, 103507 (2003); J.F. Navarro, C.S. Frank and S.D.M. White, Ap. J. **462** , 563 (1996); B. Moore et al, Ap. J. Lett. **499**, L5 (1998)
7. K. Freese, J.A. Frieman and A Gould, Phys. Rev. D **37**, 3388 (1988); G. Gelmini and P. Gondolo, Phys. Rev. D **64**, 023504 (2001); F.S. Ling, P. Sikivie and S. Wick, Diurnal and Annual Modulation of Cold Dark Matter Signals, UFIFT-HET-04–6
8. D.B. Cline: Direct Search for Dark Matter Particles with Very Large Detectors, in: *Proceedings for Beyond the Desert 2003*, Springer Proceedings in Physics v. 92, Hans Klapdor-Kleingrothaus, ed., 2004
9. M.W. Goodman and E. Witten, Phys. Rev. D **31**, 3059 (1985); A. Drukier, K. Freese and D.N. Spergel, Phys. Rev. D **33**, 3495 (1986); I. Wasserman, Phys. Rev. D **33**, 2071 (1986)
10. 10. J.R. Primack, D. Seckel and B. Sadoulet, Ann. Rev. Nucl. Part. Sci. **38**, 751(1988); P.F. Smith and J.D. Lewin, Phys. Rep. **187** 203 (1990); G. Jungman, M. Kamionkowski and K. Griest, Phys. Rep. **267**, 195 (1996)
11. D. Cline, Scientific American **288:3**, 50–59 (2003)
12. D. Cline, A. Curioni, A. Lamarina et al, Astropart. Phys. **12**, 373–377 (1999)
13. A. Bottino et al, Phys. Rev. D **69**, 037302 (2004)
14. U. Chattopadhyay and P. Nath, hep-ph/0405157
15. D.S. Akerib et al (CDMS Collaboration), Phys. Rev. D **68**, 82002 (2003)
16. A.Benoit et al, Phys. Lett. B 545 **43** (2002)
17. L. Stodolksy and F. Probst, talk at Dark Side of the Universe, Ann Arbor, May 2004
18. CDMS II; see Table 3
19. D. Cline, Y. Seo, H. Wang et al.: Status of ZEPLIN II and ZEPLIN IV Study, in: *Nuclear Physics B, Proceedings Supplements, 5th International Symposium on Search and Detection of Dark Matter and Dark Energy in the Universe*, ed. by D.B. Cline (Elsevier, Amsterdam 2003) pp 229–232
20. XENON Detector; see Table 3

21. See for example D. Cline: ZEPLIN IV: A One Ton WIMP Detector, a paper given at the Dark 2002 meeting, Capetown, January 2002, to be published in: *Proceedings of DARK 2002*, eds. H.V. Klapdor-Kleingrothaus and R. Viollier, pp 492–498
22. Private communication from H. Wang
23. GENIUS; see Table 3

Status of ZEPLIN II and ZEPLIN III

G. J. Alner[4], A. Bewick[5], R. Bissit[2], C. Bungau[4], B. Camanzi[4], M. J. Carson[6], D. B. Cline[1], J. Champer[1], Y. Chen[1], D. Davidge[5], J. Davis[6], E. Daw[6], J. V. Dawson[5], T. J. Durkin[4], T. Gamble[6], J. Gao[2], C. Ghag[7], A. S. Howard[5], W. G. Jones[5], M. K. Joshi[5], V. A. Kudryavtsev[6], T. B. Lawson[6], V. Lebedenko[5], J. D. Lewin[4], P. K. Lightfoot[6], I. Liubarsky[5], R. Lüscher[4], J. Maxin[2], J. E. McMillan[6], J. Miller[2], B. Morgan[6], A. S. Murphy[7], W. Ooi[1], S. M. Paling[6], R. M. Preece[4], J. J. Quenby[5], M. Robinson[6], G. Salinas[2], J. Seifert[2], F. Sergiampietri[1,3], N. J. T. Smith[4], P. F. Smith[1,4], N. J. C. Spooner[6], T. J. Sumner[5], D. R. Tovey[6], R. Walker[5], H. Wang[1], J. T. White[2], and X. Yang[1]

[1] UCLA, Physics and Astronomy Department, Los Angeles, CA 90095-1547
[2] Texas A&M University, Physics Department, College Station, TX 77843-4242
[3] INFN Pisa, Via F. Buonarroti 2, Ed. C, 56127 Pisa, Italy
[4] Rutherford Appleton Laboratory, Chilton, OX11 0QX, UK
[5] Imperial College, Blackett Laboratory, London SW7 2BZ, UK
[6] University of Sheffield, Physics Department, Sheffield S3 7RH, UK
[7] University of Edinburgh, Nuclear Physics Department, Edinburgh EH9 3JZ, UK

Presented by H. Wang for the ZEPLIN collaboration[1]

Abstract. We describe the ZEPLIN II (30-kg) and ZEPLIN III (7-kg) discriminating dark matter detector using two-phase xenon designed for direct detection of cold dark matter in the form of Weakly Interacting Massive Particles. These two detectors are currently being commissioned. Both detector will begin operation in the Boulby Mine, UK in 2005. ZEPLIN II & III are capable of discriminating between nuclear recoils and background events and have a design reach up to two orders of magnitude beyond current limits. These two detectors will also serve as a step in the development program for a next-generation ton-scale detector.

1 Introduction

The ZEPLIN collaboration was formed in the early 90's, after a series of research and development results obtained by ICARUS, to develop large scale liquid xenon detectors for direct WIMP (Weakly Interacting Massive Particles) dark matter search. The key results stimulated the formation of ZEPLIN are: (a) liquid xenon purification to achieve greater than 5-ms free electron life time in liquid xenon [1] and (b) first principle demonstration of gamma and alpha events discrimination [2]. Then xenon as a target for dark matter search were studied extensively [3, 4, 5, 6].

[1] wangh@physics.ucla.edu

The ZEPLIN collaboration is currently commissioning the ZEPLIN II and ZEPLIN III detector to begin operation in 2005. ZEPLIN II is a large mass (30-kg) two-phase xenon detector while ZEPLIN III is a low mass (7 kg) detector also operates in two-phase. While capable of good physics reach, these two detectors also serve as a step in the development program for a next generation ton-scale detector.

2 Xenon as Detector Target

Liquid xenon satisfies the following basic requirements for a dark matter target: (a) It is available in sufficiently large quantities with high purity [1], (b) It scintillates via two mechanisms, and respond differently to nuclear and electron recoil events, (c) It contains both odd and even isotopes, suitable for spin-dependent and scalar interactions, offering the possibility of using enriched odd or even isotopes to identify the type of interaction, (d) Its high atomic number provides a good kinematical match to the theoretically favored particle mass range of $100 - 200$ GeV.

Target masses between 100 and 1000 kg may be needed to reach the lowest predicted event rates. The 30 kg detector now under construction as ZEPLIN II represents a major step towards this, being a factor 10 larger in xenon mass than previous test chambers built at CERN and the single phase ZEPLIN I detector recently operated in the UK. The ZEPLIN design principle could subsequently be scaled up to give a total target mass 1000 kg or more. The latter would achieve sensitivity comparable to the lowest predicted neutralino event rates (0.0001–0.01/kg/d) and could detect the annual signal modulation that would confirm the Galactic origin of any signal.

3 Background Discrimination

With liquid xenon, signal discrimination can be achieved in two basic ways: (1) Scintillation pulse shape - the decay time constant differs by a factor of 2 ∼3 for nuclear recoil and background events. (2) Using an electric field to inhibit recombination and measuring (a) the 'primary scintillation' S1 and (b) drifting the ionization into a strong electric field to produce a 'secondary scintillation' signal S2. Method (2) is more powerful, involving a comparison of two distinct signals associated with each individual event. The mean value of the ratio S1/S2 differs by typically a factor > 10 for nuclear recoil and electron recoil events. Discrimination between α and γ using this technique was demonstrated in 1993 by members of the ICARUS collaboration including the UCLA/Torino groups [2]. Further tests used neutron scattering to confirm for the first time (a) that liquid xenon will give a scintillation response to recoil of its own nuclei [3], and (b) that the above discrimination processes remain effective down to energies below 5–10 KeV, as required for a dark

matter experiment. Early work demonstrated proportional scintillation in the liquid phase. The current design is based on a more advanced two-phase scheme [5]. ZEPLIN II & III introduces a liquid/gas interface, allowing the electrons to be drifted into the gas and produce an amplified scintillation pulse. The resulting energy amplification of background events removes them from the low energy signal region, while signal events produce less (or none at low field) ionization and hence little additional amplification. This increases the discrimination power, and at energies significantly above the threshold, demonstrates the possibility of full separation of signal and background. This allows the sensitivity to improve linearly with running time and mass, rather than as the square root of these.

4 The ZEPLIN II Detector

The key features of the ZEPLIN II detector are:

(a) A shallow cylindrical chamber using 7 PMTs covering the top surface, and with liquid depth (14.1 cm).
(b) Active target mass of 30 kg, to increase the number of events and to provide a realistic module for scale-up to larger masses.
(c) Due to insufficient information about ionization from low energy xenon recoils, the detector was designed using a POLYTETRAFLUOROETHYLENE (PTFE) cone to confine the liquid xenon active volume hence eliminate 'dead' regions, in which a low energy gamma signal could lose its secondary pulse and mimic a nuclear recoil event.
(d) The design of the internal vessel ensures that all of the xenon liquid is active, removing the possibility of a misinterpreted signal from an inactive volume.
(e) PMTs placed inside the detector to maximize the light collection efficiency. Custom made PMTs from Electron Tube Inc. with thin hemispherical quartz profiles and platinum underlay coating ensure high pressure and low temperature operation.
(f) ZEPLIN II is designed capable of operating at high field if the ionization from nuclear recoil is detectable. In that case a full 3-D event reconstruction and perfect background rejection can be achieved (see details in ZEPLIN III design Sect. 5).

Figure 1 shows a 3-D cut-away view of the central detector and illustrates the overall arrangement of detector, Compton veto, and shielding. The entire detector is thermal-insulated by vacuum, which is then shielded by a Compton veto and lead shield (Used for ZEPLIN I and is now being installed for ZEPLIN II). Fig. 2 shows some photos of the target assembly and commissioning using Rutherford Appleton Laboratory's dedicated facility.

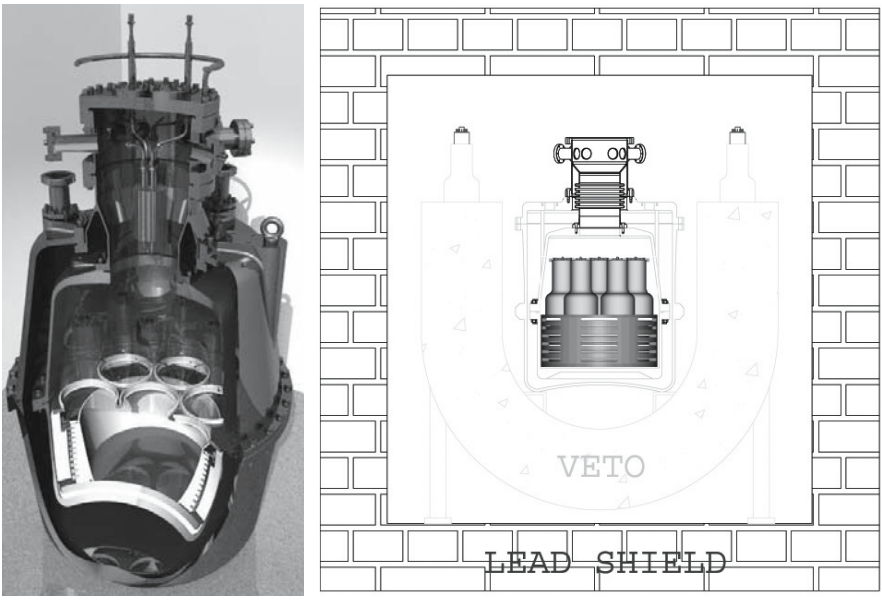

Fig. 1. The 3-D cut away view of the ZEPLIN-II central detector and the system setup (veto & lead shielding).

Fig. 2. Internal target installation. Figure shows completed PTFE cone assembly, PMT layout, PMT assembly, field shaping ring assembly with two resistor chains shown, general overview of the ZEPLIN II detector, associated infrastructure and closing up of the target.

4.1 ZEPLIN II Background Estimation and Detector Simulations

Simulation studies have been performed in ANSYS and GEANT4 to assess the ZEPLIN II target characteristics, including drift field characteristics, primary light yield and light collection uniformity, and the expected neutron background when ZEPLIN II is deployed at Boulby. These studies indicate (Details see [7]) that the main background (60 recoils/year out of 100 expected in the shielded configuration) will arise from U/Th contamination in the PMT array, which can be reduced by conversion of the Compton veto to a neutron veto through Gd loading.

ANSYS finite element analysis calculation have been performed to determine the shape and uniformity of the drift field in the liquid xenon target (Fig. 3). These simulations indicate that the expected uniformity of field will be created within the ZEPLIN II target, the PTFE having the same dielectric as the liquid xenon, thereby initially not affecting the field potentials. Four resistor chains are used to link the field shaping rings to minimize the impact of a failure of the resistors. ANSYS analysis show that if one of resisters was removed (broken), the field potential remains essentially unaffected, providing confidence that the field definition will be robust. As the PTFE is an insulator surface charge will build up following interactions within the liquid xenon. Fig. 3 also shows the effect of a fully charged PTFE surface on the field potentials. It can be seen that the direction of drift for events close to the PTFE surface will be orientated parallel to the PTFE surface at maximum charge-up. However, the total charge needed is about $1.47 \times 10^{+14}$ ions or

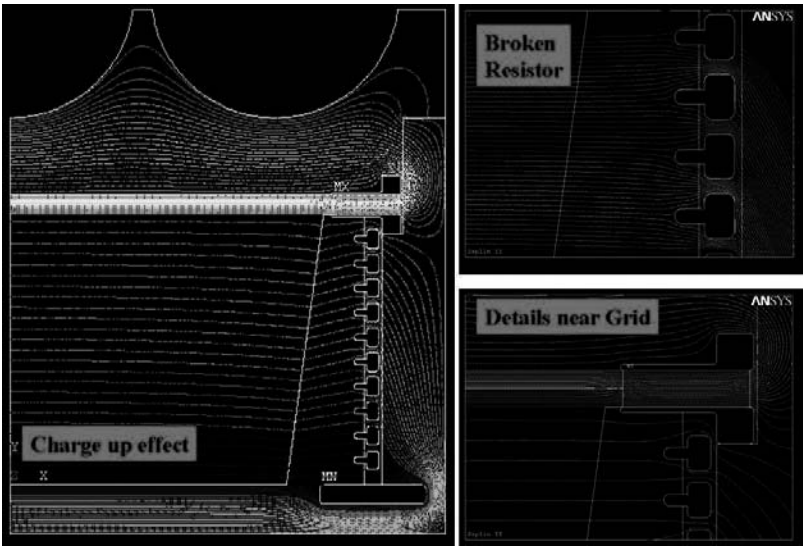

Fig. 3. Detailed electrostatic field modeling for charge-up and broken resistor effect using ANSYS, a commercial finite-element analysis package.

2.2 kTeV total Minimum-Ionizing-Particle deposition near the surface, equivalent to 8×10^{10} 122 keV γ-ray events. It is unlikely that a data run will be performed for long enough for the PTFE to charge fully.

5 The ZEPLIN III Detector

ZEPLIN III is designed to get the best possible performance from a two-phase xenon detector of intermediate mass. ZEPLIN III is expected to allow a better ultimate background discrimination than ZEPLIN II by utilizing the ionization yield from xenon nuclear recoil.

Figure 4 shows the design of ZEPLIN III and the construction in progress. A number of critical features guarantee the competitive edge of the chosen scheme. The placement of 31 PMTs inside the liquid, used to register the scintillation photons from the liquid and subsequent electroluminescence from the gas phase, as well as the thin active liquid xenon volume above the PMTs improves light collection for the primary scintillation, thus improving the energy threshold which allows deeper penetration, by a factor of five, into the cross-section parameter space. The high charge extraction electric field ensures that both primary and secondary signals are present for both nuclear and electron recoils allowing to trigger on a much larger secondary signal and therefore to locate a smaller primary as a precursor to the secondary, which not only makes the signal identification more secure but also again allows the energy threshold to be lowered. In fact these two factors make it possible to achieve a sub-keV energy threshold in detection of the primary recoil. The result is that the separation in secondary signals between electron and nuclear recoils for a given size primary is therefore, maximized. The principle of operation has been demonstrated with a prototype high-field

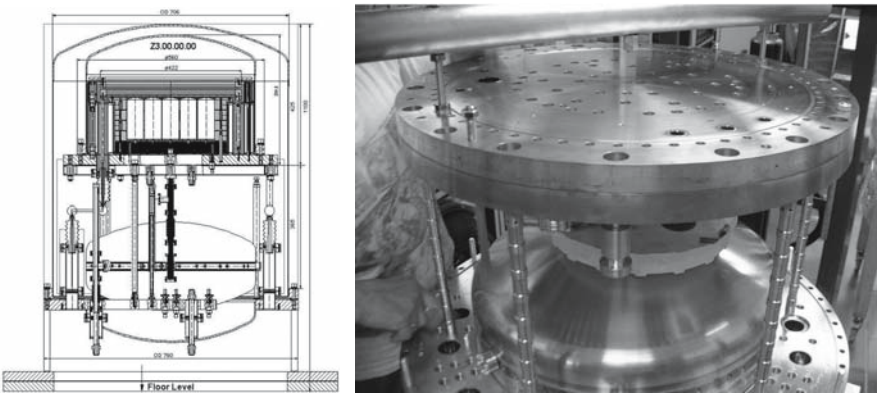

Fig. 4. ZEPLIN III side view and trial assembly of the lower base flange, the liquid nitrogen reservoir and the xenon chamber cooling ring.

detector, although it should be noted that a definitive nuclear recoil test must await deployment in a sufficiently low background environment due to event confusion at the surface.

5.1 ZEPLIN III Background Estimation

Extensive Monte Carlo simulations have also been carried out to assess the complete performance of ZEPLIN III [8, 9]. These simulations have addressed light collection from the liquid and gas phases, position reconstruction, and internally generated γ-ray and neutron backgrounds. A simulated data set has been produced, which has then been analyzed in a similar way to that proposed for real data. A fully implemented GEANT4 toolkit has been assembled. Monte Carlo simulation of position sensitivity obtained by using the gas luminescence signal has been studied by using a fine positional grid to derive templates of very good statistical quality for the hit patterns expected in each photomultiplier. The size of the fiducial volume depends on the quality of the position reconstruction, and simulations indicate a 7-kg fiducial mass. A simulation with high statistical weight was run to find the expected hit patterns from single electrons escaping from the liquid surface at random positions. This data set then analyzed to reconstruct the positions using a minimum χ^2 technique matching to the template distributions. The reconstruction is good (sub-cm), even for single electrons, over the central fiducial region.

Results of background simulations are shown in Fig. 5. A γ-ray rejection factor of 10^4–10^5 has been demonstrated by simulation. A rejection factor of 10^4 will yield an experimental sensitivity of $\sim 10^{-8}$ pb after a year of running [8]. This is partly enabled by using an all-copper construction as far as possible. However, to reach this sensitivity does require suppression of the neutron background caused by U and Th in the PMTs. ZEPLIN III will be placed inside a liquid scintillator veto designed to lower the background due to the Compton scattered γ-rays. The 10-cm nearest to the detector will be made of a passive hydrogenous shield loaded to 0.2–0.5% with a Gd salt. In combination with the liquid scintillator veto the Gd loaded shield will form part of the neutron veto. By interacting with Gd nuclei the neutrons from the cavern and ZEPLIN III components will produce γ-rays with an average energy of 4-MeV of which some significant fraction will be detected by the liquid scintillator veto. This veto system will be installed in a two stage process, starting with a simple γ-veto.

6 ZEPLIN II gas filled tests at RAL

First performance tests on this full scale system, filled with xenon gas, were completed at RAL during the summer of 2004. Performance data obtained from these tests confirms that the ZEPLIN II detector performs as designed.

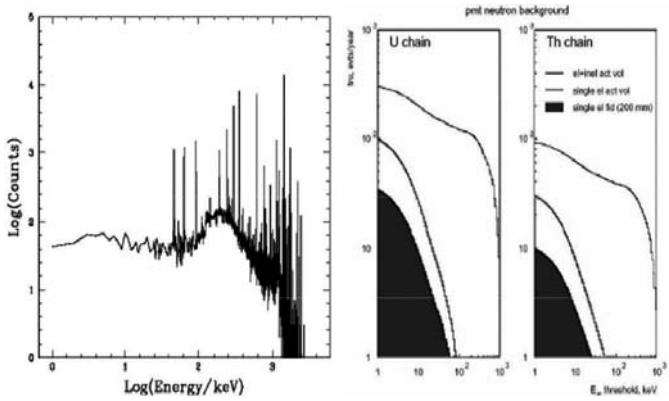

Fig. 5. Simulation of photon background expected from the measured U and Th in PMTs. Shown on the left the γ-ray background. It is dominated by Compton scatting being flat at $\sim$10 counts/keV/kg. A veto system included in the simulation will reduce the rate by a factor $\sim$3. On the right is the simulated neutron background with the total event rate as a function of energy.

Fig. 6 shows a typical high energy cosmic event. Data were taken with a ^{241}Am gamma source located below the detector. A very narrow primary pulse at $t = 0\,\mu$s followed by a gamma (at $t = 11\,\mu$s), a long cosmic track in the middle of the detector (between $31 \rightarrow 63\,\mu$s), and a shorter track near the bottom of the detector (between $66 \rightarrow 80\,\mu s$). Using the pulse area, timing,

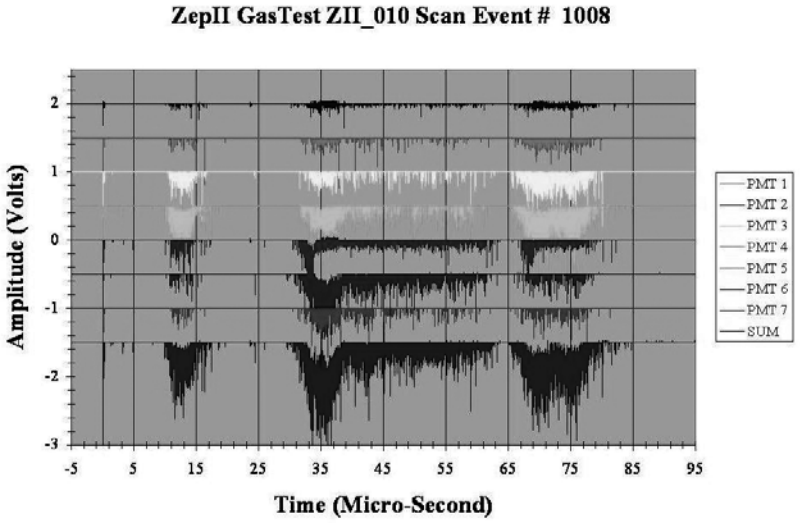

Fig. 6. A typical high energy cosmic event in the ZEPLIN II detector. The individual signals observed in the 7 PMTs and the sum signal.

and coincidence information, detector performance can be studied carefully. Due to the unique ZEPLIN II design, the performance study can be done cleanly.

A simple 2-D plot (Fig. 7 bottom, each dot represent one event and all events are plotted without any cut) shows all types of events in the ZEPLIN II detector. A: events with tracks crossing the luminescence grid into the active volume, B: events with tracks crossing the bottom of the detector, C: short cosmic tracks within the active volume, D: in red shown 60 keV source events (the slope indicates charge diffusion in gas), the primary and secondary relation of these events are shown in the middle plot of Fig. 7, E: events located between top grid and PMT also shown in upper plot near bottom axis.

Figure 8 shows the histogram of the primary pulse width. The pulse width is defined as width of the pulse between 10% and 90% of its total area. The black curve shows all events, the green curve shows events with clean secondaries, and the blue curve shows events without secondaries. Three populations are clearly seen: A, left sharp peak is due to large Cherenkov pulse mixed with gamma events; B, Middle peak is due to gamma scintillation; and C, the peak above 500-ns is due to overlap between primaries and secondaries or miss-triggers on secondaries. The red points at the bottom are events clearly not Cherenkov (97% efficiency on primary scintillation cut) and without secondaries. The energy spectrum of these events are shown in the right plot where only one event below the interested 10 keV (out of 17,288 total events).

These gas tests confirmed that gamma events produced both primary (scintillation) and secondary (ionization) pulses, as expected from the earlier work with a small test chamber. It was confirmed that some events originating above the top field grid and close to the PMTs, give also a secondary pulse due to strong reverse field. This type of events can be eliminated using the secondary signal. A few rare events very near to the PMT produce very small secondary. These events can be eliminated by pulse arrival time and compare pulse height amount triggered tubes. The gas test run with 17,288 random events show only one event pass all cuts (99.994% rejection above 5 keV). Further reduction of these events are possible using pulse shape discrimination statistically. Studies will be done when more data are available. Conditions in liquid may vary and test result will soon available when ZEPLIN II operates underground.

7 Conclusion

ZEPLIN II and ZEPLIN III design are based on R&Ds carried out by the ICARUS and the ZEPLIN collaboration during the last decade and both detectors are expected to operate under Boulby mine in 2005 with expected sensitivity of 10^{-8} Pb.

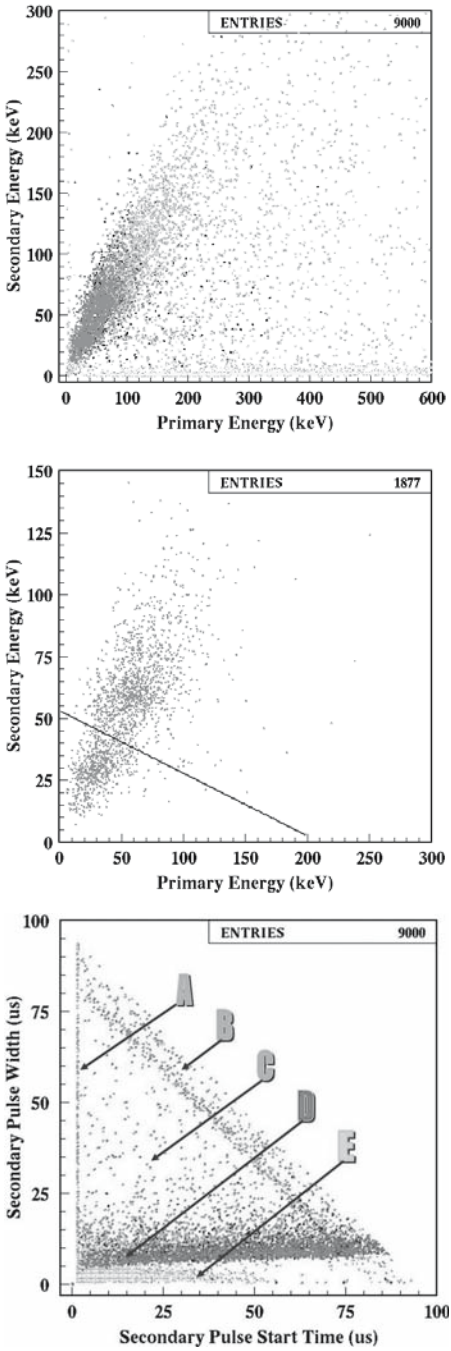

Fig. 7. The upper plot shows primary and secondary signals for all pulses taken during the first gas test. The middle plot shows removal of above-grid events by timing and secondary shape cut. The bottom plot shows 6 different types of background events in one plot.

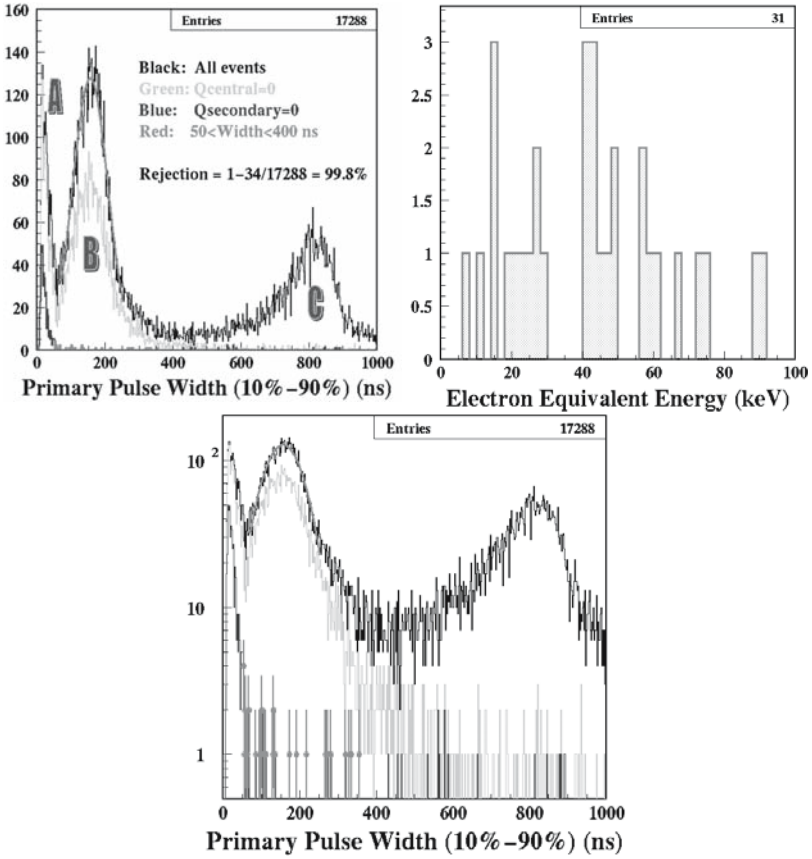

Fig. 8. Primary pulse width distribution (left: linear scale, bottom: log scale), right spectrum of final single pulse primaries after all cuts. Note that only one event below 10 keV.

Acknowledgments

The presenter wishes to acknowledge support from the U.S. Department of Energy, grant number DE-FG03-91ER40662, DE-FG03-95ER40917 and the National Science Foundation grant number PHY-0139065.

References

1. P. Benetti et al., Nucl. Instr. and Meth. A **329** 361–364 (1993).
2. P. Benetti et al., Nucl. Instr. and Meth. A **329** 203–206 (1993).
3. F. Arneodo et al., Nucl. Instr. and Meth. A **449** (2000) 147–15 7.
4. D. B. Cline et al., Nuclear Physics B - Proceedings supplements, V**124** (2003) 221–224.

5. D. Cline et al.: *Astroparticle Physics* 12 (2000)373–377.
6. H. Wang, Physics Reports, Volume 307 Issues 1–4 (1998) 263–267.
7. C Bungau et al. Astroparticle Physics (in Press)
8. T. J. Sumner, 6th Int. Symp. Sources and Detection of Dark Matter/Energy in the Universe (Marina Del Ray, California, feb. 2004).
9. J. V. Dawson, Ph.D Thesis, Imperial College London, 2003

The XENON Dark Matter Experiment

Elena Aprile (On behalf of the XENON Collaboration)

Physics Department and Columbia Astrophysics Laboratory,
Columbia University, New York, New York 10027
age@astro.columbia.edu

The XENON experiment aims at the direct detection of dark matter in the form of WIMPs (Weakly Interacting Massive Particles) via their elastic scattering off Xenon nuclei. With a fiducial mass of 1000 kg of liquid xenon, a sufficiently low threshold of 16 keV recoil energy and an un-rejected background rate of 10 events per year, XENON would be sensitive to a WIMP-nucleon interaction cross section of $\sim 10^{-46}\,\mathrm{cm}^2$, for WIMPs with masses above 50 GeV. The 1 tonne scale experiment (XENON1T) will be realized with an array of ten identical 100 kg detector modules (XENON100). The detectors are time projection chambers operated in dual (liquid/gas) phase, to detect simultaneously the ionization, through secondary scintillation in the gas, and primary scintillation in the liquid produced by low energy recoils. The distinct ratio of primary to secondary scintillation for nuclear recoils from WIMPs (or neutrons), and for electron recoils from background, is key to the event-by-event discrimination capability of XENON. A 3kg dual phase detector with light readout provided by an array of 7 photomultipliers is currently being tested, along with other prototypes dedicated to various measurements relevant to the XENON program. We present some of the results obtained to-date and briefly discuss the next step in the phased approach to the XENON experiment, i.e. the development and underground deployment of a 10 kg detector (XENON10) during 2005.

1 Introduction

The question of the nature of the dark matter in the Universe is being addressed with numerous direct and indirect detection experiments using a variety of methods, detectors and target materials. For a recent review of the field we refer to [1].

The proposed XENON experiment is among the new generation direct searches for dark matter weakly interacting massive particles (WIMPs) with the ambitious goal of a sensitivity reach which is several orders of magnitude higher than the lowest exclusion limit set by the CDMS II experiment [2] To achieve a sensitivity goal of $\sim 10^{-46}\,\mathrm{cm}^2$ XENON relies on a target mass of 1 tonne of liquid xenon (LXe), with less than about 10 background events per year. Efficient background identification and reduction is based on the

distinct ratio of the ionization and scintillation signals produced in LXe by nuclear (from WIMPs and neutrons) and electron (from gamma, beta and alpha backgrounds) recoil events [3]. The main challenge is to accomplish this event-by-event discrimination down to a few tens of keV nuclear recoil energy. Additional techniques used for background suppression are an active LXe self shield around the sensitive target, passive gamma and neutron shielding and the detector's 3-D position resolution. The position information is crucial to select single hit events characteristic of a WIMP signal and to veto multiple hit events associated with neutrons as well as other backgrounds which propagate from the edge of the detector into the fiducial volume.

To test the XENON concept and verify achievable threshold, background rejection power and sensitivity, a detector with a fiducial mass on the order of 10 kg (XENON10), is under development for underground deployment in 2005. The detector exploits several key systems which have been tested and optimized with the 3 kg prototype, but will feature significant improvement in overall performance and sensitivity down to 16 keV nuclear recoil energy. The experiment will be carried out at the Gran Sasso Underground Laboratory (3500 mwe). The depth and the expected background rejection power will allow us to reach a sensitivity a factor of 20 below the best existing measurements from CDMS II [2], of 2 dark matter events/10 kg/month, without the need of a muon veto for fast neutrons.

Another important goal of the XENON10 phase is to pave the way for the design of a 100 kg scale detector. With 3 months of operation deep underground, at a background level below 1×10^{-5} cts/keVee/kg/day after rejection, XENON100 would provide a sensitivity of $\sim 10^{-45}\,\mathrm{cm}^2$. The full 1 tonne scale experiment (XENON1T) will be realized with ten XENON100 modules.

Figure 1 shows the sensitivity projected for XENON10 experiment, in comparison to current WIMP searches, which are probing event rates at ∼0.1 evts/kg/day. The projected performance of XENON100 and XENON1T detectors is also shown. In order to continue progress in dark matter sensitivity it will be important to have a liquid xenon experiment at the 10 kg scale operational and taking science data in early 2006.

2 The XENON Detector Baseline

Figure 2 schematically shows the design of the detector proposed as unit module for the XENON experiment. It is a dual phase TPC, with the active LXe volume defined by a 50 cm diameter CsI photocathode immersed in the liquid, at about 30 cm from the first of three wire grids defining a gas proportional scintillation region. An array of compact, metal channel UV sensitive PMTs developed by Hamamatsu Photonics Co. to work at LXe temperature and recently optimized for low radioactivity content, are used for primary and secondary light detection.

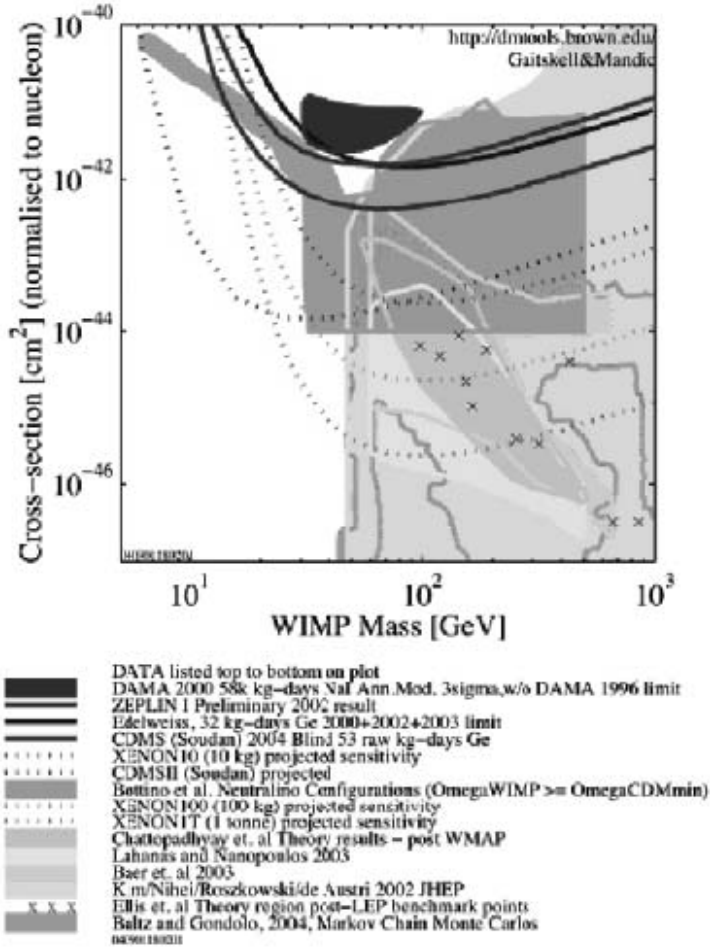

Fig. 1. Theoretically predicted regions for SUSY WIMP candidate, along with the best detection dark matter limits from current direct detection experiments. Also shown as four dotted lines (top to bottom at right) are the projected sensitivities for CDMS II at Soudan [2], and for XENON10, XENON100 and XENON1T [9].

The TPC is enclosed in a leak-tight cylindrical structure made of PTFE and OFHC. The PTFE is used as effective UV light reflector [4] and as electrical insulator. The fraction of direct light heading downward will be efficiently detected with the CsI photocathode [5]. The whole structure is immersed in a bath of LXe, serving as active veto shield against background. The LXe for shielding is readout by PMTs.

An event in the XENON TPC will be characterized by three signals corresponding to detection of direct scintillation light, proportional light from ionization electrons and CsI photoelectrons. Since electron diffusion in LXe is

Fig. 2. Schematic view of the XENON 100 dual phase detector.

small, the proportional scintillation pulse is produced in a small spot with the same X-Y coordinates as the interaction site, allowing 2D localization with an accuracy of 1 cm. With the more precise Z information from the drift time measurement, the 3D event localization provides an additional background discrimination via fiducial volume cuts. The simulated detection efficiency of the primary scintillation light is about 5 p.e./keV for the XENON100 detector.

3 Results from the 3kg XENON Prototype

R&D for the XENON program is being carried out with various prototypes dedicated to test several feasibility aspects of the proposed concept, and to measure the relevant detector characteristics such energy threshold and background discrimination as well as ionization and scintillation efficiency of Xe recoils in LXe as a function of energy and electric field. Here we limit the discussion to the results obtained to-date with a dual phase xenon prototype with ∼3 kg of active mass. The primary scintillation light (S1) from the liquid, and the secondary scintillation light (S2) from the ionization electrons extracted into the gas phase, are detected by an array of seven PMTs, operating in the cold gas above the liquid.

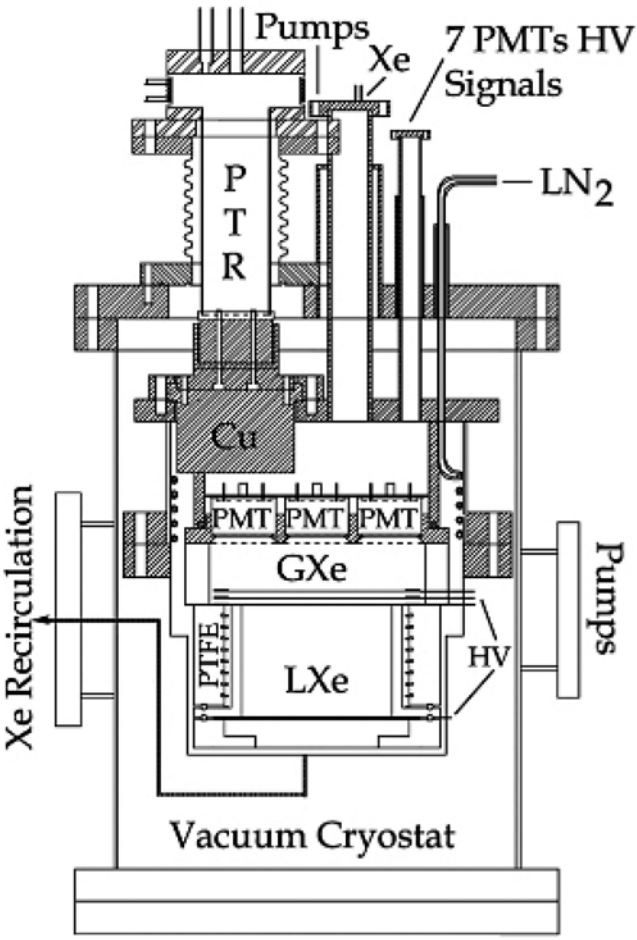

Fig. 3. Schematic drawing of the dual phase prototype.

A drawing of the 3kg XENON prototype is shown in Fig. 3 while the photo of Fig. 4 shows the integrated set-up at the Columbia University Nevis Laboratory. The sensitive volume of the TPC ($7.7\times7.7\times5.0\,\mathrm{cm}^3$) is defined by PTFE walls and grids with high optical transmission, made of Be-Cu wires with a pitch of 2 mm and 120 µm diameter. Negative HV is applied to the bottom grid, used as cathode. Grids on the top close the charge drift region in the liquid and with appropriate biasing, create the amplification region for gas proportional scintillation. Shaping rings located outside of the PTFE walls and spaced 1.5 cm apart, are used to create a uniform electric field for charge drift.

An array of seven, 2 inch PMTs (Hamamatsu R9288), mounted 2.3 cm above the top grid, is used to detect both primary and proportional light.

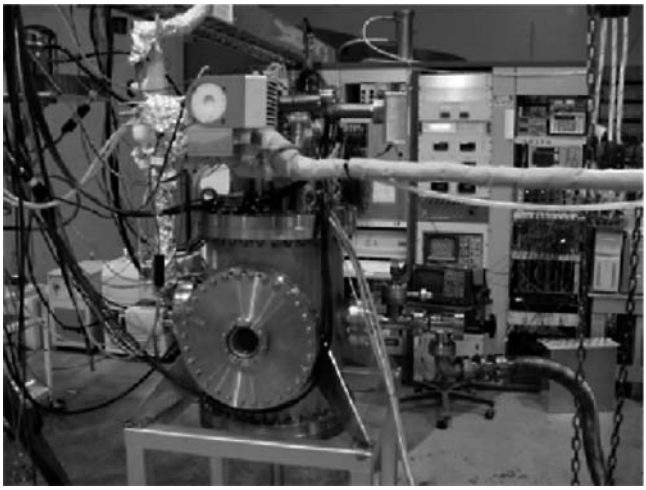

Fig. 4. The detector integrated with the vacuum cryostat, refrigerator, gas/recirculation and DAQ systems.

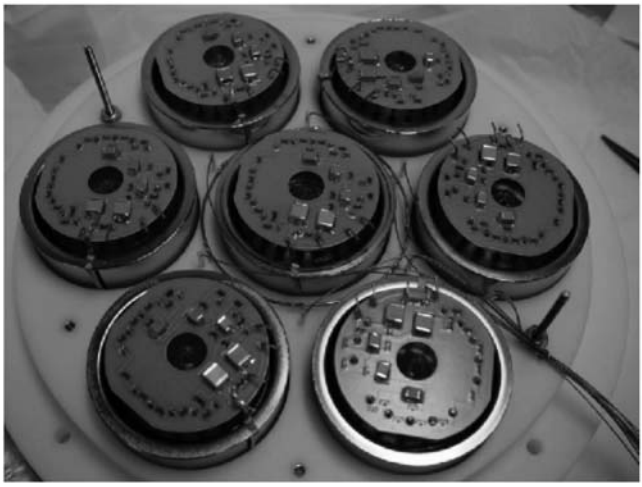

Fig. 5. An array of 7 PMTs on the top of the chamber in the gas phase.

The PMT array mounted on a PTFE frame is shown in Fig. 5. The custom-developed HV divider bases are also clearly visible. We used LEDs to measure the PMTs gain and single photoelectron response.

The LXe detector is insulated by a vacuum cryostat. A Pulse Tube Refrigerator (PTR) optimized for LXe, is used to cool down the detector, liquefy Xe gas and maintain the liquid temperature at the desired value. The typical operating temperature is -100 °C with a stability better than 0.05 °C. At this temperature the Xe vapor pressure is ∼1.8 atm. A reliable and stable cryo-

genics system is an essential requirement for the XENON experiment since both PMT's gain and the proportional light yield vary with temperature. With a cooling capacity of 100 W at 165 K the same PTR equipment will be used for XENON10 underground.

The XENON experiment requires ultra high purity LXe to enable ionization electrons to drift freely over the 30 cm proposed for the XENON100 unit module. Furthermore, the LXe purity has to be maintained during the long-term detector operation required for statistics and annual modulation analysis. A Xe purification, re-circulation and recovery system was built and operated with the 3 kg prototype [6](see Fig. 6).

For Xe gas purification, a single high temperature SAES getter was used [7]. Electron lifetime longer than 500 μsec is routinely achieved after a few days of continuous purification. A similar gas system with the addition of a Kr removal section will be used for XENON10 underground. We plan to start with commercial Xe gas with a Kr level of roughly 10 ppb to be reduced to a level well below 1 ppb by an adsorption-based system currently under

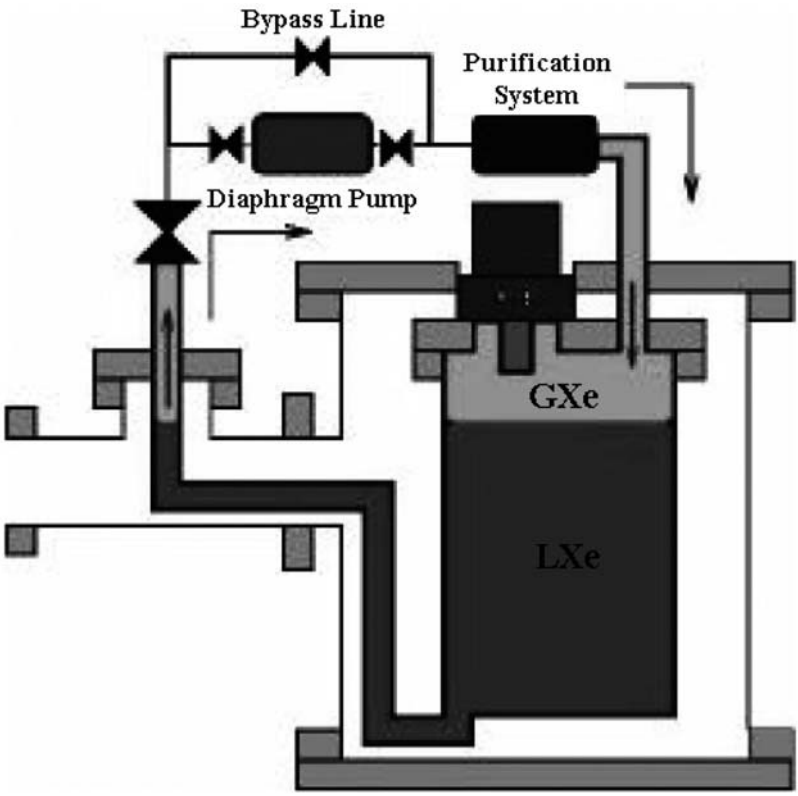

Fig. 6. Schematics of the continuous Xe circulation and purification system.

construction. The reliability and efficiency of both the cryogenics and gas purification systems have been tested with repeated experiments lasting for several weeks continuously.

To maximize the information available from time structure and amplitude of the primary (S1), secondary (S2) and possible CsI photoelectron signal (S3), the 7 PMTs are digitized by both fast (1 ns/sample, 8 bit) and slow (100 ns/sample, 12 bit) ADCs. The gain of the fast ADCs is matched to observe signals down to single photoelectrons, whereas the slow ADCs are optimized to observe the longer proportional light signals from S2/S3. The DAQ system has been developed and successfully applied to record S1, S2 and S3 signals from the current prototype (Fig. 7). The coincidence of more than one PMT signals was required to create a trigger.

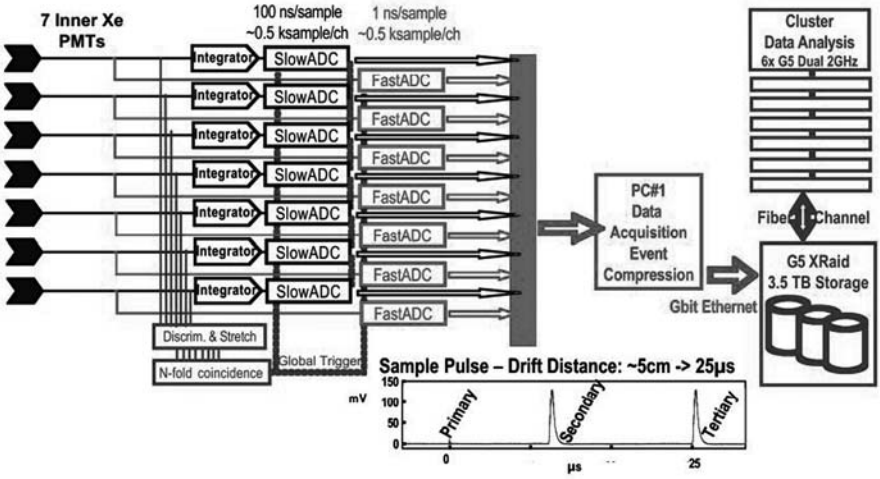

Fig. 7. The DAQ system for recording S1, S2 and S3 signals from seven PMTs.

The 3kg dual phase detector's operation was tested using low energy gamma-rays from a Co-57 source, alpha particles from Po-210 deposited on the cathode, and neutrons from an AmBe source. Two typical waveforms of the direct light produced in the liquid (S1) and the proportional light produced by electrons extracted in the gas (S2) are shown in Fig. 8, for an alpha and gamma event. The S1 signals are prompt while the S2 signals have a width of a few µsec, as expected. The time separation between S1 and S2 is dominated by the drift time in the liquid so that the position of the source along the drift axis is accurately inferred from the known drift velocity at the applied electric field. Since both the Co-57 122 keV gammas and the Po-210 5.43 MeV alphas are very localized in the dense LXe, the time separation between S1 and S2 is close to the maximum drift time of 25 µsec. The other two coordinates are inferred from the center of gravity of the proportional

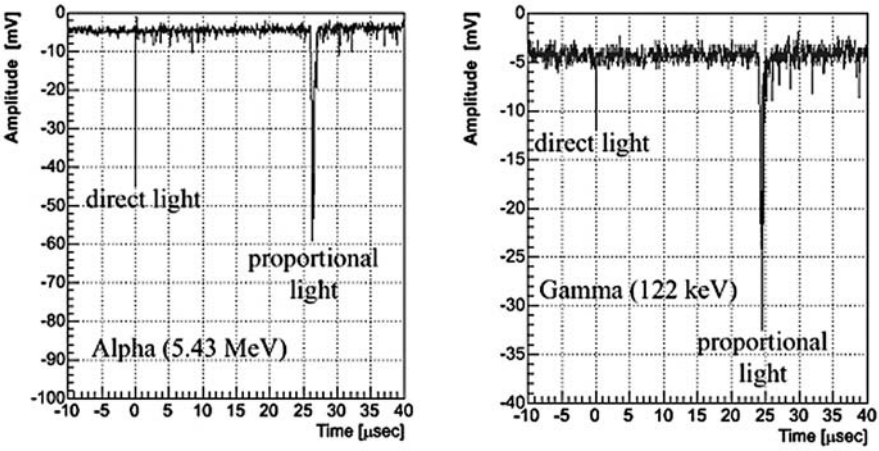

Fig. 8. Waveforms of direct and proportional light for an alpha recoil (left) and an electron recoil (right).

light emitted near the 7 PMTs. Simulations and a preliminary analysis of the alpha data show that the transverse direction of the source can be localized with an accuracy of 1 cm.

In Fig. 9(left) the S1 and S2 signals, simultaneously recorded with gamma and alpha irradiation, are plotted together. The detector was operated at 1kV/cm in the drift region and 10 kV/cm in the gas region. The two classes of events are well differentiated. Another visualization of this event separation is shown in Fig. 9 (right) where the distribution of the same events is plotted as a function of the S2/S1 ratio, in logarithmic scale. The peak from gamma rays is normalized to 1.

The measured ratio $(\mathrm{S2/S1})_\alpha/(\mathrm{S2/S1})_\gamma$ is about 0.03. The separation between alpha recoils and electron recoils is already remarkable, despite the non optimized light collection of the detector at this stage. The ratio is even larger, if we account for the fraction of primary light produced by alpha recoils which is absorbed by the ^{210}Po source disk. Another distinct feature that separates alpha recoils from electron recoils is the dependence of the light on applied electric field. While the primary light from an electron event is strongly quenched by the field because of the reduced recombination rate, this is not the case for a heavily ionizing particle such as an alpha. This means that the primary light is barely affected by the field and the S2/S1 ratio is essentially constant. The dependence of the primary light on the applied field was previously measured by Aprile et al. [8] and has been verified with data from the XENON prototypes.

The $S2/S1$ ratio in LXe for nuclear recoil events was established using a 5 Ci ^{241}AmBe source, emitting neutrons in the energy range 0–8 MeV, in conjunction with a BC501A scintillation coincidence counter to detect events

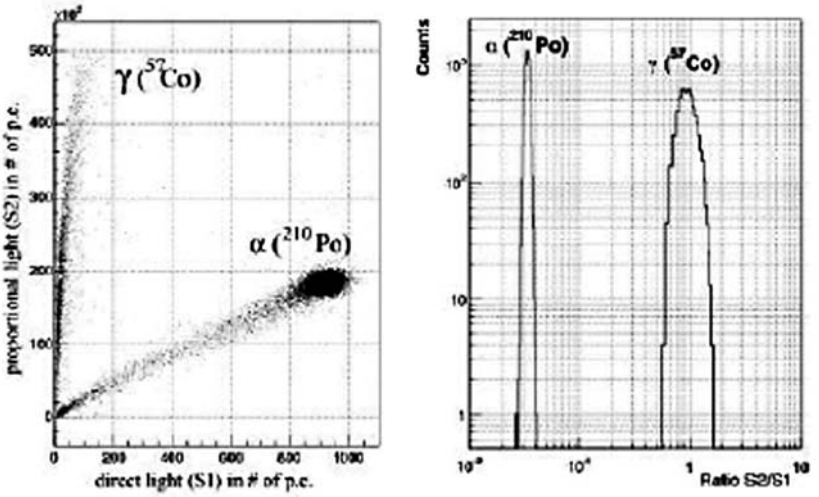

Fig. 9. Measured distribution of S2 (proportional light) versus S1 (direct light) for combined alpha and gamma events (left). Distribution of alpha and gamma events plotted as a function of the ratio S2/S1 (right).

scattering from the LXe target. The 1.4 liter BC501A counter was placed at a distance of 50 cm from the center of the LXe chamber, at a scattering angle of 130 deg.

A population of candidate neutron scattering events in the LXe was obtained by identifying events which were (i) tagged as neutron recoils in the BC501A (by pulse shape discrimination) and (ii) also had an implied ToF (time of flight) between the LXe and BC501A in a window of 40–70 ns. The selected events also contained a significant population of accidental coincidences, between gammas scattering in the LXe, and neutrons, emitted separately, which interact in the BC501A in the appropriate time window. Figure 10 shows LXe event data, for the AmBe source, in which there is a population of events with $S2/S1 \sim 1000$, associated with electron recoils, and a second population of events, with $S2/S1 \sim 100$, associated with elastic nuclear recoils. The figure also contains events arising from the inelastic scattering of neutrons from ^{129}Xe (nat. abun. 27%) and ^{131}Xe (nat. abun. 21%) which have excited states of 40 keV, and 80 keV, respectively. A simulation of the predicted event distribution $S2/S1$ vs. $S1$ is shown in Fig. 11 for comparison with the data in Fig. 10.

A histogram comparing the $S2/S1$ distributions for events $S1 < 20$ p.e. for the AmBe source, and separately a ^{137}Cs source, are shown in Fig. 12. The AmBe curve shows the two populations associated with electron and nuclear recoils. The second population is absent in the ^{137}Cs data. The leakage of electron recoil events in the ^{137}Cs data into the $S2/S1$ region for nuclear recoil events is $< 1\%$. It was established, using separate calibration work,

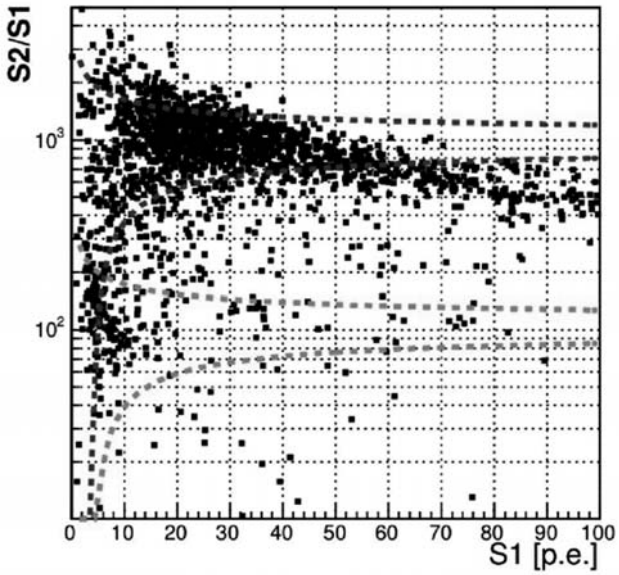

Fig. 10. Data from the 3 kg prototype obtained with an AmBe source. The value of S2/S1 is about 100 for nuclear recoils (lower band). The S2/S1 for electron recoils from gamma rays is about 1000 (upper band). The dotted lines define the statistical spread (2σ) in S1, for S2/S1 centered at 100 (for neutron) and 1000 (for gamma). Inelastic neutron scattering events are also present. Their predicted event distribution is shown in Fig. 11.

that the the $S1$ signals for electron and nuclear recoils is 0.14 p.e./keV$_{ee}$ and 0.07 p.e./keV$_r$, respectively.

The light collection efficiency of the 3kg prototype is not yet optimized, as a large fraction of UV photons are lost by total internal reflection at the liquid-gas interface. As originally proposed for the XENON baseline detector, a CsI photocathode in place of a common cathode can significantly improve light collection and lower the minimum energy threshold [9]. Monte Carlo simulations show that the primary light collection efficiency of the 3kg prototype would increase to ∼6 p.e./keV, with the cathode grid replaced by a CsI photocathode. Results from recent tests with various photocathodes are very encouraging. We have confirmed the high QE in LXe (see Fig. 13), first measured by the Columbia group more than ten years ago [5]. We have also demonstrated the effective suppression of the photon feedback connected with a CsI in a dual phase detector, using a commercial HV switch unit (PVX-4130 from Directed Energy, Inc). The normal rise and fall time of <100 nsec was slowed to 1 μsec, and not appreciable noise from the switching was observed on the PMTs in our 3 kg prototype. Proportional scintillation could be stopped as expected by deriving an appropriate gate signal from the light trigger.

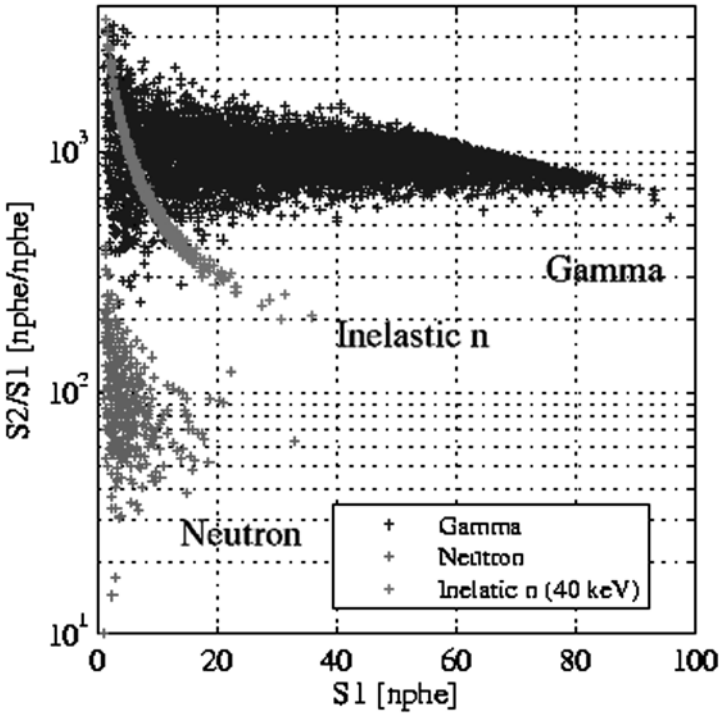

Fig. 11. Simulation of detector response, $S2/S1$ vs $S1$, for AmBe neutrons and uniform gamma spectrum. Distributions are shown for electron recoils ($S2/S1 \sim 1000$), neutron elastic recoils ($S2/S1 \sim 100$), and neutron inelastic recoils associated with ^{129}Xe 40 keV excited state. The inelastic scattering for the ^{131}Xe 80 keV excited state is not shown. The statistical fluctuations, associated with all steps in the generation of S1 and S2 signals have been considered. The variation in signals with position within the detector is not simulated for this plot.

From measurements with a CsI photocathode in the 3 kg dual phase detector we infer a similar value for QE as that measured with a simple ionization chamber without PMT and switching supply. The QE of the photocathode as a function of field (up to 3 kV/cm) is derived from a Monte Carlo simulation of the light collection efficiency and the measured signal size ratio between S2 and S4, where S2 is as explained in the text and S4 is the proportional light from the extracted photoelectrons induced by S2 on the CsI photocathode. The photocathodes used in these experiments were deposited at the same time, using the same substrate and thickness of the CsI layer. Combined results are shown in Fig. 13. We are finalizing a CsI deposition apparatus at Columbia which will enable us to optimize preparation and test CsI photocathode for maximum performance in LXe.

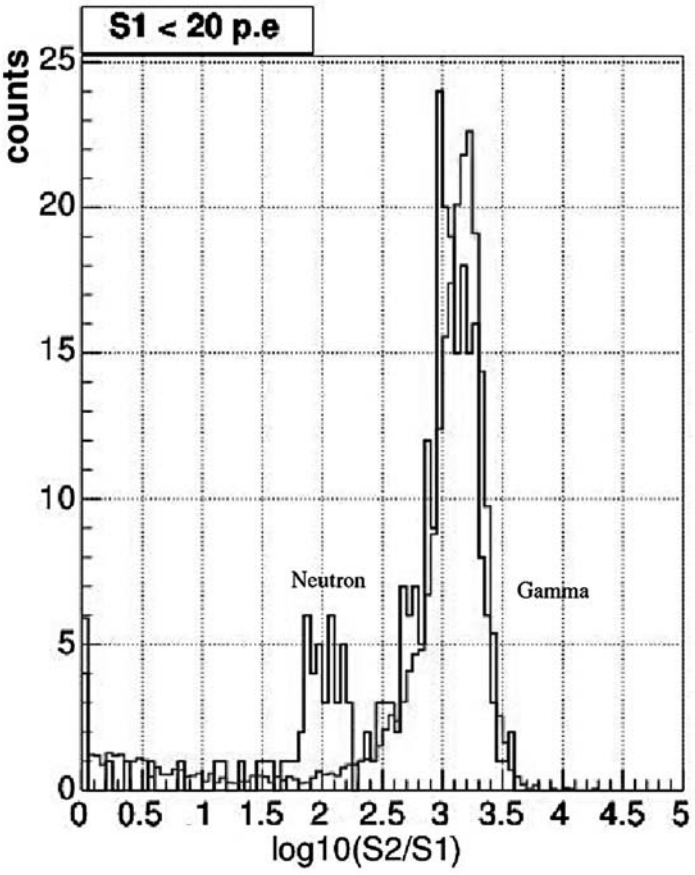

Fig. 12. The blue (dark) line shows a histogram of $S2/S1$ for events with $S1 <$ 20 p.e. taken for AmBe source data shown in Fig. 10. For comparison the $S2/S1$ distribution (red (light) line) for Compton electron recoil events, in the same $S1$ range, for a ^{137}Cs source of 662 keV gamma rays is shown. The AmBe curve shows two distinct populations associated with electron and neutron recoils at $S2/S1 \sim$ 1000 and $S2/S1 \sim 100$, respectively. The second population is absent in the ^{137}Cs data.

The experience gained with the 3kg prototype, its performance and results to-date, as well as results obtained with other detectors not presented here [10], are guiding the realization of XENON10. The 10 kg scale detector will use a light readout with a CsI photocathode in the liquid and an array of PMTs in the gas for much improved light detection efficiency and sensitivity to low energy recoils.

This work was supported by a grant from the National Science Foundation to the Columbia Astrophysics Laboratory (Grant No. PHY-02-01740).

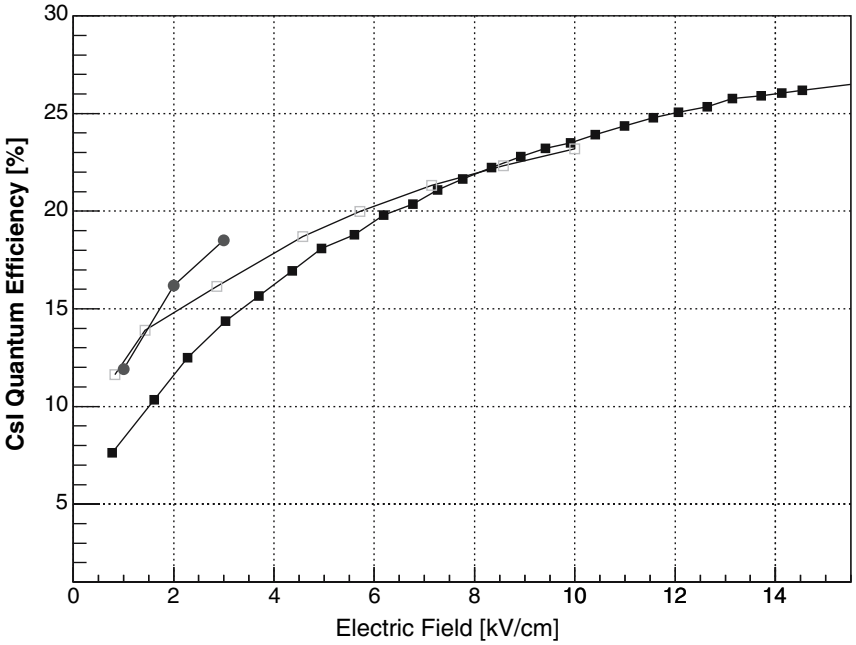

Fig. 13. CsI QE as a function of electron extraction field. The solid square data points are from [5]. The open square are from recent measurements with a similar setup as in [5]. The circle data points are inferred from the signals measured with the 3kg dual phase prototype.

References

1. R.J. Gaitskell: Annu. Rev. Nucl. Part. Sci., 54, (2004) 315–59.
2. CDMS Collaboration: Phys. Rev. Lett. 93, (2004) 211301.
3. M. Yamashita, et al.: Astropart. Phys., 20 (2003) 79–84.
4. M. Yamashita, et al.: Nucl. Inst. and Meth. A, 535 (2004) 692–698.
5. E. Aprile, et al.: Nucl. Inst. Meth. A 338 (1994) 328.
6. S. Mihara, et al.: Cryogenics, 44 (2004) 223–228.
7. SAES Pure GAS, Inc.: http://www.saesgetters.com/.
8. E. Aprile, et al.: IEEE Trans. Nucl. Sci., 37 (1990) 553.
9. XENON Collaboration: NSF proposal number 0201740, 'XENON: A Liquid Xenon Experiment for Dark Matter', proposal submitted to NSF, Particle and Nuclear Astrophysics in Sep. 2001.
10. E. Aprile, et al.: 'Scintillation Response of Liquid Xenon to Low Energy Nuclear Recoils', submitted to Phys. Rev. D.

Recent Status of the XMASS Project

Chikaori Mitsuda

Kamioka Observatory, ICRR, Univ. of Tokyo, Higashi-Mozumi,
Gifu 506-1205, Japan
mitsuda@suketto.icrr.u-tokyo.ac.jp

XMASS is an underground experiment aimed at searching rare phenomena under an ultra low background environment by using ultra pure liquid xenon in the Kamioka mine, Japan. The one of the main physics targets of XMASS is cold dark matter. So far, we have done 2 series of test experiments with a prototype liquid xenon detector. In this paper, the current status of the XMASS project, especially the first results from the second test experiment, is reported.

1 Overview of XMASS

1.1 What's XMASS

XMASS is a multi purpose detector to search for rare phenomena under an ultra low background environment by using ultra pure liquid xenon in Kamioka mine, Japan. The name of XMASS is constructed from various meanings like followings.

- Xenon MASSive detector for solar neutrino (pp/^{7}Be).
- Xenon detector for weakly interacting MASSive Particles (Dark matter search).
- Xenon neutrino Mass detector (Double beta decay).

The one of the main physics targets of XMASS is cold dark matter search. In this report, we will concentrate on the dark matter search.

1.2 Physics Goal of XMASS

The physics goal of XMASS detector is direct dark matter search via nuclear elastic scattering. The Fig. 1 shows the expected energy spectrum for the dark matter. Assuming the mass of 100 GeV dark matter, the cross section of 10^{-6} pb or proton and 0.2 of quenching factor with natural 10t Xenon, we can expect the 200 events/day/ton at the energy threshold of 5 keV.

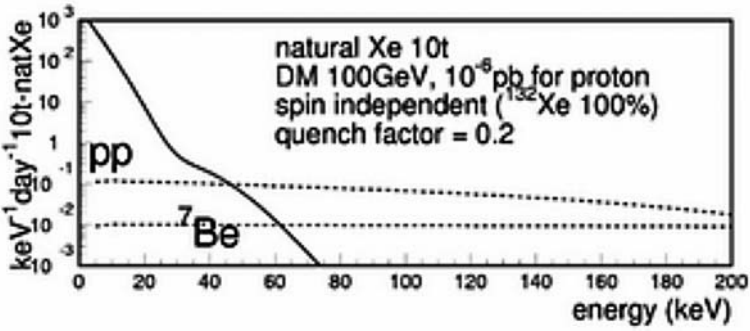

Fig. 1. The expected signal rate for dark matter. The upper and lower dashed line shows the expected pp and ^7Be solar neutrino energy spectrum respectively. The solid line shows the expected the dark matter energy spectrum.

1.3 Strategy of the XMASS Project

So far, we have developed a prototype detector and done 2 series of test experiments with it. The mass of this prototype detector is 100 kg. We are aiming at scale-up detector with the further larger volume in the future by following steps.

(1) The cubic prototype detector with 100 kg for the R&D.
(2) The spherical 800 kg detector of 1 m diameter with the 100 kg fiducial volume (F.V.) for the dark matter search.
(3) The spherical 20 ton detector of 2.5 m diameter with the 10 ton F.V. for the dark matter search and pp/^7Be solar neutrino observation.

The purpose of the prototype detector is to confirm the feasibilities of the next XMASS 800 kg detector, for example, the analysis techniques, self shielding performance, low background properties and purification techniques. In the 800 kg XMASS detector, our goal will be to search for dark matter with a factor of 100 improved sensitivity.

The advantage of the XMASS detector is the self-shielding effect. Xenon has a large atomic number (Z=54). Therefore, external gamma-ray backgrounds from outside the detector will be reduced efficiently in the F.V. by self-shielding. The reduction efficiency of 30 cm depth from outside is 10^5 for below about 500 keV like a Fig. 2. The density of liquid xenon is about 3 g/cm^3. It provides a compact detector.

The key-ideas of XMASS project are based on the various neutrino detector which produce the great results so far, for example, Kamiokande, Super-Kamiokande, SNO, and KamLAND. Their design are an uniform and simple scintillation detector. They have a large volume which achieves the low background by self-shielding. As a further advantage, it is easy to purify even after the experiment started because of using liquid media. So, the large liquid xenon detector is the most promising material.

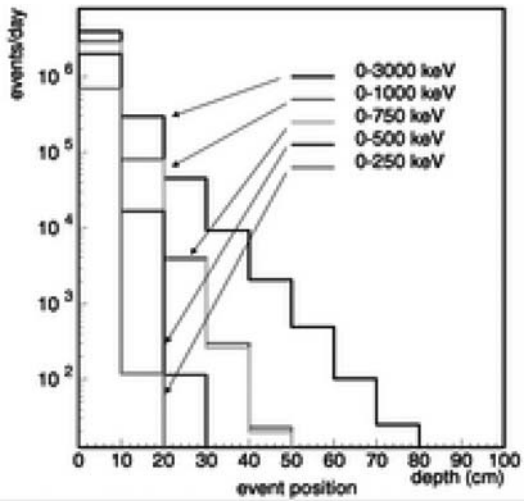

Fig. 2. The gamma-ray event rate (events/day) of the xenon depth for each energy region.

The followings are some major advantages of liquid xenon:

- Liquid xenon has a large photon yield (about 42000 photons/MeV). This feature directly provides the advantages of low threshold and high resolution.
- The wave length of the scintillation light from liquid xenon is about 175 nm. So, the scintillation light can be directory read by Photo-Multiplier Tubes (PMTs).
- Xenon has a large atomic number (Z=54). Therefore, external gamma-ray backgrounds from outside the detector will be reduced efficiently by self-shielding. The density of liquid xenon is about 3 g/cm^3. It provides a compact detector.
- Various purification methods, like distillation, can be applied. This is very effective to eliminate internal impurities.
- The melting (boiling) point of xenon is 161.4 K (165.1 K). Liquid nitrogen can be use to liquefy xenon.
- There is no long-life radioactive isotopes in xenon.

2 Current Status of XMASS

2.1 Prototype dDetector

Figure 3 shows a schematic view of the prototype detector.

The prototype detector consists of 100 kg of liquid xenon and 54 low-background PMTs. It is installed in a heavy gamma ray shield in a clean room

Fig. 3. XMASS prototype detector. 100 kg liquid xenon and 54 low-background PMTs are used. PMTs are attached to the 30 L OFHC chamber through 5 mm thickness MgF_2 windows. They are put into a heavy shield in a clean room. The XMASS prototype detector is located in Kamioka Observatory, ICRR, Univ of Tokyo, in Kamioka mine.

in Kamioka Observatory, ICRR, Univ. of Tokyo in Kamioka mine (2700 m water equivalent).

The low-background PMTs are Hamamatsu R8778, which were developed for this project. The quantum efficiency and collection efficiency are about 30% at 175 nm and about 90%, respectively. The radioactivity of the materials were measured by HPGe detector, then low-background materials were selected to assemble R8778. The remaining radio activities of a R8778 PMT are measured as follows; U: $1.5 \pm 0.3 \times 10^{-3}$ Bq, Th: $3.2 \pm 4.6 \times 10^{-3}$ Bq, and ^{40}K: $1.7 \pm 2.9 \times 10^{-3}$ Bq. These PMTs are attached to a square-shaped 30 L chamber made from OFHC (Oxygen Free High purity Copper) through 5 mm thickness MgF_2 windows. The photo coverage using 54 of low background 2-inch PMTs is about 16%. We can obtain 0.8 photo-electron(p.e.)/kev in the detector center. The heavy gamma ray and neutron shield surrounds the OFHC. They consist of 5 cm OFHC and 15 cm lead for gamma ray, 5 cm boric acid for thermal neutron, and 15 cm polyethylene for external neutron from the inner of shield. To shut out the radon from mine air, the EVOH (Ethylen Vinyl Alcohol) sheet is installed between OFHC and lead. The inside of EVOH sheet is filled with Super-Rn-Free-Air (SRFA) in order to reduce the radon background. The radon concentration of SRFA is about 3 mBq/m^3.

The charge information from the PMTs are read by 54 channels of charge sensitive ADCs and a common Flash ADC for summed signals. The threshold of each PMT is about 0.4 p.e. The data acquisition trigger is applied when there are 4 multiple hits within 100 ns time window. The typical trigger rate for normal runs is about 1.5 Hz.

So far, we have done two series of test experiments with the prototype detector. The first test run was carried out in December 2003 for about 6 days.

We took about 2 days normal runs for external background estimation. After the first run, we purified the xenon by distillation, installed new electronics, applied longer baking time of the system, and then carried out a second test run. This was from August 3 until August 11, 2004, including 6 days normal runs. The longer baking time of the system and cleaning up the detector increased the photon yield by a factor of 1.7 comparing with the first test run. Here are reported the main results from these test experiments.

2.2 Vertex and Energy Reconstruction

The vertex and energy reconstruction is performed by PMT charge pattern (not timing). The Fig. 4 shows the event hit pattern of a typical background event sample. In the figure, the QADC, FADC, and hit timing information are available for analysis.

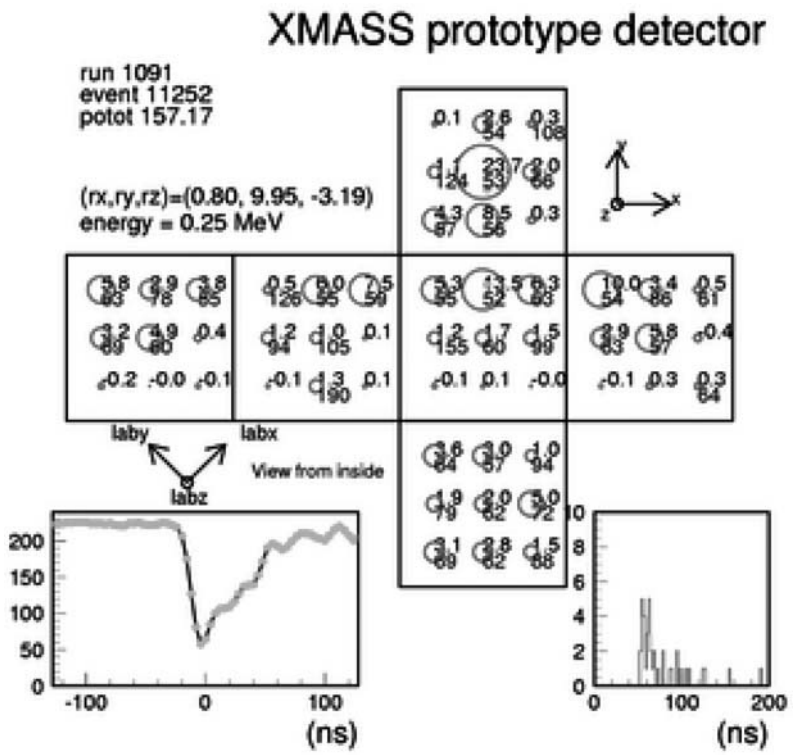

Fig. 4. The background event sample observed by the prototype detector. The circles show the QADC. The number in upper and lower column shows the energy and the hit timing, respectively. The QAD, FADC, and hit timing information are available for analysis. The reconstructed vertex point and energy are also shown for this event sample in the left upper side of this figure.

The PMT acceptances from various vertices are calculated our Monte Carlo (MC). The observed data are compared with the simulated acceptance maps by a following equation.

$$\mathrm{Log}(L) = \sum_{\mathrm{i=1}}^{\mathrm{PMT}} \mathrm{Log}\left(\frac{\exp(-\mu)\mu^{\mathrm{n}}}{\mathrm{n}}\right) , \tag{1}$$

$$\mu = \frac{\mathrm{F(x,y,z,i)}}{\sum \mathrm{F(x,y,z,i)}} \times \text{total p.e.} , \tag{2}$$

where L is likelihood function, n is observed number of p.e., and F is the acceptance for i-th PMT (MC). The MC is performed assuming the light emittance of 42 ph/keV, the absorption length of 100 cm, and scattering length of 30 cm.

2.3 The Source Run

Figure 5 shows a demonstration of the reconstruction performance of the prototype detector using ^{60}Co gamma ray source. The collimated gamma rays are injected horizontally along the detector's Z-axis. There are 3 collimators

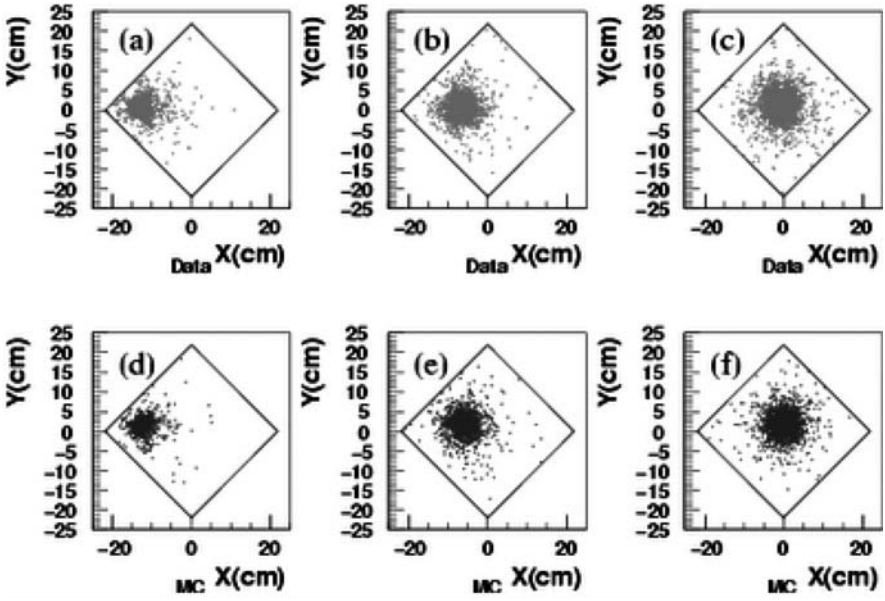

Fig. 5. Vertex reconstruction performance: (a),(b),(c) Data and (d),(e),(f) MC. The reconstructed vertex positions of collimated gamma source runs are plotted. (a),(c) Hole-C (left side), (b),(e) Hole-B (left-center), and (c),(f) Hole-A (center) are used.

on the heavy shield, that is, Hole-A, Hole-B, and Hole-C. Hole-A is located at the center of the detector. Hole-B and Hole-C are shifted to the left side on the plots. The upper plots are Data and lower plots are MC simulation. The agreement between Data and MC is good.

Figure 6 shows the self-shielding performance of the prototype detector. The horizontal axis is the distance from the injection point of collimated gamma rays.

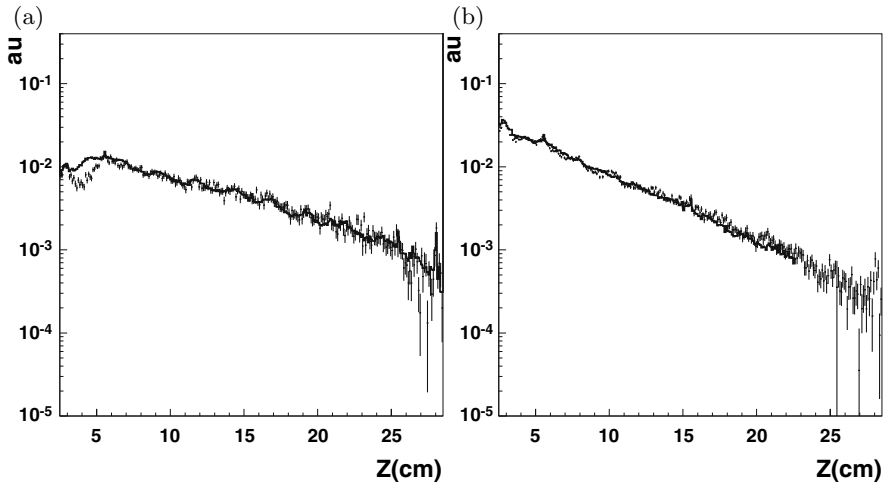

Fig. 6. Self shielding performance: (a) ^{60}Co and (b) ^{137}Cs. The solid lines and points correspond to MC and Data, respectively. The collimated gamma rays are injected horizontally from Hole-A (center) at Z=0 (cm) position. The reconstructed vertex positions are plotted. For the Data, the background data is subtracted. The wiggles are due to grid effects of the current reconstruction tool and will be improved.

The collimated gamma rays were injected from the Z=0 side horizontally. Although the reduction factor through the prototype detector is about 1 order of magnitude for ^{60}Co, it is about 2 orders for ^{137}Cs, because ^{137}Cs has a lower mean energy. In the wall of detector, there are small disagreement between Data and MC because of PMT saturation region. The self-shielding effect between Data and MC agrees well. This proves the self-shielding technique works well in the prototype detector as expected.

In this second test run, we took the every day calibration data using ^{60}Co (1132 keV) in order to confirm the energy scale stability. Figure 7 shows the performance of the energy scale stability of prototype detector.

The horizontal axis is the elapsed day. The vertical axis is the relative difference (%) which is calculated from the results of peak position using

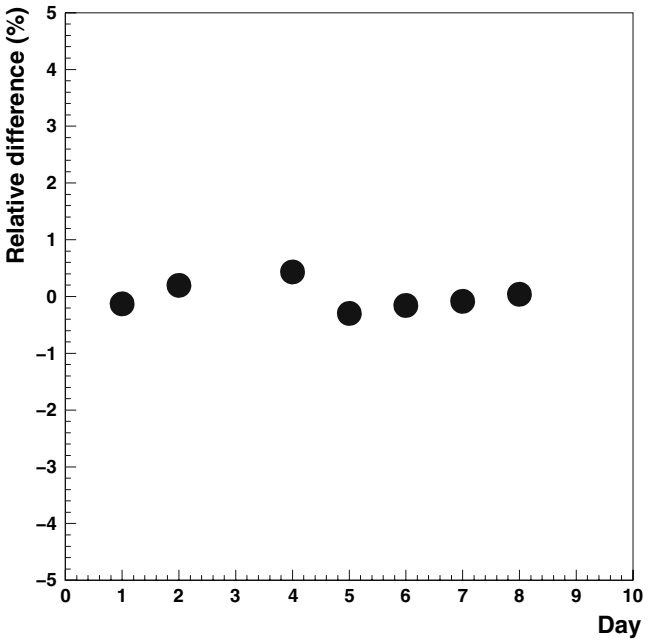

Fig. 7. The energy scale stability in the second run.

simple Gaussian fit. There is no degrading of energy scale. The data taking was done within ± 0.5% stability.

2.4 External Background Source

Figure 8 shows the MC estimation for full volume of prototype detector. Each background level was estimated from known sources which was measured by high purity Ge detector. The known sources are follows.

- Gamma rays from outside shieled.
- ^{238}U, ^{40}K, and ^{232}Th series from PMTs origin.
- ^{210}Pb in the lead shield.

Figure 9(a) shows the measured energy spectrum of the prototype detector in the heavy shield.

This data was taken during the second test run in August 2004 for about 6 days. The dashed (dotted) line shows events in a 10 cm (20 cm) F.V. in which reconstructed vertex positions must be away from the detector wall by 10 cm (5 cm). Therefore, the 10 cm (20 cm) F.V. corresponds to a 10cm (20 cm) cube and the volume inside is 1 L (8 L).

The self-shielding effect can be seen clearly around the 200–400 keV energy region.

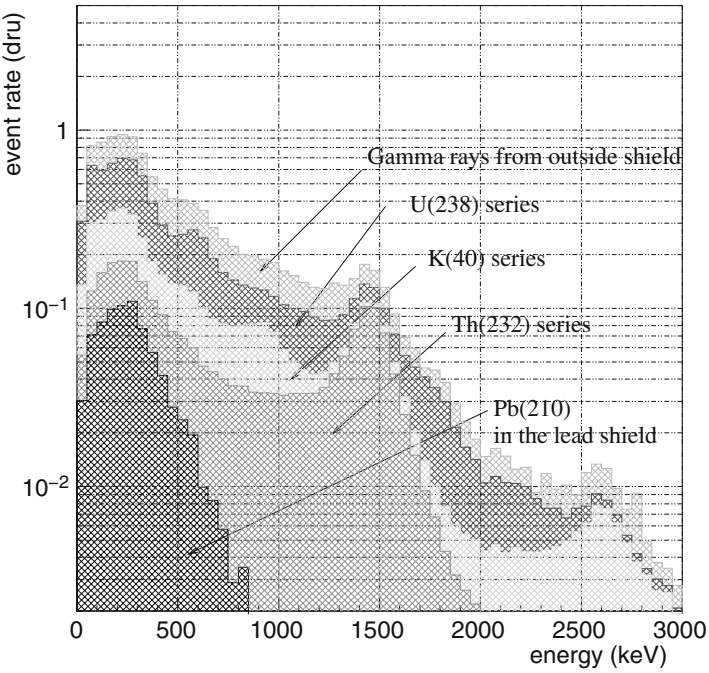

Fig. 8. The MC estimation for full volume of prototype detector using known sources. The each histogram shows each background energy spectrum of known source.

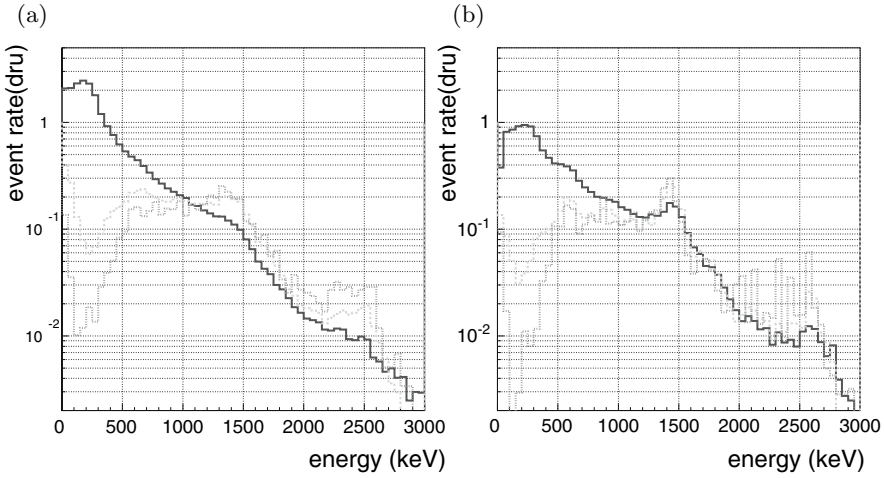

Fig. 9. Energy spectrum of normal run: (a) Data and (b) MC. The solid, dashed, and dotted lines correspond to full volume, 20 cm F.V., and 10 cm F.V., respectively. The event rate increase at the lowest energy region of dotted and dashed lines are due to the detector wall effects (see text).

The event rate increasing below 100 keV is artificial. It is due to detector wall effects of the prototype detector. The wall effects mean the dead angle from the PMTs only for the prototype detector. The scintillation light at the dead angle from PMTs give quite uniform 1p.e. level signal for PMTs. This cause miss reconstruction as if the vertex is around the center of the detector. If we use the immersing PMTs into liquid Xenon and spherical design in the future, this problem will be solved. We will eliminate this effect in the next 800 kg detector.

Those 2 plots agree within a factor of 2. Therefore, we think we have an understanding of the major sources of the remaining external background. We achieved the very low background level, 10^{-2}/kg/day/keV at 100 keV.

There are some small differences including, for example, the shape of the peak from ^{40}K (around 1.4 MeV). We are still tuning the current MC to improve these points.

2.5 Internal Background Source

We have estimated major internal background sources of the prototype detector. For radon in the Uranium and Thorium series, the time coincidence between Bi and Po decay chains was used. For ^{222}Rn in the Uranium chain, we have found 67 coincidence events during 1.8-day measurements. Actually, we took two separate runs; 0.8-day on Aug. 4 and 1.0-day on Aug. 10, 2004. The estimated Uranium contaminations from these 2 runs were $^{238}\mathrm{U} = (72 \pm 11) \times 10^{-14}$ g(U)/g(Xe) for Aug. 4 and $^{238}\mathrm{U} = (33 \pm 7) \times 10^{-14}$ g(U)/g(Xe) for Aug. 10. This decrease is consistent with the expected radon decay (half life = 3.8 days). Therefore, most of the ^{222}Rn which might come from outside the detector from storage tanks, piping, etc, will decay out.

For the ^{220}Rn in the Thorium chain, we have searched for possible peaks from Bi and Po decay chains in FADC signal. We found no coincidence during 3.2 days FADC data. This corresponds to $^{232}\mathrm{Th} < 23 \times 10^{-14}$ g(Th)/g(Xe) (90% C.L.).

Another major internal background would be ^{85}Kr. In the December 2003 run, there was a 3 ppb Kr level in xenon (measured value). We have purified 100 kg of xenon by a distillation method in March 2003, then measured Kr contamination in xenon again. The distillation system make use of the different boiling point between Xenon and Krypton (165 K and 120 K at 1 atm respectively). This method is very effective to reduce internal impurities (^{85}Kr, etc). The designed factor is 1/1000 Kr/1 pass. The measured Kr contamination decreased to (3.3 ± 1.1) ppt. So, we achieved almost designed factor for the Kr reduction.

Table 1 shows a summary of the current estimation of the internal background sources.

Table 1. Summary of the current estimation for internal background sources. The current goal is for the XMASS 800 kg detector.

Source	Estimation	Goal
^{238}U	$(33 \pm 7) \times 10^{-14}$ g/g	1×10^{-14}
^{232}Th	$< 23 \times 10^{-14}$ g/g	2×10^{-14}
^{85}Kr	(3.3 ± 1.1) ppt	1 ppt

3 Future Project and Expected Sensitivity

We are going to aim at the future project based on the results of prototype detector. Next project is a construction of the 800 kg detector for dark matter search. The diamemter is 80 cm. This detector is **full** photo-sensitivity and **spherical** geometry detector. This detector has 780 2 inch PMTs, 70% photo-coverage, and photon-yields of about 5 p.e./keV.

This detector can solve the vertex miss reconstruction problem by immersing PMTs into liquid xenon. The external gamma rays background can be reduced by self shielding effect which is already demonstrated by the prototype detector. The internal background of Kr and Radon is almost reduced to the goal level.

Assuming the 1/10 lower background PMT of current R-8778 in proceed, we can achieve the background level of $8{\times}10^{-5}$ dru (kg/day/keV) under the 50 keV energy region in the fiducial volume of 40 cm (100 kg). In this sensitivity, we can observe the dark matter signal based on the cross section of 10^{-6} pb and the energy of 50 GeV or 100 GeV for dark matter.

Assuming the 100 kg fiducial volume 5 years, the 5 keV energy threshold and 3σ discovery, we improve the sensitivity by a factor of more than $10^{2\sim3}$ for existing experiments. Especially, we can achieve the cross section of 10^{-9} pb for spin independence and 10^{-3} pb for spin dependence by the spectrum analysis of dark matter search.

4 Summary

Now, the research and development for our prototype detector is going well. The demonstration of reconstruction, self-shielding, and low background properties has been done. For the external gamma rays background, the level of 10^{-2} /kg/day/keV is already achieved. For the internal background, the Kr concentration of 3.3 ± 1.1 ppt was achieved by distillation system. This reduction factor is also consistent with designed factor. The concentration of ^{222}Rn(U) and ^{220}Rn(Th) are $33 \pm -7 \times 10^{-14}$g/g and less than 23×10^{-14} g/g, respectively. In the future, the 1/30 reduction will be achieved enough for 800 kg detector. Within a few years, we are planning to build the 800 kg detector and start to search for dark matter.

Acknowledgments

The author would like to thank the cooperation of the Kamioka Mining and Smelting Company. This work is partially supported by Grant-in-Aid for Scientific Research on Priority Areas (A) of the Japanese Ministry of Education, Science and Culture.

DRIFT and Prospects for a Large Scale Directional WIMP Detector

J.C. Davies and N.J.C. Spooner
On behalf of the DRIFT Collaboration*

Department of Physics and Astronomy, University of Sheffield, S3 7RH, UK
J.C.Davies@sheffield.ac.uk
N.Spooner@sheffield.ac.uk

The DRIFT experiment is the first directionally sensitive dark matter search. The design is based on a gaseous time projection chamber and employs carbon disulphide gas at low pressure. DRIFT-I was installed in the underground laboratory at Boulby mine in 2001 and has acquired more than 1500 hours of data. The second generation detector, DRIFT-II, is undergoing initial testing and will be installed in the new experimental hall at Boulby early in 2005.

1 DRIFT: A Directional Dark Matter Detector

The DRIFT experiment design has delivered the world's first directionally sensitive dark matter detector [1, 2]. The design concept (Fig. 1) employs time projection chambers (TPCs) with multi-wire proportional counters (MWPCs) for readout. The first generations of detector use carbon disulphide (CS_2) gas due to its electronegativity, which allows negative ions to be drifted within the TPCs, rather than electrons, and so avoids large diffusion and greatly improves the spatial resolution.

Most models suggest that the Earth is travelling through a halo of WIMPs in the Milky Way. A dark matter detector should, therefore, observe a directional 'WIMP wind' signal. A time projection chamber is well suited for dark matter detection because it enables directional track information to be recorded, and so can be used to provide the most powerful evidence for the existence of WIMPs in the Galaxy (Fig. 2) and to distinguish between postulated halo models [4, 5]. The DRIFT design has excellent background rejection potential via range-ionization discrimination [3]. It can probe the WIMP parameter space to sensitivities (defined as a minimum of the sensitivity curve) as shown in Fig. 3 [5].

*UKDMC (University of Sheffield, University of Edinburgh, R.A.L., Imperial College), Occidental College (L.A.), Temple University (Philadelphia), University of New Mexico, University of Boston, University of Thessaloniki (Greece), University of Darmstadt (Germany)

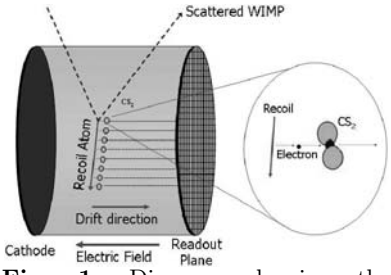

Fig. 1. Diagram showing the DRIFT detector concept.

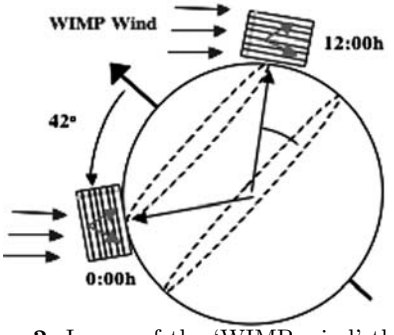

Fig. 2. Image of the 'WIMP wind' that may be seen as a directional signal by a detector such as DRIFT.

DRIFT-I is the first full-scale detector from the DRIFT collaboration [2]. It was installed underground at Boulby mine during the summer of 2001. It consists of a 1 m^3 fiducial volume within two back-to-back TPCs, with a shared central cathode, and uses two MWPC readouts mounted horizontally. This detector is placed inside a stainless steel vacuum vessel, which is filled with CS_2 gas at low pressure (standard running pressure of 40 torr, giving a target mass of 167 g). The DRIFT-I data acquisition (DAq) system was designed at SLAC.

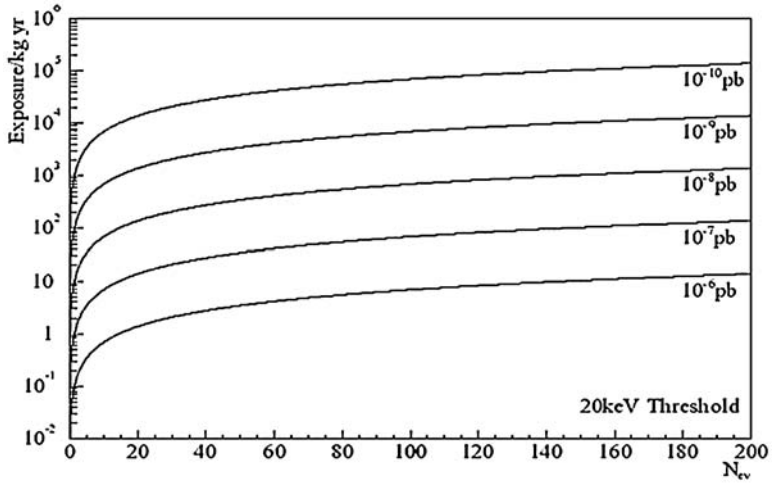

Fig. 3. Directional sensitivity that may be achieved by a DRIFT-type detector for a given exposure and number of detected events.

1.1 Simulations

Simulations investigating neutron background sources have been performed for DRIFT-I using both a 'home-grown' Monte Carlo and also the GEANT4 toolkit. The input neutron spectra were obtained from measurements of the uranium and thorium content in the DRIFT cavern and component materials, using a germanium detector in the cavern and mass spectrometry techniques for the other materials. The neutron rate predicted by the simulations for an unshielded detector is 12.6 events/kg/day due to neutrons from rock.

1.2 Operations

During the DRIFT-I (Fig. 4) running time, since 2001, there have been a number of operational issues [2], some of which have been found to have solutions that allow the detector to remain at least partially operational and so it has still been possible to take data, although not always with the full detector.

In 2004 new alpha veto hardware was installed, as was ∼8 tons of CH_2 neutron shielding –30 g/cm^2 thick on all sides – in the form of polypropylene pellets (see Fig. 5).

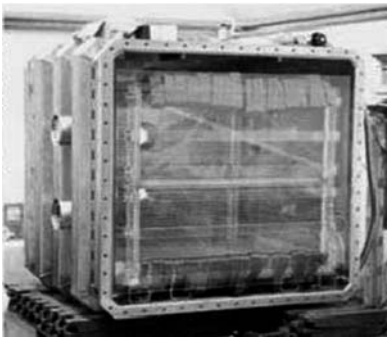

Fig. 4. Photograph of the DRIFT-I inner detector positioned inside the stainless steel vessel with the front panel removed.

Fig. 5. Photograph of the partly shielded DRIFT-I vessel in position at Boulby mine with the front section of shielding removed.

1.3 Preliminary Results

DRIFT-I has managed to acquire over 1500 hours of data and its response to neutrons, alphas, gammas and sparks has been observed. Signals from a neutron trackand a spark are shown in Figs. 6 and 7, respectively.

DRIFT-I has also attained a preliminary background measurement from 37.25 days of livetime of 28 events/kg/day, for an unshielded detector (Fig. 8).

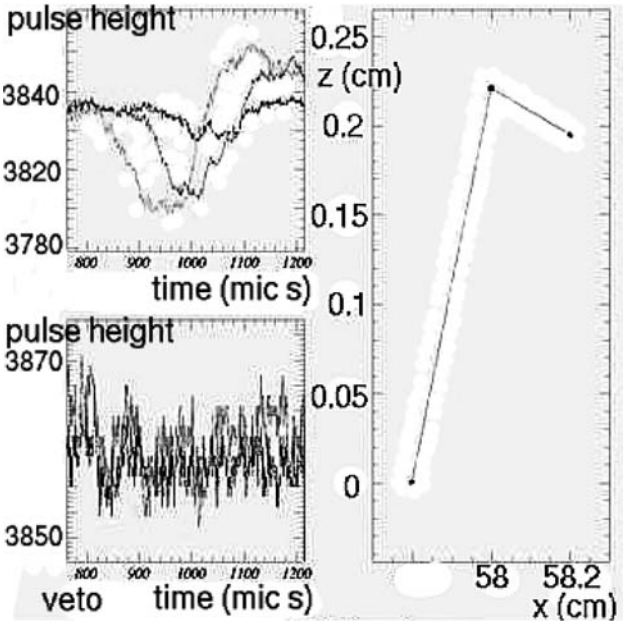

Fig. 6. Example of the signal recorded by the DRIFT-I detector due to an alpha event.

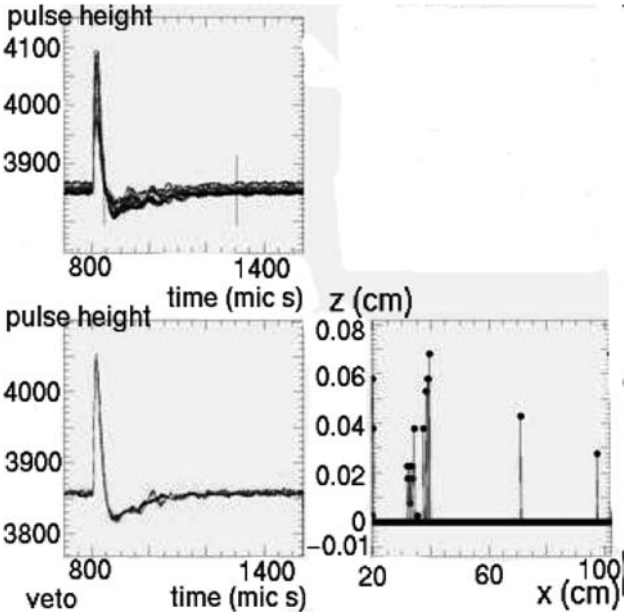

Fig. 7. Example of the signal recorded by the DRIFT-I detector due to a spark.

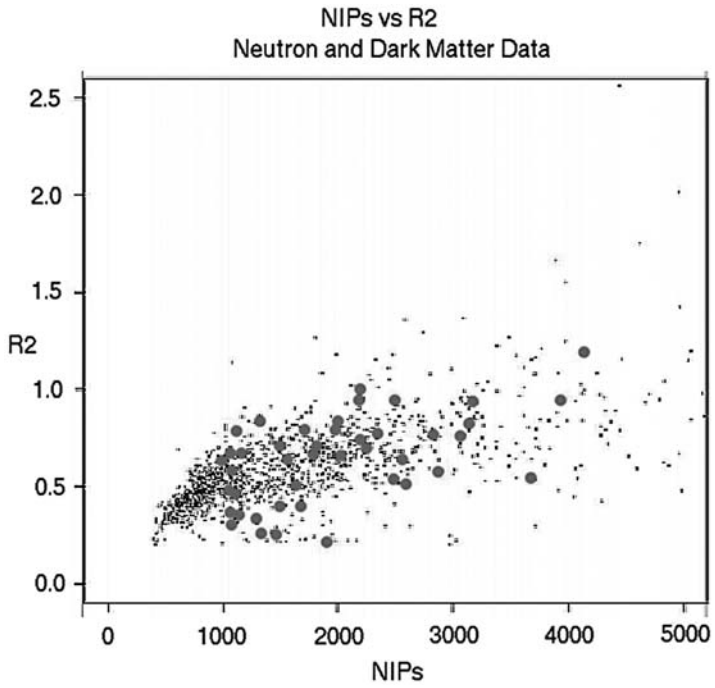

Fig. 8. Plot of the Number of Ion Pairs produced in an event against the 2-dimensional range of the event. Data from a neutron source is shown (small dots) along with background data (large dots).

The high rate, compared to that predicted by computer simulations for neutrons, may be due to neutrons from sources other than the surrounding rock, or alphas that have managed to avoid all the data cuts.

1.4 DRIFT-I Summary - Lessons Learned

The experience from installing and running DRIFT-I has allowed many invaluable lessons to be learned, both in detector engineering and in performance optimisation. These lessons have been applied to the design of the next generation detector - DRIFT-II.

2 DRIFT-II

DRIFT-II is the newest DRIFT detector and will begin taking data underground in 2005. The design is essentially an improved and expanded version of DRIFT-I (see Fig. 9) [6]. DRIFT-II will be an array of modules, with each module consisting of a stainless steel vacuum vessel of internal dimensions

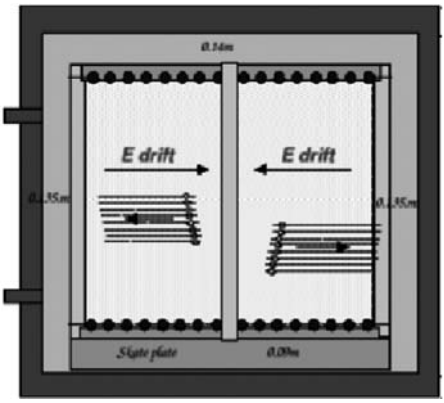

Fig. 9. Diagram showing the design of the DRIFT-II detector.

Fig. 10. Photograph of the first DRIFT-II vessel at Occidental College, L.A., where commissioning of the first DRIFT-II detector is being performed.

of $1.5 \times 1.5 \times 1.5$ m^3 and with hinged door (see Fig. 10). The vessels each contain two back-to-back time projection chambers and two MWPC read-outs mounted vertically (see Fig. 9), which will reduce the effects of falling debris and allow both MWPCs to operate in identical environments. Initially DRIFT-II will employ CS_2 gas at low pressure again, with a gas system able to maintain various pressures and flow rates. Subsequent gas systems will also be able to maintain different gas mixtures. Care has been taken in choosing the materials used for detector components to ensure they are known to be of at least a minimum purity, such as the low background stainless steel vessel, high purity copper used for the field cages and the radiopure lucite also used inside the vessel. The spatial resolution is improved, as is the 3-dimensional track reconstruction capability, and the background noise level of the data acquisition system is reduced.

Another important consideration that had to be made while designing the DRIFT-II detector array was the size and layout of the experimental hall at Boulby mine. The limited space available places a constraint on the size of vessel and amount of passive neutron shielding that can be used. By looking at these dimension constraints and taking information from computer simulations (Fig. 11), the layout of the DRIFT-II array will be as rows of four modules sharing some shielding, as shown in Figs. 11 and 12.

2.1 Data Acquisition and Commissioning

The data acquisition system for the DRIFT-II detectors includes the grid DAq, which uses a grouping technique and so records signals through only eight channels from 512 wires, using Amptek pre-amplifiers. The grid DAq also has wires at the front and back, which are used as alpha vetoes in the

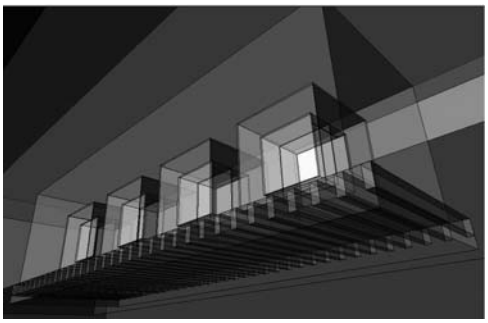

Fig. 11. VRML visualisation of the geometry used for GEANT4 simulations of DRIFT-II type detectors.

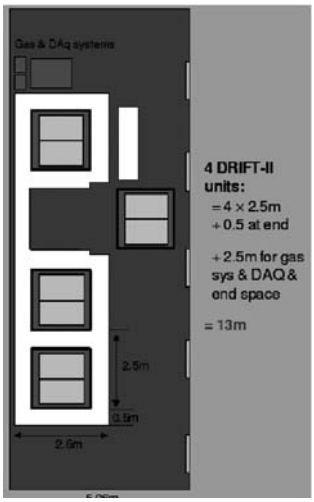

Fig. 12. Diagram of the planned layout for a group of four DRIFT-II modules with their shielding.

DRIFT y-direction. There is also an anode DAq system that simply registers hits and also has alpha vetoes in the DRIFT x-direction.

The initial commissioning of the first DRIFT-II detector module is currently underway at Occidental College, L.A. (Fig. 13), where, to date, leak testing has been done and ^{55}Fe calibration data has been taken.

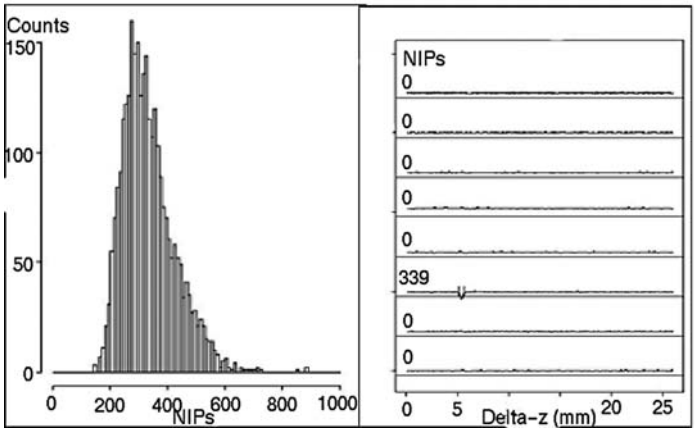

Fig. 13. Initial data plots from the commissioning of the first DRIFT-II detector showing the ^{55}Fe spectrum on the left with an ^{55}Fe signal shown on the right.

2.2 Simulations

Particle backgrounds are a big issue for dark matter detectors. It is important to investigate possible sources of these backgrounds and to use computer simulations to try to understand their effects. The main problem backgrounds for dark matter detectors are sources of neutrons because the signal seen when a neutron interacts inside the detector can be indistinguishable to that of the WIMPs being searched for. Work on simulating the neutron backgrounds for this type of detector has been performed [7] and the results have been used to make decisions on material purity and shielding requirements.

3 Future Prospects

The next generation, DRIFT-III, is expected to have a sensitivity down to about 10^{-8} pb, assuming no background and using an array of 100+ units of dimension $(1.5\,\mathrm{m})^3$. Further expansion up to a 1 ton target would give a potential sensitivity of 10^{-10} pb. This would allow the possibility of distinguishing such objects as the Sagittarius CDM stream [8]. It is also possible for future DRIFT detectors to have the capability of searching for other rare events, such as KK-axions and Universal Extra Dimensions.

While the first DRIFT detectors use CS_2 gas, future detectors may use an alternative gaseous target (single gas or gas mixtures). Research and development work on alternative charge readout devices, focussing on the possibilities of MICROMEGAS, is ongoing, along with halo modeling and computer simulation of the DRIFT detectors.

References

1. C.J. Martoff et al., Nucl. Instr. & Meth. A **440** (2000) p355.
2. G.J. Alner et al., Nucl. Instr. & Meth. A **535** (2004) p644.
3. D.P. Snowden-Ifft et al., Phys. Rev. D **61** (2000) 101301
4. C.J. Copi and L.M. Krauss, Phys. Rev. D **63** (2001) 043507.
5. B. Morgan, PhD thesis, University of Sheffield, 2004.
6. The DRIFT Collaboration, In preparation.
7. M.J. Carson et al., Proceedings of the IDM 2004 Conference.
8. K. Freese et al., Phys. Rev. Lett. **92** (2004) 111301.

COUPP, a Heavy-Liquid Bubble Chamber for WIMP Detection

J. Bolte[1], J.I. Collar[1], M.B. Crisler[2], D. Holmgren[2], D. Nakazawa[1], B. Odom[1], K. O'Sullivan[1], R. Plunkett[2], E. Ramberg[2], A. Raskin[1], A. Sonnenschein[1], and J. Vieira[1]

[1] KICP and Enrico Fermi Institute, University of Chicago, IL, USA
collar@uchicago.edu
[2] Fermi National Accelerator Laboratory, Batavia, IL, USA

Our group is presently investigating the application of bulk superheated liquids to Weakly Interacting Massive Particle (WIMP) detection. It has been possible to demonstrate [1] that relatively large volumes of heavy refrigerants can be kept in a radiation-sensitive metastable state for long enough to perform rare-event searches. For certain choices of operating pressure and temperature, the vaporization of the liquid (Fig. 1) can be produced exclusively by particles having a high stopping power (e.g., nuclear recoils like those expected from WIMPs or neutrons), making the detector insensitive to minimum ionizing backgrounds. The devices are operated at near room temperature and the industrial refrigerants used are inexpensive, non-flammable and non-toxic, with a chemical composition that maximizes sensitivity to neutralino interactions through both the spin-dependent and -independent channels [2]. For these reasons, the technique seems to be ideally fitted for the goal of building ton or even multi-ton WIMP detectors, devices able to probe most of the supersymmetric phase space where the supersymmetric dark matter may abide.

Several techniques have been identified and exploited to maximize the stability of small bubble chamber prototypes containing CF_3Br and CF_3I. Namely, avoidance of contact with rough metallic surfaces, use of an immiscible liquid "lid" above the active volume, outgassing of surface imperfections in the presence of a buffer liquid, surface cleaning techniques and wetting improvement via vapor deposition [3]. Small prototypes ($\sim$30 g) remain superheated for periods of 15 minutes on the average at the shallow 6 m.w.e. depth of the EFI underground laboratory, a nucleation rate compatible with the measured neutron flux and energy spectrum in the site [4]. The insensitivity (rejection factor) to minimum ionizing particles (MIPs) in operating conditions at which the liquids are fully responsive to low energy nuclear recoils has been measured to be $> 10^9$ using strong gamma sources [4]. This guarantees the ability to build much larger prototypes in the ton or multi-ton regime, essentially without any concern for MIPs. Calibrations using neutron sources with a well-defined endpoint energy (11.1 MeV for Am/Be and 152 KeV for ^{88}Y/Be) allowed testing the response of the liquids to nuclear

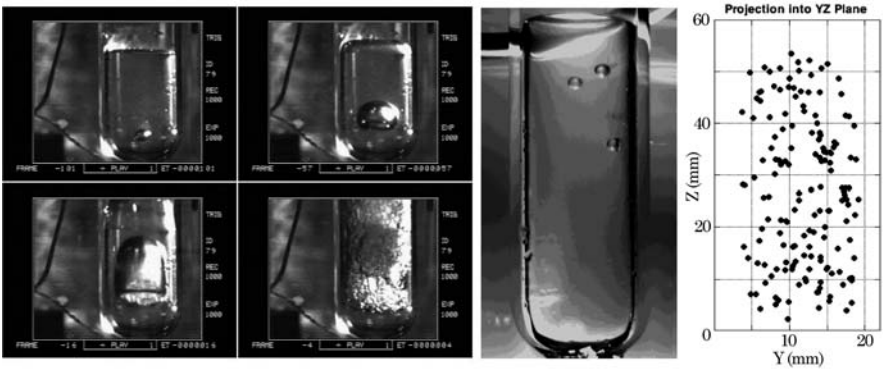

Fig. 1. Left: High-speed footage of boiling induced by a neutron source in superheated CF_3Br. The bubble diameter expansion rate is ∼1mm/ms in normal operating conditions (the depicted sequence spans 0.1 seconds). This footage can be viewed at `http://cfcp.uchicago.edu/~collar/bubble.mov`. Center: Multiple-bubble event produced by a neutron triple-scatter. Right: Automatic image analysis using LabVIEW's Vision Development Module allows precise bubble positioning and counting in 3-D (two perpendicular cameras are used).

recoils down to 4 keV in the case of CF_3I and the establishment of agreement with theoretical models of this response [4].

The construction of a 1-liter (2 kg) active volume bubble chamber is well advanced (Fig. 2): at the time of this writing, it has been operated at 6 m.w.e. for several weeks, with a nucleation rate (∼1/min) again compatible with the modelled contribution from the measured environmental fast neutron flux. The purpose of this prototype and experiment (the Chicago Observatory for Underground Particle Physics, COUPP) is to study the ultimate limits to the stability of the superheated liquid in a deeper location, with reduced neutron backgrounds. However a device of this mass can already be an extremely competitive WIMP detector, given the optimal choice of target nuclei and insensitivity to most backgrounds (Fig. 3).

While the ultimate goal is to deploy a large bubble chamber-based dark matter search in the Soudan Mine, there are considerable logistical benefits to having the initial commissioning and testing of this prototype device take place in the MINOS-near detector gallery at FNAL. Siting the initial commissioning work at Fermilab allows ready access to the detector, a critical need during the first few months of operation, until the behavior of the detector at this depth is completely understood and operation is fully automated. In this FNAL site, the experiment will profit from ∼300 ft of rock overburden. A preliminary estimate of the cosmic-ray associated backgrounds at this depth reveals that the nucleation rate assumption used to generate the projections in Fig. 3 could in principle be met there. In the presence of 30 cm of polyethylene shielding, muon-induced energetic neutrons producing a

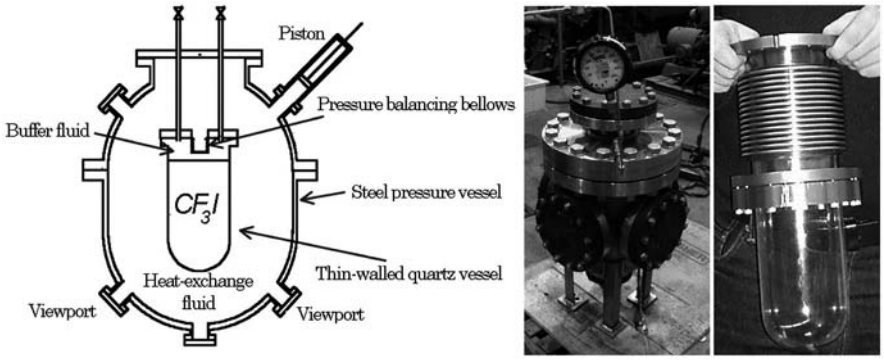

Fig. 2. Left: Conceptual design of the 2 kg CF_3I chamber to be used in the preliminary phase of COUPP. Center: the recompression vessel in this prototype. Right: inner quartz vial and pressure-compensation bellows for the same. Footage of the response of this chamber to neutrons can be seen at `http://cfcp.uchicago.edu/~collar/triple_bubble(0.4s).mov`.

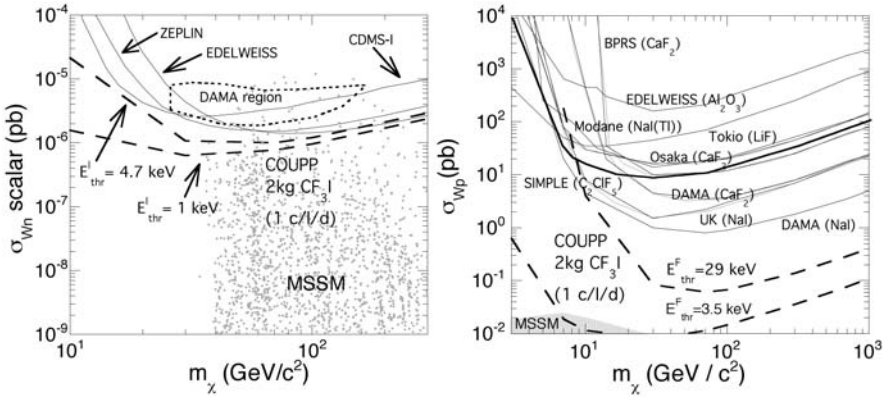

Fig. 3. Sensitivity limits in the spin-independent (left) and spin-dependent (right) neutralino parameter space achievable during the first phase of COUPP (dashed lines), compared with other experiments. The neutron background rate used for these estimates is representative of what can be expected in the Minos near detector gallery and, according to Monte Carlo calculations, *a factor of ∼100 too conservative* for the Soudan depth. The limits are plotted for two different energy thresholds, one already demonstrated with the ^{88}Y/Be neutron source calibrations and a second one (the best that can be expected before gamma background rejection is lost) soon to be tested with a ^{124}Sb/Be neutron source. *NOTE: the recently released CDMS-II limits surpass those from CDMS-I in the figure by a factor ∼4.*

few nucleations per kg/day are expected to be dominant, with only a small additional component from beam-related backgrounds. After a few months of preliminary tests at FNAL, the chamber will be transported to a final emplacement in the Soudan mine (MN).

MCNP-Polimi [5] Monte Carlo simulations of the response to a typical underground neutron flux indicate that large enough bubble chambers (few hundred liters) would have ideal features as WIMP detectors. For instance, a sizeable inner fiducial volume would be shielded against events produced by "punch-through" neutrons able to penetrate any reasonable thickness of neutron moderator. These represent the ultimate challenge for next-generation WIMP detectors. Their interactions would nevertheless be revealed in these chambers by multi-bubble events which WIMPs cannot produce (Figs. 1 and 4). To this unique feature, one can add the ability to easily exchange liquids from those containing fluorine as the heaviest atom (e.g. C_3F_8) to those containing also iodine or bromine (CF_3Br, CF_3I). For targets like these the expected WIMP and neutron induced bubble-nucleation rates can be radically different, a signature that could be exploited for WIMP discovery. The 2 kg prototype will also serve the purpose of studying the feasibility of building

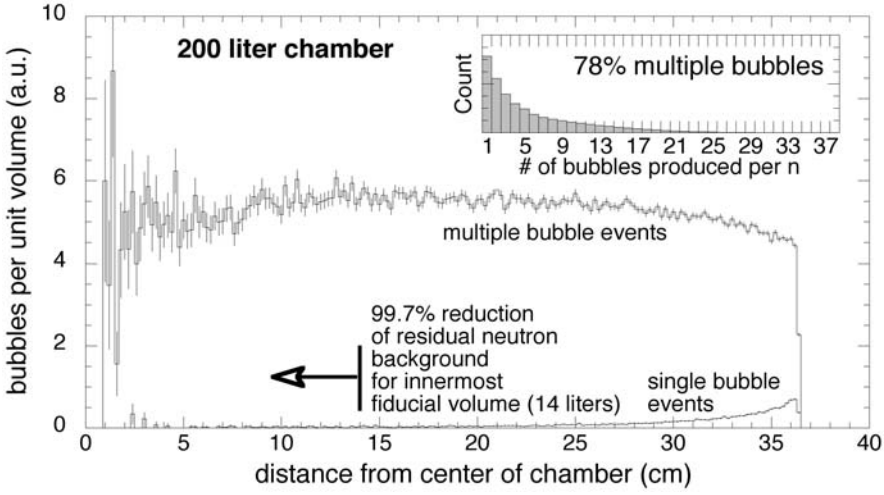

Fig. 4. Simulated distribution of bubble sites and their multiplicity, expected from a typical underground neutron spectrum (LNGS). The probability of having a fast neutron reach the center of a large volume of target liquid, produce a single bubble and exit without further interaction is seen to be extremely small. This self-shielding effect provides an additional background rejection mechanism for the innermost fiducial mass, already considerable (∼30 kg) in a 200 liter chamber (∼4 kg for 50l). WIMPs should produce a uniform distribution of singles: irreducible alpha backgrounds can do the same, but with a markedly different rate as a function of temperature [2,6].

much larger chambers. New challenges will certainly arise during its operation, besides those already envisioned (for instance, Radon emanation from metallic parts in the inner vessel can give rise to a recoiling-daughter background [4], but prospects based on BOREXINO measurements of cleaned steel parts are reassuring at $<5\mu Bq/m^2$) [7]. However, rapid upscaling to the ton or even multi-ton target mass regime seems feasible, in view of the simplicity of the method, optimal choice of target nuclei and excellent *intrinsic* background rejection ability.

References

1. L. Bond et al., Proc. *Topics in Astroparticle and Underground Physics* (TAUP 03), University of Washington, Seattle, Washington, 2003. *Nucl. Phys. B (Proc. Suppl.)* in press
2. J.I. Collar et al., Phys. Rev. Lett. **85**, 3083 (2000) (`astro-ph/0001511`); J.I. Collar et al., New J. Phys. **2**, 14.1 (2000) (`http://www.njp.org`)
3. M.A. Grolmes and H.K. Fauske, Proc. 5th Intl. Heat Transfer Conf., Tokyo 1974; M.G. Buivid and M.V. Sussman, Nature 275 (1978) 203; P. Reinke, Exp. Heat Transfer 10 (1997) 133; P. Reinke, Ph.D. Thesis no. 11598, Swiss Federal Institute of Technology, Zurich, Switzerland 1996
4. J.I. Collar et al., in preparation, to be submitted to Phys. Rev. Lett.
5. S.A. Pozzi et al., Nucl. Instr. Meth. **A513** (2003) 550
6. M. Barnabe-Heider et al., (`hep-ex/0311034`)
7. Borexino collaboration, Astrop. Phys. **18**, 1 (2002)

The SuperCDMS Experiment

R.W. Schnee[1], D.S. Akerib[1], M.J. Attisha[2], C.N. Bailey[1], L. Baudis[3], D.A. Bauer[4], P.L. Brink[5], P.P. Brusov[1], R. Bunker[6], B. Cabrera[5], D.O. Caldwell[6], C.L. Chang[5], J. Cooley[5], M.B. Crisler[4], P. Cushman[7], P. Denes[8], M.R. Dragowsky[1], L. Duong[7], J. Filippini[9], R.J. Gaitskell[2], S.R. Golwala[10], D.R. Grant[1], R. Hennings-Yeomans[1], D. Holmgren[4], M.E. Huber[11], K. Irwin[12], A. Lu[8], R. Mahapatra[6], P. Meunier[9], N. Mirabolfathi[9], H. Nelson[6], R.W. Ogburn[5], E. Ramberg[4], A. Reisetter[7], T. Saab[3], B. Sadoulet[9,8], J. Sander[6], D.N. Seitz[9], B. Serfass[9], K.M. Sundqvist[9], J-P.F. Thompson[2], S. Yellin[6], J. Yoo[4], and B.A. Young[13]

[1] Department of Physics, Case Western Reserve University, Cleveland, OH 44106, USA
schnee@case.edu
[2] Department of Physics, Brown University, Providence, RI 02912, USA
[3] Department of Physics, University of Florida, Gainesville, FL 32611, USA
[4] Fermi National Accelerator Laboratory, Batavia, IL 60510, USA
[5] Department of Physics, Stanford University, Stanford, CA 94305, USA
[6] Department of Physics, University of California, Santa Barbara, CA 93106, USA
[7] School of Physics & Astronomy, University of Minnesota, Minneapolis, MN 55455, USA
[8] Lawrence Berkeley National Laboratory, Berkeley, CA 94720, USA
[9] Department of Physics, University of California, Berkeley, CA 94720, USA
[10] California Institute of Technology, Pasadena, CA, 91125, USA
[11] Department of Physics, University of Colorado at Denver and Health Sciences Center, Denver, CO 80217, USA
[12] National Institute of Standards and Technology, Boulder, CO 80303, USA
[13] Department of Physics, Santa Clara University, Santa Clara, CA 95053, USA

1 Introduction

Nonluminous, nonbaryonic, weakly interacting massive particles (WIMPs) [1, 2] may constitute most of the matter in the universe [3]. WIMPs are expected to be in a roughly isothermal Galactic halo. They would interact elastically with nuclei, generating a recoil energy of a few tens of keV, at a rate $\lesssim 1$ event kg^{-1} d^{-1} [2, 4, 5].

Supersymmetry provides a natural WIMP candidate in the form of the lightest superpartner [5]. Figure 1 shows the WIMP masses and cross sections that are consistent with the three primary approaches to supersymmetry. Regardless of the theoretical philosophy, sensitivity from elastic-scattering experiments to WIMP-nucleon scalar cross-sections in the range 10^{-46}–10^{-44} cm^2 would be of great interest.

To probe to such small cross sections, it helps to operate without backgrounds, so that the search sensitivity is directly proportional to the detector

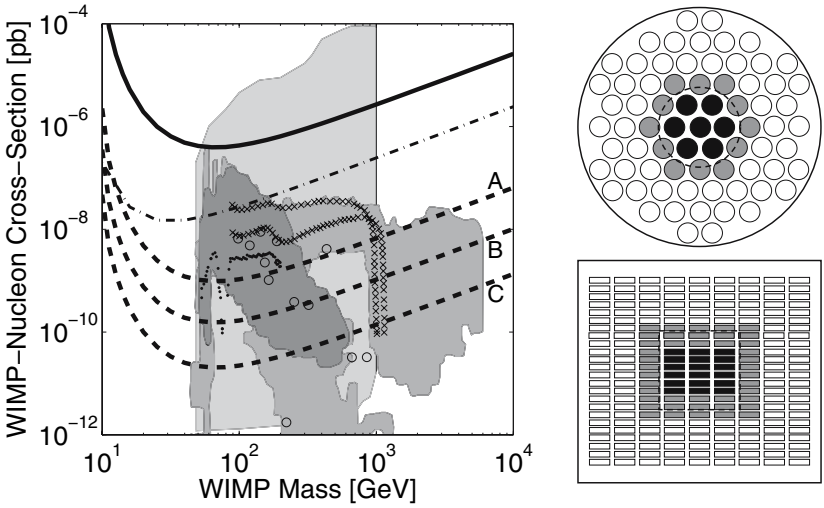

Fig. 1. Left: Reach of SuperCDMS phases A, B, and C (dashed curves) with current CDMS II limit [6] (solid curve) and sensitivity goal (dot-dashed curve). The lightest grey region results from a scan of MSSM parameter space [7]. SuperCDMS will probe nearly all split-supersymmetry models (×'s [8] and dots [9]) and much of the mSUGRA region [10] (medium grey), including most post-LEP benchmark points (circles) [11] and nearly all the subset (dark grey) consistent with a supersymmetric interpretation of the muon $g-2$ measurement. *Right*: Top view (above side view) of SuperCDMS cryostat showing deployment of 7 towers of 6 detectors each in 25 kg phase A (darkest circles), 19 towers of 12 detectors each in 150 kg phase B (grey circles), and 73 towers of 24 detectors each in 1 ton phase C (all circles). The cryostat will be 3× larger than the CDMS cryostat (dashes) in each dimension.

mass × exposure time (MT). Under subtraction of an estimated background, the sensitivity becomes proportional to $\sqrt{MT}$. Ultimately, the subtraction becomes limited by systematics, preventing further improvement in sensitivity. CDMS ZIP detectors [12] have excellent background rejection, making them the most proven means by which to operate an experiment without backgrounds.

CDMS ZIP detectors allow discrimination between WIMP nuclear recoils and background electron recoils through two effects. First, for a given energy, recoiling electrons are more ionizing than recoiling nuclei, resulting in a higher ratio of ionization to phonon signal, called "ionization yield." Second, the athermal phonon signals due to nuclear recoils have longer rise times and occur later than those due to electron recoils. For recoils within a few μm of a detector's surface (primarily from low-energy electrons), the charge collection is incomplete [13], making discrimination based on ionization yield less effective. But these events can be effectively rejected by phonon timing

cuts because they have, on the average, even faster phonon signals than those from bulk electron recoils [14, 15].

In order to probe to smaller WIMP-nucleon cross sections, we plan to increase the detector mass of the experiment in several phases, resulting in a ton-scale SuperCDMS experiment (previously called CryoArray [16, 17]). To maximize the discovery potential of the experiment, each phase will have an expected background smaller than one event. The excellent characterization of backgrounds and the information from ZIP detectors on each event would minimize the ambiguity of a discovery. The low energy thresholds and small "quenching" factors for both the ionization and the phonon measurements allow the requirement of a positive signal for both energy measurements, providing immunity to artifacts that may mimic a WIMP signal. The ∼keV energy resolutions and ∼mm position resolution would allow detailed tests of consistency with a WIMP signal. A test for annual modulation would depend only on accurately knowing the efficiency for WIMPs over time, since there would be no additional backgrounds.

To keep backgrounds negligible during the phases of SuperCDMS, improvements are needed in the level and discrimination of backgrounds, described in Sects. 2 and 3 respectively. To achieve an exposure of 500 ton d within a reasonable time and budget, manufacturability and detector production rates must be improved, as discussed in Sect. 4.

2 Reduction of Backgrounds

2.1 Neutrons

A neutron of kinetic energy ∼2 MeV can cause a recoil that is indistinguishable from one caused by a WIMP. Polyethylene shielding and an active scintillator veto are used to minimize or reject the neutron background. For the CDMS II experiment at the Soudan Mine, most neutrons that cause unvetoed nuclear recoils in Ge come from the ∼ 220 GeV muons that penetrate to and interact in the rock surrounding the CDMS II experimental hall. Simulations indicate the rate of unvetoed neutron-induced recoils from showers in the rock at Soudan is 3×10^{-4} kg^{-1} d^{-1}, sufficiently low that it should be important only for exposures significantly larger than those planned for CDMS II (1000 kg d). To reduce this background for the 10× to 500× larger exposures of SuperCDMS, we plan to build the experiment at SNOLab, where the increased depth suppresses the dominant neutron backgrounds by over two orders of magnitude compared to Soudan.

2.2 Electron and Photon Backgrounds

CDMS ZIP discrimination of electron-recoil events based on ionization yield is essentially perfect for electrons or photons interacting in the bulk of the detec-

Table 1. Mean event rates between 15–45 keV recoil energy in the inner Ge detectors of CDMS II and SuperCDMS, per 500 ton day exposure. CDMS II photon (γ) and electron (β) rates of events with full ionization yield ("Bulk") and reduced ionization yield ("Surface") are inferred from calibrations, simulations, and measurements. Leakage into the nuclear-recoil signal region with phonon-timing cuts applied is based on calibrations.

	CDMS II						SuperCDMS		
	Bulk		Surface		Leakage		Improve		Leakage
	all	singles	all	singles	wo/cuts	w/cuts	Clean	Reject	Goal
All	6×10^7	1.5×10^7	600000	170000	20000	600	2×	100×	< 1.0
γ	6×10^7	1.5×10^7	350000	100000	2500	70	2×	100×	< 0.5
β	7×10^5	2×10^5	250000	70000	17000	500	10×	100×	< 0.5

tor. However, events within ∼35 μm of the detector surface suffer ionization-yield suppression, and events in the first ∼1 μm lose so much ionization that they may be misidentified as nuclear recoils. Phonon timing provides rejection of 97% of these "surface events" while keeping 70% of true nuclear recoils.

Rejection of photon-related backgrounds in the CDMS II experiment has been measured using high-energy photon sources. Rejection of photon and electron backgrounds has been simulated using GEANT4, including tracking of low-energy electrons created by photon interactions and inferred depth-dependent ionization yield based on calibrations with an electron source [15]. The simulations and measurements both indicate that of all photon-related events (15-45 keV), 0.3% are single-scatter surface events with some ionization-yield suppression, and 1.8% of those (or 0.005% of all photon-related events) suffer enough ionization-yield suppression to be misidentified as nuclear recoils (see Table 1). Thus, rejection is 99.995% efficient based on the number of scatters and ionization yield alone, and is 99.9999% after applying the phonon-timing cut.

Table 1 shows that the background of surface singles is about twice as large as the inferred contribution from photon-related events, implying that about half the surface singles are due to surface radioactive beta contaminants. As shown in Fig. 2, surface betas cause very shallow interactions and thus suffer far higher misidentification than photon-induced events, resulting in background leakage ∼ 7× worse than that due to photons.

Background-reduction efforts will therefore center on reducing the surface beta contamination by a factor of 10 by identifying the contaminants and changing fabrication procedures to prevent their introduction. Table 2 lists screening methods for 79 beta-emitting and electron-capture isotopes. Inductively-coupled-plasma mass spectrometry (ICP-MS) would provide the quickest screening method for isotopes for which its sensitivity (typically 1 ppb to 1 ppt) is good enough. A dozen isotopes including ^{210}Pb, a crucial background candidate, can be detected by their alpha emissions. An additional 25 isotopes may be detected by low-level γ-counting.

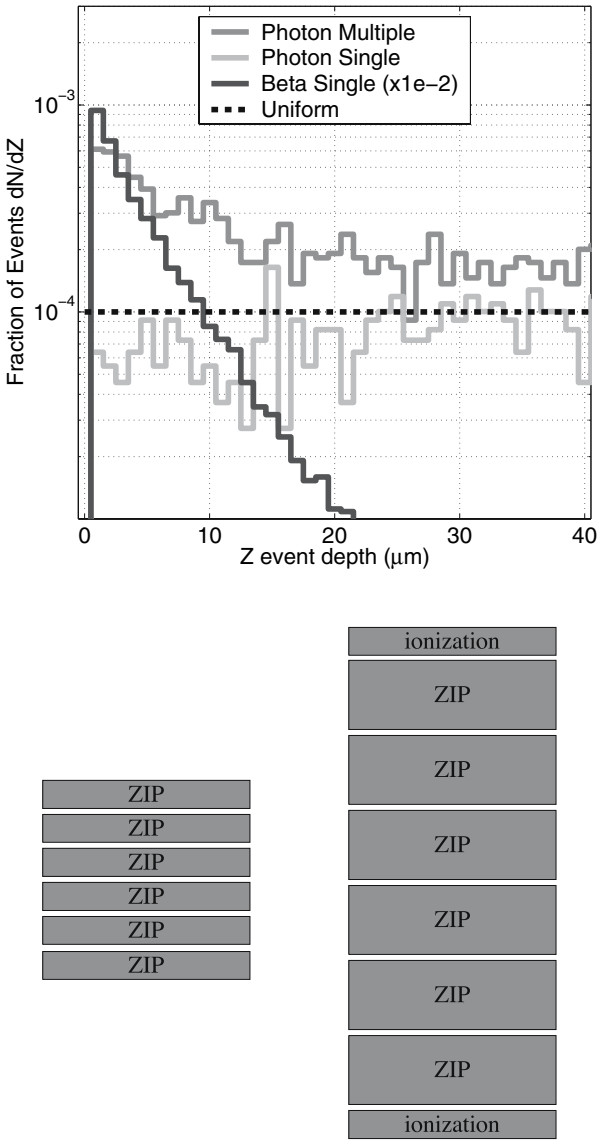

Fig. 2. Number of simulated events as a function of depth (top). Single-scatter photon-induced events (lower grey) are uniformly distributed in depth, and multiple-scatter events (upper grey) are biased toward the surface. Events from a beta emitter (black) show a steep falloff with depth, making them the most dangerous. Side views show a stack of cylindrical SuperCDMS ZIP detectors (right) which will be 2.5× thicker than CDMS ZIPs (left), with ionization endcap detectors to reduce or veto electrons incident on the outermost ZIP surfaces.

Table 2. Detection schemes for all long-lived beta-emitting isotopes. Isotopes in boldface may be detected by ICP-MS with sensitivity between 1 ppb and 1 ppt.

Method	Applicable Isotopes
ICP-MS (1 ppb)	^{40}K ^{48}Ca ^{50}V ^{87}Rb ^{92}Nb ^{98}Tc ^{113}Cd ^{115}In ^{123}Te ^{138}La ^{176}Lu ^{182}Hf ^{232}Th ^{235}U ^{238}U ^{236}Np ^{250}Cm
ICP-MS (1 ppt)	^{10}Be ^{36}Cl ^{60}Fe ^{79}Se ^{93}Zr ^{94}Nb ^{97}Tc ^{99}Tc ^{107}Pd ^{126}Sn ^{129}I ^{135}Cs ^{137}La ^{154}Eu ^{158}Tb ^{166m}Ho ^{208}Bi ^{208}Po ^{209}Po ^{252}Es
γ	^{40}K ^{50}V ^{60}Fe ^{60}Co ^{93}Zr ^{92}Nb ^{94}Nb ^{93}Mo ^{98}Tc ^{99}Tc ^{101}Rh ^{101m}Rh ^{102m}Rh ^{109}Cd ^{121m}Sn ^{126}Sn ^{125}Sb ^{129}I ^{134}Cs ^{137}Cs ^{133}Ba ^{138}La ^{145}Pm ^{146}Pm ^{150}Eu ^{152}Eu ^{154}Eu ^{155}Eu ^{157}Tb ^{158}Tb ^{166m}Ho ^{173}Lu ^{174}Lu ^{176}Lu ^{172}Hf ^{179}Ta ^{207}Bi ^{208}Bi ^{232}Th ^{235}U ^{238}U ^{236}Np ^{241}Pu
α	^{210}Pb ^{208}Po ^{209}Po ^{228}Ra ^{227}Ac ^{232}Th ^{235}U ^{238}U ^{236}Np ^{241}Pu ^{250}Cm ^{252}Es
β only	^{3}H ^{14}C ^{32}Si ^{63}Ni ^{90}Sr ^{106}Ru ^{113m}Cd ^{147}Pm ^{151}Sm ^{171}Tm ^{194}Os ^{204}Tl ^{10}**Be** ^{36}**Cl** ^{79}**Se** ^{97}**Tc** ^{107}**Pd** ^{135}**Cs** ^{137}**La** ^{154}**Eu** ^{209}**Po**

Finally, there are 12 to 21 isotopes, depending on ICP-MS sensitivity, that cannot be screened in any manner except by their emission of beta electrons. To detect these isotopes, we will develop a chamber capable of directly detecting betas emitted from surfaces. This chamber will also serve as a very low-background α screener.

Further reductions in surface backgrounds will be achieved by decreasing the exposed surface area per detector mass, as shown in Fig 2. The major thrust in detector development will be in scaling up the detector thickness from 1 cm to 2.5 cm. The thicker detectors will have a 2.5× smaller surface-to-volume ratio, thereby decreasing the background surface events per WIMP interaction by the same factor regardless of source. This increase requires new fabrication equipment and modifications to some of our present equipment. A larger voltage would be applied across these thicker detectors during their operation, resulting in only a slightly smaller drift field that would not significantly reduce the ionization yield for surface events.

Ge ionization detectors will act as an active veto shield around, above, and below the ZIP detectors. Ionization detectors cost ∼5 times less to fabricate and test than the ZIPs. These veto detectors may reduce the contamination adjacent to the ZIPs; the CDMS I experiment indicated that the Ge detector material itself has the cleanest surfaces within the detector housings. Moreover, these detectors would reject the otherwise outermost ZIP detectors' dominant background of single-detector surface events caused by photons ejecting electrons from adjacent passive materials.

3 Detector Performance Improvements

The complementary method to reduce surface-event backgrounds in SuperCDMS is to improve the detector rejection of surface events. Improved

analysis already is showing significant advances and should increase rejection by at least an order of magnitude. Further improvements can be achieved by optimization of both the charge collection and the athermal phonon sensors.

First, it is likely that we can improve the charge collection for surface events by optimizing the deposition of the amorphous-silicon layer used to prevent back-diffusion of carriers to the "wrong" electrode [13]. Older CDMS detectors with a different amorphous-silicon layer had a higher ionization yield for surface events than current detectors, resulting in >95% rejection of surface betas based on ionization yield alone [18]. Returning to and possibly improving upon the old recipe should increase the blocking effectiveness of the electrodes against surface-event charge back-diffusion.

A longer-term goal is to enhance the information in the athermal phonon signals. Reading the phonon signal from the detector substrate faster should improve the pulse discrimination. The present ZIP detectors' phonon sensors cover only 20% of one surface of the detector substrate. New phonon-readout schemes described in Sect. 4 would allow increased surface-area coverage.

The most dramatic improvement in phonon read-out would occur if *both* sides of the disc-like detectors were instrumented with phonon sensors. This double-sided readout should improve the phonon timing information by detecting the leading phonons on both faces of the detector. This design will symmetrize the detector response and allow a direct determination of the three-dimensional position of each event. The expected timing resolution of 0.5 μs at 10 keV would yield a position resolution of 1.5 mm in three dimensions.

One method of implementing this scheme keeps the same drift-field configuration used in the existing ZIP detectors. The problem then is to provide a voltage bias of up to 1 μV for the phonon sensors without adding more than a few picofarads to the capacitance of the ionization electrode, thereby degrading the ionization resolution. The best option is a high-frequency (20 MHz) AC power supply feeding a small transformer. A diode and LC filter on the secondary produce the appropriate bias. The voltage applied could be regulated at low bandwidth by monitoring the current through the readout SQUIDs, while maintaining at high bandwidth the pure voltage bias needed for the phonon sensors.

An alternative scheme [19, 20] is to interleave the ionization electrodes and the phonon collectors on both detector faces. On one face the ionization electrodes are at positive voltage and connected to one amplifier, while on the other face they are at negative voltage and connected to a second amplifier. The phonon sensors remain at ground on both faces. In this arrangement, the electric field close to the surfaces is roughly parallel to the detector face and so a surface interaction generates a signal in the near-side charge amplifier only. Bulk events experience a field perpendicular to the faces, causing the electrons and holes from an event to generate equal signals in each charge amplifier.

The interleaved design thus provides an additional means of discriminating surface events from bulk events.

Since the interleaved phonon sensors on both sides of the crystal remain at ground for the ionization measurement, the biasing electronics remain unchanged from the present implementation. If the surface identification works at the outer edges of the detector, no outer guard electrode is needed, and the readout and electronics of the two ionization channels also remain unchanged from the the present ZIP implementation of CDMS II.

4 Improving Manufacturability

At the CDMS II detector production rate of about one detector per month, or 3 kg Ge per year, deploying a ton of detectors would be impossible. Fortunately, nearly all the time associated with detector production is spent on a lengthy program of testing and repairing, which could be rendered unnecessary by improvements to the fabrication process. These improvements would allow orders of magnitude increases in detector production. Furthermore, many of these fabrication improvements also allow easier building of the experimental infrastracture and decrease the cryostat's material and heatload.

Several straightforward improvements are planned to increase fabrication yield. Changing to a whole-field mask for first-layer exposures, optimizing etching recipes, and switching from 1 µm to 2 µm features should greatly reduce photolithography errors and the resulting need for testing and repair. These changes should increase the fabrication rate by a factor of 5.

Further increases require reducing or eliminating the need for cryogenic testing of the W thin-film critical temperature. The addition of a mechanical planetary system for W film depositions may result in reproducible, uniform critical temperatures. The sensitivity of W to processing conditions has, in addition, motivated work to develop alternative films such as Al(Mn) that may be more reproducibly processed [21]. Finally, studying W film properties (crystalline phase, resistivity, film thickness, crystallite size and sputtering conditions) may lead to the establishment of room-temperature diagnostic tests.

4.1 Lower-Inductance SQUID Readout

In CDMS II the transition-edge sensors (TESs) of each phonon sensor are in series with the input coil to a SQUID array of 100 elements. A voltage is applied across the combined TES/input coil pair, and the SQUID array output measures the current through the TES. In order to have sensitivity to resolve the TES current of phonon events, the SQUID array must have many turns on the input coil for flux amplification. However, the ratio of the input inductance of the SQUID array to the operating dynamic resistance of the TES, $L_{\mathrm{in}}(\mathrm{array})/R_{\mathrm{dyn}}(\mathrm{TES})$, sets a limit on bandwidth. For the phonon

sensor readout to have sufficient bandwidth (∼100 kHz) and to be stable from electrothermal oscillations, the dynamic resistance of the phonon sensor $R_{\rm dyn} > 0.1\Omega$.

A number of the proposed advances of our phonon sensor technology described above would benefit from a decrease of $L_{\rm in}$. These include the increase of the coverage of the phonon sensors, which would require connecting more TESs in parallel; the widening of the W TES to ease the fabrication; and the use of Al(Mn), which has intrinsically lower resistivity. Moreover, the phonon rejection would likely benefit from the increased speed.

Two approaches are possible. One is to decrease the apparent input inductance through feedback. Replacing our current magnetic feedback through a feedback coil with a resistive feedback to the input of the SQUID would decrease the effective inductance by the gain of the feedback loop. This scheme requires no modification of the warm electronics and only a minor rewiring on the cold electronics stage.

A second approach is to use a single SQUID front end, so that the input inductance is physically smaller. This scheme requires a two-stage SQUID configuration, such as has been operated for many years [22]. A voltage-biased single SQUID is the initial sensor of TES current. The current from the single SQUID is amplified by a second-stage SQUID array similar to the single-stage array used in CDMS II. A two-stage system has greater current sensitivity at the first-stage input and hence greater signal to noise. The two-stage system also imposes less stringent design and fabrication requirements on the SQUID array . With a first-stage preamplifier SQUID, less gain is required in the SQUID array; the fewer turns on the input coil result in greater reliability in the SQUID fabrication and operation.

4.2 SQUID Ionization Readout

Schemes using SQUID amplifiers to read out the ionization channels would eliminate the need for tensioned signal wires going inside vacuum coax from 50 mK to 4 K, thus allowing the bulky, massive mounting hardware to be made much lighter and more flexible. Using SQUIDs would also decrease radically the power dissipated, an important consideration given the number of channels needed for SuperCDMS.

To provide enough sensitivity to measure the ionization current with SQUIDs, a high turn-ratio superconducting transformer (1:2000) would be coupled to a two-stage SQUID. The challenges of controlling stray capacitance and internal resonance for such a large transformer appear manageable, and performance at least as good as that of CDMS appears achievable [23]. This approach uses the same type of amplifier as the phonon sensors, thus simplifying the overall electronics systems.

5 Conclusions

Modest improvements in the level and/or discrimination of backgrounds are needed to keep backgrounds negligible during the three phases of Super-CDMS. By developing production designs that require only modest testing, detector production rates may be improved sufficiently to allow an exposure of 500 ton d within a reasonable time and budget. Overall, the improvement estimates described above are conservative. Previous development efforts have shown that some areas prove easier and provide larger factors while others prove more difficult. The conservative estimates together with the broad approach reduce the risk and give us confidence that we will succeed, providing the surest way to probe to WIMP-nucleon cross sections of $10^{-46}\,\mathrm{cm}^2$.

References

1. B. W. Lee and S. Weinberg, Phys. Rev. Lett., **39**, 165 (1977).
2. J. R. Primack, D. Seckel, and B. Sadoulet. Annu. Rev. Nucl. Part. Sci., **38**, 751 (1988).
3. L. Bergsrom. Rep. Prog. Phys., **63**, 793 (2000).
4. J. D. Lewin and P. F. Smith. Astropart. Phys., **6**, 87 (1996).
5. G. Jungman, M. Kamionkowski, and K. Griest. Phys. Rep. **267**, 195 (1996); J. Ellis, T. Falk, K. A. Olive, and K. Schmitt. Phys. Lett. **B413**, 355 (1997).
6. D.S. Akerib et al, (CDMS Collaboration), these proceedings.
7. Y. G. Kim et al, J. High Energy Phys. **0212**, 034 (2002)
8. G. F. Fiudice and A. Romanino, Nucl. Phys. B **699**, 65 (2004).
9. A. Pierce, Phys. Rev., **D70**, 075006 (2004).
10. E. A. Baltz and P. Gondolo, J. High Energy Phys. **0410**, 052 (2004).
11. M. Battaglia et al, Eur. Phys. J. **C33**, 273 (2004).
12. K. D. Irwin et al, Rev. Sci. Instr. **66**, 5322 (1995); R. M. Clarke et al, In: Proceedings of the Second International Workshop on the Identification of Dark Matter, ed by N.J.C. Spooner and V. Kudryavtsev (World Scientific, Singapore, 1999), pp 353–358; T Saab et al, AIP Proc. **605**, 497 (2002).
13. T. Shutt et al, Nucl. Instr. Meth. A **444**, 340 (2000).
14. R. M. Clark et at, Appl. Phys. Lett. **76**, 2958 (2000).
15. V. Mandic et al, Nucl. Instr. Meth. A **520**, 171 (2004).
16. R. J. Gaitskell, in: N. J. C. Spooner, V. Kudryavtsev (Eds.), Proceedings of the Third International Workshop on the Identification of Dark Matter, World Scientific, london, 2001, pp. 606–617.
17. R. W. Schnee, D.S. Akerib, and R. J. Gaitskell, Nucl. Phys. B (Proc. Suppl.) **124**, 233 (2003).
18. D. Abrams et al (CDMS Collaboration), Phys. Rev. **D66**, 122003 (2002).
19. P. Luke, Appl. Phys. Lett. **65**(22):2884 (1994).
20. B. Cabrera, et al, in preparation.
21. B. A. Young et al, Nucl. Instrum. and Meth. in Phys. Res. **A520**, 307 (2004); S. W. Deiker et al. Appl. Phys. Lett. **85**, 2137 (2004).
22. K. D. Irwin et al, Nucl, Instr. and Meth. in Phys. Res. **A444**, 184 (2000).
23. K. D. Irwin et al, in preparation.

WIMP-Wind Detection with an Advanced Gaseous Tracking Device

Atsushi Takeda, Kaori Hattori, Hidetoshi Kubo, Kentaro Miuchi, Tsutomu Nagayoshi, Hironobu Nishimura, Yoko Okada, Reiko Orito, Hiroyuki Sekiya, Atsushi Takada, Toru Tanimori

Cosmic-Ray Group, Department of Physics, Graduate School of Science, Kyoto University, Kitashirakawa-oiwakecho, Sakyo-ku, Kyoto, 606-8502, Japan
takeda@cr.scphys.kyoto-u.ac.jp

Measuring a wind of weakly interacting massive particles (WIMPs) blowing from the direction of the solar motion is said to be one of the most reliable methods to identify a signature of WIMPs. We have developed a micro time projection chamber (μ-TPC) with a gaseous two-dimensional micro pixel chamber (μ-PIC) readout and studied its performance as a WIMP-wind detector.

1 Introduction

Most reliable method to identify a positive sign of weakly interacting massive particles (WIMPs) which are one of the best candidates for the cold dark matter is said to be measuring direction-distribution of WIMP velocity. This distribution is expected to show an asymmetry like a wind of WIMPs at the earth due to the motion of the solar system around the galactic center. Among the many attempts to detect this WIMP-wind by measuring the recoil nuclear angles [1, 2, 3, 4, 5], gaseous detectors are one of the most appropriate devices because of their fine spatial resolution. In particular, properties of the CS_2 gas, which is sensitive to the WIMP-wind mainly via spin-independent (SI) interactions are studied by DRIFT group [6] because of its small diffusion. We have, on the other hand, evaluated the detection feasibility of WIMP-wind via spin-dependent (SD) interactions using carbon tetrafluoride (CF_4) gas taking into account the performance of an advanced gaseous detector, or micro time projection chamber (μ-TPC) with our original two-dimensional (2D) micro pixel chamber (μ-PIC) readout, because WIMPs can basically be detected via both SI and SD interactions [7]. Since fluorine was found to be one of the best nuclei for the detection of the SD coupled WIMPs [8, 9], we are focusing on the WIMP-wind detection with CF_4. We, then, found that the μ-TPC filled with low-pressure CF_4 gas can explore the theory regions predicted by minimal supersymmetric extensions of the standard model (MSSM) with a sufficient exposure ($\sim 300\,\mathrm{m}^3 \cdot \mathrm{year}$).

We have developed a prototype of μ-TPC, and studied the detector performance under low pressure condition and gas properties of CF_4 gas.

2 μ-TPC

The μ-TPC which is a gaseous time projection chamber with a μ-PIC read out has been developed for measuring three-dimensional (3D) tracks of charged particles with fine spatial resolutions [10, 11, 12, 13]. The μ-PIC is a gaseous 2D imaging detector with a fine pitch (400 μm) manufactured using printed circuit board (PCB) technology. We developed a prototype of the $10 \times 10\,\mathrm{cm}^2$ μ-PIC whose electrode structure were optimized using 3D simulators so that a high gas gain and good gain uniformity could be achieved [14]. The left and right panels of Fig. 1 show a picture of the $10 \times 10\,\mathrm{cm}^2$ μ-PIC on a mother board and a schematic structure of the μ-PIC, respectively. Anode and cathode strips are formed orthogonally on both sides of a 100 μm thick polyimide substrate with a pich of 400 μm. Since the μ-PIC is made by the PCB technology, large area detectors are in principle made at a relatively low cost, which is an inevitable feature for a WIMP search detector. Another outstanding feature of the μ-PIC is that all structures for the multiplication and the readout are on one board and would provide a stable long term operation without a serious problem of discharges. Fig. 2 shows a 2D X-ray image of a test chart and projected X-ray counts along the 0.5 mm slits obtained by the μ-PIC. Slits of 0.5 mm width can be clearly seen. From the edge image of Fig. 2, a 2D position resolution of 120 μm (RMS) was obtained, which is close to the theoretical limit of the 2D imaging detector with a 400 μm pitch.

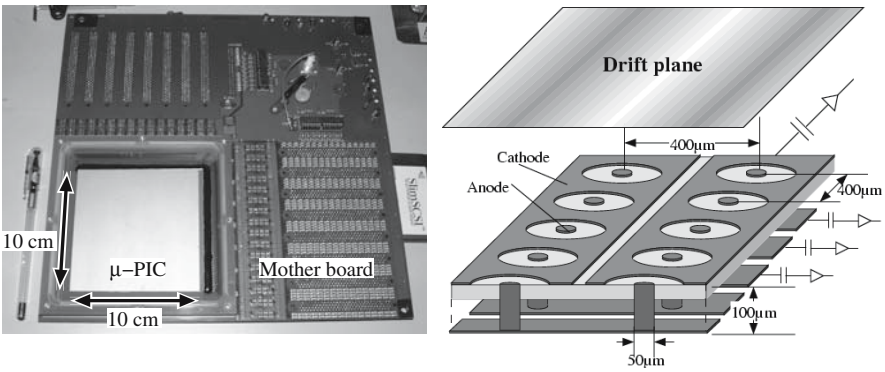

Fig. 1. A picture of the 10 cm square μ-PIC attached on a mother board (left) and schematic structure of the μ-PIC (right).

A data-acquisition (DAQ) system of the μ-TPC, consisting of amplifier-shaper-discriminator (ASD) cards, a position encoding module and a VME memory module, was developed. The ASD cards based on the ASD IC for the Thin Gap Chamber (TGC-ASD) in the LHC ATLAS Experiment have been developed so that the integration constant is suitable for the μ-PIC [15]. An-

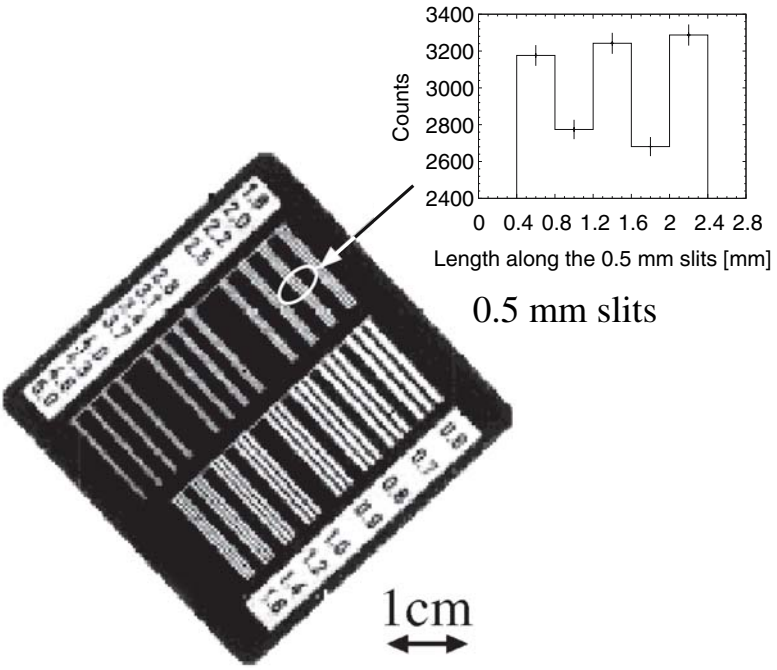

Fig. 2. Two-dimensional X-ray image of the test chart obtained by the μ-PIC and the projected X-ray counts along the 0.5 mm slits.

ode and cathode signals are discriminated into the LVDS-level digital signals in the ASD cards. Discriminated digital signals are encoded by the position encoding module consisting of five field programmable gate arrays (FPGAs), and the anode and cathode position (X and Y) and timing (Z) are recorded by the memory module with an internal clock of 50 MHz. A track of a charged particle is consequently recorded as successive points. We also record the waveform of the summed analog signals with a 8 bit 100 MHz flash ADC (FADC). This summed waveform is used to measure the deposited energy and also to decide the track sense because these summed signals basically carries the Bragg curve shapes.

We developed a prototype μ-TPC having a detection volume of $10 \times 10 \times 10\text{cm}^3$. Figure 3 shows a picture of the prototype μ-TPC in a 6 mm-thick aluminum vessel of 60 cm diameter. A field cage of 10 cm drift length which consists of a drift electrode, nine copper wires of 0.2 mm diameter with 1 cm pitch, and glass fiber reinforced plastics (GFRP) rods was set on the μ-PIC. The copper wires are set around the field area of $15 \times 15\,\text{cm}^2$, which forms a uniform electric field in the detection volume. We set the μ-TPC in the vessel as shown in Fig. 3 and studied the detector performance under low pressure condition and gas properties of CF_4 gas.

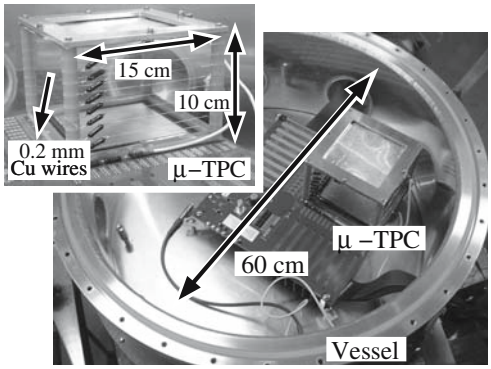

Fig. 3. A picture of the prototype μ-TPC in an aluminum vessel, and an enlargement picture of the μ-TPC (inset).

3 Performance of the μ-TPC

Several studies of the performance of the μ-TPC had been carried out with a normal pressure gas flow, and 3D tracks and Bragg curves of recoil protons with energies of between 500 keV and 1 MeV and good gamma-ray discrimination efficiency had been successfully obtained [16]. Since the required gas pressure for obtaining 3D tracks of the heavier nuclear recoil such as carbon or fluorine is 0.05–0.2 atm, we operated the μ-TPC with low-pressure chamber gas.

The experimental set-up is shown in Fig. 4. We operated the μ-TPC with a gas gain of about 3000 and irradiated the μ-TPC with neutrons from ^{252}Cf source. One fission decay of ^{252}Cf emits 3.8 neutrons and 9.7 photons on average, therefore, the μ-TPC was triggered by gamma-rays detected by the YAP scintillator. Since we put the whole mother board as shown in Fig. 4, the μ-PIC did not work stably with a lower gas pressure than 0.2 atm due to outgas from some resistances and decoupling capacitances on the mother board. We, therefore, performed the 3D tracking measurement with a gas mixture of Ar-C_2H_6 (90:10) at 0.2 atm, and detected low energy proton and carbon recoil tracks [17]. The left and right panels of Fig. 5 show typical recoil proton tracks and their Bragg curves with energies between 100 keV and 300 keV and one of the carbon track candidates and its Bragg curve, respectively. Track length known from the digital track data and the deposited energy measured from the FADC waveform are consistent with SRIM2003 calculations [18].

Some gas properties of CF_4 were measured. We irradiated with a non-collimated radioactive source of ^{55}Fe set in the vessel and measured the output charge from 32×32 pixels of the μ-PIC in a pure CF_4 gasses of various pressures. From the obtained values of the charges, the gas gains of the μ-PIC were calculated. Fig. 6 shows obtained gas gains as a function of the anode voltages using pure CF_4 gasses of 0.25 atm, 0.5 atm and 1.0 atm, respectively.

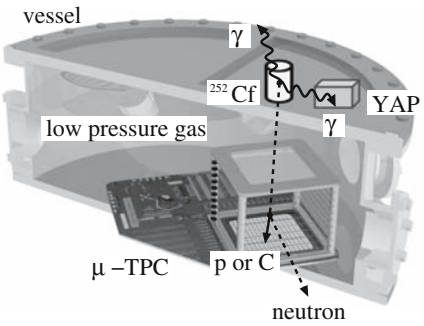

Fig. 4. Schematic drawing of the experimental setup.

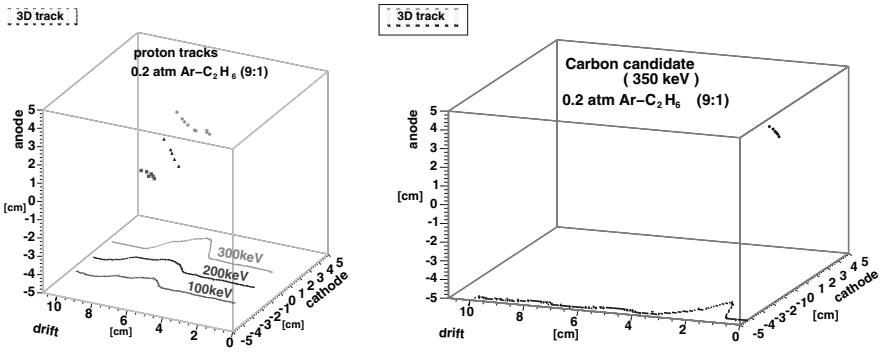

Fig. 5. Detected proton (left) and carbon tracks (right). Proton tracks of 100 keV (square), 200 keV (triangle) and 300 keV (circle) are shown.

As a result, stable operation with gas gain of more than 7000 at 0.25 atm was confirmed.

We measured the drift velocities of electrons using the time distribution of recoil nuclei caused by the elastic scatterings of the neutrons from ^{252}Cf source. Fig. 7 shows obtained drift velocities of electrons in a pure CF_4 gas of 1 atm which is consistent with the previous measurement [19]. We reconfirmed that the drift velocities of electrons in CF_4 gas are faster than them in Ar-C_2H_6 mixture gas, which is an important property to suppress the electron diffusion.

4 Prospects

A larger detection volume ($30 \times 30 \times 30\,\mathrm{cm}^3$) μ-TPC as a WIMP-wind detector is now being manufactured. We are going to measure the gamma-ray rejection power, energy and tracking resolution, and absolute efficiency by the end of 2005.

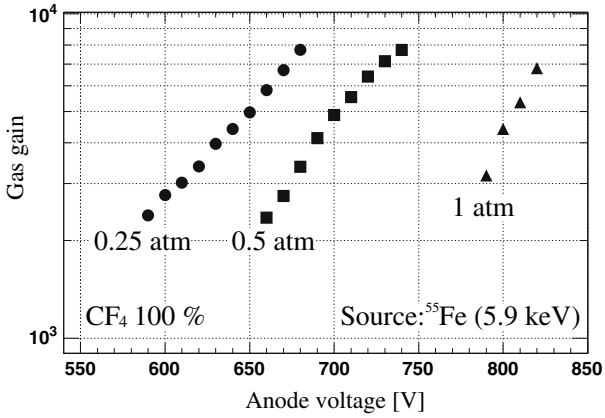

Fig. 6. Measured gas gains as a function of the anode voltages using pure CF_4 gasses of 0.25 atm (circle), 0.5 atm (squares) and 1.0 atm (triangles), respectively.

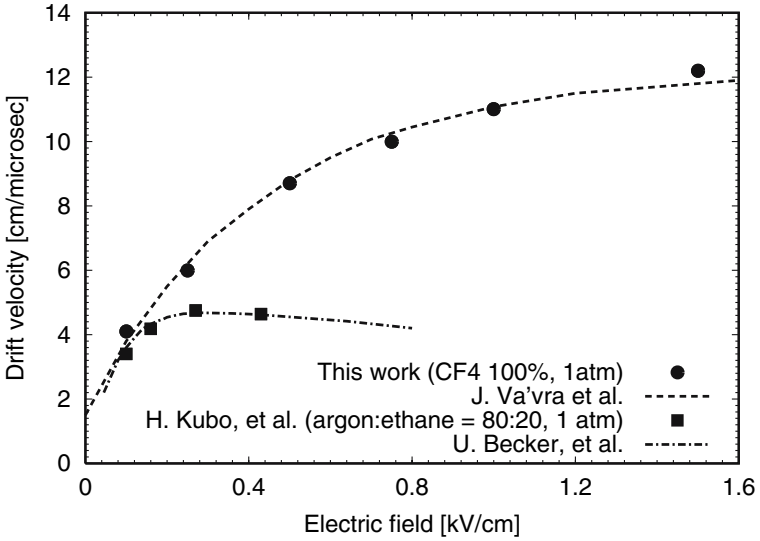

Fig. 7. Measured drift velocities of electrons as a function of the electric field in a pure CF_4 gas of 1 atm. The filled circles are in this work, and the dashed line from [19]. The filled squares are in our previous work [12] in an Ar-C_2H_6 (80:20) gas mixture of 1 atm, and the dashed-and-dotted line from [20].

5 Summary

We started investigating the performance of the μ-TPC as a WIMP-wind detector. We operated the prototype of μ-TPC having a detection volume of $10 \times 10 \times 10\,\mathrm{cm}^3$ with low pressure (0.2 atm) chamber gas. We detected low

energy proton and carbon recoil tracks and some gas properties of CF_4 for the SD coupled WIMP searches. A larger detection volume ($30 \times 30 \times 30\,\mathrm{cm}^3$) μ-TPC is now being manufactured. We hope to start the underground run after a development and performance study of a 30 cm size μ-TPC.

Acknowledgement

This work is supported by a Grant-in-Aid for the 21st Century COE "Center for Diversity and Universality in Physics";a Grant-in-Aid in Scientific Research of the Japan Ministry of Education, Culture, Science, Sports, Technology.

References

1. P. Belli, et al., Nuovo Cimento C **15**, 475 (1992); R. Bernabei, et al., Eur. Phys. J. C **28**, 203 (2003).
2. K.N. Buckland et al., Phys. Rev. Lett. **73**, 1067 (1994)
3. D.P. snowden-Ifft, et al., Nucl. Instrum. Methods A **498**, 155 (2003)
4. T. Lawson, et al., in *Proceedings of the Fourth International Workshop on "the Identification of Dark Matter", York, 2002*, edited by N.J.C. Spooner and V. Kudryavtsev, (World Scientific, 2003), p. 338.
5. Y. Shimizu, et al., Nucl. Instrum. Methods A **496**, 347 (2003); H. Sekiya, et al., Phys. Lett. B **571**, 132 (2003).
6. N. Spooner, et al., these proceedings and the references therein.
7. T. Tanimori, et al., Phys. Lett. B **578**, 241 (2004).
8. J.I. Collar, et al., Phys. Rev. Lett. **85**, 3083 (2000).
9. K. Miuchi, et al., Astropart. Phys. **19**, 135 (2003); A. Takeda, et al., Phys. Lett. B **572**, 145 (2003).
10. A. Ochi, et al., Nucl. Instrum. Methods A **471**, 264 (2001); **478**, 196 (2002).
11. T. Nagayoshi, et al., Nucl. Instrum. Methods A **513**, 277 (2003).
12. H. Kubo, et al., Nucl. Instrum. Methods A **513**, 94 (2003).
13. K. Miuchi, et al., IEEE Trans. Nucl. Sci. **50**, 825 (2003).
14. T. Nagayoshi, et al., Nucl. Instrum. Methods A **525**, 20 (2004); A. Takeda, et al., IEEE Trans. Nucl. Sci. **51**, 2140 (2004).
15. R. Orito, et al., IEEE Trans. Nucl. Sci. **51**, 1337 (2004).
16. K. Miuchi, et al., Nucl. Instrum. Methods A **517**, 219 (2004).
17. K. Miuchi, et al., in Proceedings of the Fifth International Workshop on the Identification of Dark Matter, York, 2004.
18. J.F. Ziegler, J.P. Biersack and U. Littmark, SRIM–The Stopping and Range of Ions in Matter, Pergamon Press, New York, 1985.
19. J. Va'vra, et al., Nucl. Instrum. Methods A **324**, 113 (1993).
20. U. Becker, et al., Nucl. Instrum. Methods A **421**, 54 (1999).

SIGN, a WIMP Detector Based on High Pressure Gaseous Neon

J.T. White[1], J. Gao[1], J. Maxin[1], J. Miller[1], G. Salinas[1], and H. Wang[2]

[1] Department of Physics, Texas A&M University, College Station, TX
white@physics.tamu.edu
[2] Department of Physics and Astronomy, University of California, Los Angeles, CA

A new WIMP detector concept based on the measurement of Scintillation and Ionization in Gaseous Neon (SIGN) is presented. The detector employs room temperature gaseous neon at a pressure of $\geq$100 bars as the WIMP target. The ionization is readout using either charge gain or electrofluorescence or both in a modified cylindrical proportional chamber geometry. The primary scintillation is detected by placing a CsI photocathode on the inside wall of the cylindrical chamber. The neon is doped with xenon ($\leq$0.5%) for signal enhancement. Theoretical considerations suggest that the measurement of both scintillation and ionization will provide discrimination between nuclear and electron recoils in this gas mixture.

1 Introduction – Neon as a WIMP Target

Confirmed detection of cold dark matter in the form of WIMPs (weakly interacting massive particles) may require a positive signal in a number of different experiments employing different target nuclei. Although the A^2 dependence of the coherent spin-independent (SI) WIMP-nucleus scattering cross section seems to strongly favor heavy atoms as targets for WIMP detectors, several factors maintain the attractiveness of lighter atoms for large scale detectors.

One particularly interesting potential target is neon. Neon is completely free of long-lived radionuclides and ultra-pure neon is commercially available at a relatively low cost per kilogram. In terms of kilograms, the A^2 advantage per atom of heavier nuclei reduces to a factor of A. This advantage is further reduced for light nuclei by the flatness of the form factor ($F(Q^2)\sim1$) over the momentum-transfer range of interest and by the fact that the higher recoil velocity for a given recoil energy results in a higher Lindhard efficiency [1]. The nuclear recoil spectra expected for three different WIMP masses is shown in Fig. 1. The resulting visible energy spectra (electron-equivalent) after taking account of the Lindhard efficiency is shown in Fig. 2. Both figures are for a one ton detector and cross section of 10^{-8} pb/nucleon.

In the following, it is argued that a practical neon-based detector may be realizable using pressurized neon gas at a pressure $\geq$100 bars, doped with

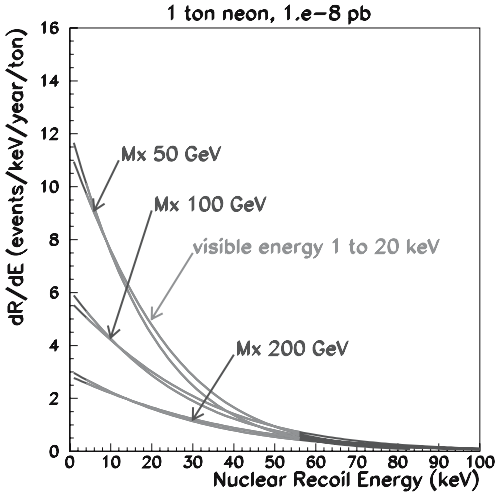

Fig. 1. Neon recoil spectra for three WIMP masses of 50, 100 and 200 GeV respectively assuming a one ton detector running for one year with a cross section of 10^{-8} pb/nucleon. The December and June spectra are shown for each mass assuming a non-rotating halo distribution. The curves indicate that a neon target will have good sensitivity for annual modulation studies.

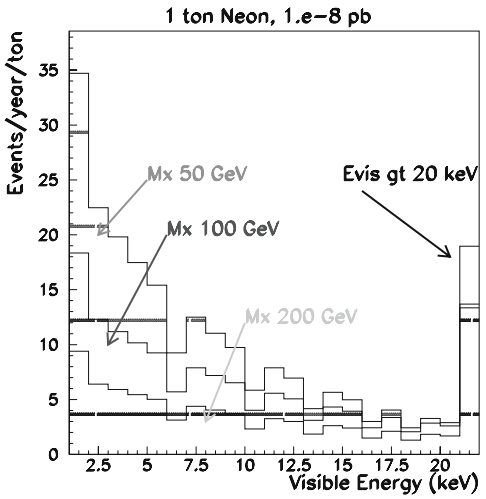

Fig. 2. The resulting visible energy spectra for the three masses (June only) taking account of the Lindhard efficiency.

xenon ($\leq$0.5%). It will be shown that this approach can potentially operate with a realistic recoil threshold of $\leq$3 keV and may also provide discrimination between electron and nuclear recoils if both scintillation and ionization are measured.

2 Proposed Detector Parameters

The motivation for considering pressurized neon gas is to maximize target density (and hence, minimize detector size) while maintaining adequate electron mobility. As is well known, free electrons in liquid neon repel the atoms and form bubbles (localized states) with diameters of a few Angstroms [2, 3]. Once the bubbles are formed the electron mobility becomes too small for use in a discriminating detector based on the correlation of scintillation to ionization. Therefore, the maximum operating pressure is determined from a physics point of view by electron mobility. Since the electron mobility in pure neon at 10% liquid density, 100 bars and at room temperature, is 10^5 cm/sec [4], and decreases only by about a factor of two up to 50% liquid density, operation at a pressure $\leq$500 bars appears feasible.

However, from an engineering point of view, it is also important to consider the possible difficulty of obtaining a pressure vessel with a reasonable mass and cost. Fortunately, ultra-light high pressure fuel tanks have been developed in recent years based on composite fiber technology. Low mass, large volume cylinders wound with carbon fibers are now commonly used in mass transit and aerospace applications. Tanks designed to hold hydrogen and methane are commercially available with pressure ratings well exceeding 300 bars. This matches well with the pressure limits due to electron mobility.

One further issue that might be a cause for concern is the required operating voltage. As will be discussed below, however, the voltage needed for proportional operation with the proposed gas mixture is sufficiently low that it will not present a major technical challenge for pressures up to a few hundred bars. Therefore, it can be concluded that a practical operating pressure in the range from 100 to 300 bars will be achievable without great difficulty.

3 Effect of the Addition of Xenon

The addition of xenon is a key feature that may greatly enhance the performance of neon as a WIMP target. It appears that the addition of a small quantity of xenon could make it possible to observe most of the inelastic component of a nuclear recoil in the form of ionization, while maintaining discrimination between electron and nuclear recoils. This is in contrast to LAr and LXe where most of the energy appears in the form of scintillation because of electron recombination [5]. Briefly, the reason this might occur is because there is a mechanism for Ne^+ - Xe interactions to result in VUV

scintillation, whereas Ne* - Xe interactions tend to result in the production of ionized xenon. Therefore, if there is strong recombination along the track of a nuclear recoil in 100 bar neon, then the high fraction of Ne* will result in a high fraction of free electrons, whereas an electron recoil will largely produce non-recombining neon ions, which will result in a larger scintillation fraction.

The production of scintillation by neon ions, Ne^+ can occur, for example, through the mechanism $Ne^+ + Xe \rightarrow Ne^+Xe \rightarrow NeXe^+ + 134$ nm. At low pressures, the Ne^+ - Xe system can produce at least four observable lines, but, at a pressure only as high as 600 torr, only the 134 nm transition is observed [6]. The 134 nm light can then escape or excite xenon, producing Xe*. All Xe* atoms produce scintillation at 175 nm through the reaction Xe* + Xe $\rightarrow$ Xe_2* $\rightarrow$ 2Xe + 175 nm. It is also possible for the Ne^+Xe molecule to interact directly with Xe to produce Xe*. It is not yet clear what happens at a pressure of 100 bars, but preliminary measurements show that a Ne-Xe mixture produces significantly more scintillation light at 175 nm than pure xenon in gamma interactions.

The production of xenon ions by excited neon atoms can occur in two ways. First, Ne* + Ne $\rightarrow$ Ne_2* $\rightarrow$ 2Ne + 80 nm, then 80 nm + Xe $\rightarrow$ Xe^+ + e-. The absorbtion length of 80 nm light in xenon at a partial pressure of 0.5 bars (0.5% at 100 bars) is 14 microns. A second mechanism is Ne* + Xe $\rightarrow$ Ne + Xe^+ + e- directly through a Penning interaction. The key issue is that xenon serves as an internal photocathode so that excited Ne* atoms efficiently convert to free electrons. This makes it possible to measure signals with a very low threshold.

4 Preliminary Test Cell Results

Preliminary studies of charge and light gain in a proportional chamber geometry were carried out in a small test cell designed to operate at pressures up to 100 bars. A stainless steel pressure vessel houses a cylindrical proportional chamber with an inside diameter of 12 mm. The cylinder also has a UV-grade sapphire view port that allows observation of the proportional scintillation light. The window has a diameter of 12.7 mm and is at a distance of 3 cm from the sense wire. A radioactive source is columnated inside the cylinder opposite to the view port so that both the proportional scintillation light and the proportional charge can be readout simultaneously. The charge is amplified by an EG&G Ortec 142AH preamplifier and the light is readout using an Electron Tubes 9214 photomultiplier tube coated with tetraphenylbutadien(TPB). (The solid angle of the view port was too small to allow studies of the primary scintillation with this chamber, but another chamber is under construction that will allow such studies.)

Figure 3 shows a typical waveform for a 5.9 keV ^{55}Fe gamma event in a gas mixture of neon-xenon(0.5%) at a pressure of 100 bars. The upper waveform shows the proportional scintillation and the bottom trace shows

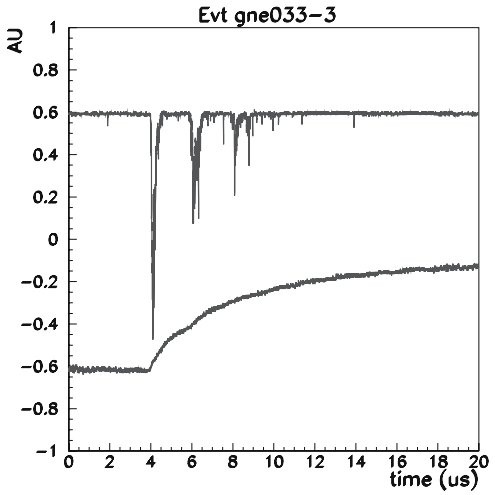

Fig. 3. Waveform of 5.9 keV gamma event. The top waveform is the proportional scintillation light output and the bottom is the charge signal.

the raw pre-amplified charge signal in coincidence. The multiple spikes in the light waveform are caused by the feedback from the photoelectric emission of electrons from the inner stainless steel surface. For this run, the sense wire diameter was 0.005 inch(127 microns) and the voltage was 4900 V. For this configuration, the light gain is estimated to be ∼2000 photons (175 nm) per electron and the charge gain is ∼500. The voltage needed for such gain is very low compared to what one would expect for a standard proportional tube at 100 bars. For example, a typical Ar-CH_4 mixture at 1 bar pressure in a similar chamber would require from 1 to 3 kV for a similar gain. Raising the pressure would raise the required voltage proportionally. The reason such a low voltage is needed for the neon-xenon mixture is a combination of at least two effects. First, the small electron-neon collision cross section results in a relatively high electron temperature for a given electric field strength [7]. Second, the electrons only need to gain sufficient kinetic energy to either ionize the xenon (12.1 eV) or excite the neon (16.6 eV) (since Ne*-Xe interactions produce ionized xenon as previously discussed). A plot showing both the light and charge spectra are shown in Figs. 4 and 5 respectively. From these spectra it can be seen that a realistic electron-equivalent threshold of $\leq$1 keV is feasible using either of the signals.

5 Conceptual Design for a Large Scale Detector

A large scale detector can be constructed using cylindrical modules containing ∼100 kg of neon each. A conceptual design for such a module is shown in

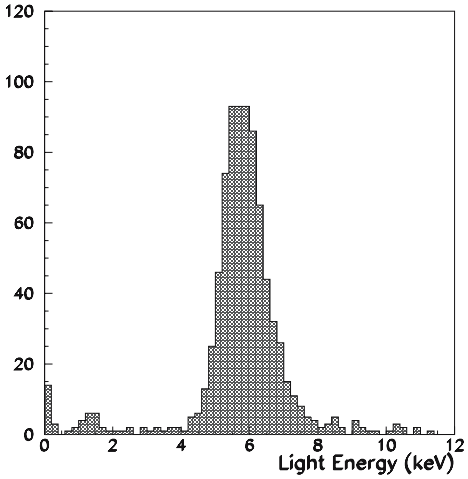

Fig. 4. Proportional scintillation spectrum from a 5.9 keV gamma source (^{55}Fe).

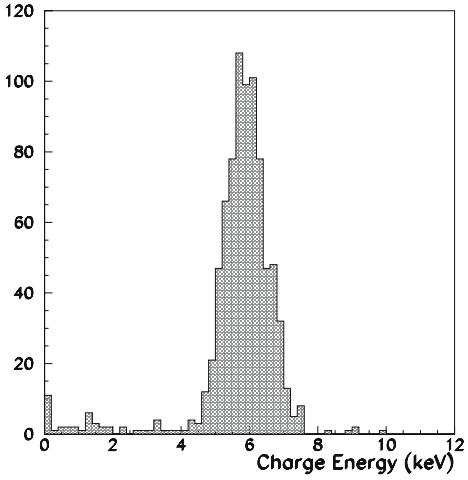

Fig. 5. Charge output spectrum from the same run.

Fig. 6. At 100 bars pressure, for example, a 100 kg module would require cylinder with a diameter of ∼60 cm and a length of 4 meters. The inside surface of the cylinder is coated with CsI to act as a photocathode for the primary scintillation. Instead of having a single sense wire, however, a series of alternating field and sense wires are spaced over an inner cylinder with a diameter from 1/3 to 1/4 the diameter of the pressure vessel. This is a key feature that makes it possible to maintain a high drift field that varies in field strength by only a factor of 3 or 4 depending on the choice of inner cylinder diameter. Fig. 7 shows an end view of the chamber.

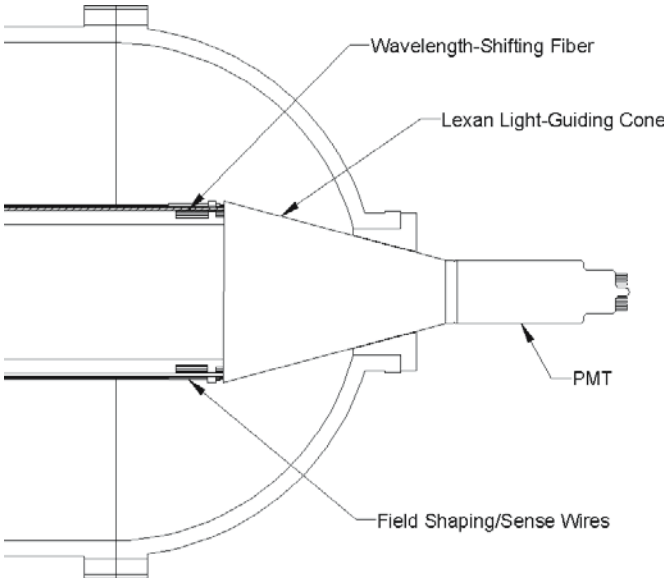

Fig. 6. Conceptual design for a detector module allowing both charge and light readout. A single module would have a target mass of about 100 kg.

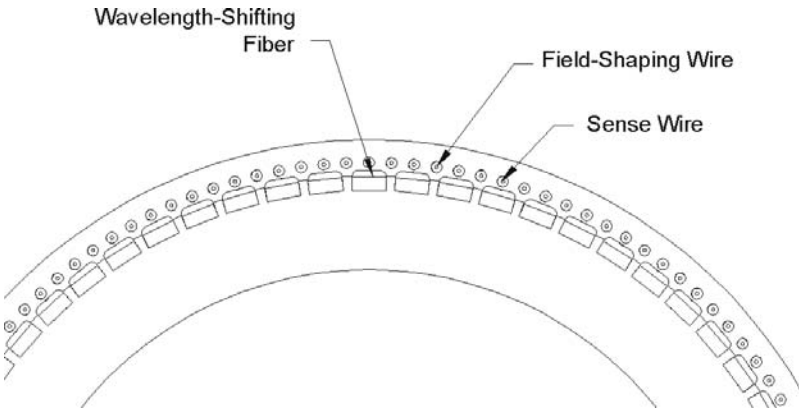

Fig. 7. End view of detector module. By alternating field and sense wires, the signal can be gated by controlling the voltage on the field wires.

Electrons reaching the sense wires undergo both charge gain (∼500) and light gain (∼2000) as discussed above. Conversion efficiency studies indicate that the proportional scintillation (secondary scintillation) can be read out with close to single electron sensitivity by placing wavelength shifting fibers (coated with TPB) under the sense wires as shown in Fig. 7. The charge can be read out using standard methods. The ionization signal will be followed by

the primary scintillation signal observed by the ejection of electrons off the CsI photocathode. This signal can be detected with good efficiency assuming a quantum efficiency $\geq$15% [8, 9] and a solid angle from 50% to almost 100% depending on event position. The 3-D event position can be determined by: 1) using the timing difference between the ionization and primary scintillation signals to determine the radius; 2) by using charge (or light) division to determine position along the sense wires; and 3) by using the sense wire signals to determine the azimuthal angle. Light reflectors on the ends of the cylinder will minimize longitudinal position dependence of primary scintillation detection efficiency. Of course a gating circuit will also be needed to prevent runaway feedback from the CsI photocathode. If the light gain is 2000, the quantum efficiency 15%, and the solid angle 50%, then the feedback gain is 2000 * 0.15 * 0.5 = 150 per electron. Simulations show that it is possible to gate the signal by pulsing the field wires between the sense wires, so it is not necessary to have a gating grid near the CsI surface.

In principle, only charge readout will be necessary, but the motivation for considering light readout is to possibly achieve single electron sensitivity for the primary scintillation and to gain information on the arrival shape of the ionization signal. The fast electroluminescence signal coupled to fast photomultipliers and read out using a 500 MHz waveform digitizer allows determination of the shape of the arriving electron cloud, which, because of diffusion, provides radial position information as well as directionality information for higher energy events (much higher than for WIMP interactions). However, since the timing between the primary scintillation and ionization signals already provides the radial position, the only issue is single electron sensitivity for the primary scintillation. It appears possible to achieve the same goal by taking advantage of the $\times$150 feedback gain. By delaying the gating pulse for two drift cycles, the primary signal will be amplified *in situ* providing a signal with a gain of 150 $\times$ 500 per single photoelectron. This is roughly equivalent to charge produced by a 5 keV gamma.

6 Summary

In summary, a new WIMP detector approach is proposed that has the potential to operate in discrimination mode with a realistic electron-equivalent threshold of $\sim$1 keV. The Lindhard efficiency for neon is $\sim$30%, so a nuclear recoil threshold of 3 keV appears achievable. Such low threshold is possible because the small quantity of xenon acts as an internal photocathode and assures that approximately 100% of the Lindhard energy is converted to ionization. The xenon also interacts with Ne^+ in such a way that scintillation at 175 nm (or perhaps 134 nm) is produced. The relatively large fraction of Ne^+ expected in electron recoils should therefore appear as an excess in the primary scintillation signal, providing background discrimination. Considering electron mobility, pressure vessel safety and operating voltage, an operating

pressure from 100 to 300 bars appears feasible. Studies are now underway to investigate nuclear recoil discrimination and to optimize chamber design.

Acknowledgements

It is a pleasure to acknowledge support from the U.S. Department of Energy, grant number DE-FG03-95ER40917 and the D.O.E. Advanced Detector Research Program.

References

1. J. Lindhard et al.: Mat. Fys. Medd. Dan. Vid. Seisk. **33** n. 10–14 (1963)
2. Y. Sakai, W.F. Schmidt, A.G. Khrapak: Chem. Phys. **164** 139 (1992)
3. W.F. Schmidt, Y. Sakai, A.G. Khrapak: Nucl. Inst. and Meth. A **327** 87 (1993)
4. L. Bruschi, M. Santini, and G. Torzo: Phys. Lett. A **102**(3) 102 (1984)
5. J. Thomas and D.A. Imel: Phys. Rev. A **36** (2) 614 (1987)
6. J. Galy et al.: J. Phys. B: At. Mol. Opt. Phys. **25** 5141 (1992)
7. L.B. Loeb: Basic Processes of Gaseous Electronics, (University of California Press, Berkley, 1961)
8. C. Lu and K.T. McDonald: Nucl. Inst. and Meth. A **343** 135 (1994)
9. P. Maier-Komor, et al.: Nucl. Inst. and Meth. A **362** 183 (1995)

Exploring Novel Signatures in Direct Neutralino Searches

J.D. Vergados[1,2]

[1] Theoretical Physics Division, University of Ioannina, Gr 451 10, Ioannina, Greece
[2] T-DO, Theoretical Physics Division, LANL, Los Alamos, N.M. 87545.
vergados@cc.uoi.gr

Abstract. Since the expected rates for neutralino-nucleus scattering are expected to be small, one should exploit all the characteristic signatures of this reaction. Such are: (i) In the standard recoil measurements the modulation of the event rate due to the Earth's motion. (ii) In directional recoil experiments the correlation of the event rate with the sun's motion. One now has both modulation, which is much larger and depends not only on time, but on the direction of observation as well, and a large forward-backward asymmetry. (iii) In non recoil experiments gamma rays following the decay of excited states populated during the Nucleus-LSP collision. Branching ratios of about 6 percent are possible (iv) novel experiments in which one observes the electrons produced during the collision of the LSP with the nucleus. Branching ratios of about 10 per cent are possible.

1 Introduction

It appears without doubts that dark matter constitutes about 30% of the energy matter in the universe. The evidence comes from the cosmological observations [1], which when combined lead to:

$$\Omega_b = 0.05, \Omega_{CDM} = 0.30, \Omega_\Lambda = 0.65$$

and the rotational curves [2]. It is only the direct detection of dark matter, which will unravel the nature of the constituents of dark matter. In fact one such experiment, the DAMA, has claimed the observation of such signals, which with better statistics has subsequently been interpreted as modulation signals [3]. These data, however, if they are due to the coherent process, are not consistent with other recent experiments, see e.g. EDELWEISS and CDMS [4].

Supersymmetry naturally provides candidates for the dark matter constituents. In the most favored scenario of supersymmetry the LSP can be simply described as a Majorana fermion (LSP or neutralino), a linear combination of the neutral components of the gauginos and higgsinos [5, 6, 7, 8]. We are not going to address issues related to SUSY in this paper, since thy have already been addressed by other contributors to these proceeding. Most

models predict nucleon cross sections much smaller the the present experimental limit $\sigma_S \leq 10^{-5} pb$ for the coherent process. As we shall see below the constraint on the spin cross-sections is less stringent.

Since the neutralino is expected to be non relativistic with average kinetic energy $< T > \approx 40\, KeV(m_\chi/100\, GeV)$, it can be directly detected mainly via the recoiling of a nucleus (A,Z) in elastic scattering. In some rare instances the low lying excited states may also be populated [9]. In this case one may observe the emitted γ rays. Finally one may be able to observe the electrons produced in the LSP-nucleus collision.

In every case to extract from the data information about SUSY from the relevant nucleon cross section, one must know the relevant nuclear matrix elements [10]–[11]. The static spin matrix elements used in the present work can be found in the literature [9].

Anyway since the obtained rates are very low, one would like to be able to exploit the modulation of the event rates due to the earth's revolution around the sun [12] [13], assuming some velocity distribution [12, 13, 14]–[15] for the LSP. One also would like to exploit other signatures expected to show up in directional experiments [16]. Finally in a novel proposal one may be able to observe the reaction produced electrons [17] instead of the standard nuclear recoils or even better to observe them in coincidence with the recoiling nuclei.

2 Rates

The differential non directional rate can be written as

$$dR_{undir} = \frac{\rho(0)}{m_\chi} \frac{m}{A m_N} d\sigma(u, \upsilon)|\upsilon| \tag{1}$$

where $d\sigma(u, \upsilon)$ was given above, $\rho(0) = 0.3\, GeV/cm^3$ is the LSP density in our vicinity, m is the detector mass and m_χ is the LSP mass

The directional differential rate, in the direction $\hat{e}$ of the recoiling nucleus, is:

$$dR_{dir} = \frac{\rho(0)}{m_\chi} \frac{m}{A m_N} |\upsilon| \hat{\upsilon}.\hat{e}\ \Theta(\hat{\upsilon}.\hat{e})\ \frac{1}{2\pi}\ d\sigma(u, \upsilon\ \delta\left(\frac{\sqrt{u}}{\mu_r \upsilon \sqrt{2}} - \hat{\upsilon}.\hat{e}\right) \tag{2}$$

where $\Theta(x)$ is the Heaviside function and:

$$d\sigma(u, \upsilon) == \frac{du}{2(\mu_r b \upsilon)^2} [(\bar{\Sigma}_S F(u)^2 + \bar{\Sigma}_{spin} F_{11}(u)] \tag{3}$$

where u the energy transfer Q in dimensionless units given by

$$u = \frac{Q}{Q_0} \quad , \quad Q_0 = [m_p A b]^{-2} = 40 A^{-4/3}\ MeV \tag{4}$$

with b is the nuclear (harmonic oscillator) size parameter. $F(u)$ is the nuclear form factor and $F_{11}(u)$ is the spin response function associated with the isovector channel.

The scalar cross section is given by:

$$\bar{\Sigma_S} = \left(\frac{\mu_r}{\mu_r(p)}\right)^2 \sigma^S_{p,\chi^0} A^2 \left[\frac{1+\frac{f^1_S}{f^0_S}\frac{2Z-A}{A}}{1+\frac{f^1_S}{f^0_S}}\right]^2 \approx \sigma^S_{N,\chi^0}\left(\frac{\mu_r}{\mu_r(p)}\right)^2 A^2 \quad (5)$$

(since the heavy quarks dominate the isovector contribution is negligible). σ^S_{N,χ^0} is the LSP-nucleon scalar cross section. The spin Cross section is given by:

$$\bar{\Sigma}_{spin} = \left(\frac{\mu_r}{\mu_r(p)}\right)^2 \sigma^{spin}_{p,\chi^0}\ \zeta_{spin}, \zeta_{spin} = \frac{1}{3(1+\frac{f^0_A}{f^1_A})^2} S(u) \quad (6)$$

$$S(u) \approx S(0) = \left[\left(\frac{f^0_A}{f^1_A}\Omega_0(0)\right)^2 + 2\frac{f^0_A}{f^1_A}\Omega_0(0)\Omega_1(0) + \Omega_1(0))^2\right] \quad (7)$$

f^0_A, f^1_A are the isoscalar and the isovector axial current couplings at the nucleon level [19].

3 Results

To obtain the total rates one must fold with LSP velocity and integrate the above expressions over the energy transfer from Q_{min} determined by the detector energy cutoff to Q_{max} determined by the maximum LSP velocity (escape velocity, put in by hand in the Maxwellian distribution), i.e. $v_{esc} = 2.84\ v_0$ with v_0 the velocity of the sun around the center of the galaxy(229 Km/s).

3.1 Non Directional Rates

In a previous paper [19] we have shown that, ignoring the motion of the Earth, the total non directional rate is given by

$$R = \bar{K}\left[c_{coh}(A,\mu_r(A))\sigma^S_{p,\chi^0} + c_{spin}(A,\mu_r(A))\sigma^{spin}_{p,\chi^0}\ \zeta_{spin}\right] \quad (8)$$

where $\bar{K} = \frac{\rho(0)}{m_{\chi^0}}\frac{m}{m_p}\ \sqrt{\langle v^2\rangle}$ and

$$c_{coh}(A,\mu_r(A)) = \left[\frac{\mu_r(A)}{\mu_r(p)}\right]^2 A\ t_{coh}(A)\ , c_{spin}(A,\mu_r(A)) = \left[\frac{\mu_r(A)}{\mu_r(p)}\right]^2 \frac{t_{spin}(A)}{A} \quad (9)$$

Table 1. The factors $c19 = c_{coh}(19, \mu_r(19))$, $s19 = c_{spin}(19, \mu_r(19))$ and $c127 = c_{coh}(127, \mu_r(127))$, $s127 = c_{spin}(127, \mu_r(127))$ for two values of Q_{min}.

Q_{min}		m_χ (GeV)							
keV		20	30	40	50	60	80	100	200
0	c19	2080	2943	3589	4083	4471	5037	5428	6360
0	s19	5.7	8.0	9.7	10.9	11.9	13.4	14.4	16.7
0	c127	37294	63142	84764	101539	114295	131580	142290	162945
0	s127	2.2	3.7	4.9	5.8	6.5	7.6	8.4	10.4
10	c19	636	1314	1865	2302	2639	3181	3487	4419
10	s19	1.7	3.5	4.9	6.0	6.9	8.3	9.1	11.4
10	c127	0	11660	24080	36243	45648	58534	69545	83823
10	s127	0	0.6	1.3	1.9	2.5	3.3	4.0	5.8

where t is the modification of the total rate due to the folding and nuclear structure effects. It depends on Q_{min}, i.e. the energy transfer cutoff imposed by the detector and $a = [\mu_r b v_0 \sqrt{2}]^{-1}$ The parameters $c_{coh}(A, \mu_r(A))$, $c_{spin}(A, \mu_r(A))$, which give the relative merit for the coherent and the spin contributions in the case of a nuclear target compared to those of the proton, are tabulated in table 1 for energy cutoff, $Q_{min} = 0$, 10 keV. Via (8) we can extract the nucleon cross section from the data.

Furthermore we have seen that ignoring the isoscalar axial current and using $\Omega_1^2 = 1.22$ and $\Omega_1^2 = 2.8$ for ^{127}I and ^{19}F respectively we find:

$$\frac{\sigma^{spin}_{p,\chi^0}}{\sigma^{S}_{p,\chi^0}} = \left[\frac{c_{coh}(A, \mu_r(A))}{c_{spin}(A, \mu_r(A))}\right] \frac{3}{\Omega_1^2} \Rightarrow \approx \times 10^4 \ (A = 127) \ , \ \approx \times 10^2 \ (A = 19) \tag{10}$$

It is for this reason that the limit on the spin proton cross section extracted from both targets is much poorer. The form factor favors the lighter system [18] both for the spin and the coherent process, $t(127) < t_(19)$. In the case of the spin this advantage is not offset by the larger reduced mass. It is even enhanced by the spin ME (see Table 1). For the coherent process, however, the light nucleus is no match (see Table 1).

If the effects of the motion of the Earth around the sun are included, the total non directional rate is given by

$$R = \bar{K} \left[c_{coh}(A, \mu_r(A)) \sigma^{S}_{p,\chi^0} (1 + h(a, Q_{min}) cos\alpha)\right] \tag{11}$$

and an analogous one for the spin contribution. h is the modulation amplitude and α is the phase of the Earth, which is zero around June 2nd. The modulation amplitude would be an excellent signal in discriminating against background, but unfortunately it is very small, less than two per cent. Furthermore for intermediate and heavy nuclei, it can even change sign for sufficiently heavy LSP [18].

3.2 Directional Rates

Since the sun is moving around the galaxy in a directional experiment, i.e. one in which the direction of the recoiling nucleus is observed, one expects a strong correlation of the event rate with the motion of the sun. In fact the directional rate can be written as:

$$R_{dir} = \frac{\kappa}{2\pi}\bar{K}\left[c_{coh}(A,\mu_r(A))\sigma^S_{p,\chi^0}(1+h_m cos(\alpha-\alpha_m\ \pi))\right] \qquad (12)$$

and an analogous one for the spin contribution. The modulation now is h_m, with a shift $\alpha_m\pi$ in the phase of the Earth α, depending on the direction of observation. $\kappa/(2\pi)$ is the reduction factor of the unmodulated directional rate relative to the non-directional one. The parameters κ , h_m , α_m strongly depend on the direction of observation.

We prefer to use the parameters κ and h_m, since, being ratios, are expected to be less dependent on the parameters of the theory. In the case of $A = 127$ we exhibit the the angular dependence of h_m for an LSP mass of $m_\chi = 100\,GeV$ in Fig. 1. We also exhibit the parameters t, h, κ, h_m and α_m for the target $A = 19$ in Table 2 (for the other light systems the results are almost identical).

The asymmetry is quite large in the direction of the sun's motion is large [18], ≈ 0.97. In the plane perpendicular to the sun's velocity the asymmetry equals the modulation.

For a heavier nucleus the situation is a bit complicated. Now the parameters κ and h_m depend on the LSP mass as well. (see Figs 2 and 3). The asymmetry and the shift in the phase of the Earth are similar to those of the $A = 19$ system.

3.3 Transitions to Excited States

Incorporating the relevant kinematics and integrating the differential event rate dR/du from u_{min} to u_{max} we obtain the total rate as follows:

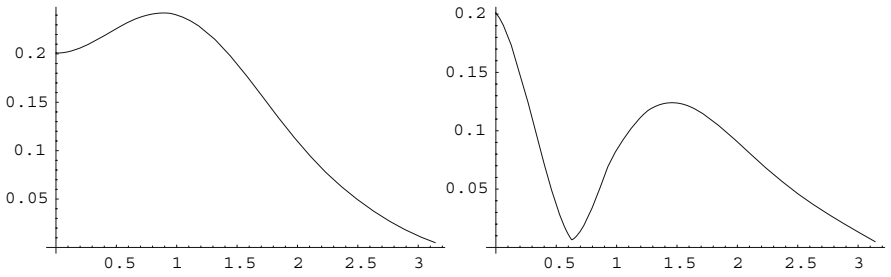

Fig. 1. The expected modulation amplitude h_m for $A = 127$ in a direction outward from the galaxy on the left and perpendicular to the galaxy on the right as a function of the polar angle measured from the sun's velocity. For angles than $\pi/2$ it is irrelevant since the event rates are tiny.

Table 2. The parameters t, h, κ, h_m and α_m for $Q_{min} = 0$. The results shown are for the light systems. $+x$ is radially out of the galaxy ($\Theta = \pi/2, \Phi = 0$), $+z$ is in the the sun's motion and $+y$ vertical to the plane of the galaxy so that $((x, y, x)$ is right-handed. $\alpha_m = 0, 1/2, 1, 3/2$ implies that the maximum occurs on June, September, December and March 2nd respectively.

type	t	h	dir	κ	h_m	α_m
dir			+z	0.0068	0.227	1
			+(-)x	0.080	0.272	3/2(1/2)
			+(-)y	0.080	0.210	0 (1)
			-z	0.395	0.060	0
all	1.00					
all		0.02				

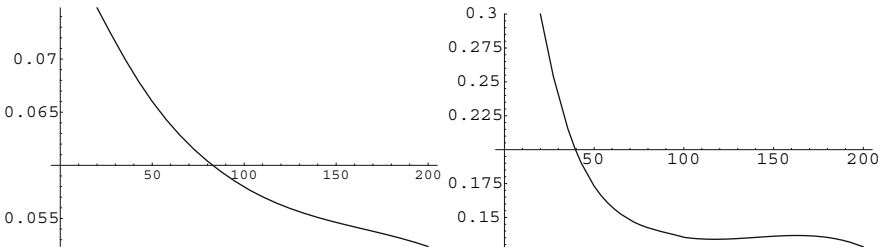

Fig. 2. The parameter κ as a function of the LSP mass in the case of the $A = 127$ system, for $Q_{min} = 0$ expected in a plane perpendicular to the sun's velocity on the left and opposite to the sun's velocity on the right.

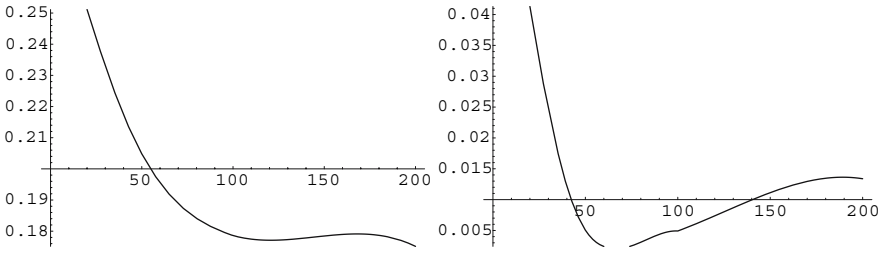

Fig. 3. The modulation amplitude h_m in a plane perpendicular to the sun's velocity on the left and opposite to the suns velocity on the right. Otherwise the notation is the same as in Fig. 2.

$$R_{exc} = \int_{u_{exc}}^{u_{max}} \frac{dR_{exc}}{du} \left(1 - \frac{u_{exc}^2}{u^2}\right) du \ , \ R_{gs} = \int_{u_{min}}^{u_{max}} \frac{dR_{gs}}{du} du \tag{13}$$

where $u_{exc} = \frac{\mu_r E_x}{A m_N Q_0}$ and E_x is the excitation energy of the final nucleus, $u_{max} = (y/a)^2 - (E_x/Q_0)$, $y = v/upsilon_0$ and $u_{min} = Q_{min}/Q_0$, Q_{min} (imposed by the detector energy cutoff) and $u_{max} = (y_{esc}/a)^2$ is imposed by the escape velocity ($y_{esc} = 2.84$).

For our purposes it is adequate to estimate the ratio of the rate to the excited state divided by that to the ground state (branching ratio) as a function of the LSP mass. This can be cast in the form:

$$BRR = \frac{S_{exc}(0)}{S_{gs}(0)} \frac{\Psi_{exc}(u_{exc}, u_{umax})[1 + h_{exc}(u_{exc}, u_{max}) \ \cos\alpha]}{\Psi_{gs}(u_{min})[1 + h(u_{min}) \ \cos\alpha]} \tag{14}$$

in an obvious notation [18]). $S_{gs}(0)$ and $S_{exc}(0)$ are the static spin matrix elements As we have seen their ratio is essentially independent of supersymmetry, if the isoscalar contribution is neglected. For ^{127}I it was found [9] to be be about 2. The functions Ψ are given as follows :

$$\Psi_{gs}(u_{min}) = \int_{u_{min}}^{(y/a)^2} \frac{S_{gs}(u)}{S_{gs}(0)} F_{11}^{gs}(u) \left[\psi(a\sqrt{u}) - \psi(y_{esc})\right] \ du \tag{15}$$

$$\Psi_{exc}(u_{exc}, u_{max}) = \int_{u_{exc}}^{u_{max}} \frac{S_{exc}(u)}{S_{exc}(0)} F_{11}^{exc}(u) \left(1 - \frac{u_{exc}^2}{u^2}\right) \left[\psi(a\sqrt{u}(1 + u_{exc}/u)) - \psi(y_{esc})\right] \ du \tag{16}$$

The functions ψ arise from the convolution with LSP velocity distribution. The obtained results are shown in Fig. 4.

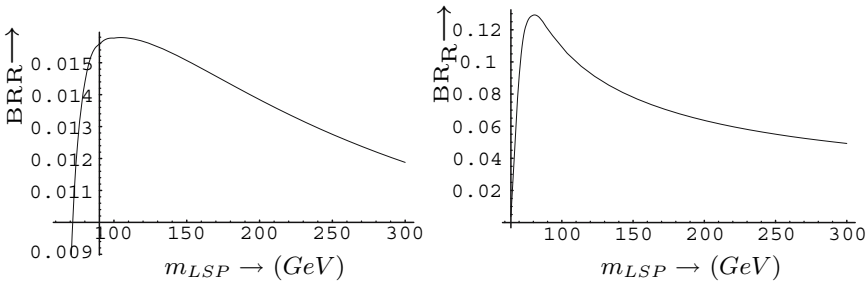

Fig. 4. The ratio of the rate to the excited state divided by that of the ground state as a function of the LSP mass (in GeV) for ^{127}I. We assumed that the static spin matrix element of the transition from the ground to the excited state is a factor of 1.9 larger than that involving the ground state, but the functions $F_{11}(u)$ are the same. On the left we show the results for $Q_{min} = 0$ and on the right for $Q_{min} = 10\,keV$.

3.4 Detecting Recoiling Electrons Following the LSP-Nucleus Collision

During the LSP-nucleus collision we can have the ionization of the atom. One thus may exploit this signature of the reaction and try to detect these electrons [17]. These electrons are expected to be of low energy and one thus may have a better chance of observing them in a gaseous TPC detector. In order to avoid complications arising from atomic physics we have chosen as a target ^{20}Ne. Furthermore, to avoid complications regarding the allowed SUSY parameter space, we will present our results normalized to the standard neutralino nucleus cross section. The thus obtained branching ratios are independent of all parameters of supersymmetry except the neutralino mass. The numerical results given here apply in the case of the coherent mode. If, however, we limit ourselves to the ratios of the relevant cross sections, we do not expect substantial changes in the case of the spin induced process.

The ratio of the our differential (with respect of the electron energy) cross section divided by the total cross section of the standard neutralino-nucleus elastic scattering, nuclear recoil experiments (nrec), takes [17] the form:

$$\frac{d\sigma(T)}{\sigma_{nrec}} = \frac{1}{4}\sum_{n\ell} p_{n\ell}|\tilde{\phi_{n\ell}}(2m_eT)|^2 \frac{\int_{-1}^{1} d\xi_1 \int_{\xi_L}^{1} d\xi K \frac{(\xi+\Lambda)^2}{\Lambda}[F(\mu_r\upsilon(\xi+\Lambda))]^2}{\int_0^1 2\xi d\xi [F(2\mu_r\upsilon\xi)]^2} m_e k dT \ . \tag{17}$$

where

$$\mathbf{K} = \frac{\mathbf{p}_\chi - \mathbf{k}}{p_\chi}, K = \frac{\sqrt{p_\chi^2 + k^2 - 2kp_\chi\xi_1}}{p_\chi}, \xi_1 = \hat{p}_\chi.\hat{k}, \xi = \hat{q}.\hat{K} \ ,$$

$\xi_L = \sqrt{\frac{m_\chi}{\mu_r}[1 + \frac{1}{K^2}(\frac{T-\epsilon_{n\ell}}{T_\chi} - 1)]}$ and $2\frac{\mu_r}{m_\chi}p_\chi\xi = 2\mu_r\upsilon\xi$ is the momentum q transferred to the nucleus and $F(q)$ is the nuclear form factor. The outgoing electron energy lies in the range $0 \leq T \leq \frac{\mu_r}{m_\chi}T_\chi - \epsilon_{n\ell}$. Since the momentum of the outgoing electron is much smaller than the momentum of the oncoming neutralino, i.e. $K \approx 1$, the integration over ξ_1 can be trivially performed.

We remind the reader that the LSP- nucleus cross-section σ_{nrec} takes the form:

$$\sigma_{nrec} = \left(\frac{\mu_r}{\mu_r(p)}\right)^2 A^2\sigma_p \int_0^1 2d\xi [F(2\mu_r\upsilon\xi)]^2 \tag{18}$$

In the case of ^{20}Ne he binding energies and the occupation probabilities are given by [17]:

$$\epsilon_{n\ell} = (-0.870, -0.048\ , -0.021)\ ,\ p_{n\ell} = (2/10, 2/10, 6/10)\ . \tag{19}$$

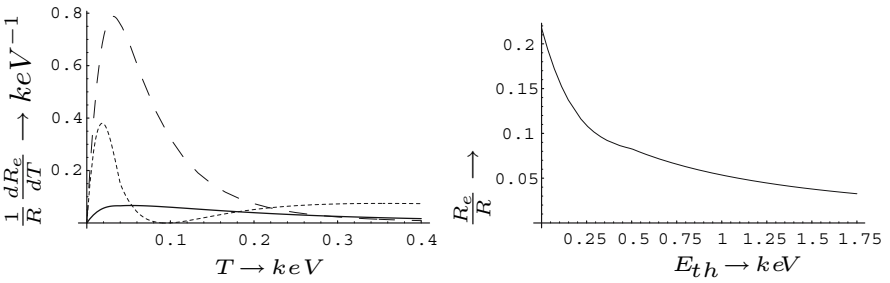

Fig. 5. Shown on the left is the differential rate, divided by the total rate associated with the nuclear recoils, as a function of the electron energy T (in keV). Each atomic orbit involved in the target ^{20}Ne is included separately. The full line, the short-dashed line and the long-dashed line correspond to the orbits $1s$, $2s$ and $2p$ respectively. Shown on the right is the ratio of the total rate for the novel process divided by that of the standard process as a function of the electron threshold energy, assuming zero threshold energy for the standard process. This ratio may increase if such a threshold is included.

in the obvious order: (1s,2s,2p). In Fig. 5 we show the differential rate of our process, divided by the total nuclear recoil event rate, for each orbit as well as the total rate in our process divided by that of the standard rate as a function of the electron threshold energy with 0 threshold energy in the standard process. We obtained our results using appropriate form factor [11].

From these plots we see that, even though the differential rate peaks at low energies, there remains substantial strength above the electron energy of $0.2\,keV$, which is the threshold energy for detecting electrons in a Micromegas detector, like the one recently [20] proposed.

4 Conclusions

Since the expected event rates for direct neutralino detection are very low [5, 8], in the present work we looked for characteristic experimental signatures for background reduction, such as:

- Standard recoil experiments
  Here the relevant parameters are t and h. For light targets they are essentially independent of the LSP mass [18], essentially the same for both the coherent and the spin modes. The modulation is small, $h \approx 0.2\%$, but it may increase as Q_{min} increases. Unfortunately, for heavy targets even the sign of h is uncertain for $Q_{min} = 0$. The situation improves as Q_{min} increases, but at the expense of the number of counts.
- Directional experiments [16] Here we find a correlation of the rates with the velocity of the sun as well as that of the Earth. One encounters reduction factors $\kappa/2\pi$, which depend on the angle of observation. The most

favorable factor is small, $\approx 1/4\pi$ and occurs when the nucleus is recoiling opposite to the direction of motion of the sun. As a bonus one gets modulation, which is three times larger, $h_m = \approx 0.06$. In a plane perpendicular to the sun's direction of motion the reduction factor is close to $1/12\pi$, but now the modulation can be quite high, $h_m \approx 0.3$, and exhibits very interesting time dependent pattern (see Table 2. Further interesting features may appear in the case of non standard velocity distributions [15].

- Transitions to Excited states
  We find that branching ratios for transitions to the first excited state of ^{127}I is relatively high, about 10%. The modulation in this case is much larger $h_{exc} \approx 0.6$. We hope that such a branching ratio will encourage future experiments to search for characteristic γ rays rather than recoils.
- Detection of ionization electrons produced in the LSP collision
  Our results indicate that one can be optimistic about using the emitted electrons in the neutralino nucleus collisions for the direct detection of the LSP. This novel process may be exploited by the planned TPC low energy electron detectors. By achieving low energy thresholds of about $0.25\,keV$, the branching ratios are approximately 10 percent. They can be even larger, if one includes low energy cutoffs imposed by the detectors in the standard experiments, not included in the above estimate.
  As we have seen the background problems associated with the proposed mechanism are not worse than those entering the standard experiments. In any case coincidence experiments with x-rays, produced following the de-excitation of the residual atom, may help reduce the background events to extremely low levels.

Acknowledgments

This work was supported in part by the European Union under the contracts RTN No HPRN-CT-2000-00148 and MRTN-CT-2004-503369. Part of this work was performed in LANL. The author is indebted to Dr Dan Strottman for his support and hospitality.

References

1. S. Hanary et al., Astrophys. J. **545**, L5 (2000); J.H.P Wu et al., Phys. Rev. Lett. **87**, 251303 (2001); M.G. Santos et al., Phys. Rev. Lett. **88**, 241302 (2002)
   P.D. Mauskopf et al., Astrophys. J. **536**, L59 (2002);
   S. Mosi et al., Prog. Nuc.Part. Phys. **48**, 243 (2002);
   S.B. Ruhl *al*, astro-ph/0212229; N.W. Halverson et al., Astrophys. J. **568**, 38 (2002);
   L.S. Sievers et al.,astro-ph/0205287;
   G.F. Smoot et al., (COBE data), Astrophys. J. **396**, (1992) L1;

A.H. Jaffe et al., Phys. Rev. Lett. **86**, 3475 (2001);
D.N. Spergel et al, astro-ph/0302209.
2. G. Jungman, M. Kamiokonkowski and K. Griest, Phys. Rep. **267**, 195 (1996).
3. R. Bernabei et al., INFN/AE-98/34, (1998); Phys. Lett. **B 389**, 757 (1996); Phys. Lett. **B 424**, 195 (1998); **B 450**, 448 (1999).
4. A. Benoit et al., [EDELWEISS collaboration], Phys. Lett. B **545**, 43 (2002); V. Sanglar,[EDELWEISS collaboration], arXiv:astro-ph/0306233; D.S. Akerib et al., [CDMS Collaboration], Phys. Rev D **68**, 082002 (2003);arXiv:astro-ph/0405033.
5. A. Bottino et al., Phys. Lett. B **402**, 113 (1997). R. Arnowitt. and P. Nath, Phys. Rev. Lett. **74**, 4952 (1995); Phys. Rev. D **54**, 2394 (1996); hep-ph/9902237; V.A. Bednyakov, H.V. Klapdor-Kleingrothaus and S.G. Kovalenko, Phys. Lett. B **329**, 5 (1994).
6. M.E.Gómez and J.D. Vergados, Phys. Lett. B **512** , 252 (2001); hep-ph/0012020.
M.E. Gómez, G. Lazarides and C. Pallis, Phys. Rev.D **61**, 123512 (2000) and Phys. Lett. B **487**, 313 (2000); M.E. Gómez and J.D. Vergados, hep-ph/0105115.
7. J.D. Vergados, J. of Phys. G **22**, 253 (1996); T.S. Kosmas and J.D. Vergados, Phys. Rev. D **55**, 1752 (1997).
8. A. Arnowitt and B. Dutta, Supersymmetry and Dark Matter, hep-ph/0204187;. E. Accomando, A. Arnowitt and B. Dutta, hep-ph/0211417.
9. J.D. Vergados, P.Quentin and D. Strottman, (to be published)
10. M.T. Ressell et al., Phys. Rev. D **48**, 5519 (1993); M.T. Ressell and D.J. Dean, Phys. Rev. C **56** (1997) 535.
11. P.C. Divari, T.S. Kosmas, J.D. Vergados and L.D. Skouras, Phys. Rev. C **61** (2000), 044612-1.
12. A.K. Drukier, K. Freese and D.N. Spergel, Phys. Rev. D **33**, 3495 (1986); K. Frese, J.A Friedman, and A. Gould, Phys. Rev. D **37**, 3388 (1988).
13. J.D. Vergados, Phys. Rev. D **58**, 103001-1 (1998); Phys. Rev. Lett **83**, 3597 (1999); Phys. Rev. D **62**, 023519 (2000); Phys. Rev. D **63**, 06351 (2001).
14. J.I. Collar et al., Phys. Lett. B **275**, 181 (1992); P. Ullio and M. Kamioknowski, JHEP **0103**, 049 (2001); P. Belli, R. Cerulli, N. Fornego and S. Scopel, Phys. Rev. D **66**, 043503 (2002); A. Green, Phys. Rev. D **66**, 083003 (2002).
15. B. Morgan, A.M. Green and N. Spooner, astro-ph/0408047.
16. D.P. Snowden-Ifft, C.C. Martoff and J.M.Burwell, Phys. Rev. D **61**, 1 (2000); M. Robinson et al., Nucl.Instr. Meth. A **511**, 347 (2003).
17. J.D. Vergados and H. Ejiri, hep-ph/0401151 (to be published).
18. J.D. Vergados, Phys. Rev. D **67** (2003) 103003; *ibid* **58** (1998) 10301-1; J.D. Vergados, J. Phys. G: Nucl. Part. Phys. **30**, 1127 (2004).
19. J.D. Vergados, to appear in the idm04 proceedings
20. Y. Giomataris and J.D. Vergados, Neutrinos in a spherical box, to appear in Nucl.Instr. Meth. (to be published) & hep-ex/0303045.

Part III

Collider and Search for Dark Matter

Indirect, Direct and Collider Detection of SUSY Dark Matter

Howard Baer

Dep't of Physics, Florida State University, Tallahassee, FL 32306
baer@hep.fsu.edu

The minimal supergravity model (mSUGRA) serves as a paradigm model for phenomenological investigations in supersymmetry. One standard prediction is that the lightest neutralino comprises the bulk of the cold dark matter in the universe. I outline expectations for detection of neutralino dark matter at the Fermilab Tevatron, CERN LHC and a future linear e^+e^- collider experiments. These collider capabilities are compared to dark matter detection capabilities of direct and indirect search experiments. In a final section, I outline motivation for going beyond the mSUGRA model, to models with scalar mass non-universality.

1 Minimal Supergravity Model

The minimal supersymmetric standard model (MSSM) is a well-motivated extension of the Standard Model (SM) which admits the prospect of gauge coupling unification. However, the 124 dimensional parameter space of the MSSM is intractable for phenomenological analysis. A much smaller parameter space can be found in the minimal supergravity (mSUGRA) model. To construct the mSUGRA model:

- Begin with the general Lagrangian for locally supersymmetric gauge theories [2].
- Specify the $SU(3)_C \times SU(2)_L \times U(1)_Y$ gauge symmetry of the Standard Model (SM).
- Elevate the SM gauge fields to gauge superfields, and the SM fermion and scalar fields to left chiral superfields. A second Higgs doublet will be needed to cancel triangle anomalies induced by the new higgsino fields.
- Specify the Kähler function $G = K + \log|\hat{f}|^2$, which includes gauge singlet hidden sector superfields $\hat{h}$, where
  - the superpotential $\hat{f} = \hat{f}_{MSSM} + \hat{f}_{hidden}$,
  - the Kähler metric $K = \sum_i \hat{S}_i^\dagger \hat{S}_i + \hat{h}^\dagger \hat{h}$ is flat.
- Specify a simple gauge kinetic function $f_{AB} = \delta_{AB} f(\hat{h})$.
- Arrange for SUSY breaking in the hidden sector, fixing parameters to yield a TeV scale gravitino mass $m_{3/2}$.
- Calculate supergravity induced soft SUSY breaking terms.

- Take the limit as $M_{Pl} \to \infty$ keeping $m_{3/2}$ fixed: the result is a globally supersymmetric renormalizable gauge theory with TeV scale soft SUSY breaking terms valid at some high scale taken to be (inspired by gauge coupling unification) M_{GUT}.
- The weak scale model is obtained via RG evolution of couplings and soft terms, and EW symmetry is broken radiatively, owing to the large top quark mass.
- The parameter space is given by:

$$m_0,\ m_{1/2},\ A_0,\ \tan\beta,\ sign(\mu)\ . \tag{1}$$

2 Allowed Parameter Space

Significant constraints on the allowed parameter space come from [3]

- limits from LEP2 that $m_{\widetilde{W}_1} > 103.5\,\mathrm{GeV}$ and $m_{H_{SM}} > 114.4\,\mathrm{GeV}$,
- the branching fraction $BF(b \to s\gamma) = (3.25 \pm 0.54) \times 10^{-4}$,
- the muon anomalous magnetic moment [4] $\Delta a_\mu = (31.7 \pm 9.5) \times 10^{-10}$ (Hagiwara et al. analysis) [5],
- The recent limit from the WMAP collaboration [6] that $\Omega_{CDM}h^2 = 0.1126 \pm 0.0090$, based on measurements of the anisotropies in the cosmic microwave background radiation.

The first of these we take as an absolute limit, since in mSUGRA the lightest Higgs scalar h is almost always SM-like. The next three we combine in a χ^2 analysis [7], but use only the WMAP upper limit $\Omega_{CDM}h^2 < 0.129$ since there may exist other forms of CDM in the universe. The results are shown in Fig 1 in the m_0 *vs.* $m_{1/2}$ plane for $\tan\beta = 10$ and 55, and for $A_0 = 0$ and $m_t = 175\,\mathrm{GeV}$. The green shading is low χ^2, red gives high χ^2 and yellow is intermediate between the two.

Several viable regions emerge.

- The bulk region at low m_0 and low $m_{1/2}$, where neutralino annihilation in the early universe is facilitated by t-channel slepton exchange. This region is severely constrained by the LEP2 Higgs mass bound, and also by $b \to s\gamma$ and Δa_μ, and is nearly excluded.
- The stau co-annihilation region, where $m_{\tilde{\tau}_1} \simeq m_{\widetilde{Z}_1}$ [8].
- The HB/FP region of Chan, Chattopadyhay and Nath [9] (see also Feng, Matchev and Moroi [10] and Baer et al. [11]) at large m_0 where $\mu \to 0$ so that the $\widetilde{Z}_1$ develops a substantial higgsino component, which facilitates annihilation to WW, ZZ and Zh final states in the early universe.
- The A annihilation funnel, which occurs at large $\tan\beta$ and where $\widetilde{Z}_1\widetilde{Z}_1$ annihilation occurs through the broad s-channel A and H resonance [12] in the early universe.

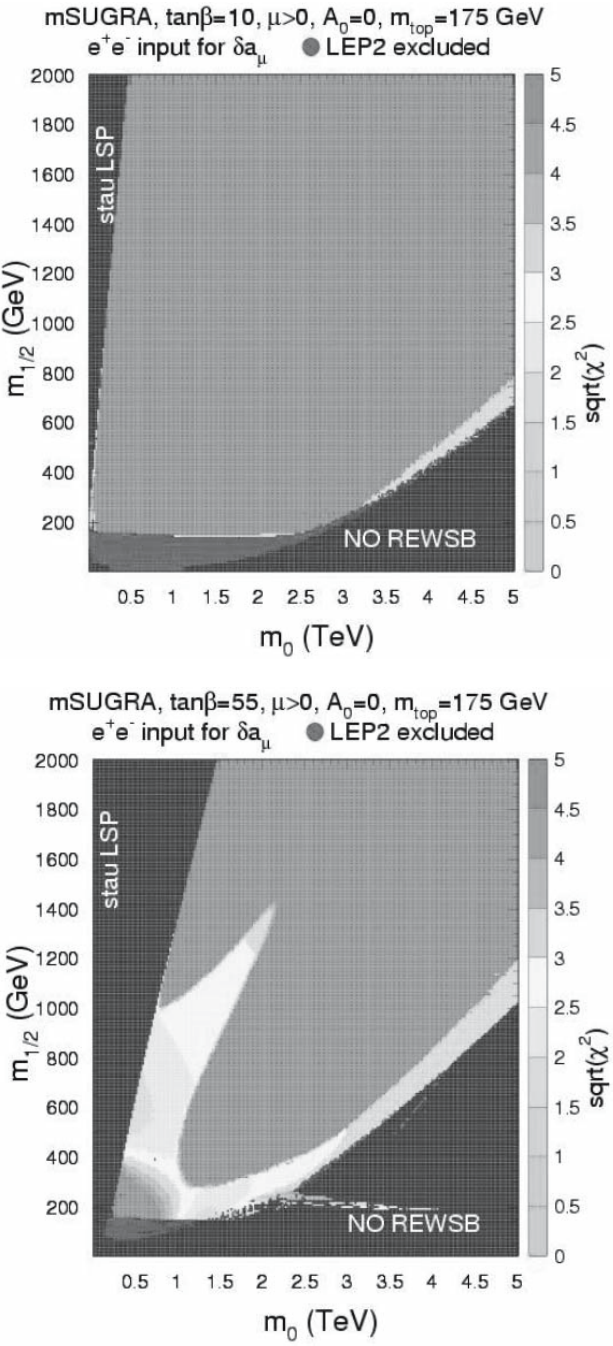

Fig. 1. Regions of preferred parameter space in the mSUGRA model in light of WMAP, $BF(b \to s\gamma)$ and $(g-2)_\mu$ data, for $\tan\beta = 10$ and 55.

3 Indirect, Direct and Collider Detection of Neutralino Dark Matter

The combined constraints on the mSUGRA model eliminate most of parameter space, but it is noteworthy that several distinct regions survive. It makes sense to then compare these regions with the reach of various collider experiments and also both direct and indirect search experiments for neutralino dark matter.

We compare the reach of the following experimental searches for supersymmetry.

- Fermilab Tevatron search for SUSY via the clean trilepton channel [13, 14] $p\bar{p} \to \widetilde{W}_1\widetilde{Z}_2 \to 3\ell + \not{E}_T$, assuming a 5σ signal with 10 fb^{-1} of data.
- CERN LHC search for SUSY in a variety of multi-lepton plus multijet $+ \not{E}_T$ modes, where a 5σ signal above SM background is required for 100 fb^{-1} of integrated luminosity [15].
- A $\sqrt{s} = 0.5$ and 1 TeV linear e^+e^- collider seach for slepton pairs, chargino pairs, and neutralino pairs, assuming 100 fb^{-1} of background [16].
- Direct detection of dark matter via underground cryogenic detectors [17]. Here, we assume Stage 3 detectors such as Genius, Xenon or Zeplin-4 with a reach of $\sim 10^{-9}$ pb as measured in the spin-independent neutralino-proton scattering cross section.
- Detection of $\nu_\mu \to \mu$ conversions in neutrino telescopes, such as IceCube, with expected sensitivity of 40 events/km^2/yr, with $E_\mu > 25\,\mathrm{GeV}$. These events originate from neutralino annihilation in the core of the sun to SM particles, which might decay to neutrinos, which can escape the sun. The rate for such events depends mainly on the neutralino-nucleon scattering rate, rather than on the neutralino-neutralino annihilation rate.
- Detection of gamma rays with $E_\gamma > 1\,\mathrm{GeV}$, where the γs arise from neutralino annihilation in the galactic core and halo to SM particles, which give rise to $\pi^0 \to \gamma\gamma$ decays. Here, we require a photon flux greater than 10^{-10}/cm^2/sec, which should be attainable by *e.g.* the GLAST experiment.
- Detection of e^+s arising from neutralino annihilation to SM particles in the galactic halo, as in the HEAT, Pamela or AMS experiments. We require a signal/background rate greater than 0.01, as in Feng et al. [18].
- Detection of $\bar{p}$s arising from neutralino annihilation to SM particles in the galactic halo. Here we require a rate of $\sim 3 \times 10^{-7}$/GeV/cm^2/s/sr, at an energy of $E_{\bar{p}} = 1.76\,\mathrm{GeV}$, as in the BESS experiment.

In these results, we use Isajet [19] for the sparticle mass spectrum calulation and event generation, IsaReD for the relic density, IsaDet for direct detection rates, and DarkSUSY [20] interfaced to Isajet for indirect detection rates.

Our first results are shown in Fig. 2. We can see immediately that the Fermilab Tevatron has enough reach to cover the light Higgs h annihilation

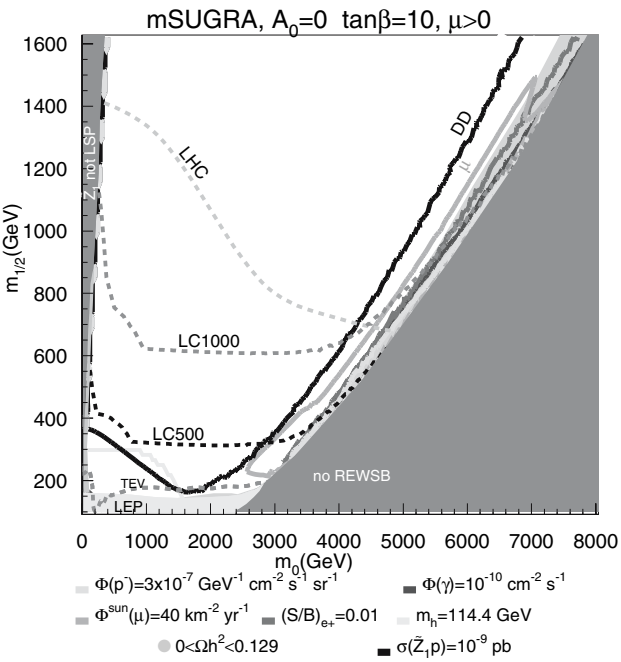

Fig. 2. Regions of parameter space in the mSUGRA model which are accessible to various collider, direct and indirect searches for supersymmetric matter. We take $\tan\beta = 10$, $\mu > 0$ and $A_0 = 0$.

region which lies just above the LEP2 excluded region [14]. The reach of the CERN LHC is also plotted [15], and can see up to $m_{\tilde{g}} \simeq 3$ TeV at low m_0 (enough to cover the stau co-annihilation region for low $\tan\beta$), and can see up to $m_{\tilde{g}} \simeq 1.8$ TeV at high m_0, *i.e.* the lower portion of the HB/FP region. An e^+e^- LC can cover most or all of the stau region. In addition, the LC reach extends far up the HB/FP region [16], where the reach of a LC exceeds even that of the CERN LHC! In the upper HB/FP region, squarks and sleptons are in the multi-TeV range, and are decoupled from LHC and LC physics. If the $\tilde{g}$ is too heavy ($\gtrsim$ 2 TeV), then it also decouples from LHC searches, and only charginos and neutralinos are relatively light. Their signals are extremely hard to extract from SM backgrounds at the LHC. However, chargino pair production at an e^+e^- LC in the HB/FP region might be kinematically possible, since in this region $|\mu| \to 0$ and charginos become light. If accessible, chargino pairs should be visible at a linear e^+e^- collider and should stand out above backgrounds [16] at a linear e^+e^- collider. Similar results are shown in Fig. 3, but this time for $\tan\beta = 55$, where the A-annihlation funnel is displayed. Here, we note the LHC covers most but not all of the stau coannihilation region, and most but not all of the A funnel.

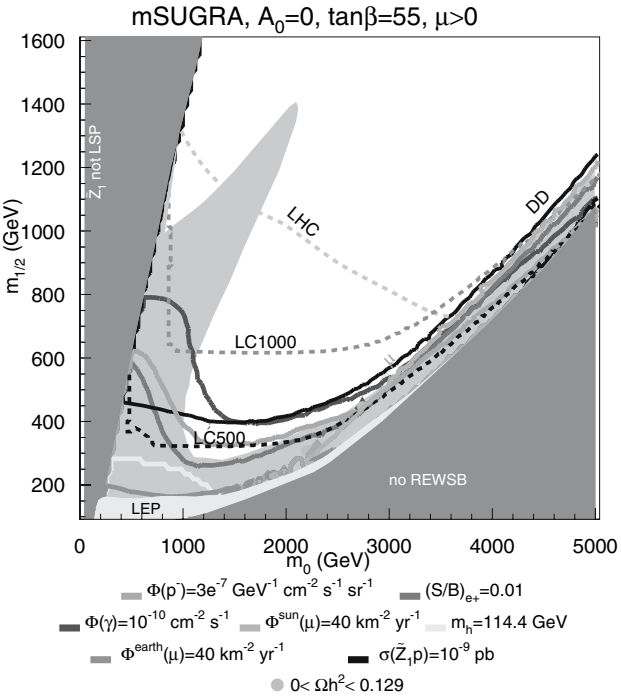

Fig. 3. Regions of parameter space in the mSUGRA model which are accessible to various collider, direct and indirect searches for supersymmetric matter. We take $\tan\beta = 55$, $\mu > 0$ and $A_0 = 0$.

The situation in the HB/FP region is qualitatively the same for all $\tan\beta$ values.

Regarding direct and indirect dark matter searches [21, 22], it is important to note that neutralino-nucleon scattering rates are large in the bulk region of parameter space, and also in the HB/FP region, where the neutralino has a substantial higgsino component. Figs. 2 and 3 show that the direct detection rates (DD contour) cover essentially all of the HB/FP region, which is a region of difficulty for LHC and even LC, in the case that $\sqrt{s} < 2m_{\widetilde{W}_1}$. Further, the IceCube contour for observable signals also covers most of the HB/FP region. Given that IceCube will be fully deployed by 2011, it is possible SUSY may be discovered there first, if parameters lie in the high $m_{1/2}$ portion of the HB/FP region. Since $\widetilde{Z}_1\widetilde{Z}_1$ annihilation rates are also large in the HB/FP region, observable signals also occur here in the γ, e^+ and $\bar{p}$ channels.

If SUSY lies in the stau co-annihilation region, then *none* of the direct or indirect signals for DM are likely observable, unless $\tan\beta$ is extremely large. In the A-annihilation funnel, neutralino pair annihilation rates are high, while neutralino-nucleon scattering rates are small. Thus, a direct detection

or neutrino telescope signal is unlikely. However, rates for γ, e^+ or $\bar{p}$ detection can be large. How large depends in part on the halo model which is assumed, especially for the γ signal, which can originate near the galactic core, where there might be a high density of neutralinos.

4 SUGRA Models with Non-Universality: NMH Model

In this last section, we note that the $BF(b \to s\gamma)$ measured rate is close to that of the SM prediction. This usually requires rather heavy top squarks, to suppress SUSY loop contributions to this decay. However, the measured value of $(g-2)_\mu$ has a $\sim 3\sigma$ difference from the SM prediction; this favors relatively light smuons or mu-sneutrinos. One way to accomodate these constraints, and to simultaneously fulfill the WMAP DM constraint, is to allow generational non-universality of soft SUSY breaking scalar masses. Dangerous FCNC effects are suppressed by keeping first and second generation scalar masses nearly equal, but a large splitting with the third generation can be allowed. In this case, we examine models with $m_0(1) \simeq m_0(2) \ll m_0(3)$, where the numbers correspond to the generations. In these models, which we call normal scalar mass hierarchy (NMH) models [23], the first and second

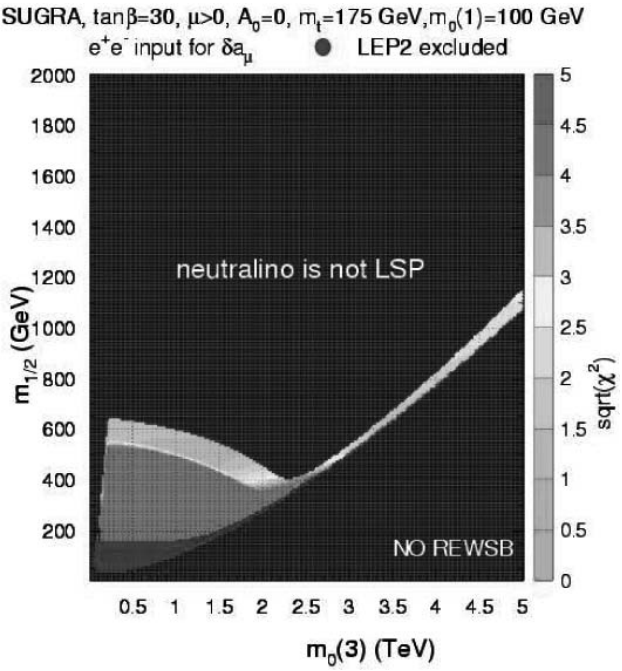

Fig. 4. Regions of various χ^2 values in the parameter space in the NMH model for $\tan\beta = 30$ and $m_0(1) = 100\,\mathrm{GeV}$. Also, $\mu > 0$ and $A_0 = 0$.

generation sleptons tend to be light- of order a few hundred GeV, while third generation scalars and squarks of the first two generations are at the TeV scale.

A χ^2 plot in the $m_0(3)$ *vs.* $m_{1/2}$ plane is shown in Fig. 4, for $m_0(1) = 100\,\text{GeV}$. The high $m_{1/2}$ regions are excluded because they give rise to a slepton LSP. However, much of the allowed region has a green shading, indicating a low χ^2 value, and good agreement with data on $\Omega_{CDM}h^2$, $BF(b \to s\gamma)$ and Δa_μ. Since these models have relatively light first and second generation slepton masses, collider events at the CERN LHC and maybe even the Tevatron can be expected to be unusually rich in isolated leptons. The relatively low lying sleptons ought to be accessible to LC SUSY searches as well.

Acknowledgments

I thank A. Belyaev, T. Krupovnickas, J. O'Farrill, A. Mustafayev and X. Tata for collaborations which led to these results.

References

1. A. Chamseddine, R. Arnowitt and P. Nath, Phys. Rev. Lett. **49** (1982) 970; R. Barbieri, S. Ferrara and C. Savoy, Phys. Lett. B**119** (1982) 343; L. J. Hall, J. Lykken and S. Weinberg, Phys. Rev. **D27** (1983) 2359; for a review, P. Nath, hep-ph/0307123
2. E. Cremmer, S. Ferrara, L. Girardello and A. van Proeyen, Nucl. Phys. **B212**, 413 (1983)
3. H. Baer, C. Balazs and A. Belyaev, J. K. Mizukoshi, X. Tata and Y. Wang, JHEP**0207**, 050 (2002)
4. T. C. Yuan, R. Arnowitt, A. Chamseddine and P. Nath, Z. Phys. **C26**, 407 (1984). See also U. Chattopadhyay and P. Nath, Phys. Rev. Lett. **86**, 5854 (2001)
5. K. Hagiwara, A. Martin, D. Nomura and T. Teubner, Phys. Rev. **D69**, 093003 (2004)
6. D. N. Spergel et al. (WMAP Collaboration), Astrophys. J. Suppl. **148**, 175 (2003)
7. H. Baer and C. Balazs, JCAP**0305**, 006 (2003).
8. J. Ellis, T. Falk and K. Olive, Phys. Lett. **B444**, 367 (1998); J. Ellis, T. Falk, K. Olive and M. Srednicki, Astropart. Phys. **13**, 181 (2000)
9. K. Chan, U. Chattopadhyay and P. Nath, Phys. Rev. **D58**, 096004 (1998)
10. J. Feng, K. Matchev and T. Moroi, Phys. Rev. **D61**, 075005 (2000)
11. See also H. Baer, C. H. Chen, F. Paige and X. Tata, Phys. Rev. **D52**, 2746 (1995) and Phys. Rev. **D53**, 6241 (1996)
12. M. Drees and M. Nojiri, Phys. Rev. **D47**, 376 (1993); H. Baer and M. Brhlik, Phys. Rev. **D57**, 567 (1998); H. Baer, M. Brhlik, M. Diaz, J. Ferrandis, P. Mercadante, P. Quintana and X. Tata, Phys. Rev. **D63**, 015007 (2001); A. Djouadi, M. Drees and J. Kneur, JHEP**0108**, 055 (2001); J. Ellis, T. Falk,

G. Ganis, K. Olive and M. Srednicki, Phys. Lett. **B510**, 236 (2001); L. Roszkowski, R. Ruiz de Austri and T. Nihei, JHEP**0108**, 024 (2001); A. Lahanas and V. Spanos, Eur. Phys. Jou. **C23**, 185 (2002)
13. D. Dicus, S. Nandi and X. Tata, Phys. Lett. **B129**, 451 (1983); A. Chamseddine, P. Nath and R. Arnowitt, Phys. Lett. **B129**, 445 (1983); H. Baer, K. Hagiwara and X. Tata, Phys. Rev. Lett. **57**, 294 (1986) and Phys. Rev. **D35**, 1598 (1987); R. Arnowitt and P. Nath, Mod. Phys. Lett. **2**, 331 (1987); H. Baer and X. Tata, Phys. Rev. **D47**, 2739 (1993)
14. V. Barger and C. Kao, Phys. Rev. **D60**, 115015 (1999); H. Baer, M. Drees, F. Paige, P. Quintana and X. Tata, Phys. Rev. **D61**, 095007 (2000); K. Matchev and D. Pierce, Phys. Rev. **D60**, 075004 (1999) and Phys. Lett. **B467**, 225 (1999). For an update, see H. Baer, T. Krupovnickas and X. Tata, JHEP**0307**, 020 (2003)
15. H. Baer, C. Balazs, A. Belyaev, T. Krupovnickas and X. Tata, JHEP**0306**, 054 (2003)
16. H. Baer, A. Belyaev, T. Krupovnickas and X. Tata, JHEP**0402**, 007 (2004); H. Baer, T. Krupovnickas and X. Tata, JHEP**0406**, 061 (2004)
17. For a recent analysis, see H. Baer, C. Balazs, A. Belyaev and J. O'Farrill, JCAP**0309**, 2003 (007); a subset of earlier work includes M. Goodman and E. Witten, Phys. Rev. D**31**, 3059 (1985); K. Griest, Phys. Rev. Lett. **61**, 666 (1988) and Phys. Rev. D**38**, 2357 (1988) [Erratum-ibid. D**39**, 3802 (1989)]; M. Drees and M. Nojiri, Phys. Rev. D**47**, 4226 (1993) and Phys. Rev. D**48**, 3483 (1993); V. A. Bednyakov, H. V. Klapdor-Kleingrothaus and S. Kovalenko, Phys. Rev. D**50**, 7128 (1994); P. Nath and R. Arnowitt, Phys. Rev. Lett. **74**, 4592 (1995); L. Bergstrom and P. Gondolo, Astropart. Phys. **5**, 263 (1996); H. Baer and M. Brhlik, Phys. Rev. D**57**, 567 (1998); J. Ellis, A. Ferstl and K. Olive, Phys. Lett. **B481**, 304 (2000) and Phys. Rev. D**63**, 065016 (2001); E. Accomando, R. Arnowitt, B. Dutta and Y. Santoso, Nucl. Phys. **B585**, 124 (2000); A. Bottino, F. Donato, N. Fornengo and S. Scopel, Phys. Rev. D**63**, 125003 (2001); M. E. Gomez and J. D. Vergados, Phys. Lett. **B512**, 252 (2001); A. B. Lahanas, D. V. Nanopoulos and V. C. Spanos, Phys. Lett. **B518**, 94 (2001); A. Corsetti and P. Nath, Phys. Rev. D**64**, 115009 (2001); E. A. Baltz and P. Gondolo, Phys. Rev. Lett. **86**, 5004 (2001); M. Drees, Y. G. Kim, T. Kobayashi and M. M. Nojiri, Phys. Rev. D**63**, 115009 (2001); see also J. Feng, K. Matchev and F. Wilczek, Ref. [18]; J. R. Ellis, A. Ferstl, K. A. Olive and Y. Santoso, Phys. Rev. D**67**, 123502 (2003); J. R. Ellis, K. A. Olive, Y. Santoso and V. C. Spanos, Phys. Rev. D**69**, 015005 (2004); see C. Munoz, hep-ph/0309346 for a recent review
18. J. Feng, K. Matchev and F. Wilczek, Phys. Rev. **D63**, 045024 (2001)
19. F. Paige, S. Protopopescu, H. baer and X. Tata, hep-ph/0312045 (2003)
20. DarkSUSY, by P. Gondolo, J. Edsjo, P. Ullio, L. Bergstrom, M. Schelke and E. Baltz, JCAP**0407**, 008 (2004)
21. H. Baer and J. O' Farrill, JCAP**0404**, 005 (2004)
22. H. Baer, A. Belyaev, T. Krupovnickas and J. O'Farrill, JCAP**0408**, 005 (2004); for related work, see J. Edsjo, M. Schelke and P. Ulio, astro-ph/0405414 (2004)
23. H. Baer, A. Belyaev, T. Krupovnickas and A. Mustafayev, JHEP**0406**, 044 (2004)

Dark Matter and Colliders

R.L. Arnowitt,[1] A. Aurisano,[1] B. Dutta,[2] T. Kamon[1], V. Khotilovich,[1]
D. Toback,[1] P. Wagner[1]

[1] Department of Physics, Texas A&M University,
College Station, TX 77807, USA
[2] Department of Physics, University of Regina,
Regina, Saskatchewan S4S 0A2, Canada

The tight bound on relic density from WMAP and other experimental results have put tremendous constraint on the minimal supergravity (mSUGRA) model parameter space. The parameter space now exhibits certain features. In this talk, we investigate the stau-neutralino co-annihilation domain where the lightest stau mass is very close to the lightest neutralino (LSP) mass. This narrow mass difference needs to be determined accurately at the colliders to verify this mSUGRA explanation of dark matter. We discuss all possible experimental constraints on the parameter space and the signals at different colliders e.g. the large hadron collider (LHC) and the linear collider (LC). We probe the Standard Model backgrounds in detail and determine the accuracy for the measurement of the stau-neutralino mass difference at a 500 GeV LC.

1 Introduction

Recently, the measurements of relic density have become very accurate. Since the Standard Model (SM) of particle physics does not explain this relic abundance, we have to search for new physics. Among the models of new physics, the most elegant and economical model is the minimal supergravity (mSUGRA) model [1, 2, 3]. The new relic abundance data from WMAP has restricted the parameter space of this model significantly [4].

Constraints on the parameter space of mSUGRA also arise from the Higgs mass bound, the $b \to s\gamma$ branching ratio, and (possibly) the muon a_μ anomaly. After including these constraints, the dark matter allowed parameter space, at present, have three distinct regions: (i) the stau neutralino co-annihilation region, (ii) the neutralino having larger Higgsino component (Focus point) and (iii) the scalar Higgs (A, H) annihilation funnel (where $2M_{\tilde{\chi}_1^0} \simeq M_{A,H}$). There still exists a bulk region where none of these above properties is observed, but this region is very small due to the existence of different experimental bounds. All of the above regions exhibit some particular features which require precise experimental measurements for confirmation. Among these regions, the stau neutralino co-annihilation region seems to be experimentally most favored and almost the entire region can be observed at the large hadron collider (LHC). This region is characterized by the lightest

stau and the lightest neutralino mass difference of about 5–15 GeV. This narrow mass difference allows the stau to co-annihilate in the early universe along with the neutralinos in order to produce the current amount of dark matter density of the universe. The co-annihilation region has a large extension for $m_{1/2}$, up to 1–1.5 TeV.

The stau-neutralino co-annihilation feature can not be explored in the dark matter experiments since these experiments only measure the mass of the neutralino, not the mass difference between the co-annihilating particles. In this situation, the colliders are the only option to test the model. The colliders which have the kinematic reach to test this region are the LHC and the linear collider (LC). The LHC will start operating from 2007 and the LC is in the planning stage. The SUSY particles will be produced directly at the colliders and the masses will be measured. In order to detect the co-annihilation region, we need to measure the mass difference between the stau and the neutralino. Since this mass difference is very small, there will be low energy taus in the signal arising from the decay of the lightest stau into the lightest neutralino. These low energy taus are hard to detect due to the presence of standard model (SM) background but their identifications are crucial to measure the mass difference.

In this talk, we discuss this possible signals and the backgrounds as well as the necessary event selection cuts to improve signal-to-noise ratio in the stau neutralino co-annihilation region at a 500 GeV LC and at the LHC. Using these cuts, we discuss the accuracy that could be obtained in measuring the narrow mass difference at a LC.

2 mSUGRA Parameter Space

The mSUGRA parameter space is determined by four parameters and one sign. These four parameters are given at the GUT (M_G) scale: m_0 (the universal scalar soft breaking mass); $m_{1/2}$ (the universal gaugino soft breaking mass at M_G); A_0 (the universal cubic soft breaking) mass; $\tan\beta = \langle H_2\rangle/\langle H_1\rangle$ at the electroweak scale (where H_2 gives rise to u quark masses and H_1 to d quark and lepton masses). The sign is associated with the μ Higgs mixing parameter in the superpotential ($W_\mu = \mu H_1 H_2$).

Various experimental constraints have already restricted the mSUGRA model parameters significantly. Among these constraints, the most important are: (1) The light Higgs mass bound from LEP [5] $M_h > 114$ GeV. Since theoretical calculations of M_h still have a 2–3 GeV error, we will conservatively assume this to mean that $(M_h)^{\text{theory}} > 111$ GeV. (2) The $b \to s\gamma$ branching ratio [6]. In our calculation, we assume a relatively broad range (since there are theoretical errors in extracting the branching ratio from the data):

$$1.8 \times 10^{-4} < \mathcal{B}(B \to X_s\gamma) < 4.5 \times 10^{-4} \tag{1}$$

The M_h and $b \to s+\gamma$ constraints produce a lower bound on $m_{1/2}$ for all $\tan\beta$ of $m_{1/2} \gtrsim 300$ GeV, which implies $M_{\tilde{\chi}_1^0} > 120\,\text{GeV}$ and $M_{\tilde{g}} > 250\,\text{GeV}$. (Note that the lightest neutralino $\tilde{\chi}_1^0$ and the gluino $\tilde{g}$ are approximately related to $m_{1/2}$ by $M_{\tilde{\chi}_1^0} \cong 0.4\ m_{1/2}$ and $M_{\tilde{g}} \cong 2.8\ m_{1/2}$.) (3) In mSUGRA the lightest neutralino, $\tilde{\chi}_1^0$, is the candidate for the observed cold dark matter relic density. The new data from WMAP [7] gives us the following 2σ bounds:

$$0.095 < \Omega_{\text{CDM}} h^2 < 0.129 \tag{2}$$

where Ω_{CDM} is the density of dark matter relative to the critical density to close the universe ($\equiv \rho/\rho_c$), and $h = H/100$ km/sec Mpc where H is the Hubble constant. The new data provides a factor of four improvement over the previous bounds from balloon flights (Boomerang, Maxima, Dasi, etc.): $0.07 < \Omega_{\text{CDM}} h^2 < 0.21$. The relic density constraint produces a narrow rising band of allowed parameter space in the m_0-$m_{1/2}$ plane. (4) The muon magnetic moment anomaly, δa_μ [8] using both μ^+ and μ^- data gives a 2.7σ deviation of the SM from the experimental result [9, 10]. This deviation is obtained using the e^+e^- data to calculate the hadronic SM contribution which appears to be more reliable in comparison to the calculation using tau decay and CVC analysis with CVC breaking [11]. Assuming future data confirms the a_μ anomaly, and the combined effects of $g_\mu - 2$ and $M_{\tilde{\chi}_1^\pm} > 104\,\text{GeV}$ only allows $\mu > 0$ and the stau neutralino co-annihilation domain of the relic density.

In order to carry out the calculations it is necessary to include a number of corrections to obtain results of sufficient accuracy, and we list some of these here: (i) two loop gauge and one loop Yukawa RGE equations are used from M_G to the electroweak scale, and QCD RGE below for the light quarks; (ii) two loop and pole mass corrections are included in the calculation of M_h; (iii) One loop corrections to M_b and M_τ are included [12]; (iv) large $\tan\beta$ SUSY corrections to $b \to s+\gamma$ are included [13]; (v) all $\tilde{\tau}_1$-$\tilde{\chi}_1^0$ co-annihilation channels are included in the relic density calculation [14]. We do not include Yukawa unification or proton decay constraints as these depend sensitively on post GUT physics, about which little is known.

We demonstrate the mSUGRA parameter space for value of $\tan\beta = 10$ with $A_0 = 0$ in Fig. 1 as well as for larger $\tan\beta$ values of 40 and 50 in Fig. 2. The yellow band is the parameter space allowed by the earlier balloon CMB experiments, while the (narrower) blue band is the region now allowed by WMAP (see (2)). The lower limit of the band comes from the rapid annihilation of neutralinos in the early universe due to co-annihilation effects as the light stau mass, $M_{\tilde{\tau}_1}$, approaches the neutralino mass as one lowers m_0. Thus the lower edge of the band corresponds to the lower bound of (2). The upper limit of the band, corresponding to the upper bound of (2), arises due to insufficient annihilation as m_0 is raised. The slope and position of the band changes, however as A_0 is changed.

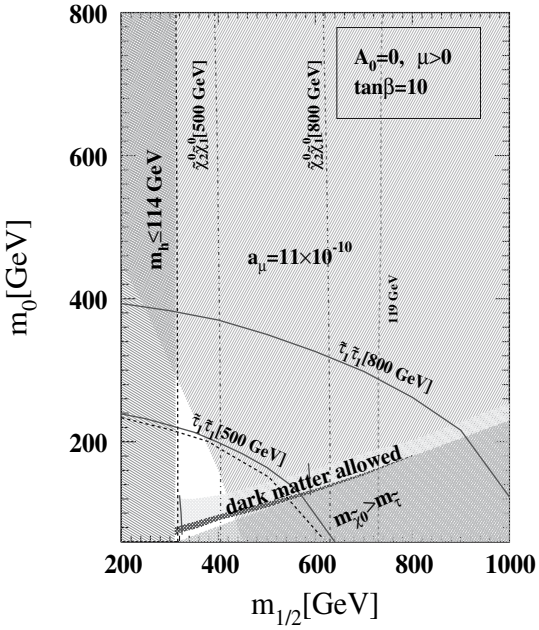

Fig. 1. Allowed region in the m_0-$m_{1/2}$ plane from the relic density constraint for $\tan\beta = 10$, $A_0 = 0$ and $\mu > 0$. The yellow region was allowed by the older balloon data, and the narrow blue band by the new WMAP data. The dotted pink vertical lines are different Higgs masses, and the current LEP bound produces the lower bound on $m_{1/2}$. The brick red region depicts the the Higgs mass region $M_h \leq 114\,\text{GeV}$. The light blue region is excluded if $\delta a_\mu > 11 \times 10^{-10}$. (Other lines are discussed in text.)

The dotted pink lines are for different Higgs masses, and the light blue region would be excluded if $\delta a_\mu > 11 \times 10^{-10}$. The three short solid lines indicate the $\sigma_{\tilde{\chi}_1^0 - p}$ values. In the case of $\tan\beta = 40$ they represent (from left) 0.03×10^{-6} pb, 0.002×10^{-6} pb, 0.001×10^{-6} pb and in the case of $\tan\beta = 50$ they represent (from left) 0.05×10^{-6} pb, 0.004×10^{-6} pb, 0.002×10^{-6} pb. In the case of $\tan\beta = 10$ they represent (from left) 5×10^{-9} pb and 1×10^{-9} pb.

Since the stau-neutralino co-annihilation region appears to be experimentally most favored, in this talk we study the detectibility of this region at a LC and the LHC. We also discuss the accuracy of mass determinations since the narrow mass difference between the lighter stau and the lightest neutralino is the crucial feature of this co-annihilation region. We first discuss the LC since this machine has the ability to measure masses very precisely.

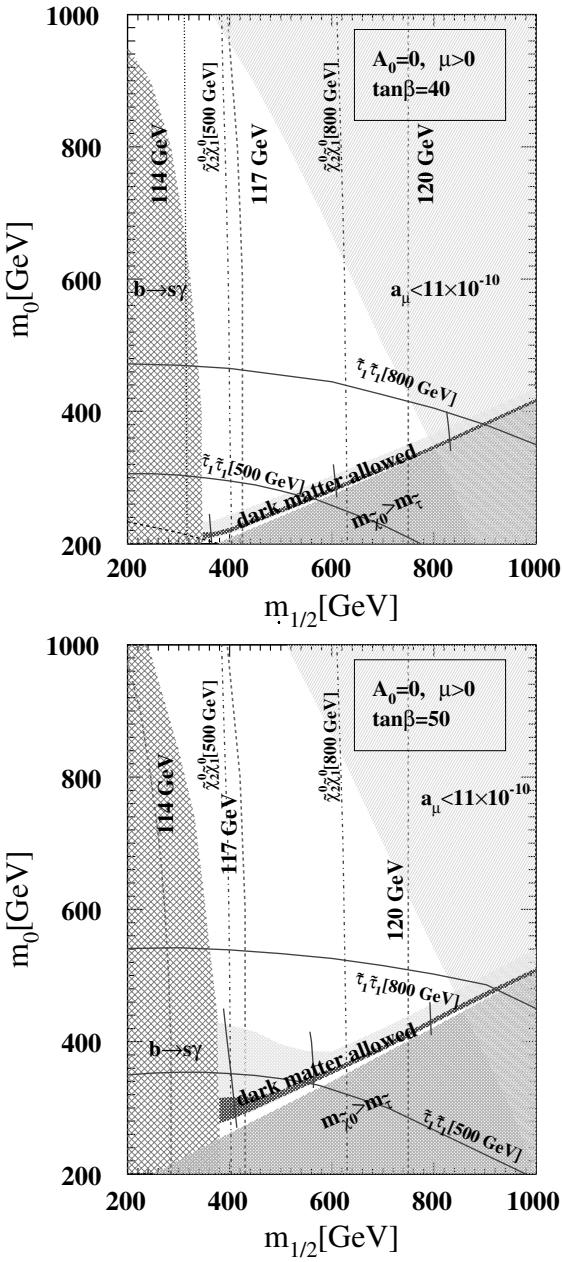

Fig. 2. Same as in Fig. 1 for $\tan\beta = 40$, and 50, $A_0 = 0$ and $\mu > 0$. The brick red region depicts the $b \to s\gamma$ constraint.

3 Linear Collider

3.1 Production and Signals of SUSY Particles

We first calculate the kinematic reach of the LCs (500 GeV and 800 GeV) for the mSUGRA parameter space. Figures 1 and 2 also show the 0.1 fb cross section limit for $\tilde{e}_R^+\tilde{e}_R^-$ (black dashed), $\tilde{\tau}_1^+\tilde{\tau}_1^-$ (blue solid), $\tilde{\chi}_1^0\tilde{\chi}_2^0$ (blue dashed-dot) and chargino pair (vertical black dot) productions. The chargino pair production is almost unobservable for any $\tan\beta$. The selectron pair production is unobservable for large $\tan\beta$. We focus on the stau pair and the neutralino pair production cross sections since the stau pair has the largest reach in $m_{1/2}$ and the neutralino pair has the largest reach in m_0. We will use the 500 GeV collider to study the signal since it seems to be the intial center-of-mass energy for the LC.

We have the following final states for $\tilde{\tau}_1^+\tilde{\tau}_1^-$ and $\tilde{\chi}_1^0\tilde{\chi}_2^0$ in mSUGRA:

$$e^+e^- \to \tilde{\tau}_1^+\tilde{\tau}_1^- \to (\tau^+\tilde{\chi}_1^0) + (\tau^-\tilde{\chi}_1^0)$$

$$e^+e^- \to \tilde{\chi}_1^0\ \tilde{\chi}_2^0 \to \tilde{\chi}_1^0 + (\tau\tilde{\tau}_1) \to \tilde{\chi}_1^0 + (\tau^+\tau^-\tilde{\chi}_1^0)$$

The analysis of the final states now is quite complicated since some of the taus have low energy due to a narrow mass difference ΔM between the lightest neutralino and the lighter stau. We need to develop appropriate cuts to extract the signal from the SM background which is dominated by the $\gamma^*\gamma^*e^+e^-$ rate. Due to the large branching ratios, we look at the hadronic final state of tau ($\tau_{\rm h}$). The final signal thus has two jets plus missing p_T ($\not{p}_T$) arising from the decay of tau.

3.2 Event Selection

We now develop the event selection cuts for three representative mSUGRA points in the stau-neutralino co-annihilation region for $m_{1/2} = 360$ GeV, $m_0 = 205$, 210 and 220 GeV, $A_0 = 0$ and $\tan\beta = 40$ (see Table 1). The mass difference for these three points are approximately 5, 10 and 19 GeV. Since both signals and background processes cross sections are affected by the choice of beam polarization, we choose appropriate beam polarization to increase the significance of the signal. The production cross-sections for $\sqrt{s} = 500$ GeV for different polarizations are given in Table 2. The right-handed (RH) polarization $\mathcal{P}(e^-) = -0.9$ enhances the $\tilde{\tau}_1^+\tilde{\tau}_1^-$ signal, and the left-handed (LH) polarization, $\mathcal{P}(e^-) = +0.9$ enhances the $\tilde{\chi}_1^0\tilde{\chi}_2^0$ signal. The SM background mentioned in table consists of $\bar{\nu}\nu\tau^+\tau^-$ states arising from processes such as WW, ZZ, and $\nu\bar{\nu}Z$ production and this background is suppressed by a RH electron beam. In addition to this, we also have two photon processes $e^+e^- \to \gamma^*\gamma^* + e^+e^- \to \tau^+\tau^-$ (or $q\bar{q}$) $+ e^+ + e^-$ where the final state e^+e^- pair are at a small angle to the beam pipe and the $q\bar{q}$ jets fake a $\tau^+\tau^-$ pair.

Table 1. Masses (in GeV) of SUSY particles in three representative scenarios of ΔM for $m_{1/2} = 360\,\text{GeV}$, $\tan\beta = 40$, $\mu > 0$, and $A_0 = 0$. These points satisfy all the existing experimental bounds on mSUGRA.

MC Point (m_0 in GeV)	$M_{\tilde{\chi}_2^0}$	$M_{\tilde{\tau}_1}$	$M_{\tilde{\chi}_1^0}$	ΔM ($\equiv M_{\tilde{\tau}_1} - M_{\tilde{\chi}_1^0}$)
1 (205)	274.2	147.2	142.5	4.7
2 (210)	274.2	152.0	142.5	9.5
3 (220)	274.3	161.6	142.6	19.0

Table 2. Cross section times branching ratio (in fb), $\sigma \times \mathcal{B}(\tau \to \tau_h)^2$, for SUSY and SM 4-fermions (4f) production in two cases of polarizations, $\mathcal{P}(e^-) = -0.9$ (RH) and $+0.9$ (LH). The SUSY cross sections were obtained using `ISAJET` [15].

	$\mathcal{P}(e^-)$	-0.9 (RH)	0.9 (LH)
SM 4f		7.84	89.8
SUSY Point 1.	$\tilde{\chi}_1^0\tilde{\chi}_2^0$	0.41	6.09
	$\tilde{\tau}_1^+\tilde{\tau}_1^-$	28.3	13.2
SUSY Point 2.	$\tilde{\chi}_1^0\tilde{\chi}_2^0$	0.40	6.00
	$\tilde{\tau}_1^+\tilde{\tau}_1^-$	26.6	12.4
SUSY Point 3.	$\tilde{\chi}_1^0\tilde{\chi}_2^0$	0.38	5.68
	$\tilde{\tau}_1^+\tilde{\tau}_1^-$	23.0	10.6

Table 3. Kinematic cuts for the LH ($\mathcal{P} = 0.9$) and the RH ($\mathcal{P} = -0.9$) cases.

Cut Variable(s)	LH ($\mathcal{P}(e^-) = 0.9$)	RH ($\mathcal{P}(e^-) = -0.9$)
$N_{jet}(E_{jet} > 3\,\text{GeV})$	2	
τ_h ID	1, 3 tracks; $M_{tracks} < 1.8\,\text{GeV}$	
Jet acceptance	$-q_{jet}\cos\theta_{jet} < 0.7$	$\lvert\cos\theta_{jet}\rvert < 0.65$
	$-0.8 < \cos\theta(j_2, p_{vis}) < 0.7$	$\lvert\cos\theta(j_2, p_{vis})\rvert < 0.6$
Missing p_T	$> 5\,\text{GeV}$	
Acoplanarity	$> 40^\circ$	
Veto on EM clusters	No EM cluster in $5.8^\circ < \theta < 28^\circ$ with $E > 2\,\text{GeV}$	
or electrons	No electrons within $\theta > 28^\circ$ with $p_T > 1.5\,\text{GeV}$	
Beam mask ($2^\circ(1^\circ)$ - 5.8°)	No EM cluster with $E > 100\,\text{GeV}$	

This background, does not change with beam polarization and we need to suppress them by appropriate cuts.

The LH polarization cuts are optimized to enhance the $\tilde{\chi}_1^0\tilde{\chi}_2^0$ signal and the RH to optimize the $\tilde{\tau}_1^+\tilde{\tau}_1^-$ signal.

The necessary cuts to suppress the background are mentioned in Table 3 where j_2 stands for second leading τ jet, p_{vis} gives the sum of visible momenta and $\theta(j_2, p_{vis})$ is the angle between them. θ_{jet} is the angle between a τ jet and the beam direction. The Monte Carlo analysis for the signal and

the background was done using the following programs: (1) `ISAJET` [15] to generate SUSY events; (2) `WPHACT` [16] for SM backgrounds.; (3) `TAUOLA` [17] for tau decay; (4) Events were simulated and analysed with a LC detector simulation [18]. The jets are reconstructed using JADE algorithm with $Y_{\rm cut} \geq 0.0025$ [19] selected with $E_{jet} > 3\,\text{GeV}$. The jet acceptance cut is required to reduce the SM background events such as WW and ZZ production. We also require no EM clusters (a) in $5.8^\circ < \theta < 28^\circ$ where the LC detector has no tracking system and (b) in the angle below 5.8° with two options of a very forward calorimeter (active beam mask). In our calculation, beamstrahlung and bremsstrahlung are included in the two photon annihilation process. The two photon background is also similar to those in [20, 21].

We summarize the number of accepted events for each class of final states for the case $\not{p}_T > 5$, 10, and 20 GeV in Table 4.

- The RH polarization strongly suppresses the SM background events (WW etc.) and the neutralino events, and combined with a 1° mask and $\not{p}_T > 5\,\text{GeV}$ it leaves a clean signal for the $\tilde{\tau}_1^+\tilde{\tau}_1^-$ events. With no mask there would be approximately 4,400 SM $\gamma\gamma$ background events swamping the SUSY signal.
- The LH polarization then allows for the detection of the $\tilde{\chi}_1^0\tilde{\chi}_2^0$ signal with $\not{p}_T > 20\,\text{GeV}$ without mask or 10 GeV with 2° mask. However, both 1° mask and $\not{p}_T > 5\,\text{GeV}$ are necessary to detect the $\tilde{\tau}_1^+\tilde{\tau}_1^-$ events and to measure ΔM to be compared with the measurements in the RH case. In the case of no mask there would be ∼9,300 SM $\gamma\gamma$ background events with $\not{p}_T > 5\,\text{GeV}$.

Table 4. Number of events for luminosity of $500\,\text{fb}^{-1}$ for Points 1, 2 and 3 corresponding to $\Delta M = 4.7$, 9.5, and 19.0 GeV, respectively. All numbers except for two-photon backgrounds are common for different options of beam mask.

		$\mathcal{P}(e^-) = 0.9$ (LH)			$\mathcal{P}(e^-) = -0.9$ (RH)		
Process		${\not{p}_T}^{min} = 5$	10	20	5	10	20
$\tilde{\chi}_2^0\tilde{\chi}_1^0$	Pt.1	374	342	260	15	14	11
	Pt.2	624	572	425	26	24	18
	Pt.3	743	697	529	29	28	22
$\tilde{\tau}^+\tilde{\tau}^-$	Pt.1	73	2	0	122	2	0
	Pt.2	524	267	11	786	437	22
	Pt.3	946	781	335	1283	1076	468
SM 4f		1745	1626	1240	129	123	100
SM $\gamma\gamma$	2–5.8° mask	535	7	0	249	4	0
	1–5.8° mask	10	0	0	4	0	0

Thus we find that the mask is essential to detect SUSY in this region of parameter space. A lower $\not{p}_T$ increases the number of events and significance. A 5 GeV $\not{p}_T$ cut is found to be feasible at a 500 GeV LC.

It should be noted that the 1° beam mask is feasible for the LC since the TESLA design (which has been accepted for the LC technology) allows a beam mask coverage down to 3.2 mrad (or 0.18°) [22]. We also note that our study is based on head-on collisions of electron and position. However, it has been shown that the active mask is still able to reduce the two-photon background events even in the case of a beam crossing [21].

The $\tilde{\tau}_1^+\tilde{\tau}_1^-$ cross-section has the largest reach along the co-annihilation band and one would use this channel to measure the mass difference. This channel needs RH polarization for enhancement. In Fig. 3, we plot the number of events for 500 fb^{-1} of luminosity as a function of ΔM for $m_0 = 203$–220 GeV ($m_{1/2} = 360$ GeV) in the RH polarization case. We see that we have more than 100 events for $\Delta M > 4.5$ GeV. In Fig. 4 we plot the acceptance as a function of ΔM for $m_0 = 203$–220 GeV with 2° mask in the case of RH polarization. We find that the acceptance drops fast as ΔM goes below 5 GeV.

Since the event acceptance mainly depends on ΔM, we estimate the 5σ reach for $M_{\tilde{\tau}_1}$ in the RH case using Table 4. The significance (σ) is simply calculated as $N_{\rm signal}/\sqrt{N_{\rm BG}}$, where the $\tilde{\chi}_1^0\tilde{\chi}_2^0$ events are also treated as backgrounds. The 5σ reach for the $\tilde{\tau}_1$ mass is found to be ≤ 231 GeV (corresponding to $m_{1/2} \leq 514$ GeV) for $\Delta M = 19.0$ GeV with a 2° beam mask and $\not{p}_T > 5$ GeV. The event acceptance for this calculation is same as Point 3 which has the same ΔM. The significance for Point 3 is 101σ for $m_{1/2} =$

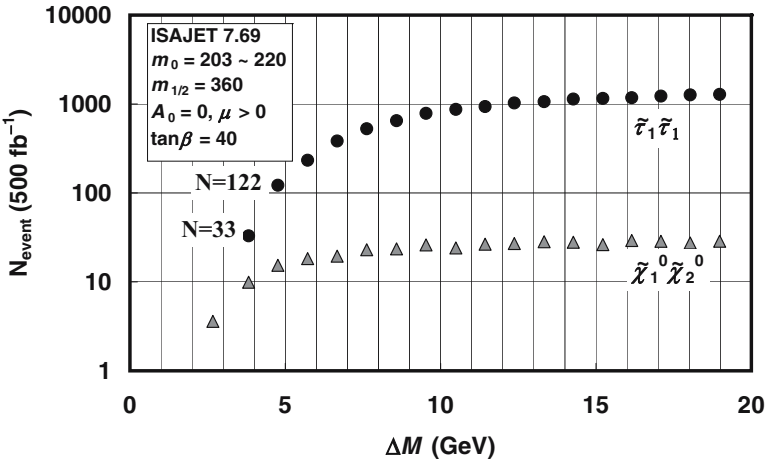

Fig. 3. Number of $\tilde{\tau}_1^+\tilde{\tau}_1^-$ (solid circles) and $\tilde{\chi}_1^0\tilde{\chi}_2^0$ (solid triangles) events as a function of ΔM (or $m_0 = 203$–220 GeV) in the RH polarization case. We assume 500 fb^{-1} of luminosity.

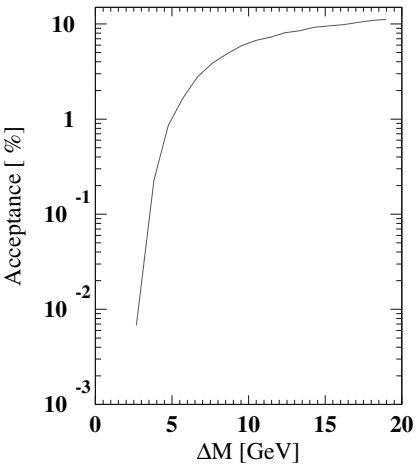

Fig. 4. Total event acceptance for $\tilde{\tau}_1^+\tilde{\tau}_1^-$ as a function of ΔM for $m_0 = 203$–$220\,\mathrm{GeV}$ in the RH polarization case.

360 GeV. Similarly, for $\Delta M = 4.7\,\mathrm{GeV}$ we find that the 5σ reach for $M_{\tilde{\tau}_1}$ is $\leq 160\,\mathrm{GeV}$ ($m_{1/2} \leq 385\,\mathrm{GeV}$). The event acceptance in this case is same as Point 1 which has 10σ significance for $m_{1/2} = 360\,\mathrm{GeV}$. The reach enhances for $\Delta M \gtrsim 5\,\mathrm{GeV}$. For example, with $\Delta M \sim 5.5\,\mathrm{GeV}$ the maximum reach for $M_{\tilde{\tau}_1}$ is 194 GeV (corresponds to $m_{1/2}$= 460 GeV). We also find that the significance decreases as $\not{p}_T$ increases.

It should be noted that our event selection cuts are optimized for a 500 GeV machine. In the case of a 800 GeV LC, the cuts need to be re-optimized based on the new SUSY backgrounds and design limitations (e.g. the lower bound on $\not{p}_T$ needs to be raised).

3.3 Measurement of Stau Neutralino Mass Difference

The measurement of small ΔM value is crucial since it would tell us the existence of the stau-neutralino co-annihilation. We propose a variable $M_{\mathrm{eff}} \equiv M(j_1, j_2, \not{E})$, an invariant mass of two τ-jets and missing energy, as a key discriminator of the signal events from its background events. We first generate high statistics MC samples for the SM and various SUSY events (by changing the m_0 value) and prepare the templates of the M_{eff} distributions for the SM, $\tilde{\chi}_1^0\tilde{\chi}_2^0$, and $\tilde{\tau}_1^+\tilde{\tau}_1^-$ events.

Figure 5 (without the data point for 500 fb^{-1}) shows examples of such templates for two m_0 values for the 2° mask in the RH polarization case. The SM cross section is fitted by a blue line, the stau pair by a green line and the neutralino pair by a red line. For smaller ΔM, the two tau signal appears like the taus from the two photon background and consequently this region requires a lower beam mask (down to 1°).

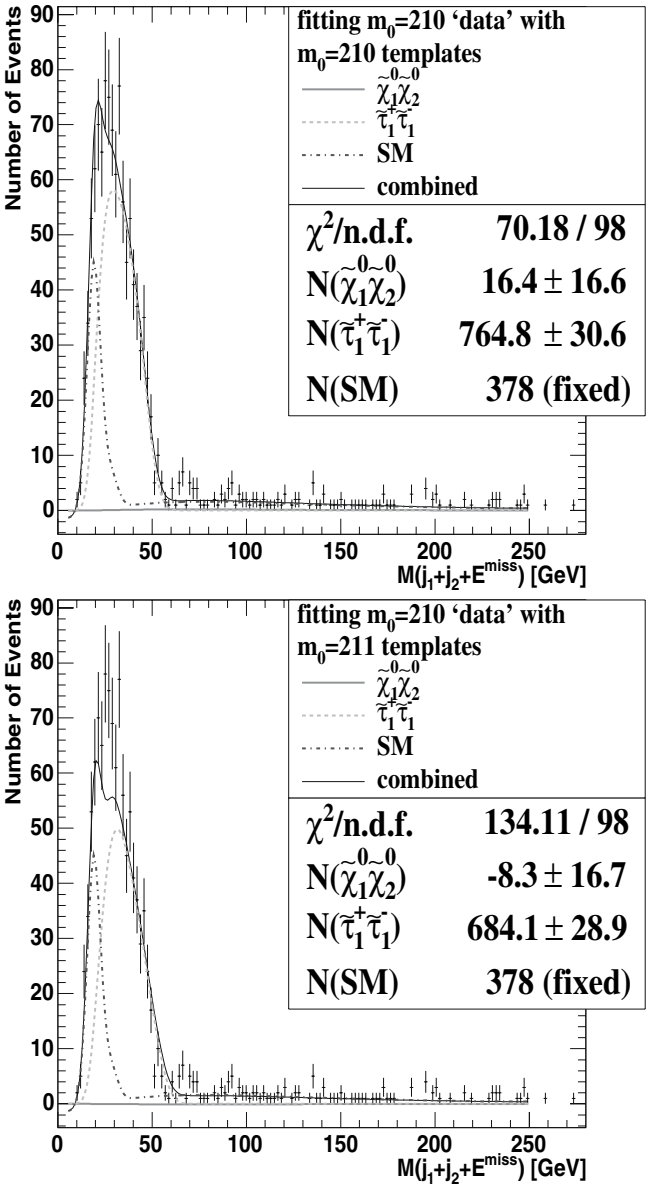

Fig. 5. Example of fitting a MC sample containing SM and SUSY ($m_0 = 210\,\text{GeV}$) events equivalent to 500 fb^{-1} to two M_{eff} templates for SM+SUSY ($m_0 = 210$ or 211 GeV). The value of χ^2/n.d.f. is minimum when the events from the same SUSY parameter are in the 500 fb^{-1} sample.

Since the initial run for a few years will generate data of 500 fb^{-1} of luminosity we generate the MC samples equivalent to 500 fb^{-1} of luminosity for particular ΔM values and fit them with the template functions generated for the high statistics sample. The black lines in Fig. 5 shows the fitting of the 500 fb^{-1} MC samples for Point 2 with the templates of two different m_0 values of 210 and 211 GeV. (Other parameters are kept at the same values as before.) We then compare the χ^2 for these fits.

We find that χ^2 for these two fits is minimum for the $m_0 = 210\,\text{GeV}$ case which means that a difference of 1 GeV of m_0 value can be distinguished from the shape analysis. We try to fit the 500 fb^{-1} MC sample for Point 2 using the range of $m_0 = 203$–$220\,\text{GeV}$ and determine the χ^2 for all these different points. We plot the χ^2 of these fits in Fig. 6 and find that 1σ in the χ^2 corresponds to $9.5 \pm 1\,\text{GeV}$. The true value of ΔM for the Point 2 is 9.5 GeV. We repeat the same study for different stau masses i.e. for different ΔM. For lower $\Delta M (\sim 5\,\text{GeV})$, we need to use a beam mask of 1°. The accuracy of mass determination for two different beam masks is summarized in Table 5. The uncertainties are found to be at a level of 10%.

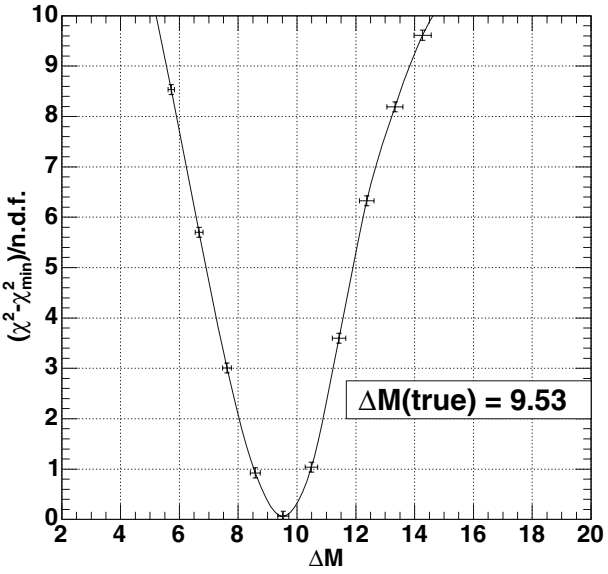

Fig. 6. χ^2 of fitting the high statistics templates against the sample point is plotted as a function of ΔM.

Table 5. Accuracy of the determination of ΔM for different beam masks.

		$N_{\tilde{\tau}_1^+\tilde{\tau}_1^-}$	ΔM("500 fb^{-1}" Experiment)	
m_0	ΔM	(500 fb^{-1})	2° Mask	1° Mask
205	4.7	122	Not Determined	$4.7^{+1.0}_{-1.0}$
210	9.5	787	$9.5^{+1.1}_{-1.0}$	$9.5^{+1.0}_{-1.0}$
213	12.4	1027	$12.5^{+1.4}_{-1.4}$	$12.5^{+1.1}_{-1.4}$
215	14.3	1138	$14.5^{+1.1}_{-1.4}$	$14.5^{+1.1}_{-1.4}$

4 Large Hadron Collider

We now discuss the signal and the detection of the co-annihilation region at the LHC. The LHC can probe larger regions of SUSY parameter space. Along the co-annihilation band, the reach in $m_{1/2}$ is up to 1–1.5 TeV.

Unlike LC, the final state of the SUSY event will dominantly be created after a series of cascade decays of gluinos and/or squarks. The final state will have multiple jets, leptons (e, μ), taus and missing energy. The main SUSY production processes are:

$$p\ p\ \rightarrow\ \tilde{q}\ \tilde{g}\ ,\tilde{q}\ \tilde{q}\ ,\tilde{g}\ \tilde{g}\ .$$

The squarks and gluinos then decay in steps.

Three dominant decay processes are:

$$\tilde{q}\ \tilde{g} \rightarrow (\tilde{\chi}_1^{\pm}\ \tilde{\chi}_1^{\mp}\ \text{ or }\ \tilde{\chi}_1^{\pm}\ \tilde{\chi}_2^0\ \text{ or }\ \tilde{\chi}_2^0\ \tilde{\chi}_2^0) + \text{jets} + \not{E}_T + X$$

The $\tilde{\chi}_2^0$ decays into the following final state:

$$\tilde{\chi}_2^0\ \rightarrow\ \tau\ \tilde{\tau}_1\ \rightarrow\ \tau\ \tau\ \tilde{\chi}_1^0\ ,$$

where one of the two taus is a low energy one. The $\tilde{\chi}_1^{\pm}$ decays into:

$$\tilde{\chi}_1^{\pm}\ \rightarrow\ \nu\ \tilde{\tau}_1\ \rightarrow\ \nu\ \tau\ \tilde{\chi}_1^0\ ,$$

where the only τ in the final state has low energy.

The same final states have been considered in [23] for a particular choice of the mSUGRA parameter space where $M_{\tilde{\chi}_1^0} = 81\,\text{GeV}$, $M_{\tilde{\chi}_2^0} = 152\,\text{GeV}$, $M_{\tilde{\chi}_1^{\pm}} = 151\,\text{GeV}$, and $M_{\tilde{\tau}_1} = 132\,\text{GeV}$. All taus in the final states are high energy taus, so that they required $p_T > 50\,\text{GeV}$ [23]. This point, however, does not account for the WMAP observed amount of dark matter.

In the narrow stau neutralino co-annihilation region, however, the low energy taus are the characteristic feature. The final states need to be chosen with taus and missing energy with one of the taus being low energy.

We look into the characteristic signal in the co-annihilation region with lower p_T threshold(s) in three ways:

1. two low-energy taus + jets + $\not{E}_T$ from $\tilde{\chi}_1^{\pm}\ \tilde{\chi}_1^{\mp}$,
2. three taus + jets + $\not{E}_T$ from $\tilde{\chi}_1^{\pm}\ \tilde{\chi}_2^0$,
3. four taus + jets + $\not{E}_T$ from $\tilde{\chi}_2^0\ \tilde{\chi}_2^0$.

At present, we are studying these signals by requiring (i) high-enery jets and $\not{E}_T$ to reduce the SM backgrounds (especially from a $t\bar{t}$ pair) and (ii) kinematical cuts on the multiple taus to distinguish the co-annihilation signal from the SUSY backgrounds [24].

5 Conclusion

We have investigated here the experimentally favored stau-neutralino co-annihilation region. This region requires a small mass difference between the co-annihilating lightest stau and the lightest neutralino in the early universe. It is important to measure the small mass difference at colliders to verify this explanation of dark matter in the context of mSUGRA. At a collider, this narrow mass difference produces low energy taus which are very hard to study due to large SM and other SUSY processes and appropriate selection cuts to do this need to be developed. In this talk, we mainly studied this region at a 500 GeV e^+e^- LC with 500 fb^{-1} of luminosity. The dominant SM background is the two-photon process. Our study was focused on the $\tilde{\tau}^+\tilde{\tau}^-$ production because it allowed us to reach large $m_{1/2}$ values in the allowed parameter space. We used a RH beam to enhance this production. We proposed $M(j_1, j_2, \not{E})$ to determine the mass difference and found that $\Delta M \equiv M_{\tilde{\tau}_1} - M_{\tilde{\chi}_1^0}$ could be determined at a level of 10% using a 2° mask except for $\Delta M = 4.7\,\text{GeV}$. For a very small mass difference ($\Delta M \simeq 5\,\text{GeV}$), a 1° mask would be crucial to suppress the two-photon background and the accuracy would be about 20%. We calculated the discovery significance of this region and determined the 5σ reach in $m_{1/2}$. We also discussed the signals and the possible backgrounds at the LHC.

Acknowledgments

This work is supported in part by a NSF Grant PHY-0101015, in part by NSERC of Canada and in part by a DOE Grant DE-FG02-95ER40917.

References

1. A.H. Chamseddine, R. Arnowitt, and P. Nath, Phys. Rev. Lett. **49**, 970 (1982).
2. R. Barbieri, S. Ferrara, and C. A. Savoy, Phys. Rev. **D119**, 343 (1982); L. Hall, J. Lykken, and S. Weinberg, Phys. Rev. **D27**, 2359 (1983); P. Nath, R. Arnowitt, and A.H. Chamseddine, Nucl. Phys. **B227**, 121 (1983).

3. For a review, P. Nilles, Phys. Rept. **110**, 1 (1984).
4. J. Ellis, K. Olive, Y. Santoso, and V. Spanos, Phys. Lett. **B565**, 176 (2003); R. Arnowitt, B. Dutta, T. Kamon, and V. Khotilovich, hep-ph/0308159; H. Baer, C. Balazs, A. Belyaev, T. Krupovnickas, and X. Tata, JHEP 0306, 054 (2003); B. Lahanas and D.V. Nanopoulos, Phys. Lett. **B568**, 55 (2003); U. Chattopadhyay, A. Corsetti, and P. Nath, Phys. Rev. **D68**, 035005 (2003).
5. See, for example, P. Igo-Kemenes, LEPC meeting, (http://lephiggs.web.cern.ch/LEPHIGGS/talks/index.html).
6. M. Alam et al., Phys. Rev. Lett. **74**, 2885 (1995).
7. D.N Spergel et al.(WMAP Collaboration), Astrophys. J. Suppl. 148, 175 (2003).
8. G. Bennett et.al., Muon (g-2) Collaboration, Phys. Rev. Lett. 92, 161802 (2004).
9. M. Davier, hep-ex/0312065.
10. K. Hagiwara, A. Martin, D. Nomura, and T. Teubner, Phys. Rev. **D69**, 093003 (2004).
11. W. Marciano, hep-ph/0411179.
12. R. Rattazi and U. Sarid, Phys. Rev. **D53**, 1553 (1996); M. Carena, M. Olechowski, S. Pokorski, and C. Wagner, Nucl. Phys. **B426**, 269 (1994).
13. G. Degrassi, P. Gambino, and G. Giudice, JHEP **0012**, 009 (2000); M. Carena, D. Garcia, U. Nierste, and C. Wagner, Phys. Lett. **B499**, 141 (2001), D'Ambrosio, G. Giudice, G. Isidori, and A.Strumia, hep-ph/0207036; A. Buras, P. Chankowski, J. Rosiek, and L. Slawianowska, hep-ph/0210145.
14. R. Arnowitt, B. Dutta, and Y. Santoso, hep-ph/0010244; hep-ph/0101020; Nucl. Phys. **B606**, 59 (2001); J Ellis, T. Falk, G. Ganis, K. Olive, and M. Srednicki, Phys. Lett. **B570**, 236 (2001); J. Ellis, T. Falk, and K. Olive, Phys. Lett. **B444**, 367 (1998); J. Ellis, T. Falk, K. Olive, and M. Srednicki, AP **13**, 181 (2000); Erratum-ibid. **15**, 413 2001; M. Gomez and J. Vergados, Phys. Lett. **B512**, 252 (2001); M. Gomez, G. Lazarides, C. Pallis, Phys. Rev. **D61**, 123512 (2000); Phys. Lett. **B487**, 313 (2000); L. Roszkowski, R. Austri, and T. Nihei, JHEP **08**, 024 (2001); A. Lahanas, D. Nanopoulos, and V. Spanos, Phys. Lett. **B518**, 518 (2001).
15. F. Paige, S. Protopescu, H. Baer, and X. Tata, hep-ph/0312045. We use `ISAJET` version 7.69.
16. E. Accomando and A. Ballestrero, Comput. Phys. Commun. 99, 270 (1997); E. Accomando, A. Ballestrero, and E. Maina, Comput. Phys. Commun. 150, 166 (2003). We use `WPHACT` version 2.02pol.
17. We use `TAUOLA` version 2.6
18. LCD Root Package version 3.5 with LD Mar01 detector parametrization
19. JADE collaboration, W. Bartl et al., Z. Phys **C33**, 23 (1986); S. Bethke et al., Phys. Lett. **B213**, 235 (1988).
20. H. Baer, T. Krupovnickas, and X. Tata, JHEP 0406, 061 (2004).
21. P. Bambade, M. Berggren, F. Richard, and Z. Zhang, hep-ph/0406010.
22. TESLA: Technical design report, part 4: A detector for TESLA, T. Behnke et.al., DESY-2001-011, DESY-2001-011D, DESY-TESLA-2001-23, DESY-TESLA-FEL-2001-05, ECFA-2001-209, March 2001. In a recent upgrade of the final focus setup, the forward calorimeter, low angle tagger or LAT, covers an angle down to 3.2 mrad.
23. I. Hinchliffe and F. Paige, Phys. Rev. **D61**, 095011 (2000).
24. Work is in progress.

Dark Matter Limits from the g-2 Experiment

P. Cushman

Physics Department, University of Minnesota, 116 Church St. SE
Minneapolis, MN 55455, USA
prisca@physics.umn.edu

1 Introduction

The anomalous magnetic moment of the muon has been measured to 0.5 ppm in a series of precision experiments at the Brookhaven Alternating Gradient Synchrotron. [1, 2, 3] The individual results for each polarity:

$$a_\mu^+ = 11\ 659\ 204(7)(5)\ \times 10^{-10} \quad \text{and} \quad a_\mu^- = 11\ 659\ 214(8)(3)\ \times 10^{-10}$$

are consistent with each other, so that we can write the average anomaly as $a_\mu(\text{exp}) = 11\ 659\ 208(6)\ \times\ 10^{\ -10}$ (0.5 ppm). A discrepancy, Δa_μ, between the measured value $a_\mu(\text{exp})$ and the Standard Model $a_\mu(\text{SM})$ is a signal for new physics. Assuming that such a discrepancy is due to contributions from supersymmetric particles provides a framework which can be used to constrain the mass of the dark matter particles, assumed to be the lightest neutral supersymmetric particles. The deviation from the standard model has varied between 1.5σ and 3σ significance, dominated by uncertainties in the hadronic contribution to the standard model calculation. Currently the standard model prediction is calculated to 0.6 ppm precision and $\Delta a_\mu = 23.5\ (9.0)\ \times 10^{-10}$ representing a 2.6σ deviation. We expect that the error on $a_\mu(\text{SM})$ will be reduced by a factor of two within the next decade. To fully utilize this improvement, a new g-2 run is proposed for the near future. If the mean Δa_μ remains the same, this would result in close to a 6σ discrepancy. In this case, we would expect to see SUSY particles at the LHC and use the g-2 results to measure tan β. If, instead, the Standard Model is confirmed to this precision, neutralinos must have masses higher than $\sim$500 GeV/c^2 and simple SUSY dark matter models will be severely constrained.

2 Historical Summary

Precision measurements are a complementary approach to investigating the highest energy, smallest scale frontier of particles and interactions. Over the last decade, E821, the Brookhaven g-2 experiment, has successfully mounted a precision challenge to the standard model. The magnetic moment is defined as $\boldsymbol{\mu} = g\frac{e\hbar}{2mc}\boldsymbol{s}$, where g is the gyromagnetic ratio. Deviations from a purely

pointlike g=2 Dirac particle are characterized by the anomaly a=(g-2)/2. The anomaly for leptons is $\sim 10^{-3}$ due to interactions with virtual particles which couple to the electromagnetic field, thus providing a laboratory for testing the Standard Model. Whereas the electron anomaly provides the most precise measurement of the fine structure constant α, the muon anomaly is more sensitive by m_μ^2/m_X^2 to virtual W and Z gauge bosons, as well as any other, as yet unobserved, particles in the hundreds of GeV mass range.

The 2.6 σ discrepancy announced four years ago sparked debate on the theoretical calculation and encouraged further work on reducing the uncertainty in the 1^{st}-order hadronic contribution. One of the more startling developments, approximately 6 months after the announcement of the first precision result (1.3 ppm), was the revelation by the Marseilles group [4] that one of the contributions to the Standard Model theory, namely the hadronic light-by-light term, had been independently assigned the wrong sign by at least two separate groups. Kinoshita [5] and Bijnens [6] studied their previous work and found that they both had used an incorrect sign convention in a matrix evaluation in a widely-used computer program. This moved the theoretical value by 17 $\times 10^{-10}$ (by more than its stated uncertainty) in the direction of the E821 result, thus reducing the discrepancy to 1.6σ. The next g-2 run, with an improved precision of 0.7 ppm, left the mean unchanged, but reduced the error bars, again indicating a 2.6 σ discrepancy with the Standard Model.

Meanwhile, in order to reduce the uncertainty on the hadronic correction, the use of vector spectral functions from the study of hadronic τ-decays in ALEPH was introduced by Alemany et al. [7]. Previously, the only handle on the hadronic vacuum polarization contribution at the low center of mass energies which are relevant for g-2 came from the dispersion relation:

$$a_\mu^{had,1} \propto \int_{(2m_\pi)^2}^{\infty} ds\ \frac{K(s)}{s} R(s) \quad where \quad R(s) = \frac{\sigma(e^+e^- \to hadrons)}{\sigma(e^+e^- \to \mu^+\mu^-)} \qquad (1)$$

R(s) is determined from a compilation of experimental results dominated by the CMD-2 experiment at Novosibirsk. When the τ-decay data were first combined with the e+e- data in 1998, it halved the error bars on the hadronic contribution to the SM calculation. However, over the past 5 years the continued operation and analysis of CMD-2 has improved the e+e- data to such an extent that the two methods were found to be in disagreement with each other. Thus, in order to quote a discrepancy with theory, it became necessary to distinguish which hadronic correction you were referring to. In 2003 the Novosibirsk collaboration completely reanalyzed their $\pi\pi$ channel [8] following the discovery of a mistake in their normalization (the t-channel leptonic vacuum polarization contribution was missing in the Bhabha scattering cross section). Their correction increased their published hadronic cross sections by 2.5%, thus reducing, but not erasing the discrepancy between the two theoretical approaches (especially for energies above 0.85 GeV).

New results from KLOE, BaBar and Belle can provide an independent method to distinguish between the two by using radiative decay to scan the center of mass energies in the region relevant to g-2 (so-called "radiative-return" method). A precise measurement of the pion form factor has been reported by KLOE [9][10]. It confirms the Novosibirsk e+e- result. Preliminary results on 4-prong final states by BaBar [11] also bolsters confidence in the e+e- data. On the other hand, branching ratios from CLEO and OPAL continue to confirm the ALEPH data, thus indicating that the τ-decay construction may be affected by a fundamental misunderstanding in how we apply CVC, isospin corrections, or the electroweak symmetry breaking. Ghozzi and Jegerlehner [12] argue that by simply allowing the mass of the charged-ρ to differ from ρ^0 is sufficient to account for this. Davier [11] shows that even assuming this modification, a detailed comparison of the shape of the pion form factor reveals some discrepancy. This in itself may be an indication of new physics. Most are agreed, however, that in any comparison of a_μ(exp) to a_μ(theory), the direct result using e+e- data is more reliable at this time.

The final g-2 experimental result was announced in January 2004 [3]. This was a 0.7 ppm result with opposite sign muons. It was consistent with the previous data sets, despite reversing the magnetic field in the storage ring. However, the mean value was slightly higher than the earlier value, serving more to emphasize than detract from any Standard Model discrepancy. In Fig. 1, the BNL g-2 results are shown together with those from the old CERN experiment. The line represents the Standard Model calculation using e+e- data [13]. Assuming CPT holds, combining all our experiments, and properly accounting for correlated systematics, the final experimental value for the anomalous magnetic moment is now at $a_\mu(\text{exp}) = 11659208(6) \times 10^{-10}$ or a precision of 0.5 ppm. This further precision also tends to increase the

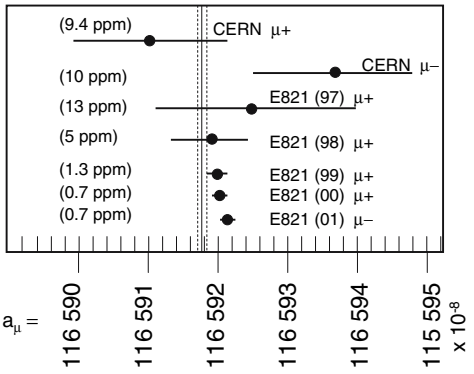

Fig. 1. An historical look at the sequence of g-2 results in improving precision. The line represents the Standard Model calculation as of early 2004, using e+e- data to deduce the hadronic contribution. The dotted lines indicate the uncertainty in the SM calculation.

significance of the discrepancy, bringing us back to the original 2.6σ significance. HowΔa_μ may change over the next several years is now in the hands of the theorists until such time as a new g-2 experiment can be mounted.

3 Current Experimental Status

Pions produced on a nickel target were directed down a beamline which momentum selected the forward-going decay muons to produce a 96% polarized muon beam. The muons were injected into the storage region via a superconducting inflector magnet. A pulsed magnetic kicker bumped the muons onto stored orbits in a uniform 1.45 T field and electrostatic quadrupoles provided vertical focusing. The spin vector of the polarized muons precesses relative to the momentum vector with an anomalous frequency ω_a, given by:

$$\omega_a \equiv \omega_S - \omega_C = a_\mu \frac{e}{m_\mu c} B \quad since \quad \omega_S = \left[1 + \gamma\left(\frac{g-2}{2}\right)\right] \underbrace{\frac{eB}{m_\mu c \gamma}}_{\omega_C} \tag{2}$$

The dependence of ω_a on E was eliminated to first order by choosing a γ which cancelled out the second term in equation 2, corresponding to a muon momentum of p = 3.094 GeV/c. The a_μ was then extracted from the ratio of the measured anomalous precession ω_a to the free proton precession frequency $\omega_p = \mu_p B/\hbar$ in the same magnetic field. The proton magnetic moment entered as the ratio $\lambda = \mu_\mu/\mu_p$ measured by the muonium hyperfine structure interval [15]. B was measured in situ every few days by a trolley with 17 NMR probes, and interpolated between trolley runs using ∼150 stationary probes.

To find ω_a, the decay positrons (electrons) from $\mu^+ \rightarrow e^+ \bar{\nu_\mu} \nu_e$ were detected by 24 lead-scintillating fiber calorimeters read out by 400 MHz waveform digitizers, yielding both time and energy information. Since this is a weak decay, the high energy positrons preferentially point in the direction of the muon spin, such that an energy threshold cut at 1.8 GeV produces a modulation in the number of positrons detected as a function of time, multiplied by the muon decay curve:

$$N(t) = N_0 \exp\left(-\frac{t}{\gamma\tau}\right)[1 + A\sin(\omega_a t + \phi_a)] \tag{3}$$

where A (or Asymmetry) is the depth of the modulation and τ is the muon lifetime at rest. Figure 2 gives a semi-log plot of the modulation curve from the 2001 g-2 data covering almost 9 muon lifetimes.

This form was modified by beam dynamics, pileup, gain corrections at early times, and muon losses coming from processes other than decay. Differences in the way in which each of these effects was treated, as well as data

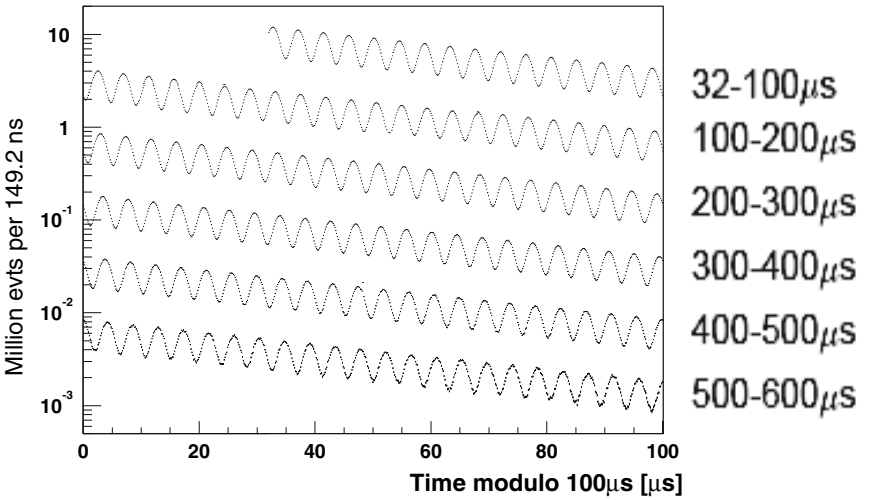

Fig. 2. The number of decay electrons detected by the calorimeters as a function of time after injection, showing the g-2 modulation superposed on the exponential decay of the parent muon (2001 negative muon data).

selection and pulse finding, resulted in four independent analyses of ω_a for the 2000 data [2] and five for the 2001 data [3], which were then averaged, with attention to their correlated uncertainties.

The analysis of ω_a and ω_p was divided into separate tasks with secret offsets for self-blinding. The value of a_μ was determined after the analyses of ω_a and ω_p had been finalized, the offsets removed, and radial E-field and pitch corrections applied. The result of the last two highest precision runs are shown in Fig. 3 together with the SM result for e+e-. The SM calculation which uses τ-decay to obtain a_μ(Had) is shown in the figure as well, in order to illustrate the degree of discrepancy between these two methods. Assuming CPT, we combined the results from μ^- and μ^+ runs to obtain $a_\mu(\text{exp}) = 11\ 659\ 208(6) \times 10^{-10}$ [3].

4 Current Theoretical Status

One can separate the components of the standard model calculation into the contributions from electromagnetic interactions, those involving weak bosons, the hadronic vacuum polarization, and the hadronic light-by-light scattering. Such a sum is shown in Fig. 4 using a subsample of Feynman diagrams. The hadronic vacuum polarization contribution cannot be calculated from perturbative QCD, but instead must be related to the measured hadron production cross section R(s) in e+e- collisions via the dispersion relation given by (1). This is graphically illustrated in the third line of Fig. 4 by a dotted line

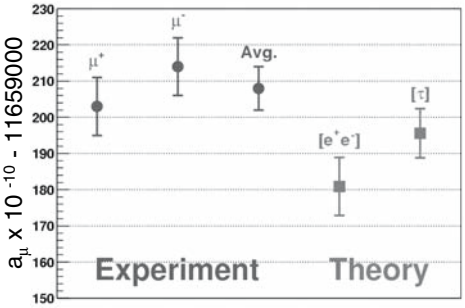

Fig. 3. Comparison of a_μ(exp) from the μ^-(2000) and μ^+(2001) BNL runs with a_μ(SM) using a_μ(Had) from both e+e- and τ-decay parameterizations.

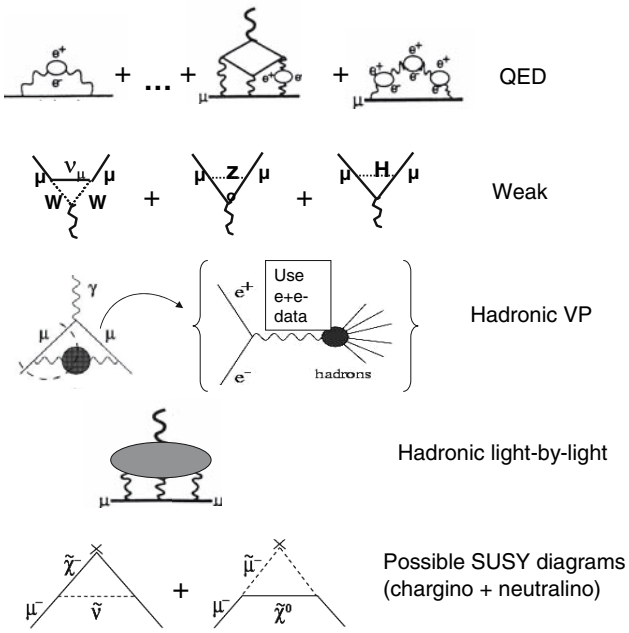

Fig. 4. A subset of the Feynman diagrams relevant to Standard Model calculation of the anomalous magnetic moment of the muon. Unlike cross section experiments, measuring the g-2 frequency is sensitive to the simple sum of a_μ contributions, rather than the square.

cutting the virtual hadronic blob to demonstrate how the real process of e+e- to hadrons is related to the virtual process which must be parametrized. The dominant SUSY diagrams are also included to illustrate how new physics might enter into the sum of contributions.

The best set of such contributions, representing the latest compilations at the time of this conference, is listed below, which when added together give $a_\mu(\mathrm{SM}) \times 10^{-10}$:

a_μ(QED) =	11658471.958	(0.143)	[17]
a_μ(Weak) =	15.4	(0.2)	[18]
a_μ(Had-LO) =	693.4	(5.3)(3.5)	[19]
a_μ(Had-NL) =	–9.8	(0.1)	[19]
a_μ(Had l-b-l) =	13.6	(2.5)	[20]

The QED component dominates, but also has the smallest error (now computed up α^4 with an estimation of α^5). An improved value for the α^4 QED term and later corrections (December 2004) by Kinoshita and Nio [17] are included. The weak contribution includes 2-loop, leading and next-leading log, but hasn't changed much in the last decade.

The largest error is in the first order hadronic vacuum polarization contribution as discussed above. Although higher order calculations rely on the same parameterization, the contribution itself is much smaller and the error does not dominate. Calculations of the vacuum polarization contribution using vector spectral functions from hadronic τ-decays [13] gives a contribution that differs significantly from the e+e− determination, dominated by Novosibirsk CMD-2 data. Since it also differs from recent KLOE and BaBar results which use radiative return to reduce the center of mass energies to those most relevant to g-2, it is no longer used in direct comparisons as it requires assumptions about CVC, isospin corrections, electroweak symmetry breaking, and the charged-ρ mass. The hadronic VP contribution chosen here therefore does not include τ-decay data, but does include the newest KLOE results [16], as well as a QCD fit at the higher center of mass energies.

The next largest uncertainty comes from the light-by-light term which is a model-dependent calculation. The listed contribution and its uncertainty come from the recent re-evaluation of this term by Melnikov and Vainshtein [20]. A smaller overall light-by-light term ($12.0(3.5) \times 10^{-10}$ due to the inclusion of some negative contributions) has been evaluated by Davier and Marciano [14], which increases the Δa_μ discrepancy to 2.7 σ significance. However, using the numbers quoted above, the g-2 discrepancy is $\Delta a_\mu = 23.5\ (9.0) \times 10^{-10}$ representing a 2.6 σ significance.

5 Muon g-2 Constraints on SUSY Dark Matter

If supersymmetry is responsible for the non-standard part of the g-2 anomaly, there exist new diagrams which can contribute to a_μ, specifically two new one-loop diagrams: one with an internal loop of smuons and neutralinos and one with a loop of sneutrinos and charginos (see Fig. 4). For minimal

supersymmetry (MSSM) parameter space in the limit of large tan β, it is the chargino contribution that can most easily generate masses large enough to explain the discrepancy. A fairly generic result for tan $\beta > 5$ is an inverse quadratic dependence on the SUSY loop mass given by

$$|a_{\mu}^{SUSY}| = 13 \times 10^{-10} \left[\frac{100GeV}{m_{SUSY}}\right]^2 tan\beta \tag{4}$$

where tan β is the ratio of vacuum expectation values of the Higgs doublet [23].

This $(m_{SUSY})^{-2}$ dependence is responsible for shapes of the shaded regions in the plot of Fig. 5, provided by T. Goto [21] for three tan β regions, under the minimal supersymmetric extension of the Standard Model and the framework of SU(5) GUT models. The current Δa_{μ} value (solid line) and its 1-σ bounds (dotted lines) are plotted on top, with vertical arrows to show how m_{SUSY} is limited by the g-2 experiment for a particular value of tan β (tan $\beta = 10$). When such constraints are translated into a 2-D plot of gaugino ($m_{1/2}$) vs slepton (m_0) mass [22] in the constrained minimal supersymmetric model (CMSSM), they form the quarter circle shape of the g-2 preferred mass region. Figure 6 shows such a plot for a particular choice of tan β and μ (the

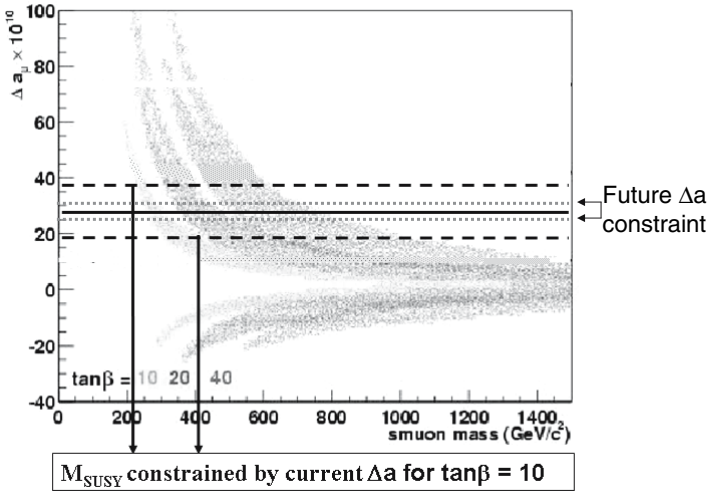

Fig. 5. The shaded regions are the allowed values for the supersymmetric contribution to a_{μ} as a function of the left-handed scalar muon mass for minimal supergravity (based on plots from T. Goto [21]. Contraints from the Higgs boson search are already imposed. Three different tan β values (10, 20, and 40) are shown. The mean and 1-σ bounds of Δa_{μ} from the most recent experiment and SM calculation provide a straight line from which to determine m_{SUSY} limits.

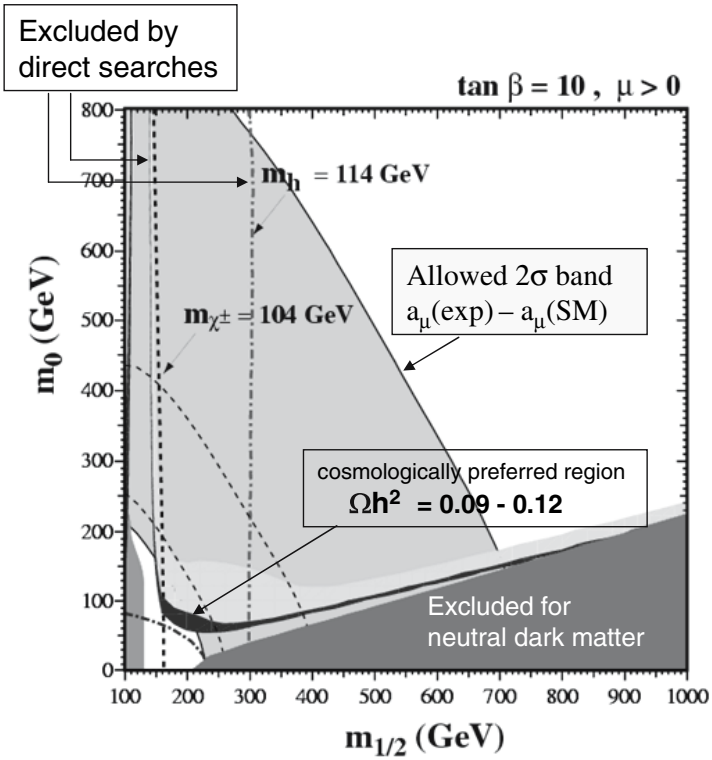

Fig. 6. Courtesy of Keith Olive. The $m_{1/2}$ vs m_0 planes in CMSSM. The cosmologically-preferred region allowed by WMAP constraint ($0.094 < \Omega_{CDM}h^2 < 0.129$) is the thinner dark boomerang. The shaded region is favored by g-2 at the 1σ level (dotted lines) and 2σ level (solid lines).

Higgs mixing parameter). The dotted lines represent the 1-σcontours and the solid lines bounding the shaded region correspond to the 2-σ contours on a g-2 discrepancy presumed to be saturated by the SUSY contribution. For this plot, Olive has used the value of $\Delta a_\mu = (23.9 \pm 9.9) \times 10^{-10}$ corresponding to the theory compilations in March 2004, but not very different from the current value quoted here. As tan β is increased the quarter circle stretches and moves to higher mass. Both the positive nature of the g-2 discrepancy and the b$\rightarrow$sγ branching ratio constraint prefer positive μ.

The power of the g-2 measurement to constrain SUSY dark matter lies in the contrasting way in which it cuts across m_0 vs $m_{1/2}$ parameter space compared to the cosmologically preferred region, which is a hyperbolically thin dark line with co-annihilation strips extending to high $m_{1/2}$ and m_0. Connecting these two high-mass extensions is the central "focus point", considerably shrunk from the fatter (light-shaded) region by the WMAP data ($0.094 < \Omega_{CDM}h^2 < 0.129$). LEP data excludes low $m_{1/2}$ regions. The requirement

that the dark matter particle be neutral eliminates the lower right triangle where the stau becomes the lowest mass SUSY particle. The next generation of collider searches will take place at CERN when the Large Hadron Collider comes on line in summer of 2007. The narrower the g-2 band, the more tan β itself will be constrained if supersymmetric particles are discovered and their mass measured at a collider.

6 Future Experiments and Theory Advances

Improvement in the g-2 constraint will depend on future advances in theory and whether or not a new g-2 experiment can be mounted at Brookhaven in the near future. Only 20% of the CMD-2 e+e- data (center of mass energies from 0.3–1.4 GeV) have been analyzed. Over the next several years one should expect the precision in the dispersion integral to improve as this work is completed. An upgrade to the VEPP-2000 collider will provide increased luminosity and an improved detector (SND) to add statistics to the Novosibirsk data sample. An intensity upgrade at the BEPS machine will increase the sample of e+e- data at the intermediate 2–5 GeV range. This energy range contributes less to the g-2 hadronic correction, since the kernel K(s) is decreasing with s, but it does provide an important handle on potential systematic bias in the region where is overlaps CMD-2 and previous experiments. BaBar, KLOE and Belle will weigh in on differential cross sections using radiative return for multiple pion states. The BaBar data will be especially interesting, since the data can be directly normalized in the same apparatus measuring e+e- $\rightarrow \mu + \mu-$. Within the decade, the error on the 1^{st} order hadronic correction should be reduced to $\delta a_\mu \sim 35 \times 10^{-11}$, which is comparable to the uncertainty on the hadronic light-by-light contribution. Since hadronic light-by-light scattering is model-dependent, it is hard to predict whether a breakthrough will occur there anytime soon. Lattice gauge calculations may have some successes in the next few years.

On the experimental side, Fig. 7 shows the evolution of the measured g-2 precision. It can be seen that each run is statistics limited and that the systematic uncertainties for ω_a and ω_p are comparable. Another run in 2009 as E969 will represent the best one can do with the modified ring and detector geometry, before becoming limited by systematics. This requires collecting 70 billion decay positrons. By doubling the number of beamline quadrupoles and using an open-ended inflector design, the number of stored muons can be increased by a factor of 5, allowing this to be done in only 21 weeks for a 0.14 ppm statistical error. The systematic error on ω_a can be reduced by injecting backward-going muons to reduce pion flash, adding another kicker module to reduce coherent betatron oscillations, segmenting calorimeters to reduce rate-dependent effects, and improving the front end electronics and data acquisition to handle the increased throughput. In situ measurement of the kicker eddy currents and mapping of the NMR probes can reduce $\delta\omega_p$.

Data Set:	1999	2000	2001	2009	2015
	1st long run	new inflector	reverse polarity	improved BNL	new facility
Statistics	1 B e^+	4 B e^+	4 B e^-	70 B e+	1 G e+/e-
(N_e above E_{thr})	**1.25 ppm**	**0.6 ppm**	**0.7 ppm**	**0.14 ppm**	**0.03 ppm**
Systematics	**0.5 ppm**	**0.4 ppm**	**0.3 ppm**	**0.15 ppm**	**0.04 ppm**
$\delta\omega_a$	0.3 ppm	0.3 ppm	0.21 ppm	0.11 ppm	0.025 ppm
Dominated by	pileup AGS mistune	coherent betatron μ loss, pileup	gain stability μ loss, pileup		
$\delta\omega_p$	0.4 ppm	0.24 ppm	0.17 ppm	0.11 ppm	0.03 ppm
Dominated by	trolley position inflector	trolley position	trolley position	trolley position	probe calibration

Fig. 7. Evolution of the statistical and systematic uncertainties in the BNL g-2 experiment. The first three columns refer to completed experimental runs. Only the most recent g-2 runs have been included. Note that the experiments have all been statistically limited. The last two columns represent future experiments: a BNL experiment in the near future with modifications to the existing beamline, storage ring and detectors, and a possible second generation experiment to be staged at JHF in Japan.

Combined with the theory precision expected a few years from now, the error on Δa_μ would then be at 4.7×10^{-10}. If the mean Δa_μ remains stable, this represents a close to 6σ departure from the Standard Model.

Looking beyond BNL, the next generation g-2 experiment would need a factor of 100 more data to make it worthwhile. Such concepts are being explored at the JPARC facility in Japan, (see, for example, Miller [24]) where JHF provides a factor of 10 increase in intensity (100 bunches/cycle every 0.7 ms) and the rest would have to come from an improved match between beam line and storage ring, etc. Another way to improve the experiment would be to increase the energy of the muons (and their dilated lifetime) so that more g-2 cycles can be measured for the same number of stored particles. This means abandoning electrostatic focusing, which can only be used at 3.1 GeV, that "magic" momentum where the radial electric field term cancels and the precession is unaffected. A new ring structure has been proposed by Farley

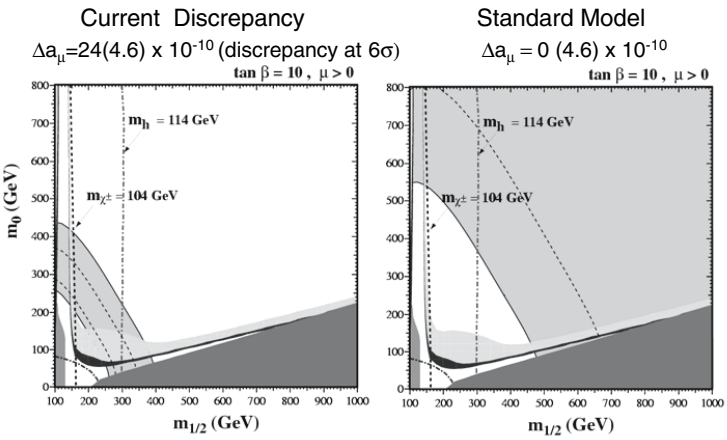

Fig. 8. The CMSSM $m_{1/2}$ vs m_0 planes for tan β=10, μ >0 as in Fig. 6 (Courtesy of Keith Olive). However, here the g-2 allowed regions correspond to two possible future scenarios, each with the reduction in uncertainty expected from a new E969 g-2 experiment and an improved hadronic VP correction as e+e- statistics increase. Left plot: Mean discrepancy remains the same to give $\Delta a_\mu = 239\ (47) \times 10^{-11}$. Right plot: The experiment matches the standard model value to give $\Delta a_\mu = 0(47) \times 10^{-11}$.

[25] which replaces electrostatic quads with edge focusing. Due to the large inhomogeneities in the field, the NMR probes must be replaced by proton calibration of the field. All such new initiatives are still more than a decade away.

Figure 8 shows how reduced errors would translate into dark matter constraints for a particular choice of tan β=10 and the preferred $\mu > 0$. Both plots include the factor of 2.5 reduction in uncertainty expected from a new run at BNL, combined with improvements in a_μ(Had) from e+e- data already collected. The plot at the left represents the case where the mean discrepancy remains stable at its present value. The plot to the right represents the case where the mean shifts down to the SM value. Due to the nature of the constraints, a reduction in the error bars which leaves the mean Δa_μ intact will significantly narrow the band of allowed masses, while a shift down to SM will widen the allowed region, but reject SUSY masses $< 500\,\mathrm{GeV/c^2}$. In both cases, this will provide significant new constraints on SUSY dark matter under the CMSSM.

7 Conclusions

On the experimental front, the BNL g-2 experiment has succeeded in its goal to improve the precision of a fundamental constant by a factor of 15 since the

last CERN experiment 30 years ago. However, the theoretical landscape has shifted considerably. Originally, the BNL experiment was designed to search for the Higgs and to confirm electroweak symmetry-breaking by measuring a_μ(weak) to 20%. As the mass limits on the Higgs moved upward over the last decade and a half of Tevatron and LEP runs, the contribution to a_μ from diagrams containing the Higgs shrank below our sensitivity. The popularity of SUSY as an answer to the hierarchy problem and as a means to unify gauge couplings has renewed interest in a_μ, especially since the hint of a discrepancy points to such convenient SUSY masses. The experimental improvement has lead theorists to uncover a number of errors, improve calculations involving both hadronic vacuum polarizations, as well as higher order QED terms, spurred further experimental work on R(s), and lead to a re-examination of CVC and pion form factors. In the end, no matter what the fad of the moment, precision measurements of fundamental constants are an enduring contribution to physics, since they confront our preconceptions with reality and guide future discussions.

References

1. H.N. Brown, et al., (Muon $(g-2)$ Collaboration), Phys. Rev. Lett. **86**, 2227 (2001)
2. G.W. Bennett, et al.,(Muon $(g-2)$ Collaboration), Phys. Rev. Lett. **89**, 101804 (2002)
3. G.W. Bennett, et al., (Muon $(g-2)$ Collaboration) [1] Phys. Rev. Lett. **bf 92**, 161802 (2004).
4. M. Knecht and A. Nyffeler: Phys. Rev. **D65**, 073034 (2002)
5. M. Hayakawa and T. Kinoshita: hep-ph/0112102 (2001)
6. J. Bijnens, E. Pallante, and J. Prades: Nucl. Phys.**B626**, 410 (2002)
7. R. Alemany, M. Davier, and A. Hocker: Eur. Phys. J. **C2**, 123 (1998)
8. R. Akhmetshin et al.: hep-ex/0308008 (2003)
9. A. Alioso et al.: hep-ex/0312056 (2003)
10. S. DiFalco, et al.: Acta. Phys. Polon. **B34**, 5207 (2003)
11. M. Davier, hep-ex/0312064 (2003).
12. S. Ghozzi and F. Jegerlehner: Phys. Lett. **B583**, 222 (2004)

[1]The g-2 Collaboration: G.W. Bennett, B. Bousquet, H.N. Brown, G. Bunce, R.M. Carey, P. Cushman G.T. Danby , P.T. Debevec , M. Deile, H. Deng , S.K. Dhawan, V.P. Druzhinin, L. Duong , F.J.M. Farley, G.V. Fedotovich, F.E. Gray , D. Grigoriev, M. Grosse-Perdekamp, A. Grossmann, M.F. Hare, D.W. Hertzog, X. Huang, V.W. Hughes, M. Iwasaki, K. Jungmann, D. Kawall, B.I. Khazin, F. Krienen, I. Kronkvist, A. Lam, R. Larsen , Y.Y. Lee, I. Logashenko, R. McNabb, W. Meng, J.P. Miller, W.M. Morse, D. Nikas, C.J.G. Onderwater, Y. Orlov, C.S. Ozben, J.M. Paley, Q. Peng, C.C. Polly, J. Pretz, R. Prigl, G. zu Putlitz, T. Qian, S.I. Redin, O. Rind, B.L. Roberts, N. Ryskulov, P. Shagin, Y.K. Semertzidis, Yu.M. Shatunov, E.P. Sichtermann, E. Solodov, M. Sossong, L.R. Sulak, A. Trofimov, P. von Walter, A. Yamamoto

13. M. Davier, S. Eidelman, A. Hocker, and Z. Zhang: Eur. Phys. J. **C31**, 503 (2003)
14. M. Davier and W.J. Marciano: Ann. Rev. Nucl. Part. Sci. **54** December (2004)
15. W. Liu et al.: Phys. Rev. Lett **82**,711 (1999)
16. KLOE collab. hep-ex/0407048 (2004)
17. T. Kinoshita and M. Nio: hep-ph/0402206v4 and Phys. Rev. **D70**, 113001 (2004)
18. A. Czarnecki, W.J. Marciano, and A. Vainshtein: Phys. Rev. **D67**, 073006 (2003)
19. K. Hagiwara, A. Martin, D Nomura, and T. Teubner: Phys. Rev. **D69**, 093003 (2004)
20. K. Melnikov and A. Vainshtein: Phys. Rev. **D70**, 113006 (2004)
21. T. Goto, Y. Okada, and Y. Shimizu: hep-ph/9908499 (1999)
22. J. Ellis, K. Olive, Y. Santoso, and V. Spanos: Phys Lett. **B565**, 176 (2003)
23. A. Czarnecki and W.J. Marciano: Phys. Rev. **D64**, 013014 (2001)
24. J. Miller: "A Future Muon (g-2) Experiment", NP02, Kyoto, Sept. 2002
25. F.J.M. Farley: hep-ex/0307024 (2003)

RPV Neutralino Searches from LEP to LHC

Silvia Costantini

Dipartimento di Fisica, Università di Roma "La Sapienza"
Piazzale Aldo Moro 2, 00185 Roma, Italy
silvia.costantini@roma1.infn.it

1 Outline

The search for supersymmetric particles will be one of the major research programs at the Large Hadron Collider. Given the large amount of proton-proton interactions per bunch crossing, the selection of processes with clean final states will be of the outmost importance. From this point of view, we discuss the present status of R-Parity Violation searches and the results expected at LHC with 10 $\text{fb}^{-1}$of integrated luminosity, corresponding to one year of data taking at the initial low luminosity value of 10^{33} cm^{-2} s^{-1}.

This paper is organized as follows: first we will review the physical conditions at LHC and the main characteristics of the general purpose detectors (Sect. 2). We will discuss in some detail the electromagnetic calorimeter of the CMS experiment (Sects. 3 and 4), which the RPV selection is based upon, and which is currently under construction in Rome. Finally we will summarize the R-Parity Violation scenario (Sect. 5), the status of RPV searches after LEP (Sect. 6) and present the results expected by ATLAS and CMS after one year of data taking at low luminosity (Sect. 7).

2 Physics and Experiments at LHC

The Large Hadron Collider (LHC) will become operational in 2007. Proton-proton collisions will occur at the center-of-mass energy of $7+7$ GeV, with an initial luminosity $\text{L} = 10^{33}$ cm^{-2} s^{-1}. The design luminosity of 10^{34} cm^{-2} s^{-1} is expected to be reached 2–3 years after the start-up. Each LHC experiment will collect an integrated luminosity per year of about 10 fb^{-1}under the initial conditions, and will reach up to about 100 $\text{fb}^{-1}$when the design luminosity will be attained. An ultimate integrated luminosity of 300 fb^{-1}per year and per experiment is foreseen. Under this conditions LHC will actually be a factory not only of Standard Model particles, but of new particles as well, like the Higgs boson(s) and the supersymmetric particles, as summarized in Table 1. Typical cross-section values are shown in Fig. 1, as a function of the center-of-mass energy $\sqrt{s}$.

With a total p-p inelastic cross-section $\sigma \simeq 70$ mb, the event rate will be between $\text{N} = \text{L}\ \sigma = 7 \cdot 10^7$ Hz and $7 \cdot 10^8$, depending on the luminosity L.

Table 1. Number of expected events at LHC, per second and per year, for some physical processes, assuming a luminosity of 10^{33} cm^{-2} s^{-1}. For comparison, the number of produced events per year at other machines is given.

Process	Events Per Second	Events Per Year	Other Machines (events per year)
W $\rightarrow e\nu$	15	10^8	LEP (10^4), Tevatron (10^7)
Z $\rightarrow$ee	1.5	10^7	LEP (10^7)
$t\bar{t}$	0.8	10^7	Tevatron (10^4)
$b\bar{b}$	10^5	10^{12}	Babar/Belle (10^8)
H (M_H = 0.8 TeV)	0.001	10^4	–

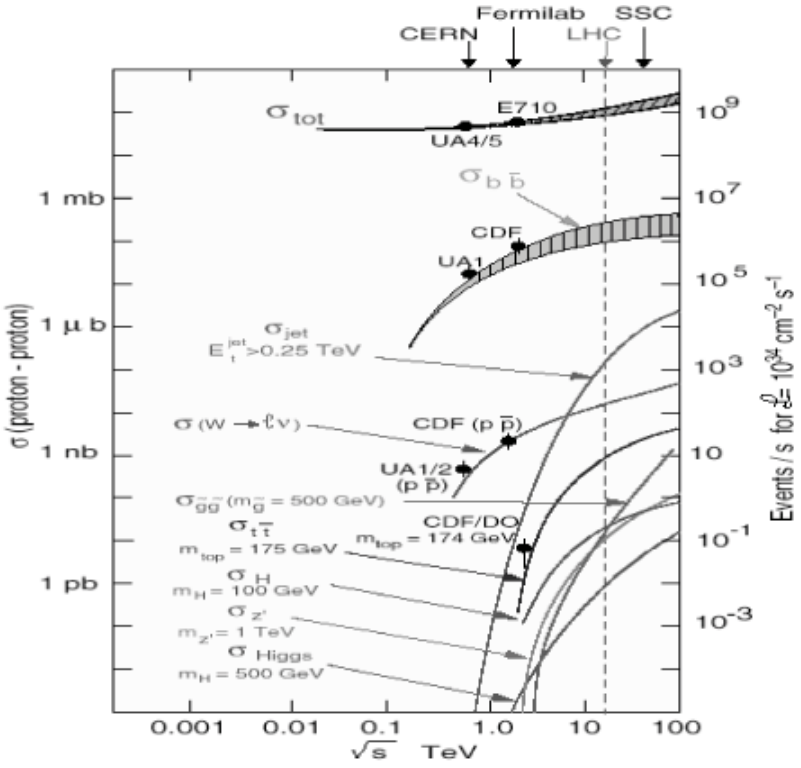

Fig. 1. Proton-proton cross-section values vertical left scale and number of expected events per second, for L = 10^{34} cm^{-2} s^{-1} (right scale), as a function of $\sqrt{s}$. The dashed line at $\sqrt{s} = 14$ TeV shows the LHC center-of-mass energy. The $\sqrt{s}$ values of other machines are shown as well.

Taking into account the bunch spacing $\Delta t = 25$ ns, the number of overlapping p-p interactions per bunch crossing will be N $/\Delta t = 2-20$, depending on L. It is therefore clear that clean final states will be needed in order to disentangle the desired signal events from the overwhelming background.

At the Large Hadron Collider there will be two so-called omni-purpose detectors, ATLAS [1] and CMS [2], which will perform a general research program, and two dedicated detectors, ALICE [3] and LHCb [4] for specific research programs, i.e. on the physics of heavy ions and on b-physics, respectively. The general purpose detectors aim at particle identification and measurement for event selection and reconstruction. At this purpose, they are based on a detector system consisting of inner tracker, calorimeters and muon chambers.

The ATLAS inner detector is a combination of discrete high-resolution pixel and strip detectors in the inner part and continuous straw-tube tracking detectors with transition radiation capability in the outer part of the tracking volume. The electromagnetic calorimeter consists of a granular Liquid Argon (LAr) sampling calorimetry with very good performance in terms of energy and position resolutions over the pseudorapidity range $|\eta| < 3.2$. The bulk of the hadronic calorimetry is provided by a scintillator tile calorimeter. The energy resolutions are given by: $\sigma/E \simeq 10\%/\sqrt{E}$ (GeV) for the electromagnetic calorimeter and $\sigma/E \simeq 50\%/\sqrt{E}$ (GeV) + 0.03 for the hadron calorimeter. The calorimetry is surrounded by the muon spectrometer with three stations of high-precision tracking chambers.

The CMS electromagnetic calorimeter is described in Sect. 3. The tracking system consists of silicon pixel detectors, choosen for their radiation hardness and small amount of material, corresponding to about 30% of the radiation length X_0.The hadron calorimeter is made by copper plates and plastic scintillator tiles.

3 The CMS Electromagnetic Calorimeter

The CMS electromagnetic calorimeter (ECAL) is currently under construction and will contain 61200 $PbWO_4$ crystals.

Scintillating crystals are the most precise calorimeters for energy measurements and provide excellent energy resolution over a wide range, as well as high detection efficiency for low energy electrons and photons. Their structural compacteness allows to have simple building blocks for mechanical assembly, hermetic coverage and fine transverse granularity. The choice of $PbWO_4$ crystals has been driven by their characteristics, as summarized in Table 2. Furthermore, $PbWO_4$ production on large scale is possible, making this material interesting for a LHC detector. The energy resolution can be parametrized as:

$$\sigma/E \simeq 2.7\%/\sqrt{E}(GeV) + 0.5\% + 150MeV/E \,, \qquad (1)$$

Table 2. Physics requirements and CMS solutions, explaining the choice of $PbWO_4$ crystals. X_0 is the radiation length.

Physics Requirements	CMS-ECAL Solution
Very good resolution for high energy e/γ	Crystal calorimeter
High LHC luminosity: L = 10^{34} cm^{-2} s^{-1}	$PbWO_4$ is radiation hard
LHC bunch separation: 25 ns	$PbWO_4$ is fast: 80% of light is collected within 25 ns
Compact detector with high granularity	$PbWO_4$ has X_0= 0.89 cm and Moliére radius = 2.2 cm
Magnetic field inside CMS: 4T	Compact solid state photodetectors

where the first term is the stochastic one and depends on the photoelectron statistics, since the measured light yield (see Sect. 4) amounts usually to only 4–5 pe/MeV; the second is the constant term, due to shower containment, crystal non-uniformity and crystal intercalibration; the last one is the noise term, which the electronic noise and the pile-up contribute to.

4 The ACCOR Measurement System

Half of the barrel crystals are being fully characterized for dimensions, optical properties and light yield in the INFN-ENEA Regional Center near Rome. The ACCOR system, described in detail in [5], consists of three measuring stations and allows the automatic measurement of crystal dimensions, optical transmission and light output. Up to 70 crystals per day can be fully characterized in two runs, feeding in turn the machine with seven trays of five crystals each. Moving belts set the trays under each measurement station.

Dimensions are reconstructed with a commercial 3D machine, by measuring five points on both the front and rear faces and eight points each on the lateral ones. The measurement reproducibility is $\pm 2\,\mu$m.

The transmission is measured with a single-beam array spectrometer, directly coupled to an integrating sphere, and by using a collimated Xenon lamp as light source in the range 300–700 nm. The array spectrometer allows to take in one single shot all data in the desired spectral range. In total twelve transmission spectra are collected for each crystal: one longitudinal (LT) and eleven transverse (TT) ones, taken every 2 cm along the crystal. The stability of the reference measurements over two minutes is better than 1% in most of the spectral range of interest (320–700 nm) and it is never worse than 2% near the edge of the UV region, where the signal intensity is lower.

Afterwards we measure the uniformity of the light output as well as the light yield (LY) at eight radiation lengths (8 X_0) from the crystal front face, distance corresponding to the shower maximum for a 50 GeV electron. The

LY is evaluated by detecting the photo-peak in the scintillation spectrum of a γ-emitting Co^{60} source, where $E_\gamma = 1.173$, 1.333 MeV. The source is moved along the crystal and 21 spectra are collected with 1 cm step, in order to check the light collection front non-uniformity (FNUF). The light yield measurement and calibration procedure are discussed in detail in [6] and [7]. The ACCOR results are calibrated with reference measurements on a classical bench, where the crystals are in optical contact with the photomultiplier and wrapped in a Tyvek sheet on the lateral faces, in order to reproduce as closely as possible the actual configuration of the CMS experiment, where the crystals will be glued to the avalanche photodiodes (APDs) and inserted in reflective alveola. Furthermore, the same five reference crystals are measured every day to check the stability of the machine. The total time needed to measure five crystals on a tray is about 55 minutes: 15 for the dimension, 20 for the transmission and 20 for the light yield measurement, respectively.

Almost 16 so-colled supermodules, out of 36 of 1700 crystals each, have been already assembled and one supermodule has been calibrated with particles [8] in 2004. Crystals not being directly calibrated will undergo an intercalibration procedure, by means of the light yield and transmission laboratory measurements [9]. The final intercalibration precision achievable before the LHC start-up will be of the order of 3–4%.

5 R-Parity Violation

R-parity is a multiplicative symmetry defined as: $R = (-1)^{3B+L+2S}$, where S is the spin, B is the baryonic quantum number and L the leptonic quantum number. R is +1 for all ordinary particles, and −1 for their supersymmetric partners. If R-parity is conserved, supersymmetric particles can be produced only in pairs and they decay in cascade to the lightest supersymmetric particle (LSP), which is stable. R-parity violating terms can be present [10] in the most general superpotential of the Minimal Supersymmetric Standard Model (MSSM) [11], which describes a supersymmetric, renormalizable and gauge invariant theory, with minimal particle content. They are:

$$\lambda_{ijk} \mathrm{L}_i \mathrm{L}_j \overline{\mathrm{E}}_k + \lambda'_{ijk} \mathrm{L}_i \mathrm{Q}_j \overline{\mathrm{D}}_k + \lambda''_{ijk} \overline{\mathrm{U}}_i \overline{\mathrm{D}}_j \overline{\mathrm{D}}_k \tag{2}$$

where λ_{ijk}, λ'_{ijk} and λ''_{ijk} are the Yukawa couplings and i, j and k the generation indices; L_i and Q_i are the left-handed lepton- and quark-doublet superfields, $\overline{\mathrm{E}}_i$, $\overline{\mathrm{D}}_i$ and $\overline{\mathrm{U}}_i$ are the right-handed singlet superfields for charged leptons, down- and up-type quarks, respectively. In order to prevent the simultaneous presence of identical fermionic fields, antisymmetry relations are required for λ_{ijk} and λ''_{ijk}, reducing to $9 + 27 + 9$ the total number of independent Yukawa couplings. The $\mathrm{L}_i \mathrm{L}_j \overline{\mathrm{E}}_k$ and $\mathrm{L}_i \mathrm{Q}_j \overline{\mathrm{D}}_k$ terms violate the leptonic quantum number L, while the $\overline{\mathrm{U}}_i \overline{\mathrm{D}}_j \overline{\mathrm{D}}_k$ terms violate the baryonic quantum number B. Their simultaneous presence would lead to a fast proton

decay (with contributions at the tree level from $\lambda'_{11k}\lambda''_{11k}$, and at one-loop level from any product $\lambda_{ijk}\lambda''_{lmn}$ or $\lambda'_{ijk}\lambda''_{lmn}$) [12], which is experimentally excluded. This can be avoided by requiring R-parity conservation, which forbids all terms in (2). However, since the absence of either the B-violating or the L-violating terms is enough to prevent a fast proton decay, there is no need to impose *a priori* R-parity conservation. As a consequence, two new kinds of processes are allowed: single production of supersymmetric particles, or LSP decays into Standard Model particles via scalar lepton or quark exchange. In the latter case, the MSSM production mechanisms are unaltered by the operators in (2).

6 Present LEP Limits

The LEP experiments have searched for pair-produced neutralinos ($e^+e^- \to \tilde{\chi}^0_m\tilde{\chi}^0_n$, with $m = 1, 2$ and $n = 1, .., 4$), charginos ($e^+e^- \to \tilde{\chi}^+_1\tilde{\chi}^-_1$), scalar leptons ($e^+e^- \to \tilde{\ell}^+_R\tilde{\ell}^-_R$, $e^+e^- \to \tilde{\nu}\tilde{\nu}$) and scalar quarks ($e^+e^- \to \tilde{q}\tilde{q}$), with subsequent R-parity violating decays, assuming that only one of the coupling constants λ_{ijk}, λ'_{ijk} or λ''_{ijk} is non-negligible. Only $\tilde{\ell}_R$ (supersymmetric partners of the right-handed charged leptons) are considered, since they are expected to be lighter than the corresponding left-handed ones. Supersymmetric particles can decay directly into two or three fermions according to the dominant interaction term, as detailed in Table 3. Indirect decays via the LSP can occur as well. In the LEP analyses, the dominant coupling is assumed to be greater than 10^{-5} [13], corresponding to decay lengths less than 1 cm.

LEP results [14] are based on about 700 pb^{-1}per experiment (about 2.7 fb^{-1}in total at LEP) and have shown a global sensitivity to cross sections of 0.01–0.03 pb, with selection efficiency values, for the various final states, in the range 30%–40%.

In the MSSM-mSUGRA framework, neutralino and chargino masses, couplings and cross sections depend on the gaugino mass parameter, M_2, the higgsino mass mixing parameter, μ, the ratio of the vacuum expectation values of the two Higgs doublets, $\tan\beta$, and the common mass of the scalar particles at the GUT scale, m_0. The results presented in this section are obtained by performing a scan in the ranges: $0 \leq M_2 \leq 1000\,\text{GeV}$, $-500\,\text{GeV} \leq \mu \leq 500\,\text{GeV}$, $0 \leq m_0 \leq 500\,\text{GeV}$ and $0.7 \leq \tan\beta \leq 40$ and by deriving overall limits from combined analyses. A point in the MSSM parameter space is excluded if the total number of expected events is greater than the combined upper limit at 95% C.L. on the number of signal events. Neutralino, chargino, scalar lepton and scalar quark analyses are combined since several processes can occur at a given point. Gaugino and scalar mass unification at the GUT scale is assumed.

Figure 2 shows the 95% C.L. lower limits on neutralino and scalar lepton masses as a function of $\tan\beta$. The $\tilde{\chi}^0_1$ and $\tilde{\chi}^0_2$ mass limits are shown for

Table 3. Possible R-parity violating decays (charged conjugate states are implied). Only supersymmetric partners of the right-handed sleptons are taken into account. Decays to more than three fermions are not listed. W^* indicates virtual W bosons.

Particle	Direct Decays			Indirect Decays
	λ_{ijk}	λ'_{ijk}	λ''_{ijk}	via $\tilde{\chi}_1^0$
$\tilde{\chi}_1^0$	$\ell_i^- \nu_j \ell_k^+$, $\nu_i \ell_j^+ \ell_k^-$	$\ell_i^- \mathrm{u}_j \bar{\mathrm{d}}_k$, $\nu_i \mathrm{d}_j \bar{\mathrm{d}}_k$	$\bar{\mathrm{u}}_i \bar{\mathrm{d}}_j \bar{\mathrm{d}}_k$	–
$\tilde{\chi}_1^+$	$\nu_i \nu_j \ell_k^+$, $\ell_i^+ \ell_j^+ \ell_k^-$	$\nu_i u_j \bar{\mathrm{d}}_k$, $\ell_i^+ \bar{\mathrm{d}}_j \mathrm{d}_k$	$\bar{\mathrm{d}}_i \bar{\mathrm{d}}_j \bar{\mathrm{d}}_k$, $\mathrm{u}_i \mathrm{u}_j \mathrm{d}_k$, $\mathrm{u}_i \mathrm{d}_j \mathrm{u}_k$	$\mathrm{W}^* \tilde{\chi}_1^0$
$\tilde{\ell}_{kR}^-$	$\nu_i \ell_j^-$, $\nu_j \ell_i^-$	–	–	$\ell_k^- \tilde{\chi}_1^0$
$\tilde{\nu}_i$, $\tilde{\nu}_j$	$\ell_j^- \ell_k^+$, $\ell_i^- \ell_k^+$	$\mathrm{d}_j \bar{\mathrm{d}}_k$, –	–	$\nu_i \tilde{\chi}_1^0$, $\nu_j \tilde{\chi}_1^0$
$\tilde{\mathrm{u}}_{iR}$	–	–	$\bar{\mathrm{d}}_j \bar{\mathrm{d}}_k$	$\mathrm{u}_i \tilde{\chi}_1^0$
$\tilde{\mathrm{d}}_{jR}, \tilde{\mathrm{d}}_{kR}$	–	$\bar{\nu}_i \mathrm{d}_j$, $\ell_i^- \mathrm{u}_j$	$\bar{\mathrm{u}}_i \bar{\mathrm{d}}_k$, $\bar{\mathrm{u}}_i \bar{\mathrm{d}}_j$	$\mathrm{d}_j \tilde{\chi}_1^0, \mathrm{d}_k \tilde{\chi}_1^0$

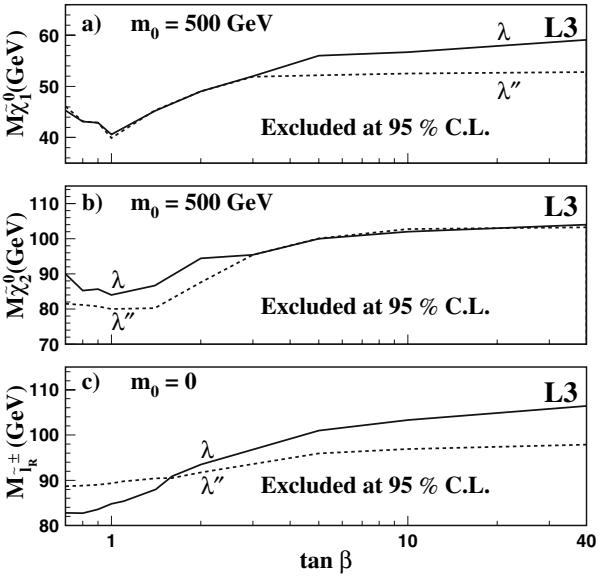

Fig. 2. MSSM mass limits from combined analyses. The solid and dashed lines, labelled with the corresponding coupling, show the 95% C.L. lower limits on the masses of (a) $\tilde{\chi}_1^0$, (b) $\tilde{\chi}_2^0$ and (c) $\tilde{\ell}_R$, as a function of $\tan\beta$, for $0 \leq M_2 \leq 1000\,\mathrm{GeV}$ and $-500\,\mathrm{GeV} \leq \mu \leq 500\,\mathrm{GeV}$. $m_0 = 500$ Gev in (a) and (b) and $m_0 = 0$ in (c). For those values of m_0 the global minima on the mass limit are obtained.

$m_0 = 500$ GeV and the $\tilde{\ell}_R$ ones for $m_0 = 0$. These values of m_0 correspond to the absolute minima from the complete scan on M_2, μ, m_0 and $\tan\beta$. The chargino mass limit is almost independent of $\tan\beta$, and is close to the kinematic limit for any value of $\tan\beta$ and m_0. For high m_0 values, neutralino and scalar lepton pair-production contributions are suppressed and the mass limits are given mainly by the chargino exclusion.

The overall 95% C.L. lower limits on the $\tilde{\chi}_1^0$ mass obtained by the LEP experiments is:

$$M_{\tilde{\chi}_1^0} > 40\,GeV\ . \tag{3}$$

7 Expectations at LHC

Analyses of R-Parity violating $\tilde{\chi}_1^0$ decays via λ or λ'' have been performed by the CMS and ATLAS experiments, respectively [15]. The experiments have assumed an integrated luminosity of 10 $\text{fb}^{-1}$and have investigated a few mSUGRA points. ATLAS shows that a precise reconstruction of the neutralino mass is possible from the 4-jets of λ''_{212} mediated decays (Fig. 3). CMS shows the feseability of the neutralino mass measurements from the

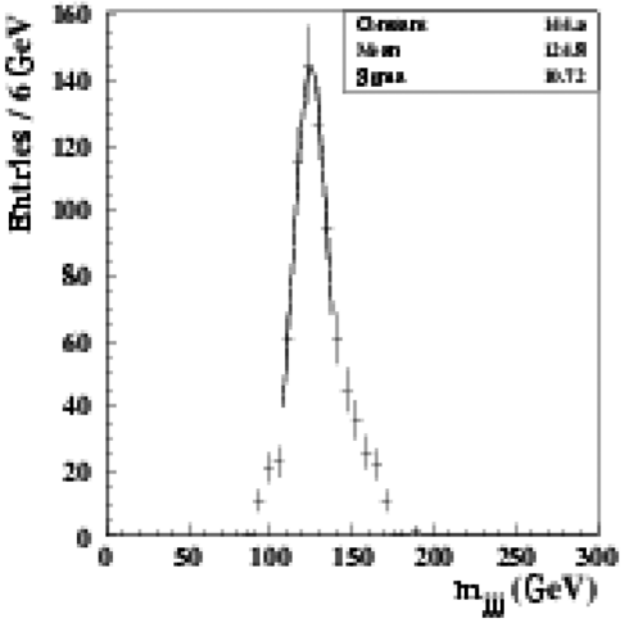

Fig. 3. Reconstructed 4-jet invariant mass for λ''_{212} mediated decays: $\text{M}_{rec} = 125 \pm 10\,\text{GeV}$. The generation parameters are: $m_0 = 100\,\text{GeV}$, $m_{1/2} = 300\,\text{GeV}$ and $\tan\beta = 1.2$, corresponding to a generated neutralino mass of 121.5 GeV.

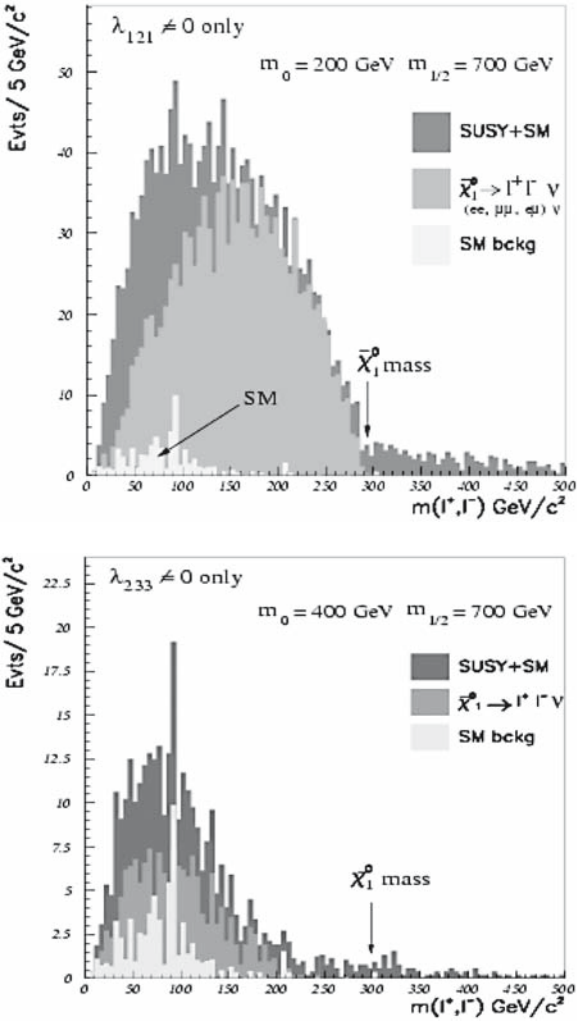

Fig. 4. Reconstructed 2-lepton invariant mass for λ_{121} (top) and λ_{233} (bottom). The generation parameters are: $m_0 = 200, 400\,\text{GeV}$, $m_{1/2} = 700\,\text{GeV}$ and $\tan\beta = 2$, corresponding to a generated neutralino mass of 300 GeV.

end-point of two-lepton mass spectrum, with λ_{121} and λ_{233}. The measurement is more difficult for final states with taus (Fig. 4).

8 Conclusions and Outlook

Results on LHC detector construction are presented, with emphasis on the CMS electromagnetic calorimeter. By exploiting the detector performances it

is expected to detect R-Parity violating SUSY particles at LHC and measure their masses up to O(100) GeV with 10 fb^{-1}, corresponding to one year of data taking at low luminosity.

Acknowledgements

I would like to thank the organizers for the invitation and for their warm hospitality.

References

1. A Toroidal LHC ApparatuS, Technical Proposal, CERN/LHCC **94–43** (1994)
2. The Compact Muon Solenoid, Technical Proposal, CERN/LHCC **94–38** (1994)
3. A Large Ion Collider Experiment at CERN LHC, ALICE Collaboration, F Carminati et al.: J. Phys. G: Nucl. Part. Phys. **30**, 1517 (2004) and references therein
4. The Large Hadron Collider beauty experiment, Technical Proposal, CERN/LHCC **98–04** (1998)
5. ACCOR is the Automatic Crystal quality COntrol system for the Rome regional center, S. Baccaro et al.: Nucl. Inst. and Meth. A **459**, 278 (2001)
6. S. Baccaro et al.: Precise determination of the light yield of scintillating crystals, Nucl. Instr. and Meth. A **385**, 69 (1997)
7. L.M. Barone et al., Improvements on $PbWO_4$ Crystal Intercalibration Precision from Light Yield Measurements at the INFN-ENEA Regional Center", CMS RN 2004/003
8. The so-called H4 test beam line at CERN is used, which provides electrons and pions of energy up to a few hundred GeV
9. S. Costantini: The CMS Electromagnetic Calorimeter: Results on Crystal Measurements, Quality Control and Data Management in the Rome Regional Center, CMS CR-2004/014; S. Costantini et al., Precise Measurements of Light Yield and Transmission of $PbWO_4$ Crystals at the INFN-ENEA Regional Center, to be published by Nucl. Inst. and Meth. A.
10. C.S. Aulakh and R.N. Mohapatra: Phys. Lett. B **119**, 136 (1982); F. Zwirner: Phys. Lett. B **132**, 103 (1983); L.J. Hall and M. Suzuki: Nucl. Phys. B **231**, 419 (1984); R. Barbieri and A. Masiero: Nucl. Phys. B **267**, 679 (1986). For a review: H. Dreiner: An introduction to explicit R-parity violation, hep–ph/9707435. In *Perspectives on Supersymmetry*, ed. G.L. Kane, World Scientific, Singapore (1998)
11. A review can be found in: H.E. Haber and G.L. Kane: Phys. Rep. **117**, 75 (1985)
12. S. Weinberg: Phys. Rev. D **26**, 287 (1982); G. Bhattacharyya and P.B. Pal: Phys. Rev. D **59**, 97701 (1999)
13. S. Dawson: Nucl. Phys. B **261**, 297 (1985)
14. ALEPH Coll.: Eur. Phys.J. C **31**, 1 (2003);
DELPHI Coll.: Eur. Phys.J. C **36**, 1 (2004) ; Eur.Phys.J. C **37**, 129 (2004);
L3 Coll.: Eur. Phys. J. C **19**, 397 (2001); Phys. Lett. B **524**, 65 (2002);

OPAL Coll.: Eur. Phys. J. C **33**, 149 (2004) (on scalar fermions); LEP-SUSYWG: www.cern.ch/LEPSUSY/ on RPV via LLE couplings: final article ready for submission
15. P. Paganini: CMS NOTE 1999/053, L. Drage and M.A. Parker: ATLAS-COMPHYS 99/029.

Tripling the LHC: The Path from Technology to Discovery

Peter McIntyre and Akhdiyor Sattarov

Department of Physics, Texas A&M University,
College Station, TX 77807, USA

The Large Hadron Collider (LHC) will dramatically extend the mass scale for finding signals from new fields of nature – the Higgs sector, supersymmetry, large extra dimensions, and ultimately superstrings. LHC will produce collisions of protons on protons with a center-of-mass energy $\sqrt{s} = 14$ TeV and a luminosity $\mathcal{L} \sim 10^{33}\text{cm}^{-2}\text{s}^{-1}$. This performance should suffice to access signals from particles conjectured in current models of the Higgs field and minimal supergravity. Even as LHC is being built, however, there have been spectacular discoveries of the past few years in astrophysics – dark matter and dark energy [1]. Among current efforts to connect these discoveries with physics at the microscale, it appears that the ∼TeV mass of LHC could prove insufficient for accessing many of these states [2] It is therefore timely to pose the question: "Is it feasible to extend LHC's mass reach by technology improvements?"

This paper presents a conceptual design for a superconducting magnet technology that could enable a tripling of LHC's energy by installing a second ring of magnets in the same tunnel, as shown in Fig. 1. The design of the Tripler dipoles is shown in Fig. 2. The Tripler dipoles would operate at 24 Tesla field strength, utilizing a hybrid coil containing windings of Nb_3Sn and Bi-2212 superconducting cables. The technology for the dipoles builds upon a decade of development of these superconductors [3] and of new methods to accommodate the stresses [4] and magnetic effects [5] that arise at such large field strength. Continued development of this technology should mature to a practical magnets for colliders within another decade, just in time to be available to upgrade LHC after its first long runs if the added energy reach appears desirable.

Also presented are first considerations for several of the most important accelerator issues that must be take into account in tripling LHC's energy. Perhaps the most important of those is the treatment of synchrotron radiation, which increases as E^4 and is already a dominant cryogenic load in LHC. Because the *spectrum* of synchrotron radiation hardens as E^3, the peak photon energy shifts from ultraviolet (which scatters in the beam tube and cannot be locally collected) to soft X-rays which can be absorbed on room-temperature photon stops located between consecutive dipoles. The room-temperature heat load should be comparable to that of LHC, even though

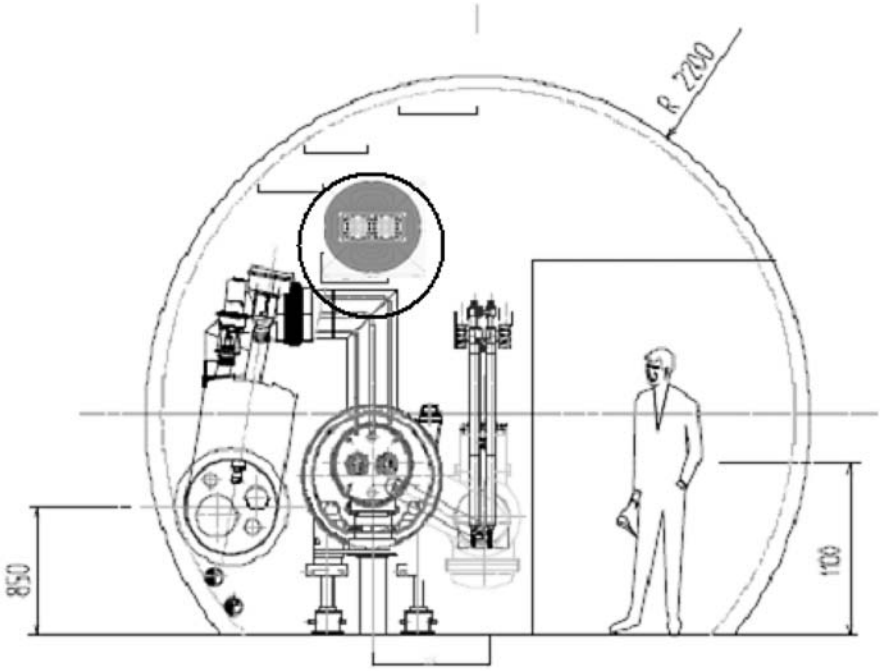

Fig. 1. Typical cross section of LHC tunnel, showing possible placement for the Tripler dual dipole.

the radiated power increases 100-fold! Indeed this increased radiation has a collateral benefit: it damps the beam emittance of the stored beam with a damping time ∼1 hour, which should provide a means to enhance and maintain luminosity during each store.

1 Discovery Reach for New Particles

In order to assess the potential of the Tripler for the discovery of new particles, Dutta [6] has calculated parton luminosities with which the constituents of colliding hadrons interact. Parton luminosities [7] are calculated for gluon-gluon scattering for the cases of the Tevatron, LHC, and the Tripler. The calculations use the CTEQ4 parton distributions [8]. The results are presented in Fig. 3 as a function of $\widehat{s}$, the c.m. energy for the colliding partons. The arrows indicate the requirement to double the mass reach at any given mass scale. Because production cross-sections scale geometrically ($\propto \widehat{s}$), increasing the mass scale by a factor 2 would require 4 times the luminosity in the gluon-gluon initial state. On the other hand beams in a collider damp adiabatically as the beam energy is increased, so that the same circulating current and same invariant emittance as LHC would yield 3 times greater

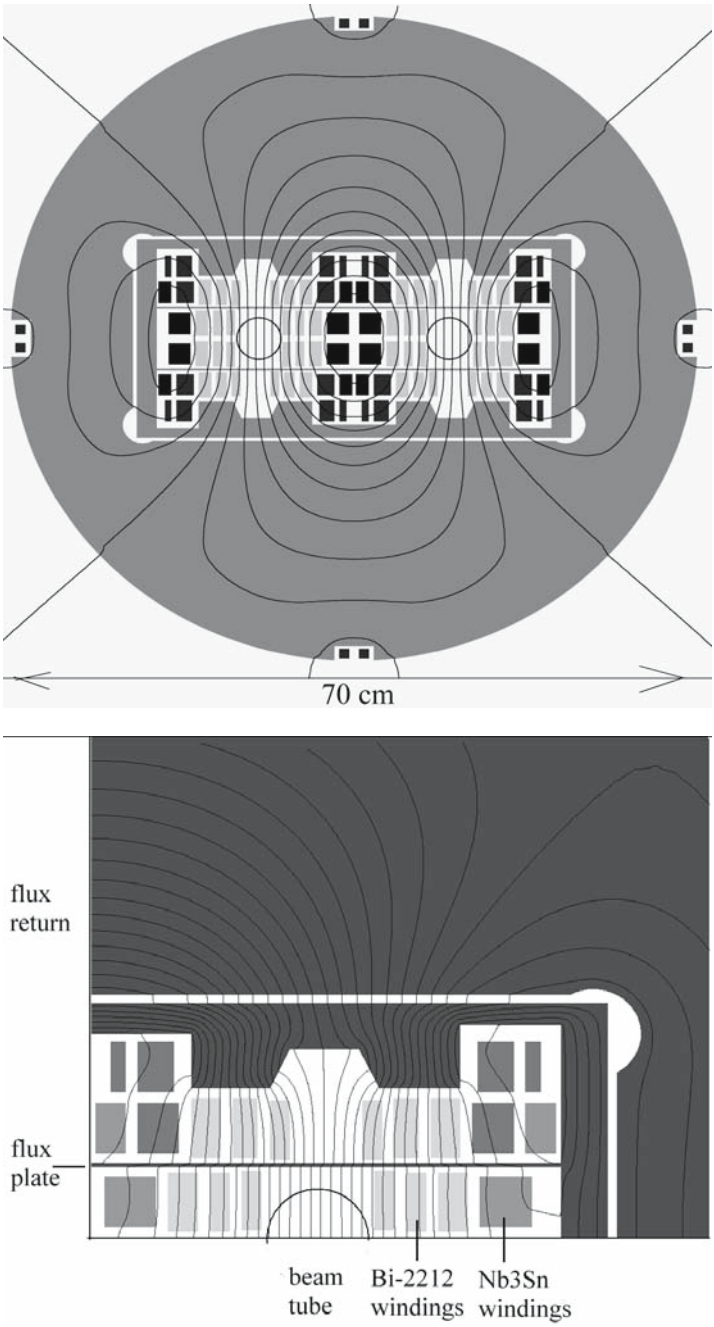

Fig. 2. Cross-section of the Tripler dipole: (a) overall view showing flux return and outer NbTi windings to suppress fringe field; (b) detail of hybrid coil region showing Bi-2212 windings, Nb3Sn windings, and flux plate.

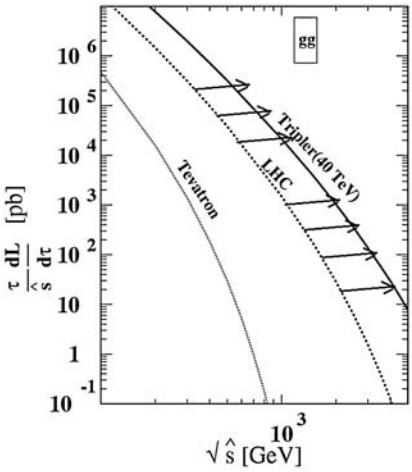

Fig. 3. Gluon-gluon luminosity vs. $\sqrt{s}$ in hadron colliding beams for the Tevatron, LHC, and LHC Tripler. Arrows indicate an increase of a factor 2 in mass reach.

luminosity in a Tripler. The arrows indicate an increase of a factor of 2 in mass scale and a factor of 4/3 in cross-section. It is seen that the Tripler would roughly double the mass reach of LHC for discovery of new particles.

To understand the significance of this factor of 2 in mass reach, one must have a model for the particle states that would result from new gauge fields. One model of current significance is the minimal supersymmetric extension of the Standard Model (MSSM). Ellis et al. [9] have calculated the masses of the lightest sparticles in MSSM, applying constraints on the range of model parameters arising from recent results from astrophysics and cosmology (CMSSM). They have mapped the parameter space of CMSSM within those constraints under variations of $m_0, m_{1/2}, A_0$, $\tan\beta$,and μ. The results are plotted in Fig. 4 for the constrained range of these parameters in order to illustrate the range of sensitivity ($\sigma > 10^{-8}$ pb) provided by underground WIMP searches (light gray dots in lower left), LHC (those plus gray crosses in center region), and the Tripler (all the previous plus square boxes in upper right). Only with the Tripler is it possible to cover the entire parameter space of CMSSM.

2 Dipole Requirements for an LHC Tripler

The mass reach of a hadron collider is determined by the field strength and field quality of its superconducting magnets. The beam momentum in the collider is determined by the collider radius R and the field strength B:

$$p[\mathrm{TeV}] = 0.3B[\mathrm{T}]\ R[\mathrm{km}]$$

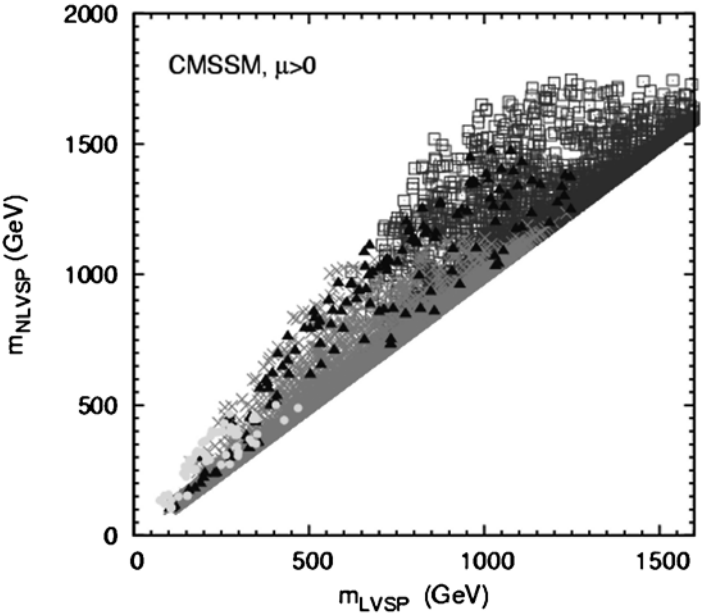

Fig. 4. Masses of the lightest visible particle (LVSP) and next-lightest visible particle (NLVSP) in cosmology-constrained CMSSM.

In turn the uniformity of the magnetic fields in the dipoles is key to sustaining the luminosity of collisions needed to create rare heavy particles of new gauge fields. Slight excitations of multipole components in the dipoles can drive the growth of non-linear instabilities through the beam-beam interaction, which would cause beam growth and loss of luminosity through the duration of a collision cycle.

The LHC dipole, shown in Fig. 5, reaches the highest performance that is possible with the classic technology of NbTi superconductor and cos θ coil geometry. That methodology was first used in the Fermilab Tevatron, later in HERA and in RHIC, and now ultimately in LHC. The design field of 8 Tesla is the highest field that is practical to attain with NbTi.

2.1 Superconductor Optimization at High Magnetic Field

The current in a superconducting coil produces the magnetic field that is used to guide the beams in a collider. This same magnetic field acts back upon the superconductor itself, however, in two key ways. With any given superconducting material, the current density that can be carried in a wire is proportional to the density of Cooper-paired electrons in the metal. Each superconducting material has an upper critical field B_{c2} at which the last Cooper pair is dissociated. The macroscopic magnetic field exerts a shear

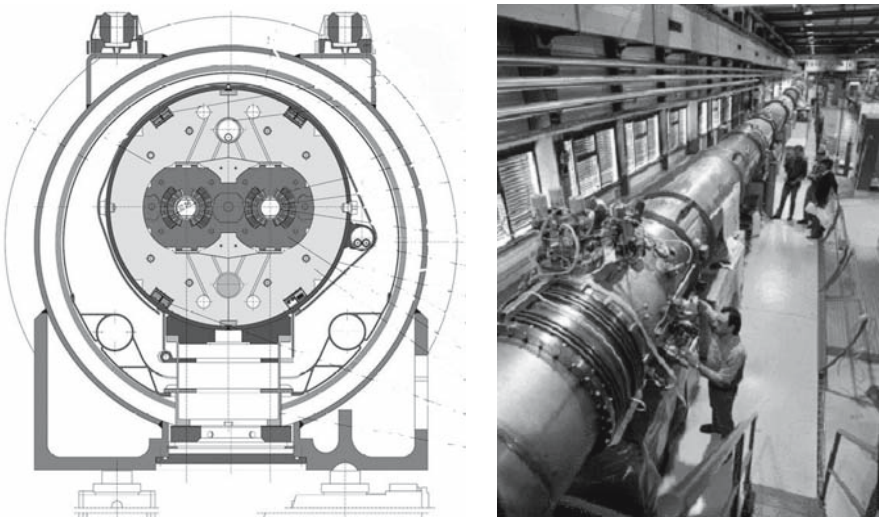

Fig. 5. LHC dipole: (a) cross section of dual dipole; (b) string test of dipoles and quadrupoles prior to tunnel installation.

force upon the Cooper pairs within the wires, so that the density of Cooper pairs (and hence the transport current density j_c that can be carried) is described by the Kramer phenomenology:

$$j_c^{1/2} B^{1/4} \propto \left(1 - \frac{B}{B_{c2}}\right)$$

Figure 6 illustrates this dependence for the superconductors NbTi, Nb_3Sn, and Bi-2212 [10]. The highest practical field for each conductor is ∼9 T for NbTi and ∼17 T for Nb_3Sn. Allowing for the distribution of field in a collider dipole, in which the maximum field stength actually occurs in the coil and is ∼10% greater than that in the bore tube, the greatest bending field attainable for dipoles is thus ∼8 T for NbTi, ∼16 T for Nb_3Sn. Thus to build a 24 T dipole for a Tripler one must utilize Nb_3Sn in the regions where $B < 18$ T, and Bi-2212 in the regions where $B > 17$ T. The technology for high-performance multifilament strand, Rutherford cables, coil winding, and heat treat and impregnation have all been matured for both Nb_3Sn [3] and Bi-2212 [11]. Until recently no one knew how to make such a hybrid dipole.

2.2 Stress Management

The second effect of the magnetic field on the superconducting coil is the Lorentz force $\boldsymbol{F}/\ell = \boldsymbol{I} \times \boldsymbol{B}$. Since the current required to produce a given field increases at least linearly, the force acting on the coils increases at least as B^2. This force acts as a lateral piston pushing the dipole open horizontally.

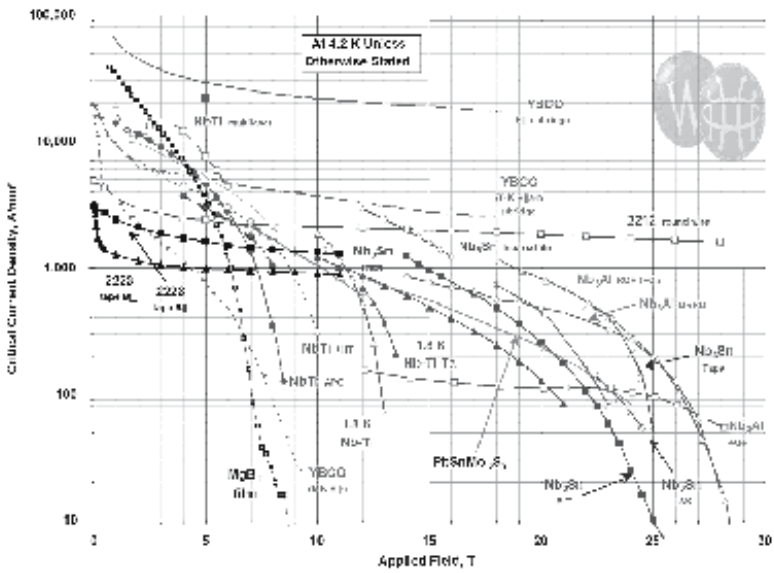

Fig. 6. The dependence of current density upon magnetic field of various superconductors at liquid helium temperature.

The forces are immense at high field, and for $B \gtrsim 12$ T approach the limit of degradation of the superconducting materials and the insulation used in the coils. Degradation is particularly troublesome with the high-field superconductors Nb_3Sn and Bi-2212, since they are brittle materials that must be formed in their superconducting phase in a high-temperature heat-treat of the final dipole after all coils are wound.

The Lorentz stress accumulates through the thickness of a superconducting coil, as the field acts upon each conductor in turn and the forces add up as they are passed to the outside structure. This is unavoidable in coils that utilize the cos θ geometry of the classic design because the entire coil is one mechanical assembly.

For managing stress in high-field dipoles, we adopt the same simple approach that is used in a multi-story building. There gravity acts on people and objects on each floor, and if there were no support structure the forces would accumulate as each occupant was pressed upon the one below. We insert floors to *intercept t*he forces acting on each floor, and walls to *bypass* those forces past the occupants in floors below. We have developed similar stress management in high-field dipoles [12]. The coils are configured in a rectangular block configuration and a support matrix of ribs and plates tis integrated within the coil to intercept the forces acting on inner windings and bypass them past outer windings to the flux return. The stragegy is summarized in Fig. 7. Three windings in a horizontal section are shown,

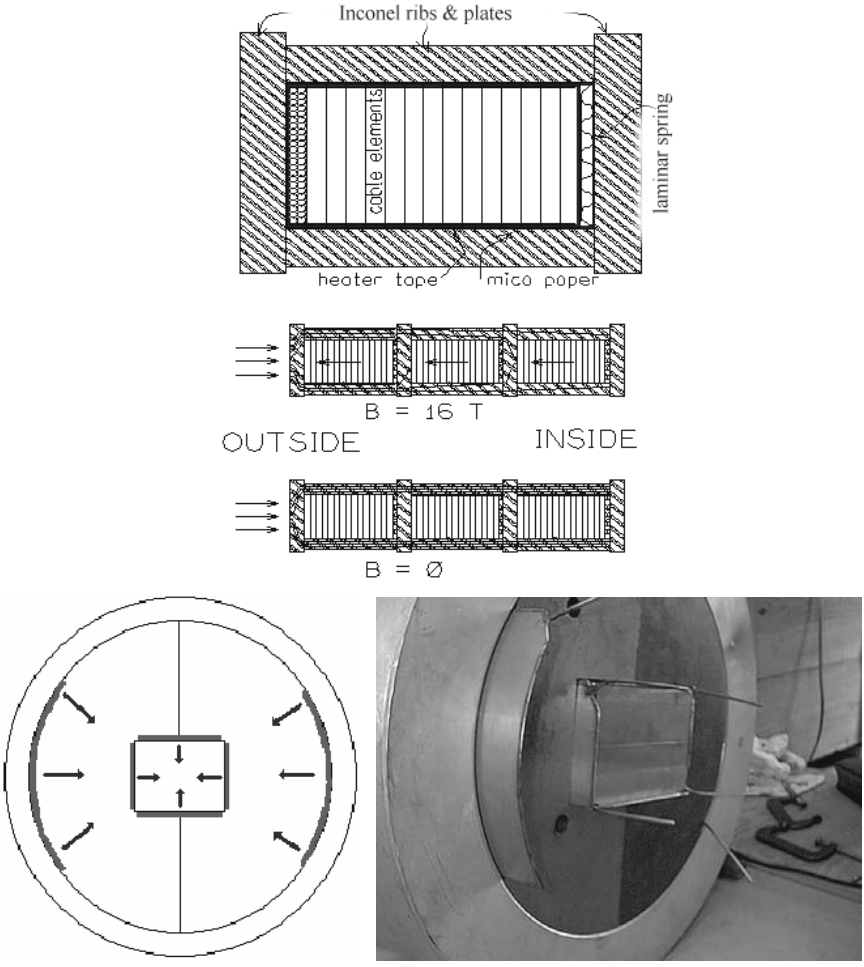

Fig. 7. Stress management in a block- coil dipole: (a) support matrix and laminar springs in coil region; (b) hydraulic bladders deliver uniform preload within coil assembly; (c) bladders assembled in flux return.

with ribs and plates of high-strength Inconel providing the support matrix. A preload is applied to the structure from the left, and Lorentz forces push to the left. A laminar spring is located at the inner end of each winding to enforce the decoupling of stress from one winding to the next. In this way, even if the overall Lorentz stress exceeds 200 MPa (which no superconductor could withstand), the stress in the windings would never exceed 70 MPa!

Figure 8 shows a design for a 14 Tesla dipole that uses Nb_3Sn superconductor and incorporates stress management [13]. We are currently building a succession of model dipoles with this design as the ultimate goal. Already

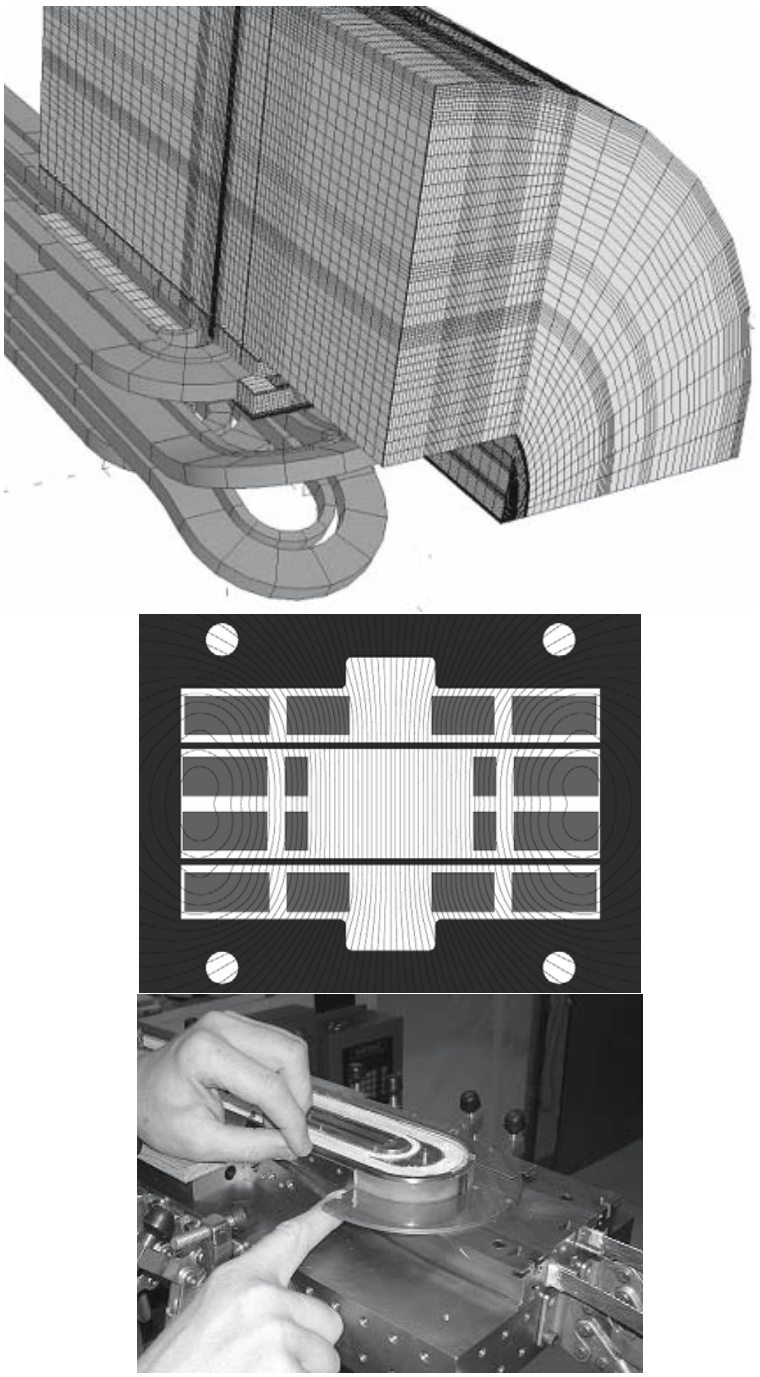

Fig. 8. 14 Tesla Nb3Sn dipole: (a) profile of dipole; (b) flux plate suppression of persistent-current multipoles; (c) close-up of coil winding.

LBNL's Supercon group has successfully tested a proof-of-principle dipole (of similar design but without central beam tube) that reached its 16 Tesla short-sample field [14].

2.3 Flux Plate Suppression of Persistent-Current Magnetization and Snap-Back

The dipole designs shown in Fig. 7 and for the Tripler in Fig. 2 also incorporate a new strategy for suppressing the magnetic multipoles that are induced by persistent currents within each strand of superconductor. When the dipole is ramped from high field (collision energy) to low field (injection of fresh beams), loops of supercurrents are induced within the filaments of each strand. Since the filament is superconducting, these induced current loops persist for very long times (hours to weeks). The magnetization from the persistent currents produces its own distribution of magnetic field in the beam tube, which can disrupt the beam at injection. This effect is further exacerbated by the "snap-back" phenomenon [5] that occurs when the current ramp is applied as the beam is accelerated. The snap-back produces a step-change in chromaticity that is already a problem to be managed at LHC and would be much worse for the larger filaments of high-field superconducting strand.

To suppress snap-back multipoles we utilize a flux plate [15] as shown in Fig. 7. The flux plates are a simple planar sheets of steel, located between winding layers just above and below the beam tube. For injections fields below the saturation of steel (1.7 T) the plates are unsaturated and produce a very strong dipole boundary condition closely coupled to the beam tube region. This boundary condition suppresses multipoles from persistent magnetization in the coils, and does so dynamically during snap-back. By this means it should be possible to control magnetization effects to a level comparable to that in LHC.

2.4 Heat Treatment for in Situ Formation of High-Field Superconductors

Both Nb_3Sn and Bi-2212 are brittle materials. If the multi-filament strands in each cable were fabricated with the final superconducting filaments within, the filaments would fracture under the bending stress of cabling and of coil winding. Over the past decade techniques have been developed to overcome this problem: the strand is fabricated as a heterogeneous composite in which each filament contains the right stoichiometry of mixed-phase materials. The coil is then heat treated to form the superconducting phase once all cabling and coil winding are finished.

This technique has been perfected for Nb_3Sn coils [4], for which the necessary heat treat is at ~650 C in an argon atmosphere, and for Bi-2212 [11], for

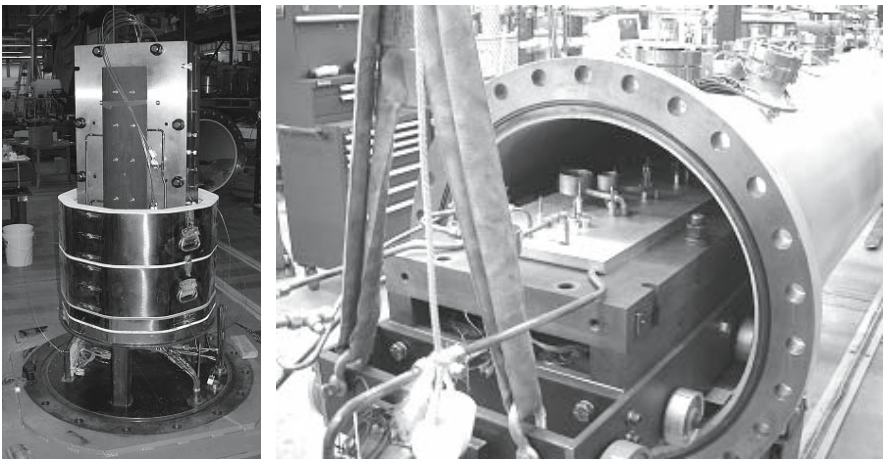

Fig. 9. Heat treat of Nb3Sn windings for the 14 Tesla dipole of Fig. 5: (a) winding assembly mounted in furnace; (b) purge manifold used for gas flow during heat treat and epoxy flow during impregnation.

which the necessary heat treat is at ∼870 C in an oxygen atmosphere. Figure 9a shows a completed Nb_3Sn coil being prepared for heat treat in a gas-purge furnace. Figure 9b shows the arrangement of purge channels that maintains gas flow throughout the coil windings during the heat treat of Nb_3Sn. and subsequently provides epoxy flow during the epoxy impregnation to stabilize the completed coil.

The challenge for a hybrid coil is that one must accomplish both of these heat treats, one for each set of windings. We have devised a means to accomplish these conflicting processes. We will first complete all of the inner Bi-2212 windings, support that portion of the coil in its final shape, and perform its heat treat. We will then wind the Nb_3Sn windings to form the outer windings and complete the coil. The box-like configuration of ribs and plates that is provided for stress management will then be used for a different purpose: to channel purge gas flow separately through the two coil regions – oxygen through the inner Bi-2212 windings and argon through the outer Bi-2212 windings. The coil will be heat treated to form the superconducting phase in the Nb_3Sn windings; the oxygen purge in the inner Bi-2212 windings during that heat treat should maintain optimum stoichiometry in the already–prepared Bi-2212 windings so that its superconducting properties will not be degraded by the second heat treat.

This 2-step process will require considerable process development, but the process should be feasible within the heat treat parameters previously established for each superconducting material when prepared individually.

3 Synchrotron Radiation and Damping

Perhaps the most obvious challenge that arises in a Tripler is the strong dependence of synchrotron radiation upon beam energy.The power per unit length that is radiated in a beam of energy E, current I and curvature radius ρ is

$$\widetilde{P} \propto \frac{E^4 I}{\rho^2}$$

So tripling the energy and keeping I and ρ constant increases the radiated power from 0.22 W/m (LHC) to 14 W/m! Already in LHC absorbing the synchrotron radiation is a major challenge, requiring an intermediate-temperature heat shield within the beam tube. It would seem at first that this issue would make a Tripler untenable.

But the *spectrum* of synchrotron light also hardens. The critical energy E_c is the peak of this spectrum:

$$E_c \propto \frac{E^3}{\rho}$$

So tripling the energy increases the critical energy from 44 eV (hard UV in LHC) to 1.2 keV (soft X-ray)! Hard UV has large cross-sections for scattering from the surface layers of anything it hits and degassing those surfaces; soft X-rays tend to penetrate into the surfaces and stop within the first ∼100 μm within the metal. It may prove possible to efficiently collect these X-rays on room-temperature photon stops located between adjacent dipoles, so that the heat budget from synchrotron radiation can be absorbed at room temperature. Figure 10 shows the conceptual design of such a photon stop from Bauer [16]. This approach has been used successfully in the arcs of some synchrotron light sources.

In another respect the enhanced synchrotron radiation may provide a significant benefit. Synchrotron radiation damps the phase space of the beam. Each proton radiates synchrotron light in a narrow cone centered on its direction of travel at the instant of radiation. Since the individual protons are describing betatron oscillations as they are focused and re-focused to the beam axis by the succession of arc quadrupoles, they radiate *transverse momentum* in this radiation. The longitudinal momentum is replaced (on average) by the RF cavities to sustain beam energy, but the transverse momentum is not, hence transverse damping.

The damping time depends strongly upon beam energy:

$$\tau = \frac{2\text{years}}{E[\text{TeV}]\ B^2[\text{T}]}$$

Transverse damping in LHC has a damping time of ∼1 day; transverse damping in the Tripler would have a damping time of ∼1 hour! It could prove useful in controlling slow beam growth and sustaining luminosity, up to limits from beam depletion from collisions and beam-beam tune shift.

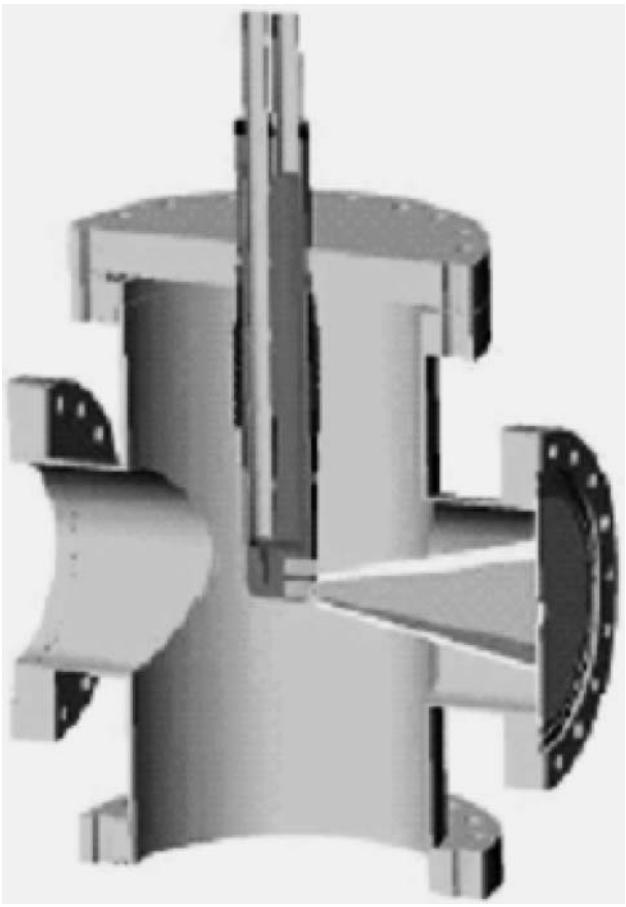

Fig. 10. Room-temperature photon stop for absorption of the fan of synchrotron light from each dipole.

4 Integration of a Tripler with LHC

The Tripler could be located directly above the LHC ring in the existing tunnel. Space in this region is very limited and it is necessary to minimize the cross-section of the Tripler while maintaining compatibility for transfer of beams from LHC (its injector) and for beam collision.

The cross-section for a high-field dual dipole is largely determined by the condition to return magnetic flux within a steel flux return structure so that the minimum fringe field is produced in the tunnel and neighboring elements. For the Tripler we have managed to shrink the size of flux return steel by utilizing a pattern of NbTi windings located on the outer surface of the flux return (see Fig. 2). The NbTi windings are used to cancel flux that would otherwise fringe beyond the steel boundary. In this way we can contain the

flux of the Tripler within a cryostat that is no larger than that of the LHC itself.

The transfer of beams from LHC to the Tripler could be done at some intermediate energy, perhaps ∼4 TeV. The dynamic range required of the Tripler dipoles would then be quite modest (6:1) compared to the 20:1 dynamic range required for the LHC dipoles.

The Tripler dipole has been designed to preserve the same beam tube spacing as that in LHC, so the crossing geometry would be similar. Of course it will be necessary to develop quadrupoles that attain the same ratio of performance to those in LHC, but in general the arc quadrupoles are less challenging to build than dipoles for a collider.

Special magnets are required in the crossing region to bring the beams to crossing and to achieve low-β focus. These magnets will be very challenging: the beams have higher stored energy and there is much greater synchrotron radiation power and greater losses from interacting protons that must be absorbed.

5 Conclusions

Thanks to developments in superconducting materials and magnet technology, it could become possible to build a Tripler for the LHC. Preliminary looks at issues of synchrotron radiation, beam transfer, and magnetic field requirements indicate that the Tripler could be feasible to operate with high luminosity. Calculation of the physics reach through gluon-gluon interactions indicates that a Tripler should provide a doubling of the mass reach for discovery of new particles of the gauge fields that have been conjectured.

The extension of superconducting magnet technology will require integration of the techniques for building, heat treating, and stabilizing windings of Nb_3Sn and Bi-2212 within a hybrid coil assembly. These techniques have been developed and proven separately, but never before integrated with one another. A great deal of technology development will be required to make hybrid-coil dipoles and to mature high-field magnets from model coil studies to manufacturable collider magnets. Given vigorous and sustained R&D support, it should be feasible to arrive at that mature technology in about a decade, in time for it to be available when the results come from the first long physics runs of LHC and we begin to ask: "Where do we go from here?"

Acknowledgements

It is a pleasure to acknowledge stimulating discussions with Richard Arnowitt and Teruki Kamon (Texas A&M University) on the impact of the Tripler on physics reach. In evaluating the physics impact, Bhaskar Dutta (University of Regina) made calculations of the gluon-gluon luminosity, and Vassilis Spanos

(University of Minnesota) provided parameter-space ivities for supergravity. Al McInturff (Texas A&M University) has been a full partner in the development of our 14 Tesla Nb_3Sn dipole and the innovations that make it feasible. Ron Scanlan and Dan Dietderich (LBNL) have pioneered the development of Rutherford cable using Bi-2212 superconducting strand, a recent successful development that is key to the feasibility of the hybrid-coil design. This work was supported in part from a grant from the US Dept. of Energy, grant DE-FG03-95ER40924.

References

1. WMAP Collaboration, D.N. Spergel et al., Astrophys. J. Suppl. **148** (2003) 175.
2. H. Baer, A. Belyaev, T. Krupovnickas and J. O'Farrill, JCAP **0408** (2004) 005; G.F. Giudice, R. Rattazzi, J.D. Wells, Nucl. Phys. **B544** (1999) 3; N. Arkani-Hamed and S. Dimopoulos, hep-ph/0409232; S. Godfrey, Phys. Rev. D**51** (1995) 1402.
3. R.A. Scanlan, "Superconducting Materials for the Next Generation Colliders", VLHC Magnet Technologies Workshop, Fermilab, May 24–26, 2000 http://tdpc02.fnal.gov/glass/vlhc_workshop/papers/SIII_P2.ppt
4. S. Gourlay, 'High field magnet R&D in the USA', IEEE Trans. On Appl. Superconductivity **14**, 333 (2004).
5. D. Finley, D. Edwards, R. Hanft, D. Johnson, A. McInturff, and J. Strait, "Time dependent chromaticity changes in the Tevatron", Proc. Particle Accel. Conf. (PAC87), Washington, DC, IEEE Cat#: 87CH2387-9, pp. 151–153; S. Sanfilippo, 'Persistent and coupling current effects in the LHC superconducting dipoles', Proc. Appl. Supercon-ductivity Conf., Houston, TX, August 4–9, 2002.
6. B. Dutta (Dept. of Physics, Univ. of Regina, Saskatchewan) calculated the parton luminosities shown in Fig. 3 (private communication).
7. E. Eichten, I. Hinchliffe, K. Lane, and C. Quigg, Rev. Mod. Phys. **56**, 579(1984).
8. CTEQ Collaboration, H. Lai et al., Phys Rev. D**55** (1997) 1280.
9. J. Ellis, K.A. Olive, Y. Santoso, and V.C. Spanos, 'Prospects for sparticle discovery in variants of the MSSM', CERN-PH-TH/2004-131, http://arxiv.org/PS_cache/hep-ph/pdf/0408/0408118.pdf
10. J. Lee and D.C. Larbalestier, "Advances in superc≥≤onducting strands for accelerator magnet application", Proc. 2003 Particle Accel. Conf., Portland, OR, May 2003.
11. Scanlan, R.M., et al, "Fabrication and test results for coils fabricated with Bi-2212 Rutherford-type cable," presented at the Applied Superconductivity Conference (ASC), Houston, TX, Aug. 4–9, 2002, SC-MAG #761, LBNL-49571.
12. N. Diaczenko et al., "Stress management in high-field dipoles", Proc. 1997 Particle Accelerator Conf, Vancouver, May 12–16, p.3443 (1997).
13. R. Blackburn et al., "Construction and testing of block-coil high-field dipoles for future hadron colliders", Proc. Appl. Superconductivity Conf., Houston, TX, August 4–9, 2002.
14. S. Mattafirri et al., "Performance analysis of HD1: a 16 Tesla Nb3Sn dipole magnet", Proc. 2004 Appl. Superconductivity Conf., Jacksonville, FL, Oct. 1–6, 2004.

15. C. Battle et al., "Optimization of block-coil dipoles for hadron colliders", Proc. Particle Accelerator Conf., New York, NY, March 30-April 1, 1999.
16. P. Bauer, et al., "Photon Stop R&D Proposal," Fermilab Technical Division Note TD-01-30.

Update on the MINOS Experiment at the Fermilab Main Injector

Robert C. Webb for the MINOS Collaboration[1]

Texas A&M University, College Station, Texas 77843-4242 USA
robert-webb@tamu.edu

Summary. The results from several experiments studying atmospheric [2, 3, 4], and solar neutrinos [5, 6, 7, 8, 9] gives a strong indication that neutrinos must have mass and therefore must oscillate. Given that neutrinos have mass and that they interact only weakly with their surroundings, they represent a portion of the dark matter contained in our universe. While it is clear that neutrinos are not the major component of this dark matter, they do represent a segment of matter for which our knowledge is rather limited. The interest in investigating the properties of these particles in more detail has lead to the staging of several "long baseline" neutrino oscillation experiments. The NuMI(Neutrinos at the Main Injector) beam at Fermilab coupled with the MINOS(Main Injector Neutrino Oscillation Search) experiment focuses on just these issues. In this paper we will describe the NuMI/MINOS programs at Fermilab and present a status report on these activities.

1 Introduction

Experiments studying the properties of atmospheric [2, 3, 4] and solar neutrinos [5, 6, 7, 8, 9] have observed fewer neutrinos than would be expected for many years. In the case of the cosmic ray induced neutrinos, the numbers of neutrinos seen are below that expected based on the flux of cosmic ray primaries on the atmosphere, and for solar neutrinos, while the observed rate of electron anti-neutrinos is below that expected from the standard solar model, the total flux of solar neutrinos in all flavors matches the solar model predictions almost perfectly [9]. These deficits of muon neutrinos for the atmospheric measurements and electron anti-neutrinos for the Sun can be explained by the oscillation of neutrinos from one flavor to another as they travel from their point of production to the point of detection. Such oscillations would arise if neutrinos had mass.

While these experiments have given a tantilizing hint of the possibility of neutrino masses, the final step in quantifying the processes involved requires a new set of long baseline neutrino oscillation experiments to be performed. One of these experiments is the Main Injector Neutrino Oscillation Search (MINOS) experiment at Fermilab using the NuMI beamline from the newly commissioned Main Injector(MI). The combination of this intense new neutrino beam and the near and far detectors of MINOS offers the opportunity to measure neutrino Δm^2 differences down to 10^{-3} eV^2.

In a long baseline experiment with both a near and far detector, we are able to measure the primary beam parameters and then project that beam flux to the far detector to compare with our observations. By having two detectors, we are able to obtain a partial cancelation of some of the systematic effects associated with our knowledge of the beam. Further, by matching the range of neutrino energies with the length of the baseline we are able to fine tune the ranges of Δm^2 we are investigating. The primary physics goal of MINOS is to measure Δm^2_{23} to the 10% level and to search for the "subdominant" oscillations of $\nu_\mu \rightarrow \nu_e$ below the levels currently set by the CHOOZ [10] experiment.

In the sections which follow, we will describe the NuMI beam and the MINOS experiment, discuss the anticipated physics reach of this program and give an update on the status of this project.

2 The NuMI Beam

The NuMI beam is produced by extracting the primary 120 GeV proton beam from the Main Injector to a pion production target in the NuMI beamline. The production target is made of carbon and has been designed to withstand the intense flux of protons(2.5×10^{13} protons per pulse) being targeted every 1.9 sec in an 8.7 msec burst. The total beam power being dissipated in the target under these conditions is 0.3 MW. The primary proton beam as well as the secondary pion beam are aimed 3.3° below the horizontal in order to have the beam strike the far detector at Soudan. A plan view of the neutrino beam is shown in Fig. 1.

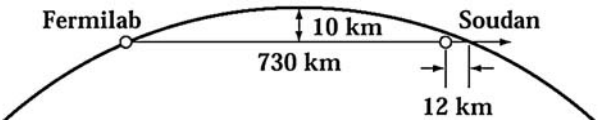

Fig. 1. A plan view of the NuMI/MINOS beam line.

The secondary π^+ beam then passes through a set of focussing horns in order to capture as much of the secondary beam flux as possible. By adjusting the relative positions of these two focussing horns with respect to the target, we are able to generate a wide range of neutrino beam energies at the location of our detectors. We classify these beam configurations as Low Energy (1–5 GeV), Medium Energy (2–10 GeV) and High Energy (7–20 GeV). The fluxes in these three beams varies in the ratio of approximately 1:2.7:5.8 respectively. By using beams of varying energy with a fixed baseline length, MINOS will be able to span a broad range of $\Delta m^2 \geq 10^{-3}$ eV^2. Figure 2 shows the energy spectra for the three beam configurations.

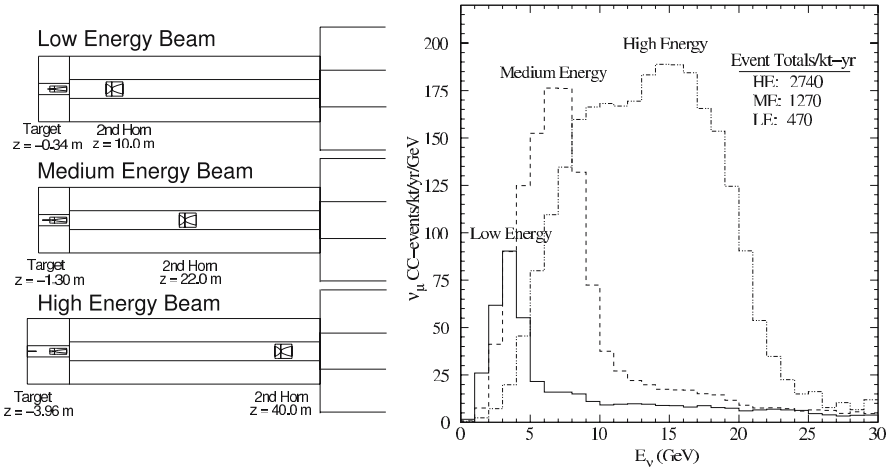

Fig. 2. This figure shows the three beam configurations to the left and the neutrino energy spectra corresponding to these NuMI beam configurations on the right.

After the pions are collected by the horns, the beam travels down a ≈ 675 meter evacuated decay pipe to allow the π^+'s to decay into μ^+ and ν_μ. The length of this decay pipe has been selected to allow for a significant fraction of the beam pions to decay in flight as they pass down this decay pipe. At 5.0 Gev/c, $\gamma c\tau \approx 200$ m for pions. At the end of the decay pipe is a hadron absorber that is designed to stop the non-interacting proton beam as well as any surviving secondaries. Following the hadron absorber is an additional ≈ 300 meters of rock absorber that is used to range out the μ^+'s in the beam. The neutrino beam then enters the near detector hall and travels through the earth 735 km to the far detector located 2500 feet below the surface at the Soudan Mine in northern Minnesota.

The civil construction of the NuMI beam line was begun in the spring of 2001. It took contractors approximately one year to dig this *down sloping* beam transport tunnel from the Main Injector extraction point to the end of the beam line in the near detector hall. The total length of this tunnel is approximately 1500 meters. From the spring of 2002 until the summer of 2004, the beamline tunnel was outfitted with beam line transport elements, target hall elements, beam line monitoring equipment and the near detector support structure. The near detector was then assembled underground in late summer of 2004 in preparation for the first NuMI beams to be delivered by the end of 2004. The first beam was successfully extracted from the Main Injector and transported to the MINOS target location and then on down the decay pipe to the hadron absorber in late November 2004 and the first neutrino interactions were observed in the near detector using NuMI beam neutrinos on January 21, 2005!

3 The MINOS Detectors

The MINOS experiment is composed of a Near Detector located at Fermilab and a Far Detector located 735 km away at the Soudan Mine. In addition to these two detectors, the collaboration has also constructed a smaller version of these detectors to be used to study the calorimetric energy response of the system to hadrons, electrons and muons. The Calibration Detector (Cal Det) was staged in several test beams at CERN to study the system's energy response over a wide range of particle energies (1–15 GeV). In the sections which follow, we will describe the overall features of these MINOS detector systems.

3.1 The Far Detector at Soudan

Each of the three MINOS detectors is composed of the same basic ingredients. All are fine grained Fe/scintillator sampling calorimeters with 2.54 cm thick steel plates and strips of extruded scintillator 1cm X 4 cm in cross section and varying lengths. In the Far Detector, each of the scintillator strips is readout from both ends using a 1.2 mm diameter wavelength shifting fiber through the scintillator coupled to a clear fiber cable on the outside of the detector. The clear fibers are then routed to the face of a multi-anode photomultiplier(M-16) for readout into the data acquisition system.

The Far Detector is composed of 8 m diameter octagonal sheets of 2.54 cm thick steel plates upon which we have mounted 8 detector modules containing 198 individual scintillator strips of varying lengths. Successive planes are rotated with respect to the axis of the detector by $\pm 45^{o}$ to provide two stereo views for tracking. There are a total of 485 such planes in the Far Detector, separated into two sections each approximately 15 meters long called supermodules. Each supermodule has a coil inserted down the axis of the octagon with the coil return traveling back down the detector along the floor. This coil is used to magnetize the calorimeter with a toroidal magnetic field that is 1.5 T at 2.0 m from the coil hole. The total mass of the Far Detector is $\approx 5,400$ tons. Figure 3 shows an end view of the completed Far Detector at the soudan Lab.

Due to cost considerations, the readout of the individual scintillator strips in the detector is multiplexed bringing 8 fibers from 8 widely spaced scintillator strips to a given pixel on a multi-anode pmt. Given that the typical lateral size of a hadronic shower in our detector is ≈ 1 m, we group fibers on a given pixel that are displaced by approximately 1 meter across the face of the detector. The multiplexing pattern on the two ends of the detector are different, allowing us to "de-multiplex" the data being readout, to position it appropriately within the fiducial volume.

In the Far Detector, we record the pulseheight and timing of every energy deposit above a fraction of a photoelectron in the detector and then ship this information to the trigger processors to develop a "trigger" and record

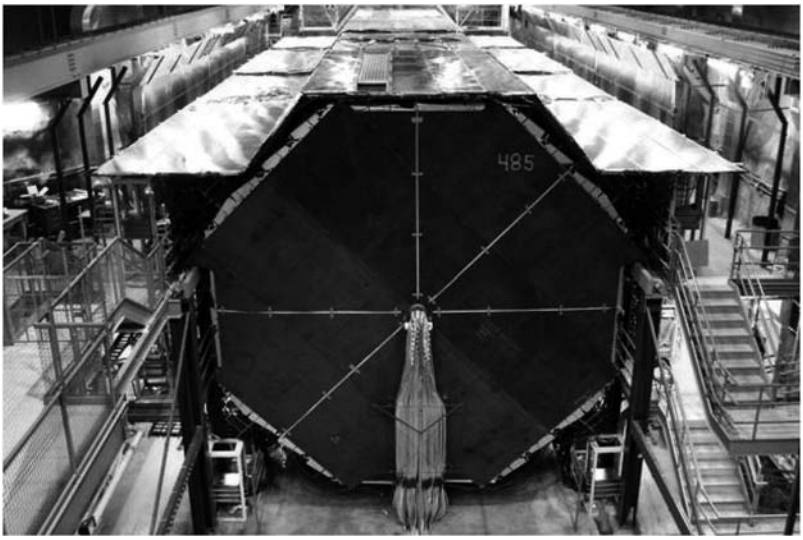

Fig. 3. Photo of the MINOS far detector after the 485th plane was hung in place on July, 2003.

data for offline analysis. The trigger processor sorts through all of the time stamped data looking for correlations in time within the detector. Once it finds a collection of energy deposits within a 100 ns time window, this data is flagged as an event and shipped to the data archive for further processing. A sample two muon event recorded with a fraction of the first supermodule is shown in Fig. 4.

The far detector construction was begun in 2000 with the excavation of the far detector hall at the Soudan Mine. By the summer of 2001 we began the assembly of the far detector and finished this job almost two years later in the summer of 2003. Since that time, the far detector has been taking cosmic ray data which we have used to commission the detector. Using real cosmic ray data to commission the detector has allowed us to confirm that the system is working properly as well as giving us a source of data that can be used to develop the analysis programs needed to mine the physics out of the coming beam neutrino data set.

3.2 The Near Detector at Fermilab

The Near Detector, located following the rock absorber in the NuMI beam line at Fermilab, is composed of elements similar in makeup to those being used for the Far Detector. However, due to the increased flux of neutrinos at the Near Detector location, the mass of detector required is only 1/5 of that in the Far Detector and even at that a different DAQ system must be used to deal with the higher rates.

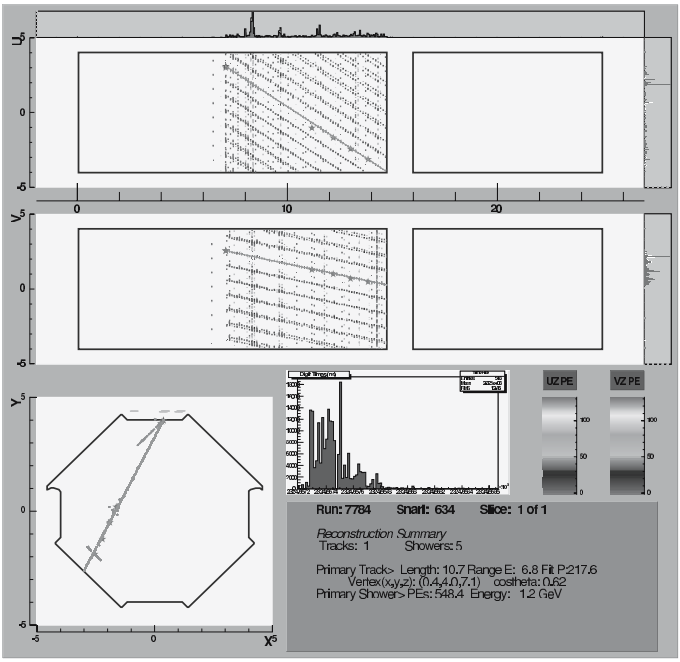

Fig. 4. A sample event display from the Far Detector showing a downward traveling muon.

The detector is again an array of steel and scintillator planes, arranged in the form of a *squashed* octagon. Each *squashed* octagon is 4.8 m wide and 3.8 m high with a coil hole slightly offset from the center of the plate. There are 282 such planes in the near detector, that are magnetized to have a toroidal field similar to that in the Far Detector. The first 120 planes contain the target and calorimeter region of the detector. In this section, 4 out of 5 planes are instrumented only on the beam side of the coil hole and every 5th plane has the entire surface of the *squashed* octagon instrumented with scintillator strips. Following these planes is 162 planes of the spectrometer section. This section is used primarily to measure muon momenta in charged current events and as such only 1 out of 5 planes in this section is fully instrumented. The near detector is 16.6 m long and has a mass of 980 tons.

The scintillator modules in the near detector are composed of the same 4.0 cm $\times$ 1.0 cm strips readout by 1.2 mm diameter wavelength shifting fibers like the Far Detector. However, for the Near Detector, we readout only one end of the fiber and have mirrored the far end to collect the light from the opposite side of the detector. The wavelength shifting fibers at the edge of the detector are then connected to clear fiber cables, which bring the light signals from the detector to the multi-anode photomultipliers(M-64) being used to readout these signals. Due to the smaller number of fibers in the

Near Detector and the larger number of pixels per tube in the M-64s, the fibers in the Near Detector are not multiplexed.

The electronics and triggering in the Near Detector are somewhat different than those described for the Far Detector due to the higher data rates found there. In the Near Detector the pulse height and timing of the energy deposits in the detector are again recorded, however this time they are stored in 5 ns time slices locked to the 19.4 nsec RF structure of the proton/pion beam. We are using a custom designed QIE based system to record this data. Pulse height and timing information from the detector is grouped by RF bucket and those buckets with non-zero data are saved for offline analysis.

The construction of the near detector elements began on the surface in the new Muon Building at Fermilab back in 2003. Then in the summer of 2004, after the collaboration was given beneficial occupancy of the detector hall, we began the installation, hook up and check out of the near detector. The near detector was completed by the end of the summer of 2004 and since that time has been taking data using cosmic rays in much the same way as we have been running the far detector since 2003. As mentioned earlier, the first beam neutrino interaction was recorded in the near detector on January 21, 2005. The display of this event is shown in the Fig. 5.

3.3 The MINOS Calibration Detector

In order to be able to maintain the systematic errors between the Near and Far Detector in the few % range, we built a third, smaller version

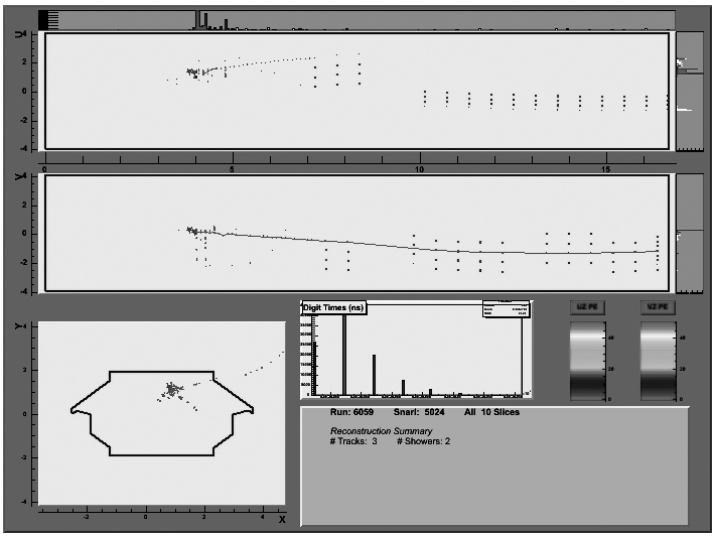

Fig. 5. Event display for the **first** neutrino event recorded in the MINOS Near detector on January 21, 2005.

of the MINOS detectors that could be setup in a testbeam. This Calibration Detector or Cal Det was staged at CERN and was made up of 60 1.0 m × 1.0 m × 2.54 cm steel plates with an equal number of specially constructed MINOS scintillator modules. The steel in the Cal Det was not magnetized.

These scintillator modules were readout in three ways during these beam tests. First, they were readout using the Far Detector electronics on both ends of the fibers being readout, then they were readout with Far Detector electronics reading out one side of the modules and with Near Detector electronics reading out the other and lastly, they were readout with only Near Detector electronics on one side and a mirrored connector on the opposite side of the modules.

We calibrated the MINOS calorimeter system in these three different electronics configurations using beams of hadrons, muons and electrons. Our first test beam run was completed in the spring of 2001 in the T11 beamline at energies up to 3.0 GeV and then there were subsequent runs in 2002 and 2003 to complete the program of calibration measurements.

We use the response of the three detectors to muons as our energy standard for setting the absolute energy scales in the Near and Far Detectors. We then monitor any drifts of this energy calibration over time using a programmable light injection system that can inject light into every fiber in the detector. Setting and maintaining the energy calibration of MINOS is critically important, since our knowledge of the total energy of each event directly impacts our measurement error on Δm^2.

From the Cal Det measurements we established that the MINOS calorimeter has a resolution of $\sigma/E = 55\%/\sqrt{E}$ for hadronic showers and has a $\sigma/E = 23\%/\sqrt{E}$ for electromagnetic showers.

4 MINOS Physics Reach

In MINOS we search for neutrino oscillation effects by comparing the rates of neutrino interactions in the Far and Near Detectors as a function of neutrino energy. We will compare the rates in the Far Detector to those based on the rates seen in the Near Detector, projected to the Far Detector accounting for beam transmission and hadron production effects. Any differences observed between the expected and observed rates will be attributable to neutrino oscillations or some other new and exotic effect.

In order to make the most convincing experiment possible, we take three basic approaches to measurement of neutrino oscillation parameters. First, we wish to make the measurement using a number of different physics signatures. Since the measurements all make use of the same beam, they are not completely free of correlated systematic error. However, the systematic errors for the different measurements will largely be uncorrelated. We should be able

to require consistency between the measurements. Second, whenever possible, we use ratios in order to limit the systematic errors involved in absolute normalizations. Finally, we wish to demonstrate clear appearance signatures for the neutrino flavor which the muon neutrinos have oscillated to. For electron neutrinos, this means identification of the electron in charged-current interactions. For tau-neutrinos, we know of no means of either explicitly reconstructing the tau mass or of observing a secondary vertex resulting from the tau decay in our detector. Hence, we resort to statistical means to identify tau appearance based on the different possible tau decay modes.

The results of simulation studies that have been carried out on charged current events can be used to illustrate the sensitivity of MINOS to neutrino oscillation effects. In Fig. 6, we show the energy spectra of charge current(CC) events expected in the Far Detector over a range of Δm^2 using the low energy beam with an exposure of 10 kt yr. This range overlaps with that suggested from the Super Kamiokande data [2]. The top plots show the un-oscillated(solid line) and oscillated spectra for the oscillation parameters noted. The bottom plots in this figure show the ratio between these spectra. Figure 7 shows the 90% CL ellipses for the three values of Δm^2 presented in the previous figure.

In addition to the data on CC events, we will be able to make measurements of other sub-dominant oscillation modes allowing us to make modest improvements in the limits from CHOOZ [10].

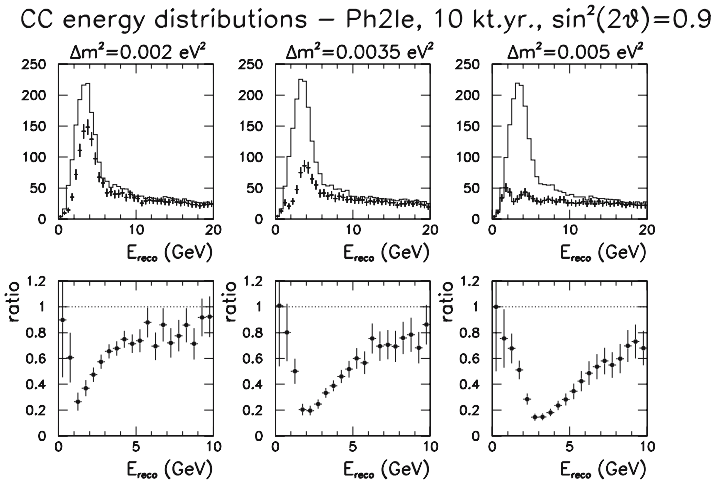

Fig. 6. MC study of Charged Current interactions from the Low Energy NuMI beam configuration with a total exposure of 10 kt yr for three different Δm^2 values as noted. The top row of plots shows the observed energy spectrum of events without (solid line) and with oscillations (data points) for these three Δm^2 values. The bottom row of plots shows the ratio of oscillated to unoscillated events as a function of energy for the three cases.

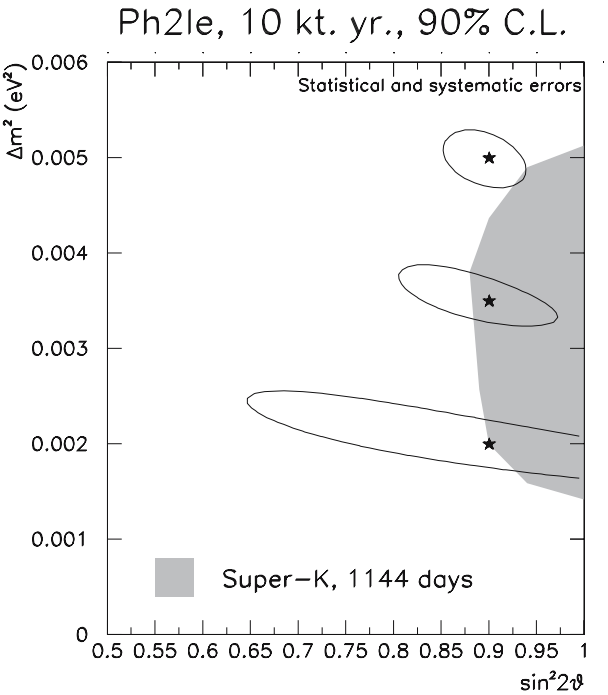

Fig. 7. The 90% Confidence Level ellipses for the three Δm^2 values compared to the Super Kamiokande results for 1144 days of data. For MINOS we are using the Low Energy beam with a 10 kt-yr exposure.

5 Summary

The MINOS experiment will open a new window on the study of neutrino oscillations as the NuMI beam comes on-line for production data taking. With the high statistics data set and control of systematics expected in 10 kt yrs of running with the NuMI beam, the collaboration is in a strong position to make direct measurements of the ν_μ oscillation parameters by early 2006.

Acknowledgements

The the author wishes to acknowledge the support of the MINOS/NuMI collaboration whose work is being presented here. Further, we wish to acknowledge the support of the MINOS/NuMI project from the United States Department of Energy and the National Science Foundation.

References

1. The MINOS collaboration is an international collaboration with participants from the following institutions: Argonne National Laboratory, University of Athens, Brookhaven National Laboratory, Caltech, Cambridge University, College de France, Fermi National Accelerator Laboratory, Harvard University, Illinois Institute of Technology, Indiana University, ITEP-Moscow, Lebedev, Livermore National Laboratory, University College London, University of Minnesota, University of Minnesota Duluth, Northwestern University, Oxford University, University of Pittsburgh, Protvino, Rutherford Laboratory, University of South Carolina, Stanford University, University of Sussex, Texas A&M University, University of Texas Austin, Tufts University, Universidade Estadual de Campinas, Universidade de Sao Paulo, Western Washington University, University of Wisconsin.
2. S. Hatakeyama et al., Phys. Rev. Lett. **81**, 2016 (1998).
3. M. Ambrosio et al., Phys. Lett. **B434**, 451 (1998).
4. W.W. Allison et al., Phys. Lett. **B449**, 137 (1999).
5. R. Davis et al., Phys. Rev. Lett., **20**, 1205 (1968).
6. M. Altmann et al., Phys. Lett. **B490**, 16 (2000).
7. J.N. Abdurashitov et al., Phys. Rev. **C59**, 2246 (1999).
8. Y. Takeuchi, Solar Neutrino Results from Super-Kamiokande, in: Proc. Ninth International Workshop on Neutrino Telescopes (ed. M. Baldo Ceolin, Venice, March, 2001), **1**, 77 (2001).
9. Q.R. Ahmad et al., Phys. Rev. Lett. **87**, 071301 (2001).
10. M. Apollonio, et al., Phys. Lett. B **466**, 415.

Part IV

Cosmology, Baryogenesis, Dark Energy

Kinematics and Dark Energy from Supernovae at $z > 1$

Adam G. Riess

Space Telescope Science Institute, 3700 San Martin Drive, Baltimore, MD 21218

Summary. We have discovered 16 Type Ia supernovae (SNe Ia) with the *Hubble Space Telescope (HST)* and have used them to provide the first conclusive evidence for cosmic deceleration that preceded the current epoch of cosmic acceleration. Joint constraints on both the recent equation of state of dark energy, w_0, and its time evolution, dw/dz, are a factor of ~ 8 more precise than its first estimate and twice as precise as those without the SNe Ia discovered with *HST*. Our constraints are consistent with the static nature of and value of w expected for a cosmological constant (i.e., $w_0 = -1.0$, $dw/dz = 0$), and are inconsistent with very rapid evolution of dark energy.

1 Introduction

Observations of type Ia supernovae (SNe Ia) at redshift $z < 1$ provide startling and puzzling evidence that the expansion of the Universe at the present time appears to be *accelerating*, behavior attributed to "dark energy" with negative pressure (Riess et al. 1998; Perlmutter et al. 1999; for reviews, see Riess 2000; Filippenko 2001, 2004; Leibundgut 2001). Direct evidence comes from the apparent faintness of SNe Ia at $z \approx 0.5$. Recently expanded samples of SNe Ia have reinforced the statistical significance of this result (Knop et al. 2003) while others have also extended the SN Ia sample to $z \approx 1$ (Tonry et al. 2003; Barris et al. 2004). Observations of large-scale structure (LSS), when combined with measurements of the characteristic angular size of fluctuations in the cosmic microwave background (CMB), provide independent (though indirect) evidence for a dark-energy component (e.g., Spergel et al. 2003). An independent, albeit more tentative investigation via the integrated Sachs-Wolfe (ISW) effect also provides evidence for dark energy (Scranton et al. 2003). The magnitude of the observed acceleration was not anticipated by theory and continues to defy a *post facto* explanation. Candidates for the dark energy include Einstein's cosmological constant Λ (with a phenomenally small value), evolving scalar fields (modern cousins of the inflation field; Caldwell, Davé, & Steinhardt 1998; Peebles & Ratra 2002), and a weakening of gravity in our $3 + 1$ dimensions by leaking into the higher dimensions required in string theories (Deffayet, Dvali, & Gabadadze 2002). These explanations bear so greatly on fundamental physics that observers have been

stimulated to make extraordinary efforts to confirm the initial results on dark energy, test possible sources of error, and extend our empirical knowledge of this newly discovered component of the Universe.

Astrophysical effects could imitate the direct evidence from SNe Ia for an accelerating Universe. A pervasive screen of grey dust could dim SNe Ia with little telltale reddening (Aguirre 1999a,b). Luminosity evolution could corrupt the measurements if SNe Ia at $z \approx 0.5$ are intrinsically fainter than their low-redshift counterparts. To date, no evidence for an astrophysical origin of the apparent faintness of SNe Ia has been found (Riess 2000; Coil et al. 2001; Leibundgut 2001; Sullivan et al. 2003). However, given the significance of the putative dark energy and the unique ability of SNe Ia to illuminate it, we need a more definitive test of the hypothesis that supernovae at $z \sim 0.5$ are intrinsically dimmer, or dimmed by absorption.

If cosmic acceleration is the reason why SNe Ia are dimmer at $z \sim 0.5$, then we expect cosmic deceleration at $z > 1$ to reverse the sign of the observed effect. The combination of recent acceleration and past deceleration is a clear signature of a mixed dark-matter and dark-energy Universe and one which is readily distinguishable from simple astrophysical dimming (Filippenko & Riess 2001).

Furthermore, assuming SNe Ia at $z > 1$ continue to trace the cosmological world model, measurements of SNe Ia in the next redshift octave provide the unique ability to discriminate between a static and evolving dark-energy equation of state. This would provide a vital clue to distinguish a cosmological constant from other forms of dark energy that change with time.

Ground-based efforts to look for past deceleration with SNe Ia have offered hints of the effect, but ultimately they have suffered from insufficient signal-to-noise ratios (Tonry et al. 2003; Barris et al. 2004). Discovering, confirming, and then monitoring transients at $I \approx 25$ mag on the bright sky is challenging even with the largest telescopes and the best conditions. A single SN Ia at $z \approx 1.7$, SN 1997ff, discovered with WFPC2 on the *Hubble Space Telescope (HST)* (Gilliland, Nugent, & Phillips 1999), provided a hint of past deceleration; however, inferences drawn from a single SN Ia, while plausible, are not robust (Riess et al. 2001; Benítez et al. 2002; Goobar & Mortsal 2001).

To study the early expansion history of the Universe, we initiated the first systematic, space-based search and follow-up effort to collect SNe Ia at $z > 1$, carried out in conjunction with the Great Observatories Origins Deep Survey (GOODS) Treasury program (Giavalisco et al. 2003) conducted with the Advanced Camera for Surveys (ACS) aboard *HST*.

2 Collecting SNe from Space

Our search was conducted in the $F850LP$ (Z-band) to an effective limit of $\sim$26.0 (Vega) magnitude covering 0.1 square degree in 5 epochs (at intervals of $\sim$45 days). Our limiting magnitude was 1 to 2 mag fainter than the expected

peak of a SN Ia over the target range of $1 < z < 1.6$, therefore SNe Ia we collected (whose intrinsic dispersion is expected to be < 0.2 mag)would not preferentially be selected from the bright tail of their intrinsic distribution. Our ToO candidates were generally too faint to anticipate useful spectral discrimination from the ground; it was therefore necessary to *initially* identify SNe Ia photometrically. To discriminate SNe Ia at $z > 1$ from SNe II and from SNe I at lower redshifts, we used a combination of photometric redshifts of the host galaxies (with 9 passbands) and rest-frame ultraviolet (UV) colors; see Riess et al. (2003) for details. Figure 1 shows the UV color diagnostic for the SNe Ia found with HST.

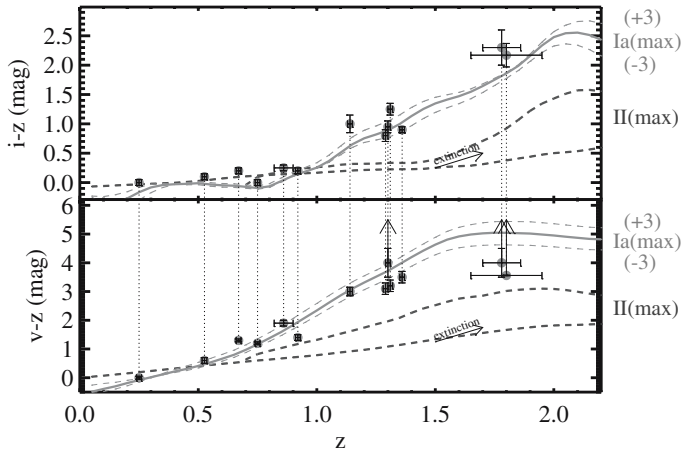

Fig. 1. Finding and classifying SNe Ia with ACS via the UV deficit. The expected $i - z$ and $v - z$ colors of SNe Ia and SNe II near maximum brightness compared to the observed colors of candidate SNe Ia found in GOODs data. SNe Ia are readily distinguishable from SNe II by their red colors. Reddened SNe II would be too faint for this magnitude-limited sample. SNe shown at $z < 1.5$ were independently confirmed to be SNe Ia.

We obtained multi-color light curves and spectroscopic redshifts for 16 new SNe Ia which uniformly sample the redshift range $0.2 < z < 1.6$. Twelve of these are classified by their spectra, 2 from their red, early-type host galaxies, and 2 by photometric diagnostics. Three of the SN spectra are at the highest redshifts yet observed for SNe (see Fig. 2). Six of the SNe Ia are among the seven highest-redshift known; all are at $z > 1.25$. These data provide a robust extension of the Hubble diagram to $1 < z < 1.6$.

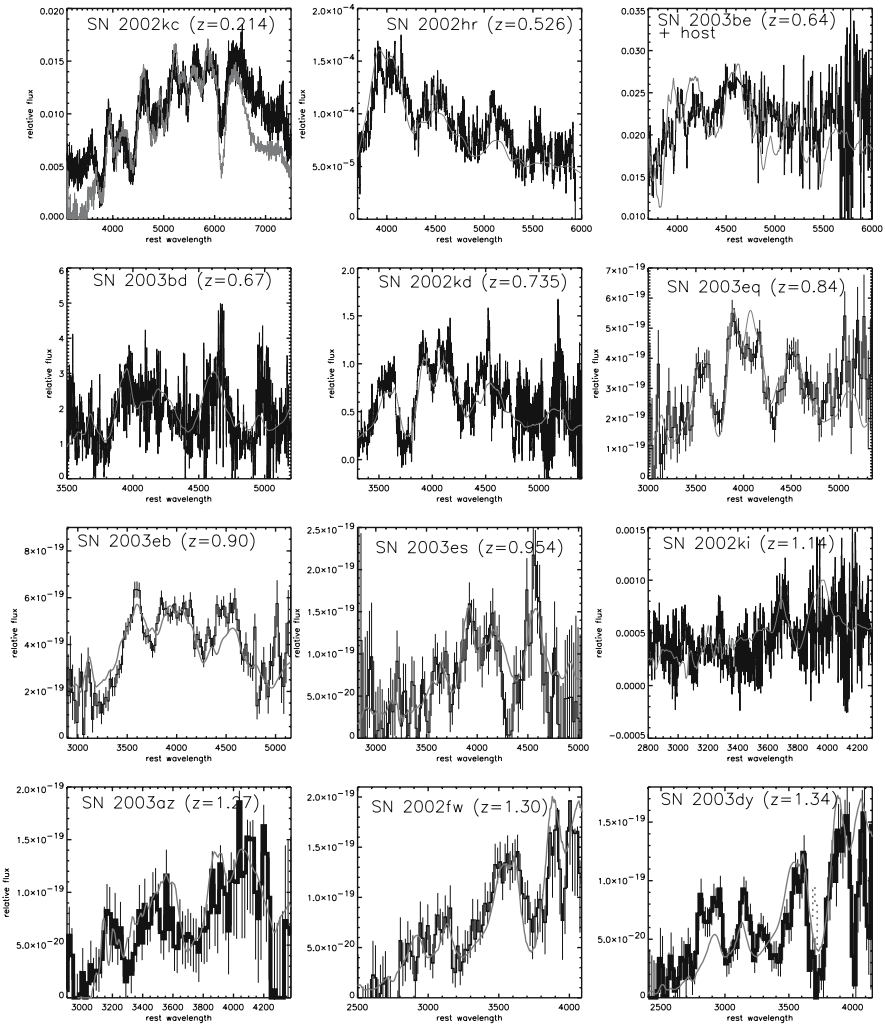

Fig. 2. Identification spectra (in f_λ) of 12 of the new *HST*-discovered high-redshift SNe Ia, shown in the rest frame. Classification features are analyzed in Sect. 2.3. The data are compared to nearby SN Ia spectra of the same age as determined by the light curves.

3 Kinematics

Here we show the Hubble diagram of distance moduli and redshifts for the new HST-discovered SNe Ia in the gold and silver sets (see Fig. 3). Although these new SNe Ia span a wide range of redshift ($0.21 < z < 1.55$), their most valuable contribution to the SN Ia Hubble diagram is in the highest-redshift region where they effectively delineate the range at $0.85 < z < 1.55$ with 11

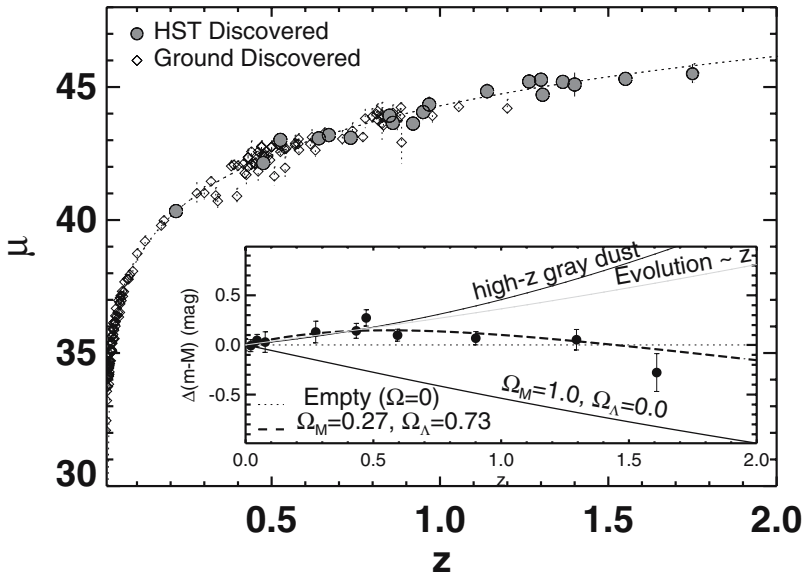

Fig. 3. MLCS2k2 SN Ia Hubble diagram. SNe Ia from ground-based discoveries in the gold sample are shown as diamonds, *HST*-discovered SNe Ia are shown as filled symbols. Overplotted is the best fit for a flat cosmology: $\Omega_M = 0.29$, $\Omega_\Lambda = 0.71$. Inset: SN Ia residual Hubble diagram comparing cosmological models and models for astrophysical dimming. Upper panel: SNe Ia from ground-based discoveries in the gold sample are shown as diamonds, *HST*-discovered SNe Ia are shown as filled symbols. Bottom panel: weighted averages in fixed redshift bins are given for illustrative purposes only. Data and models are shown relative to an empty Universe model ($\Omega = 0$).

new SNe Ia, including 6 of the 7 highest-redshift SNe known (the seventh being SN 1997ff; Riess et al. 2001).

The relationship between distance and redshift over a significant fraction of the Hubble time can be considered either empirically as a record of the (integrated) expansion history of the Universe, or theoretically as constraints on the mass-energy terms contained in the Friedman equation and affecting the expansion. Here we consider both approaches.

Given evidence that the Universe has recently been accelerating [i.e., $q(z \sim 0) < 0$], hints that it may have once been decelerating [i.e., $q(z > 1) > 0$; Riess et al. 2001; Turner & Riess 2002], and the large leverage in redshift of the current SN sample, we consider resolving $q(z)$ into two distinct components or epochs. A linear two-parameter expansion for $q(z)$ which is continuous and smooth is $q(z) = q_0 + z dq/dz$, where dq/dz is defined to be evaluated at $z = 0$.

We find that the SNe Ia favor recent acceleration and past deceleration at the 99.2% confidence level. An alternate kinematic parameterization requires

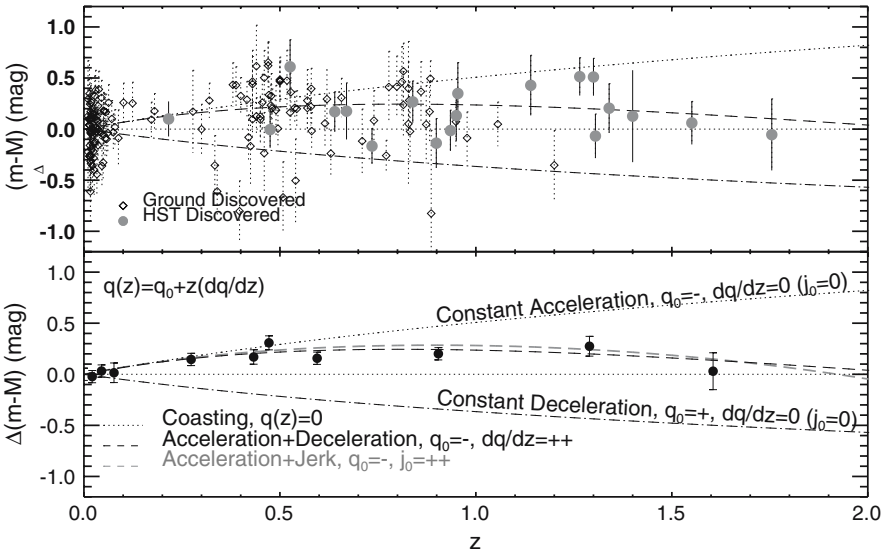

Fig. 4. Kinematic SN Ia residual Hubble diagram. Upper panel: SNe Ia from ground-based discoveries in the gold sample are shown as diamonds, *HST*-discovered SNe Ia are shown as filled symbols. Bottom panel: weighted averages in fixed redshift bins are given for illustrative purposes only. Data and kinematic models of the expansion history are shown relative to an eternally coasting model, $q(z) = 0$. Models representing specific kinematic scenarios (e.g., "constant acceleration") are illustrated.

a positive jerk (third derivative of the scale factor). The best-fit redshift of the transition between these kinematic phases is $z = 0.46 \pm 0.13$, although the precise value depends on the kinematic model employed (see Fig. 4).

4 Astrophysical Dimming or Dark Energy?

SNe Ia at $z \approx 0.5$ appear fainter by $\sim$0.25 mag relative to a Universe with $\Omega_M = 0.3$ and $\Omega_\Lambda = 0$, a result readily accommodated by a cosmological constant with $\Omega_\Lambda = 0.7$ (Riess et al. 1998; Perlmutter et al. 1999). Despite the lack of any independent evidence, an alternative explanation for this dimming could lie in the astrophysics of supernovae or in the propogation of their light to us.

We have compared the goodness-of-fit of cosmological models and simple models of astrophysical dimming. The "gold" sample of 157 SNe Ia is consistent with the "cosmic concordance" model ($\Omega_M = 0.3, \Omega_\Lambda = 0.7$) with $\chi^2_{dof} = 1.06$. The data reject at high-confidence simple, monotonic models of astrophysical dimming which are tuned to mimic the evidence for acceleration at $z \approx 0.5$. See the inset in Fig. 3. These models include either a universe filled

with gray dust at high redshift, or luminosity evolution $\propto z$. More complex parameterizations of astrophysical dimming which peak at $z \approx 0.5$ and dissipate at $z > 1$ remain consistent with the SN data (but appear unattractive on other grounds).

5 Exploring Dark Energy

Despite the results of the last section which favor the dark-energy interpretation of SNe Ia, we avoid using this conclusion as a starting point for exploring the nature of dark energy. Instead, we embark on a parallel study from the previous section. We can use distance-independent information to justify the cosmological interpretation of SNe Ia and combine with other experiments to study dark energy. Based on such evidence, we will adopt in the following analysis an a priori constraint that the net *astrophysical* contamination of SN Ia distance measures does not exceed their statistical uncertainty in their mean brightness. Quantitatively, our adopted limit on systematics is defined to be 5% per Δz at $z > 0.1$.

First we consider the SN data within an FRW cosmology of unknown curvature and mass density (with a flat prior on all parameters), with the simplest description of a dark-energy component (i.e., a cosmological constant). Joint confidence intervals in the $\Omega_M - \Omega_\Lambda$ plane were derived after numerical integration of the probability density $P(H_0) \propto \exp(-\chi^2(H_0)/2)$ over all values of H_0 and are shown in Fig. 5. Compared to the same analysis in Riess et al. (1998), the gold sample presented here reduces the area of the 1σ contour by a factor of 6 (a factor of 7 including the silver sample). With the current sample, the 4σ confidence intervals (i.e., $> 99.99\%$ confidence) are now fully contained within the region where $\Omega_\Lambda > 0$. The "concordance" model, of $\Omega_M = 0.27, \Omega_\Lambda = 0.73$ lies within the 1σ contour.

An ambitious plan and potentially more revealing approach to studying dark energy is to allow for an unconstrained value of the equation of state $w = P/\rho c^2$ (at some fiducial redshift, e.g., $z = 0$) and its time evolution, i.e., $w(z) = w_0 + w'z$, where $w' \equiv \frac{dw}{dz}|_{z=0}$. Flatness is assumed either on theoretical grounds (i.e., as a consequence of inflation) or on observational grounds from the characteristic angular size scale of the CMB fluctuations (Spergel et al. 2003, and references therein). This parameterization provides the minimum possible resolving power to distinguish a cosmological constant and a rolling scalar field from their time variation (or lack thereof). Indeed, rejection of the hypothesis that $w' = 0$ would rule out a cosmological constant as the dark energy (as would the determination that $w \neq -1$). The measured value of w' would provide an estimate of the scale length of a dark-energy potential. The only previous estimate of w', by Di Pietro & Claeskens (2003), used the set of SNe Ia from Perlmutter et al. (1999) and the constraints $\Omega_{total} \equiv 1$ and $\Omega_M \equiv 0.3$, and concluded $-12 < w' < 12$ at the 95% confidence level (best fit: $w_0 = -1.4, w' = 2.3$).

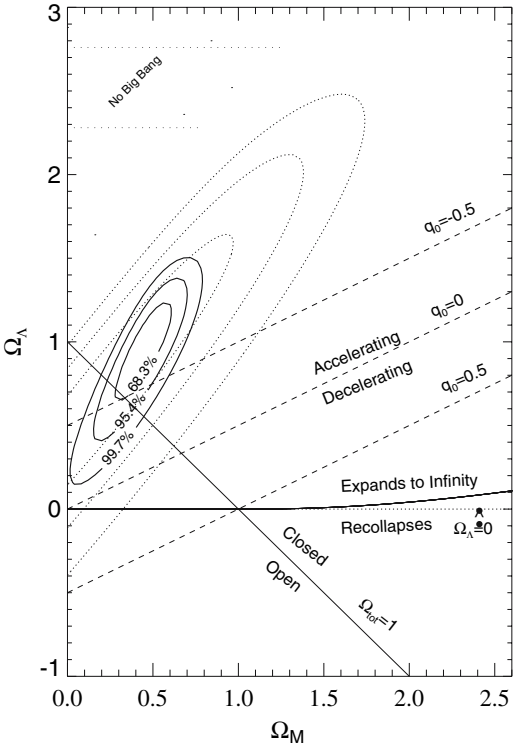

Fig. 5. Joint confidence intervals for (Ω_M,Ω_Λ) from SNe Ia. The solid contours are results from the gold sample of 157 SNe Ia presented here. The dotted contours are the results from Riess et al. (1998) illustrating the earlier evidence for $\Omega_\Lambda > 0$. Regions representing specific cosmological scenarios are illustrated. Contours are closed by their intersection with the line $\Omega_M = 0$.

For $w(z) = w_0 + w'z$, (following Linder 2003) we find joint constraints on both the recent equation of state of dark energy and its time evolution are a factor of ~ 8 more precise than its first estimate and twice more precise than those derived without the SNe Ia discovered by *HST*. Both of these dark energy properties are consistent with a cosmological constant (i.e., with $w_0 = -1.0$, $w' = 0$) and are inconsistent with very rapid evolution of dark energy (i.e., $|w'| >$ a few). See Fig. 6. The absence of rapid evolution places constraints on the time in which a simple scalar field could evolve to recollapse the Universe. Specifically, the timescale to a potential recollapse is larger than $\sim$30 Gyr. If dark energy is evolving towards more negative w, we cannot place any meaningful limit on the minimum time to a (speculative) Big Rip.

It is tempting to consider that we have reached the end of the beginning in the exploration of dark energy. Two reliable and independent routes require it in addition to a third more tentative investigation via the integrated Sachs-

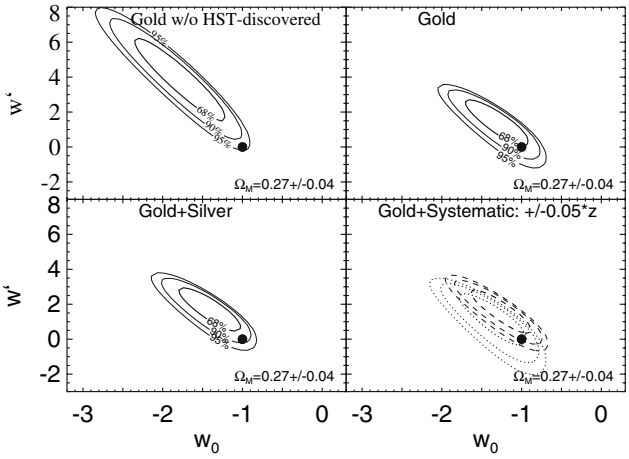

Fig. 6. Joint confidence intervals derived from SN samples for a two-parameter model of the equation of state of dark energy, $w(z) = w_0 + w'z$. For each panel, constraints from a SN sample is combined with the prior, $\Omega_M = 0.27 \pm 0.04$, to yield the indicated confidence intervals. The position of a cosmological constant $(-1, 0)$ is indicated as a filled symbol. The lower-right panel shows the impact of adding or subtracting a systematic error in distance modulus of $0.05z$ mag to the gold sample.

Wolfe effect (Scranton et al. 2003). SNe Ia continue to provide the most direct route to illuminating dark energy because their light can be measured propagating from within its era of dominance. Two clues about dark energy, its equation of state and its recent time evolution, would be invaluable aids to test and provoke theories. We suggest that the most efficient way forward in the near term is by simultaneously mining both ends of the observable redshift range: at $z < 1$ generally from the ground, and at $z > 1$ generally from space. The constraints presented here in the $w_0 - w'$ plane have reduced the allowable range of w' from a factor of ~ 10 to less than ~ 1 while retaining the constraints on w_0 within $-1.4 < w_0 < -0.7$. With continued determination,an improvement in precision by a factor of a few in this plane is expected.

Acknowledgments

We thank the organizers for a wonderful conference.

References

1. B. Barris et al., ApJ (2004) in press

2. C. Bennett et al., ApJS 148 (2003) 1
3. J.P. Blakeslee et al., ApJ (2003) in press (astro-ph/0302402)
4. R.R. Caldwell, R. Davé & P. Steinhardt, Ap&SS 261 91998) 303
5. C. Deffayet, G. Dvali & G. Gabadadze, Phys. Rev. D65 (2002) 044023
6. A.V. Filippenko, ARA&A 35 (1997) 309
7. P.M. Garnavich et al., ApJ 509 (1998) 74
8. M. Giavalisco et al., ApJL (2003) in press (astro-ph/0309105)
9. R.L. Gilliland, P.E. Nugent & M.M. Phillips, ApJ 521 (1999) 30
10. E.V. Linder, Phys. Rev. Lett. 90 (2003) 91301
11. E.V. Linder & D. Huterer, Phys. Rev. D67 (2003) 81303
12. S. Perlmutter et al., ApJ 483 (1997) 565
13. S. Perlmutter et al., ApJ 517 (1999) 565
14. A.G. Riess, PASP 112 (2000) 1284
15. A.G. Riess et al., AJ 116 (1998) 1009
16. M. Turner & A.G. Riess, ApJ 569 (2001) 18
17. R. Scranton et al., Phys. Rev. Lett. (2003) submitted (astro-ph/0307335)

Low Redshift (z < 1) Supernova Studies

Wendy L. Freedman

Carnegie Observatories, 813 Santa Barbara St., Pasadena, CA 91101, USA

Summary. The evidence for an accelerating universe, with its implication for the existence of a repulsive dark energy, is of profound significance for particle physics and cosmology. Yet the explanation for the dark energy remains a complete mystery. More precise observations are critical to characterize the nature of this acceleration. Type Ia supernovae offer a means of directly measuring luminosity distances and the change in the expansion rate with time. Moreover, potential effects due to evolution, chemical composition dependence, and changing dust properties (well-known astrophysical systematic issues), can be tested empirically. I describe briefly here several ongoing searches for supernovae at redshifts less than one: the LOTOSS, the Nearby Supernova Factory, ESSENCE, and Supernova Legacy Survey (SNLS) projects. I also provide an overview of the Carnegie Supernova Project (CSP), which differs from other projects to date in its goal of providing an I-band *restframe* Hubble diagram for type Ia supernovae (SNIa). The CSP is focused on testing for and reducing systematic uncertainties, obtaining a sample of multiwavelength observations of approximately 200 supernovae over the redshift range $0 < z < 0.6$. The goal of these studies is to measure the evolution of the expansion rate, to characterize the acceleration of the Universe, and constrain the equation of state, w, to a precision and accuracy of 10%.

1 Introduction

The comparison of nearby and distant Type Ia supernovae (Riess et al. 1998; Perlmutter et al. 1999) has revealed the surprising result that about two thirds of the total mass-energy appears to be in a new and different form: a "dark energy." This dark energy is not clumped with matter, and is causing an acceleration of the expansion of the universe. The most recent observations (Riess et al. 2004; Knop et al. 2003; Tonry et al. 2003), using HST observations, confirm this basic result, and Riess/Tonry also find evidence for the transition from a decelerating to an accelerating universe. To date there is no physical understanding of this new (dominant) component of the universe.

There are at least two major challenges to a theoretical understanding of the dark energy: 1) the small magnitude of the dark energy component relative to its expected value based on standard particle physics – a discrepancy with the observed value of 55 orders of magnitude or more, and 2) it appears

that we are living at an epoch when coincidentally the dynamics of the expansion are only now becoming dominated by the dark energy. Given these immense challenges and the current lack of a physical understanding of dark energy, further empirical characterization of the evolution of the expansion rate of the Universe is clearly needed.

In general relativity, the expansion of the Universe, described in terms of the scale factor, a(t) can be written:

$$\ddot{a}/a = -4\pi G \sum_i (\rho_i + 3P_i)$$

where ρ is the energy density and P is the pressure of the various components (matter, radiation, dark energy) of the Universe. Both energy and pressure govern the dynamics of the universe. This equation allows for the possibility of both negative as well as positive pressure, with a negative pressure acting as an effective repulsive gravity. Any component of the mass-energy density can be parameterized by its ratio of pressure to energy density, w = P /ρ.

In a universe with dark energy, the expansion rate of the Universe is given by:

$$H^2(z)/H_0^2 = [\Omega_m(1+z)^3 + \Omega_\Lambda(1+z)^{3(1+w)}]$$

where Ω_m and Ω_Λ represent the matter and dark energy densities. For ordinary matter w = 0, for radiation w = 1/3, and for the cosmological constant (dark energy) w = -1.

There are two main observational approaches that currently provide evidence for dark energy. First are measurements of the Hubble diagram using type Ia supernovae (SNIa), for which the best fit yields a model with $\Omega_m \sim 0.3$, and $\Omega_\Lambda \sim 0.7$ (Riess et al. 1998; 2004; Tonry et al. 2003; Perlmutter et al. 1999; Knop et al. 2003). Second are measurements of the angular power spectrum of the cosmic microwave background (Spergel et al. 2003, Page et al. 2003), and large-scale structure (Percival et al 2001; Seljak et al. 2004) which provide an independent check on, and a consistent set of cosmological parameters as the SNIa. The Wilkinson Microwave Anisotropy Probe (WMAP) results, combined with measurements of large-scale structure, yield results consistent with the type Ia supernova measurements, with a matter density of about one third, and the remaining two-thirds contribution from a dark energy component.

There are multiple advantages of using SNIa for measurements of Ω_Λ. First, SNIa are luminous and can observed over a wide redshift range. They offer a means of directly providing measurements of a change in the expansion rate over time, and hence for an acceleration of the Universe. (The CMB measurements provide constraints on the energy density of an additional component such as dark energy, but not on the acceleration of the Universe.) Second, the dispersion in the SNIa Hubble diagram ($\sim$0.14 mag) is small enough that the shape of the Hubble diagram can be used to separate Ω_m and

Ω_Λ, independently of the nearby, local calibration sample. Third, potential effects due to evolution, chemical composition dependence, dust properties, and gravitational lensing, can be empirically tested, calibrated, and corrected.

However, as ongoing and future supernova surveys yield larger sample sizes, the statistical uncertainties will decrease further, and systematics will dominate the total uncertainty. Tests for systematics are critical: for example, currently, the highest redshift HST observations correspond to rest-frame ultraviolet observations, where the effects of reddening by dust and chemical composition differences are largest. Models of supernovae indicate that the opacity in the atmospheres is greatest in the ultraviolet part of the spectrum, and decreases substantially through the optical and infrared. An increasing challenge for "precision measurements" in cosmology, is understanding and minimizing small systematic uncertainties, essential for characterizing the nature of the dark energy.

Riess (this meeting) has discussed HST searches for supernovae at very high redshift ($1 < z < 2$). This contribution describes ongoing supernova searches at lower redshift ($z < 1$).

2 Addressing Systematic Effects

In an era of precision cosmology, where 10% accuracy on the measurement of w and 15% on w' are desired goals, minimizing the effects of systematic errors becomes the central issue to be addressed. Observations and careful study to date have demonstrated that such systematic effects cannot explain away the observed differences in supernova luminosities for the high- and low-redshift samples. However, the requirement for increasing measurement accuracy – and the lack of a detailed theoretical understanding of type Ia supernovae, the current observations at restframe optical colors, the difficulty of obtaining accurate K- and filter-corrections – mean that even previously small effects become important to characterize and eliminate.

2.1 Reddening

An advantage of longer-wavelength photometry is the decreased sensitivity to reddening. The ratio of total-to-selective absorption increases toward shorter wavelengths:

$$R_\lambda = A_\lambda / E(B-V)$$

where the ratio of total-to-selective absorption, R, decreases from $\sim$5 for the U-band, to $\sim$ 4 for the B-band, to 1.7 for the I-band (Cardelli et al. 1989). Thus, the U-band absorption is a factor of 3 greater at U than at I. In practice, this means that even for very small reddenings, where E(B-V) < 0.03, the corrections to the restframe U-band magnitudes may be 0.15 mag;

that is, comparable to the cosmological effect being measured. Hence, at bluer restframe wavelengths, the reddening corrections are more uncertain.

2.2 Metallicity / Age:

Nearby SNIa occur in widely different stellar environments, with varying ages and metallicities of their stellar populations. The effects of age and metallicity on the observed properties of SNIa have been modeled by a number of investigators (e.g., Höflich et al. 1998, Lentz et al. 2000). These models suggest that pre-explosion metallicity can have a significant effect on the observed SNIa spectra. For example, the models of Lentz et al. (2000) indicate that scattering in the atmospheres is greatest in the U-band, and decreases through the optical to infrared. However, predictions from models to date have not yet converged on the sign or the magnitude of such effects, and therefore, empirical constraints are critical to minimize potential systematic effects in measurements of the distances to SNIa.

To date, empirical searches for environmental dependences that might correlate with the age of the supernova progenitor (host galaxy morphology, color, position in the galaxy on supernova distances have led to null results (e.g., Williams et al. 2003, Sullivan et al. 2003).

2.3 Other Systematics

Comparison of high- and low-redshift supernovae for the measurement of cosmological parameters requires accurate transformations of photometric bandpasses. The K-corrections in use today are based on observations of a few low-redshift SNIa whose overall spectral shapes from the ultraviolet through the near-infrared are adjusted to match observed broad-band colors (e.g., Nugent et al. 2002). Unfortunately, errors in I and U bands remain large (Strolger et al. 2002) due to intrinsic variations in the supernovae themselves. In addition, Stritzinger et al. (2002), have found that the peak magnitudes of supernovae can differ by up to 0.05 mag for data taken at different telescopes, despite reducing the photometry to the same local standards around the supernovae using the color terms derived for each site and instrument.

3 Ongoing Ground-Based Supernova Searches

3.1 LOTOSS ($z < 0.2$)

The Lick Observatory and Tenagra Observatory Supernova Searches (LOTOSS) is discovering supernovae over the redshift range $z = 0.003$–0.15, and obtaining $UBVRI$ light curves. Since 1998, this survey has led to the discovery of over 400 supernovae, in fields accessible to telescopes in both the northern and southern hemispheres.

3.2 The Nearby Supernova Factory (0.03 < z < 0.08)

The Nearby Supernova Factory aims to discover and analyze in detail about 300 SNIa. Their goal is to collect accurate spectra for each supernova, starting 1–2 weeks before peak brightness, and continuing for several weeks afterward. Their wide-area supernova search is being done in collaboration with the Near-Earth Asteroid Team (NEAT), whose goal is to use 1.2-meter telescopes in Hawaii and Palomar to find and catalog large asteroids and other objects near the Earth. The follow-up spectra will be obtained with a recently built, special-purpose integral-field-unit spectrograph, operating from 3200 to 10,000Å, at the University of Hawaii 2.2-meter Telescope at Mauna Kea.

3.3 Supernova Legacy Survey (0.2 < z < 1)

The SNLS is a Canadian/French collaboration, which has been using the Canada-France-Hawaii Telescope (CFHT) since 2003 to obtain deep optical (ugriz) images for 4 fields totaling 16 square degrees around the equator. The SNLS is revisiting each field every second night during a 5-month campaign per semester for 5 years. Their goal is to discover 2000 type I supernovae out to redshifts in excess of one, with 900 of those having z < 0.9.

3.4 ESSENCE (0.25 < z < 0.75)

ESSENCE is using the CTIO 4-m telescope to survey at VRI wavelengths over the redshift range between $z = 0.25$–0.75. They have just completed their third year of observing. Their observing strategy is to observe second night (but revisit each field every four nights) during one 3-month campaign every fall. ESSENCE aims to produce optical light curves for 200 SNIa over 5 years (2002–2007). To date they have observed about 100 Type Ia supernovae.

4 The Carnegie Supernova Project (CSP)

The Carnegie Supernova Project[1] is following up on the supernovae discovered as part of the surveys discussed above. That is, the CSP is not a search project, but rather focuses on obtaining more extensive (color and/or temporal) coverage of already-identified objects. It makes use of the unique resources available at the Las Campanas Observatory (LCO): the 1-m Swope, 2.5-m duPont, and two 6.5-m Magellan telescopes, instrumented with CCDs

[1]Members of the Carnegie Supernova Project include: Ray Carlberg, Alex Filippenko, Gaston Folatelli, Wendy Freedman, Mario Hamuy, Weidong Li, Barry Madore, Nidia Morrell, Eric Persson, Mark Phillips, Chris Pritchett, Nick Suntzeff, and Pamela Wyatt.

and IR cameras and CCD spectrographs. At low redshift, the goal is to provide well-observed lightcurves from the near-ultraviolet to the near-IR $(u'BVr'i'YJHK_s)$[2]. An immediate result of this effort will be a fundamental dataset on the photometric and spectroscopic sytematics of both type Ia and II SN events.

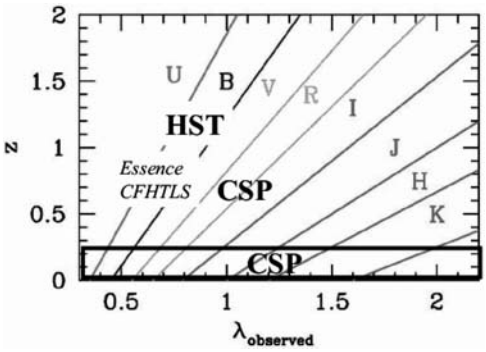

Fig. 1. Redshift and wavelength coverage. Diagonal lines indicate the rest-frame wavelength passband; the redshift and wavelength at which the object is observed can be read from the axes. At a redshift beyond z = 1, supernovae can still be observed at UB rest wavelengths using optical CCDs. The redshift/wavelength domains of several ongoing supernova projects are illustrated: HST at very high redshifts and bluer bandpasses (z > 1); ESSENCE/SNLS at more modest redshifts and optical restframe coverage; the CSP with an extension to redder restframe wavelengths using infrared arrays. Locally the CSP will provide extensive wavelength coverage from the ultraviolet through the near-infrared.

The primary aim of the CSP is to establish a rest-frame I-band Hubble diagram, while at the same time assembling an extensive database for low redshift supernovae, useful for a variety of supernova studies. For the Hubble diagram, the I band represents the best compromise wavelength to work at; shorter restframe passbands (UBV) have the advantage that they can be followed out to higher redshifts, but they suffer larger systematic uncertainties, as discussed above. The I passband offers important advantages for minimizing potential systematic effects such as reddening and metallicity; however, the objects cannot be observed to as great distances. Hence, optical and near-infrared observations remain quite complementary (see Fig. 1). However, by a redshift of 0.5, the differences amongst various cosmological models are quite significant (that is, testing for a dark energy component does not require observations to high redshifts). The I-band restframe data will thus provide both a critical test of the current shorter-wavelength restframe data, as well as an independent measure of the dark energy component.

[2]The Y-band is centered at $1\mu m$; Hillenbrand et al. 2002.

4.1 Low Redshift (0 < z < 0.2)

For the nearby sample, the goal is to obtain $u'BVr'i'YJHK_s$ photometry and optical spectroscopy for 125 low-redshift type Ia supernovae and 100 type II supernovae. Photometric observations with a precision of ∼0.03 mag will be obtained every 2–4 nights so that large gaps in the light curves, common in supernova studies to date, can be minimized. The observations are being carried out from the time of discovery through 50 days past maximum for SNIa, and through the extended plateau phase for SNII. An additional goal is to obtain optical spectroscopy every 5–7 days from discovery through 40 days past maximum.

The photometry obtained for many of the CSP supernovae will provide a unique resource for improving the precision of these objects as distance indicators, and for computing bolometric light curves for comparison with theoretical models. This nearby sample will serve as a reference for the rest-frame I and Y light curves of the sample of about 100 high-redshift SNIa that we hope to obtain. Furthermore, the infrared photometry will be valuable for independent determinations of the Hubble constant. It will also be very useful for studying the nearby peculiar flows of galaxies out to ∼10,000 km/s.

4.2 Near-Infrared Distances to Nearby Supernovae

Near-infrared observations offer the promise of improving the precision of SNIa as cosmological standard candles for the determination of H_0. Meikle (2000) and Elias et al. (1985) have noted the advantages of infrared photometry of supernovae, but the recent availability of large-format infrared arrays now allows the full potential of infrared observations to be exploited. Nearby supernova distances can be calibrated, using the local Cepheid distance scale to yield a value of H_0 at cosmologically interesting distances.

Well-known advantages of infrared photometry are reduced sensitivity to both reddening and metallicity. In addition, the JHK data for type Ia supernovae show peak absolute magnitudes in the near infrared that are nearly constant, independent of decline rate (Meikle 2000; Krisciunas et al. 2004).

4.3 Higher Redshift (0.2 < z < 0.6)

HST NICMOS observations are available for a few high-redshift supernovae (Riess et al. 2004), but due to practical limitations, the bulk of measurements at high z are UV/optical restframe. To date, very few rest-frame I-band measurements have been obtained for supernovae at high redshift. At z∼0.25 this wavelength is redshifted out of the reach of CCDs (thus requiring large-format infrared arrays), while, in addition, the objects are faint (requiring large telescopes). The higher redshift CSP supernova targets are coming from the Supernova Legacy Survey (SNLS) and the ESSENCE Project. Using the

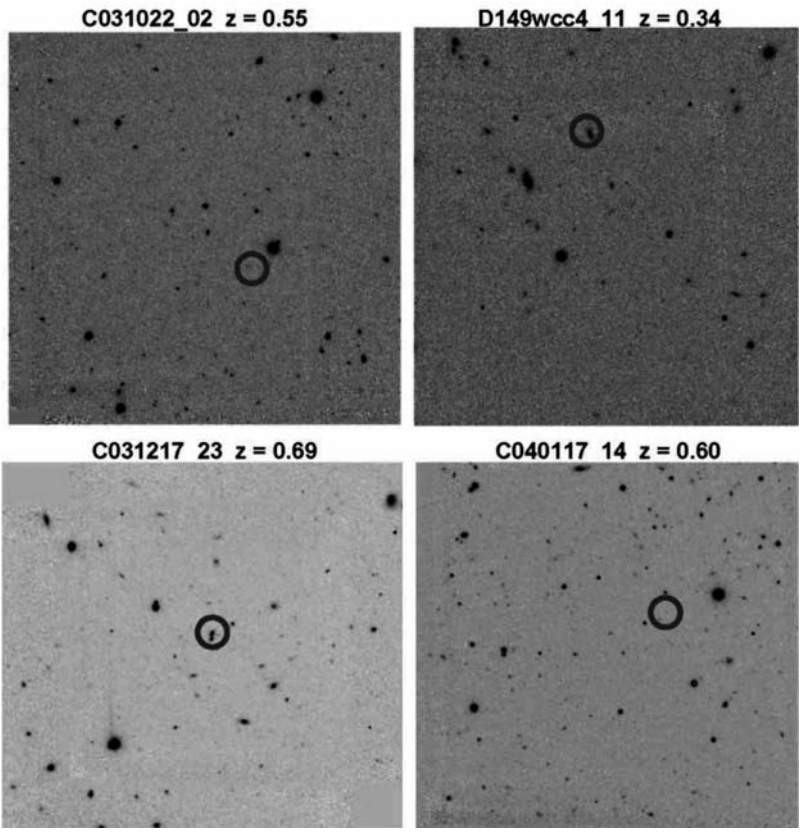

Fig. 2. J-band images of 4 supernovae observed using the Baade 6.5-meter telescope at Las Campanas and PANIC. The supernovae range in redshift from 0.34 to 0.69, and were discovered by the ESSENCE and SNLS projects.

6.5-meter Baade telescope, our goal over the course of the next five years is to observe a sample of ∼100 SNIa between z=0.2-0.6, obtaining YJ for each of the candidates. With the optical photometry from the ESSENCE and SNLS searches, these data will provide *rest-frame* BVI photometry for each supernova, yielding two colors, allowing accurate reddening corrections to be determined. We are obtaining 3-5 observations in Y and J covering the SN maximum and thereby allowing a firm measure of the peak magnitude. J-band images for four of our observed objects are shown in Fig. 2.

5 Summary

A number of ongoing ground-based supernova projects are slowly ramping up over the next 5 years. Collectively, these datasets will allow us to determine

better extinction corrections, to constrain evolutionary effects due to age and metallicity, and to improve our current estimates of the amount of dark energy and its equation of state, w. Ultimately observations from a future space mission (e.g., the Joint Dark Energy Mission) may routinely obtain multi-wavelength data for the high-redshift supernovae ($0.6 < z < 1.7$). However, the programs currently underway will provide the fiducial data from $0 < z < 1$. If we live in a universe where $w = -1$ and $w' = 0$, then this lower redshift range is the one where the cosmological effects of dark energy dominate. And should w turn out to vary with time, supernova data for redshifts less than one will provide the critical comparison data for higher redshifts required to characterize the evolution in w.

References

1. Cardelli, J.A., Clayton, G.C. & Mathis, J.S., *ApJ* **345** (1989) 245
2. Elias, J.H. et al., *ApJ* **296** (1985) 379
3. Hillenbrand, L.A., Foster, J.B., Persson, S.E., & Matthews, K., *PASP* **114** (2002) 708
4. Höflich, P., Wheeler, J.C., & Thielemann, F.K. 1998 *ApJ* **495** (1998) 617
5. Knop, R.A., et al., *ApJ* **598** (2003) 102
6. Krisciunas, K., Phillips, M.M. & Suntzeff, N.B. 2004, astro-ph/0312626
7. Lentz, E.J., Baron, E., Branch, D., Hauschildt, P.H., & Nugent, P.E., *ApJ* **530** (2000) 966
8. Meikle, W.P.S., 2000 *MNRAS* **314** 782
9. Nugent, P., Kim, A. & Perlmutter, S., 2002 *PASP* 803
10. Page, L., et al., *ApJ Suppl* **148** (2003) 175
11. Percival et al., *MNRAS* **327** (2001) 1297
12. Perlmutter, S., et al., *ApJ* **517** (1999) 565
13. Riess, A.G., et al., *AJ* **116** (1998) 1009
14. Riess, A.G., et al., *ApJ* **607** (2004) 665
15. Seljak, U. et al. 2004, astro-ph/0407372
16. Spergel, D. et al., *ApJ Suppl* **148** (2003) 175
17. Stritzinger, M. et al., *AJ* **124** (2002) 2100
18. Strolger, L.-G. et al., *AJ* **124** (2002) 2905
19. Sullivan, M., et al., *MNRAS* **340** (2003) 1057
20. Tonry, J.L. et al., *ApJ* **594** (2003) 1
21. Williams, B.F. et al., *AJ* **126** (2003) 2608

Liouville Cosmology

J. Ellis[1], N.E. Mavromatos[2], and D.V. Nanopoulos[3]

[1] TH Division, Physics Department, CERN
[2] Theoretical Physics, Physics Department, King's College London, UK
[3] Mitchell Institute for Fundamental Physics, Texas A&M University, College Station, TX 77843, USA;
Astroparticle Physics Group, Houston Advanced Research Center, Mitchell Campus, Woodlands, TX 77381, USA;
Academy of Athens, Academy of Athens, Division of Natural Sciences, 28 Panepistimiou Avenue, Athens 10679, Greece

Abstract. Liouville string theory is a natural framework for discussing the non-equilibrium evolution of the Universe. It enables non-critical strings to be treated in mathematically consistent manner, in which target time is identified with a world-sheet renormalization-group scale parameter, preserving target-space general coordinate invariance and the existence of an S-matrix. We review our proposals for a unified treatment of inflation and the current acceleration of the Universe. We link the current acceleration of the Universe with the value of the string coupling. In such a scenario, the dilaton plays an essential background rôle, driving the acceleration of the Universe during the present era after decoupling as a constant during inflation.

1 Issues in String Cosmology

Formal developments in string theory [1] over the past decade [2], with the discovery of a consistent way of studying quantum domain-wall structures (D-branes), have opened up novel ways of looking at not only the microcosmos, but also the macrocosmos.

In the microcosmos, there are novel ways of compactification, either via the observation [3] that extra dimensions that are large compared to the string scale [3] are consistent with the foundations of string theory, or by viewing our four-dimensional world as a brane embedded in a higher-dimensional bulk space-time, whose extra dimensions might even be infinite in size [4]. Such ideas are still consistent with the required large hierarchy between the Planck scale and the electroweak- or supersymmetry-breaking scale. In this modern approach, fields in the gravitational (super)multiplet of the (super)string are allowed to propagate in the bulk, but not the gauge fields, which are attached to the brane world. In this way, the weakness of gravity compared to the rest of the interactions is a result of the large compact dimensions, and the compactification is not necessarily achieved through the conventional means of closing the extra dimensions up on spatial compact manifolds, but could also involve shadow brane worlds with special reflecting properties, such as orientifolds, which restrict the bulk dimension [5]. In such approaches, the

string scale M_s is not necessarily identical to the four-dimensional Planck mass M_P. Instead, they are related by

$$M_P^2 = \frac{8M_s^2 V_6}{g_s^2} \ . \tag{1}$$

through the large compactification volume V_6.

In the macrocosmos, this modern approach has offered new insights into the evolution of our Universe. Novel ways of discussing cosmology in brane worlds have been discovered over the past five years, which may revolutionise our way of approaching issues such as inflation [6, 7]. On the other hand, mounting experimental evidence from diverse astrophysical sources presents some important issues that string theory must address if it is to provide a realistic description of Nature. Observations of distant supernovae [8] and the cosmic microwave background fluctuations, e.g., by the WMAP satellite [9], indicate that the expansion of our Universe is currently accelerating, and that 73% of its energy density consists of some unknown Dark Energy.

This cosmological development may be quite significant for string theory, requiring that we revolutionise the approach usually followed so far. If the dark energy turns out to be an honest-to-God cosmological constant, leading to an asymptotic de Sitter horizon, then the entire concept of the scattering matrix, the basis of perturbative string theory, breaks down. This would cast doubts on the very foundations of string theory, at least in its familiar formulation [10]. Alternatively, one might invoke some quintessential model for the vacuum energy, in which the vacuum energy relaxes to zero at large cosmic time. This may be consistent with the existence of an S-matrix as well as with the astrophysical data, but there is still the open issue of embedding such models in (perturbative) string theory. In particular, one must develop a consistent σ-model formulation of strings propagating in such relaxing, time-dependent space-time backgrounds.

The world-sheet conformal-invariance conditions of critical string theory, which are equivalent to the target-space equations of motion for the background fields on which the string propagates, are very restrictive, corresponding only to vacuum solutions of critical strings. The main problem may be expressed as follows. Consider the graviton world-sheet β function, which is nothing but the Ricci tensor of the target space-time background to lowest order in α':

$$\beta_{\mu\nu} = \alpha' R_{\mu\nu} \ , \tag{2}$$

in the absence of other fields. Conformal invariance requires the vanishing of $\beta_{\mu\nu}$, which implies that the background must be Ricci-flat, a characteristic of solutions to the *vacuum* Einstein equations.

The issue then arises how to describe cosmological string backgrounds, which are not vacuum solutions, but require the presence of a matter fluid, yielding a non-flat Ricci tensor. Specifically, a vacuum solution with a cosmological constant is inconsistent with conformal invariance: a de Sitter Universe

with a positive cosmological constant $\Lambda > 0$ has a Ricci tensor $R_{\mu\nu} = \Lambda g_{\mu\nu}$, where $g_{\mu\nu}$ is the metric tensor.

We now discuss how these issues may be addressed in Liouville Cosmology.

2 Universes in Dilaton Backgrounds

A proposal for obtaining a non-zero cosmological constant in string theory was made in [11], according to which dilaton tadpoles in higher-genus world-sheet surfaces produce additional modular infinities. Their regularisation would lead to extra world-sheet structures in the σ model that do not appear at the world-sheet tree level, leading to modifications of the β-function. As a result, the Ricci tensor of the space-time background is now that of a (anti) de Sitter Universe, with a cosmological constant given by the dilaton tadpole graph $J_D > 0$ ($J_D < 0$). One problem with this approach is the above-mentioned existence of an asymptotic horizon in the de Sitter case, which prevents the proper definition of asymptotic states, and hence a scattering S-matrix. However, since the perturbative world-sheet formalism is based on such an S-matrix, one may question the fundamental consistency of this approach.

A way out of this dilemma was proposed in [12], namely a dilaton background depending linearly on time in the so-called σ-model frame. Such a background, even when the σ-model metric is flat, leads to solutions of the conformal invariance conditions of the pertinent stringy σ-model that are exact to all orders in α', thereby constituting acceptable solutions from a perturbative view point. It was argued in [12] that such backgrounds describe linearly-expanding Robertson-Walker (RW) Universes, which were shown to be exact conformal-invariant solutions, corresponding to Wess-Zumino models of appropriate group manifolds. The important novelty in [12] was the identification of target time t with a specific dilaton background:

$$\Phi = \text{const} - Q\ t\ , \tag{3}$$

where Q is a constant.

The square of Q is the σ-model central charge deficit in a *supercritical* string theory [12]. Consistency of the underlying world-sheet conformal field theory, as well as modular invariance of the string scattering amplitudes, led to *discrete* values of Q^2, when expressed in units of the string length M_s. This was actually the first example of a non-critical string, with the target-space coordinates X^i, $i = 1, \ldots D-1$ playing the rôles of the pertinent σ-model fields. This non-criticality broke conformal invariance, which was compensated by Liouville dressing [13]. The required Liouville field had time-like signature, since the central-charge deficit was positive: $Q^2 > 0$ in the model of [12], and played the rôle of target time.

In the presence of a non-trivial dilaton field, the Einstein term in the effective D-dimensional low-energy field theory action is conformally rescaled by $e^{-2\Phi}$. This requires a redefinition of the σ-model-frame space-time metric $g^{\sigma}_{\mu\nu}$ to become the physical metric in the 'Einstein frame', $g^{E}_{\mu\nu}$:

$$g^{E}_{\mu\nu} = e^{\frac{2\Phi}{D-2}} g^{\sigma}_{\mu\nu} \ . \tag{4}$$

A redefinition of target time is also necessary to obtain the standard RW form of the metric in the Einstein frame:

$$ds^2_E = -dt^2_E + a^2_E(t_E)\left(dr^2 + r^2 d\Omega^2\right) \ , \tag{5}$$

where we assume for definiteness a spatially-flat RW metric. Here a_E is an appropriate scale factor, which is a function of t_E alone in the homogeneous cosmological backgrounds we assume throughout. Time in the Einstein-frame is related to time in the σ-model frame [12] by:

$$dt_E = e^{-\Phi} dt \qquad \rightarrow \qquad t_E = \int^t e^{-\Phi(t)} dt \ . \tag{6}$$

The linear dilaton background (3) therefore yields the following relation between the Einstein and σ-model time variables:

$$t_E = c_1 + \frac{c_0}{Q} e^{Qt} \ , \tag{7}$$

where $c_{1,0}$ are appropriate (positive) constants.

Thus, the dilaton background (3) scales logarithmically with the Einstein-Robertson-Walker cosmic time t_E:

$$\Phi(t_E) = (\text{const.}') - \ln\left(\frac{Q}{c_0} t_E\right) \tag{8}$$

In this regime, the string coupling, which is defined as [1]:

$$g_s = \exp\left(\Phi(t)\right) \tag{9}$$

varies with the cosmic time t_E as

$$g^2_s(t_E) \equiv e^{2\Phi} \propto \frac{1}{t^2_E} \, . \tag{10}$$

Thus, the effective string coupling vanishes asymptotically in cosmic time.

The effective low-energy action for the gravitational multiplet of the string in the Einstein frame reads [12]:

$$S^{\text{brane}}_{\text{eff}} = \int d^4x \sqrt{-g} \{R - 2(\partial_\mu \Phi)^2 - \frac{1}{2} e^{4\Phi} (\partial_\mu b)^2 - \frac{1}{3} e^{2\Phi} \delta c\} \, , \tag{11}$$

where b is the four-dimensional axion field associated with the antisymmetric tensor and $\delta c = C_{\rm int} - c^*$ is the central charge deficit, where $C_{\rm int}$ is the central charge of the conformal world-sheet theory corresponding to the transverse (internal) string dimensions, and $c^* = 22(6)$ is the critical value of this internal central charge of the (super)string theory in a flat four-dimensional space-time. The linear-dilaton configuration (8) corresponds, in this language, to a background charge Q of the conformal theory, which contributes a term $-3Q^2$ (in our normalisation (8)) to the total central charge, which also receives contributions from the four uncompactified dimensions of our world. In the case of a flat four-dimensional Minkowski space-time, one has: $C_{\rm total} = 4 - 3Q^2 + C_{\rm int} = 4 - 3Q^2 + c^* + \delta c$, which should equal 26. This implies that $C_{\rm int} = 22 + 3Q^2$ $(6 + 3Q^2)$ for bosonic (supersymmetric) strings.

An important result in [12] was the discovery of an exact conformal field theory corresponding to the dilaton background (8), i.e., a constant curvature (Milne) (static) metric in the σ-model frame or, equivalently, a linearly-expanding RW Universe in the Einstein frame. This conformal field theory corresponds to a two-dimensional Wess-Zumino-Witten (WZW) model on the world sheet, on a group manifold $O(3)$ with appropriate constant curvature, whose coordinates correspond to the spatial components of the four-dimensional metric and antisymmetric tensor fields, together with a free world-sheet field corresponding to the target time coordinate. The total central charge in this more general case reads $C_{\rm total} = 4 - 3Q^2 - \frac{6}{k+2} + C_{\rm int}$ with k a positive integer, which corresponds to the level of the Kac-Moody algebra associated with the WZW model on the group manifold. The value of Q is chosen in such a way that the overall central charge $c = 26$ and the theory is conformally invariant.

It was observed in [12] that known unitary conformal field theories have *discrete* central charges, which accumulate to integers or half-integers from *below*, and hence that the values of the central charge deficit δc are also *discrete*. From a physical point of view, this implies that the linear-dilaton Universe may either stay at such a state for ever with a fixed δc, or else tunnel through different discrete levels before relaxing to a critical $\delta c = 0$ theory corresponding to a flat four-dimensional Minkowski space-time.

The analysis in [12] also showed that there were tachyonic mass-squared shifts of order $-Q^2$ for the bosonic string excitations, but not for the fermionic ones. This in turn would imply the breaking of target supersymmetry in such backgrounds, as far as the excitation spectrum is concerned, and the appearance of tachyonic instabilities. The latter could trigger these cosmological phase transitions, since they correspond to world-sheet operators that are relevant in the renormalization-group sense. As such, they can trigger the flow of the internal unitary conformal field theory towards minimisation of its central charge, according to the Zamolodchikov c theorem [14]. As we discuss below, in semi-realistic cosmological models [15], such tachyons decouple from the spectrum relatively quickly. On the other hand, as a result of the

form of the dilaton in the Einstein frame (8), we observe that the dark-energy density for this Universe, $\Lambda \equiv e^{2\Phi}\delta c$, relaxes towards zero as $1/t_E^2$, for each of the stationary values of δc. The breaking of supersymmetry induced by the linear dilaton should therefore be considered an *obstruction* [16], rather than a spontaneous breaking, in the sense of appearing only in the boson-fermion mass splittings between the excitations, whereas the vacuum energy of the asymptotic equilibrium theory vanishes.

In [17] we went one step further than [12], considering more complicated σ-model metric backgrounds in $(D+1)$-dimensional target space-times, that did not satisfy the σ-model conformal-invariance conditions, and therefore were in need of Liouville dressing [13]. These backgrounds were even allowed to be time-dependent. Non-criticality can be introduced in many mathematically consistent ways, for instance via cosmically catastrophic events such as the collision of brane worlds [18, 19], which lead naturally to supercritical σ models. The Liouville dressing of such non-critical models results in $D+2$-dimensional target spaces with two time directions. The important point of [17] was the *identification* of the world-sheet zero mode of the Liouville field with the target time, thereby restricting the Liouville-dressed σ model to a $(D+1)$-dimensional hypersurface of the $(D+2)$-dimensional target space-time, maintaining the initial target space-time dimensionality. We stress once more that this identification is only possible in cases where the initial σ model is supercritical, so that the Liouville mode has time-like signature [12, 13]. Such an identification was shown in certain models [18, 19] to be energetically preferable from a target-space viewpoint, since it minimised certain effective potentials in the low-energy field theory corresponding to the string theory at hand.

Such non-critical σ-models relax asymptotically in the cosmic Liouville time to conformal σ models, which may be viewed as equilibrium points in string theory space. In some interesting cases of relevance to cosmology [15], which were particularly generic, the asymptotic conformal field theory was that of [12] with a linear dilaton and a flat Minkowski target-space metric in the σ-model frame. In others, the asymptotic theory was characterised by a constant dilaton and a Minkowski space-time [18]. In what follows, we describe briefly the main features of such non-critical cosmological string models, and compare them with recent observations.

3 Non-Critical Liouville String Cosmologies

We now consider in more detail the model of [15]. Although formulated in the specific framework of ten-dimensional Type-0 [20] string theory. This has a non-supersymmetric target-space spectrum, thanks to a special projection of the supersymmetric partners out of the spectrum. Nevertheless, its basic cosmological properties are sufficiently generic to be extended to the bosonic

sector of any effective low-energy supersymmetric field theory obtained from a supersymmetric string model.

The ten-dimensional metric configuration considered in [15] was:

$$G_{MN} = \begin{pmatrix} g^{(4)}_{\mu\nu} & 0 & 0 \\ 0 & e^{2\sigma_1} & 0 \\ 0 & 0 & e^{2\sigma_2} I_{5\times 5} \end{pmatrix}, \tag{12}$$

where lower-case Greek indices are four-dimensional space-time indices, and $I_{5\times5}$ denotes the 5×5 unit matrix. We have chosen two different scales for internal space. The field σ_1 sets the scale of the fifth dimension, while σ_2 parametrises a flat five-dimensional space. In the context of the cosmological models we deal with here, the fields $g^{(4)}_{\mu\nu}$, σ_i, $i = 1, 2$ are assumed to depend only on the time t.

Type-0 string theory, as well as its supersymmetric extensions that appear, e.g., in brane models, contains form fields with non-trivial gauge fluxes (flux-form fields), which live in the higher-dimensional bulk space. In the specific model of [20], there is one such field that was assumed to be non-trivial. As was demonstrated in [15], a consistent background choice for the flux-form field has a flux parallel to to the fifth dimension σ_2. This implies that the internal space is crystallised (stabilised) in such a way that this dimension is much larger than the remaining four, demonstrating the physical importance of the flux fields for large radii of compactification.

Considering the fields to be time-dependent only, i.e., considering spherically-symmetric homogeneous backgrounds, restricting attention to the compactification (12), and assuming a RW form of the four-dimensional metric, with scale factor $a(t)$, the generalised conformal invariance conditions and the Curci-Pafutti σ-model renormalisability constraint [21] imply a set of differential equations which were solved numerically in [15]. The generic form of these equations reads [13, 17, 15]:

$$\ddot{g}^i + Q(t)\dot{g}^i = -\tilde{\beta}^i, \tag{13}$$

where the $\tilde{\beta}^i$ are the Weyl anomaly coefficients of the stringy σ model on the background $\{g^i\}$. In the model of [15], the set of $\{g^i\}$ includes the graviton, dilaton, tachyon, flux and moduli fields $\sigma_{1,2}$, whose vacuum expectation values control the size of the extra dimensions.

The detailed analysis of [15] indicated that the moduli σ_i fields froze quickly to their equilibrium values. Thus, they together with the tachyon field, which also decays rapidly to a constant value, decouple from the four-dimensional fields at very early stages in the evolution of this string Universe[1].

[1]The presence of the tachyonic instability in the spectrum is due to the fact that in Type-0 strings there is no target-space supersymmetry by construction. From a cosmological viewpoint, the tachyon fields are not necessarily bad features, since they may provide the initial instability leading to cosmic expansion [15], as well as a mechanism for step-wise reduction in the central-charge deficit.

There is an inflationary phase in this scenario and a dynamical exit from it. The important point that guarantees the exit is the fact that the central-charge deficit Q^2 is a time-dependent entity in this approach, obeying specific relaxation laws determined by the underlying conformal field theory [15, 18, 19]. The central charge runs with the local world-sheet renormalisation-group scale, namely the zero mode of the Liouville field, which is identified [17] with the target time in the σ-model frame. The supercriticality [12] $Q^2 > 0$ of the underlying σ model is crucial, as already mentioned. Physically, the non-critical string provides a model of non-equilibrium dynamics, which may be the result of some catastrophic cosmic event, such as a collision of two brane worlds [7, 18, 19], or an initial quantum fluctuation [22, 15]. It also provides, as we now discuss briefly, a unified mathematical framework for analysing various phases of string cosmology, including the inflationary phase in the early Universe, graceful exit from it and reheating, as well as the current and future eras of accelerated cosmologies. It is interesting that one can constrain string parameters such as string coupling, the separation of brany worlds at the end of inflation and the recoil velocity of the branes after the collision, by fits to current astrophysical data [19].

4 Liouville Inflation: the Big Picture

As discussed in [22, 18, 19], a constant central-charge deficit Q^2 in a stringy σ model may be associated with an initial inflationary phase, with

$$Q^2 = 9H^2 > 0 \ , \tag{14}$$

where the Hubble parameter H may be fixed in terms of other parameters of the model. One can consider various scenarios for such a departure from criticality. For example, in the specific colliding-brane model of [18, 19], Q (and thus H) is proportional to the square of the relative velocity of the colliding branes, $Q \propto u^2$ during the inflationary era. As is evident from (14) and discussed in more detail below, in a phase of constant Q one obtains an inflationary de Sitter Universe.

The specific normalization in (14) is imposed by the identification of the time t with (minus) the zero mode of the Liouville field $-\varphi$ of the *supercritical* σ model. The minus sign may be understood both mathematically, as due to properties of the Liouville mode, and physically by the requirement that the deformation of the space-time relaxes following the distortion induced by the recoil. With this identification, the general equation of motion for the couplings $\{g_i\}$ of the σ-model background modes is [17]:

$$\ddot{g}^i + Q\dot{g}^i = -\beta^i(g) = -\mathcal{G}^{ij}\partial C[g]/\partial g^j \ , \tag{15}$$

where the dot denotes a derivative with respect to the Liouville world-sheet zero mode φ, and $\mathcal{G}^{ij}$ is an inverse Zamolodchikov metric in the space of

string theory couplings $\{g^i\}$ [14]. When applied to scalar inflaton-like string modes, (15) would yield standard field equations for scalar fields in de Sitter (inflationary) space-times, provided the normalization (14) is valid, implying a "Hubble" expansion parameter $H = -Q/3$[2]. The minus sign in $Q = -3H$ is due to the sign in the identification of the target time t with the world-sheet zero mode of $-\varphi$ [17].

The relations (15) generalize and replace the conformal-invariance conditions $\beta^i = 0$ of the critical string theory, and express the conditions necessary for the restoration of conformal invariance by the Liouville mode [13]. Interpreting the latter as an extra target dimension, the conditions (15) may also be viewed as conformal invariance conditions of a *critical* σ model in (D+1) target space-time dimensions, where D is the target dimension of the non-critical σ model before Liouville dressing. In most Liouville approaches, one treats the Liouville mode φ and time t as independent coordinates. However, in our approach [17, 15, 18], as already mentioned, we take the further step of restricting this extended (D+1)-dimensional space-time to a hypersurface determined by the identification $\varphi = -t$. This means that, as time flows, one is restricted to a D-dimensional subspace of the full (D+1)-dimensional Liouville space-time. This restriction arose in the work of [18, 19] because the potential between massive particles in the effective field theory was found to be proportional to $\cosh(t + \varphi)$, which is minimized when $\varphi = -t$.

However, the flow of the Liouville mode opposite to that of target time may be given a deeper mathematical interpretation. It may be viewed as a consequence of a specific treatment of the area constraint in non-critical (Liouville) σ models [17], which involves the evaluation of the Liouville-mode path integral via an appropriate steepest-descent contour. In this way, one obtains a 'breathing' world-sheet evolution, in which the world-sheet area starts from a very large value (serving as an infrared cutoff), shrinks to a very small one (serving as an ultraviolet cutoff), and then inflates again towards very large values (returning to an infrared cutoff). Such a situation may then be interpreted [17] as a world-sheet 'bounce' back to the infrared, implying that the physical flow of target time is opposite to that of the world-sheet scale (Liouville zero mode).

We now become more specific. We consider a non-critical σ model with a background metric $G_{\mu\nu}$, antisymmetric tensor $B_{\mu\nu}$, and dilaton Φ. These have the following $\mathcal{O}(\alpha')$ β functions, where α' is the Regge slope [1]:

[2]The gradient-flow property of the β functions makes the analogy with the inflationary case even more profound, with the running central charge $C[g]$ [14] playing the rôle of the inflaton potential in conventional inflationary field theory.

$$\beta^G_{\mu\nu} = \alpha' \left(R_{\mu\nu} + 2\nabla_\mu \partial_\nu \Phi - \frac{1}{4} H_{\mu\rho\sigma} H_\nu^{\rho\sigma} \right) ,$$
$$\beta^B_{\mu\nu} = \alpha' \left(-\frac{1}{2} \nabla_\rho H^\rho_{\mu\nu} + H^\rho_{\mu\nu} \partial_\rho \Phi \right) ,$$
$$\tilde{\beta}^\Phi = \beta^\Phi - \frac{1}{4} G^{\rho\sigma} \beta^G_{\rho\sigma} = \frac{1}{6} (C - 26) . \tag{16}$$

The Greek indices are four-dimensional, including target-time components $\mu, \nu, ... = 0, 1, 2, 3$ on the D3-branes of [18], and $H_{\mu\nu\rho} = \partial_{[\mu} B_{\nu\rho]}$ is the antisymmetric tensor field strength. We consider the following representation of the four-dimensional field strength in terms of a pseudoscalar (axion-like) field b:

$$H_{\mu\nu\rho} = \epsilon_{\mu\nu\rho\sigma} \partial^\sigma b , \tag{17}$$

where $\epsilon_{\mu\nu\rho\sigma}$ is the four-dimensional antisymmetric symbol. Next, we choose an axion background that is linear in the time t [12]:

$$b = b(t) = \beta t , \quad \beta = \text{constant} , \tag{18}$$

which yields a constant field strength with spatial indices only: $H_{ijk} = \epsilon_{ijk}\beta$, $H_{0jk} = 0$. This implies that such a background is a conformal solution of the full $\mathcal{O}(\alpha')$ β function for the four-dimensional antisymmetric tensor. We also consider a dilaton background that is linear in the time t [12]:

$$\Phi(t, X) = \text{const} + (\text{const})' t . \tag{19}$$

This background does not contribute to the β functions for the antisymmetric and metric tensors.

Suppose now that only the metric is a non-conformal background, due to some initial quantum fluctuation or catastrophic event, such as the collision of two branes discussed above, which results in an initial central charge deficit Q^2 (14) that is constant at early stages after the collision. Let

$$G_{ij} = e^{\kappa\varphi + Hct} \eta_{ij} , \quad G_{00} = e^{\kappa'\varphi + Hct} \eta_{00} , \tag{20}$$

where t is the target time, φ is the Liouville mode, $\eta_{\mu\nu}$ is the four-dimensional Minkowski metric, and κ, κ' and c are constants to be determined. As already discussed, the standard inflationary scenario in four-dimensional physics requires $Q = -3H$, which stems from the identification of the Liouville mode with time [17] $\varphi = -t$, that is imposed dynamically [18] at the end of our computations. Initially, one should treat φ, t as independent target-space components.

The Liouville dressing induces [13] σ-model terms of the form $\int_\Sigma R^{(2)} Q\varphi$, where $R^{(2)}$ is the world-sheet curvature. Such terms provide non-trivial contributions to the dilaton background in the (D+1)-dimensional space-time (φ, t, X^i):

$$\Phi(\varphi, t, X^i) = Q\,\varphi + (\text{const})'t + \text{const}\ . \tag{21}$$

If we choose

$$(\text{const})' = Q\ , \tag{22}$$

we see that (21) implies a *constant* dilaton background during the inflationary era, in which the central charge deficit Q is constant.

The choices (21) and (22), like the identification $\varphi = -t$, apply to the world-sheet zero modes of the Liouville field and the time coordinate. As such, they imply a constant dilaton at the mean-field (classical) level. World-sheet quantum fluctuations of the dilaton, associated with non-zero modes of these fields, do not cancel, since the identification $\varphi = -t$ is not valid for the fluctuating parts of the respective σ-model fields. This leads in turn to non-trivial fluctuations of the dilaton field during inflation. The summation over world-sheet genera turns such fluctuations into target-space quantum fluctuations. This allows one [19] to apply the phenomenology of scalar field fluctuations used in conventional inflationary models also in this case, in order to constrain physically important parameters of the non-critical string theory by means of recent cosmological data [9].

We now consider the Liouville-dressing [13] (15) for the β functions of the metric and antisymmetric tensor fields (16) at the level of world-sheet zero modes of the σ-model fields. The dilaton equation yields no independent information for a constant mean dilaton field, apart from expressing the dilaton β function in terms of the central-charge deficit as usual. For the axion background (18), only the metric yields a non-trivial constraint (we work in units with $\alpha' = 1$ for convenience):

$$\ddot{G}_{ij} + Q\dot{G}_{ij} = -R_{ij} + \frac{1}{2}\beta^2 G_{ij}\ , \tag{23}$$

where the dot indicates differentiation with respect to the (zero mode of the) world-sheet Liouville mode φ, and R_{ij} is the (non-vanishing) Ricci tensor of the (non-critical) σ model with coordinates $(t, \boldsymbol{x})$: $R_{00} = 0\ , R_{ij} = \frac{c^2 H^2}{2} e^{(\kappa - \kappa')\varphi}\eta_{ij}$. One should also take into account the temporal equation for the metric tensor:

$$\ddot{G}_{00} + Q\dot{G}_{00} = -R_{00} = 0\ , \tag{24}$$

where the vanishing of the Ricci tensor stems from the specific form of the background (20). The analogue equation is identically zero for the antisymmetric tensor background. We seek metric backgrounds of inflationary (de Sitter) RW form:

$$G_{00} = -1\ , \quad G_{ij} = e^{2Ht}\eta_{ij}\ . \tag{25}$$

Then, from (25), (20), (19) and (18), we observe that there indeed is a consistent solution with:

$$Q = -3H = -\kappa',\ c = 3,\ \kappa = H,\ \beta^2 = 5H^2, \tag{26}$$

corresponding to the conventional form of inflationary equations for scalar fields.

In this talk we do not mention ways of exiting from this inflationary phase and reheating the Universe. These issues may also be approached from a Liouville σ-model point of view, as we shall report in a forthcoming publication [23].

5 Liouville Dark Energy: the End Game

In the generic class of non-critical string models described in this talk, the σ model always asymptotes, for long enough cosmic times, to the linear-dilaton conformal σ-model field theory of [12]. However, it is important to stress that this is only an asymptotic limit, and the current era of our Universe should be viewed as close to, but still not at the equilibrium relaxation point. Thus the dilaton is almost linear in the σ-model time, and hence varies almost logarithmically in the Einstein-frame time (8). This slight non-equilibrium would lead to a time dependence of the unified gauge coupling and other constants such as the four-dimensional Planck length (1), mainly through the time-dependence of the string coupling (9) that results from the time dependence of the linear dilaton (3).

The asymptotic-time regime of the Type-0 cosmological string model of [15] has been obtained analytically, by solving the pertinent (13) for the various fields. As already mentioned, at later times the theory becomes four-dimensional, and the only non-trivial information is contained in the scale factor and the dilaton, given that the topological flux field remains conformal in this approach, and the moduli and initial tachyon fields decouple very fast at the initial stages after inflation in this model. For times long after the initial fluctuations, such as the present times where the linear approximation is valid, the solution for the dilaton in the σ-model frame, as follows from the (13), takes the form:

$$\Phi(t) = -\ln\left[\frac{\alpha A}{F_1}\cosh(F_1 t)\right] \ , \tag{27}$$

where F_1 is a positive constant, α is a numerical constant of order one, and

$$A = \frac{C_5 e^{s_{01}}}{\sqrt{2}V_6} \ , \tag{28}$$

with s_{01} the equilibrium value of the modulus field σ_1 associated with the large bulk dimension, and C_5 the corresponding flux of the five-form flux field. Notice the independence of A from this large bulk dimension.

For very large times $F_1 t \gg 1$ (in string units), one therefore approaches a linear solution for the dilaton: $\Phi \sim \text{const} - F_1 t$. From (27), (9) and (1), we thus observe that the asymptotic weakness of gravity in this Universe [15] is

due to the smallness of the internal space V_6 as compared with the flux C_5 of the five-form field. The constant F_1 is related to the central-charge deficit of the underlying non-conformal σ-model [15]:

$$Q = q_0 + \frac{q_0}{F_1}(F_1 + \frac{d\Phi}{dt}) \ , \tag{29}$$

where q_0 is a constant, and the numerical solution of (13) studied in [15]) requires that $q_0/F_1 = (1 + \sqrt{17})/2 \simeq 2.56$. However, we believe that this is only a result of the numerical approximations in the analysis of [15], and for our purposes we consider from now on

$$F_1 \sim q_0 \ , \tag{30}$$

in accord with [12], to which the model relaxes for large times. In this spirit, we require that the value of q_0 to which the central charge deficit (29) asymptotes must be, for the consistency of the underlying string theory, one of the discrete values obtained in [12], for which the string scattering amplitudes factorise. This asymptotic string theory with a time-independent central-charge deficit, $q_0^2 \propto c^* - 25$ (or $c^* - 9$ for superstring) may therefore be considered as an *equilibrium* situation, with an S-matrix defined for specific (discrete) values of the central charge c^*, generalizing the standard critical (super)string which corresponds to central charge $c^* = 25$ (=9 for superstrings) [13, 12].

Defining the Einstein frame time t_E through (6), we obtain in this case (27)

$$t_E = \frac{\alpha A}{F_1^2} sinh(F_1 t) \ . \tag{31}$$

In terms of the Einstein-frame time one obtains a logarithmic time-dependence [12] for the dilaton

$$\Phi_E = \text{const} - \ln(\gamma t_E) \ , \tag{32}$$

where

$$\gamma \equiv \frac{F_1^2}{\alpha A} \ . \tag{33}$$

For large t_E, e.g., now or in the future, one has

$$a_E(t_E) \simeq \frac{F_1}{\gamma}\sqrt{1 + \gamma^2 t_E^2} \ . \tag{34}$$

At very large times $a(t_E)$ scales linearly with the Einstein-frame cosmological time t_E [15], and hence there is no cosmic horizon. From a field-theoretical viewpoint, this would allow for a proper definition of asymptotic states and thus a scattering matrix. As we mentioned briefly above, however, from a stringy point of view, there are restrictions in the asymptotic values of the central charge deficit q_0, and there is only a discrete spectrum of values of q_0 that allow for a full stringy S-matrix to be defined, respecting modular

invariance [12]. Asymptotically, the Universe relaxes to its ground-state equilibrium situation, and the non-criticality of the string caused by the initial fluctuation disappears, giving rise to a critical (equilibrium) string Universe with a Minkowski metric and a linear-dilaton background. This is a generic feature of the models considered here and in [24], allowing the conclusions to be extended beyond Type-0 string theory to incorporate also string/brane models with target-space supersymmetry, such as those in [25, 19].

An important comment is in order at this point, regarding the form of the Einstein metric corresponding to (34):

$$g^E_{00} = -1, \qquad g_{ij} = a^2_E(t_E) = \frac{F_1^2}{\gamma^2} + F_1^2 t_E^2 \ . \tag{35}$$

Although asymptotically for $t_E \to \infty$ the above metric asymptotes to the linearly-expanding Universe of [12], the presence of a constant F_1^2/γ^2 contribution implies that the solution for large but finite t_E, such as the current era of the Universe, is different from that of [12]. Indeed, the corresponding σ-model metric (4) is not Minkoswski-flat, and the pertinent σ model does not correspond to a conformal field theory. This should come as no surprise, because for finite t_E, no matter how large, the σ-model theory requires Liouville dressing. It is only at the end-point of the time-flow: $t_E \to \infty$ that the underlying string theory becomes conformal, and the system reaches equilibrium.

The Hubble parameter of such a Universe becomes for large t_E

$$H(t_E) \simeq \frac{\gamma^2 t_E}{1 + \gamma^2 t_E^2} \ . \tag{36}$$

On the other hand, the Einstein-frame effective four-dimensional "vacuum energy density", defined through the running central-charge deficit Q^2, upon compactification to four dimensions of the ten-dimensional expression $\int d^{10}x\sqrt{-g}e^{-2\Phi}Q^2(t_E)$, is [15]:

$$\Lambda_E(t_E) = e^{2\Phi-\sigma_1-5\sigma_2}Q^2(t_E) \simeq \frac{q_0^2\gamma^2}{F_1^2(1+\gamma^2 t_E^2)} \sim \frac{\gamma^2}{1+\gamma^2 t_E^2} \ , \tag{37}$$

where, for large t_E, Q is given in (29) and approaches its equilibrium value q_0, and we took into account (30). Thus, the dark energy density relaxes to zero for $t_E \to \infty$. Notice an important feature of the form of the relaxation (37), namely that the proportionality constants in front are such that, for asymptotically large $t_E \to \infty$, Λ becomes independent of the equilibrium conformal field theory central charge q_0.

Finally, and most importantly for our purposes here, the deceleration parameter in the same regime of t_E becomes:

$$q(t_E) = -\frac{(d^2a_E/dt_E^2)\ a_E}{(da_E/dt_E)^2} \simeq -\frac{1}{\gamma^2 t_E^2} \ . \tag{38}$$

The important point to make in connection with this expression is that, as is clear from (32) and (9), it can be identified, up to irrelevant constants of proportionality which conventional normalisation sets to one, with the square of the string coupling [24]:

$$|q(t_E)| = g_s^2 \tag{39}$$

To guarantee the consistency of perturbation theory, one must have $g_s < 1$, which can be achieved in our approach if one defines the present era by the time regime

$$\gamma \sim t_E^{-1} \tag{40}$$

in the Einstein frame. This is compatible with large enough times t_E (in string units) for

$$|C_5|e^{-5s_{02}}/F_1^2 \sim |C_5|e^{-5s_{02}}/q_0^2 \gg 1 \ , \tag{41}$$

as becomes clear from (28),(33) and (30). This condition can be guaranteed either by small radii of five of the extra dimensions, or by a large value of the flux $|C_5|$ of the five-form of the Type-0 string, compared with q_0. We discuss later concrete examples of non-critical string cosmologies, in which the asymptotic value of the central charge $q_0 \ll 1$ in string units. Recalling that the relatively large extra dimension in the direction of the flux, s_{01}, decouples from this condition, we observe that there is the possibility of constructing effective five-dimensional models with a large uncompactified fifth dimension while respecting the condition (40).

The Hubble parameter and the cosmological constant continue to be compatible with the current observations in the regime (40) of Einstein-frame times, while the string coupling (39) is kept finite and of order unity by the conditions (38, 40), as suggested by grand unification phenomenology [1].

6 Dark Energy and the String Coupling

We next turn to the equation of state of our Universe. As discussed in [15], our model resembles quintessence models, with the dilaton playing the rôle of the quintessence field. Hence the equation of state for our Type-0 string Universe reads [26]:

$$w_\Phi = \frac{p_\Phi}{\rho_\Phi} = \frac{\frac{1}{2}(\dot{\Phi})^2 - V(\Phi)}{\frac{1}{2}(\dot{\Phi})^2 + V(\Phi)} \ , \tag{42}$$

where p_Φ is the pressure and ρ_Φ is the energy density, and $V(\Phi)$ is the effective potential for the dilaton, which in our case is provided by the central-charge deficit term. Here the dot denotes Einstein-frame differentiation. In the Einstein frame, the potential $V(\Phi)$ is given by Λ_E in (50). In the limit $Q \to q_0$, which we have argued should characterise the present era to a good approximation, the effective potential $V(\Phi)$ is then of order $(q_0^2/2F_1^2)t_E^{-2}$, where we

recall (c.f., (30)) that q_0/F_1 is of order one. In the Einstein frame the exact normalisation of the dilaton field is $\Phi_E = \text{const} - \ln(\gamma t_E)$. We then obtain for the present era:

$$\frac{1}{2}\dot{\Phi}^2 \sim \frac{1}{2t_E^2}, \qquad V(\Phi) \sim \frac{6.56}{2}\frac{1}{t_E^2} \; . \tag{43}$$

This implies an equation of state (42):

$$w_\Phi(t_E \gg 1) \simeq -0.74 \tag{44}$$

for (large) times t_E in string units corresponding to the present era (40). This number can be pushed lower, towards $w \to -1$, by a slight adjustment of the various parameters, improving the agreement with current cosmological data [9]. Assuming a conventional effective four-dimensional low-energy fluid Universe, which is a good picture in our situation where the moduli and other fields have decoupled at early stages of the Universe, we have:

$$q = \frac{1}{2}(1 + 3w_\Phi) \tag{45}$$

from which we obtain

$$q = -0.61 \; . \tag{46}$$

This fixes the string coupling (39) in the perturbative regime consistent with grand unification scenarios extrapolated from low energies.

So far the model does not include ordinary matter: only fields from the string gravitational multiplet have been included. Inclusion of ordinary matter is not expected to change qualitatively the result. We conjecture that the fundamental relation (39) will continue to hold, the only difference being that the inclusion of ordinary matter will tend to reduce the string acceleration:

$$q = \frac{1}{2}\Omega_M - \Omega_\Lambda \; , \tag{47}$$

where $\Omega_M(\Omega_\Lambda)$ denotes the total matter (vacuum) energy density, normalised to the critical energy density of a spatially flat Universe.

There is a remarkable coincidence in numbers for this non-supersymmetric Type-0 string Universe with the astrophysical observations, which yield q close to th value (46). The ordinary matter content of the Universe has $\Omega_{\text{ordinary matter}} \simeq 0.04$ and the dark matter content is estimated to have $\Omega_{DM} = 0.23$, while the Dark Energy content is $\Omega_\Lambda \simeq 0.73$. This yields $q = -0.595$, which is only a few per cent away from (46). In fact, if one naively used the value (46) for q, obtained in our case where ordinary matter was ignored, in the expression (47), one would find $\Omega_\Lambda \simeq 0.74$, indicating that the contribution of the dilaton field to the cosmic acceleration is the dominant one.

If the relation (39) holds after the inclusion of matter, even in supersymmetric models, one arrives at an even better value of the string coupling,

$g_s^2 \simeq 0.595$, more consistent with the unification prediction of the minimal supersymmetric standard model at a scale $\sim 10^{16}$ GeV. The only requirement for the asymptotic condition (39) to hold is that the underlying stringy σ model is non-critical and asymptotes for large times to the linear dilaton conformal field theory of [12]. It should be understood, of course, that the precise relation of the four-dimensional gauge coupling with the ten-dimensional string coupling depends on the details of compactification, which we do not discuss here.

The variation of the dilaton field at late cosmic times implies a slow variation of the string coupling (39), $\dot{g}_s/g_s = 1/t_E \sim 10^{-60}$ in the present era. The corresponding variations of the gauge couplings are too small to affect current phenomenology.

The above considerations are rather generic to models which relax asymptotically to the linear-dilaton conformal field theory solutions of [12], and from this point of view are physically interesting. We did not need to specify above the microscopic theory underlying the deviation from non criticality. For this one would need some specific example of such a deviation from a conformally-invariant point in string theory space. One such example, with physically interesting consequences, is provided by the colliding brane-world scenario, in which the Liouville string σ model describes stringy excitations on the brane worlds, at relatively long times after the collision so that string perturbation theory is valid. We now discuss this briefly.

7 A Concrete Non-Critical String Example: Colliding Branes

We now concentrate on particular examples of the previous general scenario [22], in which the non-criticality is induced by the collision of two branes as seen in Fig. 1. We first discuss the basic features of this scenario. For our purposes below we assume that the string scale is of the same order as the four-dimensional Planck scale, though this is an assumption that may be relaxed, in view of recent developments in strings with large compactification directions, as we mentioned in the Introduction.

Following [18], we consider two 5-branes of Type-II string theory, in which the extra two dimensions have been compactified on tori. On one of the branes (assumed to be the hidden world), the torus is magnetized with a field intensity $\mathcal{H}$. Initially our world is compactified on a normal torus, without a magnetic field, and the two branes are assumed to be on a collision course with a small relative velocity $v \ll 1$ in the bulk, as illustrated in Fig. 1. The collision produces a non-equilibrium situation, which results in electric current transfer from the hidden brane to the visible one. This causes the (adiabatic) emergence of a magnetic field in our world.

The instabilities associated with such magnetized-tori compactifications are not a problem in the context of the cosmological scenario discussed here.

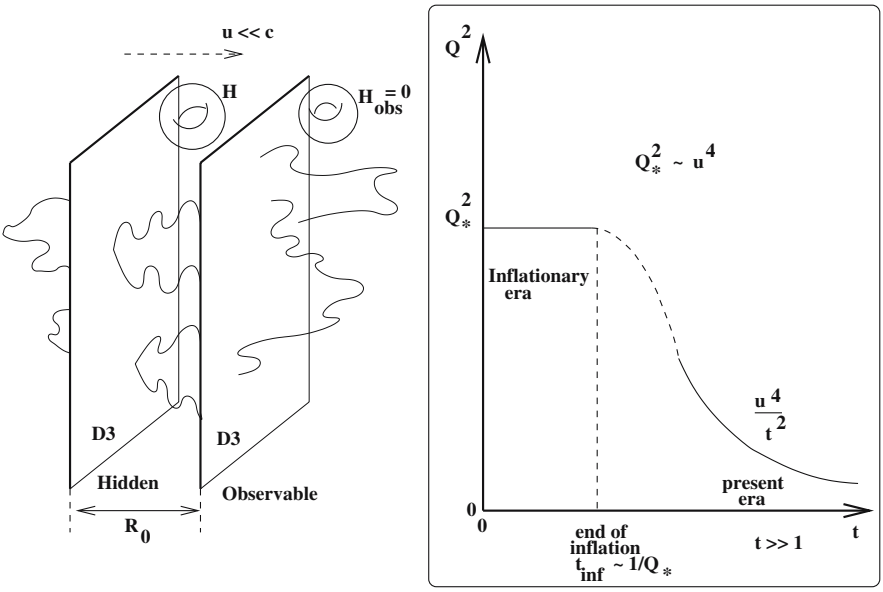

Fig. 1. A scenario in which the collision of two Type-II 5-branes provides inflation and a relaxation model for cosmological vacuum energy.

As discussed in [18], the collision may also produce decompactification of the extra toroidal dimensions at a rate much slower than any other rate in the problem. As also discussed in [18], this guarantees asymptotic equilibrium and a proper definition of an S-matrix for the stringy excitations on the observable world. We shall come back to this issue at the end of this Section.

The collision of the two branes implies, for a short period afterwards, while the branes are at most a few string scales apart, the exchange of open-string excitations stretching between the branes, whose ends are attached to them. As argued in [18], the exchanges of such pairs of open strings in Type-II string theory result in an excitation energy in the visible world. The latter may be estimated by computing the corresponding scattering amplitude of the two branes, using string-theory world-sheet methods [27]: the time integral for the relevant potential yields the scattering amplitude. Such estimates involve the computation of appropriate world-sheet annulus diagrams, due to the existence of open string pairs in Type-II string theory. This implies the presence of "spin factors" as proportionality constants in the scattering amplitudes, which are expressed in terms of Jacobi Θ functions. For the small brane velocities $v \ll 1$ we are considering here, the appropriate spin structures start at quartic order in v, for the case of identical branes, as a result of the mathematical properties of the Jacobi functions [27]. This in turn implies [18, 25] that the resulting excitation energy on the brane world is of order $V = \mathcal{O}(v^4)$, which may be thought of as an initial (approximately

constant) value of a supercritical central-charge deficit for the non-critical σ model that describes stringy excitations in the observable world after the collision:

$$Q^2 = \left(\sqrt{\beta}v^2 + \mathcal{H}^2\right)^2 > 0\ . \tag{48}$$

where, in the model of [25, 19], the proportionality factor β, computed using string amplitude computations, is of order

$$\beta \sim 2\sqrt{3} \cdot 10^{-8} \cdot g_s\ , \tag{49}$$

with g_s the string coupling $g_s^2 \sim 0.5$ for interesting phenomenological models [1, 5], as discussed above. We recall that the supercriticality, i.e., the positive definiteness of the central charge deficit (48), of the model is essential [12] for a time-like signature of the Liouville mode, and hence its interpretation as target time.

At times long after the collision, the branes slow down and the central charge deficit is no longer constant but relaxes with time t. In the approach of [18], this relaxation has been computed by using world-sheet logarithmic conformal field theory methods [28], taking into account recoil (in the bulk) of the observable-world brane and the identification of target time with the (zero mode of the) Liouville field. In that work it was assumed that the final equilibrium value of the central charge deficit was zero, i.e., the theory approached a critical string. This late-time varying deficit $Q^2(t)$ scales with the target time (Liouville mode) as (in units of the string scale M_s):

$$Q^2(t) \sim \frac{(\mathcal{H}^2 + v^2)^2}{t^2}\ . \tag{50}$$

Some explanations are necessary at this point. In arriving at (50), one identifies the world-sheet renormalisation group scale $\mathcal{T} = \ln(L/a)^2$ (where $(L/a)^2$ is the world-sheet area), appearing in the Zamolodchikov c-theorem used to determine the rate of change of Q, with the zero mode of a normalised Liouville field ϕ_0, such that $\phi_0 = Q\mathcal{T}$. This normalisation guarantees a canonical kinetic term for the Liouville field in the world-sheet action [13]. Thus it is ϕ_0 that is identified with $-t$, with t the target time.

On the other hand, in other models [15] the asymptotic value of the central-charge deficit may not be zero, in the sense that the asymptotic theory is that of a linear dilaton, with a Minkowski metric in the σ-model frame [12]. This theory is still a conformal model, but the central charge is a constant q_0, and in fact the dilaton is of the form $\Phi = q_0 t + \text{const}$, where t is the target time in the σ-model frame. Conformal invariance, as mentioned previously, requires [12] that q_0 takes on one of a discrete set of values, in the way explained in [12]. In such a case, following the same method as in the $q_0 = 0$ case of [18], one arrives at the asymptotic form

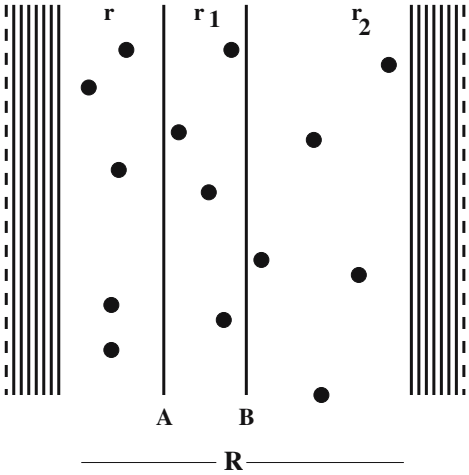

Fig. 2. A model for supersymmetric D-particle foam consisting of two stacks each of sixteen parallel coincident D8-branes, with orientifold planes (thick dashed lines) attached to them [25]. The space does not extend beyond the orientifold planes. The bulk region of ten-dimensional space in which the D8-branes are embedded is punctured by D0-branes (D-particles, dark blobs). The two parallel stacks are sufficiently far from each other that any Casimir contribution to the vacuum energy is negligible. If the branes are stationary, there is zero vacuum energy, and the configuration is a consistent supersymmetric string vacuum. To obtain excitations corresponding to interesting cosmologies, one should move one (or more) of the branes from each stack and then let them collide (Big Bang), bounce back (inflation), and then relax to their original position, where they collide again with the remaining branes in each stack (exit from inflation, reheating).

$$Q^2(t) \sim q_0^2 + \mathcal{O}\left(\frac{\mathcal{H}^2 + v^2)}{t} q_0\right) \tag{51}$$

for large times t.

The colliding-brane model of [18] can be extended to incorporate proper supersymmetric vacuum configurations of string theory [25]. As illustrated in Fig. 2, this model consists of two stacks of D8-branes with the same tension, separated by a distance R. The transverse bulk space is restricted to lie between two orientifold planes, and is populated by D-particles. It was shown in [25] that, in the limit of static branes and D-particles, this configuration constitutes a zero vacuum-energy supersymmetric ground state of this brane theory. Bulk motion of either the D-branes or the D-particles[3] results in non-zero vacuum energy [25] and hence the breaking of target supersymmetry, proportional to some power of the average (recoil) velocity squared, which

[3]The latter could arise from recoil following scattering with closed-string states propagating in the bulk.

depends on the precise string model used to described the (open) stringy matter excitations on the branes.

The colliding-brane scenario can be realized [19] in this framework by allowing (at least one of) the D-branes to move, keeping the orientifold planes static. One may envisage a situation in which the two branes collide at a certain moment in time corresponding to the Big Bang - a catastrophic cosmological event setting the beginning of observable time - and then bounce back. The width of the bulk region is assumed to be long enough that, after a sufficiently long time following the collision, the excitation energy on the observable brane world - which corresponds to the conformal charge deficit in a σ-model framework [18, 25] – relaxes to tiny values. It is expected that a ground-state configuration will be achieved when the branes reach the orientifold planes again (within stringy length uncertainties of order $\ell_s = 1/M_s$, the string scale). In this picture, since observable time starts ticking after the collision, the question how the brane worlds started to move is merely philosophical or metaphysical. The collision results in a kind of phase transition, during which the system passes through a non-equilibrium phase, in which one loses the conformal symmetry of the stringy σ model that describes perturbatively string excitations on the branes. At long times after the collision, the central charge deficit relaxes to zero [18], indicating that the system approaches equilibrium again. The Dark Energy observed today may be the result of the fact that our world has not yet relaxed to this equilibrium value. Since the asymptotic ground state configuration has static D-branes and D-particles, and hence has zero vacuum energy as guaranteed by the exact conformal field theory construction of [25, 19], it avoids the fine tuning problems in the model of [18].

Sub-asymptotically, there are several contributions to the excitation energy of our brane world in this picture. One comes from the interaction of the brane world with nearby D-particles, i.e., those within distances at most of order $\mathcal{O}(\ell_s)$, as a result of open strings stretched between them. The other contribution comes from the collision of the identical D-branes. For a sufficiently dilute gas of nearby D-particles we may assume that this latter contribution is the dominant one. In this case, one may ignore the D-particle/D-brane contributions to the vacuum energy, and hence apply the previous considerations on inflation, based on the $\mathcal{O}(v^4)$ central charge deficit, with v the velocity of the brane world in the bulk.

The presence of D-particles, which inevitably cross the D-branes in such a picture, even if the D-particle defects are static initially, distorts slightly the inflationary metric on the observable brane world at early times after the collision, during an era of approximately constant central charge deficit, without leading to significant qualitative changes. Moreover, the existence of D-particles on the branes will affect the propagation of string matter on the branes, in the sense of modifying their dispersion relations by inducing local curvature in space-time, as a result of recoil following collisions with string

matter. However, it was argued in [29] that only photons are susceptible to such effects in this scenario, due to the specific gauge properties of the membrane theory at hand. The dispersion relations for chiral matter particles, or in general fields on the D-branes that transform non-trivially under the Standard Model gauge group, are protected by special gauge symmetries in string theory, and as such are not modified.

8 Liouville's Dark Secrets

The use of Liouville strings to describe the evolution of our Universe seems generally appropriate, since non-critical strings are associated with non-equilibrium situations which undoubtedly occurred in the Early Universe, and may still occur today. It is remarkable that the departure from criticality may even enhance the predictability of string theory, although the space of non-critical string theories is much larger that of critical strings, to the point that purely stringy quantities such as the string coupling are accessible to experiment.

We have discussed in this talk Liouville cosmological models based on non-critical strings with various asymptotic configurations of the dilaton, speculating on the Big Bang itself, on the inflationary phase and the possibility of exit from it, as well the evolution of the Universe at large times, both current and future. A particularly interesting case from the physical point of view is that of a dilaton that is asymptotically linear in cosmic time. This is known to correspond to a proper conformal field theory [12]. We have observed that the string coupling is identified in such a model (up to irrelevant constants of order one) [24] with the deceleration parameter of the Universe through equation (39).

We stress once more the importance of non-criticality in arriving at (39). In critical strings, which usually assume the absence of a four-dimensional dilaton, such a relation is not obtained, and the string coupling is not directly measurable in this way.

The approach of the identification of target time in such a framework with a world-sheet renormalisation group scale, the Liouville mode [17], provides a novel way of selecting the ground state of the string theory, which may not necessarily be associated with minimisation of energy, but could be a matter of cosmic 'chance'. Indeed, it may be a random event that the initial state of our cosmos corresponds to a certain Gaussian fixed point in the space of string theories, which is then perturbed in the Big Bang by some relevant (in a world-sheet sense) deformation, thereby making the theory non-critical, and hence out of equilibrium from a target space-time viewpoint. Then the theory flows along some renormalisation-group trajectory to some specific ground state, corresponding to the infrared fixed point of this perturbed world sheet σ-model theory. This approach allows for many parallel universes to be implemented of course, and our world might be just one of these. Each

Universe, may flow between different fixed points, perturbed by different operators. Standard world-sheet renormalization-group arguments imply that the various flow trajectories do not intersect, although this is something that is far from proven in general. It seems to us that this scenario is much more specific than the landscape scenario [30], which has recently been advocated as an attempt to parametrise our ignorance of the true structure of string/M theory.

Acknowledgements

This work is based on a talk given by D.V.N. at the conference DARK 2004 in Texas A & M University in October 2004. N.E.M. wishes to thank Juan Fuster and IFIC-University of Valencia (Spain) for their interest and support. The work of D.V.N. is supported by D.O.E. grant DE-FG03-95-ER-40917.

References

1. M.B. Green, J.H. Schwarz and E. Witten, *Superstring Theory*, Vols. I & II (Cambridge University Press, 1987).
2. J. Polchinski, *String theory*, Vol. 2 (Cambridge University Press, 1998); J.H. Schwarz, hep-th/9907061.
3. N. Arkani-Hamed, S. Dimopoulos and G.R. Dvali, Phys. Lett. B **429** (1998) 263, hep-ph/9803315; I. Antoniadis, N. Arkani-Hamed, S. Dimopoulos and G.R. Dvali, Phys. Lett. B **436** (1998) 257, hep-ph/9804398.
4. L. Randall and R. Sundrum, Phys. Rev. Lett. **83** (1999) 4690, hep-th/9906064.
5. see, for instance: L.E. Ibanez, R. Rabadan and A.M. Uranga, Nucl. Phys. B **576** (2000) 285, hep-th/9905098; L.E. Ibanez, hep-ph/9905349; C.A. Scrucca and M. Serone, JHEP **9912** (1999) 024, hep-th/9912108; D.M. Ghilencea and G.G. Ross, Nucl. Phys. B **595** (2001) 277, hep-ph/0006318, and references therein.
6. D. Langlois, Prog. Theor. Phys. Suppl. **148** (2003) 181, hep-th/0209261, and references therein.
7. J. Khoury, B.A. Ovrut, P.J. Steinhardt and N. Turok, Phys. Rev. D **64** (2001) 123522, hep-th/0103239.
8. B.P. Schmidt et al. [Supernova Search Team Collaboration], Astrophys. J. **507** (1998) 46, astro-ph/9805200; S. Perlmutter et al. [Supernova Cosmology Project Collaboration], Astrophys. J. **517** (1999) 565, astro-ph/9812133; J.P. Blakeslee et al. [Supernova Search Team Collaboration], Astrophys. J. **589** (2003) 693, astro-ph/0302402; A.G. Riess et al. [Supernova Search Team Collaboration], Astrophys. J. **560** (2001) 49, astro-ph/0104455.
9. D.N. Spergel et al. [WMAP Collaboration], Astrophys. J. Suppl. **148** (2003) 175, astro-ph/0302209.
10. E. Witten, hep-th/0106109.
11. W. Fischler and L. Susskind, Phys. Lett. B **171** (1986) 383; Phys. Lett. B **173** (1986) 262.

12. I. Antoniadis, C. Bachas, J.R. Ellis and D.V. Nanopoulos, Phys. Lett. B **211** (1988) 393; Nucl. Phys. B **328** (1989) 117; Phys. Lett. B **257** (1991) 278.
13. F. David, Mod. Phys. Lett. A **3** (1988) 1651; J. Distler and H. Kawai, Nucl. Phys. B **321** (1989) 509; J. Distler, Z. Hlousek and H. Kawai, Int. J. Mod. Phys. A **5** (1990) 391; see also: N.E. Mavromatos and J.L. Miramontes, Mod. Phys. Lett. A **4** (1989) 1847; E. D'Hoker and P.S. Kurzepa, Mod. Phys. Lett. A **5** (1990) 1411.
14. A.B. Zamolodchikov, JETP Lett. **43** (1986) 730 [Pisma Zh. Eksp. Teor. Fiz. **43** (1986) 565].
15. G.A. Diamandis, B.C. Georgalas, N.E. Mavromatos and E. Papantonopoulos, Int. J. Mod. Phys. A **17** (2002) 4567, hep-th/0203241; G.A. Diamandis, B.C. Georgalas, N.E. Mavromatos, E. Papantonopoulos and I. Pappa, Int. J. Mod. Phys. A **17** (2002) 2241, hep-th/0107124.
16. E. Witten, Int. J. Mod. Phys. A **10** (1995) 1247, hep-th/9409111.
17. J.R. Ellis, N.E. Mavromatos and D.V. Nanopoulos, Phys. Lett. B **293** (1992) 37, hep-th/9207103; *Invited review for the special Issue of J. Chaos Solitons Fractals*, Vol. 10, (eds. C. Castro amd M.S. El Naschie, Elsevier Science, Pergamon 1999) 345, hep-th/9805120; Phys. Rev. D **63** (2001) 024024, gr-qc/0007044.
18. E. Gravanis and N. E. Mavromatos, Phys. Lett. B **547** (2002) 117, hep-th/0205298; N. E. Mavromatos, hep-th/0210079 (published in *Oulu 2002 (Finland), Beyond the desert* (ed. H.V. Klapdor-Kleingrothaus, IoP 2003)), 3.
19. J. Ellis, N.E. Mavromatos, D.V. Nanopoulos and A. Sakharov, gr-qc/0407089, New J. Phys. **6** (2004) 171.
20. I. Klebanov and A.A. Tseytlin, Nucl. Phys. **B 546** (1999) 155; Nucl. Phys. **B 547** (1999) 143.
21. G. Curci and G. Paffuti, Nucl. Phys. B **286** (1987) 399.
22. J.R. Ellis, N.E. Mavromatos and D.V. Nanopoulos, Mod. Phys. Lett. A **10** (1995) 1685, hep-th/9503162.
23. J. Ellis, N.E. Mavromatos, D.V. Nanopoulos and M. Westmuckett, in preparation.
24. J. Ellis, N.E. Mavromatos and D.V. Nanopoulos, hep-th/0412240.
25. J. Ellis, N.E. Mavromatos and M. Westmuckett, Phys. Rev. D **70** (2004) 044036, gr-qc/0405066; gr-qc/0501060.
26. S.M. Carroll, Living Rev. Rel. **4** (2001) 1, astro-ph/0004075.
27. C. Bachas, hep-th/9503030.
28. I.I. Kogan and N.E. Mavromatos, Phys. Lett. B **375** (1996) 111, hep-th/9512210; I.I. Kogan, N.E. Mavromatos and J.F. Wheater, Phys. Lett. B **387** (1996) 483, hep-th/9606102; J.R. Ellis, N.E. Mavromatos and D.V. Nanopoulos, Int. J. Mod. Phys. A **12** (1997) 2639, hep-th/9605046; N.E. Mavromatos and R.J. Szabo, Phys. Rev. D **59** (1999) 104018, hep-th/9808124; JHEP **0110** (2001) 027, hep-th/0106259.
29. J.R. Ellis, N.E. Mavromatos, D.V. Nanopoulos and A.S. Sakharov, Int. J. Mod. Phys. A **19** (2004) 4413, gr-qc/0312044.
30. L. Susskind, hep-th/0302219.

How Dark is 'Dark'? Electromagnetic Interactions in the Dark Sector

Kris Sigurdson

California Institute of Technology, Mail Code 130-33, Pasadena, CA 91125 USA
ksigurds@tapir.caltech.edu

Summary. We review the physical and cosmological consequences of two possible electromagnetic couplings to the dark sector: (i) a neutral lightest dark-matter particle (LDP) with nonzero electric and/or magnetic dipole moments and (ii) a charged next-to-lightest dark-matter particle (NLDP) which decays to a neutral LDP. For scenario (i) we find that a relatively light particle with mass between a few MeV and a few GeV and an electric or magnetic dipole as large as $\sim 3 \times 10^{-16} e$ cm (roughly $1.6 \times 10^{-5}\,\mu_{\rm B}$) satisfies experimental and observational bounds. In scenario (ii), we show that charged-particles decaying in the early Universe result in a suppression of the small-scale matter power spectrum on scales that enter the horizon prior to decay. This leads to either a cutoff in the matter power spectrum, or if the charged fraction is less than unity, an effect in the power spectrum that might resemble a running (scale-dependent) spectral index in small-scale data.

1 Motivation

The origin of the missing 'dark' matter in galaxies and clusters of galaxies has been an outstanding problem for over 70 years, since Zwicky's measurement of the masses of extragalactic systems [1]. Recent cosmological observations not only tell us how much dark matter exists but also that it must be nonbaryonic [2] – it is not one of the familiar elementary particles contained within the standard model of particle physics. Dark matter is a known unknown. We do not know what the underlying theory of dark matter is, what the detailed particle properties of it are, nor the particle spectrum of the dark sector.

Promising candidates for the lightest dark-matter particle (LDP) – those that appear in minimal extensions of the standard model and are expected to have the required cosmological relic abundance – are a weakly-interacting massive particle (WIMP), such as the neutralino, the lightest mass eigenstate from the superposition of the supersymmetric partners of the $U(1)$ and $SU(2)$ neutral gauge bosons and of the neutral Higgs bosons [3], or the axion [4]. There is a significant theoretical literature on the properties and phenomenology of these particles, and there are ongoing experimental efforts to detect these particles.

There has also been a substantial phenomenological effort toward placing model-independent limits on the possible interactions of the LDP. For instance, significant constraints have been made to dark-matter models with

strong interactions [5] and self-interactions [6], and various models with unstable particles have been investigated [7]. Electromagnetic interactions have also been considered, and models with stable charged dark matter have been ruled out [8] while there are strong constraints on millicharged dark-matter models [9].

Dark matter is so called because the coupling of it to photons is assumed to be nonexistent or very weak. Here we ask the question, "How dark is 'dark'?", and review several recent investigations that consider the physical and cosmological constraints to and effects of the electromagnetic interactions of the LDP and the next-to-lightest dark-matter particle (NLDP). In particular, in Sect. 2 we discuss the consequences of a neutral LDP with nonzero electric and/or magnetic dipole moments [10], and in Sect. 3 we discuss the cosmological effects of a charged NLDP which decays to a neutral LDP [11, 12].

2 Dark-Matter: Electric and Magnetic Dipole Moments

In this section we consider the possibility that the dark matter possesses an electric or magnetic dipole moment. The result of [10], illustrated in Fig. 1, is that a Dirac particle with an electric or magnetic dipole moment of order $\sim 10^{-17} e$ cm with a mass between an MeV and a few GeV can provide the dark matter while satisfying all experimental and observational constraints.[1]

The effective Lagrangian for coupling of a Dirac fermion χ with a magnetic dipole moment $\mathcal{M}$ and an electric dipole moment $\mathcal{D}$ to the electromagnetic field $F^{\mu\nu}$ is

$$\mathcal{L}_{\gamma\chi} = -\frac{i}{2}\bar{\chi}\sigma_{\mu\nu}(\mathcal{M} + \gamma_5\mathcal{D})\chi F^{\mu\nu}. \tag{1}$$

Below we summarize various physical and cosmological limits to the form of interaction shown in (1). For further details of these limits see [10].

2.1 Dark Matter: Annihilation and Relic Abundance

We assume χ particles exist in thermal equilibrium in the early Universe and their dipole interactions freeze out when T drops below m_χ. Their cosmological relic abundance is $\Omega_\chi h^2 \simeq 3.8 \times 10^7 \, (m_\chi/m_p) \ln\left(A/\sqrt{\ln A}\right)/A$ where $A = 0.038\sqrt{g_*} m_{pl} m_\chi (\sigma_{\rm ann} v)$ (see, e.g., (5.47) in [13]). Here, g_* is the effective number of relativistic degrees of freedom at the freezeout temperature $T_f \sim m_\chi/A$. χ–$\bar{\chi}$ pairs annihilate to either photons or charged pairs through the diagrams shown in Fig. 2 and $\sigma_{\rm ann} v = \sigma_{\chi\bar{\chi}\to 2\gamma} v + \sigma_{\chi\bar{\chi}\to f\bar{f}} =$

[1] We quote numbers for both the electric and magnetic dipole moments in units of e cm, where e is the electron charge. For reference, the Bohr magneton $\mu_B = e\hbar/2m_e = 1.93 \times 10^{-11}\, e$ cm in these units.

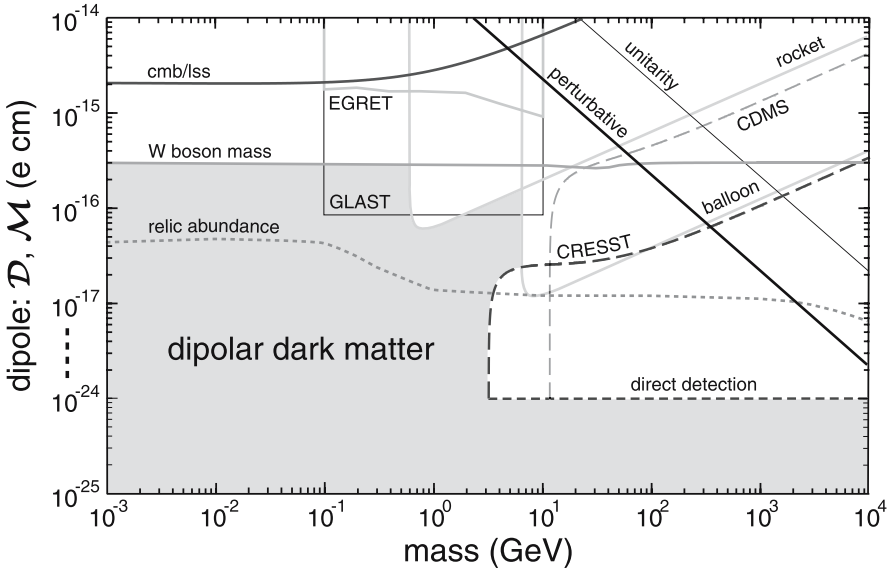

Fig. 1. The constraints to $[m_\chi, (\mathcal{D}, \mathcal{M})]$ that come from present-day searches and experiments. Viable candidates must lie in the shaded region. The short-dashed "relic abundance" curve shows where the dark matter would have a cosmological relic abundance $\Omega_\chi h^2 = 0.135$, assuming standard freezeout of annihilations via the dipole coupling to γ and no χ-$\bar{\chi}$ asymmetry.

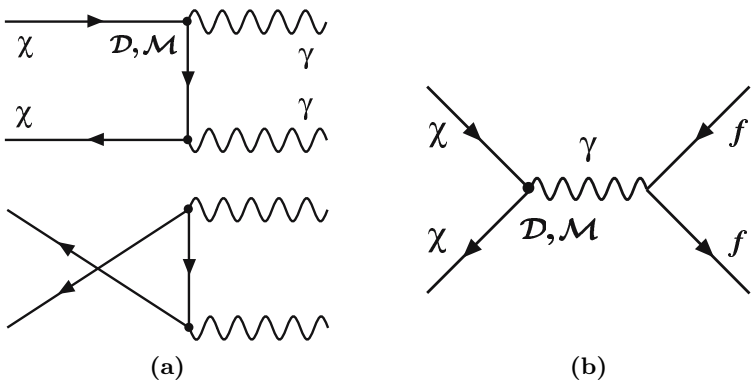

Fig. 2. Feynman diagrams for (a) annihilation of a χ–$\bar{\chi}$ pair to two photons and (b) χ–$\bar{\chi}$ annihilation to charged f–$\bar{f}$ pairs.

$(\mathcal{D}^4 + \mathcal{M}^4)m_\chi^2/2\pi + N_{\rm eff}\alpha(\mathcal{D}^2 + \mathcal{M}^2)$, where $N_{\rm eff}$ is the number of f–$\bar{f}$ pairs with $m_f < m_\chi$. If $\Omega_\chi h^2 = 0.135$ then $(\mathcal{D}^2 + \mathcal{M}^2)^{1/2} \simeq 1.0 \times 10^{-17}\, e$ cm for $m_\chi \sim 1$ GeV, as shown in Fig. 1. The present-day mass density of χ particles might differ from these estimates if other interactions are significant or there is a χ–$\bar{\chi}$ asymmetry.

2.2 Direct Detection

In the nonrelativistic limit, the differential cross section for the process shown in Fig. 3a is $d\sigma/d\Omega = Z^2e^2\left(\mathcal{D}^2+\mathcal{M}^2\right)/[8\pi^2v^2(1-\cos\theta)]$, where v is the relative velocity. Roughly speaking, $\sigma \sim (Ze)^2(\mathcal{D}^2+\mathcal{M}^2)/2\pi v^2 \simeq 6.4\times 10^{-32}\,Z^2(\mathcal{D}_{17}^2+\mathcal{M}_{17}^2)$ cm^2, using $v\sim 10^{-3}\,c$.[2] Current null searches in germanium detectors [14] thus require $(\mathcal{D}_{17}^2+\mathcal{M}_{17}^2)^{1/2}\lesssim 10^{-7}$ at $m_\chi\sim 10$ GeV — improving upon previous limits [15].

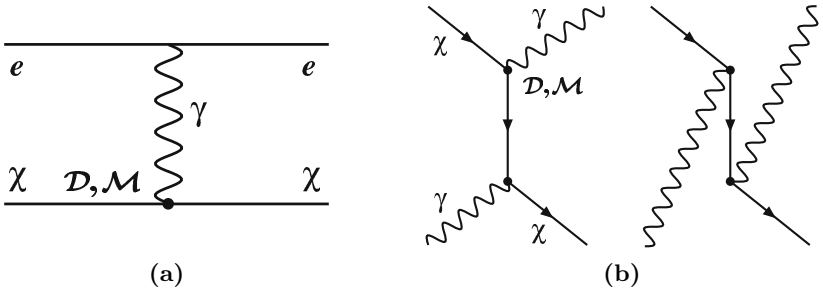

Fig. 3. Feynman diagrams for (a) the scattering of χ particles by charged particles and (b) γ-χ scattering.

However, for large enough dipole moments, χ particles will lose energy in the rock/shielding above the detector and evade detection in underground experiments. Given a shielding thickness L (in meters water equivalent), we obtain the lower bound $\mathcal{D}^2+\mathcal{M}^2 > [\frac{1}{2}m_\chi v^2 - \frac{1}{4}\frac{m_\chi m_d}{\mu[m_\chi,m_d]^2}E_{\rm th}]\times[\frac{e^2}{2\pi}L\sum_i f_i Z_i^2\frac{\mu[m_\chi,m_i]^2}{m_i^2}(1+\sqrt{\frac{m_i}{2m_\chi}})]^{-1}$, where $\mu[m_\chi,m]=m_\chi m(m_\chi+m)^{-1}$ is the reduced mass, m_d is the mass of detector nuclei, $E_{\rm th}$ is the threshold nuclear-recoil energy, the index i sums over the composition of the shielding material, and f_i is the fractional composition by weight. The most restrictive constraints for large dipoles actually come from shallow experiments with null results such as the Stanford Underground Facility run of the Cryogenic Dark Matter Search [16], and the Cryogenic Rare Event Search with Superconducting Thermometers [17]. Airborne experiments, in particular the balloon experiment of [18] and the rocket experiment of [19] provide important complimentary constraints. The bounds due to all these experiments are shown in Fig. 1.

2.3 Constraints from Precision Measurements

In [10] the effect of the dipole interaction on the anomalous magnetic moment of the muon, standard model EDMs, and corrections to Z-pole observables

[2] $[\mathcal{D}_{17},\,\mathcal{M}_{17}] = [\mathcal{D},\,\mathcal{M}]/(10^{-17}\ e\ \text{cm})$

were considered. The strongest constraint was found to arise from the contribution of χ particles to the running of α. Such running affects the relationship between G_F, m_W, and the value of α at zero momentum: $m_W^2 = (\pi\alpha)/(\sqrt{2}G_F)\left[(1 - m_W^2/m_Z^2)(1 - \Delta r)\right]^{-1}$. In the standard model $\Delta r^{SM} = 0.0355 \pm 0.0019 \pm 0.0002$ while experimentally $\Delta r^{Exp} = 0.0326 \pm 0.0023$ yielding $\Delta r^{New} < 0.003$ with 95% confidence. The dipole interaction contributes to Δr via the diagram in Fig. 4 and so $(\mathcal{D}^2+\mathcal{M}^2)^{1/2} \lesssim 3\times10^{-16}\ e$ cm is required, as shown in Fig. 1.

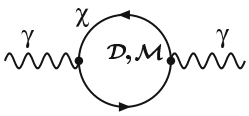

Fig. 4. One-loop correction to the photon self-energy induced by dipole moments $\mathcal{M}, \mathcal{D}$ of the dark-matter particle.

2.4 Direct Production

Missing-energy searches for light ($m_\chi \lesssim 1\,\mathrm{GeV}$) dark matter in rare B^+ decays was suggested in [20] where $Br(B^+ \to K^+ + \text{invisible}) \lesssim 10^{-4}$ was derived. This limit requires $\mathcal{D} \lesssim 3.8\times10^{-14}\ e$ cm for $m_\chi < (m_{B^+} - m_{K^+})/2 = 2.38\,\mathrm{GeV}$. Similarly, rare K^+ decays lead to the limit $\mathcal{D} \lesssim 1.5\times10^{-15}\ e$ cm for $m_\chi < (m_{K^+} - m_{\pi^+})/2 = 0.18\,\mathrm{GeV}$. These constraints are not yet competitive with other constraints shown in Fig. 1.

In order to limit dipole couplings using collider experiments an expression for the rate $f\bar{f} \to X\bar{\chi}\chi$, where X is some set of visible final-state particles, is necessary. Naive application of the effective Lagrangian in (1) is invalid because perturbation theory breaks down when the energy scale of a process satisfies $\mathcal{E} \gtrsim 1/\mathcal{D}$. Missing-energy searches from L3 ($\mathcal{E} \approx 200\,\mathrm{GeV}$) and CDF ($\mathcal{E} = 1.8$ TeV) can not be directly applied to effective dipole moments $\mathcal{D} > 10^{-16}\ e$ cm and $\mathcal{D} > 10^{-17}\ e$ cm, respectively, unless a high-energy theory is specified.

2.5 Constraints from Large-Scale Structure and the CMB

A dipole moment induces a coupling of the dark matter to the primordial plasma by scattering via the diagrams shown in Fig. 3. Dark matter couples to the plasma at early times, and subsequently decouples. When coupled to the plasma, short-wavelength modes of the dark-matter density field will grow less quickly relative to the standard case. The long-wavelength modes that enter the horizon after dark matter decoupling remain unaffected. The full calculation in cosmological perturbation theory is provided in [10].

In Fig. 5 we show the linear matter power spectrum and in angular power spectrum of the cosmic microwave background (CMB) for several values of the dipole moment and $m_\chi = 1$ GeV. Using a Markov chain Monte Carlo algorithm (see, e.g., [21], and data from SDSS [22], WMAP [23], CBI [24], VSA [25], and Type Ia supernovae [26] we find the bound shown in Fig. 1. Dipole moments as large as $\mathcal{D} \sim 10^{-17}$ e cm are thus cosmologically viable.

2.6 Gamma Rays

In the Galactic halo χ–$\bar{\chi}$ pairs can annihilate to two photons through the diagrams shown in Fig. 2a. The non-observation of a gamma-ray line by EGRET leads to the limit shown in Fig. 1. A detailed search for a line flux with GLAST may find an observable signature for $m_\chi \sim 0.1 - 1$ GeV and $\mathcal{D}_{17} \sim 10$. There may also be constraints to the annihilation rate from the low excess heat of Uranus [27].

3 The Effect of a Quasistable Charged-NLDP

In this section we discuss how the decay of a quasistable charged particle ϕ (the NLDP) to a neutral dark-matter particle χ (the LDP) suppresses the linear power spectrum on scales smaller than the horizon during the decay epoch. Prior to decay, the charged NLDPs couple to and oscillate with the primordial plasma. After decay, the plasma is coupled only gravitationally to the LDP. If all LDPs are produced through the late decay of charged NLDPs, then, as shown in [11], the power spectrum is cutoff on small scales. For a lifetime $\tau \sim 3.5$ yr this would reduce the expected number of dwarf galaxies and may solve the small-scale structure problem of cold-dark-matter theory [28]. If, instead, a fraction f_ϕ of LDPs are produced through the late decay of charged NLDPs, the linear power spectrum is suppressed only by a factor $(1 - f_\phi)^2$. This suppression might be confused with a negative running of the spectral index $\alpha_s \equiv dn_s/d\ln k$ in data that probes the power spectrum on small-scales. We describe these effects in further detail below.

3.1 Charged Decay in the Primordial Plasma

As $\phi \to \chi$, the ϕ/χ comoving density drops/increases as $\rho_\phi a^3 = m_\phi n_{\phi_0} e^{-t/\tau}$ and $\rho_\chi a^3 = m_\chi n_{\chi_0}(1 - f_\phi e^{-t/\tau})$ respectively. Here $n_{\chi_0} = \Omega_\chi \rho_{crit}/m_\chi$ is the comoving density of dark matter, f_ϕ the fraction produced through ϕ decays, a is the scale factor, and t is the cosmic time. The charged ϕ particles are tightly coupled to the baryons through Coulomb scattering. We can thus describe the combined ϕ-baryon fluid as a generalized baryon-like component β.

In the synchronous gauge the perturbation evolution equations are identical to the standard equations for the baryons (see, for example, [29]) with

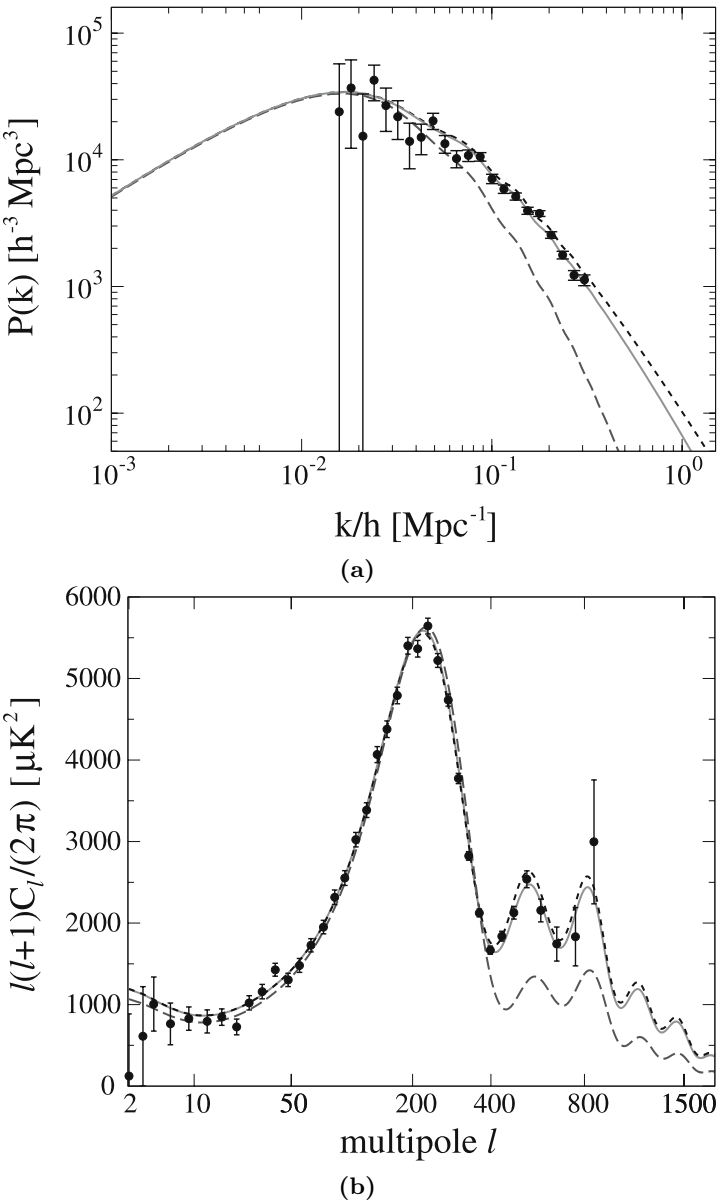

Fig. 5. The (a) matter (b) CMB power spectra including baryon-χ drag for $m_\chi = 1$ GeV. The solid curve is for $(\mathcal{D}^2 + \mathcal{M}^2)^{1/2} = 1.4 \times 10^{-15}\, e$ cm, short-dashed for $(\mathcal{D}^2 + \mathcal{M}^2)^{1/2} = 1.0 \times 10^{-16}\, e$ cm, and long-dashed for $(\mathcal{D}^2 + \mathcal{M}^2)^{1/2} = 5 \times 10^{-15}\, e$ cm. The data points are from (a) SDSS [22] and (b) WMAP [23].

the subscript b replaced by β. For the dark matter $\dot{\delta}_\chi = -ikV_\chi - \frac{1}{2}\dot{h} + \lambda_m \frac{\rho_\phi}{\rho_\chi}\frac{a}{\tau}(\delta_\beta - \delta_\chi)$, and $\dot{V}_\chi = -\frac{\dot{a}}{a}V_\chi + \lambda_m \frac{\rho_\phi}{\rho_\chi}\frac{a}{\tau}(V_\beta - V_\chi)$, where $\delta_\chi = \delta\rho_\chi/\rho_\chi$, V_χ is the bulk velocity, $\lambda_m \equiv m_\chi/m_\phi$, and an overdot is a derivative with respect to conformal time. The modifications to photon perturbation evolution are negligibly small.

Due to Compton scattering the β component and the photons are tightly coupled as a β-photon fluid at early times which supports acoustic oscillations. Since dark-matter perturbations are sourced by the perturbations of the β component, k-modes that enter the horizon prior to decay, when ρ_ϕ/ρ_χ is large, will track the oscillations in the β-photon fluid rather than growing due to gravity. After decay, when ρ_ϕ/ρ_χ is small, dark-matter modes that enter the horizon undergo the standard growing evolution. In Fig. 6 we follow the evolution of the dark-matter perturbations through the epoch of decay. We used a modified version of `cmbfast` [30].

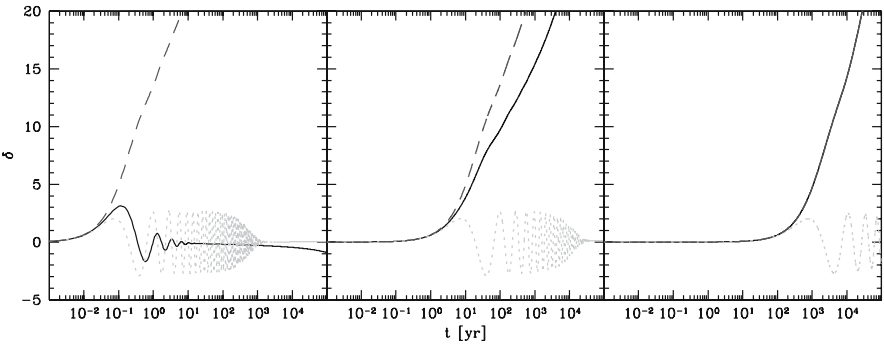

Fig. 6. The comoving $k = 30.0$ Mpc^{-1} left, $k = 3.0$ Mpc^{-1} center, and $k = 0.3$ Mpc^{-1} right δ_χ perturbation for the ΛCDM model (long-dashed) and a $f_\phi = 1$ model with $\tau = 3.5$ yr (solid). Also shown is the δ_β perturbation (short-dashed).

In Fig. 7a we plot the linear power spectrum for $f_\phi = 1$ and $\tau = 3.5$ yr. Power is cutoff for $k^{-1} \lesssim 0.3$ Mpc relative to a standard ΛCDM power spectrum, reducing the expected number of subgalactic halos and bringing predictions in line with observation [31]. In Fig. 7b we show the linear power spectrum for several values of τ and f_ϕ. The linear power spectrum is now suppressed by a factor of $(1 - f_\phi)^2$. On large scales the linear power spectrum describes the statistics of density fluctuations, but on small scales the full nonlinear matter power spectrum is required. The effects of nonlinear evolution are accounted for in [12] where it is shown that the effect of the charged-NLDP decay on the small-scale nonlinear power spectrum can be similar (but different in detail) to that of a model parametrized by a running of the spectral index $\alpha_s \equiv dn_s/d\ln k$.

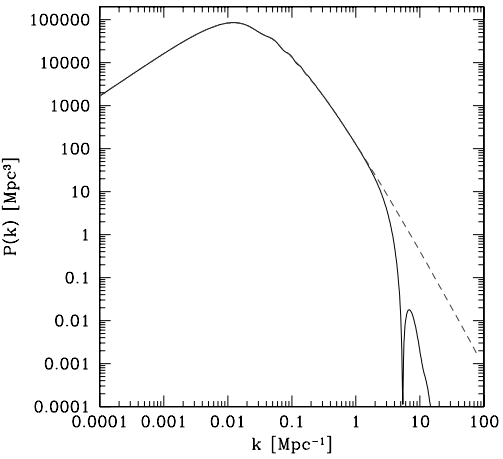

(a)

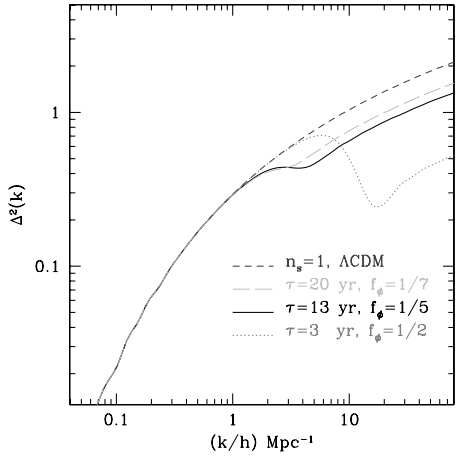

(b)

Fig. 7. (a): The linear power in the standard ΛCDM model (dashed), and a $f_\phi = 1$ charged-NLDP model (solid) with $\tau = 3.5$ yr. (b): Shown is $\Delta^2(k) = k^3 P(k)/2\pi^2$ for a $n_s = 1$ ΛCDM model (dashed) and for several charged-NLDP models.

We note that since the NLDP is charged, LDP production will be accompanied by an electromagnetic cascade. The latter could in principle reprocess the light elements produced during big bang nucleosynthesis, or induce unreasonably large spectral distortions to the CMB. In fact, the models discussed are safely below current limits [11, 12].

3.2 Particle-Theory Models of Quasistable Charged NLDPs

In the $f_\phi = 1$ case, in order to be a solution to the small-scale structure problem the charged-NLDP must have a comoving density equal to the dark-matter density today and $\tau \sim$ yr. One way to make the NDLP long lived is to suppress the LDP coupling. If LDP is a stable super-weakly–interacting particle [32], such as a gravitino $\widetilde{G}$ or the first Kaluza-Klein graviton G^1 in the universal extra-dimensions scenario [33], the NLDP can be charged and, since it decays gravitationally, have a super-weak decay rate. The required mass-spliting and lifetime can be achieved for $m_\phi \approx m_\chi \sim 100$ TeV. These masses are above the TeV range discussed in most supersymmetric phenomenology, and uncomfortably close to violating the unitary bound for thermal production [34] – nonthermal production is likely required for such large masses.

For $f_\phi < 1$, remarkably, there are configurations in the minimal supersymmetric extension of the standard model (MSSM) with the properties required here [12]. If the LDP is a neutralino quasi-degenerate in mass with the lightest stau, one can naturally obtain, at the same time, LDPs with a relic abundance $\Omega_\chi h^2 = 0.113$ [2] and NLDP lifetimes and the densities needed in the proposed scenario. Such configurations arise even in minimal schemes, such as minimal supergravity (mSUGRA) [35] and the minimal anomaly-mediated supersymmetry-breaking (mAMSB) model [36]. A detailed study of the (τ,f_ϕ) parameter space using current and future cosmological data may constrain otherwise viable regions of the MSSM parameter space. Furthermore, this scenario may be tested at future particle colliders (such as the Large Hadron Collider (LHC)) or dark matter detection experiments (See [12] for full details). The decays of staus at rest might even be studied by trapping these particles in large water tanks placed outside of LHC detectors [37]. Other methods of trapping staus have also been considered [38].

4 Conclusion

We have considered two distinct scenarios for electromagnetic interactions in the dark sector. In the first we considered the effects of a LDP with nonzero electric and/or magnetic dipole moments and found that a light particle with $m_\chi \approx$ MeV–GeV and a dipole as large as $\sim 3 \times 10^{-16} e$ cm $\approx 1.6 \times 10^{-5}\, \mu_B$ satisfies experimental and observational bounds. The second scenario examines how the decay of charged NLDPs in the early Universe results in, depending on f_ϕ, either a cutoff or suppression of the small-scale power spectrum. For a purely gravitationally interacting LDP configurations with $f_\phi = 1$ may exist, while configurations with $f_\phi < 1$ can be found within the MSSM.

Acknowledgments

We thank Robert R. Caldwell, Michael Doran, Stefano Profumo, Marc Kamionkowski, Andriy Kurylov, and Piero Ullio for collaborative work discussed in this article and the Mitchell Institute and Texas A&M University for their hospitality during DARK 2004. This research was supported in part by a NSERC of Canada Postgraduate Scholarship, NASA NAG5-9821, and DoE DE-FG03-92-ER40701.

References

1. F. Zwicky: Helv. Phys. Acta **6**, 110 (1933)
2. P. de Bernardis et al.: Nature **404**, 955 (2000); A. Lange et al.: Phys. Rev. D **63**, 042001 (2001); S. Hanany et al.: Astrophys. J. Lett. **545**, L5 (2000); N. W. Halverson et al.: Astrophys. J. 568, 38 (2002); B. S. Mason et al.: Astrophys. J. **591**, 540 (2003); A. Benoit et al.: Astron. Astrophys. **399**, L2 (2003); D. N. Spergel et al.: Astrophys. J. Suppl. **148**, 175 (2003)
3. G. Jungman, M. Kamionkowski, and K. Griest: Phys. Rept. **267**, 195 (1996); L. Bergstrom: Rept. Prog. Phys. **63**, 793 (2000)
4. M. S. Turner: Phys. Rept. **197**, 67 (1990); G. Raffelt: Phys. Rept. **198**, 1 (1990); K. van Bibber and L. Rosenberg: Phys. Rept. **325**, 1 (2000)
5. G. D. Starkman et al.: Phys. Rev. D **41**, 3594 (1990)
6. E. D. Carlson, M. E. Machacek, and L. J. Hall: Astrophys. J. **398**, 43 (1992); D. N. Spergel and P. J. Steinhardt: Phys. Rev. Lett. **84**, 3760 (2000)
7. M. S. Turner, G. Steigman and L. M. Krauss: Phys. Rev. Lett. **52**, 2090 (1984); G. Gelmini, D. N. Schramm and J. W. F. Valle: Phys. Lett. B **146**, 311 (1984); A. G. Doroshkevich, M. Yu. Khlopov, and A. A. Klypin: Mon. Not. Roy. Astron. Soc. **239**, 923 (1989); D. W. Sciama: Phys. Rev. Lett. **65**, 2839 (1990); D. Scott, M. J. Rees, and D. W. Sciama: Astron. Astrophys. **250**, 295 (1991); S. Dodelson and J. M. Jubas: Mon. Not. Roy. Astron. Soc. **266**, 886 (1994); X. L. Chen and M. Kamionkowski: Phys. Rev. D **70**, 043502 (2004)
8. A. Gould et al.: Phys. Lett. B **238**, 337 (1990)
9. S. Davidson, S. Hannestad, and G. Raffelt: JHEP **0005**, 003 (2000); S. L. Dubovsky, D. S. Gorbunov, and G. I. Rubtsov: JETP Lett. **79**, 1 (2004)
10. K. Sigurdson, M. Doran, A. Kurylov, R. R. Caldwell, and M. Kamionkowski: Phys. Rev. D **70**, 083501 (2004)
11. K. Sigurdson and M. Kamionkowski: Phys. Rev. Lett. **92**, 171302 (2004)
12. S. Profumo, K. Sigurdson, P. Ullio, and M. Kamionkowski: arXiv:astro-ph/0410714
13. E. W. Kolb and M. S. Turner: *The Early Universe* (Addison-Wesley, Redwood City 1990)
14. D. S. Akerib et al.: Phys. Rev. Lett. **93**, 211301 (2004)
15. M. Pospelov and T. ter Veldhuis: Phys. Lett. B **480**, 181 (2000)
16. D. S. Akerib et al.: Phys. Rev. D **68**, 082002 (2003)
17. G. Angloher et al.: Astropart. Phys. **18**, 43 (2002)
18. J. Rich, R. Rocchia and M. Spiro: Phys. Lett. B **194**, 173 (1987)
19. D. McCammon et al.: Astrophys. J. **576**, 188 (2002)

20. C. Bird et al.: Phys. Rev. Lett. **93**, 201803 (2004)
21. M. Doran and C. M. Mueller: arXiv:astro-ph/0311311
22. M. Tegmark et al.: Astrophys. J. **606**, 702 (2004)
23. G. Hinshaw et al.: Astrophys. J. Suppl. **148**, 135 (2003)
24. A. C. S. Readhead et al.: Astrophys. J. **609**, 498 (2004)
25. C. Dickinson et al.: arXiv:astro-ph/0402498
26. A. G. Riess et al.: Astrophys. J. **607**, 665 (2004); J. L. Tonry et al.: Astrophys. J. **594**, 1 (2003); R. A. Knop et al.: Astrophys. J. **598**, 102 (2003); B. J. Barris et al.: Astrophys. J. **602**, 571 (2004)
27. S. Mitra: Phys. Rev. D **70**, 103517 (2004)
28. G. Kauffman, S. D. M. White, and B. Guiderdoni: Mon. Not. Roy. Astron. Soc. **264**, 201 (1993); A. A. Klypin et al.: Astrophys. J. **522**, 82 (1999); B. Moore et al.: Astrophys. J. Lett. **524**, L19 (1999)
29. C. P. Ma and E. Bertschinger: Astrophys. J. **455**, 7 (1995)
30. U. Seljak and M. Zaldarriaga: Astrophys. J. **469**, 437 (1996)
31. M. Kamionkowski and A. R. Liddle: Phys. Rev. Lett. **84**, 4525 (2000)
32. J. L. Feng, A. Rajaraman, and F. Takayama: Phys. Rev. Lett. **91**, 011302 (2003); Phys. Rev. D **68**, 063504 (2003)
33. G. Servant and T. M. P. Tait: Nucl. Phys. B **650**, 391 (2003)
34. K. Griest and M. Kamionkowski: Phys. Rev. Lett. **64**, 615 (1990)
35. A. H. Chamseddine, R. Arnowitt, and P. Nath: Phys. Rev. Lett. **49**, 970 (1982); R. Barbieri, S. Ferrara, and C. A. Savoy: Phys. Lett. B **119**, 343 (1982); L. J. Hall, J. Lykken, and S. Weinberg: Phys. Rev. D **27**, 2359 (1983); P. Nath, R. Arnowitt, and A. H. Chamseddine: Nucl. Phys. B **227**, 121 (1983)
36. L. Randall and R. Sundrum: Nucl. Phys. B **557**, 79 (1999); G. F. Giudice et al.: JHEP **9812**, 027 (1998); T. Gherghetta, G. F. Giudice, and J. D. Wells: Nucl. Phys. B **559**, 27 (1999)
37. J. L. Feng and B. T. Smith: hep-ph/0409278
38. K. Hamaguchi et al.: Phys. Rev. D **70**, 115007 (2004)

Leptonic CP Violation and Baryon Asymmetry

M.N. Rebelo

Departamento de Física and Centro de Física Teórica de Partículas (CFTP), Instituto Superior Técnico, Av. Rovisco Pais, 1049-001 Lisboa, Portugal
rebelo@ist.utl.pt

The observation of neutrino masses leads to the possibility of leptonic mixing and CP violation. One of the simplest extensions of the Standard Model giving rise to neutrino masses consists of the introduction of one righthanded neutrino field per generation, singlet of SU(2). In the context of the seesaw mechanism this leads to three light and three heavy neutrinos. The charged current interactions couple the charged leptons to both the light and the heavy physical neutrinos and leptonic CP violation may occur at low energies as well as at high energies giving rise to the possibility of leptogenesis. There are special scenarios where it is possible to establish a connection between CP violation at the two different scales, an interesting example is included in this work. Furthermore, we describe how the conjecture that all phenomena of CP violation present in nature could have a common origin can be realized in the framework of a further minimal extension of the Standard Model with CP broken through the phase of the vacuum expectation value of a complex Higgs singlet.

1 Introduction

At present there is strong evidence for nonzero neutrino masses and nontrivial leptonic mixing implying for the first time the exitence of physics beyond the Standard Model. In fact in the Standard Model (SM) neutrinos are strictly massless and any extension giving rise to neutrino masses will contain new ingredients not present before in the SM. The simplest way of extending the SM in order to take into account neutrino masses is the inclusion of righthanded neutrino singlets, in analogy with all other fermions in the theory. Yet once righthanded neutrinos are included both Dirac mass terms and Majorana mass terms for righthanded neutrinos are allowed. The scale of the Dirac mass terms is the electroweak scale, v, whilst there are no constraints on the scale of the righthanded Majorana mass tems. In Grand Unified models it is natural to assume this scale, V, to be of the order of the Grand Unification scale. Mixing and CP violation in the leptonic sector naturally arise once righthanded neutrinos are included. In what follows we generally assume their number to be three although, in fact, the number of righthand neutrino fields could differ from the number of lefthanded fields. When the two scales v and

V are very different, with V much larger than v, the seesaw mechanism [1] operates providing an elegant explanation for the smallness of the observed neutrino masses. In the context of seesaw there are three light neutrinos with small masses and an additional number of very heavy neutrinos (the number of heavy neutrinos equals the number of righthanded neutrinos included) with masses that can be of the order of the Grand Unification scale. As a result there can be leptonic CP violation at low energies as well as at high energies. Leptonic CP violation at high energies could be the explanation for the generation of the observed baryon asymmetry of the Universe (BAU) via the leptogenesis mechanism [2] where a CP asymmetry generated through the out-of-equilibrium L-violating decays of the heavy Majorana neutrinos leads to a lepton asymmetry which is subsequently transformed into a baryon asymmetry by (B+L)-violating sphaleron processes [3]. In general there is no connection between CP violation at low and high energies [4] yet this connection can be established in special frameworks [5]. One can go further and ask whether there is a framework where all CP violations have a common origin. In [6] it was shown that this is indeed possible in a small extension of the Standard Model with neutrino righthanded singlets, a vectorial quark isosinglet and a complex Higgs scalar.

2 Framework

We work in the context of a minimal extension of the SM which consists of adding to the standard spectrum one right-handed neutrino per generation. After spontaneous gauge symmetry breaking, the following leptonic mass terms can be written:

$$\begin{aligned}\mathcal{L}_m &= -\left[\overline{\nu_L^0} m_D \nu_R^0 + \frac{1}{2}\nu_R^{0T} C M_R \nu_R^0 + \overline{l_L^0} m_l l_R^0\right] + h.c. \\ &= -\left[\frac{1}{2} n_L^T C \mathcal{M}^* n_L + \overline{l_L^0} m_l l_R^0\right] + h.c. \end{aligned} \tag{1}$$

where m_D, M_R and m_l denote the neutrino Dirac mass matrix, the right-handed neutrino Majorana mass matrix and the charged lepton mass matrix, respectively, and $n_L = (\nu_L^0, (\nu_R^0)^c)$ (should be interpreted as a column matrix). In order to study CP violation in a weak basis (WB) it is necessary to consider the most general CP transformation which leaves the gauge interaction invariant:

$$\begin{aligned} \mathrm{CP} l_L (\mathrm{CP})^\dagger &= U\gamma^0 \mathrm{C}\overline{l_L}^T \quad \mathrm{CP} l_R (\mathrm{CP})^\dagger = V\gamma^0 \mathrm{C}\overline{l_R}^T \\ \mathrm{CP}\nu_L (\mathrm{CP})^\dagger &= U\gamma^0 \mathrm{C}\overline{\nu_L}^T \quad \mathrm{CP}\nu_R (\mathrm{CP})^\dagger = W\gamma^0 \mathrm{C}\overline{\nu_R}^T \end{aligned} \tag{2}$$

where U, V, W are unitary matrices acting in flavour space and where for notation simplicity we have dropped here the superscript 0 in the fermion

fields. Invariance of the mass terms under the above CP transformation, requires that the following relations have to be satisfied:

$$W^T M_R W = -M_R^* \tag{3}$$

$$U^\dagger m_D W = {m_D}^* \tag{4}$$

$$U^\dagger m_l V = {m_l}^* \tag{5}$$

In [7], it was shown, making use of these equations, that the number of independent CP violating phases which appear in general in this model is $(n^2 - n)$, with n the number of generations. The same result was obtained in [8] through an analysis performed in the physical basis. In the general case where a Majorana mass term for lefthanded neutrinos is also present the number of CP violating phases would be [9] $(n^2 + n(n-1)/2)$.

In the case of three generations (three lefthanded and three righthanded neutrinos), the full neutrino mass matrix, $\mathcal{M}$ in (1), is 6×6, and has the following form:

$$\mathcal{M} = \begin{pmatrix} 0 & m \\ m^T & M \end{pmatrix} \tag{6}$$

We have dropped the subscript in m_D and M_R in order to simply the notation. Starting from a weak basis where m_l is already diagonal and real the neutrino mass matrix is diagonalized by the transformation:

$$V^T \mathcal{M}^* V = \mathcal{D} \tag{7}$$

where $\mathcal{D} = \text{diag.}(m_{\nu_1}, m_{\nu_2}, m_{\nu_3}, M_{\nu_1}, M_{\nu_2}, M_{\nu_3})$, with m_{ν_i} and M_{ν_i} denoting the physical masses of the light and heavy Majorana neutrinos, respectively. It is convenient to write V and $\mathcal{D}$ in the following form:

$$V = \begin{pmatrix} K & R \\ S & T \end{pmatrix}; \tag{8}$$

$$\mathcal{D} = \begin{pmatrix} d & 0 \\ 0 & D \end{pmatrix} . \tag{9}$$

It can be easily verified that both S and R are of order $\frac{m}{M}$ (with $R = mT^* D^{-1}$) and that K is, to an excellent approximation, the unitary matrix that diagonalizes $m_{eff} \equiv m \frac{1}{M} m^T$:

$$-K^\dagger m \frac{1}{M} m^T K^* = d \tag{10}$$

which is the usual seesaw formula. In this approximation K is a unitary matrix which coincides with the Maki, Nakagawa and Sakata matrix (V_{MNS}) [10]. The neutrino weak-eigenstates are related to the mass eigenstates by:

$$\nu_{i\,L}^0 = V_{i\alpha} \nu_{\alpha\,L} = (K, R) \begin{pmatrix} \nu_{iL} \\ N_{iL} \end{pmatrix} \quad \begin{pmatrix} i = 1, 2, 3 \\ \alpha = 1, 2, ...6 \end{pmatrix} \tag{11}$$

and thus the leptonic charged current interactions are given by:

$$-\frac{g}{\sqrt{2}}\left(\overline{l_{iL}}\gamma_\mu K_{ij}\nu_{j\,L}+\overline{l_{iL}}\gamma_\mu R_{ij}N_{j\,L}\right)W^\mu+h.c\,. \tag{12}$$

From (11), (12) it follows that K and R give the charged current couplings of charged leptons to the light neutrinos ν_j and to the heavy neutrinos N_j, respectively. In the exact decoupling limit, R can be neglected and only K is relevant.In this case two of the phases that can be factored out of K (in the approximation of exact unitarity) cannot be rotated away due to the Majorana character of the neutrino fields and, as a result, K is left with three CP violating phases (one of Dirac type and two of Majorana character). However, since we want to study the connection between CP violation relevant to leptogenesis and that observable at low energies (e.g., in neutrino oscillations) we have to keep both K and R.

The present knowledge of leptonic masses and mixing is still incomplete despite great recent progress. The evidence for solar and atmospheric neutrino oscillations is now solid and it is already established that the pattern of the leptonic mixing matrix V_{MNS} is very different from that of the quark sector (V_{CKM}), since only one of the leptonic mixing angles, θ_{13}, is small (the notation is that of the standard parametrization of V_{CKM} in [11]). Recent KamLAND results [12], a terrestreal long baseline experiment which has great sensitivity to the square mass difference relevant for solar oscillations, Δm^2_{21}, combined with those of SNO [13] and previous solar experiments [14] lead, for the 1σ range [15], to:

$$\Delta m^2_{21}\equiv|m_2^2-m_1^2|=8.2^{+0.3}_{-0.3}\times10^{-5}\ \mathrm{eV}^2 \tag{13}$$

$$\tan^2\theta_{12}=0.39^{+0.05}_{-0.04} \tag{14}$$

and corresponds to the large mixing angle solution (LMA) of the Mikheev, Smirnov and Wolfenstein (MSW) effect [16]. On the other hand, atmospheric neutrino results from Superkamiokande [17] and recent important progress by K2K [18], which is also a terrestrial long baseline experiment, are consistent with, for the 1σ range [15]:

$$\Delta m^2_{32}\equiv|m_3^2-m_2^2|=2.2^{+0.6}_{-0.4}\times10^{-3}\ \mathrm{eV}^2 \tag{15}$$

$$\tan^2\theta_{23}=1.0^{+0.35}_{-0.26} \tag{16}$$

Assuming the range for Δm^2_{32} from SuperKamiokande and K2K, the present bounds for $\sin^2\theta_{13}$ from the CHOOZ experiment [19] at 3σ lie [15] in $\sin^2\theta_{13}<0.05-0.07$. The value for the angle θ_{13} is critical for the prospects of detection of low energy leptonic CP violation, mediated through a Dirac-type phase, δ, whose strength is given by $\mathcal{J}_{CP}$:

$$\mathcal{J}_{CP}\equiv\mathrm{Im}\left[\,(V_{11}V_{22}{V_{12}}^*{V_{21}}^*\,\right]=\frac{1}{8}\sin(2\,\theta_{12})\sin(2\,\theta_{13})\sin(2\,\theta_{23})\cos(\theta_{13})\sin\delta\,, \tag{17}$$

Direct kinematic limits on neutrino masses [20] from Mainz and Troitsk and neutrinoless double beta decay experiments [21] when combined with the given square mass differences exclude light neutrino masses higher than order 1 eV. Non-vanishing light neutrino masses also have an important impact in cosmology. Recent data from the Wilkinson Microwave Anisotropy Probe, WMAP [22, 23], together with other data, put an upper bound on the sum of light neutrino masses of 0.7 eV.

3 General Conditions for Leptogenesis

The lepton-number asymmetry resulting from the decay of heavy Majorana neutrinos, ε_{N_j}, was computed by several authors [24]. The evaluation of ε_{N_j}, involves the computation of the interference between the tree level diagram and one loop diagrams for the decay of the heavy Majorana neutrino N^j into charged leptons $l_i^{\pm}$ ($i = \mathrm{e}, \mu, \tau$) leading to:

$$\varepsilon_{N_j} = \frac{g^2}{{M_W}^2} \sum_{k \neq j} \left[\mathrm{Im}\left((m^\dagger m)_{jk} (m^\dagger m)_{jk} \right) \frac{1}{16\pi} \left(I(x_k) + \frac{\sqrt{x_k}}{1 - x_k} \right) \right] \frac{1}{(m^\dagger m)_{jj}}$$
$$= \frac{g^2}{{M_W}^2} \sum_{k \neq j} \left[(M_k)^2 \mathrm{Im}\left((R^\dagger R)_{jk} (R^\dagger R)_{jk} \right) \frac{1}{16\pi} \left(I(x_k) + \frac{\sqrt{x_k}}{1 - x_k} \right) \right] \frac{1}{(R^\dagger R)_{jj}} \tag{18}$$

where M_k denote the heavy neutrino masses, the variable x_k is defined as $x_k = \frac{{M_k}^2}{{M_j}^2}$ and $I(x_k) = \sqrt{x_k} \left(1 + (1 + x_k) \log(\frac{x_k}{1+x_k}) \right)$. From (18) it can be seen that the lepton-number asymmetry is only sensitive to the CP-violating phases appearing in $m^\dagger m$ in the WB, where $M_R \equiv M$ is diagonal (notice that this combination is insensitive to rotations of the left-hand neutrinos). The simplest leptogenesis scenario corresponds to heavy hierarchical neutrinos where M_1 is much smaller than M_2 and M_3. In this limit only the asymmetry generated by the lightest heavy neutrino is relevant, due to the existence of washout processes, and ε_{N_1} can be simplified into:

$$\varepsilon_{N_1} \simeq -\frac{3}{16\,\pi v^2} \left(I_{12} \frac{M_1}{M_2} + I_{13} \frac{M_1}{M_3} \right), \tag{19}$$

where

$$I_{1i} \equiv \frac{\mathrm{Im}\left[(m^\dagger m)^2_{1i} \right]}{(m^\dagger\, m)_{11}}\ . \tag{20}$$

Thermal leptogenesis is a rather involved thermodynamical non-equilibrium process and depends on additional parameters. In the hierarchical case the baryon asymmetry only depends on four parameters [25]: the mass M_1 of the lightest heavy neutrino, together with the corresponding CP asymmetry ε_{N_1} in their decays, as well as the effective neutrino mass $\widetilde{m_1}$ defined as

$$\widetilde{m_1} = (m^\dagger m)_{11}/M_1 \tag{21}$$

in the weak basis where M is diagonal, real and positive and, finally, the sum of all light neutrino masses squared, $\bar{m}^2 = m_1^2 + m_2^2 + m_3^2$. It has been shown that this sum controls an important class of washout processes. Successful leptogenesis would require ε_{N_1} of order 10^{-8}, if washout processes could be neglected, in order to reproduce the observed ratio of baryons to photons [22]:

$$\frac{n_B}{n_\gamma} = (6.1^{+0.3}_{-0.2}) \times 10^{-10} \; . \tag{22}$$

Leptogenesis is a non-equilibrium process that takes place at temperatures $T \sim M_1$. This imposes an upper bound on the effective neutrino mass $\widetilde{m_1}$ given by the "equilibrium neutrino mass" [26]:

$$m_* = \frac{16\pi^{5/2}}{3\sqrt{5}} g_*^{1/2} \frac{v^2}{M_{Pl}} \simeq 10^{-3} \text{ eV} \; , \tag{23}$$

where M_{Pl} is the Planck mass ($M_{Pl} = 1.2 \times 10^{19}\,\text{GeV}$), $v = \langle \phi^0 \rangle / \sqrt{2} \simeq 174\,\text{GeV}$ is the weak scale and g_* is the effective number of relativistic degrees of freedom in the plasma and equals 106.75 in the SM case. Yet, it has been shown [27], [28] that successful leptogenesis is possible for $\widetilde{m_1} < m_*$ as well as $\widetilde{m_1} > m_*$, in the range from $\sqrt{\Delta m^2_{12}}$ to $\sqrt{\Delta m^2_{23}}$. The square root of the sum of all neutrino masses squared $\bar{m}$ is constrained, in the case of normal hierarchy, to be below 0.20 eV [27], which corresponds to an upper bound on light neutrino masses very close to 0.10 eV. This result is sensitive to radiative corrections which depend on top and Higgs masses as well as on the treatment of thermal corrections. In [28] a slightly higher value of 0.15 eV is found. From (19) a lower bound on the lightest heavy neutrino mass M_1 is derived. Depending on the cosmological scenario, the range for minimal M_1 varies from order 10^7 Gev to 10^9 Gev [25] [28].

4 Weak Basis Invariants and CP Violation

In this section we present WB invariants which must vanish if CP invariance holds. Non-vanishing of any of these WB invariants signals CP violation. Weak basis invariant conditions are very useful since they allow us to determine whether or not a Lagrangean violates CP without the need to go to the physical basis. Clearly they can be very useful for instance in the study of mass models with particular textures or symmetries. The strategy to build these conditions was first applied in the context of the Standard Model [29]. The starting point are (3) to (5). The technique proposed allows to build several different conditions. Different conditions may be sensitive to different CP violating phases. Furthermore some of them are identically zero under particular circumstances. This requires a careful choice of invariants.

Since leptogenesis only depends on the product $m^\dagger m$ this combination must appear in the conditions relevant for leptogenesis. From (4), (3), one obtains :

$$W^\dagger h W = h^* \qquad W^\dagger H W = H^* \tag{24}$$

where $h = m^\dagger m$, $H = M^\dagger M$. It can be then readily derived, from (3), (24), that CP invariance requires [7]:

$$I_1 \equiv \mathrm{ImTr}[hHM^*h^*M] = 0 \tag{25}$$

Analogously several other different conditions can be derived [7]:

$$I_2 \equiv \mathrm{ImTr}[hH^2M^*h^*M] = 0 \tag{26}$$

$$I_3 \equiv \mathrm{ImTr}[hH^2M^*h^*MH] = 0 \tag{27}$$

It has been shown [7] that if none of the heavy neutrino masses vanish and furthermore there is no degeneracy among them these conditions are independent and do not automatically vanish. Since there are six independent CP violating phases, one may wonder whether one can construct other three independent WB invariants, apart from I_i, which would describe CP violation in the leptonic sector. This is indeed possible, a simple choice are the WB invariants $\bar{I}_i (i = 1, 2, 3)$, obtained from I_i, through the substitution of h by $\bar{h} = m^\dagger h_l m$, where $h_l = m_l m_l{}^\dagger$. For example one has:

$$\bar{I}_1 = \mathrm{ImTr}(m^\dagger h_l m H M^* m^T h_l{}^* m^* M) \tag{28}$$

and similarly for $\bar{I}_2, \bar{I}_3$. As it was the case for I_i, CP invariance requires that $\bar{I}_i = 0$.

Since low energy physics is sensitive to m_{eff} it is possible to show that the strength of CP violation at low energies, observable for example through neutrino oscillations, can be obtained from the following low-energy WB invariant:

$$Tr[h_{eff}, h_l]^3 = 6i\Delta_{21}\Delta_{32}\Delta_{31}\mathrm{Im}\{(h_{eff})_{12}(h_{eff})_{23}(h_{eff})_{31}\} \tag{29}$$

where $h_{eff} = m_{eff} m_{eff}{}^\dagger$, $h_l = m_l m_l{}^\dagger$ and $\Delta_{21} = (m_\mu{}^2 - m_e{}^2)$ with analogous expressions for Δ_{31}, Δ_{32}.

5 Relating CP Violation at Low Energies with CP Violation Required for Leptogenesis

It is clear from (1) that it is possible to choose a weak basis where the matrices m_l and M are simultaneously diagonal. In this case all CP violating phases appear in m. There is no loss of generality in parametrizing the Dirac neutrino mass matrix by [30]:

$$m = UY_{\triangle} \tag{30}$$

with U a unitary matrix and $Y_{\triangle}$ a matrix with triangular form:

$$Y_{\triangle} = \begin{pmatrix} y_1 & 0 & 0 \\ |y_{21}|\exp(i\phi_{21}) & y_2 & 0 \\ |y_{31}|\exp(i\phi_{31}) & |y_{32}|\exp(i\phi_{32}) & y_3 \end{pmatrix} \tag{31}$$

where the y_i are real. Since U is unitary, it contains in general six phases. However, three of these phases can be rephased away through the transformation:

$$m \rightarrow P_{\xi} m \tag{32}$$

where $P_{\xi} = \mathrm{diag}\,(\exp(i\xi_1), \exp(i\xi_2), \exp(i\xi_3))$. In a WB, this corresponds to a simultaneous phase transformation of the left-handed charged lepton fields and the left-handed neutrino fields. Furthermore, $Y_{\triangle}$ defined by (31) can be written as:

$$Y_{\triangle} = P_{\beta}^{\dagger}\ \hat{Y}_{\triangle}\ P_{\beta} \tag{33}$$

where $P_{\beta} = diag(1, \exp(i\beta_1), \exp(i\beta_2))$ and

$$\hat{Y}_{\triangle} = \begin{pmatrix} y_1 & 0 & 0 \\ |y_{21}| & y_2 & 0 \\ |y_{31}| & |y_{32}|\exp(i\sigma) & y_3 \end{pmatrix} \tag{34}$$

with $\sigma = \phi_{32} - \phi_{31} + \phi_{21}$. It follows from (30), (33) that the matrix m can then be written as [7]:

$$m = \hat{U}_{\rho} P_{\alpha} \hat{Y}_{\triangle} P_{\beta} \tag{35}$$

where $P_{\alpha} = diag(1, \exp(i\alpha_1), \exp(i\alpha_2))$ and $\hat{U}_{\rho}$ contains only one phase ρ as, for example, in the standard parametrization of V_{CKM}. Therefore, in this WB, where m_l and M are diagonal and real, the phases ρ, α_1, α_2, σ, β_1, β_2 are the only physical phases and can be used to characterize CP violation in this model. It follows from here that leptogenesis is controlled by the phases σ, β_1, β_2. If these three phases vanish there is no possibility of leptogenesis, still the remaining three phases can be responsible for low energy CP violation thus it is possible to have no CP violation at high energies responsible for leptogenesis and still have leptonic low energy CP violation [7]. Conversely one may ask whether it is possible to have leptogenesis with no low energy CP violation either of Dirac or Majorana type [4]. The answer to this question can be given by going to the weak basis where both m_l and M are real and diagonal. Then from (10) one can derive:

$$m = iK\sqrt{d}O^{c}\sqrt{D}\,, \tag{36}$$

where $\sqrt{d}$ and $\sqrt{D}$ are diagonal real matrices such that $\sqrt{d}\sqrt{d} = d$, $\sqrt{D}\sqrt{D} = D$ and O^c is an orthogonal complex matrix, i.e. $O^c O^{cT} = \mathbb{1}$ but in general $O^c O^{c\dagger} \neq \mathbb{1}$. It is clear that with this parametrization the product $m^\dagger m$, relevant for leptogenesis, is insensitive to K. It is also clear from (10) that K is insensitive to the matrix O. Yet, although a connection cannot be established in general, it can be established in special frameworks.

Here we present an interesting illustrative example of such a connection [31]. Starting from the parametrization of (30) and (31) it follows that U does not play any rôle for leptogenesis since it cancels out in the product $m^\dagger m$. This suggests the simplifying choice of taking $U = \mathbb{1}$. With this choice several texture zeros were studied for the matrix $Y_\triangle$. Two patterns with one additional zero in $Y_\triangle$ where found to be consistent with low energy physics (either with hierarchical heavy neutrinos or two-fold quasi degeneracy):

$$\begin{pmatrix} y_{11} & 0 & 0 \\ y_{21}\, e^{i\,\phi_{21}} & y_{22} & 0 \\ 0 & y_{32}\, e^{i\,\phi_{32}} & y_{33} \end{pmatrix}, \qquad \begin{pmatrix} y_{11} & 0 & 0 \\ 0 & y_{22} & 0 \\ y_{31}\, e^{i\,\phi_{31}} & y_{32}\, e^{i\,\phi_{32}} & y_{33} \end{pmatrix} \tag{37}$$

Still it is possible to eliminate one of the two remaining phases and obtain viable leptogenesis together with specific predictions for low energy physics consistent with the known experimental constraints. In [31] special examples were built with strong hierarchies in the entries of $Y_\triangle$ parametrized in terms of powers of a small parameter.

The question of whether the sign of the baryon asymmetry of the Universe can be related to CP violation in neutrino oscillation experiments was addressed by considering models with only two heavy neutrinos [32]. In this case the Dirac mass matrix has dimension 3×2. The interesting examples correspond to textures of the form given above in (37) with the third column eliminated and corresponds to the most economical extension of the SM leading to leptogenesis. In this case the number of parameters is further reduced and the remaining non zero parameters are strongly constrained by low energy physics. This fact leads to a definite relative sign between $\mathrm{Im}\,(m^\dagger m)^2_{12}$ and $\sin 2\delta$.

6 A Common Origin for All CP Violations

CP violation has been observed both in the Kaon sector [34] and in the B-sector [35] [36]. The existence of a matter dominated Universe constitutes indirect evidence for CP violation. It has been established that within the framework of the SM it is not possible to generate the observed size of BAU, due in part to the smallness of CP violation in the SM. This provides motivation for considering new sources of CP violation beyond the KM mechanism.

The question of whether it is possible to find a framework where all these manifestations of CP violation have a common origin has been addressed in [6]

in the context of a small extension of the Standard Model and also in [33] in the framework of a SUSY SO(10) model. In [6] a minimal model is proposed with spontaneous CP violation, where CP breaking both in the quark and leptonic sectors arises solely from a phase α in the vacuum expectation value of a complex scalar singlet S, with $\langle S\rangle = \frac{V}{\sqrt{2}}\exp(i\alpha)$. Since S is an $SU(2) \times U(1) \times SU(3)_c$ singlet, V can be much larger than the electroweak breaking scale. Therefore, in this framework CP violation is generated at a high energy scale. In order for the phase α to generate a non-trivial phase at low energies in the Cabibbo, Kobayashi and Maskawa matrix, one is led to introduce at least one vector-like quark, whose lefthanded and righthanded components are singlets under $SU(2)$. In the leptonic sector, righthanded neutrinos play the rôle of the vector-like quarks, establishing the connection between CP breaking at high and low energies, and allowing also for the possibility of leptogenesis.

The model considered consists of adding to the SM the following fields: one singlet charge $-\frac{1}{3}$ vectorial quark D^0, three righthanded neutrino fields ν_R^0 (one per generation) and a neutral scalar singlet field, S. A Z_4 symmetry is imposed, under which the fields D^0, S, ψ_l^0 (the lefthanded lepton doublets), l_R^0 and ν_R^0 transform non trivially, all other fields remain invariant under the Z_4 symmetry.

The scalar potential will contain terms in ϕ and S with no phase dependence, together with terms of the form $(\mu^2 + \lambda_1 S^* S + \lambda_2 \phi^\dagger \phi)(S^2 + S^{*2})$ $+\lambda_3(S^4 + S^{*4})$ which, in general, lead to the spontaneous breaking of T and CP invariance [37] with ϕ and S acquiring vacuum expectation values (vevs) of the form:

$$\langle \phi^0 \rangle = \frac{v}{\sqrt{2}}, \qquad \langle S \rangle = \frac{V \exp(i\alpha)}{\sqrt{2}} \tag{38}$$

and the Z_4 symmetry is also broken.

After spontaneous symmetry breaking the leptonic mass terms are given by (1). In the model a bare Majorana mass term for the righthanded neutrinos would break the Z_4 symmetry yet, a term of this form is generated through the couplings of ν_R^0 to the scalar singlet S, after Z_4 breaking. It was shown in [6] that leptogenesis is possible in this framework. Furthermore, whenever the matrix $m^\dagger m$ is real there is also no CP violation at low energies. On the other hand the matrix $mm^\dagger$ is always real in this framework.

In the hadronic sector the phase δ_{KM}, generated through spontaneous CP violation in general is not suppressed and the Z_4 symmetry allows to find a solution [38] of the strong CP problem of the type proposed by Nelson [39] and Barr [40].

Acknowledgments

The author thanks the organizers of DARK 2004 for the warm hospitality at Texas A& M University and the stimulating Conference. This work was

partially supported by Fundação para a Ciência e a Tecnologia (FCT, Portugal) through the projects, POCTI/FNU/44409/2002, CFTP-FCT UNIT 777 which are partially funded through POCTI (FEDER).

References

1. P. Minkowski, Phys. Lett. B **67**, 421 (1977); T. Yanagida, in *Proc. of the Workshop on Unified Theory and Baryon Number in the Universe*, KEK, March 1979; S. L. Glashow, in "Quarks and Leptons", Cargèse, ed. M. Lévy et al., Plenum, 1980 New York, pp. 707; M. Gell-Mann, P. Ramond, R. Slansky, in *Supergravity*, Stony Brook, Sept 1979; R. N. Mohapatra, G. Senjanovic, Phys. Rev. Lett. **44**, 912 (1980)
2. M. Fukugita, T. Yanagida, Phys. Lett. B **174**, 45 (1986)
3. V. A. Kuzmin, V. A. Rubakov, M. E. Shaposhnikov, Phys. Lett. B **155**, 36 (1985)
4. The full proof is in: M. N. Rebelo, Phys. Rev. D **67**, 013008 (2003) [arXiv:hep-ph/0207236]; See also M. N. Rebelo, arXiv:hep-ph/0311226, Invited talk at (BEYOND 03), Castle Ringberg, Tegernsee, Germany, 9–14 Jun 2003
5. R. N. Mohapatra, X. Zhang, Phys. Rev. D **46**, 5331 (1992); H. B. Nielsen, Y. Takanishi, Phys. Lett. B **507**, 241 (2001); E. Nezri, J. Orloff, JHEP **0304**, 020 (2003) ; T. Endoh, T. Morozumi, T. Onogi, A. Purwanto, Phys. Rev. D **64**, 013006 (2001) [Erratum-ibid. D **64**, 059904 (2001)]; A. S. Joshipura, E. A. Paschos, W. Rodejohann, JHEP **0108**, 029 (2001) ; G. C. Branco, T. Morozumi, B. M. Nobre, M. N. Rebelo, Nucl. Phys. B **617**, 475 (2001); F. Buccella, D. Falcone, F. Tramontano, Phys. Lett. B **524**, 241 (2002); K. R. S. Balaji, W. Rodejohann, Phys. Rev. D **65**, 093009 (2002); G. C. Branco, R. Gonzalez Felipe, F. R. Joaquim, M. N. Rebelo, Nucl. Phys. B **640**, 202 (2002); J. R. Ellis, M. Raidal, Nucl. Phys. B **643**, 229 (2002); Z. z. Xing, Phys. Lett. B **545**, 352 (2002); J. R. Ellis, M. Raidal, T. Yanagida, Phys. Lett. B **546**, 228 (2002); S. Davidson, A. Ibarra, Nucl. Phys. B **648**, 345 (2003); P. H. Frampton, S. L. Glashow, T. Yanagida, Phys. Lett. B **548**, 119 (2002); T. Endoh, S. Kaneko, S. K. Kang, T. Morozumi, M. Tanimoto, Phys. Rev. Lett. **89**, 231601 (2002); T. Hambye, arXiv:hep-ph/0210048; G. C. Branco, R. Gonzalez Felipe, F. R. Joaquim, I. Masina, M. N. Rebelo, C. A. Savoy, Phys. Rev. D **67**, 073025 (2003) [arXiv:hep-ph/0211001]; S. F. King, Phys. Rev. D **67**, 113010 (2003) [arXiv:hep-ph/0211228]; S. Pascoli, S. T. Petcov, W. Rodejohann, Phys. Rev. D **68**, 093007 (2003) [arXiv:hep-ph/0302054]; E. K. Akhmedov, M. Frigerio, A. Y. Smirnov, JHEP **0309**, 021 (2003) [arXiv:hep-ph/0305322]; A. Broncano, M. B. Gavela, E. Jenkins, Nucl. Phys. B **672**, 163 (2003) [arXiv:hep-ph/0307058]; L. Velasco-Sevilla, JHEP **0310**, 035 (2003) [arXiv:hep-ph/0307071]; B. Dutta, R. N. Mohapatra, Phys. Rev. D **68**, 113008 (2003) [arXiv:hep-ph/0307163]; V. Barger, D. A. Dicus, H. J. He, T. j. Li, Phys. Lett. B **583**, 173 (2004) [arXiv:hep-ph/0310278]; W. l. Guo, Z. z. Xing, Phys. Lett. B **583**, 163 (2004) [arXiv:hep-ph/0310326]; W. Rodejohann, Eur. Phys. J. C **32**, 235 (2004) [arXiv:hep-ph/0311142]
6. G. C. Branco, P. A. Parada, M. N. Rebelo, arXiv:hep-ph/0307119
7. G. C. Branco, T. Morozumi, B. M. Nobre, M. N. Rebelo, in [5]

8. T. Endoh, T. Morozumi, T. Onogi, A. Purwanto, in [5]
9. G. C. Branco, L. Lavoura, M. N. Rebelo, Phys. Lett. B **180**, 264 (1986)
10. Z. Maki, M. Nakagawa, S. Sakata, Prog. Theor. Phys. **28**, 870 (1962)
11. S. Eidelman et al. [Particle Data Group Collaboration], Phys. Lett. B **592**, 1 (2004)
12. K. Eguchi et al. [KamLAND Collaboration], Phys. Rev. Lett. **90**,021802 (2003) [arXiv:hep-ex/0212021]; T. Araki et al. [KamLAND Collaboration], arXiv:hep-ex/0406035
13. S. N. Ahmed et al. [SNO Collaboration], Phys. Rev. Lett. **92**, 102004 (2004) [arXiv:hep-ex/0310030]; B. Aharmim et al. [SNO Collaboration], Phys. Rev. D **70**, 093014 (2004) [arXiv:hep-ex/0407029]
14. Y. Fukuda et al. [Kamiokande Collaboration], Phys. Rev. Lett. **77**, 1683 (1996); B. T. Cleveland et al., [Homestake] Astrophys. J. **496**, 505 (1998); W. Hampel et al. [GALLEX Collaboration], Phys. Lett. B **447**, 127 (1999); J. N. Abdurashitov et al. [SAGE Collaboration], Phys. Rev. C **60**, 055801 (1999) [arXiv:astro-ph/9907113]; M. Altmann et al. [GNO Collaboration], Phys. Lett. B **490**, 16 (2000) [arXiv:hep-ex/0006034]; S. Fukuda et al. [Super-Kamiokande Collaboration], Phys. Rev. Lett. **86**, 5656 (2001) [arXiv:hep-ex/0103033]; S. Fukuda et al. [Super-Kamiokande Collaboration], Phys. Lett. B **539**, 179 (2002) [arXiv:hep-ex/0205075]
15. M. C. Gonzalez-Garcia, arXiv:hep-ph/0410030; G. Altarelli, arXiv:hep-ph/0410101; S. Goswami, A. Bandyopadhyay, S. Choubey, arXiv:hep-ph/0409224; M. C. Gonzalez-Garcia, M. Maltoni, A. Y. Smirnov, Phys. Rev. D **70**, 093005 (2004) [arXiv:hep-ph/0408170]; A. Bandyopadhyay, S. Choubey, S. Goswami, S. T. Petcov, D. P. Roy, arXiv:hep-ph/0406328; J. N. Bahcall, M. C. Gonzalez-Garcia, C. Pena-Garay, JHEP **0408**,016 (2004) [arXiv:hep-ph/0406294]; M. Maltoni, T. Schwetz, M. A. Tortola, J. W. F. Valle, New J. Phys. **6**, 122 (2004) [arXiv:hep-ph/0405172]; G. L. Fogli, E. Lisi, A. Marrone, A. Palazzo, Phys. Lett. B **583**, 149 (2004) [arXiv:hep-ph/0309100]
16. L. Wolfenstein, Phys. Rev. D **17**, 2369 (1978); S. P. Mikheev, A. Y. Smirnov, Sov. J. Nucl. Phys. **42**, 913 (1985) [Yad. Fiz. **42**, 1441 (1985)]; S. P. Mikheev, A. Y. Smirnov, Nuovo Cim. C **9**, 17 (1986)
17. Y. Ashie et al. [Super-Kamiokande Collaboration], Phys. Rev. Lett. **93**, 101801 (2004) [arXiv:hep-ex/0404034]
18. T. Ishii [K2K Collaboration], arXiv:hep-ex/0406055 M. H. Ahn et al. [K2K Collaboration], Phys. Rev. Lett. **93**, 051801 (2004) [arXiv:hep-ex/0402017]
19. M. Apollonio et al. [CHOOZ Collaboration], Phys. Lett. B **466**, 415 (1999) [arXiv:hep-ex/9907037]
20. C. Weinheimer et al., Phys. Lett. B **460** 219 (1999) V. M. Lobashev et al., Phys. Lett. B **460**, 227 (1999)
21. H. V. Klapdor-Kleingrothaus, A. Dietz, H. L. Harney, I. V. Krivosheina, Mod. Phys. Lett. A **16**, 2409 (2001) [arXiv:hep-ph/0201231]; C. E. Aalseth et al. [16EX Collaboration], Phys. Rev. D **65**, 092007 (2002) [arXiv:hep-ex/0202026]
22. C. L. Bennett et al., Astrophys. J. Suppl. **148**, 1 (2003) [arXiv:astro-ph/0302207]
23. D. N. Spergel et al. [WMAP Collaboration], Astrophys. J. Suppl. **148**, 175 (2003) [arXiv:astro-ph/0302209]
24. L. Covi, E. Roulet, F. Vissani, Phys. Lett. B **384**, 169 (1996) ; M. Flanz, E. A. Paschos, U. Sarkar, Phys. Lett. B **345**, 248 (1995) [Erratum, ibid. B **382**, 447 (1995)]; M. Plümacher, Z. Phys. C **74**, 549 (1997)

25. W. Buchmüller, P. Di Bari, M. Plümacher, Nucl. Phys. B **643**, 367 (2002) [arXiv:hep-ph/0205349]; W. Buchmüller, P. Di Bari, M. Plümacher, Phys. Lett. B **547**, 128 (2002) [arXiv:hep-ph/0209301]; For other recent detailed studies on thermal leptogenesis see: S. Davidson, arXiv:hep-ph/0304120; S. Davidson, A. Ibarra, Phys. Lett. B **535**, 25 (2002) [arXiv:hep-ph/0202239]; as well as references in [27], [28]
26. E. W. Kolb, M. S. Turner, "The Early Universe," Addison-Wesley (1990) 547 p. (Frontiers in Physics, 69); W. Fischler, G. F. Giudice, R. G. Leigh, S. Paban, Phys. Lett. B **258**, 45 (1991); W. Buchmüller, T. Yanagida, Phys. Lett. B **302**, 240 (1993)
27. W. Buchmüller, P. Di Bari, M. Plümacher, Nucl. Phys. B **665**, 445 (2003) [arXiv:hep-ph/0302092]; W. Buchmüller, P. Di Bari, M. Plümacher, arXiv:hep-ph/0401240; W. Buchmuller, P. Di Bari, M. Plumacher, New J. Phys. **6**, 105 (2004) [arXiv:hep-ph/0406014]
28. G. F. Giudice, A. Notari, M. Raidal, A. Riotto, A. Strumia, Nucl. Phys. B **685**, 89 (2004) [arXiv:hep-ph/0310123]
29. J. Bernabéu, G. C. Branco, M. Gronau, Phys. Lett. B **169**, 243 (1986)
30. J. Hashida, T. Morozumi, A. Purwanto, Prog. Theor. Phys. **101**, 379 (2000) [Erratum-ibid. **103**, 865 (2000)] [arXiv:hep-ph/9909208]
31. G. C. Branco, R. Gonzalez Felipe, F. R. Joaquim, I. Masina, M. N. Rebelo, C. A. Savoy, in [5]
32. P. H. Frampton, S. L. Glashow, T. Yanagida, in [5]
33. Y. Achiman, Phys. Lett. B **599**, 75 (2004) [arXiv:hep-ph/0403309]
34. J. H. Christenson, J. W. Cronin, V. L. Fitch, R. Turlay, Phys. Rev. Lett. **13**, 138 (1964)
35. B. Aubert et al. [BABAR Collaboration], Phys. Rev. Lett. **86**, 2515 (2001)
36. K. Abe et al. [Belle Collaboration], Phys. Rev. Lett. **87**, 091802 (2001)
37. L. Bento, G. C. Branco, Phys. Lett. B **245**, 599 (1990)
38. L. Bento, G. C. Branco, P. A. Parada, Phys. Lett. B **267**, 95 (1991)
39. A. E. Nelson, Phys. Lett. B **136**, 387 (1984); A. E. Nelson, Phys. Lett. B **143**, 165 (1984)
40. S. M. Barr, Phys. Rev. Lett. **53**, 329 (1984)

A New Type Baryogenesis: Q-Genesis

Jihn E. Kim

School of Physics, Seoul National University, Seoul 151-747, Korea
jekim@phyp.snu.ac.kr

It is pointed out that if vector-like heavy quarks, Q, are present at a high energy scale then they can serve toward baryogenesis. We study a few phenomenological constraints on Q so that this idea is implementable.

1 Introduction

The observed facts in cosmology are (i) cosmic microwave background radiation, (ii) abundant light elements, (iii) galaxies and inter-galactic molecules, and (iv) dark matter and dark energy. We present here the work of [1] toward baryogenesis. The baryon asymmetry of universe is one of the most important cosmological observations probably explainable by a particle physics model(s). Starting from a baryon symmetric universe, Sakharov proposed three conditions for generating a baryon asymmetry in the universe from fundamental interactions applicable in cosmology [2]: the existence of $\Delta B \neq 0$ interaction which accompany C and CP violation, and their working in a non-equilibrium state in the cosmos. Grand unified theories(GUTs) seemed to provide the basic theoretical framework for baryogenesis [3], because in most GUTs $\Delta B \neq 0$ interaction is present. Introduction of C and CP violation in GUTs is always possible if not forbidden by some symmetry. The condition on non-equilibrium is possible in the evolving universe but the consistency has to be checked given a specific interaction. Namely, a cosmological evolution with $\Delta B \neq 0$ and C and CP violating particle physics model can produce a nonzero ΔB. The question is how big the generated ΔB is, which can be compared to the observed value $\Delta B \simeq 0.6 \times 10^{-9} n_\gamma$. For example, an SU(5) GUT with X, Y gauge bosons for the $\Delta B \neq 0$ interaction is not generating the needed magnitude when applied in the evolving universe. In the SU(5) GUT, two quintet Higgs are needed for an allowable magnitude [4].

GUTs seemed to be the theory for baryogenesisfor some time. However, this belief underwent a fundamental change in the mid-1980's. The spontaneously broken electroweak(EW) sector of the standard model(SM) does not allow instanton solutions. When $\mathrm{SU}(2)_{\mathrm{weak}}$ is not broken, there are EW SU(2) instanton solutions. Tunneling via these EW instantons is extremely suppressed (viz. $e^{-2\pi/\alpha_w}$), which is the zero temperature estimate. At a high

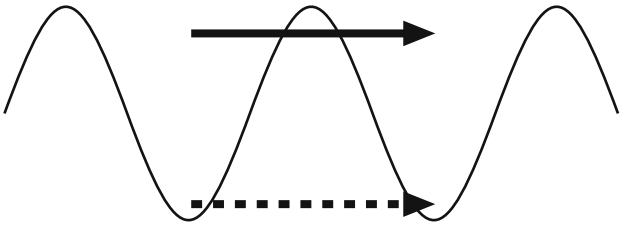

Fig. 1. Tunneling via sphaleron processes. The real(dashed) long arrow represents the high(zero) temperature tunneling.

temperature however, the transition rate can be huge and in the hot Big-Bang(BB) cosmology this effect must be considered [5]. The vacuum transition is shown schematically in Fig. 1.

We are familiar with the QCD instanton which combines a left-handed quark triplet and a left-handed anti-quark anti-triplet, $u^\alpha u^c_\alpha$, etc. Similarly, the sphaleron combines a left-handed SU(2) doublet with a left-handed SU(2) doublet, $\epsilon^{ij} q_i q_j$. The resulting effective interaction must be SU(3)×SU(2)×U(1)$_Y$ singlet. The 't Hooft diagram is shown in Fig. 2.

Due to the 't Hooft interaction, the baryon number produced during the GUT era is washed out during the EW phase transition when the temperature is of order the EW scale. Since the sphaleron interaction of Fig. 2 violates $B + L$ but conserves $B - L$, if there were a net $B - L$ in the beginning then there results a baryon asymmetry below the EW scale. If a complete washout of $B + L$ is achieved, the partition of $B - L$ into B and L is

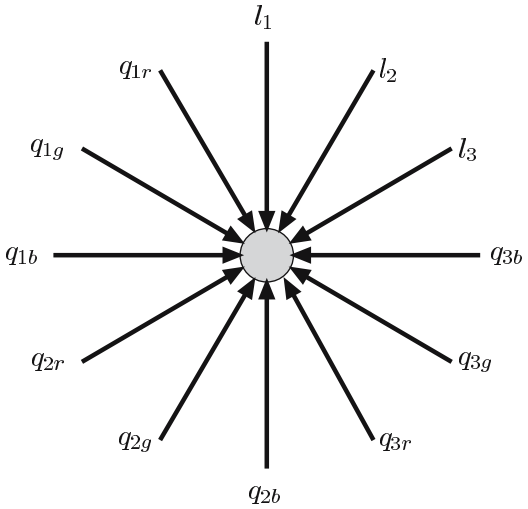

Fig. 2. The 't Hooft determinental interaction of SU(2) doublets.

$$\Delta B = \frac{1}{2}(B-L)_{\text{orig.}}\ , \quad \Delta L = \frac{1}{2}(B-L)_{\text{orig.}} \tag{1}$$

The familiar leptogenesis uses this transformation of the $B-L$ number generated by the decay of heavy Majorana neutrino(s) to the B number [6].

Thus, we need to generate a net $B-L$ number at the GUT scale, or more generally above the EW scale. The SU(5) conserves $B-L$ and hence cannot generate a net $B-L$. For baryogenesis, one has to go beyond the SU(5) GUT. There are three proposals in this regard:

(i) N-genesis known as leptogenesis [6],
(ii) neutrino(ν)-genesis [7], and
(iii) Q-genesis [1].

Among these we focus on the Q-genesis.

2 Introduction of Heavy Quarks

We will introduce heavy quarks. For baryogenesis these heavy quarks are better to be SU(2) singlets since the singlet quarks can survive the EW era not hampered by the sphaleron process of Fig. 2. We note the following toward a successful baryogenesis,

- Heavy quarks Q must mix with light quarks so that after the EW phase transition they can generate the quark number ($= \frac{1}{3}B$).
- They must live sufficiently long.
- A correct order for $\Delta B \neq 0$ should be generated.

SU(2) singlet quarks were considered before in connection with the flavor changing neutral current(FCNC) at the EW scale [8, 9], and recently in connection with the new BELLE result [10]. For the absence of the FCNC at tree level, the weak isospin T_3 eigenvalues of the mixable fermions must be the same. Thus, introducing left-handed singlets potentially introduce the FCNC problem. But in most discussions, the smallness of mixing angles with singlets were overlooked. Since quark singlets in our scheme are super heavy compared to 100 GeV, the small mixing angles are natural rather than unnatural.

For definiteness, we work out for $Q = -\frac{1}{3}$ SU(2) singlet quarks, D. So, the conditions on D must be:

1. There should be a ΔD generation,
2. 10^{-10} s $< \tau_D <$ 1 s,
3. Sphaleron should not wash out ΔD, and
4. FCNC bound must be satisfied.

The question is, "Is it natural to introduce such a heavy quark D?"

In E_6 GUT, there exist Ds in $\mathbf{27}_F$. Also, the trinification GUT has such Ds. With the notation given in [11], the branching of $\mathbf{27}_F$ is

$$\begin{aligned}\mathbf{27}_F &\to \mathbf{16}+\mathbf{10}+\mathbf{1} \to \mathbf{10}+\overline{\mathbf{5}}+\mathbf{1}+\mathbf{5}+\overline{\mathbf{5}}+\mathbf{1} \\ &\to (q+u^c+e^+)+(l+d^c)+N_5+(D+L_2)+(D^c+L_1)+N_{10} \quad (2)\end{aligned}$$

where one vector-like D appears per family.

When we consider this kind of vector-like quarks, there are three immediately related physical problems to deal with, the heavy quark axion, the Nelson-Barr type strong CP solution, and the FCNC [12]. Here, we focus on the FCNC issue.

Consider one family(the third family) first,

$$\begin{pmatrix} t \\ b \end{pmatrix}_L \quad b_R \tag{3}$$

which gives all the needed features. The mass matrix with D is

$$\begin{pmatrix} m & J \\ 0 & M \end{pmatrix} \tag{4}$$

where the entry 0 is natural since it can be obtained by a redefinition of right-handed singlets. The mass matrix can be diagonalized by considering $MM^\dagger$,

$$\begin{matrix} |m_b|^2 \\ |m_D|^2 \end{matrix} = \frac{1}{2}\left\{(|M|^2+|m|^2+|J|^2) \pm \sqrt{[(|M|+|m|)^2+|J|^2][(|M|-|m|)^2+|J|^2]}\right\} \tag{5}$$

With the hierarchy we are assuming $|M|^2 \gg |m|^2, |J|^2$, we have $|m_b| \simeq |m|$ and $|m_D| \simeq |M|$. With the vanishing phases, the b and D mass eigenstates are

$$|b\rangle \simeq \begin{pmatrix} 1 \\ -J/M \end{pmatrix} \quad , \quad |D\rangle \simeq \begin{pmatrix} J/M \\ 1 \end{pmatrix} . \tag{6}$$

Since J is the doublet VEV and M is a mass parameter or a singlet VEV, the mixing angle can be sufficiently small. This is the well-known decoupling of vector-like quarks. It can be generalized to three ordinary quarks and n heavy quarks with $(3+n)\times(3+n)$ matrix

$$M = \begin{pmatrix} M_d & J \\ J' & M_D \end{pmatrix} \tag{7}$$

can take the following form by redefining the right-handed d and D fields,

$$M = \begin{pmatrix} M_d & J \\ 0 & M_D \end{pmatrix} . \tag{8}$$

The essential feature, the decoupling of the vector-like quarks, is not changed with this generalization to $(3+n)\times(3+n)$ mass matrix. For the estimate below, we will use J with respect to the bottom quark mass, $|J| = f m_b$.

3 Q-Genesis by Heavy Quarks

In the Q-genesis the generation of D number is worked out as usual through the Sakharov mechanism. Going through the EW phase transition, this D number becomes $\frac{1}{3}B$ number.

The interaction we introduce is

$$g_{Di}X_i u^c D^c + g_{ei}X_i^* u^c e^c + \text{h.c.}\ . \tag{9}$$

To generate the D-number, we need an interference of the tree and one-loop diagrams shown in Fig. 3.

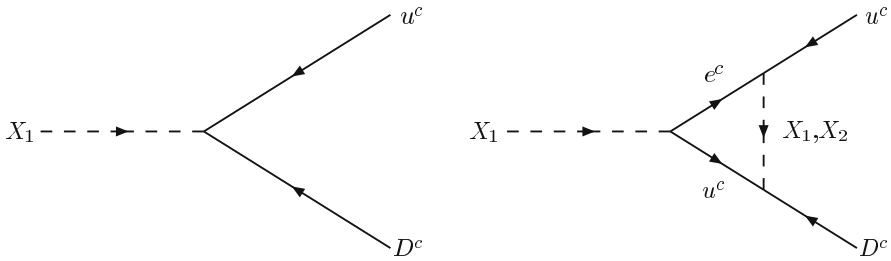

Fig. 3. The interference between tree and one-loop diagrams is needed for a nonzero ΔD generation.

The interference term contributes as

$$g_{e1}^* g_{e2}^* g_{D1}^* g_{D2}\ . \tag{10}$$

So, if we allow arbitrary phases in the Yukawa couplings, the relative phases of g_{D1} and g_{D2} can be cancelled only by the relative phase redefinition of X_2 and X_1. The same applies to g_{D1} and g_{D2}. Thus, the phase η appearing in (10) is physical. Let X_1 be the lighter among X_1 and X_2. Then, the D-number generated by this mechanism is

$$\begin{gathered} \tfrac{n_D}{n_\gamma} \simeq 0.5 \times 10^{-2}\epsilon \\ \epsilon \simeq \tfrac{\eta}{8\pi}10^{-2}[F(x) - F(x^{-1})], \quad x = \tfrac{m_{X_1}}{m_{X_2}} \\ F(x) = 1 - x\ln(x + x^{-1}) \end{gathered} \tag{11}$$

4 Lifetime Constraints

The dominant D decay modes are the processes,

$$D \to t + W, \quad b + Z, \quad b + H^0 \tag{12}$$

from which we obtain

$$\Gamma_D = \frac{G_F}{4\sqrt{2}\pi}|J|^2 m_D, \quad |J| = f m_b, \quad \epsilon = \frac{f m_b}{m_D} \,. \tag{13}$$

The lifetime of D must fall in the region

$$2 \times 10^{-11} \text{ s} < \tau_D < 1 \text{ s} \tag{14}$$

so that it must live long enough to live up the EW phase transition but must decay before the commencement of nucleosynthesis. This consideration gives a bound on ϵ

$$\frac{1}{(10^6 m_{D,\,\mathrm{GeV}})^{3/2}} < |\epsilon| < \frac{1}{(2.7 \times 10^2 m_{D,\,\mathrm{GeV}})^{3/2}} \tag{15}$$

where $m_{D,\,\mathrm{GeV}}$ is the D quark mass in units of GeV. Note that the mixing of D with b is of order ϵ(viz. (6)). For one period of oscillation, we expect that the $|\epsilon|^2$ fraction of D is expected to transform to b. Since the period of the EW phase is of order

$$\frac{1}{H} = \sqrt{\frac{3M_P^2}{\rho}} \sim \sqrt{\frac{3}{g_*}}\,\frac{M_P}{M_W^2} \,, \tag{16}$$

the following fraction of D is expected to be washed out

$$\frac{M_P m_b^2}{M_W^2 m_D} f^2 \simeq 10^{16} \frac{f^2}{m_{D,\mathrm{GeV}}} \quad . \tag{17}$$

Thus, for $m_D \sim 10^6$ GeV, we need $f < 10^{-5}$. Anyway, we need a heavy quark so that the sphaleron does not erase the D number.

5 Flavor Changing Neutral Current

For the FCNC, we may consider the processes of Z decay, B decay, and K^+ decay. These give the bounds on the relevant couplings as

process	experiment	bounds
$Z \to bb$	$z_{bb} = 0.996 \pm 0.005$	$\lvert\epsilon\rvert^2 \le 0.009$
$B \to X s l^+ l^-$		$\lvert z_{sb}\rvert = \frac{J_b J_s}{m_D^2} < 1.4 \times 10^{-3}$
$K^+ \to \pi^+ \nu\bar{\nu}$		$\lvert z_{sd}\rvert \le 7.3 \times 10^{-6}$

(18)

Note that in the last row of (18), we used the ratio

$$\frac{\mathrm{Br.}(K^+ \to \pi^+ \nu\bar{\nu})}{\mathrm{Br.}(K^+ \to \pi^0 e^+ \nu)} = \frac{3|z_{sd}|^2}{2\lambda^2} \le 2 \times 10^{-9} \,. \tag{19}$$

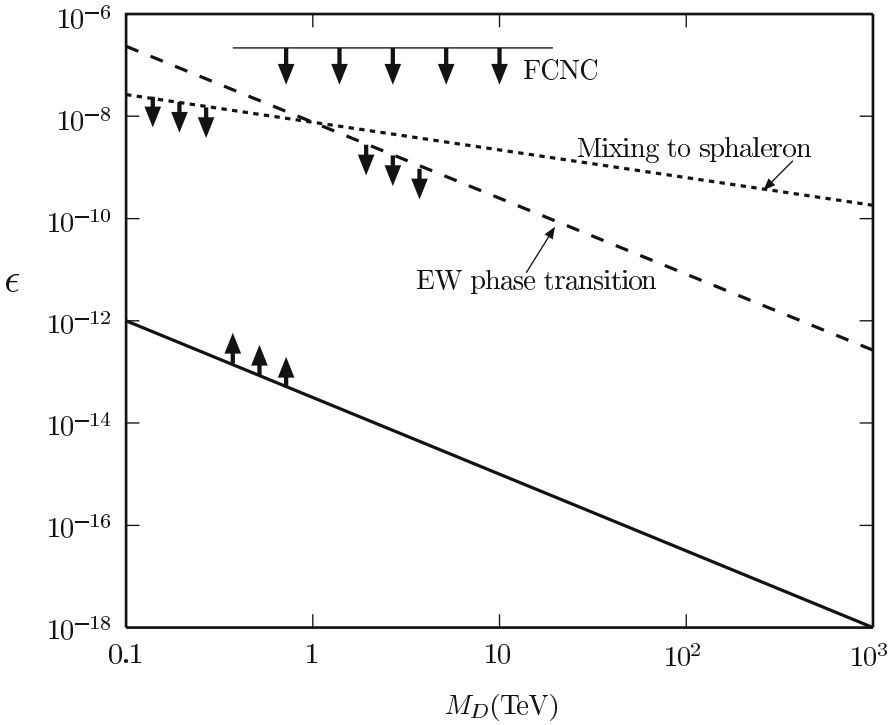

Fig. 4. The current allowed region in the $\epsilon - M_D$ plane. The allowed region is the intersection of the region above the solid line and the common region below two dashed lines.

Therefore, we obtain

$$\frac{1}{4.8 \times 10^9 \sqrt{m_{D,\,\mathrm{GeV}}}} < |f| < \frac{1}{2.1 \times 10^4 \sqrt{m_{D,\,\mathrm{GeV}}}} \tag{20}$$

All the bounds we discussed so far are summarized in Fig. 4. Note, however, that if we assume SUSY, the bound comes from the upper bound of $M_X \sim 10^9$ GeV. In that case $M_D < 1$ TeV is the bound. On the other hand, if we take $M_X \sim 10^{13}$ GeV without SUSY, M_D can be as heavy as 1000 TeV or 10^4 TeV. These are not marked in Fig. 4.

$\mathbf{Z_2}$ Symmetry

To implement the small f obtained above naturally, we can impose a discrete symmetry. Thus, let us introduce a $\mathbf{Z}_2$ parity,

$$\mathbf{Z}_2 : \; b_{L,R} \to b_{L,R}, \; D_{L,R} \to -D_{L,R} \; . \tag{21}$$

The $\mathrm{SU}(2)_W$ doublet q_L having b_L as its component has the same $Z_2 = +1$ eigenvalue as b_R. But the gauge symmetry forbid them to get a bare mass.

On the other hand, the $SU(2)_W$ singlet D can have a bare mass or obtain a mass by a large VEV of $Z_2 = +1$ singlet scalar S. All the interactions are consistent with the $\mathbf{Z}_2$ parity if L, e^c and X are $\mathbf{Z}_2$ parity odd and all the other fields are even. We can introduce two Higgs doublets, ϕ and φ,

$$\mathbf{Z}_2 : \ \phi \to \phi, \ \varphi \to -\varphi \ . \tag{22}$$

Thus, we can write the following renormalizable Lagrangian consistent with the $\mathbf{Z}_2$ parity except for the soft term m_δ^2,

$$\begin{aligned} V(\phi,\varphi) = (m_\delta^2 \varphi^\dagger \phi + h.c.) - \mu^2 \phi^\dagger \phi + M_\varphi^2 \varphi^\dagger \varphi + \lambda_1 (\varphi^\dagger \varphi)^2 + \lambda_2 (\phi^\dagger \phi)^2 \\ + \lambda_3 \varphi^\dagger \varphi \phi^\dagger \phi + \lambda_4 \varphi^\dagger \phi \phi^\dagger \varphi + (\lambda_5 \varphi^\dagger \phi \varphi^\dagger \phi + h.c.) \end{aligned} \tag{23}$$

where we assume $M_\varphi^2 \gg \mu^2 \gg |m_\delta^2| > 0$.

If $\mathbf{Z}_2$ were exact, there is no mixing of D with b and hence D would be absolutely stable, and

$$\langle \phi \rangle = v \neq 0 \ , \quad \langle \varphi \rangle = 0 \ .$$

But the existence of soft term violates the $\mathbf{Z}_2$ symmetry and a tiny VEV of φ is generated,

$$\langle \varphi \rangle = \frac{m_\delta^2 v}{M_\varphi^2} \ , \quad f_{\rm off} \bar{q}_L \varphi D_R \quad \to \quad J \simeq f_{\rm off} \frac{m_\delta^2 v}{M_\varphi^2} \tag{24}$$

or

$$f = \frac{\sqrt{2} f_{\rm off}}{f_b} \ \frac{m_\delta^2}{M_\varphi^2} \tag{25}$$

which can be made naturally small by a small ratio of m_δ / M_φ. The mass of φ can be superheavy.

Assuming no approximate discrete symmetry, proton decay can proceed via the X particle exchange $d^c u^c \to X^* \to ue$. Thus, the mass of X particle should be in the GUT scale with a small Yukawa couplings to the first family members as studied in GUT proton decay. This is the standard colored Higgs mediated proton decay.

6 Conclusion

In this talk, we presented a new type baryogenesis, the Q-genesis. There are constraints on the parameters introduced in the model. We also pointed out that a discrete symmetry such as $\mathbf{Z}_2$ can render the smallness of f natural. The interesting thing in this scenario is that this so-far unnoticed baryogenesis has an allowed region in the parameter space as shown in Fig. 4.

Finally, we summarize three classes of baryogenesis in Table 1.

Table 1. Comparison of three types of baryogenesis.

	$(B-L)_{\text{orig.}}=0$	$(B-L)_{\text{orig.}}\neq 0$	Sphaleron
N-genesis		Yes	(ν, e) converts to B
ν-genesis	Possible	Possible	(ν, e) converts to B
Q-genesis	Possible	Possible	Q decay produces B

Acknowlegments

This work is supported in part by the KOSEF Sundo Grant, the ABRL Grant No. R14-2003-012-01001-0, and the BK21 program of Ministry of Education, Korea.

References

1. H. D. Kim, J. E. Kim, and T. Morozumi, hep-ph/0409001.
2. A. D. Sakharov, Pisma Zh. Eksp. Teor. Fiz. **5**, 32 (1967) [JETP Lett. **5**, 24 (1967)].
3. M. Yoshimura, Phys. Rev. Lett. **41** (1978) 281.
4. See, for example, S. M. Barr, G. Segre, and H. A. Weldon, Phys. Rev. **D20** (1979) 2494; E. W. Kolb and M. S. Turner, *Early Universe* (Addison-Wesley Publishing Co., New York, 1990), p. 168.
5. V. A. Kuzmin, V. A. Rubakov, and M. E. Shaposhnikov, Phys. Lett. **B155** (1985) 36.
6. M. Fukugita and T. Yanagida, Phys. Lett. **B174** (1986) 45.
7. K. Dick, M. Lindner, M. Ratz, and D. Wright, Phys. Rev. Lett. **84** (2000) 4039.
8. K. Kang and J. E. Kim, Phys. Lett. **B64** (1976) 93.
9. S. L. Glashow and S. Weinberg, Phys. Rev. **D15** (1977) 1958.
10. L. T. Handoko and T. Morozumi, Mod. Phys. Lett. **A10** (1995) 309 and Mod. Phys. Lett. **A10** (1995) 1733 (E).
11. J. E. Kim, Phys. Lett. **B564** (2003) 35.
12. J. E. Kim, Phys. Rep. **150** (1987) 1.

Cosmological Constant and Gravity+Matter Self-Creation in a Cosmology with an Unbounded Hamiltonian Taking into Account Negative Energy of Gravity

V.V. Kocharovsky[1,2], E.V. Derishev[2], and Vl.V. Kocharovsky[2]

[1] Department of Physics and Institute for Quantum Studies, Texas A&M University, Texas 77843-4242, USA
vkochar@jewel.tamu.edu
[2] Institute of Applied Physics of the Russian Academy of Science, Nizhny Novgorod, 603950 Russia
kochar@appl.sci-nnov.ru

Summary. We outline a solution to the cosmological constant problem and dynamics of the Universe expansion that follow from the quantum field theory of interacting gravity and matter with an unbounded Hamiltonian taking into account a negative-energy contribution from the metric conformal factor.

1 Introduction

This paper contains notes of our DARK2004 talk on the cosmology that follows from the quantum field theory of gravity and matter suggested in [1, 2]. In Sect. 2 we review a simplified model of quantized conformally-flat gravity conformally coupled to a massive scalar field. The Lagrangian is

$$L = \frac{1}{2}(\psi^{,\mu}\psi_{,\mu} - m_\psi^2\psi^2) + \frac{1}{2}(-\phi^{,\mu}\phi_{,\mu} + m_\phi^2\phi^2) - \frac{\lambda_\psi}{4!}\psi^4 + \frac{\lambda_\phi}{4!}\phi^4 - \frac{\lambda}{4}\psi^2\phi^2 \quad (1)$$

in a Minkowski space-time with a metric $\eta_{\mu\nu} = \mathrm{diag}(1, -1, -1, -1)$, $\mu,\ \nu = 0,\ 1,\ 2,\ 3$. Here $\psi = \Omega\Psi$, the field Ψ describes matter with a mass m and a self-interaction coupling constant λ_ψ, ϕ is the gravity field (the scaled conformal factor of the spacetime metric tensor $g_{\mu\nu} = \Omega^2\eta_{\mu\nu}$, $\phi = (3/4\pi G)^{1/2}\Omega$), $\lambda = 8\pi G m^2/3$, and $\lambda_\phi = -16\pi G\Lambda/3$, where G is the universal gravitational constant and Λ is the cosmological constant. Following the renormalization-group analysis, we lay stress on a remarkable property of a co-existence of the ultraviolet and infrared asymptotical freedom in such systems.

In Sects. 3, 4 we discuss a simple cosmological (minisuperspace) model where the fields are spatially homogeneous but their amplitudes vary in time. Numerical examples (Figs. 2–4) of the classical (not quantum) dynamics imposed by this model are taken from a recent paper [3] where very rich and

unusual stability and dynamical properties of the system were demonstrated. (For a general reference on the cosmological models see, e.g., [4, 5].) For spatially homogeneous fields $\psi = x$ and $\phi = y$ the Lagrangian (1) reads

$$L = -\frac{1}{2}(-\dot{x}^2 + \omega_x^2 x^2) + \frac{1}{2}(-\dot{y}^2 + \omega_y^2 y^2) - \frac{a}{4}x^4 + \frac{b}{4}y^4 - \frac{c}{2}x^2 y^2 \ , \qquad (2)$$

where $\dot{x} = \frac{dx}{dt}$, $\dot{y} = \frac{dy}{dt}$, and $c = \lambda/2$. The partial matter (x-) and gravity (y-) oscillators have frequencies $\omega_x = m_x$ and $\omega_y = m_y$ as well as self-coupling constants $a = \lambda_\psi/6$ and $b = \lambda_\phi/6$, respectively. The canonical momenta $p_x = \frac{\partial L}{\partial \dot{x}}$ and $p_y = \frac{\partial L}{\partial \dot{y}}$ imply the Hamiltonian $H = p_x\dot{x} + p_y\dot{y} - L$ in the form

$$H = \frac{1}{2}({p_x}^2 + kx^2) - \frac{1}{2}({p_y}^2 + ky^2) + \frac{a}{4}x^4 - \frac{b}{4}y^4 + \frac{c}{2}x^2 y^2 \ . \qquad (3)$$

A distinctive feature of this Hamiltonian is that it is unbounded from below as well as from above due to the fact that the cosmological-scale y-oscillator contributes with the negative kinetic and potential energies to the total energy of the system. The case when $\omega_x = \omega_y$, $a = b$, and c are all positive constants was analyzed in [3]. When $c = 0$ the uncoupled matter ($x-$) and gravity (y-) oscillators are stable anharmonic oscillators. Simultaneous creation of the matter and gravity, i.e. the cosmological birth and growth of the Universe, occurs only due to the nonlinear coupling ($c > 0$) of matter and gravity. The Hamiltonian has to be set equal to zero, $H = 0$, which is a constraint imposed by the General Theory of Relativity in order to get the proper classical Einstein equations. Within a semiclassical analysis, the fact that the conformal factor of the spacetime metric contributes with a negative kinetic energy to the Hamiltonian has been known for a long time (see references in [1]). Within a classical, non-quantized theory, some particular examples of the Hamiltonian systems with a similar structure were studied in [6]–[11]. In this talk we present elements of an analytical description of some interesting regimes generated by the cosmological model (2)–(3). In Sect. 4 we comment on the relation of this model to cosmology and outline a possible solution to the cosmological constant problem.

2 Quantum Field Theory of Conformally-Flat Gravity Coupled to Massive Scalar Field

The original idea [1, 2] was to accept (i) a negative kinetic energy coming from a conformal factor as well as from higher-derivative terms of the gravity Lagrangian, (ii) an unboundedness of a gravity-matter Hamiltonian from below, and (iii) a corresponding negative-energy instability of an empty vacuum state (i.e., inflation and Big Bang) as a physical reality, but to quantize negative-energy fields properly. The proper quantization rules are

predetermined by the condition of convergence of a path integral representing the amplitude of the vacuum-vacuum transition and imply an opposite way to go around the poles of the propagators of the negative-energy fields as compared to that in the usual Feynman rules for the positive-energy fields. As a result, a Wick rotation of the time axes in a complex plane without crossing singularities is not possible anymore and the theory is not equivalent to the quantum statistical mechanics near a stable ground state in a Euclidean space. The theory includes nontrivial nonlinear dynamics of an unstable vacuum in a Minkowski spacetime with an indefinite metric.

Most of the formulas and methods of usual quantum field theory can be applied with small modifications to the unstable system (1). Vacuum for the system (1) is just usual tensor product of the partial vacua of ψ- and ϕ-fields. However, now it is not the ground state, but an unstable state. In order to pick out the contribution of the unstable vacuum state to the observable quantities, e. g., Green's functions, it is necessary to use the "anti-Feynman" propagator for the negative-energy field and the Feynman propagator for the positive-energy field. For the two-scalar-fields model (1), it means that one should change the sign in front of $\varepsilon \to +0$ in the Feynman propagator of the negative-energy field as well as the sign in front of the whole ϕ-propagator:

$$-- \overset{p_\phi}{\to} --= -i/\big(p_\phi^2 - m_\phi^2 - i\varepsilon\big), \quad \overset{p_\psi}{\longrightarrow}= i/\big(p_\psi^2 - m_\psi^2 + i\varepsilon\big)\,. \qquad (4)$$

As a result we obtain causal and unitary evolution of unstable field system.

We apply the method of the renormalization-group analysis to describe the behavior of interacting fields at arbitrary energy-momentum scale κp_i through the effective (running) coupling constants $\lambda(\kappa)$, $\lambda_\varphi(\kappa)$ if they are known at a given scale $\kappa_0 p_i$. For the theory (1) with $m_\psi = m_\phi = 0$ we derived the following renormalization-group equations in the one-loop approximation

$$\frac{d\lambda_\psi}{ds} = \lambda_\psi^2 - \lambda^2, \quad \frac{d\lambda_\phi}{ds} = \lambda_\phi^2 - \lambda^2, \quad \frac{d\lambda}{ds} = \frac{\lambda}{3}\big(\lambda_\psi + \lambda_\phi\big)\,, \qquad (5)$$

where $s = (3/16\pi^2)\ln(\kappa/\kappa_0)$. This result cannot come from euclidean integration because in the Minkowski momentum space the integration path along the real axis is squeezed by poles from all sides so that there is no any possibility for Wick rotation without crossing singularities. In particular, the minus sign in front of λ^2, which is crucial for the infrared&ultraviolet asymptotic freedom, appears due to a diagram with a two-vertex loop formed by virtual propagators of the field with the energy sign opposite to the sign of in- and out- fields. The exact solution of (5) for $\lambda_\psi(\lambda)$ and $\lambda_\phi(\lambda)$ is

$$\lambda_\varphi = \epsilon_\varphi\sqrt{3}\beta\lambda^3 \pm \sqrt{3\lambda^2\big(1 - \alpha\lambda + \beta^2\lambda^4\big)}, \qquad \varphi = \psi \;\text{ or }\; \phi\,, \qquad (6)$$

where arbitrary initial conditions are set by two parameters α and β at a reference scale $\kappa = \kappa_0$; ϵ_φ is equal to $+1$ for $\varphi = \psi$ and -1 for $\varphi = \phi$. The

scale dependence is given via a quadrature $s = 3\int(\lambda_\psi+\lambda_\phi)^{-1}\lambda^{-1}d\lambda$. Solution (6) takes a simple form for the plane $\lambda_\psi \equiv \lambda_\phi$, see Fig. 1. The respective scale dependence for a bounded trajectory is $s = \sqrt{3}[2\sqrt{1-\alpha\lambda}/\lambda + \alpha v]/4$, where $v = \ln|(\sqrt{1-\alpha\lambda}+1)/(\sqrt{1-\alpha\lambda}-1)|$, $\lambda(\kappa_0) = \alpha^{-1} > 0$.

Inside the separatrix cone, $\lambda_\psi\lambda_\phi > 3\lambda^2$, in the $(\lambda_\psi, \lambda_\phi, \lambda)$-space the self-interaction of fields prevails. The theory resembles either QED with infrared asymptotic freedom and ultraviolet divergence (upper part of the separatrix cone where both self-couplings are positive, $\lambda_\psi, \lambda_\phi > 0$, that corresponds to stable partial fields), or quantum chromodynamics (QCD) with ultraviolet asymptotic freedom and infrared divergence (lower part of the cone).

Outside the separatrix cone, $3\lambda^2 > \lambda_\psi\lambda_\phi$, the interaction between positive-energy and negative-energy fields is so strong that it results in a remarkable phenomenon of the co-existence of the ultraviolet and infrared asymptotic freedom. A trajectory starts at the point of freedom at $s \to -\infty$ and tends to the same point of freedom at $s \to +\infty$ without going to infinity (Fig. 1).

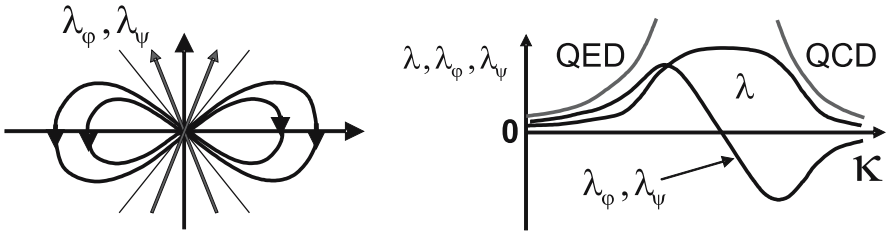

Fig. 1. Phase portrait of (5) and scale dependence of coupling constants for the case $\lambda_\psi = \lambda_\phi$.

The fact that a finite coupling and, hence, gravity-matter structure appears only within a finite range of energy-momentum scales can be related to the observed range of scales from a Planck's scale $\kappa_{max}^{-1} \sim 10^{-33}cm$ to a cosmological scale $\kappa_{min}^{-1} \sim 10^{27}cm$ on which the Universe becomes homogeneous according to the cosmological principle. The ratio $\kappa_{max}/\kappa_{min} \sim 10^{60}$ corresponds to the interval $\Delta s = (3/16\pi^2)\ln(\kappa_{max}/\kappa_{min}) \sim 3$ of the order of unity and is accounted for by quantum field theory without introducing big numbers *ad hoc*. Another consequence is the impossibility to fix arbitrarily a cosmological constant $\Lambda \propto \lambda_\phi$, in particular, to set $\Lambda \equiv 0$. It is correlated with a gravitational constant $G \propto \lambda$ and matter self-interaction λ_ψ, changes a sign, and is asymptotically small outside some interval of energy scales. Therefore, different scales (energies) contribute to the total expansion of the local, observable Universe with different weights and even signs.

3 Dynamics of a Cosmological Model

3.1 Basic Model

We assume that the gravity-matter coupling constant is positive, $c > 0$, since a change of its sign is equivalent to an interchange of the positive-energy matter x-oscillator with the negative-energy metric y-oscillator. Remember that the case $a > 0$, $b > 0$ is appropriate to the physical interpretation of the Hamiltonian (3) as describing the birth and cosmological evolution of the Universe in the process of the mutual creation of partially stable gravity (spacetime metric) and matter due to their nonlinear coupling c. In the case $b < 0$ the gravity y-oscillator is partially unstable. Hamilton's equations of motion are the coupled second order differential equations,

$$\ddot{x} + \omega_x^2 x + ax^3 + cxy^2 = 0 \quad \text{and} \quad \ddot{y} + \omega_y^2 y + by^3 - cx^2 y = 0 \,. \tag{7}$$

This, very basic model of just two coupled anharmonic oscillators already reveals many surprises coming from the unbounded Hamiltonians. First, there are no runaway solutions in the vast regions of the parameter space, i.e., despite of the unboundedness of the energy from below the nonlinear coupling can prevent from a runaway to infinity. Second, there is a fractal structure of regions with bounded and unbounded solutions in the phase space. Third, there is a dynamical chaos and variety of the stable and unstable regimes.

3.2 Bounded and Unbounded Solutions

The gravity-matter interaction ($c \neq 0$) affects the matter and gravity in quite different ways. The paper [3] demonstrates numerically an impressive nonlinear dynamics generated by the systems with the unbounded Hamiltonian. In particular, there is a wide range of parameters for which the system (3) generates very interesting unstable solutions which, contrary to the stable (bounded) solutions, approach infinity (in most cases in an explosive fashion in a finite interval of the conformal time) and are relevant to the Big Bang.

Regions of bounded (stable) and unbounded (unstable) solutions in phase space for the case $a = b$ are shown in Fig. 2 copied from [3]. In Fig. 2 and all numerical examples below the initial conditions were $(p_x, p_y, x, y) = (d, d, 0, 0)$. Generally, if a trajectory is unstable, the instability occurs very rapidly after some initial time interval $0 < t < t_{esc}$. Before the time t_{esc}, the trajectory appears to be stable and remains at small values of x and y. After the time t_{esc} unstable trajectories appear to diverge exponentially or even explosively rapidly.

Because there is an elliptic fixed point at the origin ($p_x = p_y = x = y = 0$), there will always be a small stable harmonic region in the immediate neighborhood of the origin. Within the original quantum theory of this minisuperspace model, the latter implies that the initially small vacuum spontaneous fluctuations of matter and gravity have to tunnel through a finite barrier in order to give birth and subsequent Universe inflation to a macroscopic state.

3.3 Scaling Properties

First, if the canonical variables are scaled by a factor of $\sqrt{a}$, so that $x' = x\sqrt{a}$ and $y' = y\sqrt{a}$, then the equations of motion take the form

$$\ddot{x}' + \omega_x^2 x' + x'^3 + \frac{c}{a} x' y'^2 = 0 \quad \text{and} \quad \ddot{y}' + \omega_y^2 y' + \frac{b}{a} y'^3 - \frac{c}{a} x'^2 y' = 0 \,. \quad (8)$$

Hence, as we change all three nonlinear coupling constants proportionally keeping the ratios c/a and b/a constant, the structure of the phase space motion in terms of the original variables (p_x, p_y, x, y) will be unchanged and only its overall scale will be changed. This scaling is the reason why there are stripes of stable and unstable motion along lines of constant c/a in Fig. 2.

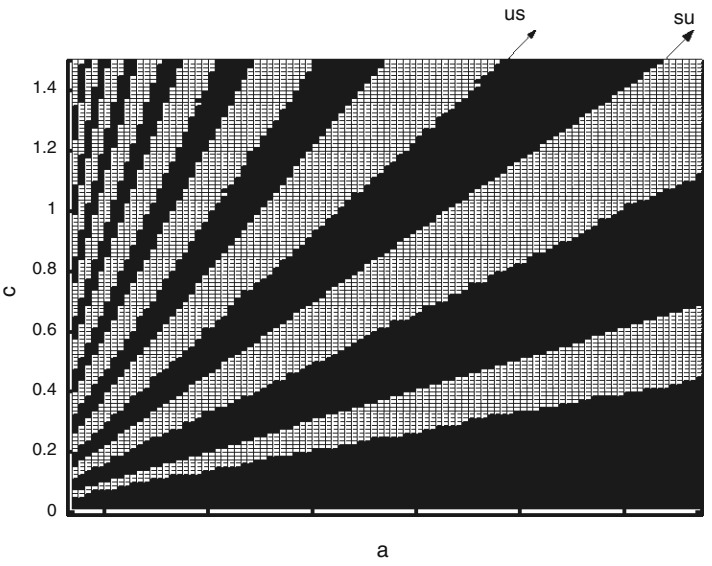

Fig. 2. A coarse-grained plot of stable and unstable regions for the system (7) as a function of parameters $a = b$ and c for $\omega_x = \omega_y = 1$. Black squares contain one stable trajectory and white squares contain one unstable trajectory. In all cases the initial conditions were $(p_x, p_y, x, y) = (d, d, 0, 0)$ with $d = 10$.

Second, if we further scale the canonical variables and time according to $x' \to |\omega_y| x'', y' \to |\omega_y| y'', t \to t/|\omega_y|$, then the motion (8) become

$$\ddot{x}'' + \frac{\omega_x^2}{|\omega_y^2|} x'' + x''^3 + \frac{c}{a} x'' y''^2 = 0, \quad \ddot{y}'' + sgn(\omega_y^2) y'' + \frac{b}{a} y''^3 - \frac{c}{a} x''^2 y'' = 0 \,. \quad (9)$$

In other words, only a ratio $(\omega_x/|\omega_y|)^2$ and a sign of ω_y^2 are important and it is enough to consider only three values $sgn(\omega_y^2) = 1, 0, -1$ which correspond to a positive, flat or negative spatial curvature, respectively.

For the limiting case $a = b = 0$ and arbitrary ω_x, ω_y, we can use an additional scaling $x \to x/\sqrt{|c|}, y \to y/\sqrt{|c|}, p_x \to p_x/\sqrt{|c|}, p_y \to p_y/\sqrt{|c|}$ that results in the equations of motion with c replaced by $sgn(c)$. Combining it with the ω_y-scaling law (9), we conclude that a stability border between stable (bounded) and unstable (unbounded) trajectories in the parameter space of initial conditions, d, gravity-matter coupling constant, c, and curvature ω_y^2 is determined by the scaling law $c = c_{cr}\omega_y^4/d^2$. Numerically it was found in [3] that there is only one critical value of the gravity-matter coupling, $c_{cr} \simeq 0.61$, and the stability border, indeed, satisfies the above scaling law.

3.4 Regime of Long Adiabatic Evolution Intermittent by Short Non-Adiabatic Crunches

Adiabatic Invariants and Averaged Equations of Motion

Some of the behavior of unstable oscillations can be understood using the theory of the adiabatic invariants [12]. Typical solutions are shown in Figs. 3–4 copied from [3]. We see some distinctive differences in the behavior for zero and nonzero $a = b$. For $a = b = 0$, the period of the y-oscillations is constant and the maximum amplitude of the y-oscillations can increase or decrease with increasing time. The x-oscillations have very small amplitude relative to those of the y-oscillator. For $a = b = 0.0015$, the period of the y-oscillations T_y can vary and appears to depend on the amplitude of the y-oscillations. Also, both the amplitude and period of the x-oscillations appear to depend on the amplitude of the y-oscillations.

Let us write $y(t) = \bar{y}(t) + \Delta y(t)$, where Δy is assumed small,

$$\bar{y}(t) = \frac{1}{T_x(t)} \int_0^{T_x(t)} y(t)\, dt\,, \tag{10}$$

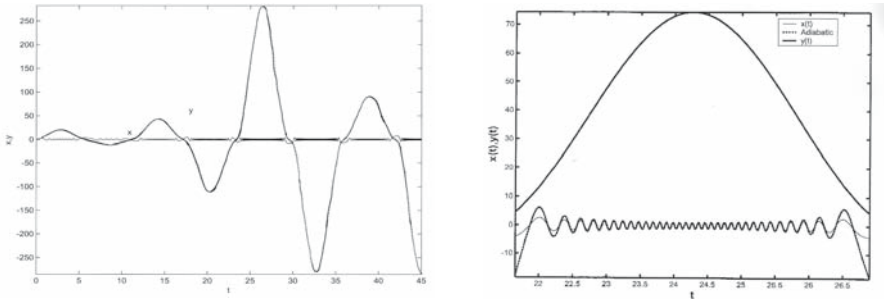

Fig. 3. (a) Plots of $x(t)$ and $y(t)$ versus t for $\omega_y = \omega_x = 1$, $a = b = 0$, $c = 0.8$, and initial momenta $d = 10$; (b) similar plots of $x(t)$ and $y(t)$ versus t for one oscillation interval of the Fig. 4(a) at $d = 1.9$.

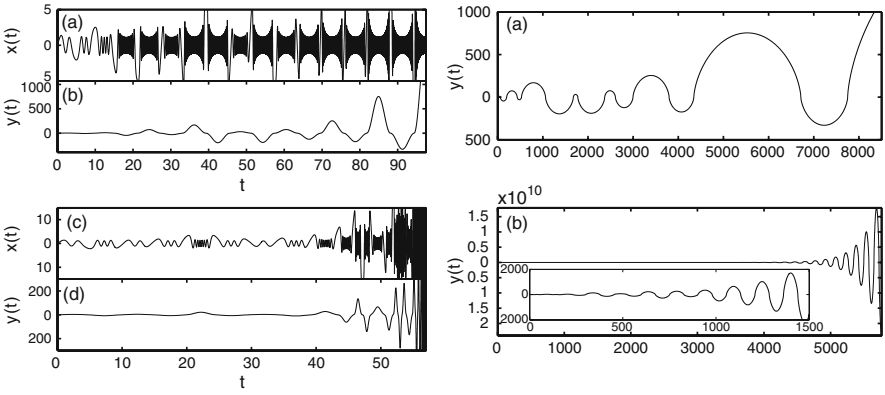

Fig. 4. Left: plots of $x(t)$ and $y(t)$ versus t for (a)–(b) $a = b = 0$ and (c)–(d) $a = b = 0.0015$. Right: plots of $y(\tau)$ versus τ for (a) $a = b = 0$ (the same case as left plot (b)) and (b) $a = b = 0.0015$ (the same case as left plot (d)). For all plots $\omega_y = \omega_x = 1$, $d = 1.9$, $c = 0.8$. The inset shows details of the early time behavior.

and $T_x(t)$ is the period of the x-oscillator at time t. If $T_x(t)$ is a slowly varying function and does not change significantly during one period of the x-oscillation, we can write $x = \bar{x}(t) + \Delta x(t)$, where Δx is assumed small and

$$\bar{x}(t) = X(t)\sin\left[\int^t \Omega_x(t)dt + \phi\right], \tag{11}$$

with $X(t)$ a slowly varying function. If we average (7) for $x(t)$ over one period, $T_x(t)$, we obtain an equation with a slowly varying frequency $\Omega_x(t)$,

$$\ddot{\bar{x}} + \Omega_x^2\bar{x} = 0, \qquad \Omega_x^2(t) = \omega_x^2 + \frac{a}{2}X^2(t) + c\bar{y}^2(t)\ . \tag{12}$$

In Fig. 3(b), we plot $x(t)$ versus t and $y(t)$ versus t for an interval of oscillations in Fig. 4(a). In the region where $y(t)$ is large enough to ensure the condition of adiabatic approximation, $|\dot{\Omega}_x| \ll \Omega_x^2$, the agreement is excellent.

Equation for $\bar{y}$ can be obtained by averaging the second equation in (7) over one period, $T_x(t)$, and has the following form

$$\ddot{\bar{y}} + \omega_y^2\bar{y} + b\bar{y}^3 - \frac{c}{2}X^2(t)\bar{y} = 0\ . \tag{13}$$

We can find $X^2(t)$ using conservation of an adiabatic invariant $\Omega_x(t)X^2(t)$ of the x-oscillator during the time interval T_y between successive non-adiabatic regions. Approximate conservation of the adiabatic invariant yields

$$X^2(t)\ \sqrt{\omega_x^2 + \frac{a}{2}X(t)^2 + c\bar{y}^2(t)} = X_{min}^2\sqrt{\omega_x^2 + \frac{a}{2}X_{min}^2 + cA^2}\ . \tag{14}$$

Here $y_{max} = A$ is a maximum value of the y-oscillator amplitude, and X_{min} is a minimum value of the x-oscillator amplitude within a particular time

interval T_y. The value X^2_{min} can be found from the equation $H = 0$ with the Hamiltonian (3) averaged over one period of oscillation T_x of the x-oscillator at the maximum of $y(t)$ where $\dot{y}(t) = 0$ and $X = X_{min}$. The result is

$$H = X^2_{min}\left(cA^2 + \frac{\omega_x^2}{2}\right) + \frac{3a}{16}X^4_{min} - \omega_y^2 A^2 - \frac{b}{2}A^4 = 0 \;\Rightarrow\; X^2_{min} = \frac{\omega_y^2}{c} + \frac{bA^2}{2c}. \tag{15}$$

Thus for $a = b = 0$ the minimum amplitude of the x-oscillator is always the same, but for $a \neq 0$ the minimum value X_{min} depends on the maximum amplitude A of the y-oscillator, as can be seen in Fig. 4(c).

For a finite $\omega_x^2 \ll c\bar{y}^2$ and small enough self-coupling a (14) yields

$$X(t) \approx X_{min}\sqrt{A/\bar{y}(t)}\,. \tag{16}$$

Thus, as the scale factor $\bar{y}(t)$ decreases away from its maximum value, the amplitude of the x-oscillations increases as in Figs. 3–4.

Dynamics of the adiabatic expansion is governed by the equation

$$\ddot{\bar{y}} + \omega_y^2\bar{y} + b\bar{y}^3 - \frac{c}{2}X^2_{min}A = 0 \quad \Rightarrow \quad T_y \sim \sqrt{\omega_y^2 + bA^2}\,, \tag{17}$$

that follows from (13). After each interval of adiabatic motion T_y, the system undergoes a relatively short interval of non-adiabatic motion (Big Crunch) where $y(t)$ approaches and crosses zero. During the nth non-adiabatic interval, the adiabatic approximation $|\dot{\Omega}_x| \ll \Omega_x^2$ is violated, and the x-oscillator acquires an additional phase shift $\Delta\phi_n$ so that its phase ϕ at the next, $(n+1)$-th interval of adiabatic motion becomes $\phi_{n+1} = \phi_n + \Delta\phi_n$. The amplitude of the y-oscillator is also changed from A_n to A_{n+1} that, for large enough A and small enough b, results in a very large change of the integral adiabatic phase shift $\int^t \Omega_x(t)dt \gg \pi$ at the $(n+1)$-th interval of adiabatic motion compared to the n-th interval. Since the result of the non-adiabatic transformation $A_n \to A_{n+1}$, $\phi_n \to \phi_{n+1}$ strongly depends on the phase with which the x-oscillator enters the non-adiabatic region, the system turns out to be very sensitive to any perturbations. The latter may explain qualitatively one of the possible mechanisms of the dynamical chaos in (2).

To study the non-adiabatic region more closely, it is convenient to introduce an amplitude y_a of the y-oscillator at which the condition of adiabaticity becomes broken, $|\dot{\Omega}_x| \simeq \Omega_x^2$, and rescale the amplitudes and time in the basic (7) as follows: $y \to y_a y$, $x \to y_a x$, and $t \to t/y_a$. The result is

$$\ddot{x} + (\omega_x/y_a)^2 x + ax^3 + cy^2 x = 0\,, \qquad \ddot{y} + (\omega_y/y_a)^2 y + by^3 - cx^2 y = 0\,. \tag{18}$$

In the limit $y_a \to \infty$ ($A \to \infty$) both partial frequencies become zero and initial conditions at the beginning of non-adiabatic region become $y = -\dot{y} = 1$ and $X = 1$. The only free parameter is the phase of the rapid x-oscillator, which eventually determines an increase (or decrease) of the maximum expansion, A, after the passage through the non-adiabatic region.

Harmonic Partial Oscillators

If the partial oscillators are harmonic (zero self-coupling nonlinearities, $a = b = 0$), $\bar{y}$ evolves as harmonic oscillator, (17), with a displaced point of equilibrium at the amplitude $y_0 = (c/2\omega_y^2)X_{min}^2 A$. The latter yields $A = 2y_0$, i.e., the point $\bar{y} = 0$ is a point of reflection. With increasing A some initial departure of Hamiltonian from zero becomes less important, so that asymptotically $H \to 0$ for the above asymptotical initial conditions.

The condition of adiabaticity means

$$|\dot{\Omega}_x|/\Omega_x^2 \ll 1 \qquad \Rightarrow \qquad \bar{y} \gg y_a = (\omega_y^2 A/c)^{1/3} \; . \tag{19}$$

At the beginning of the non-adiabatic region we have $X(y_a) = y_a$.

Depending on the entry phase, the ratio A_{n+1}/A_n varies from $(A_{n+1}/A_n)_{max} \simeq 2.15$ to $(A_{n+1}/A_n)_{min} = (A_{n+1}/A_n)_{max}^{-1}$ with the average value $\langle A_{n+1}/A_n \rangle \simeq 1.5$. Since small deviations in the amplitude of the slow y-oscillator lead to large changes in the phase increment of the rapid matter x-oscillator during its adiabatic evolution, the growth is chaotic. However, on a timescale much larger than $1/\omega_y$, the amplitude of the slow y-oscillator satisfies the equation of exponential growth,

$$\partial A/\partial t = \gamma A \; , \tag{20}$$

where the growth rate is equal to $\gamma \simeq [(\ln 1.5)/2\pi]\omega_y \simeq 0.07\omega_y$. A typical example of such behavior is shown in Fig. 3, where, in accord with the above theory, the scale factor y goes to zero exactly after each period, $\Delta t = 2\pi/\omega_y = 6.28$, of harmonic oscillations back to the point of reflection in (17) and the minimum amplitude of the rapid x-oscillator reaches the universal value, $X_{min} = \omega_y/c = 1.25$, at each maximum of y, independendly on the amplitude A of y. Moreover, the frequency of the rapid x-oscillator nicely matches the value $\Omega_x(t) = \sqrt{\omega_x^2 + c\bar{y}^2} = \sqrt{1 + 0.8\bar{y}^2}$ predicted by (12).

Effects of Self-Nonlinearity of Matter

Nonlinearity in the rapid x-oscillator becomes important when $\bar{y} < (a/c)^{1/3} y_a$. If $|a| < c$ it is important only in the non-adiabatic region. With growing amplitude of the slow oscillator, the contribution of nonlinearity to the phase increment during adiabatic evolution becomes less and less important, even if $|a| \gg c$. On the other hand, the nonlinearity changes the shape of effective potential for the slow y-oscillator near $\bar{y} = 0$. Close to $\bar{y} = 0$, the potential goes down for $a > 0$ and rises for $a < 0$.

Because of the different potential, the passage of $\bar{y} = 0$ point has different consequences. Dependence of A_{n+1}/A_n on the entry phase changes. In particular, the growth rate in (20) is considerably larger for negative a, and large ($a > c$) positive nonlinearity causes the adiabaticity to extend up to $\bar{y} = 0$. In response, the growth rate should become exponentially small.

Effects of Self-Nonlinearity of Gravity

In the presence of $b \neq 0$, independently on its sign, the slow y-oscillator almost always exhibits explosive growth. For $b < 0$ the partial y-oscillator is unstable. When it falls out of its potential well, its evolution is governed by

$$\dot{\bar{y}} = (\sqrt{|b|}/2)\bar{y}^2 \ . \tag{21}$$

If $\frac{1}{2}\sqrt{|b|/c} \ll 1$, the x-oscillator remains adiabatic and follows the slow one.

For $b > 0$ and in the limit $A \to \infty$, the time interval between subsequent passages of non-adiabatic regions is $T_y = 2\pi/\sqrt{b}A$, so that (20) becomes

$$\partial A/\partial t = \eta(\sqrt{b}/2\pi)A^2 \tag{22}$$

with some numerical pre-factor η. It also describes explosive instability (on average). In the case $b > 0$, one has $X_{min} = A\sqrt{b/2c}$ in the limit of large amplitude. The approximation of adiabaticity remains valid for $\bar{y} \gg y'_a = (b/2c)^{1/3}A$. The equality $X(y'_a) = y'_a$ as well as the condition for the importance of the nonlinearity, $\bar{y} < (a/c)^{1/3}y'_a$, remain unchanged.

3.5 Non-Adiabatic Phase Shift, Origin of Chaos, and Stochastic Explosion

Analysis of the non-adiabatic effects, chaos, and stochastic explosion can be done through a closer look at the ratio of amplitudes at subsequent y-oscillations, A_{n+1}/A_n, as a function of the non-adiabatic phase shift $\Delta\phi_n$.

This function can be calculated numerically as follows. Let us define "adiabatic" phase increment $\Delta\theta_{adiab} = \int_{t_1}^{t_2} \Omega_x(t)dt$ where t_1 and t_2 correspond to subsequent zeroes of $\bar{y}(t)$ in one variant or subsequent extrema of $\bar{y}(t)$ in another variant (see the end of this subsection). To calculate it we have to find Ω_x, (12). Hence, we need to know the relation between $X(t)$ and $\bar{y}(t)$, which can be found from (14), as well as $\bar{y}(t)$ itself that can be found from the equation

$$\ddot{\bar{y}} + \omega_y^2\bar{y} + b\bar{y}^3 = \frac{c\bar{y}}{2\Omega_x(t)}X_{min}^2\sqrt{\omega_x^2 + \frac{a}{2}X_{min}^2 + cA^2} \ . \tag{23}$$

The latter is a consequence of the (13) and (14) since $X^2(t)\Omega_x(t) = const$ is the adiabatic invariant along a given adiabatic loop. One has to substitute X_{min} from the equation $H = 0$ (see (16)).

In the numerical solution, one can determine the phase of the x-oscillator, $x(t) = X(t)\sin\theta(t)$, from the equation $\theta(t) = Arcsin(x(t)/X(t))$. This approximately corresponds to the equation $\sin\theta(t) = x(t)(\dot{x}^2(t)/\Omega_x^2(t) + x^2(t))^{-1/2}$. For $\Delta\theta_{numer} = \theta(t_2) - \theta(t_1)$, the phase shift of ϕ from one adiabatic loop to the next adiabatic loop is $\Delta\phi_n = \phi_{n+1} - \phi_n = \Delta\theta_{numer} - \Delta\theta_{adiab}$.

Another variant is to calculate phase increments (both adiabatic and numerical) between adjacent extrema of the slow y-oscillator. For the adiabatic phase it requires calculating A two times: separately for the rising and falling legs of $|\bar{y}|$-trajectory. Moreover, one needs to know the locations of extrema with precision much better than T_x. This can be done if one tries to find the best fit of the adiabatic solution as a function of parameter A to the actual solution. It is interesting to compare the results for both variants.

4 Cosmological Implications and Possible Solution to the Cosmological Constant Problem

The purpose of this section is to sketch how the dynamics of the models in (1) or (2) can be translated into cosmology. The model (2) describes an evolution of our Universe as a self-consistent process of mutual creation of the interacting gravity (spacetime metric) and matter fields from originally small quantum fluctuations. The model only describes a classical stage of the evolution when both fields have reached the macroscopic coherent values. The model (2) assumes that both fields are spatially homogeneous. Subsequent or simultaneous creation of all other spatial modes of the scalar and other matter fields, for example incoherent components of matter and radiation, could alter cosmological evolution, especially near singularities [10]. In particular, the process of reheating of the Universe due to decay and dissipation of the coherent inflaton scalar field into incoherent matter and radiation as well as the processes of spontaneous quantum creation of particles from a vacuum due to various non-adiabatic mechanisms in a non-stationary curved spacetime (e.g., like Hawking radiation near black holes) [4] could become important at some stage [5]. Obviously, all such effects should be treated on the basis of a full quantum field theory of the model (1) or of the more general models and are beyond the scope of the minisuperspace model (2).

The behavior of the model (2), so far, has only been studied in terms of the conformal time, t. In order to relate the predictions of the model with the observational cosmology, one has to use the well-known relations [4]

$$\tau = \int_0^t |\Omega(t)|dt = \sqrt{\frac{4\pi G}{3}} \int_0^t |y(t)|dt \tag{24}$$

between the conformal, t, and observable, τ, times. It is instructive to plot the conformal factor (the "radius" of the Universe) $y(\tau)$ versus τ rather than $y(t)$ versus t, see Fig. 4. For the case $a \neq 0$, while in the $y(t)$ versus t plot the y-oscillations with larger amplitude have shorter periods, in the $y(\tau)$ versus τ plot, these same y-oscillations have constant period.

The conformal field $\Omega(t)$, i.e. the y-oscillator $y = (3/4\pi G)^{1/2}\Omega$, plays the part of an overall scale factor in the Universe that stretches the observable

time τ with respect to the conformal time t. As a reference regime, let us consider a regime of the explosive evolution of the conformal factor,

$$\Omega(t) = \frac{1}{(t_\infty - t)h},\ t = \int_0^\tau \frac{d\tau}{|\Omega(\tau)|} = \frac{1 - e^{-h\tau}}{h\Omega_0} \to t_\infty = \frac{1}{h\Omega_0} \text{ at } \tau \to +\infty\ , \tag{25}$$

that ends in a singularity at a finite moment of the conformal time t_∞ ($y(t)\to\infty$ as $t\to t_\infty$) and corresponds to a standard de Sitter inflation

$$\Omega(\tau) = \Omega_0 \exp(h\tau), \qquad \Omega_0 = (ht_\infty)^{-1}\ , \tag{26}$$

over an infinite interval of the observable time with a constant Hubble parameter $h = \Omega^{-1}d\Omega/d\tau = \Omega^{-2}d\Omega/dt$. Therefore, if the model has solutions which are not stabilized dynamically at some finite level but appear to end in the singularities, these singular solutions can have a well-defined physical meaning in the Friedmann-Robertson-Walker representation and, in fact, are of great importance for they describe the observable cosmological inflation.

Such explosive solutions seem arise naturally in the present model (2). It is obvious when $b < 0$ and $a > 0$ since in this case the gravity y-oscillator is unstable by itself. For example, a pure explosive solution of the (21) yields the de Sitter inflation, (25) and (26), with the Hubble parameter $h = \sqrt{\Lambda/6}$. When $b > 0$ the explosive solutions take place due to the nonlinear interaction of the y-oscillator (gravity) with the x-oscillator (matter), even if the y-oscillator is partially stable, $b > 0$, i.e., the cosmological constant is negative, $\Lambda = -3\lambda_\phi/(16\pi G) < 0$. In this case the model exhibits a stochastic oscillatory explosion governed by (22), that corresponds to an averaged Hubble parameter $h = (\eta/\pi)\sqrt{\Lambda/6}$ with some numerical pre-factor η.

Recent observations reveal an existence of the so-called "dark energy" that constitutes about 73% of the critical mass density of the Universe, $\rho_c = 3h^2/8\pi G$, and obeys an equation of state provided by cosmological constant $\Lambda = 0.73(3h^2)$. In other words, the observed Hubble parameter is related to the cosmological constant, namely, $h_{observ} \simeq \sqrt{3}\sqrt{\Lambda/6}$, that is of the same order as the indicated above values $h \sim \sqrt{\Lambda/6}$ suggested by the simplified model (2). Thus, the field theory (1) has a potential to explain naturally inflation and simultaneously solve the cosmological constant problem.

The idea is to relate the cosmological constant to a running coupling constant of the unstable quantum field theory of interacting gravity and matter, $\Lambda = -3\lambda_\phi/16\pi G$. Together with the property of ultraviolet and infrared asymptotical freedom of the theory, this idea offers a natural explanation of the fact that cosmological constant is not zero and, at the same time, is very small (by a famous factor $\sim 10^{-120}$) compared to irrelevant vacuum energy.

The discussion above indicates that the unstable and explosive solutions are more interesting and closely related to the observational cosmology than the stable solutions. At the same time, the stable solutions which demonstrate chaotic bounded behavior are also interesting for they shed a light on how a

newly borning Universe is "hesitating" and searching for a way out of a small scale phase-space region around zero fixed point to inflationary large scales.

Other regimes relevant to the observations are possible in this system as well. Of course, for the actual explanation of the Universe evolution, along with the basic classical dynamics (2) of two oscillators the other essential properties of the original quantum field theory (1) have to be included in the analysis. Let us mention one of them which is relevant both to the problem of the cosmological constant and the acceleration of the Universe expansion.

According to the renormalization-group analysis [1, 2], the nonlinear coupling parameters λ, λ_ϕ, and λ_ψ, that is c, b, and a, are in fact the running coupling constants which are the functions of the energy scale of the process (in particular, of the momentum $\dot{y}$). This feature effectively modifies the nonlinearities of the coupled anharmonic oscillators (7). It is especially important in the regions where the self-coupling parameter $\lambda_\phi = -16\pi G\Lambda/3$ changes its sign around zero value, i.e., for relatively small cosmological constant Λ, and in the infrared and ultraviolet asymptotically free regions where all nonlinear couplings vanish. It would be interesting to check whether the original quantum field model (1), that is much more involved than the classical minisuperspace model (2), could explain a transition from a decelerating regime to an accelerating regime of the Universe expansion that, according to recent astronomical observations [13], occurs at a redshift $z \sim 0.5$. This transition means that the observable acceleration $d^2|\Omega|/d\tau^2$ after being positive at the de Sitter-like inflation, should become negative for a finite interval of time and then should change its sign to a positive value again at the latest times. An illustrative example shown in Fig. 4 is not of that complicated type since the second derivative $d^2|\Omega|/d\tau^2$ has the same sign on each interval of adiabatic motion that corresponds to the expansion of the Universe from zero size to some radius ($y = A$) with a deceleration and then contraction of the Universe again to the zero size (Big Crunch) with an acceleration. These and other effects in the original model (1), which were not included in the particular model (2), as well as a realistic cosmology based on the quantum field theory [1, 2] with the unbounded Hamiltonian will be discussed elsewhere.

5 Conclusions

The quantum field theory of interacting gravity and matter with an unbounded Hamiltonian, that takes into account a negative-energy contribution from the metric conformal factor, provides an elegant solution to the cosmological constant problem by an identification of the cosmological constant with a running coupling constant of the theory. Together with the remarkable property of the ultraviolet and infrared asymptotical freedom of this theory, this idea offers a natural explanation of the striking fact that the cosmological constant is not zero and, at the same time, is very small (by a well-known factor $\sim 10^{-120}$) compared to an irrelevant vacuum energy.

A nontrivial change of sign of the cosmological constant at some finite scale predicted by the renormalization-group equations and nontrivial dynamics of even very simplified cosmological model (2) clearly indicate that the actual dynamics of the Big Bang and cosmological expansion is more intriguing and rich than was assumed in most of the models used until recently for the interpretation of the astronomical observations in cosmology.

Acknowledgements

We are very grateful to Gursoy Akguc and Linda Reichel for the numerical analysis of the model (7) presented in [3]. We thank the grant 1744.2003.2 of the Council for Support of the Leading Scientific Schools of the Russian Federation. EVD thanks support from the Russian Science Support Foundation.

References

1. V.V. Kocharovsky and Vl.V. Kocharovsky: Found. of Physics **26**, 243 (1996)
2. V.V. Kocharovsky and Vl.V. Kocharovsky: Unstable quantum field theory solves the problem of quantum gravity (Invited lecture, Internat. School on Nonlinear Science, N. Novgorod, Sept. 1995). In: *Nonlinear Waves. Synchronization and Patterns*, part II, ed by M.I. Rabinovich, M.M. Sushchik, V.D. Shalfeev (Nizhny Novgorod Univ. Press 1995) pp 37–53
3. G.B. Akguc, L.E. Reichl, E.V. Derishev, V.V. Kocharovsky, and Vl. V. Kocharovsky: Phys. Rev. E **70**, 066210 (2004)
4. N.D. Birell and P.C.W. Davies: *Quantum Fields in Curved Space* (Cambridge Univ. Press, Cambridge London 1982)
5. E.Kolb and M.Turner: *The Early Universe* (Addison-Wesley, New York 1988)
6. E. Calzetta and C. El Hasi: Class. Quantum Grav. **10**, 1825 (1993)
7. E. Calzetta. In *Determenistic Chaos in General Relativity*, ed by A. Burd, A. Coley, and D. Hobill (Plenum, New York 1994)
8. S. Blanco et al.: Gen. Rel. Grav. **26**, 1131 (1994)
9. S. Blanco, A. Costa, and O. A. Rosso: Gen. Rel. Grav. **27**, 1295 (1995)
10. E. Calzetta and C. El Hasi: Phys. Rev. D **51**, 2713 (1995)
11. A. Helmi and H. Vucetich: Phys. Lett. A **230**, 153 (1997)
12. L.D. Landau and E.M. Lifshitz, *Mechanics (Course of Theoretical Physics, Vol. 1)* (Butterworth-Heinemann, Oxford 2000)

[13] A.G. Riess et al.: Astrophys. J. **607**, 665 (2004)

Precise Theory of Orbits in General Relativity, the Cosmological Constant and the Perihelion Precession of Mercury

G.V. Kraniotis

Texas A&M University, Physics Department, College Station TX 77843-4242, TAMU 4242, USA
kraniotis@physics.tamu.edu

Abstract. We first discuss the exact solution of the timelike geodesic and the perihelion precession in the Schwarzschild gravitational field without cosmological constant Λ. Results for the perihelion precession of Mercury and values of perihelion and aphelion are listed for different values of the invariant parameters. By use of Jacobi's inversion theorem the influence of the cosmological constant is taken into account and the modified results are presented for different values of Λ.

1 Geodesics and Perihelion Advance of Mercury

Mercury is the inner most of the four terrestrial planets in the Solar system, moving with high velocity in the Sun's gravitational field. Only comets and asteroids approach the Sun closer at perihelion. This is why Mercury offers unique possibilities for testing General Relativity [1] and exploring the limits of alternative theories of gravitation with an interesting accuracy [5].

As seen from the Earth the precession of Mercury's orbit is measured to be 5599.7 seconds of arc per century [3]. As observed, in 1859 by Urbain Jean-Joseph Leverrier there is a deviation of Mercury's orbit from Newtonian's predictions that could not be due to the presence of other planets.

Perihelion precessions of Mercury and other bodies have been the subject of experimental study from AD 1765 up to the present. In 1882 Simon Newcomb obtained the value 43 seconds per century for the discrepancy for Mercury [4]. According to Pireaux et al [5], the observed advance of the perihelion of Mercury that is unexplained by Newtonian planetary perturbations or solar oblatness is[1]

$$\begin{aligned}\Delta_{\omega_{obs}} &= 42.980 \pm 0.002 \text{ arc} - \text{seconds per century} \\ &= \frac{2\pi(3.31636 \pm 0.00015) \times 10^{-5}\text{radians}}{415.2019\text{revolutions}} \\ &= 2\pi(7.98734 \pm 0.00037) \times 10^{-8}\text{radians/revolution} \end{aligned} \quad (1)$$

[1]The observations seem to exclude Brans-Dicke theory with $\omega \sim 5$ whose post-Newtonian contribution to the perihelion shift would thus have been 39 arc-seconds per century 1) [3, 5].

In this talk I am going to describe my recent work in which the *first precise* calculation of the orbit and the perihelion precession of Mercury in General Relativity including cosmological constant contributions was performed [2]. The calculation was based on the exact solution of the time-like geodesics that describe motion of a test-particle in Schwarzschild-(anti) de Sitter spacetime. We also compare the result with observations (1). We assume that the motion of Mercury is a time-like geodesic in a Schwarzschild space-time surrounding the Sun.

In [8] a direct connection between general exact solutions of general relativity with a cosmological constant in large-scale cosmology and the theory of modular forms and elliptic curves was established.

Einstein's equations with the cosmological constant Λ are as follows

$$R_{\mu\nu} - \frac{1}{2} g_{\mu\nu} R = (8\pi G/c^4) T_{\mu\nu} + \Lambda g_{\mu\nu} \tag{2}$$

where $R_{\mu\nu}, R$ denotes the Ricci tensor and scalar respectively. Also G denotes Newton's gravitational constant and c the velocity of light. For vanishing stress-energy momentum tensor $T_{\mu\nu}$ the field equations reduce to

$$R_{\mu\nu} = \Lambda g_{\mu\nu} \tag{3}$$

The motion of a planet according to General Relativity is a time-like geodesic in a Schwarzschild space-time [12] surrounding the Sun. The Schwarzschild solution for the metric taking into account the cosmological constant (see e.g., [24]) is

$$\begin{aligned} ds^2 = c^2 \left(1 - \frac{2GM_\odot}{c^2 r} + \frac{1}{3}\Lambda r^2\right) dt^2 - \left(1 - \frac{2GM_\odot}{c^2 r} + \frac{1}{3}\Lambda r^2\right)^{-1} dr^2 \\ - r^2 (d\theta^2 + \sin^2\theta d\phi^2) \end{aligned} \tag{4}$$

where $M_\odot$ denotes the mass of the Sun. For zero cosmological constant (4) reduces to the original Schwarzschild metric element [12]. We note at this point, that by taking the time-like geodesic equation as a starting point for the subsequent calculus represents an approximation to the real situation: it is strictly true for point-like bodies with negligible mass. However, since $m_M \ll M_\odot$ where m_M denotes the mass of Mercury the approximation is adequate for all practical purposes.

The geodesic equation has the general form:

$$\frac{d^2 x^\mu}{ds^2} + \Gamma^\mu_{\alpha\beta} \frac{dx^\alpha}{ds} \frac{dx^\beta}{ds} = 0 \tag{5}$$

In Schwarzschild spacetime the orbit remains in the same plane. We choose that plane to be the equatorial plane $\theta = \pi/2$.

Furthermore, we can ignore (5) with $\mu = 1$ in favour of (4), which is a first integral of the geodesic equations. The resulting equations can be written as

$$1 = g_{\mu\nu}\frac{dx^\mu}{ds}\frac{dx^\nu}{ds} = c^2\left(1 - \frac{2GM_\odot}{c^2 r} + \frac{1}{3}\Lambda r^2\right)\left(\frac{dt}{ds}\right)^2$$
$$- \left(1 - \frac{2GM_\odot}{c^2 r} + \frac{1}{3}\Lambda r^2\right)^{-1}\left(\frac{dr}{ds}\right)^2 - r^2\left(\frac{d\phi}{ds}\right)^2 \quad (6)$$

$$\frac{d^2\phi}{ds^2} + \frac{2}{r}\frac{dr}{ds}\frac{d\phi}{ds} = 0 \quad (7)$$

$$\frac{d^2 t}{ds^2} + \frac{2\left(\frac{GM_\odot}{c^2} + \frac{1}{3}\Lambda r^3\right)}{r\left(r - 2\frac{GM_\odot}{c^2} + \frac{1}{3}\Lambda r^3\right)}\frac{dr}{ds}\frac{dt}{ds} = 0 \quad (8)$$

Next, define $v := dt/ds$ and $w := d\phi/ds$. Then (7),(8) can be written as

$$\frac{dw}{dr} + \frac{2}{r}w = 0, \quad \frac{dv}{dr} + \left[-\frac{1}{r} + \frac{1 + \Lambda r^2}{r - 2\frac{GM_\odot}{c^2} + \frac{1}{3}\Lambda r^3}\right]v = 0 \quad (9)$$

which can be integrated to yield [24]

$$w = d\phi/ds = \frac{L}{r^2}, \quad v = \frac{dt}{ds} = \frac{\mathcal{E}}{1 - \frac{2GM_\odot}{c^2 r} + \frac{1}{3}\Lambda r^2} \quad (10)$$

where $L, \mathcal{E}$ are arbitrary constants. Substituting in (6) we get the following equation after defininining a new variable $u := r^{-1}$

$$\left(\frac{du}{d\phi}\right)^2 = \frac{2GM_\odot}{c^2}u^3 - u^2 + \frac{2GM_\odot}{c^2 L^2}u - \frac{1}{3}\left(\frac{1}{u^2 L^2} + 1\right)\Lambda + \left(\frac{E'^2 - 1}{L^2}\right) \quad (11)$$

First we will solve (11) with a zero Cosmological Constant, the non-zero, more general case, will be considered in the following section. Making the following definitions,

$$\alpha_S := \frac{2GM_\odot}{c^2}, \ \beta := \frac{2GM_\odot}{c^2 L^2}, \gamma := -\frac{1 - E'^2}{L^2} \quad (12)$$

our geodesic equation reduces to:

$$\left(\frac{du}{d\phi}\right)^2 = \alpha_S u^3 - u^2 + \frac{\alpha_S}{L^2}u + \gamma \quad (13)$$

Differentiating (13) with respect to ϕ and comparing with the Newtonian term we get $cL = L_M$, where L_M is the angular momentum per unit mass of the planet [2]. Equation (13) is a cubic equation which can be reduced to the Weierstraß form using the substitution:

$$u = \frac{4}{\alpha_S}U + \frac{1}{3\alpha_S} \quad (14)$$

Then the Weierstraß representation of the geodesic equation becomes[2]

$$\left(\frac{dU}{d\phi}\right)^2 = 4\,U^3 + \left\{-\frac{1}{12} + \frac{1}{4L^2}\alpha_S^2\right\} U - \frac{1}{216} + \frac{\alpha_S^2}{48L^2} + \frac{\alpha_S^2}{16}\gamma \tag{15}$$

where the Weierstraß cubic invariants are given by:

$$g_2 = \frac{1}{12} - \frac{1}{4}\mathcal{L}c^2,\;\; g_3 = \frac{1}{216} - \frac{1}{48}\mathcal{L}c^2 - \frac{1}{16}\mathcal{L}(E^2 - c^2) \tag{16}$$

where $\mathcal{L} := \frac{\alpha_S^2}{L_M^2}$ and $E = cE'$. Then the solution of (15) is given by:

$$U = \wp(\phi + \epsilon) \tag{17}$$

and ϵ is a constant of integration. The solution in terms of the original variables is given by:

$$r = \frac{\alpha_S}{4\wp(\phi + \epsilon) + \frac{1}{3}} \tag{18}$$

For the calculation of the perihelion precesion and the orbital characteristics of Mercury we use the following values for the physical constants:

$$c = 299\;792\;458 \text{ m s}^{-1}\;\;,\;\alpha_S = 2.953\;250\;08 \text{ Km} \tag{19}$$

The data is taken from [6] and [7], respectively. The value of the speed of light in vacuum, given in (19), is exact, since a metre is the length of the path travelled by light in vacuum during a time interval of 1/299 792 458 of a second [6]. As free parameters we may use $\mathcal{L}$ and E. Then $L_M^2 = c^2L^2 = \frac{1}{\mathcal{L}}\alpha_S^2$[3]. Our free parameters are mixed through the Weierstraß invariants g_2, g_3 with exact numbers.

We find that the physically acceptable solutions that reproduce the orbital data of Mercury correspond to the case where $\Delta > 0$, $e_3 \to -\frac{1}{12}, e_2 \to -\frac{1}{12}$ and $e_1 \to 1/6$. The analytic expressions for the roots of the elliptic curve and other special orbit cases are given in appendix B in [2]. The Weierstraß function, $\wp(z)$, is an even meromorphic elliptic function of periods $2\omega, 2\omega'$ (i.e., $\wp(z + 2\omega) = \wp(z) = \wp(z + 2\omega')$, for all complex numbers z). The two half-periods ω and ω' are given by the following Abelian integrals (for $\Delta > 0$) [23]:

[2]The differential equation that the Weierstraß function satisfies is the equation of an elliptic curve and is given by : $(\wp'(z))^2 = 4\wp(z)^3 - g_2\wp(z) - g_3$, $\wp'(z) = \frac{\partial\wp(z)}{\partial z}$, see [8] for further details. The inversion of the elliptic integral $\int^U \frac{dU}{\sqrt{4U^3 - g_2U - g_3}} = \phi$, by the Weierstraß function, i.e. $U = \wp(\phi + \epsilon)$, is a simple case of the problem of inversion for elliptic integrals.

[3]The integration constant L has dimensions of length and thus scales with α_S.

$$\omega = \int_{e_1}^{\infty} \frac{dt}{\sqrt{4t^3 - g_2 t - g_3}}, \quad \omega' = i \int_{-\infty}^{e_3} \frac{dt}{\sqrt{-4t^3 + g_2 t + g_3}} \tag{20}$$

The value of the Weierstraß function at the half-periods are the three roots of the cubic. For positive discriminant Δ one half-period is real while the second is imaginary. The exact expression for the precesion of the perihelion of planet Mercury, is given by

$$\Delta_{\omega}^{\mathrm{GTR}} = 2(\omega - \pi) \tag{21}$$

which is proportional to the deviation of the real half-period ω of the Weierstraß modular form of weight 2, from the transcendental number π.

An alternative expression for the real half-period in terms of a hypergeometric function is given by

$$\omega = \frac{1}{\sqrt{e_1 - e_3}} \frac{\pi}{2} F\left(\frac{1}{2}, \frac{1}{2}, 1, \frac{e_2 - e_3}{e_1 - e_3}\right) \tag{22}$$

where $F(\alpha, \beta, \gamma, x) = 1 + \frac{\alpha.\beta}{1.\gamma} x + \frac{\alpha(\alpha+1)\beta(\beta+1)}{1.2.\gamma(\gamma+1)} x^2 + \cdots$

The exact expressions for the minimum distance of planet Mercury from the Sun (*Perihelion*) and its maximum distance (*Aphelion*) are given by[4]:

$$r_P \equiv r_{Perihelion} = \frac{\alpha_s}{4e_2 + \frac{1}{3}}, \quad r_A \equiv r_{Aphelion} = \frac{\alpha_s}{4e_3 + \frac{1}{3}} \tag{23}$$

We also note the following. Although by construction the roots of the cubic are calculated with arbitrary precision, our output for the perihelion and aphelion distances can only be displayed with nine significant figures given the nine digit accuracy of the Schwarzschild length α_S. However, their ratio which is given by:

$$\frac{r_P}{r_A} = \frac{4e_3 + 1/3}{4e_2 + 1/3} \tag{24}$$

constitutes a genuine and precise prediction[5]. Thus the theory predicts essentially the eccentricity of the orbit with an arbitrary precision. For a given choice of values for the free parameters, (21)–(24) are the output of the *precise theory* assuming zero cosmological constant, for the corresponding physical quantities, that should be tested against observations. For a particular choice of the invariant parameters $\mathcal{L}, E$ the corresponding predictions of the theory are displayed in Tables 1 and 2.

[4]We organize the roots as: $e_1 > e_2 > e_3$.

[5]In Newtonian theory the orbit of a planet is described by an ellipse with eccentricity e and semi-major axis a. For an ellipse, the perihelion (r_P^N) and aphelion (r_A^N) distances, are $a(1-e), a(1+e)$, respectively, and then $e = \frac{1 - r_P^N / r_A^N}{1 + r_P^N / r_A^N}$.

Table 1. Predictions for $\Delta_{\omega}^{\rm GTR}, r_P, r_A$ for the indicated choice for $\mathcal{L}, E$. The two half-periods are: $\omega = 3.14159290452929, \omega' = 20.409059\ i$ and the period ratio $\tau = 6.496i$. Also $L_M^2 = 7.36010550 \times 10^{38}$ cm^4 s^{-2}.

Parameters	**Roots**	**Predicted Results**
$\mathcal{L} =$	0.16666664004116	$\Delta_{\omega}^{\rm GTR} = 42.9817 \frac{\rm arcs}{\rm century}$
$1.1849947026647969\times$	-0.083333317282230892	$r_P = 4.59976206 \times 10^{12}$cm
$\times 10^{-28}$ cm^{-2} s^2		
$E =$	-0.083333322758930472	$r_A = 6.98207293 \times 10^{12}$cm
$0.029979245417779875\times$		
$\times 10^{12}$ cm s^{-1}		

Table 2. Predictions for $\Delta_{\omega}^{\rm GTR}, r_P, r_A$ for the indicated choice for $\mathcal{L}, E$. The two half-periods are: $\omega = 3.141592904522524, \omega' = 20.409391\ i$ and the period ratio $\tau = 6.4965i$. Also $L_M^2 = 7.36030420 \times 10^{38}$ cm^4 s^{-2}.

Parameters	**Roots**	**Predicted Results**
$\mathcal{L} =$	0.16666664004188	$\Delta_{\omega}^{\rm GTR} = 42.9805 \frac{\rm arcs}{\rm century}$
$1.1849627128268641\times$	-0.08333331728350096	$r_P = 4.60012605 \times 10^{12}$cm
$\times 10^{-28}$ cm^{-2} s^2		$r_P = 4.60012605 \times 10^{12}$cm
$E =$	-0.08333332275837917	$r_A = 6.98170894 \times 10^{12}$cm
$0.029979245417779875\times$		
$\times 10^{12}$ cm s^{-1}		

2 Precise Calculation of the Perihelion Advance with the Contribution of the Cosmological Constant

Including the cosmological constant effect we need to calculate the integral:

$$\int^{u} \frac{u\, du}{\sqrt{\frac{2GM_{\odot}}{c^2}u^5 - u^4 + \frac{2GM_{\odot}}{c^2L^2}u^3 - \frac{1-E'^2}{L^2}u^2 - \frac{\Lambda}{3L^2} - \frac{\Lambda}{3}u^2}} = \phi \tag{25}$$

Equation (25) defines[6] a *hyperelliptic integral* whose inversion involves genus 2, four-periodic Abelian-Siegelsche modular functions. The problem of inversion (whose solution was culminated in the Jacobisches Umkehrtheorem) of hyperelliptic integrals were first investigated by Abel [13], Jacobi, Göpel and Rosenhain [14], [15], [16]. The explicit solution of Jacobi's inversion problem in terms of higher genus theta functions was provided by Göpel and Rosenhain for the case $n = 5$ or 6, and the general solution for the hyperelliptic case (i.e. $\forall\ n\ \geq 5$) was provided by Weierstraß [17]. Riemann

[6] When all roots of the quintic are distinct.

introduced the idea of a Riemann surface to study algebraic singularities. He also introduced the Riemann theta function which served as a useful tool for solving the Jacobi's inversion problem [18].

2.1 Abel's Theorem, Jacobi's Inversion Problem and the Λ Effect

Let the genus g Riemann hyperelliptic surface be described by the equation:

$$y^2 = 4(x-a_1)\cdots(x-a_g)(x-c)(x-c_1)\cdots(x-c_g) \tag{26}$$

For $g=2$ the above hyperelliptic Riemann algebraic equation reduces to:

$$y^2 = 4(x-a_1)(x-a_2)(x-c)(x-c_1)(x-c_2) \tag{27}$$

where a_1, a_2, c, c_1, c_2 denote the finite branch points of the surface.

The Jacobi's inversion problem involves finding the solutions, for x_i in terms of u_i, for the following system of equations of Abelian integrals [19]:

$$\begin{aligned} u_1^{x_1,a_1} + \cdots + u_1^{x_g,a_g} &\equiv u_1 \\ \vdots + \cdots + \vdots \qquad &\quad \vdots \\ u_g^{x_1,a_1} + \cdots + u_g^{x_g,a_g} &\equiv u_g \end{aligned} \tag{28}$$

where $u_1^{x,\mu} = \int_\mu^x \frac{dx}{y}, u_2^{x,\mu} = \int_\mu^x \frac{xdx}{y}, \cdots, u_g^{x,\mu} = \int_\mu^x \frac{x^{g-1}dx}{y}$.

For $g=2$ the above system of equations takes the form:

$$\begin{aligned} \int_{a_1}^{x_1} \frac{dx}{y} + \int_{a_2}^{x_2} \frac{dx}{y} &\equiv u_1 \\ \int_{a_1}^{x_1} \frac{x\,dx}{y} + \int_{a_2}^{x_2} \frac{x\,dx}{y} &\equiv u_2 \end{aligned} \tag{29}$$

where u_1, u_2 are arbitrary. The solution is given by the five equations [19]

$$\frac{\theta^2(u|u^{b,a})}{\theta^2(u)} = A(b-x_1)(b-x_2) = \pm\frac{(b-x_1)(b-x_2)}{\sqrt{e^{\pi i PP'} f'(b)}}\ ; \tag{30}$$

where $f(x) = (x-a_1)(x-a_2)(x-c)(x-c_1)(x-c_2)$, and $e^{\pi i PP'} = \pm 1$ according as $u^{b,a}$ is an odd or even half-period. Also b denotes a finite branch point and the branch place a being at infinity [19]. The symbol $\theta(u|u^{b,a})$ denotes a genus 2 theta function with characteristics: $\theta(u;q,q')$ [19], where $u, = (u_1, u_2)$, denotes two independent variables, see appendix A in [2] for the definition of genus-2 theta functions that solve Jacobi's inversion problem. From any 2 of these equations, (30), the upper integration bounds x_1, x_2 of the system of differential equations (29) can be expressed as single valued functions of the arbitrary arguments u_1, u_2. For instance,

$$x_1 = a_1 + \frac{1}{A_1(x_2 - a_1)} \frac{\theta^2(u|u^{a_1,a})}{\theta^2(u)} \tag{31}$$

and

$$x_2 = -\frac{\left[(a_2-a_1)(a_2+a_1) + \frac{1}{A_1}\frac{\theta^2(u|u^{a_1,a})}{\theta^2(u)} - \frac{1}{A_2}\frac{\theta^2(u|u^{a_2,a})}{\theta^2(u)}\right]}{2(a_1-a_2)} \pm \frac{\sqrt{\left[(a_2-a_1)(a_2+a_1) + \frac{1}{A_1}\frac{\theta^2(u|u^{a_1,a})}{\theta^2(u)} - \frac{1}{A_2}\frac{\theta^2(u|u^{a_2,a})}{\theta^2(u)}\right]^2 - 4(a_1-a_2)\eta}}{2(a_1-a_2)} \tag{32}$$

where

$$\eta := a_2\, a_1(a_1-a_2) - \frac{a_2}{A_1}\frac{\theta^2(u|u^{a_1,a})}{\theta^2(u)} + \frac{a_1}{A_2}\frac{\theta^2(u|u^{a_2,a})}{\theta^2(u)} \tag{33}$$

Also, $A_i = \pm\frac{1}{\sqrt{e^{\pi i P P'} f'(a_i)}}$.

The solution can be reexpressed in terms of generalized Weierstraß functions:

$$x_k^{(1,2)} = \frac{\wp_{2,2}(u) \pm \sqrt{\wp_{2,2}^2(u) + 4\wp_{2,1}(u)}}{2}, \quad k = 1, 2 \tag{34}$$

where

$$\wp_{2,2}(u) = \frac{(a_1-a_2)(a_2+a_1) - \frac{1}{A_1}\frac{\theta^2(u|u^{a_1,a})}{\theta^2(u)} + \frac{1}{A_2}\frac{\theta^2(u|u^{a_2,a})}{\theta^2(u)}}{a_1-a_2} \tag{35}$$

and

$$\wp_{2,1}(u) = \frac{-a_1a_2(a_1-a_2) - \frac{a_1}{A_2}\frac{\theta^2(u|u^{a_2,a})}{\theta^2(u)} + \frac{a_2}{A_1}\frac{\theta^2(u|u^{a_1,a})}{\theta^2(u)}}{a_1-a_2} \tag{36}$$

Explicit expressions for the orbit in terms of genus-2 theta functions are exhibited in [2]. In the presence of the cosmological term there are five branch points for the hyperelliptic surface, (27), which are obtained by solving the quintic polynomial that appears in the time-like geodesics, (25).

For negative Λ all the roots are real. For positive Λ and depending on its magnitude and the values of the parameters $\mathcal{L}, E$ three roots are real and two complex conjugates. For some particular values all the roots are real.

When all roots are real we arrange them in *ascending* order of magnitude and denote them by $e_{2g}, e_{2g-1}, \cdots, e_0$, $g = 2$, so that e_{2i}, e_{2i-1}, are respectively c_{g-i+1}, a_{g-i+1} and e_0 is c. We then define linearly independent Abelian integrals of the first kind [19], denoted by $U_i^{x,a}$, $i = 1, \cdots g$, whose periods we want to calculate. These integrals are such that $dU_r^{x,a}/dx = \psi_r/y$, where ψ_r is an integral polynomial in x, of degree $g-1 = 1$ at most, with only real coefficients. Then the half-periods, $U_r^{e_4,e_3}$ and $U_r^{e_2,e_1}$, are *real*, while the half-periods $U_r^{e_3,e_2}$ and $U_r^{e_1,e_0}$ are purely *imaginary* [19]. For clarity, by

$U_2^{e_4,e_3}$ we denote $\int_{e_3}^{e_4} \frac{xdx}{y}$, $U_1^{e_4,e_3}$ denotes $\int_{e_3}^{e_4} \frac{dx}{y}$ and similarly for the rest of the periods.

An alternative expression for the genus-2 hyperelliptic integral for the real half-period that determines the perihelion precession can be given in terms of generalised hypergeometric functions of three-variables. This can be achieved by bringing the hyperelliptic integrals of the 1^{st} kind into Richelot's form [20]

$$\int \frac{dx}{\sqrt{x(1-x)(1-\kappa^2 x)(1-\lambda^2 x)(1-\mu^2 x)}} \tag{37}$$

then the periods satisfy a system of differential equations of the hypergeometric series [9]

$$F_1(\alpha,\beta,\beta',\beta'',\gamma,x,y,z) = \sum_{abc} \frac{(\alpha,a+b+c)(\beta,a)(\beta',b)(\beta'',c)}{(\gamma,a+b+c)(1,a)(1,b)(1,c)} x^a y^b z^c \tag{38}$$

when the following identification takes place $x=\kappa^2,\ y=\lambda^2,\ z=\mu^2$ and the constants of the series take certain arithmetical values[7]. The moduli κ,λ,μ can be expressed in terms of the five distinct roots of the quintic polynomial.

For $\Lambda = -10^{-42}\text{cm}^{-2}, \mathcal{L} = 1.1848820116975453 \times 10^{-28}\ \text{cm}^{-2}\ s^2, E = 0.0299792454178 \times 10^{12}\text{cm s}^{-1}$ the roots have been calculated in [2] which give $\omega = U_2^{e_1,e_2} = 3.14159290255$ and thus there is a substantial effect on the perihelion advance due to the cosmological constant with $\Delta_\omega^{\text{GTR}} = 42.6427 \frac{\text{arcs}}{\text{century}}$ in conflict with observations (1).

For $\Lambda = 10^{-42}\text{cm}^{-2}, \mathcal{L} = 1.1848820116975453 \times 10^{-28}\ \text{cm}^{-2}\ \text{s}^2, E = 0.0299792454178 \times 10^{12}\text{cm s}^{-1}$ $\Delta_\omega^{\text{GTR}} = 42.8689 \frac{\text{arcs}}{\text{century}}$ in conflict with observations, while for the same set of values of $\mathcal{L}, E$ and $\Lambda = 0$ the corresponding prediction was $\Delta_\omega^{\text{GTR}} = 42.9776 \frac{\text{arcs}}{\text{century}}$[2].

For the values for $\mathcal{L}, E$ chosen in table 2, and for $\Lambda = 10^{-56}\text{cm}^{-2}$, $\int_{e_2}^{e_1} \frac{udu}{y} = 3.141592904524534$ and $\Delta_\omega^{\text{GTR}} = 42.9809 \frac{\text{arcs}}{\text{century}}$ [2]. For comparison we note that in this case and for $\Lambda = 0$, $\Delta_\omega^{\text{GTR}} = 42.9805 \frac{\text{arcs}}{\text{century}}$ and $\Delta_{\omega_{obs}} = 42.980 \pm 0.002\ \frac{\text{arcs}}{\text{century}}$.

It is evident that in more accurate future experiments of the orbit of Mercury, such as ESA's mission BepiColombo [10], one can measure the Λ effect. The need to compare with other relativistic effects like the rotation of the Sun and the associated Lense-Thirring effect [11], led the author to investigate the geodesic motion for the Kerr and Kerr-(anti) de Sitter spacetimes [22]. The Kerr rotation adds longitudinal dragging to the precession discussed in this talk. The exact solution of the more complicated set of differential geodesics equations in this case was again given by modular functions. The geodesic equations were derived by integrating the Hamilton-Jacobi equation with separation of variables (completely integrable system). The application of these

[7] For m a positive integral number $(\alpha, m) = \alpha(\alpha+1)\cdots(\alpha+m-1), (\alpha,0) = 1$. The periods have also been regarded as functions of one variable, Fuchs [9].

exact solutions for the determination of the Lense-Thirring effect due to the rotation of the Sun on the perihelion precession of Mercury will be a subject of a future publication.

Acknowledgments

The author is grateful to Prof. R. Arnowitt and Prof. H.V. Klapdor-Kleingrothaus for inviting him to deliver this talk and for creating such a stimulating conference.

References

1. A. Einstein, *Sitzungsberichte der Preussischen Akademie der Wissenschaften*,(1915) 831.
2. G. V. Kraniotis, S. B. Whitehouse *Compact calculation of the perihelion precession of Mercury in general relativity, the cosmological constant and Jacobi's inversion problem*, Classical and Quantum Gravity **20**, (2003) 4817-4835.
3. C. M. Will, *Theory and experiment in gravitational physics* Cambridge University Press, Revised edition, (1993)
4. S. Newcomb, em Tables of Mercury. Astr. Pap.Am. Ephem., 6, part 2, Washington (1895-1898).
5. S. Pireaux, J.-P. Rozelot, [arXiv:astro-ph/0109032], Astrophys.Space Sci. 284 (2003) 1159-1194.
6. B. W. Petley, Nature **303**, 373 (1983)
7. E. D. Groom *et al*, Eur.Phys.J.C.15 1, K. Hagiwara *et al* Phys.Rev.D 66 (2002) 010001.
8. G. V. Kraniotis and S. B. Whitehouse, *General relativity, the cosmological constant and modular forms*, Class. Quantum Grav.**19** (2002)5073-5100, [arXiv:gr-qc/0105022]
9. J Horn, Math.Ann. **34** (1889), 544-600; L. Fuchs Crelle's Journal. f. Math. **71** (1870) 91-127.
10. ESA science missions see http://sci.esa.int/home/bepicolombo/
11. J. Lense, H. Thirring, Phys.Zeitsch.**19**, (1918) 156
12. K. Schwarzschild, Sitzungsberichte der Königlichen Preussischen Akademie der Wissenschaften (Berlin) 1916,189-196
13. N. H. Abel, *Remarques sur quelques propriétés générales d'une certaine sorte de fonctions transcendantes* Crelle's Journal f. Math. **3** (1828) 313-323.
14. C. G. J. Jacobi, Crelle's Journal.f. Math. **9** (1832)394, Crelle's Journal.f. Math. **13** (1835)55; C. G. J. Jacobi, *Ueber die vierfach periodischen Functionen zweier variablen* Ostwald's klassiker der exakten Wissenschaften, Nr.64, Wilhelm Engelmann in Leipzig (1834)1-41.
15. A. Göpel, *Entwurf einer Theorie der Abel'schen Transcendenten erster Ordnung* Crelle's Journal.f. Math. **35** (1847) 277-312.
16. G. Rosenhain, Crelle's Journal.f. Math. **40** (1850)319
17. K. Weierstraß, *Zur Theorie der Abelschen Functionen*, Crelle's Journal.f. Math.**47** (1854)289

18. B. Riemann, *Theorie der Abelschen Functionen*, Crelle's Journal.f. Math.**54** (1857)115
19. H. F. Baker *Abelian functions: Abel's Theorem and the allied theory of theta functions* Cambridge University Press , 1995 edition.
20. F. Richelot, Crelle's Journal f. Math **12** (1834) 181
21. S. Perlmutter et al. Astrophys.J. 517(1999),565; A.V. Filippenko et al, Astron.J. 116(1998)1009
22. G. V. Kraniotis, *Precise relativistic orbits in Kerr and Kerr-(anti) de Sitter spacetimes*, Class. Quantum Grav.**21** (2004) 4743-4769
23. A Treatise on the Analytical Dynamics of Particles & Rigid Bodies, E. Whittaker, Cambridge University Press, 1947
24. H. Ohanian & R. Ruffini, Gravitation & Spacetime, Norton and Company, New York, 1994.

Dark Matter and Pulsar Kicks from a Singlet Neutrino

Alexander Kusenko

University of California, Los Angeles, CA 90095-1547
kusenko@ucla.edu

Summary. A singlet neutrino with mass in the 2–20 keV range is a viable candidate for dark matter. If such a particle exists, it would be emitted from a supernova with an appreciable anisotropy due neutrino oscillations in a medium polarized by a strong magnetic field. An asymmetric emission of singlet neutrinos could explain the observed velocities of pulsars. Future X-ray telescopes may be able to detect a 1–10 keV photon line from the decays of the relic sterile neutrinos. In addition, one may be able to detect gravity waves from a pulsar being accelerated by neutrinos in the event of a nearby supernova.

Astronomical observations lead to a conclusion that there exists at least one new particle, which makes up the dark matter. The most economical solution (although not necessarily the best motivated one, from a theoretical point of view) is to add just one fermion, a singlet neutrino,with the mass ane the mixing angle consistent with dark matter [1]. It turns out that, if this particle exists, its emission from a supernova could be anisotropic [2, 3]. This anisotropy can explain the observed pulsar velocities.

The space velocities of pulsars are measured either by observation of their angular proper motions [4], or by measuring the velocity of an interstellar scintillation pattern as it sweeps across the Earth [5, 6]. Based on the data and population models, the average velocity estimates range from 250 km/s to 500 km/s [4, 7]. The distribution of velocities is non-gaussian, and there is a substantial population of pulsars with velocities in excess of 700 km/s. Some 15% of pulsars [7] appear to have velocities greater than 1000 km/s, while the fastest pulsars have speeds as high as 1600 km/s. Obviously, an acceptable mechanism for the pulsar kicks must be able to explain these very fast moving pulsars.

Pulsars are born in supernova explosions, so it would be natural to look for an explanation in the dynamics of the supernova [8]. However, state-of-the-art 3-dimensional numerical calculations [9] show that even the most extreme asymmetric explosions do not produce pulsar velocities greater than 200 km/s. Earlier 2-dimensional calculations [10] claimed a somewhat higher maximal pulsar velocity, up to 500 km/s. Of course, even that was way too small to explain the population of pulsars with speeds (1000–1600) km/s. Recent three-dimensional calculations by Fryer [9] show an even stronger

discrepancy than the earlier numerical calculations of the supernova. The hydrodynamic kick could be stronger if some large initial asymmetries developed in the cores of supernova progenitor stars prior to their collapse. Goldreich et al. [11] have suggested that unstable g-modes trapped in the iron core by the convective burning layers and excited by the ϵ-mechanism may provide the requisite asymmetries. However, according to recent numerical calculations, [12] the ϵ-mechanism may not have enough time to significantly amplify the g-modes prior to the collapse. A different kind of the seed anisotropies may develop from the north-south asymmetry in the neutrino heating due to a strong magnetic field [13]. If these asymmetries grow sufficiently during the later phases of the supernova, they may be relevant for the pulsar kicks. Evolution of close binaries [14] and asymmetric emission of radio waves [15] have been considered as possible causes of the rapid pulsar motions. However, both of these explanations fail to produce a large enough effect.

Most of the supernova energy, as much as 99% of the total 10^{53} erg are emitted in neutrinos. A few per cent anisotropy in the distribution of these neutrinos would be sufficient to explain the pulsar kicks. Alternatively, one needs (and, one is apparently lacking) a much larger asymmetry in what remains after the neutrinos are subtracted from the energy balance. Can the emission of neutrinos be anisotropic?

Neutrino production and scattering are both affected by the polarization of fermions in matter, which, in turn, is determined by the magnetic field. However, as was shown by Vilenkin et al. [18], in (approximate) thermal and chemical equilibrium these asymmetries do not result in a pulsar kick. However, if a singlet neutrino is produces through mixing with ordinary neutrinos, its production is out-of-equilibrium. Therefore, this anisotropy can explain the pulsar kick velocities. It is intriguing that the allowed range of parameters overlaps with that for dark matter. Oscillations of active neutrinos could work as well if the took place at such a density at which one of the species (ν_e) is trapped, while some other species (ν_μ or ν_τ) is free-streaming [26]. This, however, would require too large a mass for one of the active neutrino species, $\sim 10^2$ eV.

Let us consider a sterile neutrino that has a small mixing with electron neutrino:

$$|\nu_1\rangle = \cos\theta_m\,|\nu_e\rangle - \sin\theta_m\,|\nu_s\rangle \tag{1}$$

$$|\nu_2\rangle = \sin\theta_m\,|\nu_e\rangle + \cos\theta_m\,|\nu_s\rangle. \tag{2}$$

To be the dark matter and to give a kick to pulsars, sterile neutrino should have mass in the 2–20 keV range, and they should also have a small mixing ($\sin\theta\ \sim 10^{-4}$) with ordinary neutrinos, for example, the electron neutrino. Theoretical models of neutrino masses can readily produce a sterile neutrino with the required mass and mixing [16, 17].

Sterile neutrinos are produced through oscillations of active neutrinos. The relation between their mass and the abundance is very different from

what one usually obtains in freeze-out. One can trace the production of sterile neutrinos in plasma by solving the Boltzmann equation for the distribution function $f(p,t)$:

$$\left(\frac{\partial}{\partial t} - Hp\frac{\partial}{\partial p}\right) f_s(p,t) \equiv xH\partial_x f_s = \tag{3}$$

$$\Gamma_{(\nu_a \to \nu_s)} \left(f_a(p,t) - f_s(p,t)\right) \ , \tag{4}$$

where H is the Hubble constant, $x = 1\,\mathrm{MeV}a(t)$, $a(t)$ is the scale factor, and Γ is the probability of conversion. The solution [1] of this equation in the relevant range of parameters gives the following expression for the cosmological density of relic sterile neutrinos:

$$\Omega_s \approx 0.3 \left(\frac{\sin^2\theta}{10^{-9}}\right) \left(\frac{m_s}{10\ \mathrm{keV}}\right)^2 \tag{5}$$

The band of the masses and mixing angles consistent with dark matter is shown in Fig. 1.

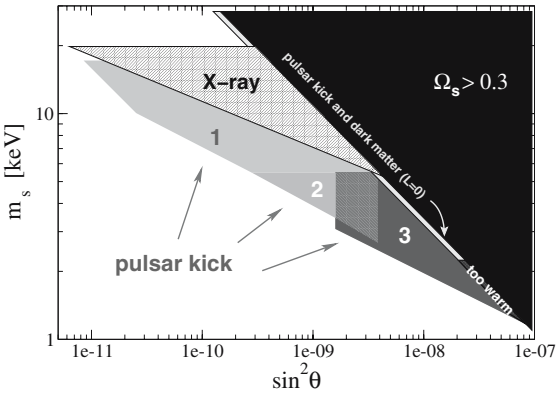

Fig. 1. The range of neutrino masses and mixing angles consistent with cosmological bounds on dark matter and with the required magnitude of the pulsar kick. The $L = 0$ band refers to the lepton asymmetry of the universe assumed small.

In the cooling neutron star, sterile neutrinos can be produced through oscillations of ordinary neutrinos in two regimes, on resonance and off resonance. Figure 1 shows the allowed range of parameters for the singlet neutrino to be dark matter and also to explain the pulsar kicks, based on the analysis of Fuller et al. [3]. In region 1, the Mikheev-Smirnov-Wolfenstein resonance deep in the core of the proto-neutron star can produce enough asymmetry for the pulsar kick. In region 2, the resonant oscillations take place outside the core, and the mechanism is somewhat different [24, 25]. Finally, in region

3, the emission of sterile neutrinos takes place deep in the core of the supernova through neutrino oscillations off resonance. A detailed discussion can be found in a recent review article [25].

There are two ways in which this mechanism can be tested. First, if the sterile neutrinos with requisite masses and mixing exist, a photon line from relic neutrino decay can be detected by X-ray telescopes [28]. The rate of the radiative decay is

$$\Gamma_\gamma \approx 6.8 \times 10^{-33}\,\mathrm{s}^{-1} \left(\frac{\sin^2 2\theta}{10^{-10}}\right) \left(\frac{m_s}{1\ \mathrm{keV}}\right)^5 . \tag{6}$$

Although $\tau = \Gamma^{-1} \sim 10^{25} - 10^{33}\,\mathrm{s}$ is much longer than the age of the universe, there are, nevertheless, enough decays in the clusters of galaxies for the photons to be observed [28]. Since $\nu_2 \to \nu_1\gamma$ is a two-body decay, the photon energy is equal $(m_s/2)$, which is in the 1–10 keV range for the masses of interest to us. These photons should be detectable by the X-ray telescopes. *Chandra* and *XMM-Newton* can exclude part of the parameter space [28] shows in Fig. 1 and labeled "X-rays". Future Constellation-X mission can probably explore the entire range of parameters.

In the event of a nearby supernova, LIGO and LISA may be able to see a characteristic signal from an asymmetric neutrino emission [29, 30].

In summary, a sterile neutrino with mass in the 2–20 keV range is a viable dark matter candidate. The emission of this particle form a supernova may be the explanation of the long-standing puzzle of pulsar velocities. Future observations of X-ray telescopes, as well as gravity wave detectors, may help confirm or rule out this explanation.

References

1. S. Dodelson and L. M. Widrow, Phys. Rev. Lett. **72**, 17 (1994); K. A. Olive and M. S. Turner, Phys. Rev. D **25**, 213 (1982); K. Abazajian, G. M. Fuller and M. Patel, Phys. Rev. D **64**, 023501 (2001); A. D. Dolgov and S. H. Hansen, Astropart. Phys. **16**, 339 (2002);
2. A. Kusenko and G. Segrè, Phys. Lett. B **396**, 197 (1997). [arXiv:hep-ph/9701311].
3. G. M. Fuller, A. Kusenko, I. Mocioiu, and S. Pascoli, Phys. Rev. D **68**, 103002 (2003).
4. A. G. Lyne, B. Anderson, and M. J. Salter, Mon. Not. R. Astron. Soc. **201**, 503 (1982); Bailes *et al.*, Astrophys. J. **343**, L53 (1989); Formalont et al., Mon. Not. R. Astron. Soc. **258**, 497 (1992); P. A. Harrison, A. G. Lyne, and B. Anderson, Mon. Not. R. Astron. Soc. **261** 113 (1993); A. G. Lyne and D. R. Lorimer, Nature 369 (1994) 127.
5. P. A. G. Scheuer, Nature **218**, 920 (1968); B. J. Rickett, Mon. Not. R. Astron. Soc. **150**, 67 (1970).

6. J. A. Galt and A. G. Lyne, Mon. Not. R. Astron. Soc. **158**, 281 (1972); Slee *et al*, *ibid.* **167**, 31 (1974); A. G. Lyne and F. G. Smith, Nature **298**, 825 (1982); J. M. Cordes, Astrophys. J. **311**, 183 (1986).
7. Z. Arzoumanian, D. F. Chernoff and J. M. Cordes, Astrophys. J. **568**, 289 (2002).
8. I. S. Shklovskii, Sov. Astr., **13**, 562 (1970) [Astr. Zh. **46**, 715 (1970)].
9. C. L. Fryer, Astrophys. J. **601**, L175 (2004) [arXiv:astro-ph/0312265].
10. A. Burrows and J. Hayes, Phys. Rev. Lett. **76**, 352 (1996); L. Scheck, T. Plewa, H. T. Janka, K. Kifonidis and E. Mueller, Phys. Rev. Lett. **92**, 011103 (2004).
11. P. Goldreich, D. Lai, and M. Sahrling, in *Unsolved Problems in Astrophysics*, ed. J. N. Bahcall and J. P. Ostriker, Princeton Univ. Press, Princeton, 1996.
12. J. Murphy, A. Burrows, and A. Heger, astro-ph/0406521.
13. K. Kotake, S. Yamada, and K. Sato, astro-ph/0409244.
14. J. R. Gott, J. E. Gunn and J. P. Ostriker, Astrophys. J. Lett. **160**, L91 (1970).
15. E. R. Harrison and E. P. Tademaru, Astrophys. J. **201**, 447 (1975).
16. Y. Farzan, O. L. G. Peres and A. Y. Smirnov, Nucl. Phys. B **612**, 59 (2001).
17. K. S. Babu and G. Seidl, Phys. Lett. B **591**, 127 (2004) [arXiv:hep-ph/0312285]. arXiv:hep-ph/0405197.
18. A. Vilenkin, Astrophys. J. **451**, 700 (1995); A. Kusenko, G. Segrè, and A. Vilenkin, Phys. Lett. B 437, 359 (1998);
19. X. d. Shi and G. M. Fuller, Phys. Rev. Lett. **82**, 2832 (1999) [arXiv:astro-ph/9810076].
20. J. F. Nieves and P. B. Pal, Phys. Rev. **D40** 1693 (1989); J. C. D'Olivo, J. F. Nieves and P. B. Pal, *ibid.*, 3679 (1989); S. Esposito and G. Capone, Z. Phys. **C70** (1996) 55; J. C. D'Olivo, J. F. Nieves and P. B. Pal, Phys. Rev. Lett., **64**, 1088 (1990); H. Nunokawa, V. B. Semikoz, A. Yu. Smirnov, and J. W. F. Valle, Nucl. Phys. **B 501**, 17 (1997); J. F. Nieves, Phys. Rev. D **68**, 113003 (2003); J. F. Nieves, arXiv:hep-ph/0403121.
21. M. B. Voloshin, Phys. Lett. B **209**, 360 (1988); G. Lambiase, arXiv:astro-ph/0411242.
22. A. Kusenko and G. Segrè, Phys. Rev. **D59**, 061302 (1999).
23. M. Barkovich, J. C. D'Olivo, R. Montemayor and J. F. Zanella, Phys. Rev. D **66**, 123005 (2002).
24. M. Barkovich, J. C. D'Olivo and R. Montemayor, Phys. Rev. D **70**, 043005 (2004) [arXiv:hep-ph/0402259].
25. A. Kusenko, arXiv:astro-ph/0409521.
26. A. Kusenko and G. Segrè, Phys. Rev. Lett. **77**, 4872 (1996). [arXiv:hep-ph/9606428].
27. E.Kh. Akhmedov, A. Lanza and D.W. Sciama, Phys. Rev. D **56**, 6117 (1997); D. Grasso, H. Nunokawa, and J.W.F. Valle, Phys. Rev. Lett. **81**, 2412 (1998); R. Horvat, Mod. Phys. Lett. A **13**, 2379 (1998); M. Barkovich, H. Casini, J. C. D'Olivo and R. Montemayor, Phys. Lett. B **506**, 20 (2001); D. V. Ahluwalia-Khalilova and D. Grumiller, in preparation.
28. K. Abazajian, G. M. Fuller and W. H. Tucker, Astrophys. J. **562**, 593 (2001)
29. L. C. Loveridge, Phys. Rev. D **69**, 024008 (2004) [arXiv:astro-ph/0309362].
30. H. J. Mosquera Cuesta, Astrophys. J. **544**, L61 (2000); Phys. Rev. D **65**, 061503 (2002); H. J. Mosquera Cuesta and K. Fiuza, arXiv:astro-ph/0403529.

Dealing with Dark Energy

Eric V. Linder

Berkeley Lab, 1 Cyclotron Rd., Berkeley, CA 94720, USA
evlinder@lbl.gov

Discoveries in the last few years have revolutionized our knowledge of the universe and our ideas of its ultimate fate. Measurements of the expansion of the universe show that it is not slowing down under normal gravity but accelerating due to an unknown, gravitationally repulsive "dark energy". This may be a clue to new properties of quantum physics or of gravity beyond Einstein. I present an overview of the puzzles of dark energy and the means for unraveling them through cosmological probes, on both a generally accessible and a technical level. I also highlight the strong benefits of meshing supernova distance and weak lensing methods. Next generation experiments such as the Supernova/Acceleration Probe (SNAP) satellite would measure the supernova distance-redshift relation to high accuracy and map the evolution of structure and dark matter through gravitational lensing. These observations will explore the frontiers of physics and aim to uncover what makes up the still unknown 95% of our universe.

1 Introduction

Discovery of the acceleration of the expansion of the universe has prompted great excitement in physics, and energized speculation about the dark energy responsible. Such physics acts contrary to the ordinarily attractive nature of gravity. It is unknown whether the answer to this extraordinary puzzle lies within modifications of gravitation or new elements of high energy physics such as a quantum vacuum.

New, high precision experiments are being developed to reveal the nature of dark energy. In this next generation, the use of simple, well understood physical probes will be crucial to reduce the systematic uncertainties in the observations due to astrophysical effects. Complementary probes will also be essential to increase the rigor of the results: to provide crosschecks, synergy leading to tighter constraints, and improved accuracy. Ideally these complementary methods would also be capable of separating a gravitational origin of dark energy from a high energy physics origin.

In Sect. 2 we discuss the basic issues regarding our current understanding of and future characterization of dark energy. Section 3 investigates the requirements for substantial progress with the next generation of experiments,

emphasizing systematics control and complementarity. In the conclusion, we summarize the possible techniques for probing the nature of dark energy and indicate the fundamental need for complementary measurements to explore the physics frontiers. Note that Sect. 2 is written at a level to make the discussion accessible to the general physicist; experts may wish to concentrate on Sect. 3 which examines more technical issues on how to reveal the physics.

2 Dark Energy – New Paradigm/New Paradox

Cosmology and fundamental physics have grown ever closer over the past few decades, with dark energy now firmly linking them together. Astrophysical observations, including Type Ia supernovae distance-redshift relations, cosmic microwave background measurements, and large scale structure properties, give clues to the expansion history of the universe: the growth in distance scales over time, $a(t)$. Within the cosmological dynamics this translates into the energy densities and physical properties of the components of the universe. These can be described in terms of present day energy densities relative to the critical density, e.g. the matter density Ω_m and the dark energy density Ω_w, and the equations of state, or pressure to energy density ratios, $w(a)$. Finally, we hope to relate these to fundamental physics, such as the potential of a high energy scalar field, $V(\phi)$.

The paradigm is to link the observational data with the underlying physics, the astrophysical with the fundamental. The new aspect is that this appears to be much more direct and of vastly greater import than before – that the current (and ultimate future) state of the expansion of the universe is intimately tied to fundamental, new physics. Acceleration of the universe is giving us tangible clues to new gravitation, new quantum physics, or even the union of the two. Illustratively we can write

$$V(\phi(a(t)))\ , \tag{1}$$

to denote the interdependence of the astrophysics measuring the expansion history, the cosmology depending on the microphysical properties of the components, and the field theory describing the fundamental physics.

The flow can, and should, go both ways. Theories of high energy physics and extended gravitation can be predictive; the implications of a specific model can be calculated and compared to the data. As well, high precision measurements of subtle variations in the expansion behavior can guide researchers toward classes of theories. A happy medium exists in a model independent parametrization of the physics, such as the key quantity of the equation of state function of the dark energy, $w(a)$.

We then proceed forward in our exploration of the universe in a manner analogous to uncovering, say, global warming of the Earth. The subtle slowing and growth of scales with time – precisely $a(t)$ – map out the cosmic environment history like the lesser and greater growth of tree rings map

out the Earth's climate history. Whether it was a cold year, a wet year – the width of the tree ring growth – tells us the climate environment just as the growth of distances between cosmological markers tells us the expansion history. The search, for decades, in astronomy was to find suitable markers covering a substantial part of the universe's 14 billion year history.

The efforts finally came to fruition in 1998 when two groups [1, 2] independently announced evidence for mapping the expansion history using Type Ia supernovae (SN Ia) as markers. These exploding stars are highly suitable for such work because they can be as bright as their entire host galaxy, and so are able to be observed at great distances and hence lookback times into the past. Crucially, they can be calibrated to about 7% in distance [3, 4] and so provide precise measurements. Furthermore, the supernova light comes from simple, clean nuclear physics and has a direct translation to the expansion history $a(t)$: with the luminosity calibrated, the flux measures the distance through the cosmological inverse square law, and hence the lookback time t, and the redshift $z = a^{-1} - 1$ measures the scale factor.

However, rather than deriving the details of the matter properties of the universe through the deceleration of the expansion under gravitational attraction, both groups found an *acceleration*. Some force was acting in a way contrary to attractive gravity. This was clearly an astonishing discovery and led to the new paradox: when is gravity not attractive?

In general relativity the gravitating mass depends on the energy-momentum tensor, not just the rest mass. For a perfect fluid, both the energy density ρ and the pressure p enter – as a specific combination $\rho + 3p$. So a component with a sufficiently negative pressure can provide an effective negative gravitating mass, and hence turn gravity into a repulsive force.

More quantitatively, consider the acceleration arising from Newton's law of gravitation,

$$\ddot{R} = -GM/R^2 = -(4\pi/3)\, G\rho R\ , \tag{2}$$

where we take a test particle a distance R from the center of a homogeneous mass M. For positive mass densities, the force is always attractive. But in Einstein gravity, the Friedmann equation of acceleration is

$$\ddot{a} = -(4\pi/3)\, G(\rho + 3p)\, a\ . \tag{3}$$

So as stated above, negative pressure can accelerate the expansion.

Since both the energy density and pressure appear in the equation, it is convenient to define their ratio, $w = p/\rho$, known as the equation of state ratio. Acceleration then occurs for $p < -(1/3)\rho$ or $w < -1/3$.

What is the physical meaning of a negative pressure? It is not as unusual as it might appear. Consider the first law of thermodynamics:

$$dU = -p\, dV\ , \tag{4}$$

where dU is the change in internal energy of a system upon expansion of the volume by dV. Expansion then decreases the energy (for positive p), as

(adiabatically) opening an oven door cools down the air inside, or breathing out through pursed lips gives a stream of cooler air than your internal temperature (contrast the feeling on your hand in front of your mouth when breathing with lips pursed vs. with mouth open).

Systems with negative pressure would have an overall positive sign for dU, increasing energy upon expansion. Everyday examples include springs, $dU = +kx\,dx$, and rubber bands, $dU = +T\,dl$, where dx, dl are displacements, k the spring constant, and T the tension. So what we need for the acceleration of the expansion of the universe is a sort of springiness of spacetime.

Quantum physics, as developed in the 1920's, predicts that the very structure of the vacuum should have properties like a simple harmonic oscillator: a spring. So the universe filled with a quantum vacuum energy will have a springiness, or tension, and measurements of the acceleration could be interpreted as direct observations of a vacuum energy with negative pressure.

To quickly review: gravity says that the acceleration of the expansion depends on energy density and pressure, $\rho + 3p$, thermodynamics says that pressure can negative, and quantum physics says that vacuum energy has such negative pressure. Cosmological "tree ring" markers can map the expansion history, measure the acceleration, and detect the vacuum energy. And they did.

The 1998 results have been strongly confirmed by further, more precise supernova observations, and by corroborating measurements of the cosmic microwave background (CMB) temperature anisotropies and of large scale structure (LSS) properties. SN Ia most directly probe the acceleration as such, saying that there is a nonzero vacuum energy and it is abundant enough to govern the expansion dynamics. CMB in combination with some large scale structure data (such as the Hubble constant, which gives the present expansion rate, or measurements of the matter density) indicates our cosmology is consistent with a spatially flat universe (total energy density equals the critical density) and one with a nonzero vacuum energy. Any two of the three data sets combine to imply that the vacuum energy, or more generically "dark energy", must account for $\sim 70 - 75\%$ of the energy density of the universe.

These are profound and exquisite experimental results. Dark energy dominates the energy of the universe, governing the expansion, accelerating it like inflation did in the first fraction of a second of cosmic history, and determining the fate of the universe. But what is it? We do not even know whether it belongs to the right hand side or left hand side of the Einstein equations, i.e. whether it is a new, physical component, arising from a high energy physics scalar field, say, or a change in the gravitational framework, an extension to general relativity due to extra dimensions, for example. Is it new quantum physics, new gravitational physics, or a sign of unification of the two?

A first attempt at a solution might be the cosmological constant, which is equally at home on the right and left hand sides. But it has two outstanding problems: the fine tuning and coincidence puzzles (for more details see, e.g.,

[5]). Thinking about the cosmological constant Λ as arising from the vacuum expectation value of a quantum zeropoint energy "sea", one can calculate that the sea level should drown the matter energy density (the "land") by a factor 10^{120} or so. Furthermore, the cosmological constant and matter energy densities evolve differently under expansion: a mere factor of 4 in expansion scale smaller (back in time) and dark energy would be undetectable, while a factor 4 larger and matter would be quite rare – we would not see a universe filled with clusters of galaxies. Dark energy cosmology is only possible today, where today means within a factor of 4 in expansion while the universe has expanded by a factor of about 10^{54} to date!

To attempt to overcome these difficulties, physicists consider dynamical models of dark energy. But guidance through the vast space of possible theories is required from observations precise enough to map the acceleration and discern subtle variations. The leading role in this endeavour is being played by SN Ia (other methods for the future are discussed in Sect. 3).

As mentioned at the beginning of this section, SN Ia have a high degree of robustness in their properties, enabling them to be calibrated to better than 10% accuracy. In a cartoon version of why nuclear physics provides a standard explosion, consider the scenario of a white dwarf star and a massive companion. The white dwarf accretes matter from the companion until it gets "full" enough, with full being related to the Chandrasekhar mass beyond which the electron degeneracy pressure can no longer support the white dwarf. Since degenerate stars have simple structures to begin with, and the explosions occur under near identical conditions, the class of SN Ia is remarkably homogeneous. The real situation is not quite so simple, but end to end computations show that a high degree of "stellar amnesia" – independence of initial conditions – occurs [6].

Moreover, each SN Ia does not merely provide a single data point, a single luminosity. They contain a rich array of information about their physical conditions in measurements of their lightcurve (flux vs. time evolution), energy spectrum, and images showing their galactic environment. Such a data set for each SN can provide robust control of systematic uncertainties [7].

Currently, of order 200 SN Ia have been analyzed, though few with the complete data characteristics just discussed at high quality. In combination with CMB and large scale structure data, they impose constraints on an *a priori* constant equation of state of $w_{\rm const} = -1.05^{+0.15}_{-0.20} \pm 0.09$ [8] or $w_{\rm const} = -1.08^{+0.18}_{-0.20}\pm?$ [9]. These appear roughly consistent with the cosmological constant value $w = -1$.

Ongoing projects to characterize many more SN include Essence (~ 200 at $0.15 < z < 0.75$ [10]), Nearby Supernova Factory (~ 300 at $0.03 < z < 0.08$ [11]), Canada-France-Hawaii Telescope Supernova Legacy Survey (~ 700 at $0.3 < z < 0.9$ [12]), Supernova Cosmology Project (~ 25 at $z > 0.8$ [13]), and Carnegie Supernova Project (optical and near infrared, and spectroscopic, follow up [14]). Additional ground based surveys are proposed. The

Supernova Cosmology Project and PANS groups are studying supernovae at high redshifts, $z > 1$, from space with the Hubble Space Telescope and may characterize $\sim 20 - 25$ such SN.

While these improvements should allow constraints on $w_{\rm const}$ without depending on combination with CMB and LSS data, they will not have the accuracy, precision, and reach to impose substantial limits on the dynamics at the heart of the physics responsible for the acceleration. Indeed, while one can use $w_{\rm const}$ to test for consistency with the cosmological constant, it is dangerous to interpret it more broadly, extrapolating to any conclusion that the dark energy *is* the cosmological constant. See [15] for examples of how assuming that $w = w_{\rm const}$ can deceive us about the true fundamental physics.

To correctly learn the new physics, we have to look for the generically expected time variation $w(z)$ – indeed essentially all models for dark energy other than the cosmological constant predict $w' = dw/d\ln a \neq 0$. Achieving robust measurements, with tight control of systematics over a long baseline of the expansion history of the universe, is a major challenge. In the next section we discuss how to address it.

3 Dark Energy – New Generation/New Physics

Data constraints in the plane of dimensionless matter density Ω_m vs. constant equation of state $w_{\rm const}$ that suggest a concordance cosmological model solution of, say, $\Omega_m = 0.3$ and cosmological constant $\Omega_\Lambda = 0.7$ could also be fit at the $\sim 1\%$ level in distance, out to redshift $z = 2$, by a very different cosmology: one containing $\Omega_m = 0.27$ with 0.73 of the critical density in a component with $w(a) = -0.8 - 0.6(1-a)$, exhibiting physics rather unlike the cosmological constant. This extreme example shows the necessity for probing the dynamics.

To have confidence in our results uncovering the new physics we need to design the next generation of experiments properly. They should possess three crucial properties:

- Longer lever arm – i.e. data covering to higher redshift, more cosmic history;
- Better statistics – many more measurements, more precisely;
- High accuracy – robust control of systematic uncertainties.

As we will discuss later, complementary methods of probing the dark energy are also critical. Together, these give the science requirements for a successful experiment.

Consider the SN Ia method. To see the most distant supernovae, space observations are required because the SN light is redshifted into the near infrared part of the spectrum, but the Earth's atmosphere is basically opaque there. Furthermore, correction of extinction – dimming due to dust – requires

a broad wavelength coverage, also pushing observations into the near infrared. Currently the only applicable space telescope is the Hubble Space Telescope (HST). HST has indeed found a few supernovae of order 10 billion years back in the cosmic expansion history (a factor 2.7 in scale factor, or $z = 1.7$). But these are exceedingly faint, about the same flux as the limit of the Hubble Deep Fields (which required commitment of a substantial part of the HST observing schedule). Yet a Hubble Deep Field has scanned (just sufficient to detect, not to characterize, SN) only 4×10^{-8} of the sky. In proportion, this is like meeting about 10 people and trying to understand the complexity of the entire US population.

A new, dedicated dark energy experiment is required. To address the science needs above, its catchphrase has to be "wide, deep, and colorful". This will 1) ensure sufficient numbers of SN for statistical and systematic analysis, 2) map a large fraction of cosmic history to pick up the subtle variations between dark energy theories, and 3) allow multiwavelength and spectral characterization of the sources to tightly control systematic uncertainties.

The Supernova/Acceleration Probe (SNAP: [16]) is a possible realization of this experiment, specifically designed to meet these criteria. The experiment will employ a two meter space telescope to obtain optical and near infrared, high accuracy observations, including spectra, of more than 2000 SN from $z = 0.1 - 1.7$ (over 70% of the age of the universe). The sky coverage will be 4 orders of magnitude greater than a Hubble Deep Field, and a wider survey aimed at using weak gravitational lensing (see later) as a partnering, complementary probe will cover 6 orders of magnitude more sky than a Hubble Deep Field, and almost as deep.

Systematics control will be a major challenge in this, as in any experiment utilizing any method. Supernovae, however, have a long history of use that has generated identification of the systematics and techniques for controlling them. We give an illustration of one approach here, but see [17, 18, 19] for specifics.

With sufficient, highly characterized supernovae, one can imagine sorting them into subsets based on their slight residual heterogeneity after calibration. Subsets might be defined based on host galaxy morphology, spectral feature strength and velocity, early time behavior, etc. – obviously requiring a comprehensive set of measurements, far beyond what a typical supernova in the current data has. Then one analyzes each subset, of supernovae occurring over the full redshift range, and derives the cosmological model. By comparison of the results from subset to subset – "like vs. like" – one can gain strong confidence that the results are free from significant systematics. Conversely, by analyzing supernovae at the same redshift *between* subsets, one can further develop systematics controls. While theories of the supernova progenitor and explosion mechanism can guide the establishment of subset criteria, such understanding is not required – only comprehensive measurements are – for robustness of the cosmological results.

Dark energy – the failure of attractive gravitation – is such a profound mystery, possibly such a clue to fundamental physics, that we should strive to probe it in as many useful, stringent ways as possible. While SN provide the most direct probe of cosmic acceleration, CMB and LSS measurements make contributions as well.

The CMB, except on very large scales, is basically a snapshot of the universe at 380,000 years old – only 0.003% its present age (when the reader was 0.003% of their present age, they were composed of merely two cells – independent of how old the reader is now!). So it is not surprising that the CMB, while fantastically precise and well understood, is not a strong probe of detailed dark energy properties, a more recent phenomenon. On large scales it can provide some rough clues, particularly in combination with full sky LSS surveys, but this is fundamentally limited by cosmic variance (there are few independent samples of large volumes, or, the sky only contains 4π steradians).

Nevertheless, it has excellent complementarity upon addition to SN data, as it breaks degeneracies between cosmological parameters [20]. Together, SN+CMB (exemplified by the SNAP SN and Planck CMB [21] experiments) can detect time variation of the dark energy equation of state, w', at the 99% confidence level (this assumes a specific model, SUGRA [22], with $w' = 0.3$; see [23] for further details and comparisons).

Large scale structure data can provide constraints on dark energy, both through breaking parameter degeneracies and through indirect measurement of the acceleration. In its most basic use, it enters not through data as such, but through a prior on, say, the matter density Ω_m. Of course this must trace back to data in some way, and often the dependence of the observations is not purely on the matter density, but also involves assumptions about the dark energy, e.g. that it is a cosmological constant. Such assumptions can sometimes be hidden quite deeply, but must be sought out for a robust cosmological analysis.

One improvement on the "prior" approach, more closely related to the data, is to employ constraints on the logarithmic growth factor, $f = d\ln\delta/d\ln a$, at some redshift, where δ is the fractional overdensity of a matter density perturbation. This is directly related to the peculiar velocity field of large scale structure. Such a prior was used for the cosmological constraint analysis the author did for [8]. An unpublished study by the author shows that this prior is roughly equivalent to an Ω_m prior. That is, ± 0.03 in Ω_m (11% uncertainty) has about the same effect as ± 0.035 in f (6% uncertainty). Note that due to its slight curvature in the Ω_m-w plane, its complementarity with SN is somewhat less than an Ω_m prior (though more realistic). Its tighter connection with data is a plus, however some doubt has been cast [24] on the intermediate step of removing the galaxy bias parameter from velocity surveys (see, for example, [25]).

Direct use of large scale structure measurements is obviously the preferred method. The most promising technique appears to be weak gravitational lensing. Since gravity bends light, we can detect mass (including that contributed by dark matter) in structures such as galaxies and clusters of galaxies through the gravitationally distorted images of distant sources – lensing. While this happens on rare instances very visibly through the production of multiple images or grossly distorted arcs (strong lensing), it occurs copiously as more subtle, percent level shearing of image shapes (weak lensing). This signal must be pulled out statistically from vast surveys of millions of resolved galaxies.

By studying the growth of massive structure over cosmic history, one can infer properties of the dark energy. While mass aggregates in an expanding universe, with gravitational attraction causing overdense regions to become more and more so, this growth shuts down in an accelerating universe. As an analogy, consider a person trying to join a group of friends standing at the bottom of a uprunning escalator. Due to the "stretching" of space between the groups, the attraction is overcome and clustering does not increase.

Weak lensing was first measured in 2000 and is rapidly developing as a cosmological probe, though it has not yet achieved the precision and accuracy to provide constraints on dark energy. Next generation experiments compiling hundreds of millions of galaxy shears over a wide area of sky with precise redshift measurements, for a three dimensional catalog, will be needed. Plans for such surveys include PanStarrs [26] and LSST [27] from the ground and SNAP from space. Ground observing can cover large areas quickly and partners well with space measurements. Space provides access to 1) a higher density of resolved images, useful for probing smaller scale structure where the growth effects are amplified by nonlinearities, 2) deeper lenses allowing mapping of the mass growth over more cosmic time, and 3) reduction of systematics such as atmospheric distortion of the shapes [28].

The combination of weak lensing and CMB data yields dark energy constraints roughly comparable to SN bounds. But the true synergy comes from bringing weak lensing and SN together. In this case complementarity is achieved on several levels. An experiment that incorporates both techniques is truly comprehensive in that no external priors are required: no outside determination of the matter density or CMB acoustic peak location is necessary. Furthermore, the two methods conjoined provide a test of the spatial curvature of the universe to $\sim 1-2\%$ (for the SNAP experiment), independent of the CMB constraint on flatness (note that the Planck CMB measurements in isolation would only determine the curvature to $\sim 6\%$ [29]). On dark energy properties, supernovae plus weak lensing methods conjoined determine the present equation of state ratio, w_0, to 5%, and its time variation, w', to 0.11 (for the SNAP experiment baseline mission, including an estimate of systematics, and in the relatively insensitive scenario of a true cosmological constant: see Fig. 1). Such an experiment can give a truly exciting view into the nature of new fundamental physics.

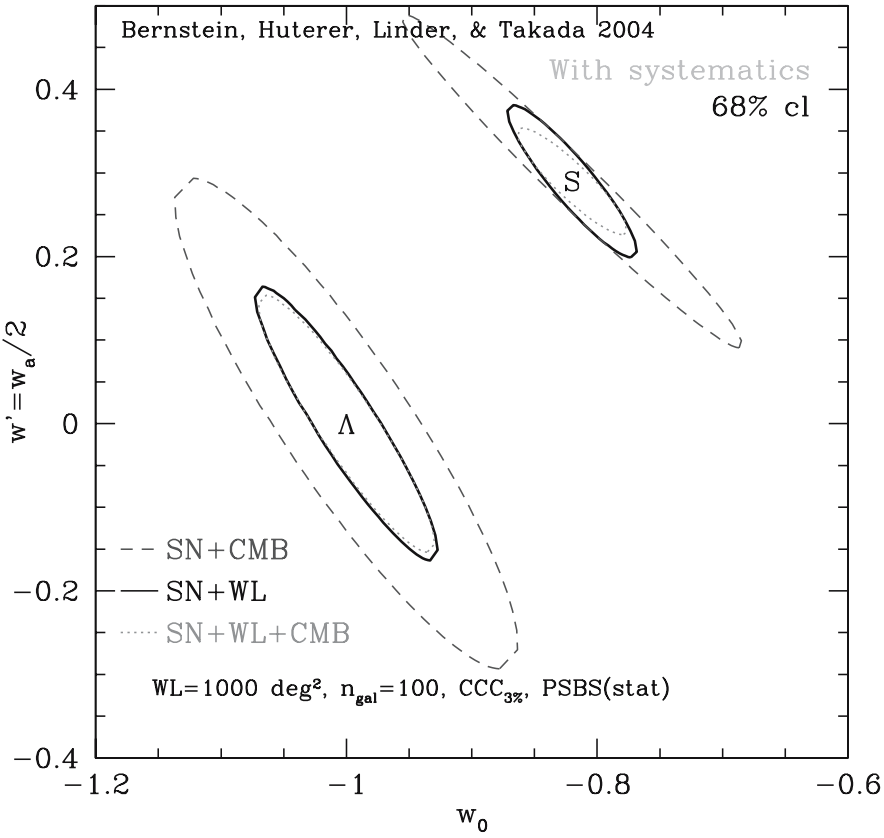

Fig. 1. Weak gravitational lensing and supernovae distances work superbly together as cosmological probes. To realize the tightest bounds requires systematics control only possible from space – point spread function resolution, stability, and low noise. Here we show constraints on two dark energy models from 2000 supernovae and a 1000 square degree weak lensing survey (employing power spectrum and bispectrum data and cross-correlation cosmography), both with systematics. No external priors are needed.

Other cosmological probes, not yet mature, may contribute to the next generation. These include angular distance-redshift tests through baryon acoustic oscillations in the matter power spectrum, growth of mass tests through cluster abundances identified by the Sunyaev-Zel'dovich effect or weak lensing, say, and possibly tests using some aspects of strong lensing or distances to another class of supernovae, Type IIs.

We must be cautious however about, first, identification, and then control of systematic uncertainties that might plague methods without a proven track record. The entanglement of astrophysical details with cosmology is another

area needing great care. One can roughly regard probes as falling into three categories of shedding light on dark energy:

- Geometric methods – a standard: like a lightbulb, where you don't need to know how the filament works, you can test it – e.g. supernovae Ia, weak lensing (crosscorrelation cosmography method), baryon oscillations, supernovae II
- Geometry+Mass methods – must understand aspects of the nonlinear mass distribution: like a flashlight, where you need to know about the lens and battery – e.g. weak lensing (shear), strong lensing
- Geometry+Mass+Gas methods – must understand aspects of hydrodynamics: like a candle, where you need to know about the wax, flame, wind – e.g. Sunyaev-Zel'dovich effect, cluster counts

4 Conclusion

The acceleration of the cosmic expansion poses a fundamental, and possibly revolutionary, challenge to physics. To probe the nature of the dark energy responsible for this behavior contrary to attractive gravity we need specially designed next generation experiments, as well as some clever theoretical ideas. We don't know whether the new physics lies within the structure of the quantum vacuum, extensions to general relativity, or a unification of high energy physics and gravitation in the form of extra dimensions or string theory.

Uncovering the dynamics of dark energy should guide us in development of new fundamental physics. To achieve this understanding requires robust, well understood cosmological probes, with greatest leverage coming from techniques working in complementarity. Our picture of the universe is one where only 5% is familiar energy components within the standard model of particle physics, 25% lies in possibly theorized dark matter, and 70% in wholly unknown dark energy. The universe is mysteriously unsimple.

When you have a mystery ailment, you want a doctor with not just a stethoscope as a tool to give a diagnosis; you want blood tests, EKG, MRI to give confidence in the results. Our universe is out of sorts, and we should seek similar complementarity to achieve fundamental understanding.

Complementary probes give (1) crosschecks, to test the results, (2) synergy, improved constraints from breaking degeneracies to reveal more of the physics, (3) robustness, through reduced influence of systematics from one approach. Currently, in maturity and application, Type Ia supernovae and weak lensing give the greatest hope of understanding dark energy. Moreover, an experiment combining the two possesses the virtues of comprehensiveness, independence from external priors, and the ability to test the framework. By mapping both the expansion history and growth history, such an experiment can distinguish between a high energy physics origin for the acceleration (e.g.

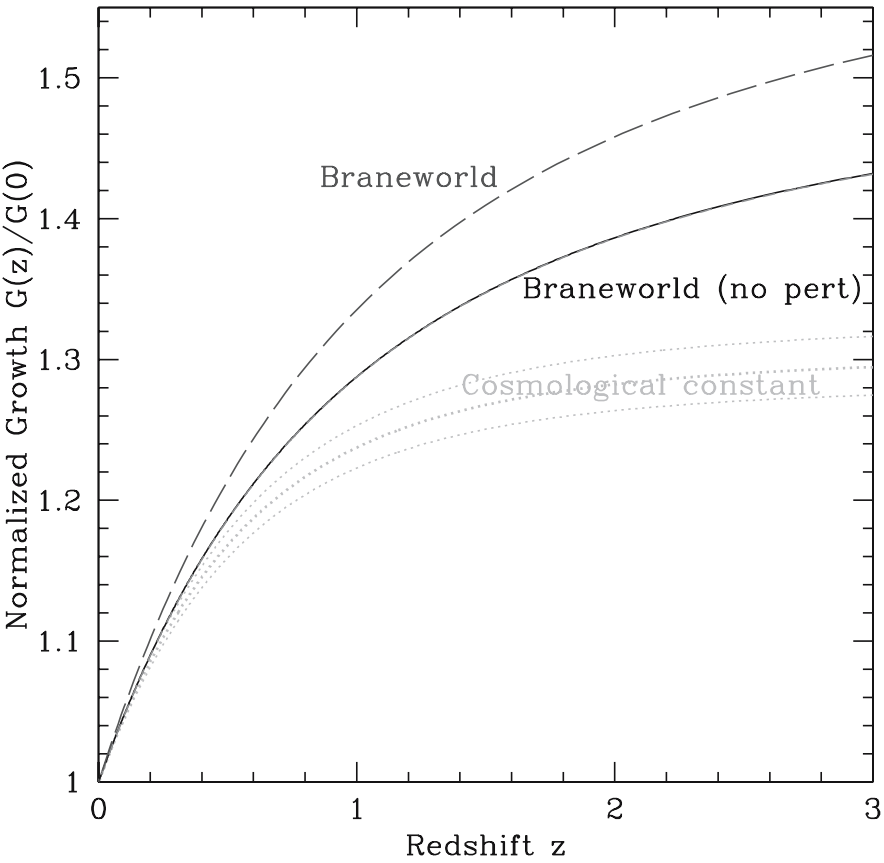

Fig. 2. The expansion history and the mass fluctuation growth history can probe different elements of the physics responsible for the acceleration of the universe. Individually they offer leverage in constraining parameters of dark energy or gravitational models, and in complementarity they can distinguish between the different physical origins. An extra dimensional braneworld model (solid, black curve) and a quintessence model with $w_0 = -0.78$, $w_a = 0.32$ (dashed, red) appear indistinguishable, but when one takes into account the effects of altered gravity on the growth history (long dashed, blue curve) this allows distinction of these models. The expansion history in turn could rule out the quintessence model degenerate with the long dashed curve. In all cases, the cosmological constant curves (dotted magenta, with outliers indicating the effect of varying Ω_m by ± 0.02) are distinct.

a scalar field) and new gravitational physics (see, e.g., Fig. 2). A space mission surveying the universe wide, deep, and colorful will naturally encompass further probes as well, and provide a bonanza for astrophysics, cosmology, and fundamental physics.

Acknowledgments

I thank Texas A&M University for unceasing hospitality throughout the DARK2004 conference. This work was supported in part by the Director, Office of Science, Department of Energy under grant DE-AC03-76SF00098.

References

1. S. Perlmutter, et al.: Ap. J. 517, 565 (1999)
2. A. Riess, et al.: Astron. J. 116, 1009 (1998)
3. M.M. Phillips: Ap. J. Lett. 413, L105 (1993)
4. L. Wang, G. Goldhaber, G. Aldering, S. Perlmutter: Ap. J. 590, 944 (2003) [astro-ph/0302341]
5. S.M. Carroll, Living Rev. Rel. 4, 1 (2001) [astro-ph/0004075]
6. P. Höflich, C. Gerardy, E. Linder, and H. Marion, in Lecture Notes in Physics, *Stellar Candles*, eds. Gieren et al.; astro-ph/0301334
7. S. Perlmutter & B.P. Schmidt, in Supernovae and Gamma Ray Bursts, ed. by K. Weiler, Lecture Notes in Physics 598, 195–217 (2003) [astro-ph/0303428]
8. R.A. Knop et al., Ap. J. 598, 102 (2003) [astro-ph/0309368]
9. A.G. Riess et al., Ap. J. 607, 665 (2004) [astro-ph/0402512]
10. Essence: http://www.ctio.noao.edu/∼wsne
11. Nearby Supernova Factory: http://snfactory.lbl.gov
12. Supernova Legacy Survey: http://cfht.hawaii.edu/SNLS
13. Supernova Cosmology Project: http://supernova.lbl.gov
14. W.L. Freedman et al.: in Observing Dark Energy, eds. S. Wolff & T. Lauer (2004) [astro-ph/0411176]
15. E.V. Linder: Phys. Rev. D 70, 061302 (2004) [astro-ph/0406189]
16. SNAP: http://snap.lbl.gov
17. G. Aldering et al.: (2004) [astro-ph/0405232]
18. D. Branch, S. Perlmutter, E. Baron, P. Nugent: in Research Book on Dark Energy, ed. E.V. Linder (2001) [astro-ph/0109070]
19. S. Perlmutter: Physics Today 56, 53 (2003)
20. J.A. Frieman, D. Huterer, E.V. Linder, and M.S. Turner, Phys. Rev. D 67, 083505 (2003) [astro-ph/0208100]
21. Planck: http://astro.estec.esa.nl/planck
22. P. Brax, J. Martin: Phys. Lett. B 468, 40 (1999) [astro-ph/9905040]
23. E.V. Linder: in Particle Physics and Cosmology, eds. J.F. Nieves, C.N. Leung, AIP Conf. Proc. 655, 193 (2003) [astro-ph/0302038]
24. R. Scoccimarro: Phys. Rev. D 70, 083007 (2004) [astro-ph/0407214]
25. E. Hawkins et al.: MNRAS 346, 78 (2003) [astro-ph/0212375]
26. Panstarrs: http://pan-starrs.ifa.hawaii.edu
27. LSST: http://www.lssto.org
28. R. Massey, A. Refregier, J. Rhodes: (2004) [astro-ph/0403229]
29. D.J. Eisenstein, W. Hu, M. Tegmark: Ap. J. 518, 2 (1998) [astro-ph/9807130]

Possible Influence of Dark Energy on the Dark Matter Relic Abundance

Antonio Masiero and Francesca Rosati

Università di Padova, Dipartimento di Fisica "Galileo Galilei" and INFN - Sezione di Padova, via Marzolo 8, 35131 Padova, Italy

Summary. Although a direct interaction between WIMP CDM candidates and scalar Quintessence fields (sources of Dark Energy) poses severe phenomenological threats, yet it is possible that the presence of Quintessence produces profound deviations in the expansion rate of the early Universe at the moment of WIMP decoupling, hence causing significant enhancements of the relic DM abundance. We consider the occurrence of such a phenomenon in a couple of physically interesting situations, kination and scalar-tensor theories of gravity where the scalar component plays the role of Quintessence. The consequences for supersymmetric DM candidates are briefly discussed.

1 Introduction

It is known that in the last years of the past century a major surprise occurred in our knowledge of the Universe: the dominance of Dark Energy (DE) in the total energy budget of the Universe, together with a close value of DE and Dark Matter (DM) energy densities in the present epoch of the Universe evolution. Indeed, their ratio is roughly two today, while one may expect it to have taken values different from O(1) even by orders of magnitude during the whole evolution of the Universe from the Big Bang until the present time. This "coincidence problem" may hint at a possible correlation between DE and DM. For instance, if one is to envisage DE as resulting from an ultralight scalar field rolling down its potential (the so-called Quintessence explanation of DE), then one could naively think that such a correlation results from a direct interaction between the DM particles and the scalar Quintessence field. However, the extreme lightness of the scalar Quintessence field, whose mass should correspond roughly to the inverse of the Hubble parameter, i.e. $O(10^{-33}\text{eV})$, and its time variation are at the basis of a host of severe phenomenological problems to be tackled (new long range forces with violations of the weak equivalence principle, time variation of the fundamental couplings, etc.). In this talk we wish to emphasize that the severe limitations we have to impose on such direct interactions between DM and DE do not prevent DE to have an indirect impact on DM. Namely, we wish to examine a couple of situations where the presence of quintessential DE in the early Universe largely influences today abundances of DM with significant changes on our prospects for direct and indirect DM searches.

According to the standard paradigm, a particle species goes through two main regimes during the cosmological evolution. At early times it stays in thermal equilibrium, until the particle interaction rate Γ remains larger than the expansion rate H. Later on, the particles will be so diluted by the expansion of the universe that they will not interact anymore and H will overcome Γ. The epoch at which Γ = H is called 'freeze-out', and after that time the number of particles per comoving volume for any given species will remain constant. This is how cold dark matter particle relics (neutralinos, for example) are generated.

As it can be easily understood, this scenario strongly depends on the evolution equation for H in the early universe, which is usually assumed to be radiation–dominated. However, as it was already noticed some time ago [1], there is little or no evidence that before Big Bang Nuclesynthesis (BBN) it was necessarily so. Non-standard scenarios are then worth exploring. In particular, if we imagine that for some time in the past the Hubble parameter was larger than usually thought (for example, due to the presence of some other component, in addition to radiation), then the decoupling of particle species would be anticipated, resulting in a net enhancement of their relic abundance.

A natural candidate for doing that is the Quintessence scalar, which is thought to consitute the Dark Energy fluid dominating the present universe. In most Quintessence models, the cosmological scalar is assumed to become the dominant component of the universe after a long period of sub-domination [2], playing little or no role in the earliest epochs. However, this has not always to be the case, as we will show in the following. We will focus on the possibility of modifying the past evolution of the Hubble paramenter H, with the double aim of respecting all the post-BBN bounds for the expansion rate and of producing a mesurable enhancement of the dark matter particles relic abundance. In particular, we will report about two possible mechanism by which the past dynamics of the Quintessence scalar could significantly modify the standard evolution of the pre-BBN universe: an early "kination" phase and a "scalar-tensor" model.

2 Kination Enhancement

If we imagine to add a significant fraction of scalar energy density to the background radiation at some time in the cosmological history, this would produce a variation in H^2, depending on the scalar equation of state w_ϕ. If $w_\phi > w_r = 1/3$, the scalar energy density would decay more rapidly than radiation, but temporarily increase the global expansion rate. This possibility was explicitly considered in [3], where it was calculated that a huge enhancement of the relic abundance of neutralinos could be produced in this way.

In a flat universe, a scalar field with potential $V(\phi)$ obeys the equations

$$\ddot{\phi} + 3H\dot{\phi} + dV/d\phi = 0 \; ; \qquad H^2 \equiv (\dot{a}/a)^2 = 8\pi\rho/3M_p^2 \; . \tag{1}$$

For any given time during the cosmological evolution, the relative importance of the scalar energy density w.r.t. to matter and radiation in the total energy density $\rho \equiv \rho_m + \rho_r + \rho_\phi$ depends on the initial conditions, and is constrained by the available cosmological data on the expansion rate and large scale structure. If the potential $V(\phi)$ is of the runaway type, the initial stage of the scalar evolution is typically characterized by a period of so–called 'kination' [2] during which the scalar energy density $\rho_\phi \equiv \dot{\phi}^2/2 + V(\phi)$ is dominated by the kinetic contribution $E_k = \dot{\phi}^2/2 \gg V(\phi)$, giving $w_\phi = 1$. After this initial phase, the field comes to a stop and remains nearly constant for some time ('freezing' phase), until it eventually reaches an attractor solution [2].

Then, if we modify the standard picture according to which only radiation plays a role in the post-inflationary era and suppose that at some time $\hat{t}$ the scalar contribution was small but non negligible w.r.t. radiation, then at that time the expansion rate $H(\hat{t})$ should be correspondingly modified. During the kination phase the scalar to radiation energy density ratio evolves like $\rho_\phi/\rho_r \sim a^{-3(w_\phi - w_r)} = a^{-2}$, and so the scalar contribution would rapidly fall off and leave room to radiation. In this way, we can respect the BBN bounds and at the same time keep a significant scalar contribution to the total energy density just few red-shifts before. The increase in the expansion rate H due to the additional scalar contribution would anticipate the decoupling of particle species and result in a net increase of the corresponding relic densities. As shown in [3], a scalar to radiation energy density ratio $\rho_\phi/\rho_r \simeq 0.01$ at BBN would give an enhancement of the neutralino codensity of roughly three orders of magnitude.

The enhancement of the relic density of neutralinos requires that at some early time the scalar energy density was dominating the Universe. This fact raises a problem if we want to identify the scalar contribution responsible for this phenomenon with the Quintessence field [4]. Indeed, the initial conditions must be such that the scalar energy density is sub-dominant at the beginning, if we want the Quintessence field to reach the cosmological attractor in time to be responsible for the presently observed acceleration of the expansion [2]. For initial conditions $\rho_\phi \gtrsim \rho_r$ we obtain instead an 'overshooting' behavior: the scalar field rapidly rolls down the potential and after the kination stage remains frozen at an energy density much smaller than the critical one. However, as shown in [5], more complicated dynamics are possible if we relax the hypothesis of considering a single uncoupled scalar. The presence of several scalars and/or of a small coupling with the dark matter fields could modify the dynamics in such a way that the attractor is reached in time even if we started in the overshooting region.

Consider a potential of the form $V(\phi_1, \phi_2) = M^{n+4} \left(\phi_1 \phi_2\right)^{-n/2}$, with M a constant of dimension mass. In this case, the two fields' dynamics enlarges

the range of possible initial conditions for obtaining a quintessential behavior today. This is due to the fact that the presence of more scalars allows to play with the initial conditions in the fields' values, while maintaining the total initial scalar energy density fixed. Doing so, it is possible to obtain a situation in which for a fixed ρ_ϕ^{in} in the overshooting region, if we keep initially $\phi_1 = \phi_2$ we actually produce an overshooting behavior, while if we choose to start with $\phi_1 \neq \phi_2$ (and *the same* ρ_ϕ^{in}) it is possible to reach the attractor in time.

Suppose, instead, that the Quintessence scalar is not completely decoupled from the rest of the Universe. Among the possible interactions, two interesting cases are the following:

$$V_b = b\ H^2\phi^2 \quad \text{or} \quad V_c = c\rho_m\phi \tag{2}$$

If we add V_b or V_c to $V = M^{n+4}\phi^{-n}$, the potential will acquire a (time-dependent) minimum and the scalar field will be prevented from running freely to infinity. In this way, the long freezing phase that characterizes the evolution of a scalar field with initial conditions in the overshooting region can be avoided. A more detailed discussion, together with numerical examples, can be found in [4].

3 Scalar-Tensor Enhancement

A different possibility arises if we consider Quintessence models in the framework of scalar-tensor (ST) theories of gravity (see [7] and references therein). These theories represent a natural framework in which massless scalars may appear in the gravitational sector of the theory without being phenomenologically dangerous, since they assume a metric coupling of matter with the scalar field, thus ensuring the equivalence principle and the constancy of all non-gravitational coupling constants [6]. Moreover a large class of these models exhibit an attractor mechanism towards GR [8], that is, the expansion of the Universe during the matter dominated era tends to drive the scalar fields toward a state where the theory becomes indistinguishable from GR.

ST theories of gravity are defined, in the so–called 'Jordan' frame, by the action

$$S_g = \frac{1}{16\pi}\int d^4x\sqrt{-\tilde{g}}\left[\Phi^2\tilde{R} + 4\,\omega(\Phi)\tilde{g}^{\mu\nu}\partial_\mu\Phi\partial_\nu\Phi - 4\tilde{V}(\Phi)\right]\ . \tag{3}$$

The matter fields Ψ_m are coupled only to the metric tensor $\tilde{g}_{\mu\nu}$ and not to Φ, *i.e.* $S_m = S_m[\Psi_m, \tilde{g}_{\mu\nu}]$. Each ST model is identified by the two functions $\omega(\Phi)$ and $\tilde{V}(\Phi)$. The matter energy-momentum tensor is conserved, masses and non-gravitational couplings are time independent, and in a locally inertial frame non gravitational physics laws take their usual form. Thus, the 'Jordan'

frame variables $\tilde{g}_{\mu\nu}$ and Φ are also denoted as the 'physical' ones in the literature. By means of a conformal transformation,

$$\tilde{g}_{\mu\nu} \equiv A^2(\varphi) g_{\mu\nu} \ , \quad \Phi^2 \equiv 8\pi M_*^2 A^{-2}(\varphi) \tag{4}$$

with

$$\alpha^2(\varphi) \equiv \ d\log A(\varphi)/d\varphi \ = \ 1/(4\omega(\Phi) + 6) \ , \tag{5}$$

it is possible to go the 'Einstein' frame in which the gravitational action takes the standard form, while matter couples to φ only through a purely metric coupling,

$$S_m = S_m[\Psi_m, A^2(\varphi) g_{\mu\nu}] \ . \tag{6}$$

In this frame masses and non-gravitational coupling constants are field-dependent, and the energy-momentum tensor of matter fields is not conserved separately, but only when summed with the scalar field one. On the other hand, the Einstein frame Planck mass M_* is time-independent and the field equations have the simple form

$$R_{\mu\nu} - \frac{1}{2} g_{\mu\nu} R = T^{\varphi}_{\mu\nu}/M_*^2 + T_{\mu\nu}/M_*^2 \ , \qquad M_*^2 \partial^2 \varphi + \partial V/\partial\varphi = -\alpha(\varphi) T/\sqrt{2} \ . \tag{7}$$

When $\alpha(\varphi) = 0$ the scalar field is decoupled from ordinary matter and the ST theory is indistinguishable from ordinary GR. The effect of the early presence of a scalar field on the physical processes will come through the Jordan-frame Hubble parameter $\tilde{H} \equiv d\log\tilde{a}/d\tilde{\tau}$:

$$\tilde{H} = H \, (1 + \alpha(\varphi) \, \varphi')/A(\varphi) \ , \tag{8}$$

where $H \equiv d\log a/d\tau$ is the Einstein frame Hubble parameter. A very attractive class of models is that in which the function $\alpha(\varphi)$ has a zero with a positive slope, since this point, corresponding to GR, is an attractive fixed point for the field equation of motion [8]. It was emphasized in [9] that the fixed point starts to be effective around matter-radiation equivalence, and that it governs the field evolution until recent epochs, when the Quintessence potential becomes dominant. If the latter has a run-away behavior, the same should be true for $\alpha(\varphi)$, so that the late-time behavior converges to GR. For this reason, we will consider the following choice ,

$$A(\varphi) = 1 + B e^{-\beta\varphi} \ , \qquad \alpha(\varphi) = -\beta B e^{-\beta\varphi}/(1 + B e^{-\beta\varphi}) \ , \tag{9}$$

which has a run-away behavior with positive slope.

In [7] it was calculated the effect of ST on the Jordan-frame Hubble parameter $\tilde{H}$ at the time of WIMP decoupling, imposing on the parameters B and β the constraints coming from GR test, CMB observations and BBN. Computing the ratio $\tilde{H}/\tilde{H}_{\rm GR}$ at the decoupling time of a typical WIMP of mass $m = 200$ GeV, it was found that it is possible to produce an enhancement of the expansion rate up to $O(10^5)$. As a further step, it was performed the

calculation of the relic abundance of a DM WIMP with mass m and annihilation cross-section $\langle\sigma_{\rm ann}v\rangle$. The effect of the modified ST gravity enters the computation of particle physics processes (like the WIMP relic abundance) through the "physical" expansion rate $\tilde{H}$ defined in (8). We have therefore implemented the standard Boltzmann equation with the modified physical Hubble parameter $\tilde{H}$:

$$dY/dx = -s\langle\sigma_{\rm ann}v\rangle(Y^2 - Y_{\rm eq}^2)/\tilde{H}\ x \tag{10}$$

where $x = m/T$, $s = (2\pi^2/45)\ h_\star(T)\ T^3$ is the entropy density and $Y = n/s$ is the WIMP density per comoving volume.

A numerical solution of the Boltzmann equation (10) is shown in Fig. 1 for a toy–model of a DM WIMP of mass $m = 50\,{\rm GeV}$ and constant annihilation cross-section $\langle\sigma_{\rm ann}v\rangle = 1 \times 10^{-7}\,{\rm GeV}^{-2}$. The temperature evolution of the WIMP abundance $Y(x)$clearly shows that freeze–out is anticipated, since the expansion rate of the Universe is largely enhanced by the presence of the scalar field φ. This effect is expected. However, we note that a peculiar effect emerges: when the ST theory approached GR (a fact which is parame-

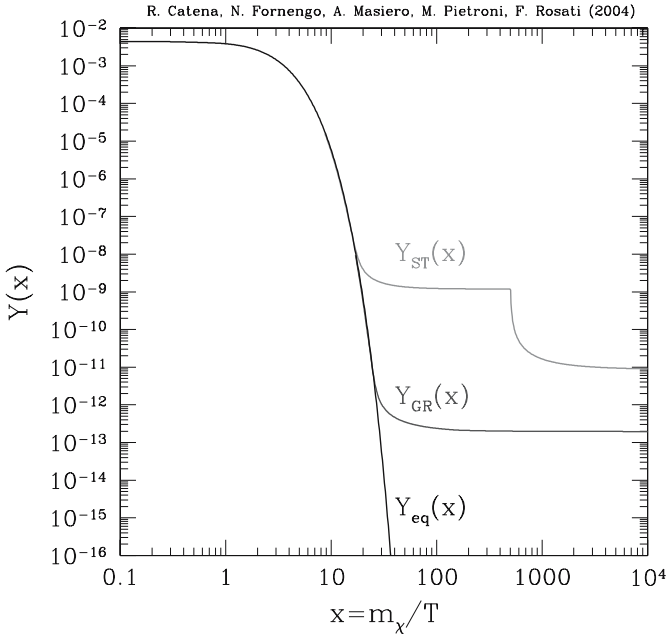

Fig. 1. Numerical solution of the Boltzmann (10) in a ST cosmology for a toy–model of a DM WIMP of mass $m = 50\,{\rm GeV}$ and constant annihilation cross-section $\langle\sigma_{\rm ann}v\rangle = 1 \times 10^{-7}\ {\rm GeV}^{-2}$. The temperature evolution of the WIMP abundance $Y(x)$ clearly shows that freeze–out is anticipated, since the expansion rate of the Universe is largely enhanced by the presence of the scalar field φ. At a value $x = m/T_\varphi$ a re–annihilation phase occurs and $Y(x)$ drops to the present day value.

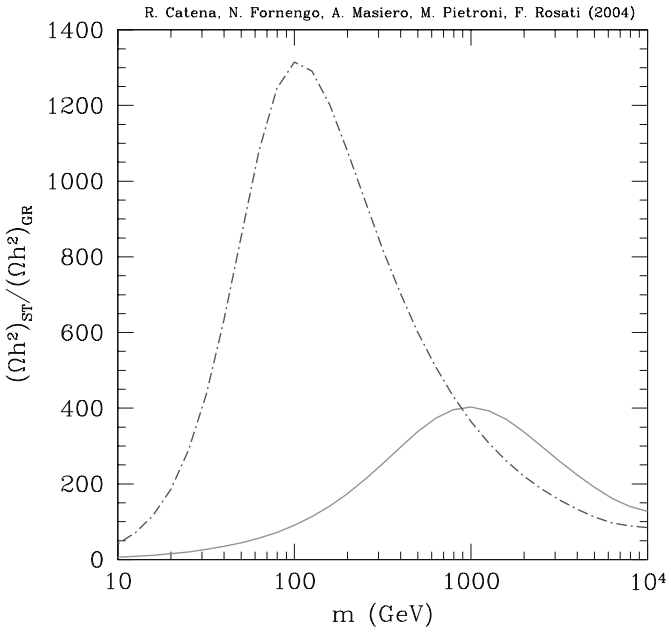

Fig. 2. Increase in the WIMP relic abundance in ST cosmology with respect to the GR case. The solid curve refers to an annihilation cross section constant in temperature, i.e. $\langle \sigma_{\rm ann} v \rangle = a = 10^{-7}\,{\rm GeV}^{-2}$, while the dashed line stands for an annihilation cross section which evolves with temperature as $\langle \sigma_{\rm ann} v \rangle = b/x = 10^{-7}\,{\rm GeV}^{-2}/x$.

trized by $A(\varphi) \to 1$ at a temperature T_φ, which in our model is 0.1 GeV), $\tilde{H}$ rapidly drops below the interaction rate Γ establishing a short period during which the already frozen WIMPs are still abundant enough to start a sizeable re-annihilation. This post-freeze-out "re-annihilation phase" has the effect of reducing the WIMP abundance, which nevertheless remains much larger than in the standard case (for further discussion on this aspect see [7]).

The amount of increase in the relic abundance which is present in ST cosmology is shown in Fig. 2. The solid curve refers to an annihilation cross section constant in temperature, i.e. $\langle \sigma_{\rm ann} v \rangle = a$, while the dashed line stands for an annihilation cross section which evolves with temperature as: $\langle \sigma_{\rm ann} v \rangle = b/x$. In the case of s–wave annihilation the increase in relic abundance ranges from a factor of 10 up to a factor of 400. For a pure b/x dependence, the enhancement can be as large as 3 orders of magnitude. Needless to say, such potentially (very) large deviations entail new prospects on the WIMP characterization both for the choice of the CDM candidates and for their direct and indirect detection probes [7, 10].

Acknowledgments

We would like to thank R. Catena, N. Fornengo, and M. Pietroni with whom part of the work reported here was done. This work was partially supported by the University of Padova fund for young researchers, research project n. CPDG037114.

References

1. J. D. Barrow, Nucl. Phys. B **208** (1982) 501; M. Kamionkowski and M. S. Turner, Phys. Rev. D **42**, 3310 (1990).
2. P. J. Steinhardt, L. M. Wang and I. Zlatev, 1999, Phys. Rev. D **59**, 123504; S. C. Ng, N. J. Nunes and F. Rosati, 2001, Phys. Rev. D **64**, 083510.
3. P. Salati, Phys. Lett. B **571** (2003) 121.
4. F. Rosati, 2003, Phys. Lett. B **570**, 5.
5. A. Masiero, M. Pietroni and F. Rosati, 2000, Phys. Rev. D **61**, 023504.
6. T. Damour, 1996, gr-qc/9606079.
7. R. Catena, N. Fornengo, A. Masiero, M. Pietroni and F. Rosati, Phys. Rev. D **70**, 063519 (2004).
8. T. Damour and K. Nordtvedt, Phys. Rev. **D48**, 3436 (1993); T. Damour and A. M. Polyakov, Nucl. Phys. **B423**, 532 (1994).
9. N. Bartolo and M. Pietroni, Phys. Rev. D **61** (2000) 023518; S. Matarrese, C. Baccigalupi and F. Perrotta, astro-ph/0403480.
10. S. Profumo and P. Ullio, JCAP **0311**, 006 (2003).

Supersymmetric Dark Matter Q-balls and their Interactions with Matter

Lee C. Loveridge

University of California at Los Angeles

1 Potential Sources of Baryogenesis

We do not know how baryogenesis occurred, but several processes have been suggested including

1. Plank scale baryogenesis
2. GUT Baryogenesis
3. Electroweak Baryogenesis
4. Leptogenesis
5. **Affleck-Dine Mechanism**

The Affleck-Dine mechanism is illustrated below.

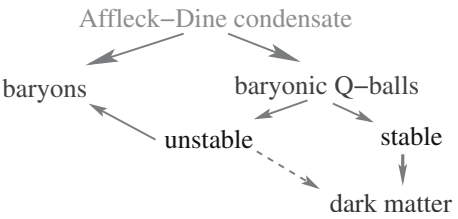

Here a scalar field gains a large value during inflation becoming the Affleck-Dine condensate. It then decays during reheating to baryons and Q-balls. The Q-balls could themselves be the dark matter or they could decay to the dark matter. This mechanism has the attractive feature that it is for baryons and dark matter to have about the same density. (Experimentally they are within an order of magnitude of each other.)

2 So What is a Q-ball

– A Q-ball is a localized region with a coherent state of squarks, sleptons, or some other scalar field. (It may be viewed as a localized remnant of Affleck-Dine Condensate)

- Unlike other solitons, it is stabilized not by topology, but by some conserved **Q**uantum Number which takes on the value $Q = \frac{1}{2i} \int \varphi^* \overleftrightarrow{\partial}_t \varphi \, d^3x$. from a variety of symmetries. For example
  - Baryon and/or Lepton Number
  - Global Abelian
  - Global Non-Abelian
  - Gauge Abelian.

3 Q-balls' Mass Behavior with Increasing Q

Depending on the Potential, the Q-ball mass may grow in different ways. If the potential is curved the mass grows linearly with Q. For a baryonic Q-ball, this will be completely stable if the mass per unit baryon number is less than the mass of a proton (the lightest baryon). If instead the potential is flat (meaning that it grows at a rate of less than ϕ^4) the mass will grow more slowly than linearly. For a completely flat potential it grows like $Q^{3/4}$. In this case the, if Q is sufficiently large, the mass per unit baryon number ω will always fall below the mass of a proton, and the Q-ball is always stable. In reality, all flat directions are eventually lifted by higher order operators, but not until $Q \sim 10^{24}$ and $\omega \sim 1$ MeV so that the Q-ball is completely stable. We will therefore focus on the stable CD Q-balls.

Linear (Curved Potential)	Less than Linear (Flat potential)
$M(Q) \sim \tilde{\mu} Q$	$M(Q) \sim m Q^{\frac{3}{4}}$
Possibly Stable	Completely Stable
	Flat directions lifted by higher dimension operators around $Q \approx 10^{24}$, $\omega \approx$MeV

4 Why the Interactions with MATTER

- A Q-ball's interactions with matter determine how we might detect them.
- Q-balls, pack baryon number more efficiently than baryons. Therefore,
  - Baryonic Matter can be absorbed into Q-balls.
  - If the consumption is fast enough, Q-balls may consume neutron stars or white dwarfs. (We focus on these, because other objects can not capture Q-balls).

5 Overview of Q-ball Matter Interactions

- Previous work (Kusenko, Shaposhnikov, Tinyakov, and Tkachev) looked only at perturbative decay of quarks in a squark background.

  - This decay was suppressed by gluino mass in gluino propagator, and therefore predicted long neutron star lifetimes.
- In reality mass mixing of quarks and gluinos creates large (O(1)) probabilities of absorbing matter into Q-balls.
- As a result, the consumption of neutron stars and white dwarfs by Q-balls is limited by matter transport processes in the star.

6 Mass in a Q-ball

- If one field has a non-zero expectation value $\langle\phi\rangle = \varphi$ then
- Interactions

$$-g\sqrt{2}T^a_{ij}(\lambda^a\sigma^2\psi_j\phi^*_i) + C.C.$$

- Become mass terms as the constant field takes the role of the mass.

$$M^a_i\lambda^a\sigma^2\psi_i$$

$$M^a_i = -g\sqrt{2}T^a_{ji}\varphi^*_j$$

7 Simplest Example for B(aryon) - Ball

For simplicity we will consider a Q-ball with the following simplified properties.

- It has a color neutral condensate of squarks.
- We will consider only one flavor of quark.
- We will include both left and right handed quarks

In this case we will have a mass matrix of the form

$$\begin{pmatrix} 0 & m & \varphi_L \\ m & 0 & \varphi_R \\ \varphi_L & \varphi_R & M \end{pmatrix} \Rightarrow \begin{pmatrix} 0 & 0 & \varphi_L \\ 0 & 0 & \varphi_R \\ \varphi_L & \varphi_R & M \end{pmatrix}$$

The Dirac mass m is negligibly small compared to the other scales in the problem and will be ignored for simplicity.

The matrix can then be diagonalized with the following prescription.

$$\begin{pmatrix} 0 & 0 & \varphi_L \\ 0 & 0 & \varphi_R \\ \varphi_L & \varphi_R & M \end{pmatrix} \Rightarrow \tilde{M}\begin{pmatrix} 0 & 0 & 0 \\ 0 & \cos^2\beta & 0 \\ 0 & 0 & -\sin^2\beta \end{pmatrix}$$

$$\begin{array}{ccc} & M_0 = 0 & \begin{pmatrix} \sin\alpha \\ -\cos\alpha \\ 0 \end{pmatrix} \\ \alpha = \arctan\frac{\varphi_R}{\varphi_L} & & \\ \varphi = \sqrt{{\varphi_L}^2 + {\varphi_R}^2} & M_+ = \tilde{M}\cos^2\beta & \begin{pmatrix} \sin\beta \begin{pmatrix} \cos\alpha \\ \sin\alpha \end{pmatrix} \\ \cos\beta \end{pmatrix} \\ \beta = \frac{1}{2}\arctan\frac{2\varphi}{M} & & \\ \tilde{M} = \sqrt{\varphi^2 + \frac{1}{4}M^2} & & \\ & -M_- = -\tilde{M}\sin^2\beta & \begin{pmatrix} \cos\beta \begin{pmatrix} \cos\alpha \\ \sin\alpha \end{pmatrix} \\ -\sin\beta \end{pmatrix} \end{array}$$

8 A Bit on Masses

It is important to know if the two mass eigenstates M_+ and M_- will in general be large or small. We will always assume that relative to the energy the condensate φ and the gluino mass $|M|$ are very large and the dirac mass m is very small.

$$\varphi, |M| \gg E \gg m$$

In this case we find that

- If the condensate is much larger than the gluino mass $\varphi \geq |M|$, then both mass states are large $M_+, M_- \gg E$.
- But if the gluino mass is much larger than the condensate $|M| \gg \varphi$, then the eigenstates still retain identity as quark and gluino states, with a small quark mass.

9 Majorana Fermion Basics

- Majorana Fermions obey the differential equation

$$i\bar{\sigma}\cdot\partial\chi + im\sigma^2\chi^* = 0\,,$$

  where $\sigma = (1, \sigma)$ and $\bar{\sigma} = (1, -\sigma)$.
- This equation has the solutions

$$\begin{array}{l} \sqrt{\sigma\cdot p}\left(Ae^{-ip\cdot x} + \sigma^2 A^* e^{ip\cdot x}\right) \; m > 0 \\ \sqrt{\sigma\cdot p}\left(Ae^{-ip\cdot x} - \sigma^2 A^* e^{ip\cdot x}\right) \; m < 0 \end{array}$$

  for positive and negative mass states respectively.
- Reflection is now a simple quantum mechanics continuity problem. If mass eigenstates change at a boundary, the wave function must be continuous. (There is no restriction on the derivative).

To solve the reflection problem we need to consider the following mass eigenstates. (At the moment I am considering only the quark state which gains a large mass).

Outside

$$\begin{pmatrix} 0 & 0 \\ 0 & M \end{pmatrix}$$

Inside

$$\begin{pmatrix} 0 & \varphi \\ \varphi & M \end{pmatrix}$$

Name	Eigenvalue	Eigenvector
Quark	$m = 0$	$\begin{pmatrix} 1 \\ 0 \end{pmatrix}$
Gluino	M	$\begin{pmatrix} 0 \\ 1 \end{pmatrix}$

Name	Eigenvalue	Eigenvector
Positive	$M_+ = \tilde{M} \cos^2 \beta$	$\begin{pmatrix} \sin \beta \\ \cos \beta \end{pmatrix}$
Negative	$-M_- = -\tilde{M} \sin^2 \beta$	$\begin{pmatrix} \cos \beta \\ -\sin \beta \end{pmatrix}$

10 Simplest Case

In the simplest case where the moment is normal to the surface, and all masses are much larger than the energy we find that the reflection coefficient is simply i.

$$M, M_+, M_- \gg E$$
$$\mathbf{p} \perp \text{boundary}$$
$$r = i$$

11 Some Implications

This has some interesting implications.

- **First there is 100 percent reflection.**
  - (This makes sense because a particle can not propagate if $M \geq E$)
- **There is also a total frequency flip.**
  - Positive (negative) frequency components are reflected as negative (positive) frequency components.
  - **So the particle must either change its handedness or particle anti-particle identity.**
- **Why?**
  - Massless particles have only a positive (negative) frequency component.
  - When $M > E$ both positive and negative frequency components must be present with equal magnitude.
  - Thus, **IF** the incoming particle matches the positive (negative) components of the states inside the Q-ball,
  - **THEN** the outgoing particle must match the negative (positive) components.

12 Some Possible Caveats

- If the gluino mass is negative then $r = -i$. This is essentially the same result.
- If the incoming momentum is not normal to the surface, the reflection coefficient is more complicated, but still implies 100 percent reflection and 100 percent frequency flipping.
- If $|M| >> \varphi$ then one of the important reflection mass can be small. In this case, frequency flipping is intact, but the reflection probability is suppressed if and only if $M_{\pm} < E$ or $\varphi^2 < |M_g E|$.
- If the condensate is mostly Stop $\tilde{t}$ or other flavors, that are not well represented in ordinary baryonic matter, the Q-ball may not couple well to protons and neutrons.

13 Effect on Incoming Quark

Of course, these results apply only to the linear combination of left and right handed quarks that gains a mass. Since, both left and right handed quarks are present in ordinary matter, an ordinary quark has a probability to be reflected and a probability to be transmitted. A chance of changing to an anti-quark and a chance of remaining a quark. These probabilities are summarized below.

Incoming Left Handed

	Quark	Anti-Quark
Trans	$\sin^4\alpha$	$\sin^2\alpha\cos^2\alpha$
Ref	$\cos^2\alpha\sin^2\alpha$	$\cos^4\alpha$

Incoming Right Handed

	Quark	Anti-Quark
Trans	$\cos^4\alpha$	$\sin^2\alpha\cos^2\alpha$
Ref	$\cos^2\alpha\sin^2\alpha$	$\sin^4\alpha$

Total ref $\cos^2\alpha = \frac{{\varphi_L}^2}{\varphi^2}$ $\sin^2\alpha = \frac{{\varphi_R}^2}{\varphi^2}$

Total anti $\cos^2\alpha = \frac{{\varphi_L}^2}{\varphi^2}$ $\sin^2\alpha = \frac{{\varphi_R}^2}{\varphi^2}$

- Total Probability to Change Handedness $= 2\sin^2\alpha\cos^2\alpha = \frac{1}{2}\sin^2 2\alpha = \frac{{\varphi_L}^2{\varphi_R}^2}{\varphi^4}$
- Averaged Total Probability to Reflect = Total Probability to Change Identity $= \frac{1}{2}$

The final result is most important. Whatever the left right composition of the condensate, if the quarks in the star are randomly left and right handed with equal probability, the total reflection probability and the total probability of changing from particle to anti-particle are both 1/2.

14 Time Dependent Effects

- Q-balls have a time dependence which we have so far ignored.

$$\langle \phi \rangle = \varphi \exp iq\omega$$

- As a result of this time dependence, if the particle (anti-particle) remains a particle (anti-particle) then the extra phases cancel with no effect.
- If instead the incoming quark is changed from a particle (anti-particle) to an anti-particle (particle), the energy is decreased (increased) by 2ω. There is also a slight increase (decrease) of the reflection probability $P \approx \frac{E_{in}}{E_{out}}$.
- This demonstrates that omega (ω) is the chemical potential of the Q-ball, i.e. the energy required to change its baryon number by one unit. Because ω roughly 1000 times smaller than the mass of a baryon, this is a very slight effect for large Q-balls.

15 Observable Effects

- We expect large Q-ball effects.
- They can leave a large signature in water Cerenkov detectors. However, the effect is so large that it is often rejected as bad data.
- Q-balls are so dense and massive that they only stop in a neutron star or a white dwarf.

16 Effects in a Neutron Star or White Dwarf

- Half of all incident quarks turn to anti-quarks.
- These annihilate with the other half.
- Therefore, **All** matter incident on the Q-ball is converted to radiation (Mostly pions).
- Because of this we might expect quick consumption. In fact, if matter in the neutron star could move toward the Q-ball at the speed of light the entire neutron star could be consumed in about 1 day.
- However, neutron and thermal transport processes inside the star will slow the process down. We are still uncertain what the exact rate would be.

17 Conclusions

1. Quarks incident on a Q-ball are converted to anti-quarks with large (O(1)) probability.

2. Even with such high conversion rates, the difficulty of getting baryonic matter to the small Q-ball remains a limiting factor on the rate at which a Q-ball can consume a neutron star or white dwarf.
3. The exact rate of consumption is unknown, but for now, Affleck-Dine Baryogenesis remains a viable mechanism and Q-balls remain a viable dark matter candidate.

Cosmology with *Chandra* Observations of Galaxy Clusters

A. Vikhlinin[1,2]

[1] Harvard-Smithsonian Center for Astrophysics, Cambridge, MA, USA
[2] Space Research Institute, Moscow, Russia

Summary. We review recent results from X-ray observations of galaxy clusters with *Chandra*. These observations lead to high-quality measurements of the global cluster properties and thus open a possibility for reliable application of several cosmological tests. Independent tests based on the observed baryon fraction in massive clusters, the shape of the cluster mass function at low redshifts, and its evolution at $z \sim 0.5$, all provide value of the matter density parameter $\Omega_m \simeq 0.26$. Observed evolution of the mass function leads to independent constraints on the Dark Energy.

1 Introduction

Dark matter is the dominant mass component of galaxy clusters and thus governs their dynamics. Observations of galaxy clusters lead to a number of well-established cosmological tests, outlined below.

Due to their large size, clusters of galaxies should represent fair samples of the Universe in the sense that the mass ratio of the baryonic and dark matter components within the cluster, f_b, is close the Universal value, Ω_b/Ω_d. If the average density of baryons is measured by an independent method, e.g. from the Big Bang Nucleosynthesis or from CMB fluctuations, observations of nearby clusters should provide a value for Ω_m. The theoretical foundations of this test were laid out by White et al. [1], followed by many observational implementations (e.g., [2, 3, 4]; see [5] for the most recent application of this test).

The real cluster baryon fraction also should be redshift-independent, while observationally derived f_b depends on the assumed distance to the cluster as $d^{3/2}$. The apparent cluster baryon fraction is therefore a distance indicator [6, 7], and measurements of $f_b(z)$ lead to cosmological tests identical to those possible with Supernovae Ia (see Linder et al. in this volume). Allen et al. [5] have recently applied this test to independently detect acceleration in the expansion of the Universe and to put constraints on the properties of Dark Energy.

Another group of cosmological tests uses the cluster mass function as a sensitive indicator of the power spectrum of the matter density perturbations, $P(k)$. Clusters are formed via the gravitational collapse of growing dark matter density perturbations. The theory of this process, which is well-developed

[8, 9, 10] and calibrated by cosmological numerical simulations (see, e.g., [11, 12, 13]), shows that the slope of the mass function is sensitive to the slope of $P(k)$ on the cluster scales, $\sim 10h^{-1}$ Mpc, and the number density of clusters with a given mass is exponentially sensitive to normalization of $P(k)$, usually expressed as σ_8, the *rms* amplitude of fluctuations on the $8h^{-1}$ Mpc scale. Cluster observations, therefore, can be used to determine these parameters (see [14] and many later works). If mass function measurements are available at high redshifts, one recovers the history of growth of perturbations, $G(z) = \sigma_8(z)/\sigma_8(0)$. The $P(k)$ slope mainly depends on the product $\Omega_m\, h$ (assuming that matter density is dominated by CDM), and growth of perturbations is sensitive to Ω_m and, more weakly, to the density and properties of Dark Energy. High quality cluster observations can, therefore, be used to constrain these cosmological parameters independently of all other astronomical methods.

High quality of the observational data is absolutely necessary for reliable application of the cosmological tests outlined above[1]. The main problems are the need for accurate measurements of the cluster total mass, and possible effects of non-gravitational processes on the observed cluster properties (see [15] for a recent review). The high-quality data are now being provided by X-ray observations of galaxy clusters with the *Chandra* X-ray observatory. X-ray telescopes directly observe the spatial distribution of density and temperature of the dominant baryonic component, the intra-cluster medium (ICM). In dynamically relaxed clusters, these data can be used to infer the total mass (including dark matter), which leads to a number of cosmological applications outlined above. A review of *Chandra* X-ray observations is the topic of this paper.

2 Self-Similarity of Cluster Profiles

Almost every cluster cosmological test is based – explicitly or implicitly – on the assumptions that clusters form from scale-free primordial density perturbations and their dynamics is driven by gravity of the CDM. The necessary consequence of these postulates is that clusters should be self-similar. Self-similarity implies, in particular, that profiles of the temperature (and density etc.) of the intra-cluster medium (ICM) should be similar when radii are scaled to the cluster virial radius, which can be estimated from the average temperature, $r_{\rm vir} \equiv r_{180} \propto \langle T \rangle^{1/2}$ (for detailed discussion see, e.g., [16]). This prediction is strongly confirmed by recent *Chandra* observations.

Chandra is well-suited for measurements of the temperature profiles to 0.5–0.6 of the virial radius thanks to its stable detector background, and fine

[1] The same is generally true for most observational techniques because the effects of the interesting cosmological parameters on the observationally derived quantities are usually small.

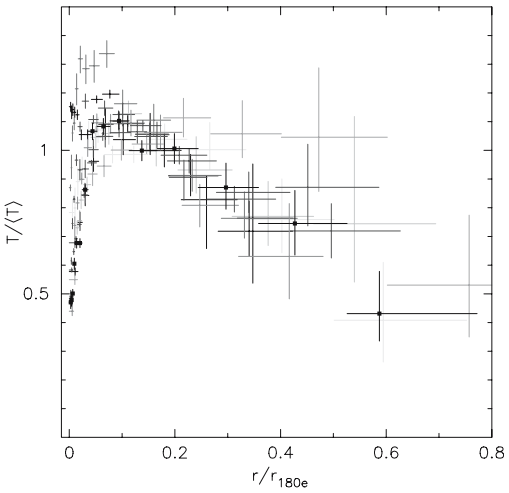

Fig. 1. Compilation of the ICM temperature profiles [17] plotted as a function of the cluster virial radius. Virial radii are estimated from the average temperature, $r_{180} = 2.74\,\mathrm{Mpc}\,(\langle T\rangle/10\,\mathrm{keV})^{1/2}$ [19].

angular resolution. To date, 11 low-redshift clusters were observed by *Chandra* with sufficiently long exposures and spatial coverage. All these objects have a very regular overall X-ray morphology and show only weak signs of dynamical activity, if any. The scaled temperature profiles for this sample show a remarkable similarity at large radii (see Fig. 1 and [17] for more details). The greatest scatter is observed at small radii, where the non-gravitational process make a non-negligible contribution to the energy budget of the ICM, as discussed below.

Chandra X-ray data allow one to trace the X-ray surface brightness distribution to the virial radius. In the soft X-ray band, the emissivity of the plasma with $T = 1{-}10\,\mathrm{keV}$ is proportional to ρ^2_{gas} and insensitive to other parameters (T, metallicity). Therefore, the X-ray imaging data can be easily deprojected to infer the density distribution of the ICM. The derived ICM density profiles (Fig. 2) also show self-similarity at large radii, $r \gtrsim 0.1 - 0.2\,r_{\mathrm{vir}}$. Just as the temperature profiles, the ICM density shows a large scatter at smaller radii.

The source of non-similarity at small radii is various non-gravitational processes which act as a significant source or sink of energy in this region. The dense ICM is subject to the radiative cooling. Another important process is periodic outbursts of the central AGN which can deposit up to 10^{61} ergs into the ICM [18]. Note that the strongest outlier on Fig. 1 is A2390 (magenta) whose central galaxy contains an unusually active central AGN.

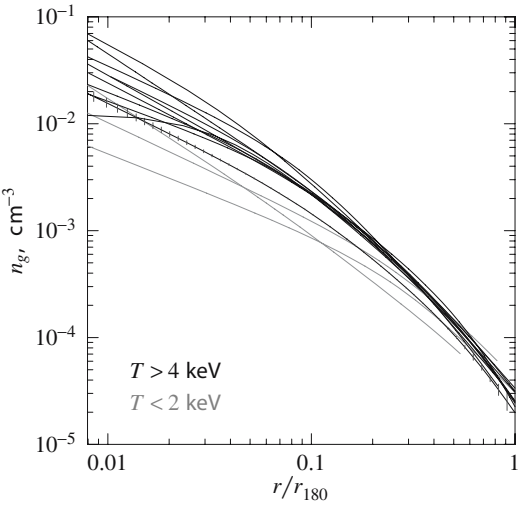

Fig. 2. Scaled ICM density profiles for the *Chandra* clusters. Density is scaled to the mean density of the Universe at the cluster redshift ($\rho \rightarrow \rho/(1+z)^3$), and radii are in units of the virial radius.

3 Baryon Fraction in Nearby Clusters

In the dynamically relaxed clusters, the X-ray data can be used to estimate the total mass as a function of radius using the hydrostatic equilibrium condition for the ICM:

$$\frac{GM_{\rm tot}}{r^2} = -\frac{\nabla P_g}{\rho_g} = -\mu\, m_p \times T/r \times \left(\frac{d\,\log n}{d\,\log r} + \frac{d\,\log T}{d\,\log r}\right)\,, \qquad (1)$$

where $T(r)$ and $n(r)$ are the temperature and density profiles derived from X-rays, and $m \simeq 0.6$ is the mean molecular weight of the fully ionized plasma. This equation can also be used to determine the mass fraction of the ICM and apply the first group of cosmological tests outlined in Sect. 1. Figure 3 shows the $f_{\rm gas}$ measurements within the radius ${r_{2500}}^2$, as a function of cluster mass. A strong trend is observed, apparently violating the assumption of universality of the baryon fraction in clusters. Recall, however, that the inner cluster regions are not self-similar and thus the trend is explainable. Universality of the gas fraction can be expected at larger radii, where the clusters are self-similar. Indeed, $f_{\rm gas}$ measured in the radial range $r_{2500} - r_{500}$, or $\approx 0.25 - 0.6$ of $r_{\rm vir}$, shows only a weak trend with mass, if any (Fig. 4).

The measurements of $f_{\rm gas}$ should be slightly corrected to determine the *baryon* mass fraction. First, ∼15% of the cluster baryons are converted into

[2]This radius is defined so that the mean cluster density, $M(r_{2500})/(4/3\pi\, r^3_{2500})$, is is a factor of 2500 higher than the critical density. For typical clusters, $r_{2500} \approx 0.25 r_{\rm vir}$.

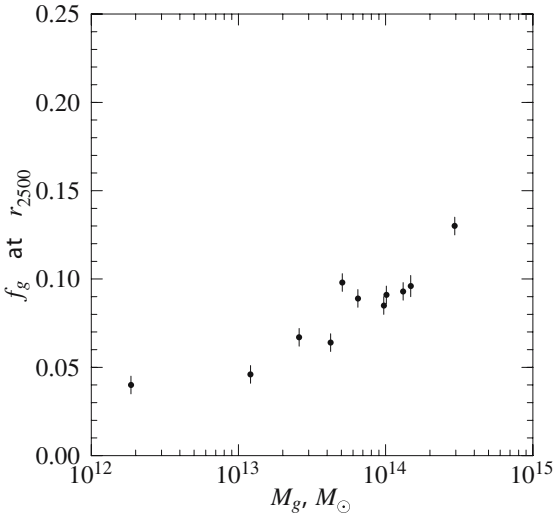

Fig. 3. Gas fraction within the radius r_{2500} ($\approx 0.25 r_{\rm vir}$) as a function of cluster mass.

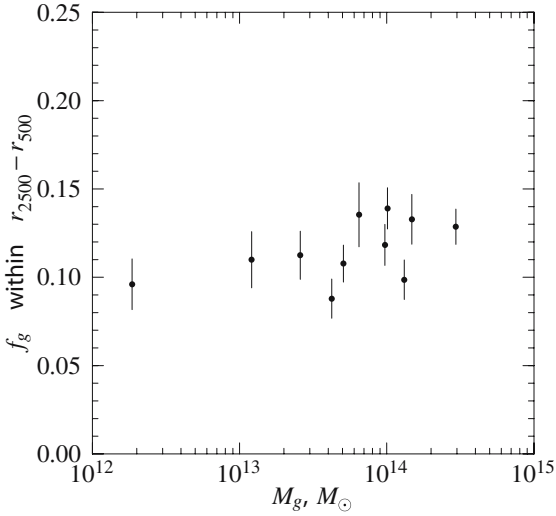

Fig. 4. Same as Fig. 3, but $f_{\rm gas}$ is measured in the spherical shell $r_{2500} - r_{500}$, or $\approx 0.25 - 0.6$ of $r_{\rm vir}$.

stars (see [20] and references therein). Second, a small decoupling of the dark matter and ICM is expected due to collisional nature of the latter. Numerical simulations show that baryons in the outer cluster regions are underdense by $\sim$7% relative to the Universal value [21]. Applying these corrections to the measurements shown in Fig. 4, we obtain the average baryon fraction $f_b = 0.153 \pm 0.008$ in the most massive clusters. This is in a good agreement

with the independent WMAP determination $f_b = 0.166 \pm 0.012$ [22]. Using the WMAP measurement of the average baryon density, the X-ray results give $\Omega_m = \Omega_b / f_b = (0.28 \pm 0.02)\,(h/0.71)^{-1/2}$.

4 Mass Function at Low Redshifts

Observationally verified universality of the gas fraction in clusters can be used to implement a new method of estimating their total mass and fitting the mass function data to the cosmological models:

$$M_{\rm tot} = 1.15 \times \Upsilon^{-1} \times M_{\rm gas} \times \frac{\Omega_M}{\Omega_b}, \qquad \Upsilon \approx 0.93\,, \tag{2}$$

where the factor 1.15 accounts for 15% of the cluster baryons being in the form of stars, and Υ is the correction for small non-Universality of the baryon fraction in clusters (see above). Gas masses can be easily derived from the X-ray imaging data for a large number of clusters, and (2) allows one to apply the mass function models to $F(M_{\rm gas})$, the number density of clusters as a function of their gas mass (see [20] for details).

Observational determination of $F(M_{\rm gas})$ for a statistically complete sample of low-redshift clusters is shown in Fig. 5. It is fully consistent with

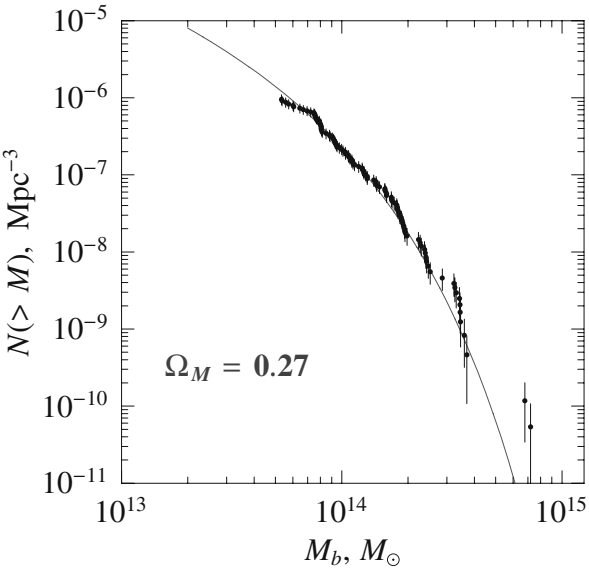

Fig. 5. Comoving number density of clusters as a function of their baryon mass, derived using a statistically complete sample at $z < 0.1$ [20]. The solid line shows the model corresponding to the best-fit WMAP cosmological parameters, with only normalization adjusted.

the theoretical prediction computed for the CDM power spectrum, corresponding to the best-fit WMAP parameters (shown by the solid line); fitting the mass function models to the data gives $\Omega_m = (0.21 \pm 0.05)\,(h/0.71)^{-1}$. The only caveat is that the best-fit normalization of the power spectrum, $\sigma_8 = 0.77 \pm 0.03$, is marginally lower than the WMAP value.

5 Evolution of Mass Function at $z \sim 0.5$

Statistically complete samples of clusters at high redshift, $z \sim 0.5$ are now provided by the X-ray surveys using the data from the *ROSAT* satellite [23]. Followup observations with *Chandra* and *XMM-Newton* can be used to accurately determine their baryon masses and thus measure the evolution in the $F(M_{\rm gas})$. Observations show that the comoving number density of clusters at a fixed mass threshold evolves by a factor of $\sim$10 between redshifts of 0.5 and 0 (Fig. 6; for details, see [24]). The observed evolution is a direct measure of the growth factor of the linear matter density perturbations at $z = 0.5$, which slightly depends on the assumed value of Ω_m: $G = 0.726 \pm 0.027$ for $\Omega_m = 0.3$ and $G = 0.760 \pm 0.045$ for $\Omega_m = 0.2$. The measurement of the perturbation growth factor leads to constraints on Ω_m and Ω_Λ which are consistent with the CMB and SN Ia results, and have a different degeneracy [24]. Under assumption of the spatially flat Universe, one can also constrain the properties of the Dark Energy. Figure 7 shows constraints for equation of state parameter of the Dark Energy, $w \equiv p_X/\rho_X$, obtained using the observed cluster

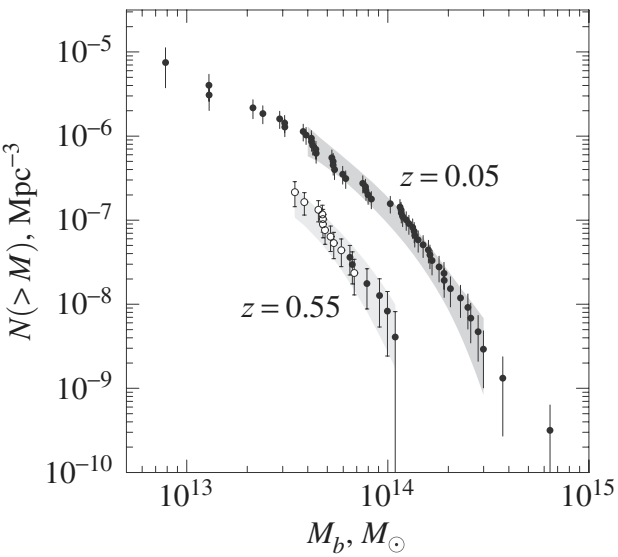

Fig. 6. Observed evolution of the cluster mass function observed at $z \sim 0.5$ [24].

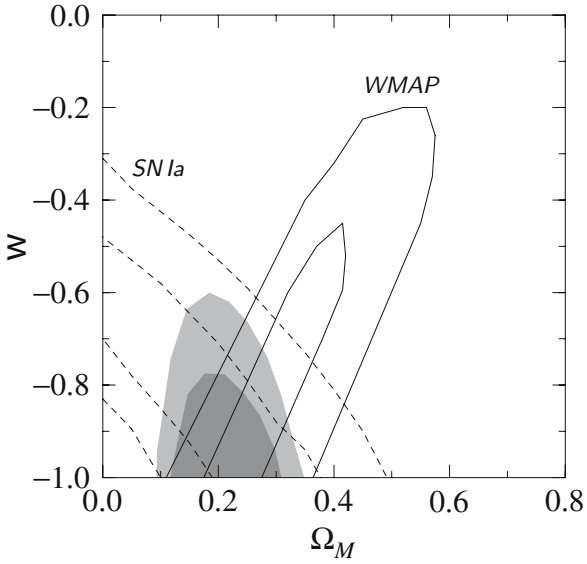

Fig. 7. Constrains on the equation of state parameter for Dark Energy obtained assuming $\Omega_{\rm tot} = 1$. Shading shows 68% and 90% confidence regions from fitting the cluster evolution data from Fig. 6.

evolution. The results agree with the SN Ia and CMB measurements, and show comparable accuracy. The on-going *Chandra* survey of distant clusters should provide a factor of ~ 2 better statistical uncertainties.

6 Conclusions

High-quality *Chandra* observations of galaxy clusters with *Chandra* lead to accurate measurements of the global cluster properties and thus open a possibility for reliable application of several cosmological tests. Independent tests based on the observed baryon fraction in massive clusters, the shape of the cluster mass function at low redshifts, and its evolution at $z \sim 0.5$, all provide value of the matter density parameter $\Omega_m \simeq 0.26$. Observed evolution of the mass function leads to independent constraints on the Dark Energy, which will be significantly improved in the near future.

I thank the organizers for their hospitality and invitation to speak. Contributions from my collaborators, A. Kravtsov, M. Markevitch, and A. Voevodkin, is gratefully acknowledged. This work was supported by NASA grant NAG5-9217 and contract NAS8-39073.

References

1. S.D.M. White, J.F. Navarro, A.E. Evrard,& C.S. Frenk, *Nature* 366 (1993) 429.
2. D.A. White & A.C. Fabian *MNRAS* 273 (1995) 72.
3. L.P. David, C. Jones & W. Forman, *Astrophysical Journal* 445 (1995) 578.
4. M. Markevitch & A. Vikhlinin, *Astrophysical Journal* 491 (1997) 467.
5. S.W. Allen, R.W. Schmidt, H. Ebeling, A.C. Fabian& L. van Speybroeck, *MNRAS* 353 (2004) 457.
6. S. Sasaki, *Publ. Astr. Soc. of Japan* 48 (1996) L119.
7. U. Pen, *New Astronomy* 2 (1997) 309.
8. W.H. Press & P. Schechter, *Astrophysical Journal* 187 (1974) 425.
9. J.R. Bond, S. Cole, G. Efstathiou & N. Kaiser, *Astrophysical Journal* 379 (1991) 440.
10. R.K. Sheth & G. Tormen, *MNRAS* 329 (2002) 61.
11. A. Jenkins, C.S. Frenk, S.D.M. White, J.M. Colberg, S. Cole, A.E. Evrard, H.M.P. Couchman, & N. Yoshida, MNRAS 321 (2001) 372.
12. A.E. Evrard, et al. *Astrophysical Journal* 573 (2002) 7.
13. W. Hu & A.V. Kravtsov, *Astrophysical Journal* 584 (2003) 702.
14. J.P. Henry & K.A. Arnaud, *Astrophysical Journal* 372 (1991) 410.
15. G.M. Voit, *Rev. Mod. Phys.* (2005) in press (astro-ph/0410173).
16. G.L. Bryan & M.L. Norman, *Astrophysical Journal* 495 (1998) 80.
17. A. Vikhlinin, M. Markevitch, S.S. Murray, C. Jones, W. Forman, L. Van Speybroeck, *Astrophysical Journal* submitted (2005) (astro-ph/0412306).
18. B.R. McNamara, P.E.J. Nulsen, M.W. Wise, D.A. Rafferty, C. Carilli, C.L. Sarazin & E.L. Blanton, *Nature* 433 (2005) 45.
19. A.E. Evrard, C.A. Metzler & J.F. Navarro, *Astrophysical Journal* 469 (1996) 494.
20. A. Voevodkin & A. Vikhlinin, *Astrophysical Journal* 601 (2004) 610
21. A. Kravtsov, D. Nagai & A. Vikhlinin, *Astrophysical Journal* submitted (2005) (astro-ph/0501227).
22. D.N. Spergel et al., *Astrophysical Journal Supl. Ser.* 148 (2003) 175.
23. P. Rosati, S. Borgani & C. Norman, *Ann. Rev. Ast. Astroph.* 40 (2002) 539.
24. A Vikhlinin et al., *Astrophysical Journal*590 (2003) 15.

Intrinsically Faint Quasars: Evidence for meV Axion Dark Matter in the Universe

Anatoly A. Svidzinsky

Department of Physics, Institute for Quantum Studies, Texas A&M University, TX 77843-4242
asvid@jewel.tamu.edu

Summary. Growing amount of observations indicate presence of intrinsically faint quasar subgroup (a few % of known quasars) with noncosmological quantized redshift. Here we find an analytical solution of Einstein equations describing bubbles made from axions with periodic interaction potential. Such particles are well-motivated cold dark matter candidate. The bubble interior possesses equal gravitational redshift which can have any value between zero and infinity. Quantum pressure supports the bubble against collapse and yields states stable on the scale more then hundreds million years. Our results explain the observed quantization of quasar redshift and suggest that intrinsically faint point-like quasars associated with nearby galaxies are axionic bubbles with masses 10^8–$10^9 M_\odot$ and radii 10^3–$10^4 R_\odot$. They are born in active galaxies and ejected into surrounding space. Properties of such quasars unambiguously indicate presence of axion dark matter in the Universe and yield the axion mass $m \approx 1$ meV, which fits in the open axion mass window constrained by astrophysical and cosmological arguments.

1 Introduction

Since their discovery in 1960's [1] quasars (QSOs) became one of the most mysterious objects in the Universe. The present-day conventional understanding of QSOs is based on the paradigm that redshift of all QSOs has cosmological origin. Hovewer, this contradicts to some observations which can not be ignored. There is a strong evidence that many low redshift (nearby) galaxies and high redshift QSOs are physically associated and, hence, these QSOs are no further away than the close galaxies and must have redshifts noncosmological in origin (see, e.g., [2, 3, 4, 5, 6, 7, 8, 9, 10, 11] and references therein). Observations indicate that such objects are ejected from nearby active galaxies or in the process of ejection from the galactic nucleus [2, 4, 9, 12, 11, 13].

In 1990 Karlsson [14] noted division of quasars into two groups with different redshift properties and concluded the following. If we select QSOs associated with most nearby, distance $d < 50-100$ Mpc, galaxies then their redshift is close to certain values (quantized), as shown in Fig. 3 below. Meanwhile, in QSO samples associated with distant galaxies no periodicity in intrinsic redshift is observed. Such a division is supported by later studies of QSOs associated with most nearby galaxies where the quantization was confirmed

[15, 16] and distant ($0.01 < z_{\rm gal} < 0.3$) galaxies for which absence of any periodicity was claimed [17].

The observations suggest existence of intrinsically faint QSO subgroup with quantized noncosmological redshift. Being intrinsically faint, such objects are not detected from large distances (which yields disappearance of redshift quantization in distant QSO samples) and constitute only a few % of the known QSO population. Typical absolute magnitude M_v of such quasars lies in the range -8 to -13 (optical luminosity $L = 10^5 - 10^7 L_\odot$) [9, 11]. They are born in nuclei of active galaxies; ejected into surrounding space and cluster at a distance upto 100−300 kpc from the parent galaxy. About 15 such objects have been discovered close to M82, the nearest active galaxy to the Milky Way [9], and about 10 in the vicinity of NGC 3628 [12].

Here we show that bubbles of dark matter with periodic interaction potential, masses $10^8 - 10^9 {\rm M}_\odot$ and radii $10^3 - 10^4 R_\odot$ can explain the intrinsically faint quasars. The redshift of such QSOs is purely gravitational. The bubble is supported against collapse by quantum pressure and decays on a time scale more than hundreds million years. Hypothetical axions, one of the leading dark matter candidate, fit well into this picture and can account for the redshift quantization. Usual baryonic matter falls into the bubble interior, heated by the release of the gravitational energy and produce electromagnetic radiation. The amount of baryonic matter trapped in the bubble we assume to be small compared to the bubble mass. Photons emitted anywhere inside the bubble interior posses identical gravitational redshift and freely propagate into surrounding space because dark matter is transparent for electromagnetic waves.

2 Dark Matter Bubbles

In this paper we study massive real scalar field φ with periodic interaction potential

$$V(\varphi) = V_0[1 - \cos(\varphi/f)] \,, \tag{1}$$

where $V_0 > 0$. This potential is quite general and derived in quantum filed theory in connection with pseudo Nambu-Goldstone bosons (PNGBs) [18]. In all such models, the key ingredients are the scales of global symmetry breaking f and explicit symmetry breaking $(V_0)^{1/4}$. One of the examples of a light hypothetical PNGB is the axion which possess extraordinarily feeble couplings to matter and radiation and is well-motivated dark matter candidate [19]. Axion arises as a solution to the strong CP problem. If the axion exists, astrophysical and cosmological arguments constrain its mass to be in the range of $m = 10^{-6} - 3 \times 10^{-3}$ eV and the global symmetry-breaking scale to lie in a window $f \approx 10^7 \,{\rm GeV} \times 0.62/m({\rm eV}) = 2 \times 10^9 - 6 \times 10^{12} \,{\rm GeV}$ [19].

We consider spherically symmetric system with metric

$$ds^2 = -N^2 dt^2 + g^2 dr^2 + r^2 d\Omega^2 \,, \tag{2}$$

where g, the radial metric, and N, the lapse, are functions of t and r with r being the circumferential radius. We introduce dimensionless coordinates and define the unit of distance, time and φ as

$$r_0 = \frac{\hbar}{mc}, \quad t_0 = \frac{\hbar}{mc^2}, \quad \varphi_0 = \frac{1}{\sqrt{4\pi G}}\,, \tag{3}$$

where c is the speed of light, G is the gravitational constant, $m = \sqrt{V_0}/f$ is the particle mass. In dimensionless units the static Klein-Gordon and Einstein equations describing the self-gravitating field φ and the metric are [20]

$$\frac{\varphi'}{g^2}\left(\frac{g^2+1}{r} - 2rg^2V\right) + \frac{\varphi''}{g^2} - \frac{\partial V}{\partial \varphi} = 0\,, \tag{4}$$

$$N' = \frac{N}{2}\left[\frac{g^2-1}{r} + r\left(\varphi'^2 - 2g^2V\right)\right]\,, \tag{5}$$

$$g' = \frac{g}{2}\left[\frac{1-g^2}{r} + r\left(\varphi'^2 + 2g^2V\right)\right]\,, \tag{6}$$

with boundary conditions

$$g(0) = g(\infty) = N(\infty) = 1\,, \quad g'(0) = N'(0) = \varphi'(0) = 0, \quad V(\varphi(\infty)) = 0\,,$$

where prime denotes $\partial/\partial r$,

$$V = \frac{1}{\alpha^2}[1 - \cos(\alpha\varphi)], \quad \alpha = \frac{1}{\sqrt{4\pi G}f} = \frac{m_{\rm pl}}{\sqrt{4\pi}f} \tag{7}$$

is the dimensionless potential and the coupling parameter respectively, $m_{\rm pl} = \sqrt{\hbar c/G} = 1.2 \times 10^{19}$ GeV is the Planck mass. The interaction potential has degenerate minima at $\varphi = 2\pi n/\alpha$, where n is an integer number. Here we show that in the limit of strong nonlinearity, $\alpha \gg 1$, equations (4)-(6) have an approximate static solution that describes a spherical bubble with surface width much smaller then its radius R. The bubble surface is an interface between two degenerate vacuum states with $\varphi = 2\pi n/\alpha$ $(r < R)$ and $\varphi = 0$ $(r > R)$. Outside the bubble (4)-(6) lead to the known Schwazschild solution

$$g^2 = \frac{1}{1 - 2M/r}, \quad N^2 = 1 - \frac{2M}{r}\,, \tag{8}$$

where M is the bubble mass in units of $m_{\rm pl}^2/m$.

Let us assume that $R \gg \alpha \gg 1$. Then, near the surface one can omit terms with $1/r$ in (4)-(6) and take $r \approx R$, we obtain

$$-2R\varphi' V + \frac{\varphi''}{g^2} - \frac{\partial V}{\partial \varphi} = 0\,, \tag{9}$$

$$N' = \frac{NR}{2}\left(\varphi'^2 - 2g^2V\right) \ , \tag{10}$$

$$g' = \frac{gR}{2}\left(\varphi'^2 + 2g^2V\right) \ . \tag{11}$$

Equations (9)–(11) can be solved analytically. Their first integral is

$$N = const, \quad \varphi'^2 = 2g^2V, \quad g' = Rg\varphi'^2 \ . \tag{12}$$

We assume $\varphi(0) = 2\pi n/\alpha$, where $n = 1, 2, 3, \ldots$ is the number of kinks at the bubble surface, and $\varphi(r)$ monotonically decreases with r. Equations (12) yield

$$\frac{1}{g} = 1 - R\int_{\varphi}^{\varphi(0)} \sqrt{2V}d\varphi, \quad \varphi' = -\frac{\sqrt{2V}}{1 - R\int_{\varphi}^{\varphi(0)} \sqrt{2V}d\varphi} \ . \tag{13}$$

For $V(\varphi)$ given by (7) the final solution is

$$\frac{4R}{\alpha^2}\ln|\sin(\alpha\varphi/2)| + \left[1 - \frac{4R}{\alpha^2}(2m-1)\right]\mathrm{arctanh}[\cos(\alpha\varphi/2)]$$

$$= \mathrm{sign}[\sin(\alpha\varphi/2)](r - R_m), \qquad \varphi \in [2\pi(n-m+1)/\alpha, 2\pi(n-m)/\alpha] \ , \tag{14}$$

where R_m is a position of the mth kink, $m = 1, 2, \ldots, n$. When the coordinate r passes through the point R_m the field $\varphi(r)$ changes from $2\pi(n-m+1)/\alpha$ to $2\pi(n-m)/\alpha$ (see Fig. 1).

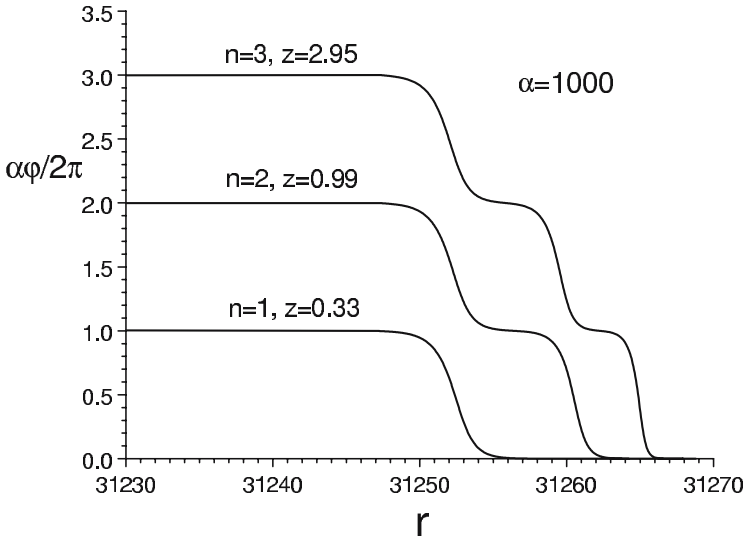

Fig. 1. Scalar field φ as a function of distance r to the bubble center for bubbles with equal radius and different quantum numbers $n = 1$, 2, 3. The unit of length is $\hbar/mc$. Note, we plot the field φ only in the vicinity of the bubble surface where it undergoes variation.

Equation (13) yields the following expression for g as a function of φ inside the bubble:

$$\frac{1}{g} = 1 - \frac{4R}{\alpha^2}[2m - 1 + \cos(\alpha\varphi/2)] \ . \tag{15}$$

Outside the bubble $\varphi = 0$, $m = n$ and $1/g = 1 - 8nR/\alpha^2$. The solution is valid if $1/g > 0$, that is $R < R_{\max} = \alpha^2/8n$. Match of the inner solution (13) with the Schwazschild solution (8) determines the mass-radius relation

$$M = 4\pi nuR^2 - 8\pi^2 n^2 u^2 R^3 \ , \tag{16}$$

where u is the surface energy density given by an integral over one potential period $u = \int \sqrt{2V} d\varphi/4\pi$. For the cosine potential (7) $u = 2/\pi\alpha^2$.

Redshift of the bubble interior $z = 1/N - 1$ can be found by matching the inner $N = const$ and the outer (8) solutions:

$$z = \frac{1}{\sqrt{1 - 2M/R}} - 1 = \frac{1}{1 - 4\pi nuR} - 1 \ . \tag{17}$$

The internal redshift monotonically increases from zero to infinity when the bubble radius R changes from zero to $R_{\max}$. Figure 2 shows the redshift of space as a function of the distance r to the bubble center. The redshift is constant in the bubble interior and monotonically decreases outside the bubble.

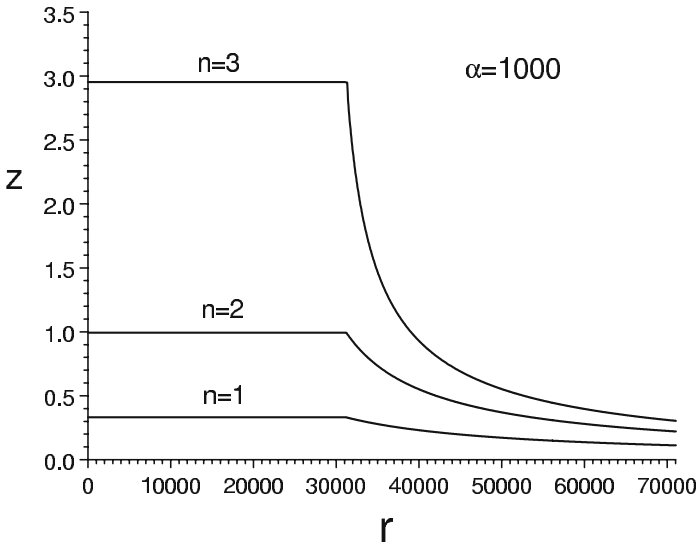

Fig. 2. Redshift z of space as a function of distance r to the bubble center for bubbles shown in Fig. 1.

2.1 Redshift Quantization

Let us make rescaling $M \to M/4\pi u$, $R \to R/4\pi u$, then (16), (17) yield

$$M = nR^2 - n^2R^3/2, \qquad z = \frac{1}{1-nR} - 1 \ . \tag{18}$$

For a given bubble mass M the redshift depends on the integer number n, which implies the redshift is quantized.

In early samples of QSOs associated with nearby spiral galaxies, Karlsson showed that the redshift distribution has a periodicity $\log(1+z_{n+1}) - \log(1+z_n) = 0.089$, where $n = 0, 1, 2, \ldots$ and $z_0 = 0.061$ [21]. It has been later confirmed by other groups [22, 15]. In a recent paper, Burbidge and Napier [16] tested for the occurrence of this periodicity in new QSO samples and found it to be present at a high confidence level. The peaks were found at $z \approx 0.30$, 0.60, 0.96, 1.41 and 1.96 in agreement with Karlsson's empirical formula. The formula also includes the peak at $z_0 = 0.061$, however, this peak does not occur for quasars, but for morphologically related objects.

The redshift periodicity is observed only in QSO samples satisfying certain selection criteria, in particular, the galaxies which are assumed to be paired to the QSOs must be *most nearby* spirals [14, 23]. This implies that redshift quantization is a property of intrinsically faint QSOs which are not detected from large distances.

It is naturally to assume that QSOs born in the same type of galaxies have approximately equal masses because their formation mechanism must be similar. Such phenomenon is well known for type Ia supernovae or neutron stars: practically all measured neutron star masses cluster around the value of $1.4\mathrm{M}_\odot$ with only a few percent deviation [24]. If dark matter bubbles are born with equal masses then, according to (18), their redshift must be quantized. For $M = 0.0601$ (in dimension units $M = 0.00752\alpha^2 m_{\rm pl}^2/m$) equations (18) have solutions for $n = 1, 2, \ldots, 8$, they are given in Table 1.

Table 1. Redshift of the bubble interior z and its radius R for $M = 0.00752\alpha^2 m_{\rm pl}^2/m$ and different kink numbers n.

n	1	2	3	4	5	6	7	8
R, in $\alpha^2\hbar/mc$	0.0329	0.0241	0.0204	0.0182	0.0168	0.0159	0.0153	0.0151
z	0.357	0.629	0.96	1.40	2.06	3.24	6.11	26.6

In Fig. 3 we plot the most recent histogram of the redshift distribution from [23] in which five peaks are clearly seen. The solid lines show the redshifts from our Table 1, they match well the observed peaks. The agreement is remarkable because the theory has only one free parameter, the bubble mass M. Such coincidence strongly suggests that the point-like quasars associated

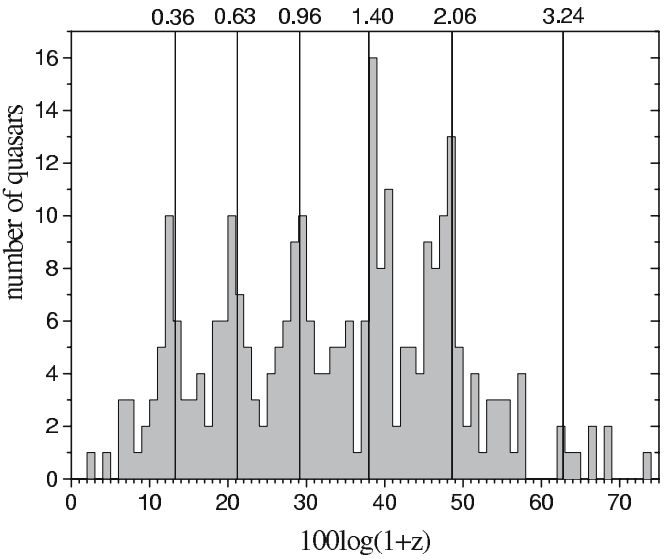

Fig. 3. Histogram of the redshift distribution of QSOs close to bright nearby active spiral galaxies or multiple QSOs with small angular separation from [23]. The solid lines represent position of the peaks from Table 1.

with nearby galaxies are dark matter bubbles composed of scalar particles with periodic interaction potential. One should mention an alternative possibility of quasar evolution. Bubbles can be originally born with the same mass and number of kinks $n = 5$ that corresponds to the 5th peak. During evolution the kinks tunnel to the bubble center and quasars sequentially decay into states with smaller n but the same mass.

For axions with $m = 0.1-3\,\mathrm{meV}$ and $f = 2\times10^9-6\times10^{10}\,\mathrm{GeV}$ (7) yields $\alpha = 5.6\times10^7 - 1.7\times10^9$. Hence, an axion bubble with the internal redshift $z = 0.36$ and $n = 1$ would have the mass $M = 3\times10^7-10^9\mathrm{M}_\odot$ and the radius $R = 3\times10^2 - 10^4 R_\odot$. Such radius range agrees with the size of the emission region expected for the intrinsically faint QSOs. Indeed, for Seyfert 1 galaxies the size of the broad-line region is $R \sim 10-100$ light days. The luminosity L of the QSOs is 5–6 orders smaller. Based on the empirical relation for Seyfert 1 galaxies $R \propto L^{1/2}$ [25], we obtain for the quasars $R \sim 10^4 R_\odot$.

2.2 Bubble Life Time

Under the influence of surface tension and gravitational attraction an initially static bubble starts to collapse. In the thin-wall approximation the initial acceleration is given by [26]

$$\ddot{R} = -\frac{2N^3}{R} - \frac{N^2 M}{(1+N)R^2}\,, \tag{19}$$

where $N = \sqrt{1-2M/R}$. For one kink thin-wall contracting bubble the conserved mass is [26]

$$M = \frac{4\pi u R^2}{\sqrt{1-(dR/d\tau)^2}} - 8\pi^2 u^2 R^3 \ , \tag{20}$$

where τ is the interior coordinate time. Based on (19), (20) one can expect a continuous contraction of the bubble to the origin on an astronomically short time scale $R/c \ll 1$yr. However, so far we treated the scalar field as classical. Quantum corrections suppress the collapse and result in appearance of long-lived bubbles. To include quantum effects it has been suggested to interpret (20) as the canonical hamiltonian of the bubble at the quantum level [27, 28, 29]. The bubble wave function $\Psi(R)$ satisfies the following stationary quantum mechanical equation in one dimension ($\hbar = 1$) [29]:

$$\left[\left(E + 8\pi^2 u^2 R^3\right)^2 + \frac{\partial^2}{\partial R^2} - 16\pi^2 u^2 R^4\right] \Psi(R) = 0 \ . \tag{21}$$

This equation possesses stationary solutions that are not possible in the classical model. Bubbles of non-negligible redshift correspond to highly excited stationary states for which the energy spectrum can be treated as quasi-continuous. At the quantum level the collapse is prevented by quantum pressure that balances the surface tension and gravitational attraction producing stationary configurations.

Let us estimate the decay time of an excited stationary state of the quantum bubble. The decay occurs by means of scalar particle emission. We estimate the decay time using the Bohr correspondence principle as the time of energy loss by the classical bubble with the radius $R(t)$ oscillating between the turning points $R(t) = R$ and $R(t) = 0$, where R is determined by (16). In the quantum picture, however, there are no such oscillations. The probability of creation a particle with the energy mc^2 by a moving bubble surface is governed by the Boltzmann factor $\exp(-mc^2/T_{\rm eff})$, where $T_{\rm eff} = a/c$ is the effective temperature and a is the acceleration of the surface [30]. For the bubble $a \approx c^2/R(t)$ and the Boltzmann factor reduces to $\exp(-R(t)/l)$ where $l = \hbar/mc$ is the surface width. Hence, emission of scalar particles is exponentially suppressed apart from small regions where $R(t) \leq l$. As a result, during one period of oscillation, $t_{\rm c} \sim R/c$, the energy loss is $\Delta E \sim (l/R)E$, which yields the bubble life time

$$t \sim \frac{R}{l} t_{\rm c} = \frac{R^2}{cl} \ . \tag{22}$$

For an axionic bubble with $R > 10^2 R_\odot$ and $l < 0.7$ cm (22) yields $t > 10^8$ yrs which is the time we need to account for the phenomenon of quasars. Indeed, if the intrinsically faint quasars cluster at a distance upto 100 - 300 kpc from the parent galaxy and their ejection speed $v \sim 0.003 - 0.04c$ [16] then the life-time turns out to be greater then $10^7 - 10^8$ yrs.

Apart from stabilization, the quantum effects lead to broadening of emission lines. An observer outside the bubble detects a line λ_0 at the wavelength $\lambda = \lambda_0(1+z)$, where $z = 1/\sqrt{1-2M/R} - 1$ is the redshift of the bubble interior. At a given bubble mass M the redshift depends on the radius R which for the quantum bubble becomes uncertain. Its distribution is determined by the square of the bubble wave function $|\Psi(R)|^2$. Hence, the emission line is detected at the redshift $z(R)$ with a probability $\propto |\Psi(R)|^2$ and, instead of a sharp line, the observer would detect a broaden peak centered near $z(R)$ corresponding to a maximum of $|\Psi(R)|^2$.

In the WKB approximation the wave function has a sharp peak near the turning point R determined by (16). Therefore, the external observer would detect a peak in the bubble radiation spectrum at the wavelength λ' as if the emission line is redshifted according to the classical (16), (17). However, the detected emission line profile $F(\lambda)$ would be different from those emitted by the atom. If for the atom $F(\lambda) \propto \delta(\lambda - \lambda_0)$ then the external observer would detect $F(\lambda) \propto \Theta(\lambda - \lambda')/\sqrt{\lambda - \lambda'}$. The line profile becomes asymmetric. However, the line width due to quantum broadening is negligible and other broadening mechanisms, e.g., atom motion, would probably wash out the quantum profile.

3 Discussion

The results obtained show that the intrinsically faint QSOs are probably bubbles of scalar field with periodic interaction potential. The observed five peaks in the quasar redshift distribution match well the theoretical result with only one free parameter, which is a strong argument in favor of our theory. The hypothetical axions fit well into the quasar picture and can account for the bubble composition.

Properties of the intrinsically faint point-like QSOs, combined with equations for the bubble mass $M = 0.00752\alpha^2 m_{\rm pl}^2/m = 2.94m(\text{eV}) \times 10^{11}\text{M}_\odot$ and the radius $R = 0.0329\alpha^2\hbar/mc = 2.73m(\text{eV}) \times 10^6 R_\odot$, allow us to determine the axion mass m. The quasar luminosity suggests that the bubble radius is larger then $10^3 R_\odot$ which yields $m > 0.4$ meV and $M > 10^8\text{M}_\odot$. From the other hand, the quasar ejection from active galaxies implies that the bubble mass M must be much smaller then the galactic mass. It is reasonable to constrain $M < 10^9\text{M}_\odot$ which leads to $m < 3\,\text{meV}$ and $R < 10^4 R_\odot$. At last, the life-time constraint $t > 10^8\,\text{yrs}$ gives $m > 0.03\,\text{meV}$. We conclude, the axion mass is $m = 0.4 - 3\,\text{meV}$. This value fits in the open window for the axion mass constrained by astrophysical and cosmological arguments [19], which unambiguously points towards the axion nature of dark matter composing the intrinsically faint point-like quasars. Current cavity search experiments in Livermore [31] and Kyoto University [19] are looking for the axion in the mass range $1 - 10\ \mu$eV which deviates by two orders of magnitude from

our result. Probably now, when the axion mass is established from quasar observations, the axion has a better chance to be discovered.

Understanding the mechanisms of quasar creation requires further detailed study. We mention only that previous three-dimensional simulation of the evolution of inhomogeneities in the axion field has demonstrated formation of bubble-like structures (see Fig. 5a in [32]). Bose-Einstein condensation of scalar particles and gravitational cooling are, probably, important processes involved in quasar nucleation [33].

At last, we mention that data on central "black hole" masses in small companion galaxies allow us to determine the axion mass more accurately and yield $m = 1.0 - 1.9$ meV. We will discuss this elsewhere. Moreover, observations show that apart from the intrinsically faint point-like objects considered here there is a subgroup of bright quasars which probably also possess noncosmological redshift. Tachyons, another dark matter candidate, can explain their nature. We discuss this in a detail paper [34].

References

1. M. Schmidt: Nature **197**, 1040 (1963)
2. H. Arp: *Quasars, redshifts and controversies*, (Interstellar Media, Berkeley 1987)
3. J.V. Narlikar: Space Sci. Rev. **50**, 523 (1989)
4. G.R. Burbidge et al.: ApJS **74**, 675 (1990)
5. G. Burbidge and A. Hewitt: In *Variability of blazars*, Eds E. Valtaoja and M. Valtonen (Cambridge University Press, Cambridge 1992), p 4
6. G. Burbidge: A&A, **309**, 9 (1996)
7. N. Benitez and E. Martinez-Gonzalez: ApJ **477**, 27 (1997)
8. H. Arp: *Seeing red: redshifts, cosmology and academic science*, (Apeiron, Montreal 1998)
9. E. M. Burbidge , G. Burbidge, H. Arp and S. Zibetti: ApJ **591**, 690 (2003)
10. H. Arp, E.M. Burbidge and G. Burbidge: A&A **414**, L37 (2004)
11. H. Arp, C.M. Gutiérrez and M. López-Corredoira: A&A **418**, 877 (2004)
12. H. Arp et al.: A&A **391**, 833 (2002)
13. P. Galianni et al.: prepint astro-ph/0409215
14. K.G. Karlsson: A&A **239**, 50 (1990)
15. H. Arp, H.G. Bi, Y. Chu and X. Zhu: A&A **239**, 33 (1990)
16. G. Burbidge and W.M. Napier: AJ **121**, 21 (2001)
17. E. Hawkins, S.J. Maddox and M.R. Merrifield: MNRAS **336**, L13 (2002)
18. C.T. Hill and G.G. Ross: Nucl. Phys. B**311**, 253 (1988)
19. R. Bradley et al.: Rev. Mod. Phys. **75**, 777 (2003)
20. E. Seidel and W. M. Suen: Phys. Rev. D **42**, 384 (1990)
21. K.G. Karlsson: A&A **13**, 333 (1971); **58**, 237 (1977)
22. J.M. Barnothy and M.F. Barnothy: PASP **88**, 837 (1976)
23. W.M. Napier and G. Burbidge: MNRAS **342**, 601 (2003)
24. N.K. Glendenning: *Compact Stars: Nuclear Physics, Particle Physics, and General Relativity*, 2nd edn (Springer Verlag, New York 2000)

25. T.G. Wang and X.G. Zhang: MNRAS **340**, 793 (2003)
26. S. K. Blau, E.I. Guendelman and A.H. Guth: Phys. Rev. D **35**, 1747 (1987)
27. V.A. Berezin et al.: Phys. Lett. B **212**, 415 (1988)
28. A. Aurilia and E. Spallucci: Phys. Lett. B **251**, 39 (1990)
29. A. Aurilia, R. Balbinot and E. Spallucci: Phys. Lett. B **262**, 222 (1991)
30. A. Gorsky and K. Selivanov: Phys. Rev. D **62**, 071702 (2000)
31. S.J. Asztalos et al.: Phys. Rev. D **69**, 011101(R) (2004)
32. E.W. Kolb and I.I. Tkachev: Phys. Rev. D **49**, 5040 (1994)
33. E. Seidel and W.M. Suen: Phys. Lett. **72**, 2516 (1994)
34. A.A. Svidzinsky: preprint astro-ph/0409064

Quantum Theory of Neutrino Spin-Light in a Dense Matter

Alexander Grigoriev[1], Alexander Studenikin[1] and Alexei Ternov[2]

[1] Department of Theoretical Physics, Moscow State University, 119992 Moscow, Russia
studenik@srd.sinp.msu.ru

[2] Department of Theoretical Physics, Moscow Institute for Physics and Technology, 141700 Dolgoprudny, Russia
a_ternov@mail.ru

Summary. The quantum theory of the spin light of neutrino ($SL\nu$) exactly accounting for the effect of the background matter is developed. Contrary to the already performed studies of the $SL\nu$, in this paper we derive expressions for the $SL\nu$ rate and power and also for the emitted photon's energy that are valid for an arbitrary value of the matter density including the case of a very dense matter. The spatial distribution of the radiation power and the dependence of the emitted photon's energy on the direction of radiation are also studied in detail for the first time. We analyze the $SL\nu$ polarization properties and show that in a wide range of the neutrino momentum and density of matter the $SL\nu$ radiation is nearly totally circular polarized. Conditions for the effective $SL\nu$ photon propagation in the electron plasma are discussed.

There are various mechanisms of an electromagnetic radiation that can be produced by a massive neutrino moving in a background environments (see, for instance, [1])[3]. Recently within the quasi-classical approach we have shown [2] that a massive neutrino moving in the background matter can emit a new type of electromagnetic radiation. This radiation has been named as "the spin-light of neutrino" ($SL\nu$) in matter. Developing the quantum theory of this phenomenon [3, 4], we have demonstrated that the $SL\nu$ appears due to the two underlying phenomena: (i) the shift of the neutrino energy levels in matter, that are different for the two opposite neutrino helicity states, and (ii) the radiation of the $SL\nu$ photon in the process of neutrino transition from the "exited" helicity state to the low-lying helicity state in matter. However, the calculations of the transition rate and radiation power have been performed in the limit of a low matter density and, therefore, the evaluation of the consistent quantum theory of the $SL\nu$ has still remained an open issue.

In this paper we develop the quantum theory of the neutrino spin-light exactly accounting for the effect of the background matter and obtain the expressions for the $SL\nu$ rate and power that are valid for any value of the matter density parameter. Thus, we present below a consistent quantum theory of

[3] A brief classification of the known mechanisms of the electromagnetic radiation by a neutrino is given in the first paper of [2]

the spin light of neutrino in matter. Within the developed theory we also obtain the expression for the emitted photon energy that is valid in the case of a very dense matter. We also consider the polarization properties of the emitted photons and find out that in a wide range of the neutrino momentum and matter density parameter the $SL\nu$ is circularly polarized. We also discuss below restrictions on the emitted photon propagation that are set by the background electron plasma.

To account for the influence of the background matter on neutrinos we use the approach [3] (similar to the Furry's representation in quantum electrodynamics) that is based on the exact solutions of the modified Dirac equation for a neutrino in matter:

$$\Big\{i\gamma_\mu\partial^\mu - \frac{1}{2}\gamma_\mu(1+\gamma_5)f^\mu - m\Big\}\Psi(x) = 0\,, \tag{1}$$

In the case of matter composed of electrons

$$f^\mu = \frac{G_F}{\sqrt{2}}(1+4\sin^2\theta_W)j^\mu\,, \tag{2}$$

where the electrons current j^μ is given by

$$j^\mu = (n, n\mathbf{v})\,, \tag{3}$$

θ_W , n, $\mathbf{v}$, being, respectively, the Weinberg angle, the number density of the background electrons, the speed of the reference frame in which the mean momentum of the electrons is zero.

Note that the modified effective Dirac equations for a neutrino interacting with various background environments were previously used in [5, 6, 7, 8, 9, 10, 11] for the study of the neutrino dispersion relations and derivation of the neutrino oscillation probabilities in matter. On the same basis the neutrino decay into an antineutrino and a light scalar particle (majoron), as well as the corresponding process of the majoron decay into two neutrinos or antineutrinos, were studied in the presence of matter [12, 13, 14]. If we neglect the contribution of the neutral-current interaction and possible effects of motion and polarization of the matter then from (1) we can get corresponding equations for the left-handed and right-handed chiral components of the neutrino field derived in [6]. The similar equation for a neutrino in the background of non-moving and unpolarized neutrons was also used in [15, 16].

As it has been shown [3] the solutions of (1) are given by

$$\Psi_{\varepsilon,\mathbf{p},s}(\mathbf{r},t) = \frac{e^{-i(E_\varepsilon t - \mathbf{pr})}}{2L^{\frac{3}{2}}} \begin{pmatrix} \sqrt{1+\frac{m}{E_\varepsilon-\alpha m}}\sqrt{1+s\frac{p_3}{p}} \\ s\sqrt{1+\frac{m}{E_\varepsilon-\alpha m}}\sqrt{1-s\frac{p_3}{p}}\;e^{i\delta} \\ s\varepsilon\sqrt{1-\frac{m}{E_\varepsilon-\alpha m}}\sqrt{1+s\frac{p_3}{p}} \\ \varepsilon\sqrt{1-\frac{m}{E_\varepsilon-\alpha m}}\sqrt{1-s\frac{p_3}{p}}\;e^{i\delta} \end{pmatrix}\,, \tag{4}$$

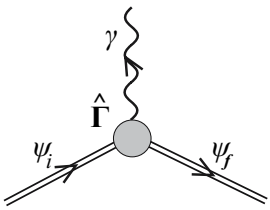

Fig. 1. The effective diagram of the $SL\nu$ photon emission process. The broad lines correspond to the initial and final neutrino states in the background matter.

where the energy spectrum

$$E_\varepsilon = \varepsilon\sqrt{\mathbf{p}^2\Big(1 - s\alpha\frac{m}{p}\Big)^2 + m^2} + \alpha m \;, \tag{5}$$

$$\alpha = \frac{1}{2\sqrt{2}}\tilde{G}_F\frac{n}{m} \;, \quad \tilde{G}_F = G_F(1 + 4\sin^2\theta_W) \tag{6}$$

depends on the neutrino helicity $s = \pm 1$ which splits the solutions into the two branches that in the limit of the vanishing matter density, $\alpha \to 0$, reproduce the positive and negative-frequency solutions for the Dirac equation in vacuum.

The amplitude of the $SL\nu$ (see Fig. 1) calculated within the developed quantum theory is given by (see also [3])

$$\begin{gathered} S_{fi} = -\mu\sqrt{4\pi}\int d^4x\bar{\psi}_f(x)(\hat{\mathbf{\Gamma}}\mathbf{e}^*)\frac{e^{ikx}}{\sqrt{2\omega L^3}}\psi_i(x) \;, \\ \hat{\mathbf{\Gamma}} = i\omega\big\{\big[\mathbf{\Sigma}\times\boldsymbol{\varkappa}\big] + i\gamma^5\mathbf{\Sigma}\big\} \;, \end{gathered} \tag{7}$$

where μ is the neutrino magnetic moment, ψ_i and ψ_f are given by (4) exact solutions of the equation (1) for the initial and final neutrino states, $k^\mu = (\omega, \mathbf{k})$ and $\mathbf{e}^*$ are the photon momentum and polarization vector, $\boldsymbol{\varkappa} = \mathbf{k}/\omega$ is the unit vector pointing the direction of the emitted photon propagation.

The integration in (7) with respect to time yields

$$S_{fi} = -\mu\sqrt{\frac{2\pi}{\omega L^3}}2\pi\delta(E' - E + \omega)\int d^3x\bar{\psi}_f(\mathbf{r})(\hat{\mathbf{\Gamma}}\mathbf{e}^*)e^{i\mathbf{kr}}\psi_i(\mathbf{r}) \;, \tag{8}$$

where the delta-function stands for the energy conservation, E and E' are the energies of the initial and final neutrino states in matter. Performing the integrations over the spatial co-ordinates, we can recover the delta-functions for the three components of the momentum. Finally, we get the law of the energy-momentum conservation for the considered process,

$$E = E' + \omega \;, \quad \mathbf{p} = \mathbf{p}' + \boldsymbol{\varkappa} \;, \tag{9}$$

where $\mathbf{p}$ and $\mathbf{p}'$ are the initial and final neutrino momenta, respectively. From (9) it follows that the emitted photon energy ω exhibits the critical dependence on the helicities of the initial and final neutrino states. In the case of electron neutrino moving in matter composed of electrons α is positive. Thus, it follows that the only possibility for the $SL\nu$ to appear is provided in the case when the neutrino initial and final states are characterized by $s_i = -1$ and $s_f = +1$, respectively. We can also conclude that in the considered process the relativistic left-handed neutrino is converted to the right-handed neutrino. A discussion on the main properties of the $SL\nu$ emitted by different flavour neutrinos moving in matter composed of electrons, protons and neutrons can be found in [3] (see also [17]).

The emitted photon energy in the considered case ($s_i = -s_f = -1$) obtained as an exact solution of the equations (9) reads

$$\omega = \frac{2\alpha m p\left[(E-\alpha m)-(p+\alpha m)\cos\theta\right]}{(E-\alpha m-p\cos\theta)^2-(\alpha m)^2}\ , \tag{10}$$

where θ is the angle between $\boldsymbol{\varkappa}$ and the direction of the initial neutrino propagation. In the case of not very high density of matter, when the parameter $\alpha \ll 1$, we can expand the photon energy (10) over the α and in the liner approximation get the result of [3, 4]:

$$\omega = \frac{1}{1-\beta\cos\theta}\omega_0\ , \tag{11}$$

where

$$\omega_0 = \frac{\tilde{G}_F}{\sqrt{2}} n\beta\ , \tag{12}$$

β is the neutrino speed in vacuum.

Using the wave functions (4) for the neutrino initial and final states in matter we calculate the spin light transition rate exactly accounting for the matter density parameter and get

$$\Gamma = \int_0^\pi \frac{\omega^3}{1+\tilde{\beta}' y} S\sin\theta d\theta\ , \tag{13}$$

where

$$S = (\tilde{\beta}\tilde{\beta}'+1)(1-y\cos\theta)-(\tilde{\beta}+\tilde{\beta}')(\cos\theta-y)\ . \tag{14}$$

Here we use the notations

$$\tilde{\beta} = \frac{p+\alpha m}{E-\alpha m},\quad \tilde{\beta}' = \frac{p'-\alpha m}{E'-\alpha m}\ , \tag{15}$$

where the final neutrino energy and momentum are, respectively,

$$E' = E-\omega\ ,\quad p' = K\omega - p\ , \tag{16}$$

and

$$y = \frac{\omega - p\cos\theta}{p'}, \quad K = \frac{E - \alpha m - p\cos\theta}{\alpha m} \ . \tag{17}$$

Performing the integration in (13), we obtain for the $SL\nu$ rate in matter

$$\begin{aligned}\Gamma = & \frac{1}{2\left(E-p\right)^2\left(E+p-2\alpha m\right)^2\left(E-\alpha m\right)p^2} \\ & \times\left\{\left(E^2-p^2\right)^2\left(p^2-6\alpha^2m^2+6E\alpha m-3E^2\right)\left(\left(E-2\alpha m\right)^2-p^2\right)^2\right. \\ & \times\ln\left[\frac{\left(E+p\right)\left(E-p-2\alpha m\right)}{\left(E-p\right)\left(E+p-2\alpha m\right)}\right]+4\alpha mp\left[16\alpha^5m^5E\left(3E^2-5p^2\right)\right. \\ & -8\alpha^4m^4\left(15E^4-24E^2p^2+p^4\right)+4\alpha^3m^3E\left(33E^4-58E^2p^2+17p^4\right) \\ & -2\alpha^2m^2\left(39E^2-p^2\right)\left(E^2-p^2\right)^2+12\alpha mE\left(2E^2-p^2\right)\left(E^2-p^2\right)^2 \\ & \left.\left.-\left(3E^2-p^2\right)\left(E^2-p^2\right)^3\right]\right\} \ , \end{aligned} \tag{18}$$

where the energy of the initial neutrino is given by (5) with $\varepsilon = -s_i = 1$.

As it follows from (18), the $SL\nu$ rate is a rather complicated function of the neutrino momentum p and mass m, it also non-trivially depends on the matter density parameter α. In the limit of a low matter density, $\alpha \ll 1$, we get

$$\Gamma \simeq \frac{64}{3}\frac{\mu^2\alpha^3p^3m}{E_0} \ , \tag{19}$$

where $E_0 = \sqrt{p^2+m^2}$. The obtained expression is in agreement with our results of [2, 3, 4]. Note that the considered limit of $\alpha \ll 1$ can be appropriate even for a very dense media of neutron stars with $n \sim 10^{33}\ \ cm^{-3}$ because $\frac{1}{2\sqrt{2}}\tilde{G}_F n \sim 1\ eV$ for a medium characterized by $n = 10^{37}\ cm^{-3}$.

Let us consider the $SL\nu$ rate for the different limiting values of the neutrino momentum p and matter density parameter α. In the relativistic case $p \gg m$ from (18) we get

$$\Gamma = \begin{cases} \frac{64}{3}\mu^2\alpha^3p^2m \ , & \text{for } \alpha \ll \frac{m}{p} \ , \\ 4\mu^2\alpha^2m^2p \, , & \text{for } \frac{m}{p} \ll \alpha \ll \frac{p}{m} \ , \\ 4\mu^2\alpha^3m^3 \ , & \text{for } \alpha \gg \frac{p}{m} \ . \end{cases} \tag{20}$$

In the opposite case $p \ll m$ we have

$$\Gamma = \begin{cases} \frac{64}{3}\mu^2\alpha^3p^3 \ , & \text{for } \alpha \ll 1, \\ \frac{512}{5}\mu^2\alpha^6p^3 \ , & \text{for } 1 \ll \alpha \ll \frac{m}{p} \ , \\ 4\mu^2\alpha^3m^3 \ , & \text{for } \alpha \gg \frac{m}{p} \ . \end{cases} \tag{21}$$

On the basis of (7) we also derive the $SL\nu$ radiation power:

$$I = \mu^2\int_0^\pi \frac{\omega^4}{1+\tilde{\beta}'y}S\sin\theta d\theta \ . \tag{22}$$

Performing the integration in (22), we obtain the total $SL\nu$ radiation power in matter

$$
\begin{aligned}
I =& \frac{5}{2\left(E-p\right)^3\left(E+p-2\alpha m\right)^3 p^2} \times \Bigg\{ (E+p)^2(E-m)^3(E+p-2\alpha m)^3 \\
& \times (E-p-2\alpha m)^2\Big(2\alpha^2 m^2 - 2\alpha m(E+\frac{1}{5}p) + E^2 - \frac{3}{5}p^2\Big) \\
& \times \ln\left(\frac{(2\alpha m - p - E)(E-p)}{(2\alpha m + p - E)(E+p)}\right) \\
& -4\alpha m p\Bigg(32\alpha^6 m^6\Big(E^4 - pE^3 - \frac{5}{3}p^2E^2 + \frac{5}{3}p^3E + \frac{8}{15}p^4\Big) \\
& -96\alpha^5 m^5\Big(E^5 - \frac{23}{30}pE^4 - \frac{83}{45}p^2E^3 + \frac{11}{9}p^3E^2 + \frac{38}{45}p^4E - \frac{1}{10}p^5\Big) \\
& +128\alpha^4 m^4\Big(E^6 - \frac{47}{80}pE^5 - \frac{511}{240}p^2E^4 + \frac{127}{120}p^3E^3 + \frac{157}{120}p^4E^2 \\
& \quad - \frac{89}{240}p^5E - \frac{7}{48}p^6\Big) \\
& -96(E^2-p^2)\alpha^3 m^3\Big(E^5 - \frac{53}{120}pE^4 - \frac{3}{2}p^2E^3 + \frac{89}{180}p^3E^2 \\
& \quad + \frac{47}{90}p^4E - \frac{19}{360}p^5\Big) \\
& +42(E^2-p^2)^2\alpha^2 m^2\Big(E^4 - \frac{32}{105}pE^3 - \frac{314}{315}p^2E^2 + \frac{4}{21}p^3E + \frac{17}{105}p^3\Big) \\
& -10\alpha m(E^2-p^2)^3\Big(E^3 - \frac{4}{25}pE^2 - \frac{17}{25}p^2E + \frac{2}{25}p^3\Big) \\
& + (E^2-p^2)^4\Big(E^2 - \frac{3}{5}p^2\Big)\Bigg)\Bigg\} . \qquad (23)
\end{aligned}
$$

In the case $\alpha \ll 1$, we get

$$I \simeq \frac{128}{3}\mu^2\alpha^4 p^4 \qquad (24)$$

in agreement with [2, 3, 4].

Let us now consider the $SL\nu$ radiation power for the different limiting values of the neutrino momentum p and matter density parameter α. From (22) we have for the relativistic neutrino, $p \gg m$,

$$I = \begin{cases} \frac{128}{3}\mu^2\alpha^4 p^4 , & \text{for } \alpha \ll \frac{m}{p} , \\ \frac{4}{3}\mu^2\alpha^2 m^2 p^2 , & \text{for } \frac{m}{p} \ll \alpha \ll \frac{p}{m} , \\ 4\mu^2\alpha^4 m^4 , & \text{for } \alpha \gg \frac{p}{m} , \end{cases} \qquad (25)$$

and for the non-relativistic neutrino, $p \ll m$,

$$I = \begin{cases} \frac{128}{3}\mu^2\alpha^4 p^4 , & \text{for } \alpha \ll 1 , \\ \frac{1024}{3}\mu^2\alpha^8 p^4 , & \text{for } 1 \ll \alpha \ll \frac{m}{p} , \\ 4\mu^2\alpha^4 m^4 , & \text{for } \alpha \gg \frac{m}{p} . \end{cases} \qquad (26)$$

Note that the obtained $SL\nu$ rate and radiation power for $p \gg m$ and $\alpha \gg \frac{m}{p}$ are in agreement with [17].

From the expressions for the $SL\nu$ rate and total power it is possible to get an estimation for the emitted photons average energy:

$$\langle\omega\rangle = \frac{I}{\Gamma} \,. \tag{27}$$

In the relativistic case $p \gg m$ we get

$$\langle\omega\rangle \simeq \begin{cases} 2\alpha\frac{p^2}{m} \,, & \text{for } \alpha \ll \frac{m}{p} \,, \\ \frac{1}{3}p \,, & \text{for } \frac{m}{p} \ll \alpha \ll \frac{p}{m} \,, \\ \alpha m \,, & \text{for } \alpha \gg \frac{p}{m} \,. \end{cases} \tag{28}$$

For the matter parameter $\alpha \gg \frac{m}{p}$ we again confirm here the result obtained in [17]. In the non-relativistic case, $p \ll m$, we have for the emitted photon average energy

$$\langle\omega\rangle \simeq \begin{cases} 2\alpha p \,, & \text{for } \alpha \ll 1 \,, \\ \frac{10}{3}\alpha^2 p \,, & \text{for } 1 \ll \alpha \ll \frac{m}{p} \,, \\ \alpha m \,, & \text{for } \alpha \gg \frac{m}{p} \,. \end{cases} \tag{29}$$

We should like to note that for a wide range of the neutrino momentum p and density parameter α the $SL\nu$ power is collimated along the direction of the neutrino propagation. The form of the radiation power spatial distribution calculated with use of (22) in the case $p > m$ for low and high matter density are shown in Figs. 2, 3, respectively. As it follows from these figures, the shape of the distribution depends on the density of matter. The shape of the spatial distribution of the radiation changes from the projector-like to the cap-like one with increase of the matter density. From (22) we derive, that in the case of $p \gg m$ for a wide range of the matter densities, $\alpha \ll \frac{p}{m}$, the direction of the maximum in the spatial distribution of the radiation power is characterized by the angle

$$\cos\theta_{max} \simeq 1 - \frac{2}{3}\alpha\frac{m}{p} \,. \tag{30}$$

It follows that in a dense matter the $SL\nu$ radiation in the direction of the initial neutrino motion is strongly suppressed, whereas there is a lighted ring on the plane perpendicular to the neutrino motion. Note that the rate of the matter-induced neutrino majoron decay, as it was shown in the second paper of [12], has the similar angular distribution.

The emitted photon polarization, together with the discussed above transition rate, emission power and photon spectrum, is a very important characteristic of the $SL\nu$. In our previous studies [3, 4] we have considered the $SL\nu$ in the low matter density limit, $\alpha \ll 1$, with account for the photon linear

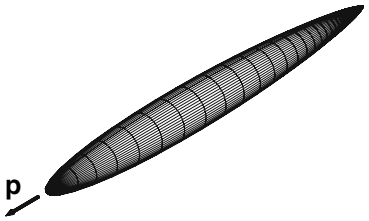

Fig. 2. The spatial distribution of the $SL\nu$ radiation power for the case $p/m = 5,\ \alpha m = 0.01$.

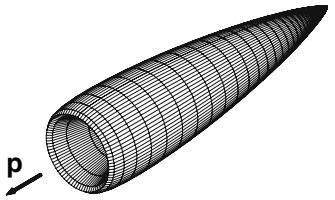

Fig. 3. The spatial distribution of the $SL\nu$ radiation power for the case $p/m = 10^3,\ \alpha m = 100$.

and circular polarizations. Let us now discuss the polarization properties of the $SL\nu$ in the case of an arbitrary value of the matter density parameter α. To specify the two different linear photon polarizations we introduce the two orthogonal vectors

$$\mathbf{e}_1 = \frac{[\boldsymbol{\varkappa} \times \mathbf{j}]}{\sqrt{1-(\boldsymbol{\varkappa}\mathbf{j})^2}}, \quad \mathbf{e}_2 = \frac{\boldsymbol{\varkappa}(\boldsymbol{\varkappa}\mathbf{j}) - \mathbf{j}}{\sqrt{1-(\boldsymbol{\varkappa}\mathbf{j})^2}}\ , \tag{31}$$

where $\mathbf{j}$ is the unit vector pointing in the direction of the initial neutrino propagation. Decomposing the neutrino transition amplitude (7) in contributions from the photons of the two linear polarizations determined by the vectors $\mathbf{e}_1$ and $\mathbf{e}_2$, we get

$$I^{(1),(2)} = \mu^2 \int_0^\pi \frac{\omega^4}{1+\beta' y} \left(\frac{1}{2} S \mp \Delta S\right) \sin\theta d\theta\ , \tag{32}$$

where

$$\Delta S = \frac{1}{2} \frac{m^2 p \sin^2\theta}{(E' - \alpha m)(E - \alpha m) p'}\ . \tag{33}$$

In the low matter density case $\alpha \ll 1$ the total radiation power of the linearly polarized photons reads

$$I^{(1),(2)} \simeq \frac{64}{3} \left(1 \mp \frac{1}{2}\right) \mu^2 \alpha^4 p^4\ , \tag{34}$$

in agreement with [3, 4]. Thus, the radiation powers for the two liner polarizations differs by a factor of three. On the contrary, in all other cases the

radiation powers for the two polarizations, $\mathbf{e}_1$ and $\mathbf{e}_2$, are of the same order,

$$I^{(1)} \simeq I^{(2)} \simeq \frac{1}{2}\big(I^{(1)} + I^{(2)}\big) \,. \tag{35}$$

It is also possible to decompose the radiation power for the circular polarized photons. The two orthogonal vectors

$$\mathbf{e}_l = \frac{1}{\sqrt{2}}(\mathbf{e}_1 + il\mathbf{e}_2) \tag{36}$$

describe the two photons circular polarizations ($l = \pm 1$ corresponds to the right and left photon circular polarizations, respectively). For the radiation power of the circular-polarized photons we obtain

$$I^{(l)} = \mu^2 \int_0^\pi \frac{\omega^4}{1+\beta' y} S_l \sin\theta d\theta \,, \tag{37}$$

where

$$S_l = \frac{1}{2}\,(1 + l\beta')\,(1 + l\beta)\,(1 - l\cos\theta)\,(1 + ly) \,. \tag{38}$$

In the limit of low matter density, $\alpha \ll 1$, we get for the power

$$I^{(l)} \simeq \frac{64}{3}\mu^2\alpha^4 p^4 \left(1 - l\frac{p}{2E_0}\right) \,. \tag{39}$$

In this limiting case the radiation power of the left-polarized photons exceeds that of the right-polarized photons

$$I^{(-1)} > I^{(+1)} \,. \tag{40}$$

In particular, this result is also valid for the non-relativistic neutrino, $p \ll m$, for a low density with $\alpha \ll 1$.

It is remarkable that in the most interesting case of a rather dense matter ($\alpha \gg \frac{m}{p}$ for $p \gg m$ and $\alpha \gg 1$ for $p \ll m$), the main contribution to the power is provided by the right-polarized photons, whereas the emission of the left-polarized photons is suppressed:

$$I^{(+1)} \simeq I, \tag{41}$$

$$I^{(-1)} \simeq 0 \,. \tag{42}$$

Thus, we conclude that in a dense matter the $SL\nu$ photons are emitted with nearly total right-circular polarization.

Finally, we should like to discuss in some detail restrictions on the propagation of the $SL\nu$ photons that are set by the presence of the background electron plasma in the case of $p \gg m$ for the density parameter $\frac{m}{p} \ll \alpha \ll \frac{p}{m}$. Only the photons with energy that exceeds the plasmon frequency

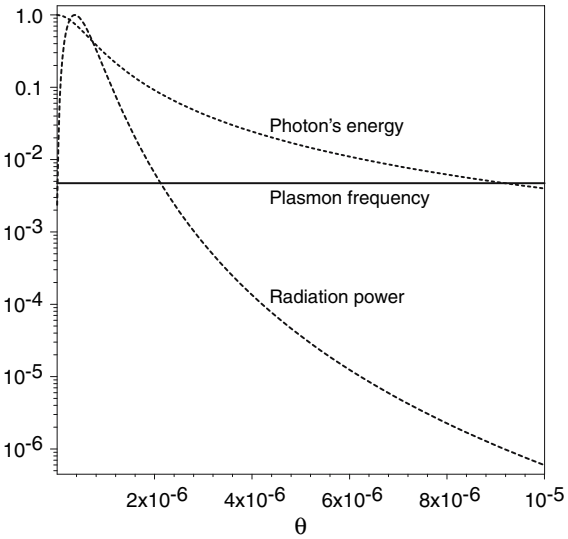

Fig. 4. The angular dependence of the emitted photon's energy and radiation power for the set of parameters: $m = 1\ eV, p = 100\, MeV, n = 10^{32}\, cm^{-3}$. The solid line denote the energy level that corresponds to the plasmon frequency.

$$\omega_{pl} = \sqrt{\frac{4\pi e^2}{m_e} n}\ , \tag{43}$$

can propagate in the plasma (here $e^2 = \alpha_{QED}$ is the fine-structure constant and m_e is the mass of the electron). From (10) and (30) it follows that the photon energy and the radiation power depend on the direction of the radiation. We can conclude that the maximal value of the photon energy,

$$\omega_{max} = p\ , \tag{44}$$

and the energy of the photon emitted in the direction of the maximum radiation power,

$$\omega(\theta_{max}) = \frac{3}{4} p\ , \tag{45}$$

are of the same order in the considered case. For the relativistic neutrino and rather dense matter the angle θ_{max}, at which the radiation power (22) has its maximum, and the angle of the maximal value (44) of the photon energy are both very close to zero (to illustrate this we show in Fig. 4 the photon energy and radiation power angular distributions for the particular case of $m = 1\, eV, p = 100\, MeV$ and $n = 10^{32}\ cm^{-3}$). In addition, as it follows from (28), the overage photon energy $\langle\omega\rangle = \frac{1}{3} p$ is also of the order of ω_{max} and $\omega(\theta_{max})$. Therefore, the effective $SL\nu$ photon energy reasonably exceeds the plasmon frequency (43) if the following condition is fulfilled:

$$p \gg p_{min} = 3.5 \times 10^4 \left(\frac{n}{10^{30}\, cm^{-3}} \right)^{1/2} eV \ . \tag{46}$$

The $SL\nu$ photon emitted by a neutrino with the momentum $p \gg p_{min}$ freely propagates through the plasma. For $n \sim 10^{33}\ cm^{-3}$ we have $p_{min} \sim 1\, MeV$.

The investigated properties of the neutrino spin light in matter (i.e., the spatial distribution of the radiation power and the angular dependence of the emitted photon's energy, as well as nearly total circular polarization of the radiation) might be important for the experimental identification of the $SL\nu$ from different astrophysical and cosmology objects and media. In conclusion, we should like to note that for the Majorana neutrino (discussion on this item can be found in [18, 19]), which has no magnetic moment [20, 21], the spin light radiation cannot be produced if not to consider the possibility of the neutrino flavour conversion due to the nonzero transition moment.

References

1. A. Ioannisiam, G. Raffelt: Phys. Rev. D **55** 7038 (1997)
2. A. Lobanov, A. Studenikin: Phys. Lett. **564** 27 (2003); Phys. Lett. B **601** 171 (2004)
3. A. Studenikin, A. Ternov: Phys. Lett. B **608** 107 (2005), hep-ph/0410297, hep-ph/0412408
4. A. Studenkin, A. Ternov, in: *Proc. of the 13th Int. Seminar on High Energy Physics "Quarks-2004"*, ed by D. Levkov, V. Matveev and V. Rubakov (Publ. Department of Institute of Nuclear Physics RAS, Moscow 2004)
5. L.N. Chang, R.K. Zia: Phys. Rev. D **38** 1669 (1988); Lett. **64** 115 (1990)
6. J. Pantaleone: Phys. Lett. B **268** 227 (1991); Phys. Rev. D **46** 510 (1992)
7. K. Kiers, N. Weiss: Phys. Rev. D **56** 5776 (1997); K. Kiers, M. Tytgat: Phys. Rev. D **57** 5970 (1998)
8. P. Mennheim: Phys, Rev. D **37** 1935 (1988)
9. D. Nötzold, G. Raffelt: Nucl. Phys. B **307** 924 (1988)
10. J. Nieves: Phys. Rev. D **40** 866 (1989)
11. W. Haxton, W-M. Zhang: Phys. Rev. D **43** 2484 (1991)
12. Z. Berezhiani, M. Vysitsky: Phys. Rev. B **199** 281 (1987); Z. Berezhiani, A. Smirnov: Phys. Rev. B **220** 279 (1989)
13. C. Giunti, C.W. Kim, U.W. Lee, W.P. Lam: Phys. Rev. D **45** 1557 (1992)
14. Z. Berezhiani, A. Rossi: Phys. Lett. B **336** 439 (1994)
15. M. Kachelriess: Phys. Lett. B **426** 89 (1998)
16. A. Kusenko, M. Postma: Phys. Lett. B **545** 238 (2002)
17. A. Lobanov: hep-ph/0411342
18. H. Klapdor-Kleingrothaus, I. Krivosheina, A. Dietz, O. Chkvorets: Phys. Lett. B **568** 198 (2004)
19. G. Altarelli: Neutrino-2004 Concluding Talk, Presented at *XXI International Confrence on Neutrino Physics and Astrophysics*, 14–19 June, 2004, Paris; hep-ph/0410101
20. I. Kobzarev, L. Okun: On electomagnetic and gravitatinal interaction of Majorana Particles. In: *Problems of Theoretical Physics. A Memorial Volume to Igor E. Tamm,* (Nakula, Moscow 1972) P. 219
21. B. Kayser, A. Goldhaber: Phys. Rev. D **28** 2341 (1983)

Part V

SUSY/SUGRA Phenomenology in Dark Matter, New Symmetries

Upper Limits on Sparticle Masses from WMAP Dark Matter Constraints with Modular Invariant Soft Breaking

Utpal Chattopadhyay[1] and Pran Nath[2]

[1] Department of Theoretical Physics, Indian Association for the Cultivation of Sciences, Jadavpur, Kolkata 700032, India
tpuc@iacs.res.in
[2] Department of Physics, Northeastern University, Boston, MA, 02115, USA
nath@neu.edu

An analysis of dark matter within the framework of modular invariant soft breaking is given. In such scenarios inclusion of the radiative electroweak symmetry breaking constraint determines $\tan\beta$ which leads to a more constrained analysis. It is shown that for μ positive for this constrained system the WMAP data leads to upper limits on sparticle masses that lie within reach of the LHC with also the possibility that some sparticles may be accessible at RUNII of the Tevatron.

1 Introduction

In this talk we will focus on modular invariant soft breaking and an analysis of dark matter within this framework [1]. We will then show the constraints of WMAP [2, 3], the flavor changing neutral current constraint arising from $b \to s + \gamma$[4, 5, 6, 7] and the constraints of radiative electroweak symmetry breaking (REWSB) put stringent limits on the sparticle masses. Specifically we will show that for the case of $\mu > 0$ the WMAP constraints lead to upper limits on sparticle masses which all lie within the reach of the Large Hadron Collider (LHC). Further, it is found that some of these particles may also lie within reach of RUNII of the Tevatron. An analysis of dark matter detection rates is also given and it is shown that for $\mu > 0$ the WMAP data leads to direct detection rates which lie within reach of the current and the next generation of dark matter detectors [8, 9, 10, 11, 12, 13, 14]. For the case of $\mu < 0$ the detection rates will be accessible to the future dark matter detectors for a part of the allowed parameter space of the models with modular invariant soft breaking and consistent with WMAP and the FCNC constraints. The outline of the rest of the paper is as follows: In Sect. 2 we give a brief discussion of modular invariant soft breaking and a determination of $\tan\beta$ with radiative electroweak symmetry breaking constraints. In Sect. 3 we give an analysis of the satisfaction of the relic density constraints consistent with WMAP and upper limits on sparticle masses for $\mu > 0$. In Sect. 4 we discuss the direct detection rates. Conclusions are given in Sect. 5.

2 Modular Invariant Soft Breaking

We begin with string theory motivation for considering a modular invariant low energy theory. It is well known that in orbifold string models one has a so called large radius- small radius symmetry

$$R \to \alpha'/R \tag{1}$$

More generally one has an $SL(2,Z)$ symmetry and such a symmetry is valid even non-perturbatively which makes it very compelling that this symmetry survives in the low energy theory. In formulating an effective low energy theory it is important to simulate as much of the symmetry of the underlying string theory as possible. This provides the motivation for considering low energy effective theories with modular invariance [15, 16, 17, 18]. With this in mind we consider an effective four dimensional theory arising from string theory assumed to have a target space modular $SL(2,Z)$ invariance

$$\begin{aligned} T_i \to T_i' &= \frac{a_i T_i - i b_i}{i c_i T_i + d_i} \ , \\ \bar{T_i} \to \bar{T_i'} &= \frac{a_i \bar{T_i} + i b_i}{-i c_i \bar{T_i} + d_i} \ , \\ (a_i d_i - b_i c_i) = 1, \quad & (a_i, b_i, c_i, d_i \in Z) \ . \end{aligned} \tag{2}$$

Under the above transformation the superpotential and the Kähler potential transform but the combination

$$G = K + ln(WW^{\dagger}) \tag{3}$$

is invariant. Further, the scalar potential V defined by

$$V = e^G((G^{-1})^i_j G_i G^j + 3) + V_D$$

is also invariant under modular transformations. We require that V_{soft} also maintain modular invariance and indeed this invariance will naturally be maintained in our analysis. Typically chiral fields, i.e., quark, leptons and Higgs fields will transform under modular transformations and for book keeping it is useful to assign modular weights to operators. Thus a function $f(T_i, \bar{T_i})$ has modular weights (n_1, n_2) if

$$f(T_i, \bar{T_i}) \to (icT_i + d)^{n_1} (-ic\bar{T_i} + d)^{n_2} f(T_i, \bar{T_i}) \tag{4}$$

Below we give a list of modular weights for a few cases (see Table. 1).

2.1 Modular Invariant V_{soft}

We begin by considering the condition for the vanishing of the vacuum energy. Using the supergravity form of the scalar potential the condition that vacuum energy vanish is given by

Table 1. A list of modular weights under the modular transformations.

Quantity	Modular Weights (n_1, n_2)
$\|W\|$	$(-\frac{1}{2}, -\frac{1}{2})$
$e^{i\theta_W}$	$(-\frac{1}{2}, \frac{1}{2})$
$\eta(T_i)$	$(\frac{1}{2}, 0)$
$2\partial_{T_i} ln\eta(T_i) + (T_i + \bar{T}_i)^{-1}$	$(2, 0)$
$\partial_{T_i} W - (T_i + \bar{T}_i)^{-1} W$	$(1, 0)$
$(T_i + \bar{T}_i)$	$(-1, -1)$
$\|\gamma_s\|$	$(0, 0)$
$\|\gamma_{T_i}\|$	$(0, 0)$
$e^{i\theta_{T_i}}$	$(1, -1)$
$e^{i\theta_S}$	$(0, 0)$
$A^0_{\alpha\beta\gamma}$	$(1, 0)$
$B^0_{\alpha\beta}$	$(1, 0)$
$1/\sqrt{f} = 1/(\prod(T_i + \bar{T}_i))^{\frac{1}{2}}$	$(\frac{1}{2}, \frac{1}{2})$

$$|\gamma_S|^2 + \sum_{i=1}^{3} |\gamma_{T_i}|^2 = 1 \tag{5}$$

where we have defined γ_s and γ_{T_i} as follows

$$\gamma_s = (S + \bar{S})G, S/\sqrt{3} = |\gamma_S| e^{i\theta_S} \tag{6}$$

$$\gamma_{T_i} = (T_i + \bar{T}_i)G, T_i/\sqrt{3} = |\gamma_{T_i}| e^{i\theta_{T_i}} \tag{7}$$

In the investigation of soft breaking we follow the usual procedure of supergravity where one has a visible sector and a hidden sector and supersymmetry breaking occurs in the hidden sector and is communicated to the visible sector by gravitational interactions. For the analysis here we choose the hidden sector to be of the form [19]

$$W_h = F(S)/\prod \eta(T_i)^2 \tag{8}$$

and for the Kahler potential we choose

$$K = D(S, \bar{S}) - \sum_i ln\left(T_i + \bar{T}_i\right) + \sum_{i\alpha} \left(T_i + \bar{T}_i\right)^{n^i_\alpha} C^\dagger_\alpha C_\alpha \tag{9}$$

where C_α are the chiral fields. Using the technique of supergravity models [20] the soft breaking potential V_{soft} is given by [19] (for previous analyses see [16, 18, 21])

$$V_{soft} = m_{3/2}^2 \sum_\alpha \left(1 + 3\sum_{i=1}^{3} n_\alpha^i |\gamma_{T_i}|^2\right) c_\alpha^\dagger c_\alpha + \left(\sum_{\alpha\beta} B_{\alpha\beta}^0 w_{\alpha\beta}^{(2)} + \right.$$
$$\left. + \sum_{\alpha\beta\gamma} A_{\alpha\beta\gamma}^0 w_{\alpha\beta\gamma}^{(3)} + H.c.\right) \qquad (10)$$

where

$$w_{\alpha\beta}^{(2)} = \mu_{\alpha\beta} C_\alpha C_\beta$$
$$w_{\alpha\beta\gamma}^{(3)} = Y_{\alpha\beta\gamma} C_\alpha C_\beta C_\gamma \qquad (11)$$

The soft breaking parameters A^0 and B^0 may be expressed in the form

$$A_{\alpha\beta\gamma}^0 = -\sqrt{3} m_{3/2} \frac{e^{D/2 - i\theta_W}}{\sqrt{f}} \Big[|\gamma_S| e^{-i\theta_S} (1 - (S + \bar{S}) \partial_S ln Y_{\alpha\beta\gamma})$$
$$+ \sum_{i=1}^{3} |\gamma_{T_i}| e^{-i\theta_{T_i}} (1 + n_\alpha^i + n_\beta^i + n_\gamma^i$$
$$- (T_i + \bar{T}_i) \partial_{T_i} ln Y_{\alpha\beta\gamma} - (T_i + \bar{T}_i) n_{\alpha\beta\gamma}^i G_2(T_i)) \Big]$$

$$B_{\alpha\beta}^0 = -m_{3/2} \frac{e^{D/2 - i\theta_W}}{\sqrt{f}} [1 + \sqrt{3} |\gamma_S| e^{-i\theta_S} (1 - (S + \bar{S}) \partial_S ln \mu_{\alpha\beta})$$
$$+ \sqrt{3} \sum_{i=1}^{3} |\gamma_{T_i}| e^{-i\theta_{T_i}} (1 + n_\alpha^i + n_\beta^i$$
$$- (T_i + \bar{T}_i) \partial_{T_i} ln \mu_{\alpha\beta} - (T_i + \bar{T}_i) n_{\alpha\beta}^i G_2(T_i))]$$

and further the universal gaugino mass is given by

$$m_{1/2} = \sqrt{3} m_{3/2} |\gamma_s| e^{-i\theta_S} \qquad (12)$$

2.2 Determination of tan β from Modular Invariant Soft Breaking and EWSB Constraints

We begin with a discussion of the front factor that appears in A^0 and B^0[3]

[3]This front factor is quite general and also appears in soft breaking arising from the intersecting D brane models [22].

$$Front\ factor = e^{D/2-i\theta_W}/\sqrt{f} \tag{13}$$

The front factor has a non vanishing modular weight and the modular invariance of V_{soft} cannot be maintained without it. There are two main elements in this front factor which are of interest to us here. First, there is factor of of $1/\sqrt{f}$ or a factor

$$1/\sqrt{\prod(T_i+\bar{T}_i)} \tag{14}$$

which produces several solutions to the soft parameters at the self dual points $T_i = (1, e^{i\pi/6})$ so that

$$f = 8, 4\sqrt{3}, 6, 3\sqrt{3} \tag{15}$$

If we include the complex structure moduli U_i then

$$\prod(T_i+\bar{T}_i) \to \prod(T_i+\bar{T}_i)(U_i+\bar{U}_i)$$
$$f = 2^n 3^{3-\frac{n}{2}} \quad (n = 0, .., 6) \tag{16}$$

Assuming that the minimization of the potential occurs at one of these self dual points one finds that there is a multiplicity of soft parameters all consistent with modular invariance. Of course, it may happen that the minimization occurs away from the self dual points. In this case there the f factor will take values outside of the sets given above. The second element that is of interest to us in the front factor is the quantity $e^{D/2}$. This factor is of significance since it can be related to the string gauge coupling constant g_{string} so that

$$e^{-D} = \frac{2}{g^2_{string}} \tag{17}$$

The importance of front factor becomes clear when one considers the electroweak symmetry breaking constraints arising from the minimization of the potential with respect to the Higgs vacuum expectation values $< H_1 >$ and $< H_2 >$. In supergravity models one of these relations is used to determine μ and the other relates the soft parameter B to $\tan\beta$. In supergravity one uses the second relation to eliminate B in favor of $\tan\beta$. However, in the model under consideration B is now determined and thus the second minimization constraint allows one to determine $\tan\beta$ in terms of the other soft parameters and $\alpha_{string} = g^2_{string}/4\pi$. Thus specifically the second constraint reads

$$-2\mu B = \sin 2\beta(m^2_{H_1} + m^2_{H_2} + 2\mu^2) \tag{18}$$

Turning this condition around we determine $\tan\beta$ such that

$$\tan\beta = \frac{(\mu^2 + \frac{1}{2}M_Z^2 + m^2_{H_1})f_\alpha^{1/2}}{\sqrt{2\pi}\mu m_{3/2}\tilde{r}_B\alpha_{string}}$$
$$(|-1+3\sum_i|\gamma_i|^2 - \sqrt{3}|\gamma_S|(1-(S+\bar{S})\partial_S ln\mu)|)^{-1} \tag{19}$$

There is one subtle point involved in the implementation of this equation. One is a relation that holds at the tree level and is accurate only at scales where the one loop correction to this relation is small. This happens when $Q \sim m_{\tilde{t}}$ or $Q \sim$ (highest mass of the spectrum)/2. Thus for the relation of (19) to be accurate we should use the renormalization group improved values of all the quantities on the right hand side of (19). This is specifically the case for the Higgs mass parameters and μ. One obtains their values at the high scale Q by running the renormalization group equations between M_Z and Q. The general analysis used is that of renormalization group analysis of supergravity theories (see, e.g., [23]). Determination of $\tan\beta$ is done in an iterative procedure. One starts with an assumed value of $\tan\beta$ and then one determines μ through radiative breaking of the electroweak symmetry, one determines the sparticle masses and the Higgs masses and uses these in (19) to determine the new value of $\tan\beta$. This iteration continues till consistency is obtained. Quite interestingly there are solutions to the iterative procedure, and the convergence is quite rapid. Thus $\tan\beta$ is uniquely determined for each point in the space of other soft parameters provided radiative electroweak symmetry breaking constraints are satisfied. In the analysis the Higgs mixing parameter μ and specifically its sign plays an important role. Interestingly there is important correlation between the sign of the supersymmetric contribution to the anomalous magnetic moment of the muon [24] and the sign of the μ parameter. It turns out the current data seems to indicate a positive supersymmetric contribution and a positive μ [25]. Thus in the analysis we will mainly focus on μ positive. However, for the sake of completeness we will also include in our analysis the $\mu < 0$ case.

3 Analysis of Supersymmetric Dark Matter

There is already a great deal of analysis of supersymmetric dark matter in the literature (For a sample of recent analyses [26] see [27, 28, 29, 30, 31, 32]). Specifically, over the past year analyses of dark matter matter have focussed on including the constraints of WMAP [33, 34, 35, 36, 37] Here we discuss the analysis of dark matter within the framework of modular invariant soft breaking where $\tan\beta$ is a determined quantity. Thus using the sparticle spectra generated by the procedure of Sect. 2 one can compute the relic density of lightest neutralinos within the modular invariant framework. Quite interesting is the fact that the relic density constraints arising from WMAP data are satisfied by the modular invariant theory in the determined $\tan\beta$ scenario. It is also possible to satisfy the FCNC constraints. One finds that the simultaneous imposition of the WMAP relic density constraints and of the FCNC constraints leads to upper limits on the sparticle masses for the case of μ postive. The sparticle spectrum that is predicted in this case can be fully tested at the LHC. Further, a part of the parameter space is also accessible at the Tevatron.

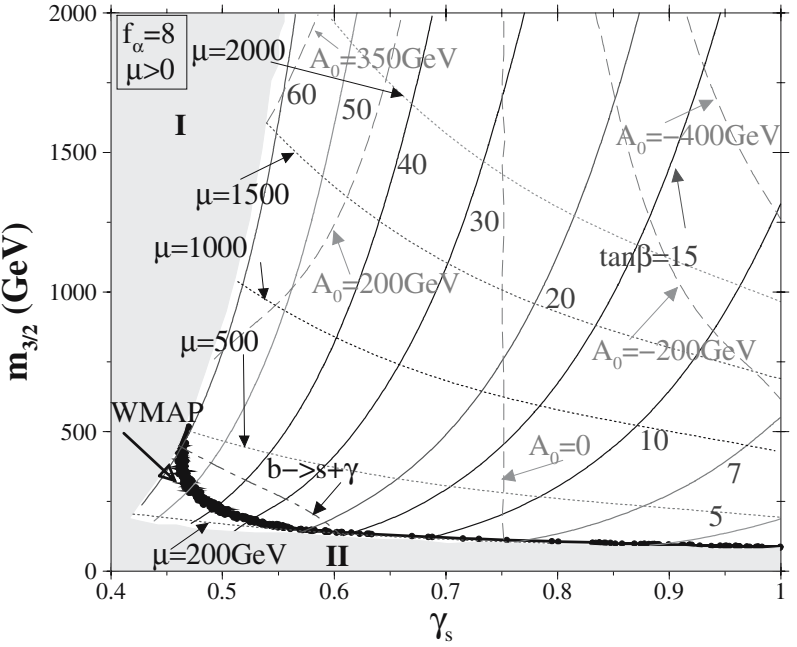

Fig. 1. Plot is given of the contours of constant $A_0, \mu, \tan\beta$ in the $(\gamma_s - m_{3/2})$ plane for the case $\mu > 0$. The constraint of $b \to s + \gamma$ decay is shown as a dot-dashed line below which the region is disallowed. The region where the WMAP relic density constraint is satisfied is shown as small shaded area in black. The gray region-I refers to the discarded region with large $\tan\beta$ where Yukawa couplings lie beyond the perturbative domain. The gray region II arises from the absence of REWSB or a $m_{\tilde{\chi}_1^\pm}$ below the experimental limit. Taken from [1].

We discuss the results now in a quantitative fashion. In Fig. 1 a plot is given of the contours of constant A_0, constant μ and constant $\tan\beta$ in the $m_{3/2} - \gamma_S$ plane. One finds that there are regions where the relic density constraints consistent with the WMAP data and the FCNC constraints are satisfied. The value of $m_{3/2}$ consistent with all the constraints has an upper limit of about 350 GeV. In Fig. 2 a plot of the sparticle spectrum as a function of $m_{3/2}$ is given for $\gamma_S = 0.75$. One finds that the sparticle masses with $m_{3/2} < 350$ GeV lie in a range accessible at the LHC. In fact, for a range of the parameter space some of the sparticles may also be accessible at the Tevatron. Thus much of the Hyperbolic Branch/Focus Point (HB/FP) region [38] seems to be eliminated by the constraints of WMAP and FCNC within the modular invariant soft breaking [1].

In Fig. 3 an analysis of the direct detection cross-section for $\sigma_{\chi-p}$ as a function of the LSP mass is given. One finds that all of the parameter space of the model will be probed in the current and future dark matter colliders.

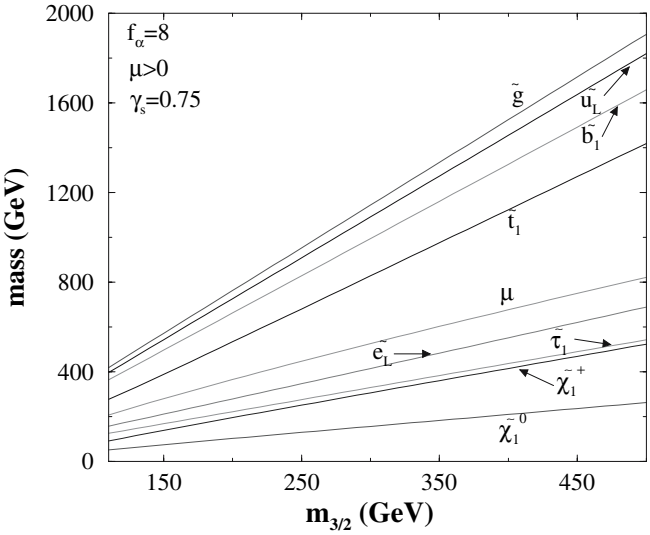

Fig. 2. An exhibition of the variation of sparticle masses with $m_{3/2}$ with $\gamma_s = 0.75$ for the case when $\mu > 0$. The WMAP constraint is not exhibited. Taken from [1].

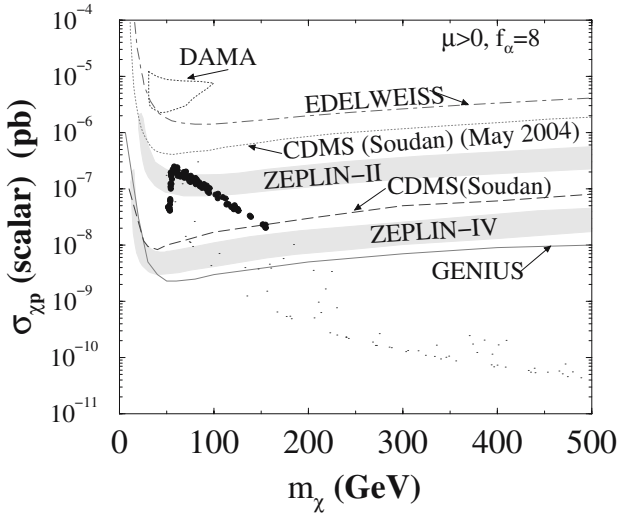

Fig. 3. A scatter plot of the spin independent LSP-proton cross section vs LSP mass for the case $\mu > 0$ when γ_s and $m_{3/2}$ are integrated. The region with black circles satisfies the WMAP constraint. Present limits (top three contours) and future accessibility regions are shown. Taken from [1].

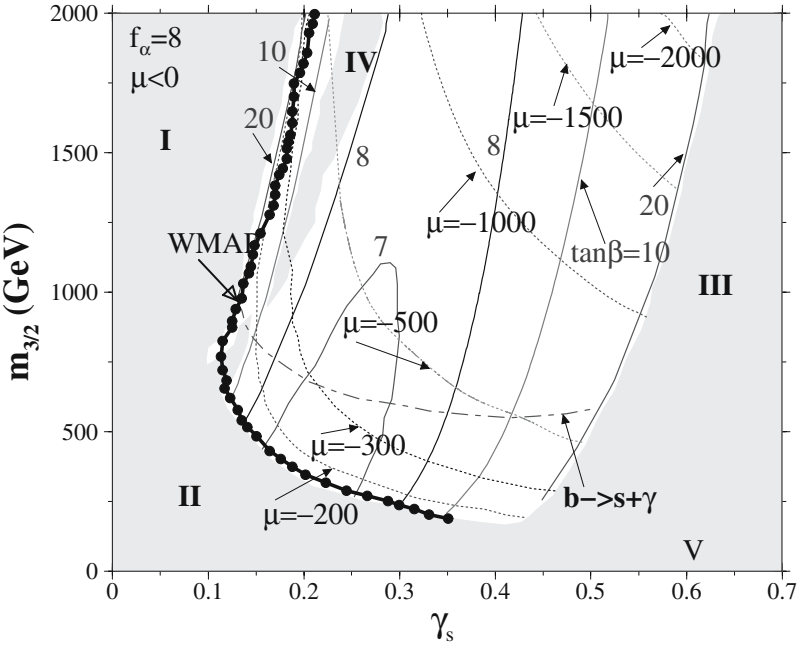

Fig. 4. Plot is given of the contours of constant $\tan\beta$ and μ in the $(\gamma_s - m_{3/2})$ plane for the case $\mu < 0$. The constraint of $b \to s + \gamma$ decay is shown as a dot-dashed line below which the region is disallowed. The region where the WMAP relic density constraint is satisfied is shown as small shaded area in black. The gray region I and III are disallowed because of the absence of consistent GUT scale inputs. The region II refers to absence of REWSB or smaller than experimental lower limits of $m_{\tilde{\chi}_1^\pm}$. The region IV is a no solution zone like I and III, but its location and extent depends on the sensitivity of the minimization scale for REWSB. Region V is the tachyonic $\tilde{\tau}_1$ zone. Taken from [1].

An analysis analogous to that of Fig. 1 but for $\mu < 0$ is given in Fig. 4 while an analysis analogous to Fig. 3 is given in Fig. 5. In this case one finds that a part of the parameter space consistent with WMAP can be probed in the current and future dark matter experiments. Finally, the analysis presented above is done under the assumption that the chiral fields have zero modular weights. For non-vanishing modular weights one needs a realistic string model and an analysis of the sparticle spectra and dark matter for such a model should be worthwhile using the above framework.

4 Conclusion

In this paper we have analyzed the implications of modular invariant soft breaking in a generic heterotic string scenario under the constraint of radiative

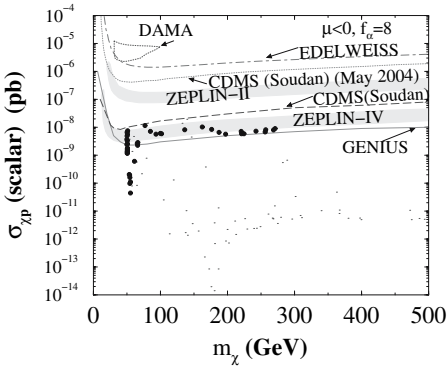

Fig. 5. A scatter plot of the spin-dependent LSP-proton cross section vs LSP mass for the case when $\mu < 0$. The region with black circles satisfies the WMAP constraint. Taken from [1].

breaking of the electroweak symmetry. It was shown that in models of this type $\tan\beta$ is no longer an arbitrary parameter but a determined quantity. Thus the constraints of modular invariance along with a determined $\tan\beta$ reduced the allowed parameter space of the model. Quite remarkably one finds that the reduced parameter space allows for the satisfaction of the accurate relic density constraints given by WMAP. Further, our analysis shows that the WMAP constraint combined with the FCNC constraint puts upper limits on the sparticle masses for the case $\mu > 0$ which are remarkably low implying that essentially all of the sparticles would be accessible at the LHC and some of the sparticles may also be visible at the Tevatron. Further, we analysed the direct detection rates in dark matter detectors in such a scenario. It is found that for the case $\mu > 0$ the dark matter detection rates fall within the sensitivities of the current and future dark matter detectors. For the case $\mu < 0$ a part of the allowed parameter space will be accessible to dark matter detectors. It should be of interest to analyze scenarios of the type discussed above with determined $\tan\beta$ in the investigation of other SUSY phenomena. Further, it would be interesting to examine if similar limits arise in models with modular invariance in extended MSSM seenarios, such as the recently proposed Stueckelberg extension of MSSM [39].

Acknowledgements

This work is supported in part by NSF grant PHY-0139967.

References

1. U. Chattopadhyay and P. Nath, hep-ph/0405157 (to appear in Phys. Rev. D)

2. C.L. Bennett et al., Astrophys. J. Suppl. **148**, 1 (2003) and astro-ph/0302207
3. D.N. Spergel et al., Astrophys. J. Suppl. **148**, 175 (2003), astro-ph/0302209
4. K. Abe et al. [Belle Collaboration], Phys. Lett. B **511**, 151 (2001), hep-ex/0103042; S. Chen et.al. (CLEO Collaboration), Phys. Rev. Lett. **87**, 251807 (2001); R. Barate et al. [ALEPH Collaboration], Phys. Lett. B **429**, 169 (1998)
5. P. Nath and R. Arnowitt, Phys. Lett. B **336**, 395 (1994), hep-ph/9406389; Phys. Rev. Lett. **74**, 4592 (1995), hep-ph/9409301; F. Borzumati, M. Drees and M. Nojiri, *Phys. Rev.* D **51**, 341 (1995); H. Baer, M. Brhlik, D. Castano and X. Tata, *Phys. Rev.* D **58**, 015007 (1998)
6. H. Baer, A. Belyaev, T. Krupovnickas and A. Mustafayev, hep-ph/0403214; K. i. Okumura and L. Roszkowski, Journal of High Energy Physics, **0310**, 024 (2003), hep-ph/0308102; M. Carena, D. Garcia, U. Nierste, C.E.M. Wagner, Phys. Lett. **B499** 141 (2001); G. Degrassi, P. Gambino, G.F. Giudice, JHEP 0012, 009 (2000); M. Ciuchini, G. Degrassi, P. Gambino and G. F. Giudice, Nucl. Phys. B **534**, 3 (1998)
7. P. Gambino and M. Misiak, Nucl. Phys. **B611**, 338 (2001); P. Gambino and U. Haisch, JHEP 0110, 020 (2001); A.L. Kagan and M. Neubert, Eur. Phys. J. C7, 5(1999); A.L. Kagan and M. Neubert, Eur. Phys. J. **C27**, 5(1999)
8. R. Abusaidi et.al., Phys. Rev. Lett.**84**, 5699(2000), "Exclusion Limits on WIMP-Nucleon Cross-Section from the Cryogenic Dark Matter Search", CDMS Collaboration preprint CWRU-P5-00/UCSB-HEP-00-01 and astro-ph/0002471
9. H.V. Klapdor-Kleingrothaus, et.al., "GENIUS, A Supersensitive Germanium Detector System for Rare Events: Proposal", MPI-H-V26-1999, hep-ph/9910205; H. V. Klapdor-Kleingrothaus, "Search for dark matter by GENIUS-TF and GENIUS," Nucl. Phys. Proc. Suppl. **110**, 58 (2002), hep-ph/0206250]
10. D. Cline, "Status of the search for supersymmetric dark matter", astro-ph/0306124
11. D.R. Smith and N. Weiner, Nucl. Phys. Proc. Suppl. **124**, 197 (2003), astro-ph/0208403]
12. [CDMS Collaboration], "First Results from the Cryogenic Dark Matter Search in the Soudan Underground Lab", astro-ph/0405033
13. G. Chardin et al. [EDELWEISS Collaboration], Nucl. Instrum. Meth. A **520**, 101 (2004); A. Benoit et al., Phys. Lett. **B545**, 43 (2002), astro-ph/0206271
14. R. Bernabei et al. [DAMA Collaboration], Phys. Lett. B **480**, 23 (2000)
15. S. Ferrara, N. Magnoli, T. R. Taylor and G. Veneziano, Phys. Lett. B **245**, 409(1990); A. Font, L. E. Ibanez, D. Lüst and F. Quevedo, Phys. Lett. B **245**, 401(1990); H. P. Nilles and M. Olechowski, Phys. Lett. B **248**, 268(1990); P. Binetruy and M. K. Gaillard, Phys. Lett. B **253**, 119(1991); M. Cvetic, A. Font, L. E. Ibanez, D. Lüst and F. Quevedo, Nucl. Phys. B **361**, 194(1991)
16. A. Brignole, L.E. Ibanez, C. Munoz and C. Scheich, Z. Phys. C **74**, 157 (1997); B. de Carlos, J.A. Casas and C. Munoz, Nucl. Phys. B **399**, 623 (1993); A. Brignole, L.E. Ibanez and C. Munoz, Phys. Lett. B **387**, 769 (1996)
17. H.P. Nilles, Phys. Lett. B **115**, 193 (1982); S. Ferrara, L. Girardello and H.P. Nilles, Phys. Lett. B **125**, 457 (1983); M. Dine, R. Rohm, N. Seiberg and E. Witten, Phys. Lett. B **156**, 55 (1985); C. Kounnas and M. Porrati, Phys. Lett. B **191**, 91 (1987)
18. P. Binetruy, M.K. Gaillard and B.D. Nelson, Nucl. Phys. B **604**, 32 (2001); M.K. Gaillard, B.D. Nelson and Y.Y. Wu, Phys. Lett. B **459**, 549 (1999); M.K. Gaillard and J. Giedt, Nucl. Phys. B **636**, 365 (2002)

19. P. Nath and T.R. Taylor, Phys. Lett. B **548**, 77 (2002), hep-ph/0209282
20. A.H. Chamseddine, R. Arnowitt and P. Nath, Phys. Rev. Lett. **49**, 970 (1982); R. Barbieri, S. Ferrara and C. A. Savoy, Phys. Lett. B **119**, 343(1982); P. Nath, R. Arnowitt and A.H. Chamseddine, Nucl. Phys. B **227**, 121 (1983); L. Hall, J. Lykken, and S. Weinberg, *Phys. Rev.* D **27**, 2359 (1983); P. Nath, "Twenty years of SUGRA", hep-ph/0307123
21. G.L. Kane, J. Lykken, S. Mrenna, B.D. Nelson, L.T. Wang and T.T. Wang, Phys. Rev. D **67**, 045008 (2003), hep-ph/0209061; B.C. Allanach, S.F. King and D.A.J. Rayner, hep-ph/0403255; P. Binetruy, A. Birkedal-Hansen, Y. Mambrini and B.D. Nelson, hep-ph/0308047; A. Birkedal-Hansen and B.D. Nelson, Phys. Rev. D **64**, 015008 (2001), hep-ph/0102075
22. B. Kors and P. Nath, Nucl. Phys. B **681**, 77 (2004), hep-th/0309167
23. R. Arnowitt and P. Nath, Phys. Rev. Lett. **69**, 725 (1992)
24. T.C. Yuan, R. Arnowitt, A.H. Chamseddine and P. Nath, Z. Phys. C **26**, 407 (1984); D.A. Kosower, L.M. Krauss, N. Sakai, *Phys. Lett.* B **133**, 305 (1983); J.L. Lopez, D.V. Nanopoulos, X. Wang, *Phys. Rev.* D **49**, 366 (1994); U. Chattopadhyay and P. Nath, Phys. Rev. D **53**, 1648 (1996), hep-ph/9507386; T. Moroi, *Phys. Rev.* D **53**, 6565 (1996); T. Ibrahim and P. Nath, Phys. Rev. D **61**, 095008 (2000), hep-ph/9907555; Phys. Rev. D **58**, 111301 (1998), hep-ph/9807501; Phys. Rev. **D62**, 015004 (2000); U. Chattopadhyay , D.K. Ghosh and S. Roy, *Phys. Rev.* D **62**, 115001 (2000)
25. U. Chattopadhyay and P. Nath, Phys. Rev. Lett. **86**, 5854 (2001); For a more complete list of references see, U. Chattopadhyay, A. Corsetti and P. Nath, hep-ph/0202275
26. See also talks by Howard Baer, Wim de Boer, Bhasker Dutta, Paolo Gondolo, Keith Olive, Leszek Roszkowski, and Ioannis Vergados in these proceedings.
27. U. Chattopadhyay, A. Corsetti and P. Nath, Phys. Rev. D **66**, 035003 (2002), hep-ph/0201001]; M.E. Gomez, G. Lazarides and C. Pallis, Phys. Rev. D **61**, 123512 (2000), hep-ph/9907261; M.E. Gomez, G. Lazarides and C. Pallis, Phys. Lett. B **487**, 313 (2000), hep-ph/0004028
28. U. Chattopadhyay and D.P. Roy, Phys. Rev. D **68**, 033010 (2003), hep-ph/0304108
29. H. Baer, A. Belyaev, T. Krupovnickas and X. Tata, JHEP **0402**, 007 (2004), hep-ph/0311351
30. P. Binetruy, Y. Mambrini and E. Nezri, hep-ph/0312155
31. R. Arnowitt, B. Dutta, T. Kamon and M. Tanaka, Phys. Lett. B **538**, 121 (2002), hep-ph/0203069
32. Y.G. Kim, T. Nihei, L. Roszkowski and R. Ruiz de Austri, JHEP **0212**, 034 (2002), hep-ph/0208069
33. U. Chattopadhyay, A. Corsetti and P. Nath, Phys. Rev. D **68**, 035005 (2003), hep-ph/0303201
34. J. Ellis, K.A. Olive, Y. Santoso and V.C. Spanos, Phys. Lett. **B565**, 176, (2003), hep-ph/0303043; H. Baer and C. Balazs, JCAP **0305**, 006 (2003), hep-ph/0303114; A.B. Lahanas and D. V. Nanopoulos, Phys. Lett. **B568**, 55 (2003), hep-ph/0303130
35. H. Baer, C. Balazs, A. Belyaev and J. O'Farrill, JCAP **0309**, 007 (2003), hep-ph/0305191; H. Baer, C. Balazs, A. Belyaev, T. Krupovnickas and X. Tata, JHEP **0306**, 054 (2003), hep-ph/0304303; R. Arnowitt, B. Dutta and B. Hu, hep-ph/0310103; J.R. Ellis, K.A. Olive, Y. Santoso and V.C. Spanos, Phys.

Lett. B **573**, 162 (2003), hep-ph/0305212; J.D. Vergados, P. Quentin and D. Strottman, hep-ph/0310365
36. For a review see, U. Chattopadhyay, A. Corsetti and P. Nath, Phys. Atom. Nucl. **67**, 1188 (2004) [Yad. Fiz. **67**, 1210 (2004)], hep-ph/0310228; A.B. Lahanas, N.E. Mavromatos and D.V. Nanopoulos, Int. J. Mod. Phys. D **12**, 1529 (2003), hep-ph/0308251
37. M.E. Gomez, T. Ibrahim, P. Nath and S. Skadhauge, Phys. Rev. D **70**, 035014 (2004), hep-ph/0404025; T. Nihei and M. Sasagawa, hep-ph/0404100; M. Argyrou, A.B. Lahanas, D.V. Nanopoulos and V.C. Spanos, hep-ph/0404286; M.E. Gomez, T. Ibrahim, P. Nath and S. Skadhauge, hep-ph/0410007
38. K.L. Chan, U. Chattopadhyay and P. Nath, Phys. Rev. D **58**, 096004 (1998), hep-ph/9710473; J.L. Feng, K.T. Matchev and T. Moroi, Phys. Rev. D **61**, 075005 (2000)
39. B. Kors and P. Nath, hep-ph/0406167; Phys. Lett. B **586**, 366 (2004), hep-ph/0402047

Dark Matter Candidates in Supersymmetric Models

Keith A. Olive

William I. Fine Theoretical Physics Institute,
University of Minnesota, Minneapolis, MN 55455, USA
olive@umn.edu

The status of the constrained minimal supersymmetric standard model (CMSSM) will be discussed in light of our current understanding of the relic density after WMAP. A global likelihood analysis of the model is performed including data from direct Higgs searches, global fits to electroweak data, $b \to s\gamma$, the anomalous magnetic moment of the muon, as well as the cosmological relic density. Also considered are models which relax and further constrain the CMSSM. Prospects for dark matter detection in colliders and cryogenic detectors will be briefly discussed.

1 Introduction

Supersymmetric models with conserved R-parity contain one new stable particle which is a candidate for cold dark matter(CDM) [1]. There are very strong constraints, however, forbidding the existence of stable or long lived particles which are not color and electrically neutral. The sneutrino [2] is one possible candidate, but in the MSSM, it has been excluded as a dark matter candidate by direct [3] and indirect [4] searches. Another possibility is the gravitino and is probably the most difficult to exclude. This possibility has been discussed recently in the CMSSM context [6]. I will concentrate on the remaining possibility in the MSSM, namely the neutralinos.

There are four neutralinos, each of which is a linear combination of the $R = -1$, neutral fermions [1]: the wino $\tilde{W}^3$, the partner of the 3rd component of the $SU(2)_L$ gauge boson; the bino, $\tilde{B}$, the partner of the $U(1)_Y$ gauge boson; and the two neutral Higgsinos, $\tilde{H}_1$ and $\tilde{H}_2$. In general, the neutralino mass eigenstates can be expressed as a linear combination

$$\chi = \alpha\tilde{B} + \beta\tilde{W}^3 + \gamma\tilde{H}_1 + \delta\tilde{H}_2 \tag{1}$$

The solution for the coefficients α, β, γ and δ for neutralinos that make up the LSP can be found by diagonalizing the mass matrix which depends on $M_1(M_2)$ which are the soft supersymmetry breaking U(1) (SU(2)) gaugino mass terms, μ, the supersymmetric Higgs mixing mass parameter and the two Higgs vacuum expectation values, v_1 and v_2. One combination of these is related to the Z mass, and therefore is not a free parameter, while the other combination, the ratio of the two vevs, $\tan\beta$, is free.

The most general version of the MSSM, despite its minimality in particles and interactions contains well over a hundred new parameters. The study of such a model would be untenable were it not for some (well motivated) assumptions. These have to do with the parameters associated with supersymmetry breaking. It is often assumed that, at some unification scale, all of the gaugino masses receive a common mass, $m_{1/2}$. The gaugino masses at the weak scale are determined by running a set of renormalization group equations. Similarly, one often assumes that all scalars receive a common mass, m_0, at the GUT scale. These too are run down to the weak scale. The remaining supersymmetry breaking parameters are the trilinear mass terms, A_0, which I will also assume are unified at the GUT scale, and the bilinear mass term B. There are, in addition, two physical CP violating phases which will not be considered here.

The natural boundary conditions at the GUT scale for the MSSM would include μ and B in addition to $m_{1/2}$, m_0, and A_0. In this case, upon running the RGEs down to a low energy scale and minimizing the Higgs potential, one would predict the values of M_Z, $\tan\beta$ (in addition to all of the sparticle masses). Since M_Z is known, it is more useful to analyze supersymmetric models where M_Z is input rather than output. It is also common to treat $\tan\beta$ as an input parameter. This can be done at the expense of shifting μ (up to a sign) and B from inputs to outputs. This model is often referred to as the constrained MSSM or CMSSM. Once these parameters are set, the entire spectrum of sparticle masses at the weak scale can be calculated. In the CMSSM, the solutions for μ generally lead to a neutralino which which very nearly a pure $\tilde{B}$.

2 The CMSSM after WMAP

For a given value of $\tan\beta$, A_0, and $sgn(\mu)$, the resulting regions of acceptable relic density and which satisfy the phenomenological constraints can be displayed on the $m_{1/2}-m_0$ plane. In Fig. 1a, the light shaded region corresponds to that portion of the CMSSM plane with $\tan\beta = 10$, $A_0 = 0$, and $\mu > 0$ such that the computed relic density yields $0.1 < \Omega_\chi h^2 < 0.3$. At relatively low values of $m_{1/2}$ and m_0, there is a large 'bulk' region which tapers off as $m_{1/2}$ is increased. At higher values of m_0, annihilation cross sections are too small to maintain an acceptable relic density and $\Omega_\chi h^2 > 0.3$. Although sfermion masses are also enhanced at large $m_{1/2}$ (due to RGE running), coannihilation processes between the LSP and the next lightest sparticle (in this case the $\widetilde{\tau}_1$) enhance the annihilation cross section and reduce the relic density. This occurs when the LSP and NLSP are nearly degenerate in mass. The dark shaded region has $m_{\tilde{\tau}_1} < m_\chi$ and is excluded. Neglecting coannihilations, one would find an upper bound of $\sim 450\,\mathrm{GeV}$ on $m_{1/2}$, corresponding to an upper bound of roughly $200\,\mathrm{GeV}$ on $m_{\tilde{B}}$. The effect of coannihilations is

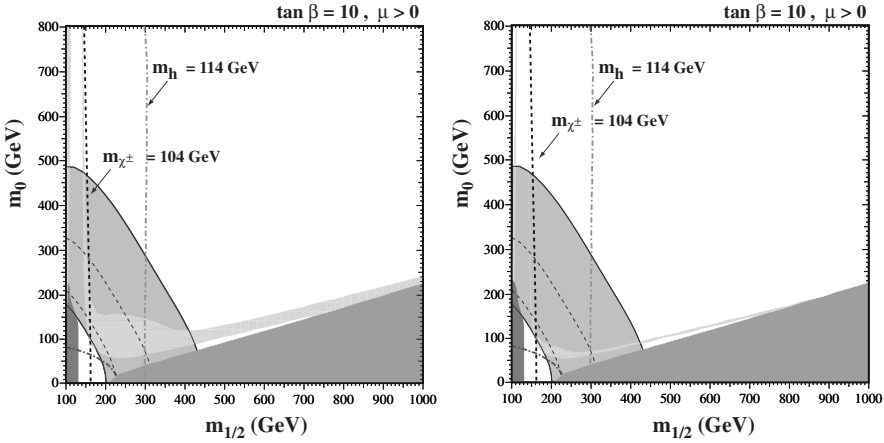

Fig. 1. The $(m_{1/2}, m_0)$ planes for (a) $\tan\beta = 10$ and $\mu > 0$, assuming $A_0 = 0, m_t = 175\,\mathrm{GeV}$ and $m_b(m_b)^{\overline{MS}}_{SM} = 4.25\,\mathrm{GeV}$. The near-vertical (*red*) dot-dashed lines are the contours $m_h = 114$ GeV, and the near-vertical (black) dashed line is the contour $m_{\chi^\pm} = 104\,\mathrm{GeV}$. Also shown by the dot-dashed curve in the lower left is the corner excluded by the LEP bound of $m_{\tilde{e}} > 99\,\mathrm{GeV}$. The medium (dark green) shaded region is excluded by $b \to s\gamma$, and the light (turquoise) shaded area is the cosmologically preferred regions with $0.1 \leq \Omega_\chi h^2 \leq 0.3$. In the dark (brick red) shaded region, the LSP is the charged $\tilde{\tau}_1$. The region allowed by the E821 measurement of a_μ at the 2-σ level, is shaded (pink) and bounded by solid black lines, with dashed lines indicating the 1-σ ranges. In (b), the relic density is restricted to the range $0.094 < \Omega_\chi h^2 < 0.129$.

to create an allowed band about 25-50 GeV wide in m_0 for $m_{1/2} \lesssim 1400\,\mathrm{GeV}$, which tracks above the $m_{\tilde{\tau}_1} = m_\chi$ contour [5].

Also shown in Fig. 1a are the relevant phenomenological constraints. These include the limit on the chargino mass: $m_{\chi^\pm} > 104\,\mathrm{GeV}$ [7], on the selectron mass: $m_{\tilde{e}} > 99\,\mathrm{GeV}$ [8] and on the Higgs mass: $m_h > 114\,\mathrm{GeV}$ [9]. The former two constrain $m_{1/2}$ and m_0 directly via the sparticle masses, and the latter indirectly via the sensitivity of radiative corrections to the Higgs mass to the sparticle masses, principally $m_{\tilde{t},\tilde{b}}$. `FeynHiggs` [10] is used for the calculation of m_h. The Higgs limit imposes important constraints principally on $m_{1/2}$ particularly at low $\tan\beta$. Another constraint is the requirement that the branching ratio for $b \to s\gamma$ is consistent with the experimental measurements [11]. These measurements agree with the Standard Model, and therefore provide bounds on MSSM particles [12, 13], such as the chargino and charged Higgs masses, in particular. Typically, the $b \to s\gamma$ constraint is more important for $\mu < 0$, but it is also relevant for $\mu > 0$, particularly when $\tan\beta$ is large. The constraint imposed by measurements of $b \to s\gamma$ also excludes small values of $m_{1/2}$. Finally, there are regions of the $(m_{1/2}, m_0)$ plane that are favoured by the BNL measurement [14] of $g_\mu - 2$ at the 2-σ

level, corresponding to a deviation from the Standard Model calculation [15] using e^+e^- data. One should be however aware that this constraint is still under active discussion.

The preferred range of the relic LSP density has been altered significantly by the recent improved determination of the allowable range of the cold dark matter density obtained by combining WMAP and other cosmological data: $0.094 < \Omega_{CDM} < 0.129$ at the 2-σ level [16]. In the second panel of Fig. 1, we see the effect of imposing the WMAP range on the neutralino density [17, 18, 19]. We see immediately that (i) the cosmological regions are generally much narrower, and (ii) the 'bulk' regions at small $m_{1/2}$ and m_0 have almost disappeared, in particular when the laboratory constraints are imposed. Looking more closely at the coannihilation regions, we see that (iii) they are significantly truncated as well as becoming much narrower, since the reduced upper bound on $\Omega_\chi h^2$ moves the tip where $m_\chi = m_{\tilde{\tau}}$ to smaller $m_{1/2}$ so that the upper limit is now $m_{1/2} \lesssim 950\,\mathrm{GeV}$ or $m_\chi \lesssim 400\,\mathrm{GeV}$.

Another mechanism for extending the allowed CMSSM region to large m_χ is rapid annihilation via a direct-channel pole when $m_\chi \sim \frac{1}{2} m_A$ [20, 21]. Since the heavy scalar and pseudoscalar Higgs masses decrease as $\tan\beta$ increases, eventually $2m_\chi \simeq m_A$ yielding a 'funnel' extending to large $m_{1/2}$ and m_0 at large $\tan\beta$, as seen in the high $\tan\beta$ strips of Fig. 2. As one can see, the impact of the Higgs mass constraint is reduced (relative to the case with $\tan\beta = 10$) while that of $b \to s\gamma$ is enhanced.

Shown in Fig. 3 are the WMAP lines [17] of the $(m_{1/2}, m_0)$ plane allowed by the new cosmological constraint $0.094 < \Omega_\chi h^2 < 0.129$ and the laboratory constraints listed above, for $\mu > 0$ and values of $\tan\beta$ from 5 to 55, in steps $\Delta(\tan\beta) = 5$. We notice immediately that the strips are considerably narrower than the spacing between them, though any intermediate point in

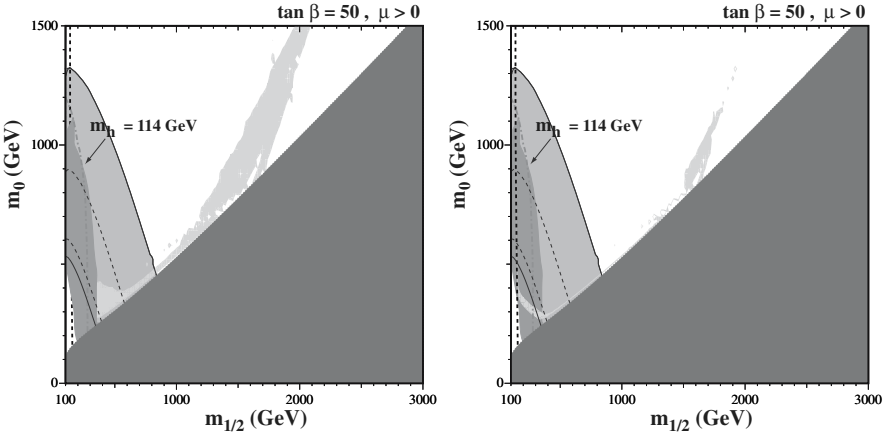

Fig. 2. As in Fig. 1 for $\tan\beta = 50$.

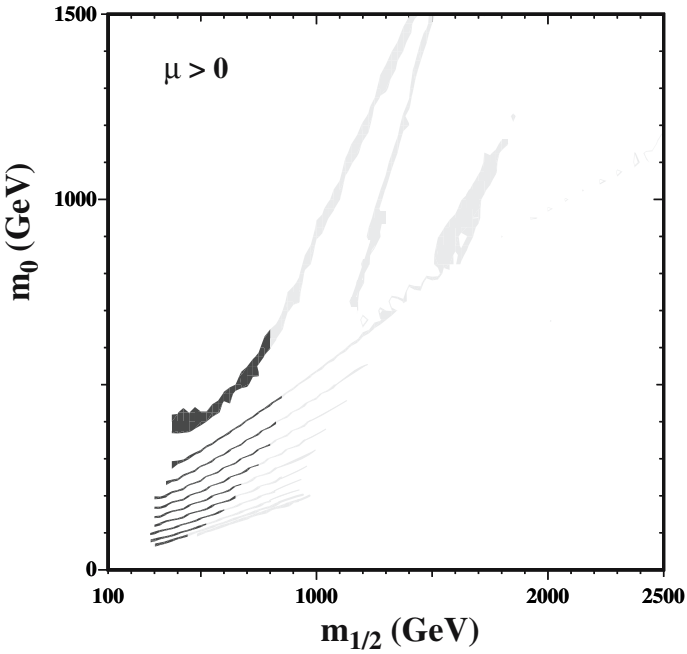

Fig. 3. The strips display the regions of the $(m_{1/2}, m_0)$ plane that are compatible with $0.094 < \Omega_\chi h^2 < 0.129$ and the laboratory constraints for $\mu > 0$ and $\tan\beta = 5, 10, 15, 20, 25, 30, 35, 40, 45, 50, 55$. The parts of the strips compatible with $g_\mu - 2$ at the 2-σ level have darker shading.

the $(m_{1/2}, m_0)$ plane would be compatible with some intermediate value of $\tan\beta$. The right (left) ends of the strips correspond to the maximal (minimal) allowed values of $m_{1/2}$ and hence m_χ. The lower bounds on $m_{1/2}$ are due to the Higgs mass constraint for $\tan\beta \leq 23$, but are determined by the $b \to s\gamma$ constraint for higher values of $\tan\beta$.

Finally, there is one additional region of acceptable relic density known as the focus-point region [22], which is found at very high values of m_0. An example showing this region is found in Fig. 4, plotted for $\tan\beta = 10$, $\mu > 0$, and $m_t = 175\,\text{TeV}$. As m_0 is increased, the solution for μ at low energies as determined by the electroweak symmetry breaking conditions eventually begins to drop. When $\mu \lesssim m_{1/2}$, the composition of the LSP gains a strong Higgsino component and as such the relic density begins to drop precipitously. These effects are both shown in Fig. 5 where the value of μ and Ωh^2 are plotted as a function of m_0 for fixed $m_{1/2} = 300\,\text{GeV}$ and $\tan\beta = 10$. As m_0 is increased further, there are no longer any solutions for μ. This occurs in the shaded region in the upper left corner of Fig. 4.

Figure 5 also exemplifies the degree of fine tuning associated with the focus-point region. While the position of the focus-point region in the

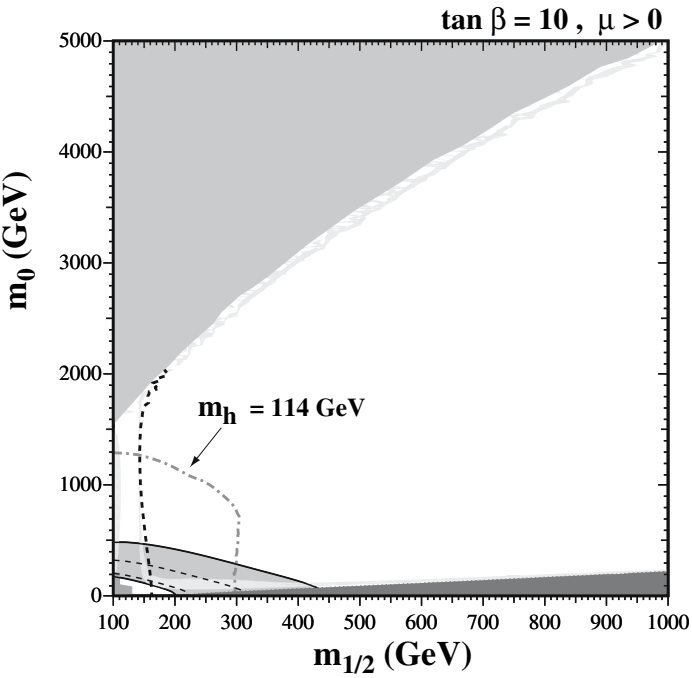

Fig. 4. As in Fig. (1a), where the range in m_0 is extended to 5 TeV. In the shaded region at very high m_0, there are no solutions for μ which respect the low energy electroweak symmetry breaking conditions.

$m_0, m_{1/2}$ plane is not overly sensitive to supersymmetric parameters, it is highly sensitive to the top quark Yukawa coupling which contributes to the evolution of μ [23, 24]. As one can see in the figure, a change in m_t of 3 GeV produces a shift of about 2.5 TeV in m_0. Note that the position of the focus-point region is also highly sensitive to the value of A_0/m_0. In Fig. 5, $A_0 = 0$ was chosen. For $A_0/m_0 = 0.5$, the focus point shifts from 2.5 to 4.5 TeV and moves to larger m_0 as A_0/m_0 is increased.

3 A Likelihood Analysis of the CMSSM

Up to now, in displaying acceptable regions of cosmological density in the $m_0, m_{1/2}$ plane, it has been assumed that the input parameters are known with perfect accuracy so that the relic density can be calculated precisely. While all of the beyond the standard model parameters are completely unknown and therefore carry no formal uncertainties, standard model parameters such as the top and bottom Yukawa couplings are known but do carry significant uncertainties. Indeed, we saw that in the case of the focus-point

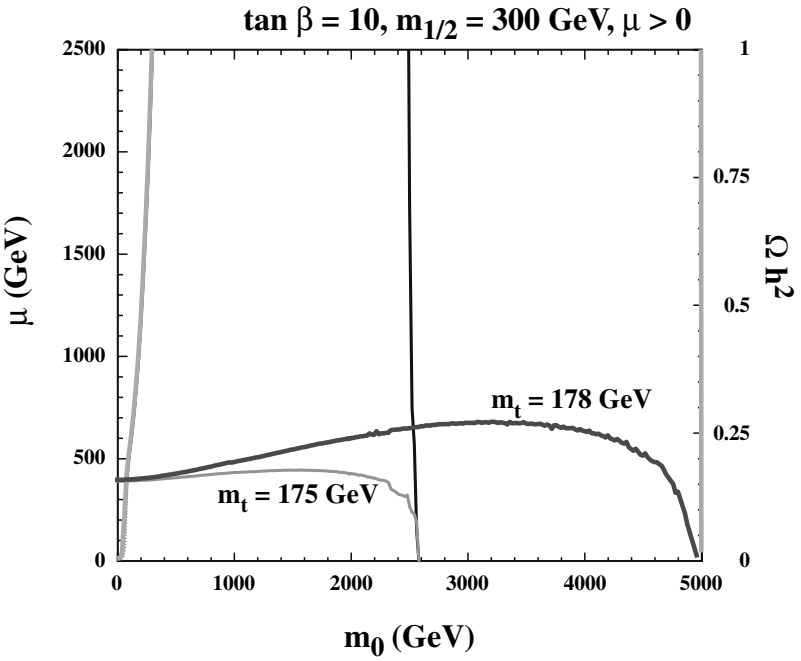

Fig. 5. The value of μ as a function of m_0 for fixed $m_{1/2} = 300\,\text{GeV}$ and $\tan\beta = 10$ for two choices of m_t as indicated. The scale on the right gives the value of Ωh^2. The curves corresponding to this is scale rise sharply at low m_0 to values much larger than 1. For $m_t = 175\,\text{GeV}$ and $m_0 \approx 2500\,\text{GeV}$, the value of Ωh^2 drops to acceptable values when μ becomes small. When the $m_t = 178\,\text{GeV}$, Ωh^2 drops at $m_0 \approx 5000\,\text{GeV}$.

region, there is an intense sensitivity of the relic density to the top quark Yukawa. Other regions in the $m_0, m_{1/2}$ plane, such as those corresponding to the rapid annihilation funnels are also very sensitive to the 3rd generation Yukawas.

The optimal way to combine the various constraints (both phenomenological and cosmological) is via a likelihood analysis, as has been done by some authors both before [25] and after [18] the WMAP data was released. When performing such an analysis, in addition to the formal experimental errors, it is also essential to take into account theoretical errors, which introduce systematic uncertainties that are frequently non-negligible. Recently, we have preformed an extensive likelihood analysis of the CMSSM [26]. Included is the full likelihood function for the LEP Higgs search, as released by the LEP Higgs Working Group. This includes the small enhancement in the likelihood just beyond the formal limit due to the LEP Higgs signal reported late in 2000. This was re-evaluated most recently in [9], and cannot be regarded as significant evidence for a light Higgs boson. We have also taken into account

the indirect information on m_h provided by a global fit to the precision electroweak data. The likelihood function from this indirect source does not vary rapidly over the range of Higgs masses found in the CMSSM, but we included this contribution with the aim of completeness.

The interpretation of the combined Higgs likelihood, $\mathcal{L}_{exp}$, in the $(m_{1/2}, m_0)$ plane depends on uncertainties in the theoretical calculation of m_h. These include the experimental error in m_t and (particularly at large $\tan\beta$) m_b, and theoretical uncertainties associated with higher-order corrections to m_h. Our default assumptions are that $m_t = 175 \pm 5\,\mathrm{GeV}$ for the pole mass, and $m_b = 4.25 \pm 0.25\,\mathrm{GeV}$ for the running $\overline{MS}$ mass evaluated at m_b itself. The theoretical uncertainty in m_h, σ_{th}, is dominated by the experimental uncertainties in $m_{t,b}$, which are treated as uncorrelated Gaussian errors:

$$\sigma_{\mathrm{th}}^2 = \left(\frac{\partial m_h}{\partial m_t}\right)^2 \Delta m_t^2 + \left(\frac{\partial m_h}{\partial m_b}\right)^2 \Delta m_b^2 \,. \tag{2}$$

Typically, we find that $(\partial m_h/\partial m_t) \sim 0.5$, so that σ_{th} is roughly 2–3 GeV.

The combined experimental likelihood, $\mathcal{L}_{exp}$, from direct searches at LEP 2 and a global electroweak fit is then convolved with a theoretical likelihood (taken as a Gaussian) with uncertainty given by σ_{th} from (2) above. Thus, we define the total Higgs likelihood function, $\mathcal{L}_h$, as

$$\mathcal{L}_h(m_h) = \frac{\mathcal{N}}{\sqrt{2\pi}\,\sigma_{th}} \int dm_h'\; \mathcal{L}_{exp}(m_h')\; e^{-(m_h'-m_h)^2/2\sigma_{th}^2} \,, \tag{3}$$

where $\mathcal{N}$ is a factor that normalizes the experimental likelihood distribution.

In addition to the Higgs likelihood function, we have included the likelihood function based on $b \to s\gamma$. The branching ratio for these decays has been measured by the CLEO, BELLE and BaBar collaborations [11], and we took as the combined value $\mathcal{B}(b \to s\gamma) = (3.54 \pm 0.41 \pm 0.26) \times 10^{-4}$. The theoretical prediction [12, 13] contains uncertainties which stem from the uncertainties in m_b, α_s, the measurement of the semileptonic branching ratio of the B meson as well as the effect of the scale dependence. While the likelihood function based on the measurements of the anomalous magnetic moment of the muon was considered in [26], it will not be discussed here.

Finally, in calculating the likelihood of the CDM density, we take into account the contribution of the uncertainties in $m_{t,b}$. We will see that the theoretical uncertainty plays a very significant role in this analysis. The likelihood for Ωh^2 is therefore,

$$\mathcal{L}_{\Omega h^2} = \frac{1}{\sqrt{2\pi}\sigma} e^{-(\Omega h^2 th - \Omega h^{2\,exp})^2/2\sigma^2} \,, \tag{4}$$

where $\sigma^2 = \sigma_{exp}^2 + \sigma_{th}^2$, with σ_{exp} taken from the WMAP [16] result and σ_{th}^2 from (2), replacing m_h by Ωh^2.

The total likelihood function is computed by combining all the components described above:

$$\mathcal{L}_{tot} = \mathcal{L}_h \times \mathcal{L}_{bs\gamma} \times \mathcal{L}_{\Omega_\chi h^2} (\times \mathcal{L}_{a_\mu}) \tag{5}$$

The likelihood function in the CMSSM can be considered a function of two variables, $\mathcal{L}_{tot}(m_{1/2}, m_0)$, where $m_{1/2}$ and m_0 are the unified GUT-scale gaugino and scalar masses respectively. Results are based on a Bayesian analysis, in which a prior range for $m_{1/2}$ is introduced in order to normalize the conditional probability obtained from the likelihood function using Bayes' theorem. Although it is possible to motivate some upper limit on $m_{1/2}$, e.g., on the basis of naturalness [27, 24, 28], one cannot quantify any such limit rigorously. Within the selected range, we adopt a flat prior distribution for $m_{1/2}$, and normalize the volume integral:

$$\int \mathcal{L}_{tot}\, dm_0\, dm_{1/2} \;=\; 1 \tag{6}$$

for each value of $\tan\beta$, combining where appropriate both signs of μ. We note that no such prior need be specified for m_0. For any given value of $m_{1/2}$, the theory is well defined only up to some maximum value of m_0, above which radiative electroweak symmetry breaking is no longer possible. We always integrate up to that point, adopting also a flat prior distribution for m_0.

In Fig. 6 the likelihood along slices through the CMSSM parameter space for $\tan\beta = 10, A_0 = 0, \mu > 0$, and $m_{1/2} = 300$ and $800\,\mathrm{GeV}$ is shown in the left and right panels, respectively, plotting the likelihood as a function of m_0. The solid red curves show the total likelihood function calculated including the uncertainties which stem from the experimental errors in m_t and m_b. The peak at low m_0 is due to the coannihilation region. The peak at $m_0 \simeq 2500(4500)\,\mathrm{GeV}$ for $m_{1/2} = 300(800)\,\mathrm{GeV}$ is due to the focus-point

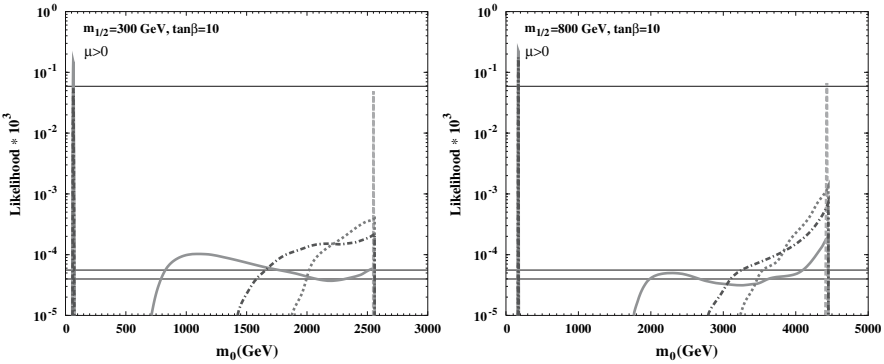

Fig. 6. The likelihood function along slices in m_0 through the CMSSM parameter space for $\tan\beta = 10, A_0 = 0, \mu > 0$ and $m_{1/2} = 300, 800\,\mathrm{GeV}$ in the left and right panels, respectively. The red (solid) curves are calculated using the current errors in m_t and m_b, the green dashed curve with no error in m_t, the violet dotted lines with $\Delta m_t = 0.5\,\mathrm{GeV}$, and the blue dashed-dotted lines with $\Delta m_t = 1\,\mathrm{GeV}$.

region. Also shown in Fig. 6 are the 68%, 90%, and 95% CL (horizontal) lines, corresponding to the iso-likelihood values of the fully integrated likelihood function corresponding to the solid (red) curve.

The focus-point peak is suppressed relative to the coannihilation peak at low m_0 because of the theoretical sensitivity to the experimental uncertainty in the top mass. We recall that the likelihood function is proportional to σ^{-1}, and that σ which scales with $\partial(\Omega_\chi h^2)/\partial m_t$, is very large at large m_0 [24]. The error due to the uncertainty in m_t is far greater in the focus-point region than in the coannihilation region. Thus, even though the exponential in $\mathcal{L}_{\Omega_\chi h^2}$ is of order unity near the focus-point region when $\Omega_\chi h^2 \simeq 0.1$, the prefactor is very small due the large uncertainty in the top mass. This accounts for the factor of $\gtrsim 1000$ suppression seen in Fig. 6 when comparing the two peaks of the solid red curves.

We note also that there is another broad, low-lying peak at intermediate values of m_0. This is due to a combination of the effects of σ in the prefactor and the exponential. We expect a bump to occur when the Gaussian exponential is of order unity, i.e., $\Omega_\chi h^2 \sim \sqrt{2}\Delta m_t\, \partial\Omega_\chi h^2/\partial m_t$. $\Omega_\chi h^2 \sim 10$ at large m_0 for our nominal value $m_t = 175\,\mathrm{GeV}$, but it varies significantly as one samples the favoured range of m_t within its present uncertainty. The competition between the exponential and the prefactor would require a large theoretical uncertainty in $\Omega_\chi h^2$: $\partial\Omega_\chi h^2/\partial m_t \sim 2$ for $\Delta m_t = 5\,\mathrm{GeV}$. This occurs when $m_0 \sim 1000\,\mathrm{GeV}$, which is the position of the broad secondary peak in Fig. 6a. At higher m_0, σ continues to grow, and the prefactor suppresses the likelihood function until $\Omega_\chi h^2$ drops to ~ 0.1 in the focus-point region.

As is clear from the above discussion, the impact of the present experimental error in m_t is particularly important in this region. This point is further demonstrated by the differences between the curves in each panel, where we decrease *ad hoc* the experimental uncertainty in m_t. As Δm_t is decreased, the intermediate bump blends into the broad focus-point peak. When the uncertainties in m_t and m_b are set to 0, we obtain a narrow peak in the focus-point region.

Using the fully normalized likelihood function $\mathcal{L}_{tot}$ obtained by combining both signs of μ for each value of $\tan\beta$, we can determine the regions in the $(m_{1/2}, m_0)$ planes which correspond to specific CLs. Figure 7 extends the previous analysis to the entire $(m_{1/2}, m_0)$ plane for $\tan\beta = 10$ and $A_0 = 0$, including both signs of μ. The darkest (blue), intermediate (red) and lightest (green) shaded regions are, respectively, those where the likelihood is above 68%, above 90%, and above 95%. Overall, the likelihood for $\mu < 0$ is less than that for $\mu > 0$ due to the Higgs and $b \to s\gamma$ constraints. Only the bulk and coannihilation-tail regions appear above the 68% level, but the focus-point region appears above the 90% level, and so cannot be excluded.

The bulk region is more apparent in the right panel of Fig. 7 for $\mu > 0$ than it would be if the experimental error in m_t and the theoretical error in m_h were neglected. Figure 8 complements the previous figures by showing

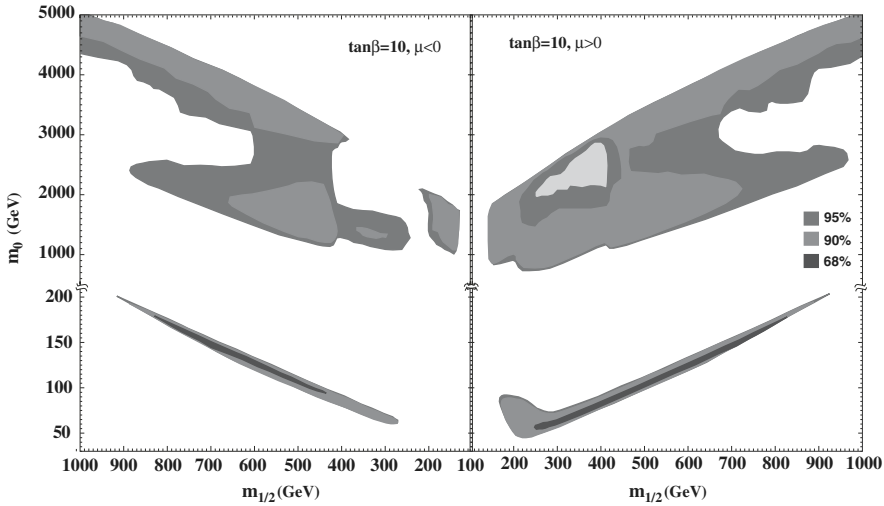

Fig. 7. Contours of the likelihood at the 68%, 90% and 95% levels for $\tan\beta = 10$, $A_0 = 0$ and $\mu > 0$ (left panel) or $\mu < 0$ (right panel), calculated using information of m_h, $b \to s\gamma$ and $\Omega_{CDM}h^2$ and the current uncertainties in m_t and m_b.

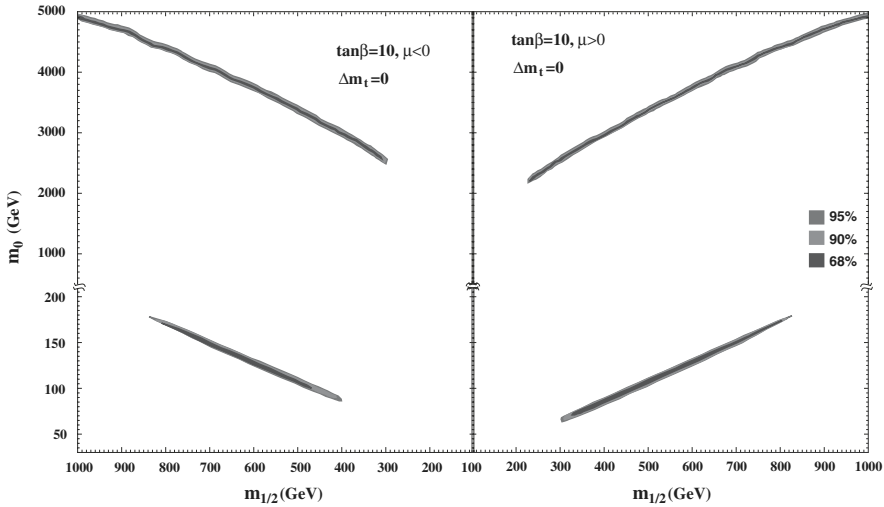

Fig. 8. As in Fig. 7 but assuming zero uncertainty in m_t.

the likelihood functions as they would appear if there were no uncertainty in m_t, keeping the other inputs the same. We see that, in this case, both the coannihilation and focus-point strips rise above the 68% CL.

Figure 9 shows the likelihood projection for $\tan\beta = 50$, $A_0 = 0$ and $\mu > 0$. In this case, regions at small $m_{1/2}$ and m_0 are disfavoured by the

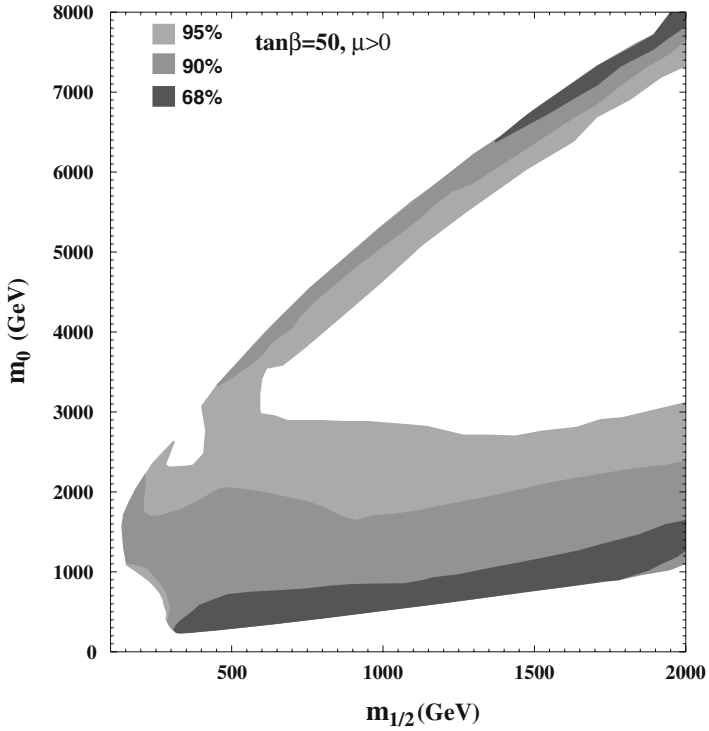

Fig. 9. Likelihood contours as in Fig. 7, but for $\tan\beta = 50$, $A_0 = 0$ and $\mu > 0$.

$b \to s\gamma$ constraint. The coannihilation region is broadened by a merger with the rapid-annihilation funnel. Both the coannihilation and the focus-point regions feature strips allowed at the 68% CL, and these are linked by a bridge at the 95% CL.

4 Beyond the CMSSM

The results of the CMSSM described in the previous sections are based heavily on the assumptions of universality of the supersymmetry breaking parameters. One of the simplest generalizations of this model relaxes the assumption of universality of the Higgs soft masses and is known as the NUHM [29] In this case, the input parameters include μ and m_A, in addition to the standard CMSSM inputs. In order to switch μ and m_A from outputs to inputs, the two soft Higgs masses, m_1, m_2 can no longer be set equal to m_0 and instead are calculated from the electroweak symmetry breaking conditions. The NUHM parameter space was recently analyzed [29] and a sample of the results are shown in Fig. 10.

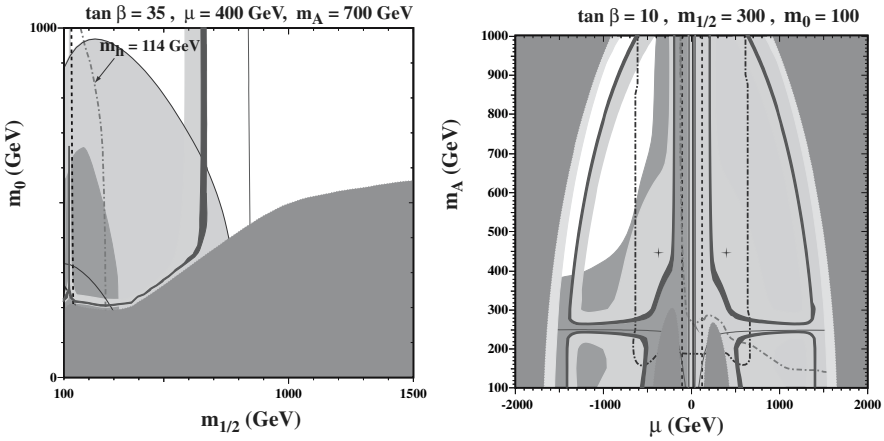

Fig. 10. a) The NUHM $(m_{1/2}, m_0)$ plane for $\tan\beta = 35$, (a) $\mu = 400\,\mathrm{GeV}$ and $m_A = 700\,\mathrm{GeV}$ b)the NUHM (μ, m_A) plane for $\tan\beta = 10$, $m_0 = 100\,\mathrm{GeV}$ and $m_{1/2} = 300\,\mathrm{GeV}$, with $A_0 = 0$. The (red) dot-dashed lines are the contours $m_h = 114\,\mathrm{GeV}$, and the near-vertical (black) dashed lines are the contours $m_{\chi^\pm} = 103.5\,\mathrm{GeV}$. The dark (black) dot-dashed lines indicate the GUT stability constraint. Only the areas inside these curves (small μ) are allowed by this constraint. The light (turquoise) shaded areas are the cosmologically preferred regions with $0.1 \leq \Omega_\chi h^2 \leq 0.3$. The darker (blue) portion of this region corresponds to the newer WMAP densities. The dark (brick red) shaded regions is excluded because a charged particle is lighter than the neutralino, and the lighter (yellow) shaded regions is excluded because the LSP is a sneutrino. The medium (green) shaded region is excluded by $b \to s\gamma$. The regions allowed by the $g-2$ constraint are shaded (pink) and bounded by solid black lines. The solid (blue) curves correspond to $m_\chi = m_A/2$.

In the left panel of Fig. 10, we see a $m_{1/2}, m_0$ plane with a relative low value of μ. In this case, an allowed region is found when the LSP contains a non-negligible Higgsino component which moderates the relic density independent of m_0. To the right of this region, the relic density is too small. In the right panel, we see an example of the m_A, μ plane. The crosses correspond to CMSSM points. In this single pane, we see examples of acceptable cosmological regions corresponding to the bulk region, co-annihilation region and s-channel annihilation through the Higgs pseudo scalar.

Rather than relax the CMSSM, it is in fact possible to further constrain the model. While the CMSSM models described above are certainly mSUGRA inspired, minimal supergravity models can be argued to be still more predictive. Let us assume that supersymmetry is broken in a hidden sector so that the superpotential can be written as a sum of two terms, $W = F(\phi) + g(\zeta)$, where ϕ represents all observable fields and ζ all hidden sector fields. We furthermore must choose $g(\zeta)$ such that when ζ picks up a vacuum expectation value, supersymmetry is broken. When the potential

is expanded and terms inversely proportional to Planck mass are dropped, one finds [30] 1) scalar mass universality with $m_0 = \langle g \rangle$; 2) trilinear mass universality with $A_0 = \langle dg/d\zeta \rangle \langle \zeta \rangle + \langle g \rangle \langle \zeta \rangle^2$; and 3) $B_0 = A_0 - m_0$.

In the simplest version of the theory [31], the universal trilinear soft supersymmetry-breaking terms are $A = (3 - \sqrt{3})m_0$ and bilinear soft supersymmetry-breaking term is $B = (2 - \sqrt{3})m_0$, i.e., a special case of the general relation above between B and A.

Given a relation between B_0 and A_0, we can no longer use the standard CMSSM boundary conditions, in which $m_{1/2}$, m_0, A_0, $\tan\beta$, and $sgn(\mu)$ are input at the GUT scale with μ and B determined by the electroweak symmetry breaking condition. Now, one is forced to input B_0 and instead $\tan\beta$ is calculated from the minimization of the Higgs potential [32].

In Fig. 11, the contours of $\tan\beta$ (solid blue lines) in the $(m_{1/2}, m_0)$ planes for two values of $\hat{A} = A_0/m_0$, $\hat{B} = B_0/m_0 = \hat{A} - 1$ and the sign of μ are displayed [32]. Also shown are the contours where $m_{\chi^\pm} > 104\,\mathrm{GeV}$ (near-vertical black dashed lines) and $m_h > 114\,\mathrm{GeV}$ (diagonal red dash-dotted lines). The excluded regions where $m_\chi > m_{\tilde{\tau}_1}$ have dark (red) shading, those excluded by $b \to s\gamma$ have medium (green) shading, and those where the relic density of neutralinos lies within the WMAP range $0.094 \leq \Omega_\chi h^2 \leq 0.129$ have light (turquoise) shading. Finally, the regions favoured by $g_\mu - 2$ at the 2-σ level are medium (pink) shaded.

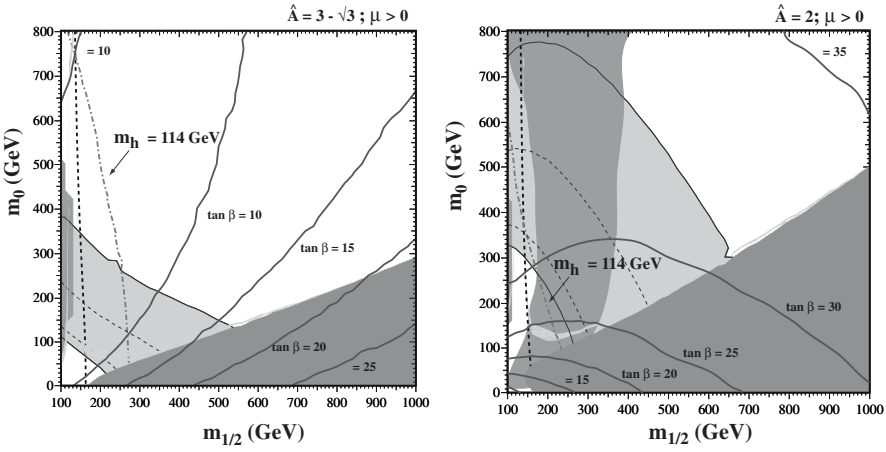

Fig. 11. Examples of $(m_{1/2}, m_0)$ planes with contours of $\tan\beta$ superposed, for $\mu > 0$ and (a) the simplest Polonyi model with $\hat{A} = 3 - \sqrt{3}, \hat{B} = \hat{A} - 1$ and (b) $\hat{A} = 2.0, \hat{B} = \hat{A} - 1$. In each panel, we show the regions excluded by the LEP lower limits on MSSM particles, those ruled out by $b \to s\gamma$ decay (medium green shading), and those excluded because the LSP would be charged (dark red shading). The region favoured by the WMAP range has light turquoise shading. The region suggested by $g_\mu - 2$ is medium (pink) shaded.

In panel (a) of Fig. 11, we see that the Higgs constraint combined with the relic density requires $\tan\beta \gtrsim 11$, whilst the relic density also enforces $\tan\beta \lesssim 20$. For a given point in the $m_{1/2} - m_0$ plane, the calculated value of $\tan\beta$ increases as $\hat{A}$ increases. This is seen in panel (b) of Fig. 11, when $\hat{A} = 2.0$, close to its maximal value for $\mu > 0$, the $\tan\beta$ contours turn over towards smaller $m_{1/2}$, and only relatively large values $25 \lesssim \tan\beta \lesssim 35$ are allowed by the $b \to s\gamma$ and $\Omega_{CDM}h^2$ constraints, respectively. For any given value of $\hat{A}$, there is only a relatively narrow range allowed for $\tan\beta$.

5 Detectability

The question of detectability with respect to supersymmetric models is of key importance particularly with the approaching start of the LHC. As an aid to the assessment of the prospects for detecting sparticles at different accelerators, benchmark sets of supersymmetric parameters have often been found useful, since they provide a focus for concentrated discussion [33, 34, 35]. A set of proposed post-LEP benchmark scenarios [33] were chosen to span the CMSSM. Five of the chosen points are in the 'bulk' region at small $m_{1/2}$ and m_0, four are spread along the coannihilation 'tail' at larger $m_{1/2}$ for various values of $\tan\beta$. Two points are in rapid-annihilation 'funnels' at large $m_{1/2}$ and m_0. Two points were chosen in the focus-point region at large m_0. The proposed points range over the allowed values of $\tan\beta$ between 5 and 50.

In Fig. 12, a comparison of the numbers of different MSSM particles that should be observable at different accelerators in the various benchmark scenarios [35], ordered by their consistency with $g_\mu - 2$. The qualities of the prospective sparticle observations at hadron colliders and linear e^+e^- colliders are often very different, with the latters' clean experimental environments providing prospects for measurements with better precision. Nevertheless, Fig. 12 already restates the clear message that hadron colliders and linear e^+e^- colliders are largely complementary in the classes of particles that they can see, with the former offering good prospects for strongly-interacting sparticles such as squarks and gluinos, and the latter excelling for weakly-interacting sparticles such as charginos, neutralinos and sleptons.

Clearly the center of mass energy of any future linear collider is paramount towards the supersymmetry discovery potential of the machine. This is seen in Fig. 12 for the benchmark points as more sparticles become observable at higher CM energy. We can emphasize this point in general models by plotting the masses of the two lightest (observable) sparticles in supersymmetric models. For example, in Fig. 13 [36], a scatter plot of the masses of the lightest visible supersymmetric particle (LVSP) and the next-to-lightest visible supersymmetric particle (NLVSP) is shown for the CMSSM. Once again, points selected satisfy all phenomenological constraints. We do not consider the LSP itself to be visible, nor any heavier neutral sparticle that decays

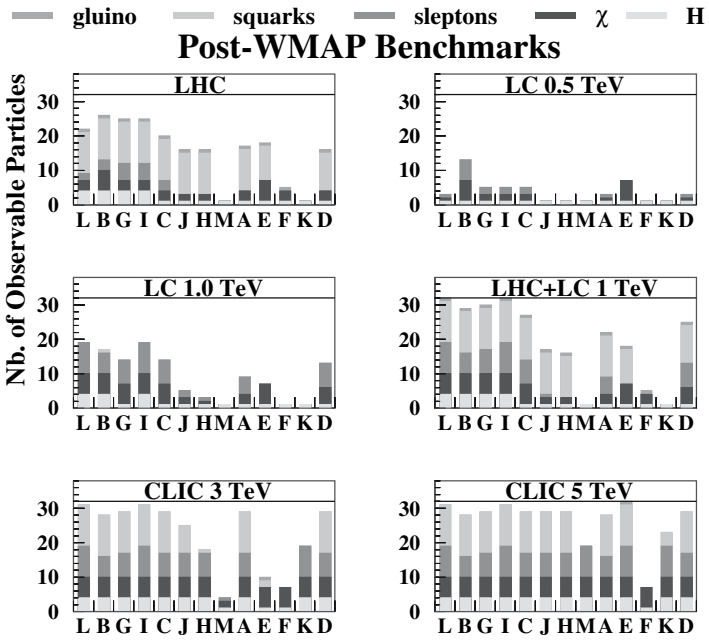

Fig. 12. Summary of the numbers of MSSM particles that may be detectable at various accelerators in the updated benchmark scenarios. We see that the capabilities of the LHC and of linear e^+e^- colliders are largely complementary. We re-emphasize that mass and coupling measurements at e^+e^- colliders are usually much cleaner and more precise than at hadron-hadron colliders such as the LHC, where, for example, it is not known how to distinguish the light squark flavours.

invisibly inside the detector, such as $\tilde{\nu} \to \nu\chi$ when $\tilde{\nu}$ is the next-to-lightest sparticle in a neutralino LSP scenario. The LVSP and the NLVSP are the lightest sparticles likely to be observable in collider experiments.

All points shown in Fig. 13 satisfy the phenomenological constraints discussed above. The dark (red) squares represent those points for which the relic density is outside the WMAP range, and for which all coloured sparticles (squarks and gluinos) are heavier than 2 TeV. The CMSSM parameter reach at the LHC has been analyzed in [37]. To within a few percent accuracy, the CMSSM reach contours presented in [37] coincide with the 2 TeV contour for the lightest squark (generally the stop) or gluino, so we regard the dark (red) points as unobservable at the LHC. Most of these points have $m_{NLVSP} \gtrsim 1.2\,\text{TeV}$. Conversely, the medium-shaded (green) crosses represent points where at least one squark or gluino has a mass less than 2 TeV and should be observable at the LHC. The spread of the dark (red) squares and medium-shaded (green) crosses, by as much as 500 GeV or more in some cases, reflects the maximum mass splitting between the LVSP and the NLVSP that is induced in the CMSSM via renormalization effects on the input mass

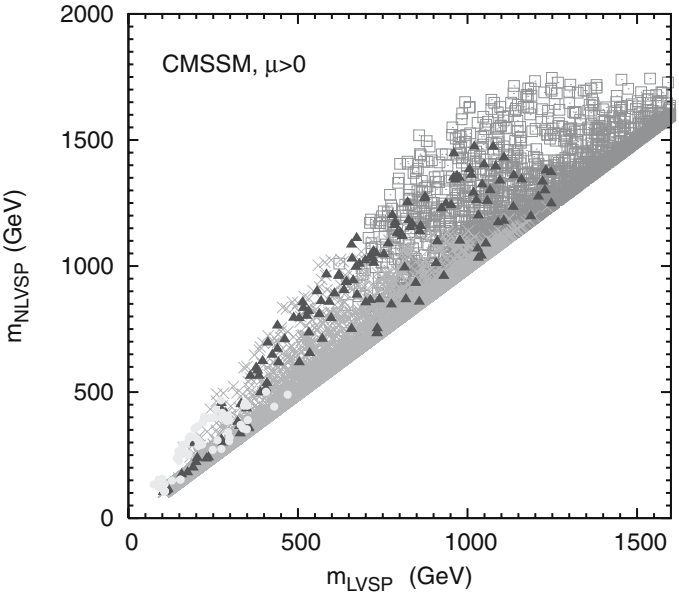

Fig. 13. Scatter plots of the masses of the lightest visible supersymmetric particle (LVSP) and the next-to-lightest visible supersymmetric particle (NLVSP) in the CMSSM for $\mu > 0$. The darker (blue) triangles satisfy all the laboratory, astrophysical and cosmological constraints. For comparison, the dark (red) squares and medium-shaded (green) crosses respect the laboratory constraints, but not those imposed by astrophysics and cosmology. In addition, the (green) crosses represent models which are expected to be visible at the LHC. The very light (yellow) points are those for which direct detection of supersymmetric dark matter might be possible.

parameters. The amount of this spread also reflects our cutoff $|A_0| < 1$ TeV, which controls the mass splitting of the third generation sfermions.

The darker (blue) triangles are those points respecting the cosmological cold dark matter constraint. Comparing with the regions populated by dark (red) squares and medium-shaded (green) crosses, one can see which of these models would be detectable at the LHC, according to the criterion in the previous paragraph. We see immediately that the dark matter constraint restricts the LVSP masses to be less than about 1250 GeV and NLVSP masses to be less than about 1500 GeV. In most cases, the identity of the LVSP is the lighter $\tilde{\tau}$. While pair-production of the LVSP would sometimes require a CM energy of about 2.5 TeV, in some cases there is a lower supersymmetric threshold due to the associated production of the LSP χ with the next lightest neutralino χ_2 [38]. Examining the masses and identities of the sparticle spectrum at these points, we find that $E_{CM} \gtrsim 2.2$ TeV would be sufficient to see at least one sparticle, as shown in Table 1. Similarly, only a LC with

Table 1. Centre-of-mass energy (in TeV) required to observe one or two sparticles at a future LC in the CMSSM and NUHM.

Model	$sgn(\mu)$	*One Sparticle*	*Two Sparticles*
CMSSM	$\mu > 0$	2.2	2.6
	$\mu < 0$	2.2	2.5
NUHM	$\mu > 0$	2.4	2.8
	$\mu < 0$	2.6	2.9

$E_{CM} \geq 2.5\,\text{TeV}$ would be 'guaranteed' to see two visible sparticles (in addition to the χ LSP), somewhat lower than the 3.0 TeV one might obtain by requiring the pair production of the NLVSP. Points with $m_{LVSP} \gtrsim 700\,\text{GeV}$ are predominantly due to rapid annihilation via direct-channel H, A poles, while points with $200\,\text{GeV} \lesssim m_{LVSP} \lesssim 700\,\text{GeV}$ are largely due to χ-slepton coannihilation.

An $E_{CM} = 500\,\text{GeV}$ LC would be able to explore the 'bulk' region at low $(m_{1/2}, m_0)$, which is represented by the small cluster of points around m_{LVSP} $\sim$200 GeV. It should also be noted that there are a few points with $m_{LVSP} \sim$ 100 GeV which are due to rapid annihilation via the light Higgs pole. These points all have very large values of m_0 which relaxes the Higgs mass and chargino mass constraints, particularly when $m_t = 178\,\text{GeV}$. A LC with $E_{CM} = 1000\,\text{GeV}$ would be able to reach some way into the coannihilation 'tail', but would not cover all the WMAP-compatible dark (blue) triangles. Indeed, about a third of these points are even beyond the reach of the LHC in this model. Finally, the light (yellow) filled circles are points for which the elastic χ-p scattering cross section is larger than 10^{-8} pb.

Because the LSP as dark matter is present locally, there are many avenues for pursuing dark matter detection. Direct detection techniques rely on an ample neutralino-nucleon scattering cross-section. The prospects for direct detection for the benchmark points discussed above [39] are shown in Fig. 14. This figure shows rates for the elastic spin-independent and spin dependent scattering cross sections of supersymmetric relics on protons. Indirect searches for supersymmetric dark matter via the products of annihilations in the galactic halo or inside the Sun also have prospects in some of the benchmark scenarios [39].

In Fig. 15, we display the allowed ranges of the spin-independent cross sections in the NUHM when we sample randomly $\tan\beta$ as well as the other NUHM parameters [45]. The raggedness of the boundaries of the shaded regions reflects the finite sample size. The dark shaded regions includes all sample points after the constraints discussed above (including the relic density constraint) have been applied. In a random sample, one often hits points which are are perfectly acceptable at low energy scales but when the parameters are run to high energies approaching the GUT scale, one or several of

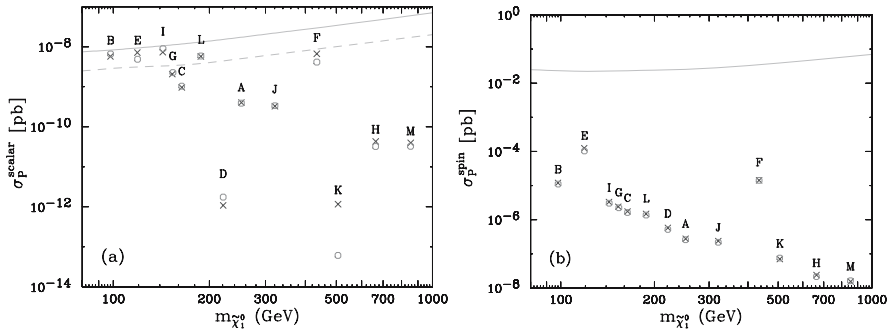

Fig. 14. Elastic cross sections for (**a**) spin-independent scattering and (**b**) spin-dependent scattering on protons. Our predictions (blue crosses) are compared with those of `Neutdriver` [40] (red circles) for neutralino-nucleon scattering. Projected sensitivities (a) for CDMS II [41] and CRESST [42] (solid) and GENIUS [43] (dashed) and (b) for a 100 kg NAIAD array [44] are also shown.

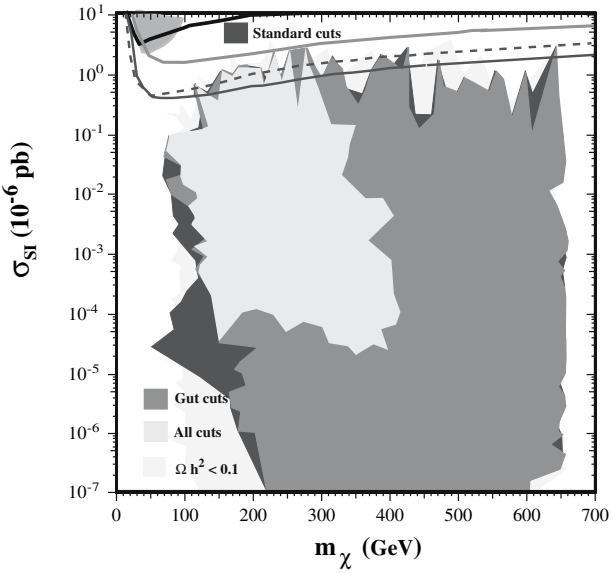

Fig. 15. Ranges of the spin-independent cross section in the NUHM. The ranges allowed by the cuts on $\Omega_\chi h^2$, m_h and $b \to s\gamma$ have dark shading, those still allowed by the GUT stability cut have medium shading, and those still allowed after applying all the cuts including $g_\mu - 2$ have light shading. The pale shaded region corresponds to the extra area of points with low relic densities, whose cross sections have been rescaled appropriately. Also shown are the limits from the CDMS [48] and Edelweiss [49] experiments as well as the recent CDMSII result [50] on the neutralino-proton elastic scattering cross section as a function of the neutralino mass. The CDMSII limit is stronger than the Edelweiss limit which is stronger than the previous CDMS limit at higher m_χ. The result reported by DAMA [51] is found in the upper left.

the sparticles mass squared runs negative [46]. This has been referred to as the GUT constraint here. The medium shaded region embodies those points after the GUT constraint has been applied. After incorporating all the cuts, including that motivated by $g_\mu - 2$, we find that the light shaded region where the scalar cross section has the range 10^{-6} pb $\gtrsim \sigma_{SI} \gtrsim 10^{-10}$ pb, with somewhat larger (smaller) values being possible in exceptional cases. If the $g_\mu - 2$ cut is removed, the upper limits on the cross sections are unchanged, but much lower values become possible: $\sigma_{SI} \ll 10^{-13}$ pb. The effect of the GUT constraint on more general supersymmetric models was discussed in [47].

The results from this analysis [45] for the scattering cross section in the NUHM (which by definition includes all CMSSM results) are compared with the previous CDMS [48] and Edelweiss [49] bounds as well as the recent CDMSII results [50] in Fig. 15. While previous experimental sensitivities were not strong enough to probe predictions of the NUHM, the current CDMSII bound has begun to exclude realistic models and it is expected that these bounds improve by a factor of about 20.

This work was partially supported by DOE grant DE-FG02-94ER-40823.

References

1. H. Goldberg, Phys. Rev. Lett. **50**, 1419 (1983); J. Ellis, J.S. Hagelin, D.V. Nanopoulos, K.A. Olive and M. Srednicki, Nucl. Phys. **B238**, 453 (1984).
2. L.E. Ibanez, Phys. Lett. **137B**, 160 (1984); J. Hagelin, G.L. Kane, and S. Raby, Nucl., Phys. **B241**, 638 (1984); T. Falk, K. A. Olive and M. Srednicki, Phys. Lett. B **339**, 248 (1994).
3. S. Ahlen, et. al., Phys. Lett. **B195**, 603 (1987);
   D.D. Caldwell, et. al., Phys. Rev. Lett. **61**, 510 (1988);
   M. Beck et al., Phys. Lett. **B336** 141 (1994).
4. see e.g. K.A. Olive and M. Srednicki, Phys. Lett. **205B**, 553 (1988);
   N. Sato et al. *Phys.Rev.* **D44**, 2220 (1991).
5. J. Ellis, T. Falk, and K.A. Olive, *Phys.Lett.* **B444** (1998) 367 [arXiv:hep-ph/9810360]; J. Ellis, T. Falk, K.A. Olive, and M. Srednicki, Astr. Part. Phys. **13** (2000) 181 [Erratum-ibid. **15** (2001) 413] [arXiv:hep-ph/9905481].
6. J.L. Feng, S. Su and F. Takayama, arXiv:hep-ph/0404231; arXiv:hep-ph/0404198; J. L. Feng, A. Rajaraman and F. Takayama, Phys. Rev. Lett. **91** (2003) 011302 [arXiv:hep-ph/0302215]; J. R. Ellis, K. A. Olive, Y. Santoso and V. C. Spanos, Phys. Lett. B **588** (2004) 7 [arXiv:hep-ph/0312262]; L. Roszkowski and R. Ruiz de Austri, arXiv:hep-ph/0408227.
7. Joint LEP 2 Supersymmetry Working Group, *Combined LEP Chargino Results, up to 208 GeV*, `http://lepsusy.web.cern.ch/lepsusy/www/inos_moriond01/charginos_pub.html`.
8. Joint LEP 2 Supersymmetry Working Group, *Combined LEP Selectron/Smuon/Stau Results, 183–208 GeV*, `http://lepsusy.web.cern.ch/lepsusy/www/sleptons_summer02/slep_2002.html`.
9. LEP Higgs Working Group for Higgs boson searches, OPAL Collaboration, ALEPH Collaboration, DELPHI Collaboration and L3 Collaboration, Phys.

Lett. B **565** (2003) 61 [arXiv:hep-ex/0306033]. *Searches for the neutral Higgs bosons of the MSSM: Preliminary combined results using LEP data collected at energies up to 209 GeV*, LHWG-NOTE-2001-04, ALEPH-2001-057, DELPHI-2001-114, L3-NOTE-2700, OPAL-TN-699, arXiv:hep-ex/0107030; LHWG Note/2002-01, `http://lephiggs.web.cern.ch/LEPHIGGS/papers/July2002_SM/index.html`.

10. S. Heinemeyer, W. Hollik and G. Weiglein, Comput. Phys. Commun. **124** (2000) 76 [arXiv:hep-ph/9812320]; S. Heinemeyer, W. Hollik and G. Weiglein, Eur. Phys. J. C **9** (1999) 343 [arXiv:hep-ph/9812472].
11. S. Chen et al. [CLEO Collaboration], Phys. Rev. Lett. **87** (2001) 251807 [arXiv:hep-ex/0108032]; BELLE Collaboration, BELLE-CONF-0135. See also K. Abe et al. [Belle Collaboration], Phys. Lett. B **511** (2001) 151 [arXiv:hep-ex/0103042]; B. Aubert et al. [BaBar Collaboration], arXiv:hep-ex/0207076.
12. C. Degrassi, P. Gambino and G. F. Giudice, JHEP **0012** (2000) 009 [arXiv:hep-ph/0009337], as implemented by P. Gambino and G. Ganis.
13. M. Carena, D. Garcia, U. Nierste and C. E. Wagner, Phys. Lett. B **499** (2001) 141 [arXiv:hep-ph/0010003]; P. Gambino and M. Misiak, Nucl. Phys. B **611** (2001) 338; D. A. Demir and K. A. Olive, Phys. Rev. D **65** (2002) 034007 [arXiv:hep-ph/0107329]; T. Hurth, arXiv:hep-ph/0106050; Rev. Mod. Phys. **75**, 1159 (2003) [arXiv:hep-ph/0212304].
14. [The Muon g-2 Collaboration], Phys. Rev. Lett. **92** (2004) 161802, hep-ex/0401008.
15. M. Davier, S. Eidelman, A. Höcker and Z. Zhang, Eur. Phys. J. **C 31** (2003) 503, hep-ph/0308213; see also K. Hagiwara, A. Martin, D. Nomura and T. Teubner, Phys. Rev. **D 69** (2004) 093003, hep-ph/0312250; S. Ghozzi and F. Jegerlehner, Phys. Lett. **B 583** (2004) 222, hep-ph/0310181; M. Knecht, hep-ph/0307239; K. Melnikov and A. Vainshtein, hep-ph/0312226; J. de Troconiz and F. Yndurain, hep-ph/0402285.
16. C.L. Bennett et al., Astrophys. J. Suppl. **148** (2003) 1; D.N. Spergel et al., Astrophys. J. Suppl. **148** (2003) 175; H.V. Peiris et al., Astrophys. J. Suppl. **148** (2003) 213.
17. J.R. Ellis, K.A. Olive, Y. Santoso and V.C. Spanos, Phys. Lett. B **565** (2003) 176 [arXiv:hep-ph/0303043].
18. H. Baer and C. Balazs, JCAP **0305** (2003) 006 [arXiv:hep-ph/0303114].
19. A.B. Lahanas and D. V. Nanopoulos, Phys. Lett. B **568** (2003) 55 [arXiv:hep-ph/0303130]; U. Chattopadhyay, A. Corsetti and P. Nath, Phys. Rev. D **68** (2003) 035005 [arXiv:hep-ph/0303201]; C. Munoz, Int. J. Mod. Phys. A **19**, 3093 (2004) [arXiv:hep-ph/0309346] R. Arnowitt, B. Dutta and B. Hu, arXiv:hep-ph/0310103.
20. M. Drees and M.M. Nojiri, Phys. Rev. **D47** (1993) 376; H. Baer and M. Brhlik, Phys. Rev. **D53** (1996) 59; and *Phys. Rev.* **D57** (1998) 567; H. Baer, M. Brhlik, M.A. Diaz, J. Ferrandis, P. Mercadante, P. Quintana and X. Tata, Phys. Rev. **D63** (2001) 015007; A.B. Lahanas, D.V. Nanopoulos and V.C. Spanos, Mod. Phys. Lett. **A16** (2001) 1229.
21. J.R. Ellis, T. Falk, G. Ganis, K.A. Olive and M. Srednicki, Phys. Lett. **B510** (2001) 236 [arXiv:hep-ph/0102098].
22. J.L. Feng, K.T. Matchev and T. Moroi, Phys. Rev. D **61** (2000) 075005 [arXiv:hep-ph/9909334].
23. A. Romanino and A. Strumia, Phys. Lett. **B 487** (2000) 165, hep-ph/9912301.

24. J.R. Ellis and K.A. Olive, Phys. Lett. B **514** (2001) 114 [arXiv:hep-ph/0105004].
25. W. de Boer, M. Huber, C. Sander and D.I. Kazakov, arXiv:hep-ph/0106311.
26. J.R. Ellis, K.A. Olive, Y. Santoso and V.C. Spanos, Phys. Rev. D **69** (2004) 095004 [arXiv:hep-ph/0310356].
27. J.R. Ellis, K. Enqvist, D.V. Nanopoulos and F. Zwirner, Mod. Phys. Lett. A **1** (1986) 57; R. Barbieri and G. F. Giudice, Nucl. Phys. B **306** (1988) 63.
28. J.R. Ellis, K.A. Olive and Y. Santoso, New J. Phys. **4** (2002) 32 [arXiv:hep-ph/0202110].
29. J. Ellis, K. Olive and Y. Santoso, *Phys.Lett.* **B539** (2002) 107 [arXiv:hep-ph/0204192].; J.R. Ellis, T. Falk, K.A. Olive and Y. Santoso, Nucl. Phys. B **652** (2003) 259 [arXiv:hep-ph/0210205].
30. For reviews, see: H.P. Nilles, Phys. Rep. **110** (1984) 1; A. Brignole, L.E. Ibanez and C. Munoz, arXiv:hep-ph/9707209, published in *Perspectives on supersymmetry*, ed. G.L. Kane, pp. 125–148; H.-P. Nilles, M. Srednicki and D. Wyler, Phys. Lett. **120B** (1983) 345; L.J. Hall, J. Lykken and S. Weinberg, Phys. Rev. **D27** (1983) 2359.
31. J. Polonyi, Budapest preprint KFKI-1977-93 (1977); R. Barbieri, S. Ferrara and C.A. Savoy, Phys. Lett. **119B** (1982) 343.
32. J.R. Ellis, K.A. Olive, Y. Santoso and V.C. Spanos, Phys. Lett. B **573** (2003) 162 [arXiv:hep-ph/0305212]; Phys. Rev. D **70** (2004) 055005 [arXiv:hep-ph/0405110].
33. M. Battaglia et al., Eur. Phys. J. **C 22** (2001) 535, hep-ph/0106204.
34. B. Allanach et al., Eur. Phys. J. **C 25** (2002) 113, hep-ph/0202233.
35. M. Battaglia, A. De Roeck, J. Ellis, F. Gianotti, K. Olive and L. Pape, Eur. Phys. J. **C 33** (2004) 273, hep-ph/0306219.
36. J.R. Ellis, K.A. Olive, Y. Santoso and V.C. Spanos, arXiv:hep-ph/0408118.
37. H. Baer, C. Balazs, A. Belyaev, T. Krupovnickas and X. Tata, JHEP **0306** (2003) 054 [arXiv:hep-ph/0304303].
38. A. Djouadi, M. Drees and J.L. Kneur, JHEP **0108** (2001) 055 [arXiv:hep-ph/0107316].
39. J. Ellis, J.L. Feng, A. Ferstl, K.T. Matchev and K.A. Olive, *Eur. Phys. J.* **C24** (2002) 311 [arXiv:astro-ph/0110225].
40. G. Jungman, M. Kamionkowski and K. Griest, Phys. Rept. **267**, 195 (1996) [arXiv:hep-ph/9506380]; `http://t8web.lanl.gov/people/jungman/neut-package.html`.
41. CDMS Collaboration, R.W. Schnee et al., *Phys. Rep.* **307** (1998) 283.
42. CRESST Collaboration, M. Bravin et al., *Astropart. Phys.* **12** (1999) 107.
43. H.V. Klapdor-Kleingrothaus, arXiv:hep-ph/0104028.
44. N.J. Spooner et al., Phys. Lett. B **473**, 330 (2000).
45. J. R. Ellis, A. Ferstl, K. A. Olive and Y. Santoso, Phys. Rev. D **67**, 123502 (2003) [arXiv:hep-ph/0302032].
46. T. Falk, K. A. Olive, L. Roszkowski and M. Srednicki, Phys. Lett. B **367** (1996) 183 [arXiv:hep-ph/9510308]; A. Riotto and E. Roulet, Phys. Lett. B **377** (1996) 60 [arXiv:hep-ph/9512401]; A. Kusenko, P. Langacker and G. Segre, Phys. Rev. D **54** (1996) 5824 [arXiv:hep-ph/9602414]; T. Falk, K. A. Olive, L. Roszkowski, A. Singh and M. Srednicki, Phys. Lett. B **396** (1997) 50 [arXiv:hep-ph/9611325].
47. J. R. Ellis, K. A. Olive, Y. Santoso and V. C. Spanos, Phys. Rev. D **69**, 015005 (2004) [arXiv:hep-ph/0308075].

48. D. Abrams et al. [CDMS Collaboration], *Phys.Rev.* **D66** (2002) 122003 [arXiv:astro-ph/0203500].
49. A. Benoit et al., *Phys.Lett.* **B545** (2002) 43 [arXiv:astro-ph/0206271].
50. D. S. Akerib et al. [CDMS Collaboration], arXiv:astro-ph/0405033.
51. DAMA Collaboration, R. Bernabei et al., *Phys. Lett.* **B436** (1998) 379.

On the Mixed Spin-Scalar Coupling Approach in Dark Matter Search

V.A. Bednyakov[1] and H.V. Klapdor-Kleingrothaus[2]

[1] Laboratory of Nuclear Problems, Joint Institute for Nuclear Research, 141980 Dubna, Russia.
Vadim.Bednyakov@jinr.ru

[2] Max-Planck-Institut für Kernphysik, Postfach 103980, D-69029, Heidelberg, Germany.
H.Klapdor@mpi-hd.mpg.de

Summary. To avoid misleading discrepancies between results of different dark matter search experiments as well as between the data and SUSY calculations it is in general preferable to use a mixed spin-scalar coupling approach in which spin-independent and spin-dependent WIMP-nucleon couplings are *both* non-zero. On the other hand one may, however, to safely neglect the subdominant spin WIMP-nucleon contribution in comparison with the spin-independent one in analysis of data from experiments with heavy enough non-zero-spin target nuclei.

The mixed coupling approach is applied to estimate future prospects of experiments with the odd-neutron high-spin isotope ^{73}Ge.

1 Introduction

In many experiments one tries to detect directly relic dark matter (DM) Weakly Interacting Massive Particles (WIMPs) χ via their elastic scattering on a target nucleus (A, Z). The nuclear recoil energy $E_{\rm R}$ ($E_{\rm R} \sim 10^{-6} m_\chi \sim$ few keV) is measured. The expected differential event rate has the form [1, 2, 3, 4, 5, 6, 7, 8]:

$$\frac{dR}{dE_{\rm R}} = N_t \frac{\rho_\chi}{m_\chi} \int_{v_{\rm min}}^{v_{\rm max}} dv f(v) v \frac{d\sigma}{dq^2}(v, q^2), \qquad E_{\rm R} = q^2/(2M_A)\,. \tag{1}$$

Here, $v_{\rm min} = \sqrt{M_A E_{\rm R}/2\mu_A^2}$, $v_{\rm max} = v_{\rm esc} \approx 600\,{\rm km/s}$, $\mu_A = \frac{m_\chi M_A}{m_\chi + M_A}$; $f(v)$ is the distribution of χ-particles in the solar vicinity, N_t is the number density of target nuclei. M_A denotes the target nuclear mass, the dark matter density is usually assumed to be $\rho_\chi = 0.3\,{\rm GeV/cm^3}$. The χ-nucleus elastic scattering cross section for non-zero-spin ($J \neq 0$) nuclei is a sum of the spin-independent (SI, or scalar) and spin-dependent (SD, axial) terms [9, 10, 11, 12]:

$$\frac{d\sigma^A}{dq^2}(v, q^2) = \frac{\sigma_{\rm SD}^A(0)}{4\mu_A^2 v^2} F_{\rm SD}^2(q^2) + \frac{\sigma_{\rm SI}^A(0)}{4\mu_A^2 v^2} F_{\rm SI}^2(q^2)\,. \tag{2}$$

For $q = 0$ the nuclear SD and SI cross sections take the forms

$$\sigma^A_{\rm SI}(0) = \frac{\mu_A^2}{\mu_p^2} A^2 \sigma^p_{\rm SI}(0)\ , \tag{3}$$

$$\sigma^A_{\rm SD}(0) = \frac{4\mu_A^2}{\pi}\frac{(J+1)}{J}\left\{a_p\langle \mathbf{S}^A_p\rangle + a_n\langle \mathbf{S}^A_n\rangle\right\}^2 \tag{4}$$

$$= \frac{\mu_A^2}{\mu_p^2}\frac{4}{3}\frac{J+1}{J}\sigma_{\rm SD}(0)\left\{\langle \mathbf{S}^A_p\rangle\cos\theta + \langle \mathbf{S}^A_n\rangle\sin\theta\right\}^2\ . \tag{5}$$

The dependence on effective χ-quark scalar $\mathcal{C}_q$ and axial $\mathcal{A}_q$ couplings and on the spin $\Delta_q^{(p,n)}$ and the mass $f_q^{(p,n)}$ structure of *nucleons* enter into these formulas via the zero-momentum-transfer proton and neutron SI and SD cross sections ($\mu_n^2 = \mu_p^2$ is assumed):

$$\sigma^p_{\rm SI}(0) = 4\frac{\mu_p^2}{\pi}c_0^2, \qquad \sigma^{p,n}_{\rm SD}(0) = 12\frac{\mu_{p,n}^2}{\pi}a_{p,n}^2; \tag{6}$$

$$c_0 = c_0^{p,n} = \sum_q \mathcal{C}_q f_q^{(p,n)}, \qquad a_p = \sum_q \mathcal{A}_q\Delta_q^{(p)}, \quad a_n = \sum_q \mathcal{A}_q\Delta_q^{(n)}\ . \tag{7}$$

The effective spin WIMP-nucleon cross section $\sigma_{\rm SD}(0)$ and the coupling mixing angle θ [13, 14] were introduced in (5):

$$\sigma_{\rm SD}(0) = \frac{\mu_p^2}{\pi}\frac{4}{3}\Big[a_p^2 + a_n^2\Big], \qquad \tan\theta = \frac{a_n}{a_p}\ . \tag{8}$$

The factors $\Delta_q^{(p,n)}$, which parametrize the quark spin content of the nucleon, are defined as $2\Delta_q^{(n,p)}s^\mu \equiv \langle p,s|\bar\psi_q\gamma^\mu\gamma_5\psi_q|p,s\rangle_{(p,n)}$. The $\langle \mathbf{S}^A_{p(n)}\rangle$ is the total spin of protons (neutrons) averaged over all A nucleons of the nucleus (A,Z). In the simplest case the SD and SI nuclear form-factors

$$F^2_{\rm SD,SI}(q^2) = \frac{S^A_{\rm SD,SI}(q^2)}{S^A_{\rm SD,SI}(0)} \tag{9}$$

have a Gaussian form (see, for example, [15]). The spin-dependent structure function $S^A_{\rm SD}(q)$ in terms of isoscalar $a_0 = a_n + a_p$ and isovector $a_1 = a_p - a_n$ effective couplings has the form [11, 12]:

$$S^A_{\rm SD}(q) = a_0^2 S_{00}(q) + a_1^2 S_{11}(q) + a_0 a_1 S_{01}(q)\ . \tag{10}$$

2 One-Coupling Dominance Approach

One can see from (2)–(7) that the direct dark matter search experiments supply us with only three different constants for the underlying SUSY theory from non-observation of a DM signal (c_0, a_p and a_n, or $\sigma^p_{\rm SI}(0)$, $\sigma^p_{\rm SD}(0)$ and $\sigma^n_{\rm SD}(0)$), provided the DM particle is the lightest SUSY particle (LSP) neutralino [16]. These constraints are traditionally presented in the form of sets

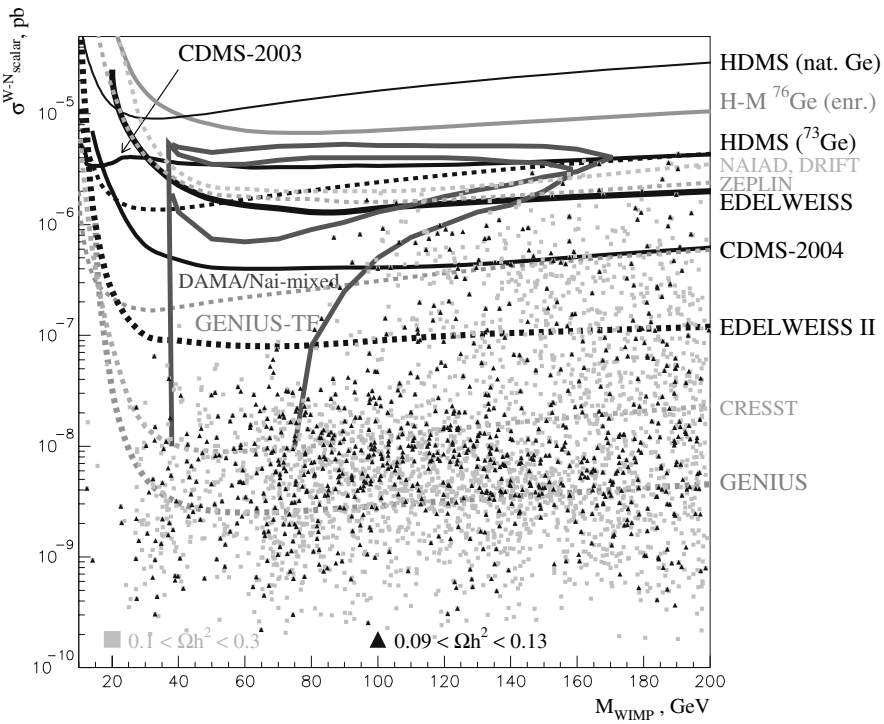

Fig. 1. WIMP-nucleon cross section limits in pb for spin-independent (scalar) interactions as a function of the WIMP mass in GeV. Shown are contour lines for some of the present experimental limits (solid lines) and some of projected experiments (dashed lines). All curves are obtained in the one-coupling dominance approach with $\sigma_{\rm SD} = 0$. For example, the closed DAMA/NaI contour corresponds to complete neglection of SD WIMP-nucleon interaction. Only the open DAMA contour is obtained in [13] with the assumption that $\sigma_{\rm SD} = 0.08$ pb > 0. From [17].

of exclusion curves for the spin-independent (scalar) nucleon-WIMP (Fig. 1), spin-dependent (axial) proton-WIMP (Fig. 2) and spin-dependent neutron-WIMP cross sections (Fig. 3) as functions of the WIMP mass. From (4) one can also see that contrary to the SI case (3) both proton $\langle \mathbf{S}_p^A \rangle$ and neutron $\langle \mathbf{S}_n^A \rangle$ spin contributions simultaneously enter into formula (4) for the SD WIMP-nucleus cross section $\sigma_{\rm SD}^A(0)$. Nevertheless, for the most interesting isotopes either $\langle \mathbf{S}_p^A \rangle$ or $\langle \mathbf{S}_n^A \rangle$ dominates ($\langle \mathbf{S}_{n(p)}^A \rangle \ll \langle \mathbf{S}_{p(n)}^A \rangle$) [17, 18].

In earlier considerations [3, 10, 15, 19, 20, 21] one reasonably assumed that the nuclear spin was carried by the "odd" unpaired group of protons or neutrons and only one of either $\langle \mathbf{S}_n^A \rangle$ or $\langle \mathbf{S}_p^A \rangle$ was non-zero. In this case all possible non-zero-spin target nuclei can be classified into n-odd and p-odd groups. Following this classification, the current experimental situation for the spin-dependent WIMP-**proton** and WIMP-**neutron** cross sections are

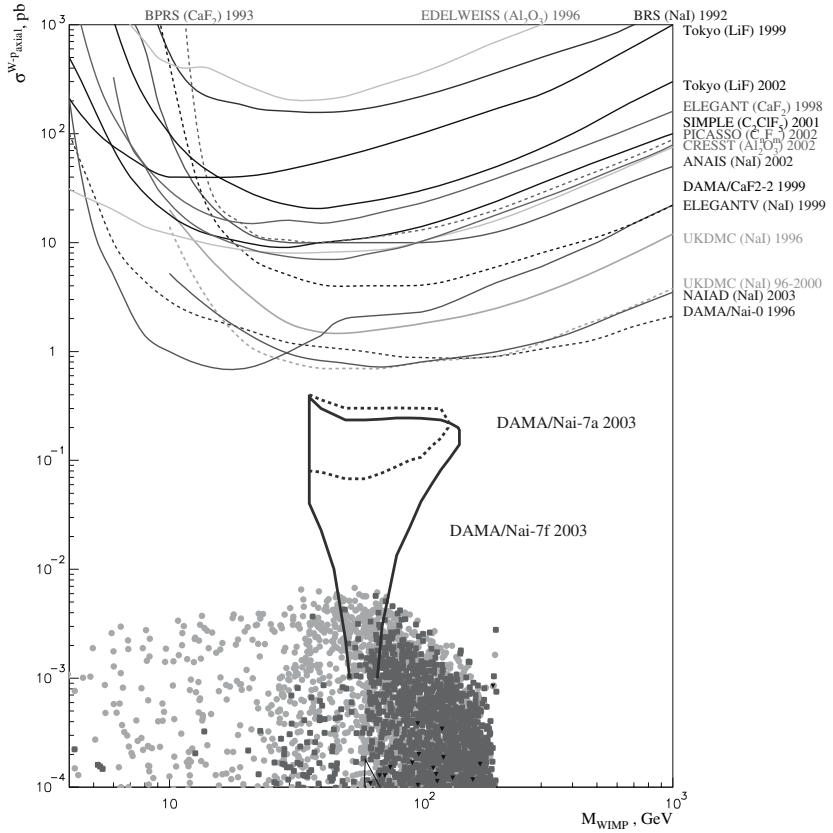

Fig. 2. Exclusion curves for the spin-dependent WIMP-proton cross sections ($\sigma^p_{\rm SD}$ as a function of the WIMP mass). All curves, except the NAIAD and Tokio-LiF, are obtained in the one-coupling dominance approach with $\sigma_{\rm SI} = 0$ and $\sigma^n_{\rm SD} = 0$. DAMA/NaI-7a(f) contours for the WIMP-proton SD interaction in ^{127}I are obtained on the basis of the positive signature of annual modulation within the framework of the mixed scalar-spin coupling approach [13, 14]. From [17].

naturally presented separately in Fig. 2 and Fig. 3. The DAMA/NaI-7 contours for the WIMP-proton SD interaction (dominating in ^{127}I) obtained on the basis of the positive signature of the annual modulation (closed contour) [13] and within the mixed coupling framework (open contour) [14] are also presented in Fig. 2. Similarly, the DAMA/NaI-7 [13] contours for the WIMP-neutron SD interaction (subdominant in ^{127}I) are given in Fig. 3. One can also expect some exclusion curves for the SD cross section from the CDMS [22] and EDELWEISS [23] experiments with natural-germanium bolometric detectors (due to a small Ge-73 admixture). The scatter plots for the SD LSP-proton and LSP-neutron cross sections calculated in the effMSSM from [17] are also given in Figs. 1–3.

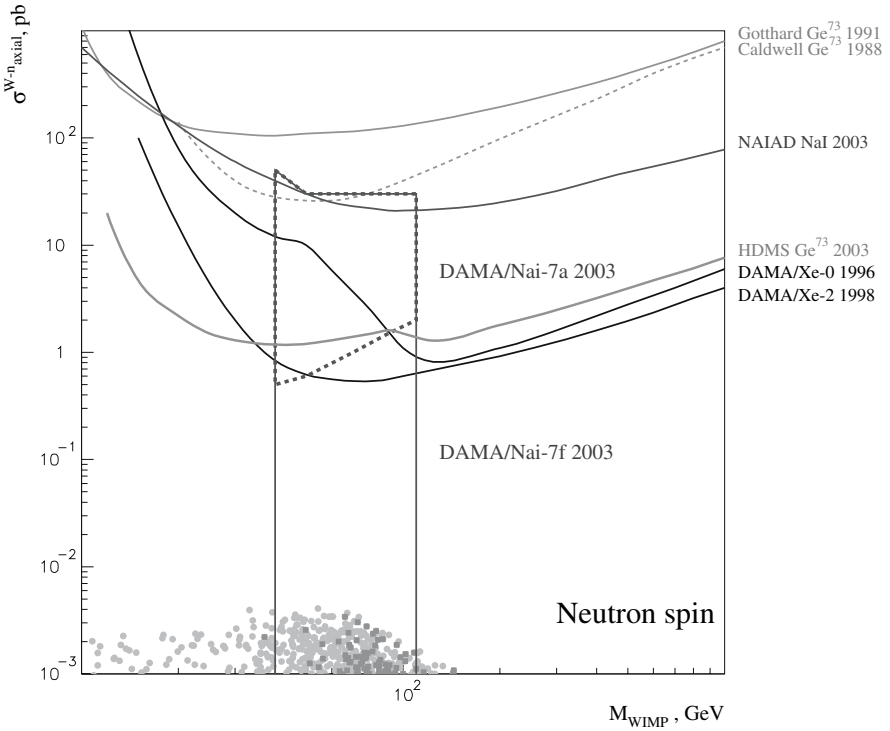

Fig. 3. Exclusion curves for the spin-dependent WIMP-neutron cross sections ($\sigma^n_{\rm SD}$ versus the WIMP mass). DAMA/NaI-7a(f) contours for the WIMP-neutron SD interaction (subdominating in ^{127}I) are obtained from the relevant figures of [13, 14]. Note that the NAIAD curve here corresponds to the WIMP-neutron SD interaction subdominant for ^{127}I. The WIMP-proton SD interaction dominates for this nucleus. The curve was obtained in the approach of [24]. It is much weaker in comparison with the both DAMA/Xe and HDMS curves. From [17].

We would like to stress that the calculated scatter plots for $\sigma^p_{\rm SD}$ (Fig. 2) are obtained without any assumption of $\sigma^n_{\rm SD} = 0$ (and $\sigma^p_{\rm SI} = 0$), but the experimental exclusion curves for $\sigma^p_{\rm SD}$ were traditionally extracted from the data with the spin-neutron (and scalar) contribution fully neglected, i.e. under the assumption that $\sigma^n_{\rm SD} = 0$ (and $\sigma^p_{\rm SI} = 0$). This **one-spin-coupling dominance scheme** (always used before new approaches were proposed in [24] and in [13, 25, 26]) gave a bit too pessimistic exclusion curves, but allowed direct comparison of sensitivities for different experiments. More stringent constraints on $\sigma^p_{\rm SD}$ can be obtained [24, 13, 25, 26] by assuming both $\sigma^p_{\rm SD} \neq 0$ and $\sigma^n_{\rm SD} \neq 0$ (although the contribution of the neutron spin is usually very small because $\langle \mathbf{S}^A_n \rangle \ll \langle \mathbf{S}^A_p \rangle$). Therefore a direct comparison of the old-fashioned exclusion curves with the new ones could in principle be misleading.

The same conclusion on the one-coupling dominance approach to a great extent concerns [13, 26] the direct comparison of the *old* SI exclusion curves (obtained with zero SD contribution, $\sigma_{\rm SD} = 0$) with the *new* SI exclusion curves (obtained with non-zero SD contribution, $\sigma_{\rm SD} > 0$) as well as with the results of the SUSY calculations. One can see from Fig. 1 that the *new-type* DAMA/NaI open contour (when $\sigma_{\rm SD} > 0$) is in agreement with the best exclusion curves of the CDMS and EDELWEISS as well as with SUSY calculations. One knows that both these experiments have natural germanium (almost pure spinless) as a target and therefore have no sensitivity to the spin-dependent WIMP-nucleon couplings (for them $\sigma_{\rm SD} \equiv 0$). Therefore, these experiments exclude only the pure SI interpretation of the DAMA annual modulation signal [22, 27, 28, 29, 30]. The statement that this DAMA result is *completely* excluded by the results of these cryogenic experiments and is inconsistent with the SUSY interpretation (see, for example, [31]) is simply wrong (see also discussions in [28, 32]).

The event-by-event CDMS and EDELWEISS background discrimination (via simultaneous charge and phonon signal measurements) is certainly very important. Nevertheless the DAMA annual signal modulation is one of a few available *positive* signatures of WIMP-nucleus interactions and the importance of its observation goes far beyond a simple background reduction. Therefore, to completely exclude the DAMA result, a new experiment, being indeed sensitive to the modulation signal, would have to exclude this modulation signal on the basis of the same or much better statistics.

Furthermore, taking seriously the positive DAMA result together with the negative results of the CDMS and EDELWEISS as well as the results of [33] one can arrive at a conclusion about simultaneous existence and importance of both SD and SI WIMP-nucleus interactions.

3 Mixed Spin-Scalar WIMP-Nucleon Couplings

More accurate calculations of spin nuclear structure (see a review in [18]) demonstrate that contrary to the simplified odd-group approach both $\langle \mathbf{S}_p^A \rangle$ and $\langle \mathbf{S}_n^A \rangle$ differ from zero, but nevertheless one of these spin quantities always dominates ($\langle \mathbf{S}_p^A \rangle \ll \langle \mathbf{S}_n^A \rangle$, or $\langle \mathbf{S}_n^A \rangle \ll \langle \mathbf{S}_p^A \rangle$). *If together* with the dominance like $\langle \mathbf{S}_{p(n)}^A \rangle \ll \langle \mathbf{S}_{n(p)}^A \rangle$ one would have WIMP-proton and WIMP-neutron couplings of the same order of magnitude (*not* $a_{n(p)} \ll a_{p(n)}$), the situation could look like that in the odd-group model and one could safely (at the current level of accuracy) neglect subdominant spin contribution in the data analysis. Indeed, very large or very small ratios $\sigma_p/\sigma_n \sim a_p/a_n$ would correspond to the neutralinos which are extremely pure gauginos. In this case Z-boson exchange in the SD interactions is absent and only sfermions make contributions to the SD cross sections. This is a very particular case which is also currently in disagreement with the experiments. We have checked the

relation $|a_n|/|a_p| \approx O(1)$ for large LSP masses in [34]. For relatively low LSP masses $m_\chi < 200\,\mathrm{GeV}$ in effMSSM [35, 36, 37, 38, 39, 40, 41] the a_n-to-a_p ratio is located within the bounds [17]:

$$0.5 < \left|\frac{a_n}{a_p}\right| < 0.8\ . \tag{11}$$

Therefore the couplings are almost the same and one can quite safely use the *clear* "old" n-odd and p-odd group classification of non-zero-spin targets and neglect, for example, the $\langle \mathbf{S}_p^A \rangle$-spin contribution in the analysis of the DM data for a nuclear target with $\langle \mathbf{S}_p^A \rangle \ll \langle \mathbf{S}_n^A \rangle$. Furthermore, when one compares in the same figure the exclusion curve for SD WIMP-proton coupling obtained without the subdominant SD WIMP-neutron contribution (all curves in Fig. 2 except the NAIAD one [42] and the Tokyo-LiF one [43]) with the curve from the approach of [24], when the subdominant contribution is included (the NAIAD and Tokyo-LiF curves in Fig. 2), one *"artificially"* improves the sensitivity of the *latter* curves (NAIAD or Tokyo-LiF) in comparison with the former ones. For the sake of consistency and reliable comparisons, one should coherently recalculate all previous curves in the new manner [13].

We note that it looks like the SI contribution is completely ignored in the SIMPLE experiment [44, 45] and the DM search with NaF bolometers [46]. Although ^{19}F has the best properties for investigation of WIMP-nucleon spin-dependent interactions (see, for example, [47]) it is not obvious that one should completely ignore spin-independent WIMP coupling with fluorine. For example, in the relation $\sigma^A \sim \sigma_{\mathrm{SD}}^{A,p}\left[\frac{\sigma_{\mathrm{SI}}^A}{\sigma_{\mathrm{SD}}^{A,p}} + \left(1+\sqrt{\frac{\sigma_{\mathrm{SD}}^{A,n}}{\sigma_{\mathrm{SD}}^{A,p}}}\right)^2\right]$, which follows from (3)–(5), it is not a priori clear that $\frac{\sigma_{\mathrm{SI}}^A}{\sigma_{\mathrm{SD}}^{A,p}} \ll \frac{\sigma_{\mathrm{SD}}^{A,n}}{\sigma_{\mathrm{SD}}^{A,p}}$, i.e. the SI WIMP-nucleus interaction is much weaker than the subdominant SD WIMP-nucleus one. At least for isotopes with an atomic number $A > 50$ [1, 8] to neglect the SI contribution would be a larger mistake than to neglect the subdominant SD WIMP-neutron contribution, when the SD WIMP-proton interaction dominates, at the current level of sensitivity of DM experiments [35, 48]. From measurements with ^{73}Ge one can extract, following [24], not only the dominant constraint for the WIMP-nucleon coupling a_n (or σ_{SD}^n) but also the constraint for the subdominant WIMP-proton coupling a_p (or σ_{SD}^p). Nevertheless, the latter constraint will be much weaker in comparison with the constraints from p-odd target nuclei, like ^{19}F or ^{127}I. This fact is illustrated by the "weak" NAIAD (NaI, 2003) curve in Fig. 3, which corresponds to the subdominant WIMP-neutron spin contribution extracted from the p-odd nucleus ^{127}I.

Therefore we would like to note that the "old" odd-group-based approach to analysis of the SD data from experiments with heavy enough targets (for example, Ge-73) is still quite suitable, especially when it is not obvious that (both) spin couplings dominate over the scalar one.

The approach of Bernabei et al. [13, 14] looks more appropriate for the mixed spin-scalar coupling data presentation, and is based on introduction of the effective SD nucleon cross section $\sigma_{\rm SD}(0)$ and the coupling mixing angle θ (8) instead of $\sigma^p_{\rm SD}(0)$ and $\sigma^n_{\rm SD}(0)$. With these definitions the SD WIMP-proton and WIMP-neutron cross sections have the form $\sigma^p_{\rm SD} = \sigma_{\rm SD} \cdot \cos^2\theta$ and $\sigma^n_{\rm SD} = \sigma_{\rm SD} \cdot \sin^2\theta$.

In Fig. 4 the WIMP-nucleon spin and scalar mixed couplings allowed by the annual modulation signature from the 100-kg DAMA/NaI experiment are shown inside the shaded regions. The regions from [13, 14] in the $(\xi\sigma_{\rm SI}, \xi\sigma_{\rm SD})$ space for $40\,{\rm GeV} < m_{\rm WIMP} < 110\,{\rm GeV}$ cover spin-scalar mixing coupling for the proton ($\theta = 0$ case of [13, 14], left panel) and spin-scalar mixing coupling for the neutron ($\theta = \pi/2$, right panel). From nuclear physics one has for the proton spin dominated ^{23}Na and ^{127}I $\frac{\langle \mathbf{S}_n \rangle}{\langle \mathbf{S}_p \rangle} < 0.1$ and $\frac{\langle \mathbf{S}_n \rangle}{\langle \mathbf{S}_p \rangle} < 0.02 \div 0.23$, respectively. For $\theta = 0$ the DAMA WIMP-proton spin constraint is the severest one due to the p-oddness of the I target (see Fig. 2).

In the right panel of Fig. 4 we present the exclusion curve (*dashed line*) for the WIMP-neutron spin coupling from the odd-neutron isotope ^{129}Xe obtained under the mixed coupling assumptions [14] from the DAMA-LiXe (1998) experiment [49, 50, 51]. For the DAMA NaI detector the $\theta = \pi/2$ means no $\langle \mathbf{S}_p \rangle$ contribution at all. Therefore, in this case DAMA gives the subdominant $\langle \mathbf{S}_n \rangle$ contribution alone, which could be compared further with the dominant $\langle \mathbf{S}_n \rangle$ contribution in ^{73}Ge.

The scatter plots in Fig. 4 give $\sigma^p_{\rm SI}$ as a function of $\sigma^p_{\rm SD}$ (left panel) and $\sigma^n_{\rm SD}$ (right panel) calculated in the effMSSM [17]. Filled circles (green) correspond to the relic neutralino density $0.0 < \Omega_\chi h^2_0 < 1.0$, squares (red) correspond to the subdominant relic neutralino contribution $0.002 < \Omega_\chi h^2_0 < 0.1$ and triangles (black) correspond to the WMAP density constraint $0.094 < \Omega_\chi h^2_0 < 0.129$ [52, 53].

The constraints on the SUSY parameter space within the mixed coupling framework in Fig. 4 are in general much stronger in comparison with the traditional approach based on the one-coupling dominance (Figs. 1, 2 and 3).

It follows from Fig. 4 that when the LSP is the subdominant DM particle (squares in the figure), SD WIMP-proton and WIMP-neutron cross sections at a level of $3 \div 5 \cdot 10^{-3}$ pb are allowed, but the WMAP relic density constraint (triangles) together with the DAMA restrictions leaves only $\sigma^{p,n}_{\rm SD} < 3 \cdot 10^{-5}$ pb without any visible reduction of allowed values for $\sigma^p_{\rm SI}$. In general, according to the DAMA restrictions, very small SI cross sections are completely excluded, only $\sigma^p_{\rm SI} > 3 \div 5 \cdot 10^{-7}$ pb are allowed. As to the SD cross section, the situation is not clear, because for the allowed values of the SI contribution the SD DAMA sensitivity did not yet reach the calculated upper bound for the SD LSP-proton cross section of $5 \cdot 10^{-2}$ pb (for the current nucleon spin structure from [54]).

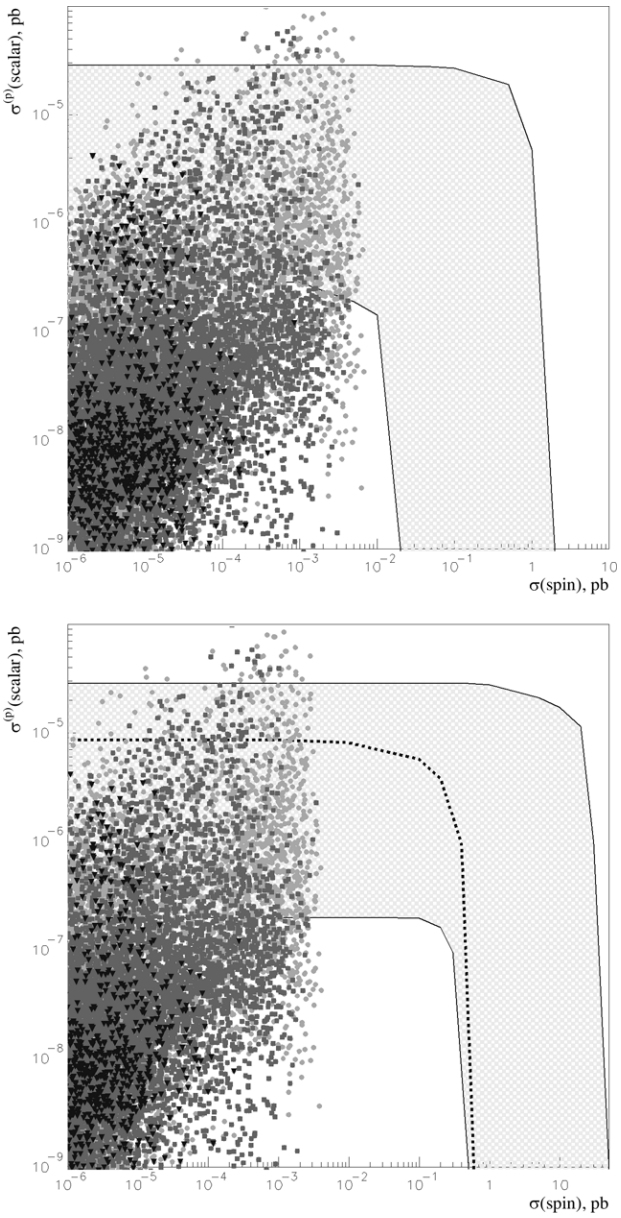

Fig. 4. The DAMA-NaI allowed region from the WIMP annual modulation signature in the ($\xi\sigma_{\rm SI}$, $\xi\sigma_{\rm SD}$) space for $40 < m_{\rm WIMP} < 110\,{\rm GeV}$ [13, 14]. The left panel corresponds to the dominating (in ^{127}I) SD WIMP-proton coupling alone ($\theta = 0$) and the right panel corresponds to the subdominating SD WIMP-neutron coupling alone ($\theta = \pi/2$). The scatter plots give correlations between $\sigma^p_{\rm SI}$ and $\sigma_{\rm SD}$ in the effMSSM ($\xi = 1$ is assumed) for $m_\chi < 200\,{\rm GeV}$ [17]. In the right panel the DAMA liquid xenon exclusion curve from [14] is given (dashed line). From [17].

4 The Mixed Couplings Case for High-Spin ^{73}Ge

There are many measurements with p-odd nuclei and there is a lack of data for n-odd nuclei, i.e. for $\sigma^n_{\rm SD}$. From our point of view this lack of $\sigma^n_{\rm SD}$ measurements can be filled with new data expected from the HDMS experiment with the high-spin isotope ^{73}Ge [55]. This isotope looks with a good accuracy like an almost pure n-odd group nucleus with $\langle \mathbf{S}_n \rangle \gg \langle \mathbf{S}_p \rangle$ (Table 1). The variation in $\langle \mathbf{S}_p \rangle$ and $\langle \mathbf{S}_n \rangle$ in the table reflects the level of inaccuracy and complexity of the current nuclear structure calculations.

Table 1. All available calculations in different nuclear models for the zero-momentum spin structure (and predicted magnetic moments μ) of the ^{73}Ge nucleus. The experimental value of the magnetic moment given in the brackets is used as input in the calculations.

^{73}Ge ($G_{9/2}$)	$\langle \mathbf{S}_p \rangle$	$\langle \mathbf{S}_n \rangle$	μ (in μ_N)
ISPSM, Ellis–Flores [15, 56]	0	0.5	−1.913
OGM, Engel–Vogel [21]	0	0.23	$(-0.879)_{\rm exp}$
IBFM, Iachello at al. [57] and [11]	−0.009	0.469	−1.785
IBFM (quenched), Iachello at al. [57] and [11]	−0.005	0.245	$(-0.879)_{\rm exp}$
TFFS, Nikolaev–Klapdor-Kleingrothaus, [58]	0	0.34	—
SM (small), Ressell at al. [11]	0.005	0.496	−1.468
SM (large), Ressell at al. [11]	0.011	0.468	−1.239
SM (large, quenched), Ressell at al. [11]	0.009	0.372	$(-0.879)_{\rm exp}$
"Hybrid" SM, Dimitrov at al. [59]	0.030	0.378	−0.920

In the mixed spin-scalar coupling case the direct detection rate (1) in ^{73}Ge integrated over recoil energy from the threshold energy, ϵ, to the maximal energy, ε, is a sum of the SD and SI contributions:

$$R(\epsilon,\varepsilon) = \alpha(\epsilon,\varepsilon,m_\chi)\,\sigma^p_{\rm SI} + \beta(\epsilon,\varepsilon,m_\chi)\,\sigma_{\rm SD}; \tag{12}$$

$$\alpha(\epsilon,\varepsilon,m_\chi) = N_T \frac{\rho_\chi M_A}{2 m_\chi \mu_p^2} A^2 A_{\rm SI}(\epsilon,\varepsilon),$$

$$\beta(\epsilon,\varepsilon,m_\chi) = N_T \frac{\rho_\chi M_A}{2 m_\chi \mu_p^2} \frac{4}{3} \frac{J+1}{J} \left(\langle \mathbf{S}^A_p \rangle \cos\theta + \langle \mathbf{S}^A_n \rangle \sin\theta\right)^2 A_{\rm SD}(\epsilon,\varepsilon);$$

$$A_{\rm SI,SD}(\epsilon,\varepsilon) = \frac{\langle v \rangle}{\langle v^2 \rangle} \int_\epsilon^\varepsilon dE_{\rm R} F^2_{\rm SI,SD}(E_{\rm R}) I(E_{\rm R})\,. \tag{13}$$

To estimate the event rate (12) one should know a number of quite uncertain astrophysical and nuclear structure parameters as well as the precise characteristics of the experimental setup (see, for example, the discussions in [13, 60]).

We neglect the subdominant contribution from the WIMP-proton spin coupling proportional to $\langle \mathbf{S}_p^A \rangle$ for ^{73}Ge. We consider only a simple spherically symmetric isothermal WIMP velocity distribution [20, 61] and do not go into details of any possible and in principle important uncertainties (and/or modulation effects) of the Galactic halo WIMP distribution [62, 63, 64, 65, 66, 67]. For simplicity we use the Gaussian scalar and spin nuclear form-factors from [56, 68]. With formulas (12) we performed a simple estimation of prospects for the DM search and SUSY constraints with the high-spin ^{73}Ge detector HDMS taking into account the available results from the DAMA-NaI and LiXe experiments [13, 25, 26, 49, 50, 51].

The Heidelberg Dark Matter Search (HDMS) experiment uses a special configuration of two Ge detectors to efficiently reduce the background [69]. From the first preliminary results of the HDMS experiment with the inner HPGe crystal of enriched ^{73}Ge [55] we can estimate the current background event rate $R(\epsilon, \varepsilon)$ integrated here from the "threshold" energy $\epsilon = 15\,\mathrm{keV}$ to the "maximal" energy $\varepsilon = 50\,\mathrm{keV}$. We obtain $R(15, 50) \approx 10$ events/kg/day. A substantial improvement of the background (up to an order of magnitude) is further expected for the setup in the Gran Sasso Underground Laboratory. In Fig. 5 solid lines for the integrated rate $R(15, 50)$ marked with numbers 10, 1.0 and 0.1 (in events/kg/day) present our exclusion curves for $m_{\mathrm{WIMP}} = 70\,\mathrm{GeV}$ expected from the HDMS setup with ^{73}Ge within the framework of the mixed SD WIMP-neutron and SI WIMP-nucleon couplings. Unfortunately, the current background index for HDMS is not yet optimized, and the relevant exclusion curve (marked with 10 events/kg/day) has almost the same strength to reduce σ^n_{SD} as the dashed curve from the DAMA experiment with liquid Xe [14] obtained for $m_{\mathrm{WIMP}} = 50\,\mathrm{GeV}$ (better sensitivity is expected with HDMS for $m_{\mathrm{WIMP}} < 40\,\mathrm{GeV}$). However, both experiments lead to some sharper restriction for σ^n_{SD} than obtained by DAMA (see Fig. 5). An order of magnitude improvement of the HDMS sensitivity (curve marked with 1.0) will supply us with the best exclusion curve for the SD WIMP-neutron coupling, but this sensitivity is not yet enough to reach the calculated upper bound for σ^n_{SD}. This sensitivity also could reduce the upper bound for the SI WIMP-proton coupling σ^p_{SI} to a level of 10^{-5} pb. Nevertheless, only an *additional* about-one-order-of-magnitude HDMS sensitivity improvement is needed to obtain decisive constraints on σ^p_{SI} as well as on σ^n_{SD}. In this case only quite narrow bounds for these cross sections will be allowed (below the curve marked by 0.1 and above the lower bound of the DAMA-NaI mixed region).

5 Conclusion

In this paper we argue that potentially misleading discrepancies between the results of different dark matter search experiments (for example, DAMA vs CDMS and EDELWEISS) as well as between the data and the SUSY

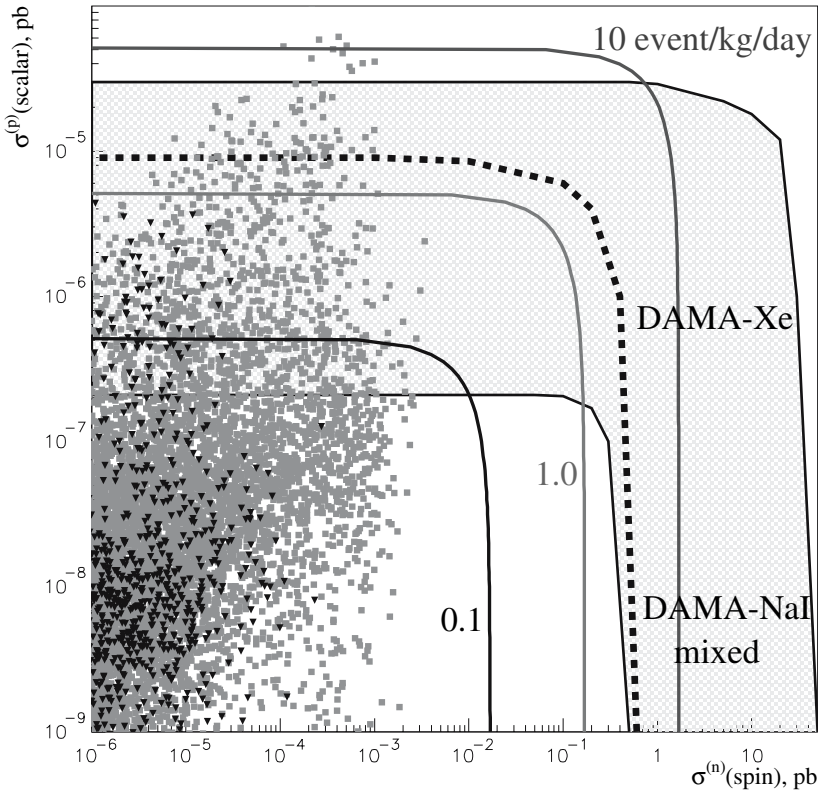

Fig. 5. Solid lines (marked with numbers of $R(15, 50)$ in events/kg/day) show the sensitivities of the HDMS setup with ^{73}Ge within the framework of mixed SD WIMP-neutron and SI WIMP-nucleon couplings. The DAMA-NaI region for the subdominant SD WIMP-neutron coupling ($\theta = \pi/2$) is from Fig. 4. Scatter plots give correlations between $\sigma^p_{\rm SI}$ and $\sigma^n_{\rm SD}$ in the effMSSM for $m_\chi < 200\,{\rm GeV}$ [17]. Squares (red) correspond to the subdominant relic neutralino contribution $0.002 < \Omega_\chi h_0^2 < 0.1$ and triangles (black) correspond to the WMAP relic neutralino density $0.094 < \Omega_\chi h_0^2 < 0.129$. The dashed line from [14] shows the DAMA-LiXe (1998) exclusion curve for $m_{\rm WIMP} = 50\,{\rm GeV}$. From [17].

calculations can be avoided by using the mixed spin-scalar coupling approach, where the spin-independent and spin-dependent WIMP-nucleon couplings are a priori considered to be *both* non-zero. There is generally some possible incorrectness in the direct comparison of the exclusion curves for the WIMP-proton(neutron) spin-dependent cross section obtained with and without the non-zero WIMP-neutron(proton) spin-dependent contribution.

On the other hand, nuclear spin structure calculations show that usually one, WIMP-proton $\langle \mathbf{S}^A_p \rangle$ or WIMP-neutron $\langle \mathbf{S}^A_n \rangle$, nuclear spin dominates and the WIMP-proton and WIMP-neutron effective couplings a_n and a_p are of

the same order of magnitude. Therefore at the current level of accuracy it looks safe to neglect subdominant WIMP-nucleon contributions when one analyses the data from non-zero-spin targets. The clear "old" odd-group-based approach to the analysis of the SD data from experiments with heavy enough targets (for example, Ge-73) is still quite suitable.

Furthermore the above-mentioned incorrectness concerns to a great extent the direct comparison of spin-dependent exclusion curves obtained with and without non-zero spin-independent contributions [13, 26]. Taking into account both spin couplings a_p and a_n but ignoring the scalar coupling c_0, one can easily arrive at a misleading conclusion especially for not very light target nuclei when it is not obvious that (both) spin couplings dominate over the scalar one.

To be consistent, one has to use a mixed spin-scalar coupling approach as for the first time proposed by the DAMA collaboration [25, 13, 26]. We applied the spin-scalar coupling approach to estimate future prospects of the HDMS experiment with the neutron-odd group high-spin isotope ^{73}Ge. Although even at the present accuracy the odd-neutron nuclei ^{73}Ge and ^{129}Xe lead to somewhat sharper restrictions for σ^n_{SD} than obtained by DAMA, we found that the current accuracy of measurements with ^{73}Ge (as well as with ^{129}Xe and NaI) has not yet reached a level which allows us to obtain new decisive constraints on the SUSY parameters.

This investigation was partly supported by the RFBR (Project 02-02-04009).

References

1. G. Jungman, M. Kamionkowski, and K. Griest, Phys. Rept. **267** (1996) 195–373.
2. J. D. Lewin and P. F. Smith, Astropart. Phys. **6** (1996) 87–112.
3. P. F. Smith and J. D. Lewin, Phys. Rept. **187** (1990) 203.
4. V. A. Bednyakov and H. V. Klapdor-Kleingrothaus, Phys. Atom. Nucl. **62** (1999) 966–974.
5. V. A. Bednyakov, S. G. Kovalenko, and H. V. Klapdor-Kleingrothaus, Phys. Atom. Nucl. **59** (1996) 1718–1727.
6. V. A. Bednyakov, H. V. Klapdor-Kleingrothaus, and S. G. Kovalenko, Phys. Rev. **D55** (1997) 503–514.
7. V. A. Bednyakov, S. G. Kovalenko, H. V. Klapdor-Kleingrothaus, and Y. Ramachers, Z. Phys. **A357** (1997) 339–347.
8. V. A. Bednyakov, H. V. Klapdor-Kleingrothaus, and S. Kovalenko, Phys. Rev. **D50** (1994) 7128–7143.
9. J. Engel, Phys. Lett. **B264** (1991) 114–119.
10. J. Engel, S. Pittel, and P. Vogel, Int. J. Mod. Phys. **E1** (1992) 1–37.
11. M. T. Ressell et al., Phys. Rev. **D48** (1993) 5519–5535.
12. M. T. Ressell and D. J. Dean, Phys. Rev. **C56** (1997) 535–546.
13. R. Bernabei et al., Riv. Nuovo Cim. **26** (2003) 1–73.

14. R. Bernabei et al., Phys. Lett. **B509** (2001) 197–203.
15. J. R. Ellis and R. A. Flores, Nucl. Phys. **B307** (1988) 883.
16. V. A. Bednyakov, H. V. Klapdor-Kleingrothaus, and S. G. Kovalenko, Phys. Lett. **B329** (1994) 5–9.
17. V. A. Bednyakov and H. V. Klapdor-Kleingrothaus, Phys. Rev. **D70**, (2004) 096006.
18. V. A. Bednyakov and F. Simkovic, Phys. of Particles and Nuclei, **36** (2004) 131.
19. M. W. Goodman and E. Witten, Phys. Rev. **D31** (1985) 3059.
20. A. K. Drukier, K. Freese, and D. N. Spergel, Phys. Rev. **D33** (1986) 3495–3508.
21. J. Engel and P. Vogel, Phys. Rev. **D40** (1989) 3132–3135.
22. D. S. Akerib et al. [CDMS Collaboration], Phys. Rev. Lett. **93**, 211301 (2004).
23. V. Sanglard, astro-ph/0406537.
24. D. R. Tovey, R. J. Gaitskell, P. Gondolo, Y. Ramachers, and L. Roszkowski, Phys. Lett. **B488** (2000) 17–26.
25. R. Bernabei et al., Phys. Lett. **B480** (2000) 23–31.
26. R. Bernabei et al., astro-ph/0311046.
27. G. Chardin, astro-ph/0411503.
28. A. Kurylov and M. Kamionkowski, Phys. Rev. **D69** (2004) 063503.
29. C. J. Copi and L. M. Krauss, Phys. Rev. **D63** (2001) 043507.
30. C. J. Copi and L. M. Krauss, Phys. Rev. **D67** (2003) 103507.
31. M. Drees, hep-ph/0410113.
32. G. Gelmini and P. Gondolo, hep-ph/0405278.
33. C. Savage, P. Gondolo and K. Freese, astro-ph/0408346.
34. V. A. Bednyakov, hep-ph/0310041.
35. V. A. Bednyakov and H. V. Klapdor-Kleingrothaus, Phys. Rev. **D62** (2000) 043524.
36. V. Mandic, A. Pierce, P. Gondolo, and H. Murayama, hep-ph/0008022, LBNL-46431, LBL-46431, UCB-PTH-00-23, MPI-PHT-2000-26.
37. L. Bergstrom and P. Gondolo, Astropart. Phys. **5** (1996) 263–278, also in Proc. of 4th Int. Symposium on Sources and Detection of Dark Matter in the Universe (DM 2000), Marina del Rey, California, 23-25 Feb 2000, ed. D. Cline, Springer (2001) 177–181.
38. P. Gondolo, hep-ph/0005171.
39. V. A. Bednyakov and H. V. Klapdor-Kleingrothaus, Phys. Rev. **D59** (1999) 023514.
40. L. Bergstrom, Rept. Prog. Phys. **63** (2000) 793.
41. A. Bottino, F. Donato, N. Fornengo, and S. Scopel, Phys. Rev. **D63** (2001) 125003.
42. B. Ahmed et al., Astropart. Phys. **19** (2003) 691–702.
43. K. Miuchi et al., Astropart. Phys. **19** (2003) 135–144.
44. F. Giuliani and T. Girard, astro-ph/0311589.
45. F. Giuliani, hep-ph/0404010.
46. A. Takeda et al., Phys. Lett. **B572** (2003) 145–151.
47. P. C. Divari, T. S. Kosmas, J. D. Vergados, and L. D. Skouras, Phys. Rev. **C61** (2000) 054612.
48. V. A. Bednyakov, Phys. Atom. Nucl. **66** (2003) 490–493.
49. R. Bernabei et al., Nucl. Phys. Proc. Suppl. **110** (2002) 88–90.
50. R. Bernabei et al., Phys. Lett. **B436** (1998) 379–388.

51. R. Bernabei et al., Nucl. Instrum. Meth. **A482** (2002) 728–743.
52. D. N. Spergel et al., Astrophys. J. Suppl. **148** (2003) 175.
53. C. L. Bennett et al., Astrophys. J. Suppl. **148** (2003) 1.
54. J. R. Ellis, A. Ferstl, and K. A. Olive, Phys. Lett. **B481** (2000) 304–314.
55. H. V. Klapdor-Kleingrothaus et al., to be Published (2005).
56. J. R. Ellis and R. A. Flores, Phys. Lett. **B263** (1991) 259–266.
57. F. Iachello, L. M. Krauss, and G. Maino, Phys. Lett. **B254** (1991) 220–224.
58. M. A. Nikolaev and H. V. Klapdor-Kleingrothaus, Z. Phys. **A345** (1993) 373–376.
59. V. Dimitrov, J. Engel, and S. Pittel, Phys. Rev. **D51** (1995) 291–295,
60. R. Bernabei et al., astro-ph/0305542, also in Proc. of 10th Int. Workshop on Neutrino Telescopes, Venice, Italy, 11–14 Mar 2003. (2003) vol. 2, 403–423.
61. K. Freese, J. A. Frieman, and A. Gould, Phys. Rev. **D37** (1988) 3388.
62. A. Kinkhabwala and M. Kamionkowski, Phys. Rev. Lett. **82** (1999) 4172–4175.
63. F. Donato, N. Fornengo, and S. Scopel, Astropart. Phys. **9** (1998) 247–260.
64. N. W. Evans, C. M. Carollo, and P. T. de Zeeuw, Mon. Not. Roy. Astron. Soc. **318** (2000) 1131.
65. A. M. Green, Phys. Rev. **D63** (2001) 043005.
66. P. Ullio and M. Kamionkowski, JHEP **03** (2001) 049.
67. J. D. Vergados, Part. Nucl. Lett. **106** (2001) 74–108.
68. J. R. Ellis and R. A. Flores, Phys. Lett. **B300** (1993) 175–182.
69. H. V. Klapdor-Kleingrothaus et al., hep-ph/0103077, and in the proc. of 3rd Int. Workshop on the Identification of Dark Matter (IDM2000), York, England, 18–22 Sep 2000, World Scientific (2001) 415–420.

Light Neutralino Dark Matter in Gaugino Non-Universal Models

Nicolao Fornengo

Department of Theoretical Physics, University of Torino and INFN - Sezione di Torino, via P. Giuria 1, 10125 Torino, Italy,
www.fornengo@to.infn.it,
www.to.infn.it:/~fornengo
www.astroparticle.to.infn.it

Summary. We [1] examine the cosmology and the astrophysical signals produced by neutralino dark matter in the frame of an effective MSSM model without gaugino-mass unification at a grand unification scale. As a consequence of the recent data on precision cosmology, we can set an absolute lower bound of 6 GeV on the neutralino mass. This limit changes to 25 GeV if the pseudoscalar higgs is heavier than 180 GeV. The light neutralinos allowed in this class of supersymmetric models provide quite sizeable direct detection rates. We show how they compare to the direct detection esperimental sensitivites: the predicted rates are largely compatible with the annual-modulation data of the DAMA Collaboration; the comparison with the upper bounds of the CDMS and EDELWEISS Collaborations shows that limits for neutralino masses below 25–30 GeV can be set for a standard isothermal halo. As for the annihilation signals, we find that only low–energy antiprotons and antideuterons are potentially able to set constraints on very low–mass neutralinos, below 20–25 GeV. The gamma–ray signal requires significantly steep profiles or substantial clumpiness in order to reach detectable levels. The up-going muon signal at neutrino telescopes is largely below experimental sensitivities for the neutrino flux coming from the Sun, while for the flux from the Earth an improvement of about one order of magnitude in experimental sensitivities with a low energy threshold can make accessible neutralino masses close to O, Si and Mg masses, for which resonant capture is operative.

1 Supersymmetry and Gaugino Non–Universality

A typical assumption of supersymmetric models is the unification condition for the three gaugino mass parameters $M_{1,2,3}$ at the GUT scale: $M_1 = M_2 = M_3$. This hypothesis implies that at the electroweak scale $M_1 \simeq 0.5\ M_2$. Under this unification condition the bound on the neutralino mass is determined to be $m_\chi \gtrsim 50$ GeV. This is derived from the experimental lower bound on the chargino mass (which theoretically depends on M_2 but not on M_1) determined at LEP2: $m_{\chi^\pm} \gtrsim 100$ GeV. By allowing a deviation from gaugino–universality, the neutralino can be lighter than in the

[1] Report on the work done in collaboration with A. Bottino, F. Donato, S. Scopel.

gaugino–universal models when $M_1 \equiv R\ M_2$, with $R < 0.5$. In this case current data from accelerators do not set an absolute lower bound on m_χ.

We consider here an extension of the MSSM which allows for a deviation from gaugino–mass universality by the introduction of the parameter R, varied here in the interval: $(0.01 \div 0.5)$ [1, 2, 3, 4]. This range for R implies that the accelerator lower bound on the neutralino mass can be moved down to few GeV for $R \sim 0.01$. The ensuing light neutralinos have a dominant bino component; a deviation from a pure bino composition is mainly due to a mixture of $\tilde{B}$ with $\tilde{H}_1^\circ$ [1, 2, 3]. Notice that our range of R includes also the usual model with gaugino–mass universality.

In the following we will discuss both the cosmology and different kinds of direct and indirect detection rates of the light relic neutralinos arising in this class of supersymmetric models. For a more detailed analysis of all these topics, as well as for a more thorough list of relevant references, see [1, 2, 3, 4].

2 Cosmology of Light Neutralinos

In the class of models we are considering here, the neutralino relic abundance $\Omega_\chi h^2$ for very light neutralinos is dominated by two competing annihilation diagrams [1, 2]: annihilation into a $\bar{b}b$ pair, proceeding through the exchange of the pseudoscalar higgs A, and annihilation into a $\bar{\tau}\tau$ pair, via stau exchange. The mixture of the dominant bino component with the subdominant, but not negligible higgsino amplitude [1, 2, 3], provides sizable yukawa–type interactions between neutralinos and higges: when the A boson is relatively light this makes the annihilation cross section into $\bar{b}b$ the dominant channel. The ensuing relic abundance is a decreasing function of the neutralino mass and it is large for light neutralinos, largely in excess of the cosmological upper bound on the cold dark matter (CDM) content of the Universe [1, 2]. The recent data on the cosmic microwave background [5, 6, 7] and other astrophysical determinations [8, 9] provide stringent limits on the cold dark matter (CDM) content of the Universe: these limits [5] allow us to set an absolute lower bound on the neutralino mass of 6 GeV [2], as shown in the top panel of Fig. 1 [10]. When the A mass is large, the relic abundance is overall larger and determined by the $\bar{\tau}\tau$ pair annihilation: in this case, as shown in the bottom panel of Fig. 1, a lower limit of about 25 GeV is obtained [2, 11, 12].

3 Searches for Relic Light Neutralinos

Relic neutralinos which act as CDM in the halo of our Galaxy can be searched for by means of different techniques: direct searches rely on the possibility to detect the recoil energy of nuclei in low–background detectors, which neutralinos scatter off; indirect techniques look for self–annihilation products: neutrinos, photons, antimatter.

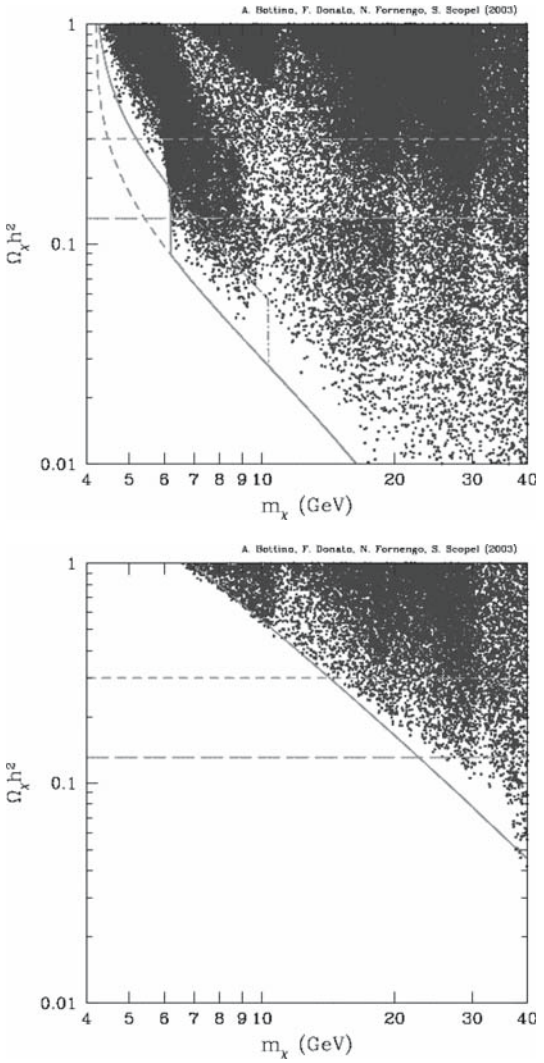

Fig. 1. Neutralino relic abundance $\Omega_\chi h^2$ as a function of the neutralino mass m_χ. Top: The solid curve denotes the analtytical lower bound for the relic abundance in the gaugino non–universal MSSM calculated for $T_{\rm QCD} = 300\,{\rm MeV}$, while the dashed and dot-dashed curves refer to the representative values $T_{\rm QCD} = 100\,{\rm MeV}$, $T_{\rm QCD} = 500\,{\rm MeV}$, respectively. The two horizontal lines denote two representative values for the maximal amount of CDM in the Universe: $\Omega_{\rm CDM}h^2 = 0.3$ (short-dashed line) and $\Omega_{\rm CDM}h^2 = 0.131$ (long-dashed line). The scatter plot is obtained by a full scanning of the supersymmetric parameter space. Bottom: The solid curve denotes the analtytical lower bound for the relic abundance in the gaugino non–universal MSSM calculated when the pseudoscalar higgs is heavy. $T_{\rm QCD}$ is set equal to 300 MeV. The scatter plot is obtained by a full scanning of the supersymmetric parameter space with $m_A > 300\,{\rm GeV}$.

3.1 Direct Detection

The relevant quantity in direct detection is the neutralino–nucleon scattering cross section $\sigma_{\rm scalar}^{\rm (nucleon)}$, multiplied by the factor ξ which defines the fractional amount of neutralinos as dark matter components of the galactic halo. As usual, the fraction ξ is defined in terms of the calculated neutralino relic abundance as: $\xi = \min[1, \Omega_\chi h^2/(\Omega_\chi h^2)_{\rm min}]$, where $(\Omega_\chi h^2)_{\rm min}$ defines the minimal value of the neutralino relic abundance below which we cannot accept that all the galactic DM is made of neutralinos: we have set $(\Omega_\chi h^2)_{\rm min} = 0.095$ [1, 3].

When neutralinos are light, with a mass close to their lower limit established in the previous Section, also the higgs masses are light [1, 3]: in this case not only the relic abundance, but also the scattering cross section is dominated by higgs exchange (in this case, by the light scalar higgs h). The consequence is that $\sigma_{\rm scalar}^{\rm (nucleon)}$ is sizeable, with peculiar properties [1, 3] which constrain the values of $\sigma_{\rm scalar}^{\rm (nucleon)}$ to lie in a very narrow range [1, 3]: the upper bound on $\sigma_{\rm scalar}^{\rm (nucleon)}$ is set by the experimental lower limit on the higgs mass; the lower limit is a consequence of the upper bound on the neutralino relic abundance, which is strongly correlated to $\sigma_{\rm scalar}^{\rm (nucleon)}$ in this class on gaugino non–universal models [1, 3]. We see in the top panel of Fig. 2 that the predicted rates are largely compatible with the annual-modulation data of the DAMA Collaboration [13], which takes into account a very large set of possible halo shapes [14]. The comparison with the upper bounds of the CDMS [15] and EDELWEISS [16] Collaborations, which are reported only for an isothermal halo with a local DM density of 0.3 GeV cm^{-3}, shows that in this case limits for neutralino masses below 25–30 GeV can be set: for more general halos, the limits imposed by these experiments may change significantly. For instance, while CDMS would allow to impose a lower limit of about 25 GeV on the neutralino mass in the case of the standard isothermal halo, when the uncertainty on the values of the local density is considered [14], only a fraction of the supersymmetric configurations at low neutralino masses are excluded and no lower limit on m_χ is determined. In any case, direct detection is a very sensitive probe for the light neutralinos of gaugino non–universal supersymmetric models, the most sensitive together with antiprotons and antideuterons searches discussed in the next Section.

3.2 Indirect Detection at Neutrino Telescopes

Indirect evidence for WIMPs in our halo may be obtained at neutrino telescopes by measurements of the upgoing muons, which would be generated by neutrinos produced by pair annihilation of neutralinos captured and accumulated inside the Earth and the Sun [4]. The top panel of Fig. 3 shows the expected upgoing muon flux for muon energies above 1 GeV, compared to present experimental upper bounds. For $m_\chi \lesssim 40$ GeV the signal from the

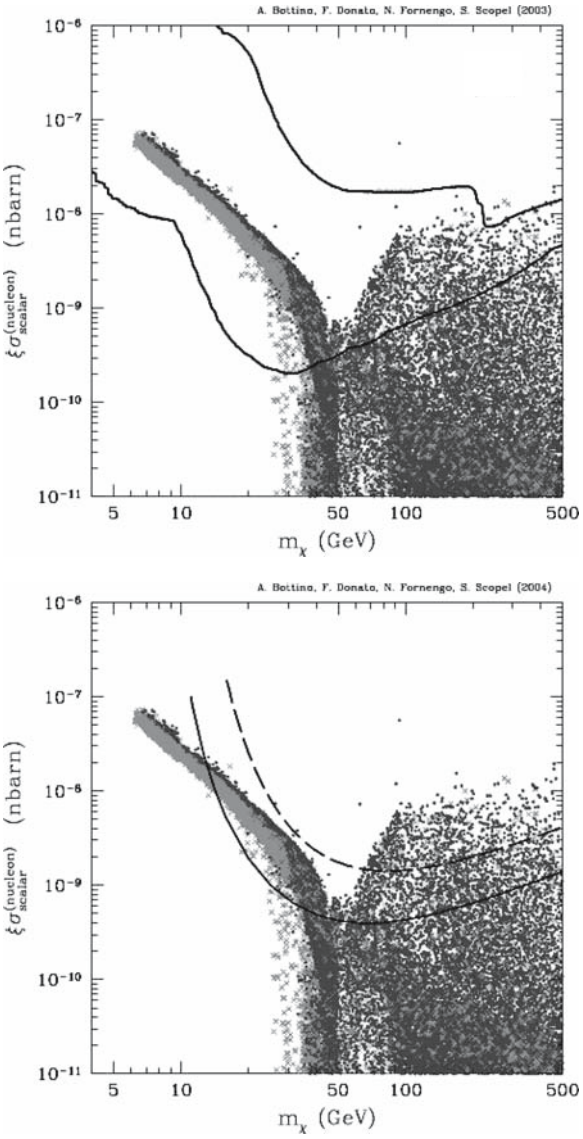

Fig. 2. Scatter plot of $\xi\sigma^{(\mathrm{nucleon})}_{\mathrm{scalar}}$ versus m_χ. Crosses (red) and dots (blue) denote neutralino configurations with $0.095 \leq \Omega_\chi h^2 \leq 0.131$ and $\Omega_\chi h^2 < 0.095$, respectively. TOP: The curves delimit the DAMA region where the likelihood-function values are distant more than 4σ from the null (absence of modulation) hypothesis [13]; this region is the union of the regions obtained by varying the WIMP DF over the set considered in [14]. BOTTOM: The solid and the dashed lines are the experimental upper bounds given by the CDMS [15] and the EDELWEISS [16] Collaborations, respectively, under the hypothesis that galactic WIMPs are distributed as a cored isothermal sphere with a standard set of astrophysical parameters.

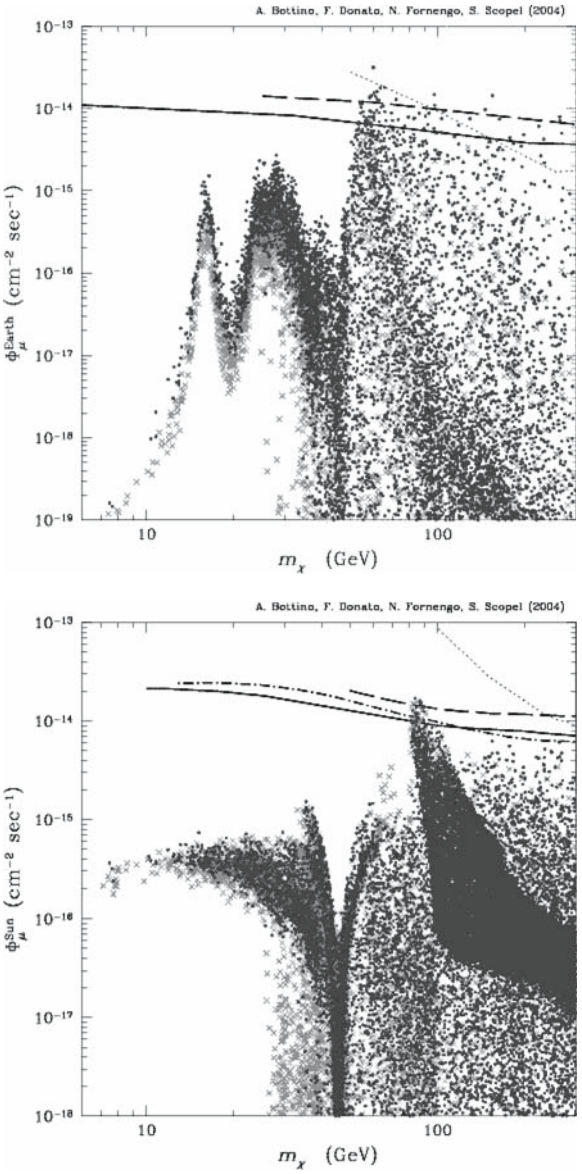

Fig. 3. Scatter plot of the flux of upgoing muons as a function of the neutralino mass. Crosses (red) and dots (blue) denote neutralino configurations with $0.095 \leq \Omega_\chi h^2 \leq 0.131$ and $\Omega_\chi h^2 < 0.095$, respectively. TOP: Signal from the Earth; the solid, dashed and dotted lines denote the experimental upper limits from SuperKamiokande [17], MACRO [18] and AMANDA [19], respectively. BOTTOM: Signal from the Sun; the solid, dashed, dot-dashed and dotted lines denote the experimental upper limits from SuperKamiokande [17], MACRO [18], Baksan [20] and AMANDA [19], respectively.

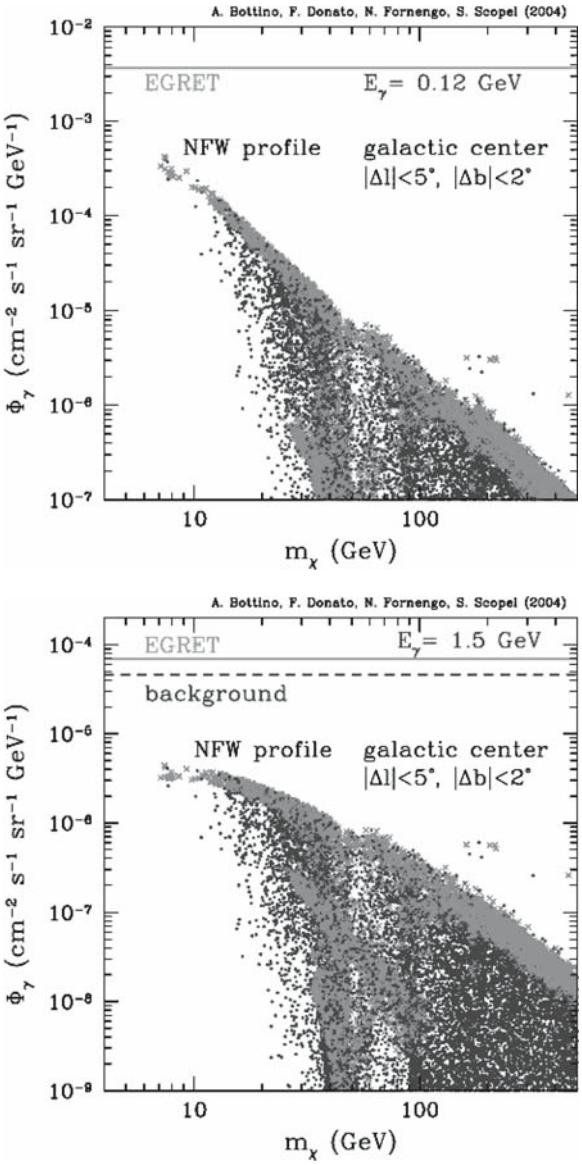

Fig. 4. Scatter plot of the gamma–ray flux from the galactic center inside the angular region $|\Delta l| \leq 5^\circ$, $|\Delta b| \leq 2^\circ$ for a NFW matter density profile. Crosses (red) and dots (blue) denote neutralino configurations with $0.095 \leq \Omega_\chi h^2 \leq 0.131$ and $\Omega_\chi h^2 < 0.095$, respectively. TOP: Flux calculated at $E_\gamma = 0.12\,\mathrm{GeV}$; the horizontal line shows the gamma–ray flux measured by EGRET [21], assumed to be compatible with the estimated background [21]. BOTTOM: Flux calculated at $E_\gamma = 1.5\,\mathrm{GeV}$; the solid horizontal line shows the gamma–ray flux measured by EGRET [21], the dashed line is an estimate of the gamma–ray background [21].

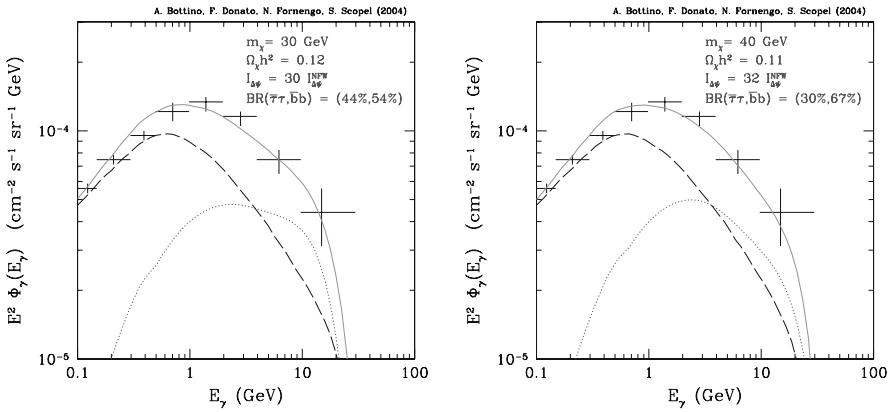

Fig. 5. Gamma–ray spectra $\Phi_\gamma(E_\gamma)$, multiplied by E_γ^2, from the galactic center inside the angular region $|\Delta l| \leq 5^\circ$, $|\Delta b| \leq 2^\circ$, as functions of the photon energy. LEFT: The dotted line is the spectrum for a neutralino with mass $m_\chi = 30\,\mathrm{GeV}$, calculated for a density profile with a factor 30 of enhancement with respect to the NFW case; the dashed line is the gamma ray background calculated in [21], reduced by 10%; the solid line is the total flux, sum of the supersymmetric signal and the background; the experimental points are the EGRET data [21]. RIGHT: The same, for $m_\chi = 40\,\mathrm{GeV}$ and for a density profile with a factor 32 of enhancement with respect to the NFW case. The numbers quoted in the legend inside parentheses denote the values of the neutralino annihilation branching ratios into $\bar{b}b$ and $\bar{\tau}\tau$.

Earth presents several peaks due to neutralino resonant capture on Oxygen, Silicon and Magnesium. Apart from the resonances, the predicted flux of light neutralinos is always very small and difficult to be accessed by experimentally [4]. In the bottom panel of Fig. 3 we show the up-going muon flux expected from the Sun. Also in this case the signal level turns out to be suppressed for $m_\chi \lesssim 50\,\mathrm{GeV}$ [4] as compared to what is obtained at higher masses. We conclude that investigations of light neutralinos by up-going muons from the Sun do not provide favourable prospects.

3.3 Gamma Rays in Space

The flux of gamma–rays produced by neutralino self–annihilation inside the galactic halo is potentially a promising tool of investigation. In Fig. 4 we show the signal from the galactic center for two different photon energies in the range of EGRET data and for a NFW [22] density profile with a core radius of 0.01 pc. The angular field of view has been chosen to match the EGRET resolution [21]. We clearly see that the small mass range is the most favourable sector of the supersymmetric model for this kind of signal (as is for all the signals which come from neutralino annihilation in the Galaxy).

Nevertheless, the predicted signal is at least one order of magnitude smaller than the detected flux [4]. In the case of steeper dark matter density

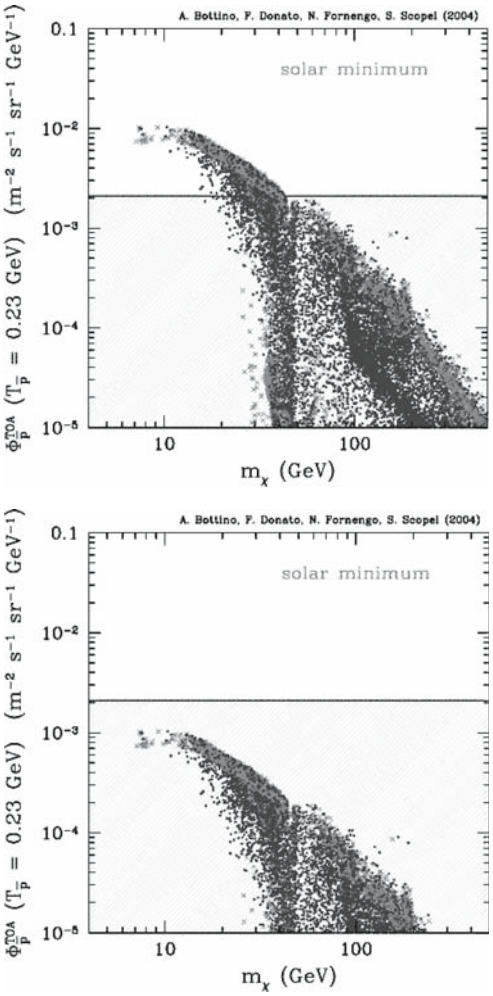

Fig. 6. Scatter plot of the antiproton flux at kinetic energy $T_{\bar{p}} = 0.23\,\mathrm{GeV}$ as a function of the neutralino mass. A spherical isothermal dark matter density profile has been used. The solar modulation is calculated at the phase of solar minimum. Crosses (red) and dots (blue) denote neutralino configurations with $0.095 \leq \Omega_\chi h^2 \leq 0.131$ and $\Omega_\chi h^2 < 0.095$, respectively. The shaded region denotes the amount of primary antiprotons which can be accommodated at $T_{\bar{p}} = 0.23\,\mathrm{GeV}$ without entering in conflict with the experimental BESS data [26, 27] and secondary antiproton calculations [28]. LEFT: The best–fit set of the astrophysical parameters which govern cosmic ray propagation is used. RIGHT: The astrophysical parameters which provide the most conservative antiproton fluxes are used.

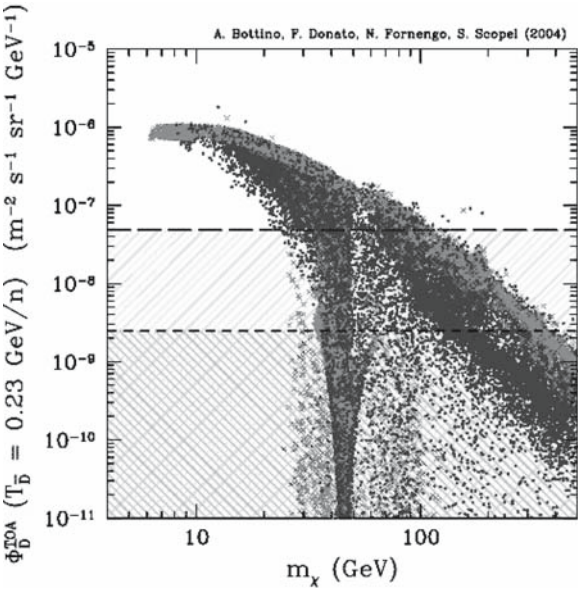

Fig. 7. Scatter plot of the antideuteron flux at kinetic energy $T_{\bar{p}} = 0.23\,\mathrm{GeV}/n$ as a function of the neutralino mass. A spherical isothermal dark matter density profile has been used. The solar modulation is calculated at the phase of solar minimum. Crosses (red) and dots (blue) denote neutralino configurations with $0.095 \leq \Omega_\chi h^2 \leq 0.131$ and $\Omega_\chi h^2 < 0.095$, respectively. The shaded region denotes the estimated sensitivity [24] to low–energy antideuterons for the AMS experiment [29] on borad of the International Space Station. The hatched region shows the estimated sensitivity for the proposed GAPS antideuteron experiment [30].

profiles, like in the case of the Moore et al. shape [23], gamma–ray studies could access the signal produced by neutralinos in the mass range below 10–20 GeV [4]. For cored isothermal halos, the predicted fluex are one order of magnitude smaller the the ones shown in Fig. 4 [4]. Fig. 5 shows that the EGRET excess [21] observed in the energy range above 1 GeV could be explained by light neutralinos in the 30–40 GeV mass range with a DM overdensity factor of about 30 with respect to a NFW profile [4].

3.4 Antimatter in Space: Antiprotons and Antideuterons

Annihilation of neutralinos in the galactic halo may lead also to the production of antiprotons and antideuterons [24] (as well as positrons, which are not considered here). Once antiprotons or antideuterons are produces, they undergo diffusion and energy losses inside the galactic halo before reaching the Earth [25]. For these reason, this kind of signals are less sensitive to the actual dark matter density profile, since they do not significantly probe the central parts of the galactic halo, where the various halo shapes mostly

differ. However, uncertainties in the modelling of propagation and diffusion instroduce large uncertainties. This has been thoroughly analyzed for the antiproton signal in [25].

These uncertainties somehow limit the capabilities of the antiproton signal [25], as it can be seen in Fig. 6. However, especially for neutralinos lighter than 20 GeV, antiprotons represent a potentially relevant probe.

Very promising is the antideuteron signal [24], shown in Fig. 7. The full neutralino mass range below 40 GeV could be probed by antideuttron searches in space.

References

1. A. Bottino, N. Fornengo, S. Scopel, Phys. Rev. D **67**, 063519 (2003).
2. A. Bottino, F. Donato, N. Fornengo, S. Scopel, Phys. Rev. D **68**, 043506 (2003).
3. A. Bottino, F. Donato, N.Fornengo, S. Scopel, Phys. Rev. D **69**, 037302 (2003).
4. A. Bottino, F. Donato, N.Fornengo, S. Scopel, Phys.Rev. D **70**, 015005 (2004).
5. D.N. Spergel et al. (WMAP), Astrophys.J.Suppl. **148**, 175 (2003).
6. T.J. Pearson et al. (CBI), Astrophys. J. **591**, 556 (2003)
7. C.L. Kuo et al. (ACBAR), Astrophys. J. **600**, 32 (2004).
8. W.J. Percival et al., MNRAS **327**, 1297 (2001).
9. R.A.C. Croft et al., ApJ **581**, 20 (2002); N.Y. Gnedin and A.J.S. Hamilton, MNRAS **334**, 107 (2002).
10. For older determinations, see: K. Griest and L. Roszkowski, Phys. Rev. D **46**, 3309 (1992); A. Gabutti, M. Olechowski, S. Cooper, S. Pokorski and L. Stodolsky, Astrop. Phys. **6**, 1 (1996); V. A. Bednyakov, H. V. Klapdor–Kleingrothaus and S. G. Kovalenko, Phys.Rev. D **55**, 503 (1997).
11. G. Bélanger, F. Boudjema, A. Pukhov and S. Rosier–Lees, *Proceedings of SUSY02*, Hamburg, Germany, June 17–23, 2002 [hep-ph/0212227].
12. D. Hooper and T. Plehn, Phys. Lett. **B562**, 18 (2003).
13. R. Bernabei et al., Riv. N. Cim. **26** n. 1 (2003) 1.
14. P. Belli, R. Cerulli, N. Fornengo and S. Scopel, Phys. Rev. D **66**, 043503 (2002).
15. D.S. Akerib et al., Phys. Rev. Lett. **93** (2004) 211301.
16. A. Benoit et al., Phys. Lett. B **545**, 43 (2002).
17. A. Habig [Super-Kamiokande Collaboration], *Proceedings of the 27th International Cosmic Ray Conferences (ICRC 2001)*, Hamburg, Germany, August 7–15, 2001 [hep-ex/0106024].
18. M. Ambrosio et al. [MACRO Collaboration], Phys. Rev. D **60**, 082002 (1999).
19. X. Bai et al. [AMANDA Collaboration], *Proceedings of the 28th International Cosmic Ray Conferences (ICRC 2003)*, Tsukuba, Japan, 31 Jul - 7 Aug 2003.
20. M.M. Boliev et al., *Proceedings of the International Workshop on Aspects of Dark Matter in Astrophysics and Particle Physics, Heidelberg, Germany, 16–20 Sep 1996.*
21. S.D. Hunter et al., Astrophys. J. **481**, 205 (1997).
22. J.F. Navarro, C.S. Frenk and S.D.M. White, Astrophys. J. **462**, 563 (1996).
23. B. Moore et al., Mon. Not. Roy. Astron. Soc. **310**, 1147 (1999).
24. F. Donato, N. Fornengo, and P. Salati, Phys. Rev. D **62**, 043003 (2000).

25. F. Donato, N. Fornengo, D. Maurin, P. Salati, R. Taillet, Phys. Rev. D **69**, 063501 (2003).
26. S. Orito, et al. (BESS Collaboration), Phys. Rev. Lett. **84**, 1078 (2000).
27. T. Maeno, et al. (BESS Collaboration), Astropart. Phys. **16**, 121 (2001).
28. F. Donato et al., Astrophys. J. **563**, 172 (2001).
29. S. Ahlen et al., Nucl. Inst. Meth. **A350**, 351 (1994).
30. K. Mori et al. Ap. J. **566**, 604 (2002).

How Can We Make Sure We Detect Dark Matter?

Paolo Gondolo

Department of Physics, University of Utah, 115 S 1400 E Rm 201, Salt Lake City, UT 84112-0830
paolo@physics.utah.edu

Summary. More and more claims of having detected WIMP dark matter are being put forward. Some are discussed here, stressing the importance of exploiting distinctive signatures to ascertain their WIMP origin. The best signals for WIMP discovery are characterized by special features that make them recognizable as due to WIMPs and nothing else. Sometimes, however, a single feature, although accountable for in theoretical models, may not be enough to make sure that we have detected WIMPs. This is because the theory of WIMPs and their distribution in the galaxy is still very uncertain, and allows for many possibilities. What are needed are *experimental* verifications of the claimed signals, either by discovering *unmistakable* features, or by detecting several kinds of signals that can all be explained by the *same* WIMP model.

One of the most intriguing results to come out of recent cosmological observations is that about 90% of the mass of the Universe is not made of protons, neutrons, electrons, or any other known particle, but of something unknown that does not shine. Discovering the composition of this so-called non-baryonic dark matter is one of the big challenges of modern physics and cosmology.

Proposals as to the nature of non-baryonic dark matter do not lack. Is it made of axions (neutral particles suggested to explain the smallness of CP violation in the strong interactions)? Or is it made of WIMPs (weakly interacting massive particles that arise naturally in extensions of the Standard Model of particle physics, such as supersymmetry)? Or is non-baryonic dark matter made of something else, or a combination of all that?

Following the tradition of experimental science, the way to find out the nature of non-baryonic dark matter is to detect its constituents, either directly by recording their collisions with a detector, or indirectly by observing products of their reactions in planets, stars, or galaxies.

The last ten years have seen more and more claims of having detected dark matter in the form of weakly interacting massive particles (WIMPs). Three of these claims will be described below: (1) a distinctive signal variation in a direct detection experiment, (2) high-energy gamma-rays from the center of our Galaxy, and (3) an excessive flux of positrons in cosmic rays.

However, explanations that do not invoke WIMPs exist for gamma-rays and positrons, and other direct detection experiments have not observed any signal from WIMPs (although straightforward comparisons are difficult).

So, has WIMP dark matter been detected? What is the real origin of the detected signals? Or more proactively: how can we make sure we detect WIMP dark matter?

This question has been asked repeatedly in the past, and several methods have been proposed to distinguish a dark matter signal from an ordinary one. In recent years, however, an excessive reliance on theory has interfered with an open-minded but critical interpretation of the experimental results. Current theories of WIMPs still leave a lot of possibilities as to their particle properties (mass, couplings, etc.) and astrophysical characteristics (density distribution, velocity distribution, etc.). Rather than theoretical arguments, what are needed are *experimental* verifications of the claimed signals, either by discovering *unmistakable* features which can only be explained by the presence of WIMPs, or by detecting several kinds of WIMP signals that can all be explained by the *same* theoretical model of WIMPs.

1 Non-Baryonic Cold Dark Matter

The existence of non-baryonic dark matter is supported by varied cosmological measurements. Of great relevance are the values of the matter and energy densities of the Universe at the present time. These densities can be determined by means of several cosmological data: the temperature fluctuations in the cosmic microwave background (CMB), the distance-luminosity relation for supernovas, the distribution of galaxies on large scales, the abundance of light elements (primordial nucleosynthesis), etc. The density values so obtained are compatible with all current astrophysical and cosmological observations, from the internal motions of galaxies and galaxy clusters to studies of weak gravitational lensing. Reference [1] finds the following values for the current matter and energy densities, Ωh^2, in units of $1.879\times10^{-29}\mathrm{g/cm^3}$ (i.e. 18.79 yg/m^3 or 1.689 nJ/m$^3c^2$):

- a negligible density in relativistic particles ("radiation"; e.g., the CMB photons contribute only $\Omega_\gamma h^2 = (2.467 \pm 0.004) \times 10^{-5}$);
- $\Omega_\Lambda h^2 = 0.36 \pm 0.04$ in a smoothly distributed component (dark energy);
- $\Omega_\mathrm{m} h^2 = 0.135^{+0.008}_{-0.009}$ in non-relativistic particles ("matter"), of which
  - $\Omega_\mathrm{b} h^2 = 0.0224 \pm 0.0009$ in protons and neutrons (baryons),
  - $\Omega_\mathrm{HDM} h^2 < 0.0076$ (95% CL) in non-baryonic hot dark matter,
  - $\Omega_\mathrm{CDM} h^2 = 0.113^{+0.008}_{-0.009}$ in non-baryonic cold dark matter.

It is the excess of total matter density ($\simeq 0.135$) over baryonic matter density ($\simeq 0.0224$) that constitutes the evidence for non-baryonic dark matter.

None of the known elementary particles can account for non-baryonic dark cold matter. The obvious Standard Model candidates would be neutrinos, but the measurements of the neutrino mass squared differences, $\Delta(m^2) \lesssim 10^{-3}$ eV^2, and the experimental upper bound of 3 eV on the mass of the neutrino produced in tritium beta decay, impose that the masses of all three known neutrinos are $m_\nu < 3$ eV. Neutrinos so light constitute *hot* dark matter, and have to be included in $\Omega_{\rm HDM}h^2 < 0.0076$ (95% CL). Thus no known particle is a candidate for non-baryonic cold dark matter.

Scores of hypothetical particles have been proposed as cold dark matter candidates over the past several decades. They range from new particles in well-founded extensions of the Standard Model, to possible particles inspired by recent theoretical ideas. To the first category belong an extra heavy neutrino, the axion, and the lightest supersymmetric particle (the neutralino, the gravitino, or the sneutrino). In the second category are particles like WIMPZILLAs, solitons (B-balls and Q-balls), self-interacting dark matter, string-inspired dark matter, Kaluza-Klein dark matter, etc.

2 Dark Matter WIMPs and Their Detection

A class of non-baryonic dark matter candidates is of interest here because of several recent claims to their detection: weakly interacting massive particles, or WIMPs. WIMPs are appealing because of a simple mechanism that can produce the observed value of their cosmic density. Assume that in the early Universe WIMPs were in thermal and chemical equilibrium with the rest of the matter and radiation. As the Universe expanded and cooled down, the chemical reactions coupling WIMPs to the rest of the world slowed down and eventually stopped, leaving a constant number of WIMPs in a volume that expands with the Universe. Numerically, the correct present-time density of WIMPs is obtained for matter-WIMP couplings of the order of electroweak couplings, and WIMP masses in the 1 GeV–100 TeV range. These characteristics give these particles their name. Examples of WIMPs are a heavy neutrino and the lightest neutralino. The latter arises in supersymmetric extension of the Standard Model, and is one of the most popular candidates for non-baryonic dark matter.

Signals from dark matter WIMPs can be either direct or indirect. Direct signals are due to collisions of dark matter WIMPs with nuclei in a detector. A very sensitive low-background detector records the amount of energy deposited by WIMPs in collisions with nuclei, and in the future also the direction of motion of the struck nucleus.

Indirect signals are due to the products of WIMP reactions in planets, stars, or galaxies. The most common reaction is WIMP annihilation: WIMPs can annihilate with anti-WIMPs, if present, or with themselves, if, like the neutralino, they are their own anti-particle. Out of the products of WIMP annihilation, neutrinos, positrons, anti-protons, and high-energy gamma-rays

are those of most interest because they are rarely produced by usual astrophysical processes. WIMP annihilations occur at a detectable rate where WIMPs are concentrated, as in the center of the Sun, the center of the Earth, and the inner regions of galactic halos, ours in particular. Neutrino telescopes, gamma-ray telescopes, and cosmic ray detectors are used to search for WIMPs indirectly.

The next three sections discuss signals that can or have been attributed to WIMPs, stressing the importance of exploiting distinctive signatures to ascertain their WIMP origin.

3 The HEAT Positron Excess

In two separate balloon flights with different detectors, the HEAT collaboration [2] has observed more cosmic ray positrons above ∼7 GeV than expected in current models of cosmic ray propagation in our galaxy. In these models, positrons arise as secondary particles in the interactions of primary cosmic rays with interstellar matter. Modifications of these models could in principle account for the extra positrons (and similar extra photons observed in EGRET [3]), but no proposed modification can yet reproduce all observable cosmic ray data (see discussion in [4], e.g.). WIMP annihilation can also be invoked to explain the extra positrons, as illustrated in Fig. 1.

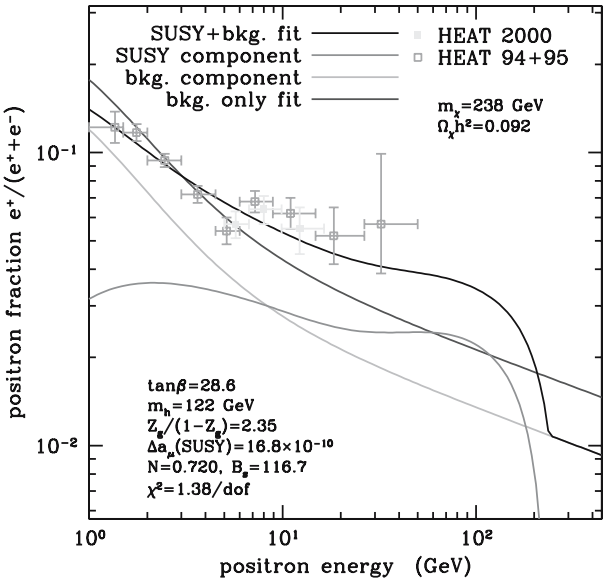

Fig. 1. The HEAT positron excess can be interpreted as due to annihilation of WIMPs, here a 238 GeV neutralino in the minimal supersymmetric standard model (from [5]).

Do the positron data distinguish between the suggested origins for the excess? Not by themselves, in that they lack a clear and unique signature that they are due to WIMPs. The positron spectrum predicted by WIMP annihilation lacks any discriminating feature, with the exception of a reduction in flux and then a cut-off as the energy increases towards the WIMP mass. Any such flux reduction can however be pushed beyond any foreseeable maximum detectable energy by simply raising the WIMP mass. In the absence of a distinguishing feature from WIMPs, it is hard to draw conclusions on the origin of the positron excess.

4 Gamma-Rays from the Galactic Center

In principle, gamma-rays from WIMP annihilation offer a characteristic signature in their spectrum: a gamma-ray line [6]. The line originates in the annihilation of WIMPs into a pair of photons, each photon carrying an energy equal to the WIMP mass, between 10 GeV and 100 TeV. No astrophysical process is known to produce a gamma-ray line at these energies. This makes the WIMP gamma-ray line an ideal signature for WIMPs.

Searches for the WIMP gamma-ray line are continuing, but no line has been detected yet. The challenge is twofold: both a large number of photons and a fine energy resolution are needed. Figure 2 shows that the space-born gamma-ray telescope GLAST, scheduled for launch in 2006, is expected to have such capabilities.

In the meantime, another source of gamma-rays from WIMPs has been used to claim their detection: the gamma-ray continuum. These are

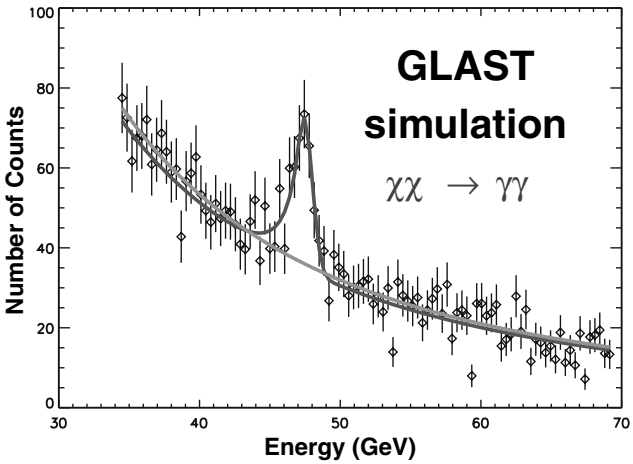

Fig. 2. Simulation showing the GLAST capability of detecting a gamma-ray line from WIMP annihilation (from [7]).

gamma-rays generated in the decay of secondary products, such as pions, produced by WIMP annihilation into quarks, W, or Z bosons. Contrary to the gamma-ray line, continuum gammas from WIMPs lack a characteristic feature, except for a flux reduction and cut-off near the WIMP mass. In this respect, they are similar to cosmic ray positrons from WIMPs. Raising the WIMP mass pushes the flux reduction beyond the observable energies.

The possibilities are limitless. For example, the early-2004 CANGAROO report of high-energy gamma-rays from the Galactic Center [8] has been interpreted as due to annihilations of $\sim 1\,\mathrm{TeV}$ WIMPs (see Fig. 3). The CANGAROO data can also be explained by appropriate modeling of accretion flows around the black hole at the Galactic Center [10]. The mid-2004 HESS observation of gamma-rays from the same region [11] has a very different spectrum from CANGAROO's, but it can also be interpreted either with appropriate (but different) accretion flows [10] or as due to WIMP annihilation, this time with $\sim 20\,\mathrm{TeV}$ WIMPs (Fig. 4). If this mass seems too high to supersymmetry aficionados, it may be amusing to see that even minimal supergravity models allow for $\sim 10\,\mathrm{TeV}$ neutralinos compatible with cosmological and astrophysical bounds and the HESS data (Fig. 5).

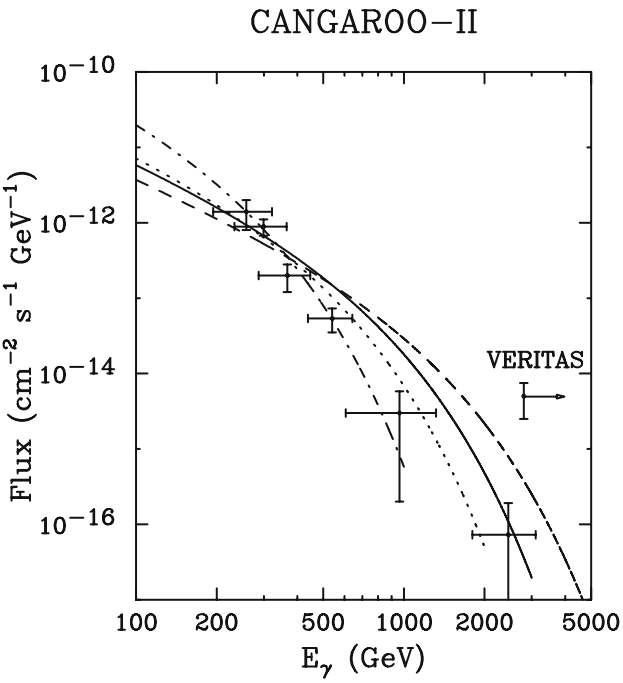

Fig. 3. WIMP annihilation can fit the CANGAROO gamma-ray data from the Galactic Center (from [9]).

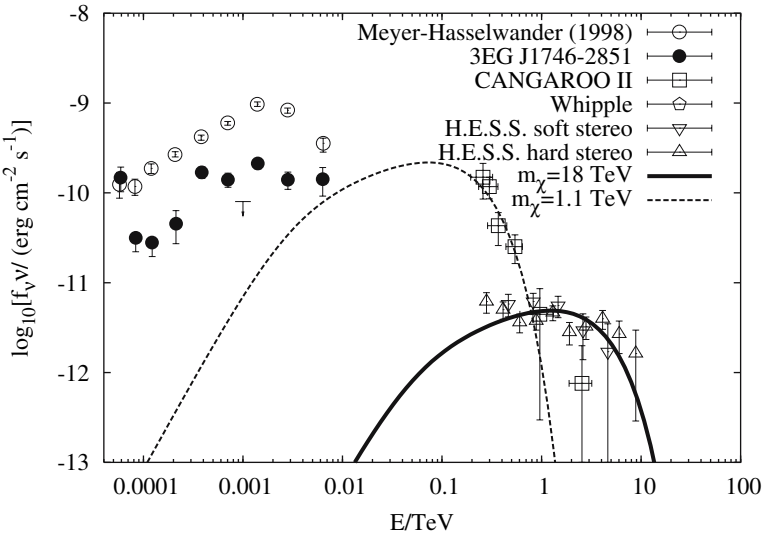

Fig. 4. Both CANGAROO and HESS Galactic Center data can be fitted to WIMP annihilation spectra, although with different WIMP masses (from [12]).

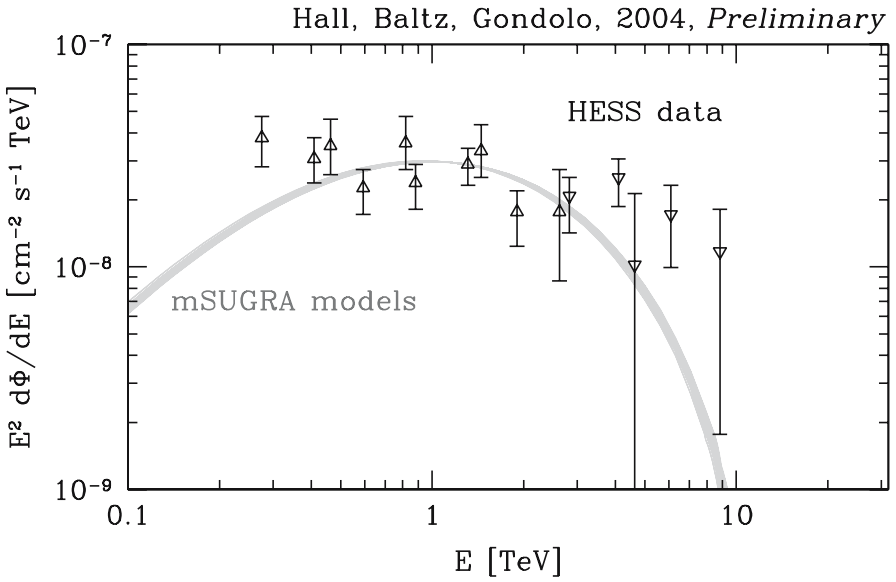

Fig. 5. The HESS spectrum can be fitted even to neutralinos in the minimal supergravity model (from [13]).

The lack of an unmistakable WIMP signature in the gamma-ray continuum makes it unsuitable as a primary indicator of the presence of WIMPs. A gamma-ray line would be desirable.

5 The DAMA Annual Modulation

An excellent signature for WIMPs in direct detection has been known for years: the annual modulation [14]. The Earth motion periodically changes the relative speed of Earth and WIMPs, causing the WIMP flux on Earth, and thus the WIMP detection rate, to vary in time and to repeat itself once every year. The details of the annual pattern depend on the WIMP velocity distribution. For example, the date of maximum rate is set by the most common arrival direction of the WIMPs, and happens in June for the canonical halo model with Maxwellian velocity distribution, but may occur in December for Sikivie's cold infall model (see [15]). Similarly, the amplitude of the modulation depends on the halo model.

The DAMA collaboration has observed an annual modulation in their sodium iodide data (Fig. 6) and has attributed it to WIMPs. No valid alternative explanation has been put forward yet, but no WIMP signal has been observed in any other direct detection experiment either. However, comparison of the various experimental results, which are obtained with different targets, is marred by the need of uncertain theoretical assumptions about the WIMP mass, interaction, and halo model. In fact, the expected event rate depends on the product of the WIMP-nucleus cross section and the WIMP flux on Earth. The cross section scales differently with the atomic mass of the target nucleus according as the WIMP interacts with the nuclear mass or the nuclear spin. The flux depends on the distribution of WIMP velocities, which is probably more complicated than an arbitrarily-assumed Maxwellian. Indeed, current hierarchical models of galaxy formation entail

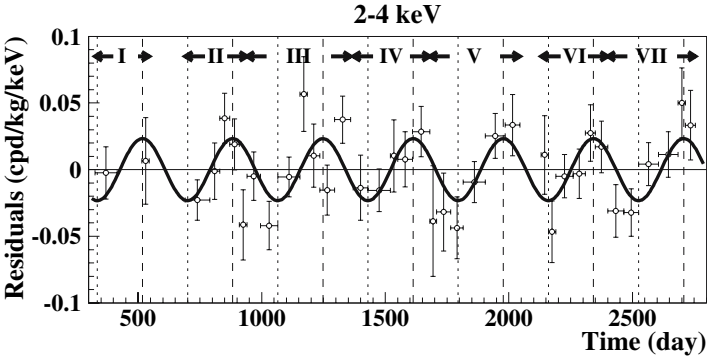

Fig. 6. The DAMA annual modulation (from [16]).

halo substructure and streams of dark matter. (Further details on the direct detection rate can be found in [17].)

Neglect of the theoretical assumptions involved has given rise to many controversies. For example, the first DAMA analysis [18] was artificially restricted to WIMPs heavier than 30 GeV, on the basis of some theoretical prejudice on the nature of the WIMPs. Under the assumption of a spin-independent cross section, the latest CDMS data [19] exclude the original DAMA region (Fig. 7-top), but relaxing the artificial restriction on the WIMP mass there remains the possibility of a (now admittedly narrow) region at low WIMP masses (Fig. 7-bottom). The moral is: do not use theoretical prejudices when analyzing data.

Another example in which the theoretical assumptions play a subtle role is the case of spin-dependent cross sections. For a canonical Maxwellian halo, if WIMPs interact predominantly with neutrons, existing data exclude the DAMA region, while if WIMPs interact predominantly with protons, the DAMA region may still be allowed, but only under further assumptions. As shown in Fig. 8, the most stringent limit on WIMP-proton spin-dependent interactions comes from the absence of indirect neutrino signals from WIMP annihilation in the Sun. This places an upper limit of $\sim$10 GeV on the WIMP mass (and a further analysis of lower energy neutrinos may lower this limit even further). However, there may be no anti-WIMPs in the Sun with which the WIMPs can annihilate, and as a consequence there may be no neutrino bounds on the spin-dependent WIMP-proton cross section. This would make the DAMA region allowed up to WIMP masses of $\sim$100 GeV. Notice that the neutralino, a fashionable candidate, is its own anti-particle, and thus for it the neutrino bounds cannot be avoided; restricting attention to the neutralino is however a theoretical prejudice.

In the face of all these difficulties of interpretation, other WIMP signatures in direct detection would be helpful. Very promising are detectors that can record not only the energy deposited by the WIMP but also the direction of motion of the nucleus after the collision. One such detector, DRIFT, is currently under construction [21]. It will be possible to use the recoil direction of the nuclei to discriminate a WIMP signal from background, for instance more WIMPs should come from the direction of motion of the Solar System than from the opposite direction.

Another signature for WIMPs has been proposed in [22] in case a stream of dark matter passes through the Solar System. Streams are common in simulations of galaxy formation, and have already been observed in our galaxy. One of them in particular, the stream associated with the tidal disruption of the Sagittarius dwarf galaxy, may pass by the Solar System. Streams through the Solar System may even enlarge the possibilities for the DAMA region, provided they come from roughly ahead of the Solar System motion (see Fig. 9). The new signature proposed in [22] is a combined annual modulation of the rate and of the highest energy that WIMPs in the stream can impart

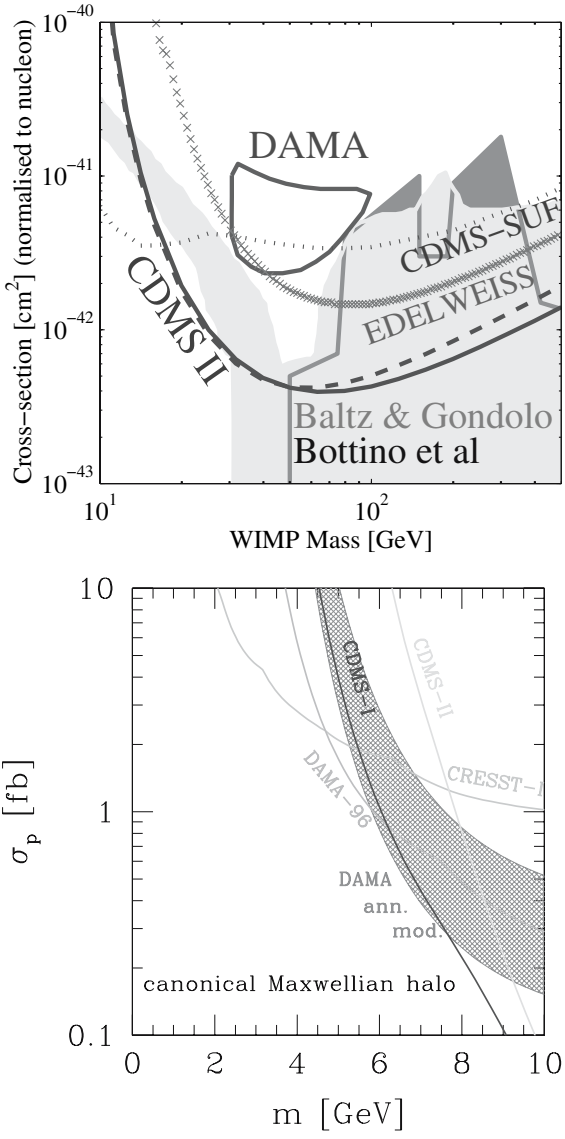

Fig. 7. Top: for spin-independent WIMP-nucleus interactions and a canonical halo with Maxwellian velocity distribution, CDMS [19] excludes the original DAMA region, which was however artificially cut at a WIMP mass of 30 GeV [18]. Bottom: relaxing the cut, the DAMA region is still (narrowly) allowed at lower masses [23].

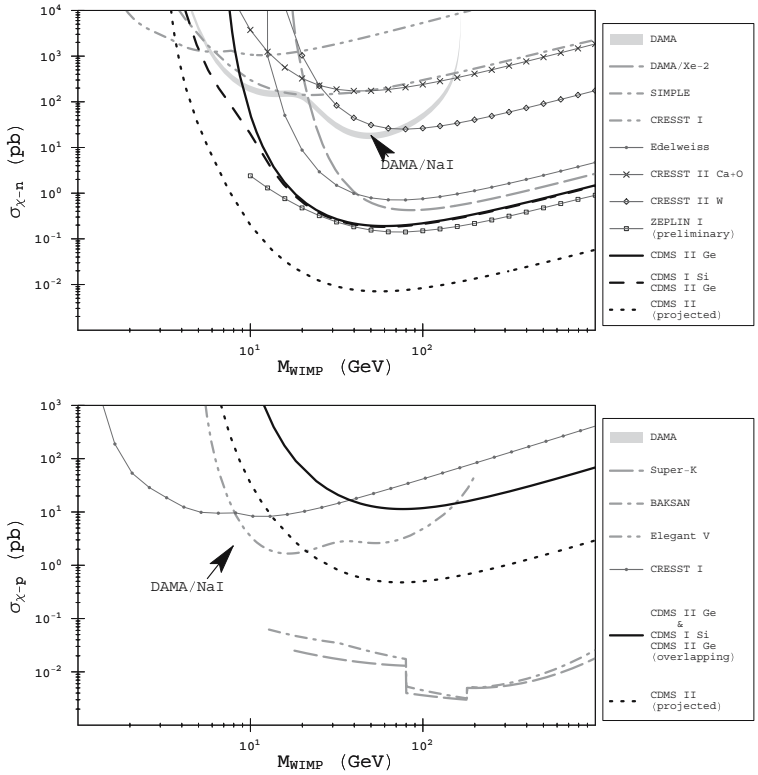

Fig. 8. Upper panel: if WIMPs interact predominantly with neutrons, existing data exclude the DAMA region for spin-dependent interactions and a canonical Maxwellian halo. Lower panel: if WIMPs interact predominantly with protons, the DAMA region may still be allowed under appropriate assumptions on WIMP annihilation in the Sun (from [20]).

to a nucleus. This highest energy shows as a step-like feature in the nucleus recoil spectrum, and the location of the step is predicted to vary in energy with a period of one year (Fig. 10). No background spectrum is expected to behave in this way.

With additional experimental signatures for WIMPs in direct detection we may be able to understand the origin of a claimed signal.

6 How Can We Make Sure We Detect Dark Matter?

The best signals for WIMP discovery are characterized by special features that make them recognizable as due to WIMPs and nothing else. For example, gamma-rays from WIMP annihilation should show a gamma-ray line in correspondence to the WIMP mass; high-energy ($\gtrsim$GeV) neutrinos from

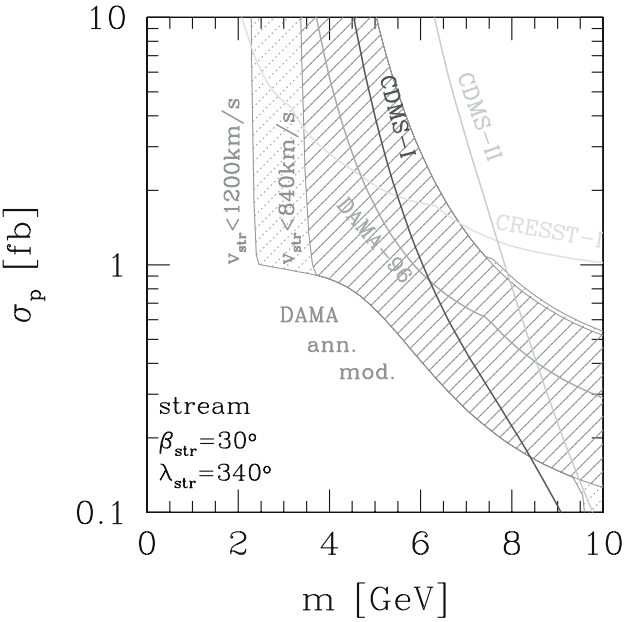

Fig. 9. Dark matter streams enlarge the possibilities for the DAMA region (from [23]).

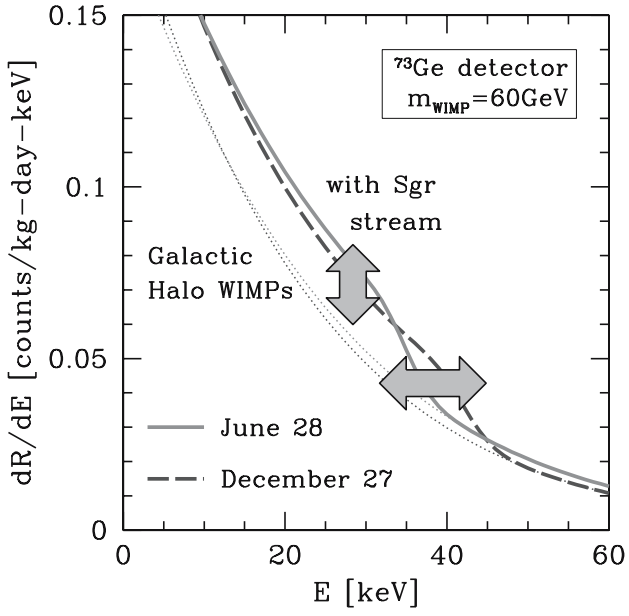

Fig. 10. A new combined modulation of both rate and end-point energy may be a powerful signature of WIMPs in a dark matter stream (from [22]).

the Sun or the Earth cannot be produced by anything else but WIMPs; the direct detection rate, and for WIMPs in a stream, the highest recoil energy, should follow a modulation with a period of a year; etc. It is these features one should look for in searching for dark matter WIMPs.

History has shown however (e.g. for the DAMA annual modulation) that a single feature, although accountable for in theoretical models, may not be enough to make sure that we have detected WIMPs. This is because the theory of WIMPs and their distribution is still very uncertain, and allows for many possibilities. What is needed is *experimental* confirmation from a variety of detectors, and perhaps from different kinds of signals that can be explained within the *same* WIMP model. Different kinds of signals will in any case be needed to determine all the interesting WIMP properties, such as mass, cross section, density, etc. Finally, to be really convinced, we will probably have to produce WIMPs in the laboratory, perhaps with high energy colliders.

References

1. C. L. Bennett et al.: Astrophys. J. Suppl. **148**, 1 (2003)
2. M. A. DuVernois et al.: Astrophys. J. **559** 296 (2001)
3. S. D. Hunter et al.: Astrophys. J. **481** 205 (1997)
4. A. W. Strong, I. V.Moskalenko, O. Reimer: Astrophys. J. **613** 962 (2004)
5. E. A. Baltz, J. Edsjö, K. Freese, P. Gondolo: Phys. Rev. **D65**, 063511 (2002)
6. M. Srednicki, S. Theisen, J. Silk, Phys. Rev. Lett. **56**, 236 (1986); **56**, 1883 (1986); S. Rudaz, Phys. Rev. Lett. **56**, 2128 (1986)
7. GLAST Science Brochure (March 2001) [http://glast.gsfc.nasa.gov/science]
8. K. Tsuchiya et al.: Astrophys. J. Lett. **606**, 115 (2004)
9. D. Hooper et al.: JCAP **09**, 002 (2004)
10. See, e.g., F. Aharonian, A. Neronov: astro-ph/0408303 (2004)
11. F. Aharonian et al.: Astron. Astrophys. Lett. **425**, 13 (2004)
12. D. Horns: astro-ph/0408192 (2004)
13. J. Hall, E. A. Baltz, P. Gondolo, in preparation.
14. A. K. Drukier, K. Freese, D. N. Spergel: Phys. Rev. **D33**, 3495 (1986); K. Freese, J. A. Frieman, A. Gould: Phys. Rev. **D37**, 3388 (1988)
15. G. Gelmini, P. Gondolo: Phys. Rev. **D64**, 023504 (2001)
16. R. Bernabei et al.: Riv. Nuovo Cim. **26N1**, 1 (2003) [astro-ph/0307403]
17. P. Gondolo: lectures at the NATO Advanced Study Institute "Frontiers of the Universe", Cargese, France (2003) [astro-ph/0403064]
18. P. Belli: presented at *TAUP 97*, LNGS, Italy [published in R. Bernabei et al., Nucl. Phys. B (Proc. Suppl.) 70 (1999) 79]; R. Bernabei et al.: Phys. Lett. **B480**, 23 (2000)
19. D. S. Akerib et al.: Phys. Rev. Lett. **93**, 211301 (2004)
20. C. Savage, P. Gondolo, K. Freese: Phys. Rev. **D70**, 123513 (2004)
21. D. P. Snowden-Ifft, C. J. Martoff, J. M. Burwell: Phys. Rev. **D61**, 1 (2000); G. J. Alner et al.: Nucl. Instrum. Meth. **A535**, 644 (2004) and references therein.
22. K. Freese, P. Gondolo, H. J. Newberg, M. Lewis: Phys. Rev. Lett. **92**, 111301 (2004); K. Freese, P. Gondolo, H. J. Newberg: astro-ph/0309279 (2003)
23. G. Gelmini, P. Gondolo: hep-ph/0405278 (2004)

From New Geometry Towards a New Symmetry. Reflexive Numbers and Berger Graphs from Calabi-Yau Spaces

L.N. Lipatov[1], A. Sabio Vera[2], V.N. Velizhanin[1] and G.G. Volkov[1,3,4,5]

[1] Petersburg Nuclear Physics Institute, Gatchina, 188 300 St. Petersburg, Russia
[2] II. Institut für Theoretische Physik, Universität Hamburg, Luruper Chaussee 149, D–22761 Hamburg, Germany
[3] Instituto de Física Teórica UAM/CSIC, C–XVI, & Departamento de Física Teórica C–XI, Universidad Autónoma de Madrid, E–28049, Madrid, Spain
[4] Laboratoire d'Annecy–Le–Vieux de Physique Théorique, LAPTH (CNRS UMR 5108), B.P. 110, Annecy–Le–Vieux, F-74941, France
[5] Theory Division, Physics Department, CERN, 1211 Geneva 23, Switzerland

1 Introduction

In this work we explore a possibility to find new symmetries similar to the Lie and Kac-Moody groups. This is done by analyzing the structure of Calabi–Yau (CY) spaces [1, 2, 3]. These spaces are interesting because they are connected to many branches of mathematics and are extensively used as candidates for compactification of extra dimensions in physical models. For example, the proof of the duality between the type IIA and IIB, and between type IIA and heterotic $E_8 \times E_8$ string theories is based on their different compactifications on CY manifolds.

A CY space can be realized as an algebraic variety $\mathcal{M}$ in a weighted projective space $\mathrm{CP}^{n-1}(\overrightarrow{k})$ where the weight vector reads $\overrightarrow{k} = (k_1, \ldots, k_n)$. This variety is defined by

$$\mathcal{M} \equiv (\{x_1, \ldots, x_n\} \in \mathrm{CP}^{n-1}(\overrightarrow{k}) : \mathcal{P}(x_1, \ldots, x_n) \equiv \sum_{\overrightarrow{m}} c_{\overrightarrow{m}} x^{\overrightarrow{m}} = 0) \,, \quad (1)$$

i.e., the zero locus of a quasi–homogeneous polynomial of degree $d_k = \sum_{i=1}^{n} k_i$, with the monomials being $x^{\overrightarrow{m}} \equiv x_1^{m_1} \cdots x_n^{m_n}$. The points in CP^{n-1} satisfy the property of projective invariance $\{x_1, \ldots, x_n\} \approx \left\{\lambda^{k_1} x_1, \ldots, \lambda^{k_n} x_n\right\}$ leading to the constraint $\overrightarrow{m} \cdot \overrightarrow{k} = d_k$. Another constraint for a CY candidate is the condition of reflexivity of the vector $\overrightarrow{k}$, which can be defined in terms of the Batyrev reflexive polyhedra [4].

Let us consider this condition in more detail. We can construct the vector $\overrightarrow{m}' = \overrightarrow{m} - \overrightarrow{1}$ where $\overrightarrow{m}' \cdot \overrightarrow{k} = 0$. Then it is convenient to define the lattice

$$\Lambda = \left\{\overrightarrow{m}' \in \mathbb{Z}^n : \overrightarrow{m}' \cdot \overrightarrow{k} = 0\right\} \quad (2)$$

with basis $\{e_i\}$. The dual of this lattice, Λ^*, has the basis $\{e_i^*\}$ with the orthonormality condition $e_i \cdot e_j^* = \delta_{ij}$. We define a polyhedron Δ as the

convex hull of the lattice Λ and the polyhedron Δ^* as the convex hull of the dual lattice Λ^*. The reflexivity condition means that the polyhedron Δ is integer, its origin $\overrightarrow{0}$ is the only interior point, and its dual Δ^* is also integer and contains only one interior point. In this case the vector $\overrightarrow{k}$ is considered to be reflexive. Using this criteria of reflexive vectors Batyrev proved the Mirror duality of $\mathrm{CY}_{3,4}$ spaces. Namely, for each CY, $\mathcal{M}$, there exists a Mirror CY partner, $\mathcal{M}^*$. This symmetry helped to derive the duality between type IIA and IIB string theories.

The correspondence between CY spaces and reflexive polyhedra led the way for their classification. In particular, for the case $\mathrm{CY}_2 = K_3$ the 4319 three–dimensional polyhedra were found in [5, 6]. Among them, 95 can be described with a single reflexive vector. The algorithm, constructed in [5, 6], gave 473 800 776 reflexive four dimensional polyhedra in the case of CY_3 spaces. A subclass of this large number can be described by one reflexive vector. Namely, 184 026 polyhedra belong to this subclass [5, 6] (see also [8, 9, 10, 11]).

Recently, an alternative to this classification was developed using some properties of the theory of reflexive vectors. This new approach was named "Universal Calabi–Yau Algebra" (UCYA)[8]. One of its main results is that all reflexive vectors of dimension n can be obtained from the reflexive vectors with lower dimension $1, \ldots, n-1$. A remarkable feature of this approach is that every reflexive vector of dimension n can be constructed from the simplest reflexive vector $\overrightarrow{k} = (1)$. The key observation to realize this program was to use the concept of the r–arity composition law (with $r = 2, \ldots, n$) for the subclass which can be described by a unique reflexive vector (in general CY spaces this subclass corresponds to the so–called level one). Using this composition law, it was shown how the level one CY_n space can be obtained from its slices of lower dimension $r = 1, \ldots n-1$, generating in this way the so–called r–arity slice classification. For example, the 2–arity composition law in K_3 space gives us 90 out of the 95 reflexive vectors described above. These 90 vectors were classified in 22 chains where each of them has the same CY_1 slice in K_3 (four of the remaining reflexive weight vectors can be obtained with the 3–arity and the last one with the 4–arity). In CY_3 a similar 2–arity classification produces 4242 chains having the same K_3 slice of CY_3 [8, 9].

To be more specific, the 22 chains in K_3 are generated by taking the reflexive vectors (1), (1,1), (1,1,1), (1,1,2) and (1,2,3) and extending them to dimension 4 by including additional zero components, i.e., (0,0,0,1), (0,0,1,1), (0,1,1,1), (0,1,1,2), (0,1,2,3) and permutations of vector components. In the 2–arity construction one should take all the possible pairs of two extended vectors and, out of them, select those "good pairs" which have a reflexive polyhedron in the intersection of the corresponding slices. Then we add these two vectors with integer coefficients. For example, from the 50 possible extended vectors we can take the pair $\overrightarrow{k}_a^{\mathrm{ext}} = (0,1,1,1)$ and $\overrightarrow{k}_b^{\mathrm{ext}} = (1,0,0,0)$. Their intersection is defined as the solution of the two

constraints $\overrightarrow{m} \cdot \overrightarrow{k}_a^{\text{ext}} = d_{k_a} = 3$ and $\overrightarrow{m} \cdot \overrightarrow{k}_b^{\text{ext}} = d_{k_b} = 1$. These equations can be also written as

$$\Lambda = \left\{ \overrightarrow{m}' \in \mathbb{Z}^4 : \overrightarrow{m}' \cdot \overrightarrow{k}_a^{\text{ext}} = \overrightarrow{m}' \cdot \overrightarrow{k}_b^{\text{ext}} = 0 \right\}, \tag{3}$$

where $\overrightarrow{m}' = \overrightarrow{m} - \overrightarrow{1}$. The lattice of solutions for $\overrightarrow{m}'$ corresponds to a two dimensional reflexive polyhedron or CY_1, and, therefore, according to UCYA, the linear combination

$$m_a \overrightarrow{k}_a^{\text{ext}} + m_b \overrightarrow{k}_b^{\text{ext}} \tag{4}$$

with $m_a \leq d_{k_b}$ and $m_b \leq d_{k_a}$ of these two vectors forms the chain with the eldest vector having unit coefficients $m_a = m_b = 1$. A simple example is the combination of two vectors, $\overrightarrow{k}_m$ with dimension m and $\overrightarrow{k}_n$ with dimension n, in the form $(\overrightarrow{k}_m, \overrightarrow{0}_n) + (\overrightarrow{0}_m, \overrightarrow{k}_n)$ which is always an eldest reflexive vector of dimension $m+n$. The three vectors (1,1,1,1), (2,1,1,1) and (3,1,1,1) produce the same two dimensional reflexive slice. This slice divides the three dimensional K_3 polyhedron in two parts. On the left and right sides of the slice the set of the points at the edges forms affine Dynkin diagrams. For example, in the reflexive polyhedra corresponding to the vector (1,1,1,1) from the (1,0,0,0) side we obtain the $A_{11}^{(1)}$–diagram and from the (0,1,1,1) side we have the graph of $E_6^{(1)}$. The (2,1,1,1) and (3,1,1,1) members of this chain generate the same slice but they contain different Dynkin graphs. This property is universal and is valid for all 22 chains. It is a generalization of the results of Candelas and Font [12, 13, 14] who found a dictionary for the Dynkin graphs of the Cartan–Lie algebra in the case of the Weierstrass slice using the type IIA and heterotic $E_8 \times E_8$ string duality. In the K_3 case a correspondence between extended reflexive vectors and Dynkin graphs was found [8, 9, 11], for example,

$$\begin{aligned}
&(0,0,0,1) \rightarrow \mathrm{A}_r^{(1)} \\
&(0,0,1,1) \rightarrow \mathrm{D}_r^{(1)} \\
&(0,1,1,1) \rightarrow \mathrm{E}_6^{(1)} \\
&(0,1,1,2) \rightarrow \mathrm{E}_7^{(1)} \\
&(0,1,2,3) \rightarrow \mathrm{E}_8^{(1)}.
\end{aligned} \tag{5}$$

Note that the maximal Coxeter label of the graphs at the right hand side of this correspondence coincides with the degree of the reflexive vectors at the left hand side. We shall discuss this point later. Our scheme offers the possibility of constructing new graphs for CY spaces in any dimension. For example, in K_3 all 4242 graphs for the reflexive numbers of level one type can be obtained following the above–mentioned approach [8]. Our analysis will help classify the structure of these large CY spaces in terms of number

theory and construct new so–called Berger graphs. These Berger graphs might correspond to unknown symmetries lying beyond Cartan–Lie algebras [15].

The number of algebraic CY_n varieties is very large and grows very rapidly with the dimension n of the space. The same situation occurs with the number of reflexive weight vectors. For example, the number of eldest reflexive vectors of 2–arity is 1, 2, 22 and 4242 [8] for dimensions $n = 2$, 3, 4 and 5, respectively. To obtain the last number 4242 for n = 5 using the arity construction we need 100 extended reflexive vectors (and all permutations of their components) (see Table 1). From UCYA one can find the approximate upper–bounds of this number for larger n: $\sim 3\ 10^{13}$, $\sim 5\ 10^{28}$, $\sim 10^{58}$, $\sim 10^{119}$, $\sim 10^{241}, \ldots$ An important point is that all reflexive weight vectors can be considered as a new type of numbers because in the framework of UCYA the arithmetic of adding and subtracting is well defined. This opens a possibility to understand the structure of CY spaces using number theory. In the "tree" classification of CY spaces the trunk line of the reflexive weight numbers corresponds to those with unit components, i.e., (1), (1,1), $(1,1,1), \ldots$ An interesting wider subclass of the full tree of them is the so–called "simply–laced" numbers. A simply–laced number $\overrightarrow{k} = (k_1, \cdots, k_n)$ with degree $d = \sum_{i=1}^{n} k_i$ is defined such that

$$\frac{d}{k_i} \in \mathbb{Z}^+ \text{ and } d > k_i \ . \tag{6}$$

For these numbers there is a simple way of constructing the corresponding affine Dynkin and Berger graphs together with their Coxeter labels. The Cartan and Berger matrices of these graphs are symmetric. In the well known Cartan case they correspond to the ADE series of simply–laced algebras. In dimensions $n = 1, 2, 3$ the numbers $(1), (1,1), (1,1,1), (1,1,2), (1,2,3)$ are simply–laced. For $n = 4$ among all 95 numbers 14 are simply–laced, as is shown in Table 1 [15, 16, 17]. The remaining 81 correspond to the non–simply–laced case. Before constructing these graphs in the next section we proceed to review the concept of reflexivity and relate it to techniques used in the functional integral approach. This section will help us understand the difference between simply and non–simply–laced numbers at a more fundamental level.

2 From Reflexive Numbers to Quantum Field Theory Methods

In this section we reconsider the condition of reflexivity first proposed by Batyrev [4]. We will do so in a new approach where the reflexive numbers are studied starting from the simply–laced case to then continue to some non–simply–laced cases. The properties of these reflexive numbers turn out to be very interesting.

Table 1. The 100 distinct types of five–dimensional extended projective vectors used to construct CY_3 spaces. The order of their permutation symmetry groups is also shown. Including these permutations, the total number of extended vectors is 10 270. The simply–laced vectors (1+1+3+14=19) are highlighted with bold face.

ℵ	${k_{5ex}}^{(i)}$	$G(Gal)$	ℵ	${k_{5ex}}^{(i)}$	$G(Gal)$
i	$(\mathbf{0,0,0,0,1})[\mathbf{1}]$	5	46	$(0,2,3,4,7)[16]$	120
ii	$(\mathbf{0,0,0,1,1})[\mathbf{2}]$	10	47	$(0,2,3,4,9)[18]$	120
iii	$(\mathbf{0,0,1,1,1})[\mathbf{3}]$	10	48	$(0,2,3,5,5)[15]$	60
iv	$(\mathbf{0,0,1,1,2})[\mathbf{4}]$	30	49	$(0,2,3,5,7)[17]$	120
v	$(\mathbf{0,0,1,2,3})[\mathbf{6}]$	60	50	$(0,2,3,5,8)[18]$	120
1	$(\mathbf{0,1,1,1,1})[\mathbf{4}]$	5	51	$(0,2,3,5,10)[20]$	120
2	$(0,1,1,1,2)[5]$	20	52	$(0,2,3,7,9)[21]$	120
3	$(\mathbf{0,1,1,1,3})[\mathbf{6}]$	20	53	$(0,2,3,7,12)[24]$	120
4	$(\mathbf{0,1,1,2,2})[\mathbf{6}]$	30	54	$(0,2,3,8,11)[24]$	120
5	$(0,1,1,2,3)[7]$	60	55	$(0,2,3,4,7)[16]$	120
6	$(\mathbf{0,1,1,2,4})[\mathbf{8}]$	60	56	$(\mathbf{0,2,3,10,15})[\mathbf{30}]$	120
7	$(0,1,1,3,4)[9]$	60	57	$(0,2,4,5,9)[20]$	120
8	$(0,1,1,3,5)[10]$	60	58	$(0,2,4,5,11)[22]$	120
9	$(\mathbf{0,1,1,4,6})[\mathbf{12}]$	60	59	$(0,2,5,6,7)[20]$	120
10	$(0,1,2,2,3)[8]$	60	60	$(0,2,5,6,13[26]$	120
11	$(\mathbf{0,1,2,2,5})[\mathbf{10}]$	60	61	$(0,2,5,9,11)[27]$	120
12	$(0,1,2,3,3)[9]$	60	62	$(0,2,5,9,16)[32]$	120
13	$(0,1,2,3,4)[10]$	120	63	$(0,2,5,14,21)[42]$	120
14	$(0,1,2,3,5)[11]$	120	64	$(0,2,6,7,15)[30]$	120
15	$(\mathbf{0,1,2,3,6})[\mathbf{12}]$	120	65	$(0,3,3,4,5)[15]$	60
16	$(0,1,2,4,5)[12]$	120	66	$(0,3,4,5,6)[18]$	120
17	$(0,1,2,4,7)[14]$	120	67	$(0,3,4,5,7)[19]$	120
18	$(0,1,2,5,7)[15]$	120	68	$(0,3,4,5,8)[20]$	120
19	$(0,1,2,5,8)[16]$	120	69	$(0,3,4,5,12)[24]$	120
20	$(\mathbf{0,1,2,6,9})[\mathbf{18}]$	120	70	$(0,3,4,7,10)[24]$	120
21	$(\mathbf{0,1,3,4,4})[\mathbf{12}]$	60	71	$(0,3,4,7,14)[28]$	120
22	$(0,1,3,4,5)[13]$	120	72	$(0,3,4,10,13)[30]$	120
23	$(0,1,3,4,7)[15]$	120	73	$(0,3,4,10,17)[24]$	120
24	$(0,1,3,4,8)[16]$	120	74	$(0,3,4,11,18[36])$	120
25	$(0,1,3,5,6)[15]$	120	75	$(0,3,4,14,21)[42]$	120
26	$(0,1,3,5,9)[18]$	120	76	$(0,3,5,6,7)[21]$	120
27	$(0,1,3,7,10)[21]$	120	77	$(0,3,5,11,14)[33]$	120
28	$(0,1,3,7,11)[22]$	120	78	$(0,3,5,11,19)[38]$	120
29	$(\mathbf{0,1,3,8,12})[\mathbf{24}]$	120	79	$(0,3,5,16,24)[48]$	120
30	$(0,1,4,5,6)[16]$	120	80	$(0,3,6,7,8)[24]$	120
31	$(\mathbf{0,1,4,5,10})[\mathbf{20}]$	120	81	$(0,4,5,6,9)[24]$	120
32	$(0,1,4,6,7)[18]$	120	82	$(0,4,5,6,15)[30]$	120
33	$(0,1,4,6,11)[22]$	120	83	$(0,4,5,7,9)[25]$	120
34	$(0,1,4,9,14)[28]$	120	84	$(0,4,5,7,16)[32]$	120
35	$(0,1,4,10,15)[30]$	120	85	$(0,4,5,13,22)[44]$	120
36	$(0,1,5,7,8)[21]$	120	86	$(0,4,5,18,27)[54]$	120
37	$(0,1,5,7,13)[26]$	120	87	$(0,4,6,7,11)[28]$	120
38	$(0,1,5,12,18)[36]$	120	88	$(0,4,6,7,17)[34]$	120
39	$(0,1,6,8,9)[24]$	120	89	$(0,5,6,7,9)[27]$	120
40	$(0,1,6,8,15)[30]$	120	90	$(0,5,6,8,11)[30]$	120
41	$(\mathbf{0,1,6,14,21})[\mathbf{42}]$	120	91	$(0,5,6,8,19)[38]$	120
42	$(0,2,2,3,5)[12]$	60	92	$(0,5,6,22,33)[66]$	120
43	$(0,2,2,3,7)[14]$	60	93	$(0,5,7,8,20)[40]$	120
44	$(\mathbf{0,2,3,3,4})[\mathbf{12}]$	60	94	$(0,7,8,10,25)[50]$	120
45	$(0,2,3,4,5)[14]$	120	95	$(0,7,8,9,12)[36]$	120

We concentrate on arithmetic properties of these numbers making use of some methods common in the study of Feynman diagrams in Quantum Field Theory.

2.1 Simply–Laced Numbers

Let us consider the simplest case with the monomial points $\{\overrightarrow{m}_i\}$ satisfying the equation

$$\sum_{r=1}^{n} \frac{m_r}{s_r} = 1\,, \tag{7}$$

where s_r are integer numbers, and

$$\sum_{r=1}^{n} \frac{1}{s_r} = 1 \tag{8}$$

due to the reflexivity requirement. Geometrically s_r is the value at which the hyperplane crosses the axis r. The vectors $(1/s_1, 1/s_2, \ldots, 1/s_n)$ satisfying the above constraint are known as the "Egyptian fractions" [19].

It is helpful to generalize the last decomposition of 1 for a general rational number $x \leq 1$

$$\sum_{r=1}^{n} \frac{1}{s_r} = x\,. \tag{9}$$

We denote the number of such decompositions by $N_n(x)$. It is convenient also to arrange the ratios $1/s_r$ as follows

$$1/s_{r+1} \leq 1/s_r\,, \tag{10}$$

corresponding to $s_{r+1} \geq s_r$. In this case we can introduce the symbol $N_n(x, 1/s)$ for the number of decompositions of x in the sum of n unit ratios $1/s_r$ satisfying the relations

$$s_r \geq s\ . \tag{11}$$

It is possible to derive the following recurrent relation for $N_n(x, 1/s)$:

$$N_n(x, 1/s) = \sum_{s'=s}^{\infty} \sum_{t=1}^{\infty} N_{n-t}\Big(x - t/s', 1/(s'+1)\Big) \tag{12}$$

with the initial condition

$$N_0(x, 1/s) = \delta_{x,0}\,, \quad N_n(x, 1/s)\Big|_{n<0} = 0\,. \tag{13}$$

For example,

$$N_1(1/s, 1/s) = 1 \tag{14}$$

and $N_1(x, 1/s) = 0$ for other x.

It is now convenient to introduce the generating function for $N_n(x, 1/s)$:

$$F_\lambda(y,\, 1/s) = \sum_{n=0}^{\infty} \sum_{x} \lambda^n\, y^x\, N_n(x, 1/s) = \prod_{t=s}^{\infty} \left(1 - \lambda y^{1/t}\right)^{-1} . \tag{15}$$

The above recurrence relation corresponds to the following equation for this function

$$F_\lambda(y,\, 1/s) = \left(1 - \lambda y^{1/s}\right)^{-1} F_\lambda(y,\, 1/(s+1)) \, . \tag{16}$$

Note that $F_\lambda(y,\, 1/s)$ contains a divergent product in t, but it does not lead to any divergence for $N_n(x, 1/s)$.

There are solutions of the above equations with all s_r different. They correspond to the polyhedron $\{\overrightarrow{m}_k\}$ without any symmetry under the transmutation of m_k. An interesting example is the following decomposition of unity

$$1 = \sum_{k=1}^{r-1} \frac{1}{2^k} + \sum_{k=0}^{r-1} \frac{1}{2^k(2^r - 1)} \, . \tag{17}$$

Provided that

$$M_r = 2^r - 1 \tag{18}$$

is a prime number $M_r = 3, 7, 31, 127, \ldots$ (which can only be for primes $r = 2, 3, 5, 7, \ldots$), in the above decomposition $1 = \sum_k 1/s_k$ the integers s_k are all divisors (except of 1) of the perfect number d

$$d = M_r(M_r + 1)/2 \, . \tag{19}$$

In this case M_r are called "Mercenna numbers" and, according to Euclid and Euler, all even perfect numbers, being the sum of all their divisors d/s_k

$$d = \sum_k \frac{d}{s_k} \, , \tag{20}$$

can be expressed in terms of Mercenna numbers. Examples of such decomposition are given here:

$$6 = 1 + 2 + 3 \, , \;\; 28 = 1 + 2 + 4 + 7 + 14 \, . \tag{21}$$

In a similar way one can construct d different $(n+1)$–dimensional polyhedrons for decompositions of other perfect numbers $d = 28, 496, \ldots$ in the sum of their n divisors. If M_r is not a prime number not all of its divisors enter in the decomposition of d. Note that there are not known odd perfect numbers.

In the next section we estimate the number of simply–laced solutions at large n.

2.2 Number of Simply–Laced Decompositions for $n \to \infty$

Let us consider the generating function

$$F_\lambda^{(\Lambda)}(y) = \prod_{t=1}^{\Lambda}(1 - \lambda\, y^{1/t})^{-1} = \sum_{n=0}^{\infty} \lambda^n \sum_x y^x\, N_n(x) \tag{22}$$

for the number $N_n(x)$ of decompositions of the rational number $x > 0$ to the sum of n unit ratios $1/s_r$ (s_r is an integer number):

$$x = \sum_{r=1}^{n} \frac{1}{s_r}\,. \tag{23}$$

The large integer number Λ is introduced to regularize the product at large values of t. In this case the equation $z = F_\lambda^{(\Lambda)}(y)$ defines a Riemann surface with a finite genus. The quantity $N_n(x)$ does not depend on Λ when its value is sufficiently large (depending on x and n).

We have the inverse relation

$$\Phi_n(y) = \sum_x y^x\, N_n(x) = \frac{1}{2\pi i} \int_L \frac{d\,\lambda}{\lambda^{n+1}}\, F_\lambda^{(\Lambda)}(y)\,, \tag{24}$$

where the integral is taken in an anti–clock–wise direction along a small closed contour L drawn around the point $\lambda = 0$.

To express $N_n(x)$ in terms of $F_\lambda(y)$ we should perform the additional integration

$$N_n(x) = \frac{1}{2\pi i\, m} \int_{l_m} \frac{d\,y}{y^{1+x}}\, \Phi_n(y)\,. \tag{25}$$

Here the closed contour of integration l_m goes m–times around the point $y = 0$ moving through other sheets of the Riemann surface $z = y^{-x}\,\Phi_n(y)$. The integer number m is chosen from the condition that the point $y = 0$ on the surface becomes regular in the new coordinate $u = y^{1/m}$.

It is possible to calculate the number of decompositions of unity $N_n(1)$ for several values of n (see [19])

$$N_1(1) = 1\,,\ N_2(1) = 1\,,\ N_3(1) = 3\,,\ N_4(1) = 14\,,\ N_5(1) = 147\,,$$

$$N_6(1) = 3462\,,\ N_7(1) = 294314\,,\ N_8(1) = 159330691\,. \tag{26}$$

Let us calculate the asymptotic behavior of $\Phi_n(y)$ using the saddle point method. For this purpose we present the generating function in the form

$$\ln F_\lambda^{(\Lambda)}(y) = \ln F_\lambda^{(\Lambda)}(1) + \Delta \ln F_\lambda^{(\Lambda)}(y)\,, \tag{27}$$

where

$$\ln F_\lambda^{(\Lambda)}(1) = -\Lambda\, \ln(1 - \lambda) \tag{28}$$

and

$$\Delta \ln F_{\lambda}^{(\Lambda)}(y) = \frac{\lambda}{1-\lambda} \ln y \sum_{t=1}^{n} \frac{1}{t} + f_{\lambda}(y) . \tag{29}$$

Here

$$f_{\lambda}(y) = \sum_{t=1}^{\infty} \left(\ln \frac{1-\lambda}{1-\lambda\, y^{1/t}} - \frac{1}{t} \frac{\lambda}{1-\lambda} \ln y \right) . \tag{30}$$

In the last expression for $f_{\lambda}(y)$ we pushed Λ to infinity, because the sum over t is convergent.

Now we apply the saddle point method to the calculation of the integral over λ, considering the extremum of the function

$$J_n^{(\Lambda)}(\lambda) = \ln F_{\lambda}^{(\Lambda)}(1) - n \ln \lambda = \Lambda \ln \frac{1}{1-\lambda} - n \ln \lambda . \tag{31}$$

From the stationarity condition $\delta J_n^{(\Lambda)}(\lambda) = 0$ one can find the saddle point

$$\tilde{\lambda} = \frac{n}{n+\Lambda} \tag{32}$$

and therefore with a quadratic accuracy in $\delta\lambda = \lambda - \tilde{\lambda}$ we obtain for this function

$$J_n^{(\Lambda)}(\lambda) = \Lambda \ln \frac{n+\Lambda}{\Lambda} + n \ln \frac{n+\Lambda}{n} + \frac{(\delta\lambda)^2}{2} \frac{(n+\Lambda)^3}{n\,\Lambda} + \dots . \tag{33}$$

It is obvious that the contour of integration over $\delta\lambda$ goes through the saddle point in a correct direction parallel to the imaginary axis. Thus, we obtain for $\Phi_n(y)$ the following expression at large n after calculating the Gaussian integral over $\delta\lambda$

$$\Phi_n(y) = \left(\frac{n+\Lambda}{\Lambda} \right)^{\Lambda} \left(\frac{n+\Lambda}{n} \right)^{n} \sqrt{\frac{\Lambda}{2\pi\, n\, (n+\Lambda)}}\, e^{\Delta \ln F_{\tilde{\lambda}}^{(\Lambda)}(y)} . \tag{34}$$

We substituted λ by its saddle point value $\tilde{\lambda}$ in the slowly changing function $\Delta \ln F_{\lambda}^{(\Lambda)}(y)$.

Let us consider now the most interesting case, when $\tilde{\lambda}$ is a small number

$$\tilde{\lambda} << 1 . \tag{35}$$

In this limit $f_{\tilde{\lambda}}(y) = 0$ and the result is significantly simplified

$$\Phi_n(y) = \left(\frac{n+\Lambda}{\Lambda} \right)^{\Lambda} \left(\frac{n+\Lambda}{n} \right)^{n} \sqrt{\frac{\Lambda}{2\pi\, n\, (n+\Lambda)}}\, y^{x} , \tag{36}$$

where

$$x = \frac{\tilde{\lambda}}{1-\tilde{\lambda}} \sum_{t=1}^{\Lambda} \frac{1}{t} \,. \tag{37}$$

Because

$$\sum_{t=1}^{\Lambda} \frac{1}{t} \approx \ln \Lambda - \Psi(1) + \frac{1}{2\Lambda} + \dots \,,$$

where $\gamma = -\Psi(1)$ is the Euler constant, we obtain that $N_n(x)$ has a maximum

$$N_n(x_m) \approx \frac{(n+\Lambda)^n}{n!} \tag{38}$$

at

$$x_m = \frac{n}{\Lambda} \left(\ln \Lambda - \Psi(1) + \frac{1}{2\Lambda} \right) . \tag{39}$$

For larger x the above saddle point method should be modified.

It turns out that when going beyond the dimension $n = 3$ not all of the reflexive weight numbers are simply–laced. A large number of them has a different structure in the sense that some of their components k_r are not divisors of the degree d. These are what we called non–simply–laced numbers. The simplest case is when each component k_r can be converted in a divisor of the difference of the degree d and another component $k_{r'}$. The next subsection is devoted to the study of this class of numbers called "quasi–simply–laced".

2.3 Classification of Quasi–Simply–Laced Numbers

Quasi–simply–laced numbers are important generalizations of the simply–laced ones. For example, in dimension $n = 4$ all 95 polyhedra with a single reflexive vector belong to this class (among them 14 are obtained from the simply–laced numbers). A simple example is the vector $\overrightarrow{k} = (1, 2, 3, 5)[11]$, corresponding to the following decomposition of unity in the sum of ratios l_i

$$1 = \frac{1}{11} + \frac{2}{11} + \frac{3}{11} + \frac{5}{11} \,.$$

For this vector $d_k = 11$ and $d_k/k_1 = 11$, $(d_k - k_1)/k_2 = 5$, $(d_k - k_2)/k_3 = 3$ and $(d_k - k_1)/k_4 = 2$.

Hence we can generalize the above ansatz for the diagonal matrix M_{ij}, assuming that the vector $\overrightarrow{l}$ satisfies the set of equations

$$s_i l_i + l_{i'} = 1 \tag{40}$$

for $i = 1, 2, \dots, n$ and $i' = i'(i)$ is also one of these numbers. Here s_i are positive integer parameters which will be later chosen from the condition that the vector $\overrightarrow{1}$ belongs to the slice of $\overrightarrow{m}$:

$$\sum_{i=1}^{n} l_i = 1 \tag{41}$$

and this point in the slice is inner following the property of reflexivity. In this section we will classify all sets of equations for quasi–simply–laced numbers in such a way that the sets obtained by a transmutation of s_i are considered as belonging to the same class.

For this purpose we introduce a diagrammatic representation where the indices i and i' in (40) are connected by a line with an arrow directed from i to i'. For each different class of sets of equations there is only one "Feynman diagram" related to the function $i'(i)$ in (40). These Feynman diagrams can be obtained from the "functional" integral $Z(\lambda)$ with the "action" L

$$Z(\lambda) = \int \frac{d\,x\,dy}{\pi}\, e^{-L}\,,\ L = |z|^2 - \lambda\, z^* e^z\,,\ \ z = x + iy \tag{42}$$

by expanding it in the "coupling constant" λ:

$$Z(\lambda) = \sum_{n=0}^{\infty} \lambda^n\, Z_n\ ,\ Z_n = \sum_r \frac{1}{G_r}\ . \tag{43}$$

Here r enumerates different Feynman diagrams in the n^{th}-order of perturbation theory (corresponding to different classes of sets of the equations shown above) and G_r are the numbers of elements in the symmetry group of transmutations of indices i for the corresponding diagram. In agreement with (40) these diagrams contain all possible vertices V_r $(r = 0, 1, 2, \ldots)$ in which r particles are absorbed (corresponding to the field z) and only one particle is emitted (corresponding to the field z^*).

Using the above expression for $Z(\lambda)$ we obtain

$$Z_n = \int \frac{d\,x\,dy}{\pi}\, e^{-|z|^2}\, \frac{z^{*n}}{n!} e^{\,nz}\,. \tag{44}$$

Therefore for the number of diagrams of order n weighted with the symmetry factors $1/G_r$ we obtain

$$Z_n = \sum_r \frac{1}{G_r} = \frac{n^n}{n!}\,. \tag{45}$$

It is natural to expect that at large n the saddle point configuration for the Feynman diagrams corresponds to an almost constant averaged symmetry factor $\frac{1}{\overline{G}(n)}$ for a subgroup of the permutation group

$$\frac{1}{\overline{G}(n)} = \frac{\sum_r 1/G_r}{\sum_r 1}\,. \tag{46}$$

In this case the number of different classes of solutions grows not very rapidly at large n

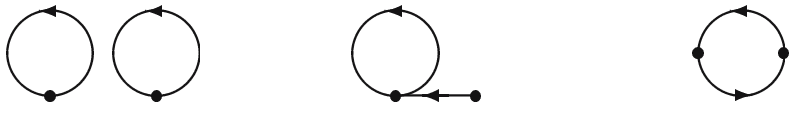

Fig. 1. Diagrams for $n = 2$.

$$\sum_r 1 \approx \overline{G}(n)\,\frac{e^n}{\sqrt{2\pi n}} \tag{47}$$

in comparison with the total number of Calabi—Yau spaces. Let us consider the Feynman diagrams for $n = 2, 3, 4, 5, \ldots$. For $n = 2$ there is one disconnected and two connected diagrams (see Fig. 1, where the symmetry weights G_r are also indicated).

The corresponding sets of equations are

$$a)\ s_1\,l_1 + l_1 = 1\,, \qquad s_2\,l_2 + l_2 = 1\,, \tag{48}$$

$$b)\ s_1\,l_1 + l_1 = 1\,, \qquad s_2\,l_2 + l_1 = 1\,, \tag{49}$$

$$c)\ s_1\,l_1 + l_2 = 1\,, \qquad s_2\,l_2 + l_1 = 1\,. \tag{50}$$

One can verify in this case the fulfillment of the relation

$$Z_2 = \frac{1}{2!} + 1 + \frac{1}{2!} = \frac{2^2}{2!} = 2\,.$$

For $n = 3$ we have 7 different Feynman diagrams and 7 different sets of equations, respectively

$$1)\ s_1\,l_1 + l_1 = 1\,, \quad s_2\,l_2 + l_2 = 1\,, \quad s_3\,l_3 + l_3 = 1;\ G = 3!; \tag{51}$$

$$2)\ s_1\,l_1 + l_1 = 1\,, \quad s_2\,l_2 + l_2 = 1\,, \quad s_3\,l_3 + l_2 = 1;\ G = 1; \tag{52}$$

$$3)\ s_1\,l_1 + l_1 = 1\,, \quad s_2\,l_2 + l_1 = 1\,, \quad s_3\,l_3 + l_2 = 1;\ G = 1; \tag{53}$$

$$4)\ s_1\,l_1 + l_1 = 1\,, \quad s_2\,l_2 + l_1 = 1\,, \quad s_3\,l_3 + l_1 = 1;\ G = 2!; \tag{54}$$

$$5)\ s_1\,l_1 + l_1 = 1\,, \quad s_2\,l_2 + l_3 = 1\,, \quad s_3\,l_3 + l_2 = 1;\ G = 2!; \tag{55}$$

$$6)\ s_1\,l_1 + l_3 = 1\,, \quad s_2\,l_2 + l_1 = 1\,, \quad s_3\,l_3 + l_2 = 1;\ G = 3; \tag{56}$$

$$7)\ s_1\,l_1 + l_2 = 1\,, \quad s_2\,l_2 + l_3 = 1\,, \quad s_3\,l_3 + l_2 = 1;\ G = 1\,. \tag{57}$$

The number of diagrams with their symmetry factors is

$$Z_3 = \frac{1}{6} + 1 + 1 + \frac{1}{2!} + \frac{1}{2!} + \frac{1}{3} + 1 = \frac{3^3}{3!} = \frac{9}{2}\,,$$

which agrees with the above relations.

For $n = 4$ there are 19 different Feynman diagrams and

$$Z_4 = \frac{4^4}{4!} = \frac{32}{3}\,.$$

For $n = 5$, 6 and 7 there are respectively 47, 130 and 342 different Feynman diagrams with the corresponding values of Z_n

$$Z_5 = \frac{5^5}{5!} = \frac{625}{24}\,,\ Z_6 = \frac{6^6}{6!} = \frac{324}{5}\,,\ Z_7 = \frac{7^7}{7!} = \frac{117649}{720}\,.$$

It is possible to calculate the number of the corresponding diagrams for larger values of n (see [20]). It turns out that the averaged symmetry $\overline{G}$ of the Feynman diagrams grows approximately linearly from $\overline{G} = 1$ for $n = 1$ up to $\overline{G}(n) \approx 10,7$ for $n = 27$.

Looking at these Feynman diagrams we can see how their connected parts contain only one loop. In this way the quasi–classical approximation for the "functional" integral should be exact:

$$Z(\lambda) = \int \frac{d\,x\,dy}{\pi}\, e^{-L} = \frac{1}{1 - z(\lambda)}\,, \tag{58}$$

where $z(\lambda)$ is the solution of the classical equation $\delta L = 0$:

$$z(\lambda) = \lambda\, e^{z(\lambda)}\,. \tag{59}$$

Solving this equation making use of perturbation theory we obtain

$$Z(\lambda) = \sum_{n=0}^{\infty} \lambda^n \frac{n^n}{n!}\,, \tag{60}$$

corresponding to

$$z(\lambda) = 1 - \frac{1}{\sum\limits_{n=0}^{\infty} \lambda^n \dfrac{n^n}{n!}} = \lambda + \lambda^2 + \frac{3}{2}\lambda^3 + \dots\,. \tag{61}$$

One can obtain a more detailed description of the Feynman diagrams in terms of the number of vertices V_r with a different number $r+1$ of lines. For this case we should consider the more general action

$$L = |z|^2 - z^* \sum_{r=0}^{\infty} g_r \frac{z^r}{r!}\,, \tag{62}$$

where g_r are the corresponding coupling constants. Here we have

$$Z = \int \frac{d\,x\,dy}{\pi}\, e^{-L} = \frac{1}{1 - a}\,, \tag{63}$$

where a is the solution of the classical equation

$$a = \sum_{r=1}^{\infty} g_r \frac{a^{r-1}}{(r-1)!} \tag{64}$$

and the perturbative expansion for Z reads

$$Z = \sum_{r_0=0}^{\infty} \frac{g_0^{r_0}}{r_0!} \sum_{r_1=0}^{\infty} \frac{g_1^{r_1}}{r_1!(1!)^{r_1}} \cdots \sum_{r_\infty=0}^{\infty} \frac{g_\infty^{r_\infty} (\sum_{k=0}^{\infty} r_k)!}{r_\infty!(\infty!)^{r_\infty}} \; \delta \left(\sum_{k=0}^{\infty} (k\,-1) r_k \right). \tag{65}$$

The coefficient in front of the product of $g_k^{r_k}$ coincides with the number of Feynman diagrams (with symmetry factors) having r_k vertices with $k+1$ lines for each $k = 0, 1, 2, \ldots$. At large orders $n = \sum_{k=0}^{\infty} r_k \gg 1$ of perturbation theory there exists a saddle point

$$\tilde{r}_k = n \, \frac{e^{-1}}{k!} \tag{66}$$

in the sums over r_k.

The simply–laced numbers are a particular case of the reflexive numbers and they can be found by the same method in higher dimensions. In [18] we list all the 147 simply–laced numbers for $n = 5$ with their corresponding dimensions d.

To find these 147 simply–laced numbers we can also use the recurrent relations in (12). Moreover, using these relations, also 3462 simply–laced numbers for $n = 6$ were calculated. But here we want to discuss a different method to generate these numbers in a recurrent way.

The generalization to a higher number of terms in the sum is trivial and one can verify that indeed the simply–laced numbers for $n = 5$ written in the form of the unit fractions can be obtained by this method from the corresponding expansions for $n = 2, 3, 4$.

It is important to note that among all unit decompositions for each n there is a decomposition with the maximal denominator corresponding to the maximal dimension $d(n) = \max d_k$. This number satisfies the simple recurrence relation

$$d(n+1) = d(n) \, (d(n) + 1) \, . \tag{67}$$

It grows very rapidly

$$d(1) = 1 \, , \; d(2) = 2 \, , \; d(3) = 6 \, , \; d(4) = 42 \, , \; d(5) = 1806 \, \ldots \, . \tag{68}$$

Note that the numbers $d(n) + 1$ are not necessarily prime because $1807 = 13 \cdot 139$.

2.4 Quasi–Simply–Laced Reflexive Weight Vectors for $n = 4$

To find all possible weight vectors in the $n = 4$ case we firstly construct all expansions of the form

$$d = k_1 + k_2 + k_3 + k_4 \tag{69}$$

which fulfill the simply–laced condition

$$\frac{d}{k_1} = s_1\,,\ \frac{d}{k_2} = s_2\,,\ \frac{d}{k_3} = s_3\,,\ \frac{d}{k_4} = s_4\,, \tag{70}$$

with $s_1,\ s_2,\ s_3,\ s_4 > 1$ being integer numbers. For this purpose we use a program based on the recurrent relation (12) for the number $N_n(x, 1/s)$ of decomposition of the rational number $x > 0$ in the ratios $1/s_k$.

To search for all possible quasi–simply–laced numbers it is helpful to apply the above classification of the classes of sets of equations. Let us consider in the following the different cases where one, two, three or four numerators of the above ratios are modified.

For one modified numerator there is only one possibility (from now $s_i \in \mathbb{Z}^+$ and $s_i > 1$)

$$\frac{d}{k_1} = s_1\,,\ \frac{d-k_1}{k_2} = s_2\,,\ \frac{d}{k_3} = s_3\,,\ \ \frac{d}{k_4} = s_4\,. \tag{71}$$

For two modified numerators there are four classes

$$\frac{d}{k_1} = s_1\,,\ \frac{d-k_1}{k_2} = s_2\,,\ \frac{d-k_1}{k_3} = s_3\,,\ \frac{d}{k_4} = s_4\,, \tag{72}$$

$$\frac{d}{k_1} = s_1\,,\ \frac{d-k_1}{k_2} = s_2\,,\ \frac{d-k_4}{k_3} = s_3\,,\ \frac{d}{k_4} = s_4\,, \tag{73}$$

$$\frac{d}{k_1} = s_1\,,\ \frac{d-k_1}{k_2} = s_2\,,\ \frac{d-k_2}{k_3} = s_3\,,\ \frac{d}{k_4} = s_4\,, \tag{74}$$

$$\frac{d}{k_1} = s_1\,,\ \frac{d-k_3}{k_2} = s_2\,,\ \frac{d-k_2}{k_3} = s_3\,,\ \frac{d}{k_4} = s_4\,. \tag{75}$$

In the case of three modified numerators seven classes exist

$$\frac{d}{k_1} = s_1\,,\ \frac{d-k_1}{k_2} = s_2\,,\ \frac{d-k_1}{k_3} = s_3\,,\ \frac{d-k_1}{k_4} = s_4\,, \tag{76}$$

$$\frac{d}{k_1} = s_1\,,\ \frac{d-k_3}{k_2} = s_2\,,\ \frac{d-k_1}{k_3} = s_3\,,\ \frac{d-k_1}{k_4} = s_4\,, \tag{77}$$

$$\frac{d}{k_1} = s_1\,,\ \frac{d-k_3}{k_2} = s_2\,,\ \frac{d-k_2}{k_3} = s_3\,,\ \frac{d-k_1}{k_4} = s_4\,, \tag{78}$$

$$\frac{d}{k_1} = s_1\,,\ \frac{d-k_3}{k_2} = s_2\,,\ \frac{d-k_4}{k_3} = s_3\,,\ \frac{d-k_1}{k_4} = s_4\,, \tag{79}$$

$$\frac{d}{k_1} = s_1\,,\ \frac{d-k_1}{k_2} = s_2\,,\ \frac{d-k_2}{k_3} = s_3\,,\ \frac{d-k_2}{k_4} = s_4\,, \tag{80}$$

$$\frac{d}{k_1} = s_1\,,\ \frac{d-k_3}{k_2} = s_2\,,\ \frac{d-k_2}{k_3} = s_3\,,\ \frac{d-k_2}{k_4} = s_4\,, \tag{81}$$

$$\frac{d}{k_1} = s_1\,,\ \frac{d-k_3}{k_2} = s_2\,,\ \frac{d-k_4}{k_3} = s_3\,,\ \frac{d-k_2}{k_4} = s_4\,. \tag{82}$$

And, finally, for four numerators six classes should be considered

$$\frac{d-k_2}{k_1}=s_1\,,\ \frac{d-k_1}{k_2}=s_2\,,\ \frac{d-k_1}{k_3}=s_3\,,\ \frac{d-k_1}{k_4}=s_4\,, \tag{83}$$

$$\frac{d-k_2}{k_1}=s_1\,,\ \frac{d-k_3}{k_2}=s_2\,,\ \frac{d-k_1}{k_3}=s_3\,,\ \frac{d-k_1}{k_4}=s_4\,, \tag{84}$$

$$\frac{d-k_3}{k_1}=s_1\,,\ \frac{d-k_3}{k_2}=s_2\,,\ \frac{d-k_1}{k_3}=s_3\,,\ \frac{d-k_1}{k_4}=s_4\,, \tag{85}$$

$$\frac{d-k_4}{k_1}=s_1\,,\ \frac{d-k_3}{k_2}=s_2\,,\ \frac{d-k_1}{k_3}=s_3\,,\ \frac{d-k_1}{k_4}=s_4\,, \tag{86}$$

$$\frac{d-k_4}{k_1}=s_1\,,\ \frac{d-k_3}{k_2}=s_2\,,\ \frac{d-k_2}{k_3}=s_3\,,\ \frac{d-k_1}{k_4}=s_4\,, \tag{87}$$

$$\frac{d-k_2}{k_1}=s_1\,,\ \frac{d-k_3}{k_2}=s_2\,,\ \frac{d-k_4}{k_3}=s_3\,,\ \frac{d-k_1}{k_4}=s_4\,. \tag{88}$$

For the simply–laced case in (70) we have 14 solutions. In the class corresponding to (71) there are 37 new solutions. In the classes shown in (72)–(75) it is possible to find 32 additional solutions. In the sets of (77)–(82) there are 10 new solutions. For the last case in (83)–(88) we only have 2 new solutions. All of these solutions are explicitly shown in [7]. The total number of quasi–simply–laced numbers is therefore 95, which is in agreement with the known number of Calabi–Yau spaces with one reflexive vector.

The simplest way to find the above–mentioned decompositions is to solve the following system of linear equations

$$l_{r'}+s_r l_r=1\,, \qquad r,r'=1,\ldots,n \tag{89}$$

$$\sum_{r=1}^{n} l_r=1 \tag{90}$$

for all integer s_r. This gives n^n sets of linear equations, which have non–trivial solutions only if the determinant of the extended $(n+1)\times(n+1)$ matrix equals zero

$$\begin{vmatrix} s_1 & 0 & \ldots & 0 & -1 \\ 0 & s_2 & \ldots & 0 & -1 \\ \vdots & \vdots & \ddots & \vdots & \vdots \\ 0 & 0 & \ldots & s_n & -1 \\ 1 & 1 & \ldots & 1 & -1 \end{vmatrix} \equiv 0\,. \tag{91}$$

Here in every row i the zero in the place i' is substituted by unity. Some of the n^n sets of linear equations are equivalent and are obtained by transmutations of indices i. For example, in the $n=4$ case there are only 19 non–equivalent

sets of equations according to the above classification of the quasi–simply–laced numbers. The corresponding matrices and numbers of solutions for each matrix are listed in Table 2, where $\tilde{s}_i = s_i + 1$ and one should add to each matrix the row with all "1" and the column with all "-1".

Table 2. Matrix and number of the corresponding equation.

Matrix	Equation	Matrix	Equation	Matrix	Equation	Matrix	Equation
$\begin{vmatrix} \tilde{s}_1 & 0 & 0 & 0 \\ 1 & s_2 & 0 & 0 \\ 1 & 0 & s_3 & 0 \\ 1 & 0 & 0 & s_4 \end{vmatrix}$	**(76)**	$\begin{vmatrix} \tilde{s}_1 & 0 & 0 & 0 \\ 0 & \tilde{s}_2 & 0 & 0 \\ 0 & 0 & s_3 & 1 \\ 0 & 0 & 1 & s_4 \end{vmatrix}$	**(75)**	$\begin{vmatrix} \tilde{s}_1 & 0 & 0 & 0 \\ 1 & s_2 & 0 & 0 \\ 1 & 0 & s_3 & 0 \\ 0 & 1 & 0 & s_4 \end{vmatrix}$	**(77)**	$\begin{vmatrix} \tilde{s}_1 & 0 & 0 & 0 \\ 0 & s_2 & 1 & 0 \\ 0 & 1 & s_3 & 0 \\ 0 & 1 & 0 & s_4 \end{vmatrix}$	**(81)**
$\begin{vmatrix} \tilde{s}_1 & 0 & 0 & 0 \\ 1 & s_2 & 0 & 0 \\ 1 & 0 & s_3 & 0 \\ 0 & 0 & 0 & \tilde{s}_4 \end{vmatrix}$	**(72)**	$\begin{vmatrix} \tilde{s}_1 & 0 & 0 & 0 \\ 0 & s_2 & 1 & 0 \\ 0 & 0 & s_3 & 1 \\ 0 & 1 & 0 & s_4 \end{vmatrix}$	**(82)**	$\begin{vmatrix} \tilde{s}_1 & 0 & 0 & 0 \\ 1 & s_2 & 0 & 0 \\ 0 & 1 & s_3 & 0 \\ 0 & 1 & 0 & s_4 \end{vmatrix}$	**(80)**	$\begin{vmatrix} s_1 & 1 & 0 & 0 \\ 1 & s_2 & 0 & 0 \\ 1 & 0 & s_3 & 0 \\ 1 & 0 & 0 & s_4 \end{vmatrix}$	**(83)**
$\begin{vmatrix} \tilde{s}_1 & 0 & 0 & 0 \\ 1 & s_2 & 0 & 0 \\ 0 & 1 & s_3 & 0 \\ 0 & 0 & 1 & s_4 \end{vmatrix}$	**(79)**	$\begin{vmatrix} s_1 & 1 & 0 & 0 \\ 1 & s_2 & 0 & 0 \\ 1 & 0 & s_3 & 0 \\ 0 & 1 & 0 & s_4 \end{vmatrix}$	**(85)**	$\begin{vmatrix} \tilde{s}_1 & 0 & 0 & 0 \\ 1 & s_2 & 0 & 0 \\ 0 & 1 & s_3 & 0 \\ 0 & 0 & 0 & \tilde{s}_4 \end{vmatrix}$	**(74)**	$\begin{vmatrix} s_1 & 1 & 0 & 0 \\ 1 & s_2 & 0 & 0 \\ 1 & 0 & s_3 & 0 \\ 0 & 0 & 1 & s_4 \end{vmatrix}$	**(86)**
$\begin{vmatrix} \tilde{s}_1 & 0 & 0 & 0 \\ 1 & s_2 & 0 & 0 \\ 0 & 0 & \tilde{s}_3 & 0 \\ 0 & 0 & 1 & s_4 \end{vmatrix}$	**(73)**	$\begin{vmatrix} s_1 & 1 & 0 & 0 \\ 1 & s_2 & 0 & 0 \\ 0 & 0 & s_3 & 1 \\ 0 & 0 & 1 & s_4 \end{vmatrix}$	**(87)**	$\begin{vmatrix} \tilde{s}_1 & 0 & 0 & 0 \\ 1 & s_2 & 0 & 0 \\ 0 & 0 & \tilde{s}_3 & 0 \\ 0 & 0 & 0 & \tilde{s}_4 \end{vmatrix}$	**(71)**	$\begin{vmatrix} s_1 & 1 & 0 & 0 \\ 0 & s_2 & 1 & 0 \\ 1 & 0 & s_3 & 0 \\ 1 & 0 & 0 & s_4 \end{vmatrix}$	**(84)**
$\begin{vmatrix} \tilde{s}_1 & 0 & 0 & 0 \\ 1 & s_2 & 0 & 0 \\ 0 & 0 & s_3 & 1 \\ 0 & 0 & 1 & s_4 \end{vmatrix}$	**(78)**	$\begin{vmatrix} s_1 & 1 & 0 & 0 \\ 1 & s_2 & 1 & 0 \\ 0 & 1 & s_3 & 1 \\ 1 & 0 & 0 & s_4 \end{vmatrix}$	**(88)**	$\begin{vmatrix} \tilde{s}_1 & 0 & 0 & 0 \\ 0 & \tilde{s}_2 & 0 & 0 \\ 0 & 0 & \tilde{s}_3 & 0 \\ 0 & 0 & 0 & \tilde{s}_4 \end{vmatrix}$	**(70)**		

Let us note that for the ansatz in (76) the above determinant is factorized, which means that this matrix corresponds to an infinite number of solutions. The vanishing condition for this determinant can be written as

$$s_1(s_3s_4 + s_2s_4 + s_2s_3 - s_2s_3s_4) = 0 \;\Leftrightarrow\; \frac{1}{s_2} + \frac{1}{s_3} + \frac{1}{s_4} - 1 = 0 \qquad (92)$$

and in fact, apart from many (non–reflexive) solutions with $s_1 = 0$, we obtain those solutions corresponding to the decompositions of unity for $n = 3$. The same is true for (83). We should neglect these two classes of sets of equations due to their degeneracy.

3 Simply–Laced Numbers as Generators of Berger Graphs

In this Section we consider the case of simply–laced Berger graphs [15, 16, 17], which can be obtained from CY_d spaces on the first level. These spaces can be described by a single reflexive weight vector. We shall firstly focus on those reflexive numbers on the level one which are simply–laced. We already stated above that these numbers generate an important subset of all the class of reflexive numbers. They lead to symmetric Berger matrices corresponding to A_r, D_r, E_6, E_7 and E_8 algebras in the Cartan–Lie case. These simply–laced Cartan–Lie algebras have the root system in Dynkin diagrams containing only simple segments connecting its nodes. Therefore their Cartan matrices are symmetric. In our study we also first consider the case of symmetric Berger matrices.

In previous works [15, 16, 17] we established a remarkable link between the simply–laced reflexive numbers and the corresponding Berger graphs. As it was discussed above, these numbers have a simple arithmetic structure. Namely, each component k_i is a divisor of its degree d_k. We recall that in dimensions $n = 1, 2, 3$ all five reflexive numbers ((1)[1], (1,1)[2], (1,1,1)[3], (1,1,2)[4], (1,2,3)[6]) are simply–laced. The situation is different when one goes to the $n = 4$ case, where for the total number 95 of all reflexive polyhedrons there are only 14 simply–laced ones. To begin with, we would like to establish relations between these $5 + 14$ simply–laced reflexive numbers and some Berger graphs.

Using the analogy with the Cartan–Lie case one can construct the corresponding "primary" Berger graph for a simply–laced reflexive number [15]. Namely, its degree d_k is assigned as a Coxeter label to the central node of the elementary graph and coincides with the maximal Coxeter label in this graph. The number of the legs going from this central node is equal to the dimension n of the vector $\overrightarrow{k}$. In each of the legs the number of nodes is $d_k/k_i - 1$, where k_i is the corresponding component of the simply–laced vector $\overrightarrow{k}$. The Coxeter labels of these nodes are the integer numbers $d_k - k_i\,,\ d_k - 2k_i\,, ..., k_i$ and decrease along the leg from the central node to its end. For example, for the vector $(1, 1, 2)[4]$ the primary graph contains three legs because its dimension is 3. The central node has the Coxeter label 4 and in the first and second legs we have additional nodes with the Coxeter labels $3, 2, 1$, i.e. these two legs contain 4/1=4 equidistant nodes (including the central node). In the remaining third leg we have 4/2=2 equidistant nodes and the Coxeter label of the additional node is 2.

For the primary Berger graph constructed in the above–mentioned way from a simply–laced number one can find the corresponding Berger matrix B_{ij} built out of scalar products (α_i, α_j) of the root vectors $\overrightarrow{\alpha}_l$ assigned to each node. The scalar product of two vectors for the nodes connected by a line is -1. Two vectors are orthogonal when the corresponding nodes are not

connected. The square of the vector assigned to an usual node is 2, but the square of the vector corresponding to the central node is $n-1$, where n is the leg number coinciding with the dimension of the reflexive vector $\overrightarrow{k}$. The squares α_i^2 are situated on the diagonal B_{ii} of the Berger matrix and the scalar products (α_i, α_j) of the root vectors are placed off the diagonal. The determinant of this matrix is zero, which is a generalization of the similar result for the affine simply–laced Cartan–Lie algebras having $\alpha_i^2 = 2$ for the root corresponding to the central node (because $n = 3$). The Coxeter labels assigned to the nodes in a Berger graph coincide with the components c_l of the eigenvector $\sum_l c_l \alpha_l$ of the Berger matrix corresponding to its vanishing eigenvalue. Note that for the vector $\overrightarrow{k} = (1,1)[2]$ the primary graph contains the central node with Coxeter label 2 and $B_{ii} = 1$, moreover, each of its two legs has one node with Coxeter label 1 and $B_{ii} = 2$.

The maximal Coxeter labels for the reflexive simply–laced numbers (1), (1,1), (1,1,1), (1,1,2), (1,2,3) are $1, 2, 3, 4, 6$, respectively, which coincide with the maximal Coxeter labels for the corresponding simply–laced algebras, A_r, D_r, E_6, E_7 and E_8. In more detail, for these cases we have, respectively: One node of A–type with Coxeter label (1), three nodes of D–type with Coxeter labels (1,2,1) (one chain), seven nodes of E_6–type with Coxeter labels (1,2;1,2;1,2;3) (three chains), eight nodes of E_7 type with Coxeter labels (1,2,3;1,2,3;2;4) (three chains) and nine nodes of E_8–type with Coxeter labels (1,2,3,4,5;2,4;3;6) (three chains).

It is important to note that the primary graphs for these numbers are generators of generalized Berger graphs in CY_d polyhedra. Namely, such Berger graphs can be built from one or several blocks of the primary graphs. These blocks are connected by lines corresponding to the Cartan matrices for the A_i–series: On each line there are several nodes with the same Coxeter label equal to the Coxeter label of the two nodes to which these lines are attached. Moreover, the Coxeter labels for all nodes and matrix elements of the Berger matrix B_{ij} inside each block are universal and coincide with those for the corresponding elementary Cartan graph. Only the square of the root corresponding to the node with the attached lines is changed by adding to it the number l of these lines l, i.e., $B_{ii} = 2 \to B_{ii} = 2 + l$ [15].

Each of the reflective vectors $\boldsymbol{k}$ with n components can be extended to extra dimensions $n \to p + n$ by adding to it several vanishing components: $\boldsymbol{k}_{p+n}^{ext} = (0, 0, ..., 0; k_1, ..., k_n)$. These extended vectors participate in the UCYA r–arity construction leading to the new reflexive vectors in higher dimensions. The topology of the Berger graphs for the polyhedrons constructed in this way depends on the number p of the zero components of the corresponding extended vectors.

In general we can use the UCYA r–arity construction to build new Calabi–Yau polyhedra (at the level one). In particular, to go from the vectors (1), (1,1), (1,1,1), (1,1,2), (1,2,3) to $n = 4$ dimensions one should take the following extended vectors (0,0,0,1), (0,0,1,1), (0,1,1,1), (0,1,1,2), (0,1,2,3) and

their permutations. Then in the framework of the 2–arity approach we can construct the linear combinations of two of these numbers with integer coefficients. For each pair one should verify that the intersection of two polyhedra corresponding to two extended vectors has the reflexivity property. This condition is fulfilled in the case of the polyhedron corresponding to the eldest vector $\boldsymbol{k}_1 + \boldsymbol{k}_2$ in the 2–arity construction. In the K_3 reflexive polyhedron for each eldest vectors one can find the primary graphs of the $A_r^{(1)}$, $D_r^{(1)}$, $E_6^{(1)}$, $E_7^{(1)}$ and $E_8^{(1)}$ types. They are situated at the two opposite sides of the polyhedra divided by the above intersection. A similar situation takes place with the reflexive K_3 polyhedron corresponding to the sum of the vectors $\boldsymbol{k}_1$ and $\boldsymbol{k}_2$ with integer coefficients. In each case in the constructed polyhedron one can find the generalized graphs corresponding to the initial primary graphs.

When one goes with the 2–arity construction to the $n = 5$ dimensional case (CY_3) then the structure of the corresponding graphs becomes more complicated although they are also built from the previous order graphs. The difference is that some of the Berger matrices corresponding to the generalized Dynkin graphs can have a 3 instead of a 2 along their diagonal. This is seen in Fig. 2 where the links between the known Berger subgraphs belong to the A_l type with modified Coxeter labels (1,2,3, ... instead of 1).

Remarkably, these five $n = 5$ Berger graphs shown on Fig. 2 generate five infinite series because their structure holds for any l in A_l. This construction can be generalized by linking with A_l–lines ($B_{ii} = 2$) not only a pair of triple nodes from corresponding primary graphs but also other nodes sharing the same Coxeter label. When this happens the diagonal element $A_{ii} = 2$ in the Cartan matrices is substituted by the matrix element $B_{ii} = 3$. The determinants of the non–affine Berger matrices (0,0,1,1,1)[3], (0,0,1,1,2)[4] and (0,0,1,2,3)[6] are equal to 3^4, 4^3 and 6^2 independently from the number of nodes along the internal line connecting two primary graphs (see Fig. 2 and table 3). Note that the labels of all the nodes along this line coincide with those of the central nodes of two connected primary graphs, i.e., they are equal to $3, 4$ and 6 respectively. Thus, these graphs produce three infinite series analogous to the graphs of the D_r–series generated by the extended reflexive number $(0, 0, 1, 1)$ in the $K3$ polyhedrons. In addition to the infinite series of the Dynkin graphs of A_r and D_r with maximal Coxeter numbers 1 and 2 there appear 3 new series with maximal Coxeter numbers $3, 4$ and 6. This construction of the infinite series of the Berger graphs for exceptional algebras could lead us to a possible generalization of the notion of the direct product for several Lie algebras, e.g., $E_8 \times E_8$ in the heterotic string.

The reflexive numbers can be generators of different Berger graphs obtained by the UCYA construction and probably should be placed in the same class. All new graphs contain inside them one or several initial graphs which are combined by various numbers of the A_i-lines. The result depends on the arity $2, 3...$ in UCYA and on the dimension of the constructed polyhedron. The reflexive polyhedra allow us to build huge classes of graphs, among

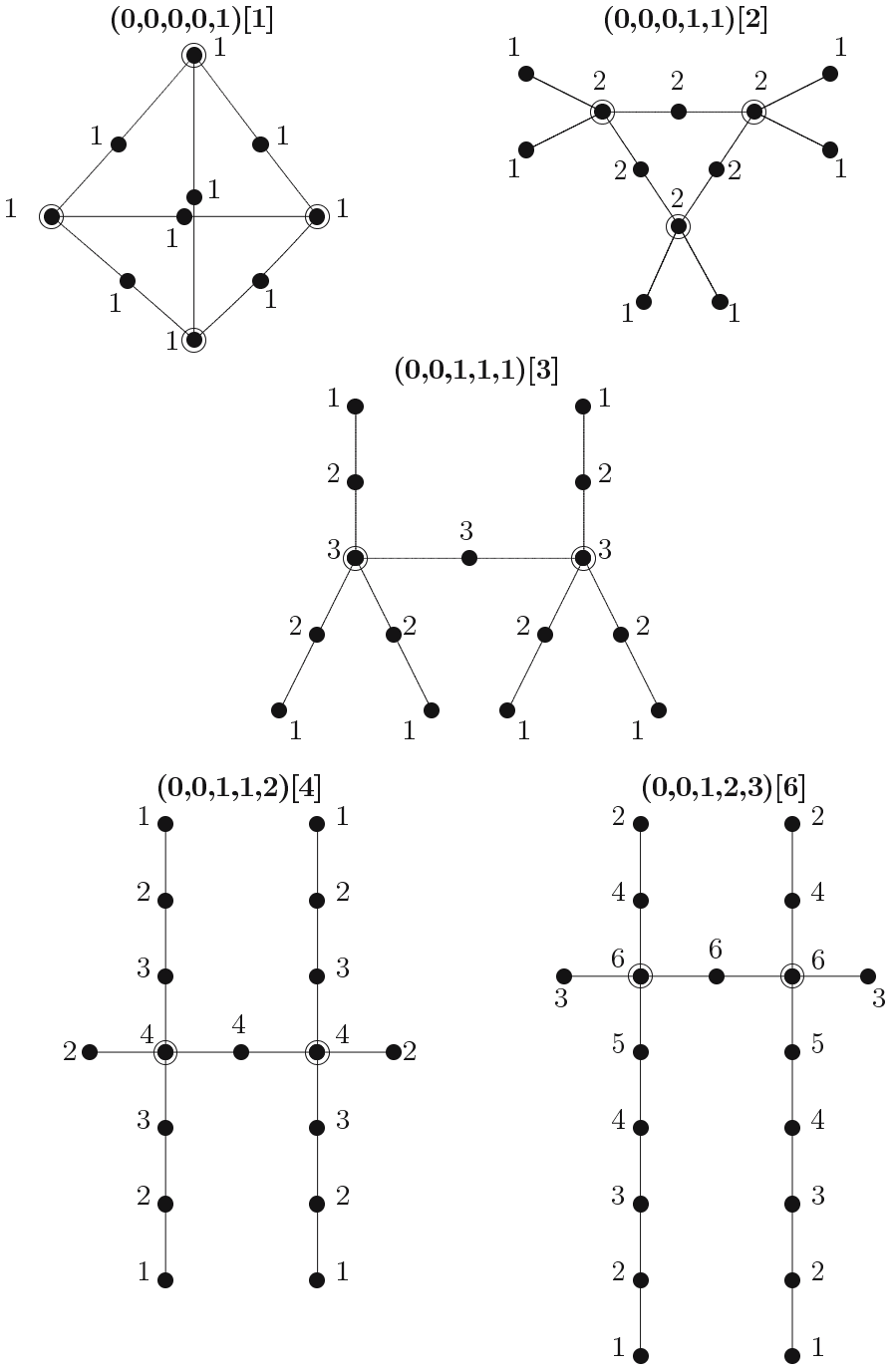

Fig. 2. Berger diagrams from a 2–arity construction in the $n = 5$ dimensional case, with the corresponding Coxeter labels at the nodes. They generate five infinite series.

which the set of usual Dynkin diagrams, related to the binary operations, is a small one, because the Dynkin diagrams and their affine generalizations are in one-to-one correspondence with finite Cartan–Lie algebras and infinite–dimensional Kac–Moody algebras, correspondingly. It was suggested in [15] that these new Berger graphs could lead to the algebras beyond the Cartan–Lie/Kac–Moody construction and, in particular, they could be related to ternary, quaternary, ... generalizations of binary algebras.

To extend the class of Dynkin diagrams it is natural to begin with a generalization of the rules for affine Cartan matrices. It was suggested in [15] that the corresponding Berger matrices should satisfy the following rules:

$$\begin{aligned} \mathbb{B}_{ii} &= 2, \text{ or } 3, \text{or } 4, ..., \\ \mathbb{B}_{ij} &\leq 0, \\ \mathbb{B}_{ij} = 0 &\mapsto \mathbb{B}_{ji} = 0, \\ \mathbb{B}_{ij} &\in \mathbb{Z}, \\ \text{Det } \mathbb{B} &= 0, \\ \text{Det } \mathbb{B}_{\{(i)\}} &> 0 \, . \end{aligned} \tag{93}$$

The constraint of a vanishing determinant for $\mathbb{B}$ is a generalization of the "affine condition" for Kac–Moody algebras. In these new rules in comparison with the usual affine Cartan case we relax the restriction on the diagonal element $\mathbb{B}_{ii} = 2$, i.e., to satisfy the affine condition we also allow for $\mathbb{B}_{ii}$ to be larger

$$\mathbb{B}_{ii} = 3, \, 4, \, \ldots \tag{94}$$

These new values $\mathbb{B}_{ii} = 3, \, 4, \, ...$ can appear in the lattice of reflexive polyhedra starting from CY_3, CY_4, ..., respectively. Below we shall check the coincidence of the graph's labels indicated on all figures with the Coxeter labels obtained from the eigenvalues of the Berger matrices. The proposed prescriptions for the Coxeter labels are universal for all Berger graphs independently from their dimension and arity construction. These prescriptions generalize the Cartan or Kac–Moody rules in a natural way. Note that the value of the diagonal term $\mathbb{A}_{ii}$ of the Cartan matrix can be related to one of the Casimir invariants of the simple Lie algebras. The number of these invariants is equal to the algebra rank. All Cartan–Lie algebras contain the Casimir operator of degree 2, but there are other invariant operators. For example, the exceptional E_6, E_7, E_8 algebras have the following degrees of Casimir invariants:

$$\begin{aligned} E_6 &: \{ \, 2, \, 5, \, 6, \, 8, \, 9, \, 12 \, \} \\ E_7 &: \{ \, 2, \, 6, \, 8, \, 10, \, 12, \, 14, \, 18 \, \} \\ E_8 &: \{ \, 2, \, 8, \, 12, \, 14, \, 18, \, 20, \, 24, \, 30 \, \} \, . \end{aligned} \tag{95}$$

By subtracting 1 from the Casimir operator degree we obtain the so–called "Coxeter exponents" of the corresponding Lie algebra. One can see that the

largest degrees of the Casimir invariants in this list, 12, 18 and 30, are equal to the Coxeter numbers of the E_6, E_7 and E_8 algebras, respectively. We should remark that the diagonal element of the Cartan matrices corresponding to each node on the (extended) Dynkin diagram is always equal to 2 and can be calculated through the Coxeter labels surrounding this node. Let us consider for example the A_r series. For each internal node N_i of the corresponding Dynkin diagram the value of the diagonal Cartan element A_{ii} satisfies the relation: $A_{ii} = (C_{i-1} + C_{i+1})/C_i = 2$, where all $C_{...} = 1$ are Coxeter labels of the nodes N_{i-1}, N_i, N_{i+1}. To generalize this argument to boundary nodes one should consider the extended Dynkin graph of the affine $A_r^{(1)}$ algebra. In this case all nodes are linked by lines with two neighbors. In the Dynkin graphs of the $D_r^{(1)}$ series apart from several nodes with two lines there are two nodes with three lines. The above relation between the Coxeter labels and the diagonal Cartan element can be easily checked for nodes with two and three lines. In particular, for a triple node N_i one obtains $A_{ii} = (C_{i+} + C_{i-1} + C_{i-})C_i = (1+2+1)/2 = 2$. For this rule to be also valid for a boundary node one can formally add an additional node with a vanishing Coxeter label. The above two examples show that the Coxeter labels 1 or 2 allow one to produce an infinite series of Dynkin diagrams. The larger values $A_{ii} \geq 3$ for triple nodes are be allowed only for some special values of the algebra rank, as we can see in the cases of E_6, E_7, E_8 algebras.

The extended reflexive number $(0, 0, 0, 0, 1)$ is the origin of the infinite series of Berger graphs with a multi–cycle topology. One can compare them with the Kac–Moody case of the $A_r^{(1)}$ infinite series where the graphs have only one cycle. The simplest example of multi–cycle topology corresponds to the tetrahedron Berger graph having 4 closed cycles with the corresponding 4×4 matrix:

$$B_3^{(1)}(00001) = \begin{pmatrix} 3 & -1 & -1 & -1 \\ -1 & 3 & -1 & -1 \\ -1 & -1 & 3 & -1 \\ -1 & -1 & -1 & 3 \end{pmatrix}$$

This matrix has the eigenvalues $\{0, 4, 4, 4\}$ for the corresponding eigenvectors $(1, 1, 1, 1)$, $(-1, 0, 0, 1)$, $(-1, 0, 1, 0)$, $(-1, 1, 0, 0)$.

The Coxeter labels are given by the zero eigenvector $\{\, 1,\ 1,\ 1,\ 1 \,\}$, which provides the well–known relation for the highest root (affine condition):

$$1 \cdot \alpha_0 + 1 \cdot \alpha_1 + 1 \cdot \alpha_2 + 1 \cdot \alpha_3 = 0 \,, \tag{96}$$

where α_i, $i = 1, 2, 3$ are the simple roots and $-\alpha_0$ is equal to the highest root α_h. For the non–affine case one should remove one node from the Berger graph. Thus the relation between the affine and non–affine Berger graphs is similar to the relation between the Cartan–Lie and Kac–Moody graphs. In the last case the Cartan–Lie algebra produces the so–called horizontal algebra of Kac–Moody algebra where the highest root participates in the construction of the additional simple root, more exactly, $-\alpha_h$.

Such non–affine Berger matrix is positive–defined and Det $B_3^{(1)}(00001) = 16$. The affine condition and the positive definiteness of the non–affine Berger matrix do not depend on the number of internal nodes with $B_{ii} = 2$.

As an example, the non–affine Berger matrix after its inversion offers the possibility to construct three $\mathbb{Z}_3$–symmetric fundamental weights:

$$\Lambda_1 = \left\{ \frac{1}{2}, \frac{1}{4}, \frac{1}{4} \right\}, \Lambda_2 = \left\{ \frac{1}{4}, \frac{1}{2}, \frac{1}{4} \right\}, \Lambda_3 = \left\{ \frac{1}{4}, \frac{1}{4}, \frac{1}{2} \right\}. \tag{97}$$

Note that in the Cartan–Lie A_r algebras there are two elementary fundamental representations, but in the Berger case we already have three elementary fundamental "representations". In our example one obtains the $\mathbb{Z}_3$ symmetry acting on the space of the fundamental representations. This new invariance could have interesting applications for the solution of the family generation problem.

A second example is related to the generalization of the D_r–infinite series of the Cartan–Lie Dynkin graphs. From our point of view the B(011) graph is exceptional. The graphs B(0011) in the K3 2–arity polyhedra produce an infinite series of D_r–Cartan–Lie Dynkin graphs. They are built from two $(1,1)[2]$ blocks connected by a segment with l–internal nodes having $B_{ii} = 2$ and Coxeter label 2. The Berger graphs B(00011) could have three blocks $(1,1)[2]$. Each two of them are connected by a line with the nodes having $B_{ii} = 2$ and the Coxeter labels equal to 2. We illustrate this by the following Berger matrix:

$$B_8^{(1)}(00011) = \begin{pmatrix} 2 & 0 & -1 & 0 & 0 & 0 & 0 & 0 & 0 \\ 0 & 2 & -1 & 0 & 0 & 0 & 0 & 0 & 0 \\ -1 & -1 & 3 & 0 & 0 & -1 & 0 & 0 & -1 \\ 0 & 0 & 0 & 2 & 0 & -1 & 0 & 0 & 0 \\ 0 & 0 & 0 & 0 & 2 & -1 & 0 & 0 & 0 \\ 0 & 0 & -1 & -1 & -1 & 3 & 0 & 0 & -1 \\ 0 & 0 & 0 & 0 & 0 & 0 & 2 & 0 & -1 \\ 0 & 0 & 0 & 0 & 0 & 0 & 0 & 2 & -1 \\ 0 & 0 & -1 & 0 & 0 & -1 & -1 & -1 & 3 \end{pmatrix}$$

For simplicity we did not include any of the internal nodes. The eigenvalues of this matrix are $\{0, 2, 2, 2, 3, 3-\sqrt{3}, 3-\sqrt{3}, 3+\sqrt{3}, 3+\sqrt{3}\}$ and the eigenvector with the vanishing eigenvalue is $\{1, 1, 2, 1, 1, 2, 1, 1, 2\}$.

To study the infinite $B(00011)$ series let us recall the usual $D_r^{(1)}$ Dynkin graphs which are described by the $B(0011)$ graphs in the $K3$ polyhedra. As an example we consider the diagram $D_8^{(1)} = B_8^{(1)}(0011)$ with three internal nodes:

$$B_8^{(1)}(0011) = \begin{pmatrix} 2 & 0 & -1 & 0 & 0 & 0 & 0 & 0 & 0 \\ 0 & 2 & -1 & 0 & 0 & 0 & 0 & 0 & 0 \\ -1 & -1 & 2 & -1 & 0 & 0 & 0 & 0 & 0 \\ 0 & 0 & -1 & 2 & -1 & 0 & 0 & 0 & 0 \\ 0 & 0 & 0 & -1 & 2 & -1 & 0 & 0 & 0 \\ 0 & 0 & 0 & 0 & -1 & 2 & -1 & 0 & 0 \\ 0 & 0 & 0 & 0 & 0 & -1 & 2 & -1 & -1 \\ 0 & 0 & 0 & 0 & 0 & 0 & -1 & 2 & 0 \\ 0 & 0 & 0 & 0 & 0 & 0 & -1 & 0 & 2 \end{pmatrix}$$

The determinant of this matrix is equal to zero. The affine condition can be written in this form:

$$1 \cdot \alpha_0 + 1 \cdot \alpha_1 + 2 \cdot \alpha_2 + 2 \cdot \sum_{i=3}^{i=5} \alpha_i + 2 \cdot \alpha_6 + 1 \cdot \alpha_7 + 1 \cdot \alpha_8 \ = \ 0, \qquad (98)$$

where $-\alpha_0$ is equal to the highest root of the D_8 Cartan–Lie algebra.

This condition relates the $D_8^{(1)}$ Kac–Moody algebra to the non–affine case of the Cartan–Lie D_8 algebra. One can construct the Cartan matrix corresponding to this algebra

$$B_8(0011) = \begin{pmatrix} 2 & -1 & 0 & 0 & 0 & 0 & 0 & 0 \\ -1 & 2 & -1 & 0 & 0 & 0 & 0 & 0 \\ 0 & -1 & 2 & -1 & 0 & 0 & 0 & 0 \\ 0 & 0 & -1 & 2 & -1 & 0 & 0 & 0 \\ 0 & 0 & 0 & -1 & 2 & -1 & 0 & 0 \\ 0 & 0 & 0 & 0 & -1 & 2 & -1 & -1 \\ 0 & 0 & 0 & 0 & 0 & -1 & 2 & 0 \\ 0 & 0 & 0 & 0 & 0 & -1 & 0 & 2 \end{pmatrix}$$

The determinant of this matrix is equal to 4 independently of the internal nodes. The determinant of the non–affine Berger matrix Det $B(00011)$ in the above example is equal to 48 and depends on the internal nodes.

The $B(0011)$ graphs help us understand the structure of the Berger graphs determined by $B(00111)$, $B(00112)$, $B(00123)$ in CY_3 reflexive polyhedra of 2–arity. In the case of $K3$ the $B(0111)$ graph generates a unique exceptional $E_6^{(1)}$ graph. In the higher dimension $n = 5$ we obtain the graph from an infinite series, constructed from two $E_6^{(1)}$ blocks in which we should change two nodes $A_{ii} = 2 \rightarrow B_{ii} = 3$.

To obtain the non–affine Berger graph, i.e. the analog of the Cartan–Lie case, one should remove one root with the Coxeter label equal to one. This means that the simple roots α_i on the Berger graph define the highest root $\alpha_h = -\alpha_0$ (the affine condition), i.e.,

$$\alpha_0 + \sum_i C_i \cdot \alpha_i = 0 \ , \qquad (99)$$

where C_i are the Coxeter labels.

In the non–affine case one can check that the determinant of the Berger matrix is equal to 81, a value which does not depend on the number l of the internal nodes. Also, all principal minors are positive–defined in a similar way to the Cartan–Lie case. In a complete analogy with the Cartan case the Berger non–affine graph also defines the fundamental weights [15, 16, 17]

The Dynkin diagrams for the Cartan–Lie/Kac–Moody algebras can have the nodes with the maximal number of edges equal to 3. For example, let us take the $E_6^{(1)}$,$E_7^{(1)}$, $E_8^{(1)}$ graphs and consider the vertex–nodes having three edges and having the Coxeter labels equal to 3, 4 and 6, respectively. It is known that in the case of the Cartan–Lie algebras the number of Casimir

invariants coincides with the algebra rank. The r-degrees of these Casimir take values from 2 up to the maximum equal to the Coxeter number. The important cases correspond to the degrees of invariants for the three above–mentioned algebras equal to the following sums: $\mathrm{Cas}_i = C_{i-1} + C_{i+} + C_{i-} = 2 + 2 + 2 = 6$, Cas$= 3 + 3 + 2 = 8$, Cas$= 5 + 4 + 3 = 12$, respectively. The diagonal elements of the Cartan matrices for the nodes in these cases are equal to $A_{ii} = \mathrm{Cas}/C_{ii} = 6/3 = 2$, $A_{ii} = \mathrm{Cas}/C_{ii} = 8/4 = 2$, $A_{ii} = \mathrm{Cas}/C_{ii} = 12/6 = 2$.

The relation between the Coxeter labels and B_{ii} is also valid for all nodes with 2, 3, 4,... edges. Here the diagonal elements of the Berger matrix are $B_{ii} = 3, 4, \ldots$.

The extension of the $A_r^{(1)}$ series for the $B_{ii} = 3$ case gives a new infinite series $B(00001)$ in which for all triple nodes N_i we have $B_{ii} = (C_{i-1} + C_{i+} + C_{i-})/C_i = 3$, where all $C_{\ldots} = 1$. Hence one can get the infinite series of graphs both for the Cartan nodes $A_{ii} = 2$ and for the Berger nodes with $B_{ii} = 3$. Note that all Coxeter labels for the Berger graphs $B(0 \ldots 01)$ are equal to 1.

A similar extension of the $D_r^{(1)}$ series is $B(00011)$, where apart from the Cartan nodes $A_{ii} = 2$ there appear two nodes $B_{ii} = 3$ with 4 edges. Here one has $B_{ii} = (C_{i-1} + C_{i+1} + C_{i+} + C_{i-})/C_i = (2 + 2 + 1 + 1)/2 = 3$. Note that for the Berger graphs the maximal Coxeter label is equal to 2. Therefore for all Berger graphs we have only two possibilities for Coxeter labels, 1 or 2. In the Cartan–Lie case one obtains just two infinite series of simply–laced Dynkin diagrams, with the maximal Coxeter labels equal to 1 and 2. For other examples of simply–laced Cartan–Lie algebras their maximal values are 3, 4 and 6. This is related to the fact that the corresponding algebras are exceptional.

Apart from the five types of infinite series, which can be interpreted as generalizations of the corresponding Cartan–Lie simply–laced graphs, we also found 14 exceptional completely new graphs (see Fig. 3) which correspond to 14 simply–laced numbers inside the 95 K_3 reflexive numbers as shown in Table 3.

As it was mentioned above, the affine graphs have symmetric Berger matrices with their determinant equal to zero, which correspond to the Kac–Moody type of infinite-dimensional algebras. Removing one node with a minimal Coxeter label we can obtain the non–affine graph generalizing the Cartan–Lie case. For the corresponding Berger matrix the determinant is positive–defined and all principal minors are also positive, see Table 3.

We see that for the Berger graphs one can build the infinite series with the maximal Coxeter labels 3, 4, 6 due to the presence of new nodes with $B_{ii} = 3$. These new nodes lead to the appearance of 14 exceptional simply-laced Berger graphs with their maximal Coxeter labels: 4, 6, ..., 42. When we introduce the new nodes $B_{ii} = 4$ these 14 exceptional cases produce new 14 infinite series of Berger graphs. This could be a key point to understand the nature of exceptional algebras in Cartan–Lie and Berger algebras.

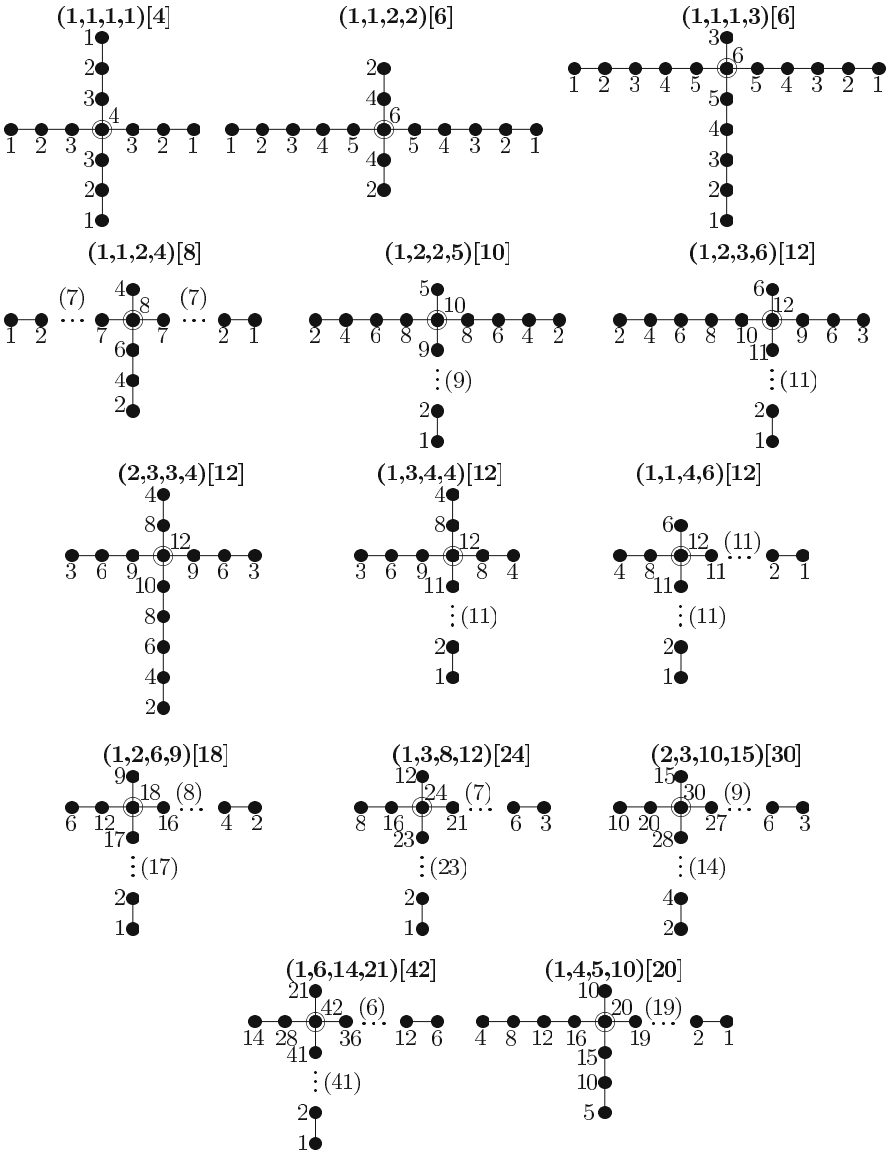

Fig. 3. 14 exceptional new Berger diagrams with the Coxeter labels at the nodes.

Table 3. In this table we give the Rank, the Coxeter number h (equal to the sum of the Coxeter labels for the affine Berger graphs), the Casimir depending on B_{ii} (equal to the sums of all Coxeter labels for the nodes in the nearest circle around the node $B_{ii} = 3$) and the determinants for the non–affine exceptional Berger graphs. The maximal Coxeter labels for these graphs coincides with the degree of the corresponding reflexive simply–laced vector. The determinants in the last column for the infinite series (0,0,1,1,1)[3], (0,0,1,1,2)[4] and (0,0,1,2,3)[6] are independent from the number l of internal binary $B_{ii} = 2$ nodes. The numbers 1_3 and 2_3 denote the number of nodes with $B_{ii} = 3$.

$\boldsymbol{k}^{\rm ext}_{3,4}$	Rank	h	Casimir(B_{ii})	Determinant
$(0,1,1,1)$[3]	$6(E_6)$	12	6	3
$(0,1,1,2)$[4]	$7(E_7)$	18	8	2
$(0,1,2,3)$[6]	$8(E_8)$	30	12	1
$(0,0,1,1,1)$[3]	2_3+10+l	$18+3(l+1)$	9	3^4
$(0,0,1,1,2)$[4]	2_3+13+l	$32+4(l+1)$	12	4^3
$(0,0,1,2,3)$[6]	2_3+15l	$60+6(l-1)$	18	6^2
$(0,1,1,1,1)$[4]	1_3+11	28	12	16
$(0,2,3,3,4)$[12]	1_3+12	90	36	8
$(0,1,1,2,2)$[6]	1_3+13	48	18	9
$(0,1,1,1,3)$[6]	1_3+15	54	18	12
$(0,1,1,2,4)$[8]	1_3+17	80	24	8
$(0,1,2,2,5)$[10]	1_3+17	100	30	5
$(0,1,3,4,4)$[12]	1_3+17	120	36	3
$(0,1,2,3,6)$[12]	1_3+19	132	36	6
$(0,1,4,5,10)$[20]	1_3+26	290	60	2
$(0,1,1,4,6)$[12]	1_3+24	162	36	6
$(0,1,2,6,9)$[18]	1_3+27	270	54	3
$(0,1,3,8,12)$[24]	1_3+32	420	72	2
$(0,2,3,10,15)$[30]	1_3+25	420	90	4
$(0,1,6,14,21)$[42]	1_3+49	1092	126	1

The Cartan graphs of dimension 1, 2, 3 are well known and correspond to the classical Cartan–Lie algebras. The main purpose of this paper was to enlarge their list with graphs generated by the reflexive weight vectors of dimension four (corresponding to CY_3). In this dimension, corresponding to $K3$–sliced CY_3 spaces, we have singled out the following 14 reflexive weight vectors from the total of 95 $K3$–vectors (1,1,1,1)[4], (1,1,2,2)[6], (1,1,1,3)[6], (1,1,2,4)[8], (2,3,3,4)[12], (1,3,4,4)[12], (1,2,3,6)[12], (1,2,2,5)[10], (1,4,5,10)[20] 1,1,4,6)[12], (1,2,6,9)[18], (1,3,8,12)[24], (2,3,10,15)[30], (1,6, 14,21)[42]. The Coxeter labels for the nodes in the Berger graphs were

assigned consistently from the geometrical and algebraic points of view. These Berger matrices have simple properties: they are symmetric and affine. In addition, each of these graphs and matrices is not "extendible", i.e. other graphs and Berger matrices cannot be obtained from them by adding more nodes to any of the legs. In this sense these graphs are "exceptional". Similarly to classical non–exceptional graphs, one can construct infinite series containing them. Apparently these fourteen vectors are the only set of vectors with symmetric Berger matrices among the total 95 reflexive vectors.

4 Conclusions

In this paper we continued the study of the graphs firstly obtained from $CY_{3,4,...}$ reflexive polyhedra. The important correspondence between $CY_{3,4}$ spaces and reflexive polyhedra was discovered several years ago by Batyrev [4]. In previous works we found a very intriguing relation between reflexive vectors and Dynkin [8] and Berger graphs [15] with dimensions $n = 4$ and $n = 5, 6, ...$, respectively. It was shown, with the use of the Universal Calabi–Yau Algebra (UCYA) and the arity construction, that the structure of the reflexive polyhedra can be completely understood in terms of the Berger graphs [15, 16, 17]. For the Calabi–Yau spaces of the level one in any dimension, $CY_{2,3,4,..}$, the Dynkin diagrams belong to a small subclass of a huge amount of Berger graphs. To understand and develop this interesting result we concentrated here on the study of the structure of the reflexive vectors [8, 18]. In particular, we studied the properties of the reflexive numbers and their relation to number theory [18]. A very interesting subclass of them corresponds to the simply–laced reflexive numbers which are related to the so–called "Egyptian fractions" [19]. As a first step of generalization we considered the quasi–simply–laced vectors [18]. They satisfy the reflexivity constraint. The classes of the simply–laced numbers were shown to be in correspondence with certain Feynman diagrams [18]. We studied the structure of the simply–laced and quasi–simply–laced reflexive vectors, their relation to the structure of the Berger graphs, the asymptotics of their number at large dimensions n, and the link with UCYA. It was demonstrated that the simply–laced reflexive numbers are generators of the n–dimensional Berger graphs [18].

Summing up the above discussion, we conclude that one can construct not only diagrams for the non-affine Berger (Det $B > 0$) and affine Berger (Det $B = 0$, Det $B_i > 0$) algebras, but also from the generalized Berger graphs it is possible to obtain some information about the roots and weights for extended algebraic structures. In particular these graphs allow one to generalize the known simply–laced series A_r and D_r and exceptional simply–laced algebras $E_{6,7,8}$ and $E^{(1)}_{6,7,8}$. The Berger matrices for the new simply–laced graphs in dimensions $n = 4, 5, ...$ share a number of properties with the Cartan matrices in dimensions $n = 1, 2, 3$.

Table 4. Evolution of Geometry, Algebras and Symmetries: Towards New Symmetries using Berger graphs.

SEARCH FOR NEW SYMMETRIES				
	Known Results		New Results and Project	
Algebra	Cartan–Lie Standard Model (SM)	Kac–Moody String Theory (ST)	Non–Affine Berger Inside SM?	Affine Berger Beyond ST?
	⇕	⇕	⇕	⇕
Simple–Root Graphs	Dynkin Graphs	Affine Dynkin Graphs	Berger Graphs	Affine Berger Graphs
	⇕	⇕	⇕	⇕
Geometry	Regular Polyhedra (G) – – – – – Klein–Du Val $\mathcal{C}^2/G$ Sings $G \subset$ SU(2)	K3–Refl. Polyhedra (G) – – – – – ADE–Sings. (K3) SU(2) Holonomy Group	? – – – – – $\mathcal{C}^3/G$ Sings.? $G \subset$ SU(3)	CY_3 Refl. Polyhedra (G)? – – – – – K3 Sings. (CY_3)? SU(3) Holonomy Group

The interest in the construction of new algebraic structures beyond the Lie algebras started from the investigation of $SU(2)$–conformal field theories [21, 22]. One can expect that geometrical concepts, in particular, algebraic geometry, are a natural and promising way to discover new algebras. Historically the marriage of algebra and geometry was useful for these both fields of mathematics. In particular, to prove mirror symmetry of Calabi–Yau spaces the powerful techniques of the Newton reflexive polyhedra was used. Further, the ADE–type singularities [23, 24] in $K3 = \mathrm{CY}_2$ spaces [12, 13] and their resolution were related to the Dynkin diagrams for the Cartan–Lie algebra. We formulate these relations in the following way (see Table 4):

1. The algebraic origin of Cartan–Lie algebras is the Torus and $SU(2)/U(1)$.
2. The geometrical origin of the Cartan–Lie algebras is S^1 and $CP^1 \cong S^2$.

One can continue this correspondence to the Berger graphs (see Table 4):

1. The algebraic origin of the Berger graphs is the Torus and $SU(3)/SU(2) \times U(1)$.

2. The geometrical origin of Berger algebras is S^1 and CP^2?

Another interesting possibility to understand the structure of the Berger graphs is connected with the resolution of the quotient singularities. Calabi–Yau spaces are defined by their holonomy groups [1, 25, 26]. Typical quotient singularities C^n/G are characterized by the list of finite subgroups $G \subset H$ of the holonomy groups, $H = SU(2), SU(3), ...$ For the case of the $SU(2)$ holonomy group there are five well–known Klein–Du–Val singularities of A–D–E type [23, 24]. And the crepent resolution of A–D–E–types singularities in $K3$ gives us the corresponding Dynkin diagrams in the $K3$ polyhedra. So it is natural to find the Berger graphs in CY_3 polyhedra through the resolution of the C^3/G quotient singularities, where G are finite subgroups of $SU(3)$. Although this problem is under study we can briefly mention that the first five finite subgroups are isomorphic to the five subgroups of $SU(2)$ and one can assume that they could be the origin of our five Berger graphs $B(00001), B(00011), B(00111), B(00112), B(00123)$ discussed above. To clarify this discussion one can look at the Table 4.

It is possible to imagine that the Berger graphs could be linked to the existence of new algebras which could be realized in quadratic matrices. The main question at this point is how to unify in one single approach Cartan–Lie algebras and new hypothetical algebras.

The search of new symmetries in the theories describing the interaction of elementary particles is traditional. Especially important are gauge symmetries of the Standard Model $SU(3) \times SU(2) \times U(1)$ and the symmetries used in Cosmology. But there could be hidden symmetries which may lead to the integrability of the theory in some special cases. As an example, the equations describing the high energy behaviour of scattering amplitudes in multi-colour QCD are integrable [27], this being related to the hidden Virasoro and dual symmetries [28].

Calabi-Yau spaces can contain also some hidden ("dark") symmetries, which can be used for the explanations of the parameters of SM, for the construction of more general models of elementary particles and for solving the problem of dark matter in Cosmology..

Acknowledgments

We are grateful to Ugo Aglietti, Enrique Álvarez, Luis Álvarez–Gaumé, Ignatios Antoniadis, Patrick Aurenche, Jochen Bartels, Geneviève Bélanger, John Ellis, Belén Gavela, George Girardi, César Gómez, Richard Kerner, Paul Sorba, Emilio Torrente-Lujan and Jean–Bernard Zuber for support and helpful discussions. We also would like to thank the Laboratoire d'Annecy–Le–Vieux de Physique Théorique (LAPTH), DESY Theory Group, II. Institut für Theoretische Physik at the University of Hamburg, CERN Theory Division, Instituto de Física Teórica UAM/CSIC and Departamento de Física

Teórica at the Universidad Autónoma de Madrid, Laboratoire de Physique Théorique et Hautes Energies (LPTHE) and Petersburg Nuclear Physics Institute for their hospitality. This work was supported by the Alexander von Humboldt Foundation and by INTAS and RFBR grant 04-02-17094, RSGSS-1124.2003.2.

References

1. M. Berger, *Sur les groupes d'holonomie des varietés a connexion affine et des variétés riemannienes*, Bull. Soc. Math. France **83**, (1955), 279–310.
2. E. Calabi, *On Kahler Manifolds with Vanishing Canonical Class*, in *Algebraic Geometry and Topology*, A Symposium in Honor of S. Lefshetz, 1955 (Princeton University Press, Princeton, NJ (1957)).
3. S.–T. Yau, *Calabi's Conjecture and Some New Results in Algebraic Geometry*, Proc. Nat. Acad. Sci. **74** (1977), 1798.
4. V. Batyrev, *Dual Polyhedra and Mirror Symmetry for Calabi–Yau Hypersurfaces in Toric Varieties*, *J. Algebraic Geom.* **3** (1994) 493.
5. M. Kreuzer and H. Skarke, *Reflexive Polyhedra, Weights and Toric Calabi-Yau Fibrations*, HUB-EP-00/03, TUW-00/01, math.AG/0001106, Rev. Mat. Phys. 14 (2002) 343–374.
6. M. Kreuze and H. Skarke, *Complete classification of reflexive polyhedra in four dimensions* , hep–th/0002240, Adv. Theor. Math. Phys. 4 (2002) 1209–1230; *Reflexive polyhedra, weights and toric Calabi–Yau fibrations*, math.AG/0001106, Rev. Math. Phys. 14 (2002) 343–374.
7. L. N. Lipatov, A. Sabio Vera, V. N. Velizhanin and G. G. Volkov, hep-th/0501101.
8. F. Anselmo, J. Ellis, D. V. Nanopoulos and G. G. Volkov, *Towards an Algebraic Classification of Calabi-Yau Manifolds I: Study of K3 Spaces*, Phys. Part. Nucl. **32** (2001) 318–375 [Fiz. Elem. Chast. Atom. Yadra **32** (2001) 605–698] [arXiv:hep-th/0002102].
9. F. Anselmo, J. Ellis, D. V. Nanopoulos and G. G. Volkov, *Results from an Algebraic Classification of Calabi–Yau Manifolds*, Phys. Lett. B **499** (2001) 187–199 [arXiv:hep-th/0007115].
10. F. Anselmo, J. Ellis, D. V. Nanopoulos and G. G. Volkov, *Universal Calabi–Yau Algebra: Towards an Unification of Complex Geometry*, Int. J. Mod. Phys. A **18** (2003) 5541–5612 [arXiv:hep-th/0207188].
11. F. Anselmo, J. Ellis, D. V. Nanopoulos and G. G. Volkov, *Universal Calabi–Yau algebra: Classification and enumeration of Fibrations*, Mod. Phys. Lett. A **18** (2003) 699–710 [arXiv:hep-th/0212272].
12. P. Candelas and A. Font, *Duality Between the Webs of Heterotic and Type II Vacua*, Nucl. Phys. **B511** (1998) 295.
13. M. Bershadsky, K. Intriligator, S. Kachru, D.R. Morrison, V. Sadov, and C. Vafa, *Geometric Singularities and Enhanced Gauge Symmetries*, Nucl. Phys. **B481** (1996) 215.
14. E. Perevalov and H. Skarke, *Enhanced Gauge Symmetry in Type II and F–Theory Compactifications: Dynkin Diagrams from Polyhedra*, Nucl. Phys. **B505** (1997) 679.

15. G. G. Volkov, *Hunting for the new symmetries in Calabi–Yau jungles*, Int. J. Mod. Phys. A **19** (2004) 4835 [arXiv:hep-th/0402042].
16. E. Torrente–Lujan and G. G. Volkov, *Root Systems from Toric Calabi-Yau Geometry: Towards new Algebraic Structures and Symmetries in Physics?*, hep-th/0406035.
17. J. Ellis, E. Torrente–Lujan and G. G. Volkov, *The Classification of the Simply Laced Berger Graphs from Calabi–Yau CY_3 spaces*, hep-th/0806035.
18. L. Lipatov, A. Sabio-Vera, V.Velizhanin and G. G. Volkov, *Reflexive Numbers and Berger Graphs from Calabi-Yau Spaces*, To be published [arXiv:hep-th/0501101].
19. R. K. Guy, *Unsolved Problems in Number Theory, D11* Springer (1994), 44–139,
http://www.research.att.com/projects/OEIS?Anum=A002966
Egyptian fractions: 1, 1, 3, 14, 147, 3462, 294314, 159330691.
20. F. Bergeron, G. Labelle and P. Leroux, *Combinatorial Species and Tree–Like Structures*, Cambridge (1998), 41–209,
http://www.research.att.com/projects/OEIS?Anum=A001372
Sequence: 1, 1, 3, 7, 19, 47, 130, 343, 951, 2615, 7318, 20491, 57903, 163898, 466199, 1328993, 3799624, 10884049, 31241170, 89814958, 258604642, 745568756, 2152118306, 6218869389, 17988233052, 52078309200, 150899223268, 437571896993.
21. A. Capelli, C. Itzykson and J.-B. Zuber, *The ADE classification of Minimal and $A_1^{(1)}$ Conformal Invariant Theories*, Commun. Math. Phys.**184** (1987), 1-26, MR **89 b**, 81178.
22. P. Di-Francesco and J.-B. Zuber, *SU(N) Lattice Integrable Models Associated with Graphs*, Nucl.Phys. **B 338** (1990), 602-646.
23. F. Klein, *The Icosahedron and the Solution of Equations of Fifth Degree*, Dover, New York, 1956.
24. P. Du Val, *Homographies, Quaternions and Rotations* (Clarendon Press, Oxford (1964)).
25. A. Beauville, *Riemannian Holonomy and Algebraic Geometry*, math.AG/9902110.
26. R. Bryant *Recent advances in the theory of holonomy*, math.DG/9910059, Seminaire Bourbaki, Volume 1998/99, Asterisque 266 (2000), 351–374.
27. Lipatov L.N. *High energy asymptotics of multi-colour QCD and exactly solvable lattice models*, Padova preprint DFPD/93/TH, hep-th/9311037, unpublished.
28. Lipatov L.N. Nucl.Phys. **B548** (1999) 328. duality symmetry of reggeon interactions in multicolour qcd

List of Participants

Elena Accomando
Dipartimento di Fisica Teorica
Universita di Torino
ITALY
Email: accomand@infn.it

Roland E. Allen
Department of Physics
Texas A&M University
College Station
Texas 77843-4242
USA
Tel: 1-979-845-4341
Fax: 1-979-845-2590
Email: allen@tamu.edu

Elena Aprile
Columbia University
Physics Department
550W 120th St
New York, NY 10027
USA
Tel: 212-854-3258
Fax: 212-854-8121
Email: age@astro.columbia.edu

Richard Arnowitt
Department of Physics
Center for Theoretical Physics
Texas A&M University
College Station, TX 77843-4242
USA
Tel: (979) 845-7746
Fax: (979) 845-2590
Email: arnowitt@physics.tamu.edu

Howard Baer
Dep't of Physics
Florida State University
Tallahassee
FL 32306, USA
Tel: 850-644-3523
Email: baer@hep.fsu.edu

Charles L. Bennett
Department of Physics & Astronomy
The Johns Hopkins University
3400 North Charles Street
Baltimore, MD 21218, USA
Tel: (410) 516-6177
Email: (410) 516-7239

Piero Belli
INFN sez. ROMA c/o Dip. di Fisica
Universita' di Roma "La Sapienza"
p.le A. Moro, 2, 00185 Roma
ITALY
Tel: +39-06/49914335
Fax: +39-06/49914335
Email: Rita.Bernabei@roma2.infn.it

Alain Blanchard
LATT, Observatoire Midi-Pyrenees
14, Avenue Edouard Belin
31400 Toulouse
FRANCE
Tel: 33 (5) 61 33 28 42 (intern.)
Fax: 05 61 33 28 40
Email: alain.blanchard@ast.obs-mip.fr

Wim de Boer
Universität Karlsruhe
Inst. für Exp. Kernphysik
Physikhochhaus
Postfach 6980
D-76128 Karlsruhe
GERMANY
Tel: +49 (721) 608 3593
Tel: +41 22 767 3529
+49 (721) 608 7930
Email: wim.de.boer@cern.ch

Paul Louis Brink
Physics Department
Varian Physics Bldg
382 Via Pueblo Mall
Stanford, CA 94305-4060, USA
Tel: 001 650 725-9304
Email: pbrink@stanford.edu

Riccardo Cerulli
Laboratori Nazionali del Gran Sasso
S.S. 17 BIS km. 18.910
I-67010 Assergi L'Aquila
ITALY
Tel: +39 0862 437296
Fax: +39 06 72594825
Email: riccardo.cerulli@lngs.infn.it

David Cline
Astrophysics Division
Department of Physics & Astronomy
University of California
Los Angeles, CA 90095
USA
Tel: 310 825-1673
Fax: 310-206-1091
Email: dcline@physics.ucla.edu

Silvia Costantini
Dipartimento di Fisica
gruppo CMS
Universita' di Roma "La Sapienza"
Piazzale Aldo Moro 2
I-00185 Roma
ITALY
Tel: +39-06-4451642
Fax: +39-06-4453829
Email: Silvia.Costantini@cern.ch
Email: silvia.costantini@roma1.infn.it

Prisca Cushman
Physics Department
University of Minnesota
116 Church St. SE
Minneapolis, MN 55455
USA
Email: prisca@physics.umn.edu

Dore, Olivier
Dpt of Astrophysical Sciences
Princeton University
Princeton, NJ08540
USA
Tel: 609 258 3809
Email: olivier@astro.princeton.edu

Jerome Drexler
25440 Becky Lane
Los Altos Hills, CA 94022-4520
USA
Email: drexlerastro@aol.com

Bhaskar Dutta
Department of Physics
University of Regina
Regina, Saskatchewan S4S 0A2
CANADA
Tel: 306 585 5384
Fax: 306 585 5659
Email: dut-tabh@yogi.phys.uregina.ca

Andreas Eckart
I Physikalisches Institute
Zülpicher Str. 77
Köln, 50937
GERMANY
Tel: +49 221/470-3546
Fax: +49 221/470-5162
Email: eckart@ph1.uni-koeln.de

Ryoji Enomoto
5-1-5 Kashiwa-no-ha, Kashiwa-city
Chiba 277-8582
JAPAN
Tel: +81-4-7136-5116
Fax: +81-4-7136-3133
Email: enomoto@icrr.u-tokyo.ac.jp

Nicolao Fornengo
Department of Theoretical Physics
University of Torino
and INFN - Torino
via P. Giuria 1
I-10125 Torino
ITALY
Tel: +39 011 670 7243
Fax: +39 011 670 7214
Email: fornengo@to.infn.it

Wendy Freedman
Carnegie Observatories
813 Santa Barbara St.
Pasadena, CA 91101
USA
Tel: 626-304-0204
Fax: 626-304-0266
Email: wendy@ociw.edu

Burkhard Fuchs
Astronomisches Rechen-Institut
Mönchhofstrasse 12-14
D-69120 Heidelberg
GERMANY
Tel: +49-06221 405-126
Fax: +49-06221 405-297
Email: fuchs@ari.uni-heidelberg.de

Paolo Gondolo
Department of Physics
University of Utah
115 S 1400 E Rm 201
Salt Lake City
UT 84112-0830, USA
Tel: 801-581-7788
Fax: 801-581-6256
Email: paolo@physics.utah.edu

Patrick Greene
Department of Physics and Astronomy
University of Texas at San Antonio
San Antonio, TX 78249
USA
Email: patrick.greene@utsa.edu

Kim Griest
Physics Department 0319
University of California, San Diego
La Jolla, CA 92093
USA
Tel: 858-534-0924
Fax: 858-534-0173
Email: kgriest@ucsd.edu

Jihn E. Kim
Seoul National University
School of Physics
Seoul National University
Seoul 151-747
KOREA
Tel: +82 2 880 6605
Fax: +82 2 884 7167
Email: jekim@phyp.snu.ac.kr

Hans Volker Klapdor-Kleingrothaus
Max-Planck-Institut für Kernphysik
Saupfercheckweg 1
D-69117 Heidelberg
GERMANY
Tel: +49-(0)6221-516-262
Fax: +49-(0)6221-516-540
Email: H.Klapdor@mpi-hd.mpg.de

Vitaly V. Kocharovsky
Department of Physics
Texas A&M University
College Station, TX 77843-4242
USA
Tel: (979) 862-1652 or (979) 845-2012
Fax: (979) 845-2590
Email: vkochar@jewel.tamu.edu

Rocky Kolb
Fermilab, Box 500
Batavia, Illinois 60510
USA
Email: rocky@rigoletto.fnal.gov

George V. Kraniotis
Texas A&M University
Physics Dept
College Station TX 77843-4242
TAMU 4242
USA
Tel: (979)-458 2169
Fax: (979)-845 2590
Email: kraniotis@physics.tamu.edu

Irina Vladimirovna Krivosheina
Max-Planck-Institut für Kernphysik
Saupfercheckweg 1
D-69117 Heidelberg
GERMANY
and Radiophysical Research Institute
ul. Bolshaja-Pecherskaja 25
603005, Nishnij-Novgorod
RUSSIA
Tel: +49-(0)6221-516-262
Fax: +49-(0)6221-516-540
Email: irina.krivosheina@mpi-hd.mpg.de

Alexander Kusenko
Department of Physics & Astronomy
University of California
Los Angeles, CA 90095-1547
USA
Tel: 310-825-3440
Fax: 310-206-5668
Email: kusenko@ucla.edu

Eric V. Linder
1 Cyclotron Rd
MS 50R5008
Berkeley Laboratory
Berkeley, CA 94709
USA
Tel: +1 510 486 5568
Fax: +1 510 486 6738
Email: evlinder@lbl.gov

Rafael Lopez-Mobilia
Department of Physics
and Astronomy
University of Texas
at San Antonio
San Antonio, TX 78249
USA
Email: rmobilia@utsa.edu

Lee C. Loveridge
UCLA Physics Department
Box 951547
Los Angeles
CA 90095-1547
USA
Tel: 310-923-6245
Fax: 310-206-5668
Email: leecl@physics.ucla.edu

Roland Lüscher
Rutherford Appleton Laboratory
Chilton
Didcot
OX11 0QX
UK
Tel: +44/(0)1235 44 6139
Tel: +44/(0)1235 44 5702
Fax: +44/(0)1235 44 6733
Email: r.luscher@rl.ac.uk

Antonio Masiero
Dipartimento di Fisica "G. Galilei"
Università di Padova
Via Marzolo, 8
35131 Padova
ITALY
Tel: +39-0498277183
Fax: +39-0498277112
Email: antonio.masiero@pd.infn.it

Peter McIntyre
Department of Physics
Texas A&M University
College Station, TX 77807
USA
Tel: (979)845-7727
Email:
p-mcintyre@physics.tamu.edu

Chikaori Mitsuda
Kamioka Observatory, ICRR
University of Tokyo
Higashi-Mozumi, Gifu 506-1205
JAPAN
Tel: +81-578-5-9642
Fax: +81-578-5-2121
Email: mitsuda@suketto.icrr.u-tokyo.ac.jp

Dante Nakazawa
Department of Physics
The Enrico Fermi Institute
University of Chicago
5640 S. Ellis Ave., LASR 214
Chicago, IL 60637
USA
Tel: 1-773-702-5014
Fax: 1-773-834 8279
Email: nakazawa@uchicago.edu

Dimitri V. Nanopoulos
Texas A&M University
College Station
TX 77843-4242
USA
Tel: TAMU: 979 845-7790
Fax: 979 845-2590
Tel: HARC: 281 363-7955
Fax: 281 364-6052
Email: dimitri@physics.tamu.edu

Pran Nath
Department of Physics
Northeastern University
Boston, MA, 02115
USA
Tel: +617-373-4669
Fax: +617-373-2943
Email: nath@neu.edu or
nath@curie.physics.neu.edu

Margarida Nesbitt Rebelo
Department de Fisica
Instituto Superior Tecnico
Av. Rovisco Pais
P-1049-001 Lisboa
PORTUGAL
Tel: + 351 -21 8419010
Fax: + 351 - 21 841 9143
Email: rebelo@alfa.ist.utl.pt
Margarida.Rebelo@cern.ch

Adam G. Riess
Space Telescope Science Institute
3700 San Martin Drive
Baltimore, MD 21218
USA
Email: ariess@stsci.edu

Leszek Roszkowski
Astro-Particle Theory
and Cosmology Group
Dept. of Physics and Astronomy
University of Sheffield
Sheffield S3 7RH
ENGLAND
Tel: +44(0)114-222-35-80
Fax: +44(0)114-272-80-79
Email: l.roszkowski@shef.ac.uk

Richard W. Schnee
Department of Physics
Case Western Reserve University
10900 Euclid Ave.
Cleveland, OH 44106-7079
U.S.A.
Tel: (216)-368-3009
Fax: (216)-368-4671
Email: schnee@casino.PHYS.cwru.edu

Kris Sigurdson
California Institute of Technology
Mail Code 130-33
1200 East California Boulevard
Pasadena, California 91125
USA
Fax: 626-796-5675
Email: ksigurds@tapir.caltech.edu

Neil Spooner
University of Sheffield
Department of Physics & Astronomy
Hicks Building
Hounsfield Road
Sheffield, S3 7RH
UNITED KINGDOM
Email: N.Spooner@sheffield.ac.uk

Anatoly A. Svidzinsky
Department of Physics
Institute for Quantum Studies
Texas A&M University
TX 77843-4242, USA
Tel: +1-011-979-845-5644
Email: asvid@jewel.tamu.edu

Atsushi Takeda
Cosmic-Ray Group
Department of Physics
Faculty of Science, Kyoto University
Kitashirakawa, Sakyo-ku
Kyoto 606-8502
JAPAN
Tel: 81-75-753-3868
Fax: 81-75-753-3799
Email: takeda@cr.scphys.kyoto-u.ac.jp
takeda@suketto.icrr.u-tokyo.ac.jp

John D. Vergados
Theoretical Physics Division
University of Ioannina
Gr 451 10, Ioannina
GREECE
Email: vergados@cc.uoi.gr

Alexey Vikhlinin
Space Research Institute
84/32 Profsoyuznaya
Moscow, 117997
RUSSIA
Tel: 7-095-333-3377
Fax: 7-095-333-5377
Email: alexey@hea.iki.rssi.ru
and Harvard-Smithsonian Center
for Astrophysics, 60 Garden St.
Cambridge MA, 02138, USA
Tel: 1-617-495-7044
Fax: 1-617-495-7356
Email: avikhlinin@cfa.harvard.edu

Hanguo Wang
Department of Physics & Astronomy
University of California
at Los Angeles
475 Portola Plaza
Los Angeles, CA 90095-14757
U.S.A.
Tel: +1-310-206-3656
Fax: +1-310-206-1091
Email: wangh@physics.ucla.edu

Robert C. Webb
Texas A&M University
Physics Department
4242 TAMU, College Station
TX 77843-4242, USA
Tel: 979-845-4012
Fax: 979-845-2590
Email: webb@physics.tamu.edu

James T. White
Department of Physics
Texas A&M University
College Station
TX 77843-4242
USA
Email: white@physics.tamu.edu

Author Index